

Conference Proceedings

2nd INTERNATIONAL CONFERENCE

ON

RECENT ADVANCES IN MATERIAL SCIENCE
AND NANOTECHNOLOGY

Volume 9, Issue 13, May-June-2022

SOUVENIR



RAMAN 2022

12th - 14th May 2022



Organized by

Department of Physics

G. S. Tompe Arts, Commerce & Science College,

Chandur Bazar

In Collaboration with

I.Q.A.C.,

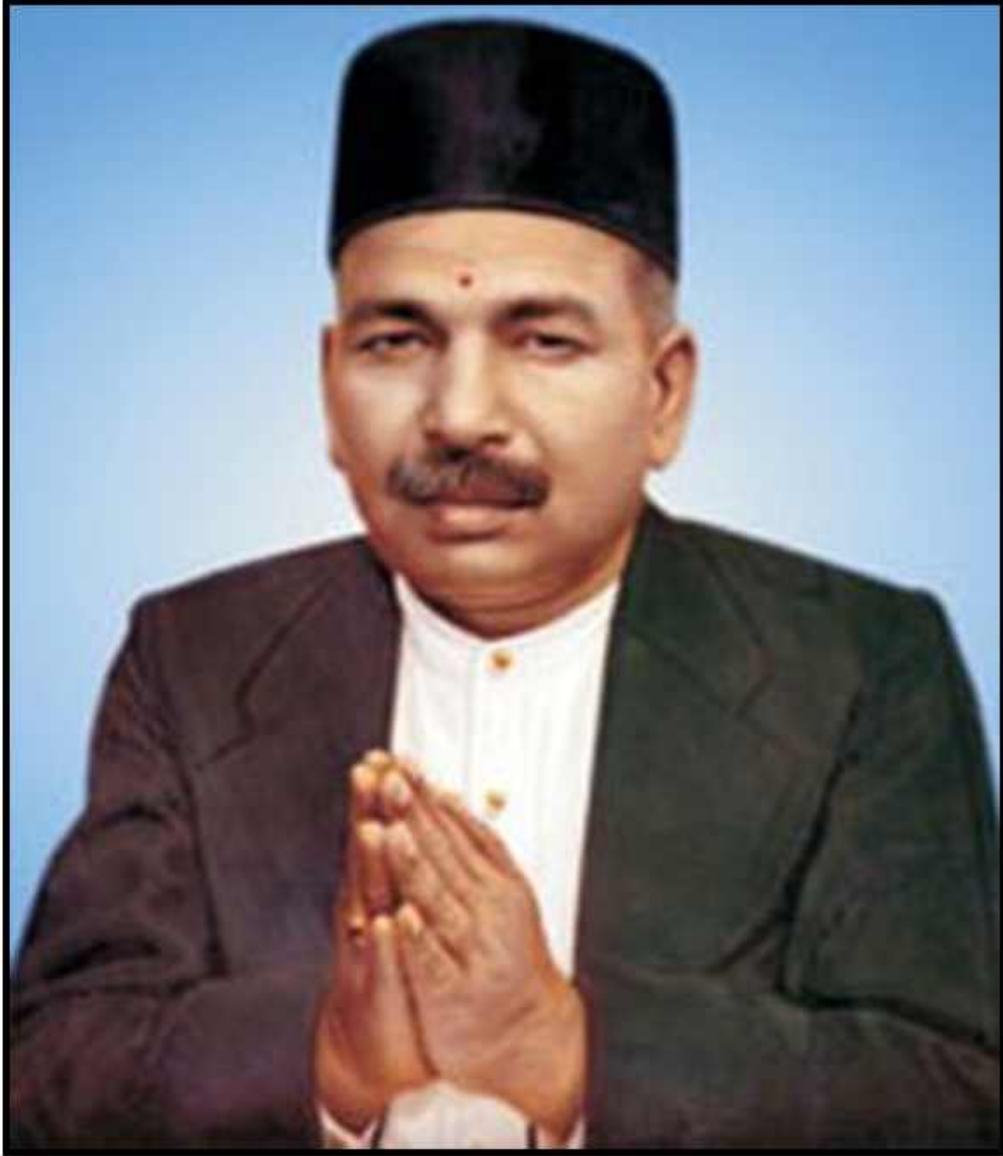
Sant Gadge Baba Amravati University, Amravati. (M. S.)

In Association with

International Journal of Scientific Research in Science and Technology

Online ISSN : 2395-602X | Print ISSN : 2395-6011

OUR INSPIRATION



Late. Shri. Govindrao Sitaramji Tompe

Founder

G.S. Tompe Mahavidyalaya, Chandur Bazar

Conference Proceedings

2ND INTERNATIONAL CONFERENCE

**RECENT ADVANCES IN MATERIAL SCIENCE
AND NANOTECHNOLOGY**

RAMAN 2022

Organized by

Department of Physics

G. S. Tompe Arts, Commerce & Science College, Chandur Bazar

In Collaboration with

I.Q.A.C.,

Sant Gadge baba Amravati University

● Editors ●

Dr. P. S. Deole
Dr. D. R. Bijwe
Prof. M. N. Pawar
Dr. A. V. Rajgure
Dr. P. P. Chaudhary

● Publisher ●

Dr. R. S. Ramteke

Principal

G. S. Tompe Arts, Commerce
& Science College,
Chandur Bazar, Dist.- Amravati (M. S.)

● Date of Publication : 12th May 2022 ●

About the College

G. S. Tompe Arts, Commerce and Science College, is one of the oldest colleges of the Amravati district having completed its 50th years in 2018. The college was established in 1968 by Late Govindraoji Sitaramji Tompe, a renowned philanthropist of his time. His schooling cannot be traced out and perhaps this might be the reason which grieved him too much and consequently motivated him to provide the higher education to the students of adjacent area, the education which he himself could not get and remained thirsty all through his life and kept on yearning in desire to gain it.

Nevertheless, the vision that he possessed cannot tag him as an illiterate person, rather he may be called an unschooled person having great vision and mission of life.

G. S. Tompe Arts, Commerce and Science College is located in Chandur Bazar which is a taluka place surrounded by the rural area. The tribal area called 'Melghat', known for its 'Tiger Reserve Project' is near from it. The college is affiliated to Sant Gadge Baba Amravati University, Amravati. The College is on the forefront of the town and Amravati-Chandur Bazar highway passes right from its main gate. Its taluka place in Amravati district. It deserves special mention that the area is known for the orchards of Orange.

The college falls in the category of co-education (grant-in-aid) and every year in an average 2000 students are admitted for various academic pursuits. As far senior section of the college is concerned, almost 1800 students are accommodated in the various streams and programmes offered by the college. To carry out all the functioning of the college, almost 100 teaching and non-teaching staff has been striving tirelessly since its establishment and the college has been continuously trying to ascend its progress graph having no feeling of satiety.

Conference Structure

Conference will have key note speaker, Plenary talks, Invited talks and Oral Presentations. Hardcopy of the certificate will be posted on the institutional registered address of the participants

Background Recent Advances in Material Science and Nanotechnology has borne fruit in bringing together young and dynamic researchers, academicians and industrialists to explore ,their knowledge and novel ideas to improve the concepts in this vital multidisciplinary area of research for economic growth and sustainable development of the society. 'RAMAN-2022' is timely need to produce many need-based products in different industrial sectors.

The conference aims to provide open discussion forum through e-platform and bringing together academicians, young scientists, researchers and technologists to meet the global demand of novel materials and challenges in the field of Material Science and Nanotechnology. Outstanding Academic Excellence Award Applications are invited for 'Outstanding Academic Excellence Award' along with the following documents Photocopy of PhD degree obtained Teaching and research experience Publication details (Papers, Books, etc) Awards at National/International level Talk delivered/Chaired session in National/International conferences PhD awarded under supervision

Conference Topics

- * Nanomaterials and Application
- * Nanoscience and Nanotechnology
- * Material Science
- * Ultrasonic and Acoustics Liquid Dielectric
- * Thin Film and Polymers
- * Semiconductor Materials and Devices
- * Ceramic Advanced Smart Materials
- * Chemical Materials and its Characterization
- * Bio-materials and Biosensors
- * Cosmetic Materials
- * Ultrasonic Transducer Materials
- * Non-destructive Testing and Evaluation
- * Nanobiophysics
- * Mathematical Physics
- * Green Chemistry

RAMAN 2022

2ND INTERNATIONAL CONFERENCE

RECENT ADVANCES IN MATERIAL SCIENCE
AND NANOTECHNOLOGY

RAMAN 2022

Organized by
Department of Physics
G. S. Tompe Arts, Commerce & Science College, Chandur Bazar
In Collaboration with
I.Q.A.C.,
Sant Gadge baba Amravati University

• Patron •



Hon. Mr. Keshavdada Tompe
Chairman, G. S. Tompe Mahavidyalaya
Sarvajanic Trust's, Chandur Bazar

• Co-Patron •



Hon. Mr. Bhaskardada K. Tompe
Secretary, G. S. Tompe Mahavidyalaya
Sarvajanic Trust's, Chandur Bazar



Dr. Vijay K. Tompe
Member, G. S. Tompe Mahavidyalaya
Sarvajanic Trust's, Chandur Bazar

• Chairman •



Dr. R. S. Ramteke
Principal
G. S. Tompe Mahavidyalaya

• Chairman •



Prof. Dr. S. A. Waghuley
Director, IQAC SGBAU, Amravati

• Convener •



Dr. D. R. Bijwe
Dept. of Physics
G. S. Tompe Mahavidyalaya

• Org. Secretary •



Dr. P. S. Deole
HOD Dept. of Physics
G. S. Tompe Mahavidyalaya

Co-Convener



Dr. A. V. Rajgure
Dept. of Physics
G. S. Tompe Mahavidyalaya



Ms. M.N Pawar
Dept. of Physics
G. S. Tompe Mahavidyalaya



Dr. A. R. Bansod
Dept. of Physics
Dr. Ambedkar College Nagpur



Dr. U. P. Manik
Dept. of Physics
Sardar Patel Mahavidyalaya,
Chandrapur



MESSAGE

Hon'ble Bhaskardada Tompe

Secretary,

G. S. Tompe Mahavidyalaya Sarvajanik Trust's,
Chandur Bazar

It gives me great pleasure that the Department of Physics of our College is organizing a DST-SERB sponsored three days 2nd International Conference on "Recent Advances in Material Science and Nanotechnology" during May 12-14, 2022 in collaboration with I.Q.A.C., Sant Gadge Baba Amravati University, Amravati.

I am sure that this international conference will share latest path breaking developments in the field from eminent scientist to new researchers and promote research regarding advanced technologies in material science.

I take this opportunity to appreciate the efforts of organizers and in particular congratulate the faculty members of Physics Department for organizing such an important conference.

I wish a grand success to this International conference.

Mr. Bhaskardada Tompe

Secretary

G. S. Tompe Mahavidyalaya Sarvajanik Trusts
Chandur Bazar

PROF. DR. DILEEP N. MALKHEDE

M.E., Ph.D.

VICE-CHANCELLOR



SANT GADGE BABA
AMRAVATI UNIVERSITY
AMRAVATI - 444 602
MAHARASHTRA (INDIA)



MESSAGE

I am delighted to know that, G. S. Tompe Arts, Commerce & Science College, Chandur Bazar and I.Q.A.C., Sant Gadge Baba Amravati University, Amravati is jointly organizing "2nd International Conference on "Recent Advances in Material Science and Nanotechnology (RAMAN - 2022)" on 12th to 14th May, 2022.

As the conglomeration of eminent personalities like Sr. Research Scientists & Academicians would deliberate on various important themes of the Conference I believe, it will help to enhance recent trends in science & nanotechnology. This conference will also strengthen capabilities of all the participants and promote them towards the future advancement of research.

I extend my warm greetings to the Principal, editorial board and student contributors to keep the good work. I wish them all a magnificent success.

(Dr. Dileep Malkhede)

Dr. Rajendra Ramteke
Principal,
G. S. Tompe Arts, Commerce &
Science College,
Chandur Bazar, Distt. Amravati

MESSAGE



It gives me an immense pleasure to know that G. S. Tompe Arts, Commerce & Science College is going to organize an International Conference on "Recent Advances in Material Science and Nanotechnology (RAMAN-2022)" during May 12-14, 2022.

Nanotechnology and its microscopic universe do offer enormous possibilities for contemporary science and industry. Nanotechnology and nanomaterials can be applied in all kinds of industrial sectors. They are usually found in these areas including but not limited to electronics, energy, biomedicine, environment, food, textile, etc. However, the environmental, health and safety risks of nanotechnology and concerns related to its commercialisation should be addressed scrupulously and properly.

I do believe that this conference will be able to provide an excellent opportunity to the researchers related with the subject with a view to congregate at one place and exchange their outcome of research and expertise, as envisaged by the organizers of the conference.

I congratulate the college on this occasion and wish the organizers a grand success with the hope that their endeavour will definitely help address the challenging issues in contemporary material sciences nanotechnology, so that new benchmarks would be established in near future.

Dr. S. V. Dudul,

I/C Dean,
Faculty of Science and Technology,
Sant Gadge Baba Amravati University,
Amravati



MESSAGE

It gives me immense pleasure to know that Department of Physics of G.S. Tompe Arts, Commerce & Science College of Chandur bazar in collaboration with I.Q.A.C. of Sant Gadge Baba Amravati University, Amravati. is organizing 02nd International conference on Recent Advances in Material Science and Nanotechnology from 12th May 2022 to 14th May 2022.

It is also a matter of pride that a souvenir is being released on this notable occasion. This conference will witness Researchers, academicians and eminent experts working in different field of material science and nanotechnology. A collaborative link between likeminded people across the globe will encourage acquiring novel knowledge in the field of nanotechnology. I am very confident that this conference will prove to be prolific and will substantiate the chosen topics.

It is certainly commendable effort of G.S. Tompe College to organize such a conference on such an extensive scale with experts and participants across the globe.

I extend my best wishes for the success of the conference and for publication of the souvenir.

Dr. S.S.Yawale

Director
Pre-IAS Training Centre, Amravati.

प्रो० देवराज सिंह

निदेशक

प्रो०राजेन्द्र सिंह (रज्जू भइया) भौतिकीय विज्ञान

अध्ययन एवम् शोध संस्थान

Prof. Devraj Singh

Director

Prof. Rajendra Singh (RajjuBhaiya) Institute
of Physical Sciences for Study and Research



वीर बहादुर सिंह पूर्वाञ्चल विश्वविद्यालय,

जौनपुर- 222003 (उ. प्र.)

Veer Bahadur Singh Purvanchal University,

Jaunpur 222003 (U.P.)

E-Mail.:devraj2001@gmail.com

Mob.: +91-9810549461

02 MAY 2022

Message

I feel happy to know that G.S. Tompe Arts, Commerce & Science College, Chandur Bazar is organizing “Second International Conference on Recent Advances in Materials Science & Nanotechnology (RAMAN-2022)” in association with IQAC Cell, Sant Gadge Baba Amravati University during 12th-14th May, 2022. To mark the occasion a souvenir is also being released.

The conference will witness the participation from research scholar, professors and scientists working in different fields of materials science & nanotechnology. A common platform will encourage gaining the new insight in the field of materials science & nanotechnology.

I strongly believe that the conference will result in actual output in the support of its topics.

I hope that the entire participants will enjoy this academic fest.

I wish all the success for the conference.

Devraj Singh

02/05/2022

(Prof. Devraj Singh)

Prof. (Dr.) Devraj Singh

Professor & Head, Department of Physics,

Director, Prof. Rajendra Singh (Rajju Bhaiya)

Institute of Physical Sciences for Study & Research,

Veer Bahadur Singh Purvanchal University,

Jaunpur-222003, U.P., India



Phone : 011-26131577 - 78, 80
011-29581000
Website : www.aicte-india.org

Dr. Shrishail Kamble
Assistant Director



सत्यमेव जयते

अखिल भारतीय तकनीकी शिक्षा परिषद्
(भारत सरकार का एक सांविधिक निकाय)
(मानव संसाधन विकास मंत्रालय, भारत सरकार)
नेल्सन मंडेला मार्ग, वसंत कुंज, नई दिल्ली-110070

ALL INDIA COUNCIL FOR TECHNICAL EDUCATION
(A Statutory Body of the Govt. of India)
(Ministry of Human Resource Development, Govt. of India)
Nelson Mandela Marg, Vasant Kunj, New Delhi-110070

28-04-2022

Greetings,

I am delighted to express my BEST WISHES to the organizing team of 2nd International Conference on Recent Advances in Material Science and Nanotechnology. May this conference be characterized by fruitful scientific discussions and lead to the betterment of society. I'm sure that your conference will be a great success considering the effort organizing team putting in this event in quality and diversity in the speakers.

My best wishes are to the Convenor, the staff, and everyone else connected with 2nd International Conference on Recent Advances in Material Science and Nanotechnology for a successful "RAMAN 2022".

S.P.K.
28/04/22
Dr. Shrishail Kamble



From the Principal's Desk



It is a moment of pride for me to host this International conference. I warmly welcome to all the dignitaries, scientist, delegates and students participating in three days 2nd International conference on "Recent Advances in Material Science and Nanotechnology" hosted by the college. The college established in the year 1967-68 is affiliated to Sant Gadge Baba Amravati University, Amravati and accredited by NAAC with B+ grade. The college offers Arts, Commerce & Science with B. Sc., M. Sc., B. A., M. A., B. Com., M. Com. and recently started three years degree course in B. Voc.

The event is focused on the Recent Advances in Material Science and Nanotechnology. The conference aims to provide common platform for researcher, academicians etc for the exchange of ideas , experience relevant to the various themes. I am sure that the themes and contents of the event will be beneficial for the society.

Finally I would like to express our sincere gratitude towards G. S. Tompe Mahavidyalaya Sarvajanic Trusts, Department of Science and Technology, New Delhi, Sant Gadge Baba Amravati University, Amravati and the sponsors who have whole heartedly extended their kind support for the successful organization of the conference.

I am very glad that the Department of Physics has taken the much needed initiatives of organizing the conference of this stature and I wish them all success in their tireless endeavor.

Dr. R. S. Ramteke

Chairman, RAMAN-2022

Principal

G. S. Tompe Arts, Commerce & Science College,
Chandur Bazar

From the desk of Chairman RAMAN-2022



On behalf of the Organizing Committee, it is a great pleasure for me to welcome all the Eminent Scientist and Researchers, Academicians, Patrons, Principals and Advisers to "Second International Conference on Recent Advances in Material Science and Nanotechnology" (RAMAN-2022). The RAMAN Conference series is held in various places of India and this time G.S. Tompe Arts, Commerce and Science College, Chandur Bazar has the honor to organize this prestigious event.

The aim of the Conference is to provide a forum for delegates from the industry, research labs and academia to exchange ideas and presenting their research works. In addition, it is an ideal venue for interactions and for them to establish the all-important contacts with each other.

This is a momentous and remarkable occasion in moulding our thoughts towards the applications of Physics/Materials Science to the society with innovative materials and nano-devices. The Key-note lectures, Plenary talks, Invited talks and Paper presentations of stalwarts will open up a new vista of knowledge before blooming researchers and scientists.

The staff of Sant Gadge Baba Amravati University has indeed contributed its' mite towards ensuring its success. I am also grateful to the Department of Physics, G.S. Tompe Arts, Commerce & Science College, Chandur Bazar and Sponsors for their collaboration and liberal support.

I am extremely grateful to Hon'ble Vice Chancellor Prof. (Dr.) Dileep N. Malkhede and other authorities whose enthusiasm and excellent support has given us great strength and encouragement for this important international event.

Finally, I would like to thank everybody involved in the organization of this event. I wish all the participants a very successful Conference with fruitful discussions and a memorable stay during the conference.

Looking forward to the international conference and welcoming you all once again.

Best wishes.



Prof. (Dr.) Sandeep A. Waghuley

Director, IQAC

Dept. of Physics,

Sant Gadge Baba Amravati University, Amravati.



MESSAGE

I welcome you to 2022 RAMAN 2nd International Conference on Recent Advances in Material Science and Nanotechnology being held at G. S. Tompe Arts, Commerce and Science College, Chandur Bazar, India during May 12-14, 2022.

This conference was planned by Prof Dr Devraj Singh and Dr V B Pawade, Founders of RAMAN Conference Series under the guidance and valuable suggestions by the esteemed members of Executive Council. First, I wish to thank all the members of Executive council and members of International and National advisory committees of RAMAN-2022 who have endeavoured to establish the conference.

The RAMAN-2022 is hosted by the Department of Physics, G. S. Tompe Arts, Commerce and Science College, Chandur Bazar and IQAC, SGB Amravati University, Amravati. Principal Dr R S Ramteke and Prof Dr S A Waghuley, Conference Chair, Dr D R Bijwe, Convener, Dr P S Deole, Organizing Secretary, Co-conveners and chairs of various committees are working hard to make the RAMAN-2022 succeed.

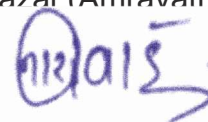
I hope the RAMAN-2022 will provide a unique opportunity for the teachers, educators, experts and scholars of higher education from all over the world to convene and share novel ideas on the field and trends in higher education development. Further, the RAMAN-2022 is organized with an aim, to exchange new thoughts and share the latest knowledge in field of material science and Nanotechnology by the eminent experts and to motivate budding Scientist and young researchers. I trust all the participants and delegates would be with some value addition to their current knowledge after attending the conference.

The RAMAN-2022 will be endorsed by a strong scientific and technical program and by the attendance of academicians, scientists, researchers and delegates from various countries. I believe that it is very important for us to discuss interesting topics and exchange ideas. The RAMAN Conference Series will be continued to stimulate and inspire the researchers.

I would like to give special thanks to G. S. Tompe Mahavidyalaya Sarvajanic Trust's, Chandur Bazar, DST-SERB, New Delhi and all organizational sponsors of the RAMAN-2022.

I wish the RAMAN-2022 will be an enjoyable, memorable and productive for the participants. I believe all delegates will benefit substantially from the conference through the presentations of expert speakers and exchange of ideas with one another.

I hope you have an enjoyable stay at the RAMAN-2022 in Chandur Bazar (Amravati), India and I'm looking forward to seeing you there.



Dr. N. R. Pawar

Founder
RAMAN Conference Series



From the Convener's Desk

It is my great privilege to welcome you all to the 2nd International Conference on "Recent Advances in Material Science and Nanotechnology" being organized by the Department of Physics, G. S. Tompe Arts, Commerce & Science College, Chandur Bazar, Dist.- Amravati . In Collaboration with I.Q.A.C., Sant Gadge Baba Amravati University, Amravati. It is a matter of great pleasure for me to present a souvenir on the occasion of the International Conference. It's a collection of abstracts of accepted research papers from various learned scholars and faculties.

This conference has been a meeting place for researchers, academicians, scientist in various branches of Physics and Chemistry to come together and exchange ideas and understand one another. It is a golden opportunity for young researchers to participate in the conference. The founts of our inspiration are Hon'ble Mr. Keshavdada Tompe, President, Hon'ble Mr. Bhaskardada Tompe, Secretary and Hon'ble Dr. Vijay K. Tompe, Member of G. S. Tompe Mahavidyalay Sarvajanic Trust's. I am deeply indebted to our dynamic principal Dr. R. S. Ramteke for valuable suggestions, constant support and encouragement. I must acknowledge the keen interest and remarkable co-operation of Advisory committee member. Their support and motivation always boost us throughout this mammoth task.

It is truly said for every success there is some one behind it. It is the support of delegates from various organizations for this conference. We have been blessed by receiving the message from Hon'ble Vice-Chancellor Dr. Dilip Malkhede sir, , S. G. B. A.U. Amravati and Dr. S. S. Yawale madam, Director Pre-IAS Academy, Amravati for their cooperation in this souvenir. I am extremely grateful to Prof. Vladimir V. Petrov and Dr. Luca Pellegrino for accepting our invitation for the talk. The staff of entire college has indeed taken pains ensuring the success of conference, it cannot be successful being one. I am grateful to the management of our Institute for financial and liberal support.

The organizing committee is indebted to keynote and invited speakers for their kind consent, providing summary of their research contribution and sharing their knowledge for growth of material science in India. I am also thankful to all the learned participants for their overwhelming response. Thanks are also due to our International, National and Local advisory committee for their thought provoking interventions and suggestions. The financial assistance provided by DST-SERB, New Delhi, Sant Gadge Baba Amravati University, Amravati are also gratefully acknowledged. My deep sense of appreciation and thanks to advertisement or sponsorship.

I must acknowledge the strong and active support received from Dr. P. S. Deole, organizing secretary, Dr. A. V. Rajgure, Prof. M. N. Pawar & Dr. A. R. Bansod Co-convener of the conference. This event would not have been possible without the relentless efforts of all my colleagues, non-teaching staff, P. G. students and members of organizing committee. I thank them all from the core of my heart. I also extend my sincere thank to Vikasdada Satpute and Mr. Shekhar for souvenir & other printing in stipulated span of time.

Last but not the least, I thank all the delegates, invited guests, audience for their presence and cooperation in the conference.

Dr. D. R. Bijwe
Convener, RAMAN-2022

MESSAGE

I am pleased to bring the book of Abstract of Research Paper of the three days DST-SERB, New Delhi Sponsored 2nd International Conference on 'Recent Advances in Material Science and Nanotechnology (Raman 2022)' on behalf of G. S. Tompe Arts, Commerce and Science College Chandur Bazar, Amravati, Maharashtra. it is my honour to Welcome the eminent personalities of various nationally recognized Departments and Institutes to the Conference.

Raman 2022 serves as Global platform for various form of knowledge sharing irrespective of differences in time and geography. This conference serve as an excellent forum to explore the innovative research in Physics particular and general science specifically. I express my sense of gratitude to Honorable Shri. Keshavdada Tompe, President, G. S .Tompe Sarvjanik Trust, Chandur Bazar, Amravati whose blessings are always with us and it is their support that always strengthen us and his words motivate us to conduct various conference and programs in our college.

I am thankful to Honorable Shri. Bhaskardada Tompe, Secretary, G. S . Tompe Sarvjanik Trust, Chandur Bazar, Amravati whose dynamic leadership and consistent support have provided us inspiration to organise this conference.

I sincerely thank to the Principal of our college Dr. R. S. Ramteke for his support, motivation and encouragement without which this event could not have been organised. I am grateful to all resource persons and eminent personalities of the conference.

I extend my regards to the members of international Advisory Committee, National Advisory Committee, Members of local Organising Committee, Researchers, Participants & Students for their kind co- operation and encouragement. I am thankful to teaching and non- teaching staff of our college who burn the Midnight oil for the success of this event.

I am thankful to those who have contributed directly or indirectly to make this event extremely successful.

Dr. Priya S. Deole

Organising Secretary & Head, Dept. of Physics

RAMAN 2022



MESSAGE

It is a great privilege for us to welcome you all at the outset of the Abstract book of the three days DST-SERB, New Delhi Sponsored 2nd International conference on Recent advances in material science and nanotechnology (Raman 2022)

The world has witnessed the rapid advancement in the field of Science & Technology. This Conference aims at providing a forum for Scientists, Researchers, academicians,, industry executives and other Professionals to discuss the recent advancement and share Knowledge .

In fact substantial result impartation is possible only through collective vision and collaborative approach there fore this is one such attempt to move in this direction.

Our college with proactive support and guidance from management is taking number of initiative to improve the quality of education. We extend our sincere thanks to our petron honorable Keshav Dada Tompe, President, G.S. Tompe Sarvjanik Trust Chandur Bazar Amravati for his whole hearted support to this conference.

We are also thankful to honorable Bhaskardada Tompe, secretary G.S . Tompe sarvjanik Trust, Chandur Bazar, Amravati, for their constant and generous support & encouragement in this respect.

We are also thankful to the eminent members of the advisory Committee members. We sincerely thank to the principal of our college Dr R.S Ramteke for their precious guidance for organizing this event.

Our thanks to teaching and non teaching staff members of our college for their whole hearted co- operation for the success of this event. Last but not least , We thank all the resource persons, invited Guests , delegates for their active & enthusiastic response.

Dr. Ashutosh V. Rajgure & Miss. Manjusha N. Pawar
Dept. Of Physics & Co- Convenor of Raman 2022.

CONTENTS

<i>Sr. No</i>	<i>Article/Paper</i>	<i>Page No</i>
1	Simulation of Linear Array Transducer with Center Frequency 10 MHz Dr. S. A. Rodge, S. K. Shelke, Dr. S. A. Ghogare, V. G. Gabhane, H. E Salve	01-07
2	Physico-Chemical, Spectroscopic Characterization and Adsorption Study of Prepared Activated Carbon from Limonia Acidissima Vaishali A. Shirbhate, Deepali P. Gulwade	08-17
3	Synthesis and Experimental Studies of Heterocyclic Chalcone Gotmare P. A., Ingle G. B, Dr. Kolhe S. V	18-22
4	To Study the Adsorption Behaviour of Cobalt (II) Metal Ions from Aqueous Solution Using Low-Cost Adsorbent A. K. Wanjari, U. E. Chaudhari, R.S. Talegaonkar	23-26
5	A Comparative Dielectric Study of Methanol-Water and Glycerol-Water Mixtures Using TDR Bharose N .A., Chavan S.D., Kumbharkhane A. C.	27-31
6	Chalcone: Synthesis and Experimental Study of New Promising Medicinal Compound Ingle G. B., Gotmare P. A., Dr.Kolhe S. V.	32-37
7	Study of Structural and Magnetic Properties of Bi Substituted Nickel Spinel Ferrites D. D. Mathankar, N. S. Meshram, K. G. Rewatkar	38-43
8	Morphological and Structural Characterization of Polyaniline Doped Cadmium Telluride Nanocomposite Pritesh J. Jadhao, Kamlesh R. Banarse, S. P. Yawale, S. S. Yawale	44-47
9	The Crystallization Behaviour of Silver Doped Lead Borate Dr. M. A. Giri	48-51
10	Formulation and Development of Skin Cleansing Gel with Self Exfoliation K. S. Misar, A. A. Paranjape, K. S. Tiwari, M. P. Bokde	52-58
11	Formulation and Development of Two-Phase Facial Cleansing System K. Misar, R. Gajbhiye, A. Thakker, M. Taywade	59-65

12	Formulation, Development and Evaluation of Self Foaming No Rinse Body Wash K. S. Misar, S. A. Bhankhede	66-71
13	Molecular Interaction Study through Molar Volume, Available Volume and Free Volume for Ternary Liquid Mixture of Alcohol + Tri-Ethylamine + Acetic Acid P J Thakare	72-75
14	Synthesis of Silver Nanoparticle Material Using Plant Parkia Biglodulosa S. V. Narsing, S. E. Bhandarkar, B.P Khobragade, V. A. Shirbhate	76-78
15	In-Vitro Selection of Salt Tolerant Tomato Plant (Lycopersicon Esculentum Mill) V. Y. Charjan, B. Abraham, P. J. Ninawe	79-86
16	Evaluation of Biological Activities of Nanocrystalline Tetragonal Zirconia Synthesized Via Sol-Gel Method V. G. Thakare, P. A. Wadegaokar	87-91
17	Microwave Assisted Synthesis and Biological Evaluation of Pyrazoline Derivatives A. R. Bijwe, B. P. Khobragade, S. E. Bhandarkar	92-95
18	Study of the Optical Constants of the Polymer Blends R Y Bakale, Y G Bakale, Y S Tamgadge, R P Ganorkar, S V Khangar, A B Patil	96-101
19	Synthesis and Photoluminescence Studies of UV emitting Mg₂P₂O₇: Gd Phosphor R. S. Khan, M. A. Wani, S. D. Sawarkar, M. V. Talan, Z. S. Khan	102-106
20	Study of Structural, Magnetic and Dielectric Properties of Calcium Substituted Ni Ferrites S. N. Kachhwah, Y. D. Choudhari, K. G. Rewatkar	107-116
21	Fabrication and Characterization of Co Modified SmFeO₃ Thick Film R. B. Mankar, V. D. Kapse	117-122
22	Aurone : A Comprehensive Review on Synthesis and Physical Properties of the Interesting Natural and Emerging Synthetic Compound Chaware T. S., Pinjarkar A.P., Ingle G.B., Dr. Kolhe S. V.	123-127
23	To Study the Potency Of Newly Synthesized Substituted Thiocarbamidonaphthol by Conductometrically Saleem Khan R. Khan, D. T. Tayade	128-131

24	Investigation of Structural, Magnetic, And Microwave Absorption Properties of Bi Supplemented Calcium Hexaferrite	132-138
	Y. D. Choudhari, P. J. Chaware, K. G. Rewatkar	
25	Synthesis and Characterization of LiBaB₉O₁₅ : Gd³⁺ Phosphor by Recrystallization Method	139-144
	N. D. Kherde, A. O. Chauhan, P. A. Nagpure, S. K. Omanwar	
26	Preliminary Phytochemical Screening of Medicinal Plants used in Cosmeceutical Formulation	145-151
	R. Gajbhiye, D. Wasule	
27	Trends in the Technology of Radar Absorbing Materials	152-158
	P. R. Thote, A. R. Bansod	
28	Organic Inorganic Metal Halide Perovskite Solar Cells	159-165
	S. K. Bhonge, A. R. Bansod	
29	Refractive Indices and Densities of Binary Mixtures of Benzene-Ethanol and Benzene-Acetone at Room Temperature	166-169
	M. P. Bhise, Javed Khan, N.D. Kapse, S. A. Athawale	
30	Physico Chemical Assessment of Soil Samples from Rama (Sahur) Region, Amravati District, Maharashtra (India)	170-174
	M. P. Bhise, S. A. Athawale, N. A. Junghare	
31	Process Optimization of Plant Based Silver Nanoparticle Synthesis using Response Surface Methodology	175-186
	Harsha Sonaye, Vidya Sabale	
32	Preparation and Structural Characterization of Polyaniline Doped Zinc Oxide Nanocomposite	187-191
	Kamlesh R. Banarse, Pritesh J. Jadhao, S. P. Yawale, S. S. Yawale, D. R. Bijwe	
33	Novel Synthesis of 2-3 Substituted Quinoxaline & Study of Its Physical Parameters	192-198
	Pinjarkar A. P, Chaware T. S, Dr. Kolhe S. V	
34	Viscometric Properties of Aqueoussodium Salt of L-Alanine	199-202
	M. B. Dhande, D. T. Tayade	
35	Effect of Sintering Temperature on Structural and Dielectric Properties of Lead Titanate	203-208
	A. U. Bajpeyee, N. V. Galande, S. H. Shamkuwar	
36	Proximate and Nutritional Analysis of Leaves of Gmelinaphillippensis Cham	209-214
	Nida S. Shaikh, Rahim S. Shaikh	

37	Analysis of Structure and Surface Morphology, Synthesis of Nickel Oxide Nanoparticles by Hydrothermal Method Sonu Patwa, Dr. Hemant Kumar Singh, Navin Chaurasiya, Sandip Kumar Singh, Deep Prakash Singh	215-220
38	Syntheses of Copper Oxide Nanoparticle by Hydrothermal Method and Its Structural & Surface Morphological Studies Harshen Yadav, Navin Chaurasiya, Hemant Kumar Singh, Deep Prakash Singh, Sandip Kumar Singh, Kumkum Kumari	221-227
39	Synthesis of Some Novel Heterocycles from Variously Substituted Chalcones by Microwave Irradiation and Their Medicinal Assay D. R. Deshmukh, Dr. R. D. Isankar	228-231
40	The Fourier Transform Infra-Red Spectroscopical Analysis of Andrographis Paniculata Plant Extracts R. P. Ganorkar, Y.S.Tamgadge, R. Y. Bakale	232-236
41	Synthesis and Thermal Properties of Copper Doped KNbO₃ Crystal A. R. Khobragade, A. R. Bansod	237-241
42	To Study the Impact of Concentration and Temperature on Intermolecular Interaction Between Dextrose and Electrolyte Solution Sandhya D. Pinge, Urvashi P. Manik, Paritosh L. Mishra	242-246
43	Synthesis and Physical Properties of Mn Doped KNbO₃ Crystal A. R. Khobragade, A. R. Bansod	247-250
44	Synthesis and Thermal Properties of Fe Doped KNbO₃ Crystal A. R. Khobragade, A. R. Bansod	251-256
45	The Divergence of the Laser Beam Emitted By This Segment Would Have Less Angle of Divergence Because the Plasma Has Less Thickness A. P. Pachkawade	257-261
46	Behaviour Investigated As Tunneling Behaviour of Electrolytic Solution Using DC Glow Discharge A. P. Pachkawade	262-266
47	Variation of Energy Band Gap in Composites of N-doped Titanium Dioxide for Preparation of Dye-sensitized Solar Cell Shivam Yadav, Rupali Patel, Vinita Dhulia	267-274
48	Electrical Properties of Lead Sulphide Amalgam under Influence of Aluminium Doping Deposited by Chemical Spray Pyrolysis S. G. Ibrahim, S. A. Waghuley	275-278

49	Thermodynamic and Viscometric Study of Aminopyrimidine Derivatives in 80% DMF-Water Solvent M M Mhasal	279-285
50	Green Synthesis of Iron Nanoparticles and Its Characterization Using Brassica Oleracea Var.Capitata Leaf Extract Shaikh Ruqqaiya, R.D. Isankar	286-288
51	Synthesis and Characterization of Some 2- (Substituted Thiocarbamido) Aminophenothiazine B. R. Deshmukh, R. D. Isankar	289-292
52	Thermal Decomposition Kinetics of VO (IV) and Zr (IV) Complexes of Hydrazone Schiff Bases Prashant R. Mandlik, Pallavi R. Deshmukh, Pratik K. Deshmukh	293-299
53	Study the pH of Different Water Samples in Amravati City Vaishnavi Pramod Gulhane, Kaiwalya Jwala Nagale	300-302
54	IOT Based Blood Glucose Measurement Using Optical Spectroscopy Nilima Jajoo, Dr. Gopaldas Agrahari, Dr. Deepak Dhote	303-308
55	Synthesis and Physico-Chemical Parameters of Thiazine Almas Farheen Khan, Dr. Kolhe S. V	309-312
56	Photo Degradation Study of LDPE/PEG Thin Film Dr. V. S. Sangawar, S. A. Umale, S. O. Sharma	313-319
57	Ultrasonic Velocity and Other Acoustical Parameters of Leaf Extract Solution of Psidiumgujavain Two Different Solvents: A Comparative Study S. S. Kamble, S. R. Aswale, S. S. Aswale	320-329
58	Synthesis of Substituted-4, 6-Diaryl-2-Imino-6h-2, 3-Dihydro-1, 3-Thiazine A. S. Dighade	330-335
59	Insight Details Of X-Ray Diffraction Analysis and Infrared Spectra of Polypyrrole Composites Decorated With TiO₂ and SnO₂ Metal Oxides Aditya V. Tiwari, A. P. Deshmukh, P. S. Awandkar, S. P. Tiwari, S. P. Yawale	336-343
60	Photoluminescence Properties of Cs₂Ba (MoO₄)₂: Eu³⁺ Red Emitting Phosphor A. S. Khobragade, B. V. Tupte, D.H. Gahane, S. V. Moharil	344-349
61	Ultrasonic Velocity, Adiabatic Compressibility, Intermolecular Free Length and Other Acoustical Parameters of Leaf Extract	350-356

	Solution of Cymbopogon Citratus	
	S. S. Kamble, S. R. Aswale, S. S. Aswale	
62	Synthesis and Optical Properties of Lanthanium Doped Nanocrystalline Tin Dioxide Thick Films	357-363
	L. P. Chikhale, F. I. Shaikh, A. V. Rajgure, S. S. Suryavanshi	
63	Synthesis and Structural Properties of Lanthanium Doped Tin Dioxide Nanocrystalline	364-369
	L. P. Chikhale, F. I. Shaikh, A. V. Rajgure, S. S. Suryavanshi	
64	Effect of Synthesis Temperature on Structural, Electrical and Optical Properties of Mn₃O₄ Thin Films	370-375
	K. S. Iqbal, M. S Dixit, A. U Ubale	
65	Synthesis of Some Substituted 4H-Chromene Derivatives by Using Nanostructured Doped Polyaniline as a Catalyst	376-382
	Sharad N. Pawar, Deepak M. Nagrik	
66	Synthesis of Substituted Triazine and Its Derivatives, with Their Study of Antimicrobial Activity	383-386
	Pratibha S. Deulkar, Ramkrushna P. Pawar	
67	Study of Molecular Interaction in Various Liquid Mixtures by Acoustical Technique : A Review	387-392
	Krishna Kumar Pandey, Shilpa Kundrakpam	
68	A Synthesis and Fluorescence Properties of Trivalent Europium Doped Yttrium Vanadate and YVO₄ : Eu³⁺ @SiO₂ for Biological Application	393-397
	R. G. Korpe, K. A. Koparkar, G. V. Korpe, S. K. Omanwar	
69	MgSe Thin Films Deposited By Successive Ionic Layer Adsorption and Reaction Method	398-401
	Kailas C. Shinde, Raghavendra J. Topare, Yogesh S. Sakhare	
70	To Study the Adsorption Efficiency of Pb (II) from Aqueous Solution Using Low-Cost Adsorbent	402-405
	Anil R. Somwanshi	
71	Photoluminescence Investigation Of Li₂Al₂Si₂(PO₄)₄ Eu³⁺ for WLEDs Lighting Applications	406-412
	R.G. Deshmukh, P. A Fartode	
72	Degradation Studies of UV Irradiated Polystyrene/ Polyisoprene Thin Films	413-420
	Dr. V. S. Sangawar, S. O. Sharma, S. A. Umale	

73	Refractometric Studies of 2,4,6-Triazin substituted thio-Carbamides In Dioxane-Water Systems P. V. Raut, K. P. Jumde, M. S. Lunge, D. T. Tayade	421-427
74	Preparation & PL Analytical Study of Red and Blue Emitting K₂CaPO₄ Phosphor for Lighting Industry G. R. Rahate, V. R. Panse, K. V. Sharma, N. S. Bajaj, Odi Martin Ntwaeaborwa	428-437
75	Synthesis and Photoluminescence Properties of ZnB₄O₇: Eu³⁺ Phosphor V. R. Kharabe	438-442
76	Application of Graphene Oxide - Cadmium Oxide Nano Composite as Photo Catalyst in Degradation of Nitro Benzene M. N. Zade, D. T. Tayade	443-447
77	Synthesis of 3- (4-Substituted Phenyl) 2- Chloractamide and Its Some Physical Aspects Miss. Raibole Shital, Dr. Kolhe S.V	448-451
78	Synthesis and Characterization of Copper Oxide (CuO) Doped Conducting Polymer Polyaniline M. N. Pawar, D.R. Blije, A. V. Rajgure, P. S. Deole, S. Kavitar, M. S. Khandekar	455-458
79	To Study the Potency Of Newly Synthesized Substituted Thiocarbamidonaphthol by Conductometrically Saleem Khan R. Khan, D. T. Tayade	459-462
80	pH Metric Studies of Some Substituted 2-Oxo-2H-Chromene-3-Carbohydrazone Derivatives at 0.1 M Ionic Strength at 52°C P. P. Choudhari, P. R. Yawale, S. S. Ubarhande, M. P. Wadekar	463-469
81	Structural Characterisation of Ppy/Rhodamine-B Dye Composites Synthesized by Simple Chemical Oxidation Method N. S. Dixit, M.S. Dixit, S. G. Khobragade, A. S. Dixit	470-473
82	Morphometric Analysis using Remote Sensing and GIS of Bahiram Ka Sand River (Pili River) Basin Amravati District, Maharashtra Akshay D. Ghatol, Pravin S. Parimal	474-479
83	Ionic Ratios of Groundwater in Northern part of Akola District, Maharashtra P. S. Parimal	480-484
84	Molar Concentration Dependent Capacitive Performance of Ultrasonic Spray Pyrolysed Ruthenium Oxide (RuO₂) Thin Films	485-489

	B. Y Fugare, A.V. Rajgure, G.T. Chavan, P. K. Tawalare, B. J. Lokhande	
85	Synthesis and Electronic Study of Iron Nanoparticles of Trigonella Foenum-Graceum Saifuddin Quazi, Dipak Tayade	490-492
86	Evaluating The Performance of Artificial Recharge Structures Towards Ground Water Recharge in Amravati District, Maharashtra Sumit D. Ingle, Ketki A. Jadhav	493-502
87	A Discriminatively Trained Fully Connected Conditional Random Field Model for Blood Vessel Segmentation in Fundus Images Durgeshwari Vairale, Dr. Ram K. Nawasalkar	503-509
88	EEG Signal Processing for Fetus and Mother Using MATLAB Ankita Gurjar, Dr. Ram K. Nawasalkar	510-515
89	Line width-Tolerant Joint Digital Signal Processing for 16QAM Nyquist Wdm Super Channel Avantika Upase, Dr. Ram K. Nawasalkar	516-522
90	Green Synthesis of Magnesium Oxide Nanoparticles using Aloe Vera and its Application D. R. Bijwe, A.V. Rajgure, A.M. Shirbhate, S. S. Kawar	523-527
91	Green Synthesis and Characterisation of Copper Oxide Nanoparticles using Azadirachta indica (Neem Leaves) D. R. Bijwe, A. R. Rajgure, P. S. Deole, M. N. Pawar, G. P. Gorle, S. P. Deshmukh, D. A. Pund	528-532
92	Green Synthesis of Zinc Oxide (ZnO) Nanoparticles Using Ocimum Tenuiflorum Leaves P. S. Deole, D. R. Bijwe, A. V. Rajgure, M. N. Pawar, K. H. Chavhan, A. R. Bodkhe	533-537
93	Green Synthesis and Characterization of Copper Oxide Nanoparticle Using Ficus Panda Leaf (Mehendi) Aqueous Extract A.V. Rajgure, D. R. Bijwe, P. A. Mandale, N. C. Ingle, N. G. Pokle	538-541
94	Green Synthesis and Characterization of Mgo Nanoparticles by Using Neem Leaves D. R. Bijwe, S. P. Deshmukh, G. P. Gorle, A. R. Bhojane, R. V. Barde	542-546

95	Molecular Interaction Between the Monosaccharide and Salt Solution by Acoustical Approach	547-552
	Akshay M. Jirkuntwar, Urvashi P. Manik, Paritosh L. Mishra	
96	Molecular Interaction and Thermodynamic Properties of Potassium Nitrate at Various Concentrations and Temperatures by Ultrasonic Method	553-558
	Neha Pathan, Dr. Urvashi Manik, Paritosh Mishra	
97	Measurement of Thermo-Acoustic and Volumetric Properties of Zinc Sulphate in Aqueous Solution of Monosaccharide	559-563
	Pooja V. Lande, Urvashi P. Manik, Paritosh L. Mishra	
98	A Physico-Chemical and Thermo-Acoustical Study of Aqueous Potassium Sulphate at Different Temperature and Concentrations	564-571
	Pooja R. Sonune, Urvashi P. Manik, Paritosh L. Mishra, Mohini G. Wankhade	
99	An Acoustical Study to Explore the Interaction Between Dextrose and Electrolyte Solution Using Ultrasonic Technique	572-576
	Prajakta S. Mohare, Paritosh L. Mishra, Urvashi Manik	
100	Intermolecular Interaction Between Ascorbic Acid & Salt Solution: A Thermo-Acoustical Study	577-581
	Rahul J. Raut, Urvashi P. Manik, Paritosh L. Mishra	
101	Ultrasonic Characterization on Solution of Niacinamide in Aqueous Sodium Sulphate	582-586
	Sanchit M. Bhatarkar, Urvashi P. Manik, Paritosh L. Mishra	
102	Enhancement of Electrical Conductivity in PVA Film by Doping with Li⁺ ion	587-591
	A. S. Wadatkar, A. V. Turkhade	



Simulation of Linear Array Transducer with Center Frequency 10 MHz

Dr. S. A. Rodge¹, S. K. Shelke¹, Dr. S.A. Ghogare², V. G. Gabhane¹, H. E Salve¹

¹Department of Electronics, Adarsha Science J.B. Arts and Birla Commerce Mahavidyalaya, Dhamangaon Rly-444709, Maharashtra, India

²Department of Computer Science, Adarsha Science J.B. Arts and Birla Commerce Mahavidyalaya, Dhamangaon Rly-444709, Maharashtra, India

ABSTRACT

Over the past decades, ultrasound imaging technology has satisfied outstanding improvement in obtaining significant diagnostic information from patients in a fast, noninvasive approach. Piezoelectric transducers are important elements of various broadband ultrasonic systems, either pulse-echo or through-transmission, used for imaging and detection purposes [1]. In ultrasonic broadband applications such as medical imaging, or non-destructive testing, piezoelectric transducers should generate/receive ultrasonic signals with good efficiency over a large frequency range. This implies the use of piezoelectric transducers with high sensitivity, broad bandwidth and short-duration impulse responses. High sensitivity provides large signal amplitudes which determine a good dynamic range for the system and the short duration of the received ultra-sonic signal provides a good axial resolution. This paper presents the simulation of 32-element linear array transducers with center frequency 10 MHz, using Field-II GUI program for ultrasonic measurements.

Keywords:-Detected image, Field-II GUI, Linear array Transducer, medical imaging, TX/RX Fields, TX/RX Axial slice, TX/RX lateral slice, Ultrasonic.

I. INTRODUCTION

For the period of the second half of 20th current century the medical imaging is grown through Ultrasound tool speedily. The part of novel technology is the use of computers to decide problems by simulating theoretical models (Numerical simulations) that has taken place alongside pure theory and experiment during the last few decades. These numerical simulations permit one to resolve problems that may not be accessible to direct experimental study or too complex for theoretical analysis. Computer simulations can link the gap between analysis and experiment [2].

More than the last half century much development has been made in medical device technology. One particular medical technology that has enhanced speedily over the last 30 years is ultrasound. This advancement in technology however has brought with it the rapid obsolescence of system design. The

accomplishment of modern electronics is built on the possibility to precisely predict system performance by the use of simulation tools. This model can be extended to components such as piezoelectric transducers attached to the electronics [3]. The ability to simulate both piezoelectric transducer and electronics together renders possible efficient optimizations at system level, i.e. minimizing size, price and power consumption [4].

II. SPATIAL IMPULSE THEORY

The pressure field generated by the aperture is found by the Rayleigh integral [5]

$$p(\vec{r}_1, t) = \frac{\rho_0}{2\pi} \int_s \frac{\partial v_n(\vec{r}_2, t - \frac{|\vec{r}_1 - \vec{r}_2|}{c})}{|\vec{r}_1 - \vec{r}_2|} ds \quad (1)$$

Where the field point is denoted by \vec{r}_1 and the aperture by \vec{r}_2 , is the velocity normal to the transducer surface. Using the velocity potential, and assume that the surface velocity is uniform over the aperture making it independent of \vec{r}_2 , then: where the field point is denoted by \vec{r}_1 and the aperture by \vec{r}_2 , is the velocity normal to the transducer surface. Using the velocity potential, and assume that the surface velocity is uniform over the aperture making it independent of \vec{r}_2 , then:

$$\Psi(\vec{r}_1, t) = v_n(t) * \int_s \frac{\partial(t - \frac{|\vec{r}_1 - \vec{r}_2|}{c})}{2\pi |\vec{r}_1 - \vec{r}_2|} \quad (2)$$

Where * denotes convolution in time. The integral in this equation

$$h(\vec{r}_1, t) = \int_s \frac{\partial(t - \frac{|\vec{r}_1 - \vec{r}_2|}{c})}{2\pi |\vec{r}_1 - \vec{r}_2|} \quad (3)$$

Represent the spatial impulse response. The continuous wave field can be found from the Fourier transform of

$$p(\vec{r}_1, t) = \rho_0 \frac{\partial v(t)}{\partial t} * h(\vec{r}_1, t) \quad (4)$$

The impulse response includes the excitation convolved with both the transducers electro-mechanical impulse response in transmit and receive. The final signal for a collection of scatters is calculated as a linear sum over all signals from the different scatters [6-7].

III. SIMULATION OF LINEAR ARRAY TRANSDUCER

The linear array is the fundamental type of multi-element transducer and it scans the region of interest by exciting the elements situated over the region. The field is focused on the region by introducing time delay in the excitation of the concerned individual elements, so initially concave beam is emitted. Here a Fig.1 shows general design format of 16 element linear array transducer having height, width and kerf of individual

element are taken as 5 mm, 0.2 mm and 0.02 mm respectively. The transducers are situated at the center of the coordinate system. To achieve focal length of 30 mm from the center of transducer the electronic focusing is included.

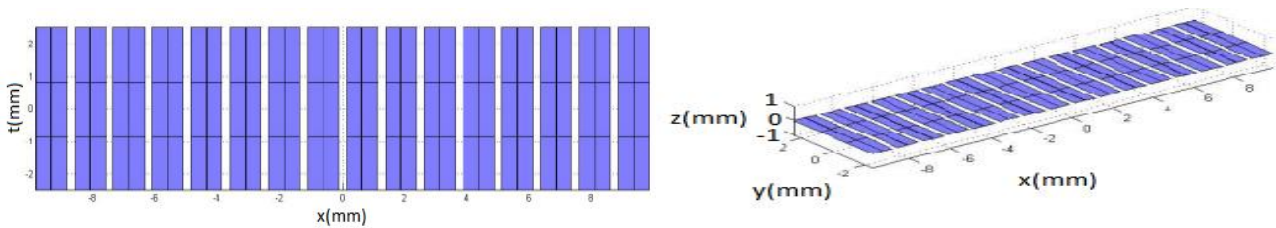


Fig. (1) Design format of linear array transducer (Height=5mm, Width=0.25mm, Kerf=0.02mm)

In this paper a linear array transducer of 16 elements is simulated using FIELD-II program with center frequencies 5MHz. For this specified linear array transducer, acoustic field generated is propagated through human body tissues and is observed at a focal distance i.e. (0, 0, 30)

IV. RESULT AND DISCUSSION

The calculation of the impulse response is facilitated by projecting the field point onto the plane of the aperture. In this way, the problem became two-dimensional and the field point is given as a (x, y) coordinate set and a height z above the plane. The spatial impulse response is, thus, determined by the relative length of the part of the arc that intersects the aperture [8]. Thereby it is the crossing of the projected ultrasonic waves with the edges of the aperture that determines the spatial impulse responses as a function of time. In this paper by using FIELD-II program created a 32-element linear array transducer with center frequency $f_0 = 10\text{MHz}$. The speed of sound in tissue is $c = 1540\text{m/s}$, The sampling frequency used was $f_s = 100\text{MHz}$. The elements had a width and height of 0.25mm and 5mm respectively. The focal-point was set to 30mm.

Table: 1 shows the parameters for 32element array transducer, excitation pulse and medium used for this center frequency (f_0) used is 10 MHz Figs. (a-m) shows; Element impulse response for 32 element array, TX Field image for 32 element array, TX Axial waveform for 32 element array, TX Lateral beam plot for 32 element array, TX/RX Field image for 32 element array, TX/RX Axial waveform for 32 element array, TX/RX Lateral beam plot for 32 element array, K- space TX/RX field image for 32 element array, K-space axial slice for 32 element array, K-space lateral slice for 32 element array, Detected image for 32 element array, Detected image axial slice for 32 element array and Detected image lateral slice for 32 element array.

Linear Array		QUIT	
Transducer Parameters			
Number of Elements	32	General Settings	
Kerf (mm)	0.02	Sampling Frequency (MHz)	100
Width (mm)	0.2	Sound Speed (m/s)	1540
Height (mm)	5	Target Type:	
Focal Pt. [lat elev axial] (mm)	0 0 30	Number of Axial Points	1
Center Frequency (MHz)	10	Dist. b/t Axial Points (mm)	0.5
Fractional Bandwidth (%)	50	Axial Dist. from Focus (mm)	0
Image Size			
Lateral ROI Range (mm)	2	Number of Lateral Points	1
Lateral Increment (mm)	0.02	Dist. b/t Lateral Points (mm)	0.5
Excitation Pulse:			
Center Frequency (MHz)	Sine 10	Lat. Dist. from Focus (mm)	0
Number of Cycles	5		
Save filename		testing	

Table: 1

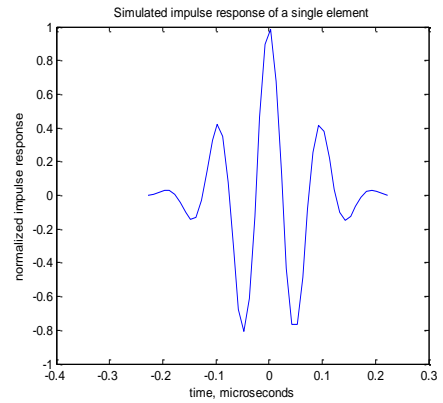


Fig.(a) Element impulse response

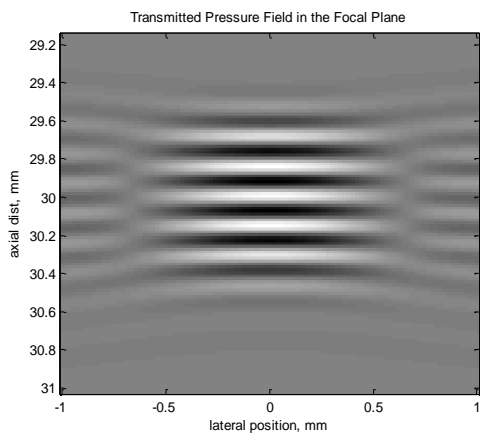


Fig. (b) TX Field image

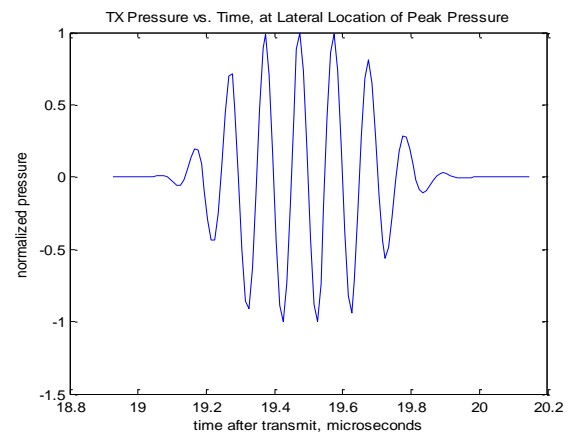


Fig. (c) TX Axial waveform

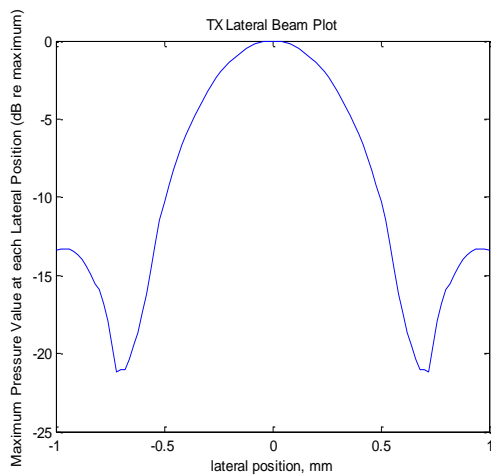


Fig. (d) TX Lateral beam-plot

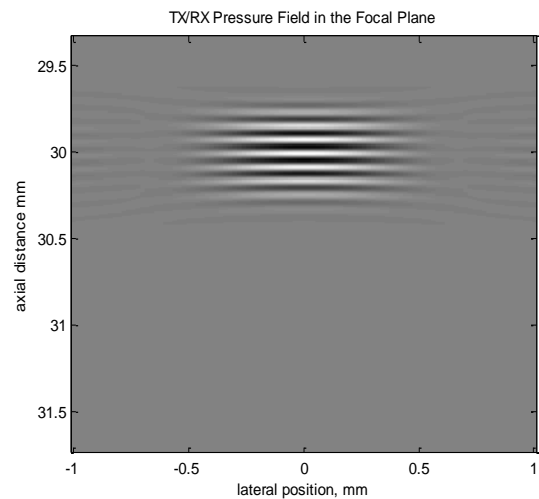
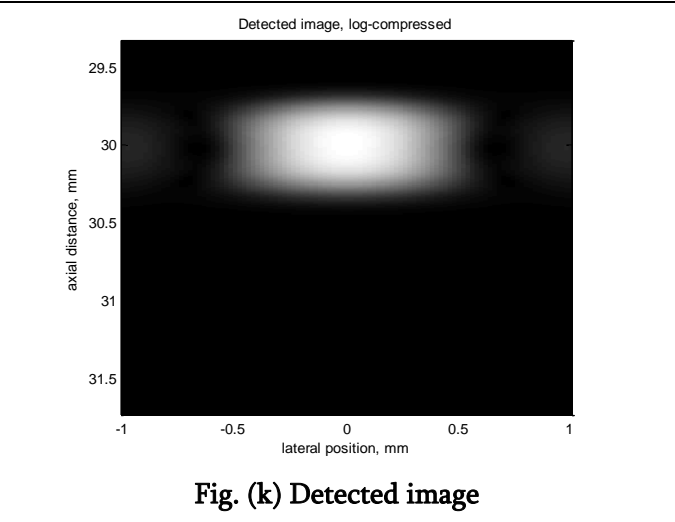
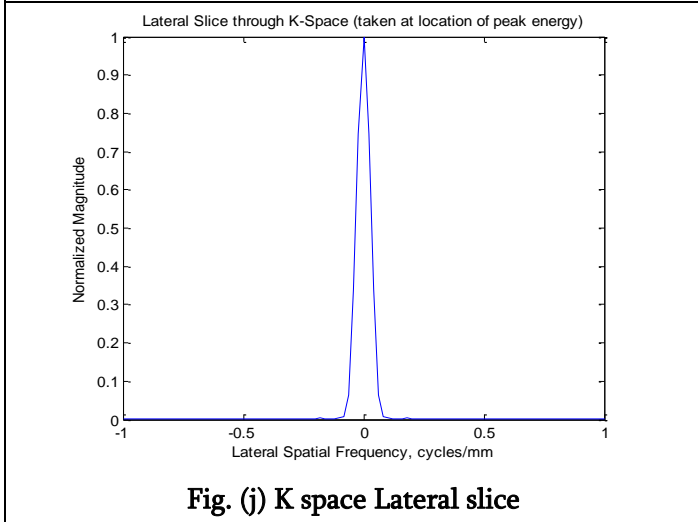
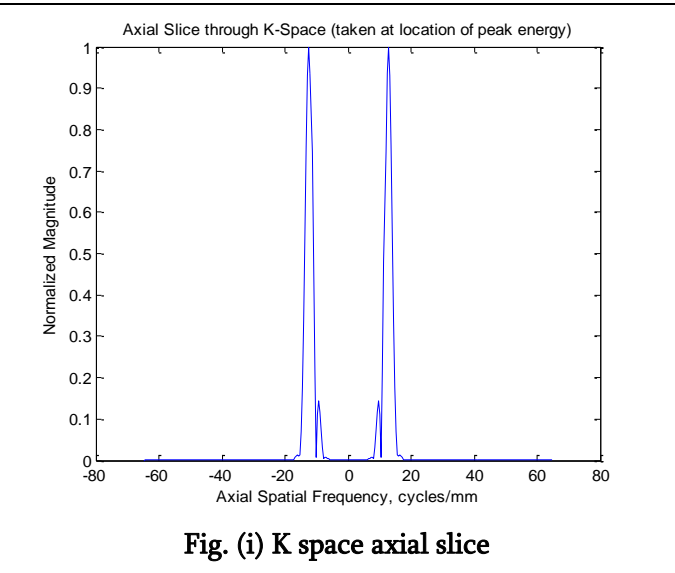
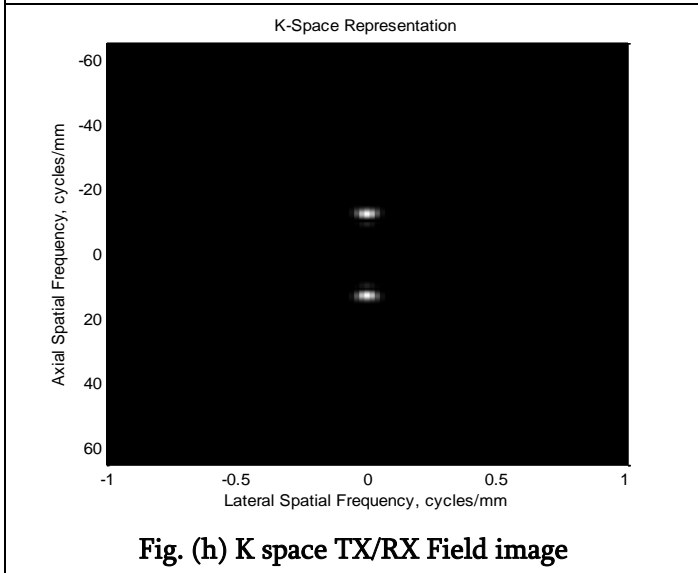
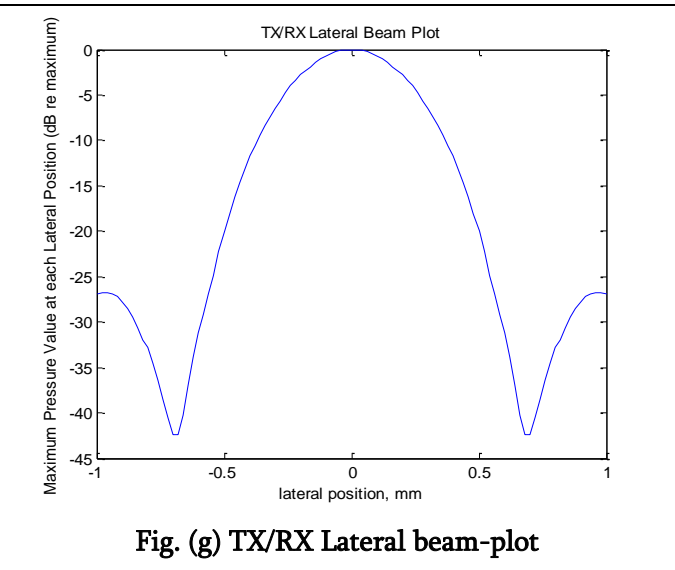
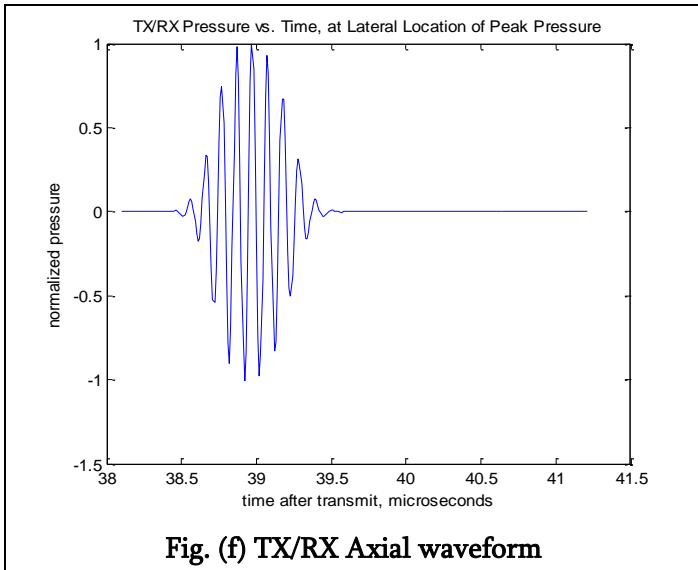
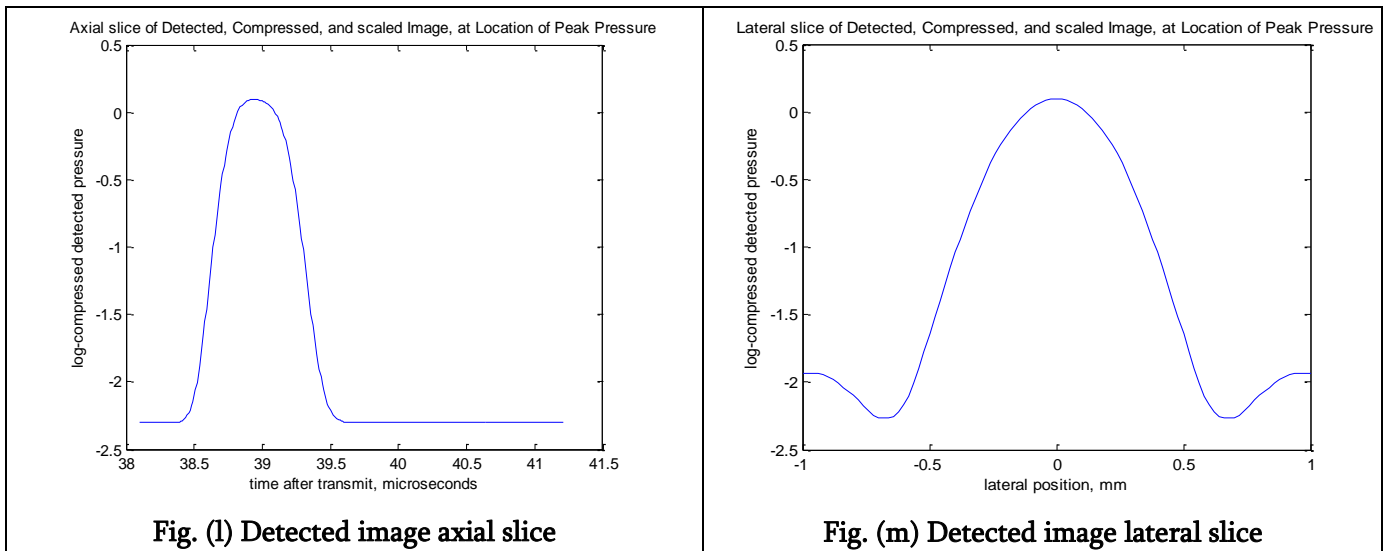


Fig. (e) TX/RX Field image





V. CONCLUSION

The paper attempts to present a coherent analysis of the focusing strategies for 2-D array transducer design and properties, based on linear acoustics. The delays on the individual transducer elements and their relative weight or apodization are changed continuously as a function of depth. This yields near perfect focused images for all depths and has increased the contrast in the displayed image, thus, benefitting the diagnostic importance of ultrasonic imaging. If the center frequency and number of elements in transducer is increased then contrast in the detected image is increased, this also increases the diagnostic status of ultrasonic imaging

VI. REFERENCES

- [1]. T. R. Meeker, "Thickness mode piezoelectric transducers," *Ultrasonics* 10, 26–36, 1972.
- [2]. Gandole, Y. B. (2012). Computer Modeling and Simulation of Ultrasonic System for Material Characterization. <http://www.oalib.com/search?kw=Y.%20B.%20Gandole&searchField=authors>.
- [3]. R. Krimholtz, D. Leedom, and G. Matthaci, "New equivalent circuits for elementary piezoelectric transducers," *Electron. Lett.* 6, 398–399, 1970
- [4]. P. Marchal, F. Levarssort, L.-P. Tran-Huu-Hue, and M. Lethiecq, "Effects of acoustical properties of a lens on the pulse-echo response of a single element transducer," *IEEE*
- [5]. International Ultrasonics, Ferroelectrics, and Frequency Control Joint 50th Anniversary Conference, pp. 1651–1654, 2004.
- [6]. Jensen, J.A, A New Approach to Calculating Spatial Impulse Responses, *IEEE*
- [7]. International Ultrasonic Symposium, Toronto, Canada, 1997
- [8]. P. Marchal, F. Levarssort, L.-P. Tran-Huu-Hue, and M. Lethiecq, "Effects of acoustical properties of a lens on the pulse-echo response of a single element transducer," *IEEE*

- [9]. International Ultrasonics, Ferroelectrics, and Frequency Control Joint 50th Anniversary Conference, pp. 1651–1654,2004.
- [10]. JENSEN, J.A., Field: A program for simulating ultrasound systems, 10th Nordic-Baltic Conference on Biomedical Imaging, in: Medical & Biological Engineering & Computing, 1996, 34, Supplement 1, 351–353.
- [11]. Jensen, J.A., N.B. Svendsen, Simulation of advanced ultrasound systems using field II, Biomedical Imaging: Nano to Macro, 2004. IEEE International Symposiumon, 15-18 April 2004 Page(s):636–639 Vol.-1.

Physico-Chemical, Spectroscopic Characterization and Adsorption Study of Prepared Activated Carbon from Limonia Acidissima

Vaishali A. Shirbhate¹, Deepali P. Gulwade¹

¹Department of Chemistry, Govt. Vidarbha Institute of Science and Humanities Amravati University,
Amravati-444604, Maharashtra, India

ABSTRACT

In the present study the removal of Ni(II) by adsorption on Limonia Acidissima Shell as adsorbent has been investigated in the batch experiment. Physico-chemical characteristics of prepared activated carbon such as Bulk density, Porosity determination, Moisture content determination, Ash Content, water-soluble matter, have been carried out for adsorbent. The equilibrium data were well described by Langmuir and Freundlich adsorption isotherms. Spectroscopic Characterizations were studied to analysing internal structure of carbon by Scanning Electron Microscopy, X-ray Diffraction which provides information about the arrangement of crystal and Fourier Transform Infrared Spectroscopy has been used to detect functional groups present in the sample.

Keywords-Adsorption, impregnate, Physico-chemical Characterizations, Limonia Acidissima Shell Activated Carbon (Kavat Shell)

I. INTRODUCTION

Industrial development has caused the release of various pollutants including toxic metals into the environment⁽¹⁾. Carbonaceous material showing a well developed surface area and porous texture called activated carbon depend on the physical and chemical properties of precursor and also the activation method⁽²⁾. Activated carbon is form of carbon has been processed to make it extremely porous and having a very large surface area for adsorption or chemical reactions. The carbonized carbon is converted to activated form through physical or chemical activation⁽³⁾.

II. MATERIALS AND METHODS

Kavat Shell was used as a precursor for preparation of activated carbon purchased from local market of Amravati, Maharashtra. Analytical grade chemicals potassium hydroxide and Nickel nitrate and use as activating agent as well as % removal Ni(II).

Adsorbent Preparation-Kavat Shell are collected from local market and remove the pulp, washed with distilled water and sun dried for three days to remove impurities dried at 105° c for 24 hours in hot box oven then carbonized at 400° c for 1 hour in muffle furnace (i-therm AI-7981). The carbonized sample cool and crushed with mortar and grinded with electric grinder. The sample Sieved by 250 MICS (Standard test Sieve). Activated carbon were prepared by first impregnating Kavat Shells in KOH solution followed by carbonization. Concentrations such as 20%, 60%, 100% prepared by dissolving KOH in distilled water.

Characterization

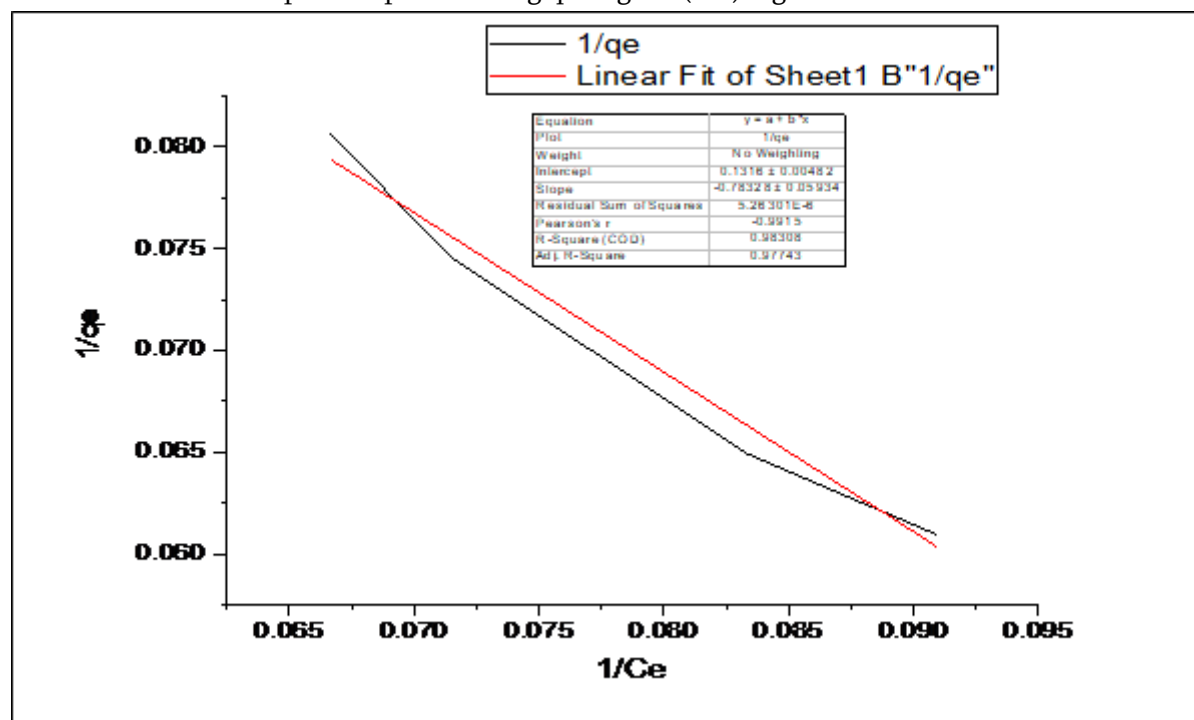
Parameters	20%	60%	100%
Bulk density	2.63	2.56	2.78
Porosity	0.0536	0.05408	0.05673
Moisture Content(%)	66	76	89
Ash Content	29	21	13
Water soluble matter (gm)	0.2	0.1	0.3

Table No-1 Langmuir and Freundlich Isotherm Adsorption Study

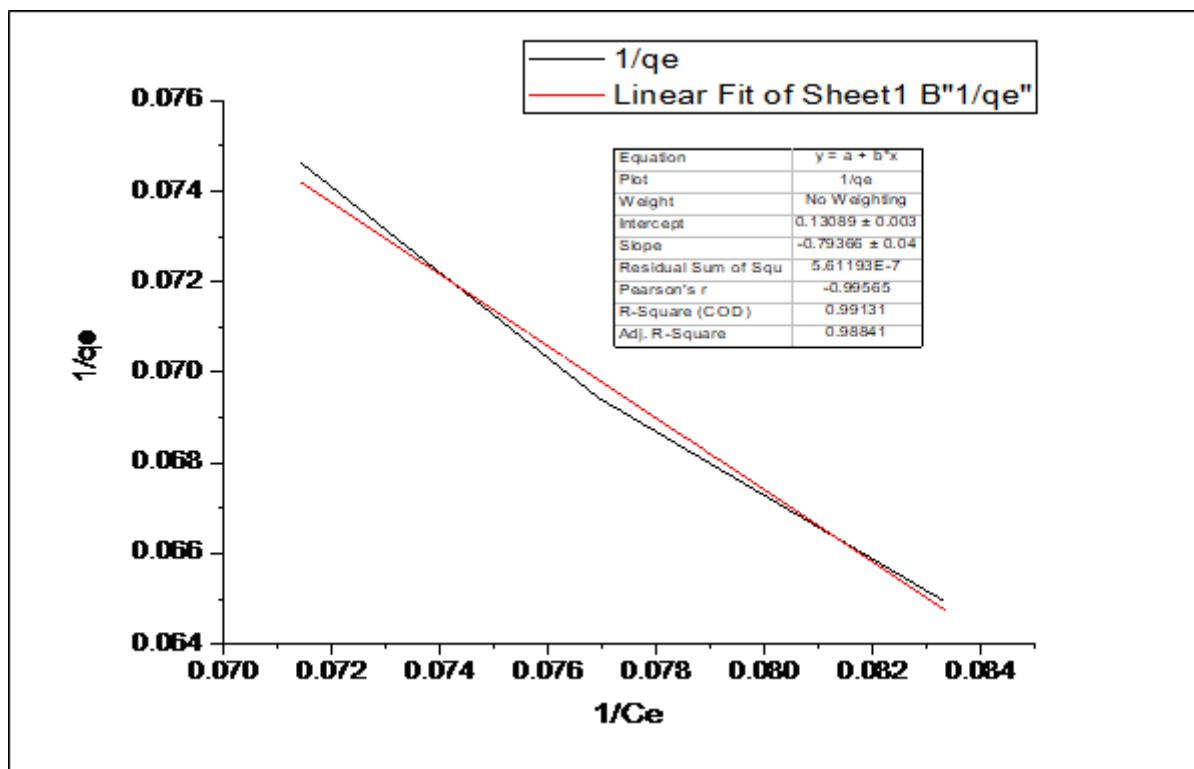
The adsorption isotherm data fitted to both the Langmuir and Freundlich isotherm equation, it help to describe the sorption interaction and adsorption capacity of adsorbent. The chemical equation were given below.

1) Langmuir isotherm adsorption expression- $\frac{1}{q_e} = \frac{1}{KLq_{max}} \cdot \frac{1}{C_e} + \frac{1}{q_{max}}$

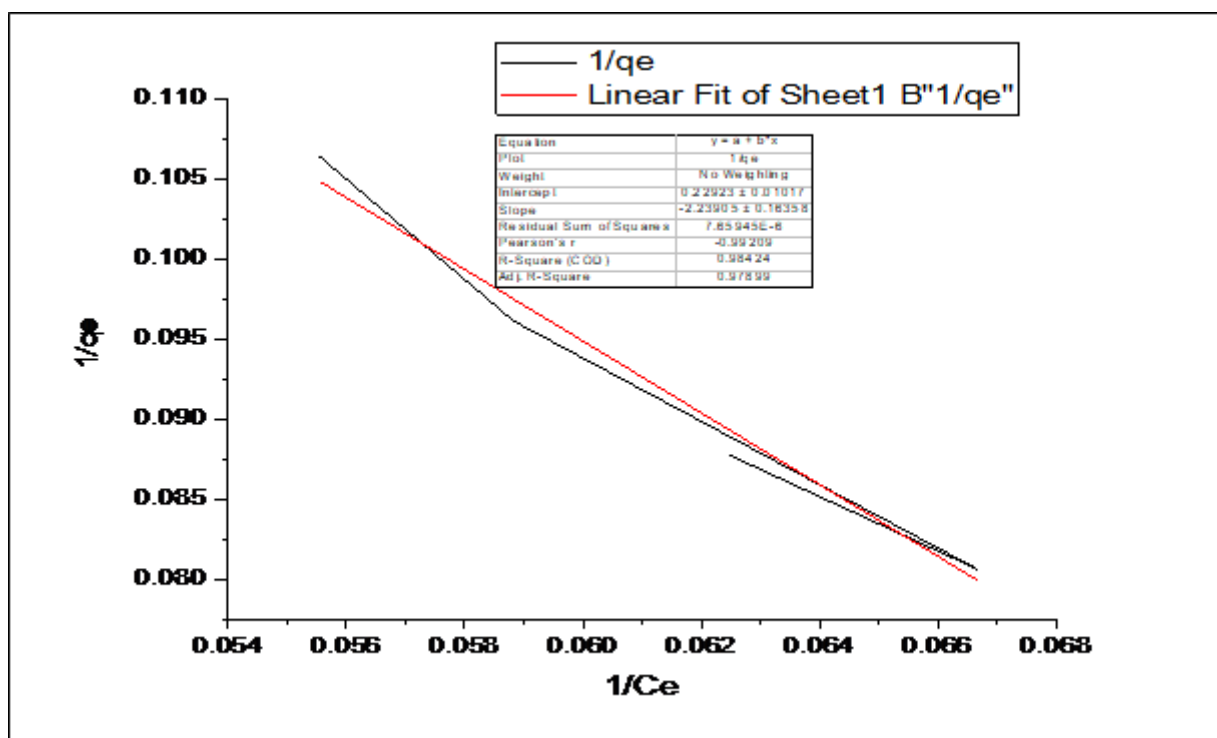
2) Freundlich isotherm adsorption expression- $\log q_e = \log K_F + (1/n) \log C_e$



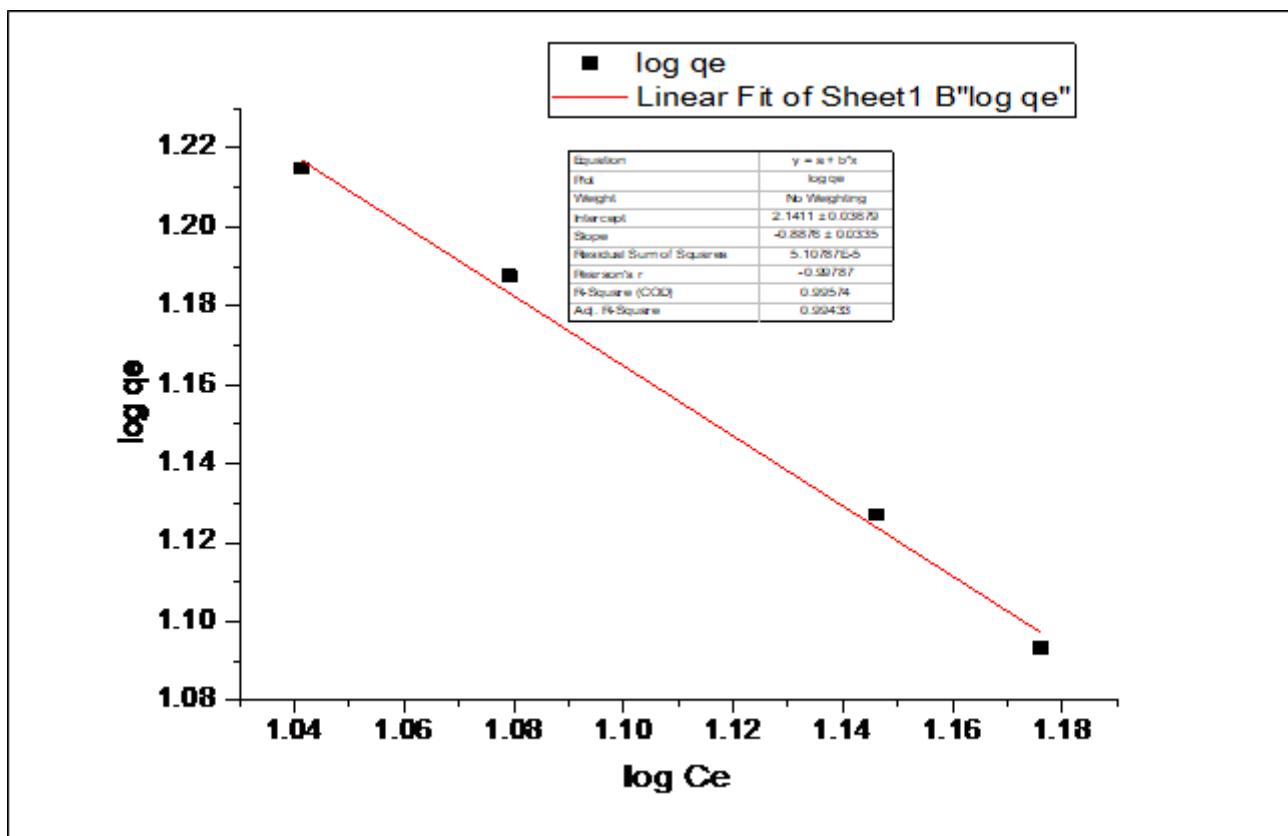
A)Langmuir adsorption isotherm Ni(II)20% AC



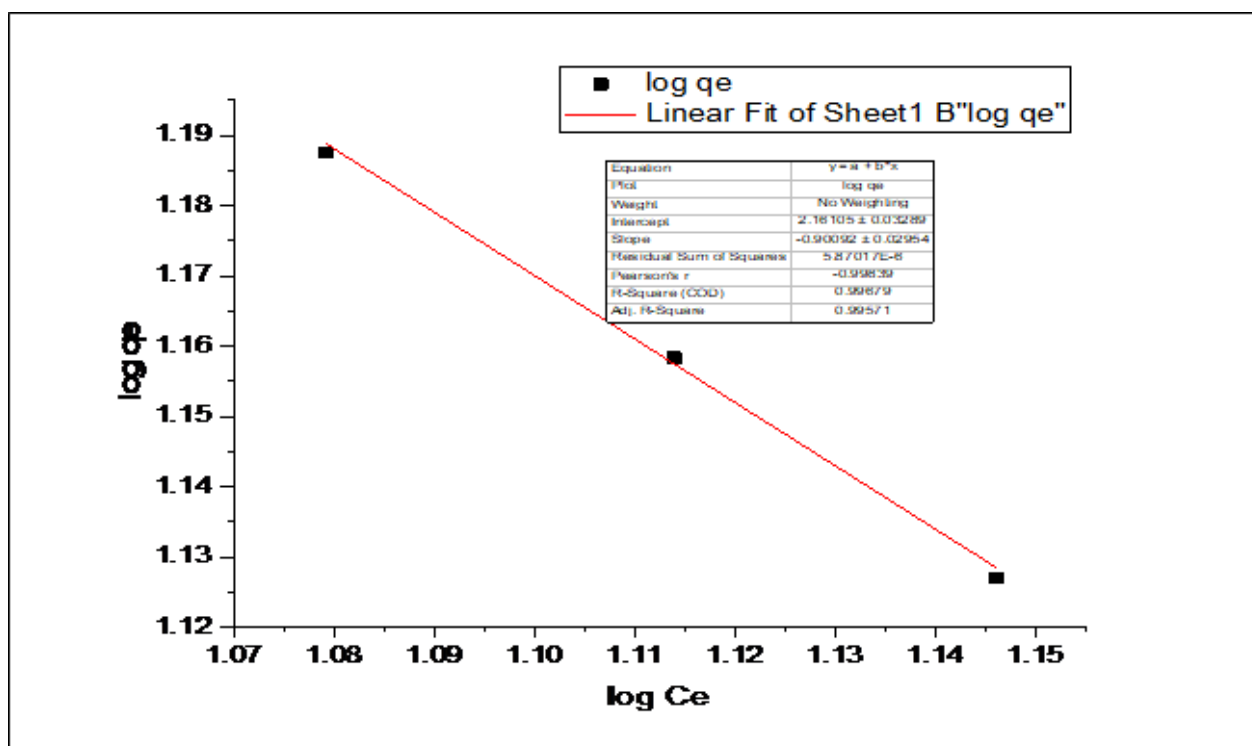
B)Langmuir adsorption isotherm



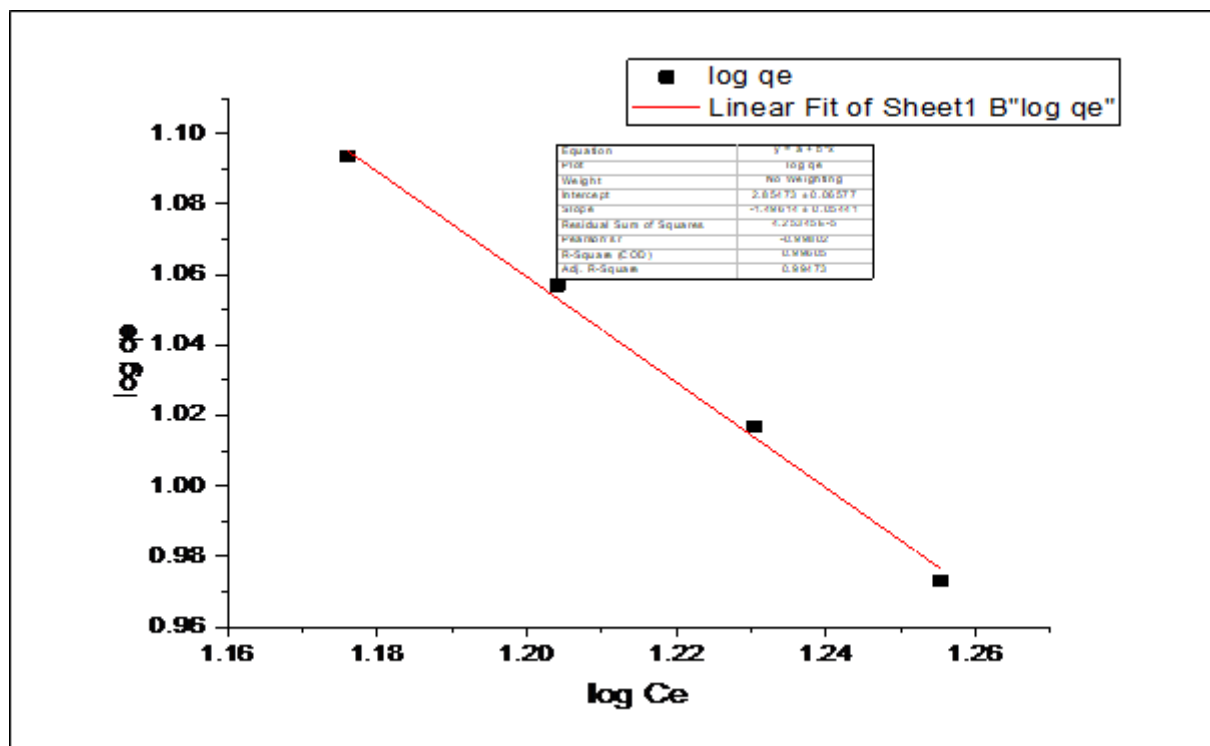
C)Langmuir adsorption isotherm Ni(II)100% AC



D) Freundlich adsorption



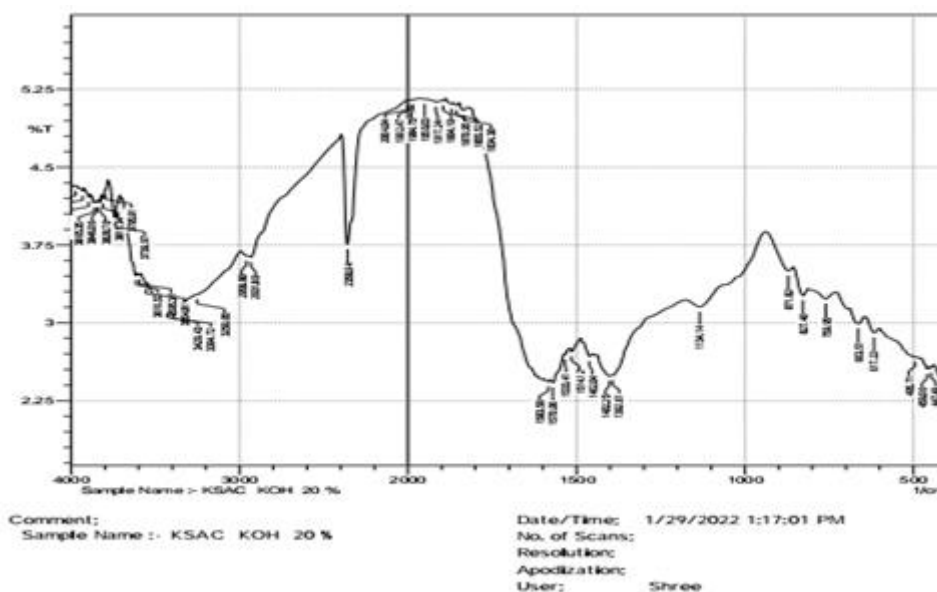
E) Freundlich adsorption isotherm Ni(II)60% AC



F) Freundlich adsorption isotherm Ni(II)100% AC

III. RESULT AND DISCUSSION

FTIR Analysis-Figure 3- 20%,60%, 100% concentrations of activated carbon FTIR results evident that broad peak were found between 3500-3000 cm^{-1} which indicates presence of O-H functional groups. Also C-H stretching found at frequency between 2850-2960 cm^{-1} . The peak at 1570.06 cm^{-1} was due the presence of C=C and C-H stretching.



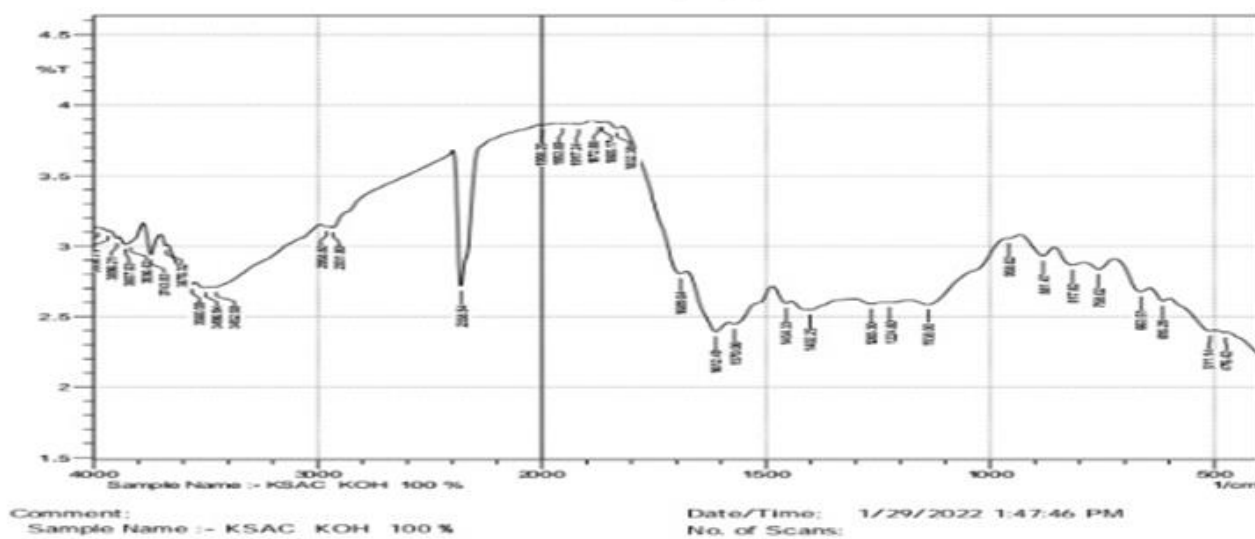
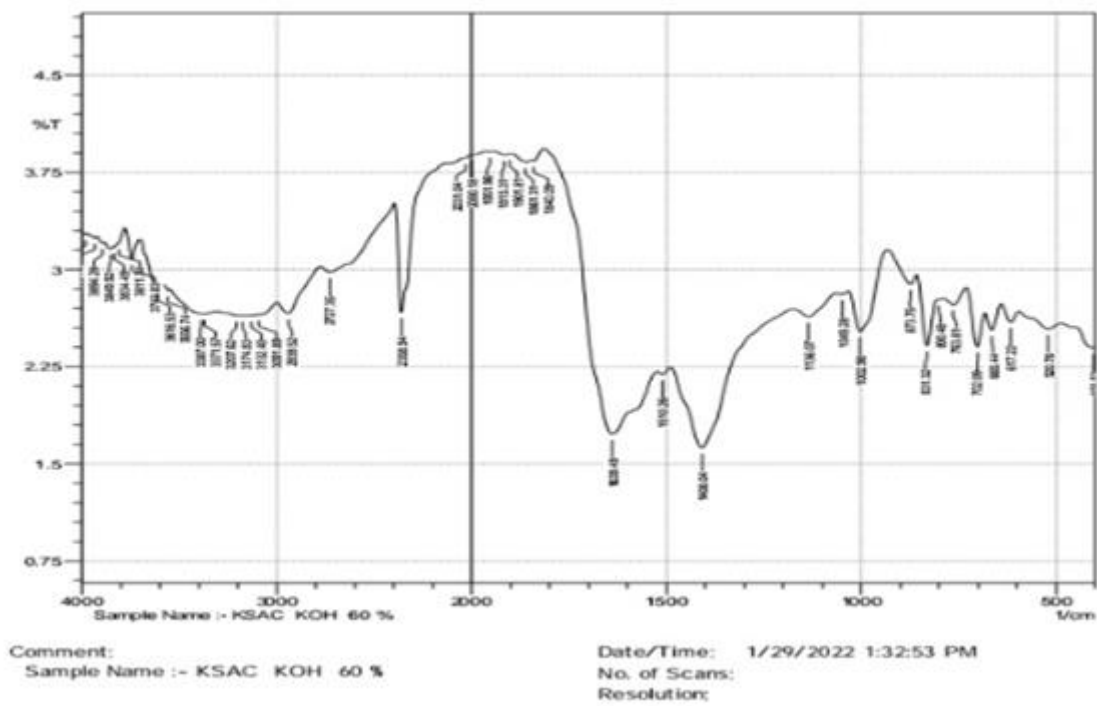


Figure 3.- FTIR monographs of 20%,60%,100% activated carbon

XRD Analysis –

The activated carbon of *Limonia acidissima* 20% exhibited peak 2 theta= 11.71°,60% peak 2theta=11.85°,100% peak 2theta=20°. XRD analysis proved that the sample have a perfect amorphous structure.

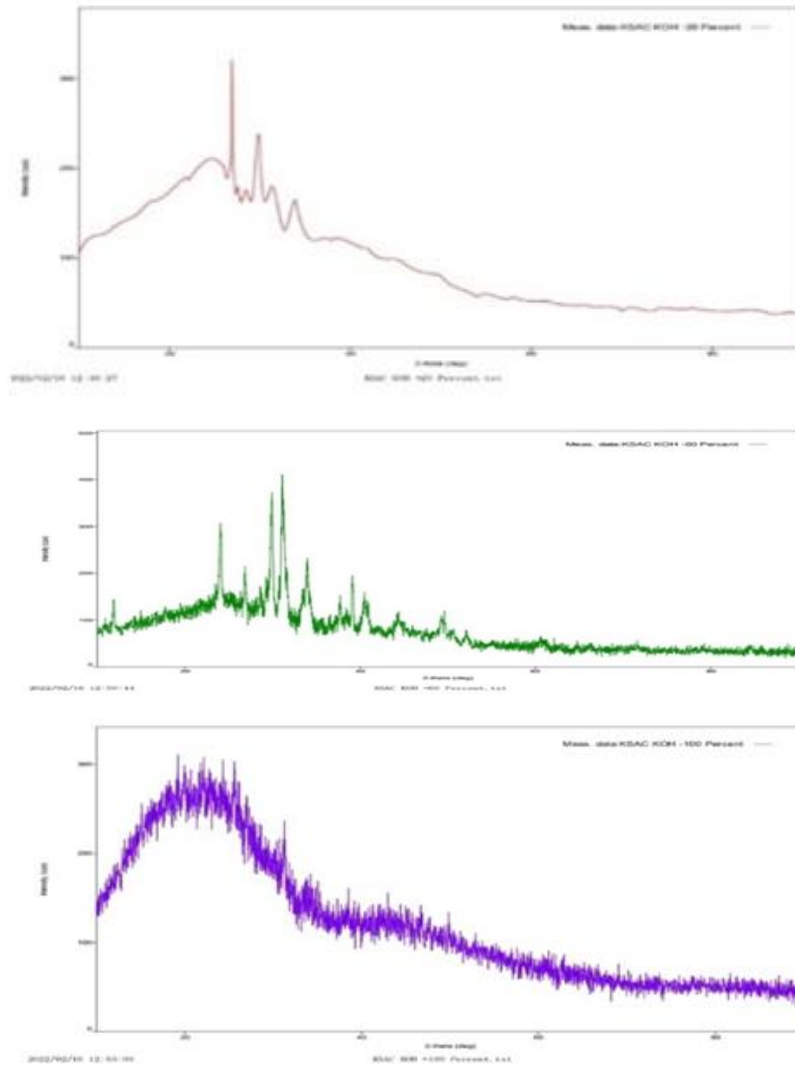


Figure 4.-XRD monographs of 20%,60%,100% activated carbon

SEM

Scanning electron micrographs of *Limonia Acidissima* after characterization are shown in figure- respectively from figure-5. It was seen that *Limonia Acidissima* has a porous surface

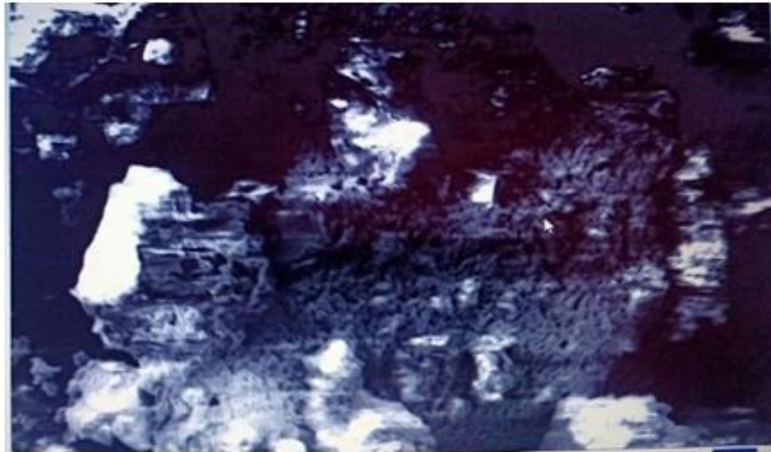
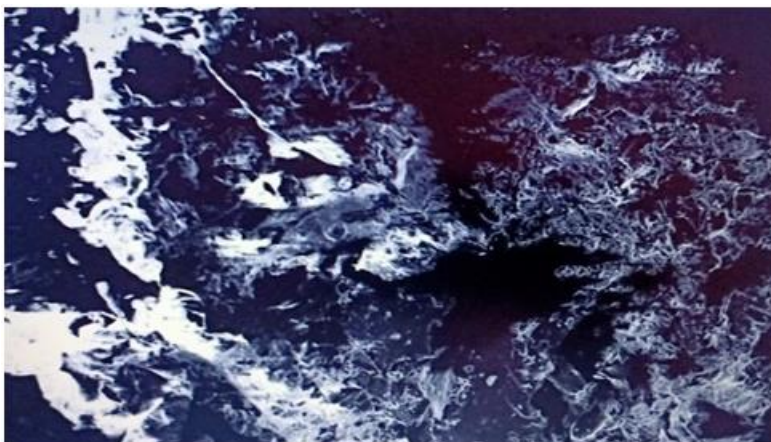


Fig5 -A) SEM Image of 20% AC



B) SEM Image of 60% AC



C) SEM Image of 100% AC

Figure-5.

IV. CONCLUSIONS

- In this study the adsorption of from aqueous solution was investigates using activated carbon of Limonia Acidissima as an adsorbent.
- The adsorptive removal of Ni(II)by activated carbon of a Limonia Acidissima was found to be effective. The result obtained characterization suggests that the prepared KOH activated carbon has well defined pore size with majority of macropores.
- The prepared activated carbon was characterized for bulk density, porosity, moisture content, Ash content, water soluble matter, percentage yield (Table No.-1) and used for removal of Ni(II) by adsorption phenomenon.The activated carbon was also further characterized by XRD ,FTIR and SEM (figure: 3-5).
- Langmuir and Freundlich isotherm adsorption revealsfollowing conclusion(Table No.-2,3,4,5,6, 7)

Intercept	Slope	$q_{\max}(\text{mg/g})$	KL	RL	R^2
0.1316	-0.78328	7.598784	-9.70124	-264.814	0.9774

Table no.-2Langmuir adsorption isotherm Ni(II)20% AC

Intercept	Slope	$q_{\max}(\text{mg/g})$	KL	RL	R^2
0.13193	-0.80863	7.579777	-9.3736	-255.837	0.98297

Table no.-3 Langmuir adsorption isotherm Ni(II) 60% AC

Intercept	Slope	$q_{\max}(\text{mg/g})$	KL	RL	R^2
0.22923	-2.23905	4.362431	-1.94834	-52.3845	0.97899

Table no.-4 Langmuir adsorption isotherm Ni(II) 100% AC

Intercept	Slope	1/n	K_f	R^2
2.1411	-0.8876	-0.8876	138.388	0.99433

Table no.-5 Freundlich adsorption isotherm Ni(II)20%

Intercept	Slope	1/n	K_f	R^2
2.16105	-0.90092	-0.90092	144.893	0.99571

Table no.-6 Freundlich adsorption isotherm Ni(II)60%

Intercept	Slope	1/n	K_f	R^2
2.8547	-1.49614	-1.49614	215.65	0.99473

Table no.-7 Freundlich adsorption isotherm Ni(II)100%

V. REFERENCES

- [1]. E.W.NSI,A.E.AKPAKPAN,E.J ULPONG,U.D AKPABIO,“preparation and characterzation of activatedcarbon from Hura Crepitans Linn seed shells”,int. J. of engineering and sci. vol5 (9), 2016,pp-2319-1813
- [2]. Stela Nhandeyara do Carmo Ramos,Amalia Luisa Pedrosa Xavier,Fillipe simoes Teodoro,Laurent Frederic Gil,Leandro Vinicius Alves Gurgel,“Removal of cobalt(II), copper(II),nickel (II) ions from aqueous solutions using phthalate-functionalized surgarcanebagasse: mono and multicomponent adsorption in batch mode”,industrial crops and products,vol79, 2016,pp.116-130
- [3]. Muthanna J.Ahmed,“preparation of activated carbons from date stoneby chemical activation method using FeCl₃and ZnCl₂ as activating agents”,journal of engineering vol 17,Aug 2011
- [4]. Shivdas Dowlatshahi, Ahmad Reza Haratinezhad Torbati, Mahshid Loloei,“Adsorption of copper,lead and cadmium from aqueous solution by activated carbon prepared from saffron leaves”,Environmental Health Engineering and Management Journal,Vol1(1),2014,pp.37-44
- [5]. Joshi Sahira,Adhikari Mandira,Pokhrel prasad, Pradhananga,Raja Ram,“Effect of activating agents on the activated carbonsprepared from Lapsi seed stone”,Research J. Chemical Sci. vol 3(5),may,2013, pp-19-24
- [6]. Akpa J.G And Nmegbu C.G.J,“Adsorption of bezene on activated carbon fromagricultural waste materials”,research journal of chemical science, Vol4(9) ,september 2014,pp-34-40

Synthesis and Experimental Studies of Heterocyclic Chalcone

Gotmare P.A.^{1*}, Ingle G.B¹, Dr.Kolhe S.V¹

¹Department of Chemistry, Shri Shivaji Arts, Commerce and Science College, Akot-444101, Maharashtra, India

ABSTRACT

A new chalcone was synthesized by Claisen-Schmidt condensation. The solute and solvent interaction were studied on the basis of physicochemical properties like density, viscosity, refractive index etc. The physicochemical properties are varies by changing concentration, temperature and solvent etc.

Key Words: Physicochemical, Chalcone synthesis. Solvent solute interaction etc.

I. INTRODUCTION

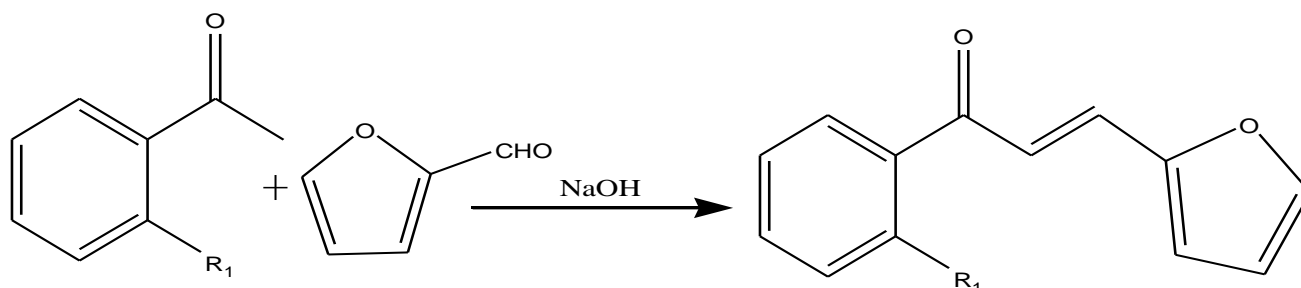
Chalcones are natural or synthetic compounds belonging to the flavonoid family¹. Chalcones have been used as intermediates for the preparation of compounds having therapeutic value^{2,3}, Chalcones possess various multipronged activities such as antimicrobial⁴, antioxidant⁵, anticancer⁶, antiviral⁷, antitumor⁸, antimalarial⁹, antifertile¹⁰, cardiovascular¹¹, antidepressants¹², antiplasmodial¹³, anti-aids¹⁴, and insect antifeedant activities^{15,16}. In advanced form, these compounds are widely distributed in foods and beverages such as vegetables, fruits, tea, soy-based foodstuff and spices^{17,18}. The physicochemical study of chalcone has analytical, medicinal agricultural, industrial, pharmaceutical significance¹⁹⁻²⁶

Chalcone shows various properties hence in the present work, the novel chalcone derivative was prepared and experimentally studied its properties like density, viscosity, refractive index etc. in different solvent and at different concentrations.

II. EXPERIMENTAL

Synthesis of Heterocyclic chalcone

The heterocyclic chalcone was prepared by mixing of aromatic substituted acetophenone (0.01M) and Furfuraldehyde (0.01M) along with ethanol as solvent. The reaction mixture was stirring and drop wise added dilute sodium hydroxide. The product chalcone was obtained which kept overnight. Later on chalcone was acidified and filter. The structure of synthesized chalcone was confirmed by IR, ¹H NMR and mass spectral data.



Parameters of synthesized heterocyclic chalcone

Sr. No.	Compound	Substitution R ₁	Molecular Formula	Molecular Weight	Yield
1	Chalcone	OH	C ₁₃ H ₁₀ O ₃	214	74%

Physical parameters of synthesized heterocyclic chalcone

The physical parameters of synthesized heterocyclic chalcone were studied indifferent solvents (DMSO and DMF) at different concentrations and temperatures.

a) Density: The density (ρ) is elementary physical property of matter. For a homogeneous object it is defined as the ratio of its mass (m) to its volume (v). The density (ρ) of chalcones were studied by using pycnometer. In this case measures volume (V) and a balance is used to determine mass (m), then weighing. Density is calculated by $\rho = m/V$.

b) Viscosity: Fluids are used in mechanical system as lubricants to reduce the wear and tear of the system. Hence viscosity plays an important role in assessing the performance of the mechanical systems. Here the viscosity of synthesized heterocyclic chalcone was measured by using Ostwald viscometer.

c) Refractive Index: The refractive index of synthesized heterocyclic chalcone was measured by using Abbe's refractometer and sodium lamp in different solvents, concentration and temperatures,

III. RESULTS AND DISCUSSION

Density and viscosity:-

The experimental values of density (ρ), and viscosity (η), at different solvents, different temperature and different concentration are mention in following tables

Temperature: 303.15 K

Conc. (M).	DMSO Solvent		DMF Solvent	
	Density (ρ)(g.cm ⁻³)	Viscosity (η .10 ⁻³) poise	Density (ρ)(g.cm ⁻³)	Viscosity (η .10 ⁻³) poise
0.05	1.1193	12.3426	0.9642	8.1748
0.04	1.1187	12.2827	0.9632	8.0917
0.03	1.1181	12.2428	0.9624	7.9438
0.02	1.1176	12.1985	0.9607	7.7782
0.01	1.1170	12.1584	0.9596	7.5394

Conc. (M).	DMSO Solvent		DMF Solvent	
	Density (ρ)(g.cm ⁻³)	Viscosity (η ,10 ⁻³) poise	Density(ρ) (g.cm ⁻³)	Viscosity (η ,10 ⁻³) poise
0.05	1.1186	11.7285	0.9628	7.3185
0.04	1.1179	11.6327	0.9620	7.1215
0.03	1.1164	11.2477	0.9615	6.8246
0.02	1.1124	11.0982	0.9602	6.6487
0.01	1.1106	11.0224	0.9598	6.4761

Temperature: 308.15 K

Temperature: 313.15 K

Conc. (M).	DMSO Solvent		DMF Solvent	
	Density (ρ)(g.cm ⁻³)	Viscosity (η ,10 ⁻³) poise	Density(ρ)(g.cm ⁻³)	Viscosity (η ,10 ⁻³) poise
0.05	1.1182	10.2864	0.9622	6.6279
0.04	1.1174	10.2627	0.9616	6.5984
0.03	1.1142	10.2319	0.9606	6.4399
0.02	1.1108	10.1964	0.9598	6.4194
0.01	1.1060	10.1831	0.9590	6.3820

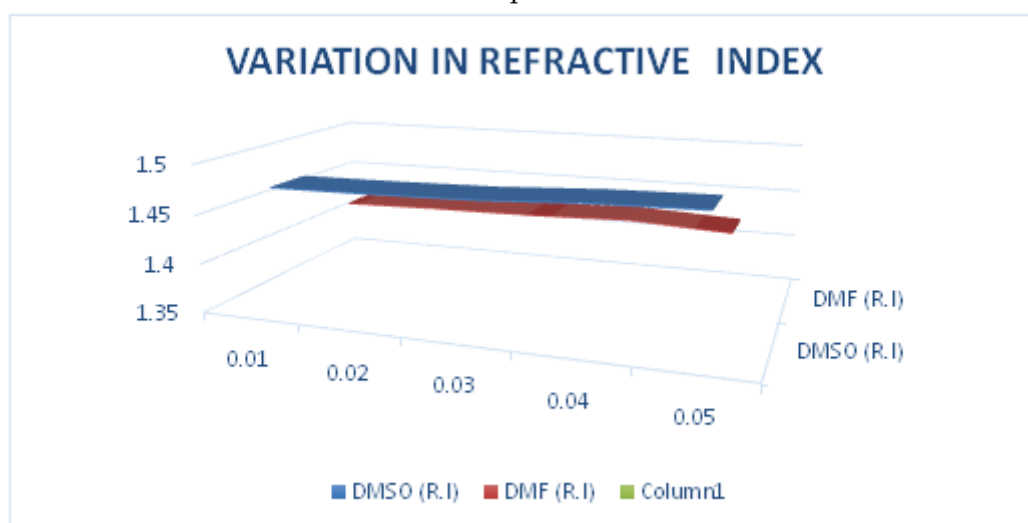
The knowledge of the coefficient of viscosity and its variation with temperature helps us to choose a suitable lubricant for specific machines. In light machinery thin oils (for example, lubricant oil used in clocks) with low viscosity is used. In heavy machinery, highly viscous oils (example: grease) are used. In this experiment it's clear that, the temperature and concentration decreases the viscosity decreases due to a decrease in solute-solute interactions. The viscosity in DMF solvent is lower than DMSO is due to density and less interaction between solute and solvent molecules.

Refractive Index:

The experimental values of refractive index of synthesized heterocyclic chalcone in different solvents are given in following table

CONC.	DMSO	DMF
(M)	R.I.	R.I.
0.01	1.472	1.423
0.02	1.473	1.425
0.03	1.475	1.426
0.04	1.480	1.429
0.05	1.482	1.434

Graph-01



Refractive index is useful to measure the optical density of the medium. A medium having a greater value of refractive index is said to be optically denser than that having a lower value. The current study explains that DMSO has a greater optical density than DMF. The refractive index changes by changing the solvent due to different solute-solvent interactions. The above data clearly shows that the concentration of the solution is directly proportional to the refractive index.

IV. CONCLUSION

It is concluded that properties like density and viscosity change by changing solvents, temperature, and concentration due to different interactions of solute-solvent molecules, and the value of the refractive index changes due to the polarity and the hydrogen bonding ability of the solvents.

V. REFERENCES

- [1]. F.Lunardi, M. Guzela, A.T. Rodrigues, R. Correia, I. Eger-Mangrich, M.steindel, E.C.Grisard, J.Assreuy, J.B.Calixto, R.S.Santos .Trypanocidal and leishmanicidal properties of substitution-containing chalcones. *Antimicrob. Agents Chemother.*, 47(4), 1449–1451(2003).
- [2]. B. A. Bhat, K. L. Dhar, A. K. Saxena and M. Shanmugavel, *Bioorg. Med. Chem.*, 15(3)177 (2005).
- [3]. L. E. Michael, M. S. David and S. S. Parsad, *J. Med. Chem.*, 33, 1948 (1990).
- [4]. M.Sivakumar, S.Phrabu Sreeneivasan, V.Kumar, M.Doble; *Bioorg.Med.Chem.Lett.*, 17(10), 3169 (2007).
- [5]. M.W.Weber, L.A.Hunsaker, S.F.Abcouwer, L.M.Decker, D.L.Vander Jagat; *Bioorg.Med. Chem.*13, 3811(2005).
- [6]. K.L.Lahtchev, D.I.Batovska, St.P.Parushev, V.M.Ubiyovok, A.A.Sibirny; *Eur.J.Med.Chem.* 43(1),1 (2008).

- [7]. V.S.Parmer, K.S.Bishit, R.Jain, S.Singh, S.K.Sharma, S.Gupta, S.Malhotra, O.D.Tyagi, A.Vardhan, H.N.Pati, D.V.Berghe, A.J.Vlietnek; *Indian J.Chem.*, 35(B), 220 (1996).
- [8]. (a) A.Modzelewska, C.Pettit, G.Achanta, N.E.Davidson, P.Huang, S.R.Khan; *Bioorg.Med.Chem.*, 14, 3491 (2006); (b) B.Ngameni, M.Touaibia, R.Patnam, A.Belkaid, P.Sonna, B.T.Nagaduji, B.Annabi, R.Roy; *Phytochem.*, 67,2573 (2006).
- [9]. J.N.Dominguez, C.Leon, J.Rodrigues; *J.IL Farmaco.*, 60(4), 307 (2005).
- [10]. Y.Xia, Z.Y.Yang, P.Xia, K.F.Bastow, Y.Nakanishi, K.H.Lee; *Bioorg.Med.Chem. Lett.*,10, 609 (2006).
- [11]. K.Miki, A.Kosho, Y.Hayashida; *Exp.Physiol.*,87(1), 2281 (2010).
- [12]. (a) X.Liu, M.L.Go; *Bioorg.Med.Chem.*, 14, 153 (2006); (b) L.Delmulle, A.Bellahcene, W.Dhooge, F.Comhaire, F.Roelens, K.Huvaere, A.Heyerick, V.Castronovo, D.D.Keukeleire; *Phytomed.*, 13, 732 (2006).
- [13]. R.Arulkumaran, R.Sundararajan, G.Vanangamudi, M.Subramanian, K.Ravi, V.Sathiyendiran, S.Srinivasan, G.Thirunarayanan; *IUP J.Chem.*, 3(1),82 (2010).
- [14]. J.Deng, T.Sanchez, Q.A.M.Lalith; *Bioorg.Med. Chem.*, 15(14), 4985 (2007).
- [15]. G.Thirunarayanan; *J.Indian Chem.Soc.*, 84, 447 (2008).
- [16]. G.Thirunarayanan, S.Surya, S.Srinivasan, G.Vanangamudi, V.Sathyendiran; *Spectrochim Acta.*, 75A, 152 (2010).
- [17]. D. Israf, T. Khaizurin, A. Syahida, N. Lajis, S. Khozirah, Cardamonin inhibits COX and iNOS expression via inhibition of p65NF-kappa-B nuclear translocation and I-kappa-B phosphorylation in RAW 264.7 macrophage cells, *Mol.Immunol.*, 44,673 (2007).
- [18]. D.W. Kim, M.J. Curtis-Long, H.J. Yuk, Y. Wang, Y.H. Song, S.H. Jeong, K.H. Park, Quantitative analysis of phenolic metabolites from different parts of *Angelica keiskei* by HPLC-ESI MS/MS and their xanthine oxidase inhibition, *FoodChem.*, 153, 20 (2014).
- [19]. R. Kidal and N. H. Ince, *Ultrasonics*, 13(2), 195 (2006).
- [20]. P. D. Singh, S. R. Hashim and R. G. Singhal, *Int. J. Drug Dev. Res.*, 2(4), 810-815(2010).
- [21]. S. Noorulla, N. Sreenivasulu, *Int. J. Res. Pharm. Bio. Sci.*, 2(3), 1100-1106 (2011).
- [22]. C. K. Rath, N. C. Raut, S. P. Das and P. K. Mishra, *Abstract of Volume*, 8(2), (2012).
- [23]. S. Baluja, K. P. Vaishnani, R. Gajera and N. Kachhadi, *Lat. Am. Appl. Res.*, 40(3),249-254 (2010).
- [24]. M. N. Roy, D. Ekka, I. Banik and A. Majumdar, *Thermochimica Acta*, 5(47), 89-98(2012).
- [25]. P. B. Raghuwanshi and A. D. Deshmukh, *Int. J. Chem. Sci.*, 11(1), 313-320 (2013).
- [26]. S. N. Khattab, S. Y. Hassan, A. A. Bekhit, A. M. Elmassry, V. Langer and A. Amer, *J.Eur. J. Med. Chem.*, 45, 4479-4489 (2010).



To Study the Adsorption Behaviour of Cobalt (II) Metal Ions from Aqueous Solution Using Low-Cost Adsorbent

A. K. Wanjari*, U. E. Chaudhari, R.S. Talegaonkar

Department of Chemistry, Mahatma Fule Arts, Commerce and Sitaramji Chaudhari Science College, Warud, Maharashtra, India

ABSTRACT

Water contaminated with cobalt (II) cause various deceases in leaving and non-leaving organisms. Removal of such kind of metal ion`s is the need of current era. Present study deals with the removal of cobalt(II) metal ions from the aqueous solution using low-cost adsorbent. The activated charcoal prepared from bone char used as a low-cost adsorbent. The various parameters like effect of pH, adsorbent dose, contact time and effect of temperature was examined for the retrieval of Co(II). Surface characterization of adsorbent was done by using SEM and FTIR. The experimental data fitted with Langmuir and Freundlich adsorption isotherm.

Keywords:-Cobalt(II), Adsorption, Bone Char, Langmuir, Freundlich

I. INTRODUCTION

Rapid urbanization and industrialization cause the contamination of water with toxic metal ions because of their known toxic effects on the receiving environment and also on the performance of biological treatment processes [1-3]. Removal of these kind of toxic metal ions from wastewater is now very important. On the other hand, the performance of wastewater treatment processes in terms of metal. Therefore, recovery of heavy metals from wastewater became an important environmental issue, recently[4-5]. Environmental pollution has become a key focus of concern for all the nations worldwide, as not only the developing countries but developed nations as well are affected by and suffer from it [6-8]. The water of aquatic systems gets polluted by domestic activities, mining activities, municipal wastes, modern agricultural practices, marine dumping, radioactivewastes, oil spillage, underground storage leakages and industries. Conventional methods for the removal of Co(II) from wastewaters include chemical precipitation, ion exchange, filtration, chemical reduction, electrodepositing and adsorption on activated carbon [8-10]. But due to operational demerits and high cost of the treatment, some new technologies have been tried for a long time. Among them less expensive non conventional adsorbents are being investigated. Many reports have appeared on preparation of activated carbon from cheaper and readily available materials [8,11].

II. MATERIAL AND METHOD

Preparation of solutions

The stock solution of Co(II) were prepared by dissolving $\text{Co}(\text{NO}_3)_2 \cdot 6\text{H}_2\text{O}$ in double distilled water. The analytical grade salts used for analysis. The desired solutions were obtained by diluting the stock solution in double distilled water.

BATCH STUDY METHOD

Effect of pH

pH plays an important role while removing the metal ions from aqueous solution or wastewater. In this study effect of was studied in the pH range 2-6. In the study it was observed that on increasing pH the metal ions uptake on adsorbent also increases. At higher pH the effect of competition from H^+ ions decreases and metal ions get adsorbed on the surface of adsorbent. The optimum pH was chosen for adsorption of Co(II) 4.0 shown in fig-I.

Effect of Contact Time

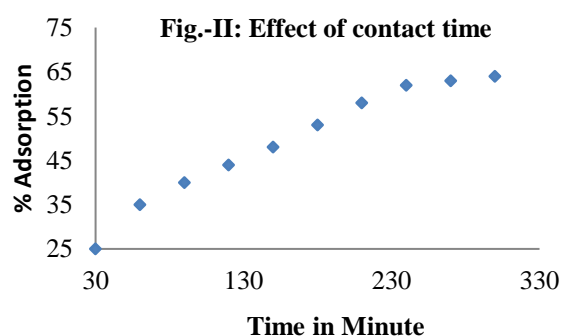
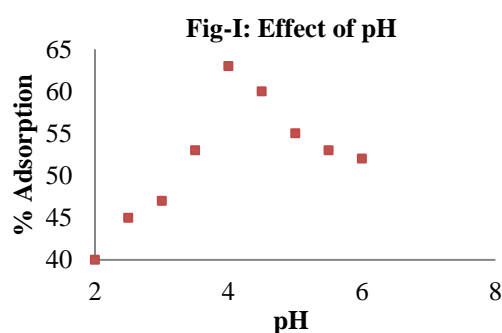
The effect on contact time on the uptake of the studied cations on to the adsorbent is shown in Fig.2.this was achieved by varying the contact time from 30 to 300 minutes. Equilibrium contact time was found to be 360 minutes for Co(II). The removal efficiency for Co(II) at these contact time was 66%. Result shown in Fig-II.

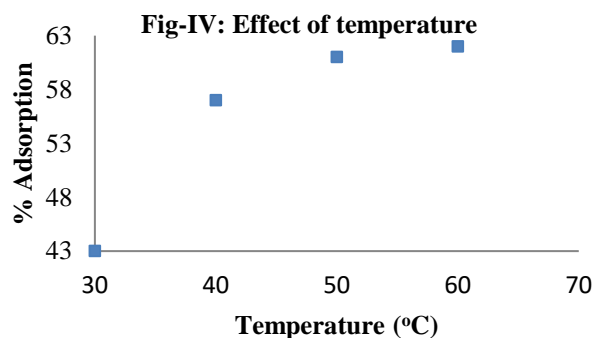
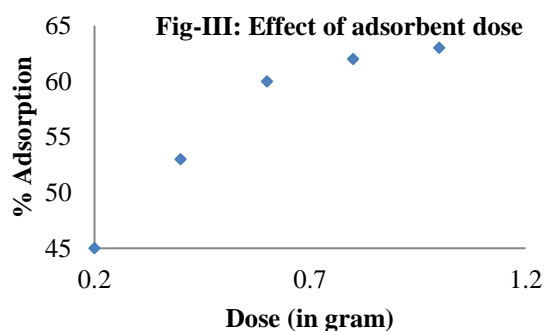
Effect of Adsorbent Dose

The effect of varying the adsorbent dosage from 0.2–1 gram for adsorption of Co (II) from their aqueous solutions having known volume of initial concentration was studied at respective pH as studied earlier. It has been found that the percent removal of Co (II) increases with increase in adsorbent dose up to some extent, thereafter further increase adsorbent dose. This is due to availability of more functional groups and surface area at higher dosages. Result shown in fig-III.

Effect of Temperature

Effect of temperature was studied by varying the temperature from 30°C to 60°C with working volume 200 ml having known concentration. Study was carried out at pH 5.0 and at 1000 rpm with contact time 3 hours. As the temperature increases porosity increases and percent of adsorption increases up to certain extent and then remains constant this is due to chemisorptions process.Result shown in fig-IV.





ADSORPTION ISOTHERMS

Equilibrium isotherm equations are used to describe the experimental adsorption data. The parameters obtained from the different models provide important information on the sorption mechanisms and the surface properties and affinities of the adsorbent. The most widely accepted surface adsorption models for single-solute systems are the Langmuir and Freundlich models. The correlation with the amount of adsorption and the liquid-phase concentration was tested with the Langmuir and Freundlich isotherm equations. Linear regression is frequently used to determine the best-fitting isotherm, and the applicability of isotherm equations is compared by judging the correlation coefficients.

Langmuir Adsorption Isotherm: -

In Langmuir adsorption isotherm Q_0 values found to be comparable with commercial activated carbon. Value of R_L lies between 0 and 1 indicate the favourable adsorption. It indicates the applicability of Langmuir adsorption isotherm. The calculated value R^2 confirms the applicability of Langmuir adsorption isotherm shown in table 1.

Freundlich Adsorption isotherm: -

Freundlich plot for the adsorption of Co (II) on AC-PETB shows that the values of adsorption intensity $1/n < 1$, reveal the applicability of Freundlich adsorption shown in table 1.

Table 1: Adsorption Isotherm Constants

System	Langmuir Isotherm				Freundlich Isotherm		
	Q_0	b	R_L	R^2	K_f	$1/n$	R^2
Activated Charcoal of bone char	6.2562	0.0187	0.1425	0.999	2.1254	0.2015	0.998

III. CONCLUSION

Adsorption of Co(II) metal ions from aqueous solutions using activated charcoal as adsorbent was studied. The following results were obtained: These studies show that activated charcoal prepared from the bone char is an inexpensive adsorbent for Co(II) removal from aqueous solutions. The adsorption of Co(II) ions on activated charcoal was dependent on the pH, quantity adsorbent dose, temperature and contact time. Amount of

removal of Co(II) metal ions from aqueous solution on activated charcoal was found to be maximum at pH 4. The equilibrium time for the adsorption of Co(II) ions on activated charcoal from aqueous solutions is estimated 300 minutes. The adsorption process of Co(II) ions can be described by Langmuir isotherm and Freundlich isotherm model. The process of adsorption is economically feasible, easy to handle in small scale and large scale also. Regeneration studies are not necessary with the view that the cost of the adsorbent is very low and it can be disposed of safe. It is calculated that the adsorbent prepared from bone char could be exploited for commercial application.

IV. REFERENCES

- [1]. A.K. Wanjari, Evaluation of Adsorption Efficiency of *Ferronia Elefantum* Fruit Shell for Rhodamine-B Retrieval from Aqueous Solution, *International Journal Of Pharmaceutical And Chemical Sciences*, Vol. 2 (1) Jan-Mar 2013, 457-460.
- [2]. A.K. Wanjari and U. E. Chaudhari, Removal Of Cr(VI), Pb(II), Mn(II) And Bi(III) From Aqueous Solutions Using Granular Activated Charcoal Prepared From *Cordia Macleodii* Tree Bark. *Rasayan J. Chem.*, 10(1), 82-85(2017) [Http://Dx.Doi.Org/10.7324/Rjc.2017.1011556](http://dx.doi.org/10.7324/Rjc.2017.1011556)
- [3]. Bareket, G., Aroguz, A.Z., Ozel, M.Z., 1997. Removal of Pb(II), Cd(II) and Zn(II) from aqueous solution by adsorption on bentonite. *J. Colloid Interface Sci.* 187, 338–343.
- [4]. Petrov, N., Budinova, T., Khaveson, I., 1992. Adsorption of zinc, cadmium, copper and lead ions on oxidized anthracite. *Carbon* 30, 135–139.
- [5]. M.A.A. Zaini, K. Yoshihara, R. Okayama, M. Machida, H. Tatsumoto, Effect of out gassing of ZnCl₂-activated cattle manure compost (CMC) on adsorptive removal of Cu(II) and Pb(II) ions, *TANSO* 234, 220–226, 2008.
- [6]. Wanjari AK et al., Physico-Chemical Investigation of Quality of Drinking Water Affected by Ganapati Visarjan in Maharashtra, India. *American Journal of PharmTech Research* 2015.
- [7]. Babel S. and Kurniawan T.A. Cr (VI) removal from synthetic wastewater using coconut shell charcoal and commercial activated carbon modified with oxidizing agents and/or chitosan. *Chemosphere*, 5(7), 951-967, 2004.
- [8]. Atul K. Wanjari, Adsorption of manganese (II) by nitric acid treated granular activated charcoal prepared from *Cordia Macleodii* tree bark, *Der Pharma Chemica*, 2016, 8(18):87-94.
- [9]. C. Moreno-Castilla, M.A. Alvarez-Merino, M.V. Lopez-Ramon, J. Rivera-Utrilla, "Cadmium ion adsorption on different carbon adsorbents from aqueous solutions. Effect of surface chemistry, pore texture, ionic strength, and dissolved natural organic matter", *Langmuir* 20, 8142– 8148, 2004.
- [10]. Namasivayam.C. Kadirvelu, K., 1994. Coirpith: an agricultural waste by-product for the treatment of dyeing wastewaters. *Bioresour. Technol.* 48, 79–81.
- [11]. Kumar, P., Dara, S.S., 1980. Modified barks for scavenging toxic metal ions. *Indian J. Environ. Health* 22, 196–202.



A Comparative Dielectric Study of Methanol-Water and Glycerol-Water Mixtures Using TDR

Bharose N.A.¹, Chavan S.D.¹, Kumbharkhane A.C.¹

¹School of Physical Sciences, SRTM University, Nanded, Maharashtra, India

ABSTRACT

Time domain reflectometry (TDR) technique has been used in frequency range 10MHz to 20GHz to determine the dielectric parameters at room temperature. A comparative dielectric study have been done between methanol-water and Glycerol-water mixture. Relaxation time gives orientation relation between two mixtures. Dielectric constant & Kirkwood correlation factor have been studied for molecular interaction between two mixtures.

Keywords: - Methanol, Glycerol, water, TDR, dielectric parameters

I. INTRODUCTION

Primary alcohol methanol is hydrogen bonded alcohol, having formula CH_3OH and molecular weight 32.04 g/mol and density 0.792 g/cm³. Methanol-water H_2O mixtures dielectric properties have been studied previously [1]. Alcohols are an associating liquid that can donate and accept the hydrogen bonds in the water mixture. Since solution properties of alcohols particularly in aqueous solution are of considerable interest due to their non-ideal nature and hydrogen bonding network [1-4]. Extensive experimental dielectric studies have been carried out on alcohol-water mixtures in order to investigate the hydrogen bond structure and intermolecular rotation in these mixtures.[1-4]. The static and dynamic dielectric properties of alcohols-water mixtures have also been studied. Glycerol [5] have chemical formula $[\text{C}_3\text{H}_5(\text{OH})_3]$ and molecular weight 92.09 g/mol and density 1.261g/cm³. Methanol and Glycerol both the liquids have industrial importance and also both are soluble in water. There are some basic differences between both the liquids, methanol has one carbon atom and glycerol have 3 carbon atoms. Molecular weight of glycerol is three times greater than the methanol. Therefore in this paper we studied comparative differences of dielectric properties between these two aqueous solutions.

II. EXPONENTIAL TECHNIQUE

The dielectric permittivity of all alcohol-water mixtures were measured by TDR in the frequency range between 10 MHz to 20GHz. The Hewlett Packard HP54750 sampling oscilloscope with HP 5475A. A TDR plug in module has been used. A fast rising step voltage pulse of about 40ps rise time was propagated through

a coaxial line system. SMA sample cell with 3.5mm outer diameter and 1.35mm effective Pin length was used. All measurements were done under open load conditions. The time window chosen for the measurements was kept at 5ns. First, the reflected pulse $R_1(t)$ and $R_x(t)$ without and with sample in the cell, respectively was recorded. The pulse Reflected through the sample $R_x(t)$ was compared with the reflected pulse without sample $R_1(t)$. [6-8]

III. RESULT AND DISCUSSION

The dielectric relaxation parameters namely such as static dielectric constant (ϵ_0), relaxation time (τ) and distribution parameters (α and β) are obtained by the non-linear least squares method to the Havriliak-Negami expression. [9]

$$\epsilon^*(\omega) = \epsilon_\infty + \frac{(\epsilon_0 - \epsilon_\infty)}{[1 + (j\omega\tau)^{1-\alpha}]^\beta} \quad (1)$$

With ϵ_0 , ϵ_∞ , τ , α and β are the fitting parameters. The equation includes the Cole-Cole ($\beta = 1$), Davison-Cole ($\alpha = 0$) and Debye ($\alpha = 0, \beta = 1$) relaxation model. The values of the errors are estimated by assuming 2% errors in the values of ϵ' and ϵ'' from the goodness of fit of the data with eq.(1).

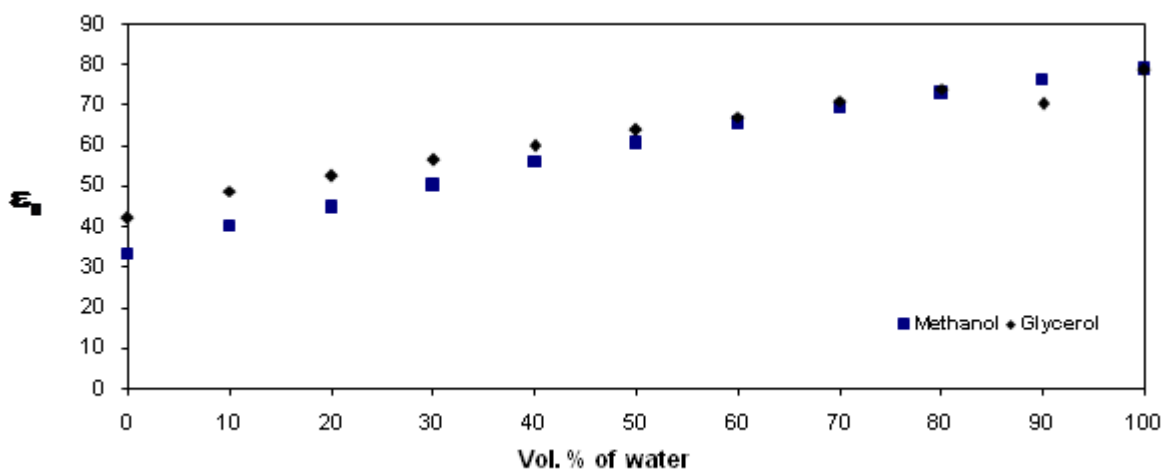


Fig.1. Static dielectric constant Vs Vol. % of water of methanol and Glycerol

Variation of the static permittivity (ϵ_0) as a volume fraction of water concentration is shown in Fig.1. The static permittivity increases as the concentration of water in methanol increases. Similar pattern is observed in static dielectric constant of glycerol-water mixture at room temperature. Glycerol-Water mixture have same pattern like methanol-water mixture but glycerol-water mixture have greater value than the methanol-water mixture. It may be due to larger no. of carbon atoms in glycerol than methanol. Dielectric constant of pure glycerol is greater than the pure methanol.

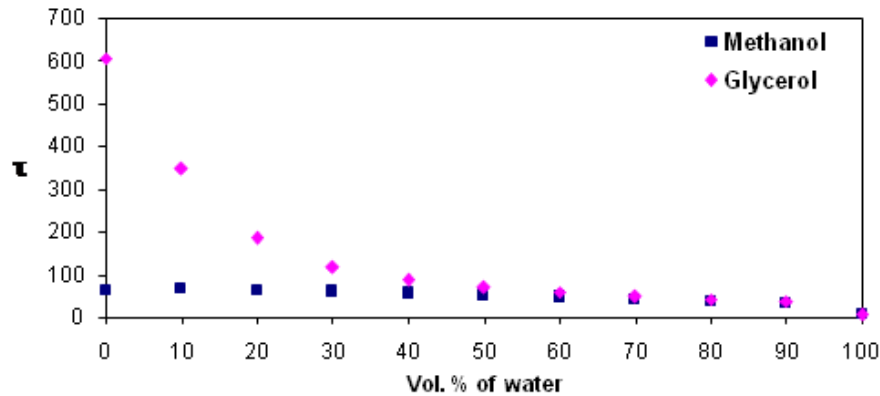


Fig.2. Relaxation time Vs Vol. % of water of methanol and Glycerol

Relaxation time (τ) of methanol-water and glycerol-water mixtures are as shown in Fig.2. The relaxation time (τ) decreases as the concentration of water increases in both the mixtures. But the relaxation time of glycerol-water mixture decreases sharply as compare to methanol-water mixture. There is large difference in relaxation time between methanol and glycerol because due to two extra carbon atoms in glycerol than methanol and also due to molecular weight of glycerol is nearly three times greater than methanol.

The Kirkwood correlation as determined from the dielectric constant gives information about collective orientation correlation between molecules.[10-12] The calculation of Kirkwood correlation factor ' g ' provides information regarding the hindrance of molecular orientation by neighbouring molecules. The deviation of ' g ' from unity is a measure of degree of hindered relative molecular motion arising from short range intermolecular forces. When the molecules tend to direct themselves with parallel dipole moments, ' g ' will be greater than unity. If the molecules prefer an ordering with anti parallel dipoles, ' g ' will be smaller than unity.

For a mixture, the Kirkwood correlation factor ' g ' can be expressed as follows:

$$\left[(\epsilon_{0i} - \epsilon_{\infty i}) (2\epsilon_{0i} + \epsilon_{\infty i}) / 9\epsilon_{0i} \right] = 4\pi/9kT \sum_{i=1}^2 g_i \rho_i \mu_i^2 \quad (2)$$

where $i=1,2$ represent water and alcohol, respectively; μ_i is their dipole moment in gas phase, ρ_i is the density, k is the Boltzmann constant, T is the temperature, ϵ_{0i} and $\epsilon_{\infty i}$ are the static dielectric constant and dielectric constant at high frequency. ' g_i ' is the Kirkwood correlation factor for the i^{th} liquid system.

The interpretation of the dielectric phenomena in terms of the Kirkwood correlation factor is very difficult for mixtures of associating compound.

(i) In the first model, we have assumed that the mixture can be represented by one correlation factor g^{eff} as follows:

$$\left[(\epsilon_{0m} - \epsilon_{\infty m}) (2\epsilon_{0m} + \epsilon_{\infty m}) / 9\epsilon_{0m} \right] = [4\pi/9kT] g^{\text{eff}} [\rho_m \mu_m^2] \quad (3)$$

To calculate g^{eff} values, we have taken dipole moment of methanol, glycerol and water as 1.70D, 2.67D and 1.84D respectively. The value ($\epsilon_{\infty m}$) is taken as the square of the refractive index data. We believe that g^{eff}

defined by eq.(3) is a reasonable measure of the molecular correlation. Fig.3 shows that the value of methanol-water twice of glycerol-water. The high values of g^{eff} indicate average parallel orientation of electric dipoles in a molecule. It can be seen that as water is added in methanol and glycerol at regular steps in the mixture, the difference in the values of g^{eff} between methanol and glycerol shows association variation between two aqueous solutions. The correlation factor is essentially connected to the total orientation polarization and the dominating contribution to it is embodied in $(\epsilon_{0m} - \epsilon_{\infty m})$. To calculate the Kirkwood correlation factor (g^{eff}) from eq. (3) is not fully legitimate since in the investigating binary system, the water-water, water-methanol, water-glycerol and methanol-methanol, glycerol-glycerol correlation exist.[13]

(ii) It is impossible to determine ' g_1 ' and ' g_2 ' from a single value of the static dielectric constant without some assumption. In the second model, the Kirkwood correlation factors for individual species $i = 1, 2$ are modified by assumed for methanol-water, glycerol-water mixtures that two kinds of intermolecular hydrogen bonds exist. One is the hydrogen bond between the water-water molecules, another is the hydrogen bond between the methanol, glycerol and water molecules. These new correlations (g_1 and g_2) are described by the relation as follows

$$g_1 = 1 + Z_{11} \cos\varphi_{11} + Z_{12} \cos\varphi_{12} (\mu_2/\mu_1) \tag{4}$$

$$g_2 = 1 + Z_{21} \cos\varphi_{21} (\mu_1/\mu_2) \tag{5}$$

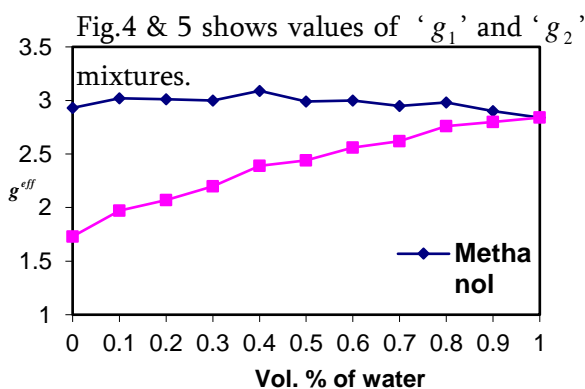


Fig.3

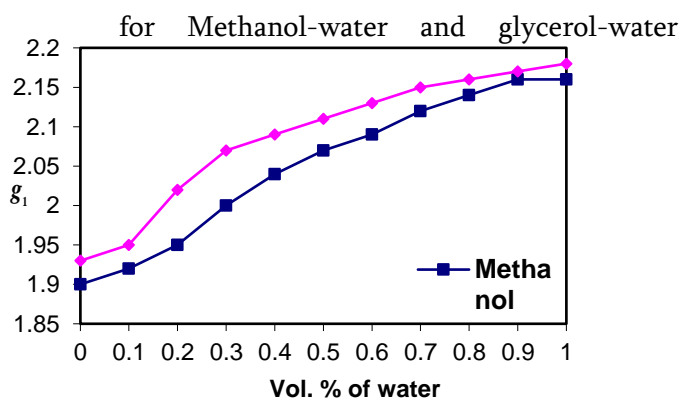


Fig.4

Fig.3. Variations of g^{eff} values for methanol and Glycerol with water mixtures.

Fig.4. g_1 values for different methanol and Glycerol with water mixtures.

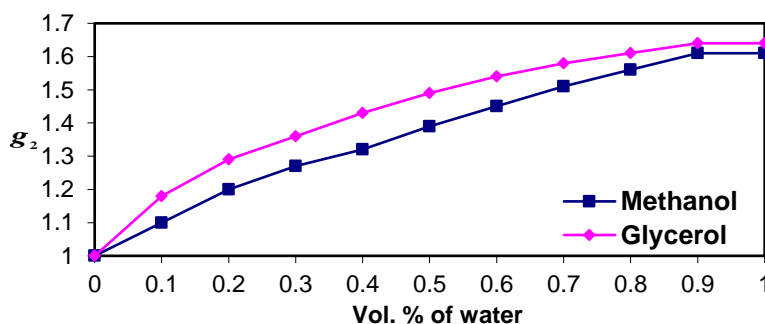


Fig.5. g_2 values for different methanol and Glycerol with water mixtures.

IV. CONCLUSIONS

In this paper comparative dielectric study have been done between methanol and glycerol aqueous solutions. Static dielectric constant of both the mixture have same pattern but there is large difference in glycerol-water mixture and methanol-water mixture due to maximum no. of carbon atoms in glycerol. Relaxation time of methanol-water mixture have smaller values than glycerol-water mixtures because molecules of glycerol are more bulky. We found the Kirkwood correlation factor for both mixtures shows difference in association effect.

V. ACKNOWLEDGMENT

Sincere thanks to Dr.A.C.Kumbharkhane for his constant support in research activity.

VI. REFERENCES

- [1]. K S Kanse, S D Chavan, C S Mali, A C Kumbharkhane and S C Mehrotra, Indian J. Phy., 80(3) (2006) 265.
- [2]. H Tanaka and G E Gubbins, J. Chem. Phys., 97 (1992) 2626.
- [3]. A Laaksonen, P G Kusalik and I M Svishchev, J. Phys. Chem., A101 (1997) 5910.
- [4]. G Palinkas, E Hawlicka and K Heinzinger, Chem. Phys., 158 (1991) 65.
- [5]. S D Chavan, A C Kumbharkhane and S C Mehrotra, J. Indian Chem.Soc., 84 (2007) 354.
- [6]. S M Puranik, A C Kumbharkhane & S C Mehrotra, J. Microwave Power & Electromagnetic Energy, Vol. 26(3) (1991) 119.
- [7]. A C Kumbharkhane, S M Puranik & S C Mehrotra, J. Chem. Soc. Faraday Trans., 87(10) (1991) 1569.
- [8]. A C Kumbharkhane, S N Helambe, S Doraiswamy & S C Mehrotra, J. Chem. Phys., 99 (4) (1993) 2405.
- [9]. S Havriliak & S Negami, Polymer, 8 (1967) 161.
- [10]. J B Hasted, "Aqueous Dielectric", (London : Chapman and Hall) (1973)
- [11]. A C Kumbharkhane, S N Helambe, S Doraiswamy, S C Mehrotra, J. Chem. Phys., 99(4) (1993) 2405.
- [12]. A C Kumbharkhane, S M Puranik, S C Mehrotra, J. Mol. Liq., 51(1991) 307.
- [13]. J B Hasted, "Aqueous dielectric", [Chapman and Hall London.] (1973)

Chalcone: Synthesis and Experimental Study of New Promising Medicinal Compound

Ingle G.B.^{1*}, Gotmare P.A.¹, Dr.KolheS.V.¹

¹Department of Chemistry, Shri Shivaji Art's, Commerce and Science College, (Affiliated To Sant Gadge Baba Amravati University, Amravati), Akot-444101, Maharashtra, India

ABSTRACT

Chalcone is a common natural pigment and one of the important intermediates in flavonoid biosynthesis. Medicinal chemists continue to be fascinated by chalcone derivatives because of their simple chemistry, ease of hydrogen atom manipulation, straightforward synthesis, and a variety of promising biological activities. The present work was undertaken to study about method of synthesis, characterization done by NMR, Mass, and IR spectroscopic techniques and different physical properties with experimental data such as molecular weight, density, refractive index and viscosity of chalcones.

Keywords : Chalcone, Molecular weight, Density, Refractive index, Viscosity etc.

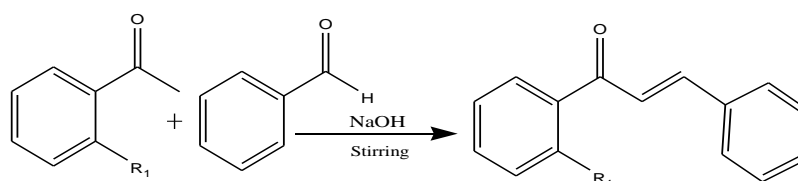
I. INTRODUCTION

Chalcone, 1, 3-diphenyl-1-propen-1-one is a very important compound in nature. Chalcones contain two aromatic rings and one carbon atom α , β -unsaturated. Chalcone, as a precursor of flavonoids and isoflavonoids that are widely found in Indonesian plants. Chemically, chalcone consists of open chain flavonoids in which two aromatic rings join with three carbons in the α , β -unsaturated carbonyl system¹. Chalcone is synthesized by Claisen-Schmidt condensation, which involves the cross-Aldol condensation of aldehydes and ketones with a base or acid catalyst followed by a dehydration reaction. Chalcone is a common natural pigment and one of the important intermediaries in flavonoid biosynthesis². Studies revealed that compounds with a chalcone-based structure possess a wide variety of biological activities⁴, such as anti-inflammatory⁵, anti-bacterial^{6,7}, anti-fungal⁸⁻¹⁰, anti-oxidant¹¹ and anticancer activities^{12,13}. Chalcones are multifunctional molecules, since one particular structure can show multiple biological activities. These compounds are known to be excellent scaffolds for synthetic manipulation with multiple pharmacological properties¹⁴⁻¹⁷. Various other industrial and pharmaceutical applications of chalcones have also been reported¹⁸⁻²¹.

It was reported to have wide range of applications in the fields of biology and biochemistry^{22,23} such as antitumor^{24,25}, anti-inflammatory²⁶⁻²⁸, and antimalaria²⁹ agents. Besides, it is also reported in its photochemical and photo physical properties as well, including being used as photo alignment and photo cross linking unit in polymerization process³⁰, fluorescent dyes, light-emitting diodes (LEDs), and so forth³¹.

II. EXPERIMENTAL

I. Synthesis: The experiment was started by adding substituted acetophenone and benzaldehyde in a round bottom flask, and then ethanol was added to the flask. Then to the mixture was added base solution, the addition was done with stirring. After mixing, the mixture is allowed to stand for 24 hours at room temperature. Then the crude product formed is filtered and washed. Furthermore, recrystallization with ethanol is carried out, then the filtered filtrate is evaporated and dried at room temperature. The yield of hydroxyl substituted chalcone was higher than the compound which was not substituted. It can be concluded that the synthesis results in hydroxyl substituted chalcone derivatives have higher yields compared to chalcone derivatives without hydroxyl substitution.



II. Physicochemical studies of synthesized chalcone: Refractive Index along with density, molecular mass and specific volume is very useful in the evaluation of various thermodynamics properties of chemical materials. Further, solution crystallization is a key step for industrial purification process, which control product quality such as purity, yield, and crystal size distribution.

The solvents dimethyl formamide (DMF i.e. solvent A) and dimethyl sulfoxide (DMSO i.e. solvent B) were used for the physicochemical studies. Various concentrations of solution were taken for the study and also the temperatures a variation was taken into considerations.

Table: 1: Physical parameters of synthesized Chalcone.

Sr. No.	Compound	Substitution	Molecular Formula	Molecular Weight	Yield
1	Chalcone	OH	C ₁₅ H ₁₁ O ₂	223	77 %

Measurement of density and viscosity:

The density measurements of pure solvents and solutions of chalcone have been done. The Ostwald's viscometer was used for the viscosity measurement. The flow time of water (*t_w*), and the flow time of solution, (*t_s*) were measured with a digital stop watch.

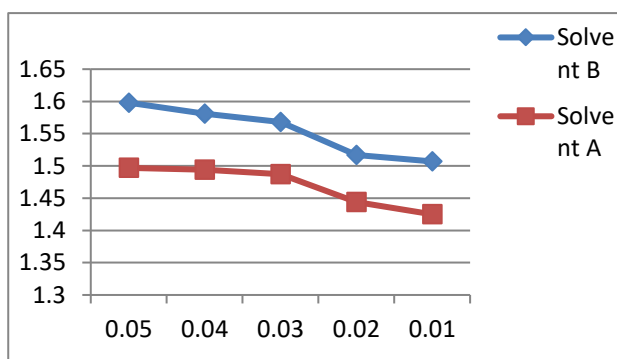
Refractive index:

The Abbe refractometer was used for the measurement of refractive index of solutions of synthesized compounds at 313.15 K.

III. RESULTS AND DISCUSSIONS:

I. Refractive Index of synthesized Chalcone: Values of refractive index are varies with various concentrations of solution at 313.15 K temperatures. The below table shows the dynamic values of refractive index.

Conc. (M) At 313.15 K	Solvent A	Solvent B
	RI	RI
0.05	1.497	1.598
0.04	1.494	1.581
0.03	1.487	1.568
0.02	1.444	1.517
0.01	1.425	1.507



II. Density and Viscosity of synthesized Chalcone:

The table below shows the dynamic experimental values of density (ρ), and viscosity (η), at different temperature and different concentrations.

Conc. (M) At 303.15K	Solvent A		Solvent B	
	Density(ρ) (g.cm^{-3})	Viscosity ($\eta \cdot 10^{-3}$)poise	Density(ρ) (g.cm^{-3})	Viscosity ($\eta \cdot 10^{-3}$)poise
0.05	0.9518	6.7452	1.1223	11.812
0.04	0.9493	6.7497	1.1213	11.778
0.03	0.9491	6.7551	1.1209	11.698
0.02	0.9489	6.7588	1.1202	11.641
0.01	0.9485	6.7623	1.1197	11.523

Conc. (M) At 308.15K	Solvent A		Solvent B	
	Density(ρ) (g.cm^{-3})	Viscosity($\eta \cdot 10^{-3}$)poise	Density(ρ) (g.cm^{-3})	Viscosity ($\eta \cdot 10^{-3}$)poise
0.05	0.9595	6.7295	1.1175	11.314
0.04	0.9591	6.7187	1.1168	11.265
0.03	0.9588	6.7110	1.1165	11.158
0.02	0.9581	6.7088	1.1121	11.113
0.01	0.9570	6.7023	1.1111	11.098

Conc. (M) At 313.15K	Solvent A		Solvent B	
	Density(ρ) (g.cm^{-3})	Viscosity(η , 10^{-3})poise	Density(ρ) (g.cm^{-3})	Viscosity (η , 10^{-3})poise
0.05	0.9614	6.583	1.1113	10.023
0.04	0.9609	6.494	1.1108	9.881
0.03	0.9604	6.437	1.1095	9.725
0.02	0.9599	6.382	1.1090	9.659
0.01	0.9587	6.284	1.1081	9.611

The above physical parameters show that, decrease in concentration of solution, the density and viscosity are decreased, while the same values were increased in increased temperatures. Table 1 shows the experimental values of refractive index of solutions of the new synthesized compound in solvent A and solvent B at 313.15 K. All tables shows the dynamic values of densities and viscosities of compound in various concentration and various temperatures with solvent A and solvent B.

IV. CONCLUSIONS

From above experimental values it is concluded that densities, viscosities and refractive index of solution are changes by changing temperatures and by changing the solvent due to solute-solvent interaction. It is also concluded that physicochemical properties of a compound depends on its structure and solvents in which it is dissolved. For compounds having same central moiety, nature of substitution plays an important role in solution due to which interactions changes in different solvents thereby affecting properties. Further, position of substitution in a compound also affects physicochemical properties.

V. REFERENCES

- [1]. Syam S., Abdelwahab S.I., Al-Mamary M.A.,Mohan S., *Molecules* 17(6), pp. 617 - 6195,2012
- [2]. Choudhary A. L.,JuyalV., *Int J Pharm Pharm Sci.* 3(3), pp. 125–128,2011.
- [3]. Mahapatra D. K., Bharti S. K., Asati V., *Eur J Med Chem* 98, pp. 69–114,2015.
- [4]. Dimmock JR, Elias DW, Beazely MA and Kandepu NM:Bioactivities of Chalcones *Curr Med Chem* 6: 1125-1149, 1999.
- [5]. Cheng JH, Hung CF, Yang SC, Wang JP, Won SJ and Lin CN:Synthesis and cytotoxic, anti-inflammatory, and anti-oxidantactivities of 2',5'-dialkoxychalcones as cancer chemo-preventitativeagents. *Bioorg Med Chem* 16: 7270-7276, 2008.
- [6]. Avila HP, Smania EF, Monache FD and Smania A Jr:Structure–activity relationship of antibacterial chalcones. *BioorgMed Chem* 16: 9790-9794, 2008.

- [7]. Tomar V, Bhattacharjee G, Kamaluddin and Kumar A: Synthesis and antimicrobial evaluation of new chalcones containing piperazine or 2,5-dichlorothiophene moiety. *Bioorg Med Chem Lett* 17: 5321-5324, 2007.
- [8]. Lopez SN, Castelli MV, Zacchino SA, Dominguez JN, Lobo G, Charris-Charris J, Cortes JC, Ribas JC, Devia C, Rodriguez AM and Enriz RD: In vitro antifungal evaluation and Structure activity relationships of a new series of chalcone derivatives and synthetic analogues, with inhibitory properties against polymers of the fungal cell wall. *Bioorg Med Chem* 8: 1999- 2013, 2001.
- [9]. Vargas MLY, Castelli MV, Kouznetsov VV, Urbina GJM, Lopez SN, Sortino M, Enriz RD, Ribas JC and Zacchino S: In vitro antifungal activity of new series of homoallylamines and related compounds with inhibitory properties of the synthesis of fungal cell wall polymers. *Bioorg Med Chem* 11: 1531-1550, 2003.
- [10]. Sortino M, Delgado P, Juarez S, Quiroga, J, Abonia R, Insuasty B, Nogueras M, Rodero L, Garibotto FM, Enriz RD and Zacchino SA: Synthesis and antifungal activity of (Z)-5-aryliden- γ -butyrolactones. *Bioorg Med Chem* 15: 484-494, 2007.
- [11]. Katsori AM and Hadjipavlou-Litina D: Chalcones in cancer: Understanding their role in terms of QSAR. *Curr Med Chem* 16:1062-1081, 2009.
- [12]. Achanta G, Modzelewska A, Feng L, Khan SR and Huang P: A boronic-chalcone derivative exhibits potent anticancer activity through inhibition of the proteasome. *Mol Pharmacol* 70: 426-433, 2006.
- [13]. Modzelewska A, Pettit C, Achanta G, Davidson NE, Huang P and Khan SR: Anticancer activities of novel chalcone and bischalcone derivatives. *Bioorg Med Chem* 14: 3491-3495, 2006.
- [14]. Maydt D., De Spirt S., Muschelknautz C., Stahl W., Muller T.J.J., Chemical reactivity and biological activity of chalcones and other α , β -substituted carbonyl compounds, *Xenobiotica*, 43(8), 711, 2013.
- [15]. Jandial D., Danielle A., Blair C., Zhang S., Krill S.L, Zhang Y.B., Zi X., Molecular targeted approaches to cancer therapy and prevention using chalcones, *Curr. Cancer Drug Targets*, 14, 181, 2014.
- [16]. Shah M.S., Khan S.U., Ejaz S.A., Afridi S., Rizvi S.U.F., Haq N., Iqbal J., Cholinesterases inhibition and molecular modeling studies of piperidyl-thienyl and 2-pyrazoline derivatives of chalcones, *Biochem. Biophys. Res. Comm.*, 482(4), 615, 2017.
- [17]. Wieslaw S., Grzegorz G., Aleksandra R., Isoflavones, their glycosides and glyco conjugates. Synthesis and biological activity, *Curr. Org. Chem.*, 21(3), 218, 2017.
- [18]. Zhou B., Xing C., Diverse molecular targets for chalcones with varied bioactivities, *Med. Chem.*, 5, 388, 2015.
- [19]. Ramkumar V., Anandhi S., Kannan P., Gopalakrishnan R., Substitution effect on chalcone Based materials for corrosion and photo cross linking applications, *RSC Adv.*, 5, 586, 2015.
- [20]. Tielas D., Graña E., Reigosa M.J., Sánchez-moreiras A.M., Biological activities and novel Applications of chalcones, *Planta Daninha*, 34(3), 607, 2016.
- [21]. Singh P., Anand A., Kumar V., Recent developments in biological activities of chalcones: A Min review, *Eur. J. Med. Chem.*, 85, 758, 2014.

- [22]. Bukhari S.N.A., Jasamai M., Jantan I., and Ahmad W, "Reviews of methods and various catalysts used for chalcone synthesis "Mini-Reviews in Organic Chemistry, vol. 10, pp. 73– 83, 2013.
- [23]. Bukhari S. N. A., Jasamai M., and Jantan I., "Synthesis and biological evaluation of chalcone derivatives (mini review)," Mini Review of Medicinal Chemistry, vol. 12, no. 13, pp. 1384– 1403, 2012.
- [24]. Saydam G., Aydin H. H., Sahin F. et al., "Cytotoxic and inhibitory effects of 4,4-dihydroxy chalcone (RVC-588) on proliferation of human leukemic HL-60 cells," Leukemia Research, vol. 27, no. 1, pp. 57– 64, 2003.
- [25]. Mishra L., Sinha R., Itokawa H. et al., "Anti-HIV and cytotoxic activities of Ru(II)/Ru(III) Polypyridyl complexes containing 2,6-(2-benzimidazolyl)-pyridine/chalcone as co-ligand," Bioorganic and Medicinal Chemistry, vol. 9, no. 7, pp. 1667–1671, 2001.
- [26]. Ko H.-H., Tsao L.-T., Yu K.-L., Liu C.-T., Wang J.-P., and Lin C.-N., "Structure-activity relationship studies on chalcone derivatives: the potent inhibition of chemical mediators release," Bioorganic and Medicinal Chemistry, vol. 11, no. 1, pp. 105–111, 2003.
- [27]. Tuchinda P., Reutrakul V., Claeson P. et al., "Anti-inflammatory cyclohexenyl chalcone derivatives in *Boesenbergia pandurata*," Phytochemistry, vol. 59, no. 2, pp. 169–173, 2002.
- [28]. Bukhari S. N. A., Jantan I., and Jasamai M., "Anti-inflammatory trends of 1, 3-diphenyl-2 – propen-1-one derivatives," Mini-Reviews in Medicinal Chemistry, vol. 13, pp. 87–94, 2013.
- [29]. J. N. Domínguez, C. León, J. Rodrigues, N. G. De Domínguez, J. Gut, and P. J. Rosenthal, "Synthesis and evaluation of new antimalarial phenylurenyl chalcone derivatives," Journal of Medicinal Chemistry, vol. 48, no. 10, pp. 3654–3658, 2005.
- [30]. Shi D. M., Song D. M., Jung K. H., and Moon J. H., "Photochemical transformation of chalcone derivatives," Journal of Photoscience, vol. 8, no. 1, pp. 9–12, 2001.
- [31]. Suwunwong T, Syntheses and fluorescent properties of chalcone derivatives and Heteroarylchalcones [M.S. thesis], Prince of Songkla University, Thailand, 2010.



Study of Structural and Magnetic Properties of Bi Substituted Nickel Spinel Ferrites

D. D.Mathankar¹, N. S. Meshram², K. G. Rewatkar²

¹Department of Physics, Dr. Ambedkar College Deekshabhoomi, Nagpur-440001, Maharashtra, India

²Vidya Vikas Arts, Commerce and Science College, Samudrapur, Maharashtra, India

ABSTRACT

Microwave-assisted sol-gel auto combustion was used to make spinel ferrite nanoparticles (NPs) of $Ni_{(1-(3/2)x)}Bi_xFe_2O_4$ with $x=0.0, 0.2$ and 0.4 (NPS).. X-ray diffraction (XRD) was used to determine the crystallite size of the produced NPs, which was found to be 28 and 40 nm, respectively. Coercivity H_c (167.82 Oe to 137.95 Oe), Magnetic Saturation M_s (37.257 to 25.543 emu/g), and retentivity M_r (9.0094 to 3.4970 emu/g) of $NiFe_2O_4$ and Bi^{3+} Substituted $NiFe_2O_4$ were measured using a Vibrating Sample Magnetometer. The substitution of trivalent metal ions (Bi^{3+}) alters the crystallite size and cation distribution in the tetrahedral and octahedral positions, causing structural and magnetic alterations.

Keywords: - Sol-gel Auto combustion, Nickel ferrites, Bismuth Ferrites, XRD, VSM, etc.

I. INTRODUCTION

Ferrites have long been investigated because they constitute an important class of magnetic materials with technological uses. It is well known that they may be used in applications ranging from low to high frequencies.[1] A ferrite has the typical chemical formula AFe_2O_4 , where A is a divalent element. The cubic ferrites feature an $MgAl_2O_4$ type spinel crystal structure. Ferrite is the spinel having the highest molar concentration of the metal ion Fe^{3+} , and it has ferrimagnetic characteristics [2]. Spinel's structure and crystal chemistry have been extensively studied in the literature. A spinel structure's unit cell includes 32 oxygen atoms packed closely together. Eight cations occupy the tetrahedral A-site, while sixteen occupy the octahedral site, forming a face centered cubic close-packed structure[3], [4]. The ionic radii, diameters of interstices, temperature, valences, and electrostatic energy all influence cation occupancy. The magnetic properties of ferrite are controlled by Fe^{3+} ions, which fluctuate in appearance as divalent (Fe^{2+}) or trivalent (Fe^{3+}) ions.

II. EXPERIMENTAL

The $Ni_{(1-(3/2)x)}Bi_xFe_2O_4$ spinel ferrites were prepared by the using analytical grade reagents [5]. Starting materials included the compounds ferric nitrate, bismuth nitrate, nickel nitrate, and urea. To make a

homogenous mixture, an aqueous solution of ferric nitrate, nickel nitrate, and bismuth nitrate were added in order, stirring constantly at 60–70 °C. A clear solution was formed from the brown–color citrate mixture [6]. Within five minutes, it is placed in the microwave oven, where brown fumes begin to emerge from the oven and the thick solution produced is fired to make a dark brown floppy powder. The powder is crushed for around 3 hours in a pestle mortar before being calcined at 800 °C for 4 hours and crushed again for 1 hour to obtain a nano ferrites sample ready for characterization. [5-6]

III. RESULTS AND DISCUSSION

1. Structural analysis

Figure 1 shows the X-ray diffraction (XRD) patterns of ferrite nanoparticles $\text{Ni}_{(1-(3/2)x)}\text{Bi}_x\text{Fe}_2\text{O}_4$ with $x=0.0, 0.2$ and 0.4 (NPS). The indexed plane of (220), (311), (222), (400), (422), (511), and (440) along with the JCPDS Card: 9006317 indicates the formation of cubic spinel ferrite with space group $\text{Fd-}3\text{m}$. [7] The XRD data show that pure NiFe_2O_4 has a single phase spinel structure. The inclusion of bismuth in small amounts does not alter the spinel structure of the ferrite system, but the presence of additional peaks in bismuth-containing samples indicates the presence of a secondary phase. [8] the effect of Bi^{3+} substitution on NiFe_2O_4 by utilizing the relation below to calculate crystallite size, lattice dimension, X-ray density, bulk density-spacing, lattice strain, dislocation density, hopping length, and porosity. [9] As the concentration of bismuth is increased, the crystallite size decreases. As indicated in table 1, it ranges from 28 to 40 nanometers. The crystallite size of the highest intense peak (311) was calculated using the Debye-Scherrer formula, [10]

$$D = \frac{0.9\lambda}{\beta \cdot \cos\theta} \quad (1)$$

where β is the FWHM of the resultant crystallite size in radians, θ is Bragg's angle, k is the spherical shape factor ($k=0.9$), and λ is the X-ray wavelength.

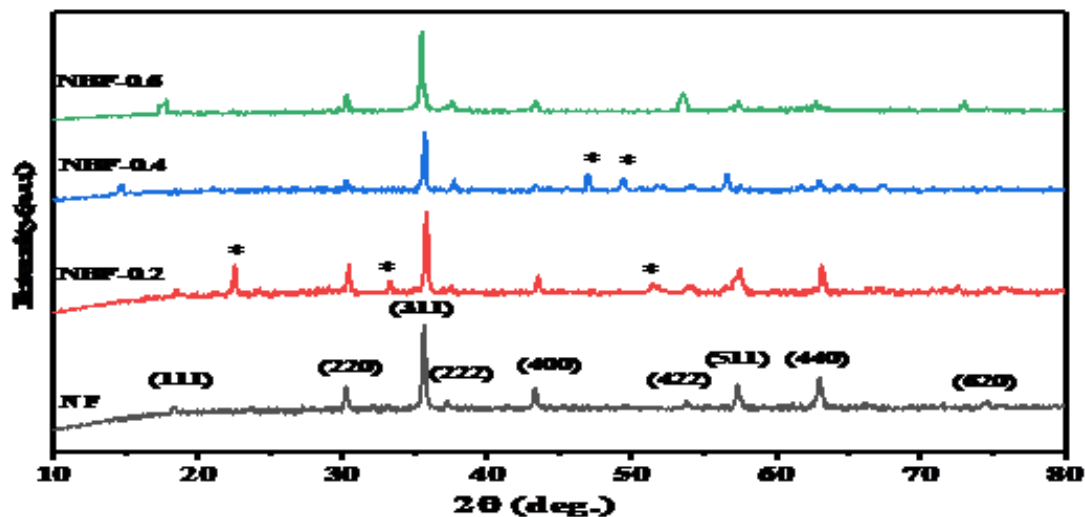


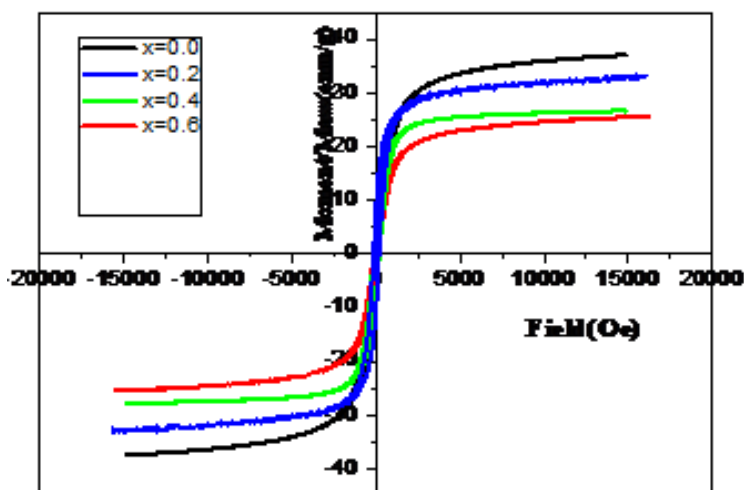
Figure 1 : XRD Image of $\text{Ni}_{(1-(3/2)x)}\text{Bi}_x\text{Fe}_2\text{O}_4$ ($x=0.0, 0.2, 0.4, 0.6$) Ferrites

Table 1: crystallite size, lattice parameter, x-ray density, bulk density of Ni_{(1-(3/2)x)} Bi_x Fe₂O₄ (x =0.0, 0.2, 0.4, 0.6) Ferrites

Compound name	Ni Fe ₂ O ₄	Ni _{0.7} Bi _{0.2} Fe ₂ O ₄	Ni _{0.4} Bi _{0.4} Fe ₂ O ₄	Ni _{0.1} Bi _{0.6} Fe ₂ O ₄
<i>d</i> [Å]	2.5182	2.5098	2.5034	2.5033
<i>D</i> [nm]	40.13	39.20	31.52	28.80
<i>a</i> [Å]	8.3522	8.3234	8.3031	8.3030
ρ_x [g/cm ³]	5.3426	5.9539	6.5603	7.1218
ρ_m [g/cm ³]	3.7426	5.1094	6.4351	5.1260
<i>M</i> [g/mol]	234.36	258.54	282.72	306.91
<i>P</i> [%]	29.86	14.18	19.08	28.02
<i>Lattice stain</i>	9.2782	9.4649	11.7441	12.8520
<i>Dislocation density</i> (10 ³ lines/cm ²)	6.20	6.50	10.06	12.06
<i>Hopping length L_A</i>	3.6166	3.6043	3.5953	3.5953
<i>Hopping length L_B</i>	2.9529	2.9429	2.9356	2.9355
Bond length A-O (0.125) <i>a</i> √3	1.8083	1.8022	1.7977	1.7976
Bond length A-O (0.25) <i>a</i>	2.0881	2.0808	2.0757	2.0757

The lattice constant (*a*) decreases from 8.3522 to 8.3030 as the concentration of Bi³⁺ ions rises, as shown.[11] This could be attributed to the partial replacement of smaller ionic radius Ni²⁺ (0.69) ions with higher ionic radius Bi³⁺ (1.31) ions at octahedral positions, resulting in Lattice strain in the material crystal structure. [12] Changes in cationic radii, as well as the injection of dopant ions into the spinel matrix, cause a change in the behavior of numerous lattice parameters, which follows Vegard's rule and implies linear dependency. [13] Lattice parameter is inverse relation of crystallite size. When crystallite size increases then lattice parameter is decreases. The concentration of Bi³⁺ increases then hopping length and bond length also decreases as shown in table.

2. Magnetic analysis

Figure 2: VSM image of Ni_{(1-(3/2)x)} Bi_x Fe₂O₄ (x =0.0, 0.2, 0.4, 0.6) Ferrites

Magnetic hysteresis loops of the $\text{Ni}_{(1-(3/2)x)}\text{Bi}_x\text{Fe}_2\text{O}_4$ ($x = 0.0, 0.2, 0.4, 0.6$) Nano ferrites were captured to determine the magnetic properties of the samples. [13] Figure 2 show the VSM hysteresis loops at room temperature. All samples exactly show the S-shaped hysteresis loops which confirm the ferrimagnetic nature of the prepared ferrites. The doping of Bi in NF ferrite affected the magnetic properties of the spinel ferrite. [2] It can be seen that the magnetic remanence, saturation and saturation of magnetization decreased with the increases addition of Bi concentration because of the value of crystallite size of NF and BNF. Table 2 shows The dopant Bi significantly increases the value of the saturation magnetization M_s also decreases may be due to the spin-glass-like surface layer on the nano-crystalline nickel–bismuth ferrite with a ferri-magnetically aligned core. Samples indicate the soft nature of the ferrite nanomaterials. Various magnetic properties such as saturation magnetization (M_s), remanence (M_r), and coercivity (H_c) are calculated from the M-H loop. The behavior of saturation magnetization, remanence, and coercivity as a function of Bi content is shown in table 2 . The value of coercivity decreases from 167.82 Oe to 137.95 Oe. If the concentration of Bismuth increases then Bohr magneton, anisotropy constant also decreases. [15] If M_r/M_s is between 0.05 and 0.5, the particle interacts with a pseudo-single domain via magnetostatic couplings,. All of the samples show squareness ratios ranging from 0.27073 to 0.13690, indicating that the nanoparticles are pseudo-single domain in nature.

Table 2: M_s , H_c , M_r , SQR ratio of $\text{Ni}_{(1-(3/2)x)}\text{Bi}_x\text{Fe}_2\text{O}_4$ ($x = 0.0, 0.2, 0.4, 0.6$) Ferrites

Bi content	Coercivity [H_c] (Oe)	saturation magnetization [M_s] (emu g^{-1})	Remanence [M_r] (emu g^{-1})	Bohr magneton	Anisotropy constant* 10^3	Squareness ratio
X=0	167.82	37.257	9.0094	1.5633	6.380	0.16272
X=0.2	160.02	33.278	6.0625	1.5405	5.5470	0.27073
X=0.4	158.41	27.228	5.601	1.3783	0.8802	0.20570
X=0.6	137.95	25.543	3.4970	1.4036	3.670	0.13690

IV. CONCLUSION

The sol-gel microwave-assisted auto combustion method was used to make nanocrystalline nickel–bismuth ferrite with varied Bi^{3+} ion concentrations ($x = 0, 0.2, 0.4, 0.6$). Using the XRD method, the typical nanocrystalline sizes were calculated to be around 28 to 40 nm. With increasing ' Bi^{3+} ' substitution, the saturation magnetization (M_s), coercivity, and remanence magnetization diminish. The spin-orbit coupling is reduced when magnetic Fe^{3+} ions are replaced with nonmagnetic Bi^{3+} cations, resulting in a drop in the anisotropy constant of ferrites. Soft magnetic behavior is observed in Bi^{3+} -substituted nickel ferrites.

V. REFERENCES

- [1]. K. Chandra Babu Naidu and W. Madhuri, "Microwave processed bulk and nano NiMg ferrites: A comparative study on X-band electromagnetic interference shielding properties," *Materials Chemistry and Physics*, vol. 187, pp. 164–176, Feb. 2017, doi: 10.1016/j.matchemphys.2016.11.062.
- [2]. M. J. Nasr Isfahani, M. J. Fesharaki, and V. Šepelák, "Magnetic behavior of nickel-bismuth ferrite synthesized by a combined sol-gel/thermal method," *Ceramics International*, vol. 39, no. 2, pp. 1163–1167, Mar. 2013, doi: 10.1016/j.ceramint.2012.07.040.
- [3]. J. L. Xie, M. Han, L. Chen, R. Kuang, and L. Deng, "Microwave-absorbing properties of NiCoZn spinel ferrites," *Journal of Magnetism and Magnetic Materials*, vol. 314, no. 1, pp. 37–42, Jul. 2007, doi: 10.1016/j.jmmm.2007.02.124.
- [4]. J. L. Xie, M. Han, L. Chen, R. Kuang, and L. Deng, "Microwave-absorbing properties of NiCoZn spinel ferrites," *Journal of Magnetism and Magnetic Materials*, vol. 314, no. 1, pp. 37–42, Jul. 2007, doi: 10.1016/j.jmmm.2007.02.124.
- [5]. M. I. Arshad et al., "Impact of Mg doping on structural, spectral and dielectric properties of Cd–Cu nano ferrites prepared via sol-gel auto combustion method," *Physica B: Condensed Matter*, vol. 599, Dec. 2020, doi: 10.1016/j.physb.2020.412496.
- [6]. S. K. Gore et al., "The structural and magnetic properties of dual phase cobalt ferrite," *Scientific Reports*, vol. 7, no. 1, Dec. 2017, doi: 10.1038/s41598-017-02784-z.
- [7]. Y. Peng, C. Xia, M. Cui, Z. Yao, and X. Yi, "Effect of reaction condition on microstructure and properties of (NiCuZn)Fe₂O₄ nanoparticles synthesized via co-precipitation with ultrasonic irradiation," *Ultrasonics Sonochemistry*, vol. 71, Mar. 2021, doi: 10.1016/j.ultsonch.2020.105369.
- [8]. A. Houbi, Z. A. Aldashevich, Y. Atassi, Z. Bagasharova Telmanovna, M. Saule, and K. Kubanych, "Microwave absorbing properties of ferrites and their composites: A review," *Journal of Magnetism and Magnetic Materials*, vol. 529. Elsevier B.V., Jul. 01, 2021. doi: 10.1016/j.jmmm.2021.167839.
- [9]. F. Gao, D. L. Zhao, and Z. M. Shen, "Preparation and microwave absorbing properties of Cu-doped Ni-Zn spinel ferrites," in *Advanced Materials Research*, 2010, vol. 105–106, no. 1, pp. 293–296. doi: 10.4028/www.scientific.net/AMR.105-106.293.
- [10]. S. Joshi, M. Kumar, S. Chhoker, G. Srivastava, M. Jewariya, and V. N. Singh, "Structural, magnetic, dielectric and optical properties of nickel ferrite nanoparticles synthesized by co-precipitation method," *Journal of Molecular Structure*, vol. 1076, pp. 55–62, 2014, doi: 10.1016/j.molstruc.2014.07.048.
- [11]. B. Sattibabu, T. D. Rao, A. K. Bhatnagar, V. S. Murthy, J. A. Chelvane, and S. Rayprol, "Structural and magnetic properties of Bi substituted nickel ferrite," in *Materials Today: Proceedings*, 2020, vol. 39, pp. 1482–1486. doi: 10.1016/j.matpr.2020.05.371.
- [12]. S. Deepapriya, P. A. Vinosha, John. D. Rodney, S. Krishnan, J. E. Jose, and S. J. Das, "Effect of Lanthanum Substitution on Magnetic and Structural Properties of Nickel Ferrite," *Journal of Nanoscience and Nanotechnology*, vol. 18, no. 10, pp. 6987–6994, Jun. 2018, doi: 10.1166/jnn.2018.15528.

- [13]. S. K. Gore et al., "The structural and magnetic properties of dual phase cobalt ferrite," *Scientific Reports*, vol. 7, no. 1, Dec. 2017, doi: 10.1038/s41598-017-02784-z.
- [14]. M. K. Anupama, B. Rudraswamy, and N. Dhananjaya, "Investigation on impedance response and dielectric relaxation of Ni-Zn ferrites prepared by self-combustion technique," *Journal of Alloys and Compounds*, vol. 706, pp. 554–561, 2017, doi: 10.1016/j.jallcom.2017.02.241.
- [15]. S. O. Aisida et al., "The role of polyethylene glycol on the microstructural, magnetic and specific absorption rate in thermoablation properties of Mn-Zn ferrite nanoparticles by sol-gel protocol," *European Polymer Journal*, vol. 132, Jun. 2020, doi: 10.1016/j.eurpolymj.2020.109739.



Morphological and Structural Characterization of Polyaniline Doped Cadmium Telluride Nanocomposite

Pritesh J. Jadhao¹, Kamlesh R. Banarse¹, S.P. Yawale¹, S.S. Yawale²

¹Govt. Vidarbha Institute of Science and Humanities, Amravati-444604, Maharashtra, India

²Pre-IAS Training Centre, Amravati, Maharashtra, India

I. INTRODUCTION

From last two decades, there has been growing interest in research on nanostructures of conducting polymers. As they exhibit important properties in different areas, like transistors, sensors, actuators, muscles, etc. [1]. The composite of the polymer gives interesting mechanical and thermal properties that are not to be accomplished with any other material. It has wide applications in industries, automobiles, aerospace engg., military, building and construction industries etc.[2]

Considering different conducting polymers, polyaniline has very important properties such as hardness with doping or without doping. It has an extraordinary applications like anticorrosion coatings, [3], synthetic detecting, batteries [4], electromagnetic impedance protecting, microelectronics [5-6], The composites formed with polymers have improved optical and electronic properties due to the fillers in the chain during polymerization. Polymerization of polyaniline-graphene oxide nanocomposites showed enhanced electrical conductivity of 9.2 S/cm [7]. The conductivity of SnO₂/PANI nanocomposites is found to be 1.75×10⁻¹S/cm by some researchers [8]. Maximum conductivity of PANI/SnO₂ nanocomposite was found to be 6.4×10⁻³ s/cm at 9 wt%. Liu *et al* [9] prepared TiO₂/PANI solar cells..

In this work, nanoparticles of polyaniline and polyaniline-CdTe nanocomposites are synthesized by chemical oxidative polymerization method. Their morphological and structural characterization is done by scanning electron microscopy technique and x-ray diffraction technique. Crystalline nature of the nanocomposite with agglomeration of crystals over polymer and nanosized particles in nanocomposite is observed in the results.

II. SYNTHESIS OF MATERIALS

2.1 Synthesis of Polyaniline nanoparticles:

Polyaniline nanoparticles were synthesized by chemical oxidative polymerization method [10]. 2.59 gm of aniline hydrochloride was dissolved in 50 ml distilled water in a volumetric flask. Similarly 5.71 g of ammonium persulfate (APS) was dissolved in 50 ml distilled water kept for 1 h. at room temperature (303 K), During additions, mixture is stirred for 2 hr. Then resulting dark green precipitate of PANI was filtered and washed with HCl and acetone. Obtained precipitate was kept in oven to dry for about 5 hrs. at 80 °C.

2.2 Preparation of Polyaniline-CdTe Nanocomposite:

In the present work polymer composite with CdTe was prepared by *in-situ* polymerization method [11] with Cadmium Telluride (CdTe) 4 wt.%. CdTe nanoparticles were dispersed into the APS solution of 50 ml DD water and stirred for 1 hr. Aqueous solution of 2.59 g of aniline hydrochloride in 50 ml DD water added slowly in APS under vigorous stirring for 2 h. The resulting dark green precipitate was filtered and washed with HCl and then with acetone. Then kept in oven for about 5 h. at 80 °C.

III. CHARACTERIZATION

3.1 Scanning Electron Microscopy (SEM):

The SEM micrographs of all the samples of PANI and CdTe doped with PANI are shown in figure below. From the SEM micrographs of the film doped with CdTe, it is found that image show certain types of crystallinity may be due to the CdTe. Morphology of PANI doped with CdTe shows further drastic improvement of surface morphology. Nanoparticles formed are not of homogeneous size.

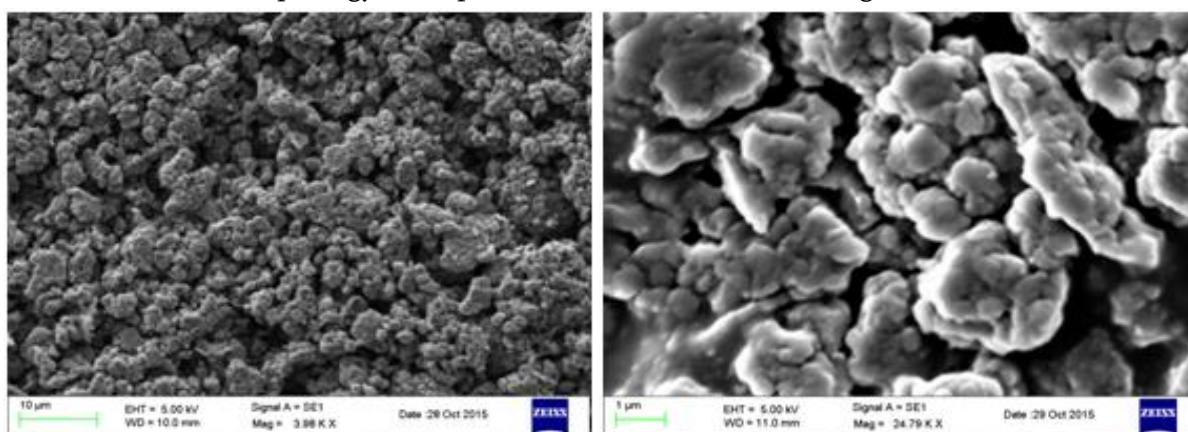


Fig.: Scanning Electron Microscopy images of (a) PANI (b) PANI+CdTe (4%)

There is agglomeration of crystallites which is clearly seen from Figure. A fine microspheroidal surface was observed with poor matrix. From the SEM of CdTe shows the crystalline nature where small crystallites of CdTe are seen. PANI is completely amorphous in nature whereas PANI-CdTe nanocomposite shows partly crystalline as well as amorphous phase. Nanoparticles were not of homogenous size but of different sizes ranging from 15-268 nm for PANI. These materials are polycrystalline in nature. Particle sizes of PANI- CdTe nanocomposite are found in the range 50 to 340 nm. Amorphous structure with very fine particles is seen. CdTe nanoparticles are seen which are deposited on surface of PANI.

3.2 X-Ray Diffraction (XRD):

The X-Ray diffraction has been used to determine the possible crystallinity in the composite films. The X-ray diffraction was carried out in the 2θ range from 0 to 100°. The XRD spectra of Pure PANI and PANI-CdTe nanocomposites with 4 wt % of CdTe are shown.

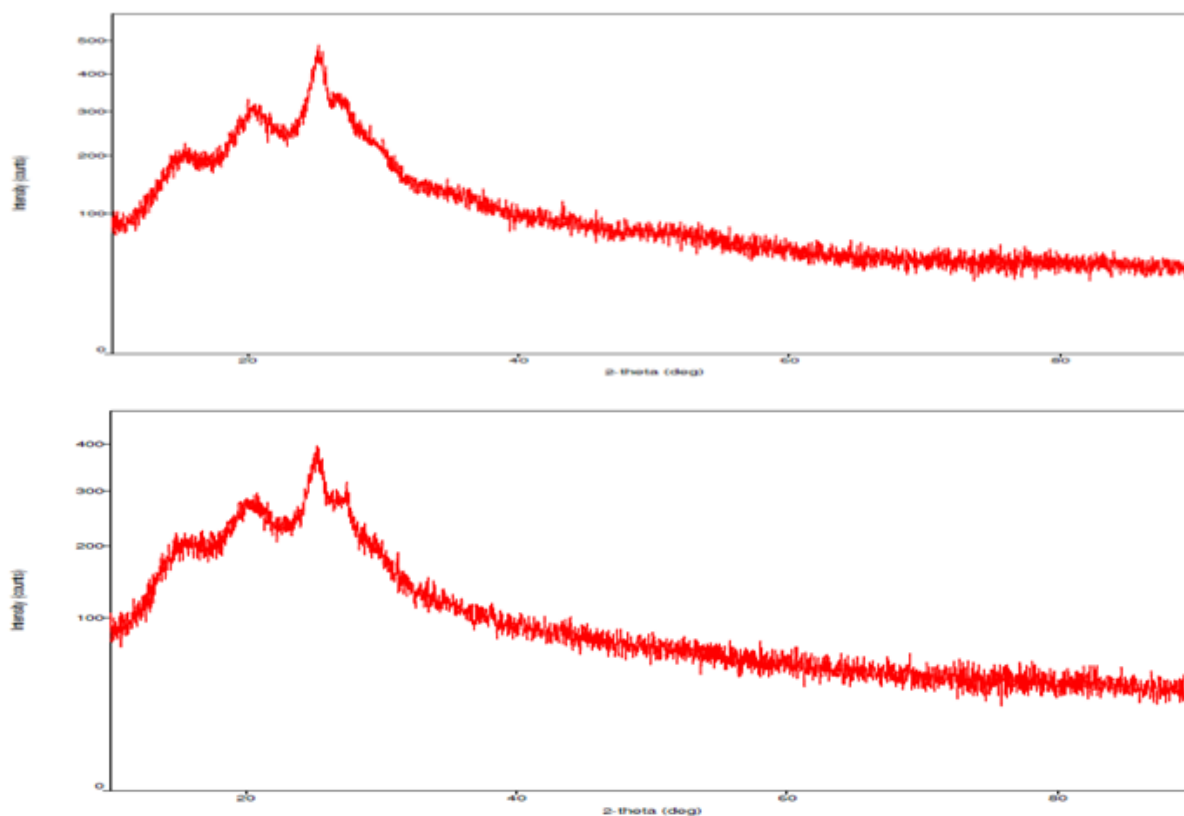


Fig.: X-Ray Diffraction images of PANI and PANI+CdTe (4%)

Absence of peak in the intensity versus 2θ curve represents complete amorphous state of sample [12]. Indication of peak or peaks in the curve suggests formation of phase of phases in the composite during polymerization process.

The degree of crystallinity increased in PANI-CdTe nanocomposite than pure PANI, clearly indicated the homogeneous distribution of nanoparticles in the polymer matrix. The crystallite size can be determined using Debye Scherrer formula $[(0.9 \lambda)/(\beta \cos \theta)]$ and it is found that the crystallite size of PANI-CdTe nanocomposite is 50 nm. The XRD pattern of PANI shows the three broad peaks at $2\theta = 15.13^\circ, 20.34^\circ, 25.20^\circ$. The SEM analysis shows that the particles are held together by a porous irregular network for CdTe [13]. PANI showed two broad hallos at $2\theta = 20.34^\circ$ and 25.20° . The entire sample has an amorphous nature [14]. A nanocomposite show the greater crystallinity due to the addition of CdTe in PANI matrix as compared to pure PANI and shows the peaks related to CdTe with increasing concentration in PANI matrix as seen from figure.

IV. CONCLUSION

SEM micrograph shows the partly crystalline behaviour as well as amorphous morphology of Polyaniline doped with Cadmium Telluride (CdTe). Nanoparticles formed are not of homogeneous size. Nanocomposites with crystal agglomeration was seen. Polycrystalline nature of the nanocomposite is seen. The morphology changes to smooth surface. Also the addition of CdTe shows further drastic improvement of surface

morphology of polymer composite. The average size of the particles PANI and PANI-CdTe nanocomposite are found to be range between 15-268 nm, and 50-340 nm respectively.

From the X-Ray diffraction technique it was observed that Polyaniline doped with CdTe indicating the partly crystalline and partly amorphous in nature. The sharp peak observed in PANI-CdTe nanocomposite is due to the presence of CdTe in the nanocomposite. A nanocomposite shows greater crystallinity due to the addition of CdTe in PANI matrix as compared to pure PANI.

V. REFERENCES

- [1]. Lijia Pan, Hao Qiu, Chunmeng Dou, Yun Li, Lin Pu, Jianbin Xu and Yi Shi, *Int. J. Mol. Sci.* 11, (2010), 2636-2657.
- [2]. Yu-Kai Han, Yi-Jang Lee, Pei-Chen Huang, *J. of Electrochem. Society*, 1564, (2009), K37-K43.
- [3]. Jiaying Huang, *Pure Appl. Chem.*, 78, 1, (2006), 15-27.
- [4]. Guoqing Zhang, Xinxi Li, Haitao Jia, Yahui Wang, et.al *Int. J. Electrochem. Sci.*, 7, (2012), 830 – 843.
- [5]. A.C.V. de Araújo, R.J. de Oliveira, et.al, *Synth. Met.* 160, (2010), 685-690.
- [6]. Na Li, Yinghong Xiao, Chong. Xu, Huihui Li, et.al *Int. J. Electrochem. Sci.*, 8, (2013), 1181-1188.
- [7]. S.B. Lee, S.M. Lee, N.I. Park, S. Lee, D.W. Chung, *Synth. Met.* 201 (2015) 61-66.
- [8]. Libo Sun, Yuanchang Shi, Zhaopin He, Bo Li, Jiurong Liu, *Synth. Metals* 162 (2012), 2183-2187.
- [9]. Ziran Liu, Jingran Zhou, Hailin Xue, Liang Shen, *Synth. Metals* 156, (2006), 721-723.
- [10]. J. Stejskal, R.G. Gilbert, *Pure Appl. Chem.*, No. 5, 74 (2002) 857.
- [11]. Ozcan Koysuren & H. Nagehan Koysuren, *Journal of Macromolecular Science, Part A, pure and applied chem.*, Taylor & Francis, (2019).
- [12]. Renu Chadha, *J. Sci. and Ind. Res.*, 65 (2006), pp.459-469.
- [13]. Snehal R. Kargirward, R. Elilarassi, S. Maheshwari & G. Chandrashekhara (2010) *Optoelectronics Adv Mater. Res.* 4(3)309-312., Pelagia Research Library, 1 (1), (2010), 166-173.
- [14]. Trindade T., Neves M.C. & Barros A.M.V., *Scr. Mater.* 43 (2000) 567.



The Crystallization Behaviour of Silver Doped Lead Borate Glasses

Dr. M. A. Giri

Department of Physics, Gramin Mahavidyalaya, Vasantnagar, Tq. Mukhed Dist. Nanded, Maharashtra, India

ABSTRACT

The differential scanning calorimetric technique of characterization of glasses (5-30 mol% Ag₂O) was obtained to study the glass transition and crystallization behavior of amorphous solids. The quality control for monitoring glass synthesis because the overall behavior of the glass depends on glass transition temperature (T_g) and the different phase formation in the samples.

Keywords: Lead silver borate glasses, dc electrical conductivity, ionic conduction, Ag⁺ ions.

I. INTRODUCTION

The structure of glass was proposed by Zachariasen (1932). In borate glasses B₂O₃ is a basic glass former because of its higher bond strength lower cation size, smaller heat of fusion and valence (=3) of B. In borate glasses B³⁺ ions triangularly co-ordinated by oxygen form glasses easily. In B₂O₃ the units are triangles, which are covalently bonded in a random configuration (Yawale *et al* 2000)

The evolution of the ionic conduction have been reported in (AgI)_x-(Ag₂O)_y-(B₂O₃)_{1-(x+y)} glasses containing Nano crystallites of α-AgI. The predominant role of Au/AgI Nanoparticles is discussed (Kiyoshi Nozaki et al 2006; Zacheo et al ,2011).

This paper reports the glass transition and crystallization of Lead silver borate glasses on with the help of X-ray and DSC to determine the structure of borate glasses.

GLASS PREPARATION:-

The glasses of different compositions were prepared from pure Gradeamounts in mole % of PbO₂, Ag₂O and B₂O₃ in powder form were weighted having accuracy ±0.00001 g. and mixed thoroughly in acetone in an agate mortar. The dried mixture was taken in porcelain crucible and heated at moderate rate up to 1100°C ± 10°C.

The general formula of the present system are (100 - 3x) PbO₂-xAg₂O-2xB₂O₃ the ratio of Ag₂O/B₂O₃ was kept constant say 0.5.

The molten mass soaked at a temperature 323K above the melting point for two hours to achieve homogeneity and to minimize the dispersion of resistivity of the material. The molten mass was then finally, quenched between two flat surfaces of metallic block at room temperature in air. The circular samples thus

obtained were immediately transferred into an annealing furnace pre-maintained at a constant temperature of 100°C for two hours. The effect of annealing is to remove the air bubbles.

The conducting silver paint applied on two surfaces of the glass sample, provide two electrodes, without any air gap between the surface of the sample.

II. RESULTS AND DISCUSSION

In the present work the calorimetric investigation of $\text{PbO}_2\text{-Ag}_2\text{O-B}_2\text{O}_3$, glasses is made in the temperature range of 303 to 1100 K at heating rate of 10° K/min. The DSC studies helps in understanding the glass transition and crystallization behavior of solids.

The DSC technique has been employed to determine glass transition temperature (T_g), change in heat capacity (ΔC_p), crystallization temperature (T_c), crystallization enthalpy (ΔH_c) obtained from the thermo grams are reported in table for different compositions of lead silver borate glasses.

The values of T_g for the glasses studied here are in well agreement with the values reported by many workers for borate and other glasses (Soppe *et al* 1988, Selvaraj *et al* 1989, Ghosh 1995 and Chaudhary 1995). From the DTA/DSC curves the glass transition temperature (T_g) change in heat capacity (ΔC_p) and crystallization enthalpy (ΔH_c) are evaluated. The glass transition temperature variation with Ag_2O mol % for different ratio of $\text{Ag}_2\text{O/B}_2\text{O}_3 = 0.5$, are shown in figures 1 . The glass transition temperature (T_g) decreases up to 15 mol % of Ag_2O and then increases glasses, the decreasing T_g with Ag_2O concentration suggested the network structure of glass and consequently at higher concentration of Ag_2O more than 15 mol % the (T_g) increases sharply which is an indication of strong network structure of glass. It is noted that the glass transition temperature (T_g) varies from 336 to 932.8°C for entire series of glasses.

The decrease in the T_g decreases in case like vibrational frequency of the most mobile species in the tissue portion of the glass such as Ag^+ ion. According to the cluster model of glass transition the clusters are the more order groups and the tissue is disorder and distorted regions of the glass structures with the addition of Ag_2O .

The increasing (T_g) value after specific mol % Ag_2O in all the glasses of the series, suggests that with increasing composition of PbO_2 at the cost of Ag_2O , strengthen the network structure of the glass which ultimately decreases the formation of the non bridging oxygen.

Variation of change in heat capacity (ΔC_p) with Ag_2O mol% in glass transition region figure 2. From the figures it is observed that were $\text{Ag}_2\text{O/B}_2\text{O}_3 = 0.5$ the change in specific heat increases and is maximum at 25 mol% of Ag_2O where as in other two cases ΔC_p is found to be maximum at 30 mol% of Ag_2O . The magnitude of ΔC_p is generally indicative of the nature of bonding and is higher for ionic glasses and lower for covalent ones. The higher magnitude of ΔC_p in these glasses indicative of ionic bonding

The area under exothermic peak gives crystallization enthalpy (ΔH_c). The variation of (ΔH_c) with Ag_2O mol % is shown in figure 3 For the $\text{Ag}_2\text{O/B}_2\text{O}_3 = 0.5$ glass series, ΔH_c decreases up to 10 mol % of Ag_2O and then increases for higher composition of Ag_2O .

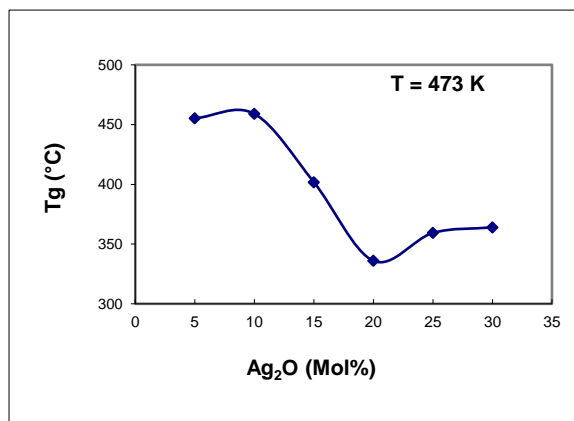


Fig.1

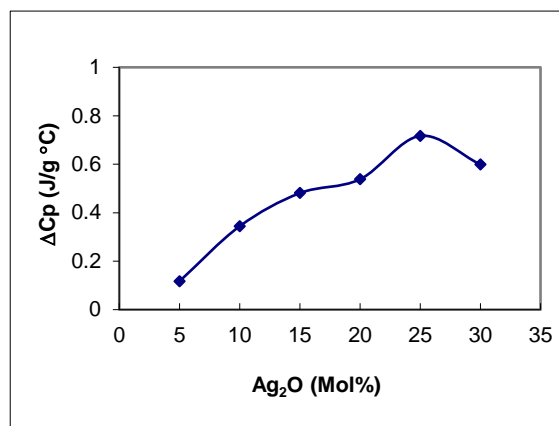


Fig.2

Fig. 1: Variation of glass transition temperature T_g with Ag_2O (mol%) for ratio $Ag_2O/B_2O_3 = 0.5$

Fig. 2 : Variation of change in heat capacity (ΔC_p) with Ag_2O (mol%) in glass transition region for ratio $Ag_2O/B_2O_3 = 0.5$

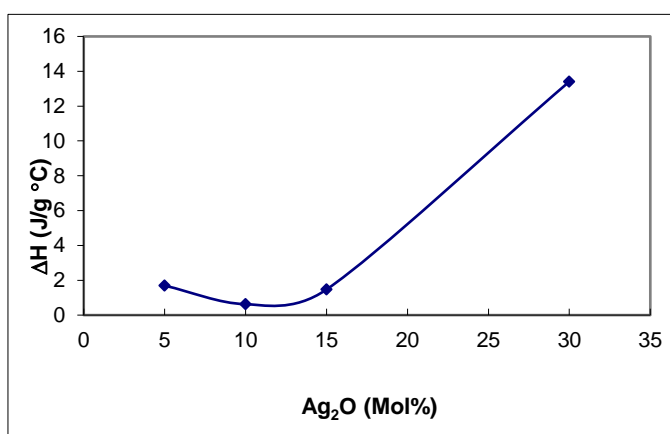


Fig. 3 : Variation of change in enthalpy (ΔH_c) with Ag_2O (mol%) in glass transition region for ratio $Ag_2O/B_2O_3 = 0.5$

Table : Thermal parameters for $Ag_2O/B_2O_3 = 0.5$ glasses

Sr. No.	Glass Composition	Total Weight loss (%)	T_g (°C)	ΔC_p (J/g)	ΔH (J/g)	E_a (J/g-mole K)
1	10PbO ₂ -30Ag ₂ O-60B ₂ O ₃	07.38	363.98	0.599	13.4079	-
2	25PbO ₂ -25Ag ₂ O-50B ₂ O ₃	28.992	359.31	0.717	-	-
3	40PbO ₂ -20Ag ₂ O-40B ₂ O ₃	7.60	336.00	0.538	-	-
4	55PbO ₂ -15Ag ₂ O-30B ₂ O ₃	7.87	401.80	0.481	1.4726	10157.37
5	70PbO ₂ -10Ag ₂ O-20B ₂ O ₃	6.78	558.97	0.344	0.6273	1071.153
6	85PbO ₂ -5Ag ₂ O-10B ₂ O ₃	12.61	455.24	0.197	1.6927	10173.05

It is concluded that the glasses are not soft because they have higher values of T_g glass transition temperature.

III. CONCLUSIONS

From differential scanning calorometric (DSC/DTG) technique, the glass transition temperature (T_g), the change in heat capacity (ΔC_p), crystallization enthalpy (ΔH_c) is determined. The results are discussed on the basis of vibrational heat capacity. The glass transition temperature variation with Ag_2O mol% for different ratio of Ag_2O/B_2O_3 is presented. The magnitude of ΔC_p is generally indicative of the nature of bonding and is higher for ionic glasses and lower for covalent ones. The higher magnitude of ΔC_p in these glasses indicative of ionic bonding. The exothermic peaks gives crystallization enthalpy (ΔH_c). The variation of ΔH_c with Ag_2O mol% is presented.

In DSC/DTG curves no prominent exothermic peaks are seen curves shows exothermic peaks around 550°C and 630°C which could correspond to the formation of $Ag_2O-4B_2O_3$ and $Ag_2O-2B_2O_3$.

IV. REFERENCES

- [1]. Boulos E N and Kreidl N J, The American Ceramic Society, Chicago 34 (1971) 71. Chaudhary B K, Bull Mater Sci18 (1995) 127-46.
- [2]. De Carli F D, "Anhydrous Borate of silver, Barium and Zinc", Atti.Accad.Lincei,5(6) (1927) 27-41. Ghosh A, Bull Mater Sci18 (1995) 153-60.
- [3]. Kiyoshi Nozaki and Toshio Itami Journal of Physics: Condensed Matter 18 (2006)
- [4]. Selvaraj W Kershava, Sunder H G and Rao K J, J ChemSoc Faraday Trans 185(2) (1989) 251-267. Soppe W and Marel V, J Non Cryst Solids103 (1988) 102.
- [5]. Yawale S S, Yawale S P and Adgonkar C S, Ind J Engg Mater Sci7 (2000) 150. Zachariasen W H, J Am Chem Soc54 (1932) 46.
- [6]. Zaccheo, B.A., Crooks, R.M.Langmuir 27, (2011) 11591-11596.



Formulation and Development of Skin Cleansing Gel with Self Exfoliation

K. S. Misar^{*1}, A. A. Paranjape¹, K.S. Tiwari¹, M.P.Bokde¹

^{*1}Department of Cosmetic Technology, Kamla Nehru Mahavidyalaya, Nagpur, Maharashtra, India

ABSTRACT

The aim of present work was to study formulation and development of skin cleansing gel with self-exfoliation. The idea of formulation of self-exfoliating gel was conceptualized by observing that the products available in mass market were not so gentle on the skin surface when exfoliated. Hence, exfoliating gel with Carbomer 940 and Cetrimonium Chloride was formulated with its own unique self-exfoliation property with deep cleansing effect. Cetrimonium chloride was validated by physical and chemical methods like colour, odour, pH and appearance. Suitable gel base was formulated with various concentrations of Cetrimonium chloride and the formulations were evaluated for the functional parameters. Exfoliating gel thus prepared was subjected to stability study for parameters like- colour, odour and pH at different temperatures like at room temperature, at 45^o C and at 4^oC. Subjective evaluation of gel was carried out to study the functional parameters like ease of spreadability, self-exfoliating efficacy, cleansing effect, improvement in skin texture and irritancy on skin, on human volunteers. The study showed that exfoliating gel with 10% Cetrimonium chloride was the best formulation for self-exfoliation with deep skin cleansing effect and improvement in texture of the skin.

Key words: Cetrimonium chloride, Gel base, Self exfoliating, Cleansing of skin

I. INTRODUCTION

The Skin:

The skin is the largest organ of the body, with total area of about 20 square feet in adult. The skin protects us from the harmful effects of external environment, helps regulate body temperature and permits the sensation of touch, heat and cold[1]. Skin has three layers-epidermis, dermis and deeper subcutaneous tissue (hypodermis)[2]. Skin's epidermis produces fresh skin cells every day. They are pushed up by the arrival of newer cells to the top of the skin[3]. After which they are dead and supposed to flake off by themselves in a process called desquamation. Unfortunately, the procedure often doesn't reach its completion in some areas of the body; so dead cells cling on and pile up which results in thickening of skin[4]. The thickness of the skin cannot be seen, but can be observed and experienced with fingertips and nails. However, the thicker it gets, the more exfoliation it needs [5]. In addition to this there might be other routine ways through which skin

might get damaged such as environmental pollution, photo damage, improper diet, lack of cleansing and use of unnecessary chemicals[6].

Exfoliation:

As skin grows older, rate of cell turnover slows down dramatically. Majorly dead cells found on facial skin surface may result in fine lines and can make complexion dull and dead [7]. To remain healthy and of good appearance, the skin surface requires frequent cleansing to remove grime, sebum and other secretions, and dead cells [8]. Exfoliation has become one of the most dominant activities in skin care and is considered by many to be beneficial as it refreshes the skin and removes dead cells [9]. Proper exfoliation removes the barrier of dead skin cells clogging the skin and uncovers fresh new cells below. This opens the way for moisturizing products to penetrate more deeply into the skin, which makes them more effective. In short, a regular exfoliating routine will leave skin fresh and healthy [10].

II. SKIN CLEANSING GEL WITH NATURAL EXFOLIATION

Skin cleansing gel is a type of exfoliator, but include no conventional scrubs, micro-dermabrasions, AHA, peel, etc. The purpose of the skin cleansing gel with natural exfoliation is to exfoliate the dead skin without abrasive material, doesn't tingle skin like glycolic acid does, it is effective but gentle, and also provides a sense of achievement when we experience the dead skin coming off. The skin appears much more clear, translucent, smooth and soft without stripping its natural oil after each application [11].

Exfoliating gel:

In the present study Exfoliating gel with popular carbomer 940 and cetrimonium chloride was formulated to have its own unique self-exfoliation and good skin conditioning property. Easy to use, easy to formulate and mild exfoliation feel with deep cleansing effect are ideal characteristics of the formulae. Some benefits of the exfoliating gel includes unclogging of skin pores, removal of dirt, grime and extra sebum, it allows penetration of creams, lotions, and other similar types of all topically applied products to deeper layers of skin and maintain skin's health. And, a modest approach to formulate and develop a product which can be applied on skin regularly for removal of dead skin cells without using any harsh chemicals or physical exfoliating agents was the key objective during this project work.

III. CETRIMONIUM CHLORIDE

Cetrimonium Chloride is transparent liquid, with characteristic odor and it is soluble in water. It has a molecular formula-C₁₉H₄₂ClN. It is reported that it shows antimicrobial, emulsifying agent, preservative and surfactant. Its use level are 0.25 – 10 % for rinse off preparations [12,13].

IV. MATERIAL AND METHODS

Analysis of Cetrimonium Chloride:

Cetrimonium Chloride was procured for the present study from N V Organics Pvt. Ltd., Delhi., along with Certificate of Analysis. The procured sample was validated by performing tests, such as colour, odor, pH, Ash and solubility. The results are summarized in table no. 1.

Formulation and Development of Skin Cleansing Gel with self-exfoliation

Sr. No.	Ingredient	Uses of ingredients	Quantity for 100g in Percentage (%)			
			Trial 1	Trial 2	Trial 3	Trial 4
1	Water (Distill)	Vehicle	70	78	85	65
2	Ethyl Alcohol	Astringent	20	15	10	10
3	Glycerin	Humectant	5	5	3	2
4	Propylene Glycol	Humectant	-	2	2	3
5	Propanediol	Humectant	-	-	2	5
6	Carbomer 940	Gelling agent	2	2	2	2
7	Ethyl LauroylArginate	Preservative	0.5	0.5	0.5	0.5
8	GlycerylCaprylate	Preservative	0.5	0.5	0.5	0.5
9	Cetrimonium Chloride	Neutralizer	2	5	7	10
	Total		100	100	100	100

Gel base was selected by taking different trials for base and self-exfoliating gel was formulated with four different concentrations of Cetrimonium chloride i.e. 2%, 5%, 7% and 10% and studied for having its own unique self-exfoliation property as well as good skin conditioning ability

Study of Functional parameters of Self Exfoliating Gel:

The Self exfoliating gel formulations were subjected to study the functional parameters like Consistency, Clarity, Exfoliation and Cleansing. The results are summarized in table no. 3.

Analysis of Gel base: All the Gel base formulations were subjected to study parameters like Spreadability, Tackiness and after use feel on the skin [14]. The results are summarized in table no.4.

Accelerated Stability Study: The objective of accelerated stability studies is to predict the shelf life of a product by accelerating the rate of decomposition preferably by increasing the temperature. This information is then projected to predict shelf life or used to compare the relative stability of alternative formulations. This usually provides an early indication of the product shelf life [15]. In the present study after analyzing all the four formulations on the basis of functional parameters it was observed that formulation (Trial-4) with 10% concentration of Cetrimonium Chloride was giving satisfactory results. Hence, the Trial-4 was selected for further study of accelerated stability test (i.e. trial-4 was observed for Colour, Odor and pH changes at room temperature, at 45°C and at 40°C) and subjective evaluation [16]. The results are summarized in table no. 5.

Subjective evaluation: Self exfoliating gel containing 10% Cetrimonium Chloride (i.e. Trial 4) was given to 10 volunteers of age group between 19-30 years for 4 weeks to carry out the subjective evaluation on the basis of

their feed back. The subjects were asked to use exfoliating gel twice a week for 4 weeks and note the changes they observed on the surface area of the body where they applied the product. Subjective evaluation was carried out on the basis of rating (1-5) the parameters like Appearance, Ease of Spreadability, Self-Exfoliation efficacy, Improvement in skin Texture and Irritancy in skin.

V. RESULT AND DISCUSSION

Analysis of Cetrimonium Chloride:

Cetrimonium Chloride was analyzed; results were noted and compared with values mentioned in Certificate of Analysis of Cetrimonium Chloride. It passed all the tests and hence was used for incorporation in exfoliating gel formulations. The results are summarized in table no.1.

Table No.1: Analytical test results of Cetrimonium Chloride

Sr. No.	Characteristic	Requirement As Per Certificate of Analysis of Cetrimonium Chloride	Result	Inference
1.	Color	No Color	No Color	Passes the test.
2.	Odor	Characteristics	Characteristics	Passes the test
3.	Appearance	Liquid type	Liquid type	Passes the test
4.	pH	5.0-8.0	7.12	Passes the test
5.	Ash	0.1 Max	0.04	Passes the test
6.	Solubility	Water Soluble	Water Soluble	Passes the test

Study of Functional parameters of Self Exfoliating Gel:

In the present study after analyzing all the four formulations on the basis of functional parameters it was observed that formulation (Trial-4) with 10% concentration of Cetrimonium Chloride was giving satisfactory results. Hence, the Trial-4 was selected for further study. The results are summarized in table no.3.

Sr.No.	Formulations	Observed Parameters				Inference
		Consistency	Clarity	Exfoliation	Cleansing	
1	Trial1	Less Viscous	NotClear	Noexfoliation	Poor	Increased CetrimoniumChloride
2	Trial2	More Viscous	NotClear	Noexfoliation	Poor	Increased CetrimoniumChloride
3	Trial3	More Viscous	NotClear	Less exfoliation	Fine	Increased CetrimoniumChloride
4	Trial4	Satisfactory Viscous	Clear	Enough exfoliation	Good	Good

Table No. 3: Result of Selection of Gel with self-exfoliation

Analysis of Gel base: From the results of analysis of all the Gel base formulations (i.e. Trial-1,2,3,and 4)it was observed that Trial-4 was satisfactory with respect to Spreadability, Tackiness and After use feel on the skin, hence it was selected for further study. The results are summarized in table no.4.

Sr. No.	Parameters	Trial1	Trial2	Trial3	Trial4
1	Spreadability	Fine	Fine	Good	Good
2	Tackiness	Tacky	Tacky	Slightly Tacky	Non Tacky
3	After use feel on skin	Fine	Fine	Fine	Good

Table No. 4: Result of Analysis of Gel base

Accelerated Stability Study: From the result of accelerated stability study it was observed that the self-exfoliation gel with 10% concentration of Cetrimonium Chloride (Trial-4)was stable with respect to physical and chemical parameters like colour, odour and pHfor 30 days, and also the product was passed cyclic temperature test for 3 cycles.

Sr.No.	Characteristic	Requirement	Observation
1.	Cyclic temperature test	To pass the test	Passes the test
2.	Accelerated stability test		
	Colour,	To pass the test	Passes the test
	Odor	To pass the test	Passes the test
	pH	4-9	4.8

Table No. 5: Result of Chemical and Physical testing of self-exfoliation gel (Trial-4)

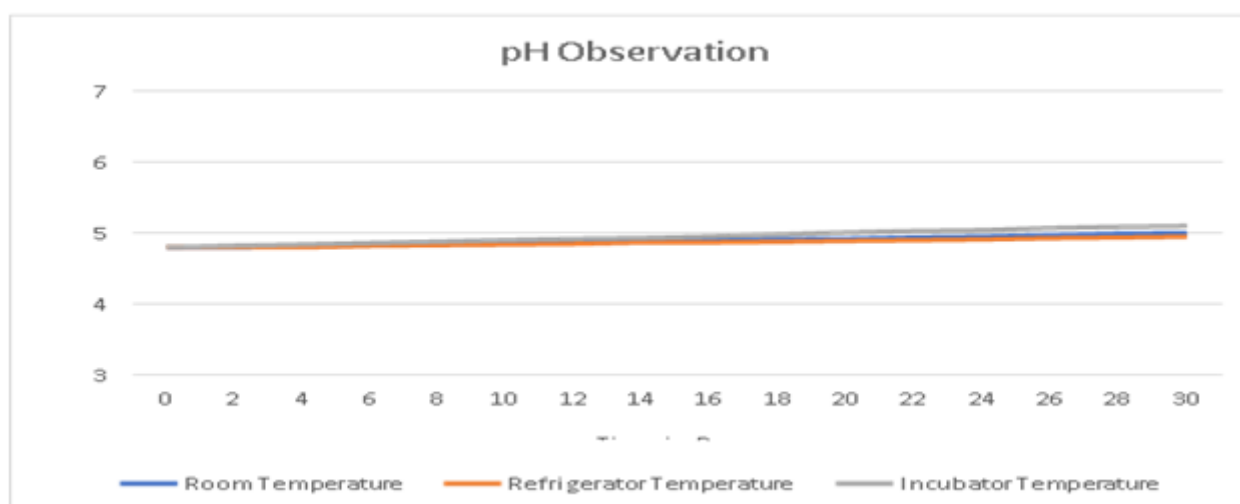


Figure no. 1: Change in pH at different Temperature (Accelerated stability test-Trial-4)

Subjective evaluation: From the subjective evaluation, it was observed that self-exfoliation gel (Trial-4)was well appreciated. It caused no irritation on regular application. It showed good self-exfoliation with deep skin cleansing effect and improvement in texture of the skin.

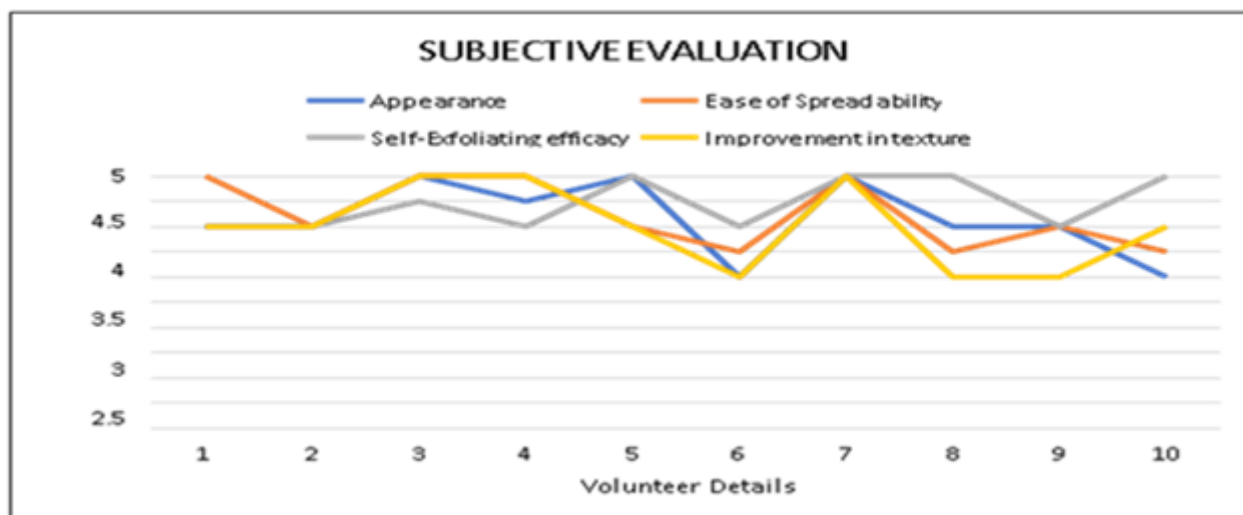


Figure No. 2: Graph of Subjective evaluation

VI. CONCLUSION

After formulating and evaluating the skin cleansing gel with self-exfoliation, it is observed that product can be a useful addition in the portfolio of other mild exfoliating products available in market. Being an indifferent approach in the theory of exfoliation, the gel can be efficiently used for removal of dead skin cells, without harming the skin.

VII. REFERENCES

- [1]. J.M. Abdo, N.A. Sopko S.M. Milner ,The applied anatomy of human skin: A model for regeneration, journal homepage: www.elsevier.com/locate/wndm, Wound Medicine 28 (2020) 100179 Available online 18 January 2020,1-10.
- [2]. H.Yousef; M. Alhaji; and S. Sharma, Anatomy, Skin (Integument), Epidermis, StatPearls- NCBI, November 19, 2021. https://www.ncbi.nlm.nih.gov/books/NBK470464/#_ncbi_dlg_citbx_NBK470464
- [3]. B. Pecoraro, M. Tutone et.al., Predicting Skin Permeability by means of Computational Approaches: Reliability and Caveats in Pharmaceutical Studies, Journal of Chemical Information and Modeling, DOI: 10.1021/acs.jcim.8b00934 • Publication Date (Web): 18 Jan 2019, 1-3
- [4]. P. K. NAG et.al. Occupational Skin Diseases, ENVIS NIOH, Vol. 5, No. 2, Apr-Jun, 2010, <http://www.osh.dol.govt.nz/order/catalogue/pdf/occskin.pdf> , 1-8.
- [5]. G.H. Ta, C.F.Weng,et.al.,In silico Prediction of Skin Sensitization: Quo vadis? published:04May2021doi:10.3389/fphar.2021.655771,1-18 <https://www.frontiersin.org/journals/pharmacology>
- [6]. E. Drakaki,C. DessiniotiandChristinaV.Antoniou* Air pollution and the skin, ENVIRONMENTAL SCIENCE MINI REVIEWARTICLE published: 15May2014 doi: 10.3389/fenvs.2014.00011, 1-4.

- [7]. C. T. Nemade, N. Baste., Formulation and Evaluation of a Herbal Facial Scrub, World Journal of Pharmaceutical Research Volume 3(3) , April 2014:4367-4371
- [8]. S.Lawton,<https://www.nursingtimes.net/clinical-archive/dermatology/skin-1-the-structure-and-functions-of-the-skin-25-11-2019/>
- [9]. P. B. Murphy; A. R. Atwater; M. Mueller, Allergic Contact Dermatitis, StatPearls-NCBI <https://www.ncbi.nlm.nih.gov/books/NBK459230/>
- [10]. V. C. Maurizio, Topical Delivery Systems Based on Polysaccharide Microspheres, Technology, Applications, and Formulations Personal Care & Cosmetic Technology 2005,273-282
- [11]. R. Kandasamy, Skin Care with Herbal Exfoliants, Functional Plant Science and Biotechnology 5 NilaniPackianathan, (Special Issue 1), 94-97 ©2011 Global Science Books.
- [12]. Fuizz and C. Richard, 2012.Transdermal delivery system. US Patent 5736154
- [13]. Nguyenbachemical.com first indexed by Google in January 2014 <http://nguyenbachemical.com/file/CTAC.pdf>
- [14]. A. Khan, S. Kotta, S. Ansari,et.al Formulation development, optimization and evaluation of aloe vera gel for wound healing, Pharmacognosy Magazine | October-December 2013 | Vol 9 | Issue 36 (Supplement); S6-S10
- [15]. S. Bajaj, D. Singla, and N. Sakhuja, Stability Testing of Pharmaceutical Products Journal of Applied Pharmaceutical Science 02 (03); 2012: 129-138
- [16]. S.Mahajan*, D. Gayakwad, A. Tiwari,G. N. Darwhekar. Formulation and Evaluation of Herbo-Mineral Facial Scrub, Journal of Drug Delivery & Therapeutics. 2020; 10(3):195-197

Formulation and Development of Two-Phase Facial Cleansing System

K. Misar*, R. Gajbhiye, A. Thakker, M. Taywade

*Department of Cosmetic Technology, Kamla Nehru Mahavidyalaya, Nagpur, Maharashtra, India

ABSTRACT

The present work was undertaken to formulate and develop Two-Phase Facial Cleansing system to serve gentle cleansing feel with a unique way of application and attractive container. Two phase cleansing system was developed containing emulsion with Sodium bicarbonate and gel with Citric acid. The reaction between sodium bicarbonate and citric acid results in the formation of water and bubbles of CO₂ which gives delightful chunks that bubbles on the skin giving a refreshing feel and therapeutic benefit because it is formulated with unique chemistry and exclusive packaging. The formulation was carried out with 5 different trials of emulsion and 4 different trials of gel and finalized a stable system with emulsion (F-5) and Gel (F-4). Both the phases i.e. gel with citric acid and emulsion with sodium bicarbonate, were filled in a two-way container so that when the actuator button is pressed both the phases come out on the skin together as a final product. Both phases were evaluated for functional parameters as per BIS for Skin Creams (IS 6608:2004) and for gel pH, colour, odour, and consistency. The product was subjected to an accelerated stability study to check the stability of the product with respect to colour, odour, and pH. Subjective evaluation of the product was carried out on a panel of human volunteers. The study showed that a two-phase facial cleansing system gives excellent cleansing effect with improved skin condition in a joyful manner.

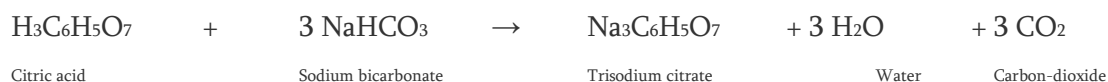
Keywords: Two-Phase facial Cleansing System, Sodium bi-carbonate emulsion, Citric acid gel.

I. INTRODUCTION

At the end of a long day, nothing feels quite as good as cleansing the face. As the first step in skincare rituals is removing every trace of dirt, sweat, and makeup which allows the skin to breathe, and helps to repair and renew skin by itself [1]. Having a spotless surface also helps other skincare products to penetrate the skin more deeply and perform their tasks more efficiently [2]. The two-phase facial cleansing system contains two products with unique characteristics and different pH. It governs the self-foaming effect on the skin when applied together which feels like quick gentle cleansing to the skin. A two-phase facial cleansing system can prove the best way to reward the skin for making a tough fight against pollution and stress throughout the day for all skin types in any weather [3]. People like those delightful chunks that bubble and crackle on the skin with a refreshing feel and therapeutic benefit in a unique way because it is formulated with unique chemistry and packed in an iconic two-way container that is capable of storing and discharging two kinds of

contents. As the system has 2 phases with different pH, they were filled in a two-way container so that when the actuator button is pressed both the phases come out on the skin together as a final product, from a single opening with neutral pH [4-5].

A two-phase facial cleansing system is far away different from routine cosmetic cream or gel. Sodium bicarbonate is having great ionic reactivity with the acids; hence sodium bicarbonate is taken as alkali and citric acid is a well-accepted, highly stable, and non-hazardous acid that is in use for a very long period in cosmetics [6-9]. Interaction between these two ingredients generates carbon dioxide which improves skin oxygenation immediately and it's also claimed to increase blood flow when topically administered to the skin by previous studies [10].



This formulation provides with unique double chamber and outlet in a single container which gives gentle cleansing and ease of application and handling. A two-way container used in this study is given in figure no.1.



Figure no. 1. A two-way container

II. MATERIALS AND METHODS

Selection of Base

The cleansing system is conceptualized with two phasic system as it contains two phases i.e., emulsion (cream) and gel. Both the phases are different from each other and both phases have reactions with each other due to differences in pH and electrolytic charge. Two phases of the system are as follows:

1. Emulsion (cream) with sodium bicarbonate
2. Gel with Citric acid

Collection / Procurement of Ingredients

This work is done on focusing the development of citric acid and sodium bicarbonate reaction on application. Both the ingredients citric acid and sodium bicarbonate have extremely high and extremely low pH hence it needs to be stabilized with speciality ingredients, hence two ingredients i.e. Sepiplus 400 and Seppimax Zenwere procured for the present study from Yasham Specialty Chemicals, Mumbai, along with the Certificate of Analysis.

Formulation and Development of Two-phase facial cleansing system

Formulation and Development of Two-Phase facial cleansing system was designed to give better cleansing with different pH. Two phases consist of two different products. Hence this product consists of two formulas i.e., Emulsion with sodium bicarbonate and gel with citric acid. The formulation was carried out with 5 different trials (F-1, F-2, F-3, F-4 and F-5) of emulsion and 4 different trials of gel (F-1, F-2, F-3, and F-4) and finalized a stable system by selecting emulsion (F-5) and Gel (F-4). The formulation with different trials is summarized in table no. 1 and 2.

Sr. No.	Ingredients	Uses of Ingredients	Quantity (%) w/w				
			F-1	F-2	F-3	F-4	F-5
Phase A							
1.	Distilled Water	Vehicle	78.25	77.95	71.95	67.95	69.95
2.	Propylene Glycol	Humectant	5	5	10	10	10.0
Phase B							
3.	Cetearyl Alcohol	Emulsifier	1	3	3	3	3.0
4.	Steareth-21	Non-ionic emulsifier	-	-	1	2	2.0
5.	Light Liquid Paraffin	Conditioning agent	2	5	5	8	8.0
6.	Sepiplus 400 [Polyacrylate-13 (and) Polyisobutene (and) Polysorbate 20]	Emulsion stabilizer	1.15	1.15	1.15	1.15	1.15
Phase C							
7.	Perfume	Mask odour of the other ingredients	3.0	0.3	0.3	0.3	0.3
8.	Tocopherol	Anti-oxidant	0.3	0.3	0.3	0.3	0.3
	Euxyl PE 9010 [Phenoxyethanol (and) Ethylhexylglycerin]	Preservative	1.0	1.0	1.0	1.0	1.0
9.	Sodium bicarbonate	Remove dead skin cells	10.00	8	8	8	6.0
	Check/adjust pH; approx. 8						

Table no. 1. Formulation and Development of Emulsion (cream) with sodium Bicarbonate

S. N.	Ingredients	Uses of Ingredients	Quantity (%) w/w			
			F-1	F-2	F-3	F-4
1	Distilled Water	Vehicle	92.5	91.0	92.8	91.7
2	Glycerine	Humectant	0.5	1	1	2
3	Citric acid	Skin exfoliator	4	4	4	4.

4	PVP	Film former	2	-	-	-
5	Sepimax (Polyacrylate crosspolymer-6)	Neutralized polymer	-	-	0.7	1.3
6	Xanthan Gum	Thickening agent	-	3	0.5	-
7	Euxyl PE 9010 [Phenoxyethanol (and) Ethylhexylglycerin]	Preservative	1	1	1	1
Check/adjust pH; approx. 4.0						

Table no. 2. Formulation and Development of Gel with Citric acid

Analysis of Two-phase facial cleansing system

Both the selected formulations of the two-phase facial cleansing system were subjected to analysis, i.e., for gel pH, colour, odour, and consistency were checked and for emulsion as per BIS for skin creams (IS 6608: 2004), all the functional parameters were checked [11-13]. The results are summarized in table no. 3 and table no. 4.

Accelerated Stability Study

The accelerated stability test is essential to evaluate a product's shelf life. The product samples are placed in different temperature environments and the product reactions to these conditions are observed over a set amount of time. Warmer temperature conditions will accelerate any reactions that may occur under normal shelf-life conditions and the 4°C sample is usually used as a control sample as the cold temperature will slow down any changes that may occur [14]. For selected formulations of emulsion and gel, accelerated stability studies were carried out for 1 month. The samples were kept at room temperature, in a fridge (4°C) and in an oven (45°C), for the observation of changes in colour, odour, pH, and consistency. The results were noted.

Subjective Evaluation

Subjective evaluation was carried out on the basis of different parameters of sensory evaluation like softness, smoothness, cleansing, shine, and absence of oil before and after application [15]. Parameters evaluated by 20 human volunteers were noted and proportional representation is given in figure no. 2.



Figure no.2. Graphical representation of Subjective evaluation Testing

From the above evaluations, it can be concluded that the cleansing effect of Two phasic cleansing system gives better effect as compared to non-treated skin in all the five parameters of sensory evaluation protocol by sensory evaluation panel.

III. RESULTS AND DISCUSSION

The formulation was carried out with 5 different trials of emulsion and 4 different trials of gel and finalised a stable formulation system by selecting emulsion (F-5) and gel (F-4). Gel with citric acid has a 4.16 pH and emulsion with sodium bicarbonate have a pH of 8.14. From the two way container, when both the products come out together on the skin from the single opening, the products get mixed together which shows neutral pH i.e., around 7 which is suitable for the skin.

The functional parameters of the selected formulation of emulsion (F-5) and gel (F-4) of the two-phase facial cleansing system were studied, they were found to be satisfactory, and the results are summarized in **table no. 3**.

Sr. No.	Parameters	Selected emulsion base (F-5)	Selected gel base (F-4)
1.	Colour	White	Transparent
2.	Odour	Good	Good
3.	Consistency	Semisolid	Semisolid
4.	pH	8.14	4.16

Table no. 3: Results of Functional parameters of selected emulsion (F-5) and Gel formulation (F-4)

The emulsion (F-5) was analyzed as per BIS of Skin creams (IS 6608: 2004) and the gel was analyzed for pH and Total viable count, the results showed that both the formulations passes the test. The results are summarized in **table no. 4**.

Sr. No.	Characteristics	Requirements [IS 6608: 2004]	Results	
			Emulsion [IS 6608: 2004]	Gel
1.	Thermal Stability	To Pass the Test	Pass the test	Not applicable
2.	pH	4.0-9.0	8.14	4.16
3.	Total Fatty Substance content, percent by mass, <i>Min.</i>	5.0	12.4	Not applicable
4.	Total Viable Count, cfu/g,	Not more than 1000 cfu/g	700 cfu/g	600 cfu/g

Table no. 4: Results of Analysis of Two-phase facial cleansing system

From the result of the accelerated stability study, it was observed that both the selected formulations of emulsion and gel were stable with respect to colour, odour, pH, and consistency.

From the results of subjective evaluation, the reaction of users to the application and review regarding the product was well appreciated. It also showed a skin cleansing effect along with excellence in terms of smoothness, softness, shine, and absence of oil from the skin.

IV. CONCLUSION

From the above study, it can be concluded that the formulation of a two-phase facial cleansing system with compact, innovative packaging is so unique in feel and can be well accepted and appreciated by the users. The study showed that a two-phase facial cleansing system gives excellent cleansing effect with improved skin condition in a joyful manner.

V. REFERENCES

- [1]. Noor, N. M., Muhamad, N. J., Sahabudin, N. A., & Mustafa, Z. (2018). Development of Skin Care Routine Support System. *Advanced Science Letters*, 24(10), 7830–7833. <https://doi.org/10.1166/asl.2018.13026>
- [2]. Zhang, L., Adique, A., Sarkar, P., Shenai, V., Sampath, M., Lai, R., Qi, J., Wang, M., & Farage, M. A. (2020). The Impact of Routine Skin Care on the Quality of Life. *Cosmetics*, 7(3), 59. <https://doi.org/10.3390/cosmetics7030059>
- [3]. Hawkins, S., Dasgupta, B. R., & Ananthapadmanabhan, K. P. (2021). Role of pH in skin cleansing. *International Journal of Cosmetic Science*, 43(4), 474–483. <https://doi.org/10.1111/ics.12721>
- [4]. P, M., P, N., B, S., & E, B. (2017). Trends in Cosmetic Packaging: a Review. *International Research Journal of Pharmacy*, 7(12), 1–4. <https://doi.org/10.7897/2230-8407.0712136>
- [5]. Lee Dohon.,(2015), Cosmetic container capable of storing and discharging two kinds of contents, WO2015026168A1. Source: <https://patents.google.com/patent/WO2015026168A1/en#patentCitations>
- [6]. Giyatmi, & Lingga, D. K. (2019). The effect of citric acid and sodium bicarbonate concentration on the quality of effervescent of red ginger extract. *IOP Conference Series: Earth and Environmental Science*, 383(1). <https://doi.org/10.1088/1755-1315/383/1/012022>
- [7]. Fiume, M. M., Heldreth, B. A., Bergfeld, W. F., Belsito, D. V., Hill, R. A., Klaassen, C. D., Liebler, D. C., Marks, J. G., Shank, R. C., Slaga, T. J., Snyder, P. W., & Andersen, F. A. (2014). Safety Assessment of Citric Acid, Inorganic Citrate Salts, and Alkyl Citrate Esters as Used in Cosmetics. *International Journal of Toxicology*, 33(Supplement 2), 16S–46S. <https://doi.org/10.1177/109158181452689>
- [8]. Luki 'c, M. L., Panteli 'cpanteli 'c, I., & Savi 'c, S. D. (2021). cosmetics Towards Optimal pH of the Skin and Topical Formulations: From the Current State of the Art to Tailored Products. <https://doi.org/10.3390/cosmetics8030069>
- [9]. Mazzarello, V., Piu, G., Ferrari, M., & Piga, G. (2019). Efficacy of a Topical Formulation of Sodium Bicarbonate in Mild to Moderate Stable Plaque Psoriasis: a Randomized, Blinded, Inpatient, Controlled Study. *Dermatology and therapy*, 9(3), 497–503. <https://doi.org/10.1007/s13555-019-0302-5>
- [10]. Niikura, T., Iwakura, T., Omori, T., Lee, S. Y., Sakai, Y., Akisue, T., Oe, K., Fukui, T., Matsushita, T., Matsumoto, T., & Kuroda, R. (2019). Topical cutaneous application of carbon dioxide via a hydrogel for improved fracture repair: Results of phase i clinical safety trial. *BMC Musculoskeletal Disorders*, 20(1), 1–14. <https://doi.org/10.1186/s12891-019-2911-7>

- [11]. Indian Standard; Toilet Soap-Specification; IS2888: 2004; Bureau of Indian standard; Government of India; 3rd Revision; 1-3
- [12]. Indian Standard; Skin Cream-Specifications; IS6608: 2004; Bureau of Indian standard; Government of India; 2nd Revision; 1-5
- [13]. Indian Standard; Method for yeast and mould count of foodstuffs and animal feeds; IS5403: 1999; Bureau of Indian standard; Government of India; 1-3
- [14]. Kirkbride, L., Humphries, L., Kozielska, P., & Curtis, H. (2021). Changing Retail Landscape. *Samudra Report*, 55, 0-3.
- [15]. Civille, G. V., & Carr, B. T.; *Sensory Evaluation Techniques*, fourth edition; CRC Press Taylor & Francis Group; 1-5



Formulation, Development and Evaluation of Self Foaming No Rinse Body Wash

K.S. Misar*, S.A. Bhankhede

*Department of Cosmetic Technology, Kamla Nehru Mahavidyalaya, Nagpur, Maharashtra, India

ABSTRACT

The 2018 edition of UN World Water Development Report stated that nearly 6 billion people will suffer from clean water scarcity by 2050. Cutting back on water usage and saving the environmental balance is already seen as a focus area among the consumers, 27% global consumers are trying to reuse or use less water. Now a day it is the need of the hour to use less water while bathing. Hence, the present study was undertaken with the aim to formulate and develop self-foaming no rinse body-wash by using Methylperfluorobutylether as an active material. Methylperfluorobutylether is colourless, odourless, nontoxic, non-flammable liquid. It has self-foaming and cleansing property. Self-foaming no rinse bodywash were developed with two different concentrations of Methylperfluorobutylether; and final formulation with 3.5% of active was evaluated for functional parameters such as pH, colour, odour, appearance, cleansing effects, foaming ability, irritancy on skin. Also, the product was subjected to stability studies and subjective evaluation on panel of human volunteers. The results showed that the self-foaming no rinse bodywash (T-II) effectively cleanses skin with its self-foaming activity without using water and causing any harsh effects on skin.

Keywords:-Self-foaming no rinse bodywash, Methylperfluorobutylether, skin cleansing

I. INTRODUCTION

The worldwide water shortage is a huge area of concern. According to UNICEF 700 million people can be displaced by extreme water scarcity by 2030 [1]. The 2018 edition of UN World Water Development Report stated that nearly 6 billion people will suffer from clean water scarcity by 2050 [2]. Cutting back on water usage and saving the environmental balance is already seen as a focus area among the consumers, 27% global consumers are trying to reuse or use less water. Now a day it is the need of the hour to use less water while bathing. More than one in five adults have made changes into their bathroom routines for saving environment [1]. To save water and assure its sustainability, several companies are showing their dedication to reducing the water footprint of their systems. This approach includes sourcing sustainable raw materials, creating waterless, fast rinse-off or non-rinse formulas, finding an alternative water source [3].

The general purpose for skin cleansing is to lower the sebum, exogenous contaminants, to control odour and the skin microbiome. The surfactants in cleansers solubilize hydrophobic materials into the aqueous phase and enable their successive removal from the skin surface. The amphiphilic structure of surfactants,

consisting of a hydrophilic polar head group and a nonpolar lipophilic tail, drives surfactants to oil/water interfaces to facilitate cleansing [4]. Bodywash is employed as a skin cleansing agent in the shower or bath. It contains milder surfactant bases than shampoos [5]. A self-foaming no rinse body wash composition that is applied topically to cleanse and mask and/or deodorize a biological entity, human and animal, does not require rinsing with water [6]. Hence, the present study was undertaken with the aim to formulate and develop self-foaming no rinse body-wash by using Methylperfluorobutylether as an active material to serve as a water saving gentle skin cleansing aid in its unique way.

Perfluoro butyl methyl ether also known as Methylperfluorobutylether, is a type of colourless and odourless, nontoxic, non-corrosive, non-combustible liquid substance, having molecular formula : $C_4F_9OCH_3$ [7]. It is reported that, the fluorine compound mentioned in present study is colourless, tasteless, low irritant, and have oxygen carrying capability, and therefore, gasification power is good, has cleaning capacity.0.01 to 20% by weight is preferable usage level of Methylperfluorobutylether for cosmetic preparations [8].

II. MATERIALS AND METHODS

2.1 Analysis of Methylperfluorobutylether

Methylperfluorobutylether was procured for the present study from Chemico Health and Beauty India, Pvt., Ltd., Thane, along with Certificate of Analysis. The procured sample was validated for parameters, such as colour, odour and heavy metals (Table 3).

2.2 Formulation of self-foaming no rinse bodywash

Two different formulations of base for self-foaming no rinse bodywash were formulated, and Trial II formulation was selected for further study as it gave satisfactory consistency (Table1).

S.N.	Ingredients	Use	Trial I (Quantity in %)	Trial II (Quantity in %)
Phase A				
1.	Sodiumlaurylethersulphate	Primary surfactant	30%	30%
2.	Cocamidopropylbetaine	Secondary surfactant, Foam booster	3.33%	3.33%
3.	Glycerine	Humectant	3.33%	3.33%
Phase B				
4.	Sodium Chloride (NaCl)	Viscosity modifier, Thickener	2.000%	2.905%
5.	Liquid germall plus	Preservative	0.1%	0.1%
6.	Colour (orange)	Aesthetic appearance	0.15%	0.15%
7.	Perfume (orange)	For pleasant smell	0.75%	0.4%
Phase C				
8.	Water	Vehicle , Solvent	Upto 100 (60.34%)	Upto 100 (59.785%)

Table no.1.Formulation of self-foaming bodywash base

All the ingredients of phase A, phase B and phase C were taken in separate clean and dried beakers. Phase A was added into phase C and stirred. Phase B was added into mixture of phase A and phase C. The contents in the beaker were subjected to stirring with the help of mechanical stirrer at low shear. Then self-foaming no rinse bodywash was transferred to suitable container.

Since formulation Trial II gave a satisfactory consistency hence it was selected as a suitable self-foaming no rinse bodywash base for incorporation of Methylperfluorobutylether. Two different concentrations of Methylperfluorobutylether (i.e. 3% and 3.5%) was incorporated in base formulation (Trial II) to formulate two formulations of self-foaming no rinse bodywash (i.e. T-I, T-II) respectively (Table 2).

S.N.	Ingredients	Quantity in%	
		T-I	T-II
1.	Self-foaming no rinse bodywash base	97%	96.5%
2.	Methylperfluorobutylether	3%	3.5%

Table no. 2. Formulation of Self-foaming no rinse bodywash with Methylperfluorobutylether (Active)

2.3 Study of functional parameters:-

The self-foaming no rinse bodywash formulations i.e. selected base (Trial-II),T-I (Methylperfluorobutylether3%) andT-II(Methylperfluorobutylether 3.5%) was subjected to study functional parameter like pH, colour, odour, appearance, cleansing effects, foaming ability, irritancy on skin. The results are summarized in table no4, 5, 6 and graph 1, 2, and 3.

2.3.1 Analysis of self-foaming no rinse bodywash.

Formulations under study i.e. T-I (Methylperfluorobutylether3%) and T-II (Methylperfluorobutylether3.5%) was subjected to analysis of foaming power and cleaning ability. The results are summarized in table no.4.

2.3.2 Accelerated stability study.

A stability study is a routine operation which ensures the maintenance of product safety, quality and efficacy throughout the shelf life [9]. The data generated during the stability testing is an important necessity for regulatory approval of any formulation [10]. Such information can be helpful in terms of creating successful products, and product development [11]. The preferred stability test is the accelerated method, which requires shorter test times [12]. The above mentioned formulations [selected base (Trial II), T-I (Methylperfluorobutylether3%) and T-II (Methylperfluorobutylether3.5%)] were subjected to accelerated stability studies [13]. Changes in parameter like colour, odour, pH at three temperatures [i.e., in oven at (45°C), in refrigerator at (4°C) and at room temperature] was recorded for 30 days, at the interval of 5 days. The results were noted.

2.3.3 Subjective evaluation.

Since the cleansing ability and foaming power of T-II (Methylperfluorobutylether 3.5%) formulation was greater, it was selected for further study on human volunteers. It was given to 30 human volunteers of age group between 17 to 62 years to carry out the subjective evaluation on the basis of their feedback. Subjective evaluation was carried out on the basis of parameters such as, appearance, cleansing effects, self-foaming effect and irritancy on skin.

III. RESULTS AND DISCUSSION

To save water is the need of the hour, hence the present study was undertaken with the aim to formulate self-foaming no rinse body wash formulation with Methylperfluorobutylether, which produces the foam by itself after being rubbed on the skin and cleanses the skin without using water. From the analysis of Methylperfluorobutylether it was observed that procured sample passed the test as per certificate of analysis and hence was used for incorporation in base formulation (Table no.3).

S.N.	Characteristic	Requirement as per Certificate of Analysis of Methylperfluorobutylether	Result	Inference
1.	Colour	Clear colourless liquid	Clear colourless liquid	Passes the test
2.	Odour	Slight characteristic	Slight characteristic	Passes the test
3.	Heavy metals [14].	Not more than 20 ppm	Passes the test	Passes the test

Table no. 3. Results for Analysis of Methylperfluorobutylether

Two different formulations of self-foaming no rinse bodywash base were prepared and Trial-II was selected, as it gave satisfactory consistency, for incorporation of Methylperfluorobutylether. Two different formulations T-I (Methylperfluorobutylether 3%) and T-II (Methylperfluorobutylether 3.5%) were prepared by using Trial-II as base. From the results of analysis of T-I and T-II, it was observed that formulation T-II (Methylperfluorobutylether 3.5%) has more foaming power and cleaning ability than formulation T-I (Methylperfluorobutylether 3%). The results are summarized in table no 4.

S.N.	Name of test	Requirements	Formulations		Inference
			T-I	T-II	
1.	Determination of Foaming power [15]	Minimum 50ml	96ml	118ml	Passes the test
2.	Cleaning ability	Should clean oil, dirt and give fresh feeling	Average cleaning	Good cleaning	Passes the test

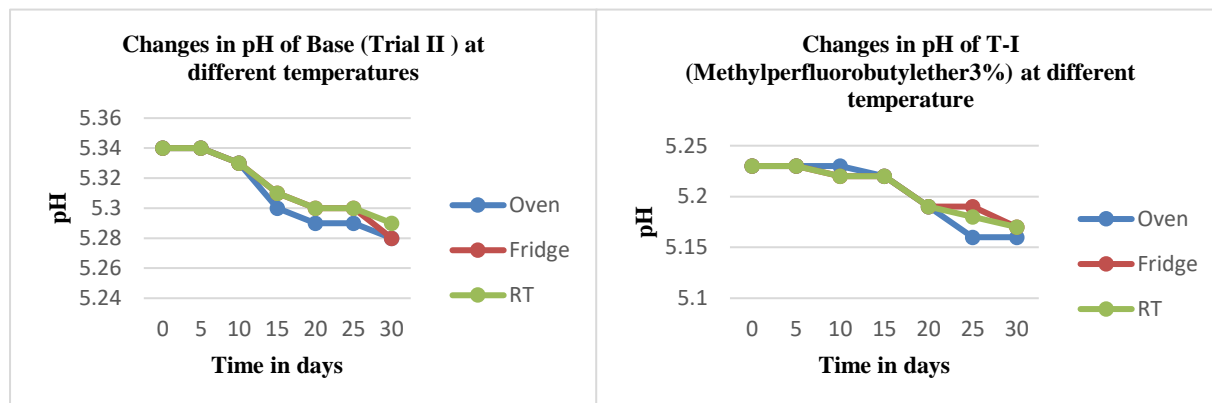
Table no.4. Results of Determination of foaming power and cleaning ability of self-foaming no rinse bodywash

From the results of stability study, it was observed that formulations [i.e. Base (Trial II), T-I (Methylperfluorobutylether 3%), T-II(Methylperfluorobutylether 3.5%)] was stable with respect to colour, odour and pH at three different temperatures (Table no.5; Graph No. 1,2 and 3).

S.N	Formulations	Parameters	Oven(45°C)	Refrigerator (4°C)	Room Temperature
1.	Base (Trial II)	Odour	No change	No change	No change
		Colour (light orange)	No change	No change	No change
2.	T-I (Methylperfluorobutylether 3%)	Odour	No change	No change	No change
		Colour (light orange)	No change	No change	No change

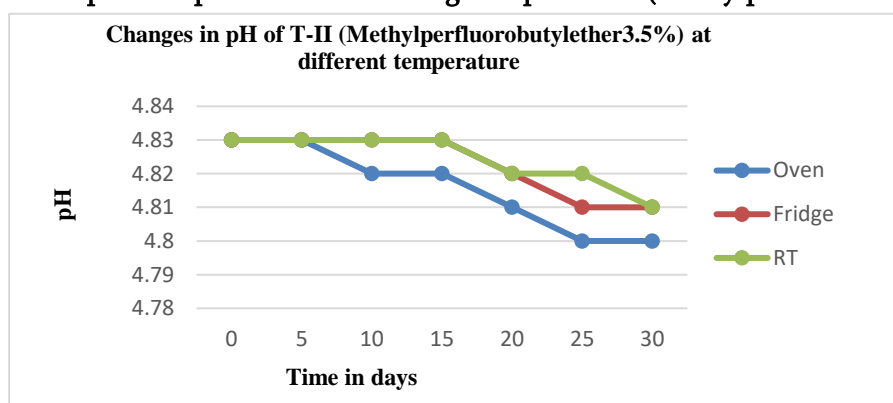
		orange)			
3.	T-II (Methylperfluorobutylether 3.5%)	Odour	(light	No change	No change
		Colour	orange)	No change	No change
				No change	No change

Table no. 5. Results of Accelerated stability study



Graph 1. Graphical representation of changes in pH of base (Trial II).

Graph 2. Graphical representation of changes in pH of T-I (Methylperfluorobutylether 3%).



Graph 3. Graphical representation of changes in pH of T-II (Methylperfluorobutylether 3.5%).

Since formulation T-II (Methylperfluorobutylether 3.5%) gave satisfactory cleansing and foaming effect it was used for subjective evaluation. From the result of subjective evaluation, it was observed that self-foaming no rinse bodywash with 3.5% of Methylperfluorobutylether was well appreciated. It caused no irritation during usage and after removal. It also showed excellence in terms of cleansing effect .Results are summarized in table no 6

Table no.6. Results of Subjective evaluation of T-II

S.N.	Parameters	Formulation T-II (3.5%)
1.	Appearance	Good
2.	Cleansing effect	Excellent
3.	Irritancy on skin	None
4.	Self-foaming effect	Excellent

IV. CONCLUSION

From the above study it can be concluded that the self-foaming no rinse bodywash T-II (Methylperfluorobutylether 3.5%) is good formulation in terms of appearance, odour, and cleansing, foaming property. It cleanses skin in a gentle way with its self-foaming activity without using water on skin.

V. REFERENCES

- [1]. M. Priyanka & Kavana. "Waterless Products: The Growing Trend in Beauty Products".course5i, 20July2021,<https://www.course5i.com/blogs/trend-in-beauty-products/>
- [2]. A. Boretti and L. Rosa. "Reassessing the projections of the World Water Development Report". Nature partner journal. 31July 2019. 1
- [3]. J. B. Aguiar, A. M. Martins, C. Almeida, H. M. Ribeiro, J. Marto. "Water sustainability: A waterless life cycle for cosmetic products". Elsevier. 9April2022 .1
- [4]. G. Mao, E. T. Gunn, S. Hornby. "Cleansing Formulations That Respect Skin Barrier Integrity". Dermatology Research and Practice .25June2012.2
- [5]. Lawton ; "The Structure & Function Of Skin" ; Nursing times ; December 2019 ; Vol 115; Issue 12 ; 33
- [6]. Edwin De La Cruz ;5 august 2010; Rinseless bodywash composition ; US 2010/0197544A1
- [7]. Zhu Hongji, Ren Huifang, Fan Wen , Geng Weli, Wang Zhihui, Yu Kaoming, Chen Weifeng ; 24 November 2017 ; A kind of preparation method of methyl perfluro butyl ether ; CN107382678A
- [8]. Kim Da-Hye, Han Na-Kyeong, Choi Jong-Wan, Lee Gi-Yong, Kim Hae-Min ;23 September 2015 ; Mask sheet cosmetic composition with self-foaming function and manufacturing method thereof ; CN1049219601
- [9]. G .Rao, A .Goyal. "Development of stability indicating studies for pharmaceutical products: an innovative step". International Journal of Pharmaceutical Chemistry and Analysis.110
- [10]. M. S. Charde et al. "Development of analytical and stability Testing method for Vitamin-A palmitate formulation". International Journal of Pharmaceutical Chemistry. ISSN:2249-734X.2014.39
- [11]. K .Edwards. "Stability Testing Guidance for Product Safety and Shelf life Insight".Cosmetic&Toiletries.18December2018.<https://www.cosmeticsandtoiletries.com/testing/method-process/article/21837281/stability-testing-guidance-for-product-safety-and-shelflife-insight>
- [12]. Iskandarsyah et al. "Accelerated stability testing of anti-aging cream: Formulation of myristic acid and stearic acid as degradation product". International journal of applied pharmaceutics. 2018. Vol 10. Issue 1.1
- [13]. A .M .Juncan, L .L .Rus. "Influence of Packaging and Stability Test Assessment of an Anti-aging Cosmetic Cream". Materiale plastice.2018.426
- [14]. Indian standard; Skin Creams-Specifications; IS6608:2004; Bureau of Indian Standards; 2nd Revision; 2004; 4
- [15]. Indian standard; Toothpaste -Specifications; IS6356:2001; Bureau of Indian Standards;3rd Revision;2001;8-9



Molecular Interaction Study through Molar Volume, Available Volume and Free Volume for Ternary Liquid Mixture of Alcohol + Tri-Ethylamine + Acetic Acid

P J Thakare

Department of Chemistry, Shri Shivaji College of Arts, Commerce and Science, Akola, Maharashtra, India

ABSTRACT

The density, viscosity and ultrasonic velocity of ternary liquid mixture of Alcohol + Tri-ethylamine (TEA) + Acetic acid have been measured at three different temperatures 30DEG, 35DEG and 40DEG. From these measured values, molar volume, available volume and free volume have been calculated. The nature of molecular interactions between component molecules is investigated through above parameters. The experimental results are used to interpret the molecular interactions in ternary liquid mixture.

Keywords: ternary liquid mixture, molar volume, available volume, free volume

I. INTRODUCTION

The study of molecular interaction in binary and ternary liquid mixtures plays an important role in the study of development of molecular science. Since long, thermodynamic and transport properties of liquid mixtures have been used to study the departure of real liquid mixture behaviour from ideal one¹⁻⁴. Acoustical parameters are important to understand different kinds of association, the molecular packing, molecular motion and various types of intermolecular interactions and their strength. When two liquids are mixed together, the resulting changes in physical and thermodynamic properties can be considered as a sum of several contributions due to free volume change, change in energy, change in molecular orientations, steric hindrances etc⁵. By looking at the importance, in the present study ultrasonic velocity, density, and viscosity measurements have been carried out at different concentrations and different temperature for the determination of ultrasonic parameters such as molar volume, available volume and free volume.

II. THEORY

If ρ_{mix} is the density of mixture, then molar volume is given by

$$V_{m} = \frac{\bar{M}}{\rho_{mix}} \quad (1)$$

If mole fractions are changed the \bar{M} then ρ_{mix} are also found to change. This suggests that molar volume changes with concentration when temperature is constant.

Available volume is the direct measure of compactness and strength of binding the molecule of liquid or liquid mixture. This parameter can be calculated from ultrasonic velocity as⁶;

$$V_a = V [1 - U/U_\infty] \text{ m}^3\text{mol}^{-1} \quad (2)$$

Where

V_a = Available Volume

U_∞ = the Schaaf's limiting value taken as 1600 m/s for liquid mixture.

V = molar volume of liquid mixture

U = Ultrasonic velocity

Free volume in terms of Ultrasonic velocity (U) and the Viscosity of the liquid (η) can be express as;⁷

$$V_f = [M_{\text{eff}}U/K\eta]^{1/2} \quad (3)$$

Where, M_{eff} is the effective molecular weight.

III. EXPERIMENTAL STUDY

In the present work density was measured by using density bottle (corning made certified 10 ml). Stopper is used in order to avoid evaporation of chemicals. Weight of bottle was taken by monopan balance(model no. K15) supplied by, K-Roy and Company, Varanasi. For the measurement of viscosity Ostwald viscometer was used. The liquids used for the work were of BDH AR grade. For the present work the chemicals used viz. Alcohol, tri-ethylamine (TEA), and acetic acid were procured SD fine Mumbai and from E Merk chemicals Ltd India. A crystal controlled interferometer, model No. M8 15 supplied by Mittal enterprises, New Delhi, was used for determination of ultrasonic velocity. Measurements are made at frequency 2 MHz.

IV. RESULT AND DISCUSSION

The Fig 1a shows the decreasing trend of molar volume with concentration of acetic acid. This reveals the presence of specific interaction between the components in the ternary system. Decrease in molar volume V_m is probably due to the reason that the molar volume is directly proportional to the molecular weight.

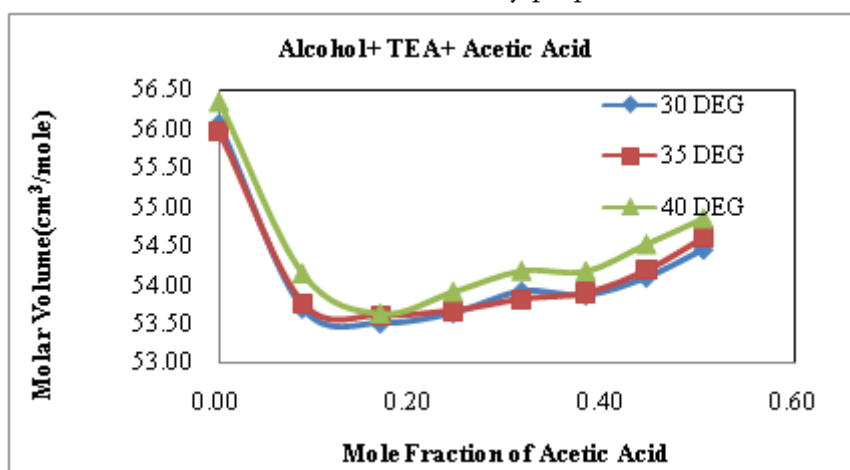


Fig: 1a

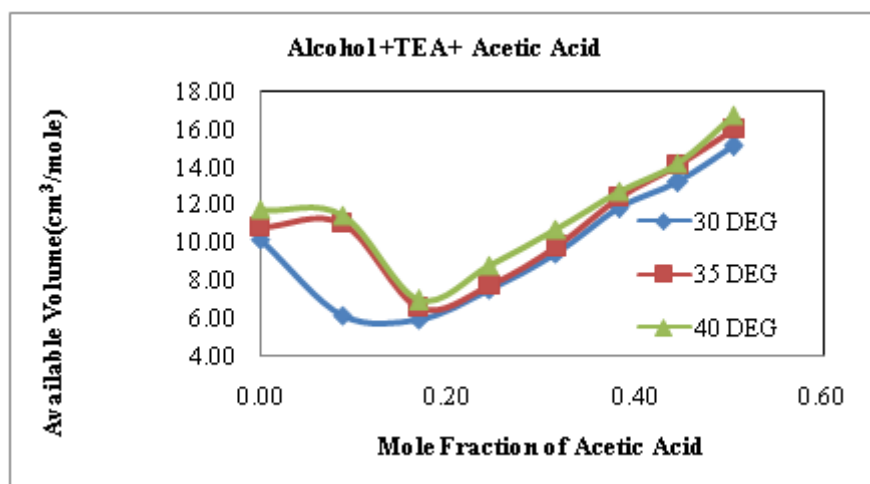


Fig: 1b

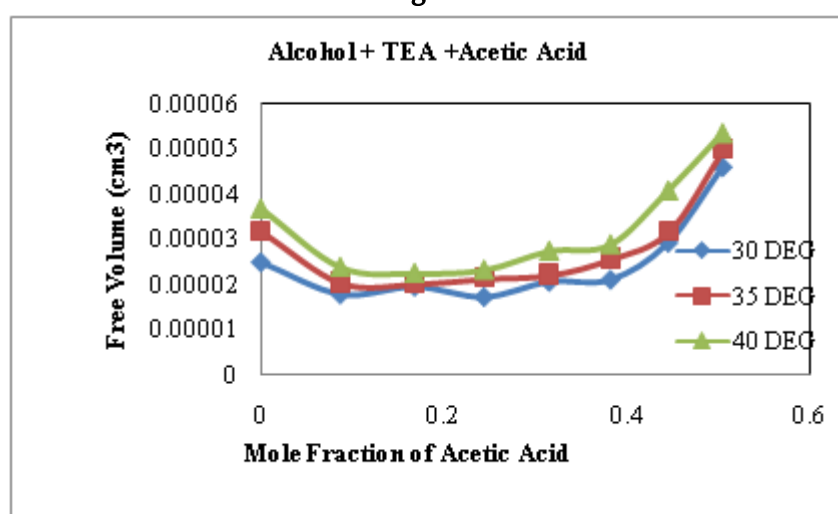


Fig: 1c

Since TEA (101.19) has higher molecular weight in the solution as compared to acetic acid, hence as mole fraction of acetic acid (60.05) increases V_m decreases. This may be due to decrease in the percentage of TEA in the mixture. Further, the molar volume increases with temperature slightly which is due to increase in molecular separation in liquid mixture.

Available volume V_a is the direct measure of compactness and strength of binding the molecule of liquid or liquid mixture. Fig: 1b shows that available volume V_a decreases with the increase in mole fraction of carboxylic acid, attains minimum and increases again with mole fraction of carboxylic acid. The decrease in V_a is due to the net packing of molecules inside the shell which may be formed by complexation between unlike molecules through hydrogen bonding in the ternary liquid mixture.

It is seen that increase in concentration of acetic acid results in considerable increase in intermolecular spaces between the molecules. Thus a progressive increase or decrease in free volume (Fig: 1c) clearly indicates the existence of molecular interaction, due to which the structural arrangement is considerably affected. It proves that there is a weak interaction between the solute and solvent molecules at lower and higher concentration of acid in mixture⁸.

V. REFERENCES

- [1]. Z T Fidkowaski, M F Doherty and M F Malone, (1993), AICHE Journal, vol.39,no.8,pp.1303.
- [2]. R Tiyyagarajan , L Palaniappan,(2008), Indian J. Pure and Appl.22) Shahla P, Maimoona Yasmin, Manisha Gupta and Jagdish Prasad Shukla, (2010), Thermoacoustical and Excess Properties of binary mixtures of ethyl butyrate with methanol and vinyl acetate, Int. J. Thermodynamics, vol.13,pp. 59-66. Phys. Vol.46, pp.852-856
- [3]. G Thomas,(1996), Chem for Pharma and Life Sci, Prentice Hall, London, Chap:2,pp.15-24.
- [4]. V D Bhandakkar et al.,(2003) Indian J. Pure and App. Phy., vol.41, pp 849-854.
- [5]. Shahla P, Maimoona Yasmin, Manisha Gupta and Jagdish Prasad Shukla, (2010), Thermoacoustical and Excess Properties of binary mixtures of ethyl butyrate with methanol and vinyl acetate, Int. J. Thermodynamics, vol.13,pp. 59-66.
- [6]. Sabesan R, Varadarajan R, (1984), Ultrasonic studies of thermodynamic luctuations of pressure, volume and temperature in liquids in relation to isomerism, Journal of Acoustical Society of India, vol. 12(03),38-40.
- [7]. Reddy Raveendranatha K, Rama Murthy S, Moorthy Rama L, (1991) Free volume and internal pressure study in aqueous solutions of methylene blue and auramine. The Journal of Acoustical Society of India, vol. 19(4), 22- 25.
- [8]. Bedare, G R. Bhandakkar, V D. and Suryavanshi, B M. (2012). Journal of Chemistry and Pharmaceutical Res., 4(2),1028.



Synthesis of Silver Nanoparticle Material Using Plant *Parkia Biglodulosa*

S. V. Narsing, S. E. Bhandarkar, B.P Khobragade, V. A. Shirbhate

Department of Chemistry, Govt. Vidarbha Institute of Science and Humanities Amravati University,
Amravati 444604, Maharashtra, India

ABSTRACT

Nanoparticle and nanotechnology open new theme in chemical, agriculture, industrial and life Sciences. The medicinal properties of plant due to some bioactive chemical constituents which are present in it. Silver has been recognized as a non-toxic, safe antibacterial / antifungal agent used for centuries. Silver shows a lot high potential for a variety of biological applications, especially in the form of nanoparticles. It is in harmony with nature. Blending methods are becoming increasingly popular in chemical technologies as well as environmental needs. We synthesized silver nanoparticles from plant leaves of *Parkia Biglodulosa*. Spectroscopic techniques such as Ultra violet radiation(UV), X-ray diffraction (XRD), Fourier Transform Infrared spectroscopy(FTIR) was carried out for characterization. Scanning electron Microscopy(SEM) technique was employed to observe the surface morphology of nanomaterial. Synthesized nanoparticles were studied for their biological activities and found to be most active.

Keywords- Synthesis, Silver nanoparticle, *Parkia Biglodulosa*, Characterization, Biological activity

I. INTRODUCTION

Nanotechnology refers to an emerging field of science that includes synthesis and development of various nanomaterials. ^[1] The object ranging size from 1- 100 nm and may differ from the bulk material is called as nanoparticles. ^[2] Presently, different metallic nanomaterials are being produced using copper, zinc, titanium, magnesium, gold, alginate and silver. ^[3] Nanoparticles it is used in different purpose such as medical treatment as well as industrial production of solar and oxide fuel batteries for energy storage, to wide incorporation into diverse materials of everyday use such as cosmetics or clothes. ^[4] incorporation into diverse materials of everyday use such as cosmetics or clothes. ^[5] The application of nanotechnology in medical applications, commonly referred to as “nanomedicine”, seeks to deliver a new set of tools, devices and therapies for the treatment of human disease. Nanomaterials that can act as biological mimetics, “nanomachines”, biomaterials for tissue engineering, shape-memory polymers as molecular switches, biosensors, laboratory diagnostics and nanoscale devices for drug release, are just a few of the applications being explored. ^[6]

II. MATERIAL AND METHOD

The preparation of metal nanoparticle as view of environmental and physical ways are as follows, Effective and externally stimulated heating can be delivered at cellular levels through alternating magnetic field (Ito et al, 2006), in research must be based on botanical plant like Parkia Biglodulosashows taxonomical study as shown

Common name : African locust bean

Botanical name : Parkia Biglodulosa

Kingdom: Plantae

Phylum: Spermatophyt

Subphylum: Angiosperm

Class: Dicotyledonae

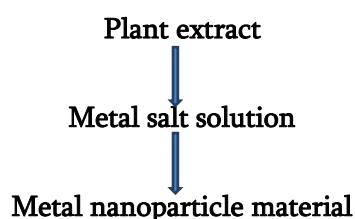
Order: Fabales

Family: Fabaceae

Genus: Parkia

Species: Parkia Biglodulosa

As also shows some of the plants must be as parkia filicoidea, Azadirachta indica,acalypha indica, medicago sativa etc showing the synthesis ofnanoparticlesmaterial like Au,Ag, Fe,Zn, etc. Step involving formation of metal nanoparticles ,



III. CHARACTERIZATION

XRD- X-ray diffraction measurements were taken on maxima X XRD-7000(Shimadu, Tokya, Japan operating at voltage of 40KVand 20mA electrical current radiation source in region of 2θ from 40° to 80° c.

FTIR analysis

FTIR analysis of silver nanoparticles synthesized by using leaf extract of Parkia Biglodulosa. It is found that nanoparticle possessed definite surface morphology. FTIR spectrum reveals prominent bonds at 3425cm^{-1} , 3195cm^{-1} , 2335cm^{-1} , 1915cm^{-1} , 1608cm^{-1} , 1028cm^{-1} . The groups are responsible for the synthesis and stabilization of generated silver nanoparticles.

SEM- The morphology and geometry of AuNPs were investigated by 200 scanning electron microscopy shown microporous surface area.

UV-vis spectroscopy is one of the most widely used simple and sensitive technique for the analysis of nanoparticle synthesis. The silver nanoparticles synthesized by Parkia Biglodulosaleaf extract were confirmed by uv-vis spectrophotometer. It showed the peak at 422.03 nm which correspond to absorbance of silver nanoparticles.

Antimicrobial and antifungal study - silver nanoparticles generated by leaves extract of Parkia Biglodulosaleaf tested for the antimicrobial activity. Silver nanoparticles were found most active against E-coli, *Staphylococcus aureus*, *Proteus mirabilis* and fungus *Aspergillus niger*.

IV. CONCLUSIONS

Silver Nanoparticles material from Parkia Biglodulosa was synthesised and characterized by using spectroscopic techniques .The synthesized nanoparticles may be used to treat diseases caused by test pathogens only if they do not cause side effects.

V. ACKNOWLEDGEMENT

The authors are thankful to Director, Govt. Vidarbha Institute of Science and Humanities Amravati for providing necessary laboratory facility.

VI. REFERENCES

- [1]. Saba Hasan , international science congress association , (2015);4:1-3
- [2]. Fatimah, I., journal of advanced research, (2016) , 961–969.
- [3]. Paul N.S. and Raman P. ,Yadav.,Asian Journal of Biomedical and Pharmaceutical Sciences, 5(45),2015, 26-28.
- [4]. Albrecht M.A, Evan C.W, Raston C.L.,Green Chem (2006); 8: 417-432.
- [5]. Dahl AJ, Bettye L, Maddux S, Hutchison EJ., Greener Synthesis. Chem. Rev. 2007; 107: 2228–2269.
- [6]. Gurunathan S, Kalishwaralal K, Vaidyanathan, R, Deepak V, Pandian S, Muniyandi J., Colloids Surf. B (2009); 74: 328–335.

In-Vitro Selection of Salt Tolerant Tomato Plant (*Lycopersicon Esculentum Mill*)

V. Y. Charjan¹, B. Abraham¹, P. J. Ninawe²

¹Department of Botany, Kamla Nehru Mahavidyalaya, Nagpur, Maharashtra, India

²Department of Botany, D.R.B. Sindhu Mahavidyalaya, Nagpur, Maharashtra, India

ABSTRACT

The given study is based on identification of salt tolerance trait from the seeds of Tomato (*Lycopersicon esculentum Mill.*). Genetic diversity can be seen within a particular species. To identify a trait in a given variety is difficult to find out using morphological data. In the present study the hypocotyl were isolated and grown in increasing salt concentration of 0.5%, 1.0% and 1.5%. The tolerance observed may be due to genetic diversity or soma clonal variation within in the variety and thus can be selected for micropropagation, hybridization and other experiments.

Keywords:- In-vitro, somaclonal variation

I. INTRODUCTION

Tissue culture is the in vitro aseptic culture of cells, tissues, organs or whole plant under controlled nutritional and environmental conditions (Thorpe T, 2007) often to produce the clones of plants. The resultant clones are true-to type of the selected genotype. The controlled conditions provide the culture an environment conducive for their growth and multiplication. These conditions include proper supply of nutrients, pH medium, adequate temperature and proper gaseous and liquid environment. Plant tissue culture technology is being widely used for large scale plant multiplication.

Apart from their use as a tool of research, plant tissue culture techniques have in recent years, become of major industrial importance in the area of plant propagation, disease elimination, plant improvement and production of secondary metabolites. Small pieces of tissue (named explants) can be used to produce hundreds and thousands of plants in a continuous process. A single explant can be multiplied into several thousand plants in relatively short time period and space under controlled conditions, irrespective of the season and weather on a year round basis (Akin-Idowu et al,2009) . Endangered, threatened and rare species have successfully been grown and conserved by micropropagation because of high coefficient of multiplication and small demands on number of initial plants and space. In addition, plant tissue culture is considered to be the most efficient technology for crop improvement by the production of somaclonal and gametoclonal variants. The micropropagation technology has a vast potential to produce plants of superior quality, isolation of useful variants in well-adapted high yielding genotypes with better disease resistance and stress tolerance capacities

(Brown DCW; Thorpe TA, 1995). Certain type of callus cultures give rise to clones that have inheritable characteristics different from those of parent plants due to the possibility of occurrence of somaclonal variability (George EF, 1993), which leads to the development of commercially important improved varieties. Commercial production of Tissue culture is an important tool of biotechnology which can be used to improve productively of crop via rapid availability of superior planting material (Bhatia and Ashwath, 2004) in vitro techniques are important tools for modern plant improvement program to develop suitable cultivars in a minimum time (Tagi et al.,2002)

The regeneration of shoots from callus has been found to depend on factors such as genotype, explant type, composition of media, quantity of media, plant growth regulators used in media gelling agent, light intensity and quality, photoperiod provided, temperature, culture container (Reed, 1999; Bhatia et al., 1994).

The tomato is the edible [fruit](#) of *Solanum lycopersicum* which belongs to family, [Solanaceae](#). In 1753, Linnaeus placed the tomato in the genus *Solanum* (alongside the potato) as *Solanum lycopersicum*. In 1768, Philip Miller moved it to its own genus, naming it *Lycopersicon esculentum* (International Plant Name Index) This name came into wide use.

The species originated in [Central](#) and [South America](#). The plants typically grow to 1–3 meters (3–10 ft) in height and have a weak stem that often sprawls over the ground and vines over other plants. It is a [perennial](#) in its native habitat, and grown as an [annual](#) in temperate climates. Tomato fruit is classified as a [berry](#). As a true fruit, it develops from the ovary of the plant after fertilization, its flesh comprising the pericarp walls. Tomato is consumed in diverse ways, including raw, as an ingredient in many dishes, sauces, [salads](#), and drinks. While tomatoes are [botanically berry](#)-type fruits, they are considered [culinary vegetables](#), being ingredients of savory meals.

For propagation, the seeds need to come from a mature fruit, and be dried or fermented before germination. In 2014, world production of tomatoes was 170.8 million [tonnes](#), with China accounting for 31% of the total, followed by [India](#), the United States and [Turkey](#) as the major producers (table) In 2014, tomatoes accounted for 23% of the total fresh vegetable output of the [European Union](#), with more than half of this total coming from Spain, Italy and Poland. In 2013, global tomato exports were valued at 88 billion US dollars. ([Food and Agriculture Organization](#), Statistics Division. 2016).

Effect of salinity

Salt stress has three fold effects which reduces water potential and causes ion imbalance and toxicity. Salt stress affects some major processes such as germination, speed of germination, root/shoot dry weight and Na^+/K^+ ratio in root and shoot . Salinity tolerance is critical during the life cycle of any species. Large genetic variation of tolerance to salt level exists among tomato genotypes. However, salt tolerance breeding programs have been restricted by the complexity of the trait, insufficient genetic and physiological knowledge of tolerance-related traits, and lack of efficient selection domain. Most commercial cultivars of tomato are sensitive to moderate levels of salinity up to 2.5 dSm^{-1} , without significant yield reduction. Correcting saline condition in field and greenhouse would be expensive and temporary while selection and breeding for salt tolerance can be a wise solution to minimize salinity effects as well as improve production efficiency. So

breeding tolerant cultivars of tomato under saline conditions is needed. Genetic characterization of useful germplasm is the first step toward releasing tolerant cultivars. This study tried to find any level of tolerance to saline conditions Salt stress cause blossom-end rot (BER) of tomato fruit when grown hydroponically. Fruit growth rate, water status, cuticle permeability and induction of blossom-end rot (BER) of tomato fruit Hossain & Nonami (2012).

The present investigation was carried out to develop protocol for efficient selection of salt tolerant varieties of tomato by in-vitro selection.

II. MATERIALS AND METHODS

The seeds of Tomato PKM – 1 variety of 'seedco quality seeds' were purchased from Krishi kranti Kendra, Nagpur. In the present investigation B5 media (Gamborg et al., 1968) was used. The stock solutions were prepared by dissolving the chemicals in distilled water. These were added one at a time to avoid precipitation. To avoid precipitation of phosphate salt and calcium, the stock of $\text{CaCl}_2 \cdot 2\text{H}_2\text{O}$ and macro salts containing phosphate moiety were prepared separately. For preparation of media, concentration stock solutions were used. Usually the stock solutions were prepared in 20X and 1000X concentration.

Plant growth regulators stock (Narayanswamy, 1994)

- Stock (10mg/10ml) was prepared by dissolving 10mg of NAA first NAA in small volume of 1N NaOH, and gradually diluted to 10ml with double distilled water and stored in refrigerator at -20°C .
- 2,4 -D stock (10mg/10ml) was prepared by dissolving 10mg of 2,4-D first in small volume of ethanol, and gradually diluted to 10ml with double distilled water and stored in refrigerator at -20°C .
- Kinetin stock (10mg/10ml) was prepared by dissolving 10mg of kinetin first in small volume of 1N HCL and gradually diluted to 10ml with double distilled water and stored in refrigerator at -20°C .
- 6 Benzylamino purine stock (10mg/ml) was prepared by dissolving 10mg of 6 Benzyl amino purine first in small volume of 1N HCL, and gradually diluted to 10ml with double distilled water and stored in refrigerator at refrigerator at -20°C .

Preparation of Agar media (solid) :

The 1 L of the medium was prepared by adding, each stock. Each stock was completely mixed before adding the next.

Explant type and sterilization:

The hypocotyl region of seedlings of tomato PKM-1 variety reaching a height of 3-4 cm length were taken as explants. The explants were sterilized using 0.1% HgCl_2 for 3 mins followed by repeated washing with distilled water for 5 mins each.

Standardization of media:

1. Media used to determine the tolerance level of explants to NaCl stress:

The media consisted of full strength Gamborg B5 media (Gamborg et al., 1968). The media were supplemented with hormones and NaCl. Hormones include 6 Benzylamino purine (BAP) $4.4 \mu\text{M}$, Kinetin (KIN) $18.4 \mu\text{M}$,

Naphthaleneacetic acid (NAA) 2.7 μ M. in this media different concentration of NaCl (0%, 1%, 1.5%, 2%) was added to determine the salt tolerance of the PKM-1 variety.

2. Media used for selecting salt tolerant explants at 1% NaCl Stress:

Same as the above medium with 1% NaCl.

3. Media used for Callus induction:

Full strength Gamborg B5 media (Gamborg et al., 1968) supplemented with

i. 6 Benzylamino purine (BAP) 4.4 μ M, Kinetin (KIN) 18.4 μ M, Naphthaleneacetic acid (NAA) 2.7 μ M (Subculture I).

ii. 6 Benzylamino purine (BAP) 8.8 μ M, Naphthaleneacetic acid (NAA) 1.0 μ M (Subculture II).

In B5, the amount of $\text{COCl}_2 \cdot 6\text{H}_2\text{O}$ and $\text{CuSo}_4 \cdot 5\text{H}_2\text{O}$ was very small, their stocks were prepared separately. For that 2mg of $\text{CuSo}_4 \cdot 5\text{H}_2\text{O}$ was dissolved in 2ml of double distilled water and 2mg of $\text{CuSo}_4 \cdot 5\text{H}_2\text{O}$ in 2ml of double distilled water and then added 250 μ g of each to micronutrient stock.

III. RESULT AND DISCUSSION

The results obtained in the study are presented as under.

Effect of different concentration of sterilizing agent and hormone on germination:

The seeds of tomato germinated under normal condition within 10-12 days. The prerequisite for invitro culture is sterilization of seeds, and then inoculating in culture medium. This avoids contamination in media. Therefore the seeds were sterilized with 0.1% HgCl_2 . It was observed that when seeds were sterilized with 0.1% HgCl_2 for 3 mins followed by rinsing thoroughly with distilled water, did not show any germination. In order to increase the germination percentage the seeds were first treated with 0.5% gibberellic acid for 24 hrs followed by treatment with 0.1% HgCl_2 . The seeds were then washed thoroughly and was inoculated in autoclaved Petri Dish with wet filter paper. The Petri Dish was kept in culture room for germination. It was observed that there was still no germination. Therefore in next attempt the seeds were directly treated with 0.5% gibberellic acid and kept for germination in culture room. There was 100% germination in 5 days. The seeds were only treated with 0.5% gibberellic acid and once seedlings were 7 days old it was sterilized with 0.1% HgCl_2 and was used as source of explants. (Table 1)

Table 1: Effect of different concentration of sterilizing agent and hormone on germination

Sr.no	Nature of Treatment	No. of Days	% of Germination
1	Control	12	100%
2	0.1% HgCl_2	-	0%
3	0.5% Gibberellic acid (GA)	5	100%
4	0.1% HgCl_2 and 0.5% Gibberellic acid (GA)	-	0%

Effect of salt stress on explants:

The media used was Gamborg B5 supplemented with hormones BAP 4.4 μ M, KIN 18.4 μ M, NAA 2.7 μ M. The same media along with different concentration of NaCl (0.0%, 1.0%, 1.5%, 2.0%) was used to determine the effect of salt stress. It was found that salt stress above 1.0% was lethal for explants growth. (Table 2)

Table 2: Effect of Salt Stress on ExplantsB5 media with BAP 4.4 μ M, KIN 18.4 μ M, NAA 2.7 μ M

Sr.no	Concentration of NaCl	No. of explants	Survival
1	0.0%	16	16
2	1.0%	16	0
3	1.5%	16	0
4	2.0%	16	0

Result show that at 1.0% and above no explant

Selection of explants tolerant to 1.0% NaCl:

The media used was Gamborg B5 supplemented with hormones BAP 4.4 μ M, KIN 18.4 μ M, NAA 2.7 μ M and NaCl 1.0% was used to select a salt tolerant explants.

Out of 64 explants inoculated 3 explant survived at this concentration of salt. This 3 explants were used for further studies. (Table 3)

Table 3: Subculturing and Selection of explants tolerant to 1.0% NaCl.B5 media with BAP 4.4 μ M, KIN 18.4 μ M, NAA 2.7 μ M

Sr.no.	No. of Explants	Survival
1	16	3

Sub culture I: Shoot induction media

The Shoot induction media used was Gamborg B5 supplemented with hormones BAP 4.4 μ M, KIN 18.4 μ M, NAA 2.7 μ M. in this media salt stress was not given to enhance the growth of explants. Out of the three explants two explants were lost due to contamination in the medium. After three weeks of inoculation shoot formation was not observed only swelling of explants was observed. Hence it was cultured in callus induction media. (Table 4)

Table 4: Subculture IB5 media with BAP 4.4 μ M, KIN 18.4 μ M, NAA 2.7 μ M ; 0.0% NaCl.

Sr.no	No. of explants for subculture	Survival
1	3	1

Sub culture II: Callus induction media

The Callus induction media used was Gamborg B5 supplemented with hormones BAP 8.8 μ M, NAA 1.0 μ M. Callus was observed after 2 weeks of inoculation. (Table 5)

Table 5: Subculture IIB5 media with BAP 8.8 μ M, NAA 1.0 μ M ; 0.0% NaCl.

Sr.no	No. of explants for subculture	Result
1	1	Callus induction

Thus out of 64 explant used 1 was successfully selected for callus induction.

IV. CONCLUSION

Plant tissue culture is a technique through which large clones of selected plant genotype. It is widely used for large scale plant multiplication. We can also use it for invitro selection of salt tolerant varieties. On sub-culturing and organogenesis we can get salt tolerant plants.

V. REFERENCES

- [1]. Akin-Idowu PE, Ibitoye DO, Ademoyegun OT (2009) Tissue culture as a plant production technique for horticultural crops. *Afr. J. Biotechnol.* 8(16): 3782-3788.
- [2]. Bhatia P, Ashwath N, Senaratna T and Midmore D, 2004. Tissue culture studies of tomato (*Lycopersicon esculentum*). *Plant Cell Tiss. Organ Cult*, 78:1-21.
- [3]. Brichkova GG, Maneshina TV and Kartel NA, 2002. Optimization of nutrient medium for effective regeneration of tomatoes (*Lycopersicon esculentum*) in vitro.
- [4]. Brown DCW, Thorpe TA (1995) Crop improvement through tissue culture. *World J. Microbiol & Biotechnol.* 11: 409-415.
- [5]. Chen LZ & Adachi T (1994) Plant regeneration via somatic embryogenesis from cotyledon protoplasts of tomato (*Lycopersicon esculentum* Mill). *Breed. Sci.* 44: 337-338
- [6]. El-Farash EM, Abdalla HI, Taghian AS & AhmadMH (1993) Genotype, explant age and explant type as effecting callus and shoot regeneration in tomato. *Assiut J. Agri. Sci.* 24: 3-14
- [7]. El-Farash EM, Abdalla HI, Taghian AS & AhmadMH (1993) Genotype, explant age and explant type as effecting callus and shoot regeneration in tomato. *Assiut J. Agri. Sci.* 24:3-14.
- [8]. Fari M, Szasz A, Mityko J, Nagy I, Csanyi M & Andrasfalvy A (1992) Induced organogenesis via the seedling decapitation method (SDM) in three solanaceous vegetable species. *Capsicum Newsletter*: 243-248 Food and Agriculture Organization, Statistics Division. 2016
- [9]. George EF (1993) *Plant propagation by Tissue Culture*. Eastern Press, Eversley. Tagi A, Kumar PP and Lakshmanan P, 2002. *In Vitro Plant Breeding*, Food Products Press, New York, 167 pp.
- [10]. Gill R, Malik KA, Sanago MHM & Saxena PK (1995) Somatic embryogenesis and plant regeneration from seedling cultures of tomato (*Lycopersicon esculentum* Mill.). *J. Plant Physiol.* 147: 273-276
- [11]. Gresshoff PM & Doy CH (1972) Development and differentiation of haploid *Lycopersicon esculentum* (tomato). *Planta* 107: 161-170

- [12]. Handa AK, Bressan RA, Handa S & Hasegawa PM (1982a) Characteristics of cultured tomato cells after prolonged exposure to medium containing polyethylene glycol [PEG]. *Plant Physiol.* 69: 514–521
- [13]. Handa AK, Bressan RA, Handa S & Hasegawa PM (1983a) Clonal variation for tolerance to polyethylene glycon-induced water stress in cultured tomato cells. *Plant Physiol.* 72: 645–653
- [14]. Handa AK, Bressan RA, Park ML & Hasegawa PM (1982b) Use of plant cell cultures to study production and phytotoxicity of *Alternaria solani* toxin(s). *Physiol. Plant Pathol.* 21: 295–309
- [15]. Handa S, Bressan RA, Handa AK, Carpita NC & Hasegawa PM (1983b) Solutes contributing to osmotic adjustment in cultured plant cells adapted to water stress. *Plant Physiol.* 73: 834–843
- [16]. Handa S, Handa AK, Hasegawa PM & Bressan RA (1986) Proline accumulation and the adaptation of cultured plant cells to water stress. *Plant Physiol.* 80: 938–945
- [17]. Hossain MM; Nonami H (2012) Effect of salt stress on physiological response of tomato fruit grown in hydroponic culture system. 39: 26-32.<http://www.fao.org/faostat/en/#data/QC/visualize>
- [18]. Hulme A. (Ed.), *The Biochemistry of Fruits and their Products*. New York: Academic Press. pp. 337-482.
- [19]. Kalloo G (1991). Introduction. In: Kalloo G (eds) *Monographs on Theoretical and Applied Genetics 14, Genetic Improvement of Tomato* (pp. 1–9). Springer-Verlag, Berlin, Heidelberg, New York
Lycopersicon esculentum, International Plant Name Index
<http://web.archive.org/web/20110606004439/http://www.ipni.org/ipni/idPlantNameSearch.do?id=146898-2>
- [20]. Moghaleb REA, Saneoka H and Fujita K, 1999. Plant regeneration from hypocotyls and cotyledon explants of tomato (*Lycopersicon esculentum*). *Soil Sci. Plant Nutr*, 45: 639-646.
- [21]. Muhlbach HP (1980) Different regeneration potentials of mesophyll protoplasts from cultivated and a wild species of tomato. *Planta* 148: 89–96.
- [22]. Narayanswami S, (1994) *Plant tissue culture*; Tata Mc Graw-Hill pub.co. New Delhi 51-56.
- [23]. Newman PO, Krishnaraj S & Saxena PK (1996) Regeneration of tomato (*Lycopersicon esculentum* Mill.): somatic embryogenesis and shoot organogenesis from hypocotyl explants induced with 6-benzyladenine. *Int. J. Plant Sci.* 157: 554–560
- [24]. Novak FJ & Maskova I (1979) Apical shoot tip culture of tomato. *Sci. Hort.* 10: 337–344
- [25]. Rahman MM & Kaul K (1989) Differentiation of sodium chloride tolerant cell lines of tomato (*Lycopersicon esculentum* Mill.) cv. Jet Star. *J. Plant Physiol.* 133: 710–712
- [26]. Raziuddin S, Salim HJ, Chaudhary T, Mohammad A and Ali S, 2004. Hormonal effect on callus induction in Tomato. *Sarhad J. Agric.* (2092): 223-225.
- [27]. Reed BM 1999. Design a Micropropagation system: workshop presentation from the 1998 SIVB Congr. On in vitro Biology. *In vitro Cell Dev. Biol. Plant.*, 35: 275-284.
- [28]. Singh J. ; et al (2012) Effect of salinity on tomato (*Lycopersicon esculentum* Mill.) during seed germination stage. 18: 45-46.
- [29]. Thorpe T (2007) History of plant tissue culture. *J. Mol. Microbial Biotechnol.* 37: 169-180.

- [30]. Tomsone S, Gertnere D and Novikova D, 2004. The influence of Thidiazuron on shoot regeneration and proliferation of rhododendrons in vitro. *Acta Universitatis Latviensis, Biology*, 676: 239-242.
- [31]. Toyoda H, Shimizu K, Chatani K, Kita N, Matsuda Y & Ouchi S (1989) Selection of bacterial wilt-resistant tomato through tissue culture. *Plant Cell Rep.* 8: 317–320
- [32]. Varghese TM & Yadav G (1986) Production of embryoids and calli from isolated microspores of tomato (*Lycopersicon esculentum* Mill.) in liquid media. *Biol. Planta* 28: 126–129



Evaluation of Biological Activities of Nanocrystalline Tetragonal Zirconia Synthesized Via Sol-Gel Method

V.G. Thakare*¹, P.A. Wadegaokar²

¹Department of Physics, Shri Shivaji College of Art's, Commence and Science Akola, Maharashtra, India

²Department of Biotechnology, SGB Amravati University, Amravati-444 602, Maharashtra, India

ABSTRACT

The objective of the following study was synthesis of nanocrystalline tetragonal zirconia (ZrO_2) using simple sol-gel method and evaluation of its structural and biological properties. The sample was characterized by powder X-ray diffraction (XRD), Field Emission Scanning Electron Microscopy (FESEM), Evaluated for cell growth study using 3T3 mouse fibroblast cells. The XRD pattern shows that the tetragonal phase of nanocrystalline zirconia was obtained at relatively low temperature i.e. 300°C. The FESEM images showed that the prepared sample consists of particles in the range of 35-69 nm and homogenous particle size distribution. The sample of zirconia has excellent tissue biocompatibility, higher cell growth and does not shows the toxicity towards normal 3T3 mouse fibroblast cells. Nanocrystalline tetragonal zirconia show higher cell growth. Hence it can be used for various biomedical applications.

Keywords: Nanocrystalline Zirconia; sol-gel route; antimicrobial action; biomedical application.

I. INTRODUCTION

Zirconia ceramics has been increasingly used as implant biomaterials [1-3]. The excellent electrical, mechanical, optical and thermal properties of Zirconia, makes it a good choice for application such as: structural materials [4], dental crowns [5], femoral heads for total hip replacement [6], solid oxide fuel cell electrolytes [7], air-fuel ratio sensors for automotive applications [8], Catalytic application [9]. Pure zirconia exhibits three polymorphs of monoclinic, tetragonal and cubic symmetries. The monoclinic phase is stable at room temperature and transforms to the tetragonal phase at 1170°C during heating, while this phase transforms to the cubic one at 2370°C [10-11]. To overcome these limitations, nanocrystalline materials are expected to show improved mechanical properties and the nanometric features in the surface of the prostheses seem to reduce the risk of rejection and to enhance the proliferation of osteoblasts (bone-forming cells) [12-13]. It is well known that nano structured materials exhibited unique physiochemical properties that are unseen in conventional bulk materials. Nano- ZrO_2 exhibits much better chemical and physical properties as compared to normal ZrO_2 powder, due to the small particle diameter which will result in better sintering ability [14-15].

II. MATERIALS AND METHODS

SOL-GEL SYNTHESIS

The entire precursor taken of AR grade (99.99% pure) procured from SD fine scientific which included Zirconium n-propoxide, n-propanol, Hydroxpropoly methyl cellulose and ammonia. Initially, n-propanol was added to Zirconium n-propoxide (70 wt %). Then resulting solution was hydrolysis using drop by drop addition of ammonia and distilled water with a P_H value of 9 to 10. 3g Hydroxpropoly methyl cellulose was added to the solution under vigorous stirring. After homogenization, the solution was stirred at room temperature for an hour so the resulting gel was polymerized [4]. The gel was dried in an oven at a temperature of 100°C for 12 hrs and sintered by using microwave furnace at 300°C for 2 hrs. The resulting powders was then compacted into mould and made a pellets with the help of die and punch in a hydraulic dry press at a load of 4 Ton for 10 min with a diameter of 10 mm and thickness of 2 mm. Each pellet consists of 0.25 g powder without any binder added and given the name P1, P2, and P3. The flow chart of Sol-gel synthesized zirconia as shown in fig 1.

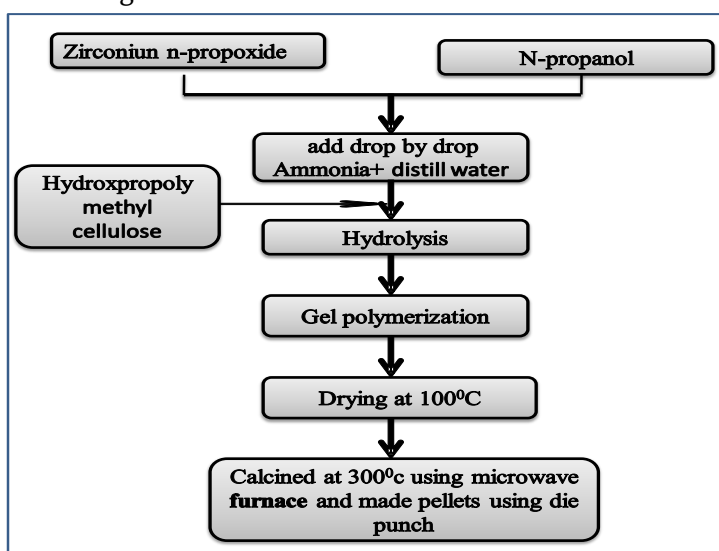


Fig. 1 Flow chart of ZrO₂ synthesized by Sol-Gel method

EVALUATION OF CELL GROWTH

The zirconia powder pellets were sterilized by autoclaving at 120°C and immersed in culture medium for 1, 2, 3, 4 and 6 days. The resulting media were used to culture mouse fibroblasts 3T3 cells in Eagle's Dulbecco essential medium (DMEM) containing fetal bovine serum (10%) along with antibiotics evenly spread and growing in monolayer. About 2.5 X 10⁵ cells in 100µl of immersion medium were seeded into each well of 96 well plates and were cultured for 1, 2, 3, 4, and 6 days. The pellets P1, P2 and P3 were put in triplicate. Cells growth was determined by counting cells using heamocytometer. In addition, the pellets of zirconia were placed in to 80 mm dish and immersed in 75% alcohol for sterilization. After 24 hrs, the residual alcohol on the pellets was removed by washing the pellets with the culture medium. About 2.5 X 10⁵ mouse fibroblasts 3T3 cells were seeded onto the pellets and incubated at a 5% CO₂ atmosphere for 2, 6, days at 37°C so that

cells were grown near pellets and staining by crystal violet stain. The morphology of the cells to pellets was observed with an inverted contrast-phase microscope.

III. RESULTS AND DISCUSSIONS

X-RAY DIFFRACTION (XRD) ANALYSIS

The structural properties are studied by X-Ray diffraction technique. The XRD pattern of ZrO_2 as shown in Fig. 1(a), which is well matched with standard ICDD file no, 01-079-1764 of ZrO_2 as shown in Fig. 1(b). ZrO_2 has a single pure phase with a tetragonal crystal structure which was obtained at $300^\circ C$. The diffraction peaks in zirconia crystal structure, as shown in Fig. 2(a), viz., (101), (110), (200), (211), (212), are matched well with the peaks shown in fig 2(b) and

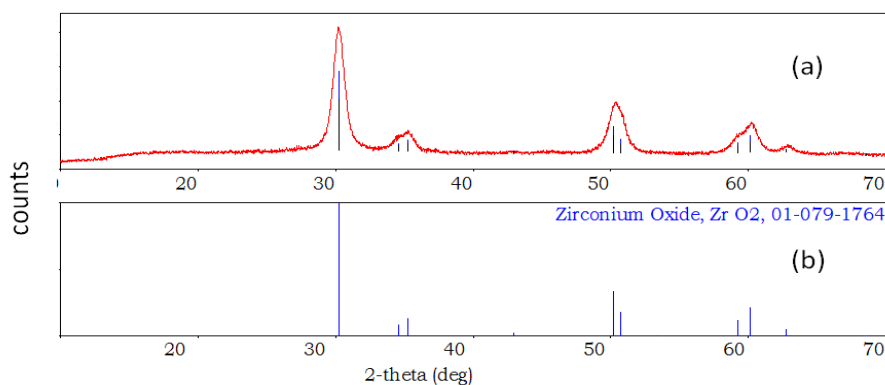


Fig. 2 (a) XRD patterns of ZrO_2 sintered at $300^\circ C$ and (b) standard ICDD file of ZrO_2

FESEM ANALYSIS

The FESEM image for ZrO_2 Fig. 3(a-c) at different magnification shows uniform distribution of particles and spherical like morphology. The image 3(a) shows the particles in the range of 35-69 nm. The formation and composition of Crystalline of ZrO_2 nanoparticles are confirmed from EDX analysis, Fig. 3 (d) which reveals that the Zr and O as the only elements in the sample, high purity and no any other impurity in the sample.

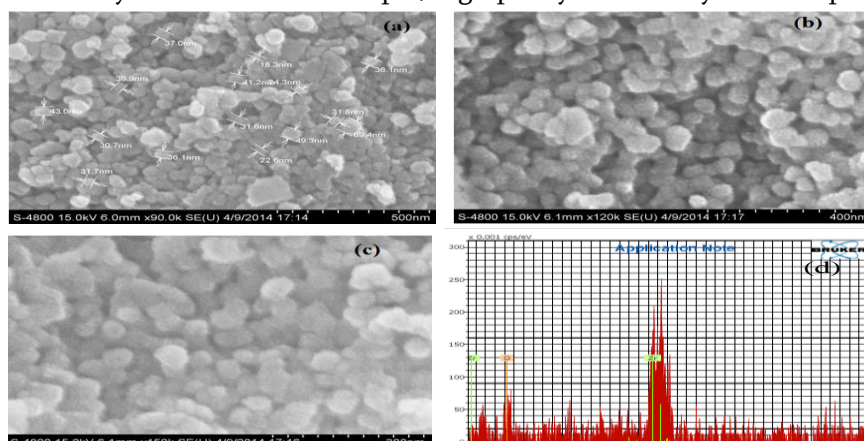


Fig. 3 FE-SEM images of (a-c) ZrO_2 at different magnification, (d) EDAX spectrum of ZrO_2

CELLS GROWTH ASSESSMENT OF ZrO₂

The behavior of cells in contact with the surface of nanocrystalline ZrO₂ pellets P1, P2 and P3 after 1, 2, 3, 4 and 6 days was similar. Cells growth and regular morphological characterization for ZrO₂ pellets was studied. The Fig.4 shows cells growth along with control well (in absence of pellets) and pellets P1, P2 and P3 which is counted by hemocytometer after 1, 2, 3, 4, and 6 days. For the P1 pellet the growth of cell increase after 1 day. After 6 days it increases 95% as compared to the control. For the pellets P2 and P3 the cells growth is 94% and 98 % respectively. This shows that the growth of cells along with pellets of ZrO₂ is same to the control. It means that nanocrystalline ZrO₂ powder does not show any sign of cytotoxicity. Fig 5(a-c) shows images of 3T3 fibroblast cell in contact with ZrO₂ pellets which shows that after 2 days the growth of cell was found in control with reference cultures. After 6 days the amount of cell growth is greater as compared to 2 days. In the photographs of cell culture regular fibroblast patterns are visible, which are characteristic for test conducted on ZrO₂ pellets studied. The study of cytotoxicity of sample of ZrO₂ conducted *in vitro* shows very high biocompatibility of materials produced. Nanocrystalline ZrO₂ was considered nontoxic. Also the numbers of living cells near the ZrO₂ pellets examined increased regularly, and were comparable to the controls. The present's data reveals the no signs of cytotoxicity and the rate of cell growth is higher in the case of nanocrystalline ZrO₂ pellets.

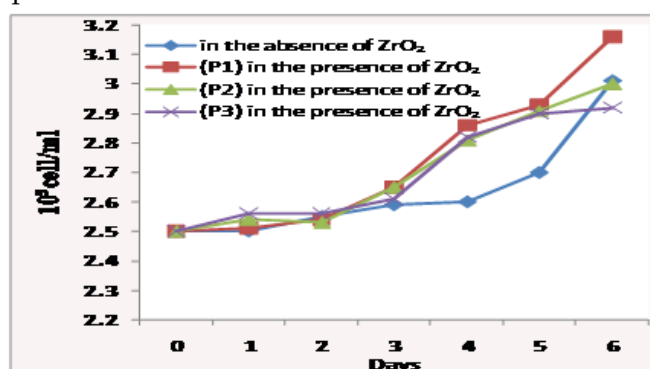


Fig. 4 Growth of Mouse Fibroblast in the presence of ZrO₂ pallets

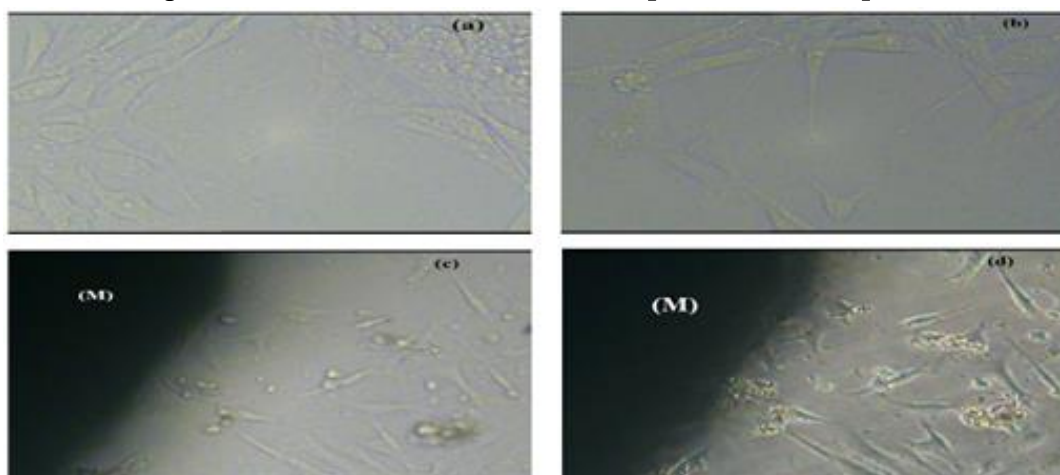


Fig 5 (a-d) optical microscope images of a culture of mouse fibroblasts after 2 days and 6 days contact with the ZrO₂ pellet, (M) area of pellet

IV. CONCLUSIONS

In this study, our aim was to synthesis nanocrystalline zirconia by using simple sol-gel method with good antibacterial property. The formation of tetragonal crystalline phase of ZrO_2 was confirmed by powder XRD analysis at relatively low temperature using microwave furnace. The morphology, particle size and nanostructure were analyzed using field effect scanning electron microscopy. Nanocrystalline zirconia show higher cell growth towards normal 3T3 mouse fibroblast cells.

V. REFERENCES

- [1]. Piconi C, Maccauro G. Review: Zirconia as a ceramic biomaterial. *Biomaterials*. 1999;20:1-25.
- [2]. Thamaraiselvi TV, Rajeswari SV. Biological evaluation of bioceramic materials -a review. *Trends Biomater Artif Organs*. 2004;18:9-17.
- [3]. Thakare VG. Progress in synthesis and applications of zirconia. *Int J eng Res Dev*. 2012;5:25-28.
- [4]. Heshmatpour F, Aghakhanpour R. Synthesis and characterization of nanocry- stalline zirconia powder by simple sol-gel method with glucose and fructose as organic additives. *Powder Technology*. 2011;205:193-200.
- [5]. Oetzel C, Clasen R, Preparation of zirconia dental crowns via Electrophoretic deposition. *J Mater Sci Tech*. 2011;27:8130-8137.
- [6]. Elshazly ES, Elhout SM, Ali M. Yttria tetragonal zirconia biomaterial: Kinetic investigation. *J Mater Sci Tech*. 2011;27:332-337.
- [7]. Luo J, Ball R, Stevens R. Gadolina doped ceria/yttria stabilized zirconia electrolytes for solid oxide fuel cell application. *J Mat Sci*. 2004;39:235-240.
- [8]. Lee J, Review on zirconia air-fuel ratio sensors for automotive application. *J Mat Sci*. 2003;38:4247-4257.
- [9]. Krumov E, Dikova J, Starbova K, Popov D, Kolev K, Laude L. Thin ZrO_2 sol-gel films for catalytic application. *J Mater Sci Tech : Mater Elec*. 2003;14:332-337.
- [10]. Siddiquia M, Wassila A, Otaibib A, Mohfouza R. Effect of precursor on the morphology and size of ZrO_2 nanoparticles synthesized by sol-gel method in non-aqueous medium. *Materials Research*. 2012;15:986-989.
- [11]. Dev VG, Venugopal J, Sudha S, Deepika G, Ramakrishna S. Dyeing and antimicrobial characteristics of chitosan treated wool fabric with henna dye. *Carbohydr Polym*. 2009;75:646-650.
- [12]. Stoimenov PK, Klinger RL, Marchin GL, Klabunde KJ. Metal Oxide Nanoparticles as Bactericidal Agents. *Langmuir*. 2002;18:6679-6686.
- [13]. G. Mohamed, Nano-zirconium oxide and nano-silver oxide/cotton gauze fabrics for antimicrobial and wound healing acceleration. *J. Ind. Tex*. 2012;41:222-240.

Heterocyclic nitrogenous compounds and their fused analogs represent an important class of heterocyclic compounds. They exist in numerous natural products, display a wide range of biological and pharmaceutical activities. Heterocyclic nitrogenous compounds and their fused analogs represent an important class of heterocyclic compounds. They exist in numerous natural products, display a wide range of biological and pharmaceutical activities.

Heterocyclic nitrogenous compounds and their fused analogs represent an important class of heterocyclic compounds. They exist in numerous natural products, display a wide range of biological and pharmaceutical activities.

Heterocyclic fused nitrogenous cyclic compounds like pyrazoline having wide range of biological and pharmaceutical activities. 3-(2-Hydroxy -3,4-Benzophenyl-5- Methoxy) 5-Aryl -1-Substituted Pyrazolines were synthesised by green method that is by using microwave and biological study was carried out for the synthesised compounds for their antimicrobial and antifungal activities. The synthesized compounds were characterized by elemental analysis, UV, ¹H NMR and IR Spectroscopy. Thin Layer Chromatography on silica gel-G, was used to check the purity of the compounds. Biological study was carried out for all newly synthesized compounds and showed an excellent results.

I. INTRODUCTION

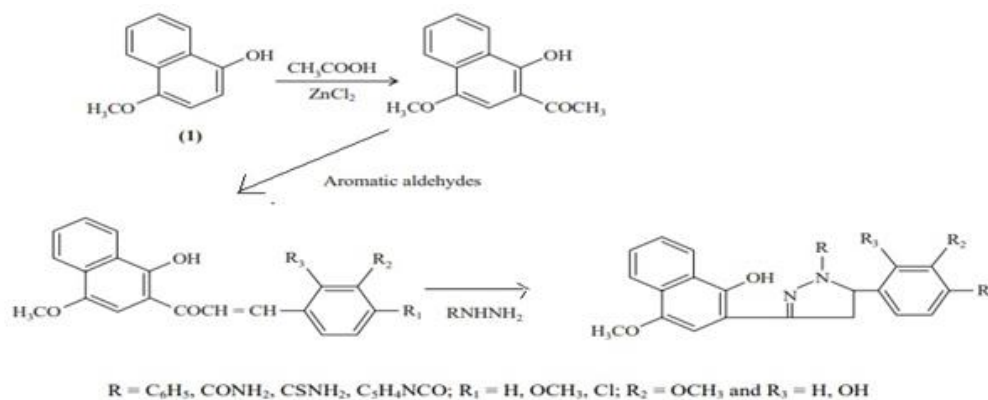
A heterocyclic compound is a cyclic compound that has atoms of at least two different elements as members of its ring(s). Pyrazolines are well known and important nitrogen containing five membered heterocyclic compounds and various methods have been worked out for their synthesis¹⁻⁴. Derivatives of pyrazolines have played a crucial role in the history of heterocyclic chemistry and these have been used extensively as important pharmacophores and synthons in the field of organic chemistry and drug designing. Pyrazolines possess fungicidal⁵, bactericidal⁶ and insecticidal⁷ properties. Several pyrazolines are important as pharmaceuticals and they have been found to possess analgesic⁸, antipyretic⁹, and anti-inflammatory¹⁰ properties. Pyrazoline derivatives acquire antiimplantation activity¹¹ and cerebroprotective¹² also. Due to the vital biological role of pyrazolines derivatives^{13,14}. It was thought of interest to synthesize titled pyrazolines. It has been observed that substituted chalcones are best starting compounds for the preparation of the substituted pyrazolines. Present work deals with the synthesis of some new pyrazolines and their characterization by elemental analysis, IR and ¹H NMR analysis.

II. MATERIALS AND METHODS

Melting points were determined in open capillary tubes and are uncorrected. All the chemicals and solvents used were of laboratory grade and solvents were purified by suitable methods. The purity of the compounds was ascertained by thin layer chromatography on aluminium plates precoated with silica gel G (Merck) in various solvent systems using iodine vapors as detecting agent. Elemental analysis was done using Carlo Erba 1106 CHN analyzer.

Synthesis of pyrazoline derivatives :

A mixture of the chalcone and semicarbazide was dissolved in acetone and ethanol, respectively. Basic alumina was added and stirred vigorously. After 5 min, the solvent was removed under vacuum and the dry powder was irradiated in a microwave oven for the appropriate time, at 650 W. After completion of the reaction the product was eluted with acetone. Removal of the solvent under reduced pressure yielded the product which was recrystallized from acetone-ethanol mixture.



III. DISSCUSSION OF RESULTS

It was found that the yield of synthesized compound was more by green synthesis that is by microwave instead of the conventional method. Above synthesized pyrazoline derivatives have been studied for their antimicrobial activity against *escherichia coli*, *proteus mirabilis*, *staphylococcus aureas*, *A.Nigar*. The culture of each species was incubated at 37^o C and the zone of inhibition was measured after 24 hr. Most of these compounds were found active. Thus from above results, it was observed that these heterocyclic compounds were found effective against *escherichia coli*, *proteus mirabilis*, *staphylococcus aureas*, and *A. Niger*. So all synthesised compounds can be easily be used for the treatment of diseases caused by these above pathogens, only when they does not have poisons and other side effects.

Physical Properties of synthesised compounds :

Compd.	R	R ₁	R ₂	R ₃	Melting point (°C)
1	--	--	--	--	99°C
2	--	H	H	H	102°C
3	--	H	H	OH	110°C
4	--	OCH ₃	OCH ₃	H	160°C
5	--	Cl	H	H	140°C
6	CONH ₂	H	H	H	208°C
7	CONH ₂	H	H	OH	210°C
8	CONH ₂	OCH ₃	OCH ₃	H	222°C
9	CONH ₂	Cl	H	H	240°C

IV. ACKNOWLEDGEMENT

The authors are thankful to Prof. A. K. Tithe, Principal, Late K. Z. S. Science College, Bramhni, Kalmeshwar for providing facilities

V. REFERENCES

- [1]. S.E. Bhandarkar, *Oriental Journal of Chemistry*, 30 (1), 361-363, 2016
- [2]. S.E.Bhandarkar, V.M.Sherekar , *American Journal of Pharm Tech Research (AJPTR)* 6 (5), 560-5655, 2017
- [3]. Pyrazoles, Pyrazolines, Pyrazolidines, Indazoles and Condensed Rings, in *The Chemistry of Heterocyclic Compounds*, Vol. 22, A Weissberger (Ed.), Intersci. Pub., New York, (1967) 108 p. 180.
- [4]. J. Elguero, in *Comprehensive Heterocyclic Chemistry II*, Vol. 3, A. R. Katritzky, C. W. Rees and E. F. Scriven (Eds.) Pergamon Press, Oxford (1996) p. 1
- [5]. N. B. Das and A. S. Mitra, *Indian J. Chem.*, 16B, 638 (1978).
- [6]. H. Z. Katri and S. A. Vunii, *J. Indian Chem., Soc.*, 58, 168(1981).
- [7]. S. G. Roelofan, C. Arnold and Wellmgak, *J. Agric. Food Chem.*, 27, 406 (1979).
- [8]. M. A. Metwally, M. Y. Yusuf, A. M. Tsmail and F. A. Amer, *J. Indian Chem., Soc.*, 62, 54 (1985).
- [9]. V. G. Vornin, Z. I. Sharmova, S. Ya. Shachilova, L. D. Kulikova and A. S. Zaks. *Khim, Farm. Zh.*, 19, 1208, (1985); *Chem. Abstr.*, 104, 61668m (1986).
- [10]. J. P. Dusza, J. P. Josheph and S. Burnstun, *US. US4 360 680 (CI 548 362 CO7D, 231/06)* (1982).
- [11]. Y. U. M. Batulin, *Chem. Abstr.*, 70, 2236a (1969).
- [12]. G. E. H. Elgemeie, A. M. E. Attia, D. S. Farag and S. M. Sherif, *J. Chem. Soc. Perkin Trans.*, 1, 1285 (1994).
- [13]. Y. J. Fernandes and H. Parekh, *J. Indian Chem. Soc.*, 74, 59 (1997).
- [14]. S. S. Ganguli, M. S. Vadaria and A. R. Parikh, *J. Inst. Chem.*, 68, 1920 (1996).



Study of the Optical Constants of the Polymer Blends

R Y Bakale^{1*}, Y G Bakale², Y S Tamgadge¹, R P Ganorkar³, S V Khangar⁴, A B Patil¹

¹Department of Physics, Mahatma Fule Arts, Commerce and Sitaramji Chaudhari Science Mahavidyalaya, Warud, Maharashtra, India

²Department of ESH, Kavikulguru Institute of Technology and Science, Ramtek, Maharashtra, India

³Department of Chemistry, Mahatma Fule Arts, Commerce and Sitaramji Chaudhari Science Mahavidyalaya, Warud, Maharashtra, India

⁴Department of Physics, Shri Shivaji Education Society, Congress Nagar, Nagpur, Maharashtra, India

ABSTRACT

The aim of the present work is concerned with the study of the optical constants of the PVC/PMMA blend at different ratio, were prepared with different concentration. The absorption spectra of PVC/PMMA blends at different concentration showed absorption changes in the wavelength range, which depends on the polymer type, and the concentration of the polymer blends. It was found that 50%PVC+50%PMMA ratio from these polymers showed higher absorption values in comparison with the other blend. The absorption spectra have been recorded in the wavelength range (300-1400) nm. The absorption coefficient(α), extinction coefficient(k), refractive index(n) has been evaluated.

Keywords: Optical constants, Optical properties, PVC/PMMA blend.

I. INTRODUCTION

Polymer composites have steadily gained growing importance in the past decade. The incorporation of transition metal salts into polyvinyl polymers, either pure or blended in multiphase systems can induce pronounced changes in various parameters of polymers [1,2,3]. Polymeric materials have attracted the scientific and technological researchers, because of their wide applications. This is mainly due to the lightweight, good mechanical strength, optical properties and make them to be multifunctional materials. Optical properties of polymers constitute an important aspect in study of electronic transition and the possibility of their application as optical filters, a cover in solar collection, selection surfaces and green house. The information about the electronic structure of crystalline and amorphous semiconductors has been mostly accumulated from the studies of optical properties in wide frequency range [4]. PMMA is one of the earliest and best-known polymers. PMMA was seen as a replacement for glass in a variety of applications and is currently used extensively in glazing applications. The material is one of the hardest polymers, and is rigid, glass-clear with glossy finish and good weather resistance. PMMA is naturally transparent and colorless. The transmission for visible light is very high. Polymeric composites of

PMMA are known for their importance in technical applications.[5] Poly (methyl methacrylate) is one of the best organic optical materials and has been widely used to make a variety of optical devices, such as optical lenses. It is known that its refractive index changes upon UV irradiation, either in the pure [6, 7] or doped state [8], which provides a means to fabricate structures, such as gratings or waveguides. Polyvinylchloride(PVC) is one of the most important commercial polymer that has wider range of applications [9]. L. JOSHI et al [10] study the polyblend of polyvinyl chloride (PVC) and polystyrene (PS), in the weight ratio 5: 1 using 1.25 gm of PVC and 0.25 gm of PS by casting method. The two polymers PVC and PS and dopant Polyaniline dissolved separately in tetrahydrofuran. Polyaniline (PANI) has been used as dopant and with 0.5 %, 1.0%, 1.5%, 2.0% and 2.5 % of the total weight of the two polymer they prepared five samples. The amorphous nature in all samples were observed from XRD. On the basis of optical absorbance and transmittance measurements at normal incidence of light in the wavelength range 500- 1000 nm, the absorption coefficient (α), optical energy gap (E_{opt}), refractive index (n_0), optical dielectric constant (ϵ), constant (B) and ratio of carrier concentration to the effective mass (N/m^*) have been reported for polyaniline doped PVC-PS blend. They found the behavior of all the optical parameters found to be non-linear. It can be concluded that the evaluated optical parameters such as absorption coefficient, optical energy gap, optical dielectric constant, refractive index, constant B, measure of extent of band tailing (n_0B)-1 are found to be bidden direct transition. The refractive index (n_0) calculated in the region 500 to 1000 nm is found to be non-linear. The ratio of carrier concentration to the effective mass N/m^* is found to be of the order of 10^{21}cm^{-3} .

II. EXPERIMENTAL

Preparation of sample

The polyvinyl chloride (PVC) of standard grade product supplied by Polychem Industries Mumbai and polymethylmethacrylate (PMMA) supplied by Dental Product of India Ltd., Mumbai was used for the study. The two polymers PVC and PMMA were taken in the percentage (75%PVC+25%PMMA, 50%PVC+50%PMMA, 25PVC+75PMMA) Two polymers PVC and PMMA were add in 10 ml of tetrahydrofuran (THF), allowing them to dissolve completely, after allowing them to dissolve completely the two solutions were mixed together. The solution was heated at constant temperature 333K for the two hours to allow polymers to dissolve completely to yield clear solution. A glass plate (15cmx15cm) thoroughly cleaned with hot water and then with acetone was used as a substrate. To achieve perfect leveling and uniformity in the thickness of the film, the films were prepared on a thoroughly cleaned optically plane glass plate kept floating in a pool of mercury. The whole assembly was placed in dust free chamber maintained at constant temperature (313K). In this way the film was prepared by isothermal evaporation technique [11, 12]. The film was subjected to 12hrs has heated at constant temperature 323K and another 12hrs at room temperature to remove the traces of solvent. Finally, the film was

as removed from the glass plate. It was cut into small pieces of suitable size, which were washed with ethyl alcohol to remove the surface impurities.

Thickness measurement

For greater accuracy and resolution, a compound microscope in conjunction with a micrometer, which gives least count 13µm and 3.3µm at the magnification of 1:10 and 1:100 respectively, was used. A small section of the sample was taken and mounted vertically to get a clear sectional view of the thickness. The films used for the present study are thickness about 80µm.

III. RESULT AND DISCUSSION

The optical constants are very important because they describe the optical behavior of the materials. The absorption coefficient of the material is very strong function of photon energy and band gap energy [13]. The variation of absorption with wavelength of the incident light the absorption was recorded using double beam Shimadzu UV/VIS- 1650 PC in the wavelength optical a range (300-1400) nm for polymer blend.

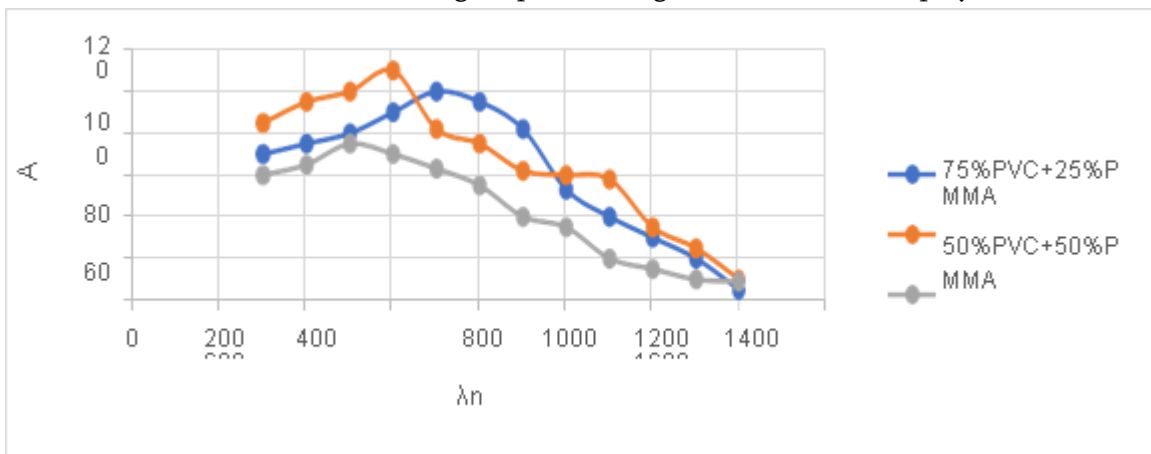


Figure (1): Variation of absorption for (PVC/PMMA) with wavelength.

Figure (1) The figures show absorption spectrum in range (300-1400) nm reveals a strong absorption probability below 250-290 nm respectively. 75%PVC+25%PMMA; 50%PVC+50%PMMA; 25%PVC+75%PMMA. there is a sudden decrease in the absorption values observed above the limits. For 50%PVC+50%PMMA the decrease was even slower. 50%PVC+50%PMMA blend showed the high absorption than the other blend for polymer blend. and all the films showing the same behavior

Absorption coefficient (α) is defined as the ability of a material to absorb the light of a given wavelength [14]

$$\alpha = \frac{2.303A}{t} \dots\dots\dots (1)$$

Where ‘A’ is the absorption of the material and ‘t’ is the thickness in cm

Figure (2) shows the relationship of the absorption coefficient with photon energy of different weight percentages of PVC/PMMA. it shows high absorption edge for 50%PVC+50% PMMA.

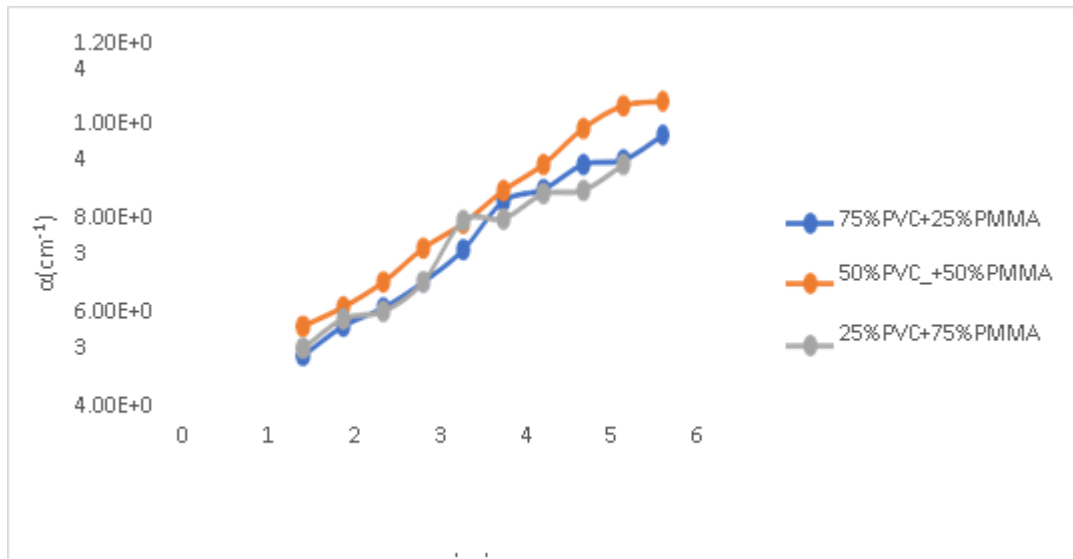


Figure (2): Absorption coefficient for (PVC/PMMA) photon energy

The values of the refractive index (n_0) and dielectric constant (ϵ') is observed to be nonlinear for all samples. Such nonlinear behavior is observed for amorphous materials as reported [15, 16]. The value of refractive index and optical dielectric constant are calculated for wavelength range 400 nm to 1000 nm. The values of refractive des are found to be more or less same throughout the wavelength range (400 nm to 1000 nm). Therefore, average value n_0 are reported in this wavelength region. The refractive index (n_0) can be measured by equation

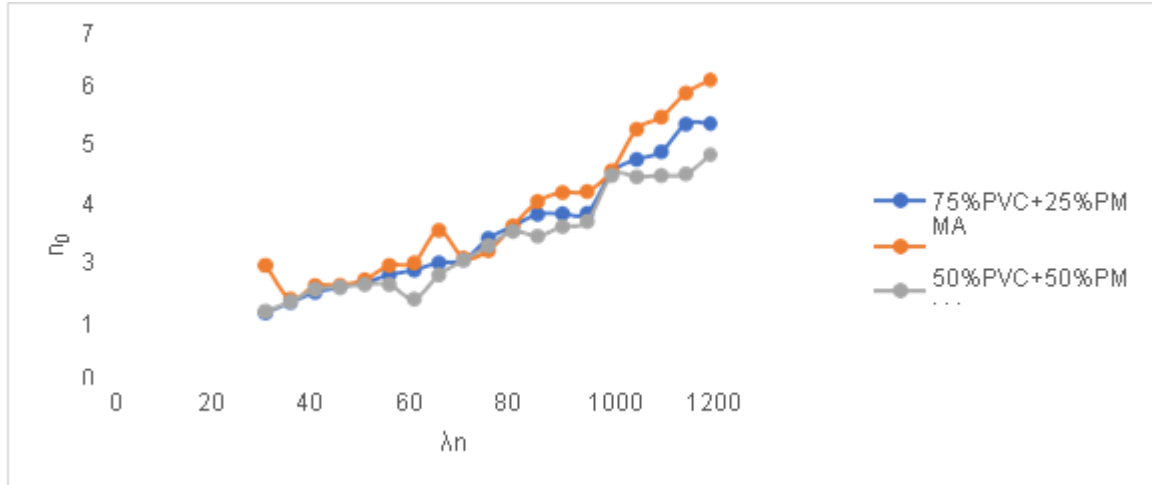


Figure (3) Refractive indices as a function of wavelength for polymer blend

Figure (3) Shows the variation of n_0 as a function of wavelength, the value of the refractive index from this we can say that the refractive index for 50%PVC and 50%PMMA is more in compare with the other two

Table (1): Represents the parameters of optical properties of polymer blend

Polymer blend	α (cm ⁻¹)	A%	K 10 ⁻³	n
75%PVC+25%PMMA	100.45	0.95	1.0E-03	1.42800
50%PVC+50%PMMA	306.163	1.51	1.64E-03	2.587151
25%PVC+75%PMMA	294.94	0.60	4.1E-03	1.62220

IV. CONCLUSION

It can be concluded that the evaluated optical parameters of polymer blends (PVC / PMMA) With various concentrations. It was found that 50%PVC+50%PMMA ratio from these polymers showed higher absorption values in comparison with the other blend. The absorption spectra have been recorded in the wavelength range (300-1400)nm. And it is observed that at 50%PVC+50%PMMA blend film shows the best optical property

V. ACKNOWLEDGEMENT

The authors are extremely thankful to Principal, Shri Shivaji Science College, Amravati for providing necessary laboratory facilities during the course of this work. The authors also wish to put on record sincere thanks to Regional Sophisticated Instrumentation Centre, Chennai for characterization Facilities.

VI. REFERENCES

- [1]. F H Abd El-Kader and S A Gaafar, J. Polym. Mater 10, 245(1993).
- [2]. W H Osman, J Mater Sei. Mater in Electronics 7, 1(1996).
- [3]. N H Barkoula and Karger Kocsis, J Mater Sci 37, 3807(2002).
- [4]. G.Pinto and A.Maaroufi,"Critical filler concentration for electro conductive polymer composites", Society of Plastics Engineers (SPE),2011.
- [5]. T.Hamad, M. Abdul nabi and W.Musa," The optical properties of Poly methyl methacrylate (PMMA) polymers doped by Potassium Iodide with different thickness", Vol.8(2) " Baghdad Science Journal", pp.538- 542,2011.
- [6]. C.Wochnowski, S. Metev, and G. Sepold, "UV—laser-assisted modification of the optical properties of polymethylmethacrylate," Applied Surface Science, vol. 154,pp. 706–711, 2000.
- [7]. A. Baker and P. Dyer, "Refractive-index modification of polymethylmethacrylate (PMMA) thin films by KrF-laser irradiation," Applied Physics A, vol. 57, no. 6, pp. 543–544,1993.
- [8]. T. Kardinahl and H. Franke, "Photoinduced refractive-index changes in fulgide-doped PMMA films," Applied Physics A, vol. 61, no. 1, pp. 23–27, 1995.
- [9]. Wang Q.; Storn B. K.; Polymer Testing, 24,290.2005.

- [10]. L.Joshi, M. Deshmukh, P. Deshmukh, D.burghate and S. Shilaskar “Optical Band Gap in Polyaniline Doped PVC- PS Blend” J. Polym. Mater. Vol. 28, No. 1,pp.93-100,2011.
- [11]. A. Narayan and H.P. Singh, Indian J. Pure. Appl. Phys.25, 1983, pp.30.
- [12]. R. Bahri and B.R. Sood, “Thin solid film”100L5,1983.
- [13]. E. Mizher ., Ph. D., PhD Thesis, "University of Baghdad, College of Science", (2005).
- [14]. S.Hutagalwng.andB.Lee,2007,Proceedingofthe2ndinternationalconferenceNano/MicroEngineered and Molecular systems, January,Bangkok,Thailand.
- [15]. SH Deshmukh, PhD Thesis (SGB Amravati University. Amravati(2007).
- [16]. E Kh. Shokr, Indian J Pure Appl Phys30, 271(1992)



Synthesis and Photoluminescence Studies of UV emitting $Mg_2P_2O_7: Gd$ Phosphor

R. S. Khan, M. A. Wani, S. D. Sawarkar, M. V. Talan, Z. S. Khan*

Department of Physics and Electronics, Government Vidarbha Institute of Science & Humanities, Amravati
444604, Maharashtra, India

ABSTRACT

Gadolinium doped $Mg_2P_2O_7$ phosphor is prepared with slow vaporization method. The phase analysis of this synthesized material was determined using powder X-ray diffraction (XRD). Photoluminescence properties of UV emitting phosphor $Mg_2P_2O_7: Gd^{3+}$ with varying concentration of Gd^{3+} was studied. Crystal structure and co-ordination of prepared phosphor was confirmed using powder X-ray diffraction and FTIR. SEM images of prepared powder samples show the irregular grains with agglomeration phenomena. Under the excitation of 274 nm phosphor materials show two emissions at 304 nm and 312 nm, which could be applicable in phototherapy. These lines correspond to the $6P_{5/2} \rightarrow 8S$ and $6P_{7/2} \rightarrow 8S$ transitions of the Gd^{3+} ion, respectively. The maximum intensity of luminescence in synthesized materials was investigated.

I. INTRODUCTION

Most of the researchers are in search of good material doping with diverse rare earths (RE) elements by means of specific methods for their synthesis [1-4]. Apart from them, rare earth doped phosphate phosphors have attracted attention due to considerable belongings including high luminous efficiency, low synthesis temperature, high chemical stability and high color purity reputation [5,6]. Not only doped but also pure pyrophosphates are supposed to be very important because of their multipurpose belongings including luminescent, dielectric, semiconductor, catalytic, magnetic, fluorescent and ion-exchange properties [7]. Gupta et al put forward the photoluminescence studies of $Zn_2P_2O_7$ with Eu^{3+} , Sm^{3+} as well as Mn for a choice of discrepancy. [8-10] while some other researchers [11-13] have notice into the energy transfer mechanism in the phosphor for its preferred purpose in LEDs. We have already study rare earth doped phosphors by solution combustion synthesis method [14-17]. Divalent / Trivalent rare earth ions doped inorganic compounds phosphors are found to be applicable for white light emitting diodes [18]. Low energy consumption, higher lifetime and higher efficiency made these LEDs protagonist materials [19]. We have prepared polycrystalline samples of $Mg_2P_2O_7: Gd$ by low cost low temperature slow vaporization method keeping in mind its luminescence properties applicable for UV-Light Emitting Diode.

II. EXPERIMENTAL

2.1 Synthesis and doping of RE³⁺

Polycrystalline Mg₂P₂O₇: Gd³⁺ phosphor is prepared by slow vaporization method [20]. Magnesium nitrate [Mg (NO₃)₂] and diamonium hydrogen orthophosphate [(NH₄)₂HPO₄] is added together with Gd₂O₃ (activator). Doubled distilled water is added in this combination. Mixing thoroughly about 10 minutes, milky solution is obtained. Now this solution is kept for slow evaporation at 100 °C for about 8 hours. The obtained white precipitate was kept under hot light for a complete night. The powder is then thoroughly mixed in the agate mortar. Now this powder is kept in previously heated furnace at 800 °C for 1 hour. The entire samples are now ready for characterizations. The procedure is shown in figure 1.

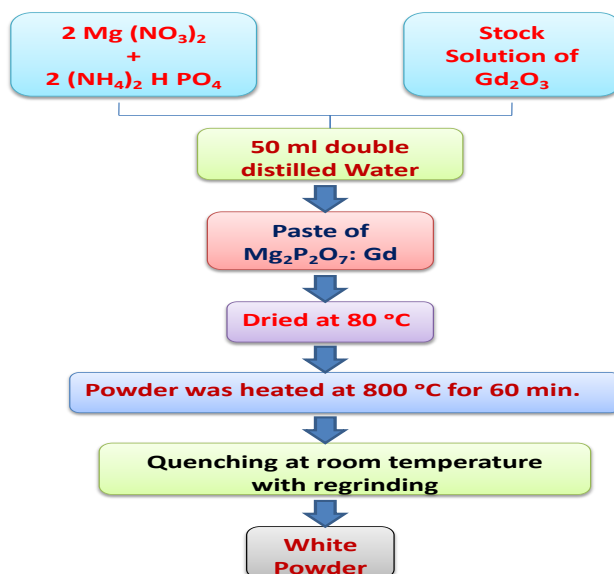


Fig 1 Experimental procedure for the Synthesis of Mg₂P₂O₇: Gd³⁺ phosphor

2.2 Characterizations

The prepared sample was confirmed by RigakuMiniflex X-Ray Diffractometer with scan speed of 2.00 deg/min and with Cu K α radiation ($\lambda = 1.5406 \text{ \AA}$). Scanning Electron Microscope images of the sample are taken. The XRD image is as shown in the figure 2.

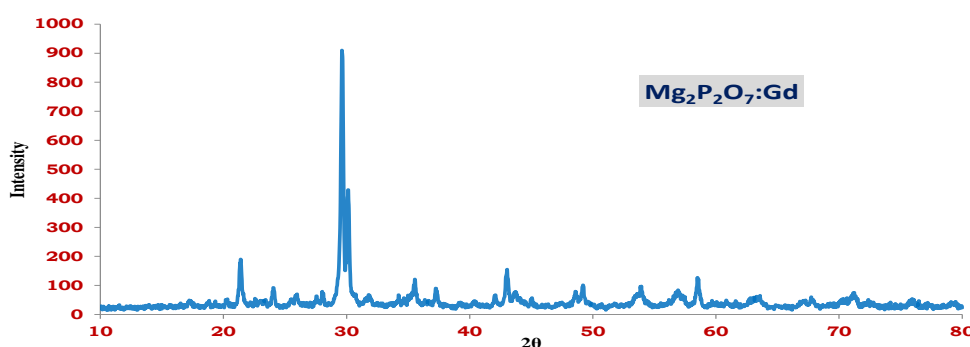


Fig 2 XRD image of the prepared phosphor Mg₂P₂O₇: Gd³⁺

III. RESULTS AND DISCUSSION

3.1 Morphology of $Mg_2P_2O_7: Gd^{3+}$ Phosphor

SEM image is represented in Fig. 3 for $Mg_2P_2O_7: Gd^{3+}$ material. The material shows irregular shape expanded particle structure. It shows the sizes of particles from 0.5 μm to 5 μm range.

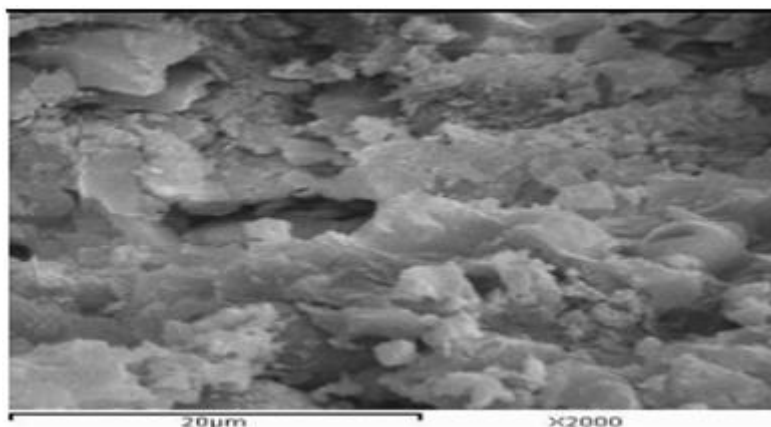


Fig 3 SEM image of the phosphor $Mg_2P_2O_7: Gd^{3+}$

3.2 FTIR analysis of $Mg_2P_2O_7: Gd^{3+}$ Phosphor

Fig. 4 represents the Fourier transformed infrared spectroscopy (FTIR) spectra for $Mg_2P_2O_7: Gd^{3+}$ Material. The FTIR revealed prominent absorption with peaks for $Mg_2P_2O_7: Gd$ are at 3670 cm^{-1} , 2971 cm^{-1} , 1065 cm^{-1} , 1029 cm^{-1} , 1009 cm^{-1} , 949 cm^{-1} , 720 cm^{-1} , 607 cm^{-1} as shown in figure. The IR peak at about 1029 and 1065 cm^{-1} is for P-O asymmetric stretching bonds used for the preparation of $Mg_2P_2O_7: Gd^{3+}$. The peaks at about 909 cm^{-1} and 990 cm^{-1} P-O symmetric stretching bonds. The IR absorption at wave numbers smaller than 500 cm^{-1} mainly originates from the lattice dynamic modes. A distinguished peak at 723.93 cm^{-1} is from the OH hydroxyapatite group is visible in spectrum. The absence of peaks in the range of 1550 - 2500 cm^{-1} supports the complete removal of residual nitrate and organic matter. The peaks at about 550 cm^{-1} is for O-P-O bonding. The IR spectrum confirms the existence of both trigonally and tetrahedrally coordinated boron atoms, consistent with the results obtained from the crystallographic study [21-23]

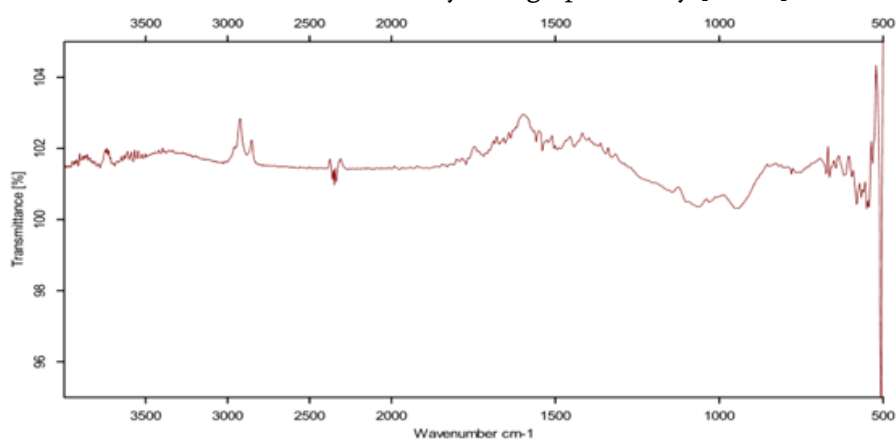


Fig 4 FTIR image of $Mg_2P_2O_7: Gd^{3+}$ Phosphor

3.3 Photoluminescence Studies of $Mg_2P_2O_7: Gd^{3+}$ Phosphor

Fig. 5 represents emission and excitation spectra of $\text{Mg}_2\text{P}_2\text{O}_7:\text{Gd}^{3+}$. Under the excitation of 274 nm phosphor materials show two emissions at 304 nm and 312 nm, which could be applicable in phototherapy. These lines correspond to the $6P_{5/2} \rightarrow 8S$ and $6P_{7/2} \rightarrow 8S$ transitions of the Gd^{3+} ion, respectively.

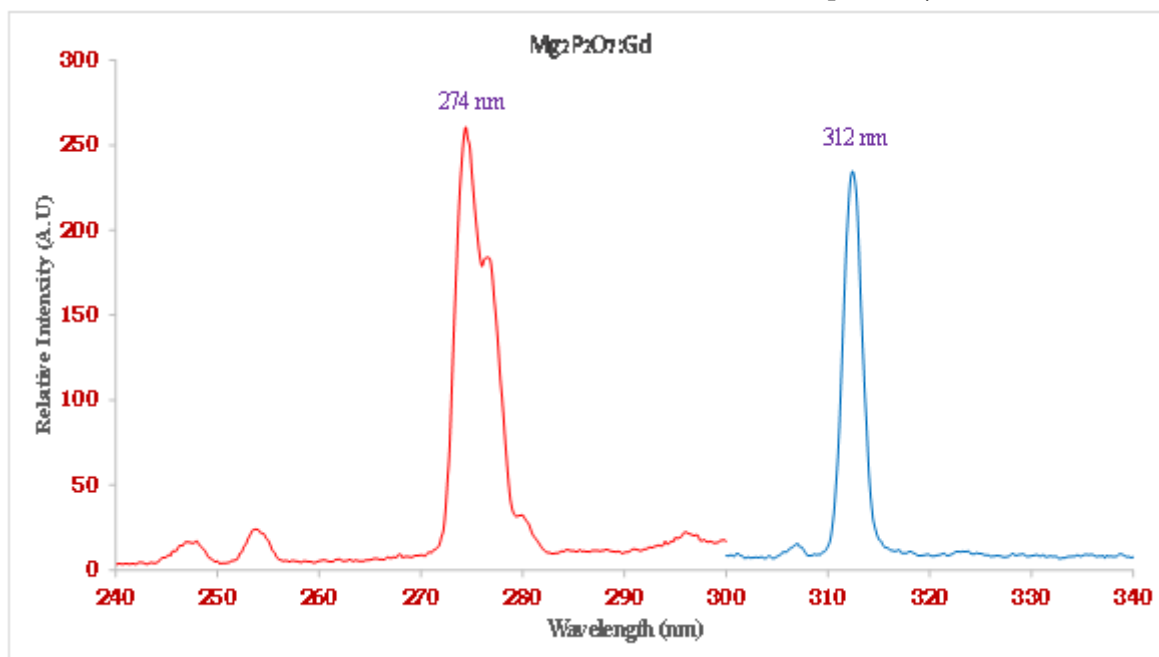


Fig 5 Excitation and Emission Spectra of $\text{Mg}_2\text{P}_2\text{O}_7:\text{Gd}^{3+}$ Phosphor

IV. CONCLUSIONS

In summary, a novel green phosphor $\text{Mg}_2\text{P}_2\text{O}_7:\text{Gd}^{3+}$ was obtained via the slow vaporization method. Under the excitation of 274 nm phosphor materials show two emissions at 304 nm and 312 nm, which could be applicable in phototherapy. These lines correspond to the $6P_{5/2} \rightarrow 8S$ and $6P_{7/2} \rightarrow 8S$ transitions of the Gd^{3+} ion, respectively. The doped phosphor exhibits an intense green emission under the ultraviolet excitation.

V. REFERENCES

- [1]. Z. S. Khan, N. B. Ingale, S. K. Omanwar, Adv. Sci. Lett. 2016, 22, 164
- [2]. D. N. Game, S. T. Taide, Z. S. Khan, N. B. Ingale, S. K. Omanwar, AIP Conference Proceedings 2016, 1728, 020488.
- [3]. Z. S. Khan, N. B. Ingale, S. K. Omanwar, Int. J. Lumin. And Appl. 2015, 5, 471.
- [4]. Z. S. Khan, N. B. Ingale, S. K. Omanwar, AIP Conference Proc. 2018, 1953, 070024.
- [5]. A. K. Bedyal, V. Kumar, O.M. Ntwaeaborwa, H.C. Swart, Mater. Res. Exp. 2014, 1 015006.
- [6]. Z. S. Khan, N. S. Bajaj, N. B. Ingale, S. K. Omanwar, International Journal of Basic and Applied Research 2014, 1, 59.

- [7]. EEU Tien Yew, PANG Xie Guan, LEOU Ting Qiao, Zuahiri Ibrahim, RosliHussin, *Advanced Materials Research* 2014, 895, 265.
- [8]. Santosh K. Gupta, M. Mohapatra, S. V. Godbole, V. Natarajan, *RSC Adv.* 2013, 3, 20046.
- [9]. Santosh K. Gupta, NimaiPathak, ManjulataSahu, V. Natarajan, 2014, 25, 1388.
- [10]. SantoshK.Gupta, R. M. Kadam, R. Gupta, ManjulataSahu, V. Natarajan, *Materials Chemistry and Physics*, 2014, 145, 162.
- [11]. MengjiaoXu, Luxiang Wang, DianzengJia, Fuje Le, *J lumin.*2015, 158, 125.
- [12]. MengjiaoXu, Luxiang Wang, DianzengJia, Lang Liu, *Mat Res Bull.* 2015, 70, 691.
- [13]. Ran Pang, Wenzhi Sun, Jipeng Fu, Haifeng Li, YongleiJia, Da Li, Lihong Jiang, Su Zhang, Chengyu Li, *RSC Advances*, 2015, 5, 82704.
- [14]. Z. S. Khan, N. B. Ingale, S. K. Omanwar, *Environ Sci. Pollut. Res.* 2016, 23, 9295.
- [15]. Z. S. Khan, N. B. Ingale, S. K. Omanwar, *Opt-Int J Light Electron Opt.* 2016, 127, 9679.
- [16]. Z. S. Khan, N. B. Ingale, S. K. Omanwar, *Opt-Int J Light Electron Opt.* 2016, 127, 6062.
- [17]. Zamir Khan, Z. S. Khan, N. B. Ingale, S. K. Omanwar, *AIP Conference Proceedings* 2104, 1, 030035.
- [18]. D.P. Dutta, A. Ballal, J. Nuwad and A.K. Tyagi, *J. Lumin.* 2014, 148, 230.
- [19]. S. Mukherjee, D.P. Dutta, N. Manoj and A.K. Tyagi, *J. Lumin.* 2013, 134, 880.
- [20]. M. Rathod, Z. S. Khan, N. B. Ingale, S. K. Omanwar, *J of Emerging Tech and Innovative Res.* 2019, 6, 460.
- [21]. N. Khay, A. A. Ennaciri, M. Harcharras, *VibSpectrosc.* 2001, 27, 119.
- [22]. N. Khay, A. A. Ennaciri, *J Alloys Compd*2001, 323, 800.
- [23]. M. S. Idrissi, L. Rghioui, R. Nejjar, L. Benarafa, M. S. Idrissi, A. Lorriaux, F. Wallart, *SpectrochimActa Part A* 2004, 60, 2043.
- [24]. R. P. Rao, *J. Electrochem. Soc.* 2003, 150, H165.
- [25]. Z. S. Khan, N. B. Ingale, S. K. Omanwar, *Journal of Advances in Applied Sciences and Technology* 2014, 1, 277.



Study of Structural, Magnetic and Dielectric Properties of Calcium Substituted Ni Ferrites

S.N. Kachhwah, Y.D. Choudhari*, K.G. Rewatkar

Department of Physics, Dr. Ambedkar College, Deeksha Bhoomi, Nagpur-10, Maharashtra, India

ABSTRACT

Calcium-doped nickel ferrites with the composition $\text{Ni}_{1-x}\text{Ca}_x\text{Fe}_2\text{O}_4$ ($x = 0.3$ and 0.9) are synthesized via microwave-induced sol-gel auto combustion method to analyze their structural, magnetic, and dielectric characteristics at extending frequency range. The X-ray reaction (XRD) and transmission electron microscopy (TEM) were employed to analyze the prepared composition's nanostructure and exterior topography. The development of pure spinel ferrites is revealed by XRD patterns. The results demonstrate that as the calcium content in material increases, the lattice parameter of the Ni ferrite decline, as does the grain boundary. The saturation magnetization and coercivity of Ni-Ca ferrites decreased as the Calcium substitution raised. Due to the expanded boundary, the huge grains may have trapped pores within them, affecting the sample's density, resistivity, and dielectric constant. Following the Verway hopping mechanism, the dielectric constant drops with increasing frequency.

Keywords: Ni-Ca ferrite, XRD, SEM, TEM, VSM, Saturation magnetization etc.

I. INTRODUCTION

Nanotechnology, which deals with the design, manufacturing, and application of nanostructures or nanomaterials, is sometimes referred to be the technology of the century. There is also an understanding of how distinct physical and chemical qualities are related to the material's size. There has been a growing consensus in the last decade that nanotechnology is a developing, cross-disciplinary technology that has made significant contributions to many different professions and disciplines including physics and materials science as well as optics and electronics[1]. The extensive structural chemistry of spinel ferrite systems provides significant chances for comprehending and fine-tuning the many features of nanoparticles by chemical manipulations. Ferrites made from nanocrystalline mixed spinel ferrites are employed in a wide range of technological applications, including antenna shrinking, microwave dielectric properties, and antenna performance improvement[2]. Researchers have focused on nickel ferrites as a soft magnet and low-loss material at high frequencies because of their enticing features. High electrical and low eddy current losses make calcium substituted nickel ferrites more appropriate for microwave devices than conventional nickel ferrites. T. Vigneswari et al. successfully synthesized spinel ferrite of $\text{Ni}_{1-x}\text{Ca}_x\text{Fe}_2\text{O}_4$ nanoparticles via co-precipitation. The creation of a cubic spinel structure with a single phase of nanoparticles was demonstrated

by XRD and FTIR spectra. The lattice constant and crystallite size have been found to increase with Ca²⁺ substitution[3]. Saturation magnetization increases up to x=0.2 and then declines as Ca²⁺ concentration increases. The current study examines the structural, dielectric, and magnetic properties of nanoparticles of Ca²⁺ substituted nickel ferrites synthesized using the sol-gel auto-combustion process, as well as their structural and magnetic properties as measured by X-ray diffraction, TEM, and VSM[4].

II. MATERIAL PREPARATION

The microwave-induced sol-gel auto-combustion technique was used to synthesize calcium substituted nickel ferrite [Ca_xNi_{1-x}Fe₂O₄ (x=0.3 and 0.9)]. The synthesizing technique employs a mix of metal nitrates and urea. Equimolar amounts of Ca(NO₃)₂·4H₂O, Fe(NO₃)₃·9H₂O, and Ni(NO₃)₂·6H₂O, and urea are stirred in distilled water in a beaker. The gel was burned in a microwave oven; initially, the mixture boiled at 80-90 °C and dehydrates, emitting a significant amount of gases in the process[5].

When the liquid reaches the point of self-initiated combustion, it ignites and emits a huge quantity of heat, combusting the entire solution in a moment and solidifying, at temperatures greater than 500 °C. By igniting the mixture, calcium substituted nickel ferrite powder can be produced in much less than a few minutes in a microwave oven. To create nanoparticles, the nanocomposite was grinded for three hours in a pestle and mortar and then calcining the substances for 5 hours at 800 °C in a muffle furnace[6].

III. RESULT AND DISCUSSIONS

3.1 XRD Analysis

The X-ray diffraction patterns of Ni-Ca ferrite for (x = 0.3 and 0.9) are shown in **Error! Reference source not found.** All material has been shown to have a cubic spinel structure phase that matches the JCPDS file number 00-036-1451. The detected maxima are fairly sharp due to the nanocrystalline size. The lattice parameter (a) has been calculated using

the most prominent peaks denoted by (220), (311), (222), (400), (422), and (511). The ionic radius of Ca (1.02Å) is significantly bigger than the ionic radius of Ni (0.69Å), causing the lattice parameter (a) to decrease and confirming that Ca²⁺ has reached the regular spinel lattice state[7]. The Scherrer formula has been used to determine the

crystallite size (D). $D = k \lambda / \beta \cos \theta$

Where λ is the X-ray beam's wavelength, K is the form factor, and θ is the angle of diffraction. The average crystalline size (D) is reduced as the Ca²⁺ ratio has increased, reaching a minimum of 42 nm at x = 0.9, which is consistent with the report of T. Vigneswari et al. The x-ray density (Xd) and bulk density both decrease with Ca²⁺ substitution. The improved porosity (P) of each sample (Table 1) reflects crystal defects. The discrepancy in densities occurs as a result of porosity in the crystal formation, which is dependent on stoichiometry, processing method, and heat treatment parameters[3].

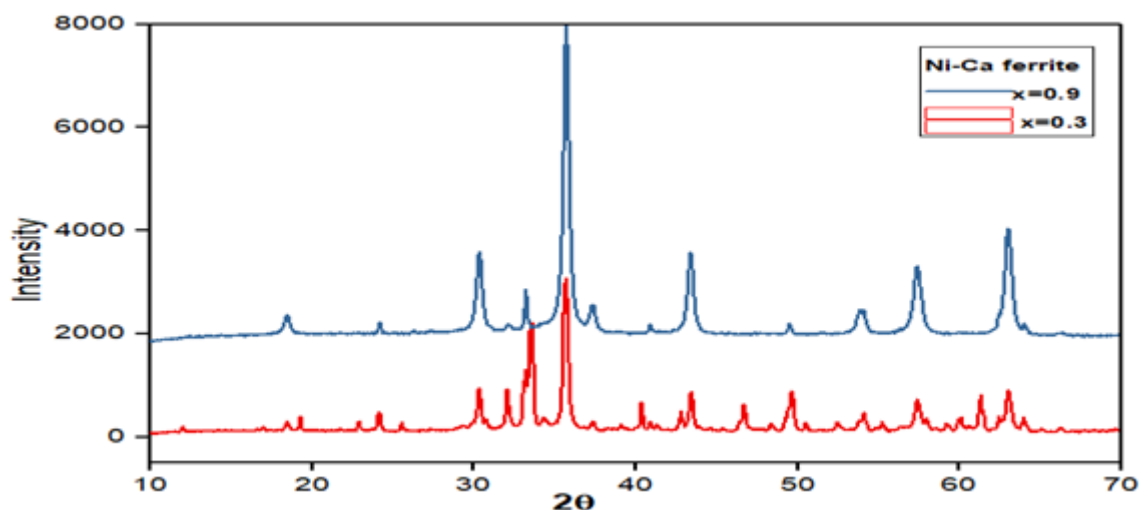


Figure 1: XRD graph of $\text{Ni}_{1-x}\text{Ca}_x\text{Fe}_2\text{O}_4$ ($x=0.3$ and 0.9) ferrite

Table 1: Lattice parameter, X-ray density and Crystallite size of $\text{Ni}_{1-x}\text{Ca}_x\text{Fe}_2\text{O}_4$ ($x=0.3$ and 0.9) ferrite

Conc. (x)	Molecular weight	Lattice parameter (Å)	X-ray density (gm/cm^3)	Bulk density (gm/cm^3)	Porosity (%)	Crystallite size (nm)
0.3	221.35	8.3723	5.38	3.797	29	52
0.9	228.79	8.3712	5.24	3.573	32	42

3.2 FTIR Analysis

The presence of two essential absorption bands attributed to inverse spinel ferrites is displayed by FTIR spectra in **Figure 1**. The assigned stronger recurring absorption bands were seen between 400 and 700 cm^{-1} , and these vibration bands correlate to a midpoint of oxygen and metal ions as they approach tetrahedral and octahedral sites[8]. Single-phase inverse spinel ferrites are known for their distinctive absorption bands, ν_1 is assigned to a high repetition band of the metal-oxygen stretching to the vibration for tetrahedral metal-oxygen vibration, whereas ν_2 is given to a reduced recurrence band of the octahedral metal-oxygen vibration. This absorption model elucidates the inverse spinel lattice structure and the variation is related to the bond period sequence in tetrahedral A-sites. Additionally, octahedral B-sites are less abundant than A-sites. The intensity increases when the Ca^{2+} ion element is increased, implying that the ionic bonding is strengthened, and it was discovered that the inter-ionic distances between the anion exchange reduce as the Ca^{2+} ion increases[9]. The bands found between 3400 and 1600 cm^{-1} correspond to the H–O–H and extending modes of consumed water molecules, respectively. Additionally, it is worth noting that the difference in peak positions is mostly determined by the amount of substituent, particle size, and also production procedure. Thus, the peak shifts observed in the FT-IR spectrum, along with the variation in lattice parameters as determined by XRD data, indicate crystal lattice scattering and cation redistribution caused by the expansion of higher rare earth cations[10].

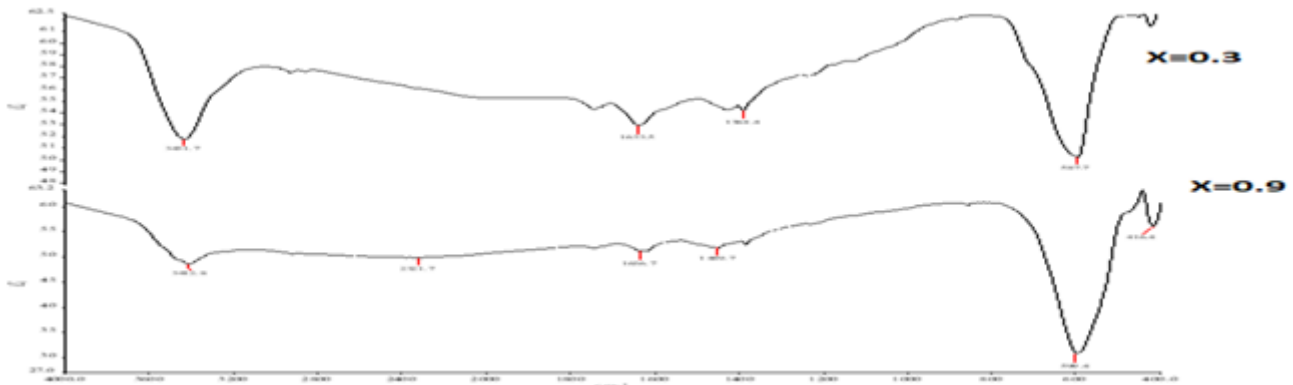


Figure 1: FTIR image of $Ni_{1-x}Ca_xFe_2O_4$ ($x=0.3$ and 0.9) ferrite

3.3 SEM- EDX Analysis

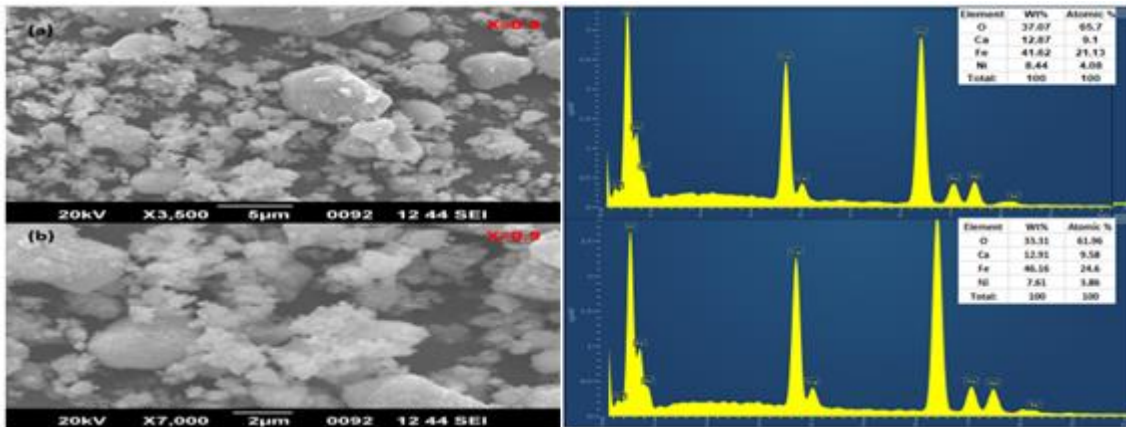


Figure 2 shows SEM micrographs for the compositions $x = 0.3$ and 0.9 . Nano dimensions and nearly uniform sizing of ferrite particles have shown in the micrograph. The microscopic particles appear to have clumped together. Also

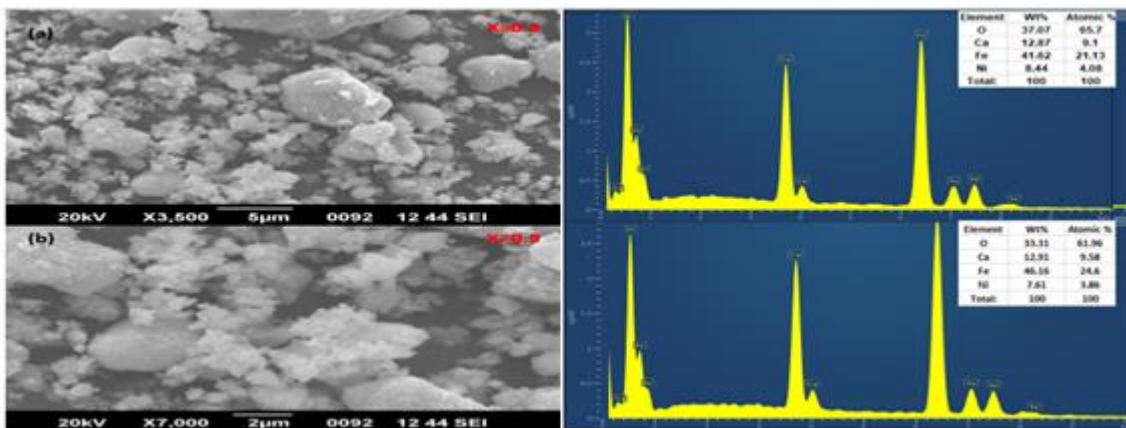


Figure 2 shows the results of the energy dispersive X-ray (EDX) analysis on the produced samples [11]. The existence of Ni, Ca, Fe, and O peaks have revealed in the EDX spectrum of Nickel - Calcium ferrite nanoparticles calcined at $800\text{ }^{\circ}\text{C}$. EDX analysis confirmed that all of the constituent elements are present in

the desired ratio in the synthesized ferrite samples. The pattern also confirms that after being doped with Nickel ferrite, the crystal structure of Ni-Ca spinel ferrite has decreased[12].

3.4 TEM analysis

The crystallite morphology of the materials was confirmed by TEM analysis (Transmission Electron Microscopy). As shown by the TEM images, the particle size distribution in the dynamically processed samples is in excellent agreement with that of the grain size[13]. The particle diameter was determined using the Debye-Scherrer formula and prominent XRD peaks associated with the cubic spinel phase. The synthesized samples' grain size was found to be between 29 and 32 nm, as presented in

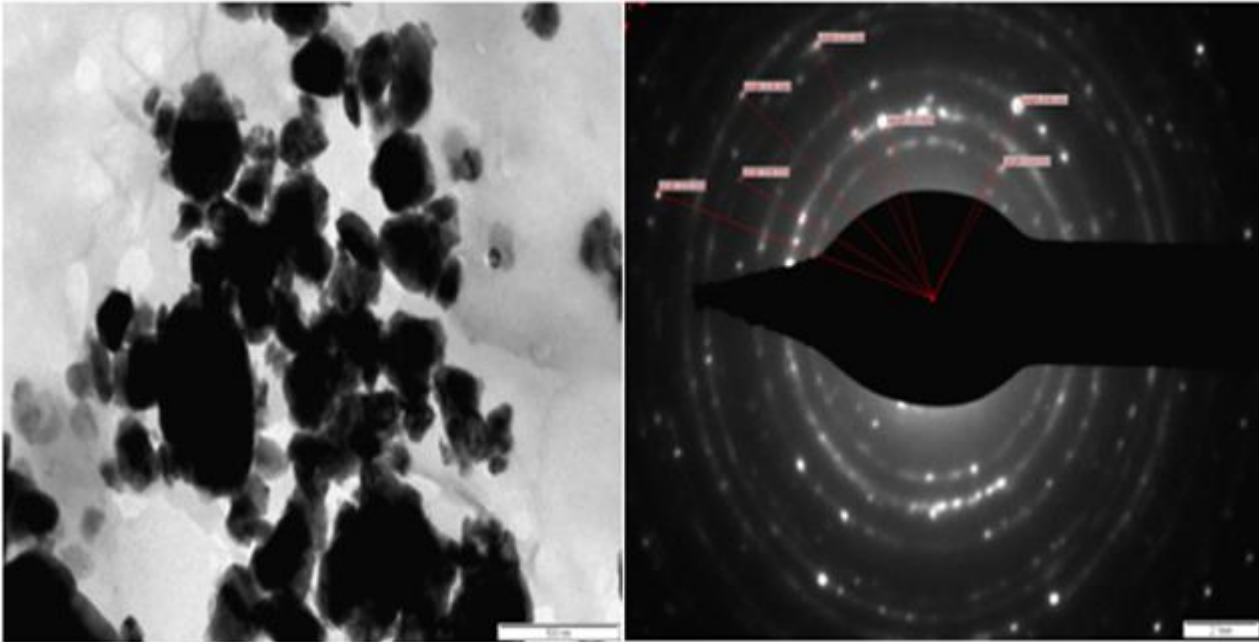


Figure 34[14].

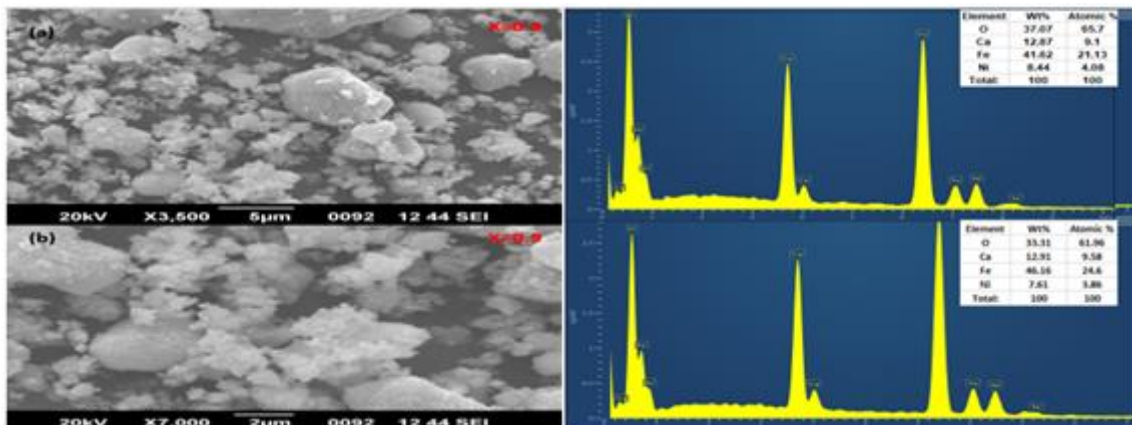


Figure 2: SEM and EDX image of $Ni_{1-x}Ca_xFe_2O_4$ ($x=0.3$ and 0.9) ferrite

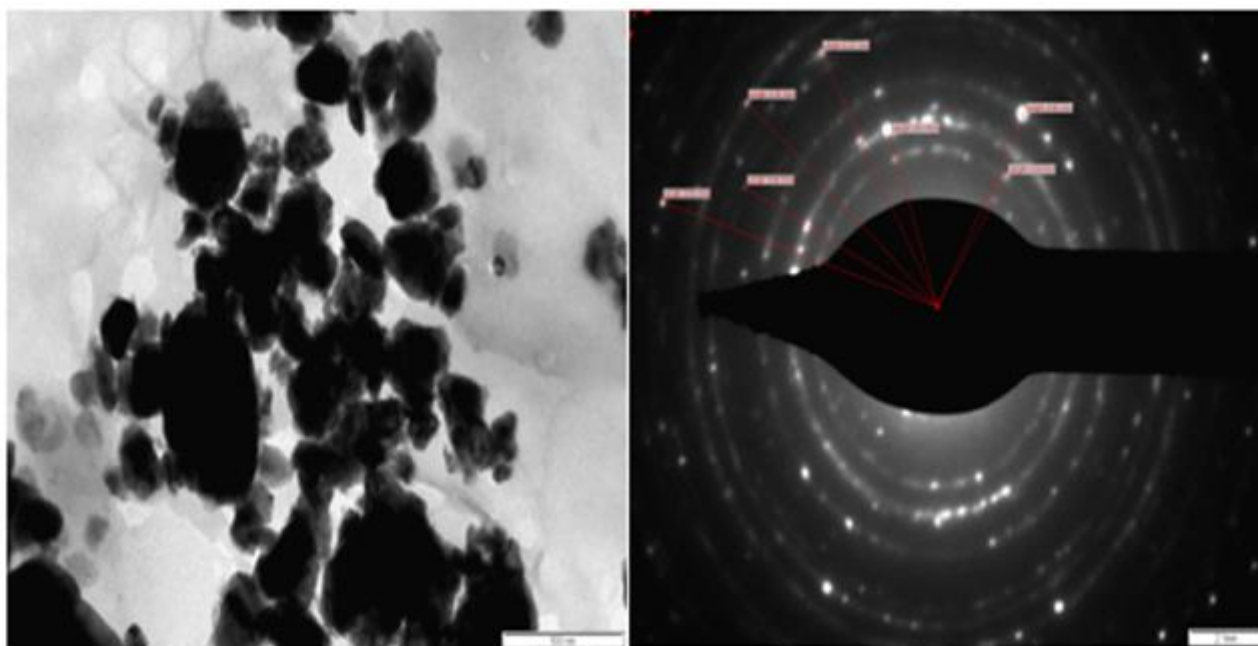


Figure 3: TEM and SAED image of $\text{Ni}_{1-x}\text{Ca}_x\text{Fe}_2\text{O}_4$ ($x=0.3$) ferrite

3.5 VSM Analysis

VSM has been used in the study of magnetic properties including saturation magnetization, retentivity, and coercive field. It is possible to calculate the Bohr magneton by applying the following relationship:

$$\mu_B = \frac{M * M_s}{5585}$$

The ferrite sample's molecular weight is M , the magnetic factor is 5585, while the observed saturation magnetization is M_s . The VSM investigations were done at room temperature because the spins regulate more consistently at this temperature[15].

Conc. x	Saturation Magnetization M_s (emu/g)	Retentivity $M_r * 10^{-3}$ (emu/g)	Coercivity (H_c) (Oe)	Bohr magneton $\mu_B * 10^{-1}$	SQR Ratio (M_r/M_s)
0.3	0.42632	17.275	21.043	1.42	0.0405
0.9	0.42603	15.248	20.635	0.82	0.0358

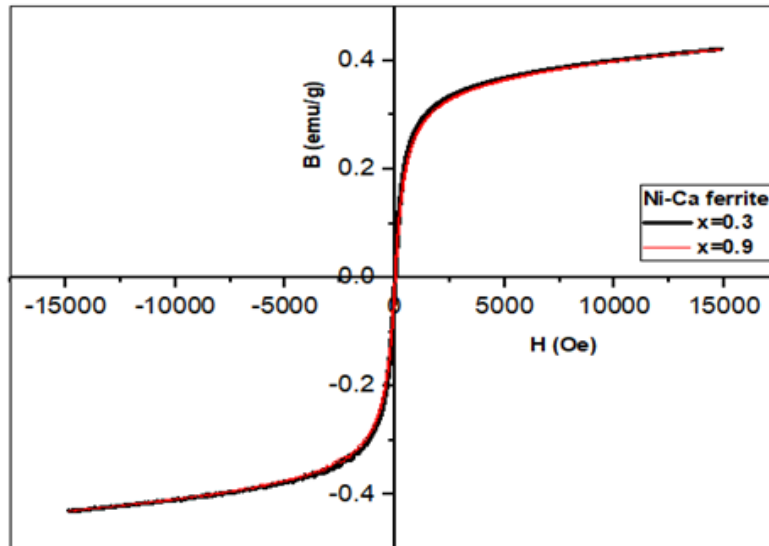
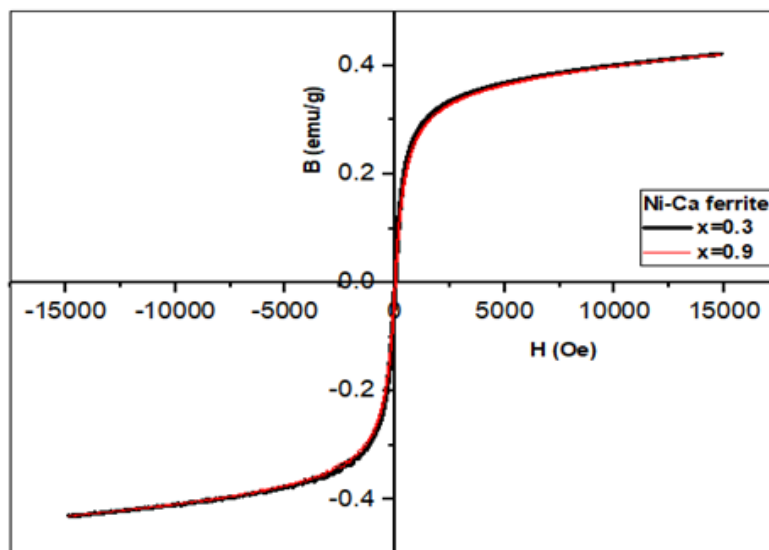


Figure 4 illustrates the hysteresis loops of the Ni-Ca ferrite system. The materials thin hysteresis loop refers, that they are magnetically soft, have low coercivity, and are ferrimagnetic. There is a large concentration of Ca^{2+} ions at A sites, but it is only distributed partially between A and B[8]. The values of the Bohr magneton have been observed to decrease when the Ca^{2+} volume increases. This is because the A–B exchange interaction grows stronger, as Ni^{2+} ions are replaced by Ca^{2+} ions at the appropriate locations[4]. The M_s and H_c values are reduced from 0.42632 to 0.42603 emu/g and 21.043 to 20.635 Oe.

Table 2 : M_s , M_r , H_c of Ni-Ca ferrite

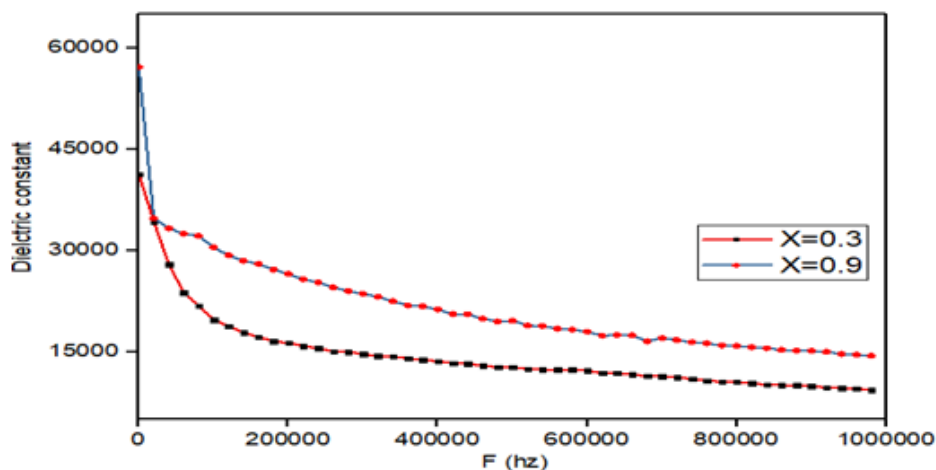


Conc. x	Saturation Magnetization M_s (emu/g)	Retentivity $M_r \cdot 10^{-3}$ (emu/g)	Coercivity (H_c) (Oe)	Bohr magneton $\mu_B \cdot 10^{-1}$	SQR Ratio (M_r/M_s)
0.3	0.42632	17.275	21.043	1.42	0.0405
0.9	0.42603	15.248	20.635	0.82	0.0358

Figure 4: VSM image of $\text{Ni}_{1-x}\text{Ca}_x\text{Fe}_2\text{O}_4$ ($x=0.3$ and 0.9) ferrite

3.6 Dielectric Analysis

One of the most essential aspects of ferrite nanoparticles is their dielectric constant (ϵ'), which is heavily influenced by the preparation conditions, uniting time, temperature, material type, and quality. Electrodes were placed on both sides of the disc using a thin layer of silver paste to create a capacitance[16]. An LCR-meter device was used to evaluate the specimens' true dielectric constant, tangential loss factor, and electrical conduction in the range of 20 Hz to 10 Mhz. Dielectric constant changes in the high-frequency range at room temperature are shown in **Error! Reference source not found.**

Figure 6: Dielectric constant vs Frequency of $\text{Ni}_{1-x}\text{Ca}_x\text{Fe}_2\text{O}_4$ ($x=0.3$ and 0.9) ferrite

When frequency increases, the dielectric constant begins to decline until it approaches a fixed value at higher frequencies[17]. That implies that ferrites are naturally dielectric. Using the Kopp theory, it is possible to explain the massive drop in dielectric coefficient at low frequencies. Dielectric materials with a heterogeneous microstructure can be viewed as grain structures with strong electrical conductivity, separated by several thin resistive layers. Space charge polarization occurs when the sample's voltage drops significantly after passing through the grain boundaries, and this is what causes the voltage to be reduced in this situation. The free charges on the grain boundaries regulate the polarization of the space charge and conductivity of the samples. The migration of iron ions from octahedral sites to tetrahedral sites and the consequent drop in the electron hopping between Fe^{3+} and Fe^{2+} may be the causes of a decrease in the dielectric constant when calcium levels are raised[18]

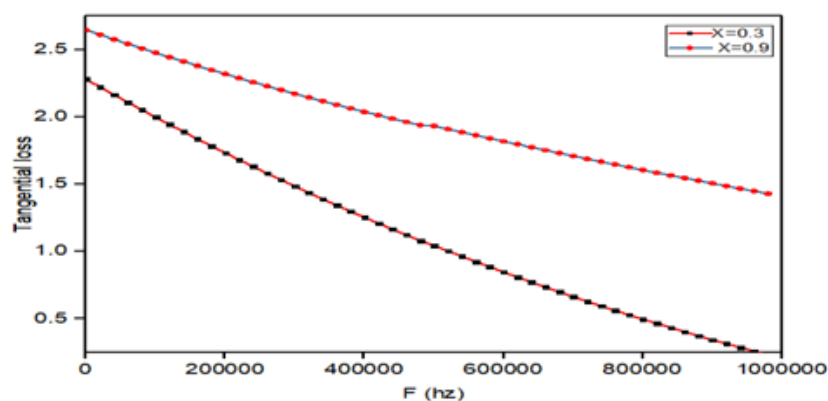


Figure 5 depicts the relationship between conductivity and temperature. It is clear from these graphs that the conductivity enhances gradually. Localized majority carriers are responsible for its conduction. Electrons are significantly concentrated on cations in a confined model, according to this theory. The strong interaction between electrons and phonons in these materials allows polaron to be used to reveal conduction. Temperature and frequency are both important factors when it comes to the band structure of the conductivity of polaron. The higher the temperature, the hopping process is initiated by heat radiation[19]. A strong magnetic contact between the carriers and the magnetic sub-lattice may be responsible for the localization of the electron-phonon interactions. Fe^{2+} ions may be distributed unevenly over octahedral and tetrahedral positions in the spinel lattice, resulting in an extra localization of the ions. Small polaron conduction-related trends are also evident in the current scenario[20].

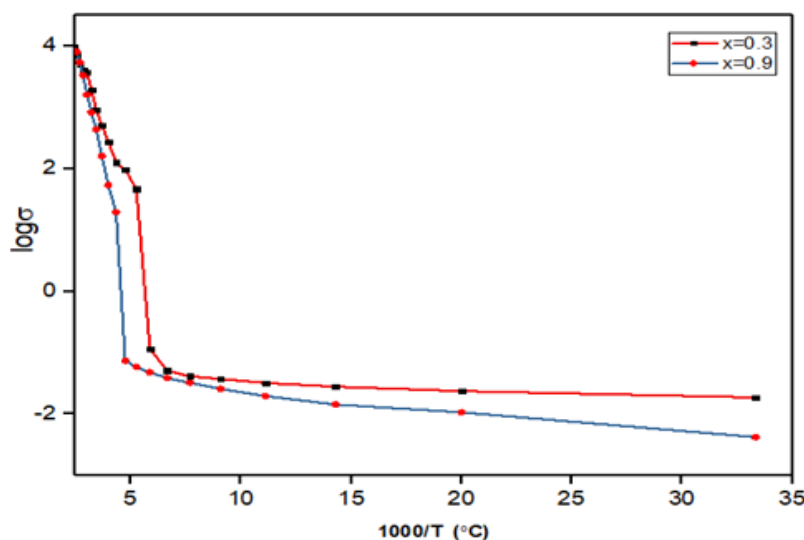


Figure 5: Log σ vs $1000/T$ of $\text{Ni}_{1-x}\text{Ca}_x\text{Fe}_2\text{O}_4$ ($x=0.3$ and 0.9) ferrite

IV. CONCLUSION

The sol-gel auto combustion approach was used to successfully produce Ca^{2+} substituted nickel ferrites with the chemical formula $\text{Ni}_{1-x}\text{Ca}_x\text{Fe}_2\text{O}_4$ ($x=0.3$ and 0.9). The creation of a single-phase spinel structure was confirmed by X-ray diffraction investigation. Approximately 42nm to 52nm in crystallite size was discovered.

The lattice parameter dropped as Ca^{2+} concentration increased. The results of the XRD-based nanosize measurements were validated by a TEM investigation. A decrease in saturation magnetization and coercivity was observed because the substitution of ions by non-magnetic Ca^{2+} ions decreases the sublattice connection and lowers the magnetic moment of each unit cell in nickel ferrite.

V. ACKNOWLEDGMENT

The authors would like to thank the Sophisticated Test and Instrumentation Centre (STIC), Cochin University, Kerala, India, for the XRD and FE-SEM, as well as IIT Guwahati for the VSM instrumentation characterization.

VI. CONFLICT OF INTEREST

The authors declare there is no conflict of interest.

VII. REFERENCES

- [1]. M.A. Borikar, D.M. Borikar, N.S. Meshram, K.G. Rewatkar, Characterization of nanostructured spinel $\text{NiCr}_x\text{Fe}_{2-x}\text{O}_4$ obtained by sol gel auto combustion method, *J. Phys. Conf. Ser.* 1913 (2021). <https://doi.org/10.1088/1742-6596/1913/1/012079>.
- [2]. W. Da Oh, Z. Dong, T.T. Lim, Generation of sulfate radical through heterogeneous catalysis for organic contaminants removal: Current development, challenges and prospects, *Appl. Catal. B Environ.* 194 (2016) 169–201. <https://doi.org/10.1016/j.apcatb.2016.04.003>.
- [3]. T. Vigneswari, P. Raji, Structural and magnetic properties of calcium doped nickel ferrite nanoparticles by co-precipitation method, *J. Mol. Struct.* 1127 (2017) 515–521. <https://doi.org/10.1016/j.molstruc.2016.07.116>.
- [4]. N.N. Sarkar, D.J. Roy, S.M. Butte, W.S. Barde, K.G. Rewatkar, Synthesis and Magnetic studies of Co-Sn doped Nanoscale Calcium Hexaferrites, 25 (2020) 57–67.
- [5]. D.M. Borikar, M.A. Borikar, A.S. Kakde, K.G. Rewatkar, Nano copper spinel ferrite : Synthesis & characterization by sol-gel auto combustion technique, 5 (n.d.) 7–10.
- [6]. A.S. Kakde, B.A. Shingade, N.S. Meshram, K.G. Rewatkar, STRUCTURAL AND MAGNETIC PROPERTIES OF SN-ZR SUBSTITUTED CALCIUM NANO-HEXAFERRITE ., 1 (2014) 60–63.
- [7]. V.S. Kiran, S. Sumathi, Comparison of catalytic activity of bismuth substituted cobalt ferrite nanoparticles synthesized by combustion and co-precipitation method, *J. Magn. Mater.* 421 (2017) 113–119. <https://doi.org/10.1016/j.jmmm.2016.07.068>.
- [8]. H.R. Dehghanpour, Physical and chemical properties of NiFe_2O_4 nanoparticles prepared by combustion and ultrasonic bath methods, *Russ. J. Appl. Chem.* 89 (2016) 80–83. <https://doi.org/10.1134/S10704272160010122>.

- [9]. J.T. Adeleke, T. Theivasanthi, M. Thiruppathi, M. Swaminathan, T. Akomolafe, A.B. Alabi, Photocatalytic degradation of methylene blue by ZnO/NiFe₂O₄ nanoparticles, *Appl. Surf. Sci.* 455 (2018) 195–200. <https://doi.org/10.1016/j.apsusc.2018.05.184>.
- [10]. J. Massoudi, M. Smari, K. Nouri, E. Dhahri, K. Khirouni, S. Bertaina, L. Bessais, E.K. Hlil, Magnetic and spectroscopic properties of Ni-Zn-Al ferrite spinel: From the nanoscale to microscale, *RSC Adv.* 10 (2020) 34556–34580. <https://doi.org/10.1039/d0ra05522k>.
- [11]. M. Shandilya, S. Thakur, R. Rai, Study of phase transitional behavior and electrical properties of relaxor Ba_{0.85}Ca_{0.15}Zr_{0.05}Ti_{0.95}O₃ lead free ceramic, *Ferroelectr. Lett. Sect.* 46 (2019) 8–18. <https://doi.org/10.1080/07315171.2019.1647705>.
- [12]. P. Dipak, D.C. Tiwari, S.K. Dwivedi, Synthesis of Polymer Blend Ferrite Composite for Microwave Absorption at X-Band Frequency, *Open J. Met.* 09 (2019) 33–41. <https://doi.org/10.4236/ojmetal.2019.94004>.
- [13]. P. Chaware, A. Nande, S.J. Dhoble, K.G. Rewatkar, Structural, photoluminescence and Judd-Ofelt analysis of red-emitting Eu³⁺ doped strontium hexa-aluminate nanophosphors for lighting application, *Opt. Mater. (Amst.)* 121 (2021) 111542. <https://doi.org/10.1016/j.optmat.2021.111542>.
- [14]. Y. Liu, X. Su, X. He, J. Xu, J. Wang, Y. Qu, C. Fu, Y. Wang, Dielectric and microwave absorption properties of ZrB₂/Al₂O₃ composite ceramics, *J. Mater. Sci. Mater. Electron.* 30 (2019) 2630–2637. <https://doi.org/10.1007/s10854-018-0538-3>.
- [15]. M.A. Borikar, D.M. Borikar, A.S. Kakde, K.G. Rewatkar, Nickel nano spinel ferrites: Synthesis and characterization, *Int. Conf. Electr. Electron. Optim. Tech. ICEEOT 2016.* (2016) 3251–3253. <https://doi.org/10.1109/ICEEOT.2016.7755306>.
- [16]. M.N. Ashiq, M.J. Iqbal, I.H. Gul, Structural, magnetic and dielectric properties of Zr-Cd substituted strontium hexaferrite (SrFe₁₂O₁₉) nanoparticles, *J. Alloys Compd.* 487 (2009) 341–345. <https://doi.org/10.1016/j.jallcom.2009.07.140>.
- [17]. R.K. Panda, R. Muduli, D. Behera, Electric and magnetic properties of Bi substituted cobalt ferrite nanoparticles: Evolution of grain effect, *J. Alloys Compd.* 634 (2015) 239–245. <https://doi.org/10.1016/j.jallcom.2015.02.087>.
- [18]. M. Aliuzzaman, M. Manjurul Haque, M. Jannatul Ferdous, S. Manjura Hoque, M. Abdul Hakim, Effect of sintering time on the structural, magnetic and electrical transport properties of Mg_{0.35}Cu_{0.20}Zn_{0.45}Fe_{1.94}O₄ ferrites, *World J. Condens. Matter Phys.* 4 (2014) 13–23.
- [19]. S.M. Kabbur, S.D. Waghmare, U.R. Ghodake, S.S. Suryavanshi, Synthesis, morphology and electrical properties of Co²⁺ substituted NiCuZn ferrites for MLCI applications, *AIP Conf. Proc.* 1942 (2018) 2–6. <https://doi.org/10.1063/1.5029072>.
- [20]. V.S. Shinde, S.G. Dahotre, L.N. Singh, Synthesis and characterization of aluminium substituted calcium hexaferrite, *Heliyon.* 6 (2020) e03186. <https://doi.org/10.1016/j.heliyon.2020.e03186>.

Fabrication and Characterization of Co Modified SmFeO₃ Thick Film

R.B.Mankar*, V.D.Kapse

*¹Department of Physics, Smt. Radhabai Sarda Arts, Commerce and Science College, Anjangaon Surji 444705, Maharashtra, India

²Department of Physics, Arts, Science and Commerce College, Chikhaldara 444807, Maharashtra, India

ABSTRACT

In present work dipping method was employed for surface modification of SmFeO₃ thick films. SmFeO₃ thick films were fabricated on glass substrate by screen printing technique and fired at 500 °C for 30 min. As-prepared pure SmFeO₃ thick films were dipped into 0.1 M aqueous solution of Cobalt Chloride for 1 min and then fired at 550 °C for 30 min to obtain Co modified SmFeO₃ thick films. Structural and morphological properties of unmodified and Co modified SmFeO₃ thick films were investigated by Field Effect Scanning Electron Microscopy (FE-SEM) and Energy Dispersive X-Ray Analysis (EDS) techniques. The effect of cobalt doping on microstructure and surface morphology of pure SmFeO₃ thick film was discussed.

Keywords: SmFeO₃, Surface modification, Perovskite, Gas sensor, dipping technique.

I. INTRODUCTION

In past few decades, semiconductor metal oxides have attracted considerable attention due to their promising applications in gas sensor. Different semiconducting metal oxides including complex metal oxides have been investigated for gas sensing characteristics [1-2]. Among them perovskites of type ABO₃ (A: rare earth, B: transition metal) have been reported to exhibit great technological versatility because of their interesting properties such as ionic and electronic conductivity, thermal and chemical stability [3-4]. Their properties can be further improved by partial substitutions at A-site, B-site and/or both A-site and B-site. SmFeO₃ is typical rare earth orthoferrite which has been extensively investigated as a gas sensor material. Being p-type semiconducting material, it is widely used for detection of oxidizing gases such as ethanol, O₃ and NO₂ [5-7]. However due to reducibility and lower electrical conductivity of SmFeO₃ for reducing gases, its use is restricted to oxidizing gas sensor only. Both reduction stability and electrical conductivity depends on nature of A and B cations. With ABO₃ type perovskite structure of SmFeO₃ modification in reduction stability and electrical conductivity is possible by partial substitution at A-site and/or the B-site. For enhancement in reduction stability, doping of A-site with bigger cation was reported [8]. Researchers have reported the advantages of introducing CO at B-site. M. Zhao et al have reported that Co doped SmFeO₃ improves the electrical conductivity of perovskite as well as prevents it from decomposing under reducing conditions [9].

Since the physic-chemical properties of SmFeO_3 depend on size and surface morphology, synthesis of SmFeO_3 nanoparticles of well defined surface morphology and size is of interest. For the synthesis of SmFeO_3 perovskite different methods like sol-gel method and hydrothermal method have been adopted [10-11]. Sol-gel method in citric system has advantage of providing SmFeO_3 perovskite powder with high sensitivity and selectivity.

We have previously reported the synthesis of pure SmFeO_3 perovskite powder by Sol-gel method in and fabrication of SmFeO_3 thick films on glass substrate by screen printing technique [12]. In present work dipping method was employed for surface modification of SmFeO_3 thick films.

II. METHODS AND MATERIAL

2.1 Synthesis of SmFeO_3 powder:

Fine powder of SmFeO_3 perovskite oxide was prepared by sol-gel method. Samarium nitrate $\text{Sm}(\text{NO}_3)_3 \cdot 6\text{H}_2\text{O}$, iron nitrate $\text{Fe}(\text{NO}_3)_3 \cdot 9\text{H}_2\text{O}$ and citric acid monohydrate were mixed according to desired stoichiometry. The mixture was grounded in Agate mortar for 30 minutes. To this mixture, Ethylene glycol was added with constant stirring at 75°C for 2 hours to obtain a gel. The gel was then dried in oven at 110°C for 12 hours and calcined at 800°C for 4 hours to obtain fine powder of SmFeO_3 .

2.2 Fabrication of SmFeO_3 thick films:

The thixotropic paste was prepared by mixing the fine powder of SmFeO_3 with the solution of ethyl cellulose in a mixture of organic solvent by keeping the ratio of inorganic to organic part as 75:25. This paste was then screen-printed on glass substrate in desired pattern. The films were fired at 500°C for 30 min. and termed as pure SmFeO_3 thick film.

2.3 Surface modification of thick films :

As-prepared pure SmFeO_3 thick film was surface modified by dipping method. Pure SmFeO_3 thick film was dipped into 0.1 M aqueous solution of cobalt chloride for 1 min. After drying, these films were fired at 550°C for 30 min and termed as Co surface modified SmFeO_3 thick film.

III. RESULT AND DISCUSSION

3.1 X-ray diffraction analysis :

We have reported the analysis of X-ray diffraction pattern of synthesized pure SmFeO_3 powder in our previous paper [12]. The crystallite size was found to be 50.08 nm.

3.2 Surface morphology analysis :

Surface morphology and microstructure of both pure and Co modified SmFeO_3 thick films were studied by using FE-SEM. Fig. 1 depicts the FE-SEM image of pure SmFeO_3 thick film fired at 500°C for 30 min. The

micrograph shows the presence of large number of grains with grain size ranging from 53 nm to 131 nm on the film. Grains are subjected to sintering due to firing temperature. The films were observed to be highly porous. The presence of α -terpineol favored the sintering of grains. Fig. 2 represents FE-SEM image of Co modified SmFeO₃ thick film fired at 550 °C for 30 min. The micrograph shows the distribution of smaller particles around the larger grains. The smaller particles may be attributed as Co species. The modified thick film appears to have comparatively high porosity and large surface area for oxygen adsorption.

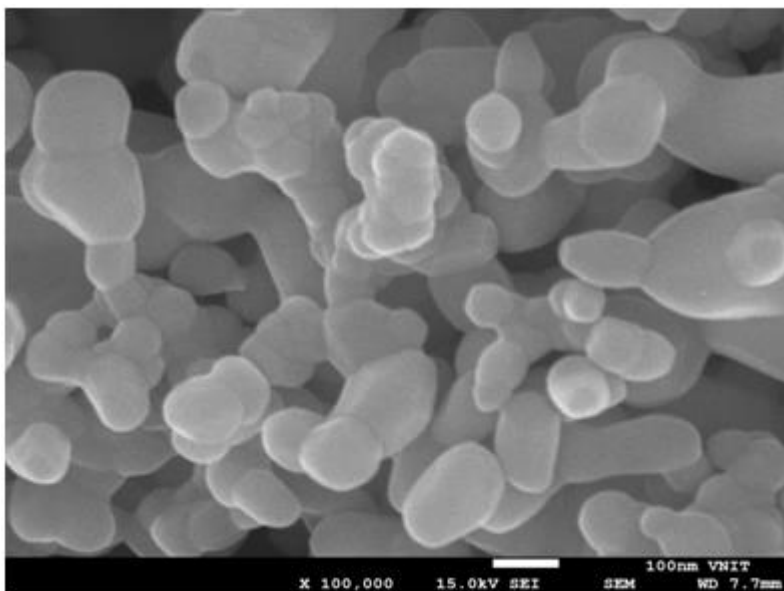


Fig. 1: FE-SEM of pure SmFeO₃ thick film.

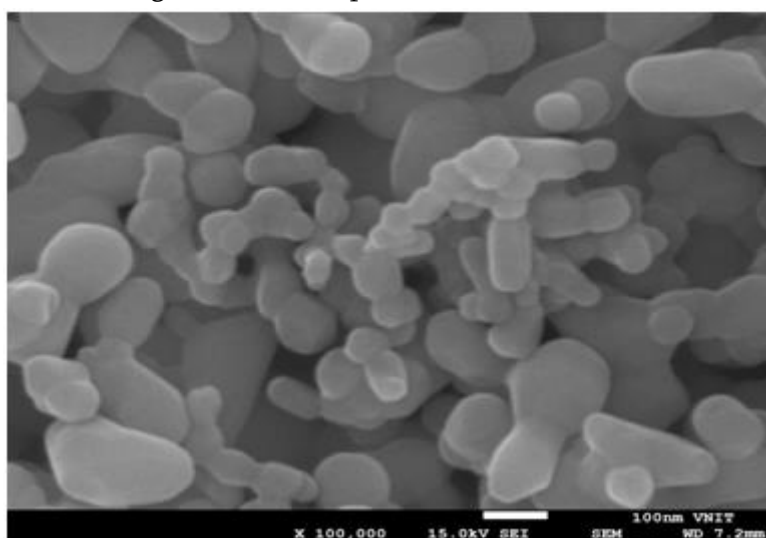
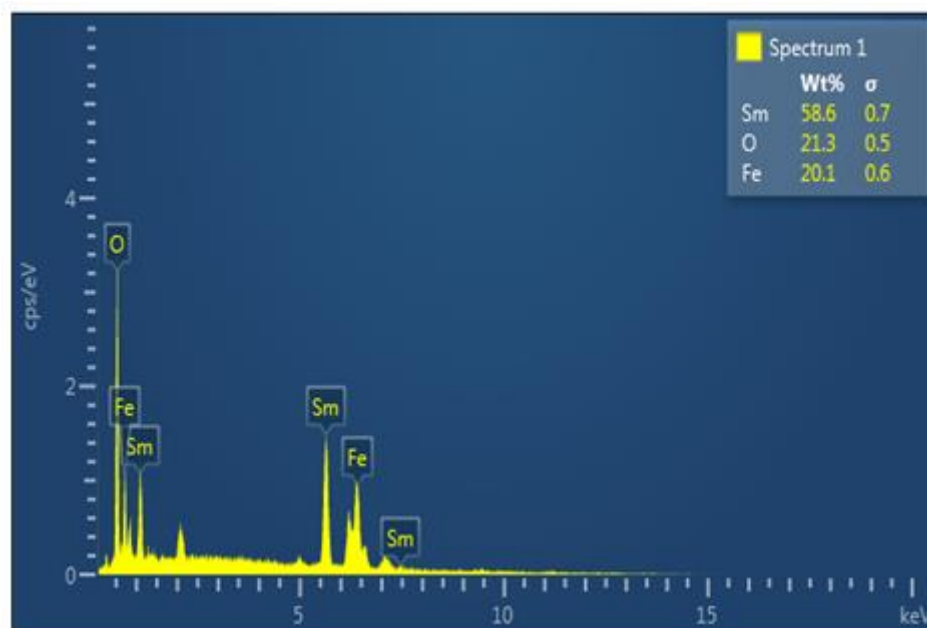
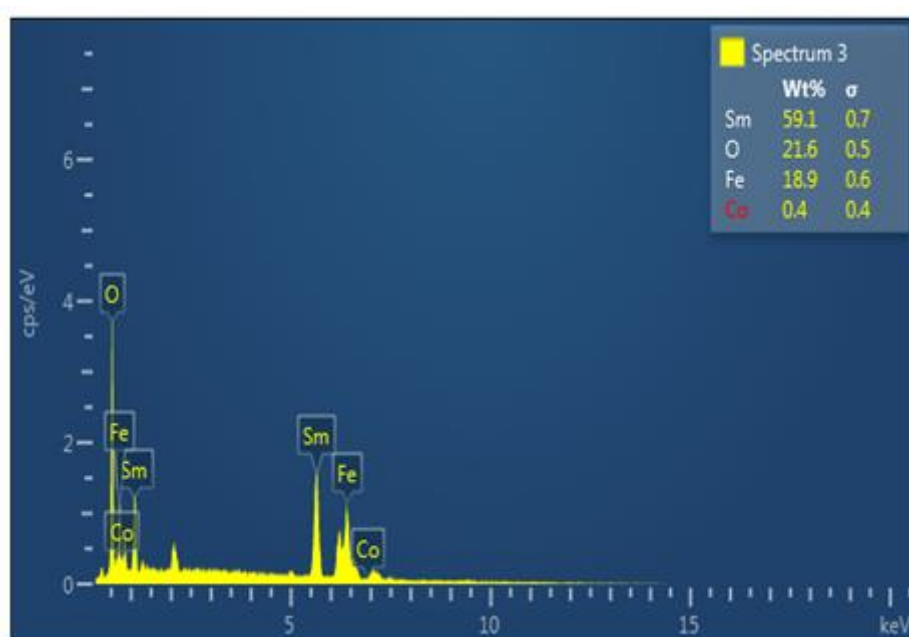


Fig. 2: FE-SEM of Co doped SmFeO₃ thick film.

3.3 Elemental composition analysis :

Elemental composition analysis of both pure and Co modified SmFeO₃ thick films were carried out by EDS technique. Fig. 3 and Fig. 4 respectively represent EDS images of pure and Co modified SmFeO₃ thick films.

Fig. 3: EDS of pure SmFeO₃ thick film.Fig. 4: EDS of Co doped SmFeO₃ thick film.

It is observed from EDS images that in Co doped SmFeO₃ thick film, weight percentage of Fe was decreased due to Co doping. This confirms that partial substitution at B-site is possible by dipping technique and it may result in better conductivity and sensitivity. Moreover, Co doped is oxygen deficient which facilitate increased oxygen adsorption.

IV. CONCLUSIONS

The FE-SEM analysis and EDS analysis respectively confirm the structural morphology and the elemental composition of both pure and Co modified SmFeO₃ thick films. Hence surface modification of SmFeO₃ thick films can be achieved by dipping technique for increased oxygen adsorption.

V. ACKNOWLEDGEMENT

Authors would like to acknowledge VNIT, Nagpur for providing characterization facilities.

VI. REFERENCES

- [1]. S. Ramachandran and A. Sivasamy, "Synthesis and characterization of nanocrystalline N-doped semiconductor metal oxide and its visible photocatalytic activity in the degradation of an organic dye," *J. Environ. Chem. Eng.*, vol. 6, no. 3, pp. 3770–3779, 2018.
- [2]. N. A. Shah, M. Gul, M. Abbas, and M. Amin, "Synthesis of Metal Oxide Semiconductor Nanostructures for Gas Sensors," *Gas Sens.*, vol. 1, p. 101, 2019.
- [3]. D. Sánchez-Rodríguez, H. Wada, S. Yamaguchi, J. Farjas, and H. Yahiro, "Self-propagating high-temperature synthesis of LaMO₃ perovskite-type oxide using heteronuclearcyano metal complex precursors," *J. Alloys Compd.*, vol. 649, pp. 1291–1299, 2015.
- [4]. Y. Hakuta, H. Takashima, and M. Takesada, "Hydrothermal synthesis of perovskite metal oxide nanoparticles in supercritical water," *Ferroelectrics*, 2019.
- [5]. H.-T. Huang, W.-L. Zhang, X.-D. Zhang, and X. Guo, "NO₂ sensing properties of SmFeO₃ porous hollow microspheres," *Sens. Actuators B Chem.*, vol. 265, pp. 443–451, 2018.
- [6]. H. Zhang, H. Qin, P. Zhang, and J. Hu, "High Sensing Properties of 3 wt% Pd-Doped SmFe_{1-x}Mg_xO₃ Nanocrystalline Powders to Acetone Vapor with Ultralow Concentrations under Light Illumination," *ACS Appl. Mater. Interfaces*, vol. 10, no. 18, pp. 15558–15564, 2018.
- [7]. Z. Anajafi, M. Naseri, and G. Neri, "Gas sensing and electrochemical properties of rare earth ferrite, LnFeO₃ (Ln= Nd, Sm)," *Ceram. Int.*, vol. 46, no. 17, pp. 26682–26688, 2020.
- [8]. S. M. Bukhari and J. B. Giorgi, "Effect of cobalt substitution on thermal stability and electrical conductivity of Sm_{0.95}Ce_{0.05}FeO_{3-δ} in oxidizing and reducing conditions," *Solid State Ion.*, vol. 181, no. 8–10, pp. 392–401, 2010.
- [9]. M. Zhao, H. Peng, J. Hu, and Z. Han, "Effect of cobalt doping on the microstructure, electrical and ethanol-sensing properties of SmFe_{1-x}CoxO₃," *Sens. Actuators B Chem.*, vol. 129, no. 2, pp. 953–957, 2008.
- [10]. Q. Lin, C. Lei, J. Lin, Y. He, J. Dong, and L. Wang, "Effect of substitution on the structural and magnetic properties of Sm³⁺-doped/SmFeO₃ in nickel-copper-zinc mixed ferrite nanoparticles," *Ceram. Int.*, vol. 46, no. 2, pp. 2523–2529, 2020.

- [11]. K. Li et al., "High methanol gas-sensing performance of Sm₂O₃/ZnO/SmFeO₃ microspheres synthesized via a hydrothermal method," *Nanoscale Res. Lett.*, vol. 14, no. 1, pp. 1–13, 2019
- [12]. R. B. Mankar, V. D. Kapse, "Synthesis and characterization of pure and Ce modified SmFeO₃ thick film," *Int. J. Scientific research in Science and Technology*, vol. 8, p. 371-375, 2021.

Aurone : A Comprehensive Review on Synthesis and Physical Properties of the Interesting Natural and Emerging Synthetic Compound

Chaware T.S.^{1*}, Pinjarkar A.P.¹, Ingle G.B.¹, Dr. Kolhe S.V.¹

¹Department of Chemistry, Shri Shivaji Art's, Commerce and Science College (Affiliated to Sant Gadge Baba Amravati University, Amravati), Akot-444101, Maharashtra, India

ABSTRACT

Aurones constitute a subclass of naturally occurring compounds which are structurally isomeric to flavones, biogenetically related to chalcones, and are responsible for imparting beautiful yellow colors to some of the flower petals¹⁻⁴. Recent investigations have shown that these compounds have potent and promising biological activities, in some cases even more potent than chalcones and flavones⁵⁻⁷. The current research is focused on study the physical properties with experimental data such as density, conductance, absorbance etc. of synthesized Aurone.

Keywords: Aurones, flower petals, Solubility, Density, Conductance, Absorbance, etc.

I. INTRODUCTION

The first examples of aurones were characterized in 1940 in Asteraceae⁸, the family of sunflowers, which synthesize the most common 4-deoxy-derivatives of the family including sulfuretin, maritimetin, leptosidin and their corresponding glycosides. The species *variabilis* and *sulphureus* mainly express sulfuretin and its glycosylated counterparts in leaves and petals. In the *bidens* species, maritimetin has been isolated while, in the genus *Coreopsis*, compounds such as sulfuretin, maritimetin, but also leptosidin may be found.

In the early twentieth century, Gustav Klein coined the term anthochlor (anthos = flower, chl⁻ or ós = yellowish) to define a class of water-soluble pigments conferring color to plants able to synthesize them as secondary metabolites⁹. It included a restricted group of derivatives known as aurones (aurum = gold), due to the bright yellow/gold color that these compounds give to plants in which they are located. Aurone provides intense yellow pigmentation to some fruits and flowers¹⁰. However, they are also found in leaves, barks, seeds and woods of various plants. Aurone derivatives also show various range of pharmacological activities such as antiviral, antifungal, antioxidant, anticarcinogen, antidiabetes^{11,12}. Actually, to date, the chemical structures of more than 100 different aurones have been identified, characterized by distinctive hydroxylated, methoxylated, and glycosylated substitution patterns. Moreover, their effective potential to predict viable therapeutic uses has begun to be unveiled¹³⁻¹⁶. Therefore, they represent a worth deepening class of natural compounds intended to provide bioactive compounds in the near future.

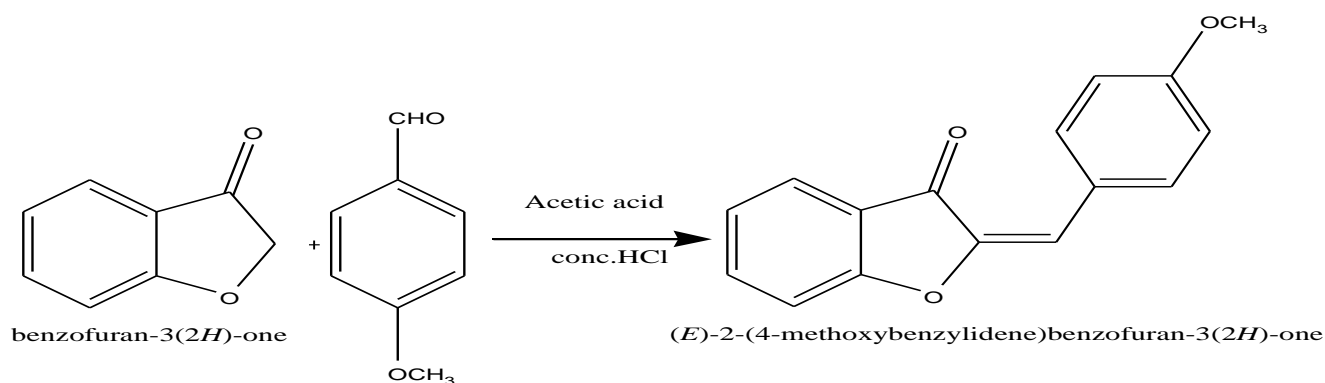
The chalcones are accessed through synthesis by the Claisen-Schmidt reaction of 2-hydroxyacetophenone and benzaldehyde or their derivatives in the presence of aqueous NaOH, KOH or Ba(OH)₂¹⁷⁻²¹. These chalcones further cyclized in various solvents to get desired substituted aurones.

II. EXPERIMENTAL STUDIES

2.1 Synthesis:

Substituted Aurone have been synthesized by cyclization of substituted chalcone in presence of various solvents and their general structures were confirmed by IR, ¹H NMR and mass spectral data. Tables below show the various physical parameters of new synthesized Aurone.

The experiment was started by adding benzofuran and benzaldehyde derivative in a round bottom flask, and then acetic acid was added to the flask. Then to the mixture was added conc. acid solution, the addition was done with stirring to produce desired product.



2.2 Physicochemical studies:

Properties	Colour	Chemical Name	Chemical Formula	Molecular Weight	Yield	Phase
Observations	Golden/Yellow	Aurone	C ₁₆ H ₁₂ O ₃	252	75%	Solid

The synthesized Aurone was crystallized from DMF and DMSO. The solvent A i.e. DMF and B. i.e. DMSO were used for the physicochemical studies.

2.3 Density, Viscosity, Conductance and Absorbance:

Solutions of different concentrations were made in solvent A and solvent B of the synthesized compounds. The conductance of solutions was measured using conductivity meter at various temperatures. Vis spectrophotometer was used to determine the absorbance of all the solutions. Table 1 shows the absorbance of synthesized Aurone at various temperatures and various concentrations.

III. RESULTS AND DISCUSSIONS

3.1 Density and Viscosity of synthesized Aurone:

Table 1: The table below shows density (ρ), and viscosity (η), at different concentrations and at 308.15K.

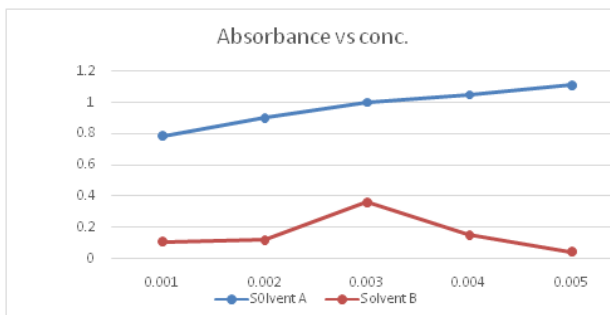
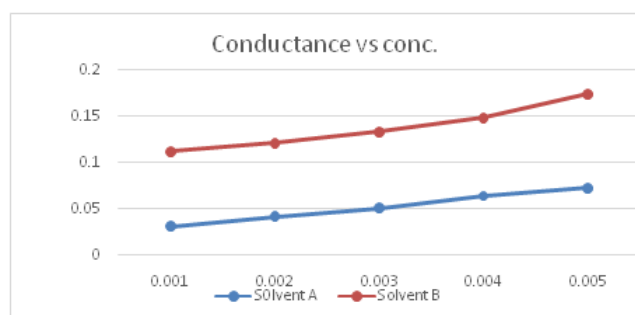
Conc.	Solvent A Density(ρ) (g.cm^{-3})	Solvent A Viscosity ($\eta.10^{-3}$)poise	Solvent B Density(ρ) (g.cm^{-3})	Solvent B Viscosity ($\eta.10^{-3}$)poise
0.05	0.967	6.9751	1.023	11.245
0.04	0.965	6.7685	1.011	11.210
0.03	0.964	6.6787	1.002	11.113
0.02	0.963	6.5989	0.997	11.047
0.01	0.962	6.5756	0.991	10.958

I. Conductance and Absorbance:

The table below shows values of conductance and absorbance of various concentrations of solution at 308.15 K. (Absorbance- λ_{max} for solvent A-380 nm and λ_{max} solvent B-400nm).

Table 2: Conductance and absorbance of various concentrations.

Concentrations	Conductance (S/cm ⁻³) Solvent A	Conductance(S/cm ⁻³) Solvent B	Absorbance Solvent A	Absorbance Solvent B
0.005	0.073	0.175	1.112	1.045
0.004	0.064	0.149	1.051	0.887
0.003	0.051	0.134	1.002	0.361
0.002	0.042	0.121	0.901	0.152
0.001	0.031	0.112	0.785	0.045



The above data clears the variation of conductance with concentration for both the solvents. It is observed that conductance increases with concentration and values are less in Solvent A than that in Solvent B i.e. there is linear increase in conductance with concentration.

IV. CONCLUSIONS

From above experimental values it is concluded that densities, viscosities and conductance and absorbance of solution are changes by changing temperatures and by changing the solvent due to solute-solvent interaction.

V. REFERENCES

- [1]. Nakayama, T.; Sato, T.; Fukui, Y.; Sakakibara, K.Y.; Hayashi, H.; Tanaka, Y.; Kusumi, T.; Nishino, T. *FEBS Lett.*, 499, 107–111, 2001.
- [2]. Jain, A.C.; Rohatagi, V.K.; Seshadri, T.R. *Indian J.Chem.*, 7, 540–543, 1969.
- [3]. Nakayama, T. *J. Biosci. Bioeng.*, 94, 487–491 2002.
- [4]. Olesen, J.M.; Ronsted, N.; Tolderlund, U.; Cornett, C.; Molgaard, P.; Madsen, J.; Jones, C.G.; Olsen, C.E. *Nature.*, 393, 529, 1998.
- [5]. Okombi, S.; Rival, D.; Bonnet, S.; Mariotte, A.M.; Perrier, E.; Boumendjel, A. *J. Med.Chem.*, 49, 329–333, 2006.
- [6]. Haudecoeur, R.; Boumendjel, A. *Curr. Med. Chem.*, 19, 2861–2875, 2012.
- [7]. Manjulatha, K.; Srinivas, S.; Mulakayala, N.; Rambabu, D.; Prabhakar, M.; Arunasree, K.M.; Alvala, M.; Rao, M.V.B.; Pal, M. *Bioorg. Med. Chem. Lett.*, 22, 6160–6165, 2012.
- [8]. Geissman, T.A.; Heaton, C.D. Anthochlor pigments. IV. The pigments of *Coreopsis grandiflora*, Nutt. *J. Am. Chem. Soc.*, 65, 677–683, 1943.
- [9]. Klein, G. Studien uber das Anthochlor. *Sitzb. Akad. Wiss. Wien.*, 129, 341–395, 1920.
- [10]. Jagtap S. V., A. A. Khan, Synthesis and biological activities of aurones: A Review, *Int. J.Pure App. Biosci.* 4 (2) 137-155, 2016.
- [11]. Sui G, Zhang T, Li, B., Wang R., Hao H., Zhou W, Recent advances on synthesis and biological activities of aurones, *Bioorg. Med. Chem.* 29, 115895, 2021.
- [12]. Bandichhor R., Hazardous Reagent Substitution: A Pharmaceutical Perspective *Green Chemistry Series* 52, 2018.
- [13]. Zwergel, C.; Gaascht, F.; Valente, S.; Diederich, M.; Bagrel, D.; Kirsch, G. Aurones: Interesting natural and synthetic compounds with emerging biological potential. *Nat. Prod. Commun.*, 7, 389–394, 2012.
- [14]. Boucherle, B.; Peuchmaur, M.; Boumendjel, A.; Haudecoeur, R. Occurrences, biosynthesis and properties of aurones as high-end evolutionary products. *Phytochemistry*, 142, 92–111, 2017.
- [15]. Alsayari, A.; Muhsinah, A.B.; Hassan, M.Z.; Ahsan, M.J.; Alshehri, J.A.; Begum, N. Aurone: A biologically attractive scaffold as anticancer agent. *Eur. J. Med. Chem.*, 166, 417–431, 2019.
- [16]. Sui, G.; Li, T.; Zhang, B.; Wang, R.; Hao, H.; Zhou, W. Recent advances on synthesis and biological activities of aurones. *Bioorg. Med. Chem.* 29, 115895–115917, 2021.
- [17]. Babu KR, Kumar KV, Vijaya M, Madhavarao V. A novel solid supported synthesis of flavones. *Inter. J Pharm Technol*; 4(1):3943-3950, 2012.
- [18]. Chee CF, Lee YK, Buckle MJC, Rahman NA. Synthesis of (\pm)-kuwanon V and (\pm)-dorsterone methyl ethers via Diels–Alder Reaction. *Tetrahedron Lett*; 52(15):1797-1799, 2011.
- [19]. Chimenti F, Fioravanti R, Bolasco A, Chimenti P, Secci D, Rossi F et al. A new series of flavones, thioflavones, and flavanones as selective monoamine oxidase-B inhibitors. *Bioorg. Med. Chem.*; 18(3):1273-1279, 2010.

- [20]. Susanti EVH, Matsjeh S, Wahyuningsih TD, Mustofa,Redjeki T. Synthesis, characterization and antioxidantactivity of 7-hydroxy-3',4'-dimethoxyflavone Indo. J Chem.; 12(2):146-151,2012.
- [21]. Stoyanov EV, Champavier Y, Simon A, Basly J. Efficient liquid-Phase synthesis of 2' Hydroxychalcones. Bioorg.Med. Chem. Lett; 12(19):2685-2687,2002.



To Study the Potency Of Newly Synthesized Substituted Thiocarbamidonaphthol by Conductometrically

Saleem Khan R.Khan, D.T.Tayade

Department of Chemistry, Government Vidarbha Institute of Science and Humanities, Amravati -444 604, Maharashtra, India

ABSTRACT

To foster more intensity drugs since microorganisms become more dynamic than past one. Numerous physicist and scientists has gotten an extraordinary consideration in the perspective on human powerlessness and insurance of conditions. According to the need of this age they combined many mixtures and particles and prime to evaluate their meanings and applications in different fields. Conductometric concentrate on got more qualities. Conductometric examination fostered an interconnecting join in the middle to substance science and life sciences. Consider above reality as a top priority present examination plot planned as to concentrate on the strength of 5-phenylthiocarbamido-1-naphthol at blended dissolvable media. In which decided the conductometric boundaries and thermodynamics boundaries of 5-phenylthiocarbamido-1-naphthol at various fixations and 310 K in 60% ethanol-water combination. Present work assists with understanding various associations like solute-dissolvable connection, solute cooperation, solute dissolvable collaboration and solute-dissolvable communication that are utilized in present work. This study assists with figuring out Pharmacodynamics of the recently integrated atoms.

Keywords: 5-Phenylthiocarbamido-1-naphthol, conductometric parameters, thermodynamic parameters and conductometric study.

I. INTRODUCTION

Portability of particles in electrolytic arrangement is known as conductivity. As medications action perspective versatility of particles got more qualities since it worries to the conductivity particle in arrangement that additionally assists with figuring out the separation of solute in dissolvable. Separation of solute additionally called as ionization of solute that impact the portability and bioavailability of solute particles. Conductivity of medication assists with understanding the pharmacodynamics of medication. Versatility of particles is additionally treated as transmission of particles. Ionic transmissions of electrolyte in electrolytic arrangement firmly impact on solvency and penetrability of medications proficiently Shuiqin Li et al¹ reported green synthesis of gold nanoparticles using aqueous extract of Mentha Longifolia leaf and investigation of its anti-human breast carcinoma properties in the in vitro condition. Shengmei Chen et al² carried out Ziziphoraclinopodioides Lam leaf aqueous extract mediated novel green synthesis of iron

nanoparticles and its anti-hemolytic anemia potential: A chemobiological study. Elsayed M. AbouElleef et al³ studied Conductometric Association Parameters for Cd Br in the Presence and Absence of Ceftazidime in Water and 30% Ethanol–Water Mixtures. BingxiFenget al⁴ studied Self-template synthesis of spherical mesoporous tin dioxide from tin-polyphenol-formaldehyde polymers for conductometric ethanol gas sensing. ReemAlzahrani et al⁵ carried out Synthesis and characterization for new Mn(II) complexes conductometry, DFT, antioxidant activity via enhancing superoxide dismutase enzymes that confirmed by in-silico and in-vitro ways. GhenadiiKorotcenkov et al⁶ reported their Electrospun Metal Oxide Nanofibers and Their Conductometric Gas Sensor Application, in Nanofibers and Features of their Forming. ArwaAlharbiet al⁷ carried out Studies on new Schiff base complexes synthesized from d¹⁰metal ions: Spectral, conductometric measurements, DFT and docking simulation. Dafne Musino et al⁸ studied Hydroxyl groups on cellulose nanocrystal surfaces formnucleation points for silver nanoparticles of varying shapes and sizes. K.V. Stepurskaet al⁹ carried out Feasibility of application of conductometric biosensor based on acetylcholinesterase for the inhibitory analysis of toxic compounds of different nature. Ahmad I.Ayesh et al¹⁰ studied Conductometric graphene sensors decorated with nanoclusters for selective detection of Hg traces in water. PheerayaJaikang et al¹¹ reported their Conductometric determination of ammonium ion with a mobile drop. AgnieszkaChylewska et al¹² studied Spectrophotometric, potentiometric, and conductometric studies of binary complex formation between copper(II) and three forms of vitamin B6 in aqueous solutions. Considering these above realities present exploration work intended to assurance of thermodynamic boundaries (viz. ΔH ; ΔS and ΔG) and conductometric boundaries of 5-phenylthiocarbamido-1-naphthol conductometrically at various focuses and 310 K in 60% ethanol-water blend. This review assists with understanding the different bury and intra-atomic communication like dissolvable, solute-dissolvable and solute-dissolvable associations. That data assists with understanding the pharmacodynamics of recently blend particle.

II. MATERIALS AND EXPERIMENTAL METHODS

Newly pre-arranged arrangements are utilized through current work. All AR grade synthetics are utilized through present examination. The solvents were decontaminated by standard strategy before utilized. To arranged 0.01M, 0.005M, 0.0025M and 0.0012M convergences of 5-phenyl thiocarbamido-1-naphthol 60% ethanol-water blend. Warm balance kept up with at temperatures 310 K) of medications arrangement by utilizing indoor regulator individually. Conductivity estimated for every focus arrangement in the wake of getting warm balance.

III. RESULT AND DISCUSSION

Arranged the arrangement of 0.01 M grouping of 5 phenylthiocarbamido-1-naphthol then by utilizing sequential weakening strategy arranged arrangements of 0.005M, 0.0025M and 0.0012M with 60% ethanol-water combination separately. To estimated conductance for every arrangement by utilizing Conductivity

Bridge at 310 K. The got result classified in given in Table-1 and Table-2. Noticed conductance (G), explicit conductance (k) and molar conductance (μ) were analyzed with helps of known writing technique from resultant information.

TABLE – 1 - CONDUCTOMETRIC MEASUREMENTS AT DIFFERENT CONCENTRATIONS OF 5-PHENYLTHIOCARBAMIDO-1-NAPHTHOL				
DETERMINATION OF G, k and μ AT DIFFERENT CONCENTRATIONS AND DIFFERENT TEMPERATURES IN 60% E-W MIXTURE				
Temp	Concentration C (M)	Observed conductance (G) mS	Specific conductance (k) mSm ⁻¹	Molar conductance (μ) mSm ² mol ⁻¹
310 K	0.01	0.04608	0.0023084 X10 ⁻³	0.23084
	0.005	0.03502	0.031848 X10 ⁻³	0.63696
	0.0025	0.03064	0.021365 X10 ⁻³	0.8546
	0.0012	0.02912	0.021147X10 ⁻³	0.17622

Noticed conductance (G), explicit conductance (k) diminishes and molar conductance (μ) values are arranged in Table 1. Here G, k and μ increments alongside diminishing fixations and G, k and μ increments alongside expanding temperatures. The particular conductance increments with expanding temperature. Determined values the particular steady (Ksp), log (Ksp) and thermodynamic boundaries viz. (ΔG), (ΔS) and (ΔH) of 5-phenylthiocarbamido-1-naphthol by known writing techniques at various fixation with various temperatures. Gotten outcome figured in Table 2.

TABLE – 2 - CONDUCTOMETRIC MEASUREMENTS AT DIFFERENT CONCENTRATION AND DIFFERENTS TEMPERATURES OF 5-PHENYLTHIOCARBAMIDO-1-NAPHTHOL						
DETERMINATION OF Ksp, log Ksp, ΔG , ΔH and ΔS AT DIFFERENT CONCENTRATIONS AND DIFFERENT TEMPERATURES						
SYSTEM: L ₂ [PTCN]			MEDIUM - 60% Ethanol-Water Mixture			
Temp.(K)	Conc. M	Ksp	Log Ksp	ΔG kJmlo ⁻¹	ΔH kJmlo ⁻¹	ΔS kJK ⁻¹ mlo ⁻¹
310 K	0.01	0.05595	-4.58701	-2705092	-88357.6	377.639
	0.005	0.03930	-5.03159	-29672.75	-96920.5	413.007
	0.0025	0.03507	-5.29433	-31224.52	-101989	435.5
	0.0012	0.033584	-5.44574	-32115.3	-104898	447.837

IV. CONCLUSION

From above table - 1 and 2 it is reasoned that the variety in molar fixations firmly connected with conductometric and thermodynamic boundaries upsides of 5-phenylthiocarbamido-1-naphthol. As noticed, the μ values increment with diminishing in focus that shows less solvation or higher portability of particles.

This is because of the way that more prominent bond breaking because of weakening. Additionally regrettable upsides of ΔG showed the response is unconstrained. Negative upsides of enthalpy change (ΔH) recommended the response is exothermic. Good at lower temperature and positive worth of (ΔS) delights entropically great. The adjustment of thermodynamic boundaries esteems firmly impacted by molar fixations and rate pieces. Additionally solute (drug)- dissolvable collaborations, dissolvable connections, dissolvable solute associations and - solute-dissolvable communications significantly impact on these boundaries. Interior calculation as well as inward and intra hydrogen holding are likewise answerable for the variety of these boundaries.

V. REFERENCES

- [1]. Shuiqin Li, Fahad A. Al-Misned , Hamed A. El-Serehy , Linlin Yang, Arabian Journal of Chemistry, 2021, 14, 102931.
- [2]. ShengmeiChen, Ailing Fang , Yanfa Zhong , Jin Tang, Arabian Journal of Chemistry, 2022,15, 103561.
- [3]. Elsayed M. AbouElleef, Mahmoud N. Abd El-Hady, Esam A. Gomaa, Anwer G. Al-Harazie, Journal of Chemistry Engineering Data, 2021,2, 66, 878–889.
- [4]. BingxiFeng ,Youyou Feng , Jing Qin , Zheng Wang , Yalong Zhang , Fei Du , Yongxi Zhao, Jing Wei, Sensors & Actuators: B. Chemical,2021 , 341, 129965,.
- [5]. Reem Alzahrani ,IsmailAlthagafi ,AmerahAlsoliemy ,KhloodS.Abou-Melha ,Abdulmajeed F.Alrefaei ,GaberA.M.Mersal ,Nashwa El-Metwaly, Journal of Molecular Structure, 2021, 1243,130855.
- [6]. GhenadiiKorotcenkov, Nanomaterials, 2021,11, 1544.
- [7]. Arwa Alharbi ,SerajAlzahrani ,FatmahAlkhatib ,Khulood Abu Al-Ola ,Alia AbdulazizAlfi, RaniaZaky ,Nashwa M.El-Metwaly, Journal of Molecular Liquids, 2021,334, 116148.
- [8]. Dafne Musino ,CamilleRivard ,Gautier Landrot ,Bruno Novales ,Thierry Rabilloud Isabelle Capron, Journal of Colloid and Interface Science, 2021, Volume 584, 360-371.
- [9]. K.V. Stepurska, Soldatki, I.S. Kucherenko, V.M. Arkhypova ,S.V. Dzyadevych, A.P. Soldatkin, Analytica Chimica Acta, 2015,854, 161–168.
- [10]. Ahmad I. Ayesh ,Zainab Karam ,Falah Awwad ,Mohammed A. Meetani, Sensors and Actuators B: Chemical, 2015, Volume 221, 201-206.
- [11]. PheerayaJaikang ,KateGrudpan ,TinakornKanyanee, Talanta, 2015,Volume 132, 884-888.
- [12]. Agnieszka Chylewska, MałgorzataOgryzek, Lech Chmurzyński , Mariusz Makowski, Journal of Coordination Chemistry, 2015, Vol. 68, No. 21, 3761–3775.



Investigation of Structural, Magnetic, And Microwave Absorption Properties of Bi Supplemented Calcium Hexaferrite

Y.D. Choudhari¹, P. J. Chaware², K.G. Rewatkar²

¹Department of Physics, Dr. Ambedkar College, Deeksha Bhoomi, Nagpur-10, Maharashtra, India

²Vidya Vikas Arts, Commerce and Science College, Samudrapur, Maharashtra, India

ABSTRACT

Calcium hexaferrite ($\text{CaFe}_{12-x}\text{Bi}_x\text{O}_{19}$, $x=0.2$ to 0.8) was successfully brewed through a microwave-induced sol-gel auto-combustion technique with Bi^{3+} as a substitute. The impact of added Bi^{3+} ions on the structure, morphology, magnetic, and dielectric properties of calcium hexaferrite was analyzed using an X-ray powder diffractometer (XRD), Field emission scanning electron microscopy (FE-SEM), vibrating sample Magnetometry (VSM), The peak position in the XRD pattern confirms the development of single-phase hexagonal ferrite nanoparticles with a space group of $P6_3/mmc$ and an average crystalline size of 46 to 56 nm. Magnetic analysis revealed that when the Bi^{3+} ion is added to Ca ferrite, the material's coercive force improves, but the saturation magnetization decreases. A vector network analyzer was used to record the microwave absorption properties for the X-band (VNA). Reflection loss values were computed within the frequency range of 8–12 GHz using transmittance line theory for a given thickness of 1.2 mm. The material properties of the bismuth substituted calcium hexaferrite material can predict the layer dimension and frequency, resulting in reduced reflection loss. The most significant loss is obtained at 10.2 GHz (-9.27 dB, 75 % loss), related to the appropriate magnetic material composition.

Keywords: Calcium Hexaferrite, Bismuth, XRD, FE-SEM, VSM, VNAetc.

I. INTRODUCTION

Hexagonal substances have been segmented into five categories based on their chemical formulas and degree of crystallinity: M, W, X, Y, and Z. The industrial and scientific communities are mainly interested in M-type hexaferrite $\text{BaFe}_{12}\text{O}_{19}$ and $\text{SrFe}_{12}\text{O}_{19}$ [1]. Compared to other elements like barium and strontium, calcium is widely available on our planet. M-type calcium hexaferrite is a viable material for low-cost permanent magnets because of its chemical stability and uniaxial solid magnetocrystalline anisotropy along the hexagonal c-axis[2]. It has excellent magnetic, electrical, mechanical, and thermal properties. This hexaferrite's electric and magnetic properties could be improved by replacing paramagnetic and diamagnetic cations with iron (Fe^{3+})[3]. To make calcium hexaferrite enriched with cobalt and zirconium, J. N. Christy et colleagues; employed the microwave-aided auto combustion sol-gel method. The synthesized samples have particle sizes of less than 50 nm. Due to their capacity to create a sufficient signal-to-noise ratio, the

synthesizing compounds can be used in a medium with a high recording density[4]. The dielectric constant and dielectric loss tangent decreased as the frequency increased, indicating that these nanocomposites are suitable for high-frequency applications[5]. The current work uses the microwave-induced sol-gel auto-combustion method to make M-type calcium hexaferrite with the formula $\text{CaBi}_x\text{Fe}_{12-x}\text{O}_{19}$ ($x=0.2$ to 0.8). The sol-gel auto combustion technique is superior to the others because it is a simple, safe, and fast procedure that achieves excellent homogeneity, purity, and time efficiency. Calcium hexaferrite's structure and microwave characteristics were investigated when bismuth was substituted at the Fe^{3+} sites.

II. MATERIAL PREPARATION

The microwave-induced sol-gel auto-combustion procedure might be used to make $\text{CaBi}_x\text{Fe}_{12-x}\text{O}_{19}$ ($x=0.2$ to 0.8) M-type bismuth substituted calcium hexaferrite. The synthesis technique involves a mixed reaction in which metal nitrates act as an oxidizing reactant and urea work as a reducing reactant to initiate ignition[6]. Equimolar amounts of AR grade $\text{Ca}(\text{NO}_3)_2 \cdot 4\text{H}_2\text{O}$, $\text{Fe}(\text{NO}_3)_3 \cdot 9\text{H}_2\text{O}$, and $\text{Bi}(\text{NO}_3)_3 \cdot 9\text{H}_2\text{O}$, as well as urea, are combined in deionized water in a beaker. The gel was burned in a microwave oven; the solution first boils at 70-90 °C and dehydrates, then decomposes, generating many odors[7]. The mixture begins to inflame when it acquires the connotation of self-initiated burning. It produces a lot of heat, which rapidly vaporizes the entire solution and turns it into a solid at temperatures above 500°C. Bismuth substituted calcium hexaferrite powder can be created in less than a few minutes by burning the material in a microwave oven. The composite material was crushed in a pestle and mortar to form nanoparticles[8]. To create nanocomposite materials, the fine particles were calcined in an electric furnace for 5 hours at 800 °C.

III. RESULTS AND DISCUSSIONS

3.1 Structural Analysis :

The phase and structural composition of Ca-Bi hexaferrite were determined using the XRD spectrum; the trend is shown in Figure. JCPDS file 49-1586 was used to reference the observed peaks. The x-ray diffraction patterns of calcium hexaferrite were indexed using the magnetoplumbite structure and space group $P63/mmc$ (SG:194)[9]. The (107) plane produced the maximum intensity diffraction peak. The XRD tests included conventional reflecting planes (006), (107), (002), (1000), (213), (126), (307) and (007) for m-type hexaferrite shown in **Figure 1**. In the (107) and (200) planes, the Bi^{3+} percentage considerably impacted the diffraction peak intensity[10]. Bi^{3+} doped calcium hexaferrite crystallite size, lattice parameters a and c , lattice volume, c/a ratio, surface area, bulk density, and x-ray density (X_d) are shown in **Table 1**. The prominent (107) peak point was moved to a lower inclination by Bi^{3+} ion replacements, as evidenced in x-ray diffraction patterns[11]. The peak location moved because of differences in Fe^{3+} (0.64) and Bi^{3+} (1.06) ionic radii. As the Bi^{3+} ion density grows, this movement causes homogenous strain and elastic deformation in the structure, causing the lattice constants a and c , lattice volume, and crystallinity size to decrease[12]. Crystallite diameters in all specimens are in the nanoscale range. This magnetoplumbite crystal structure has five Fe

locations: 2a, 2b, 12k, 4f₁, and 4f₂. 2a, 12k, and 4f₂ are octahedral, whereas 4f₁ is a tetrahedral site, 2b is a bi-pyramidal site, and 4f₁ is a tetrahedral site. The correlation coefficient (c/a) was within the estimated 3.84–4.06, indicating that an M-type hexagonal structure had been created[13].

Figure 1: XRD image of CaBi_xFe_{12-x}O₁₉ (x=0.2, 0.4, 0.6, and 0.8) hexaferrite

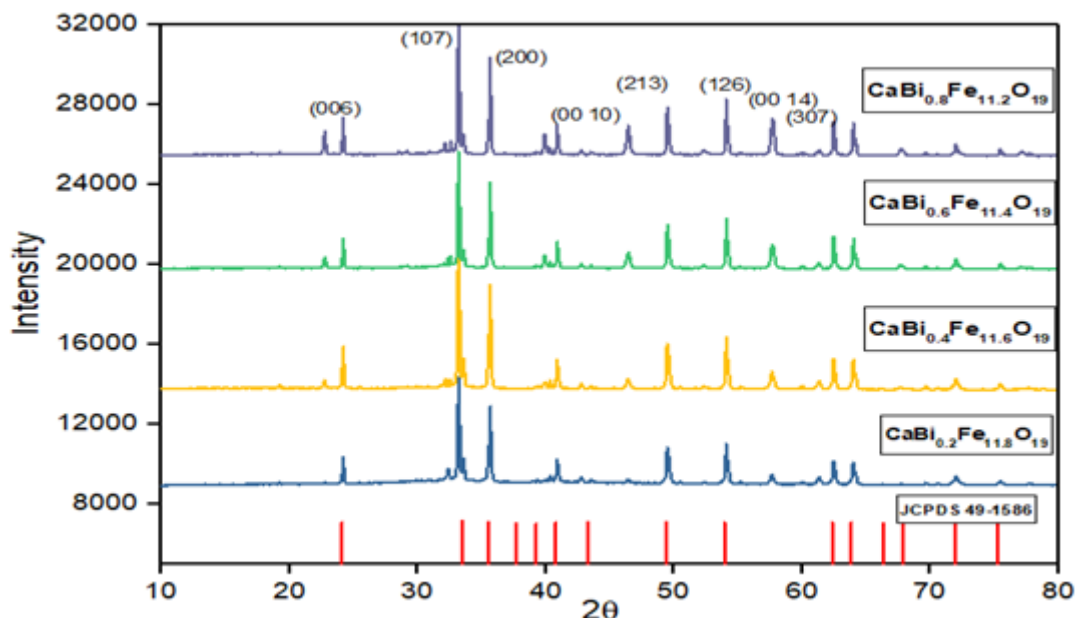


Table 1: Lattice parameter, x-ray density bulk density and particle size of Ca-Bi hexaferrite

Compound Name		CaBi _{0.2} Fe _{11.8} O ₁₉	CaBi _{0.4} Fe _{11.6} O ₁₉	CaBi _{0.6} Fe _{11.4} O ₁₉	CaBi _{0.8} Fe _{11.2} O ₁₉
Lattice parameter	a=b (Å)	5.8320	5.8132	5.8115	5.8112
	C (Å)	22.3584	22.3603	22.3618	22.1542
Crystalline Size (nm)		55.76	53.23	49.76	46.21
c/a		3.846	3.846	3.848	4.062
Molecular Weight (gm/mol)		1044.845	1075.472	1106.099	1136.726
Volume (Å ³)		653.994	649.840	649.50	643.61
X-ray density (gm/mol ³)		5.305	5.495	5.655	5.862
Bulk Density (gm/mol ³)		3.152	3.327	3.356	3.422
Porosity (%)		40.58	39.45	40.65	41.62
Surface area (*10 ⁷ cm ² /g)		20.28	20.51	21.32	22.14

3.2 Magnetic analysis :

Figure 2 shows the hysteresis loop of $\text{CaBi}_x\text{Fe}_{12-x}\text{O}_{19}$ ($x=0.2$ to 0.8) samples. These hysteresis loops indicated the ferromagnetic property of synthesized samples[3]. These curves have been used to calculate magnetic properties such as saturation magnetization (M_s), coercivity (H_c), and remanence (M_r); these parameters are influenced by a variety of factors, including the synthesis technique, processing temperature, and duration, and the proportion of crystalline solids used. The H_c ranges from 169 to 2696 Oe, as seen in **Table 2**[14]. It was discovered that H_c and D vary in opposite directions, with higher D values corresponding to lower H_c levels and vice versa. As shown in the table below, some of the materials exhibited H_c values substantially greater than 1200 Oe, making them acceptable for high-density perpendicular magnetic recording media[15]. As the concentration of Bi^{3+} grew, M_s and M_r values decreased steadily. M_s fluctuates between 0.8 and 0.4 emu/g, while M_r fluctuates between 0.145 and 0.10 emu/g[16]. The positioning of Bi^{3+} ions in the Fe^{3+} ions in five crystallographic sublattices, including one tetrahedral sublattice ($4f_1$), one bipyramidal sublattice ($2b$), and three octahedral sublattices, could explain this reduction ($12k$, $2a$, and $4f_2$). $12k$, $2a$, and $2b$ are spin-up sites in the hexagonal lattice, while $4f_1$ and $4f_2$ are spin-down sites[17].

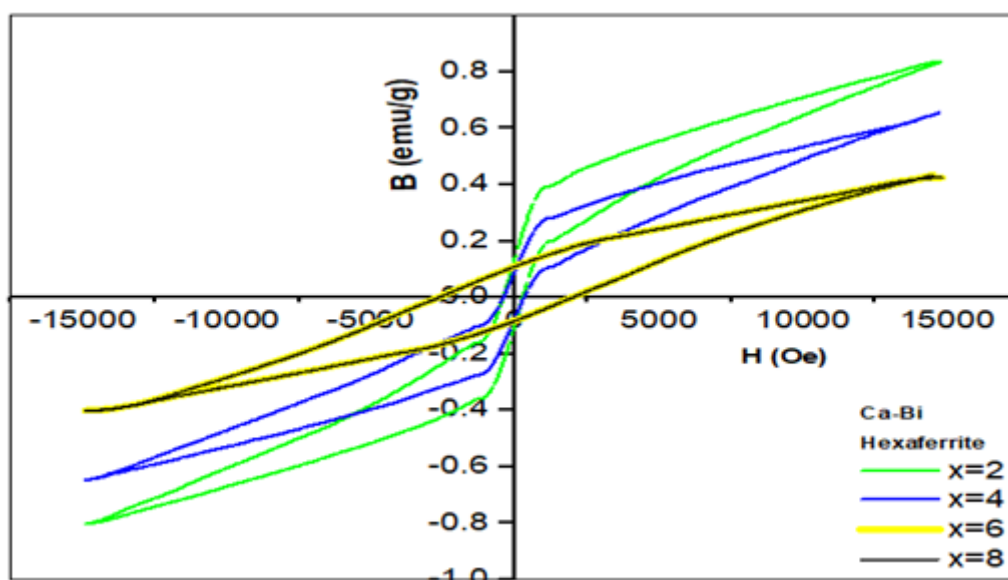


Figure 2: VSM image of $\text{CaBi}_x\text{Fe}_{12-x}\text{O}_{19}$ ($x=0.2, 0.4, 0.6, \text{ and } 0.8$) hexaferrite

Table 2: M_s , M_r , H_c of Ca-Bi hexaferrite

Conc. x	Saturation Magnetization $M_s(\text{emu/g})$	Retentivity M_r (emu/g)	Coercivity (H_c) (Oe)	Bohr magneton $\mu_B \times 10^{-1}$	SQR Ratio (M_r/M_s)
0.2	0.82383	0.14569	169.75	1.54	0.1768
0.4	0.65385	0.11929	222.73	1.25	0.1824
0.6	0.42603	0.10945	2415.9	0.84	0.2569
0.8	0.40991	0.10423	2696.4	0.83	0.2543

3.3 Microwave analysis :

The reduction of EM wave reflection from the EM absorbing layer is measured in reflection loss (RL) in decibels (dB)[18]. The EM wave reflection loss is defined by transmission line theory as

$$RL = 20 \log \left| \frac{Z_{in} - 1}{Z_{in} + 1} \right|$$

Z_{in} is the free space input impedance. An EM absorbing layer's input impedance can be written as:

$$Z = \sqrt{\frac{\mu^*}{\epsilon^*} \tan(J \frac{2\pi t}{\lambda})} \sqrt{\epsilon^* \mu^*}$$

where d is the absorbing layer thickness, c is the light speed, and f is the EM wave frequency[19].

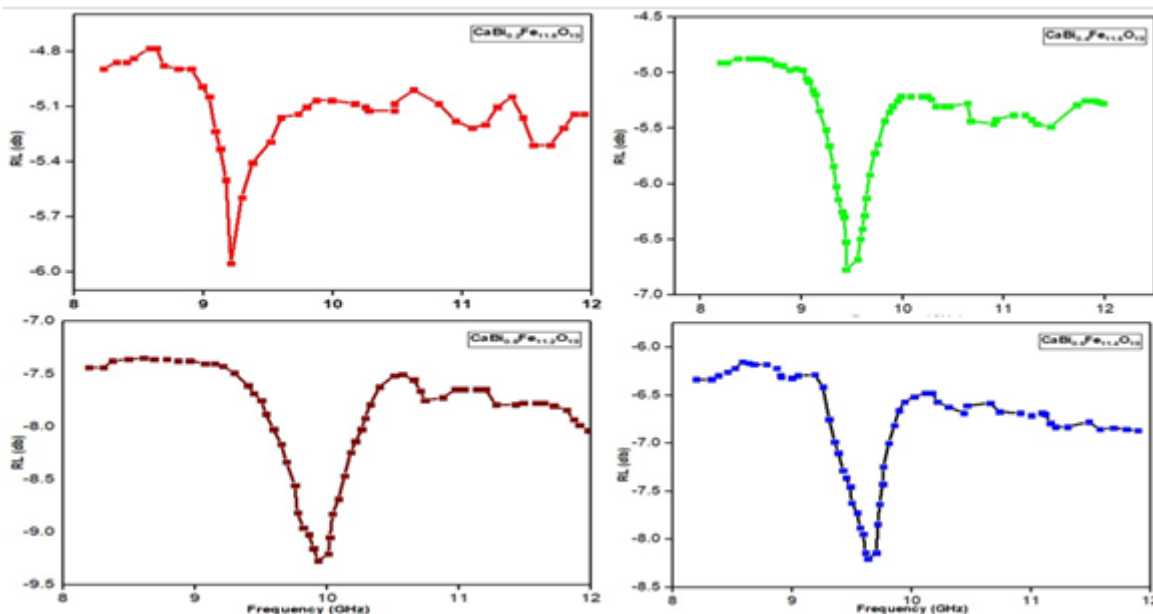


Figure 3: Reflection loss vs frequency of $\text{CaBi}_x\text{Fe}_{12-x}\text{O}_{19}$ ($x=0.2, 0.4, 0.6, \text{ and } 0.8$) hexaferrite

The reflection coefficients for $\text{CaFe}_{12-x}\text{Bi}_x\text{O}_{19}$ ($x=0.2$ to 0.8) composite material are shown in **Figure 3** as a function of frequency. All samples demonstrate absorption in the frequency range of 8 to 12 GHz. The microwave reflection losses of the composite are depicted in the graph[20]. The minimum reflection loss by the composite of thickness 2 mm for bismuth inserted calcium hexaferrite is found to be -5.98 dB at the frequency 9.2 GHz for $x=0.2$, -6.77 dB at the frequency 9.5 GHz for $x=0.4$, -8.2 dB at the frequency 9.7 GHz for $x=0.6$, and -9.27 dB at the frequency 9.9 GHz for $x=0.8$, which corresponds The reflection coefficient of a good absorber should be increased[21]. Compared to other samples, it was discovered that the composite material had the best electromagnetic absorption performance. Only the spin-rotation resonance contributes significantly to the magnetic loss[22].

IV. CONCLUSION

Microwave-induced sol-gel auto combustion was used to successfully produce $\text{CaFe}_{12-x}\text{Bi}_x\text{O}_{19}$ ($x = 0.2$ to 0.8) nanoparticles. The existence of a single crystalline phase in materials with the space group $P63/mmc$ was confirmed by X-ray investigation. M_s and M_r have been observed to decrease with Bi^{3+} concentration because Bi^{3+} ions conquer $4f_1$ sites (tetrahedral sites). The generated samples have a high coercivity (H_c) value, indicating acceptable for recording medium applications. Because the reflection loss of the $\text{CaBi}_{0.8}\text{Fe}_{11.2}\text{O}_{19}$ (-9.27 dB, 75 % loss) sample is higher than that of other samples, we discovered that it could be used as a ferrite composite microwave absorber and for RADAR applications.

V. REFERENCES

- [1]. G.B. Teh, N. Saravanan, D.A. Jefferson, A study of magnetoplumbite-type (M-type) cobalt-titanium-substituted barium ferrite, $\text{BaCo}_x\text{Ti}_x\text{Fe}_{12-2x}\text{O}_{19}$ ($x = 1-6$), *Mater. Chem. Phys.* 105 (2007) 253–259. <https://doi.org/10.1016/j.matchemphys.2007.04.054>.
- [2]. M.A. Almessiere, Y. Slimani, H. Güngüneş, S. Ali, A. Baykal, I. Ercan, AC susceptibility and hyperfine interactions of Mg-Ca ions co-substituted $\text{BaFe}_{12}\text{O}_{19}$ nano-hexaferrites, *Ceram. Int.* 45 (2019) 10048–10055. <https://doi.org/10.1016/j.ceramint.2019.02.050>.
- [3]. Y.D. Choudhari, K.G. Rewatkar, Journal of Magnetism and Magnetic Materials Influence of Bi^{3+} ions substitution on structural, magnetic, and electrical properties of lead hexaferrite, *J. Magn. Magn. Mater.* 551 (2022) 169162. <https://doi.org/10.1016/j.jmmm.2022.169162>.
- [4]. J.N. Christy, K.G. Rewatkar, P.S. Sawadh, Structural and Dielectric Properties of Substituted Calcium Hexaferrites, *Int. J. Eng. Res. Technol.* 8 (2019) 178–182. www.ijert.org.
- [5]. M. Javed Iqbal, M. Naeem Ashiq, I. Hussain Gul, Physical, electrical and dielectric properties of Ca-substituted strontium hexaferrite ($\text{SrFe}_{12}\text{O}_{19}$) nanoparticles synthesized by co-precipitation method, *J. Magn. Magn. Mater.* 322 (2010) 1720–1726. <https://doi.org/10.1016/j.jmmm.2009.12.013>.
- [6]. S. Shakoor, M.N. Ashiq, M.A. Malana, A. Mahmood, M.F. Warsi, M. Najam-Ul-Haq, N. Karamat, Electrical, dielectric and magnetic characterization of Bi-Cr substituted M-type strontium hexaferrite nanomaterials, *J. Magn. Magn. Mater.* 362 (2014) 110–114. <https://doi.org/10.1016/j.jmmm.2014.03.038>.
- [7]. A.S. Kakde, B.A. Shingade, N.S. Meshram, K.G. Rewatkar, Structural And Magnetic Properties Of Sn-Zr Substituted Calcium Nano-Hexaferrite, *J. Magn. Magn. Mater.* 1 (2014) 60–63.
- [8]. M.A. Borikar, A.S. Kakde, K.G. Rewatkar, D.M. Borikar, Structural And Electrical Behavior Of Co-Ti Substituted Nickel Nano Ferrite Prepared By Sol-Gel Auto Combustion Route, *J. Magn. Magn. Mater.* 1 (2015) 128–130.
- [9]. C. Mamatha, M. Krishnaiah, C.S. Prakash, K.G. Rewatkar, B.M. Nagabhushana, Structural, electrical and magnetic properties of aluminum substituted nanocalcium hexaferrites, *Int. J. ChemTech Res.* 6 (2014) 2165–2167.
- [10]. D.M. Borikar, M.A. Borikar, A.S. Kakde, K.G. Rewatkar, Nano copper spinel ferrite: Synthesis & characterization by sol-gel auto combustion technique, *J. Magn. Magn. Mater.* 5 (n.d.) 7–10.

- [11]. S.N. Sable, K.G. Rewatkar, V.M. Nanoti, Structural and Magnetic Behavioral Improvisation of Nanocalcium Hexaferrites, *Mater. Sci. Eng. B Solid-State Mater. Adv. Technol.* 168 (2010) 156–160. <https://doi.org/10.1016/j.mseb.2009.10.034>.
- [12]. S.W. Lee, S.Y. An, I.B. Shim, C.S. Kim, Mössbauer studies of La-Zn substitution effect in strontium ferrite nanoparticles, *J. Magn. Magn. Mater.* 290-291 PA (2005) 231–233. <https://doi.org/10.1016/j.jmmm.2004.11.190>.
- [13]. N.N. Sarkar, D.J. Roy, S.M. Butte, W.S. Barde, K.G. Rewatkar, Synthesis and Magnetic studies of Co-Sn doped Nanoscale Calcium Hexaferrites, 25 (2020) 57–67.
- [14]. T.T. Carol T., J. Mohammed, B.H. Bhat, S. Mishra, S.K. Godara, A.K. Srivastava, Effect of Cr–Bi substitution on the structural, optical, electrical and magnetic properties of strontium hexaferrites, *Phys. B Condens. Matter.* 575 (2019) 411681. <https://doi.org/10.1016/j.physb.2019.411681>.
- [15]. R.U. Mullai, P.P. Pradeep, G. Chandrasekaran, Synthesis And Characterization Of Lanthanum Doped Mg-Zn Ferrite Nanoparticles Prepared by SOL-GEL Method, 5 (2012) 78–85.
- [16]. A.S. Kakde, R.M. Belekar, G.C. Wakde, M.A. Borikar, K.G. Rewatkar, B.A. Shingade, Evidence of magnetic dilution due to unusual occupancy of zinc on B-site in NiFe₂O₄ spinel nano-ferrite, *J. Solid State Chem.* 300 (2021) 122279. <https://doi.org/10.1016/j.jssc.2021.122279>.
- [17]. M.A. Almessiere, Y. Slimani, H. Gungunes, A. Manikandan, A. Baykal, Investigation of the effects of Tm 3+ on the structural, microstructural, optical, and magnetic properties of Sr hexaferrites, *Results Phys.* 13 (2019) 102166. <https://doi.org/10.1016/j.rinp.2019.102166>.
- [18]. O. Dotsenko, K. Frolov, D. Wagner, Effect of Temperature on the Magnetic Permeability of Hexagonal Ferrites, 781 (2018) 36–40. <https://doi.org/10.4028/www.scientific.net/KEM.781.36>.
- [19]. S.M. Kabbur, U.R. Ghodake, R.C. Kambale, S.D. Sartale, L.P. Chikhale, S.S. Suryavanshi, Magnetic, Electric and Optical Properties of Mg-Substituted Ni-Cu-Zn Ferrites, *J. Electron. Mater.* 46 (2017) 5693–5704. <https://doi.org/10.1007/s11664-017-5616-4>.
- [20]. J. Singh, C. Singh, D. Kaur, S.B. Narang, R. Joshi, S.R. Mishra, R. Jotania, M. Ghimire, C.C. Chauhan, Tunable microwave absorption in Co[sbnd]Al substituted M-type Ba[sbnd]Sr hexagonal ferrite, *Mater. Des.* 110 (2016) 749–761. <https://doi.org/10.1016/j.matdes.2016.08.049>.
- [21]. S.S.S. Afghahi, A. Mirzazadeh, M. Jafarian, Y. Atassi, A new multicomponent material based on carbonyl iron/carbon nanofiber/lanthanum-strontium-manganite as microwave absorbers in the range of 8-12 GHz, *Ceram. Int.* 42 (2016) 9697–9702. <https://doi.org/10.1016/j.ceramint.2016.03.058>.
- [22]. J.L. Lv, S.R. Zhai, C. Gao, N. Zhou, Q. Da An, B. Zhai, Synthesis of lightweight, hierarchical cabbage-like composites as superior electromagnetic wave absorbent, *Chem. Eng. J.* 289 (2016) 261–269. <https://doi.org/10.1016/j.cej.2016.01.003>.



Synthesis and Characterization of $\text{LiBaB}_9\text{O}_{15}:\text{Gd}^{3+}$ Phosphor by Recrystallization Method

N. D. Kherde¹, A. O. Chauhan², P. A. Nagpure^{1*}, S. K. Omanwar³

¹Department of Physics, Shri Shivaji Science College, Amravati 444 603, (Affiliated to S.G.B.A. University, Amravati), Maharashtra, India

²Department of Physics, Vidya Bharati Mahavidyalaya, Amravati 444 602, (Affiliated to S.G.B.A. University, Amravati), Maharashtra, India

³Department of Physics, S.G.B.A. University, Amravati 444 602, Maharashtra, India

ABSTRACT

$\text{LiBaB}_9\text{O}_{15}:\text{Gd}^{3+}$ phosphor was synthesized first time by recrystallization method. The phosphor was characterized by X-ray diffraction (XRD), Photoluminescence (PL). The Phase purity and crystallinity of phosphor is confirmed by X-ray diffraction (XRD) analysis. The photoluminescence properties of the $\text{LiBaB}_9\text{O}_{15}:\text{Gd}^{3+}$ sample was investigated by PL excitation and emission spectra. Under UV excitation of 277 nm, the phosphor shows maximum intensity emission peak at 312 nm. This result shows that the $\text{LiBaB}_9\text{O}_{15}:\text{Gd}^{3+}$ phosphor is suitable for Phototherapy application.

Keyword: XRD, Photoluminescence, UV excitation

I. INTRODUCTION

The electromagnetic spectrum shows UV radiation lies between X-rays and visible light. The ultraviolet radiation divided into three parts such as UV-C: the rays that do not pass through the earth's atmosphere (200–280 nm), UV-B: the rays responsible for nearly all biological effects following sun light exposure including tanning, burning and skin cancer(280–315 nm) and UV-A: those rays closest to the visible spectrum that pass through glass and are the least harmful to the skin (315–400 nm).The biological study shows that human skin is most sensitive to UV-B and UV-A radiations and these radiations with different wavelengths have different energy levels and also different penetration characteristic. The depth of penetration increases with increasing wavelength. [1] The requirements of the phosphors vary with different applications. UV emitting phosphors having different applications, such as photocopying, phototherapy etc. [2]

Rare earth orthoborates, RBO_3 (R=Y, La, Gd), doped with rare earth ions (Eu^{3+} and Tb^{3+}) are interesting luminescent materials [3]. Rare earth borates doped with Eu^{3+} are potential red emitting phosphor. Gadolinium borate phosphors ranging from orthoborates to pentaborates have proved to be potential candidates for practical applications in optoelectronic devices due to their high efficiency [4-8]. Due to their large electronic band gaps, borate materials are excellent host lattices for luminescent ions. Lithium barium

borate $\text{LiBaB}_9\text{O}_{15}$ is a cost effective luminescent host material with excellent physical and chemical properties. Additionally, it can be doped with various rare earth ions. There are many good phosphors from borate group, $\text{LaB}_5\text{O}_9:\text{Ce}^{3+}$ [9], $\text{LaMgB}_5\text{O}_{10}:\text{Ce}^{3+}$ [10], $\text{Na}_2\text{La}_2\text{B}_2\text{O}_7:\text{Ce}^{3+}$, $\text{LiSrBO}_3:\text{Gd}^{3+}$ [11].

A.O.Chauhan *et.al.* had reported the synthesis of $\text{LiSr}_4(\text{BO}_3)_3:\text{Gd}^{3+},\text{Pr}^{3+}$ phosphor by solid state diffusion method and PL study shows that this phosphor is suitable for UV-B phototherapy application. [12]

A.A. Sharma *et.al.* have reported another phosphor Gd^{3+} doped YP_3O_9 which was synthesized by citric sol-gel method.[13]The Gd^{3+} activated inorganic lanthanum phosphate (LaPO_4) has been successfully synthesized using re-crystallization method. [14]

V. Singh *et.al.* have reported the $\text{SrY}_2\text{O}_4:\text{Gd}^{3+}$ phosphor by using sol-gel synthesis method. The Gd^{3+} doped- SrY_2O_4 phosphors applicable for phototherapy lamp applications with required UV emission. [15]

In this present paper we had studied the first time synthesis of $\text{LiBaB}_9\text{O}_{15}:\text{Gd}^{3+}$ phosphor by recrystallization method. The phosphor was characterized by X-ray diffraction (XRD), Photoluminescence (PL).

II. EXPERIMENTAL

Synthesis Method :

The phosphor $\text{LiBaB}_9\text{O}_{15}:\text{Gd}^{3+}$ was first time prepared by a recrystallization method. There are some primary advantages of this method are offering a comparatively low temperature route, higher controllability and easy to soluble. [16] The Stoichiometric amounts of high purity starting materials Lithium nitrate (LiNO_3), Barium nitrate $\text{Ba}(\text{NO}_3)_2$, Boric acid, Gadolinium nitrate($\text{Gd}(\text{NO}_3)_2$), have been used for the preparation of phosphor. The starting materials Lithium nitrate and Barium nitrate were firstly dissolving in small amount of double distilled water. The stock solution of Gd_2O_3 was added in the nitrate form and stirred continuously on magnetic stirrer for few minutes. Boric acid was dissolved in double distilled water by continuous stirring on 50°C for few minutes. This solution was then added dropped by drop in above mixture. The entire homogenous solution was then placed on a hot plate at 70°C for slow evaporation of excess water. The dried precursor was finally crushed and heated at 800°C for 2 hours to get white crystalline powder of $\text{LiBaB}_9\text{O}_{15}:\text{Gd}^{3+}$. The resultant powder sample was then characterized using powder XRD and Spectrophotometer.

III. RESULT AND DISCUSSION

The crystallinity of the prepared materials are confirmed by the XRD analysis. The excitation and emission spectra were measured by using fluorescence spectrophotometer.

3.1 XRD Analysis :

The phase purity and crystalline structure of the prepared phosphor was confirmed by XRD pattern which was studied using Rigaku miniflex II X-Ray Diffractometer. Fig 1.shows the XRD pattern of the $\text{LiBaB}_9\text{O}_{15}:\text{Gd}^{3+}$. It shows that all the diffraction peaks coincide well with the standard data of the

LiBaB₉O₁₅:Gd³⁺ can be indexed as pure phase of the prepared sample. The sharp and strong diffraction peaks indicates the sample is well crystallized. The reitveld refinement data shows the lattice parameters a=10.994117, b=10.994117 and c = 17.014416 which belongs to the structure of non-centrally symmetric R-3c:H space group. Also $\alpha = 90.00$, $\beta = 90.00$, $\gamma = 120.00$ with volume = 1773.273 & Z = 6. Finally the refinement converged to the goodness of fit coefficient values of $R_b = 10.33\%$ and $R_{wb} = 14.63\%$.

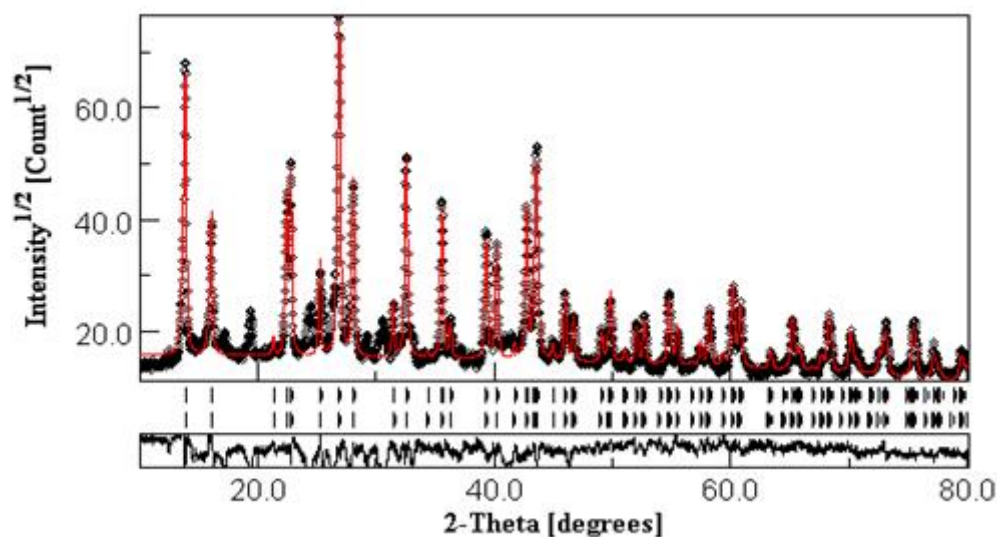


Fig1- Reitveld analysis patterns for X-ray powder diffraction data of LiBaB₉O₁₅:Gd³⁺ .

3.2 Photoluminescence Spectroscopy :

The excitation and emission spectra of the LiBaB₉O₁₅:Gd³⁺ were measured on (Hitachi F-7000) fluorescence spectrophotometer at the room temperature, which are shown in following figure. The phosphor shows excitation spectra at 277nm having corresponding transition $^8S_{7/2} \rightarrow ^6I_{7/2}$. Under the excitation of 277nm the phosphor exhibits emission at 312 nm having corresponding transitions $^6P_{7/2} \rightarrow ^8S_{7/2}$. PL intensity increased with increase in concentration of dopant Gd³⁺ ions up to 2mol%, after which intensity started decreasing as a result of concentration quenching, as shown in fig2. Concentration quenching occurs mainly due to non-radiative energy transfer in dopant ion, multipole–multipole phonon interaction and radiation reabsorption. The probability of energy transfer between activator ions depends on the nth power of distance between activator ions. Thus, with increase in dopant ion concentration, distance between them will decrease and energy transfer will enhance. We can find the critical energy transfer distance (R_c).

Critical energy transfer distance can be found by using the equation given below:

$$R_c = 2 \left[\frac{3V}{4\pi X_c Z} \right]^{\frac{1}{3}}$$

Where R_c is the critical distance, V corresponds to the volume of the unit cell, Z is the number of cations in the unit cell, X_c is the critical concentration of activator ion (Gd³⁺). By using the values of V=1773.273, X_c=0.02 and Z=6, the critical energy transfer distance was found to be 19.17Å. There are mainly three processes that are responsible for nonradiative energy transfer, these are exchange interaction, radiative

reabsorption and multipole–multipole interaction. Radiative reabsorption takes place when excitation spectra match with emission spectra, whereas exchange interaction is taken into account when critical distance is less than 5 Å. Hence, both mechanisms are not applicable in this case. [17]

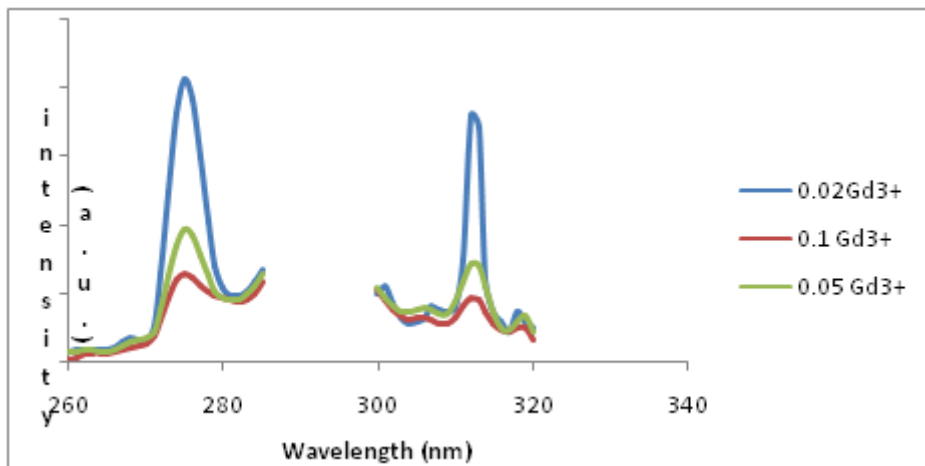


Fig2-PL excitation and emission spectra of LiBaB₉O₁₅:Gd³⁺

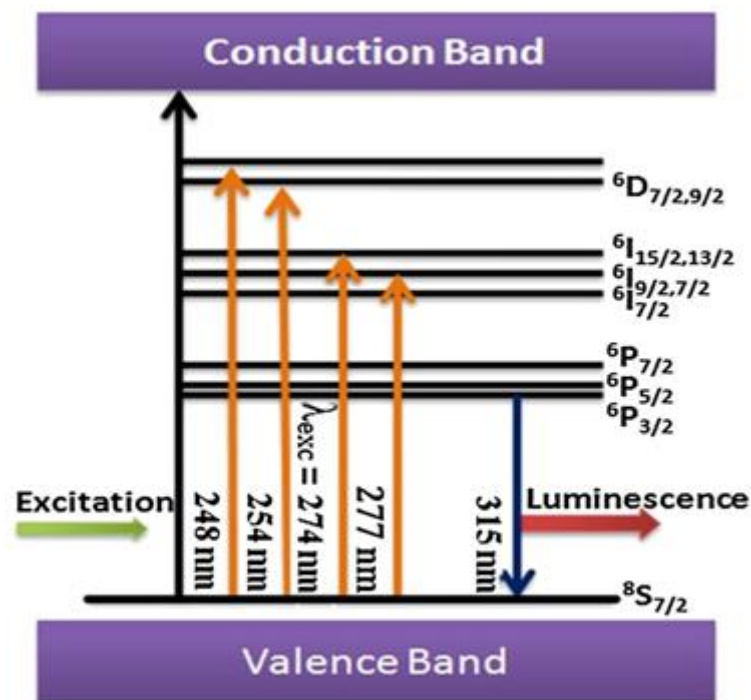


Fig3- Energy level scheme of Gd³⁺

IV. CONCLUSION

The LiBaB₉O₁₅:Gd³⁺ powder phosphor was successfully synthesized via soft chemical route by the recrystallization method. The phase purity was confirmed by X-ray diffraction analysis. The photoluminescence spectra illustrate that under the excitation of 277 nm phosphor emits sharp and intense

emission in Narrow band UVB region (i.e. 312 nm). The obtained result shows that the prepared phosphor $\text{LiBaB}_9\text{O}_{15}:\text{Gd}^{3+}$ could be potential candidate for Phototherapy Application.

V. REFERENCES

- [1]. P. A. Nagpure, S. K. Omanwar, UV emitting borate phosphors for phototherapy lamps, *Indian Journal of pure and Applied Physics*, 53(2015) pp. 77-81.
- [2]. Ting Li, Panlai Li, Nian Fu, Zhijun Wang, Shuchao Xu, Qiongyu Bai and Zhiping Yang, Introducing Eu^{2+} into yellow phosphor $\text{LiBaB}_9\text{O}_{15}:\text{Ce}^{3+}$, Dy^{3+} as blue emitting source to realize white emission, *Journal of Solid State Chemistry*. (2018)
- [3]. P. A. Nagpure, S. K. Omanwar, UV emitting borate phosphors for phototherapy lamps, *Indian Journal of pure and Applied Physics*, 53(2015) pp.77-81
- [4]. P. S. Hemne, R. G. Kungthakar, S. J. Dhoble, S.V. Moharil, V. Singh, Phosphor for phototherapy: Review on psoriasis, *The journal of biological and chemical luminescence*, 32 (2017) 260–270.
- [5]. E Runkle, *UV Radiation and Applications in Horticulture*, 2018
- [6]. Ya Zhuo, J. Zhong, J. Brgoch, Controlling Eu^{2+} Substitution towards a Narrow-Band Green-Emitting Borate Phosphor $\text{NaBaB}_9\text{O}_{15}:\text{Eu}^{2+}$, *ChemRxiv* (2019)
- [7]. X. Liu, B. Lei, Y. Liu, *The Application of Phosphor in Agricultural field*, Springer Science, (2016)
- [8]. N. Singh, Jung-Kul Lee, M. Mohapatra, R.M. Kadam, V. Singh, UV emitting Gd incorporated $\text{LiBaB}_9\text{O}_{15}$ phosphors: An ESR and photoluminescence investigation, *journal of luminescence*, 223 (2020) pp. 117239
- [9]. X. Lei, Gen Li, M. Zeng, B. Zhou, Z. Yuan, Y. Hu, H. Gu, Y. Li, Wei Chen, Europium-doped $\text{NaBaB}_9\text{O}_{15}$ phosphors with controllable blue/red dual-band emissions through self-reduction for plant growth LEDs, *Journal of luminescence*, 237(2021), pp.118166
- [10]. P. A. Nagpure, S. K. Omanwar, UV emitting borate phosphors for phototherapy lamps, *Indian Journal of pure and Applied Physics*, 53(2015) pp. 77-81
- [11]. P. A. Nagpure, S. K. Omanwar, Red and blue emitting borate phosphor excited by near Ultraviolet Light, *Journal of Optics*, 46-2(2016) pp. 91-94
- [12]. A. O. Chauhan, N. S. Bajaj and S. K. Omanwar, Synthesis and photoluminescence study of narrow-band UVB-emitting $\text{LiSr}_4(\text{BO}_3)_3:\text{Gd}^{3+}$, Pr^{3+} phosphor *Bulletin of Material Science*, 40- 1, (2017), pp. 1–6.
- [13]. A. A. Sharma, A. O Chauhan, C. B. Palan, S. K. Omanwar, Synthesis and Photoluminescence study of Gd^{3+} doped YP_3O_9 phosphor prepared by Citric sol-gel method, *International Journal of Scientific Research*, 8-1(2021), pp.65-69
- [14]. S. Tamboli, G. B. Nair, S.J. Dhoble, D.K. Burghate Energy transfer from Pr^{3+} to Gd^{3+} ions in $\text{BaB}_8\text{O}_{13}$ phosphor for phototherapy lamps, *Physica B* (2017)
- [15]. V. Singh, K. Swapna, S. Kaur, A.S. Rao and J.L. Rao, "Narrow-Band UVB-Emitting Gd-Doped SrY_2O_4 Phosphors", *Journal Of Electronics material*, vol 49, pp. 5-13, 2020.

- [16]. A.O. Chauhan, A.B. Gawande, S.K. Omanwar, Narrow band UVB emitting phosphor LaPO₄:Gd³⁺ for phototherapy lamp, *Optik* 127 (2016) 6647–6652.
- [17]. S. Tamboli, B. Rajeswari and S. J. Dhoble, Investigation of UV-emitting Gd³⁺-doped LiCaBO₃ phosphor, *The journal of biological and chemical luminescence* (2016) *Luminescence*, 31(2016) pp. 551–556.

Preliminary Phytochemical Screening of Medicinal Plants used in Cosmeceutical Formulation

R. Gajbhiye, D. Wasule

Department of Cosmetic Technology, L. A. D. & Smt. R. P. College for Women, Nagpur, Maharashtra, India

ABSTRACT

Qualitative phytochemical screening determination of three selected medicinal plants viz. *Albizia Lebbeck* L. Benth. (Shirisha), *Acacia Catechu* L.f. Willd (Khadira), and *Hemidesmus Indicus* L. R. Br. (Sariva) were carried out to know about the presence of secondary metabolites. Plant materials subjected to screening include stem-bark of *Albizia Lebbeck*, *Acacia Catechu*, and root of *Hemidesmus Indicus*. Six different solvents viz. water, ethanol, isopropyl alcohol, acetone, chloroform, and petroleum ether were used for extractions. These plants were analyzed for the presence of twelve important secondary metabolites such as tannins, alkaloids, anthraquinone glycosides, cardiac glycosides, flavonoids, phenol, terpenoids, steroids, saponins, carbohydrates, proteins, and amino acids using standard methods. Preliminary screening of these plant species revealed the presence of secondary metabolites which were predominantly found in aqueous and ethanolic extract followed by acetone, isopropyl alcohol, and chloroform fractions and rarely observed in petroleum ether. The presence of these secondary metabolites may be the ones responsible for the therapeutic properties. The present work is planned to study the effect of metabolites in skincare preparations.

Keywords: *Albizia Lebbeck*, *Acacia Catechu*, *Hemidesmus Indicus*, secondary metabolites, therapeutic properties, skincare

I. INTRODUCTION

Skincare products are the medicinal preparations intended to be used on the external part of the skin surface that manifest beneficial topical actions and provide protection against degradative skin conditions. The use of plant extracts in skincare products is highlighted by consumer demands, as they are relatively safer alternatives offering therapeutic properties than synthetic ingredients/chemical substances [1]. Medicinal plants traditionally used in skincare products generally contain a complex mixture of chemical compounds and is considered a key element for skincare. Generally, all classes of organic compounds find some uses in skincare; some of them like polyphenols, flavonoids, saponins, alkaloids, glycosides, and other phytosterols, show the highest variety of relevant biological properties in dermatology and skin care [2]. *Albizia lebbeck* L. Benth.(Shirisha), *Acacia Catechu* L.f. Willd.(Khadira) belongs to the family Fabaceae, and *Hemidesmus Indicus* L. R. Br. (Sariva) belongs to the family Apocynaceae are used in traditional medicines of India. Scientific studies showed that the stem-bark of *Albizia lebbeck*, *Acacia Catechu*, and root of *Hemidesmus*

Indicus contains tannins, alkaloids, glycosides, flavonoids, phenols, and terpenoids which are responsible for their antioxidant, anti-inflammatory, and antimicrobial activities [3,4,5]. This study investigates the presence of phytochemical constituents in these plants with six different solvents i.e., water, ethanol, isopropyl alcohol, acetone, chloroform, and petroleum ether by using the standard methods

II. MATERIALS AND METHODS

Collection of Plant material :

The stem bark of *Albizia lebbbeck*, *Acacia Catechu*, and root of *Hemidesmus Indicus* was purchased from the local market of Itwari, Nagpur between November 2021 which was identified and authenticated by Prof. (Dr.) Nitin. Dongarwar, Dept of Botany, RTMNU, Nagpur.

Pre-extraction procedure :

The barks and roots were cleaned well with running tap water to remove the dust particles and shade dried for about 18 days. After drying, the barks and roots were powdered and stored in clean airtight containers until used.

Preparation of plant extracts :

Maceration- Powdered material of *Albizia lebbbeck* (L.) Benth., *Acacia Catechu* (L.f.) Willd bark, and *Hemidesmus Indicus* (L.) R. Br. root (10gm) was taken for maceration with 100ml of different solvents viz., water, ethyl alcohol, isopropyl alcohol, acetone, chloroform, and petroleum ether for 15 days at room temperature with vigorous shaking after every 24 hrs. The bark and root extract were filtered using normal filter paper. All the extracts were stored in the amber-colored bottle for preliminary phytochemical analysis.

Fig.1: (a) *A. lebbbeck* stem-bark (b) *A. Catechu* stem-bark (c) *H. Indicus* root



Solvents used :

Water, ethyl alcohol, isopropyl alcohol, acetone, chloroform, and petroleum ether were used as the solvent for the preparation of plant extracts.

Preliminary Phytochemical analysis :

Preliminary phytochemical screening was carried out as per the standard procedure [6,7,8]. As per the protocol, the crude plant material was subjected to solvent extraction method. For this extraction, the

sequence of solvents used were water, ethanol, isopropyl alcohol, acetone, chloroform and petroleum ether. The occurrence of the active constituents is confirmed by its presence and it is subjected to standard chemical test methods. It shows that as per the polarity of the active constituents are extracted with their complimentary solvents whereas the traces of the active constituents also provide us the qualitative test.

III. RESULTS

Preliminary Phytochemical screening was carried out with three selected medicinal plant species. The results are depicted in the following Tables.

Table No.1: Phytochemical Qualitative test of *Albizia Lebbeck* plant extract in six solvents

S.N.	Tests	<i>Albizia Lebbeck</i> L. Benth. (AL)					
		AQ	ET	IPA	AE	CF	PE
1.	Alkaloids Test						
	Dragendorff's test	+	+	++	+	++	+
	Wagner's test	+	++	+	+	++	+
	Hager's test	+	+	+	+	++	++
	Iodine test	-	++	-	+	++	++
2.	Flavonoids Test						
	Shinoda test	+	++	-	-	-	-
	NaOH test	+	+	+	+	-	-
3.	Tannins Test						
	Ferric chloride test	++	++	+	+	-	-
	Lead acetate test	+	++	++	+	-	-
4.	Phenols Test						
	Ferric chloride test	+	+	-	+	-	-
	Ellagic acid test	++	++	-	+	-	-
5.	Terpenoid Test						
	Salkowski's test	+	+	+	+	++	+
6.	Steroids Test						
	Salkowski's test	-	+	+	+	+	++
7.	Cardiac glycoside Test						
	Keller-Kiliani test	-	+	+	-	+	-
8.	Anthraquinone glycoside Test						
	Borntrager test	-	+	-	-	-	-
9.	Saponins Test						
	Foam test	+	-	-	+	-	-
10.	Carbohydrates Test						

	Molisch's test	+	+	-	-	+	+
	Seliwanoff's test	+	+	-	+	+	+
11.	Protein Test						
	Biuret test	+	+	-	+	-	+
12.	Amino acid Test						
	Ninhydrin test	+	+	-	+	+	-

Key: ++ Highly Present; + Present; - Absent; AQ-Aqueous; ET- Ethanol; IPA- Isopropyl alcohol; AE-Acetone; CF-Chloroform; PE-Petroleum ether

Table No.2: Phytochemical Qualitative test of *Acacia Catechu* plant extract in six solvents

S.N.	Tests	<i>Acacia Catechu</i> L.f. Willd (AC)					
		AQ	ET	IPA	AE	CF	PE
1.	Alkaloids Test						
	Dragendorff's test	+	+	-	+	+	+
	Wagner's test	+	++	++	-	++	+
	Hager's test	+	++	+	+	++	-
	Iodine test	+	++	-	-	+	++
2.	Flavonoids Test						
	Shinoda test	++	++	+	+	+	-
	NaOH test	+	+	-	+	-	-
3.	Tannins Test						
	Ferric chloride test	+	++	-	+	-	-
	Lead acetate test	++	++	+	-	-	-
4.	Phenols Test						
	Ferric chloride test	+	++	-	+	-	-
	Ellagic acid test	++	+	+	+	-	-
5.	Terpenoid Test						
	Salkowski's test	-	+	-	+	+	+
6.	Steroids Test						
	Salkowski's test	-	+	-	-	-	-
7.	Cardiac glycoside Test						
	Keller-Kiliani test	+	+	-	-	+	-
8.	Anthraquinone glycoside Test						
	Borntrager test	-	+	+	-	-	-
9.	Saponins Test						
	Foam test	-	+	-	-	-	-
10.	Carbohydrates Test						
	Molisch's test	+	+	-	-	+	-

	Seliwanoff's test	-	+	-	-	+	-
11.	Protein Test						
	Biuret test	+	+	+	+	+	+
12.	Amino acid Test						
	Ninhydrin test	-	-	-	-	-	-

Table No.3: Phytochemical Qualitative test of *Hemidesmus Indicus* plant extract in six solvents

S.N.	Tests	<i>Hemidesmus Indicus</i> L. R. Br. (HI)					
		AQ	ET	IPA	AE	CF	PE
1.	Alkaloids Test						
	Dragendorff's test	+	+	-	+	-	+
	Wagner's test	+	++	++	++	-	+
	Hager's test	+	++	+	+	+	++
	Iodine test	+	+	-	++	-	++
2.	Flavonoids Test						
	Shinoda test	+	++	+	++	-	-
	NaOH test	+	+	+	+	-	-
3.	Tannins Test						
	Ferric chloride test	+	+	-	+	-	-
	Lead acetate test	+	++	++	+	+	-
4.	Phenols Test						
	Ferric chloride test	+	+	-	+	-	-
	Ellagic acid test	+	+	-	+	-	-
5.	Terpenoid Test						
	Salkowski's test	-	+	+	+	+	+
6.	Steroids Test						
	Salkowski's test	-	+	-	-	+	+
7.	Cardiac glycoside Test						
	Keller-Kiliani test	+	+	+	-	+	+
8.	Anthraquinone glycoside Test						
	Borntrager test	-	++	+	-	+	-
9.	Saponins Test						
	Foam test	+	+	-	+	-	-
10.	Carbohydrates Test						
	Molisch's test	+	+	+	-	+	-
	Seliwanoff's test	+	+	+	+	+	-
11.	Protein Test						

	Biuret test	+	+	+	+	+	+
12.	Amino acid Test						
	Ninhydrin test	+	+	+	+	-	-

IV. DISCUSSION

Investigation of twelve phytochemicals in the three selected plants revealed that most of them were present in the ethanolic and aqueous extract as compared to the other fractions. The reason for the presence and absence of secondary metabolites is mainly due to the polar and non-polar nature of extracts and secondary metabolites. The order of polarity of solvents from high to low is water>ethanol>isopropyl alcohol>acetone>chloroform>petroleum ether. *A. lebbeck* stem bark showed the presence of tannins, flavonoids, phenols, saponins, terpenoids, alkaloids, carbohydrates, protein, and amino acids in all fractions of aqueous and ethanolic extracts. Whereas, acetone, isopropyl alcohol, and chloroform also showed some traces but were absent in petroleum ether extract. Other findings showed that steroids and alkaloids have marked presence in petroleum ether as compared to the other solvents. With respect to the presence of cardiac glycosides and anthraquinone glycosides, these were found in ethanolic extract but were absent in the other solvents.(Table No.1.)

Phytochemical analysis of all six extracts of *A. Catechu* stem bark revealed that the presence of tannins, flavonoids, phenols, saponins, steroids, cardiac glycosides, anthraquinone glycosides, carbohydrates, and protein in all ethanolic fractions followed by aqueous extract. Whereas, amino acid is absent in all the extracts. Also, the qualitative presence of alkaloids and terpenoids was observed in petroleum ether, chloroform, and ethanolic fractions.(Table No.2)

The result of *H. Indicus* root extract revealed the presence of secondary metabolites viz., tannins, flavonoids, phenols, saponins, alkaloids, carbohydrates, proteins, and amino acids mostly in ethanolic and aqueous extract followed by qualitative presence in acetone, isopropyl alcohol, chloroform, and petroleum ether. Also, terpenoids, steroids, cardiac glycosides, and anthraquinone glycosides showed their presence in ethanol, chloroform, and petroleum ether fractions. (Table No.3)

Phytochemicals are important for skincare cosmeceutical preparations due to their antioxidant, anti-inflammatory, and anti-microbial properties. Above test results showed that all the twelve secondary metabolites (i.e., Phytochemicals) are present in good amount in all three selected plant species.

V. CONCLUSION

AlbiziaLebbeck, *Acacia Catechu*, and *Hemidesmus Indicus* extracts are rich in various active constituents which have therapeutic properties. The use of ethanol and aqueous extracts of these plants are likely to enhance the bioavailability of active constituents and therefore can be used in skincare/cosmeceutical formulations.

VI. REFERENCES

- [1]. Emerald, M., et al. (2016). Perspective of Natural Products in Skincare. *Pharmacy & Pharmacology International Journal*, 4 (3). <https://doi.org/10.15406/ppij.2016.04.00072>
- [2]. Burlando. B., et al. (2010). *Herbal Principles in Cosmetics-Properties and Mechanisms of Action*. 1st edition, CRC Press, Taylor and Francis group, Boca Raton, London; 9
- [3]. Abriham, H., & Paulos, B. (2016). In vitro Antioxidant and Antibacterial Activity of Albizia lebbeck (L) Benth Stem Bark. *Science, Technology and Arts Research Journal*, 4(2), 204-206. <https://doi.org/10.4314/star.v4i2.25>
- [4]. Stohs, S. J., & Bagchi, D. (2015). Antioxidant, Anti-inflammatory, and Chemoprotective Properties of Acacia catechu Heartwood Extracts. *Phytotherapy Research*, 29 (6), 818-824. <https://doi.org/10.1002/PTR.5335>
- [5]. Kutumbarao. B., Suryanarayana. V., (2018). PHYTOCHEMICAL SCREENING, ANTIOXIDANT, AND ANTI-MICROBIAL ACTIVITY OF HEMIDESMUS INDICUS (INDIAN SARSAPARILLA). *World Journal of Pharmaceutical Research*, 7 (03), 1020–1035. <https://doi.org/10.20959/wjpr20183-10885>
- [6]. Musa Aisha, Ahmed Kalid, & Alagbe Olujimi John. (2020). PRELIMINARY PHYTOCHEMICAL SCREENING OF Albizia lebbeck STEM BARK. *International Journal on Integrated Education*, 3(12), 112–116. <https://doi.org/10.31149/ijie.v3i12.944>
- [7]. Khandelwal, K. R. (2008). *Practical Pharmacognosy*. 19th edition: Nirali Prakashan, Pune, 149-156
- [8]. Kokate, C. K., Purohit, A. P., Gokhale, S. B., *Textbook of Pharmacognosy*, 7: 133-166

Trends in the Technology of Radar Absorbing Materials

P. R. Thote*, A. R. Bansod

*Department of physics, Dr. Ambedkar College, Dikshabhoomi, Nagpur-10, Maharashtra, India

ABSTRACT

This paper will discuss the different types of cutting edge materials being designed as radar absorbing materials (RAM). It will define the type of RAM and its general performance. I will discuss the plausible use of each material and provide details on what aspects must be improved or further researched. Overall a general path for future RAM will be proposed and discussed.

Keywords: Radar Absorbing Material (RAM), Radar Cross Sections (RCS), United States Air Force (USAF), Halpern Anti Radar paint (HARP), Radio Detection and Ranging (RADAR), etc.

I. INTRODUCTION

The word Radar is new- an artificial word. It is abbreviation of “Radio Detection and Ranging”- what was called “Radio-location” until the middle of the second world war, when the new word came into general use. Radar is relatively new invention developed by a team of British scientists led by Sir Robert Watson- Watt in the years before and during the second world war. But its principle is too old. In fact, Nature developed it millions of years ago to help the bats to fly at night without bumping into things. They send out short bursts of squeaks- audible to them, inaudible to us- catching the echo when it rebounds from an obstacle.[1]

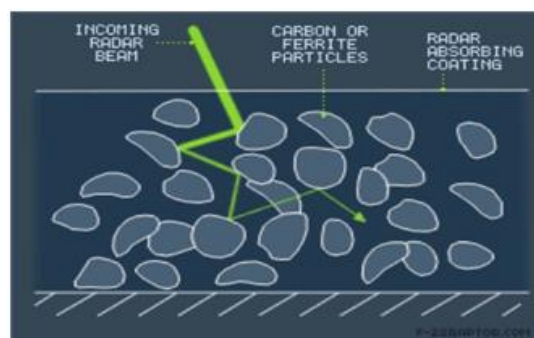


Fig.1 Radar Absorbing Material- Stealth Technology

Much scientific and technical research, most of it carried out since the 1880s, was necessary to make Radar possible: the discovery of electro-magnetic waves and the invention of equipment to produce and receive them; research into the miniature world of atom, and the discovery and study of electron; the invention of valves for the production and amplification of streams of electrons; the invention of wireless telegraphy and

telephony- radio, as we call it now; and, finally, the development of electronic precision instruments capable of dealing with infinitesimal time intervals and very high frequency Radar gave the allies a tremendous advantage over their enemies during the second world war; to-day, it is firmly established in peaceful navigation at sea and in the air.

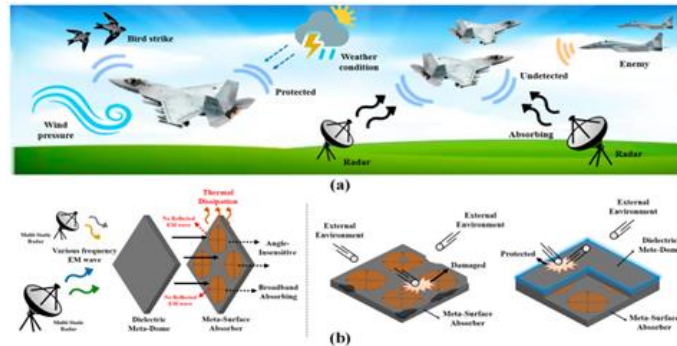


Fig.2 Meta-dome for Broadband Radar Absorbing Structure

Application

- It has three main purposes
- It warns ships and aircraft of obstacles in their way, and helps them to avoid collisions.
- It assists ships and aircraft in the navigation of difficult courses, such as coastal waters or harbours crowded with ships, cross mountain flights or complicated landings.
- It helps ships and aircraft to find whales or icebergs, vessels in distress or storm clouds.

Similarly, Radar detects distant objects, and measures their directions and ranges, by sending out short bursts of radio waves and catching their echoes when they rebound from solid things.

Radar is the most common technique for the detection and tracking of aircraft. Although radar is an indispensable tool in aviation traffic management, it is a problem in offensive military operations which require aircraft to attack their target and then escape without being detected. Radar involves the transmission of electromagnetic waves into the atmosphere; they are then reflected off the aircraft back to a receiving antenna. [2] Conventional aircraft, such as passenger airliners, are easily detected by radar because of their cylindrical shape together with bumps from the engines and tail plane. Metals used in the aircraft are also strong reflectors of electromagnetic waves, and can be easily detected using radar. Composites are also detected using radar, although usually not as easily as metals.

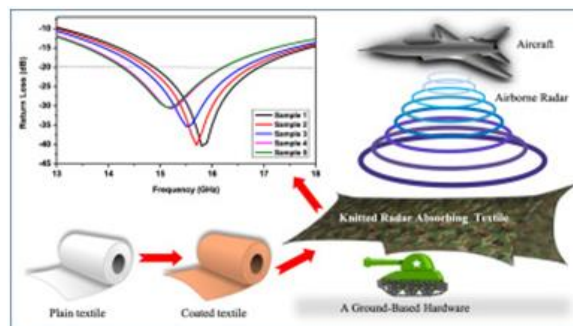


Fig.3 Knitted Radar Absorbing Material

II. WHAT IS RAM?

Radar-absorbing material (RAM) is a specialist class of polymer-based material applied to the surface of stealth military aircraft, such as the F-22 *Raptor* and F-35 *Lightning II* to reduce the radar cross-section and thereby make them harder to detect by radar. These materials are also applied in stealth versions of tactical unmanned aerial systems, such as the Boeing X-45. RAM is applied over the entire external skin or (more often) to regions of high radar reflection such as surface edges. [3] RAM works on the principle of the aircraft absorbing the electromagnetic wave energy to minimize the intensity of the reflected signal. RAMs are used in combination with other stealth technologies, such as planar design and hidden engines, to make military aircraft difficult to detect. It is possible to reduce the radar cross-section of a fighter aircraft to the size of a mid-sized bird through the optimum design and application of stealth technologies.

Information about the composition of RAMs is guarded by the military. Most RAMs consist of ferromagnetic particles embedded in a polymer matrix having a high dielectric constant. One of the most common RAMs is called iron ball paint, which contains tiny metal-coated spheres suspended in an epoxy-based paint. [4] The spheres are coated with ferrite or carbonyl iron. When electromagnetic radiation enters iron ball paint it is absorbed by the ferrite or carbonyl iron molecules which causes them to oscillate. The molecular oscillations then decay with the release of heat, and this is an effective mechanism of damping electromagnetic waves. The small amount of heat generated by the oscillations is conducted into the airframe where it dissipates.

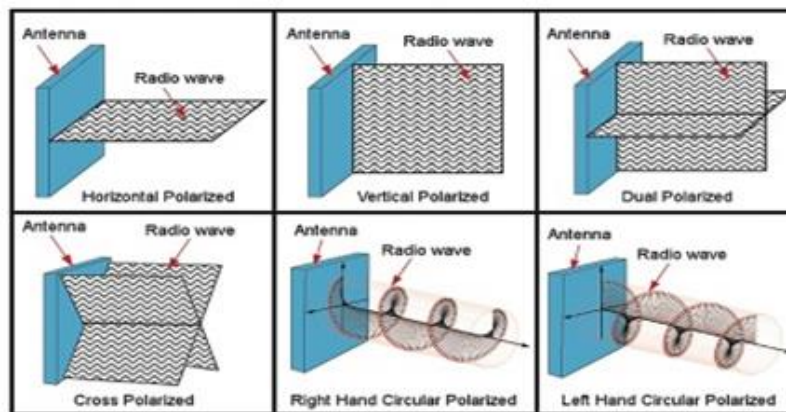


Fig.4 Radar Absorbing Materials Mechanism and Effective Parameters

Another type of RAM consists of neoprene sheet containing ferrite or carbon black particles. This material, which was used on early versions of the F-117A *Nighthawk*, works on the same principle as iron ball paint by converting the radar waves to heat. [5] The USAF has introduced radar-absorbent paints made from ferrofluidic and nonmagnetic materials to some of their stealth aircraft. Ferrofluids are colloidal mixtures composed of nano-sized ferromagnetic particles (under 10 nm) suspended in a carrier medium. Ferrofluids are superparamagnetic, which means they are strongly polarised by electromagnetic radiation. When the fluid is subjected to a sufficiently strong electromagnetic field the polarisation causes corrugations to form on the surface. The electromagnetic energy used to form these corrugations weakens or eliminates the energy of the reflected radar signal. [6] RAM cannot absorb radar at all frequencies. The composition and morphology of the material is carefully tailored to absorb radar waves over a specific frequency band.

III. THE EVOLUTION OF RAMs

Although the commercial production of RAMs started during the 1950s, the research on it was well underway even during the 1930s. The first absorber material to be patented was the one developed in the Netherlands in 1936 (Naamlooze Vennootschap Machinerieën 1936). This was a quarterwave resonant material in the 2 GHz region, in which carbon black was used to achieve dissipation, and TiO₂ to achieve a high dielectric constant. As pointed out earlier, with the advent of radars during the World War II, the quest for absorbers intensified. Germany and the United States began to work on projects to develop such materials. It is interesting to know the contrast between the ultimate motives of the two countries; Germany was primarily looking for absorbers for radar camouflage, while in the US, the research was directed primarily toward absorbers that would improve the radar performance (Emerson 1973). Two types of materials (MacFarlane 1945; Schade 1945) were successfully developed in Germany for use in submarines. The first, called Wesch material consisted of a semiflexible rubber sheet loaded with carbonyl iron powder, and was resonant around 3 GHz. The second material, Jaumann absorber was developed by a multilayer approach. This provided reflection coefficients, typically lower than -20 dB over a wide band (2-15 GHz) near normal incidence. In the US, two types of absorbers, generally called HARP (Halpern-anti-radar paint) were developed during the same time (Halpern & Johnson), which offered a reflection reduction of 15-20 dB at resonance. [7] The airborne version, MX-410, was actually akin to a paint which utilised artificial dielectric materials of high relative permittivity. The second type was a rugged shipboard version consisting of a high concentration of iron particles in a neoprene binder. As with the MX-410, this too could operate in the X-band with a typical thickness of 0-07 inch. A salient feature of this version was the broadening of absorption around the resonant frequency (Montgomery et al 1948). A well-known absorber developed around the same time as HARP, was the Salisbury screen (Salisbury 1952). A resistive sheet placed at quarter wavelength from the scatterer, was spaced by a low dielectric material. Salisbury screens operate by resonant technique, and were widely used in earlier anechoic chamber designs. Yet another resonant absorber in wide use, was the Dallenbach layer (Ruck et al 1970). It consisted of a homogeneous lossy layer on a metal plate. The thickness of the lossy layer was selected so as to match its input impedance with the intrinsic impedance of the free space. [8] As discussed above, the absorbers developed in earlier stages were mostly narrow band in nature. This necessitated research towards obtaining broad band RAMs. Probably the very first approach to be tried was a multilayer structure (c.f. Jaumann absorbers discussed above). Most of the practical broad band RAMs were constructed using this technique. For example, the broadening of bandwidth of Salisbury screens was achieved by introducing additional layers of resistive sheets and spacers (Emerson 1973). In some applications bulk absorbers were also used in place of sheets/layers. The conductivity of the bulk material reduces upon infusion of carbon in a matrix of spongy urethane foam. Based on this approach, the US Naval Research Laboratory developed a broad band absorber in the early 1950s. The conductivity was reduced here, by dipping or spraying carbon onto a mat of loosely spun animal hair. These bulk absorbers could be readily used for controlling reflections for both, the indoor (anechoic) as well as the outdoor antenna measurement ranges. During the late 1950s the focus shifted to problems of anechoic chamber implementation, such as (i)

development of RAMs with reflection coefficients of - 40 to - 60 dB, (ii) lowering the operational frequency limit, and (iii) improved measurement techniques for RAM/anechoic chamber. Attempts were also made to modify the resonant absorbers. For example, circuit analog RAM (CA-RAM) were obtained as Salisbury screen derivatives. CA-RAMs were obtained by depositing lossy material in geometric patterns on a thin lossless film (Severin 1956; Ruck et al 1970). The thickness of the deposit controlled the effective resistance of the layer, while the geometry of the pattern controlled its effective inductance and capacitance. Thus, the layer could be tailored into any value of impedance and its characteristic analysed in terms of lumped elements. The advantage of the CA-RAMs was that better performance could be obtained with comparatively less thickness. In the 1960's, the possibility of using magnetic materials as RAM was explored intensively. Thin magnetic RAMs (e.g. the ferrites) with low reflection coefficients were fabricated which could operate at lower resonant frequencies than had earlier been feasible with the dielectric materials (Bowman 1968). Although thinner compared to the dielectrics, these materials are much heavier and prone to disintegration at higher frequencies. It came to light in the 1980s by serendipity, that some biotech products have ultrawide band absorption characteristics. [9] Subsequent experiments confirmed that substantial RCS reduction was indeed possible by dissolving these compounds in aircraft structural materials. Following this spectacular revelation, the Department of Defense, US, immediately classified the compound. There are, however, conjectures that this ultrawide band RAM is a retinyl compound belonging to the class of Schiff-base salts. This is a powdery black substance which is much lighter (1/10) than the ferrites; it is also said to have been used in making RAM paints for stealth aircraft (Adam 1988). More recently, a new class of homogeneous materials, making use of the chiral property have also found applications as RAMs (Jaggard&Enghetta 1989). Such chiral RAMs depend upon their optical activity and circular dichroism, and the backscatter RCS is independent of polarisation. [10] As compared to the dielectric and magnetic RAMs discussed above, the chiral RAMs have vastly superior RCS reduction characteristics (Jaggard et al 1990, 1991).

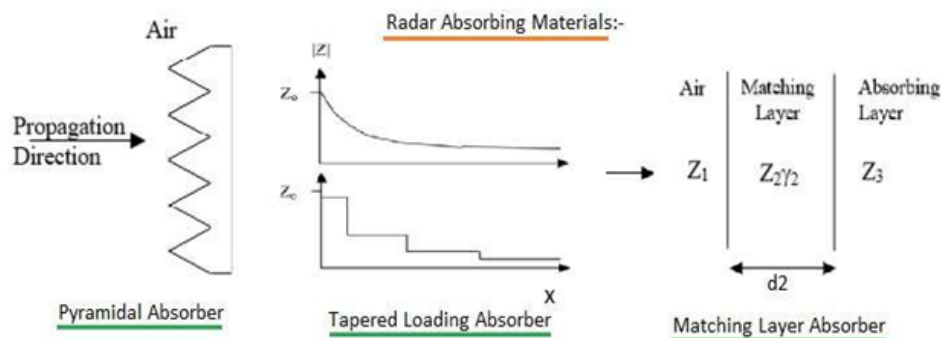


Fig 5. Radar Absorbing Paint

IV. APPLICATIONS OF RAM

Although initially intended for camouflaging aircraft, and for enhancing radar performance, RAMs have found their way into numerous other areas. Some of the important applications of the RAMs are given below.

4.1 RCS reduction of aerospace vehicles:

RAMs are primarily used to achieve broad band RCS reduction for aircraft (Walkington&Huster 1979; Sweetman 1982, 1987; McCluggage 1987; Schmitman& Warwick 1990; Cobucci 1991; Brown 1992; Martin 1992) and missiles (Hanson &Kiehle 1982). Ferrite-based paints are one such class of materials developed earlier that were found to be useful, not only over wide band but also at the lower frequencies. Lighter RAMs were fabricated subsequently, but most of them are still on the classified list.

4.2 Improvement of radar performance :

Absorber sheets are used to shield such reflecting objects in the vicinity of the radar that may otherwise cause spurious effects on radar signals at the base of the radome, parts of the antenna mechanism etc. In shipboard applications, the mast and the bulkhead are also covered with absorbers. Similarly, treating the buildings near an air traffic control radar with RAM, improves radar performance (Emerson 1973).

4.3 Reduction of antenna RCS :

In some military applications it becomes necessary to keep the RCS of antennas as low as possible. Covering the aperture with an absorber coating can lead to considerable RCS reduction. In a typical case with a circular waveguide termination (Lee et al 1985), this RCS reduction can be as much as 13 dB.

V. CONCLUSION

The research in Radar Absorbing Materials (RAMs) as a viable means for RCS reduction has been actively pursued for at least four decades. The RAMs fabricated initially were based upon transmission line approach and were narrow band absorbers. The applicability of these resonant absorbers was enhanced by multilayering to obtain broad band absorbers. Analyses have however shown that the ultrawide band radars can be effectively used as electronic countermeasures against broad band absorbers. This has motivated the current search for ultrawide band RAMs. Compared to the transmission line approach and multilayer concept, the initial successes reported in the area of ultrawide band RAMs have come from the completely novel approach of chirality and by exploring even biochemical products for this purpose. In order to overcome the penalty of weight imposed by multilayered dielectric or ferrite RAMs coated on the aircraft structures, there is a decided shift towards using Radar Absorbing Structures (RAS) where the RAMs are embedded in the polymeric composite matrix. The concept of RAS is compatible with the trend of using increasing volumes of composites in the fabrication of the latest and of future generation fighter aircraft. A comparison with our concurrent study in radomes has shown that several RAMs are actually radome materials. This observation is significant since the RAMs in general are classified, whereas extensive information on the radome materials is available in the open literature. Besides the obvious military applications, RAMs have many prevailing and potential applications in the industrial and even domestic sectors. RAM has thus emerged as a typical dual-use technology, where commercially viable research and development can be pursued independent of the defense sector. An awareness of the underlying principles of RAM analysis, design and fabrication methods,

and the actual materials used as RAMs, could enable material scientists to indigenise and even pioneer the next generation of RAMs.

VI. REFERENCES

- [1]. Yong-Bao Feng, Tai Qiu, Chun-Ying Shen, and Xiao-Yun Li. "Electromagnetic and Absorption Properties of Carbonyl, Iron/rubber Radar Absorbing Materials." *IEEE Transactions on Magnetics* 42.3 (2006): 363-68.
- [2]. Franchitto, M. , R. Faez, A.J. F. Orlando, M. C. Rezende, and M. Martin. *SBMO/IEEE MTi-S IMOC 2001 Proceedings* (2001): 13740.
- [3]. Pitkethly, M. J. "Radar Absorbing Materials and Their Potential Use in Aircraft Structures." (n.d.): n. pag.
- [4]. Fan, Y., H. Yang, X. Liu, H. Zhu, and G. Zou. "Preparation and Study on Radar Absorbing Materials of Nickel-coated Carbon Fiber and Flake Graphite." *Journal of Alloys and Compounds* 461.1-2 (2008): 490-94.
- [5]. Jun, Zeng, Tao Peng, Wang Sen, and Xu Jincheng. "Preparation and Study on Radarabsorbing Materials of Cupric Oxide nanowire-covered Carbon Fibers." *Applied Surface Science* 255.9 (2009): 4916-920.
- [6]. K.L. Zhang, C. Rossi, C. Tenailleau, P. Alphonse, J.Y.C. Ching, *Nanotechnology* 18 (2007) 275607.
- [7]. Zhang, Zhengquan, Tiehu Li, Deqi Jing, and Qiang Zhuang. "Fabrication and Optimization of Radar Absorbing Structures Composed of Glass/carbon Fibers/epoxy Laminate Composites Filled with Carbon Nanotubes." *COMMAD 2008*, 12.
- [8]. Oh, J., K. Oh, C. Kim, and C. Hong. "Design of Radar Absorbing Structures Using Glass/epoxy Composite Containing Carbon Black in X-band Frequency Ranges." *Composites Part B: Engineering* 35.1
- [9]. Oraizi, Homayoon, A. Abdolali, and N. Vaseghi. "Introduction of a New Class of Materials Called Double Zero Media Having the Real Parts of Epsilon and MU Equal to Zero." (n.d.): n. pag.
- [10]. Oraizi, H., A. Abdolali, And N. Vaseghi. "Application Of Double Zero Metamaterials As Radar Absorbing Materials For The Reduction Of Radar Cross Section." *Progress In Electromagnetic Research* 101 (2010): 323337.

Organic Inorganic Metal Halide Perovskite Solar Cells

S. K. Bhonge*, A. R. Bansod

*Department Of Physics, Dr. Ambedkar College, Deekshabhoomi, Nagpur-10, Maharashtra, India

ABSTRACT

A revolutionary all-solid-state, hybrid solar cell based on organic-inorganic metal halide perovskite ($\text{CH}_3\text{NH}_3\text{PbX}_3$) materials has piqued academics' interest around the world and is rated one of the top ten scientific accomplishments of 2013. Because of its advantages, perovskite materials can be employed not only as a light-absorbing layer, but also as an electron/hole transport layer, and also Because of its high extinction coefficient, high charge mobility, extended carrier lifespan, and long carrier diffusion distance, it has a very high extinction coefficient. The photoelectric effect. Perovskite solar cells' power conversion efficiency has increased from 3.8 percent in 2009 to 22.1 percent in 2016, making them more efficient than conventional solar cells. Perovskite solar cells are the best choice for a new generation of solar cells that will eventually replace traditional silicon solar cells. We detail the specific function of each layer in this study, as well as the development and process of perovskite solar cells. Concentrate on improving the function of such layers and their impact on cell performance. The methods of synthesis are then discussed. The performance features of the perovskite light-absorbing layer are discussed. Finally, the obstacles and hopes for the future are discussed. Perovskite solar cell development is also briefly discussed.

Keywords: Organic/inorganic perovskite, Mesoporous Structure, Plane Heterostructures, power conversion efficiency etc.

I. INTRODUCTION

Traditional fossil energy sources cannot satisfy the sustainable growth of human society due to rising global energy consumption and pollution. The use of clean, renewable energy sources has become a priority. It is a requirement for the advancement of human society. Among a group of the many new energy sources, solar power is unquestionably one of the most promising. Solar cell is a device that converts light energy into electrical energy directly. And, Photovoltaic effects or photochemical reactions provide energy.

Becquerel, a French physicist, discovered the photovoltaic effect for the first time in 1839. Adams et al., a group of British scientists, discovered in 1876 that a selenium semiconductor could generate electricity when exposed to sunlight. Fritts created the first semiconductor/metal junction solar cell with a piece of germanium coated with a thin layer of gold in 1883, despite the fact that the efficiency was only 1%. Pearson et al. of US Bell Labs produced the first crystalline silicon solar cell in 1954, with a conversion efficiency of 4.5 percent, ushering in a new era for solar power utilisation. The photovoltaic conversion efficiency of monocrystalline

silicon/polycrystalline silicon solar cells currently used in industrial applications is higher than 20%. However, silicon-based solar cells are expensive, require difficult preparation, and pollute the environment significantly. In the laboratory, cadmium telluride and copper indium gallium selenium thin-film solar cells have reached high photovoltaic conversion efficiency, but industrial applications are limited by high production costs, pollution, and other issues.

Dye-sensitized solar cells, as a representative of the third-generation solar cells, have recently reached a photoelectric efficiency. In the lab, there was a conversion efficiency of more than 13%, and have grown significantly as a result of their significant advantages. Low cost, simple process, and high efficiency are just a few of the benefits. Dye-sensitized cells, on the other hand, have two drawbacks. To begin with, the absorbing layer is thick ($>10\ \mu\text{m}$) to assure total absorption of sunlight's energy because it is difficult to achieve complete light absorption in solid-state cells with a smaller absorbing layer. Second, light bleaching is a problem that organic dyes cannot prevent. Researchers have developed outstanding all-solid dye compounds as a result of these two issues.

The organic metal halide perovskite, discovered by Japanese scientists Kojima et al. in 2009, is comparable to dyes and can absorb sunlight. Teperovskite can be used as a sensitizer in dyesensitized solar cells with a liquid electrolyte to obtain a 3.8 percent power conversion efficiency (PCE). For the first time, Kim et al. announced all-solid-state perovskite solar cells with a PCE of 9.7% in 2012. Perovskite solar cells have gotten a lot of attention from academics around the world because of their high efficiency and inexpensive cost, and they've progressed quickly in recent years. The best conversion efficiency to date was 22.1 percent in 2016, according to the National Renewable Energy Laboratory (NREL). Further advancements in perovskite solar cell performance are projected to break the conversion efficiency and production cost bottlenecks. Perovskite solar cells are of considerable scientific and practical significance as one of the most promising new photovoltaic cells. Figure 1 depicts the significant rise in the number of publications on perovskite solar cells, as well as the greatest NREL-certified efficiencies. This report outlines recent developments in perovskite solar cells. This study reviews recent achievements in perovskite solar cells and delves into the architectures and operating principles of perovskite solar cells, as well as the specific function and characteristics of each layer and the methods used to create perovskite light-absorbing layers. Finally, based on the findings, we propose future study directions.

II. PEROVSKITE MATERIAL FOR SOLAR CELLS

The calcium titanate (CaTiO_3) chemical, which has a molecular structure of type ABX_3 , is used to make the perovskite material. Because of their cubic lattice-nested octahedral layered structures and unique optical, thermal, and electromagnetic properties, perovskite materials have gotten a lot of interest. Perovskite materials used in solar cells are a type of organotinorganic metal halide compound with the perovskite structure, in which Group A (**methylammonium**, CH_3NH_3^+ , MA^+ , or **formamidinium**, $\text{CH}(\text{NH}_2)_2^+$, FA^+) is located in the vertex of the face-centred cubic lattice, and metal cation B (Pb^{2+} , Sn^{2+} , etc.) and halogen anion and halogen anion X (Cl, Br, or I, or a coexistence of many halogens) are located in the core and apex of the

octahedra. A stable three-dimensional network structure is formed by joining metal-halogen octahedra together.

Figure 2 depicts the crystal structure.

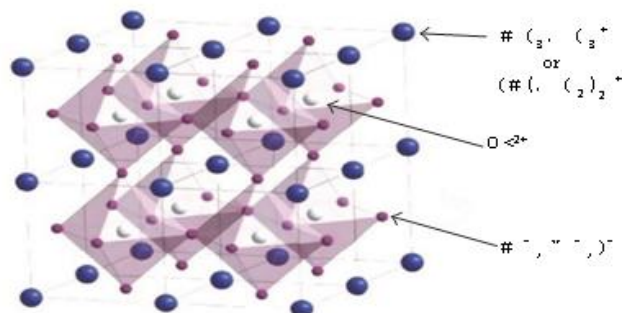


Figure 2: Typical perovskite cubic lattice structure. Reprinted from

The following are the properties of materials with this structure:

The materials with this structure have the four characteristics listed below. To begin with, the materials have good photoelectric characteristics, a low exciton binding energy, and high optical absorption coefficients (up to 10^4 cm^{-1}). Second, perovskite, as a light-absorbing layer, can efficiently collect solar energy. Third, the materials have a high dielectric constant, which allows electrons and holes to be efficiently transported and collected. Finally, electrons and holes can be transported at the same time, with transmission distances of up to 100 nm or even more than 1 μm .

If these properties are used in solar cell devices, they result in a high open-circuit voltage (V_{oc}) and a high short-circuit current density (J_{sc}). When exposed to sunlight, the perovskite layer absorbs photons first, and then produces those excitons (electron-hole pairs). These excitons can produce free carriers (free electrons and holes) to generate a current or recombine into excitons due to differences in the exciton binding energy of the perovskite materials. The diffusion distance and lifetime of the carrier are lengthy due to the low carrier recombination probabilities of $\text{CH}_3\text{NH}_3\text{PbI}_3$ (MAPbI₃) and other perovskite materials, as well as the increased carrier mobility. The carrier diffusion distance for MAPbI₃ is at least 100 nm and greater than 1 μm for MAPbI_{3-x}Cl_x. The increased performance of perovskite solar cells is due to the greater diffusion distance and carrier lifetime. Then, an electron transport material (ETM) and a hole transport material (HTM) gather these free electrons and holes (HTM). Electrons are transmitted from the perovskite material to TiO₂, which is then employed in the ETM layers before being collected by FTO. The holes are transmitted to the HTM layer and collected by the metal electrode at the same time. Finally, the photocurrent is generated in the outside circuit by connecting the FTO and metal electrode.

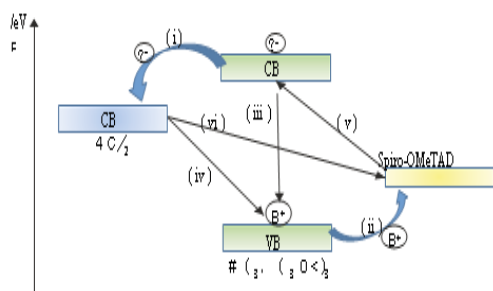


Figure 3: Schematic diagram of energy levels and transport processes in an HTM/perovskite/TiO₂ cell.

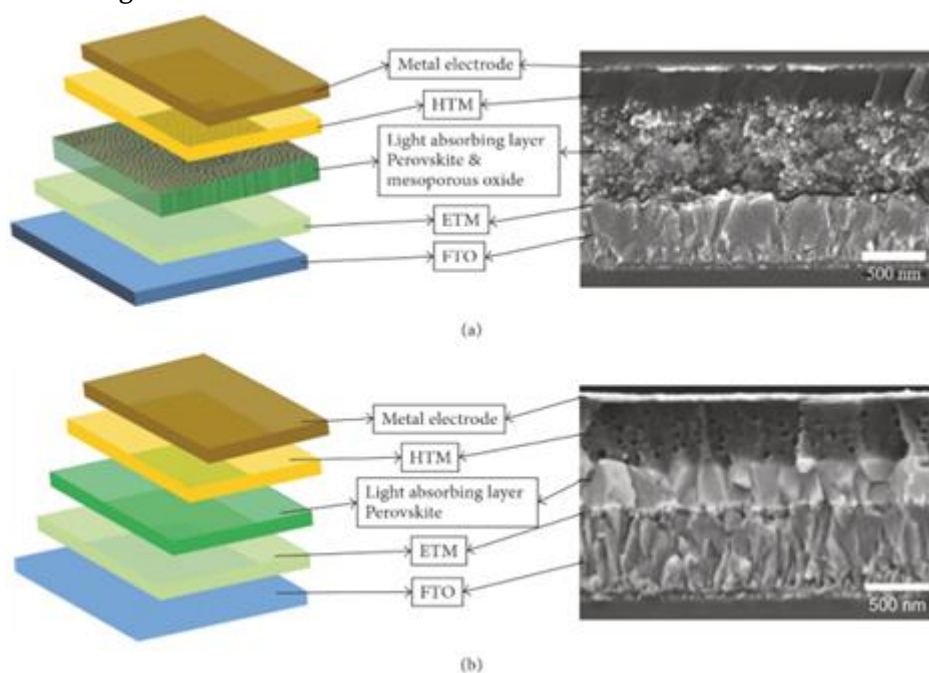
Marchioro et al. theorised that electron-hole pairs separated at the TiO₂/perovskite and Spiro-OMeTAD/perovskite heterojunction interfaces, with electrons injecting into TiO₂ (process I in Figure 3) and holes injecting into HTM (process (ii)) to achieve charge transfer. Simultaneously, a number of deleterious cell behaviours such as exciton annihilation (process (iii)), photoluminescence, or nonradiative recombination, as well as reverse transmission of electrons and holes (process (iv) and (v)) and recombination at the TiO₂/HTM interface (process (vi)) would occur. Figure 3 depicts the electron and hole transport pathways in an HTM/perovskite/TiO₂ cell.

III. MESOPOROUS STRUCTURE

Because of their high porosity and enormous specific surface area (up to 1000 m²/g), mesoporous materials have been extensively explored and widely utilised. The use of mesoporous materials in perovskite solar cells allows the perovskite absorber to cling to the mesoporous metal oxide framework, expanding the photosensitive material's light-receiving area and increasing the device's efficiency. A typical mesoporous solar cell has an FTO electrode, a dense electron transport layer, a mesoporous oxide layer, a perovskite layer, a hole transport layer, and an electrode layer, as shown in Figure 4(a). By solution spin-coating perovskite nanocrystals into the pores of mesoporous TiO₂ and forming an interconnected absorbent layer, TiO₂ is the most common mesoporous framework material. TiO₂ has a significant functional role in this structure, such as conveying electrons, blocking holes, and limiting the recombination of electron-hole pairs in the FTO conductive substrate, all of which contribute to the device's improved photoelectric conversion efficiency. Mesoscopic metal oxides, such as ZnO₂, Al₂O₃, and ZrO₂, are often utilised frame materials in addition to TiO₂. The hole transport layer receives holes created in the perovskite absorbing layer and transports them to the metal electrode's surface. Spiro-OMeTAD (2,2',7,7'-Tetrakis[N,N-di(4-methoxyphenyl)amino]-9,9'-spirobifluorene) is the most often employed hole transport substance. Noble metals including Au, Ag, and Pt are commonly utilised as counterelectrode materials. This type of structure can not only effectively prevent electron and hole recombination, but also offer the requisite diffusion length for effective electron and hole collecting.

All-solid-state MAPbI₃ solar cells based on the mesoscopic structure of porous nano-TiO₂ were reported by Kim et al. and Burschka et al. The filling factors (FF) were 0.62 and 0.73, respectively, and the PCEs were 9.7%

and 15.0 percent. The high-quality perovskite films generated by the two-step solution deposition process are largely responsible for the significant improvement. Burschka et al. theorised that the conversion takes place within the nanoporous host as soon as the two components (MAI and PbI_2) come into contact, allowing for far more control over perovskite shape. Using mesoscopic $\text{TiO}_2/\text{FAPbI}_3$ perovskite solar cell architecture, Yang et al. reported a PCE greater than 20% at the end of 2014. Qiu et al. developed all-solid-state perovskite solar cells with an oc of 0.82 V and a PCE of 4.87 % using a one-dimensional TiO_2 nanoarray mesoscopic structure with MAPbI_2Br as the light-absorbing layer. Qiu et al. found that when the length of the one-dimensional TiO_2 nanowire extended, the PCEs first increased, then declined, indicating a balance between electron transport and perovskite loading. Many scientists have researched the framework of perovskite cells using Al_2O_3 as the mesoscopic material because the perovskite solar cells based on mesoscopic TiO_2 require high-temperature sintering.



Unlike TiO_2 , Al_2O_3 serves only as a support layer in the device and does not play the same role in photoanode electron transport as TiO_2 . As a result, the Al_2O_3 particle interaction becomes less critical, preventing high-temperature sintering. The electrons generated by light irradiation in perovskite light-absorbing materials are not injected into the Al_2O_3 conduction band, but are instead transferred directly from the perovskite to the FTO conductive layer. Lee et al. developed MAPbI_3 perovskite solar cells with Al_2O_3 as the support material in 2012, achieving an oc of 980 mV, an FF of 0.63, and a PCE of 10.9 percent. The device's conversion efficiency climbed to 12.3% when the process conditions were optimised. To increase the PCE of Al_2O_3 -based devices, Au@SiO_2 nanoparticles with a core-shell configuration were doped into the Al_2O_3 layer to lower the exciton binding energy, resulting in a 11.4% photoelectric conversion efficiency. Insulating support layers such as Al_2O_3 , ZrO_2 , and SiO_2 can also be employed. The solar cells with ZrO_2 nanoparticles in MAPbI_3 exhibit an V_{oc} of 1070 mV and a PCE of 10.8%. Hwang et al. compared a series of perovskite solar cells with different sized SiO_2 nanoparticles (15–100 nm) as the support layer and found that the PCE was 11.45% when the SiO_2

nanoparticles were 50 nm, which was slightly higher than the PCE (10.29%) of the devices with the same-sized TiO₂ nanoparticles.

IV. PLANE HETEROSTRUCTURE

Figure depicts a typical planar heterojunction configuration of perovskite solar cells (b). The planar structure differs from the mesoscopic structure in that it does not include the porous metal oxide framework. The perovskite materials and the two layers (the electron transport layer and the hole transport layer) form two interfaces. As a result, the electron transport layer and the hole transport layer separate the electron hole pairs quickly and effectively. The research on perovskite solar cells with a planar heterojunction structure aids in the knowledge of light absorption and electron-hole separation mechanisms, as well as the flexibility of device optimization for the development of highly efficient lamination perovskite solar cells. The FTO/TiO₂/MAPbI₂Cl/spiro-OMeTAD/Ag planar heterojunction structure of perovskite solar cells published by Snaith's group had a PCE of 1.8%. Thereafter developed a set of planar solar cells with a maximum PCE of 15.7%, an oc of 1.03 V, and an FF of 0.749 under optimum manufacturing conditions.

By employing yttrium-doped TiO₂ as the electron transport material and modifying the ITO to lower the working function, Zhou et al. were able to achieve greater electron mobility. The device's open-circuit voltage and short-circuit current were considerably improved, with a PCE of 19.3 %. Malinkiewicz et al. developed MAPbI₃perovskite solar cells with a PCE of 12 percent by replacing the dense TiO₂flm with poly(3,4-ethylenedioxythiophene): polystyrene sulfonate (PEDOT:PSS). An inverted planar heterostructure is a type of structure that can be used to make flexible perovskite solar cells.

V. SUMMARY AND OUTLOOK

The principles and basic architectures of perovskite solar cells are reviewed in this work, as well as current improvements in recent developments. The adaptability of perovskite light-absorbing layer manufacturing techniques, which include solution-deposition, vapour-deposition, and vapour-assisted solution procedures, is appealing, and these methods are also reviewed.

Perovskite solar cells have advanced rapidly, however several crucial variables may limit their progress. To begin with, external environmental conditions (such as humidity, temperature, and UV light) have a significant impact on the stability of organic lead halide perovskite, resulting in low device stability and significant difficulties in encapsulating cells later on. As a result, developing a high-stability device composition, including the light-absorbing layer, electron/hole transport layer, and electrode materials, as well as a simple and effective device-packaging process, will be critical in promoting the practicability of such devices. Second, the hole-transporting substance SpiroOMeTAD, which is utilised in perovskite solar cells, is costly (10 times the market price of gold) and the synthesis procedure is difficult. As a result, novel hole transport materials must be designed and synthesised in order to advance practical applications of perovskite solar cells. Finally, because it is difficult to deposit a wide area of continuous perovskite film using the

standard methods mentioned above, other methods should be improved in the future to manufacture high-quality, big-area perovskite solar cells for commercial manufacturing. Fourth, the Pb element used in perovskite solar cells is exceedingly hazardous, which will stymie perovskite solar cell development and industrialization. As a result, a low-toxicity or nontoxic component must be found to replace Pb in the future. Finally, a thorough knowledge of the nanoscale physics mechanism of perovskite solar cells is lacking. As a result, a comprehensive theoretical model is required to explain the reasons behind the increased conversion efficiency. Theoretical research will not only help to increase the performance of perovskite solar cells, but will also provide suggestions for developing new materials and structures that are simpler and/or more efficient.

In a nutshell, all of the above concerns must be overcome before perovskite solar cells may be fully utilised.

VI. REFERENCES

- [1]. Perovskite Solar Cells Technology And Practices; By Kunwu Fu; Anita Wing Ho-Baillie Hemant Kumar Mulmudi; Pham Thi Thu Trang.
- [2]. Hybrid Perovskite Solar Cells Characteristics And Operation; By Hiroyuki Fujiwara.
- [3]. Review Of Current Progress In Inorganic Hole-Transport Materials For Perovskite Solar Cells SinghRahul , Singh PramodK, Bhattacharya B , Rhee HeeWoo.
- [4]. Perovskite-Based Solar Cells: Materials, Methods, And Future Perspectives Zhou Di , Zhou Tiantian,Zhu,Xiaolong, Tu, Yufang.
- [5]. A Perspective On The Recent Progress In Solution-Processed Methods For Highly Efficient Perovskite Solar Cells Chilvery,AshwithDas, Sanjib, Guggilla, Padmaja, Brantley, Christina, SundaMeya, Anderson.
- [6]. Alternatives Assessment Of Perovskite Solar Cell Materials And Their Methods Of Fabrication Llanos, Yekani R, Demopoulos, G.P., Basu N.
- [7]. Perovskites-Based Solar Cells: A Review Of Recent Progress, Materials And Processing Methods Shizhengqi, Jayatissa, Ahalapitiya
- [8]. Physics Of Solar Cells: From Principles To New Concepts Peter Wiirefel.
- [9]. Flexible Solar Cells Antonio Luque, Steven Hegedus.
- [10]. Flexible Solar Cells Antonio Luque, Steven Hegedus.

Refractive Indices and Densities of Binary Mixtures of Benzene-Ethanol and Benzene-Acetone at Room Temperature

M. P. Bhise¹, Javed khan¹, N.D. Kapse², S. A. Athawale¹

¹Department of Chemistry, Govt. Vidarbha Institute of Science and Humanities, Amravati, Maharashtra, India

²MCT's Rajiv Gandhi Institute of Technology, Andheri (West) Mumbai, Maharashtra, India

ABSTRACT

Densities and refractive indices, of pure acetone, benzene, ethanol and their binary mixtures have been measured experimentally at room temperature. Molar refraction for the benzene-ethanol and benzene-acetone system was calculated theoretically. Experimental values and theoretical values of molar refraction were compared from these data. It has been suggested that the molar refraction is additive and constitutive property. Further, it is also observed that, the intermolecular interactions contribute nothing to molar refraction. Densities decreases as mole fraction increases suggesting that molecular interaction is weaker.

Keywords: Molar refraction, Refractive indices, Binary mixtures of benzene acetone and ethanol

I. INTRODUCTION

Mixed solvents are frequently used as suitable media for many chemical, industrial and biological processes, as they provide a wide range of mixtures with desired properties. In recent years' numerous researchers have studied the thermodynamic and physico-chemical behavior of binary mixtures of benzene-cyclohexane¹ benzene-isomer of butanol², benzene+ tert-butyl alcohol³ and benzene 1-hexanol/propyl propanoate,⁴ using different experimental techniques. Verification of the molar refraction as an additive and constitutive property of binary liquid mixtures of benzene-ethanol and water-ethanol⁵. The study of liquid systems by means of refractive methods has a long history⁶ and still attracts considerable interest⁷. Ever since the early work of Gladstone and Dale⁸ physical properties of a substance depends on the internal structure or the constitution of the molecules. Therefore, the determination of properties such as refractive index, molar refraction, molar polarization, electronic polarization, etc. can provide valuable information's about the structure of molecules, binary mixture of liquid. In addition to with the refractive index and density, deviation in refractive index, molar refractions deviation in molar refractions and excess -molar volume have been calculated⁹⁻¹¹. To the best of our knowledge there has been no study of binary liquid mixtures of benzene-ethanol and benzene-acetone system of volumetric and refractive index at room temperature. The present paper explains the result of experimental and the theoretical values of molar

refractions, refractive indices and various other parameters for the liquid mixture of benzene -ethanol and benzene-acetone.

Refractive indices and other related parameters are determined for the binary mixture of ethanol with water and benzene with ethanol. Though a large number of preliminary investigations are available in the literature, but no comprehensive study has yet been reported related to binary studies.

II. EXPERIMENTAL

All the chemicals used were of L.R. grades (s.d. fine chemicals, India,) All chemicals were purified according to the standard procedures.⁹ The chemicals were stored over 0.4nm molecular sieves for several days to reduce the water content, if any. Solutions were prepared by mole fraction method. Nine bottles of each system were kept in special air tight stopper glass bottles so as to avoid evaporation. The weighing was done by using electronic balance with precision of ± 0.1 mg.

The densities of pure liquids and their binary mixtures were measured using a single capillary pycnometer made of Borosil glass having a bulb capacity of 8×10^{-6} m³. Refractive indices were measured with a thermostat Abbe refractometer at room temperature. The calibration of the refractometer was done by measuring the refractive indices of pure water and benzene at 298.15K as describe by Bhatia et al ¹². The accuracy in refractive index data was quite satisfactory. The temperature of pure liquids and their binary mixtures was maintained to an accuracy of ± 0.02 K in an accuracy in the density and refractive index. The refractive index measurements were ascertained by comparing the experimental values of pure liquids and their mixtures with theoretically values.

III. RESULTS AND DISCUSSION

The experimental values of density and refractive indices of pure liquids and their binary mixtures as a function of mole fraction of binary mixture of benzene – acetone and acetone-water at room temperature are given in table [1, 2 & 3]. By using above experimental values of refractive indices and densities, molar refraction and electronic polarization was calculated by using the following formulae.

$$R_m = [(n^2-1)/(n^2+2)]M/d \quad (1)$$

Where, R_m - Molar refraction; n -Refractive index; M -Molar mass; d - density
and for binary mixture, equation (1) becomes-

$$R_{ms} = [(n^2-1)/(n^2+2)] [(M_1x_1+M_2x_2)/d] \quad (2)$$

Where, R_{ms} - molar refraction of solution; n - Refractive index of solution; M_1 - Molar mass of 1st compound; x_1 -mole fraction of 1st compound; M_2 -Molar mass of IInd compound; x_2 - mole fraction of IInd compound.

Table-1: For Pure Liquids at room temperature

S.No.	Compound	Molar Mass	Refractive Index (n)	d, densities (g/ml)	Δn^2 electronics polarization	Observed molar Refraction $R_{m_{obs}}$ (cm^3/mol)	Calculated molar refraction $R_{m_{cal}}$ (cm^3/mol)
1.	Acetone	58.00	1.3534	0.7978	1.0084	15.1314	16.06
2.	C ₂ H ₅ O ₆	46.07	1.3797	0.8508	0.7239	12.5355	12.961
3.	C ₆ H ₆	78.00	1.5218	0.8978	0.8060	26.5267	26.289

Table-2: Benzene-Acetone at room temp

S.No.	Compound		Refractive Index (n)	Δn^2 electronics polarization	densities (g/ml)	$R_{m_{obs}}$ ($cm^3/mole$)	$R_{m_{cal}}$ ($cm^3/mole$)
	Mole fraction of Acetone (x_1)	Mole Fraction of Benzene (x_2)					
1	0.1	0.9	1.5178	2.303717	0.90831	25.34656	25.2661
2	0.2	0.8	1.49782	2.243466	0.8966	24.18499	24.2432
3	0.3	0.7	1.48477	2.204542	0.8833	23.35218	23.2203
4	0.4	0.6	1.46871	2.157109	0.8644	22.54064	22.1974
5	0.5	0.5	1.45365	2.113098	0.8457	21.75991	21.1745
6	0.6	0.4	1.44159	2.078185	0.8291	21.04565	20.1516
7	0.7	0.3	1.43155	2.047335	0.8041	20.62531	19.1287
8	0.8	0.2	1.41547	19.200355	0.7934	19.52424	18.5415
9	0.9	0.1	1.39939	19.58292	0.7822	18.5705	17.105

Table-3: Benzene-Ethanol at room temp

S.No.	Compound		Refractive Index (n))	Δn^2 electronics polarization	Densities (g/ml)	$R_{m_{obs}}$ ($cm^3/mole$)	$R_{m_{cal}}$ ($cm^3/mole$)
	Mole fraction of Benzene (x_1)	Mole fraction of Ethanol (x_2)					
1	0.1	0.9	1.3946	1.9455	0.8227	14.3525	14.2938
2	0.2	0.8	1.4198	2.0158	0.8362	15.8714	15.6266
3	0.3	0.7	1.4324	2.0158	0.8449	17.1019	16.9594
4	0.4	0.6	1.4459	2.0906	0.8533	18.3979	18.2922

5	0.5	0.5	1.4574	2.1240	0.8588	19.7014	19.6250
6	0.6	0.4	1.4720	2.1668	0.8663	21.1039	20.9578
7	0.7	0.3	1.4825	2.1978	0.8730	22.3854	22.2906
8	0.8	0.2	1.4974	2.2437	0.8789	23.9115	23.6234
9	0.9	0.1	1.5146	2.2940	0.8883	25.4155	24.9534

From the observation Table- [1, 2 and 3], it is suggested that the experimental values of molar refraction of pure solvent and binary mixture systems are in good agreement with the calculated values of molar refractions. Density of binary mixture of benzene-acetone is decreased as mol fraction increases as shown in table [1] indicating that as the mol fraction of benzene decreases density also decreases similar trends observed for the benzene-ethanol as shown in the table [2]. Suggesting that mol fraction of benzene increases density also increases. Refractive indices of binary mixture of benzene-acetone decreases as mol fraction of benzene decreases and increases as mol fraction of benzene increases as shown in table [2 & 3]. Observed molar refraction of binary mixture of both the system and pure solvent values were compared with the calculated values.

Hence it is confirmed that the intermolecular interactions do not play any role in the contribution of molar refractions. Indicating that the contribution for molar refraction is only due to the atoms and bonds present in the molecules or mixtures.

Hence it is confirmed that molar refractions (R_m) is an additive and constitutive property and the refraction of molecule is sum of contribution of atoms and bonds.

IV. REFERENCES

- [1]. Patterson, D.J. *Solution Chem.* 1994, 23, 105.
- [2]. Bhardwaj, U., Maken, S, Singh, K.C.J. *Chem. Thermodyn.* 1996, 28, 1173.
- [3]. Larsen, G., Ismail, Z.K., Herreros, B., Parra, J. *Phys. Chem.* 1998, 102, 4734
- [4]. Garabal, S. Segade, S., Cabeza, O., Franjo, C., Jimene, E.J. *Chem. Thermody.* 2003, 35, 1129.
- [5]. Javedkhan, M., Farooqui, S.H., Quadri, Rasayan J. *Chem.* 2011, 4, 944-946.
- [6]. Arago, D.F., J.B., *Mem. Acad. Fr.* 1806, 7-9
- [7]. Li, W.B., Segre, P.N., Gammon, R.W., Sengers, J.V., Lamvik, M. *J. Chem Phys. Phys.*, 1994, 101, 5058-5069.
- [8]. Y. Jayalakshmi, J.S. Van Duijneneldt, D. Beysens. *J. Chem. Phys.*, 1994, 100, 604.
- [9]. Arthur I. Vogel, *A text book of Practical Organic Chemistry including Qualitative Analysis*, New impression with corrections and additions, 3rd edition, 1031.
- [10]. P.W. Atkins, *Physical chemistry*, Oxford University Press, Oxford Melbourne Tokyo, 6th edition, 1998., 654.
- [11]. LLYOD N. Ferguson, *The modern structural theory of organic chemistry*, Prentice-Hall of India Pvt.Ltd, New Delhi, 1969, 196.
- [12]. Bhatia, S.C., Tripathi, N., Dubey, G.P., *Indian J. Chem.* 2002, 41, 266.



Physico Chemical Assessment of Soil Samples from Rama (Sahur) Region, Amravati District, Maharashtra (India)

M. P. Bhise¹, S. A. Athawale¹, N. A. Junghare²

¹Department of Chemistry, Government Vidarbha Institute of Science and Humanities Amravati, Maharashtra, India

²MCT's Rajiv Gandhi Institute of Technology, Andheri (Waste) Mumbai, Maharashtra, India

ABSTRACT

The present study, deals with physico chemical assessment of soil samples from field which were collected from Rama village (Sahur). the study was primarily focused on testing of soil quality from various sampling stations. eleven representative samples were analyzed for its WHC, CaCO₃, pH, E.C., organic carbon, organic matter, Potassium, Sodium, Calcium, Magnesium.

KEYWORDS: Physico-chemical, WHC, EC, OC, OM, Potassium, Sodium, Calcium, Magnesium

I. INTRODUCTION

Soil is a vital component, medium of unconsolidated nutrients and materials forms the life layer of plants. The soil supports the plants that provide us with food, fiber and forest product. due to soil contamination, the productivity of crop diminished seriously and poses the problem of shortage of food. Hence, in recent year, study of physiochemical parameter of soil to monitor soil pollution and nutritional value of soil become important.

Number of review studies had been performed to assess the quality of soil M Akter, S Sultana, A K C Chaudhary, M A H Chaudhary (2010) have studied Physiochemical Characteristic of soil in tropical Sal (Shorearobusta Garten.) forest in eastern Nepal [1-2].

TukuraBirtusWokhe, Yahaya Mohammad and Madhu Paschal Chima (2013) [3] have studied Evaluation of physiochemical and biological properties of irrigated soil and showed that Physical and chemical properties of the soil differed according to farm [4]. The most common chemical involved in causing soil pollution are petroleum hydrocarbon [5], heavy metals[6]. Municipal wastes increase the nitrogen, pH, cation exchange capacity, percentage base saturation and organic matter [7-8]. Organic waste [9] can provide nutrients for increase plant growth and such positive effect will likely encourage continued land application of this waste however excessive waste in soil may increase heavy metal concentration in the soil and underground water. Heavy metal may have harmful effects on soil, crop and human health [10-11].

II. MATERIALS AND METHOD

1. WATER HOLDING CAPACITY AND CaCo₃ CONTENT:

i) WATER CONTENT :

Water contain capacity was measured by taking 20g samples in pre weigh aluminum pan and placed it an oven at 110°C. The sample was dry after overnight heating. Cool the sample in desiccators at room temperature.

ii) CaCo₃ CONTENT

Place a 5g of sample on filter paper in a funnel and remove carbohydrate by washing with 10% HCl, after removing bubbling of carbon dioxide rinse with deionized water. Dry the sample in oven at 110°C. after a week place the sample in desiccator for a while

2. pH:

Take 20g of soil in 40ml distilled water and stir. Calibrate the pH meter with two buffers, (4.0 and 7.0 or 9.2). shake the soil suspension and calculate the pH on the pH meter.

3. ELECTRICAL CONDUCTIVITY:

The conductivity of a saturation extract is generally recommended for appraising soil salinity in relation to plant growth. In the range of EC, suitable for plant growth.

Electrical conductivity of soil sample was measured by 'Solution Bridge'. by adding 10 gm soil sample in ml distilled water. after stirred for 15 min. leave overnight. after calibration dip the conductivity cell in the supernatant soil. and measure the conductance

4. OC and OM (ORGANIC CARBON AND ORGANIC MATTER) :

OC and OM percentage calculated by Walkley- Black Method using the the following formula

a. Percentage of easily oxidizable organic carbon (OC) :

$$\% C = \frac{(B - S) \text{ M of Fe (II) } 12 * 100}{\text{grams of soil} * 4000}$$

where,

B= ml of Fe (II) solution used to titrate blank

S= ml of Fe (II) solution used to titrate sample

12/4000= mill equivalent weight of C in grams

b. calculating percent of organic matter (OM)

% of OM = %C * 1.72

5. ESTIMATION OF POTASSIUM AND SODIUM :

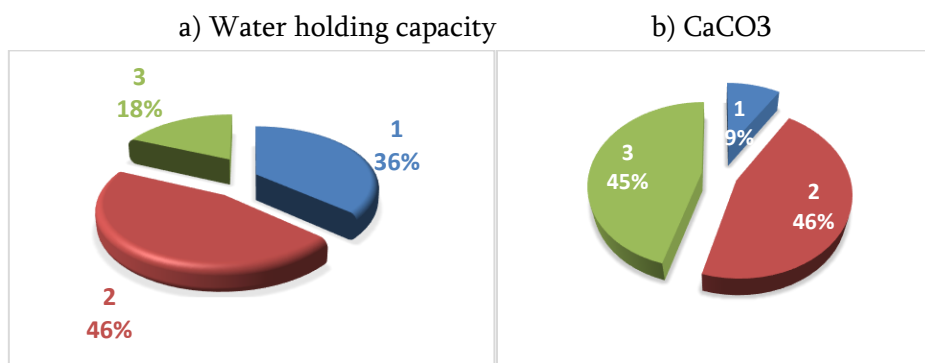
Weight 5g of sample in 25ml of neutral ammonium acetate solution. shake it for 5 min. Feed the filtrate into the atomizer of flame the photometer. For standard curve take the 1000 ppm solution of K and Na for estimation of potassium and sodium respectively and dilute the stock solution 20 times to get 50 ppm of K solution. Take the reading by feeding solution of different concentrations.

III. RESULT AND DISCUSSION

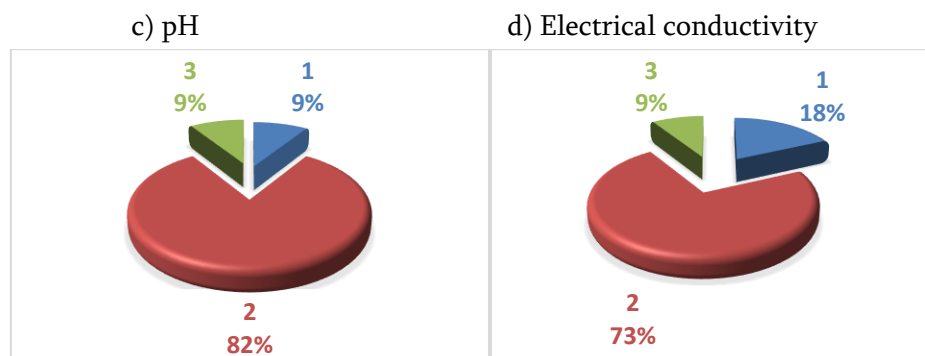
Number of parameters were studied are as follows

Sample no.	% of Moisture	% CaCO ₃	pH	E.C. in Mhos/cm-1	%OC	%OM	KKg/hc	Na kg/hc	%Ca	%Mg
1	135	10	8.22	0.92 X 10 ⁻³	2.79	4.80	333.76	246.4	1.66	2.82
2	145.24	13.8	8.1	0.27 X 10 ⁻³	2.56	4.40	174.72	327.04	1.57	2.64
3	117.30	16.8	7.42	0.38 X 10 ⁻³	3.00	5.17	192.64	259.84	1.6	2.64
4	105.43	0.6	8.31	0.30 X 10 ⁻³	3.00	5.17	212.8	268.8	1.1	0.75
5	100.67	11.6	7.35	0.34 X 10 ⁻³	3.57	6.14	172.48	152.32	1.44	2.24
6	110.52	16.4	6.3	0.19 X 10 ⁻³	3.36	5.26	176.96	159.04	1.53	1.53
7	118.44	10	8.27	0.45 X 10 ⁻³	3.39	6.23	248.64	219.52	1.66	2.46
8	120.50	4.4	7.53	0.20 X 10 ⁻³	2.82	4.85	192.64	201.6	0.86	1.42
9	129.35	16.2	8.4	0.67 X 10 ⁻³	3.27	5.62	203.84	185.92	0.92	1.82
10	127.94	9.4	8.61	0.65 X 10 ⁻³	2.82	4.85	201.6	206.08	0.94	2.50
11	110.21	8	8.32	0.31 X 10 ⁻³	3.00	5.32	421.12	383.04	0.64	2.04

Graphical representation of calculated parameter as follow:



WHC 18% sample highest value (130-150%)45% samples show strongly calcareous



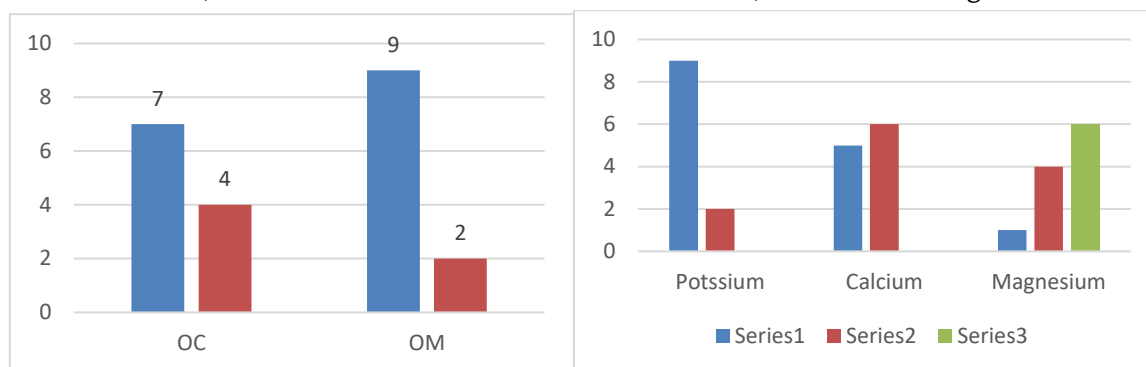
9%, 82%, 95 sample shows normal(acidic) 18 sample shows low amount of salt

and above the normal range (alkaline) respectively

73% sample shows normal range, 9% sample shows H.C.

e) OC and OM

f) % K, % Ca, %Mg



OC- 2.56-3.57%

Potassium- 152-383.04 Kg/

OM- 4.40-6.14% Calcium- 0.86-1.66%

Magnesium- 0.75-2.86%

IV. CONCLUSION

Out of 11 samples, 5 samples show 45% moderately calcareous behaviour. 5 samples show 45% strong calcareous due to accumulation and precipitation of CaCO_3 in semi-arid condition. WHC shows optimum level range from 100.67-145.27 which is high due to high Na content. pH in this area shows normal range i.e. 6.5-8.5. The nature of most of the soil is slightly alkaline due to process of accumulation of CaCO_3 . EC in this region are found satisfactory. 73% sample shows normal EC. OM and OC are found in optimum level, high level of OM is supportive for the microbial activity of soil. In present study amount of available K in the soil present satisfactory range which is very essential nutrient for plant. Ca and Mg are required trace quantity for the plant. In present study the level of both cations is up to the marks. out of 11 samples 5 samples of soil show low level of Ca, level of mg is somewhat high, 55% of sample show Mg level above the desirable level, which causes faster rate of photosynthesis.

From the above result it concludes that the development of salinity or sodicity soil is in progress but all other Physico-chemical parameters are found in optimum level and hence soil in Rama (Sahur) area is good for the farming.

V. ACKNOWLEDGEMENT

The author is thankful to HOD Department of Chemistry G.V.I.S.H. Amravati, for their valuable support and co-operation.

VI. REFERENCES

[1]. M. Akter, S. Sultana, A. Chowdhary, M. Chowdhury, (2010), In J Biores, 2(9), 25-31.

- [2]. S. Paudel, J. Sah, (2003), Him. J. sell (2), 107-110.
- [3]. T. Bitrus, Wokhe, Y. Mohammed, M. Paschal Chima, (2013) Evaluation of Physicochemical properties of Irrigated Soil Journal of Natural Sciences Research,9, 135.
- [4]. K. Chaudhary (2013),Advances in Applied Science Research, 4(6), 246-248.
- [5]. P. Jain, D. Singh, (2014). Scholarly Journal of Agricultural Science,4(2), 103-108.
- [6]. S.Sumithra, C.Ankalaiah, J. Rao, R. Yamuna, India International Journal of Geology, Earth and Environmental Sciences (2013), (2), 28-34.
- [7]. S. Paudel, J.Sah, (2003). J. Sci. 1(2), 107 110.
- [8]. H. Solanki, N. Chavda, (2012), Life sciences Leaflets, 8, 62-68.
- [9]. B. Adelekan, A. Alawode (2011), J. Appl.Biosci. 40, 7227-2737.
- [10]. M. Anikwe, K. Nwobodo, (2001),BiosourTechnol, 83(3), 241-250.
- [11]. C. Nyle, R. Ray, (1999) The Nature and Properties of Soils. 12th Ed. United States of America, 743-785.



Process Optimization of Plant Based Silver Nanoparticle Synthesis using Response Surface Methodology

Harsha Sonaye^{*1}, Vidya Sabale²

¹Dadasaheb Balpande College of Pharmacy, Besa, Nagpur-440037, Maharashtra, India

²Taywade College of Pharmacy, Koradi, Nagpur-441111, Maharashtra, India

ABSTRACT

Nanoparticle research has sparked a lot of interest in recent decades, particularly in terms of developing more efficient techniques to synthesise them. The aim of the research is to study the plant mediated synthesis of silver nanoparticles using silver nitrate and plant extract concentration as a reducing agent. To get a high yield, processing parameters were statistically optimised. Response Surface Methodology was used to explore AgNPs and optimization (RSM). Based on the synthesis of AgNPs, which was measured using a UV-vis spectrophotometer at 390nm, the results suggest that all three parameters evaluated (AgNO₃, plant extract concentration, and stirring time) contributed considerably to the production. UV-vis analysis was used to characterize the synthesised AgNPs under optimal conditions.

Keywords: Silver nanoparticle, Response Surface Methodology, *Gloriosa superba*

I. INTRODUCTION

The creation of experimental processes for the synthesis of nanoparticles of different sizes, shapes, and controlled dispersity is a significant aspect of nanotechnology[1]. In recent days, nanotechnology is one of the most exciting/well-known development technologies that deal with materials of scale between 1-100 nm[2]. Due to the efficacy of different metal nanoparticles against many pathogenic microorganisms, such as bacteria[3], fungi[4], algae, yeast[5], and viruses[6], a vast potential has been recognized in nanotechnology over the past decade. There are several drawbacks to microbe-mediated synthesis methods, such as the identification of potent strains, the maintenance of aseptic conditions for abundant microorganism growth, chances of infection, contamination[7]. Biological synthesis of microorganism-using nanoparticles are relatively expensive than plant-using[8,9,10]. Above all, the method of microbial synthesis is very time-consuming[10] and takes around 2-3 days for a potent strain to grow and another 1-2 days for nanoparticle synthesis and purification. Scientists have therefore turned their interest towards plant systems for the manufacture of biocompatible nanomaterials. Approximately 200 plants belonging to different families have been tested for their ability to synthesise different metal nanoparticles using this green chemistry method, including silver[11,12,13,14], gold[15,16,17], iron[18], palladium[19,20,21], lead[22], copper[23,24], magnesium[25], zinc[26] and alginate[27]. AgNPs were, however, developed to be simplest since they have

fair antimicrobial activity against different microorganisms. Nanostructured materials are commonly used in the food industry[28], in dentistry[29], in the treatment of waste water[30], in electrochemical sensors[31], and medicines[32]. Due to its specific characteristics, the applications of silver nanoparticles have been widely reported in the diagnostic[33], antibacterial[34], conductive[35] and optical[36] groups. As stabilizing and reducing agents for the synthesis of AgNPs, biomolecules such as proteins, amino acids, enzymes, flavonoids, and terpenoids from many plant extracts have been used [37].

There has been a significant rise in study into the synthesis and characterisation of AgNPs. AgNPs of various sizes and shapes have diverse plasmon resonance bands, resulting in a variety of coloured suspensions. Since high yield nanoparticle synthesis and size analysis have been a critical focus of intense research many researchers have reported on the synthesis of AgNPs, such as spherical AgNPs.[38] and the creation of triangular AgNPs [39].

Aside from that, there has been a lot of research on optimising process parameters in AgNPs synthesis, primarily to improve product stability and yield, especially in bulk production; for example, stirring time has been discovered to affect surface plasma resonance (SPR) [40]. Saat et al. [41] mention the typical one-factor-at-a-time (OFAT) strategy is a missed interaction between several variables in order to precisely assess the probable interactions accurately. The design of experiments (DOE) and a face centred central composite design (FCCCD) must be used under response surface methodology (RSM) can be a powerful tool for improving complex processes.

However, to the best of our knowledge, no published approach for enhancing the yield of spherical AgNP synthesis using statistical optimization techniques has yet been reported in the literature. We reported an optimal process for AgNPs manufacture by adjusting several parameters such as AgNO₃ and plant extract concentrations, as well as stirring time, in this study. The DOE and data analysis were both done with statistical computer tools. The optimum levels of the three specified process parameters were determined using a three-level FCCCD with duplicate centre points. UV-vis analyses was used to characterise the AgNPs that were formed.

II. MATERIAL AND METHOD

2.1 AgNPs synthesis

Typically the experiment begins with 90ml of 2mM AgNO₃ was added in 10µg/ml ethanolic extract of *Gloriosa superba*. The reduction process begins with the colour change and the solution turns dark brown.[42] The amount of extract entrapped in prepared silver nanoparticles was estimated by the centrifugation method. 1gm of silver nanoparticles was taken and suspension was sonicated using a bath sonicator for 20minutes. Later this solution was placed in a centrifugation tube and centrifuged at 14000 rpm for 30minutes. 0.5ml of supernatant was withdrawn, diluted and absorbance was measured to determine yield using a UV spectrophotometer at 590nm [43, 44].

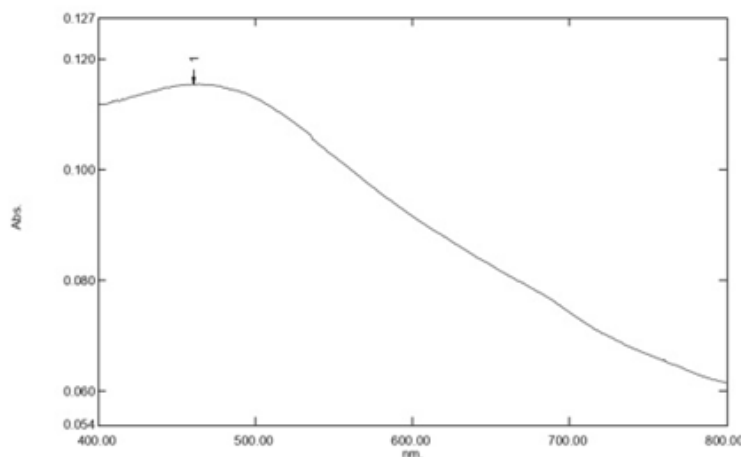


Figure1: UV-vis spectra of AgNP.

The size of interest is 115 nm of AgNPs represented by absorbance from 590 nm, insert visual dark brown colour of AgNPs solution.

2.2 Statistical optimization of process parameters for AgNPs synthesis

To optimize the synthesis parameter of AgNPs with respect to high yield, DOE and data analysis was carried out with the help of a statistical software Design Expert (Version 7.0.0). According to the DOE, with three parameters (AgNO_3 , extract concentration and stirring time) and at three levels, FCCCD suggested 17 experimental runs. The response is represented by yield which is the estimated area under the wavelength 590 nm

2.3 Characterization of AgNPs

AgNPs have unique optical properties as they are extraordinarily efficient at absorbing and scattering light. Spherical AgNPs have Surface Plasmon Resonance (SPR) at the wavelength of 590nm. AgNPssynthesis that gave highest yield at 590 nm was characterised via UV-vis analysis.

III. RESULT AND DISCUSSION

3.1 Statistical process optimization of AgNPsproduction using response surface methodology (RSM)

A central composite design under Response Surface methodology (RSM) was employed to identify the most prominent interaction between significant parameters for high yield AgNPs production and to develop a system model with their feasible interaction within a minimum number of experimental runs[45]. RSM is a combination of mathematical and statistical techniques that could be used to appropriate and optimise a system from several responses and different types of experimental runs[46].shows the FCCCD of three parameters along with AgNPs yield as the response. The highest response, 81.23was found at the centre point (run11), whereas the lowest response 23.05 was found at run 1

Table 1: The CCD design of three variables along with AgNPs yield as the response

Run	A	B	C	Yield
1	160	10	1	23.05
2	120	15	1.5	35.08
3	120	15	2.34	53.50
4	120	6.59	1.5	25.91
5	80	20	1	47.74
6	120	23.41	1.5	37.98
7	120	15	1.5	35.39
8	80	20	2	76.81
9	160	10	2	32.88
10	80	10	1	43.75
11	52.73	15	1.5	81.23
12	120	15	1.5	34.48
13	187	15	1.5	30.99
14	160	20	2	42.02
15	120	15	0.66	26.75
16	120	15	1.5	34.48
17	120	15	1.5	34.78
18	80	10	2	70.47
19	120	15	1.5	35.39
20	160	20	1	66.18

A three level factorial design was used to achieve all possible combinations of input variable that are able to optimize the response within the region of 3-D space. According to the analysis of variance (ANOVA), the quadratic model was found to be significant at p value less than 0.05. Some values were not significant; hence model reduction was done using response methodology (RSM). The values are presented in Table 2. Fisher's statistical analysis proved the adequacy of the developed model.

The second order regression equation presented the dependence of a high yield of AgNP synthesis on plant extract conc, stirring time and silver nitrate concentration during reaction. The relation between the selected parameters and each response was established using a second order polynomial equation in terms of coded factors.

$$\text{Sqrt(AgNPs yield)} = -11.65 * A + 6.07 * B + 16.33 * C + 9.00 * A^2 + 0.46 * B^2 + 3.35 * C^2 + 5.24 * A * B - 8.77 * A * C - 3.96 * B * C$$

Equation 1

The statistical equation 1, indicates that the positive values have a synergistic effect on the response (AgNP yield) and the negative values represents an antagonistic effect on the response, where "A" is plant extract concentration, "B" is stirring time and "C" is AgNO₃ concentration. In this equation, the coefficient of

one factor presented the effectiveness of this particular factor. To analyse the AgNPs yield through the coefficient values from the equation, it is clear that silver nitrate concentration gives a higher positive effect as compared to the other parameters. Values of “Prob>F” was less than 0.05 indicating that the model terms were significant, where a lower probability value represents a higher significance for the regression model and in this model p- value < 0.0005. The F-test value presents how the mean square of the model compares to the mean square of the residuals. The model F- test value of 10.98 implies that model is significant and suggesting that there is only a 0.04% chance that a “Model F value” this large could occur due to noise. In this model A, B, C A², AC are significant model terms.

To check the fitness of the model, the coefficient of determination (R²) was used. An R² value close to 1 implies the better correlation between experimental and predicted responses. Thus, it is important for a good model R² to be within the range of 0-1, and the closer it is to 1, the more fit the model is deemed to be [47]. In this model the correlation coefficient (R²) value of 0.9081 is in a reasonable agreement with the adjusted determination coefficient (R²adj) value of 0.8253 in terms of a high significance of model. The adequate precision measures the signal to noise ratio. A ratio greater than 4 is desirable and values less than 4 is considered appropriate for the desired model. In the developed model ratio of 11.138 indicates an adequate signal. This model can be used to navigate the design space.

A 3D surface response plot is the graphical representation of the regression equation obtained from the established model, which is used for (1) to study the interaction among the parameters and (2) to define the optimum condition of each parameter for maximum AgNPs yield production. Further, the plot is based on the function of two variables while the third variable is at its optimum condition. Additionally, the elliptical or saddle shape plot will be obtained when there are a perfect interaction among independent variables [48]. Figure 2 and 3 demonstrate the 3D plot of AgNPs yield using the interactions of all three variables used. Figure 2, when both extract concentration and AgNO₃ concentration increase, the yield increases. Next, Figure 3, 3D response surface curve were suggesting that there were optimized conditions of AgNO₃ concentration effect on AgNPs yield and the stirring time effect on yield production is almost constant. The surface plot indicates that the optimal condition of high yield AgNPs depends on extract concentration and AgNO₃ concentration and it was clearer in the perturbation plot discussed further on.

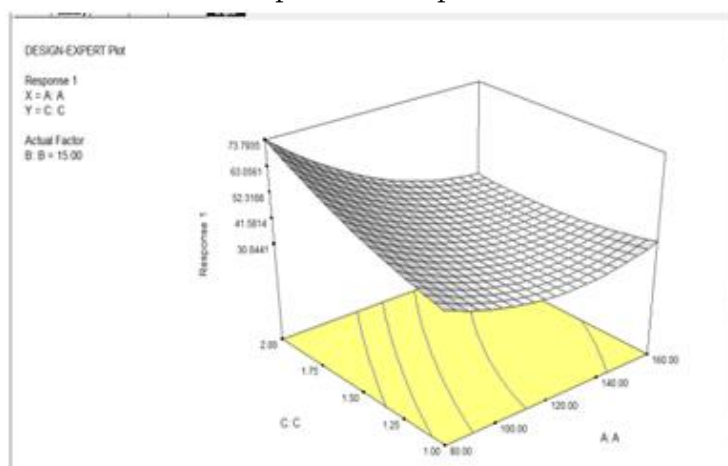


Figure.2. A 3D interaction plot of AgNPs yield, interaction of plant extract concentration and AgNO₃.

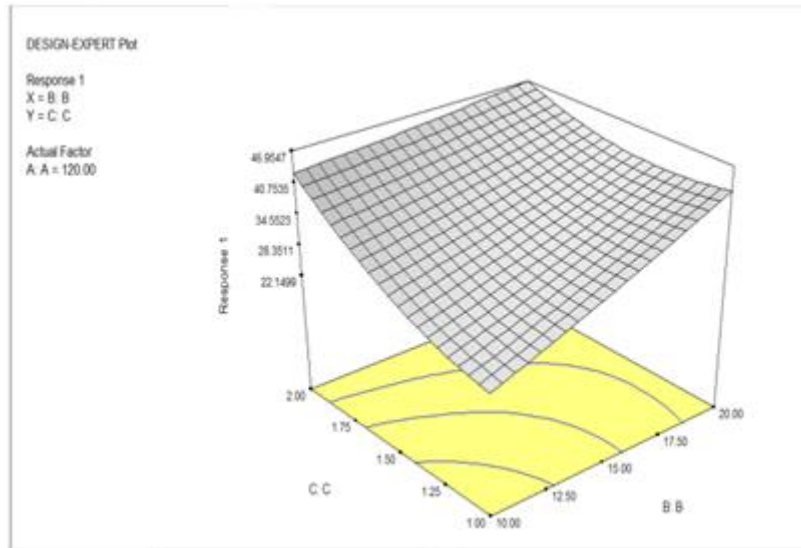


Fig.3. A 3D interaction plot of AgNPs yield, interaction of stirring time and AgNO₃.

Additionally, interactions between the variables can also be clearly seen from the perturbation plot in figure 4, which came up by default from the design expert software and perturbation theory using mathematical methods for finding an optimized condition to solve the problem. The reference point in figure 4 is the interaction of the line, where X=0.00 and the actual conditions at the side point. Extract concentration as A and stirring time as B has a linear relation. Based on the statistical and perturbation plot analysis, the optimum production condition for AgNPs for a developed model is 120µg/ml extract concentration, 15 min stirring time and 1.5 mM AgNO₃ with 35.08 % of AgNPs yield production. It can be seen that AgNO₃ concentration is the most prominent variable of the model obtained from equation 1.

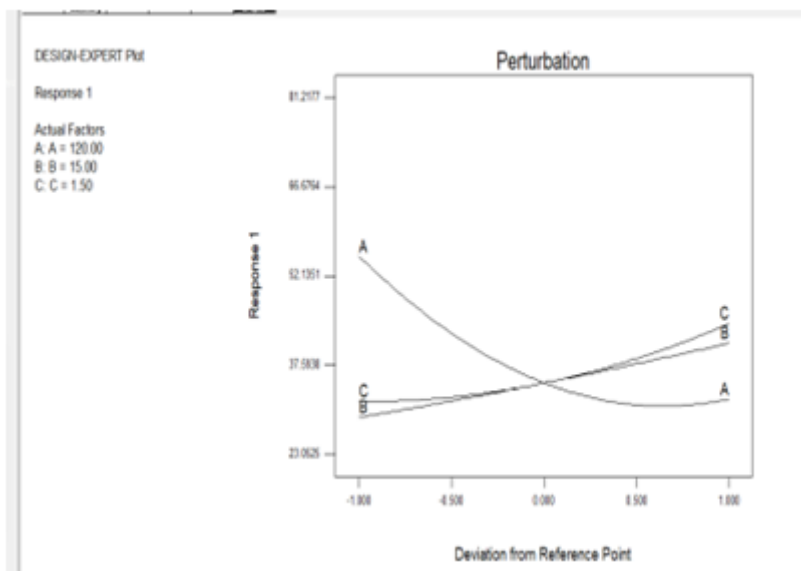


Figure.4. Perturbation plot of AgNPs

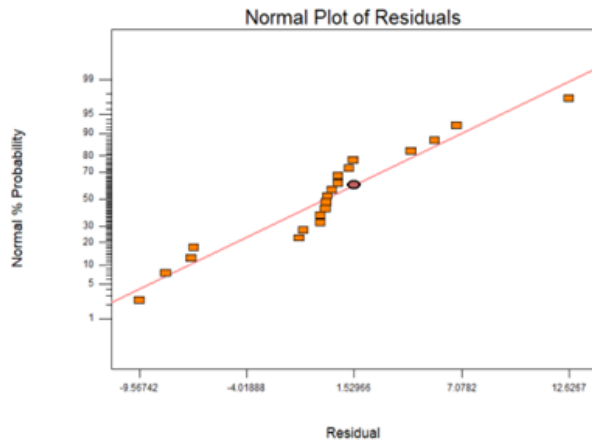


Figure. 5 Normal plot of residual Yield optimization

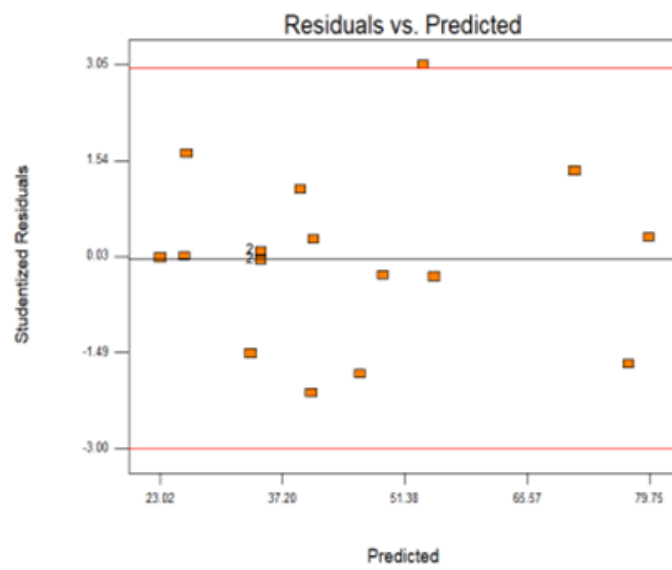


Figure.6. Normal probability plot of residuals vs. predicted

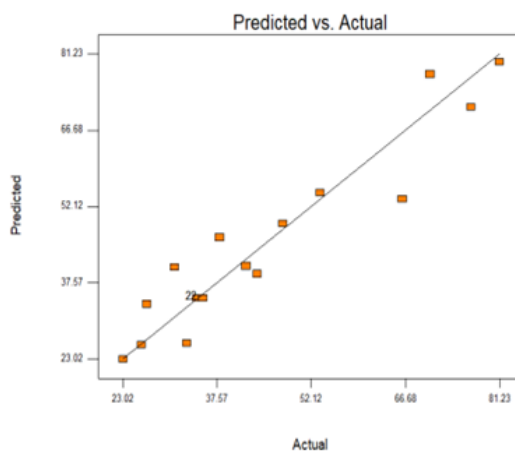


Figure.7. Relationship between predicted and experimental values of Ag NP yield

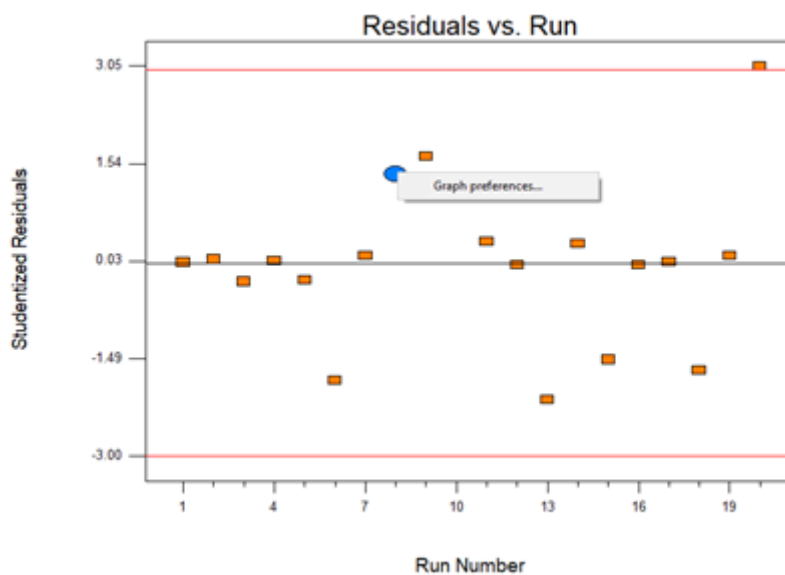


Figure.8.residuals vs. observation order

3.2 Model validation using residuals

Residual analysis was executed owing to achieve close approximation of the real system. Residuals (r_i) were obtained from the following regression;

$$r_i = Y_i \text{ observed} - Y_i \text{ predicted} \text{----- Equation 2}$$

Where, r is residuals, y is response and i is observation. The value of all observation residuals used in the residual plot containing (i) normal plot of residuals, ii) residuals vs predicted plot and iii) residuals vs observation order plot. The normal plot of residuals, residuals vs predicted plot and residuals vs observation order plot of the response for high yield AgNPs production are presented in figure 5,6 and 8 respectively, which is the most important diagnostic for the model. According to [49] a linear relationship proved normality in the error terms and our data showed no signs of problems, which indicate that error follow a normal distribution and support the experimental model. Further, there is a random scatter pattern found from the residuals vs predicted plot in figure 6. The residuals are well distributed in positive and negative residuals in the range of $-2 < r_i < +2$ (r_i is actual residuals). However, there is no pattern that follows the residuals vs observation order plot in figure 8, which means that all residuals are not correlated with each other as an effect of time related factors. The developed model is acceptable and there is no purpose to infer any violation of the objectivity or constant variance hypothesis.

IV. CONCLUSION

In this study we documented a *Gloriosa superba* mediated AgNPs synthesis and optimized different parameters in the reaction medium to develop a high yield of AgNPs synthesizing techniques. Subsequently, the DOE employed FCCCD under RSM was used for the complex process optimization of three important parameters. The optimized conditions for high yield of 81.23% AgNP synthesis are 52.73 $\mu\text{g/ml}$ of plant extract

concentration, 1.5mM AgNO₃ with 15 mins stirring time, and it is believed that these parameters are highly suitable for in bulk production of spherical AgNPs with diameter of 115 nm.

V. REFERENCES

- [1]. Dubey M., Bhadauria S, Kushwah BS, Green Synthesis of Nanosilver Particles from Extract of *Eucalyptus Hybrid*(Safeda) Leaf. *Digest Journal of Nanomaterials and Biostructures* 2009; 4(3); 537 – 543
- [2]. Okafor F, Janen A, Kukhtareva T, Edwards V, Curley M, Green synthesis of silver nanoparticles, their characterization, application and antibacterial activity, *Int J Environ Res Public Health* 2013; 10; 5221–5238.
- [3]. Kim JS, Antimicrobial effects of silver nanoparticles, *Nanomedicine Nanotechnology, Biol Med* 2007; 3(1); 95-101.
- [4]. Kim SW, Jung JH, Lamsal K, Kim YS, Min JS, and Lee YS, Antifungal effects of silver nanoparticles (AgNPs) against various plant pathogenic fungi, *Mycobiology* 2012; 40(1); 53-58.
- [5]. Dorobantu LS, Toxicity of silver nanoparticles against bacteria, yeast, and algae, *J Nanoparticle Res* 2015; 17(4).
- [6]. Khandelwal N, Kaur G, Kumar N, Tiwari A, Application of silver nanoparticles in viral inhibition: A new hope for antivirals, *Dig J NanomaterBiostructures* 2014; 9(1); 175-186.
- [7]. Khan T, Yasmin A, Townley HE, An evaluation of the activity of biologically synthesized silver nanoparticles against bacteria, fungi and mammalian cell lines, *Colloids and Surfaces B Biointerfaces* 2020. <https://doi.org/10.1016/j.colsurfb.2020.111156>
- [8]. Dhillon GS, Bra SK, Kaur S, Verma M, Green approach for nanoparticle biosynthesis by fungi: current trends and applications. *Crit Rev. Biotechnol* 2012; 32; 49–73.
- [9]. Luangpipat T, Beattie IR, Chisti Y, Haverkamp RG, Gold nanoparticles produced in a microalga. *J Nanopart Res* 2011; 13; 6439–6445.
- [10]. Narayanan KB, Sakthivel N, Biological synthesis of metal nanoparticles by microbes. *Adv. Colloid Interface Sci.* 2010; 156; 1–13.
- [11]. Bar H, Bhui DK, Sahoo GP, Sarkar P, De SP, Misra A, Green synthesis of silver nanoparticles using latex of *Jatropha curcas*. *Colloids Surf. A* 2009; 339; 134–139.
- [12]. Krishnaraj C., Jagan EG, Rajasekar S, Selvakumar P, Kalaichelvan PT, Mohan N., Synthesis of silver nanoparticles using *Acalypha indica* leaf extracts and its antibacterial activity against waterborne pathogens. *Colloids Surf. B Biointerfaces* 2010; 76, 50–56.
- [13]. Kumar V, Yadav SC, Yadav SK, *Syzygium cumini* leaf and seed extract mediated biosynthesis of silver nanoparticles and their characterization. *J. Chem. Technol. Biotechnol.* 2010; 85;1301–1309.
- [14]. Sathishkumar M, Sneha K, Won S, Cho CW, Kim S, Yun YS, Cinnamon *zeylanicum* bark extract and powder mediated green synthesis of nano crystalline silver particles and its bactericidal activity. *Colloids Surf. B Biointerfaces* 2009; 73, 332–338.

- [15]. Ghodake GS, Deshpande NG, LeeYP, Jin ES, Pear fruit extract-assisted room temperature biosynthesis of gold nanoplates. *Colloids Surf. B Biointerfaces* 2010; 75; 584–589.
- [16]. Song JY, Kim BS, Rapid biological synthesis of silver nanoparticles using plant leaf extracts. *Bioprocess. Biosyst. Eng.* 2009; 32; 79–84.
- [17]. Song JY, Jang HK, Kim BS, Biological synthesis of gold nanoparticles using *Magnolia kobus* and *Diopyros kaki* leaf extracts. *Process Biochem.* 2009; 44; 1133–1138.
- [18]. Njagi EC, Huang H, Stafford L, Genuino H, Galindo HM, Collins JB, Hoag GE, Suib S., Biosynthesis of iron and silver nanoparticles at room temperature using aqueous sorghum bran extracts. *Langmuir* 2011; 27; 264–271.
- [19]. Petla RK, Vivekanandhan S, Misra M, Mohanty AK, Satyanarayana N, Soybean (*Glycine max*) leaf extract based green synthesis of palladium nanoparticles. *J. Biomater. Nanobiotechnol* 2012; 3; 14–19.
- [20]. Roopan SM, Bharathi A, Kumar R, Khanna VG, Prabhakarn AA, Roopan SM, Bharathi A, Kumar R, Khanna VG, Prabhakarn A, Acaricidal, peel as biomaterial for the reduction of palladium salts into nanoparticles. *Colloids Surf. B Biointerfaces* 2012; 92; 209–212.
- [21]. Yang X, Li Q, Wang H, Huang j, Lin L, Wang W, Green synthesis of palladium nanoparticles using broth of *Cinnamomum camphora* leaf. *J. Nanopart. Res* 2010; 12; 1589–1598.
- [22]. Joglekar S, Kodam K., Dhaygude M, Hudlikar M, Novel route for rapid biosynthesis of lead nanoparticles using aqueous extract of *Jatropha curcas* L. latex. *Mater Lett* 2011; 65; 3170–3172.
- [23]. Lee HJ, Song JY, Kim BS, Biological synthesis of copper nanoparticles using *Magnolia kobus* leaf extract and their antibacterial activity. *J. Chem. Technol. Biotechnol* 2013; 88, 1971–1977.
- [24]. Valodkar M, Nagar PS, Jadeja RN, Thounaojam, MC, Devkar RV, Thakore S, Euphorbiaceae latex induced green synthesis of non-cytotoxic metallic nanoparticle solutions: A rational approach to antimicrobial applications. *Colloids Surf. A* 2011; 384, 337–344.
- [25]. Kalidindi SB; Jagirdar BR, Highly Monodisperse Colloidal Magnesium Nanoparticles by Room Temperature Digestive Ripening, *Inorg. Chem.* 2009; 48(10); 4524–4529.
- [26]. Koupaei MH, Shareghi B, Saboury AA, Davar F, Semnani A and Evini M, Green synthesis of zinc oxide nanoparticles and their effect on the stability and activity of proteinase K, *RSC Adv* 2016; 6(48); 42313–42323.
- [27]. Paques JP, Linden EV, Rijn GJ and Sagis LC, Preparation methods of alginate nanoparticles, *Adv. Colloid Interface Sci* 2014; 209; 163–171.
- [28]. He X, Deng H, Hwang H, The current application of nanotechnology in food and agriculture, *J. Food Drug Anal* 2019; 27; 1–21.
- [29]. AlKahtani RN, The implications and applications of nanotechnology in dentistry: a review, *Saudi Dent. J* 2018; 30; 107–116.
- [30]. Hashima N, Paramasivamb M, Tanb JS. Green mode synthesis of silver nanoparticles using *Vitis vinifera*'s tannin and screening its antimicrobial activity / apoptotic potential versus cancer cells, *Materials Today Communications*, 2020; 25; 101511.

- [31]. Luo X, Morrin A, Killard AJ, SmythMR, Application of nanoparticles in electrochemical sensors and biosensors, *Electroanalysis* 2006; 319–326.
- [32]. Salata OV, Applications of nanoparticles in biology and medicine, *J Nanobiotechnology* 2004; 1–16.
- [33]. Maldonado RM, Sotelo J, Pineda B, Cruz VP, Angel AS, Pedro NY, López ER, Application of nanoparticles on diagnosis and therapy in gliomas, *Biomed Res Int* 2013 ; 1–20.
- [34]. Sharma VK, Yngard RA, Lin Y, Silver nanoparticles: green synthesis and their antimicrobial activities, *Adv Colloid Interface Sci* 2009; 145; 83–96.
- [35]. Alshehri AH, Jakubowska M, Młoziniak A, Horaczek M, Rudka D, Free C, Carey JD, Enhanced electrical conductivity of silver nanoparticles for high frequency electronic applications, *ACS Appl Mater Interfaces* 2012; (4); 7007–7010.
- [36]. Mahmudin L, Suharyadi E, Utomo ABS, Abraha K, Optical properties of silver nanoparticles for surface plasmon resonance (SPR)-Based biosensor applications, *J Mod Phys* 2015; 6; 1071–1076.
- [37]. Khan T, Yasmin A, Townley HE, An evaluation of the activity of biologically synthesized silver nanoparticles against bacteria, fungi and mammalian cell lines, *Colloids and Surfaces B: Biointerfaces* 2020.
- [38]. Kim JS. Antimicrobial effects of silver nanoparticles. *Nanomedicine: Nanotechnology, Biology and Medicine*, 2007; 3(1); 95-101.
- [39]. Mansouri SS and Ghader S, Experimental study on effect of different parameters on size and shape of triangular silver nanoparticles prepared by a simple and rapid method in aqueous solution. *Arabian Journal of Chemistry*, 2009; 2(1); 47-53.
- [40]. Balavandy SK. Stirring time effect of silver nanoparticles prepared in glutathione mediated by green method. *Chemistry Central Journal*, 2014; 8(1); 11.
- [41]. Saat MN. Effects and optimization of selected operating variables on Laccase production from *Pycnoporus Sanguineus* in stirred tank reactor. *International Journal of Chemical Reactor Engineering*, 2012; 10(1).
- [42]. Chowdhury S, Yusof F, Faruck MO, Sulaiman N. Process Optimization of Silver Nanoparticle Synthesis using Response Surface Methodology. *Procedia Engineering* 148(2016) 992 – 999.
- [43]. Gurunathan, S., et al., Biosynthesis, purification and characterization of silver nanoparticles using *Escherichia coli*. *Colloids and Surfaces B: Biointerfaces*, 2009. 74(1): p. 328-335.
- [44]. Noroozi, M., et al., Green formation of spherical and dendritic silver nanostructures under microwave irradiation without reducing agent. *International journal of molecular sciences*, 2012. 13(7): p. 8086-8096.
- [45]. Salihu, A., et al., Optimization of lipase production by *Candida cylindracea* in palm oil mill effluent based medium using statistical experimental design. *Journal of Molecular Catalysis B: Enzymatic*, 2011. 69(1): p. 66-73.
- [46]. McDonald, D.B., et al., Global and local optimization using radial basis function response surface models. *Applied Mathematical Modelling*, 2007. 31(10): p. 2095-2110.

- [47]. Reddy, L., et al., Optimization of alkaline protease production by batch culture of *Bacillus* sp. RKY3 through Plackett–Burman and response surface methodological approaches. *Bioresource Technology*, 2008. 99(7): p. 2242-2249
- [48]. Muralidhar, R., et al., A response surface approach for the comparison of lipase production by *Candida cylindracea* using two different carbon sources. *Biochemical Engineering Journal*, 2001. 9(1): p. 17-23.
- [49]. Draper, N.R. and H. Smith, *Applied regression analysis* 2014: John Wiley & Sons



Preparation and Structural Characterization of Polyaniline Doped Zinc Oxide Nanocomposite

Kamlesh R. Banarse¹, Pritesh J. Jadhao¹, S. P. Yawale¹, S.S. Yawale², D.R.Bijwe³

¹Govt. Vidarbha Institute of Science and Humanities, Amravati-444604, Maharashtra, India

²Pre-IAS Training Centre, Amravati, Maharashtra, India

³G.S.Tompe Arts, Commerce & Science College, Chandur Bazar, Amravati-444704, India

ABSTRACT

Polyaniline doped with Zinc Oxide (ZnO) nanocomposites are prepared by using chemical oxidative polymerization method. Preparation is done in aqueous medium with ammonium persulphate as an oxidant at room temperature. ZnO with 25 wt% is used for preparing nanocomposite. Structural characterization of the prepared samples was done by X-ray diffraction (XRD) and scanning Electron Microscopy (SEM) technique. Agglomeration of the crystals were seen. These materials are polycrystalline in nature. Amorphous structure with very fine particles is seen. ZnO nanoparticles are seen which are deposited on surface of PANI. A nanocomposite show greater crystallinity due to addition of ZnO in PANI matrix as compared to pure PANI. The crystallite size of PANI-ZnO nanocomposite was estimated from X-ray line broadening using Scherer's equation and found around 30 to 60 nm. The X-ray diffraction pattern shows that degree of crystallinity of PANI-ZnO composite is higher than that of PANI.

Keywords: Polyaniline, ZnO, XRD, SEM

I. INTRODUCTION

In recent years, there has been developing interest in research on conducting polymer nanostructures. Conducting polymers show different promising applications in various fields, for example in transistors, sensors, actuators/ muscles, [1-2]. The blend of the segments in a polymer composite outcomes in interesting mechanical and thermal properties that are infeasible to be accomplished with any material. It has advanced applications in industries aerospace, shipbuilding, automotive, military, building and construction industries. Among group of conducting polymers, polyaniline has incredible solidness in its doped, de-doped form. It has an extraordinary applications like anticorrosion coatings, [3], synthetic detecting, batteries [4], electromagnetic impedance protecting, microelectronics, etc. [5-6], Polymer composites have improved optoelectronic properties due to the expansion of fillers. Polymerization of polyaniline-graphene oxide nanocomposites showed enhanced electrical conductivity of 9.2 S/cm [7]. The conductivity of SnO₂/PANI nanocomposites is found to be 1.75×10⁻¹S/cm by some researchers [8]. Maximum conductivity of PANI/SnO₂

nanocomposite was found to be 6.4×10^{-3} s/cm at 9 wt%. Liu *et al* [9] prepared TiO₂/PANI solar cells. The composite of (ZnO/PANI) was found electrically responsive to humidity in a closed chamber.

In the present work, nanoparticles of polyaniline and polyaniline-ZnO nanocomposites are prepared by chemical oxidative polymerization method. Their structural characterization is done by scanning electron microscopy technique and x-ray diffraction technique. We are getting crystalline nature of the nanocomposite with agglomeration of crystals over polymer and nanosized particles in nanocomposite.

II. PREPARATION OF MATERIALS

2.1 Preparation of Polyaniline (PANI) nanoparticles:

In this process polyaniline nanocomposite was synthesized by chemical oxidative polymerization method [10]. 2.59 gm of aniline hydrochloride was dissolved in 50 ml distilled water in a volumetric flask. Similarly 5.71 g of ammonium persulfate (APS) was dissolved in 50 ml distilled water kept for 1 h. at room temperature (303 K), During additions, mixture is stirred for 2 hr. Then resulting dark green precipitate of PANI was filtered and washed with HCl and acetone. Obtained precipitate was kept in oven to dry for about 8 hrs. at 50-60 °C.

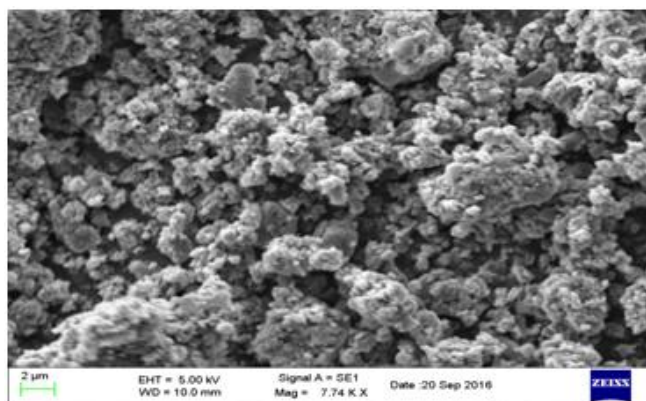
2.2 Preparation of Polyaniline-Zinc Oxide Nanocomposite:

In the present work polymer composite with ZnO was prepared by *in-situ* polymerization method [11] with Zinc Oxide (ZnO) 20 wt.%. ZnO nanoparticles were dispersed into the APS solution of 50 ml DD water and stirred for 1 hr. Aqueous solution of 2.59 g of aniline hydrochloride in 50 ml DD water added slowly in APS under vigorous stirring for 2 h. The resulting dark green PANI-ZnO precipitate was filtered and washed with HCl and acetone. Then kept in oven for about 8 h. at 50-60 °C. In this way PANI-ZnO nanoparticles were formed.

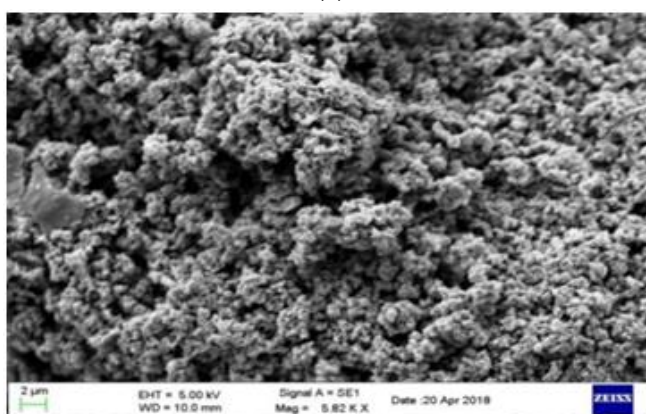
III. CHARACTERIZATION

3.1 Scanning Electron Microscopy (SEM):

The SEM micrographs of all the samples of PANI and ZnO doped with PANI are shown in figure below. From the SEM micrographs of the film doped with ZnO, it is found that image show certain types of crystallinity may be due to the ZnO. Morphology of PANI doped with ZnO shows further improvement of surface morphology. Nanoparticles formed are not of homogeneous size.



(a)



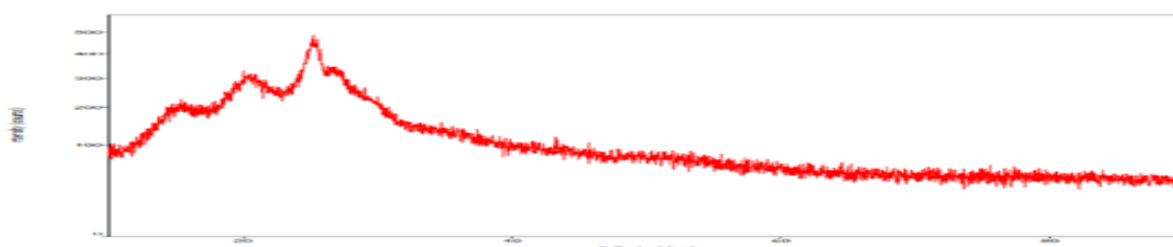
(b)

Fig.: Scanning Electron Microscopy images of (a) PANI (b) PANI+ZnO (20%)

There is agglomeration of crystallites which is clearly seen from Figure. A fine microspheroidal surface was observed with poor matrix. The fine islands in micro meter size are observed with matrix having nano size particles. PANI is completely amorphous in nature whereas PANI-ZnO nanocomposite shows partly crystalline as well as amorphous phase. Nanoparticles were not of homogenous size but of different sizes ranging from 100-250 nm for PANI. These materials are polycrystalline in nature. Particle sizes of PANI-ZnO nanocomposite are found in the range 50 to 340 nm. Amorphous structure with very fine particles is seen. ZnO nanoparticles are seen which are deposited on surface of PANI.

3.2 X-Ray Diffraction Technique (XRD):

The X-Ray diffraction has been used to determine the possible crystallinity in the composite films. The X-ray diffraction was carried out in the 2θ range from 0 to 100° . The XRD spectra of Pure PANI and PANI-ZnO nanocomposites with 25 wt % of ZnO are shown in figure



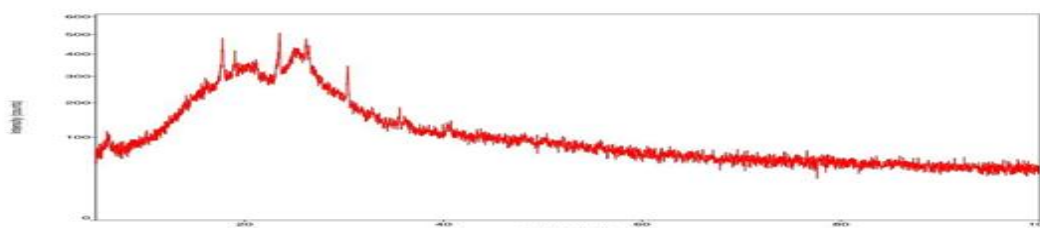


Fig.: X-Ray Diffraction images of PANI and PANI+ZnO (20%)

PANI showed two peaks at $2\theta=20.34^\circ$ with planes of (010) which represents the characteristic distance between the ring planes of benzene rings in adjacent chains or the close contact inter-chain distance and at 25.20° with planes of (200) which represents the scattering from PANI chains at interplanar spacing (12, 13) and very low intensity of the observed peak indicates that the Polyaniline has amorphous nature with low crystallinity.

For to study the effect of doping of ZnO nanoparticles analysis of the position of the XRD peak indicates that there is a shifting in peak's position towards lower 2θ value. These results are in good agreement with the results reported before. The shifting of the peak's position shows that ZnO nanoparticles are incorporating into the PANI matrix [14]. The crystallite size of PANI-ZnO nanocomposite was estimated from X-ray line broadening using Scherer's equation and found around 30 to 60 nm. The X ray diffraction pattern shows that degree of crystallinity of PANI-ZnO composite is higher than that of PANI. This shows that the amorphous nature of PANI may affect the crystallisation of ZnO [15]

IV. CONCLUSION

SEM micrograph shows the partly crystalline behaviour as well as amorphous morphology of Polyaniline doped with Zinc Oxide (ZnO). Nanoparticles formed are not of homogeneous size. Agglomeration of the crystals were seen. These materials are polycrystalline in nature. The surface morphology changes severely from rough to smooth. Also the addition of ZnO shows further drastic improvement of surface morphology of polymer composite. The average size of the particles PANI and PANI-ZnO nanocomposite are found to be range between 200-550 nm, and 100-250 nm respectively.

From the X-Ray diffraction technique it was observed that Polyaniline doped with ZnO indicating the partly crystalline and partly amorphous in nature. The sharp peak observed in PANI-ZnO nanocomposite is due to the presence of ZnO in the nanocomposite. A nanocomposite show greater crystallinity due to the addition of ZnO in PANI matrix as compared to pure PANI.

V. REFERENCES

- [1]. Lijia Pan, Hao Qiu, Chunmeng Dou, Yun Li, Lin Pu, Jianbin Xu and Yi Shi, Int. J. Mol. Sci. 11, (2010),2636-2657.

- [2]. Yu-Kai Han, Yi-Jang Lee, Pei-Chen Huang, *J. of Electrochem. Society*, 1564, (2009), K37-K43.
- [3]. Jiaxing Huang, *Pure Appl. Chem.*, 78, 1, (2006), 15–27.
- [4]. Guoqing Zhang, Xinxi Li, Haitao Jia, Yahui Wang, et.al *Int. J. Electrochem. Sci.*, 7, (2012), 830 – 843.
- [5]. A.C.V. de Araújo, R.J. de Oliveiraa, et.al., *Synt. Met.* 160, (2010), 685–690.
- [6]. Na Li, Yinghong Xiao, Chong. Xu, Huihui Li, et.al *Int.J.Electrochem. Sci.*, 8, (2013), 1181–1188.
- [7]. S.B. Lee, S.M. Lee, N.I. Park, S. Lee, D.W. Chung, *Synth. Met.* 201(2015) 61–66.
- [8]. Libo Sun, Yuanchang Shi, Zhaopin He, Bo Li, Jiurong Liu, *Synt. Metals* 162 (2012), 2183–2187.
- [9]. Ziran Liu, Jingran Zhou, Hailin Xue, Liang Shen, *Synt. Metals* 156, (2006), 721–723.
- [10]. J. Stejskal, R.G. Gilbert, *Pure Appl. Chem.*, No. 5, 74 (2002) 857.
- [11]. Ozcan Koysuren & H. Nagehan Koysuren, *Journal of Macromolecular Science, Part A, pure and applied chem.*, Taylor & Francis, (2019).
- [12]. Feng W., Sun E., et.al, (2000), *Bulletin of the Chemical Society of Japan*, 73, 2627-2633
- [13]. Min S., Wang F., & Han Y., (2007), *Journal of Materials Science*, 42, 9966-9972.
- [14]. Megha Sawarkar, S APande, P S Agrawal, (2015) *Int. Research J. of Engg. & Tech.* pp. 2429.
- [15]. Pouget J.P., Hsu C.H., MacDiarmid A.G., & Epstein, A. J., (1995), *Synt. Met.*, 69, 119-120.

Novel Synthesis of 2-3 Substituted Quinoxaline & Study of Its Physical Parameters

Pinjarkar A.P^{1*}, Chaware T.S¹, Dr.Kolhe S.V¹

¹Department of Chemistry, Shri Shivaji Arts Commerce and Science College, Akot-444101, Maharashtra, India

ABSTRACT

Quinoxaline & its derivative is a privileged that has broad-spectrum applications in the various fields. The work emphasis on the synthesis of quinoxaline derivative, and evaluation of the physical properties like, conductance, spectrophotometric analysis, viscosity, density, solubility, etc. was studied for quinoxaline in different solvents at different concentration.

Keywords: - Quinoxaline, Conductance, Spectrophotometric, Viscosity etc.

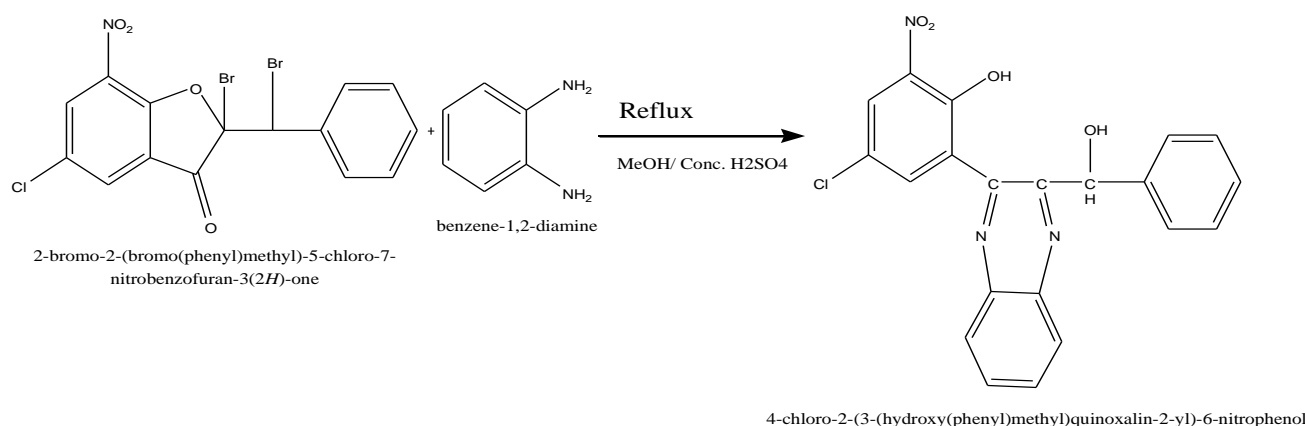
I. INTRODUCTION

A quinoxaline, also called a benzopyrazine, in organic chemistry, is a heterocyclic compound containing a ring complex made up of a benzene ring and a pyrazine ring¹. Quinoxaline and its derivatives are mostly of synthetic origin. Nitrogen containing heterocyclic compounds are indispensable structural units for both the chemists and biochemists. Among the various classes of benzene fused six-membered nitrogen containing heterocyclic compounds, quinoxaline derivatives form an important class of compounds². Quinoxalines are a class of N-heterocycles which are present in a variety of natural and synthetic compounds. They act as a versatile building block in synthesizing novel heterocyclic scaffolds and are important intermediates in many bioactive compounds. They have achieved immense significance in organic as well as medicinal chemistry. Several synthetic approaches have been developed to afford a variety of quinoxaline derivatives³. Quinoxalines are an important class of heterocycle compounds, where N replaces some carbon atoms in the ring of naphthalene. Its molecular formula is C₈H₆N₂, formed by the fusion of two aromatic rings, benzene and pyrazine. It possesses the dipole moment of zero.⁴ Considering these properties, various research workers have shown a keen interest in this small heterocyclic moiety as target structure for evaluation of many pharmacological activities. It is rare in natural state, but their synthesis is easy to perform. The quinoxaline constitutes the useful intermediate in the organic synthesis⁵. This substructure plays an important role as a basic skeleton for the design of a number of heterocyclic compounds with different biological activities⁶, making this type of compounds important in the fields of medicine: antitumor, anticonvulsant, antimalarial, anti-inflammatory, anti-amoebic, antioxidant, antidepressant, antiprotozoal, antibacterial, and anti-HIV agents and technology: fluorescent dyeing agents, electroluminescent materials,

chemical switches, cavitands, and semiconductors⁷. The quinoxaline derivatives are beneficial compounds because of their various medicinal and industrial applications⁸. They are well-known for application in organic light emitting devices, polymers and pharmaceutical agents⁹. The quinoxaline-containing polymers are applicable in optical devices due to their thermal stability and low band gap¹⁰.

II. EXPERIMENTAL PROCEDURE

Take 0.01 M Aurone & 0.01 M benzene-1,2-diamine in round bottom flask and add 30 ml methanol to this mixture, 2,3 drops of concentrated H₂SO₄ was added & reflux the reaction mixture for 3^{1/2}hrs. cool the mixture and decomposed with slightly acidic distilled water resulting solid was extract with ether and separate out.



Physical Parameters:-

Parameters analysed by using Instruments –1) Digital Spectrophotometer: Range 340-960 nm with facility for automatic concentration, % Transmission and absorbance measurements. Wavelength resolution 5nm, 3^{1/2} digit LED display with a set of 10 test tubes. Optical System Single Beam Brand LABTRONICS Model No / Item Code LT-392) Equiptronic Digital Conductivity Meter:, 0.05 Ms To 200 Ms, Model Name/Number: EQ-660B Model Name/Number EQ-660B Brand Equiptronic Conductivity 0.05 mS to 200 mS.3) Glass Ostwald Viscometer, For Laboratory

Solubility – The Solubility of Quinoxaline was studied under different solvent.

Table -1:

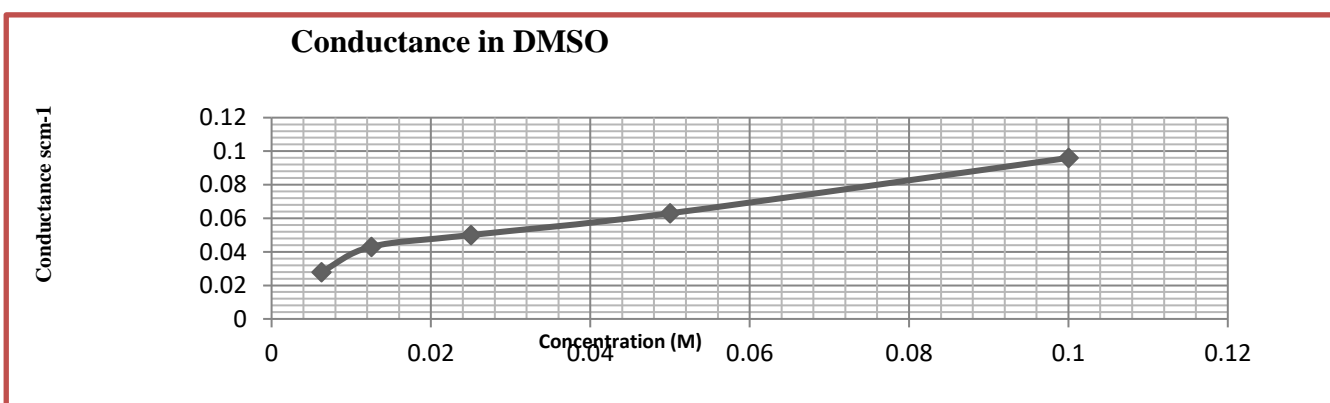
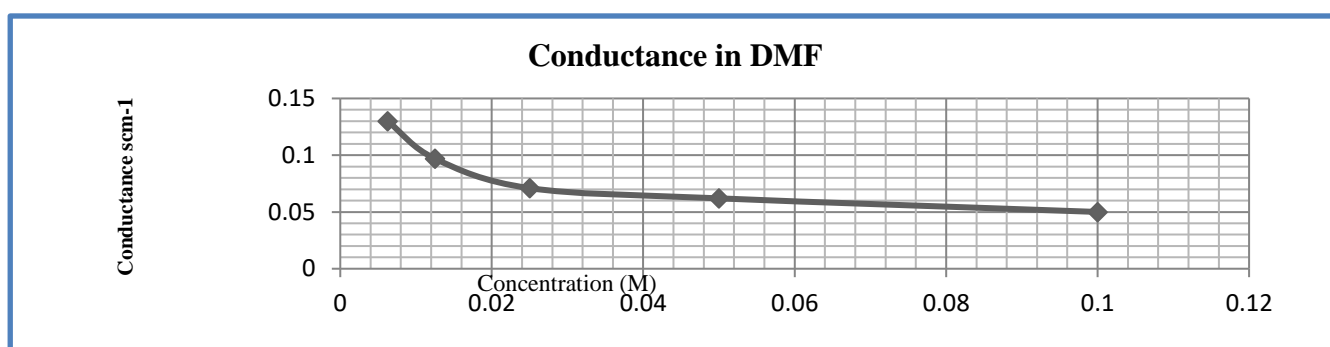
Sr no	Solvent	Solubility
1	Water	Insoluble
2	HCl	Insoluble
3	Pyridine	Insoluble
4	DMF	Soluble
5	Benzene	Insoluble
6	DMSO	Soluble

Physical parameters of quinoxaline in DMF solvent DMSO Solvent.- as the synthesized quinoxaline is soluble in DMF & DMSO the physical parameter are analyzed in the following solvent –

- DMF – Solvent A , DMSO – Solvent B

Table 2 – Temperature – 311K,

Solvent -A				Solvent-B		
Sr .no	Concentration (M)	Conductance (scm^{-1})	Absorbance	Concentration (M)	Conductance (scm^{-1})	Absorbance
1	0.1	0.050 scm^{-1}	1.605	0.1	0.096 scm^{-1}	1.951
2	0.05	0.062 scm^{-1}	1.635	0.05	0.063 scm^{-1}	1.950
3	0.025	0.071 scm^{-1}	1.610	0.025	0.050 scm^{-1}	1.592
4	0.0125	0.097 scm^{-1}	1.542	0.0125	0.043 scm^{-1}	1.490
5	0.00625	0.130 scm^{-1}	1.540	0.00625	0.028 scm^{-1}	1.480



Compounds with strong conductivity dissociate completely into charged atoms or molecules, or ions, when dissolved in water. These ions can move and carry a current effectively. Carbon compounds are poor electrical conductors because they form covalent bonds, and they do not give rise to free electrons because all electrons are used to create the covalent bond. Also carbon compound does not dissociate itself into ions. High electrical conductivity can be a property of a purely organic compound that is characterized by a metallic energy-band system. Absorbance is directly proportional to the concentration of the substance. The

higher the concentration, the higher its absorbance. This is proportional to the number of molecules to which it interacts.

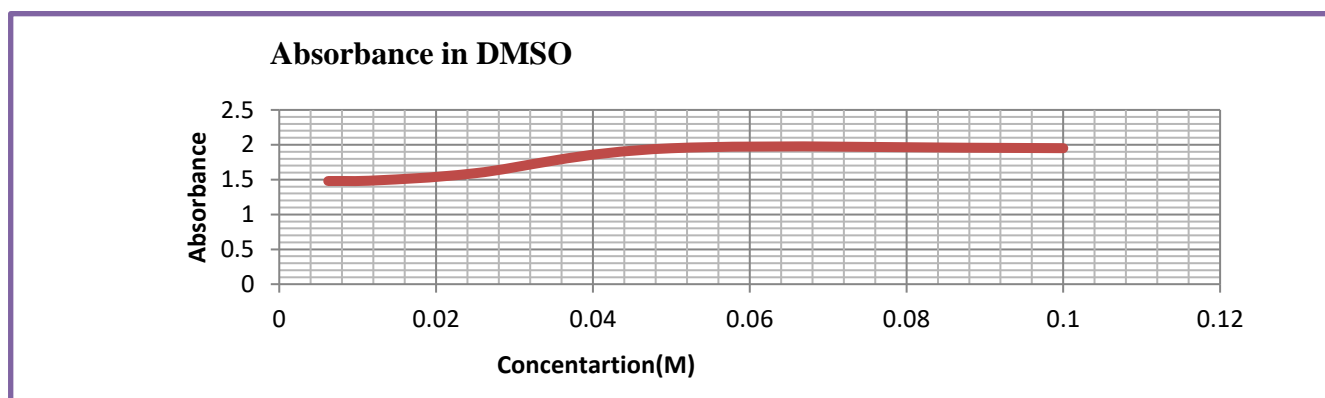
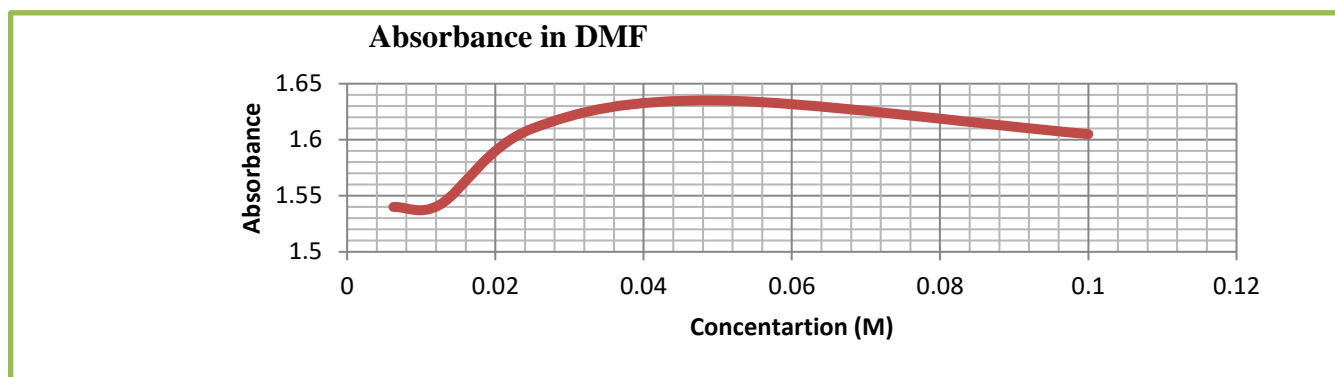


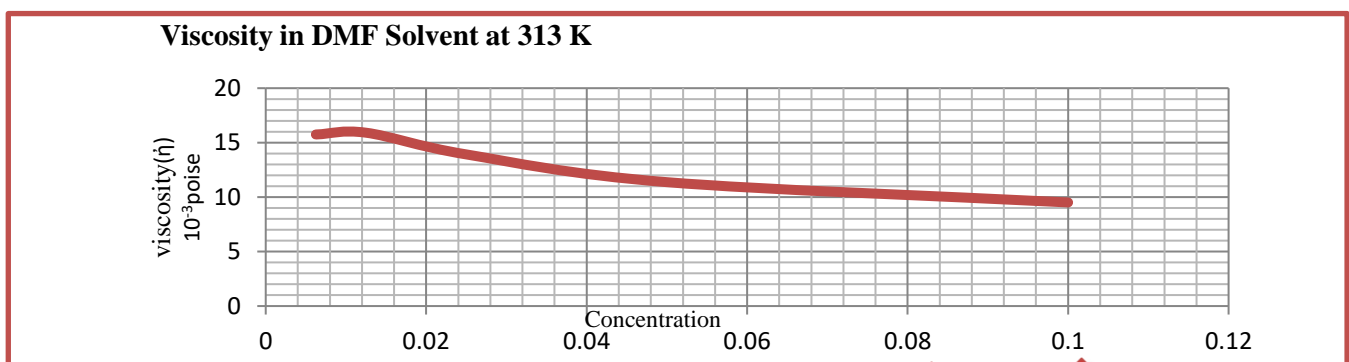
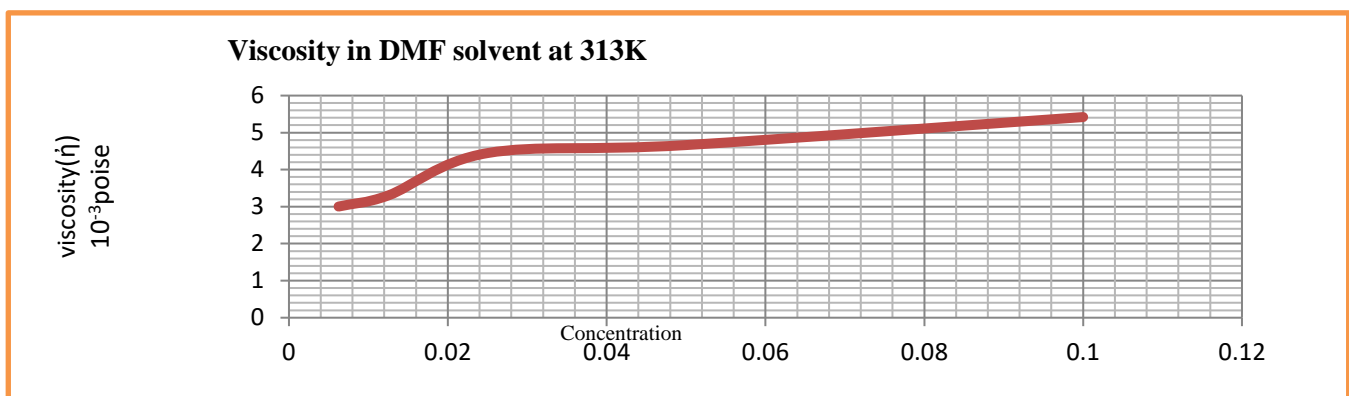
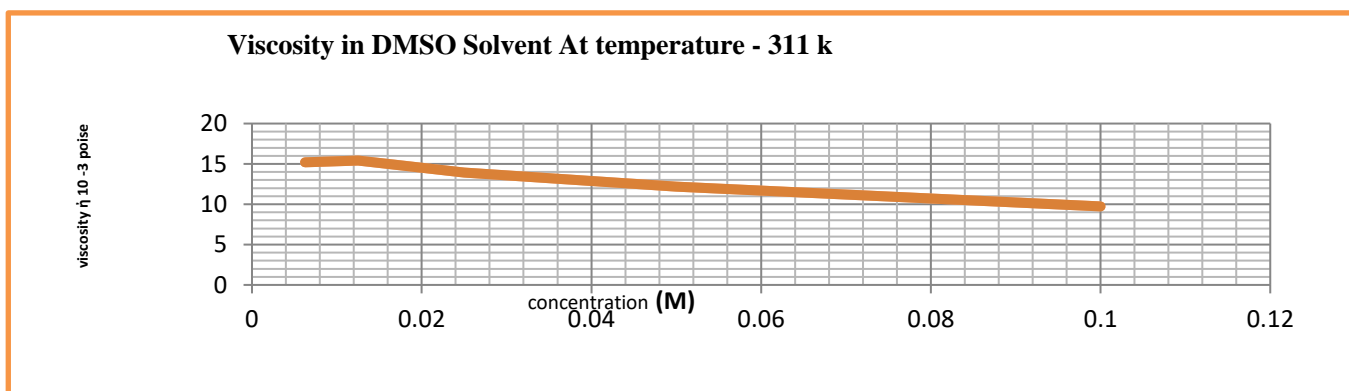
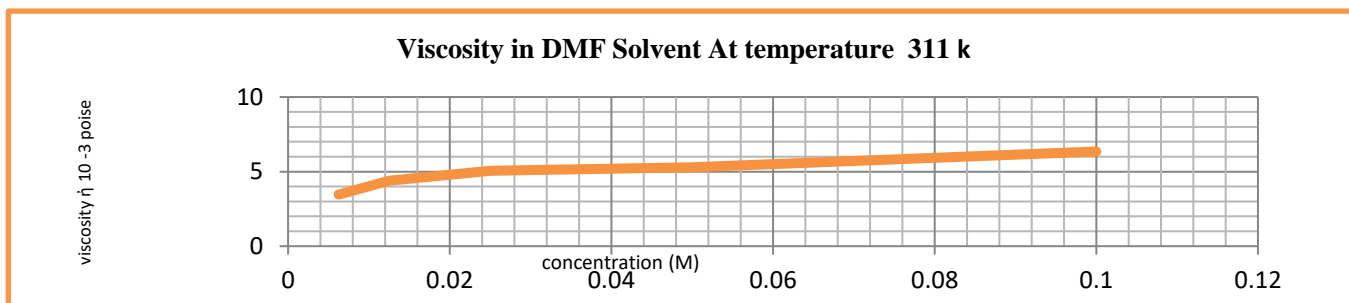
Table 3– Temperature – 311K

Solvent-A				Solvent-B		
Sr .no	Concentration (M)	Density (g/cm ³)	Viscosity($\dot{\eta}$) 10 ⁻³ poise	Concentration (M)	Density (g/cm ³)	Viscosity($\dot{\eta}$) 10 ⁻³ poise
1	0.1	2.830	6.3466	0.1	3.249	9.730
2	0.05	2.830	5.2888	0.05	3.249	12.170
3	0.025	2.829	5.0580	0.025	3.246	13.92
4	0.0125	2.827	4.395	0.0125	3.234	15.413
5	0.00625	2.823	3.4607	0.00625	3.188	15.197

Table 4 – Temperature – 313 K

Solvent-A				Solvent-B		
Sr .no	Concentration (M)	Density (g/cm ³)	Viscosity($\dot{\eta}$) 10 ⁻³ poise	Concentration (M)	Density (g/cm ³)	Viscosity($\dot{\eta}$) 10 ⁻³ poise
1	0.1	2.832	5.4201	0.1	3.268	9.5110

2	0.05	2.832	4.6634	0.05	3.269	11.374
3	0.025	2.821	4.4472	0.025	3.265	13.920
4	0.0125	2.829	3.3022	0.0125	3.254	15.914
5	0.00625	2.825	3.0032	0.00625	3.254	15.750



If Changing the concentration of a solution which changes the density of the solution. Density is the ratio of mass and volume whereas concentration is the ratio of minor part i.e. is solute to the major part i.e. solvent. Viscosity measurement of different concentration of solution Of DMF & DMSO -The viscosity of liquids decreases rapidly with an increase in temperature, and the viscosity of gases increases with an increase in temperature. The maximum large molecules you have exerting drag and interacting with each other. Higher concentration leads to a higher viscosity measurement.

III. CONCLUSION

The conductance was analyzed in both solvent it was found that for the solvent A as the concentration decreases the conductance increases but for solvent b as the concentration of organic molecules decreases the conductance also decreases this is due to DMSO is more polar than DMF. In both solvent as the concentration decreases absorbance decreases. In case of solvent A as the concentration decreases the viscosity also decreases & for solvent B as the concentration of organic molecule decreases and solvent increases the viscosity increases.

IV. REFERENCES

- [1]. Sujiti Srivastava "Quinoxaline as a potent heterocyclic moiety"-IOSR Journal of Pharmacy (IOSRPHR) gitanjali college of pharmacy Nomi Shrestha Sunsari Technical College, 2017.
- [2]. Karim-Dânoun, Younes-Essamlali, Othmane-Amadine, Hassan Mahi Mahi & Mohamed Zahouily "Eco-friendly approach to access of quinoxaline derivatives using nanostructured pyrophosphate $\text{Na}_2\text{PdP}_2\text{O}_7$ as a new, efficient and reusable heterogeneous catalyst." Article number: 6 2020.
- [3]. Vipin K. Maikhuri, Ashok K. Prasad, Amitabh Jhab and Smriti Srivastava "Recent advances in the transition metal catalyzed synthesis of quinoxalines" 2017
- [4]. Joana A. Pereira a , Ana M. Pessoa b, c , M. Natalia D.S. Cordeiro c , Rúben Fernandes a, d , Cristina Prudencio, Joao Paulo Noronhaf , Monica Vieira "Quinoxaline, its derivatives and applications" 2018.
- [5]. Chao Ma¹, Mohammed S. Taghour, Amany Belal, Ahmed B. M. Mehany, Naglaa Mostafa, Ahmed Nabeeh, Ibrahim H. Eissa and Ahmed A. Al-Karmalawy Design and "Synthesis of New Quinoxaline Derivatives as Potential Histone Deacetylase Inhibitors Targeting Hepatocellular Carcinoma." 2014.
- [6]. Mousa Soleymani and Mahdiah Chegani "The Chemistry and Applications of the Quinoxaline Compounds" Volume 23 , Issue 17. DOI: 10.2174/1385272823666190926094348.
- [7]. Morton Goldweber and Harry P. Schultz "The Preparation and Physical Properties of Some 2-Hydroxy-3-alkylquinoxalines" Cite this: J. Am. Chem. Soc. 1954, 76, 1, 287-288 Publication Date: January 1, 1954.
- [8]. Y. Deepika P.S. Nath K. Sachin S. Shewta "Biological activity of quinoxaline derivatives" International Journal of Current Pharmaceutical Review and Research 2(1):33-46 February 2011.

- [9]. Nesma A. Abd El-Fatah, Ahmed F. Darweesh*, Mostafa E. Salem, Ismail A. Abdelhamid,* and Ahmed H. M. Elwahy “Microwave assisted synthesis of novel 1, ω -bis(quinoxalin-2-yl)phenoxy)alkanes or arenes” The Free Internet Journal for Organic Chemistry 2019.
- [10]. Poonam M More*, Shradha R Jedge, Sandip S Kshirsagar and Rajesh J Oswal “to study the effect of solvent on the synthesis of novel quinoxaline derivatives” Open Access Scientific Reports October 31, 2012.

Viscometric Properties of Aqueous sodium Salt of L-Alanine

M. B. Dhande¹, D. T. Tayade²

¹Department of Chemistry, HPT Arts and RYK Science College, Nashik-422005, Maharashtra, India

²Department of Chemistry, Government Vidarbha Institute of Science and Humanities, Amravati, Maharashtra, India

ABSTRACT

Amino acid salts are considered as an attractive alternative to alkanolamine solvents for post combustion CO₂ capture from flue gases, due to their low volatility, stability towards oxidative degradation, higher surface tension and fast absorption rates. In this work, the viscosities of aqueous solutions of sodium salt of L-alanine were measured at 298.15 and 303.15K for concentrations range 0.01 to 0.15mol L⁻¹. Furthermore, the Jones-Dole coefficient (B) and constant A were calculated from the experimental viscosity data.

Keywords:- Sodium salt of amino acid; CO₂; viscosity; Jones-Dole coefficient.

I. INTRODUCTION

The world is facing an uncontrolled environmental problem: global warming¹. The main contributor to global warming is excessive CO₂ emissions from a variety of sources- industrial as well as human activities².

The removal of carbon dioxide (CO₂) from a process gas stream is an important step in many industrial processes and can be required for operational, economical and/or environmental reasons. CO₂ capture technologies comprise ways to separate CO₂ from flue gas, before the flue gas is released into the atmosphere. In such operations, alkanolamine-based absorbents and their blends are being extensively applied³. Alkanolamines undergo degradation in oxygen-rich atmosphere, usually encountered in the treatment of flue gases, resulting in very toxic degradation products⁴. These demerits of amine-based solvents restrict their use for CO₂ removal processes.

Amino acid salts have been found as attractive alternatives to amines and various researchers have studied their reactions with CO₂^{5,6}. Though amino acids are more expensive than alkanolamines, they have certain unique advantages like stability towards oxidative degradation, negligible volatility, higher surface tension and fast absorption rates.

Physicochemical properties are necessary in the design of gas-liquid contactors, modelling simulation, operation of the equipment and the evaluation of suitable absorbents for CO₂ capture^{7,8}. These data are also necessary to deduce chemical reaction kinetics from CO₂ absorption rate experiments^{9,10}.

For aqueous viscosities of aqueous solutions of sodium salt of L-alanine, such properties have not yet been reported in the open literature at lower concentrations. Thus, in the present work, we presented new experimental data on viscosity and Jones-Dole coefficient (B) for aqueous sodium salt solutions of L-alanine.

II. EXPERIMENTAL SECTION

Materials and amino acid salt preparation.

The amino acid L-alanine (CAS No. 56-41-7) was supplied by S D Fine-Chem Ltd., India. sodium hydroxide (NaOH, CAS No. 1310-73-2, GR, 98 % purity) was purchased from Merck. The aqueous amino acid salt solutions were prepared by neutralizing amino acid dissolved in triply distilled water with an equimolar amount of NaOH. Weight was taken on Dhona balance accurate to ± 0.1 mg.

Viscosity measurements

Dynamic viscosity measurements were undertaken by using Ubbelohde suspended-level viscometer^{11, 12}. All of the measurements were made at atmospheric pressure. Measurements were made for amino acid salt concentrations range from 0.01 to 0.15 m and at 298.15 and 303.15 K temperatures. Viscometer was calibrated with triply distilled water. For measurements of viscosity of aqueous solutions at different temperatures, glass walled thermostat was used.

III. RESULTS AND DISCUSSION

The measured viscosity values for aqueous solution of sodium salt of amino acid at various concentrations and temperatures are given in Table 1. The viscosity is observed to increase with concentration and decrease with increasing temperature. Due to the increase in the temperature thermal energy increases which leads to the breaking of amino acid salt/water aggregates. From Table 1, it is observed that density increase with molality of the solutions and decrease with increasing temperature. The B value of amino acids salts decreases with increase in the temperature.

The dynamic viscosities (η) of the pure liquids were calculated using

$$\frac{\eta}{\eta_0} = \frac{\rho t}{t_0 \rho_0} \quad 1$$

where ρ , ρ_0 , t , t_0 , η , and η_0 are density, flow time, and viscosity of pure liquids and water, respectively.

The Jones-Dole Equation equation was used to analyse the viscosity data.

$$\eta / \eta_0 = 1 + Am^{0.5} + Bm \quad 2$$

where η and η_0 are the viscosities of solution and solvent, respectively. A is constant and gives information regarding the strength ion-ion interactions in the solution. Equation 2 can be rearranged as

$$[(\eta / \eta_0) - 1] / m^{0.5} = A + Bm^{0.5} \quad 3$$

Equation 3 is similar to the equation of straight line ($y = mx + c$) with slope equal to B and intercept equal to A . The values of $[(\eta/\eta_0)-1]/m^{0.5}$ reported in Table 2. Jones-Dole coefficient (B) and constant A were obtained by the use of least square method is a measure of structural modifications induced by the solute–co-solute interactions. Table 3 includes the values of B and constant A for sodium salt of alanine at (298.15 and 303.15) K. The values of B are positives and A are negative.

Table 1, 2 and 3: Viscosities (η), $[(\eta/\eta_0)-1]/m^{0.5}$ and (B), (A) values of sodium salt of L-alanine at different temperatures respectively.

m (kg.mol ⁻¹)	η (m ⁻¹ .kg.s ⁻¹)		m (kg.mol ⁻¹)	$[(\eta/\eta_0)-1]/m^{0.5}$		Parameter	298.15 K	308.15 K
	298.15 K	308.15 K		298.15 K	308.15 K			
Sodium Alanate			Sodium Alanate			Sodium Alanate		
0.0000	0.8903	0.7975	0.0100	0.02529	0.03253	B	0.36582	0.35427
0.0100	0.8926	0.8001	0.0296	0.05202	0.05782	A	-0.01126	-0.003
0.0296	0.8983	0.8054	0.0512	0.07147	0.07713			
0.0512	0.9047	0.8114	0.0731	0.08748	0.09297			
0.0731	0.9114	0.8175	0.0921	0.1002	0.10499			
0.0927	0.9175	0.823	0.1083	0.10893	0.1137			
0.1083	0.9222	0.8273	0.1348	0.12304	0.12697			
0.1348	0.9305	0.8347	0.1506	0.13083	0.13433			
0.1506	0.9355	0.8391						

IV. CONCLUSION

The B value of amino acid salt decreases with increase in the temperature. The positive values B for studied amino acid salt + water system suggests strong interactions between water and amino acid salt. Therefore, it can be concluded that amino acid salt is water structure maker.

V. REFERENCES

- [1]. Le Quere, C., Andrew, R. M., Friedlingstein, P., Sitch, S., Pongratz, J., Manning, A. C., and Zhu, D. (2018). Global carbon budget 2017. *Earth System Science Data*, 10(1), 405-448.
- [2]. Olivier, J. G. J., and Peters, J. A. H. W. (2020). Trends in global CO₂ and total greenhouse gas emissions. PBL Netherlands Environmental Assessment Agency: The Hague, The Netherlands.

- [3]. Ping, T., Dong, Y., and Shen, S. (2020). Energy-efficient CO₂ capture using nonaqueous absorbents of secondary alkanolamines with a 2-butoxyethanol co-solvent. *ACS Sustainable Chemistry and Engineering*, 8(49), 18071-18082.
- [4]. Vitillo, J. G., Smit, B., and Gagliardi, L. (2017). Introduction: carbon capture and separation. *Chemical Reviews*, 117(14), 9521-9523.
- [5]. Xu, X., Myers, M. B., Versteeg, F. G., Adam, E., White, C., Crooke, E., and Wood, C. D. (2021). Next generation amino acid technology for CO₂ capture. *Journal of Materials Chemistry A*, 9(3), 1692-1704.
- [6]. Liu, M., and Gadikota, G. (2020). Single-step, low temperature and integrated CO₂ capture and conversion using sodium glycinate to produce calcium carbonate. *Fuel*, 275, 117887.
- [7]. Guo, H., Li, H., and Shen, S. (2018). CO₂ capture by water-lean amino acid salts: absorption performance and mechanism. *Energy and Fuels*, 32(6), 6943-6954.
- [8]. Bian, Y., Shen, S., Zhao, Y., and Yang, Y. N. (2016). Physicochemical properties of aqueous potassium salts of basic amino acids as absorbents for CO₂ capture. *Journal of Chemical and Engineering Data*, 61(7), 2391-2398.
- [9]. Li, H., Guo, H., and Shen, S. (2020). Water-lean blend mixtures of amino acid salts and 2-methoxyethanol for CO₂ capture: Density, viscosity and solubility of CO₂. *The Journal of Chemical Thermodynamics*, 150, 106237.
- [10]. Li, H., and Shen, S. (2019). Kinetics of carbon dioxide absorption into water-lean potassium proline/ethylene glycol solutions. *Industrial and Engineering Chemistry Research*, 58(23), 9875-9882.
- [11]. Einfeldt, J. (2001). Comments on high-accuracy viscosity measurements using capillary viscometers. *Metrologia*, 38(5), 459.
- [12]. Wankhede, D. S., Lande, M. K., and Arbad, B. R. (2005). Densities and viscosities of binary mixtures of paraldehyde + propylene carbonate at (288.15, 293.15, 298.15, 303.15, and 308.15) K. *Journal of Chemical and Engineering Data*, 50(1), 261-263.



Effect of Sintering Temperature on Structural and Dielectric Properties of Lead Titanate

A. U. Bajpeyee, N. V. Galande*, S. H. Shamkuwar

*Department of Physics, Shrimati Narsamma Arts, Commerce and Science College, Kiran Nagar, Amravati
444606, Maharashtra, India

ABSTRACT

Ferroelectric lead titanate (PbTiO_3) has been made by using wet chemical reaction method. Single-phase PbTiO_3 perovskite nanocrystalline powders were obtained by sintering at different temperatures 650°C , 700°C and 750°C for 4 hours. Synthesized powders of Lead Titanate PT (PbTiO_3) were subjected to X-ray diffraction [XRD] studies. XRD of the lead titanate reveals 29.66 nm, 25.90 nm and 25.15 at 650°C , 700°C and 750°C calcinations. As sintering temperature is increased, The PbO present in the material is vanished and pure phase PbTiO_3 is obtained. The influence of sintering temperature on structural and dielectric properties of the synthesized PbTiO_3 is discussed in this paper.

Key words: PbTiO_3 , Sintering , XRD, Dielectric properties.

I. INTRODUCTION

Lead titanate (PbTiO_3) PbTiO_3 is a well-known perovskite-type ferroelectric material with a large spontaneous polarization and a small dielectric constant. However, synthesis of the large PbTiO_3 single crystal is very difficult because it cracks spontaneously when passing through its phase transformation temperature during cooling. [1] Possible applications to electronic and optical devices have brought much attention to the preparation of pure PbTiO_3 .

Lead titanate (PbTiO_3 , PT) is a ferroelectric nanocrystalline powder that has not only been proved to be a technologically important material but also it is a significant component material in electronics such as capacitors, ultrasonic transducers, thermistors, and optoelectronics. These systems are due to their potential applications as ferroelectric materials.[2] The improvement in the piezoelectric and pyroelectric properties is also described by replacing Pb in the A site of the ABO_3 structure. Large c/a ratio in PbTiO_3 at low temperature confer tetragonal phase, it disintegrates into powder when cooled through the Curie point. Synthesis of PbTiO_3 by wet chemical methods offer advantages because of high-purity, good stoichiometry and controlled particle size.[3-5]

The conventional solid-state reaction has a tendency to produce a coarse PbTiO_3 powder with compositional in homogeneity and a degree of particle agglomeration if the processing parameters are not carefully optimized.[6] Therefore, many chemistry-based processing routes, including co-precipitation, sol-gel

synthesis, hydrothermal and citrate routes have been devised for the preparation of an ultrafine, sintering-reactive PbTiO_3 powder. Our method of synthesizing PbTiO_3 relies on the reaction between Lead Nitrate [$\text{Pb}(\text{NO}_3)_2$] and Titanium Isopropoxide [$\text{C}_{12}\text{H}_{28}\text{O}_4\text{Ti}$] at high temperature.[7-12]

II. EXPERIMENTATION

Molar proportions of $\text{Pb}(\text{NO}_3)_2$ (Lead Nitrate) is dissolved in Titanium Isopropoxide [$\text{C}_{12}\text{H}_{28}\text{O}_4\text{Ti}$] in liquid. The lead titanate were prepared by dissolving solid lead nitrate powder in pure water and stirred for 1 hr at 100°C in reaction flask, when the lead nitrate was dissolved in water, then a stoichiometric amount of titanium Isopropoxide was added to the solution and the solution was refluxed at 100°C for 1 h and the solution was kept at 100°C for 4 h to get nanocrystalline powder. Nanocrystalline powders with various crystallite sizes were obtained by calcining the powder at different temperatures at 650°C , 700°C and 750°C . Structure and phase transformation analyses were investigated by XRD in the range of 0° – 90° . The average crystallite size was calculated from the full width at half maximum of the diffraction lines using Scherrer's relation.

III. RESULTS AND DISCUSSIONS

X-RAY DIFFRACTION:

XRD pattern of the PbTiO_3 sintered at 650°C , 700°C and 750°C is shown in Fig.1 at 650°C ; the crystallization of tetragonal lead titanate phase began along with traces impurity phase. At 650°C all peaks can be indexed to the PbTiO_3 with a tetragonal structure. No peak corresponding to any of the source materials or allotropic forms was found, suggesting that a pure crystalline compound exists. The crystallite size of the particles calcined at various temperatures could be calculated by the Scherrer's equation: $t = k\lambda/\beta\cos\theta$ (where t is the average size of the particles, assuming particles are spherical, $k=0.9$, λ is the wavelength of X-ray radiation, β is the full width at half maximum of the diffracted peak and θ is the angle of diffraction). The crystallite size obtained from XRD data at 650°C , 700°C and 750°C were 29.66 nm, 25.90 nm and 25.15 respectively. The peak related to the plane 100 is getting suppressed with the elevated sintering temperature. This peak belongs to the excess amount of PbO present in the material. As sintering temperature is increased, the peak belonging to PbO is vanished and pure phase PbTiO_3 is obtained.

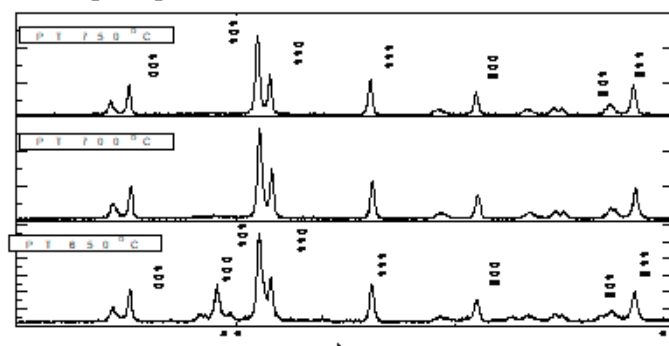


Fig. 1 XRD Analysis

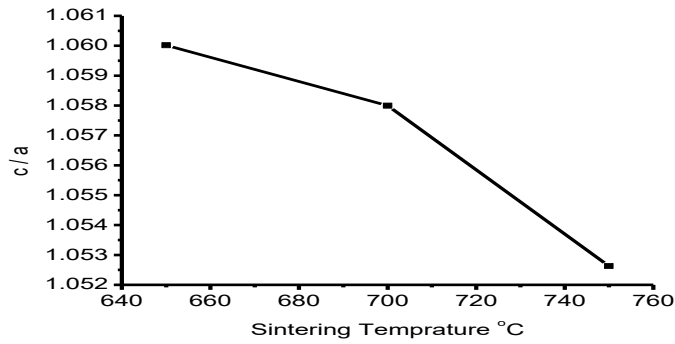


Fig.2: Variation of c/a with sintering temperature.

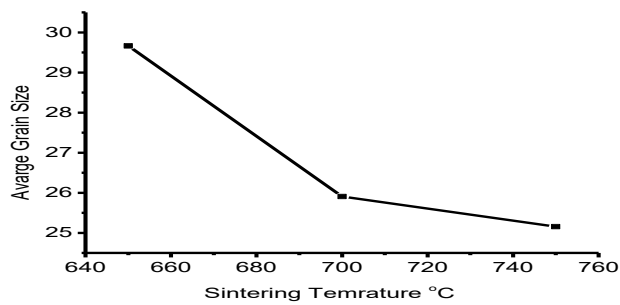


Fig.3: Variation of average grain size with Sintering temperature

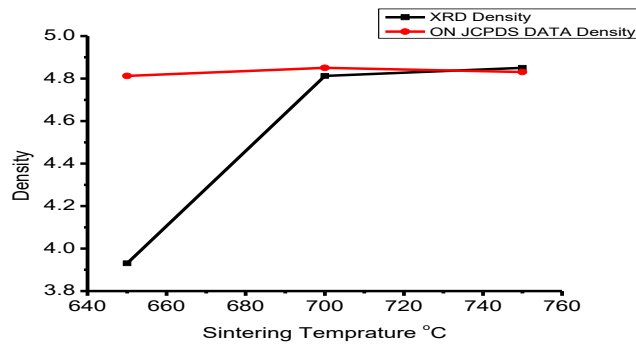


Fig.4: Variation of cell Volume with sintering Sintering temperature

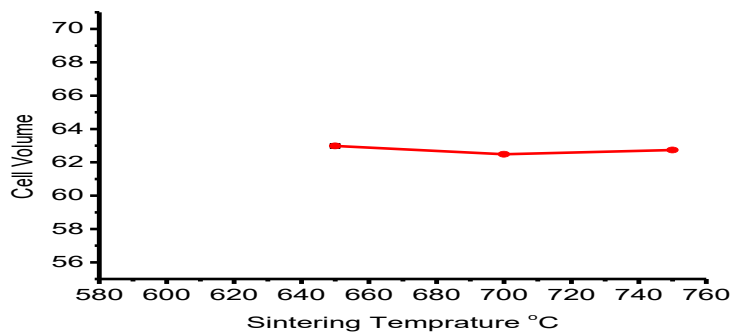


Fig.5: Variation of density with temperature.

Fig.2. shows the variation of c/a ratio with the sintering temperature, which clearly indicates decrease in c/a ratio with increasing sintering temperature. Decrease in c/a ratio afterwards indicates dispersion from

tetragonality and an approach to the cubic phase with higher sintering temperature. Fig.3 shows the variation of average grain size with sintering temperature indicating decrease in average grain size with increasing sintering temperature. The cell volume doesn't show any prominent change with increasing sintering temperature. The density of the material is initially increases and then becomes stable which means highly dense structures can be obtained if we increase sintering temperature.

Dielectric Properties:

The dielectrics properties of PT (Lead Nitrate) nanoparticles were studied to determine various electrical parameters with respect to frequency. Figure 6.shows the dielectric constant (k) of the PT nanocrystalline powders as a function of frequency at room temperature. The dielectric constant decreases with respect to frequency. The decrease in frequency is rapid in low frequency region and becoming constant in high frequency region representing dielectric dispersion. The dielectric dispersion with frequency shown by the material is due to Maxwell-Wagner type interfacial polarization. The large value of dielectric constant at low frequency is attributed to the presence of all types of polarization, whereas at higher frequencies the dominant contribution to dielectric constant is from electronic polarization only. Fig.6 shows variation of the dielectric constant with respect to sintering temperature. The graph shows increase in dielectric constant w.r.to sintering temperature indicating that the charge holding capacity of the material increases with increased sintering temperature in the given range.

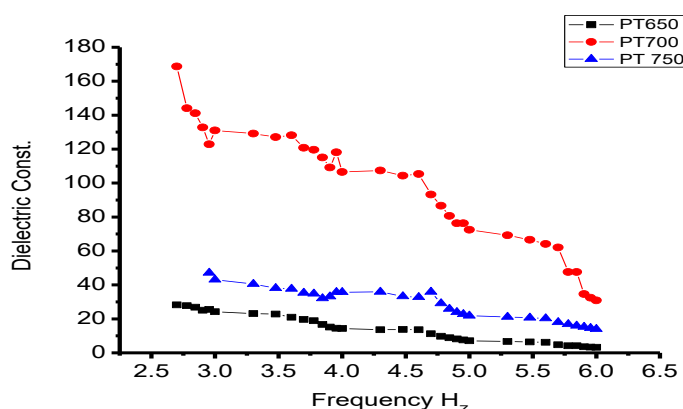


Fig.6: Variation of dielectric constant sintering temperature

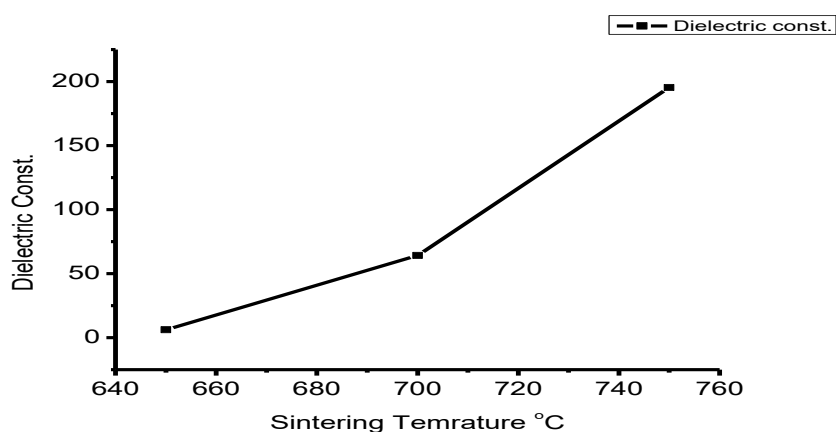


Fig.7: Variation of dielectric constant with with frequency

IV. CONCLUSION

Nanocrystalline PbTiO_3 were synthesized successfully using wet chemical method. The average crystallite size 29.66 nm, 25.90 nm and 25.15 at 650°C, 700°C and 750°C calcinations was assured from XRD peaks. The variation in c/a ratio showed that increase in sintering temperature favours shift from tetragonal phase to cubic phase. Sintering temperature also affects charge holding capacity of the material. More is the sintering temperature, more is dielectric constant. The grain size also decreases with increased calcinations temperature. Cell volume of the material is almost constant with increased sintering temperature. Highly dense materials can be obtained with increased sintering temperature. The Dielectric properties the large value of dielectric constant at low frequency attributed to the presence of all types of polarization, whereas at higher frequencies the dominant contribution to dielectric constant is from electronic polarization only. With increased sintering temperature, charge holding capacity of the material increases.

V. REFERENCES

- [1]. V. D. Kapse, A. U. Bajpeyee, P. A. Murade, International journal of chem. Tech. Research. Vol.6 No.3, PP2096-2098 May-June 2014.
- [2]. Alexandre H. Pinto, Flavio L Souza, Adenilson J. Chiquito, Elson Longo, Material Chemistry and Physics 8 Aug. 2010 pp. 1051-1056.
- [3]. S. Supriya, S. Kalainathan and S.Swaroop, International Journal of Chem. Tech. Research, vol. 3 No. 1 pp. 488-494 Jan-Mar 2011
- [4]. A.A.Abd El-razek, E.M.Saed M. K. Gerges. International Journal of computational Engineering research vol.04 Sept. 2014.
- [5]. Archana Shukla, Namrata Shukla, R.N.P. Choudhary, R. Chatterjee, Elsevier Physics B 448 pp. 219-222, 2014.
- [6]. B. Ravel, N. Sicron, Y. yacoby, E. A. Stern, F. Dogan. And J.J. Rechr. Gordon and Breach Science Publishers. S.A.vol.164 pp. 265-277.1994.
- [7]. Sergio de Lazaro, Elson Longo, Julio Ricardo Sambrano Armando Beltran.Surface Science 552 pp. 149-159.
- [8]. E. C. Paris, M.F.C. Gurgel, T.M.Boschi, M.R.Joya, P.S.Pizani, A.G. Souza, E.R.Leite, J.A. Varela, E. Longo, Journal of Alloys and compounds 462 pp. 157-163, 2008.
- [9]. Archana Shukla, R.N.P. choudhary, A.K. Thakur, D.K.Pradhan, Physica B 405 pp. 99-106, 2010.
- [10]. A. Penton-Madrigal, Y. mendez-Gonzalez, A. Pelaiz-Barranco,F.Calderon-Pinar, L.A.S.deOliveira, J.Belhadi and Y. Gagou, Powder Diffraction Vol. 31 No.1 2016.
- [11]. DING Shiwen, Wang Jing, QIN Jianglei, and LI Ximao, Science in China (Series B) Vol. 44 No. 6 pp.657-659, 2001.
- [12]. Bajpeyee A. U., Ph. D. Thesis SGB Amravati University, Amravati (Maharashtra) India, 2012.

- [13]. O. P. Martinez, J. M. Saniger, E. T. Garcia, J. O. Flores, F. C. Pinar, J. C. Llopiz, A. P. Barranco, J. Mater. Sci. Lett. Vol. 16(13) 1161-3 (1997).
- [14]. C. Sudhama, J. Kim, J. Lee, V. Chikarmane, W. Shepherd and E. R. Myers, J. Vac. Sci. Technol., B 11, issue 4 pp. 1302-9 (1993).
- [15]. G. A. Rossetti Jr, L. E. Cross, J. P. Cline, Journal of Materials Science, Volume 30, Issue 1 pp. 24-34. (1995).
- [16]. P. S. Pizani, J. A. Eiras, Applied Physics Letters, Volume 72, Issue 8 pp. 897-899 (1998).
- [17]. S. B. Majumder, S. Bhaskar, P. S. Dobal & R. S. Katiyar, Integrated Ferroelectrics: An International Journal, Volume 23, Issue 1-4 pp. 127-148 (1999).
- [18]. Hans Theo Langhammer, Thomas Müller, Karl-Heinz Felgner, Hans-Peter Abicht, Journal of the American Ceramic Society, Volume 83, Issue 3 pp. 605-11 (2000).
- [19]. Wenhua Jiang and Wenwn Cao, Applied Physics Letters, Volume 77 pp. 1387-1392 (2000).
- [20]. S. Bhaskar, S. B. Majumdar, M. Jain, P.S. Dobal, R. S. Katiyar, Materials Science and Engineering: B, Volume 87, Issue 2 pp. 178-190 (2001).
- [21]. S. B. Majumdar, M. Jain, R.S. Katiyar, Thin Solid Films, Volume 402, Issues 1-2 pp. 90-98 (2002).
- [22]. Jong-Jin Choi, Sang-Wook Kim and Hyoun-Ee Kim, Journal of the American Ceramic Society, Volume 85, Issue 3 pp. 733-735 (2002).
- [23]. S. B. Majumdar, R. S. Katiyar, F. A. Miranda, F. W. Van Keul, Applied Physics Letters, Volume 82, Issue 12 pp. 1911-3 (2003).
- [24]. Jun Chen, Xianran Xing, Ranbo Yu and Guirong Liu, Journal of the American Ceramic Society, Volume 88, Issue 5 pp 1356-1358 (2005).
- [25]. Arabjit Singh, O. P. Thakur, Chandra Prakash, K. K. Raina, A Multinational Journal, Vol. 78, Issue 7-8, pp 655-667 (2005).
- [26]. A. V. Chaudhari; G. K. Bichile; Smart Materials Research, volume 2013 pp 1-9, 2013.



Proximate and Nutritional Analysis of Leaves of *Gmelinaphillippensis* Cham

Nida S.Shaikh¹, Rahim S.Shaikh²

¹Department of Chemistry, Government Vidarbha Institute of Science and Humanities, Amravati-444604, Maharashtra, India

²Department of Chemistry, Institute of Science, Nagpur, Maharashtra, India

ABSTRACT

The goal of this study is to evaluate the entire nutritional profile of *Gmelinaphillippensis* Cham. While mineral content was determined using an atomic absorption spectrophotometer. All the essential micro and trace metals were discovered in the leaves of *G. phillippensis* Cham. Potassium, calcium, iron, zinc, and magnesium were found to be present in it. The spectroscopic method identified and characterized all the major compounds that were of biological significance. Furthermore, the mineral content of *G. phillippensis* Cham. Leaves can be used as a supplement to combat malnutrition, particularly among rural folk, and the nutritional content can serve as an excellent source of natural antioxidants. Thus, numerous important minerals can be identified from the leaves of *Gmelina phillippensis* Cham.

I. INTRODUCTION

We are aware of the importance of medicinal plants in drug development, and humans have used them for a variety of diseases since the dawn of time (1). Traditional folk medicine derived from wild plants has always inspired researchers to seek out novel medications to promote a healthy lifestyle for humans and animals (2). Furthermore, some medicinal plants remain obscured within the plant and must be scientifically evaluated (3). The common name for *Gmelinaphillippensis* Cham. is Badhara, and the parrot's peak is a member of the Verbenaceae family. It is a small tree that grows to a height of 3–8 m and has pendant branches that are 3–4 cm wide, entire or slightly lobed, and smooth. Yellow blossoms emerge from a pendant structure of overlapping bracts in exotic flowers (4). The flower is shaped like a parrot's beak. The fleshy, smooth, yellow pear-shaped fruit is about 2 cm long (flowers of India). It is indigenous to the Philippine Islands, India, and Southeast Asia. It is also available in the US, Australia, Vietnam, Thailand, Malaysia, Indonesia, Myanmar, and Bangladesh (5).

In the Philippines, the juice of the fruit is practiced to foot eczema. It's also a leech repellent. In Peninsular Malaysia, the crushed fruit is used as a throat home remedy to treat coughs. The root juice is used as a mild laxative to treat drowsiness in Indo-China. Internally, the root extract is used as a stimulant, a resolvent, and in the treatment of joint and nerve diseases. Externally, a leaf extract is also used (6),(7).

The proximate analysis included the solubility of powdered leaves in cold water, hot water, and dil.NaOH,dil.HCl and estimation ofmoisture content, ash content, and acid insoluble ash(8).The qualitative analysis emphasizes several aspects of detecting the physical and physicochemical properties of herbal drugs due to the presence of various constituents present. This type of analysis not only aids in the primary identification of herbs but also indicates an indication of the quality of herbs used in phytopharmaceutical formulations(9). Aside from phytoconstituent identification, it is also critical to analyze plants for their proximate and mineral compositions to expand knowledge of their nutritional health benefits. The review of the literature revealed that no previous work on the proximate analysis and mineral content of Gmelinaphillippensischam had been conducted. As a result, we are interested in researching the proximate analysis and mineral content of Gmelinaphillippensischam.

II. MATERIALS AND METHODS

Plant materials were obtained from the Botanical Garden of the Govt. Vidarbha Institute of Science and Humanities in Amravati, Maharashtra, India. To remove dirt and damaged leaves, the collected fresh plant leaves were washed with tap water and then with double distilled water. The washed leaves are then dried at room temperature for 14 days before being ground into powder form with a mechanical grinder and stored in an airtight container for future use.

Proximate Analysis:-

The determination of physicochemical parameters such as moisture content, total ash value, acid-insoluble ash value, and solubility of the sample was carried out by following the procedure as described by (10).

The Solubility of the sample was checked in cold water, hot water, and dil.NaOH and dil.HCl.andthe percentage was calculated by using the formula:-

$$\% \text{ of solubility} = (\text{loss of weight of sample}) / (\text{weight of sample taken}) \times 100$$

Determination of moisture content Principle:-

The purchase of raw drugs with excess water is not only uneconomical, but it also leads to the activation of enzymes and the multiplication of microorganisms when combined with a suitable temperature. Moisture equalization is based on the weight loss of the sample being tested, which is caused primarily by the water content and, in some cases, by small amounts of other volatile substances. Because it combines the drying process and weight recording, the moisture balance is well suited for handling large sample quantities.(11)

2.1 Procedure:-

The oven-drying method was used to determine moisture. The weight of the empty crucible was recorded and kept in the oven for 1 hour at 1100C, then 1 gm of dried sample was placed in a crucible (W1) and kept in the oven for 1 hour at 1100C. It was then cooled and weighed until the weight remained constant (W2).

The moisture content (%) was calculated by using the formula:-

$$\% \text{ Moisture} = \frac{w1 - w2}{W} \times 100$$

Where W1 = Initial weight of crucible + Sample; W2 = Final weight of crucible + Sample; W = Weight of sample

Determination of ash values:

Principle:-

The total ash method is intended to determine the total amount of material that remains after ignition. This includes both physiological ash, which is produced by plant tissue, and non-physiological ash, which is the residue of foreign substances (such as sand and earth) that adhere to the plant's surface. When herbal drugs are burned, they produce inorganic ash known as total ash in some plants. This is significant because it demonstrates the care taken in the drug's manufacture. Carbon must be removed at the lowest temperature possible (450°C), or else alkali chlorides, which can be volatile at high temperatures, will be lost. Carbonates, phosphates, silicates, and silica acid are common constituents of total ash.(12)

Procedure

An ignited and weighed silica crucible which contains 1 gm of the powdered sample was incinerated slowly by raising the temperature in a muffle furnace at 450°C for 4 – 5 hours. The sample was carbon-free. It was cooled in desiccators and weighed. The procedure was repeated until a constant weight was obtained. The percentage of total ash was calculated.

% of total ash = $\frac{\text{Weight of the ash} \times 100}{\text{Weight of the sample}}$

Acid Insoluble Ash:-

Principle

The residue obtained after boiling all of the ash with dilute hydrochloric acid and igniting the remaining insoluble matter is known as acid-insoluble ash. This metric assesses the amount of silica present, particularly sand and silica. When whole ash is treated with dilute hydrochloric acid, minerals react to form soluble salts, and the residue, which is mostly silica, is the acid-insoluble ash.(13)

Procedure

The ash was boiled with 25 ml of 40% concentrated hydrochloric acid in a silica crucible for 5 minutes. The insoluble ash was collected on ashless filter paper by filtration and washed with hot water. The filter paper was rinsed repeatedly with hot water until the filtrate was free from acid. The insoluble ash was transferred into a preweighed silica crucible. The percentage of acid-insoluble ash was calculated. The filter paper containing the insoluble matter was transferred to the original crucible, dried on a hot plate, and ignited to a constant weight in the muffle furnace at 450-500 °C. The silica crucible was removed from the muffle furnace and allowed to cool in the desiccator for 30 minutes, and then weighed without delay.

% acid-insoluble ash = $\frac{\text{Weight of acid-insoluble residue}}{\text{Weight of the sample taken}} \times 100$

The acid-insoluble ash was calculated and the results are shown in Table-1.

Table No.1

Sr.No	Solubility in	loss of wt. of sample	Amount of sample taken	%
1	Cold water	0.39	1 gm	39%
2	Hot Water	0.48	1 gm	48%

3	Dil.NaOH	0.26	1 gm	26%
4	DilHCl	0.352	1 gm	35.2%
5	Total Ash Value	0.004	1 gm	4%
6	Moisture Content	0.1	1 gm	10%
7	Acid Insoluble Ash	0.08	1 gm	8%

Mineral Analysis:

The powdered sample was digested with nitric acid and perchloric acid. The mineral content of the sample (sodium, potassium, calcium, and magnesium) was determined using atomic absorption spectrophotometry. All essential dietary minerals were found to be abundant in *G.phillippensis* Cham.It was a good source of potassium, sodium, and calcium, which are the most common macroelements, and the order decreases as $K > Ca > Na$. Table 2 shows the mineral content of *G.phillippensis* Cham. in mg/100 g dry tissue, as well as the reference daily intake based on the older recommended dietary allowance from 1968, the Council for Responsible Nutrition, and the biological importance of the respective elements. In addition to evaluating the various macro and microelements in the sample, screening for the presence of heavy metals was accomplished, as their presence in soil is a clear result of geo-climatic conditions and environmental pollution.

Table No.2

Name of Mineral	Biological significance
Sodium	Electrolyte balance, nerve tissue excitability
Potassium	Electrolyte balance, nerve tissue excitability
Calcium	An essential role in blood clotting, muscle contraction, nerve transmission, and bone and tooth formation
Magnesium	Cofactor for enzyme systems
Manganese	Involved in the formation of bone, as well as in enzymes involved in amino acid, cholesterol, and carbohydrate metabolism
Iron	Component of haemoglobin and numerous enzymes; prevent microcytic hypochromic anaemia
Cobalt	Act as a cofactor and stimulate erythropoiesis
Zinc	Component of multiple enzymes and proteins; involved in the regulation of gene expression
Copper	

III. RESULT AND DISCUSSIONS

The results of the proximate analysis support the use of the leaves as a food supplement. From the result, it was found that the total ash content obtained from dry leaves is 4%. Ash content is generally taken to be a

measure of the mineral content of original food. The moderate moisture content provides for an activity of water-soluble enzymes and coenzymes needed for the metabolic activities of the plant. The total moisture content is 10% and the total acid insoluble ash is 8%. The proximate composition of the plant is depicted in table no.1.

The study also reveals the presence of several micro and macro elements in the leaves of *G. Phillippensis* Cham, including zinc, copper, iron, potassium, calcium, sodium, and phosphorus as shown in table no.2. These are thought to be nutritionally valuable and healthy. These nutrients may not be strictly medicinal, but they may be useful in preventing diseases associated with malnutrition. Minerals are required for normal growth, muscle and skeletal development (such as calcium), cellular activity and oxygen transport (copper and iron), chemical reactions in the body and intestinal absorption (magnesium), fluid balance, and nerve transmission (sodium and potassium), and acid-base balance regulation (phosphorus).

IV. CONCLUSION

The results of the proximate analysis support the use of the leaves as a food supplement. This study establishes the complete nutritional profile and reveals the presence of several pharmacologically active components in the leaves of *Gmelinaphillippensis* Cham. With its nutritional profile in mind, the leaves of *Gmelinaphillippensis* Cham can be encouraged to be included in daily diet for better health.

Conflicts of Interest:-

There are no conflicts of interest.

V. REFERENCES

- [1]. Ganie SA, Yadav SS. *Holoptelea integrifolia* (Roxb .) Planch : A Review of Its Ethnobotany , *Holoptelea integrifolia* (Roxb .) Planch : A Review of Its Ethnobotany, Pharmacology, and Phytochemistry. 2014;(September).
- [2]. Sofowora A. Research on medicinal plants and traditional medicine in Africa. *J Altern Complement Med.* 1996;2(3):365–72.
- [3]. Wight W. Evaluation of Phytochemical, antioxidant, the antibacterial and anti-cancerous activity of *Ficus auriculata* Lour. and *Osyris wightiana*. 2018;7(July):64–70.
- [4]. Chen JJ, Cheng MJ, Liao HR, Sung PJ, Wang TC, Chang TH, et al. *Gmelinoiridoside*, a new iridoid glycoside from *Gmelina philippensis*. *Chem Nat Compd.* 2014;50(6):1005–8.
- [5]. *Bulletin of Pharmaceutical Sciences CULTIVATED IN EGYPT.* 2018;41:55–80.
- [6]. Stem L. Phytochemical and Antioxidant Studies on Methanolic Extract of *Gmelina* Phytochemical and Antioxidant Studies on Methanolic Extract of *Gmelina asiatica* Linn Stem. 2014;(October).
- [7]. Islam F, Choudhury SR, Sharmin T. *For A ut ho r ' s Pe rs se.* 2015;(January 2013).

- [8]. Adegbesan SI. Proximate Composition, Qualitative and Quantitative Phytochemical Screening of Aqueous Extract of *Aspilia africana* (Asteraceae) C.D Adams Leaves. *Biomed J Sci Tech Res*. 2019;22(2).
- [9]. Forsido F. Proximate, mineral, and anti-nutrient compositions of underutilized plants of Ethiopia: Figl (*Raphanus sativus* L.), Girgir (*Eruca sativa* L) and Karkade (*Hibiscus sabdariffa*): implications for in-vitro mineral bioavailability. *Food Res Int* [Internet]. 2020;109724. Available from: <https://doi.org/10.1016/j.foodres.2020.109724>
- [10]. Sree LT, Vijayalakshmi K. Proximate Composition, Nutritional Evaluation and Mineral Analysis in the Leaves of an Indigenous Medicinal Plant, *Alternanthera Sessilis*. *Int J Heal Sci Res* [Internet]. 2018;8(7):55. Available from: www.ijhsr.org
- [11]. Adamu AU, Paul ED, Gimba CE, Ndukwe IG. Phytochemical and proximate analysis of *Aspillia kotschy* (Sch. bipex, hochst) Oliv. *Niger J Technol*. 2018;36(4):1135.
- [12]. Kumar S, Chelle S, Avasarala H. Journal of Traditional and Complementary Medicine Profiling and determination of phenolic compounds in poly herbal formulations and their comparative evaluation. *J Tradit Chinese Med Sci* [Internet]. 2019;9(4):319–27. Available from: <https://doi.org/10.1016/j.jtcme.2017.12.001>
- [13]. Achi NK, Onyeabo C, Ekeleme-egedigwe CA, Onyeonula JC. Phytochemical, Proximate Analysis, Vitamin and Mineral Composition of Aqueous Extract of *Ficus capensis* leave in South Eastern Nigeria. 2017;7(03):117–22.

Analysis of Structure and Surface Morphology, Synthesis of Nickel Oxide Nanoparticles by Hydrothermal Method

Sonu Patwa¹, Dr. Hemant Kumar Singh², Navin Chaurasiya², Sandip Kumar Singh², Deep Prakash Singh²

¹Department of Mechanical Engineering, Veer Bahadur Singh Purvanchal University Jaunpur, Uttar Pradesh, India

²Assistant Professor, Department of Mechanical Engineering, Veer Bahadur Singh Purvanchal University Jaunpur, Uttar Pradesh, India

ABSTRACT

Nickel Oxide (NiO) nanoparticles were synthesized by the hydrothermal method using Nickel Chloride Hexahydrate (NiCl₂.6H₂O) as the precursor. The synthesized precursor was calcined at 300°C for 4 hours. The XRD analysis depicts the calcined sample has a cubic structure with an average crystal size of around 18.02 nm. The FTIR analysis ensures the presence of a functional group of nickel oxide. The UV analysis presents a bandgap of 3.8 eV. And the SEM analysis confirms the morphology.

Keywords:- NiO nanoparticles, XRD, FTIR, UV, SEM

I. INTRODUCTION

Nano-particle oxides of transition metals have influenced researchers. These materials have unique properties which are used in many advanced applications [1-3]. Nano-structured nickel oxide is a good example having a large exciton binding energy and a wide band gap ranging from 3.6 to 4.0 eV [4,5]. This p-type semiconductor can be used in many fields as optical, electronic, catalytic and super-paramagnetic devices like transparent conductor films, gas sensors, alkaline battery cathodes, dye-sensitized solar cells and solid oxide fuel cells [4-11].

II. EXPERIMENTAL

2.1 Chemical Used

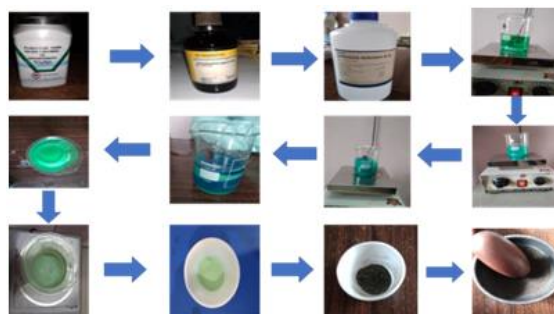


FIGURE.1 Photograph of synthesis of NiO

The Molychem Nickel Chloride Hexahydrate ($\text{NiCl}_2 \cdot 6\text{H}_2\text{O}$) chemical, the Merck Polyethylene Glycol (PEG) solution, the Paskem Ammonia (NH_3) solution and the PBPL distilled water as dispersing solvent were used as the raw material in the synthesis of Nickel Oxide (NiO).

2.2 Synthesis of Nickel Oxide:-

Nickel oxide (NiO) nanoparticles were prepared by hydrothermal method under continuous stirring for 4 h at the room temperature. The Polyethylene Glycol and Ammonia were used by drop wise. The prepared solution was then kept into autoclave and heated at 100°C for 15 h. After cooling, the light green precipitate was formed and washed with distilled water several times to remove impurities. The green precipitate was dried at Thermo Scientific HERATHERM Oven at 80°C for 10 hours. The obtained precursor was calcined at 300°C for 4 hours. The black nanoparticles were obtained and grinded as shown in FIGURE.1. The result was black Nanocrystalline powder received.

III. CHARACTERIZATION DETAILS

The calcined Nickel Oxide (NiO) nanoparticles were examined by Rigaku Smart Lab X-ray Diffractometer (XRD) with radiation source of wavelength $\lambda = 1.5406 \text{ \AA}$, scanned for a diffraction angle (2θ) in the range 20° to 80° to obtain crystal structure, phase composition, purity, crystalline size and average size. The BRUKER ALPHA II Fourier transform infrared spectrometer (FT-IR) confirms the existence of functional group of NiO and the spectrum of nickel oxide (as pellets in KBr) shows many bands ranges from $(4000-400) \text{ cm}^{-1}$. The UV-Visible spectrum of NiO nanoparticles was measured by using a UV-PLUS UV VISIBLE SPECTROPHOTOMETER of MOTRAS SCIENTIFIC in the range 300-700nm and dispersion was in absolute ethanol to get absorption edge and band gap. Scanning electron microscope (SEM) was used to identify the surface morphological behavior of Nickel oxide (NiO) nanoparticles.

IV. RESULTS AND DISCUSSION

4.1 X-ray diffraction (XRD) analysis:-

The Peak Position from 2θ was obtained from FIGURE.2. The noticed diffraction peaks or Miller Indices are shown in Table 1. The standard structure is cubic with $a=b=c=4.180 \text{ \AA}$ from JCPDS Card. The sharp and high-intensity peaks ensures that the synthesized NiO nanoparticles are crystalline in nature and there is no impurity peaks. To calculate d-spacing Bragg's equation is used:

$$d = \frac{n\lambda}{2\sin\theta}$$

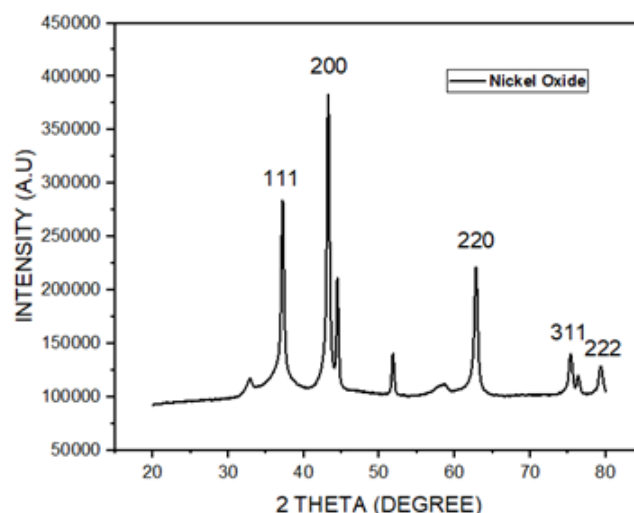


FIGURE.2 XRD spectrum of NiO nanoparticles

Where d is d-spacing in \AA , n is order of diffraction (1), λ is wavelength of x-ray (1.5406\AA), θ is Bragg's diffraction angle. So, calculated value of d-spacing is correspondence to standard value from JCPDS Card. Most intense reflection {200} at $2\theta=43.22^\circ$ is selected. To calculate Lattice constant for cubic crystal system following formula is used:

$$\frac{1}{d^2} = \frac{h^2 + k^2 + l^2}{a^2}$$

Where, d is d-spacing, h, k, l is miller indices and 'a' is lattice constant. So, calculated value of lattice constant is correspondence to the standard value from JCPDS Card. The Crystallite size was calculated by the Scherer equation:

$$D = \frac{k\lambda}{\beta \cos\theta}$$

Where, D is the crystallite size of the powder in nm, K is 0.9 (Scherer Constant), λ is 0.15406nm , the wavelength of the x-ray sources, β is the full width at half-maximum (FWHM) in radians, θ is Bragg's diffraction angle in radians. FWHM (β) was obtained from peak fitting. So, the value of β is 0.53503° , 0.46809° , 0.44051° and 0.58845° . So, the calculated value of D was 15.66nm , 18.25nm , 21.13nm and 17.05nm . The average crystallite size is $D=18.02\text{nm}$. The average crystallite size of produced NiO powder confirms the formation of the nano-crystalline structure.

Planes (hkl)	2 θ values (Degree)		d-spacing values d(\AA)		Lattice Constant a (\AA)		FWHM B
	JCPDS	Experimental	JCPDS	Experimental	JCPDS	Experimental	
111	37.22	37.18	2.41	2.48	4.180	4.259	0.53
200	43.25	43.22	2.09	2.13	4.180	4.259	0.46
220	62.82	62.82	1.47	1.48	4.180	4.259	0.44
311	75.34	75.36	1.26	1.26	4.180	4.259	0.58

Table 1 Compared values of miller indices, 2 θ , d-spacing and lattice constant with JCPDS card.

4.2 Fourier transform infrared spectroscopy (FTIR) analysis:-

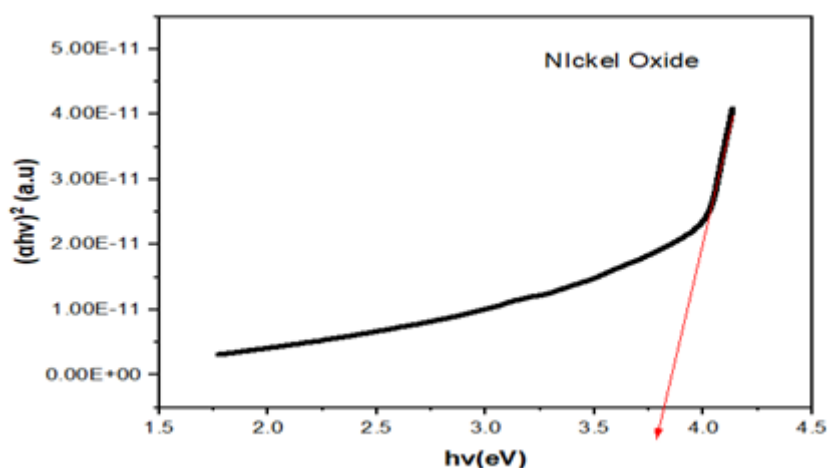
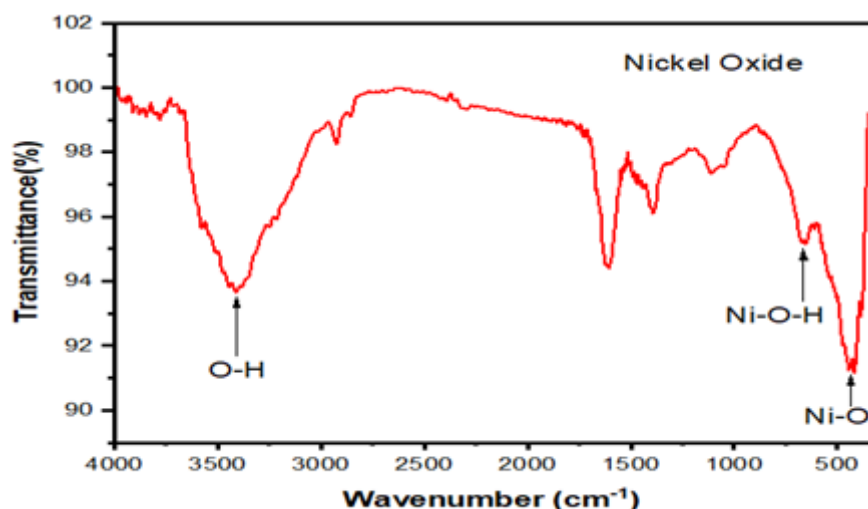


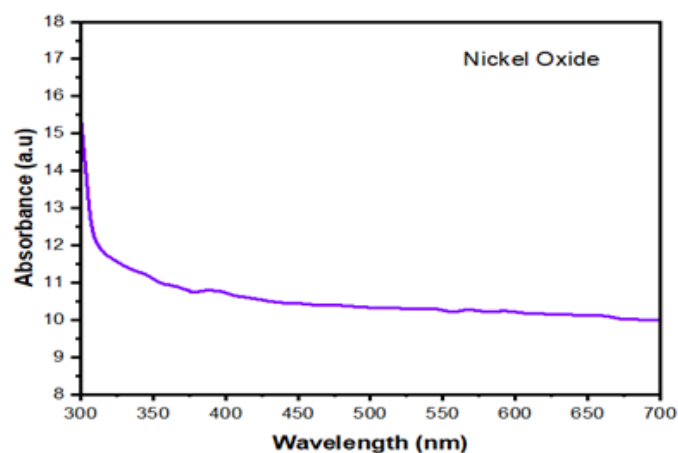
FIGURE.3 FTIR spectrum of NiO nanoparticles

FIGURE.3 shows the FTIR spectrum of NiO nanoparticles and presence of functional group of inorganic compounds. There are several absorption peaks exists in the spectrum of NiO nanoparticles at 3404cm^{-1} , 2925cm^{-1} , 1603cm^{-1} , 1389cm^{-1} , 1113cm^{-1} , 645cm^{-1} and $(419 \text{ and } 446)\text{cm}^{-1}$. The peak at 3404cm^{-1} in the FT-IR spectrum is related to O-H bond. The bond at 2925cm^{-1} is correspondence to C-H stretching mode. The absorption at 1603cm^{-1} attributed to hydroxyl groups. The absorption bonds at 1389cm^{-1} and 1113cm^{-1} indicates the existence of carbonates. But absorption bond at 645cm^{-1} is assigned to Ni-O-H stretching bond. The absorption bonds at 419 and 446cm^{-1} are associated to Ni-O vibration bond. The above information confirms the formation of pure NiO nanoparticles from reference [12] [13] [14].

4.3 UV-visible spectroscopy (UV-Vis) analysis



(a)



(b)

FIGURE.4 UV-visible spectrum of NiO nanoparticles and $(\alpha h\nu)^2$ vs. $(h\nu)$ spectrum of NiO nanoparticles

FIGURE.4 (a) shows the UV-visible spectrum of NiO nanoparticles after calcination in the range 300-700nm. The observed absorption edge is in the range 300-375nm. The blue shift of the absorption edges is related to the size decrease of particles due to the quantum confinement effect of nanoparticles for different sized nanocrystals [14]. The direct band gap values of the NiO samples were determined by Tauc's relation [15]:

$$\alpha h\nu = \alpha_0 (h\nu - E_g)^{1/2}$$

Where $h\nu$, α_0 and E_g are photon energy, a constant and optical band gap of the nanoparticles, respectively, α is absorption coefficient. Absorption coefficient (α), $h\nu$, $\alpha h\nu$ and $(\alpha h\nu)^2$ of NiO nanoparticles can be calculated from the absorption spectra. Then values of E_g were determined by extrapolations of the linear regions of the plot of $(\alpha h\nu)^2$ versus $E_g = h\nu$ as shown in FIGURE.4 (b). The obtained energy band gap was found to be 3.8 eV for pure NiO.

4.4 Scanning electron microscopy (SEM) analysis:-

The morphology of NiO nanoparticles is shown in FIGURE 5 a, b, c. Figure 7 shows FESEM images of NiO nanoparticles at different magnification. So morphology was confirmed by FESEM analysis. Particles are agglomerated in nature it is clear from the images. Cause of overlapping or aggregating of smaller particles larger particles is also present. The images clearly show that randomly distributed grains with smaller size and the porous cubic topography particles as compared to XRD are observed. 1 μm nano particle has 15.00 KX magnifications, 200 nm nano particles have 50.00 KX magnification and 20 nm nano particles have 200.00 KX magnification.

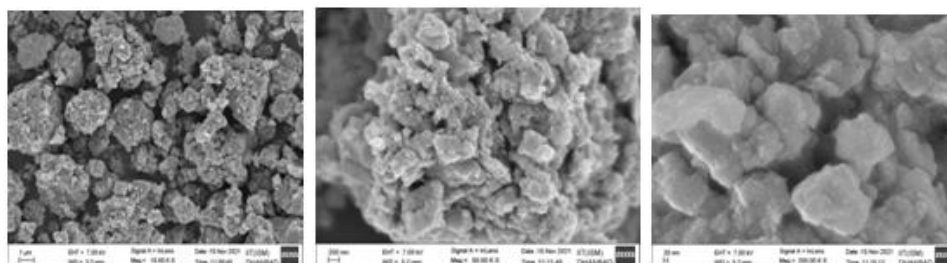


FIGURE.5 SEM images of NiO nanoparticles

V. CONCLUSION

The nanoparticles of NiO have been successfully synthesized by hydrothermal method and calcined at 300°C for 4 hours at room temperature. The formation of NiO nanoparticles by the hydrothermal method is simple, less dangerous, and has a short synthesized time. XRD analysis confirms the cubic structure and 18.02nm average crystal size. FTIR analysis presents the functional group of NiO and confirms the formation of NiO nanoparticles. In UV analysis, absorption edge is observed in the range 300-375nm and obtained energy band gap at 3.8 eV. And the SEM analysis confirms the agglomerate NiO nanoparticles forming porous cubic topography particles.

VI. ACKNOWLEDGEMENTS

The authors are thankful to the Department of Mechanical Engineering, UNSIET, V.B.S. Purvanchal University, Jaunpur-222003, India for providing experimental support.

VII. REFERENCES

- [1]. P. Duran, J. Tartaj, C. Moure, J. Am. Ceram. Soc., Vol. 86 (8), 2003, pp. 1326–1329.
- [2]. J. Wang, L. Gao, J. Am. Ceram. Soc., Vol. 88 (6), 2005, pp. 1637–1639.
- [3]. M. Mazaheri, A.M. Zahedi, M.M. Hejazi, Mater. Sci. Eng. A, Vol. 492, 2008, pp. 261–267.
- [4]. J. Bahadur, D. Sen, S. Mazumder, S. Ramanathan, J. Sol. Sta. Chem., Vol. 181, 2008, pp. 1227–1235.
- [5]. H. Sato, T. Minami, S. Takata, T. Yamada, Thin Solid Films, Vol. 236, 1993, pp. 27.
- [6]. B.L. Cushing, V.L. Kolesnichenko, C.J. O'Connor, Chem. Rev., Vol. 104, 2004, pp. 3893–3946.
- [7]. Y. Bahari Molla Mahaleh, S.K. Sadrnezhaad, and D. Hosseini, J. Nanomat., Vol. 2008, 2008, pp. 1-4.
- [8]. Q. Hongxia, W. Zhiqiang, Y. Hua, Z. Lin, Y. Xiaoyan, J. Nanomat., Vol. 2009, 2009, pp. 1-5.
- [9]. S.A. Needham, G.X. Wang, and H.K. Liu, J. Power Sources, Vol. 159 (1), 2006, pp. 254–257.
- [10]. S.S. Kim, K.W. Park, J.H. Yum, Y.E. Sung, Sol. Energy Mater. Sol. Cells, Vol. 90, 2006, pp. 283–290.
- [11]. M. Ghosh, K. Biswas, A. Sundaresan, C.N.R. Rao, J. Mat. Chem., Vol. 16, 2006, pp. 106–111.
- [12]. A.Sharma, Pallavi, S.Kumar., S.Dahiya , N.Budhiraja, Advances in Applied Science Research. 4(2013)124-130
- [13]. F.Davar.,Z.Fereshteh., M.Salavati-Niasari, Journal of Alloys and Compounds.476(2009)797–801.
- [14]. A. Rahdar, M. Aliahmad, Y. Azizi, Journal of Nanostructures, 5 (2015) 145- 151.
- [15]. J .Tauc,Optical Properties of Solids.Academic Press Inc, New York (1966) 155.



Syntheses of Copper Oxide Nanoparticle by Hydrothermal Method and Its Structural & Surface Morphological Studies

Harshen Yadav¹, Navin Chaurasiya¹, Hemant Kumar Singh¹, Deep Prakash Singh¹, Sandip Kumar Singh¹,
Kumkum Kumari²

¹Department of Mechanical Engineering, UNSIET, Veer Bahadur Singh Purvanchal University Jaunpur, Uttar Pradesh, India

²Assistant Professor, Department of Mechanical Engineering, UNSIET, Veer Bahadur Singh Purvanchal University Jaunpur, Uttar Pradesh, India

ABSTRACT

This research demonstrates a simple and versatile approach for producing copper oxide powder on a large scale. Copper oxide powder (CuO) was synthesized by the hydrothermal method using copper sulphate (CuSO₄·5H₂O) as a precursor material. According to the XRD study, copper oxide has a monoclinic crystal structure with a grain size of 23 nm. The resulting nano-CuO has an irregular homogenous shape, based on SEM analysis. FTIR spectroscopy at 1136 cm⁻¹ confirmed the presence of metal-oxygen (CuO) stretching vibrations in copper oxide nanoparticles. According to the UV-Vis investigation, the copper oxide nanoparticle exhibits an energy gap of 4.1 eV.

Keywords : Nanoparticles, Hydrothermal synthesis, Copper Oxide, Quantum confinement

I. INTRODUCTION

Nanoscience is a relatively recent discipline of science concerned with the study of extremely small particles or nanoscale particles. To put it another way, it's the study of processes in the nanoscale [1]. Nanoparticles (NPs) are granular-size materials with at least one dimension of fewer than 100 nanometers [2]. Nanomaterials are classified as zero-dimensional (quantum dots), one-dimensional (nanorods, nanotubules and nanowires) and two-dimensional (nanosheet, graphene, quantum well).

Copper Oxide (CuO) may be employed in a broad range of technological sectors due to its distinctive features, including gas sensors [3-4], active catalysts [5], high selectivity magnetic recording media [6], solar cell applications [7].

II. METHODS AND MATERIALS

2.1 Chemical used

We used the following materials to make CuO nanoparticles in various environments. Components include copper sulphate [CuSO₄·5H₂O], polyethylene glycol [PEG], sodium hydroxide [NaOH], and double distilled

water. Merck Specialists Private Limited (Mumbai, India) supplied all chemicals. In the synthesis process, Borosil glassware was used. Only distilled water was used for the synthesis.

2.2 Synthesis Method:-

The hydrothermal process is employed to create nanocrystal samples in this study. The main reason we want to focus on hydrothermal methods is that they have a number of advantages, including the ability to use high uniformity of shape and size of nanoparticles, low waste of materials, low equipment, and, finally, the ability to produce large quantities of nanoparticles at low cost.

2.3 Preparation of Copper oxide nanoparticles:-

Copper oxide (CuO) nanoparticles were synthesized using a simple hydrothermal method. In brief: 2 moles of Copper Sulphate ($\text{CuSO}_4 \cdot 5\text{H}_2\text{O}$) as a precursor material were dissolved in distilled water named solution (A) in a beaker under a continuous magnetic stirring at room temperature. After 2-hour, 10 ml PEG (Polyethylene glycol) was added dropwise into an aqueous solution (A) and stirred for 1 hour to ensure that the Solution (A) mixed thoroughly and a Blue (Cyan) colour solution appeared. Again, stirring for several minutes, another named as (solution B) prepared from NaOH (3 gm) dissolved with double distilled water (10 ml) was added into (solution A) under a magnetic stirrer at 1800 rpm for 2.5 hours till the colour of the combination modified to Reddish Brown.

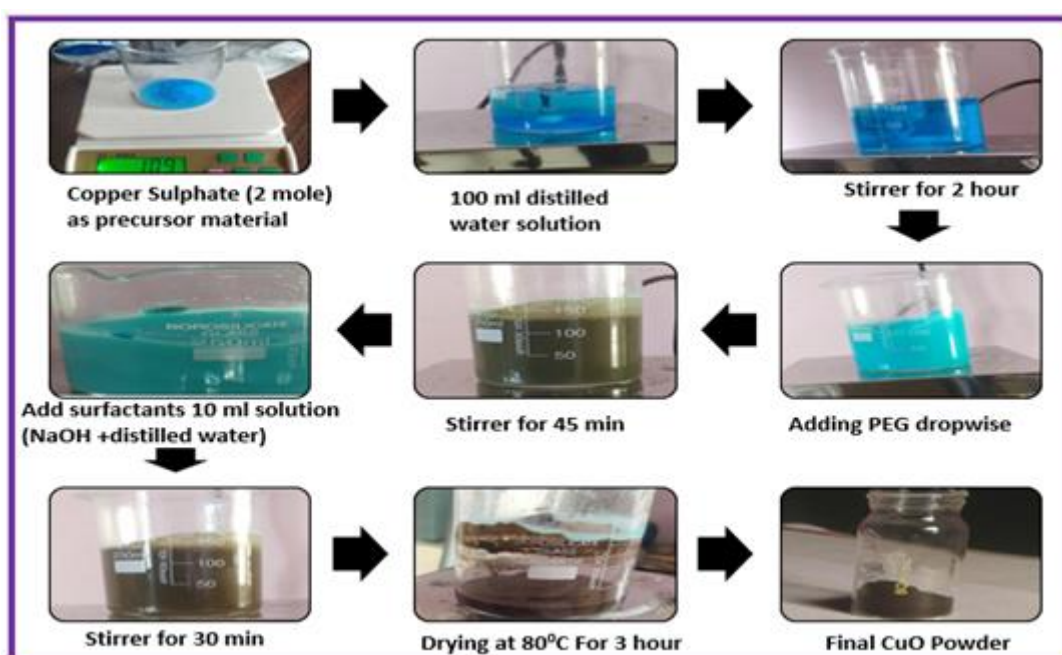


Fig1. Synthesis of Copper Oxide Nanoparticles

After cooling to room temperature, the reaction mixture was filtered, and the precipitate was washed three times with absolute water to remove impurities. Furthermore, it was kept in a crucible and annealed at 300°C for 4 hours to obtain the black coloured copper oxide nanoparticles.

III. RESULTS AND DISCUSSION

3.1 Fourier Transform Infrared Spectroscopy Analysis (FTIR)

FTIR alpha 11 BRUKER was utilized to examine the structural spectrum characteristics of copper oxide (CuO). As demonstrated in the graph of transmittance versus wavenumber, the recorded transmission spectra ranged from 300 cm^{-1} to 4000 cm^{-1} (fig 1). Peaks at wavenumbers of 1630 cm^{-1} and 1114 cm^{-1} , which are related to symmetric and asymmetric stretching, demonstrate flaws in the hydrocarbon group, such as (CH, CH₃) [8]. The vibration band at 3441 cm^{-1} indicates the presence of the O-H bond (hydroxide group). It could be mainly due to the availability of water on the copper oxide nanoparticle's surface, which is a chemical reaction that could be avoided by simply raising the temperature.

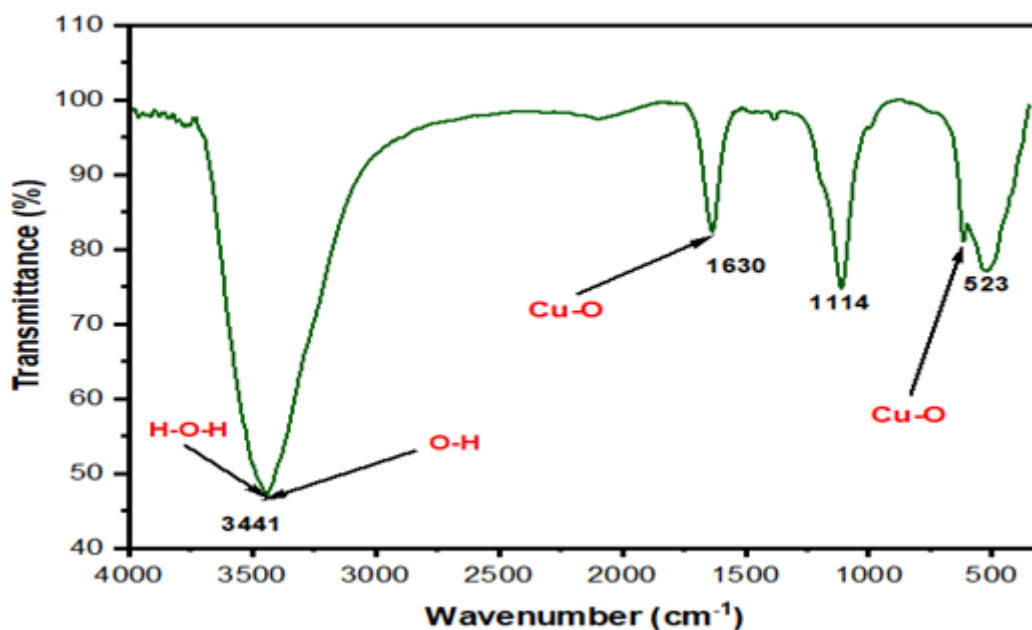


Fig 1- FTIR spectrum of CuO nano particles

Peaks at 523 cm^{-1} and 1114 cm^{-1} indicate that Cu-O bonds have unique bending vibrations. The Cu-O bond of copper (II) oxide nanoparticles is being stretched, as indicated by the wavenumber at 1630 cm^{-1} .

3.2 UV-Vis Spectroscopic Studies

UV-Visible spectroscopy was performed on a MOTRAS SCIENTIFIC UV spectrometer with bandgap energy calculations. Fig 2 shows the UV-visible absorption spectrum of copper oxide nanoparticles. Capturing UV-Vis data, the copper oxide was initially dissolved in ethanol by sonography with absolute ethanol was chosen as reference fluid. The absorption spectrum (Fig. 2) of the UV-visible region of the CuO nanoparticles obtained indicates two maximum absorption peaks at approximately 233 nm and 243 nm , which might be the usual bands of CuO.

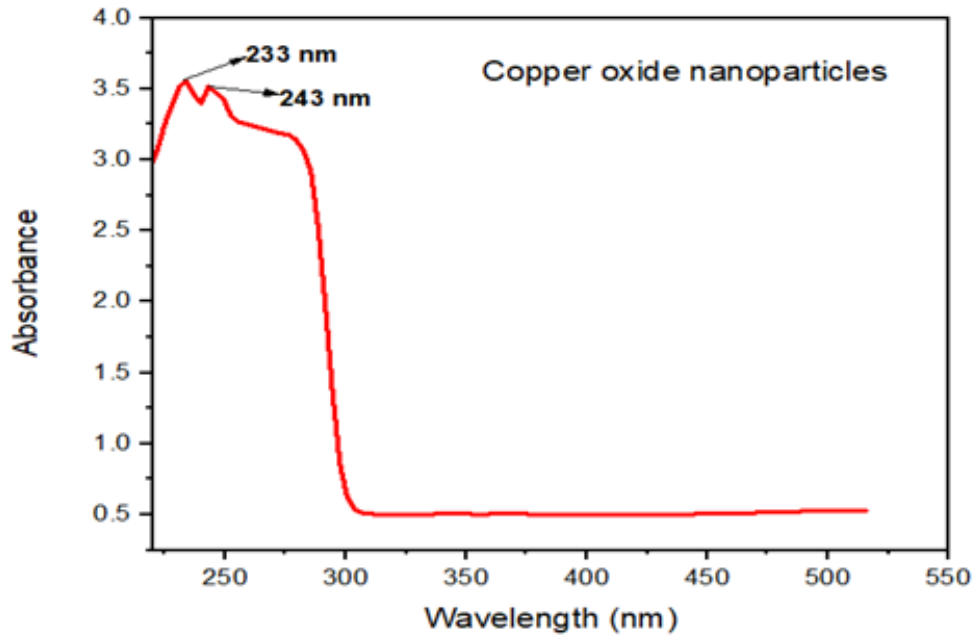


Fig 2 – Graph showing the two maxima absorption band at 233 nm and 243 nm

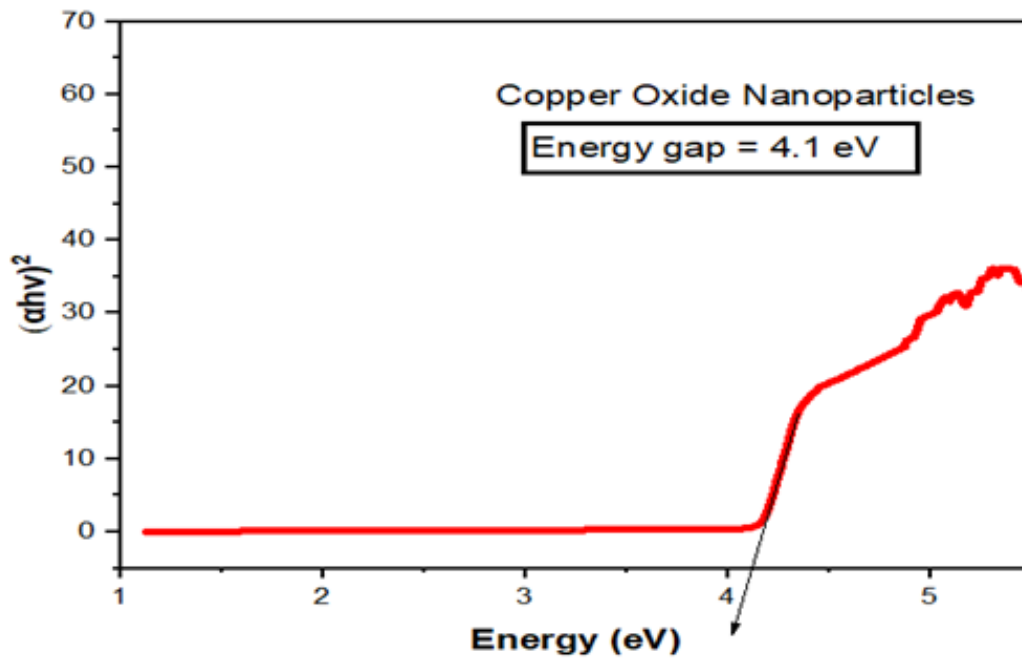


Fig 3- Graph showing the energy band gap of CuO nanoparticles

The calculated band gap for the copper oxide nanoparticle sample is 4.1 eV shown in fig. 3.

3.3 X-ray Diffraction Studies

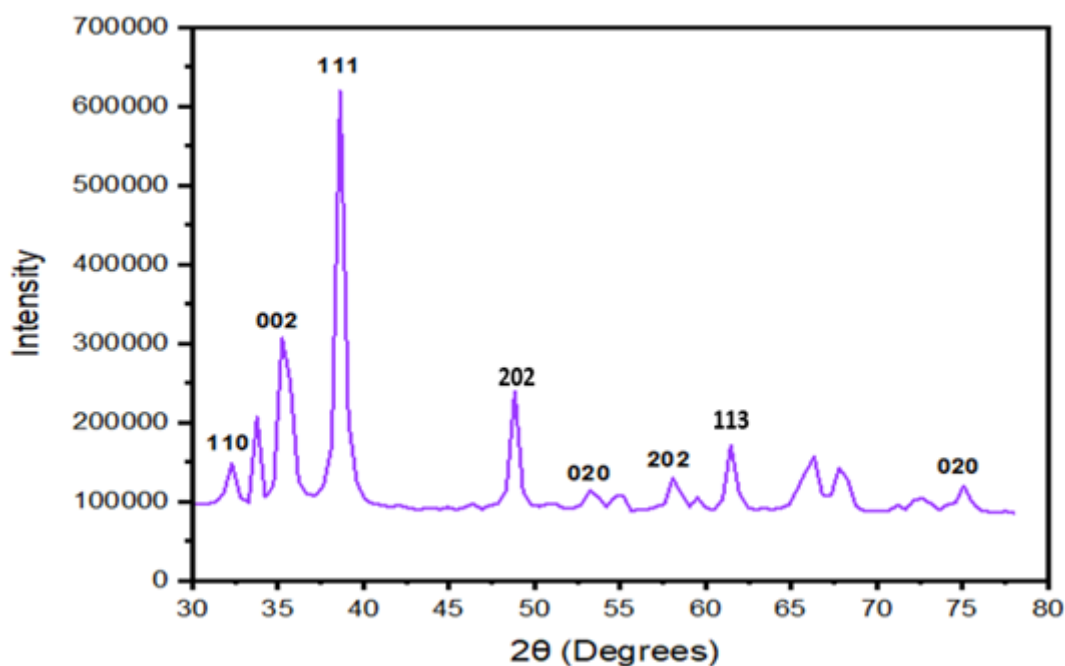


Fig 4 – X-Ray diffractometer of Copper Oxide nano powder

X-ray diffraction studies were performed on a RIGAKU Smart Lab X-ray diffractometer using $\text{CuK}\alpha 1$ radiation (1.5406 Å). The peaks shown in Fig. 4 suggest that the copper oxide nanoparticles were well-crystallized; no other peaks on the copper oxide were observed. The diffraction peaks of copper oxide powder are well described and correlate with JCPDS card number 05-0661. It shows CuO powder has a monoclinic structure. The Peaks were observed at 32.27, 35.41, 38.65, 48.81, 53.42, 58.19, 61.50 and 75.07 which corresponds to (h k l) values of (110), (002), (111), (202), (020), (202), (113) and (004) respectively.

The average particle size (D) was found to be 23 nm which is lying in between the experimental range of CuO i.e., 20 nm-95 nm. The average particle size was calculated by using Debye-Scherrer formula [9-10].

$$D = \frac{0.89 \lambda}{\beta \cos \theta} \quad \text{where, } D = \text{Average crystal Size, } \lambda = \text{X-Ray wavelength used (1.5406 \text{ \AA})}$$

β = Full width at Half Maxima (FWHM), θ = Bragg's angle

3.4 Scanning Electron Microscopy (SEM) Analysis :-

The morphology and composition of the synthesized nanoparticles are shown in fig 5. The SEM images show the formation of nanoparticles that clump together to make larger agglomerates. The SEM images demonstrate that the structure of the synthesized CuO nanoparticles is not homogenous, and the size does not match the nanoscale level. These SEM photos show that only a few spherical nanoparticles were synthesized.

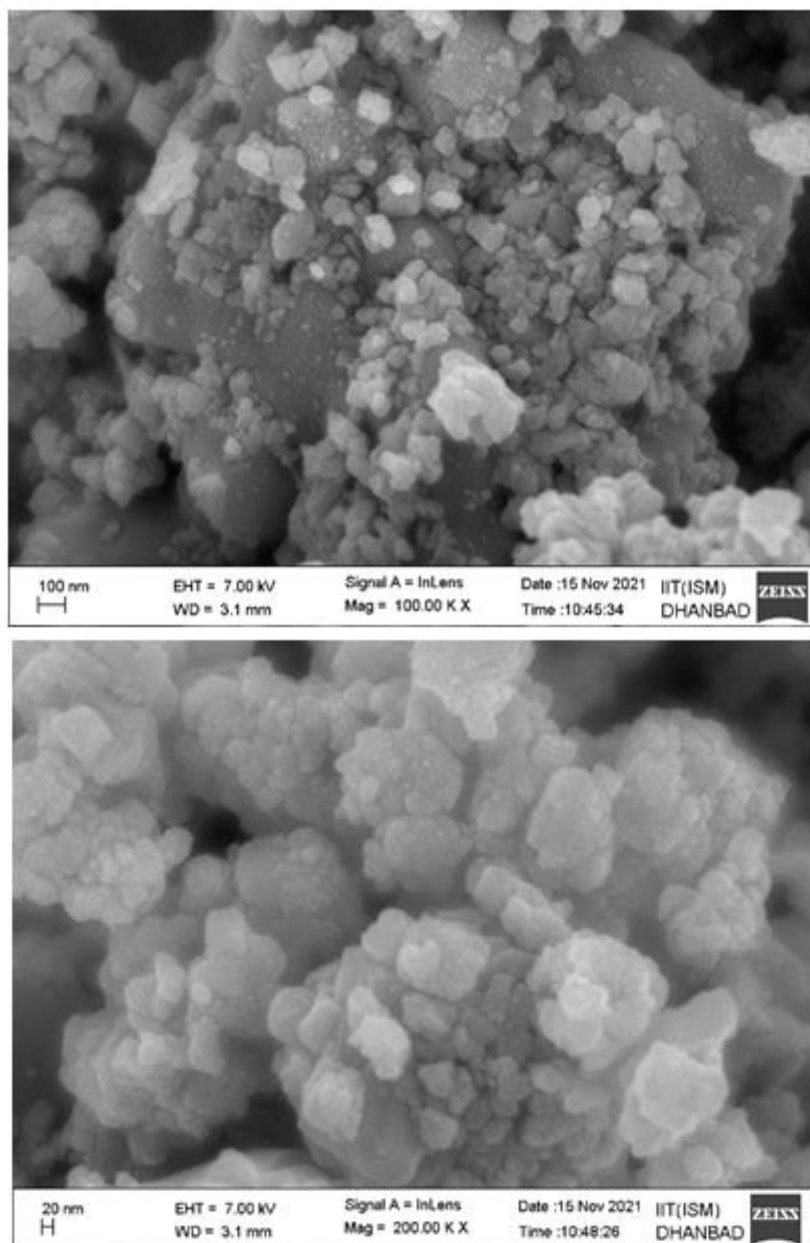


Fig.5 :SEM images of copper oxide nanoparticle

IV. CONCLUSION

Copper oxide nanoparticles, their production, and characterisation were all described in detail in this paper. A simple hydrothermal method was used to process copper oxide nanoparticles. Copper oxide nanostructures were also discussed for some of their distinguishing properties that set it apart from other metallic transition oxides. Future study should focus on better understanding the synthesis, morphology, characterisation, and structure of copper oxide nanoparticles, as well as approaches to exploit the fascinating features of these nanostructures.

V. REFERENCES

- [1]. Yousaf S.A., Ali S. Journal of Faculty of Engineering & Technology, (2007-2008), P.11-20.
- [2]. Forge D., Gossuin Y., Roch A., Laurent S., Elst L.V., Muller R.N. Development of magnetic chromatography to sort polydisperse nanoparticles in ferrofluids. Contrast media & molecular imaging, 2010, 5(3), P.126-132.
- [3]. D'Anna F., Grilli M.L., Petrucci R., Feroci M. WO₃ and ionic liquids: A synergic pair for pollutant gas sensing and desulfurization. Metals, 2020, 10(4), P.475.
- [4]. Tran T.H., Nguyen V.T. Copper oxide nanomaterials prepared by solution methods, some properties, and potential applications: a brief review. International scholarly research notices, 2014.
- [5]. Chang Y., Zeng H.C. Controlled synthesis and self-assembly of single-crystalline CuO nanorods and nanoribbons. Crystal growth & design, 2004, 4(2), P.397-402.
- [6]. Aslani A., Oroojpour V. CO gas sensing of CuO nanostructures, synthesized by an assisted solvothermal wet chemical route. Physica B: Condensed Matter, 2011, 406(2), P.144-149.
- [7]. Li Y., Liang J., Tao Z., Chen J. CuO particles and plates: synthesis and gas-sensor application. Materials Research Bulletin, 2008, 43(8-9), P.2380-2385.
- [8]. Yechezkel Y., Dror I., Berkowitz B. Catalytic degradation of brominated flame retardants by copper oxide nanoparticles. Chemosphere, 2013, 93(1), P.172-177.
- [9]. Kumar V., Masudy-Panah S., Tan C.C., Wong T.K., Chi D.Z., Dalapati G.K. Copper oxide based low cost thin film solar cells. In 2013 IEEE 5th international nanoelectronics conference (INEC), 2013, P.443-445.
- [10]. Wang X., Xu X., Choi S.U. Thermal conductivity of nanoparticle-fluid mixture. Journal of thermophysics and heat transfer, 1999, 13(4), P.474-480.



Synthesis of Some Novel Heterocycles from Variously Substituted Chalcones by Microwave Irradiation and Their Medicinal Assay

D. R. Deshmukh, Dr. R.D. Isankar

G.V.I.S.H. Amravati, Maharashtra, India

ABSTRACT

Variously substituted chalcones (I) have been converted into 1, 3, 5- tri substituted pyrazolines (III). These pyrazolines have been obtained by reacting chalcones (I) with isoniazide (2a) and thiosemicarbazide (2b) in stichometric proportion in microwave oven. The reaction mixture was irradiated with in microwave oven for 1 min at 150 watt. The yields obtain with these techniques are higher and purity of compound obtain is better as compare to classical method of synthesis. The structures of all these pyrazolines Δ^2 have been conformed on the basis of elemental analysis and spectroscopic data. These compounds were screened for their anti-microbial activity.

Keywords: - Synthesis of 1.3.5- tri substituted pyrazolines, microwave irradiation, anti microbial testing.

I. INTRODUCTION

Synthesis of varies chalcones are reported in the literature ¹⁻². In recent past researchers have been actively engaged in the synthesis of various heterocycles having more than one heteroatome with structural and functional novelty. In fact amongst varied substituted heterocycles, benzimidazol, thiozole, isonizaide have gained grete interest due to their successful practical application in clinical and pharmaceutical chemistry.

II. RESULTS AND DISCUSSIONS

Isoniazide and 1- chloro phenyl- 3-2 hydroxyl 5- methyl phenyl chalcone was reacted in presence of 1-2 dropes of ethanol in beaker. The reaction was occurring microwave oven for 1 minute and coloured solid was separated and recrystallized from ethanol, Melting point observed was 130⁰ C. The elemental analysis indicates the Molecular Formula as of the product as C₂₂H₁₆N₃O₂Cl.

The IR spectral analysis of the product indicated the presence of ν (OH) 3460.5 cm⁻¹, ν (C = O) 1645.7 cm⁻¹, ν (N-N) 1213.0 cm⁻¹, ν (C-N) 1563.5 cm⁻¹

On the basis of all above facts the compound (2a) has been assigned the structure 1- isonicotinoyl- 3- (2 hydroxyl- 5 methyl phenyl)- 5-p- chloro phenyl) pyrazoline. The other pyrazolines (2a 1-2a5) were prepared by extending this reaction to other chalcones in good yield. (Table- 1)

Synthesis of 1, 3, 5- tri substituted Δ^2 pyrazolines**Reactant- Isonizide (IIa), and chalcone (Ia)**

Reactant- IIa	Reactant- Ia	Product- IIIa	Yield	M. pt.
Isonizide	1-p- chlorophenyl- 3-2- hydroxyl- 5-methyl phenyl chalcone	1-isonicotinoyl-3 (2 hydroxyl- 5- methyl phenzyl)- 5-p- chlorophenyl pyrazoline	87 %	130°C.
Isonizide	1- (3-methyl- 5 acetyl phenyl)- 3-2 hydroxyl- 5- methyl phenyl chalcone	1- isonicotinoyl-3 (2 hydroxyl-5- methyl phenyl)- 5- (3-methyl- 5- acetyl phenyl) pyrazoline	90 %	190°C.
Isonizide	1- methyl- 3-2- hydroxyl-5- methyl- phenyl chalcone	1- isonicotinoyl-3 (2 hydroxyl-5- methyl phenyl) 5- methyl pyrazoline	56 %	210°C.
Isonizide	1- phenyl- 3-2- hydroxyl-5- methyl phenyl chalcone	1- isonicotinoyl-3 (2 hydroxyl-5- methyl phenyl) 5- phenyl pyrazoline	67 %	102°C.
Isonizide	1-methoxy phenyl -3-2 hydroxyl-5- methyl phenyl chalcone	1- isonicotinoyl-3 (2 hydroxyl-5- methyl phenyl) 5- (4-methoxyl phenyl) pyrazoline	37 %	82°C.

The thiosemicarbazide and 1 phenyl 3-(2- hydroxyl 5- methyl phenyl) chalcone was reacted in presence of 1-2 drpes of ethanol. The reaction was occurring in microwave for 1 min and coloured solid was separated and recrystallized from ethanol. M.P. 110° C. The elemental analysis indicated the M.F. of the product as $C_{17}H_{15}N_3OS$. The IR spectral analysis of the product indicated the presence of ν (OH) 3350 cm^{-1} , ν (-NH) $3262.1-3174.9\text{ cm}^{-1}$, ν (N-N) 1215.6 cm^{-1} , ν (C-N) 1343.2 cm^{-1} .

On the basis of all the above facts. The compound (2b) has been assigned structure as 1-thioamido-3 (2- hydroxyl-5 methyl phenyl) 5- phenyl pyrazoline. The other compounds from (2b2-2b5) were prepared by extending the above reaction of other pyrazolines (2b1-2b5) and other chalcones were isolated in good yield (Table 2)

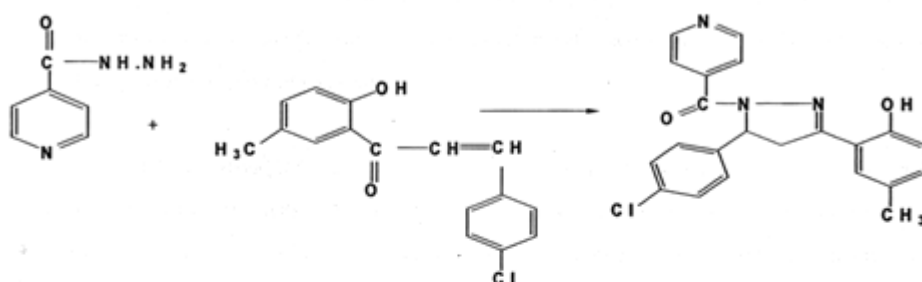
Synthesis of 1, 3, 5- tri substituted Δ^2 pyrazolines**Reactant- Thiosemicarbazide (IIb), and chalcone (Ia)**

Reactant- IIb	Reactant- Ia	Product- IIIa	Yield	M. pt.
Thiosemicarbazide	1-p- chlorophenyl- 3-2- hydroxyl- 5-methyl phenyl chalcone	1-thioamido-3 (2 hydroxyl- 5- methyl phenzyl)- 5-p- chlorophenyl pyrazoline	69.97 %	140°C.
Thiosemicarbazide	1- (3-methyl- 5 acetyl phenyl)- 3-2 hydroxyl-5- methyl phenyl chalcone	1-3 (2 thioamido hydroxyl-5- methyl phenyl)- 5- (3-methyl- 5- acetyl phenyl) pyrazoline	66.35 %	165°C.
Thiosemicarbazide	1- methyl- 3-2- hydroxyl- 5- methyl- phenyl chalcone	1-3 (2 thioamido hydroxyl-5- methyl phenyl)- 5- methyl	70 %	180°C.

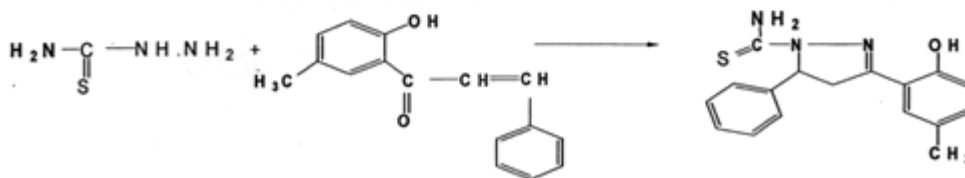
		pyrazoline		
Thiosemicarbazide	1- phenyl- 3-2- hydroxyl-5- methyl phenyl chalcone	1-thioamido-3 (2 hydroxyl- 5- methyl phenyl)- 5- phenyl pyrazoline	73.2 %	110°C.
Thiosemicarbazide	1-methoxy phenyl -3-2 hydroxyl-5- methyl phenyl chalcone	1- thioamido- 3 (2 hydroxyl- 5- methyl phenyl)-5- (4- methoxyphenyl) pyrazoline	47.8 %	90°C.

Formation of IIIa and IIIb can be shown as follows :

Scheme I:-



Scheme II:-



III. EXPERIMENTAL

The melting point are recorded using hot paraffin bath and are uncorrected. Reaction of Isoniazide with 1-p-chloro-3 2 hydroxy 5 methyl phenyl chalcones; formation of 1- isonicotionyl-3 2 hydroxy- 5 methyl phenyl 5- p- chlorophenyl pyrazolines. (2a)

Isoniazide (0.005) and 1-p-chlorophenyl-3-2 hydroxy-5-methyl phenyl chalcone (0.005) in (1-2 drope) ethanol was added to it moisten the mixture. The beaker was covered with a watch glass and irradiated in a microwave oven for 1 min. After completion of reaction the beaker was remove from the oven and mixture

was cooled to room temp. the product was crystallized from ethanol. Yield (79 %) and M.P. was found to be 130°C. Molecular formula of compound was found to be $C_{22}H_{16}N_3O_2Cl$.

On extending the above reaction to other isoniazide pyrazolines were isolated a good yield.

Reaction of Thiosemicarbazide with 1 phenyl-3-2 hydroxyl 5 methyl phenyl chalcone. Formation of 1 thioamido-3- (2-hydroxyl-5 methyl phenyl) 5 phenyl pyrazolines (2b)

Thiosemicarbazide (0.005) and 1-phenyl-3-2-hydroxyl-5-methyl phenyl chalcone (0.005) in (1-2 drope) ethanol was added to it to moisten the mixture. The beaker was covered with a watch glass and irradiated in microwave oven for 1 minute. After completion of reaction the beaker was removed from the oven and mixture was cooled to room temp. the product was crystallized from ethanol. Yield (73.2 %) and M.P. was found to be 110° C. molecular formula of compound was found to be $C_{17}H_{15}N_3OS$. On extending the above reaction to other thiosemicarbazide pyrazolines were isolated good yield.

IV. REFERENCES

- [1]. Shashikant R. Pattan, TalathSirajunisa&PattanJayashri Indian J. Chem, Vol 43 B 2004, 439-441.
- [2]. Kreuzlerger A.E. J. Heterocyclic Chem, 19, 1978, 753.
- [3]. Magharley MA & Hassan AA, Indian J. Chem, 208 B, 1967, 256.
- [4]. Benzimidazole and Congeneric Tricyclic Compound Part-2, Chap 10, edited by P.N. Preston (Wiley Intrescience New York), 1980, Prestone P.N. Chem Rev. 74, 1974, 279.
- [5]. Grimmett M R, Comprehensive Heterocyclic Chemistry, Vol 5, Chap- 408.
- [6]. Bahadur Surendra & Srivastava Neru, J. Indian Chem Soc, 60, 1983, 168.
- [7]. J. Fried, H Mrozk, G.E. Arth, T.S. Bry, N. Cr. Steinberg M. Tischer, R. Hirshmann and S.L. Steelman, J. Am Chem Soc, 85, 1963, 236.

The Fourier Transform Infra-Red Spectroscopical Analysis of *Andrographis Paniculata* Plant Extracts

R. P. Ganorkar¹, Y.S.Tamgadge², R.Y.Bakale²

¹Department of Chemistry, Mahatma Fule Arts, Commerce and Sitaramji Choudhari Science Mahavidyalaya, Warud, Dist. Amravati-444906, Maharashtra, India

²Department of Physics, Mahatma Fule Arts, Commerce and Sitaramji Choudhari Science Mahavidyalaya, Warud, Dist. Amravati- 444906, Maharashtra, India

ABSTRACT

The sample of *Andrographis Paniculata* Plant have been studied Fourier Transform Infra Red Spectroscopical Analysis of extraction in distilled water, ethanol, ethyl acetate and chloroform have been studied. FT-IR spectroscopic analysis is one of such powerful techniques used as an effective tool in phytochemical group investigation by identifying and characterizing chemical bonds present in biological samples including plant parts. The presence of characteristic functional group ketones, Aldehydes, carboxylic acids, Nitro, Ester, Amines, Alkane, Ether and Amides are responsible for various medicinal property of *Andrographis Paniculata* Plant.

Keywords:- *Andrographis Paniculata*, plant extract, FTIR, functional groups.

I. INTRODUCTION

A large number of medicinal plants are used as alternate medicine for diseases of animals and man since most of them are without side effects when compared with synthetic drugs. The investigation of FTIR spectrum of *Tribulus terrestris* leaf extract, shows the carboxylic acid, alkane, aldehyde, unsaturated ketone, phenol, anhydride and halogen compound have been studied¹. Fourier Transform Infrared Spectral, phytochemical and Antimicrobial investigation of solvents extracts of *Urginea indica* (Roxb.) Kunth (Liliaceae) and *Cyclopeltata* Arn. ex Wight (Menispermaceae), results were clearly exposed that the plant contained different bioactive compounds such as of Alkaloids, Anthoquinones, Coumarins, Steroids and Flavonoids compounds were rich in the extracts of *Urginea indica* (Liliaceae) and *Cyclopeltata* (Menispermaceae) are associated with resistance mechanism against many microorganisms. These plants have antimicrobial activity against some gram positive and gram negative bacteria such as, *E.coli*, *Pseudomonas fluorescens*, *Salmonella typhi*, *Bacillus subtilis*, *Klebsiella pneumoniae*, *Staphylococcus aureus*, *Streptococcus*, *Yeast candida*, *Aspergillus niger*².

FTIR Spectroscopy method was performed as the spectroscopical analysis find out the characteristic peak values and functional groups present in the extracts of the root of *Hemidesmus Indicus* and

Dioscorea Bulbifera from Nagthana, in various solvent like acetone, distilled water, ethanol and petroleum ether have been studied. FTIR spectroscopic analysis revealed the presence of values of different functional groups such as ketones, Aldehydes, carboxylic acids, Ether, Ester, Amines, Alkane, and Amides³. The FTIR analysis of methanol leaf extracts of *Phyllanthus amarus*, *Senna auriculata*, *Phyllanthus maderaspatensis* and *Solanum torvum* confirmed the presence of amide, alcohols, phenols, alkanes, carboxylic acids, aldehydes, ketones, alkenes, primary amines, aromatics, esters, ethers, alkyl halides and aliphatic amines compounds, which showed major peaks. The results of the study generated the FTIR spectrum profile for the medicinally important plants of *Phyllanthus amarus*, *Senna auriculata*, *Phyllanthus maderaspatensis* and *Solanum torvum* can be used in the aquaculture industry⁴. The FTIR analysis of aqueous methanolic leaf extracts of *Bauhinia racemose* for phytochemical compounds was done by Gauravkumar et.al.⁵ Kareru et.al. detected saponins in crude dry powder of 11 plants using FTIR spectroscopy. [6]

The Fourier transform Infrared) Spectroscopic analysis of *Nicotiana plumbaginifolia*, an ethno-medicinally important plant. The phytochemical group analysis of the plant has been performed by FT-IR method. Different phytochemical groups present in the plant sample give an indication of its medicinal potency⁷. FT-IR analysis shows the presence of different functional group such as carboxylic acids, aromatics, alkenes, alcohols, phenols, aliphatic amines, alkenes and amino groups in the *Myristica Dactyloids* fruit extract⁸. *Mentha spicata* L. or garden mint cultivated under normal atmospheric situation was investigated for FTIR and spectral lines have shown different distinguishing peaks of functional groups. As a result, alkanes, alkenes, alcohols, phenols, and aromatics etc. have been investigated⁹.

Phytochemical and FT-IR spectral analysis of *Carallumageniculata* Grev. Et Myur. The result of the studies showed the presence of valuable compounds present in the plant. The study also justified the uses of the plant in the treatment of various diseases, ornamental and edible values. Prolongation of study on the same plant is required to identify, isolate, differentiate and make clear the structure of bioactive compounds present in it as there is no comprehensive study on this plant¹⁰. The FTIR method was performed, which was used to detect the characteristic peak values and their functional groups. The results of the study generated the FTIR spectrum profile for the medicinally important plants of *wedeliabiflora* can be used in the industry¹¹. The FT-IR analysis shows the presence of different functional groups such as alcohols, phenols, alkanes, carboxylic acids, aldehydes, ketones, alkenes, primary amines, aromatics, esters, ethers, alkyl halides and aliphatic amine compounds, which showed major compounds present in the leaf extracts. The study generated the FTIR spectrum profile for the medicinally important plant *Grewia tilifolia*¹². Hence, an attempt is made in the present study to analyse the functional groups of *Andrographis paniculata* plant was selected in Chikhaldara in Maharashtra.

II. EXPERIMENTAL

Collection of Plant :-

Site for *Andrographis paniculata* plant was selected in Chikhaldara, Dist-Amravati of Maharashtra State. Before picking the whole plant, the soil was moistened. The collected plant was washed smoothly by distilled

water and was shed dried at room temperature. Sample was crushed separately in pestle-mortar to isolate fine powder. This powder was treated as sample powder for various analyses.

Preparation of Solvent extract:-

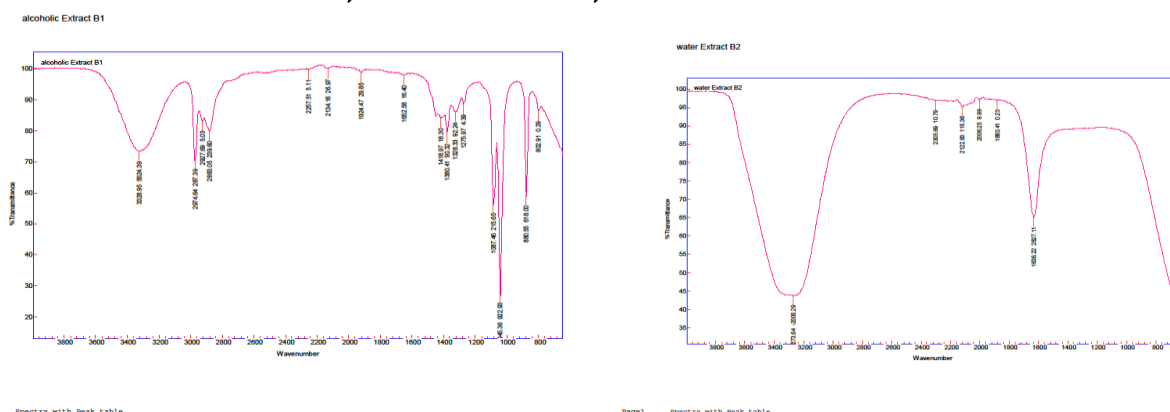
Powdered plant material, 5 g. portion was each separately dispersed in 100 ml of each water, ethanol, ethyl acetate and chloroform. The solution was left to stand at room temperature for 24 hrs and that solution was filtered with whatman No. 1 filter paper. The filtrate was used for the Fourier Transform Infra-Red Spectroscopical Analysis.

Preparation of sample for Infrared Spectrophotometer [FTIR] analysis :-

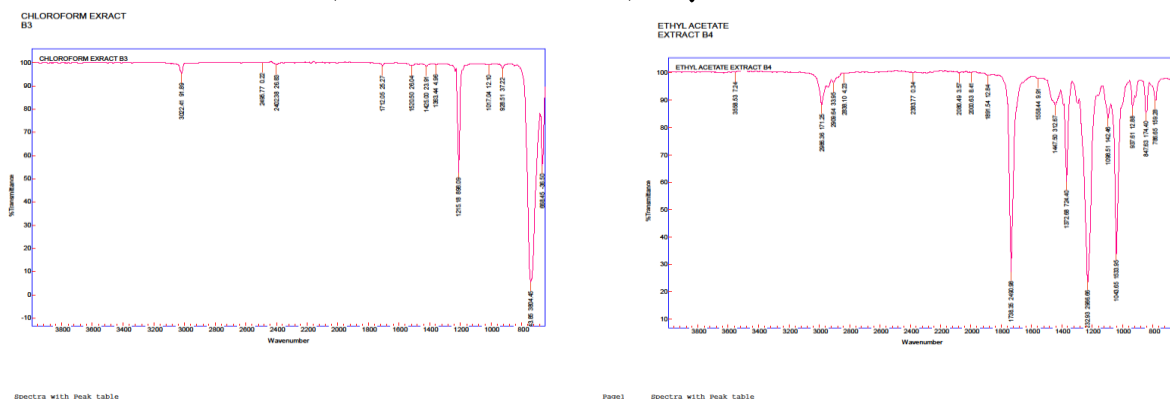
The extract was compressed separately in KBr pellet, to prepare lucent sample discs. The sample was loaded in Fourier Transform Infra-Red spectroscope (Agilent Technologies Ltd., Model No. Cary 630.) with scan range from 600 to 4000 cm^{-1} .

A) FTIR Spectral Data Interpretation of *Andrographis paniculate* plant.

1) Ethanol extract:- 2) Distilled Water extract:-



3) Chloroform extract:- 4) Ethyl Acetate extract:-



III. RESULTS AND DISCUSSION

1) Alcohol (B₁)

Exhibited a characteristic band at 3328 cm^{-1} for (N-H) amines, amides, at 2974 cm^{-1} for (C-H) alkanes at 2883 cm^{-1} for (-C-H) alkanes at 1380 cm^{-1} for (-NO₂) nitro, at 1275 cm^{-1} for (-C-O) alcohol, phenol, ether, ester

etc. at 1087 cm^{-1} for (-C-O) alcohol ,phenol ether ester etc. at 880 cm^{-1} for (=C-H) alkenes ,at 802 cm^{-1} (=C-H) meta substituted benzene.

2) Water (B₂)

Exhibited a characteristic band at 3273 cm^{-1} for (= C-H) Acetylenic at 2122 cm^{-1} for terminal alkynes (-C≡C-H) at 1636 cm^{-1} for (-C=C-) alkenes.

3) Chloroform (B₃)

Exhibited a characteristic band at 3022 cm^{-1} for (=C-H) ethylenic & aromatic, 1712 cm^{-1} for (>C=O) Ketone at 1215 cm^{-1} for (-C-O) alcohol , phenol , ether , ester etc. at 743 cm^{-1} for (ortho substituted benzene , at 668 cm^{-1} for N-H & NH₂.

4) Ethyl acetate (B₄)

Exhibited a characteristic band at 2986 cm^{-1} for (-C-H) alkanes , at 1738 cm^{-1} for (R-C-H) aldehyde,at 1447 cm^{-1} for (-NO₂) nitro ,or CH₃ bending at 1232 cm^{-1} for (-C-O) alcohol , phenol , ether , ester etc. at 1098 cm^{-1} for (-C-O) alcohol , phenol , ether ester ,etc. at 1043 cm^{-1} for (S=O) or (C-O) alcohol , phenol ,ether ,ester, etc. at 937 cm^{-1} for stretch alkenes (=C-H) ,at 847 cm^{-1} for (=C-H) para substituted benzene . At 786 cm^{-1} for (meta substituted benzene.)

IV. CONCLUSION

The presence of characteristic functional group ketones, Aldehydes, carboxylic acids, Nitro, Ester, Amines, Alkane, Ether and Amides are responsible for various medicinal property of *Andrographis Paniculata* Plant. Phytopharmaceuticals also called as herbal drugs are playing a major role in the treatment of diseases. The above functional groups are present in the nucleus of the drug like Ibuprofen, Paracetamol, Gatifloxin, Amoxilin etc. hence may be used as a drugs after further investigations.

V. REFERENCES

- [1]. G. Ambedkar, S. Pragalathan, A. Sabaridasan, K. Gandhimaniyan, S. Dineshkumar, (2019) FTIR Spectrum Analysis and Antibacterial Activity of *Tribulus terrestris* Leaves Extract, *Research & Reviews: A Journal of Microbiology and Virology*, 9, 3, 25-30.
- [2]. U. S. Patil, O.S.Deshmukh and R.P.Ganorkar;(2015) Studies On The Phytochemical, Spectroscopic Characterisation And Antibacterial Efficiency Of *Urginea Indica*(Roxb.) Kunth (Liliaceae) and *Cyclea Peltata* Arn.Ex Wight (Menispermaceae). *European Journal Of Pharmaceutical and Medical Research*, 2(6), 171-176.
- [3]. R.P.Ganorkar, D.D.Kale and Y.S.Tamgadge, (2020) The Fourier Transform Infra-Red Spectroscopical Analysis Of Root Of *Hemidesmus Indicus* And *Dioscorea Bulbifera*. *Journal of Emerging Technologies and Innovative Research*,7(4),1729-1737.

- [4]. R.Ashokkumar and M.Ramaswamy,(2014) Phytochemical screening by FTIR spectroscopic analysis of leaf extracts of selected Indian Medicinal plants, International Journal of Current Microbiology and Applied Sciences,3(1),395-406.
- [5]. Gaurav Kumar, L., Karthik and BhaskaraRao,K.V.(2010) Phytochemical composition and in vitro Antimicrobialactivity of Bauhinia racemosa Lamk(CAESALPINIACEAE). International Journal of Pharmaceutical Sciences and Research 1(11): 51-58.
- [6]. Kareru, P.G., Keriko, Gachanja, J.M., and Kenji, A.N.(2008) African Journal of Traditional, Complementary and Alternative Medicines.; 5(1): 56-60.
- [7]. Sayani Chandra,(2019) Fourier transform Infrared (Ft-Ir) Spectroscopic analysis of Nicotianaplumbaginifolia (Solanaceae) 7(1):82-85.
- [8]. P.Rajiv, A. Deepa, P. Vanathi, D. Vidhya(2017) Screening For Phytochemicals and FTIR Analysis Of Myristica Dactyloids Fruit Extracts, International Journal of Pharmacy and Pharmaceutical Sciences 9(1) 315-318,2017.
- [9]. A. T. Muhammad and S. A. Muhammad Abbasi (2020) FTIR Spectroscopic Analysis of Mentha spicata L. (Garden Mint), Asian Journal of Chemical Sciences,7(1): 1-5.
- [10]. V. Asha1, S. Jeeva and K. Paulraj (2014) Journal of Chemical and Pharmaceutical Research, 6(7),:2083-2088.
- [11]. J.GowriEt.Al.(2015) Phytochemical screening by FTIR spectroscopic analysis of leaf and stem Extracts of wedeliabiflora. International Journal Nano Corrosion Science and Engineering 2(5), 322-334.
- [12]. D. R. Devi, G. R. Battu,(2019)Qualitative Phytochemical Screening And Ftir Spectroscopic Analysis Of Grewia Tilifolia (Vahl) Leaf Extracts,Internationa Journal of Current Pharmaceutical Research ,11, 4, 100-107.



Synthesis and Thermal Properties of Copper Doped KNbO₃ Crystal

A. R. Khobragade^{1*}, A. R. Bansod²

¹Department of Chemistry, Rajee Dharamrao College of Science, Aheri, Maharashtra, India

²Department of Chemistry, Dr. Ambedkar College Deekshabhoomi Nagpur, Maharashtra, India

ABSTRACT

This study Ferroelectric ceramics have been synthesized from powders formulate from individual oxides also called mixed oxide process. The XRD studies of the sample were carried out to determine the lattice parameters. The XRD studies revealed the lattice parameters of Cu doped KNbO₃ single crystals as $a=b=c= 4.0214 \text{ \AA}$. With an cubic structure at room temperature. It actually deviates from the regular orthorhombic structure of KNbO₃.

Key Words: Cubic ,Ferroelectric ceramics, single crystals, orthorhombic.

I. INTRODUCTION

The Potassium niobate (KNbO₃) is very important ferroelectric material having perovskite structure. To its isomorphous analog, BaTiO₃, it shows the cubic - tetragonal -orthorhombic - rhombohedral phase transformations on cooling. Unlike tetragonal BaTiO₃, KNbO₃ is orthorhombic at room temperature, with space group. The spontaneous polarization vector is parallel to the c axis.

II. GROWTH OF KNbO₃ SINGLE CRYSTALS

In the present work it was decided to undertake the crystal growth studies in detail, and to see how the techniques of crystal growth are reflected in the physical properties of the crystal. The importance of the studies is great if the anisotropy is high, and the impurity interactions are complex. Deshmukh and Ingle¹ found that at phase transition temperature 235°C the conductivity in 'a' domains is about 10⁷ times larger as compared to that in 'c' domains. Also there are many complex impurity interactions. Most of the work on dielectrics, conductivity and domain studies are by Ingle and his coworker¹⁻⁹. Since the development of their technique to grow large clear crystals of KNbO₃ of some sufficiently high domain width. In the present work, this technique is explored in details both theoretically and experimentally, and the technique has been used with advantage with better results. The physical properties of KNbO₃ have been investigated experimentally and theoretically¹⁰⁻¹⁸. Recently, the KNbO₃-based crystals have been used in the photorefractive hybrid¹⁹ and self-pumped photorefractive two-beam coupling²⁰. Because of certain legal

restrictions on use of toxic lead, recently there has been great interest in lead-free materials²¹⁻²³ to replace PbTiO₃-based materials which are the widely used acoustic sensors and transducers. There has been a flurry of activity to study KNbO₃-based ferroelectrics owing to good piezoelectric performance among lead-free materials. A site cations (such as Fe, Na and Mn) doped KNbO₃ have been investigated for their desirable dielectric properties^{18,19-30-32}.

III. SYNTHESIS

KNbO₃ single crystals

The growth of single crystals of KNbO₃ by flux method was reported by Jolly³³. In this Present work by using Flux method of single crystals of KNbO₃ are grown from melt which is composed of mixture potassium carobate and niobium oxide in the molar composition of 1.2:1 with an impurity of CuO (10mg). The mixture was grounded together in a mortar for 5-6 hours and put into a 50 ml platinum crucible. The mixture was heated in furnace up to 1100°C. The mixture was soaked at this temperature for 24 hours and cooled slowly at the rate of 20°C/hr up to 900°C. It was reheated till 1000°C and kept at this temperature for 18 hours. Finally, the crucible was cooled at the rate of 20°C /hr till room temperature and the large sized single crystals were obtained.

The reheating mechanism is important in order to get large sized single crystals. Conventional method supports stray nucleation due to which small crystallites develop. The reheating is expected to re-dissolve the number of small crystals that might be nucleated initially as a result of stray nucleation. In the reheating process, the smaller crystallites dissolve rapidly, while the larger crystallites are also attacked and get reduced in size. Gradually, while during re-soaking and re-cooling process the crystallites in the solution act as a crystal growth centers or as seeds for crystal growth and large crystal growth takes place. The crystals obtained by this method were pale yellow transparent ranging from 40 to 400 mesh in size.

IV. CuO DOPED KNbO₃ CHARACTERIZATION

4.1 XRD studies

The XRD studies revealed the lattice parameters of Cu doped KNbO₃ single crystals as $a = b = c = 4.0214 \text{ \AA}$. With a cubic structure at room temperature. It actually deviates from the regular orthorhombic structure of KNbO₃.

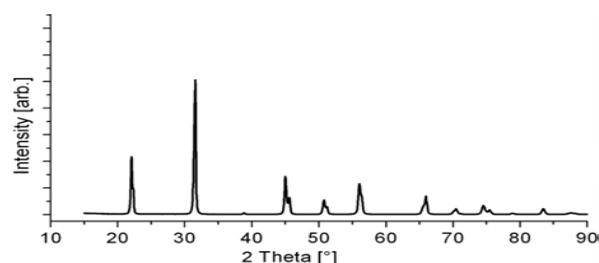


Fig.4.1: XRD of Cu Doped KNbO₃

4.2 Scanning electron microscope (SEM)

The microstructure obtained of Cu doped KNbO₃ sample are found to be having large grains from approximately 10 to 50 μ m with mostly homogeneity in grains.

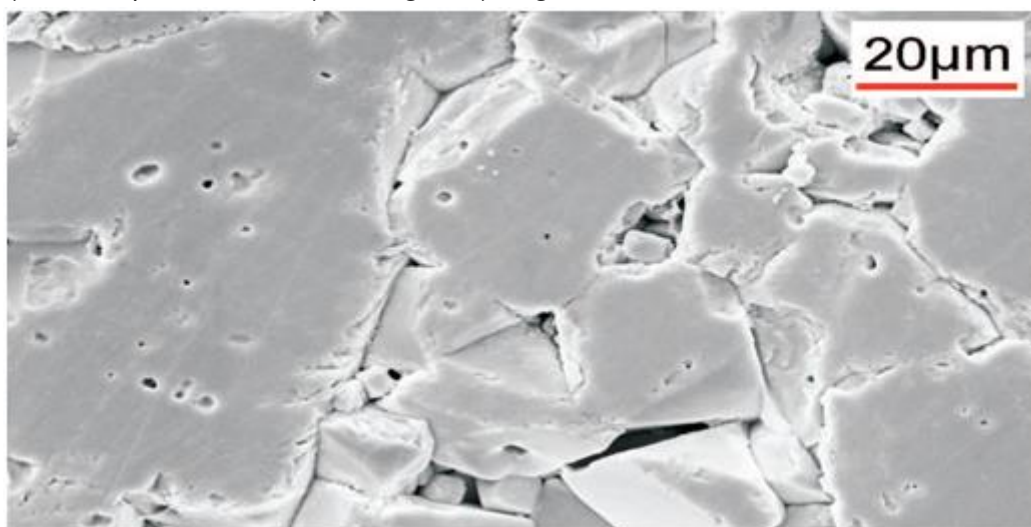


Fig. 4.2. Microstructure of Cu doped KNbO₃

4.3 Thermal analysis

Differential thermal analysis (DTA) curves of the Mn doped KNbO₃ nanoparticles are displayed in Figure 4.19 . The curves were recorded from T_r to 900 °C with heating rate of 10 °C/minutes

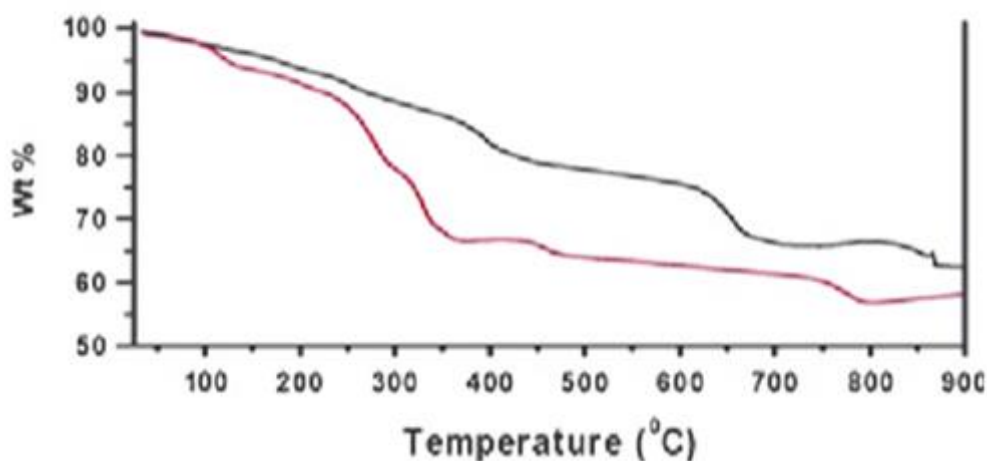


Fig.4.3: DTA Wt% curve of CuO doped KNbO₃

The curves shows that the maximum weight loss (\sim 38%) occurs in case of doped CuS nanoparticles, CuS nanoparticles shows that it is of endothermic nature, as curves lies below zero base line level all throughout the analyzed temperature range.

V. CONCLUSIONS

This study Ferroelectric ceramics have been synthesized from powders formulate from individual oxides also called mixed oxide process. The XRD studies of the sample were carried out to determine the lattice parameters. The theoretical lattice constant is 3.977 \AA , which is in good accord with the experimental data of pure KNbO_3 within the difference of 0.6%. This value is better than results, The XRD studies revealed the lattice parameters of Cu doped KNbO_3 single crystals as $a=b=c= 4.0214 \text{ \AA}$. With an cubic structure at room temperature. It actually deviates from the regular orthorhombic structure of KNbO_3 .

VI. REFERENCES

- [1]. Deshmukh, K.G. and Ingle, S.G. Curr. Sci., No. 16, 39 (1970) 368.
- [2]. Deshmukh, K.G. and Ingle, S.G. J. physics D: Appl. Physics, 4 (1974 a) 124.
- [3]. Deshmukh, K.G. and Ingle, S.G. J.Phys. D: Appl.Phys. 4(1971 b) 1633.
- [4]. Deshmukh, K.G. and Ingle, S.G. Ind. J. Pure and Appl.Phys. 10 (1972 a) 29.
- [5]. Deshmukh, K.G.and Ingle, S.G.Ind. J. Pure and Appl. Phys. 10 (1972 b) 353.
- [6]. Kulkarni, R.H. and Ingle, S.G. Ind. J. Phys. D: Appl. Phys., Vol. 6 (1972).
- [7]. Kulkarni, R.H. and Ingle .S.G. J. Phys. D: Appl. Phys. Vol. 6 (1973).
- [8]. Mishra, M.B. and Ingle, S.G. J. Appl.Phys. 45 (1974) 5152.
- [9]. Mishra, M.B. and Ingle S.G. J. Phys., D: Appl. Physics, Vol. 10 (1977) 1149.
- [10]. R. Pattnaik, J. Toulouse, Phys. Rev. Lett. 79 (1997) 4677.
- [11]. J. Sigman, D.P. Norton, H.M. Christen, P.H. Fleming, L.A. Boatner, Phys. Rev. Lett. 88 (2002) 097601.
- [12]. T. Neumann, G. Borstel, C. Scharfschwerdt, M. Neumann, Phys. Rev. B 46 (1992) 10623.
- [13]. A.V. Postnikov, T. Neumann, G. Borstel, Phys. Rev. B 48 (1993) 5910.
- [14]. R.D. King-Smith, David Vanderbilt, Phys. Rev. B 49 (1994) 5828.
- [15]. D.J. Singh, Phys. Rev. B 53 (1996) 176.
- [16]. C.M.I. Okoye, J. Phys.: Condens. Mat. 15 (2003) 5945.
- [17]. O. Die'guez, K.M. Rabe, D. Vanderbilt, Phys. Rev. B 72 (2005) 144101.
- [18]. M.J. Deer, Appl. Phys. Lett. 88 (2006) 254107.
- [19]. G. Cook, J.L. Carns, M.A. Saleh, D.R. Evans, Phys. Rev. B 73 (2006) 174102.
- [20]. E. Cross, Nature 432 (2004) 24.
- [21]. Y. Saito et al., Nature 432 (2004) 84.
- [22]. S.K. Mishra, N. Choudhury, S.L. Chaplot, P.S.R. Krishna, R. Mittal, Phys. Rev. B 76 (2007) 024110.
- [23]. C. Medrano, M. Zgonik, I. Liakatas, P. Gu'nter, J. Opt. Soc. Am. B 13 (1996) 2657.
- [24]. G. Sa'ghi-Szabo', R.E. Cohen, Phys. Rev. B 59 (1999) 12771.
- [25]. H. Fu, R.E. Cohen, Nature 403 (2000) 281.
- [26]. S.A. Prosandeev et al., Phys. Rev. B 70 (2004) 134110.
- [27]. N. Choudhury, Z. Wu, E.J. Walter, R.E. Cohen, Phys. Rev. B 71 (2005) 125134.

- [28]. R.E. Cohen, Nature 441 (2006) 941.
- [29]. Z. Feng, X. Ren, Appl. Phys. Lett. 91 (2007) 032904.
- [30]. R.-P. Herber, G.A. Schneider, S. Wagner, M.J. Hoffmann, Appl. Phys. Lett. 90 (2007) 252905.
- [31]. B.P. Burton, T. Nishimatsu, Appl. Phys. Lett. 91 (2007) 092907.
- [32]. M.D. Segall, P.J.D. Lindan, M.J. Probert, C.J. Pickard, P.J. Hasnip, S.J. Clark, M.C. Payne, J. Phys.: Condens. Mat. 14 (2002) 2717.
- [33]. Jolly, A, Ann. Sci.De l' e Cole Norm.Suppl.Paris, 6 (1877) 164.
- [34]. Fakuda, T., Uematsu, Y. and Ito, T.J. Crystal Growth, 24(1979) 450.

To Study the Impact of Concentration and Temperature on Intermolecular Interaction Between Dextrose and Electrolyte Solution

Sandhya D. Pinge*, Urvashi P. Manik, Paritosh L. Mishra

*PG, Department of Physics, Sardar Patel Mahavidyalaya, Chandrapur-442401, Maharashtra, India

ABSTRACT

Densities and Ultrasonic velocity of Dextrose in electrolyte solution have been determined experimentally at 283.15K, 288.15K, 293.15K and 298.15K with different concentration. From these experimental data the Adiabatic compressibility (β_s), Acoustic impedance (Z), Intermolecular free length (Lf), Non-linearity parameter (β/A), will be calculated. The variation in concentration and temperature is useful in understanding the nature of molecular interaction in terms of physical parameters. On the basis of trends obtained for different parameter, it is cleared that there exist solute-solvent interaction shows greater molecular association through hydrogen bonding.

Keywords: Acoustic parameters, Adiabatic compressibility, Density, Dextrose and Ultrasonic velocity.

I. INTRODUCTION

Ultrasonic techniques are widely applied to estimate the acoustic property and the intermolecular interaction between the liquid mixture and ionic interaction of dextrose in electrolyte solution. [1] By these technique velocity, density and related parameter of electrolyte solution (NaCl) can be determine. And also, in the mixture of solute-solute, solute-solvent system we evaluate the structure making and nature of the system. Characterizing the physico-chemical behaviour of liquid mixtures. Further, they play an important role in many chemical reactions. Due to their ability of self-association with manifold internal structure. [2-3] The interaction of solute-solvent is understanding by Ultrasonic technique. The implementation of Ultrasonic methods for probing the structural vital of polysaccharides has been the theme of extensive research. [4] Carbohydrates is one of the main nutrients which gives energy to our body, tissues. And Dextrose is a example of carbohydrates which is soluble in water and these biomolecules of significant importance present in the biological system. Dextrose gives calories and may be given drip in combination of amino acid and fats. [5] To study the thermodynamic properties in electrolyte solution is an important process to understanding the behaviour biological fluids including different ionic species and study the stability. [6]

II. MATERIAL AND METHODS

The monosaccharide dextrose {[CAS No. 50-99-7] [Molecular weight – 180.16 g/mol]} used in the present work is of analytical reagent (AR) grade with 99% purity which is used as a solute and the fresh distilled water + NaCl [Molecular wt. -18.051528 g/mol and 58.44g/mol] with density [1000 kg/m³] is used as a solvent. This process was done at different temperature (283.15K, 288.15K, 293.15K, 298.15K) which were maintained by using a digital water bath.

The measurement of weight was done by using a digital weighing machine having an accuracy of ±0.1mg some basic parameters like [(a) Ultrasonic velocity were measured on a digital Ultrasonic interferometer with a 2MHz frequency having an accuracy of 0.1%. (b) The Ultrasonic density of this solution was accurately determined by a using a 10ml density gravity bottle.] By using these two basic parameters of dextrose solution measured at different temperatures and concentrations, we can estimate other various acoustical parameters.

Defining Relation:

1. **Adiabatic Compressibility (β):** It is the fractional change (decrease) in volume per unit increase of applied pressure when no heat flows in or out of the system. Quantitatively, the reciprocal of bulk modulus, $\beta = 1/ U^2 \rho$
2. **Acoustic Impedance (Z):** It is the ratio of sound pressure to particle velocity at a single frequency and is expressed as 'rayals'. It is depending on the density of the medium and the speed of the sound wave. $Z = U \rho$
3. **Non – linearity parameter (B/A):** It is a basic parameter for determining the degree of waveform distortion. From the Non - linearity Parameter we can gather information about some physical properties of the liquid mixture such as internal pressure and structural behaviour etc.
4. **Relative Association (RA):** It is a parameter used to assess the association in any solution relative to the association existing in solvent. It is estimated using the following relation, $RA = \{(\rho/\rho_0) (U/U_0)^{1/3}\}$
5. **Intermolecular free length (L_f):** It is the distance between the surfaces of neighbouring molecules in the medium. The intermolecular free length can be calculated from the relation, $L_f = \{K(\beta)^{1/2}\}$
6. **Isothermal Compressibility:** Isothermal Compressibility is a useful concept in determining the compressible properties of the reservoir. $K_T = \gamma \cdot B_a$

III. RESULT AND DISCUSSION

The oversufficiency of thermo-acoustic parameters which plays an important role to understanding the nature of molecular interaction of liquid mixtures have been studied by several researchers. The variation obtained by experimentally determined values of Ultrasonic velocity, density and other acoustical parameters of dextrose solution at different temperatures (283.15K, 288.15K, 293.15K, 298.15K) and different concentration as shown in fig. 1-8.[7]

Ultrasonic velocity is a major parameter which provide information and it is greatly affected by the concentration and the temperature. It depends upon the change in elastic properties of liquid solution during its propagation. Ultrasonic velocity of the solution increases with increase in concentration and temperature as shown in fig.1. Compressibility of the solution decreases with the increase in concentration therefore ultrasonic velocity increases which clearly denote that rise in solute-solvent interaction shows greater molecular association through hydrogen bonding one of the Constituent in the solution.

The density of dextrose in the present investigation increases with increase in concentration and decrease with increase in temperature (as shown in fig.2) as the temperature increases, the particle become weakly packed Therefore the density is decrease.[8] Adiabatic compressibility decreases with increase in concentration and temperature, this decrease value of adiabatic compressibility indicates strong intermolecular Association between the dextrose and solvent (NaCl+ water) as shown in fig. 3. because adiabatic compressibility depends on electron donor and acceptor capacity. Water is universal polar solvent when Dextrose is added, the association of solute -solvent molecules shows the close packing of molecules.[9]

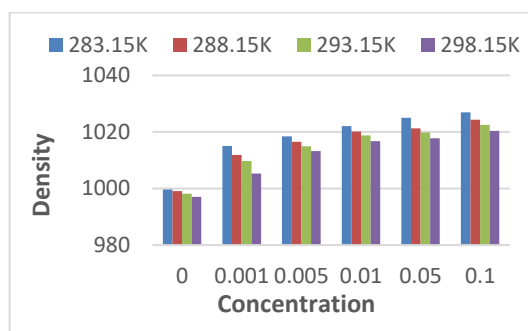
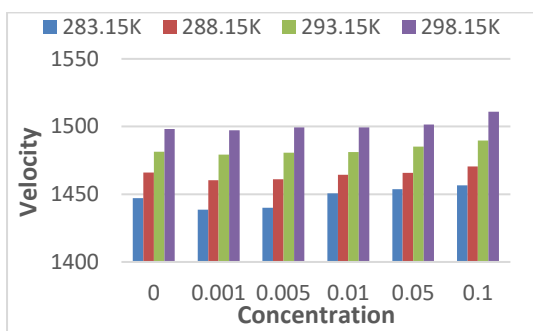


Fig. 1. Variation of Ultrasonic Velocity with Concentration and temperature.

Fig. 2. Variation of Density with concentration and temperature.

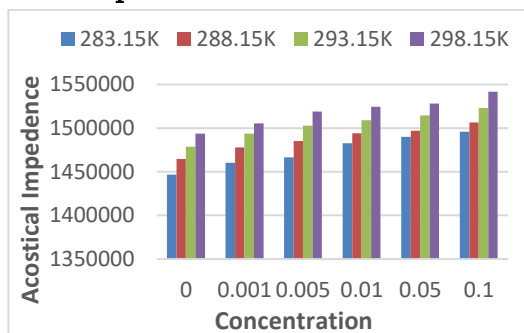
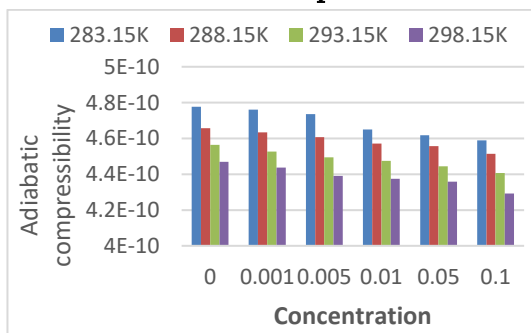


Fig.2. Variation of adiabatic compressibility with Concentration and temperature.

Fig. 4. Variation of Acoustic Impedance with Concentration and temperature..

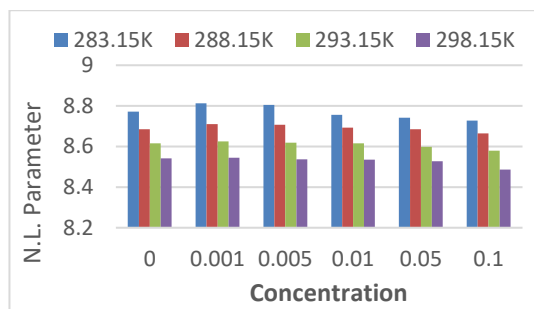


Fig. 5. Variation of Non Linearity Parameter with Concentration and temperature.

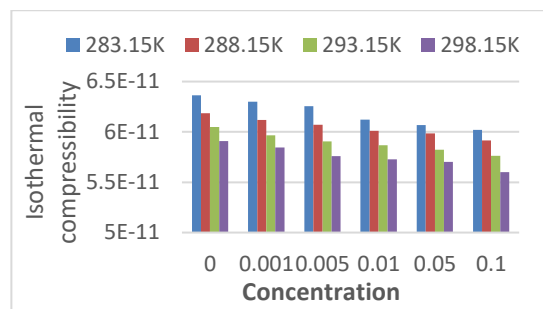


Fig. 6. Variation of Isothermal Compressibility with Concentration and temperature..

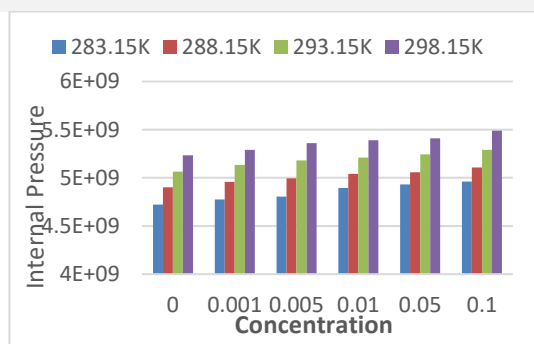


Fig. 7. Variation of Internal Pressure with Concentration and temperature.

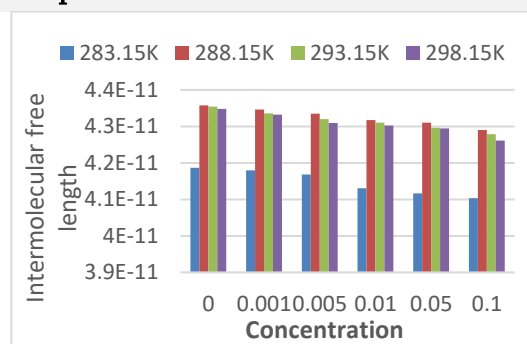


Fig. 8. Variation of Intermolecular free length with Concentration and temperature.

Acoustical Impedance values increase with increase in concentration of dextrose at all temperature in fig. 4. It is found that accords with experimental data the values of velocity and density both increases with increase concentration of solute. The increasing of impedance shows that effective solute-solvent interaction. From the fig.5 shows that the Non linearity Parameter for Dextrose as a function of concentration and temperature. From it is observed that the value of B/A decreasing with increase in temperature. This process indicates that less array value of B/A and confirms the less interaction at low temperature.[10]

The all over observation of the isothermal compressibility (K_T) are as shown in fig. 6 from the trend it is found that the decreasing the Isothermal compressibility with increasing concentration and temperature. From these the result of dextrose decreasing free volume and average Kinetic energy of the constituent solute-solvent molecules in the solution.[11] The trend of Internal Pressure increases with increasing concentration and temperature as resulting the association through ionic bonding. It gives the increasing magnitude of interaction between Dextrose and NaCl in fig. 7. [12]

Intermolecular free length is used to determining the mobility and understanding the nature as well as strength of interaction between solute-solvent. From the fig.8 it observed that the Intermolecular free length decreases with increasing concentration.[13]

IV. CONCLUSION

Ultrasonic Technique is a very efficient, sensitive and powerful probe for characterizing the acoustical and physico-chemical parameters, such as measure values are velocity and density of the dextrose in the solvent at different temperature and concentrations. The impact of concentration and temperature on the above parameters were observed and derived the presence of strong interaction between solute-solvent and greater molecular association through hydrogen bonding or ionic bonding and in some parameter, interaction is weak and to understanding the effective nature of solute-solvent.

V. REFERENCES

- [1]. B. Swain, R. Mishra, U. Dash., J. Pure Appl. Ultraso.39(2017), pp-8-12.
- [2]. D. Ahlawat, M. Gill, J. Pure Appl. Ultraso. 39(2017) pp-23-26.
- [3]. A. Mugugkar, A. Maharolkar., Ind. J. Adv. Chem. Sci. 2(2014), pp249-252.
- [4]. S.K Swain, P.P Priyadarshini., Ind. J. Pure Appl. Phy. 48(2010) pp-539-542.
- [5]. Y. Akhtar, M. A. Albalawi, S.M. Yasin., Curr. Res. Dev.Chem. Vol-2. (2020) pp-86-93
- [6]. A P Mishra., Ind.J. Chem. Vol-43A. (2004), pp-730-733.
- [7]. P.B. Nalle, B. R. Shinde, S. U. Shinde, R.G.Dorik, K.M. Jadhav., J. Pure Appl. Ultraso.39(2017) pp-1-7.
- [8]. V. A. Giratkar, R. B. Lanjewar, S. M. Gadegone.,Int. J. Res. Bioscience Ag. Tech. 5(2017) pp-41-45.
- [9]. S. Rathika, K. R. Devi, S. Geetha, A. Gomathiyalini., IOSR J. Appl. Phy. 6 (2014) pp-19-24.
- [10].P.L.Mishra, A. B. Lad, U. P. Manik.,Int. Res. J. Sci. Eng.(2020) pp-260-265.
- [11].P.L.Mishra, A. B. Lad, U. P. Manik., J. Pure Appl. Ultraso. 43(2021) pp-27-34.
- [12].A. S. Dange, O. P. Chimankar., Int. J. Sci. Eng. (2020) pp-874-877.
- [13].V.G. Dudhe, V.A. Tabhane, O. P. Chimankar., Int. J. Sci. Res. 5(2016) pp-2398-2401.

Synthesis and Physical Properties of Mn Doped KNbO₃ Crystal

A. R. Khobragade^{1*}, A. R. Bansod²

¹Department of Chemistry, Raje Dharamrao College of Science, Aheri, Maharashtra, India

²Department of Chemistry, Dr. Ambedkar College, Deekshabhoomi, Nagpur, Maharashtra, India

ABSTRACT

This study Ferroelectric ceramics have been synthesized from powders formulate from individual oxides also called mixed oxide process. The XRD studies are found to be very much important to find the lattice parameters. The XRD pattern of Mn doped KNbO₃ is exhibited here in the Fig. 3.2. The lattice parameters are determined as $a = 4.0 \text{ \AA}$, $b = 5.6 \text{ \AA}$, $c = 5.7 \text{ \AA}$. It is orthorhombic structure.

Key Words: Ferroelectric ceramics, single crystals, orthorhombic.

I. INTRODUCTION

Potassium niobate (KNbO₃) is a well-known lead free ferroelectric material with high Curie temperature¹. Interestingly, KNbO₃ exists in two ferroelectric phases, orthorhombic and tetragonal above room temperature. Solid solution of KNbO₃ and NaNbO₃, is one of the most promising candidates of lead-free piezoelectric materials because previous research has indicated that NKN has not only an excellent piezoelectric property but also a high Curie temperature ($T_c > 400 \text{ }^\circ\text{C}$)^{2,3}. It also exhibits a variety of properties like piezoelectricity, nonlinear optical response, electromechanical coupling, and photo-catalytic activity^{4,5}. Hence it attracts considerable interest in fundamental research and for applications in sensors, actuators, and transducers and other technological fields⁶. Inducing ferromagnetism in this ferroelectric KNbO₃ would give rise to multiferroic behavior making it a potential material for the fabrication of multifunctional devices such as data storage elements, magnetic resonance devices controlled via electric field, and transducers with electrically controlled piezoelectric devices⁷. Room temperature ferromagnetism can be induced by the doping of transition metal ions (TM). An approach of this kind has been successful in the case of diluted magnetic semiconductors, in which ferromagnetism is induced in the host semiconducting materials (CuO,⁸ ZnO,⁹⁻¹² and SnO₂¹³⁻¹⁵) by doping them with TMs like Fe, Mn, Cr, Co, and Ni. Based on the idea, some studies on Co doped KNbO₃¹⁶, report ferromagnetic nature in the doped samples at room temperature. There are a few reports of doping of Mn in KNbO₃^{17,18} and their electrical properties. In this paper, a systematic study on the effect of Mn doping in structural, morphological, magnetic, dielectric, and ferroelectric properties of KNbO₃ has been carried out¹⁹. Dielectric behavior of pure and Mn doped KNbO₃ as a function of (with respect to) frequency and temperature has also been studied. Magneto-dielectric response of Mn doped KNbO₃ is the first time report²⁰.

II. EXPERIMENTAL

The growth of single crystals of KNbO_3 by flux method was reported by Jolly²¹. In this Present work by using Flux method of single crystals of KNbO_3 are grown from melt which is composed of mixture raw materials were high-purity (99.99%) powders of K_2CO_3 , Nb_2O_5 and in the molar composition of 1.2:1.0. with Mn_2O_3 (10 mg). The mixture was grounded together in a mortar for 5-6 hours and put into a 50 ml platinum crucible. The mixture was heated in furnace up to 1100°C . The mixture was soaked at this temperature for 24 hours and cooled slowly at the rate of 20°C/hr up to 900°C . It was reheated till 1000°C and kept at this temperature for 18 hours. Finally, the crucible was cooled at the rate of 20°C/hr till room temperature and the large sized single crystals were obtained. The crystals obtained by this method were transparent ranging from 30 to 200 mesh in size. The molten solution is cooled very slowly in the presence of seeds. Single crystals by Kyropoulos techniques were also grown by Fakuda²² et. al. They controlled the growth rates and orientation of seed precisely. The melt composition of K_2CO_3 , 52.5 mol % and Nb_2O_5 , 47.5 mol % seed orientation along the pseudo-cubic $\{001\}$ and seed orientation of 30 r.p.m. , were the conditions used for crystal growth . The crystals were pooled by applying a 1kV/cm d.c. field at about 180°C in a Silicone Oil bath. The various controls were exercised precisely , and therefore ,this method of crystal growth become quite elaborate ,further ,the cooling at a very slow rate (of order of 0.5°C/hour) required a lot of time for crystal growth . The application of d.c. field during the polling produces high stress regions. Riesman et.al²³. used polycrystalline KNbO_3 with excess of K_2CO_3 (52.5 mol %) as a flux. The charges were heated to 960°C at 10 min. and soaked for 20 hrs at this temperature to obtain equilibrium. The melt was then cooled at the rate of 1°C/min . The crystals obtained by this method were Mn-doped KN crystals were brownish white transparent in colour ranging from 40 to 400 mesh in size.

III. RESULTS AND DISCUSSION OF PHYSICAL PROPERTIES OF Mn_2O_3 DOPED KNbO_3

3.1 XRD studies

The XRD studies are found to be very much important to find the lattice parameters. The XRD pattern of Mn doped KNbO_3 is exhibited here in the Fig. 3.1. The lattice parameters are determined as $a = 4.0 \text{ \AA}$, $b = 5.6 \text{ \AA}$, $c = 5.7 \text{ \AA}$. It belongs symmetry group $\text{Amm}2$ with orthorhombic structure.

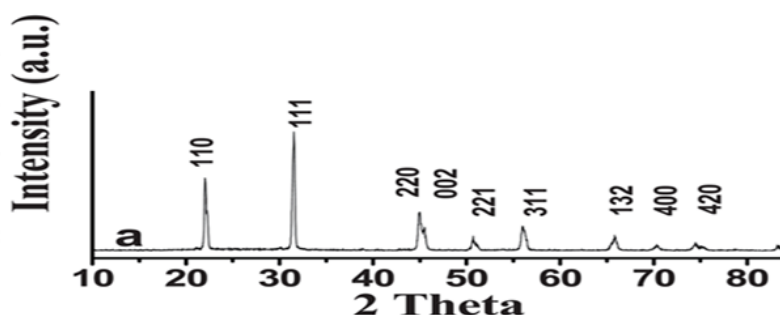


Fig.3.1: XRD study of Mn Doped KNbO_3 Crystal

The intensities and positions of these diffraction peaks were found to be consistent with the standard diffraction data for KNbO_3 (JCPDS 32-0822), indicating good formation of KNbO_3 with orthorhombic symmetry.

3.2 Scanning electron microscope (SEM)

The microstructure of the sintered samples was analysed using a scanning electron microscope (Leica 440). The surface was polished with a water-free solution and then etched with a H_2O - HCl - HF solution. The microstructure revealed large grains from approximately 11 to $20\mu\text{m}$ with linearly dimensions and some grains.

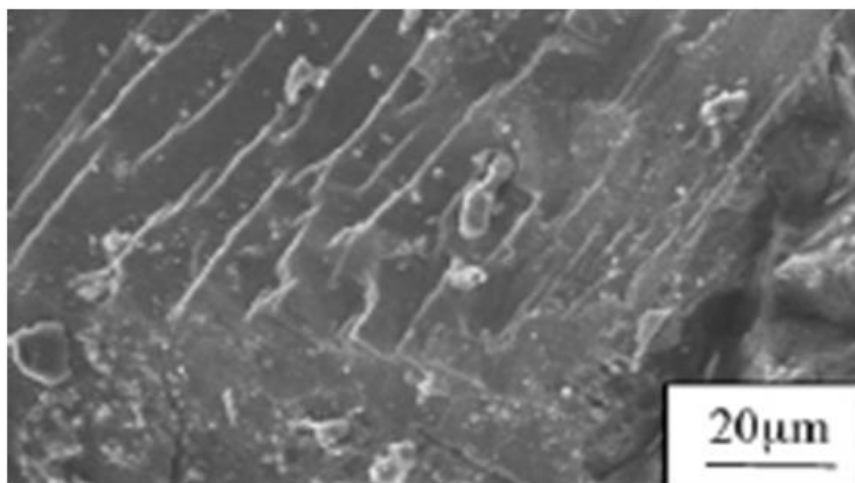


Fig.3.2: SEM micrographs of Mn doped KNbO_3

3.3 Thermal analysis

DSC measurement confirmed that Mn was substituted in the perovskite-type structure of Mn Doped KN because the orthorhombic-tetragonal phase-transition temperature (T_{o-t}) and T_c shifted to a higher temperature by Mn-doping as shown in Fig. 3.3. T_{o-t} and T_c of Mn-doped Mn doped KN crystals were 194.1 and 417.9 °C, respectively.

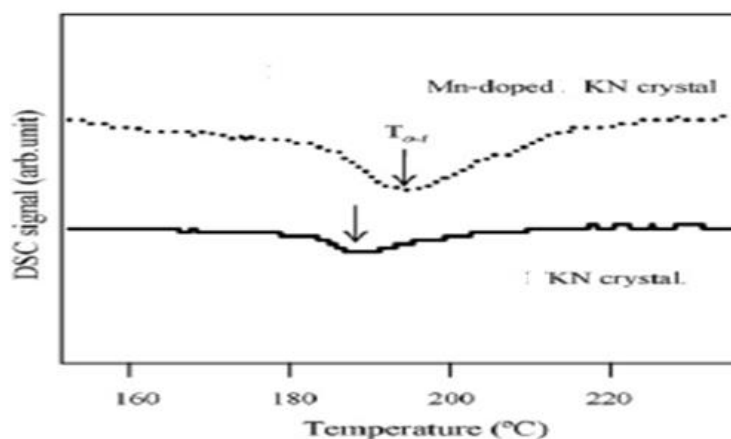


Fig.3.3: DSC of Mn_2O_3 doped KNbO_3

From these results, it was found that Mn was substituted in the structure of KN, but a part of doped Mn was segregated out due to the function of purification.

IV. REFERENCES

- [1]. Deshmukh, K. G. and Ingle, S. G. Nuclear physics and Solid State physics Symposium, Abstract No. 594 (December 28-31, 1969).
- [2]. Egerton, L. and Dillion, D. M., Piezoelectric and dielectric properties of ceramics in the system potassium–sodium niobate. *J. Am. Ceram. Soc.*, 1959, 42, 438–442.
- [3]. Saito, Y., Takao, H., Tani, T., Nonoyama, T., Takatori, K., Homma, T., Nagaya, T. and Nakamura, M., Lead-free piezoceramics. *Nature*, 2004, 432, 84–87.
- [4]. D. Fu, M. Itoh, and S. Y. Koshihara, *J. Appl. Phys.* 106, 104104 (2009).
- [5]. K. Min, F. Huang, X. Lu, Y. Kan, J. Zhang, S. Peng, Y. Liu, J. Su, C. Zhang, Z. Liu, and J. Zhu, *Solid State Commun.* 152, 304 (2012).
- [6]. T. Delahaye, A. Al-Zein, M. H. Berger, X. Bril, and J. F. Hochepped, *J. Am. Ceram. Soc.* 97, 1456 (2014).
- [7]. G. Singh, V. S. Tiwari, and P. K. Gupta, *Integr. Ferroelectr.* 117, 1 (2010).
- [8]. Y. Li, M. Xu, L. Pan, Y. Zhang, Z. Guo, and C. Bi, *J. Appl. Phys.* 107, 113908 (2010).
- [9]. R. K. Singhal, M. Dhawan, S. Kumar, S. N. Dolia, Y. T. Xing, and E. Saitovitch, *Physica B* 404, 3275 (2009).
- [10]. Y. Liu, Y. Yang, J. Yang, Q. Guan, H. Liu, L. Yang, Y. Zhang, Y. Wang, M. Wei, X. Liu, L. Fei, and X. Cheng, *J. Solid State Chem.* 184, 1273 (2011).
- [11]. W. Chen, L. F. Zhao, Y. Q. Wang, J. H. Miao, S. Liu, Z. C. Xia, and S. L. Yuan, *Solid State Commun.* 134, 827 (2005).
- [12]. P. K. Sharma, R. K. Dutta, and A. C. Pandey, *J. Magn. Magn. Mater.* 321, 3457 (2009).
- [13]. S. A. Ahmed and S. H. Mohamed, *J. Magn. Magn. Mater.* 324, 812 (2012).
- [14]. S. A. Ahmed, *Solid State Commun.* 150, 2190 (2010).
- [15]. W. Chen and J. Li, *J. Appl. Phys.* 109, 083930 (2011).
- [16]. A. Astudillo, J. L. Izquierdo, A. Gomez, G. Bolaños, and O. Moran, *J. Magn. Magn. Mater.* 373, 86 (2015).
- [17]. K. Matsumoto, Y. Hiruma, H. Nagata, and T. Takenaka, *Ceram. Int.* 34, 787 (2008).
- [18]. N. Yawata, H. Nagata, and T. Takenaka, *Ferroelectrics* 458, 158 (2014).
- [19]. P. Manimuthu, N. P. Shanker, K. S. Kumar, and C. Venkateswaran, *Physica B* 448, 354 (2014).
- [20]. T. Sakakura, J. Wang, N. Ishizawa, Y. Inagaki, and K. Kakimoto, *IOP Conf. Ser.: Mater. Sci. Eng.* 18, 022006 (2011).
- [21]. Jolly, A, *Ann. Sci.De l' e Cole Norm.Suppl.Paris*, 6 (1877) 164.
- [22]. Fakuda, T., Uematsu, Y. and Ito, T.J. *Crystal Growth*, 24(1979) 450.
- [23]. Riesman, A.andHoltzberg, F.J.*Am.Chem. Soc.* 77 (1955) 2155.



Synthesis and Thermal Properties of Fe Doped KNbO₃ Crystal

A. R. Khobragade^{1*}, A. R. Bansod²

¹Department of Chemistry, Rajee Dharamrao College of Science, Aheri, Maharashtra, India

²Department of Chemistry, Dr. Ambedkar College, Deeksha bhoomi, Nagpur, Maharashtra, India

ABSTRACT

This study Ferroelectric ceramics have been synthesized from powders formulate from individual oxides also called mixed oxide process. The XRD studies of the sample were carried out to determine the lattice parameters. The XRD studies revealed the lattice parameters of fe doped KNbO₃ single crystals The lattice parameters of Fe doped KNbO₃ single crystals are found as a = 5.69195 Å, b = 3.96691 Å and c = 5.71130 Å. with orthorhombic structure.. It actually deviates from the regular orthorhombic structure of KNbO₃.

Keywords: Ferroelectric ceramics, single crystals, orthorhombic.

I. INTRODUCTION

Potassium niobate (KNbO₃) is a well-known lead free ferroelectric material with high Curie temperature¹. Interestingly, KNbO₃ exists in two ferroelectric phases, orthorhombic and tetragonal above room temperature. Solid solution of KNbO₃ and NaNbO₃, is one of the most promising candidates of lead-free piezoelectric materials because previous research has indicated that NKN has not only an excellent piezoelectric property but also a high Curie temperature (T_c > 400 °C)^{2,3}. It also exhibits a variety of properties like piezoelectricity, nonlinear optical response, electromechanical coupling, and photo-catalytic activity^{4,5}. Hence it attracts considerable interest in fundamental research and for applications in sensors, actuators, and transducers and other technological fields⁶. Inducing ferromagnetism in this ferroelectric KNbO₃ would give rise to multiferroic behavior making it a potential material for the fabrication of multifunctional devices such as data storage elements, magnetic resonance devices controlled via electric field, and transducers with electrically controlled piezoelectric devices⁷. Room temperature ferromagnetism can be induced by the doping of transition metal ions (TM). An approach of this kind has been successful in the case of diluted magnetic semiconductors, in which ferromagnetism is induced in the host semiconducting materials (CuO,⁸ ZnO,⁹⁻¹² and SnO₂¹³⁻¹⁵) by doping them with TMs like Fe, Mn, Cr, Co, and Ni. Based on the idea, some studies on Co doped KNbO₃¹⁶, report ferromagnetic nature in the doped samples at room temperature. There are a few reports of doping of Mn in KNbO₃^{17,18} and their electrical properties. In this paper, a systematic study on the effect of Mn doping in structural, morphological, magnetic, dielectric, and ferroelectric properties of KNbO₃ has been carried out¹⁹. Large effective trap densities at near-infrared wavelengths were obtained in crystals

doped with Fe, Ni, Rh, and Mn–Rh. This result may lead to large exponential gains. From the calculated photorefractive sensitivities, we conclude that crystals doped with Rh, Fe, Mn, and Mn–Rh show promising results at 860 nm. At longer wavelengths only Rh-doped crystals presented photorefractive sensitivities at least four times larger than the Fe-doped crystals.²⁰ suggest that the introduction of dopants in BaTiO₃ crystals may produce the adequately active species for the response in the near-infrared wavelength region. Few attempts to extend the photorefractive sensitivity of KNbO₃²¹⁻²³ to the infrared have been performed.

II. EXPERIMENTAL

The growth of single crystals of KNbO₃ by flux method was reported by Jolly²⁴. In this Present work by using Flux method of single crystals of KNbO₃ are grown from melt which is composed of mixture raw materials were high-purity (99.99%) powders of K₂CO₃, Nb₂O₅ in the molar composition of 1.2:1 with impurity Fe₂O₃ (10mg). The mixture was grounded together in a mortar for 5-6 hours and put into a 50 ml platinum crucible. The mixture was heated in furnace up to 1100°C. The mixture was soaked at this temperature for 24 hours and cooled slowly at the rate of 20°C/hr up to 900°C. It was reheated till 1000°C and kept at this temperature for 18 hours. Finally, the crucible was cooled at the rate of 20°C /hr till room temperature and the large sized single crystals were obtained. The reheating mechanism is important in order to get large sized single crystals. Conventional method supports stray nucleation due to which small crystallites develops. The reheating is expected to re-dissolve the number of small crystals that might be nucleated initially as a result of stray nucleation. In the reheating process, the smaller crystallites dissolve rapidly, while the larger crystallites are also attacked and get reduced in size. Gradually, while during re-soaking and re-cooling process the crystallites in the solution acts as a crystal growth centers or as seeds for crystal growth and large crystal growth takes place. The charges were heated to 960°C at 10 min. and soaked for 20 hrs at this temperature to obtain equilibrium. The melt was then cooled at the rate of 1°C/min., The crystals obtained by this method were transparent ranging from 30 to 200 mesh in size. The molten solution is cooled very slowly in the presence of seeds. Single crystals by Kyropoulos techniques were also grown by Fakuda²⁵ et. al. They controlled the growth rates and orientation of seed precisely. The melt composition of K₂CO₃, 52.5 mol % and Nb₂O₅, 47.5 mol % seed orientation along the pseudo-cubic {001} and seed orientation of 30 r.p.m., were the conditions used for crystal growth. The crystals were pooled by applying a 1kV/cm d.c. field at about 180°C in a Silicone Oil bath. The various controls were exercised precisely, and therefore, this method of crystal growth become quite elaborate, further, the cooling at a very slow rate (of order of 0.5°C/hour) required a lot of time for crystal growth. The application of d.c. field during the polling produces high stress regions. Riesman et.al²⁶. used polycrystalline KNbO₃ with excess of K₂CO₃ (52.5 mol %) as a flux. The charges were heated to 960°C at 10 min. and soaked for 20 hrs at this temperature to obtain equilibrium. The melt was then cooled at the rate of 1°C/min. The high-temperature heat capacity of KNbO₃ in the temperature ranges from 280 K to 820 K was measured using a DSC (TA, Q2000). According to the American Society for Testing Materials (ASTM) standard, the measurements of heat capacity were performed in a dynamic model with a heating rate of 10 K/min under the high purity argon atmosphere

(99.998%, 50 mL/min)²⁷⁻³⁰. The crystals obtained by this method were Fe-doped KN crystals were white transparent in colour ranging from 40 to 400 mesh in size.

III. Fe₂O₃ DOPED KNbO₃ CHARACTERIZATION

3.1 XRD studies

The lattice parameters of Fe doped KNbO₃ single crystals are found as $a = 5.69195 \text{ \AA}$, $b = 3.96691 \text{ \AA}$ and $c = 5.71130 \text{ \AA}$. with orthorhombic structure. The sample is found to be in more crystalline form but with larger crystalline size as compared to that of aluminum doped KNbO₃ crystal.

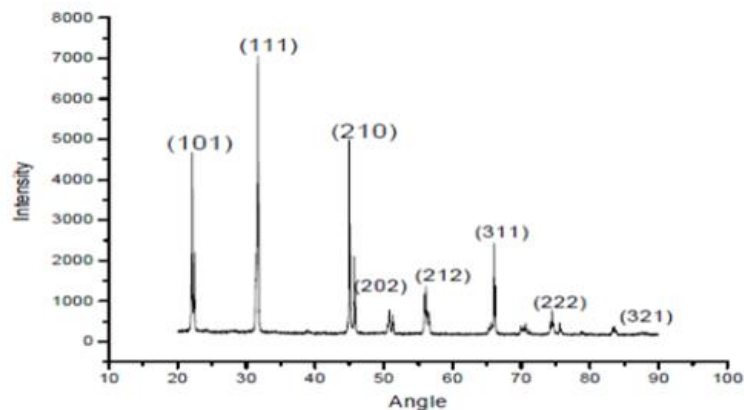


Fig. 3.1 X-ray diffraction of Fe doped KNbO₃ sample.

3.2 Scanning electron microscope (SEM)

The figures 4.16 show well-developed cubic/orthorhombic morphology of crystal structure with well-separated crystal grains. The SEM micrographs show the single crystalline nature of the sample, with almost rectangular grains of different sizes uniformly distributed throughout the sample surface. A good amount of porosity can be observed from the SEM micrograph. The microstructure obtained of Fe doped KNbO₃ sample are found to be having large grains from approximately 2 to 10 μm with mostly homogeneity in grains.

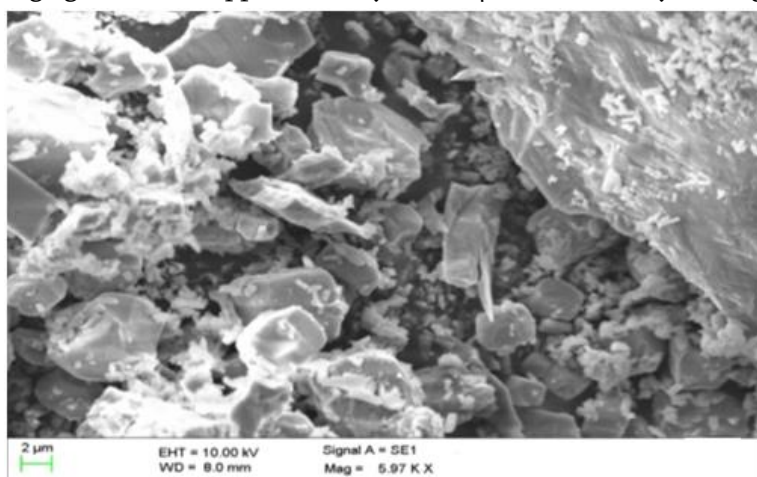


Fig. 3.2 SEM Micrograph of Fe Doped KNbO₃

3.3 Thermal analysis

The DTA shows small endotherm at 240°C followed by one another at 450°C. These correspond to some phase transitions. Lossless mass transitions are indicated the phase transition.

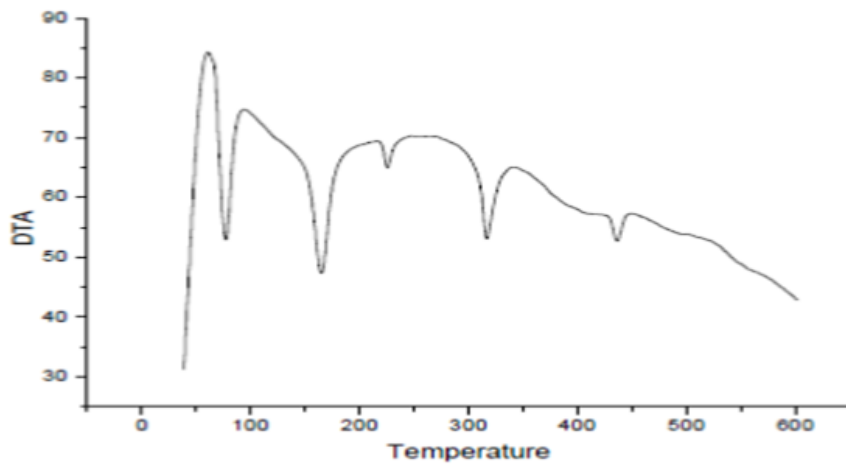


Fig. 4.17 DTA curve of Fe₂O₃ doped KNbO₃.

3.4 DSC

The DSC results show that KNbO₃ undergoes four-stages of phase transitions during the heating process. The KNbO₃ undergoes phase transformations from triclinic system to orthorhombic system at 258.6 K and the corresponding enthalpy is 72.47 J·mol⁻¹. The phase transformation occurs at 486.2 K is assigned to the KNbO₃ crystal from orthorhombic system to tetragonal system, and the phase transformation enthalpy is 317.71 J·mol⁻¹.

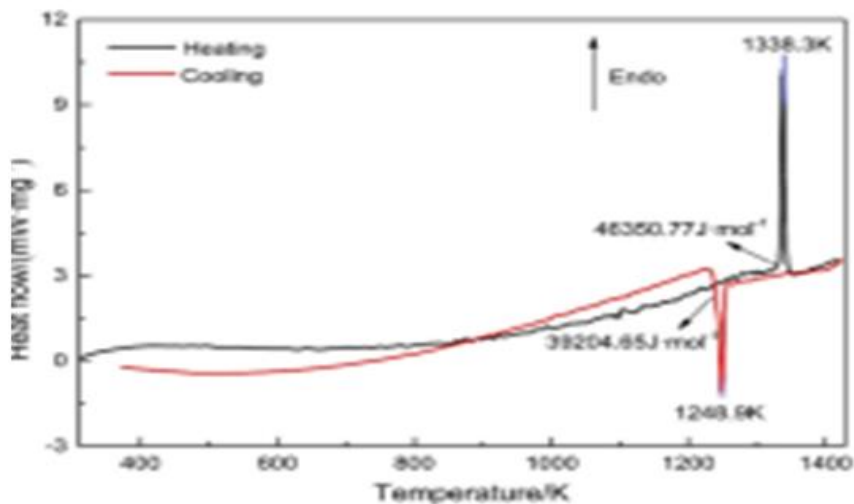


Fig.3.4 DSC curve of KNbO₃ with a heating and cooling rate of 10 K/min

The phase transformation occurring at 699.4 K is due to crystal changing from tetragonal system to cubic type and the phase transformation enthalpy is 506.89 J·mol⁻¹. The sharp endothermic effect at 1333.7 K corresponded to the fusion of KNbO₃ and the enthalpy of fusion ΔH_f is equal to 46,350.77 J·mol⁻¹.

IV. REFERENCES

- [1]. Deshmukh, K. G. and Ingle, S. G. Nuclear physics and Solid State physics Symposium, Abstract No. 594 (December 28-31, 1969).
- [2]. Egerton, L. and Dillion, D. M., Piezoelectric and dielectric properties of ceramics in the system potassium–sodium niobate. *J. Am. Ceram. Soc.*, 1959, 42, 438–442.
- [3]. Saito, Y., Takao, H., Tani, T., Nonoyama, T., Takatori, K., Homma, T., Nagaya, T. and Nakamura, M., Lead-free piezoceramics. *Nature*, 2004, 432, 84–87.
- [4]. D. Fu, M. Itoh, and S. Y. Koshihara, *J. Appl. Phys.* 106, 104104 (2009).
- [5]. K. Min, F. Huang, X. Lu, Y. Kan, J. Zhang, S. Peng, Y. Liu, J. Su, C. Zhang, Z. Liu, and J. Zhu, *Solid State Commun.* 152, 304 (2012).
- [6]. T. Delahaye, A. Al-Zein, M. H. Berger, X. Bril, and J. F. Hochepped, *J. Am. Ceram. Soc.* 97, 1456 (2014).
- [7]. G. Singh, V. S. Tiwari, and P. K. Gupta, *Integr. Ferroelectr.* 117, 1 (2010).
- [8]. Y. Li, M. Xu, L. Pan, Y. Zhang, Z. Guo, and C. Bi, *J. Appl. Phys.* 107, 113908 (2010).
- [9]. R. K. Singhal, M. Dhawan, S. Kumar, S. N. Dolia, Y. T. Xing, and E. Saitovitch, *Physica B* 404, 3275 (2009).
- [10]. Y. Liu, Y. Yang, J. Yang, Q. Guan, H. Liu, L. Yang, Y. Zhang, Y. Wang, M. Wei, X. Liu, L. Fei, and X. Cheng, *J. Solid State Chem.* 184, 1273 (2011).
- [11]. W. Chen, L. F. Zhao, Y. Q. Wang, J. H. Miao, S. Liu, Z. C. Xia, and S. L. Yuan, *Solid State Commun.* 134, 827 (2005).
- [12]. P. K. Sharma, R. K. Dutta, and A. C. Pandey, *J. Magn. Magn. Mater.* 321, 3457 (2009).
- [13]. S. A. Ahmed and S. H. Mohamed, *J. Magn. Magn. Mater.* 324, 812 (2012).
- [14]. S. A. Ahmed, *Solid State Commun.* 150, 2190 (2010).
- [15]. W. Chen and J. Li, *J. Appl. Phys.* 109, 083930 (2011).
- [16]. A. Astudillo, J. L. Izquierdo, A. Gomez, G. Bolaños, and O. Moran, *J. Magn. Magn. Mater.* 373, 86 (2015).
- [17]. K. Matsumoto, Y. Hiruma, H. Nagata, and T. Takenaka, *Ceram. Int.* 34, 787 (2008).
- [18]. N. Yawata, H. Nagata, and T. Takenaka, *Ferroelectrics* 458, 158 (2014).
- [19]. P. Manimuthu, N. P. Shanker, K. S. Kumar, and C. Venkateswaran, *Physica B* 448, 354 (2014).
- [20]. C. Medrano, E. Voit, P. Amrhein, and P. Guñter, “Optimization of the photorefractive properties of KNbO₃ crystals,” *J. Appl. Phys.* 64, 4668 (1988).
- [21]. X. Ma, Z. Xing, and D. Shen, “Investigation of non-Fe doped KNbO₃ crystals,” in *Photorefractive Materials, Effects, and Devices*, Vol. 14 of 1991 OSA Technical Digest Series (Optical Society of America, Washington, D.C., 1991), postdeadline paper 1.
- [22]. C. Medrano, M. Zgonik, N. Sonderer, C. Beyeler, S. Krucker, J. Seglins, H. Wu“ est, and P. Gu“ nter, “Photorefractive effect in Cu- and Ni-doped KNbO₃ in the visible and near infrared,” *J. Appl. Phys.* 76, 5640 (1994).

- [23]. Y.Ding, H. J. Eichler, Z. G. Zhang, B. Burfeindt, F. Willig, D. Z. Shen, X. Y. Ma, and J. Y. Chen, "New dopants in KNbO₃ for photorefractive self-pumped phase conjugation: extension into the near infrared," in Conference on Lasers and Electro-Optics, Vol. 15 of 1995 OSA Technical Digest Series (Optical Society of America, Washington, D.C., 1995), p.48.
- [24]. Jolly, A, Ann. Sci.De l' e Cole Norm.Suppl.Paris, 6 (1877) 164.
- [25]. Fakuda, T., Uematsu, Y. and Ito, T.J. Crystal Growth, 24(1979) 450.
- [26]. Riesman, A.andHoltzberg, F.J.Am.Chem. Soc. 77 (1955) 2155.
- [27]. Jinxiang Youa , GuanghuiLia,b , ShuhuiZhanga , Xin Zhanga , Jun Lua , MingjunRaoa,b,* , ZhiweiPenga,bSynthesis, characterization and thermodynamic properties of KNbO₃Vol. 13, No. 11/November 1996/ J. Opt. Soc. Am. B 265729 May 2021 .
- [28]. G.S. Pei, J.Y. Xiang, X.W. Lv, G. Li, S.S. Wu, D.P. Zhong, W. Lv, High-temperature heat capacity and phase transformation kinetics of NaVO₃, J. Alloy. Compd. 794 (2019) 465–472,
- [29]. A.N. Mansurova, R.I. Gulyaeva, V.M. Chumarev, S.A. Petrova, High-temperature heat capacity and temperatures of phase transformation of the FeNb₂O₆, J. Alloy. Compd. 695 (2017) 2483–2487,
- [30]. G.S. Pei, J.Y. Xiang, L.L. Yang, X. Jin, X.W. Lv. Thermodynamic properties of sodium pyrovanadate (Na₄V₂O₇) at high temperature (298.15–873 K) Calphad 70, 2020, 1–6. <https://doi.org/10.1016/j.calphad.2020.101802>.



The Divergence of the Laser Beam Emitted by this Segment Would Have Less Angle of Divergence Because the Plasma Has Less Thickness

A. P. Pachkawade

Department of Physics, Rajarshree Shahu Science College, Chandur Rly, Dist. Amravati, Maharashtra, India

ABSTRACT

The angle of divergence of output beam are different for Copper Vapour Laser and pulsed laser. The angle of divergence determine the photon flux when the beam is focused using focusing optics. Further the output beam is focused the diverging beam converges and get focused at the same point. In the present work, the analytical expressions are obtained for the peak power output of the CVL without mirror, the intensity of the laser radiation across the laser beam and peak power angle of divergence along the diameter of the discharge tube. The angle of divergence is determined by the absorption coefficients, initial inversion density and the dimensions of the laser plasma column in a direction perpendicular to the direction of propagation of the beam. The angle of divergence also increase with the dimensions of the plasma column in a direction perpendicular to the direction of propagation of the beam. From the calculation of peak power across the laser beam desired angle of divergence may be obtained. The half peak power angle of divergence for initial inversion density 0.2 and 0.4 are 20mrad and 30mrad respectively in Copper Vapour Laser.

Keywords:- Copper Vapour Laser, laser radiation, inversion density, dimensions of the laser plasma.

I. INTRODUCTION

Especially in the copper vapour laser the vapours of the chemical elements are extensively used as the active medium [1]. In some designs the bids of copper metal are used as the source of copper. The laser beam is characterized by spectral band-width, the wavelength, output power, polarization and angle of divergence. The most important characteristics of any laser is the divergence of its output radiation which plays very important role in the determination of photon flux. The angles of divergence of output beams are different for CV lasers and pulsed lasers. In case of pulsed lasers the divergence may vary during the formation of the output pulse. The angle of divergence determines the photon flux when the beam is focused using focusing optics. Further when the output beam is focused the diverging beam converges and gets focused at some point. There are many methods for measuring the angle of divergence, such as the methods of sections, recording of the angular distribution and of intensity methods of focal spot [2]. A method for on line analysis by line scanning of a focal spot is suggested in work of A.P.Anerovov et al [3]. However, all these methods are not sufficient to give the idea about the evolution of the divergence during the formation of output pulse. O.

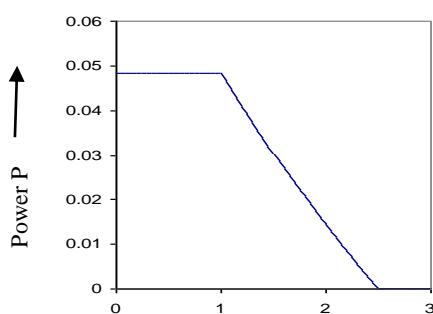
Burihinskir [4] describe a method for recording changes in the divergence during the formation of output pulse.

The stimulating action in the laser medium starts with the signal produced by spontaneous emission and subsequent amplification of the radiation by the laser medium. In case of cyclic lasers, X-ray laser and high power solid state lasers the gain of the amplifying medium is relatively high and the amplification rate is also high and the intensity builds up immediately after the production of spontaneous emission. In case of copper vapour laser [5,6], nitrogen laser [7,8], lead vapour laser [9] the gain of the media is high and the production of population inversion is transient phenomenon, the single pass of the radiation is sufficient for building up of the laser intensity. On the other hand the laser like He-Ne [10], He-Cd [11] and He-Zn [12], the optical gain of the medium is small and multiple pass of the radiation is essential for building up of the laser intensity. In case of multiple pass laser the radiation having less angle of divergence gets amplified. However, in transient laser the spontaneous radiation gets amplified and comes out of the cavity in a very short interval of time consequently the radiation having large angle of divergence gets amplified. Thus, the pulsed laser having narrow pulse width, have large angle of divergence and the CW lasers have low angle of divergence [13]. Being high gain lasers the X-ray lasers and high power solid state lasers have large angle of divergence.

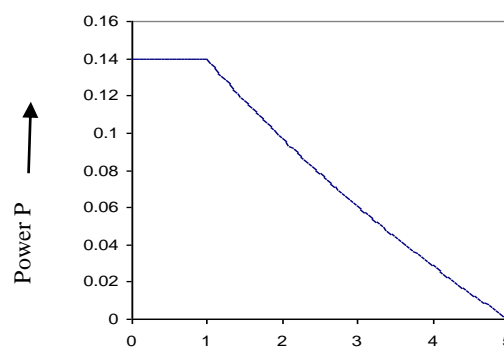
The theoretical and experimental study has not been extensively done as far as the angle of divergence is concerned. But few computations in the branch of angle of divergence of pulsed laser are carried out by Pawar and his co-workers [14].

In the present work the analytical expressions are obtained for the peak power output of the CVL without mirror, the intensity of the laser radiation across the laser beam and half peak power angle of divergence of the copper vapour laser beam. The angle of divergence is obtained by graphical method. The peak output power of the laser beam at various inversion density and at various radial points across the laser beam is studied.

The absorption coefficient of the transition of 3371Å pulsed nitrogen laser is about 0.4 per cm. The dimension of laser plasma lies between 0.1 to 1 cm. Therefore the operating parameters of the pulsed ultraviolet nitrogen laser are very much similar to the copper vapour laser. Hence the behavior of the angle of divergence in nitrogen and X-ray lasers are very much similar to that in the copper vapour laser.



Distance edge of the plasma column X
Fig 1: The laser power across the laser beam
 [Horizontal div for $N_{ti}=0.2$]



Distance edge of the plasma column X
Fig 2: The laser power across the laser beam
 [Horizontal div for $N_{ti}=0.2$]

The figures 1 and 2 show that the power across the laser beam is nearly constant between B and C in if the inversion density is uniform across the laser medium. If the point P on the observation plane shifts from B' to D' i.e. from $x = 0$ to $x = L'D/L$. The beam intensity increases very slowly. For the points beyond D the beam power goes on decreasing as x increases and it becomes zero for $x = x_0 = L d \alpha_0 n(t_i)/2$ or for a beam traveling in the direction making an angle $\theta_0 = d\alpha_0 n(t_i)/2$ with the plane of the nearest edge of the laser tube. It may be clearly stated that, if θ_0 , d and α_0 are known, $n(t_i)$ may be calculated using above relation. Hence, the value of initial inversion density may be obtained by measuring θ_0 . The inversion experienced by photon flux traveling parallel to laser axis and the photon flux traveling in oblique direction is the same. The energy stored in terms of inversion density is shared by two fluxes. Hence, the inversion density obtained by this method may be slightly lower than the actual value of the inversion density.

We also calculated peak power for different values of x along the diameter of the discharge tube at different diameters and results are plotted in figures 3 and figure 4 for the initial inversion density 0.1, and 0.3 respectively. The results clearly indicate that as the initial inversion density goes on increasing, the peak power goes on increasing. The magnitude of the peak power is unchanged as the diameter of the laser tube is changed. Thus, we may conclude that the output peak power depends on initial inversion density rather than the diameter of the discharge tube.

From the calculations of peak power[21,22] across the laser beam desired angle of divergence may be obtained. The half peak power angle of divergence for $n(t_i) = 0.2$ and 0.4 are 20 mrad and 30

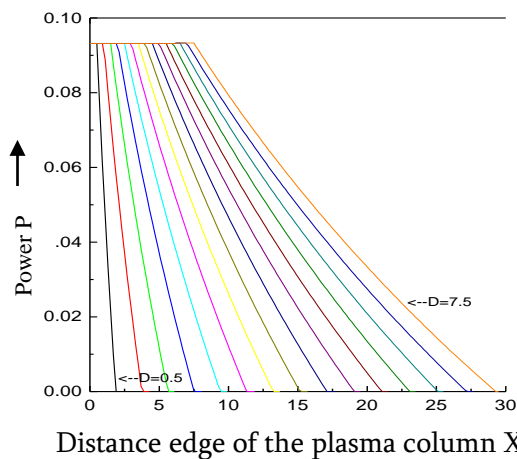


Fig 3: The peak power for the different values for the diameter of the discharge tube at different diameter at initial inversion density is 0.1

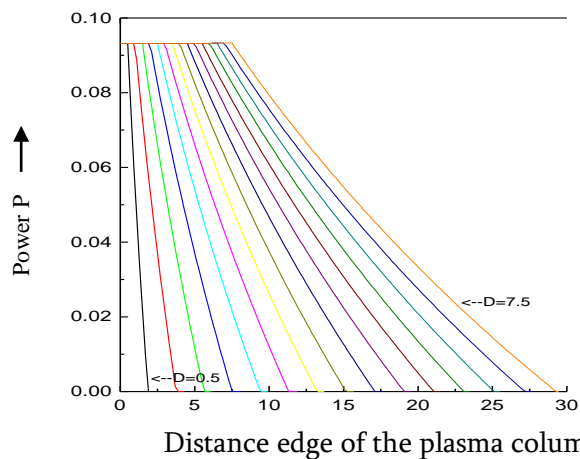


Fig 4: The peak power for the different values for diameter of the discharge tube at different diameter at initial inversion density is 0.1

mrad respectively in T.E. field pumped CVL. In this we may say that also the leading part of the output laser beam has large angle of divergence and that of lagging part has less angle of divergence. In case of the A.E. field pumped CVL the angle of divergence is much less than the above mentioned figures. This is because reason that the laser beam makes many passes before coming out of the laser cavity and the rate of production

of population inversion is relatively low compared T. E. field pumped laser as the current density is low in case of A. E field pumped laser. The results of the experimental measurements of the angle of divergence may be compared with the computation carried out in the present work. The comparison shows good agreement between the theoretical calculations and the experimental results.

While obtaining the results in the present work, it is assumed that the initial inversion density in the laser medium is constant across the discharge tube. But it has been shown that the electron temperature is not constant across the discharge tube and the population density of the upper and lower laser states are different. This leads to the variation in the inversion density across the discharge tube. The study of the angle of divergence now becomes crucial and the calculation of angle of divergence becomes complicated if the beam becomes annular in shape while it is easy when beam is not annular. The laser discharge consists of thin hollow, cylindrical shells of constant inversion densities. This indicates that a part of the cylindrical shell parallel to the laser axis treated as segment of discharge and the angle of divergence may be calculated. The divergence of the laser beam emitted by this segment would have less angle of divergence because the plasma has less thickness.

II. RESULTS AND DISCUSSION

We assume that the initial inversion density is constant through out the laser medium for calculating radial variation of peak power across the laser beam of copper vapour laser operating at 5106A or 5782A. The length of the laser discharge tube is taken to be about 100cm and the diameter is to be 1 cm (specification of these values due to our laser parameters). The plane of observation is assumed to be located at a distance of 100cm from the exit end of the laser. The absorption cross section for the copper atoms at wavelengths 5106A or 5782A is about 0.393 cm^{-1} . The initial inversion density is about 0.25 when the laser discharge conditions are optimized. We have calculated peak power for different values of x along the diameter of the discharge tube by using equation 17 and the results are plotted in figures 1 and 2 for the initial inversion densities of 0.2 and 0.4 respectively. The figures show that if the value of x is increased, the peak power also increases till the point comes to a position for which $x = L'd/L$ for the values of x more than Ld/L the peak power of the laser radiation go on decreasing as the value of x is increased. Finally the peak power goes to zero for a certain value of x .

III. REFERENCES

- [1]. A.M.Prokaorov, Laser Hand book (in Russian), Vol., Sover Skoe Rads, Mascow (1978).
- [2]. E.P.VysokorovKubarev, N.Morozov and V.R.Provin Izmer Proc.No.5, PP. 32, (1973).
- [3]. V.P.An dronov etal Prib. Tel. RKSS, (1978).
- [4]. O.I.Buzhinskir, S.A.Kuznetsova, I.A.Slivitskaya and A.A.Shivitskir. ov.J.Quantum electron, Vol.10, No.2, (1950).
- [5]. S.Gabay, I.Smilansky and 2, Karny IEEE J. Quantum electronics, QE14, PP.427, (1978).

- [6]. J.J.Kim and K.Im J. Opt. Soc. Amer. A – 1, PP.1242, (1984).
- [7]. W.A.Citzsimmons, L.W.Anderson, C.E.Reidhauser and J.M.Vertilek JEEEJ. Quantum Electronics, PP. 624 – 633, (1976).
- [8]. T. Kasuya and D.R.Lide Appl. Optics, Vol.6, No.1, PP. 69 – 80, (1967).
- [9]. G.R.Fowels and A.W.T.Silfvast Appl. Phys.lett, Vol.6,PP.236–237 (1966)
- [10]. K.G.Hernquvist and D.C.Pultorak Rev. Sci. Instrum., Vol. 43 No.2, PP. 290 – 292, (1971).
- [11]. M.Mori, M.Murayana, T.Goto and S.Hattori JEEE J. Quantum Electronic, QE – 14, PP. 427, (1978).
- [12]. P.Gill and C.E.Webb J.Phys. D:Appl. Phys, Vol.11,PP.245–254, (1978).
- [13]. S.N.Thakur Presented in Work shop, I.A.T., March (1988).
- [14]. B.H.Pawar, S.P.Bhandari and L.V.Thakare M. U. Journal, (1992).
- [15]. W. G. Wanger and B. A. Lengyl J. Appl. Phys., Vol.34, PP. 2040, (1963)
- [16]. P.Richter, J.D.Kimal and G.C.Motton. Appl. Optics, Vol.15, PP.756, (1976)
- [17]. D.W. Coutts and D.J. W. Brown Appl. Opt. 34, PP. 1502-1512, (1995)
- [18]. R.Riva, J.T. Watanuki, B.Christ, C.Schwab and N.A.S. Rodrigues Revista de Fisica Aplicada, Vol.12, No.4, (1997)
- [19]. B Singh, S. R. Daultabad, V.V.Subramaniam and A. Chakraborty Proc. Sixth DAE-BRNS National Laser Symposium, (2006)
- [20]. I.I. Balchev, N.I. Minkovski, I.K. Kostadinov and N.V. Sabotinov Bulg. J. Phys. 33 PP.39-47 (2006)
- [21]. F.Pedaci, Y. Wang, M. Berrill, B.Luther, E. Granados and J.J. Rocca Optics Letters, Vol.33, Issue5, PP. 491- 493 (2008)
- [22]. J. hao, Q.L. Dong and J. Zhang Optics Letters, Vol.32, Issue5, PP.491-493 (2007)
- [23]. Y.Liu, Y.Wang, M.A.Larotonda, B.M.Luther, J.J.Rocca and D.T. Attwood Optics Letters, Vol.14, Issue26, PP. 12872-12879 (2006) 113, ISSN 1549-3636 (2006)



Behaviour Investigated As Tunneling Behaviour of Electrolytic Solution Using DC Glow Discharge

A.P.Pachkawade

Department of Physics, Rajarshree Shahu Science College, Chandur Rly, Dist. Amravati, Maharashtra, India

ABSTRACT

Phenomenon of discharge of electricity through the study of property of ionized gases has proved to be fruitful for the investigation. The dc glow discharge spectrometry is the most essential part of the electrical and spectral emission studies of the molecules, atoms and ions in the interface of solid and liquid. We measured the intensity of radiation emitted by dc glow discharge as a function of discharge current for the different electrolytes along with V-I characteristics. The voltage-ampere characteristics during a glow discharge in the atmospheric pressure gas using an electrolytic solution as the anode and metal electrode like tungsten as a cathode were carried out. Under the study of glow discharges of various elements, a monochromatic light at various wavelengths generated. Few species shows a change in the color of the glow when discharge current increased. We investigated negative resistance of solutions. This behavior investigated as tunneling behavior of electrolytic solution using DC glow discharge.

Keywords: Glow discharge, interface, radiation intensity, tunneling.

I. INTRODUCTION

Electrical and spectral characterization of the glow discharge [1-7] of the material helps in studying the chemical composition of the material. The elements in the material may be excited in the plasma [8] produced between liquid and solid interface. The neutral atoms, ionized atoms and molecules are excited and they emit characteristic spectrum and hence atomic, ionic or molecular species may be identified. Spectral study of the glow discharge [3,4,7,9] of the material helps in studying the chemical composition of the material. The solid liquid junction is formed when current is passed through the junction; a plasma film is generated along the interfaces between solid and liquid. The plasma pressure is very near to the atmospheric pressure [10,11,12]. [The plasma parameters in DC glow discharge may be generated by a current source [13].] The method is very low cost and quick results may be obtained and therefore has wide applications.

When electric discharge is passed to a conducting solution from an electrode, which is placed in the gas space above the liquid surface, reactions take place in the liquid phase and the process is referred to as "Glow Discharge Electrolysis (GDE)". The dc glow discharge continues to be the subject of spectroscopic research [15] and analytical method development. Glow discharges [14] are used for a variety of technological, physical and analytical applications, ranging from plasma etching and deposition systems in the micro-

electronics industry, to lasers or even plasma monitors. Traditionally [14] dc-glow discharge optical emission spectroscopy is mainly applied in the materials sciences where it is used for bulk and surface analysis, pellets containing the adsorbed liquid and direct analysis of the liquid samples by use of adequate sample introduction techniques. Liquids can be analyzed directly at atmospheric pressures, when applying the atmospheric electrolyte cathode glow discharge cell approach with detection by emission spectroscopy as described by Cserfalvi and Mezei [3].

II. MATERIAL AND METHODS

The experimental arrangement used for the investigation of dc glow discharge is simple and. It is inexpensive arrangement and it is very much cost effective. It consists of tungsten electrode of length 40 mm and diameter 3mm fused in glass capillary tube and suspended axially in a hollow slotted stainless steel cylinder, of length 6 cm and internal diameter 2.54 cm. The stainless steel cylinder served as another electrode i.e. anode in the glow discharge. The suspended end of tungsten rod was carefully rounded. The tungsten electrode can be used as cathode by connecting it to the dc power supply of 700 V capacity having 1.5 A current capacity. In this arrangement the hollow cylinder was dipped in a electrolytic aqueous solution taken in a glass beaker. The depth of immersion of the tungsten electrode in electrolyte solution could be adjusted with the help of micrometer adjustable stand. By using this arrangement the tip of tungsten electrode could be just brought in touch with the upper surface of the solution or the distance between the solution surface and the electrode may be adjusted. In this way the solution itself acts as another electrode.

The different 28 electrolytic solutions have been taken for investigation using the glow discharge system. With the help of the above-mentioned experimental arrangement the following properties may be studied.

III. RESULT AND DISCUSSIONS

Variation of electrolytic current with the applied dc-voltage during glow discharge in atmospheric pressure gas using 28 electrolytic solutions as the anode and cathode were carried out. The colors emitted on the glow are observed and listed in table 1. As an example we consider the electrolytic aqueous solution of $0.5N \text{ Cd}(\text{NO}_3)_2 \cdot 4\text{H}_2\text{O}$ as the anode, the electrolytic process leading to a luminescent glow is best depicted by the standard voltage-current curve as shown in figure 1. The curve may be divided in to several regions and its behavior may be studied.

In the region AB the curve is almost linear, the Ohms law is satisfied and conventional electrolysis found with tiny bubbles of gas around both material electrodes-tungsten electrode and stainless steel electrode. At the voltage corresponding to point B in curve, a smooth evolution of gas bubbles is disturbed and layer of steam is seen at the tungsten cathode. In the region between B and C, the pointer of voltmeter and ammeter widely fluctuates. In this region the characteristics like current passing through the electrode and voltage applied found as unstable.

The behavior of region BC, CD and DE can be explained as follows. Because of increase in the applied dc voltage, the rate of gas evolution is increased with the formation of large size gas bubbles at a fast rate.

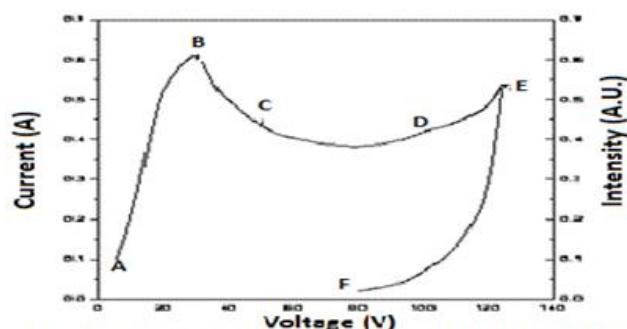


Fig.1: V- I Characteristics of 0.5N Electrolytic Solution of $\text{Cd}(\text{NO}_3)_2 \cdot 4\text{H}_2\text{O}$

This decreases the rate of migration of the ions and charge transfer process at the electrodes. When voltage is further increased more fluctuations are obtained in both voltage and current readings with fall in current. This unstable decreased current is shown by line BC. In the neighborhood of point C it is found that fluctuation rate decreases and now hissing sound occurs. When the applied dc voltage reaches to the point C, there is intermittent sparking. The formation of gas bubbles around the tungsten electrode has now stopped. After increasing the applied dc-voltage to a still higher value the formation of movable thin vapor film around the tungsten cathode takes place, which at times produces the vortex motion and visible glow spark of greenish-blue color is found in the gap between cathode and solution phase. Due to vortex motion, electrolyte periodically touches to the tungsten cathode surface. This produces local heating at the tungsten cathode surface and visible glow spark of bluish-green color. Due to the local heating process there produces the vapor jet and nearby liquid molecules tried to take its place. The region CD of V- I characteristics shows this situation. Thus the region B to C represents the negative slope as seen in the curve. When the electrolyte current decreases to the corresponding point D, the violent gas evolution stops and slope of the curve changes sign from negative to positive. After the point D, with the applied dc voltages the current starts increasing and thereby producing a stable superheated insulating layer around the cathode (tungsten electrode). At this situation a continuous bluish-green glow is developed at the cathode surface. For a further increase in applied dc voltage, the intensity of the glow increases continuously with the increase in current also as shown in figure 1. Thus the region beyond D i.e. along DE appears to be true glow discharge. This happens due to the discharge of accumulated ions through the insulating layer. This situation produces intense glow of bluish-green color and it sometimes can be pictured as corona discharge. Thus under the observation, it is quite obvious that the superheated insulating layer around the cathode is the governing factor responsible for the bluish-green glow.

Tunnel Behavior Under V-I Characteristics of DC-glow Discharge

The discharge parameter like V-I characteristics of dc-glow discharge between the solid and liquid interfaces behaves like that of Tunnel diode. This has been investigated under the observation of V-I characteristics of aqueous solution of different concentrations. The energy band diagrams of cathode type and anode type (plasma band) materials as shown in figure 2. (a, b and c) can be used to explain the Tunneling phenomenon.

When the cathode type material (tungsten electrode) is joined, the energy band diagram under no bias condition becomes as shown in figure 2. (a). The junction barrier produces only a rough alignment of the two materials and their respective valence and conduction bands, hence no tunneling occurs. Initially when a lower voltage in equal step is applied, the energy band diagram become as shown in figure 2. (b). Due to the downward movement of the cathode region, the anode region valence band becomes exactly aligned with the cathode region conduction band. At this stage, electrons tunneling takes place as shown in figure and it 54

For this investigation taking the example of V-I characteristics for aqueous solution of 0.5 N KOH by dc glow discharge as shown in figure 3. With initially gradually increasing dc-voltage, the significant electrolyte current rises to its peak value say I_p and the corresponding applied voltage reaches to a value say V_p (at point B).

When applied voltage is increased to a value greater than V_p , the electrolyte discharge current starts decreasing till it achieves its minimum value called valley current I_v corresponding to valley voltage V_v (at point D). For the voltages greater than V_v current starts increasing again as in any ordinary junction diode.

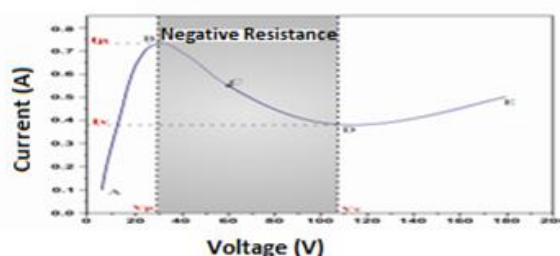


Fig.3: Tunnel Behavior Under V -I Characteristics of 0.5 N KOH Electrolytic Solution

In a similar way to negative resistance of the Tunnel diode it is seen from the figure in the region between peak point B and valley point D that the electrolyte current decreases with increase in the applied voltage. This behavior of the characteristics is similar to the electrolytic cell possesses negative resistance in this region. In fact this contributes the most useful property of the diode. Instead of absorbing power a negative resistance produces power.

IV. CONCLUSION

DC Glow discharge using a solution as the anode and the metallic electrode as the cathode for the investigation of phenomenon of spectrometry shows that, a sensitive and inexpensive technique and very much cost for the elemental analysis of electrolytic solutions.

V. REFERENCES

- [1]. T. Cserfalvi and P. Mezei (1996), Operating Mechanism of the Electrolytic Cathode Atmospheric Glow Discharge, Fresenius Journal of Analytical Chemistry(Springer Link), pp: 83-89

- [2]. Michael R. Webb, Francisco J. Andrade, Gerardo Gamez, Robert McCrindle and Gray M. Hieftje, (2005), Spectroscopic and Electrical Studies of a Solution Cathode Glow Discharge, *J. Anal. At. Spectrom.*, 20, pp: 1218- 1225
- [3]. T Cserfalvi, P Mezei and P Apai, (1993), Emission Studies on a Glow Discharge in Atomic Pressure Air using Water as a Cathode, *J. Phys. D*, , 26, 2184-2188
- [4]. Stephane Baude, Jose A.C. Broekaert, Daniel Delfosse, Norbert Jakubowski, Lars Fuechtjohann, Nestor G. Orellana-Velado, Rosario Pereiro and Alfredo Sanz- Medel (2000), Glow discharge atomic spectrometry for the analysis of environmental samples-a review, *J. Anal. At. Spectrom.* 2000, Vol. 15, pp: 1516-1525
- [5]. John Marshal, Simon Chenery, E. Hywel Evans and Andrew Fisher (1998), Atomic Spectrometry Update- Atomic Emission Spectrometry, *Journal of Analytical Atomic Spectrometry*, June 1998, Vol. 13, pp: 107R- 130R
- [6]. A A Garamoon, A Samir, F F Elakshar and E F Kotp (2003), Electrical Characteristics of a DC glow discharge, *Plasma Sources Science Technol.* 12(2003), pp: 417-420
- [7]. Tamas Cserfalvi and P. Mezei, *J. Anal. At. Spectrom* (1994), Direct solution analysis by glow discharge: electrolyte cathode discharge spectrometry, *J. Anal. At. Spectrom.* 1994, 9, pp: 345-349
- [8]. Z. Machalaa, M. Jandaa, K. Hensela, I. Jedlovsky, L. Leatinska, V. Foltinc, V. Martiaovita and M. Morvova (2007), Emission spectroscopy of atmospheric pressure plasmas for biomedical and environmental applications, *J. of Molecular Spectroscopy*, Vol. 243, Issue 2, pp: 194-201
- [9]. Michael R. Webb, George C.-Y. Chan, Francisco J. Andrade, Gerardo Gamez, and Gary M. Hieftje (2006), Spectroscopic characterization of ion and electron population in a solution – Cathode Glow discharge, *J. Anal. At. Spectrom.* 2006, 21, pp 525- 530.
- [10]. David Staack, Bakhtier Farouk, Alexander Gutsol and Alexander Fridman (2005), Characterization of a DC atmospheric pressure normal Glow Discharge, *Plasma sources Sci. Technol.* 14, 2005, pp. 700-711
- [11]. Christoph Gerhard, Tobiasweins, Daniel Tasche (2013), Atmospheric Pressure plasma treatment of fused silica related surface and near surface effects and applications, *Plasma Chemistry and Plasma Processing*, 2013, 33(5), pp. 895 – 905.
- [12]. Santak V, Zaplotnik R, Tarle Z, Milosevic S (2015), Optical Emission spectroscopy of an atmospheric pressure plasma jet during tooth bleaching Gel Treatment, *Appl. Spectrosc.*, 2015, pp. 1327 – 1333.
- [13]. Mohammed Khalaf, Osday A Hammadi Firas J. Kahim (2016), Current Voltage Characteristics of DC plasma Discharges Employed in Sputtering Techniques, *IJAP*, 2016, 12(3), pp. 11 – 16.
- [14]. Norbert Jakubowaski, Volkar Hoffmann, Annemie Bogaerts (2003), Foreword: Glow discharge spectrometry, *J. Anal. At. Spectrom.* 2003, 20, pp. 19N-22N
- [15]. John Marshall, Simon Chenery, E. Hywel Evans, Andrew Fisher (1998), Atomic Spectrometry Update- Atomic emission spectrometry, *J. Anal. At. Spectrom.*, 1998, 13, 107R-130R.



Variation of Energy Band Gap in Composites of N-doped Titanium Dioxide for Preparation of Dye-sensitized Solar Cell

Shivam Yadav, Rupali Patel, Vinita Dhulia

Department of Physics, N.E.S Ratnam College of Arts Science and Commerce, Maharashtra, India

ABSTRACT

TiO₂ (Titania) is one of the prominent transition metal oxides, which is a widely used nanomaterial, for various applications, due to its stability, abundance, non-toxicity, and high reactivity. It is also one of the components widely used for solar cell applications. The large band-gap of TiO₂ which is approximately 3.2 eV for the anatase phase limits visible light absorption. It is only stimulated in the region of ultraviolet (UV) light i.e. wavelength less than 387 nm. We have made composites of the dye-sensitized solar cell (DSSC) with the objective of reducing the band-gap to enhance the absorption of solar spectra. Pure and N-doped TiO₂ nanoparticles are synthesized by the Sol-Gel method. Composites were prepared by taking varying concentration of Nitrogen and pure TiO₂. Energy band-gap for the composites were studied using absorption spectra obtained from characterization using a UV visible spectrophotometer. Doped TiO₂ displayed a narrow band-gap compared to the pure TiO₂ nanoparticles. IV characteristics were analysed to check the efficiency of DSSC. It is observed that the energy band gap is reduced with increasing concentration of nitrogen.

Keywords: Dye-Sensitized Solar Cell (DSSC), TiO₂ nanoparticle, N-doped TiO₂, Spectrophotometer, energy band-gap.

I. INTRODUCTION

Nanoscience is a new ability to modify and characterize matter at the level of a single atom. In the last two decades, nanosized materials have received considerable attention to discover the novel properties of nanoscale clusters which are significantly different from properties of the bulk scale (Michael Dahl, 214). When Semiconductor nano-material such as TiO₂ (Titania) is reduced to nanometre scale, its physical as well as chemical properties change dramatically resulting in unique properties (Shalini Reghunath, 2021). The band-gap of TiO₂ is wide which confines the absorption of visible light, this in turn limits the use of solar irradiation. The recent research shows, when TiO₂ is doped with Nitrogen (N) it reduces the band-gap to promote light absorption in visible range (Shahzad Abu Bakar, 2016). This property is used in making Dye-Sensitized Solar Cell which is an alternative to a non-renewable energy source which can be used either on large scale or small scale. (Mahmud, 2021) (Nurul Diyana Zainal, 2015). However, some disadvantages in the DSSC design are that ITO plates should have low resistance and the liquid electrolyte used in DSSC is

temperature sensitive and may cause some physical damage to DSSC at low temperature or high temperature (Baba Alfa, 2012).

Despite these drawbacks,the DSSC is a low cost and promising alternative to fossil fuels.

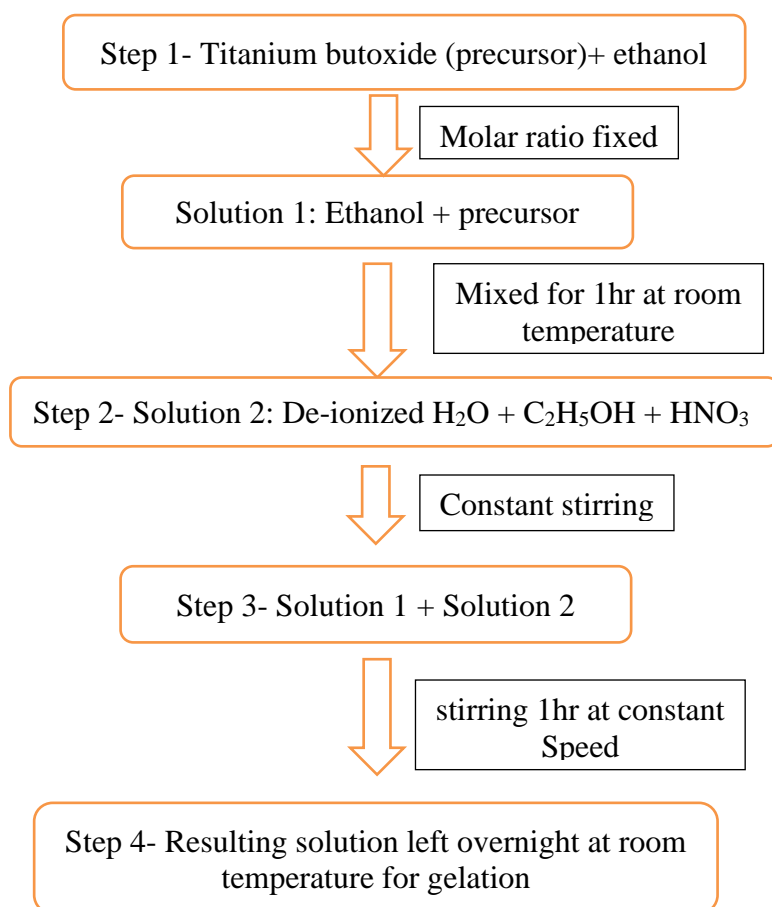
In this paper we have investigatedthe effect of Nitrogen doping in TiO_2 to reduce its band-gap and prepared DSSC with various concentrations. Three samples - one pure TiO_2 and other two Nitrogen doped samples, 2.5 % and 3% respectively.

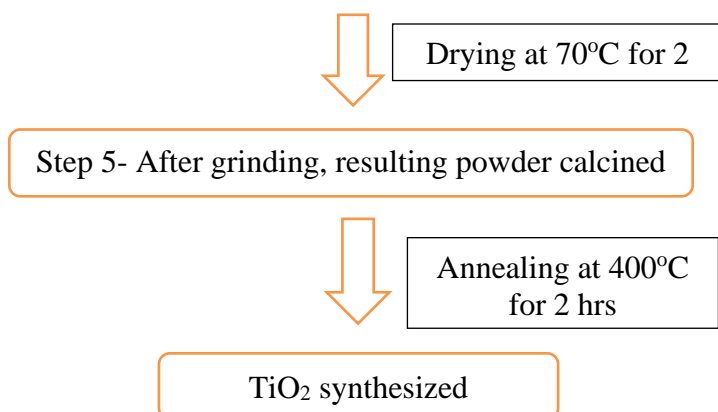
II. EXPERIMENTS

2.1 Synthesis of TiO_2 nanoparticles by Sol-Gel method:

Sol-Gel process is the easiest way to synthesize TiO_2 nanoparticles with their tailor-ability to attain the required optical and physical properties. The procedure used for synthesizing pure TiO_2 nanoparticles is as shown in Flowchart 1. Titanium butoxide, Ethanol ($\text{C}_2\text{H}_5\text{OH}$), De-ionized water, Nitric acid (HNO_3) are taken in the ratio 1/20/0.5/0.1respectively(A. Yadav, M. Yadav, S. 2018) and preparation of N doped TiO_2 nanoparticles consists of same ratio with Tri-ethylamine used as a Nitrogen source. It is added to the mixture of Nitric acid and distilled water before keeping the solution for gelation (Refer step 2, Flowchart-1) doping with 2.5% and 3% of Nitrogen. The sample is then washed twice with deionized water and twice with ethanol.

Flowchart1:





2.2 DSSC Preparation

For the preparation of DSSC, the materials used are listed below.

i. ITO (Indium Tin Oxide) plates

Dimension- 25mm×25mm×0.7mm

Resistivity-less than equal to 10 ohms/sq.

ii. Methyl Red Indicator

iii. Iodine electrolyte solution was prepared locally.

iv. Acetic acid solution was prepared locally (pH=3)

TiO₂ powder was mixed with Acetic acid solution and a thick paste was produced. A thick layer as well as a mesoporous layer is needed to absorb more light. This paste was coated on ITO plate using Doctor Blading technique. It was kept for drying for 1hr, the coated ITO plate was then dipped in Methyl red solution for 24hrs for proper absorption of dye molecules. (Mahmud, 2021)

Counter electrode was prepared by taking another ITO plate and passing the conductive side through a candle flame several times to create a layer of soot. (Darshna D. Potphode, 2019) An Iodine electrolyte solution was added after the preparation of DSSC (refer figure 1B)

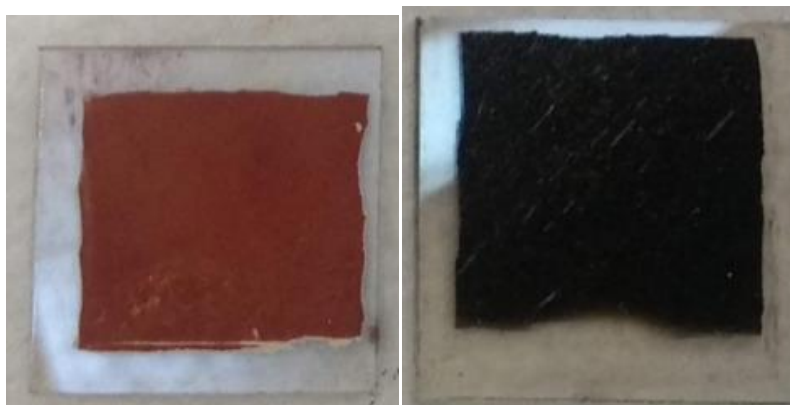


Figure 1A- ITO plated with TiO₂ and counter electrode.

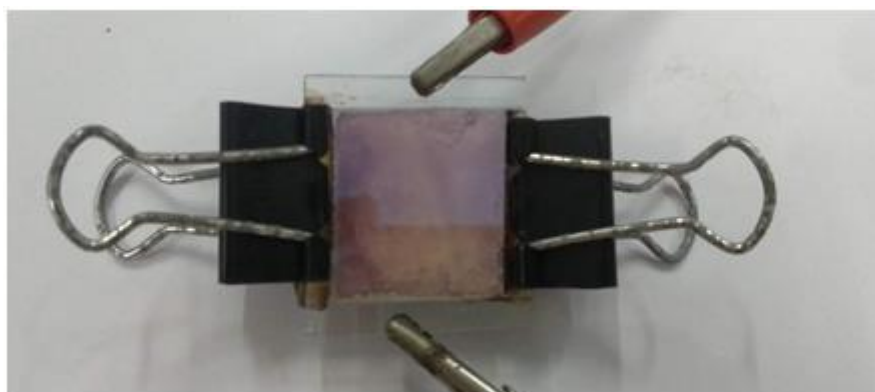


Figure 1B- A typical assembled DSSC

2.3 Characterization of Nanomaterials

Prepared nanomaterials were characterized via X-ray diffraction techniques (XRD) to determine the structural characterization for all sample and UV-Visible spectrometer with integrating sphere for absorption characteristics of solid TiO_2 powder and doped TiO_2 powder.

I-V Characteristics of a DSSC was used to calculate the fill factor.

III. RESULTS AND DISCUSSION

3.1 X-ray Diffraction (XRD)

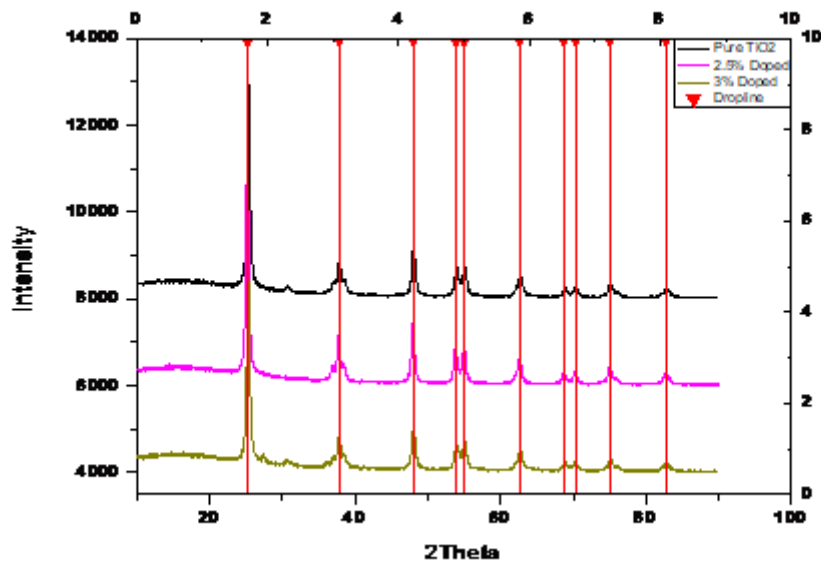


Figure 2. XRD analysis of (a) TiO_2 , (b) 2.5% N doped TiO_2 (c) 3% N doped TiO_2

The XRD spectra of the pure TiO_2 and N doped TiO_2 powder prepared by Sol-Gel method with post annealing at 450°C are presented in fig 2. The diffraction peak of Nitrogen doped TiO_2 at different doping ratio were

obtained at 25.32°, 37.87°, 48.056°, 53.91°, 55.08°, 62.7°, 68.76°, 70.31° and 75.12°. The TiO₂ doped with 2.5% and 3% Nitrogen shows same peaks as pure TiO₂. This can be assigned to crystal planes (101), (004), (200), (105), (211), (204), (116), (220) and (215) that corresponds to anatase phase of titania and agrees with JCPDS card np.21-1272.

The average crystalline particle size is calculated by applying Scherrer expressions in equation (1)

$$D = \frac{0.9 \lambda}{\beta \cdot \cos \theta} \quad \text{--- (1)}$$

The λ is X-ray wavelength of 1.5406 Å of Cu K α radiation. β is the line broadening at maximum intensity (FWHM) and θ is the Bragg angle. The particle size is recorded in table 1. The average crystalline particle size for pure TiO₂ was 13 nm and increases up to 17 nm with nitrogen doping. As seen in XRD pattern the diffraction peak may sharpen because of faster growth rate and by increased crystallite size (Khan, et al., 2021)

Table 1 The average particle size of the sample

Sample	2 θ	FWHM (Full Width Half Maxima)	Average particle size (nm)
Pure TiO ₂	25.302	0.6177	13
2.5% doped TiO ₂	25.212	0.46283	17
3% doped TiO ₂	25.327	0.49174	16

The anatase phase was observed with crystalline size ranging from 13 nm – 17 nm confirming the nanocrystalline form. The anatase phase is found to be suitable for DSSC application.

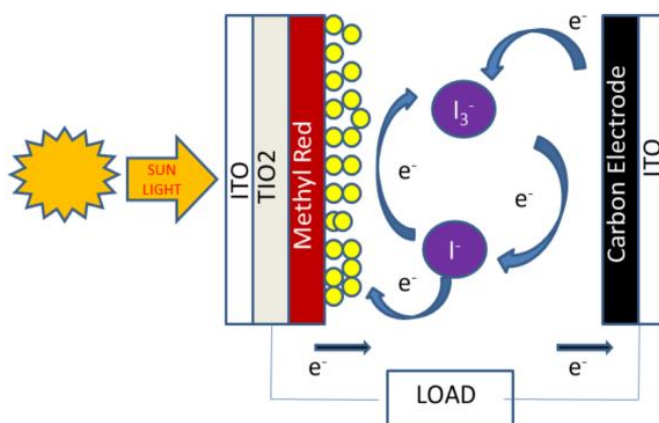


Figure 3-Schematic for working principle of DSSCs

3.2 UV-visible Spectroscopy:

The UV Visible absorption spectra of TiO₂ and N-doped TiO₂ samples are presented in fig.4. As seen from the characterization the absorbance edge is shifted resulting in lower band gap, as the amount of incorporated nitrogen increases. This increases the visible light absorption in N-doped TiO₂ sample. Similarly decreasing band gap of TiO₂ leads to decreasing recombination of charges as compared to the pure TiO₂. (Gang Liu, 2009) The band gap of doped sample is obtained by converting UV-Visible spectra into Tauc plot by using Kubelka-Munk formula reported in equation (2)

$$\alpha hv = A(hv - E_g)^2 \text{ --- (2)}$$

where α is absorbance coefficient, h is the Plank's constant ($4.136 \times 10^{-15} \text{eV}$), A is constant (1), ν is frequency and E_g is band gap, factor 2 is taken for indirect allowed transition. Table 2 shows the band gap energy for pure and doped TiO_2 .

Table 2 Bandgap energy for all samples

Sample	Band Gap(eV)
Pure TiO_2	3.096
2.5% doped TiO_2	3.017
3% doped TiO_2	2.915

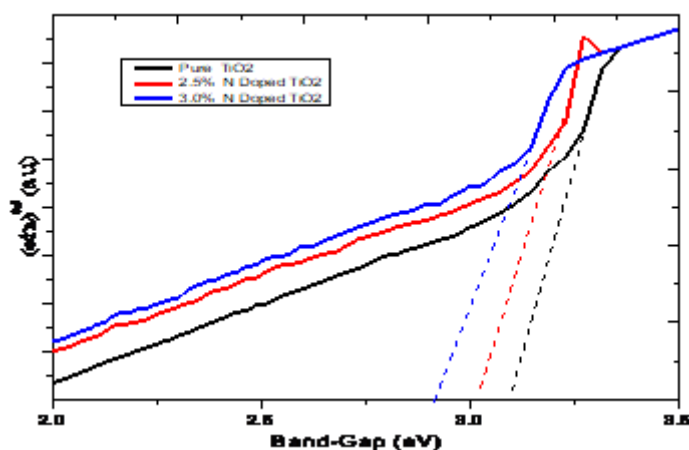


Figure 4: UV-Visible spectroscopy of pure TiO_2 and N doped TiO_2 with different Nitrogen concentration

3.3 I-V characteristic

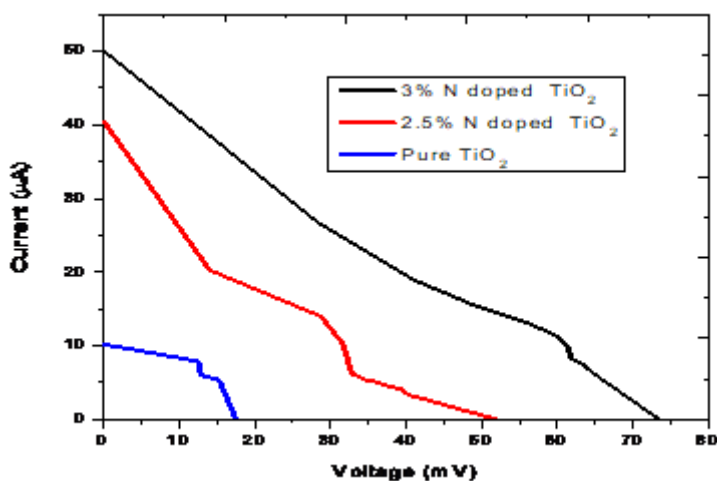


Figure 5: I-V curve of DSSC

The DSSC performance of pure TiO_2 and N-doped TiO_2 with different concentration are reported in figure 5, It has been observed that the DSSC performance improved for 3% N-doped TiO_2 as compared to the pure

TiO₂. Also, the higher value of fill factor of the 3% N doped TiO₂ sample indicated improved lifetime of electron(R. Raja, 2016). Open circuit voltage Voc, Short Circuit current I_{sc} and Fill Factor FF of all samples are reported in table 3.

Table 4: Photovoltaic characteristics of DSSC

samples	Short Circuit current I _{sc} (μ A)	Open circuit voltage Voc (mV)	Fill Factor
Pure TiO ₂	0.1022	17.5	0.128
2.5% doped TiO ₂	40.5	52	0.134
3% doped TiO ₂	50.1	73.5	0.205

IV. ACKNOWLEDGEMENT

We are thankful to N.E.S. Ratnam College for providing laboratory facilities, we would also like to thank department of Chemistry for providing the essential chemicals, Sophisticated Analytical Instrument Facility (SAIF) IIT Bombay for providing UV-Vis Spectrometer data and DoctorNainesh Patel for providing XRD data.

V. CONCLUSION

Dye Sensitized Solar Cell (DSSC) has become approved and capable device to replace solid state junction device to convert solar energy in to electricity. Recent research developments indicate the reduced band gap of TiO₂ by doping with foreign elements leading to absorption of solar light across visible spectrum and also resulting in higher efficiency of DSSC.The work carried out on DSSC device which is made using nitrogen doped TiO₂ with methyl red dye as working electrode and locally prepared carbon electrode as counter electrode shows improved efficiency than pure TiO₂ due to the good absorption of visible light by the dye and nitrogen doped TiO₂.

VI. REFERENCES

- [1]. A. Yadav, M.Yadav, S. Gupta, Y. Papat, A. Gangan, B. Chakraborty, L.M. Ramaniah, R. Fernandes, A. Miotello, M.R. Press, N. Patel, 2018. Effect of graphene oxide loading on TiO₂: Morphological, optical, interfacial charge dynamics-A combined experimental and theoreticalstudy. Carbon, Volume 143, pp. 51-62.
- [2]. Baba Alfa, 2012. Fabrication and Characterisation of Titanium Dioxide Based Dye Sensitized Solar Cell using Flame of the Forest Dy. Applied Physics Research, Volume 04, pp. 48-56.
- [3]. Darshna D. Potphode, 2019. Candle Soot Carbon as Electrode Materials for Energy Storage Applications.
- [4]. Gang Liu 2009. Visible Light Responsive Nitrogen Doped Anatase TiO₂ Sheets with Dominant {001} Facets Derived from TiN. Journal of the American Chemical Society, pp. 12868-12869.

- [5]. Hytham Elbohy, Amit Thapa, Prashant Poudel, Nirmal Adhikary, Swaminathan Venkatesan, Qiquan Qiao, 2015. Vanadium oxide as new charge recombination blocking layer for high efficiency dye-sensitized solar cells. *Nano Energy*, Volume 13, pp. 368-375.
- [6]. Khan, T. et al, 2021. Synthesis of N-Doped TiO₂ for Efficient Photocatalytic Degradation of Atmospheric NO_x. *Catalysts* 2021, pp. 1-13.
- [7]. Mahmud, M, 2021. A literature survey of nanomaterials for dye sensitized solar cells. *International Journal of Chemical and Biological Sciences*, Volume 03, pp. 36-38.
- [8]. Michael Dahl, 2014. Composite Titanium Dioxide Nanomaterials. *Chemical Reviews*, Volume 114, p. 9853–9889.
- [9]. Nurul Diyana Zainal, 2015. Synthesis and characterization of nitrogen-doped titania nanomaterials of. *Malaysian Journal of Fundamental and Applied Sciences*, Volume 11, pp. 111-113.
- [10]. R. Raja, M., 2016. Effect of TiO₂/reduced graphene oxide composite thin film as a blocking layer on the efficiency of dye-sensitized solar cells. *Journal of Solid State Electrochemistry*, 21(891-903).
- [11]. Shahzad Abu Bakar, C. R., 2016. Nitrogen-doped Titanium Dioxide: an overview of material design and dimensionality effect over modern applications. *Journal of Photochemistry and Photobiology C: Photochemistry*.
- [12]. Shalini Reghunath, D. P. S. D. K., 2021. A review of hierarchical nanostructures of TiO₂: Advances and applications. *Applied Surface Science Advances*, Volume 03.



Electrical Properties of Lead Sulphide Amalgam under Influence of Aluminium Doping Deposited by Chemical Spray Pyrolysis

S. G. Ibrahim^{*1}, S. A. Waghuley²

^{*1}Department of Engineering Physics, Prof. Ram Meghe College of Engineering & Management, Badnera-444701, Maharashtra, India

²Department of Physics, Sant Gadge Baba Amravati University, Amravati-444602, Maharashtra, India

ABSTRACT

Nanotechnology is one of the most demanding areas in the field of science and engineering. Due to this, it has become possible to engineer devices at the nanometer scale which can be utilised in the production and application of materials, structures, devices, and systems. The effect of Al doping on the electrical properties of chemically spray deposited lead sulphide thin films was investigated in this study. The films are polycrystalline in nature, with a cubic lattice, and have a direct band gap on the order of 1.49 eV, which increases to 1.62 eV as doping concentration increases. The electrical resistivity of the pure films was $2.68 \times 10^3 \Omega \text{cm}$, but it dropped to $1.35 \times 10^3 \Omega \text{cm}$ with further Al doping. Both undoped and doped thin films show p-type conductivity, according to the thermo-emf measurement.

Keywords: Thin films; Nanostructures; Spray pyrolysis; Electrical properties.

I. INTRODUCTION

Lead chalcogenides and associated alloys play an important role in today's materials technology because of their crystalline and polycrystalline essence, which work as infrared detectors and can be utilized as infrared emitters for solar applications. In recent years, lead sulfide a group IV–VI semiconductor has become one of the most appealing semiconducting materials due to its wide variety of uses, low cost, and ease of availability. In bulk form, it has a low band gap of (~ 0.41 eV) at ambient temperature with direct transition and generally shows p-type conducting nature [1-4]. According to requirements and applications materials can be moulded by using a process called doping. Doping of different materials / Various metal ions is an important concept for tuning many properties of semiconducting materials. The type and concentration of dopants play a critical role in achieving desirable characteristics and better efficiency for nanostructured semiconducting materials. Electrical conductivity is a fundamental feature of semiconductors, and it is directly dependent on the mobility and concentrations of free charge carriers. The electrical characteristics are affected by doping as well as the quantity of doping. In the present research work we have used aluminium (Al) as dopant and studied the effect of doping on the electrical properties of lead sulfide thin films.

II. EXPERIMENTAL DETAILS

For the deposition of doped and undoped lead sulfide thin films glass substrate was used. Cleaning process is discussed elsewhere [5]. Lead nitrate (PbNO_3) and Thiourea ($\text{CH}_4\text{N}_2\text{S}$) were used to deposit the doped and undoped lead sulfide films and Aluminium III chloride (AlCl_3) was used as source for (Al) precursors, respectively. PbNO_3 and $\text{CH}_4\text{N}_2\text{S}$ were taken in equal molar ratio(1:1). The total solution (10mL) was made by adding doubled distilled water. Aluminium doping was carried out by adding the appropriate concentrations 5% (wt.%) into the complete lead sulfide solution. An optimized temperature of 573 K was maintained for film deposition and the nozzle to the substrate distance was 28 cm.

III. RESULT AND DISCUSSION

3.1 Electrical analysis

The electrical properties in any material play a vital role. The capacity of a material to be suited for a certain electrical engineering application is determined by its electrical characteristics. In the present investigation, electrical resistivity and thermoelectric properties were studied.

“The two-probe method is one of the standards and most commonly used method for the measurement of resistivity for very high resistive samples like sheets/films of polymers” [6]. In the existing research work for making ohmic contacts to pure lead sulfide and Al doped lead sulfide thin films silver paste was used. The nature of pure and doped/Ag contacts was tested up to 30 V. (Figure 1) shows the linear nature of I–V characteristics.

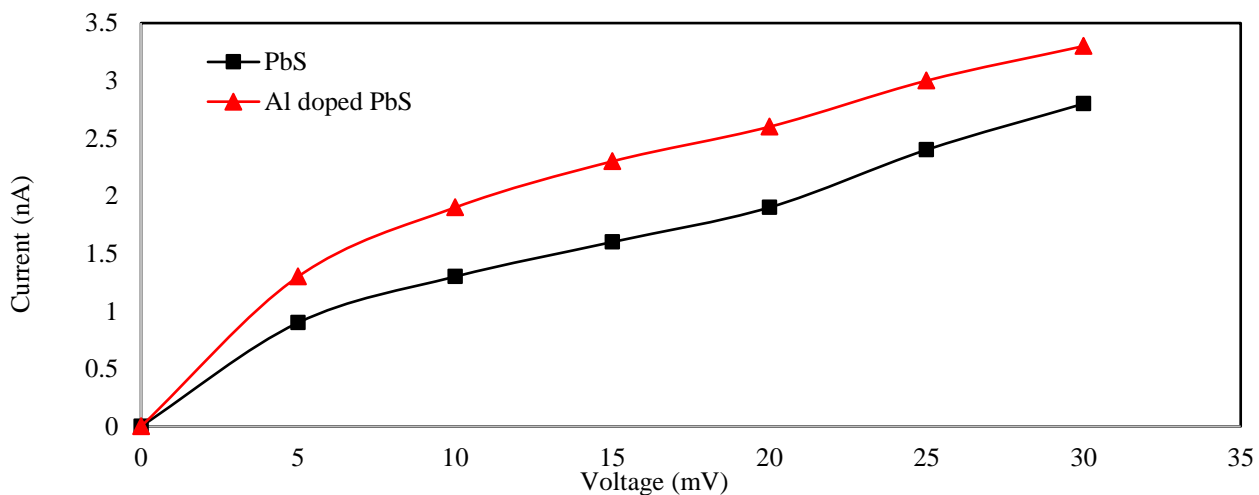


Figure 1: I-V characteristics of spray deposited lead sulfide and Al doped lead sulfide thin film

By varying the temperature from 300K to 500K the relation between resistivity with temperature for pure and Al doped thin films was studied. The electrical resistivity of the pure films was $2.68 \times 10^3 \Omega\text{cm}$, but it reduces to $1.35 \times 10^3 \Omega\text{cm}$ with addition of the dopant (Al). As the decrease in resistivity is observed with increase in temperature, we may say the material is behaving like semiconductor.

Figure 2 shows the graph between deviations of the log of resistivity with $(1/T)$ for pure and doped lead sulfide thin films. For the calculation of thermal activation energy following relation is used,

$$\rho = \rho_0 \exp(E_0/kT) \text{----- (1)}$$

Where “ ρ ” denotes resistivity, “ ρ_0 ” is a constant, and Boltzmann constant “ k ”.

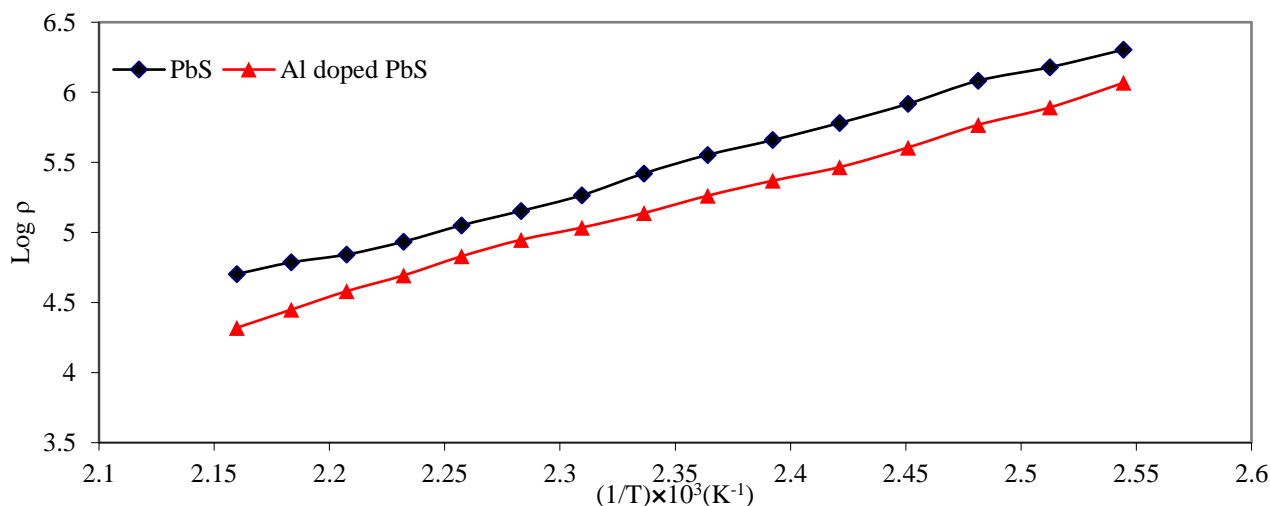


Figure 2: Variation of Log of resistivity with $1/T$ for spray deposited lead sulfide and Al doped lead sulfide thin film

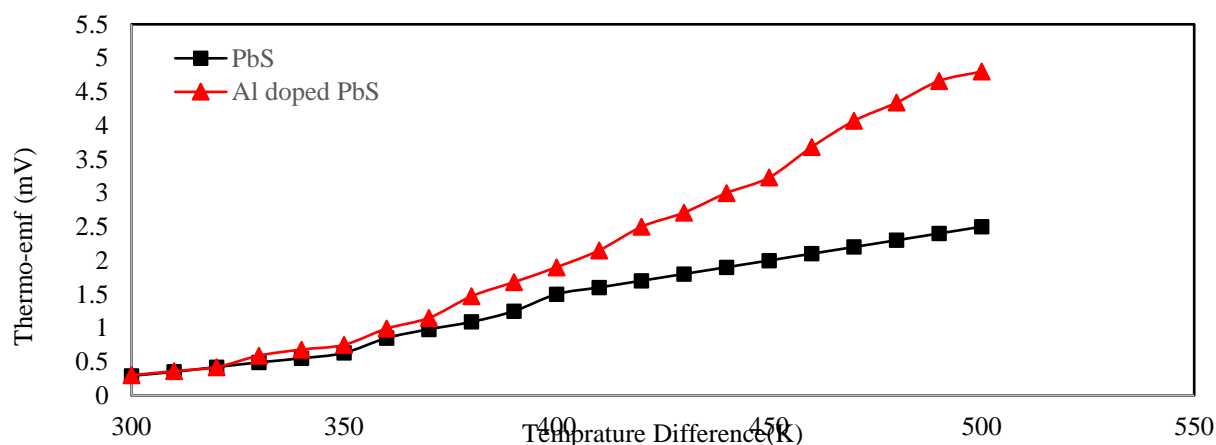


Figure 3: Variation of thermo emf (mV) with temperature difference for spray deposited lead sulfide and Al doped lead sulfide thin film

The calculations related to (E_0) activation energy was done using the resistivity plots, from which the value obtained is 0.059 eV for pure films and 0.048 for doped lead sulfide thin films also it is observed that it depends on the deposition temperature and nature of the deposition process.

In the present research work, the thermo electric power (TEP) was measured as a function of temperature in the range of 300–500K (Figure 3). The polarity of the thermoelectric voltage confirms that the as-deposited films have p-type conductivity which is in good agreement with the reported data [7]

IV. CONCLUSION

The effect of Al doping on the electrical properties of chemically spray deposited lead sulphide thin films was studied. The deposited films were polycrystalline in nature, having a cubic lattice, with direct band gap of order 1.49 eV, which increases to 1.62 eV with increase in doping concentration. The electrical resistivity of the pure films was found to be $2.68 \times 10^3 \Omega \text{cm}$, which decreases to $1.35 \times 10^3 \Omega \text{cm}$ with Al doping. Thermo-emf measurement shows that, both undoped and doped thin films possess p-type conductivity.

V. REFERENCES

- [1]. Zogg, H, Arnold, M. (2006). Narrow spectral band monolithic lead chalcogenide on Si mid-IR photodetectors. *Nuclear Instruments and Methods in Physics Research Section A: Accelerators, Spectrometers, Detectors and Associated Equipment*, 568(1), 459–461. doi:10.1016/j.nima.2006.05.206
- [2]. Kumar, S., Khan, Z. H., Majeed Khan, M. A., & Husain, M. (2005). Studies on thin films of lead chalcogenides. *Current Applied Physics*, 5(6), 561–566. doi:10.1016/j.cap.2004.07.001
- [3]. Beddek, L., Messaoudi, M., Attaf, N., Aida, M. S., & Bougdira, J. (2016). Sulfide precursor concentration and lead source effect on PbS thin films properties. *Journal of Alloys and Compounds*, 666, 327–333. doi:10.1016/j.jallcom.2016.01.088
- [4]. Rex Rosario, S., Kulandaisamy, I., Deva Arun Kumar, K., Arulanantham, A. M. S., Valanarasu, S., Youssef, M. A., & Awwad, N. S. (2019). Deposition of p-type Al doped PbS thin films for heterostructure solar cell device using feasible nebulizer spray pyrolysis technique. *Physica B: Condensed Matter*, 411704. doi:10.1016/j.physb.2019.411704
- [5]. S. G. Ibrahim, A.U. Ubale, Structural, electrical and optical properties of nanostructured Cd_{1-x}Fe_xS thin films deposited by chemical spray pyrolysis technique, *J. Mol. Struct.* 1076 (2014) 291–298 DOI: <https://doi.org/10.1016/j.molstruc.2014.07.065>
- [6]. A.U. Ubale, S. G. Ibrahim, Effect of acetic acid complex on physical properties of nanostructured spray deposited FeCdS₃ thin films. *Journal of Alloys and Compounds*, 509(5)(2011) 2364–2367 DOI:10.1016/j.jallcom.2010.11.020
- [7]. S. Rex Rosario, I. Kulandaisamy, K. Deva Arun Kumar, A.M.S Arulanantham, S. Valanarasu, Maha.A.Youssef, Nasser SAwwad, Deposition of p-type Al doped PbS thin films for heterostructure solar cell device using feasible nebulizer spray pyrolysis technique. *Physica B: Condensed Matter*, 575(2019), 411704. doi:10.1016/j.physb.2019.411704



Thermodynamic and Viscometric Study of Aminopyrimidine Derivatives in 80% DMF-Water Solvent

M M Mhasal

Department of Chemistry, Shri Shivaji College of Arts, Commerce, Science, Akola, Maharashtra, India

ABSTRACT

Viscosity measurement of aminopyrimidine derivatives was carried out in different percentage of binary solvent mixture. The viscometric measurement of recently synthesized drug viz 2-Amino[4-(3-nitrophenyl)-6-phenyl-1,6-dihydro]-1,3-pyrimidine (L_A), 2-Amino[4,6-diphenyl-1,6-dihydro]-1,3-pyrimidine (L_B) were carried out at several variation in concentration of solute as well as variation in temperature. The value of coefficient A and B was calculated from Jones Dole equation. The viscometric and thermodynamic parameters free energy change (ΔG), enthalpy change (ΔH) and entropy change (ΔS) were also evaluated. The result obtained during this investigation have been used to compute molecular interaction either solute-solute or solute-solvent and structure/ breaking ability of component in binary solvent mixture.

Keywords: 2-Amino[4-(3-nitrophenyl)-6-phenyl-1,6-dihydro]-1,3-pyrimidine, 2-Amino[4,6-diphenyl-1,6-dihydro]-1,3-pyrimidine, Viscosity, Thermodynamic parameters, Molecular interaction.

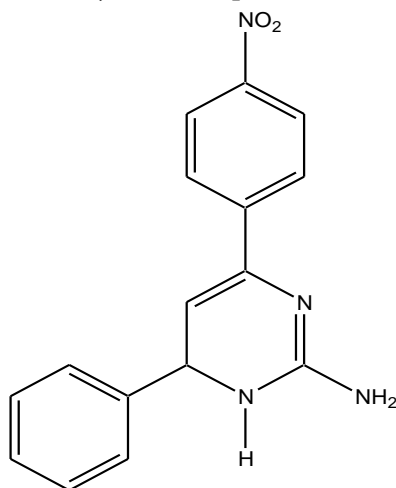
I. INTRODUCTION

For decades medicinal chemists explore interesting pharmacological properties of the aminopyrimidine. 2-aminopyrimidine ring is also found in many cytotoxic natural products. 2-aminopyrimidine derivatives, though well known for a long time, have attracted considerable interest recently because of their applications in various fields especially in pharmaceutical research. For example, the use of 2-aminopyrimidines have been reported as glucokinase activators or selective inhibitors of neuronal nitric oxide synthase¹. There are large number of synthetic compounds with properly substituted pyrimidine nucleus used for analgesic, anti-inflammatory^{ii, iii}, antibacterial^{iv, v}, anticancer, antifungal^{vi}, antihistaminic^{vii}, antinociceptive^{viii}, antitumoral^{ix, x}, pesticidal activities^{xi}, antiulcer^{xii}, antihypertensive^{xiii}, non-nucleoside HIV-1 reverse transcriptase inhibitory activity^{xiv} and antiprotozoans^{2, xv} tranquilizing^{xvi}, adenosine receptor antagonist^{xvii}, CDK inhibitor^{xviii}, analgesic^{xix}, and antidiabetic^{xx} activities.

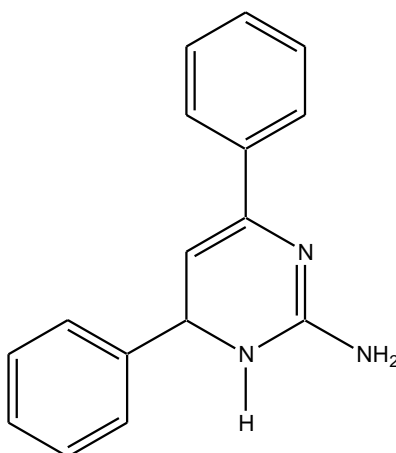
Viscosity measurement of liquids plays a major role in judging the frictional properties of the liquid^{xxi}. The resistance to the flow of liquids is called viscosity. Viscosity of liquids mainly depends upon the size and shape of the particles and the attraction between them. Liquids that flow slowly have high viscosity like

glycerine or honey and liquids that flow rapidly have low viscosity like ether or gasoline^{xxii}.Densities of solutions of glycine, l-alanine, and l-serine have been measured respectively with an oscillating-tube densimeter at 298.15K in ethylene glycol + water mixtures with mass fractions of ethylene glycol ranging from 0 to 0.50.Effect of N-acetyl glycine on volumetric, acoustic and viscometric behavior of aqueous amoxicillin solutions is studied^{xxiii}.Experimental results of viscosity measured in large concentration of electrolytes in aqueous solutions and the solvent-solvent interaction are available in the literature^{xxiv}.Viscometric and thermodynamic data provide valuable information regarding the solute-solute, solute-solvent and solvent-solvent interactions^{xxv}. Solution behavior of drugs has been extensively investigated with the aim to explore their physiological action^{xxvi,xxvii}.Volumetric and viscometric studies of molecular interactions in systems containing tartaric acid in water/aqueous-L-arginine solutions at 303.15 K^{xxviii}

Present work deals with the study, viscometric and thermodynamic study of aminopyrimidine derivative was carried out. From the effect of temperature, the density, relative viscosity and value of thermodynamic parameters like change in free energy(ΔG), enthalpy (ΔH) and entropy (ΔS) was calculated. It gives very important information about change in viscosity with temperature.



(LA): 2-Amino [4-(3-nitro phenyl)-6-phenyl-1,6-dihydro]-1,3- pyrimidine



(LB): 2-Amino [4,6-diphenyl-1,6-dihydro]-1,3- pyrimidine.

II. METHODS AND MATERIAL

Sample Preparation:For the viscosity investigation of Ligand (L_A), Ligand (L_B) is prepared in 80% DMF–water mixture at different temperature 303K, 305K, 307K, 309K respectively.The viscometer was kept in Elite thermostatic water bath and temperature variation was maintained at 30°C (± 0.1) for each measurements, sufficient time was allowed to attain thermal equilibrium between viscometer and water bath. The flow time of solutions were measured by using digital clock of racer company having error (± 0.01 Sec).

Instrumentation:The instrument that is used to measure the viscosity of fluids is called viscometer. Ostwald viscometer is a commonly used viscometer which is also known as a U-tube viscometer or capillary viscometer.All the chemicals used of A.R grade and doubly distilled water was used. Weighing was made one pan digital balance (petit balance AD-50B) with an accuracy of ± 0.001 gm.Densities of solutions were determined by a bicapillarypyknometer ($\pm 0.2\%$) having a bulb volume of about 10 cm³ and capillary having an internal diameter of 1mm and calibrated with deionised doubly distilled water . The accuracy of density measurements were within ± 0.1 kgm³.

III. RESULT AND DISCUSSION

Viscometric study with variation in concentration

Viscometric study of synthesized aminopyrimidine derivative L_A and L_B at different concentration using 80% DMF-water system as a solvent have been prepared in table 1. The data obtained were used to calculate relative viscosity, specific viscosity and density of aminopyrimidine derivatives. The relative viscosity, specific viscosity and density decreases with decrease in concentration. The graphs are plotted between η_{sp}/\sqrt{C} and \sqrt{C} and are presented in Fig.1 to 2 and gives linear straight line. which shows the validity of Jones-Dole equation for all the tested ligand^{xxix}. The slope of this graph shows the value of B-coefficient and intercept gives the value of coefficient A. The relative viscosities of solutions at different concentration are presented in table 1.

Table 1: Densities (d) and viscosities (η_r) of substituted aminopyrimidine of different concentration in 80% (DMF+ water) solvent at 303K

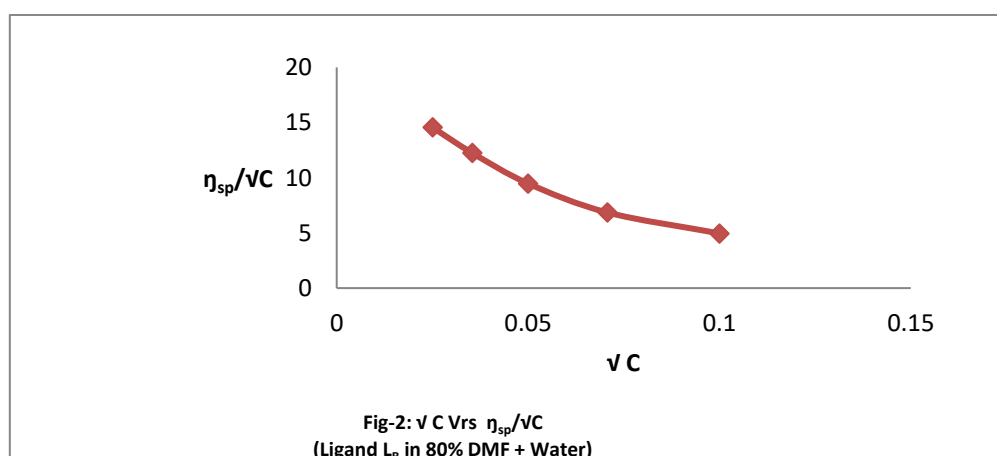
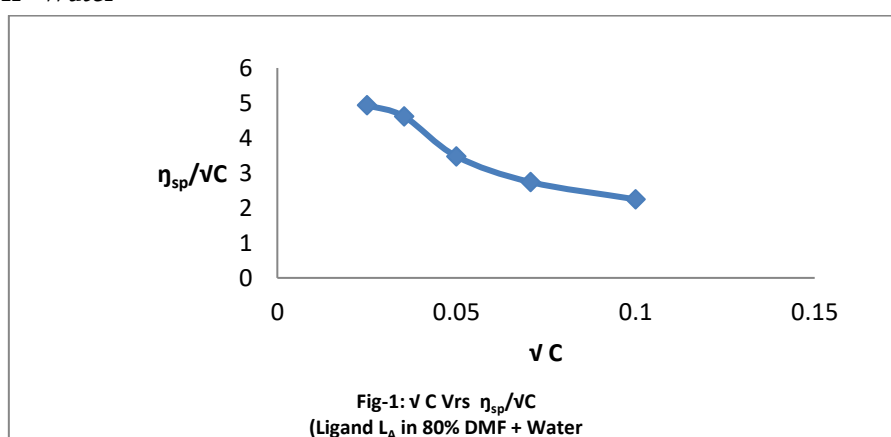
Conc(C) (mol/lit)	L_A			L_B		
	Density (gm/cc)	Relative Viscosity	Specific Viscosity $\eta_{sp} = \eta_r - 1$	Density (gm/cc)	Relative Viscosity	Specific Viscosity $\eta_{sp} = \eta_r - 1$
0.01	1.0137	1.2245	0.2245	1.0183	1.4957	0.4958
0.005	1.0124	1.1936	0.1936	1.0174	1.4846	0.4846
0.0025	1.0121	1.1737	0.1737	1.0169	1.4740	0.4740
0.00125	1.0115	1.1632	0.1632	1.0161	1.4336	0.4336
0.000625	1.0108	1.1233	0.1233	1.0155	1.3641	0.3641

Table 2: A and B Coefficient values

Ligand	80% (DMF+ Water) system	
	A (lit ^{3/2} mol ^{-1/2})	B (lit/mol ⁻¹)
L _A	5.704	-37.41
L _B	16.74	-126.6

It was observed from table 2 that the values of A are positive in both the ligand for L_A and L_B shows strong solute-solute interaction. medium. On the other hand the value of B-coefficient is negative shows weak solute-solvent interaction which indicates the good drug activity which is in favor of pharmacodynamics and pharmacokinetics activity^{xxx}. These different results for all the tested ligands may be due to different polarity index of solvent DMF-Water^{xxxi}

Medium: 80% DMF-Water



Viscometric study with variation in temperature

The viscosity was determined at different temperature were used to evaluate thermodynamic parameters like enthalpy change, entropy change and free energy change for aminopyrimidine derivative of two different ligands, using 80% DMF-water system as a solvent. The relative viscosity, density of a liquid generally

decreases with rise in temperature in the solvent (table 3). The graph was plotted between $\log \eta_r$ and $1/T$ which gives the straight line with positive value of slope fig 3 and 4. The various thermodynamic parameters were calculated by using following expression and the result obtained were computed in table 4 and 5.

$$\Delta G = -2.303 \times R \times \text{slope}$$

$$\log \eta_{r1} - \log \eta_{r2} = (\Delta H / 2.303) \times (1/T_1 - 1/T_2)$$

$$\Delta S = (\Delta G - \Delta H) / T$$

Table – 3 Medium: 80% DMF-Water

Ligand L_A					
Temp (K)	1/T x 10 ⁻³	Density (kgm ⁻³)	Time Flow (s)	Relative Viscosity (η_r)	log η_r
303	3.30033	1.0168	125	1.2282	0.0893
305	3.278689	1.0142	120	1.2124	0.0836
307	3.257329	1.0135	116	1.1974	0.0782
309	3.236246	1.0112	112	1.1687	0.0677
Ligand L_B					
Temp (K)	1/T x 10 ⁻³	Density (kgm ⁻³)	Time Flow (s)	Relative Viscosity (η_r)	log η_r
303	3.30033	1.0229	152	1.5025	0.1768
305	3.278689	1.0223	146	1.4869	0.1722
307	3.257329	1.0216	142	1.4775	0.1695
309	3.236246	1.0211	139	1.4647	0.1657

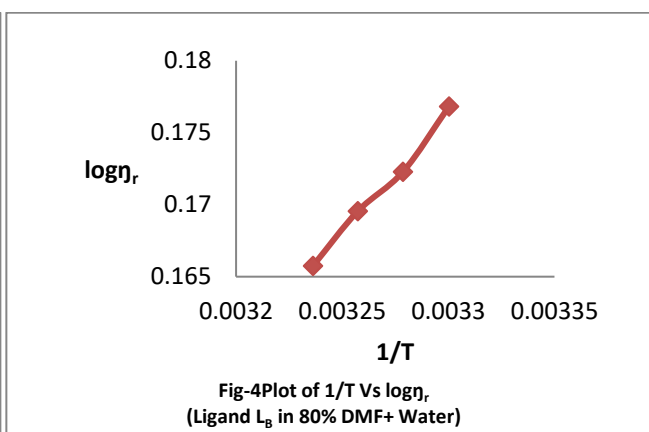
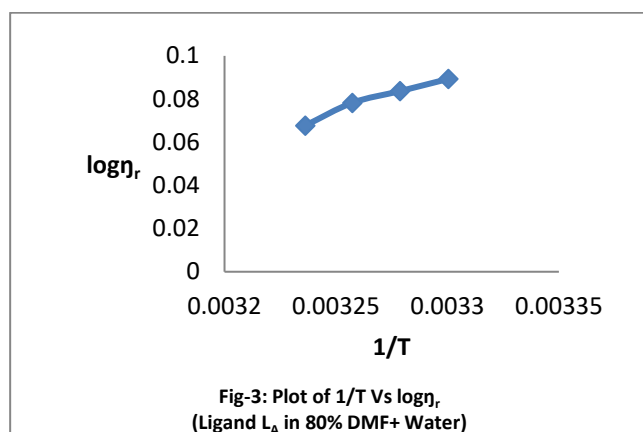
Table – 4 Values of Thermodynamic Parameters for temperature difference 309K – 307K

Ligands	ΔG (J mol ⁻¹)	ΔH (J mol ⁻¹)	ΔS (J mol ⁻¹ K ⁻¹)
System : 80% (DMF + Water)			
L _A	-6278.35	-3147.87	10.1309
L _B	-3224.38	-1133.06	6.7680

Table – 5 Values of Thermodynamic Parameters for temperature difference 309K – 303K

Ligands	ΔG (J mol ⁻¹)	ΔH (J mol ⁻¹)	ΔS (J mol ⁻¹ K ⁻¹)
System : 80% (DMF + Water)			
L _A	-6278.35	-9733.85	-11.1829
L _B	-3224.38	-4997.13	-5.7370

Medium: 80% DMF-Water



The values of thermodynamic parameter are negative shows spontaneous and exothermic reaction between solute and solvent. We know the entropy measure the randomness in the system. Positive values of entropy shows the randomness of solute molecule in the solvent indicate endothermic reaction.

IV. CONCLUSION

In the present study, the relative viscosity, specific viscosity, density of solution of aminopyrimidine derivatives decreases with decrease in concentration of solution. Positive value of A shows strong solute-solute interaction. On the other hand the value of B-coefficient is negative shows weak solute-solvent interaction which is in favor of pharmacodynamics and pharmacokinetics activity. Thermodynamic study shows negative value of Gibbs' free energy and values of thermodynamic parameter are negative shows spontaneous and exothermic reaction. The positive values of change in enthalpy indicate endothermic reaction. The values of entropy is positive shows the randomness of solute molecule in the solvent.

V. REFERENCES

- [1]. Aicher, T. D., S. A. Boyd, M. J. Chicarelli, K. R. Condroski, R. J. Hinklin, and A. Singh US Pat. 20090156603, (2007).
- [2]. Lawton, G. R., H. R. Ranaivo, L. K. Chico, P. Martasek, L. J. Roman, D.M. Watterson, and R. B. Silverman, *Bioorg. Med. Chem.*, no.17 (2009): 2371.
- [3]. Ahmed, A. Fayed, H. M. Hosni, E. M. Flefel, Abd El-Galil E. Amr., *World J. Chem.*, no.4 (2009): 58.
- [4]. Sondhi, S. M., M. Dinodia, R. Rani, R. Shukla, and R. Raghbir, *Indian J. Chem.*, No. 49B (2009): 273.
- [5]. a. Abunada, N. M., H. M. Hassaneen, and N. G. Kandile, *Molecules*, no. 13 (2008):1501. b. Fathalla, O. A., I. F. Zeid, and A. M. Soliman, *World J. Chem.*, no.2 (2009): 127. c. Basavaraja, H. S., and K.V. Jayadevaiah, *J. Pharm. Sci. Res.*, no.2 (2010): 5. d. Mistry, R. N., and K. R. Desai, *E-J. Chem.*, no. 2 (2005): 30. e. Naik, T. A., K. H. Chikhalia, *E-J. Chem.*, no. 4 (2007): 60. f. El-Saghiera, A. M., and F. S. Matough, *Jordan J. Chem.*, no.3 (2008): 223. g. Orzeszko, B., and A. E. Laudy, *Acta Poloniae Pharm.*

- Drug Rev., no. 61(2004): 455. h. Vaghasia, S. J., and V.H. Shah, J. Serb. Chem. Soc., no. 72 (2007): 109. i. Munawar M. A., M. Azad,H. L. Siddiquia, and F. H. Nasimb, J. Chin. Chem. Soc., no. 55 (2008): 394.
- [6]. Sadanandan, Y.S., N. M. Shetty, and P. V. Diwan, Chem.Abstr., no. 117 (1990):7885.
- [7]. Mosharef Hossain Bhuiyan, M. D., M. D. Khandker, M. Rahman, M. D. Kamrul, H. A. Rahim, M. I. Hossain, and M. A. Naser, Acta Pharm., no. 56 (2006):441.
- [8]. Rahaman,A.,Y. R. Pasad, P. Kumar, and B. Kumar, J.Saudi Pharma.,no.17 (2009):259.
- [9]. Pore,Y., and B. Kuchekar, Digest J. Nanomater. Biostruct., no. 3 (2008): 293.
- [10]. Quintero A., A. Pelcastre, and J. D. Solano, J. Pharm. Sci., no. 2 (1999):108.
- [11]. Singh, N., S.K. Pandey, and N. Anand, Bioorg. Med. Chem., no. 21 (2011): 4404.
- [12]. Bretschneider T., R. Fischer, and F.Maurer, Int. Patent Appl. WO 02/067684 A1,(2002).
- [13]. Abdel-Rahman, B. A., El-gazzar, Hoda A. R. Hussein, and H. N. Hafez., Acta Pharma., no. 57 (2007): 395.
- [14]. Press,J. B., R. K. Russel, and U. S. Petent, no. 4 (1987): 670.
- [15]. Sriram,D., T. R. Bal, and P. Yogeeswari, ibid., no. 1 (2005): 277.
- [16]. Katiyar, S. B., I. Bansal, and J. K. Saxena, Bioorg. Med.chem. Lett.,no.15(2005),15, 47.
- [17]. Kumar,A., and J. K. Saxena, Med. Chem., no. 4 (2008): 577.
- [18]. Angelo, R., B. Olga, and S. Silvia, Chem.Abstr., no.23 (1986): 128.
- [19]. Yaziji, V., D. Rodri guez, and H. Gutie, J. Med. Chem., no. 54 (2011), 457.
- [20]. Chu X., W. Depinto, and D. Bartkovitz, J. Med. Chem., no. 49 (2006),6549.
- [21]. Russel, R. K., J. B. Press, and R. A. Rampilla, Chem.Abstr., no. 117 (1990): 7785.
- [22]. Michida Pharmaceutical Co. Ltd., JP, no. 81(127), (1981): 383.
- [23]. Viscosity of liquids: Theory, Estimation, Experiment and Data by Vishwanath Ghosh.
- [24]. Barne, H. A., J. F. Hultton,and K. Walters, Elsevier, (1989).
- [25]. Kumar, H., M. Singla, and A. Katal, Thermochim. Acta, no.583 (2014): 49.
- [26]. Ottain, S., D. Vitalini, F. Comeli and C. Costellari, J. Chem. Eng. Data., No. 47 (2002),1197.
- [27]. Dack, M. R. J., K. J. Bird, and A. J. Parker, Aust. J. Chem., no.28 (1975): 955.
- [28]. Banipal,T. S., H. Singh, and P. K. Banipal , J. Chem. Eng. Data, no.55 (2010): 3872.
- [29]. Chauhan,S.,V. K. Syal, M. S. Chauhan, and P. Sharma, J. Mol. Liq., no. 136(2007):161.
- [30]. Deosarkar,S.D., A.D. Arsule, R.T.Sawale, V.G. Pingale, . J. Mol. Liq., No 323 (2021): 114925
- [31]. Jones,G., and M Dole; J. Am. Chem. Soc., no. 51(10)(1929): 2950-2964.
- [32]. Quazi ,S. A., D.T Mahajan, N. Mohammad, M.L. Narwade, V. Masand, M.R. Ingale, Ind. J. Res. Pharm.Biotechnol., no. 3(1)(2015): 13-14.
- [33]. Kalaskar, Monali M., H. S. Chandak and M. P. Wadekar, J. of Chemical, Biological and Physical Sciences, no.5(4) (2015):3868-3874.



Green Synthesis of Iron Nanoparticles and Its Characterization Using Brassica Oleracea Var. Capitata Leaf Extract

Shaikh Ruquaiya¹, R.D. Isankar²

¹Department of Chemistry, Dr. Rafiq Zakaria Campus Maulana Azad College, Aurangabad-431001, Maharashtra, India

²Department of Chemistry, Government Vidarbha Institute of Science and Humanities, Amravati-444604, Maharashtra, India

ABSTRACT

Nanoscience is a vital area of science which deals with study of small dimensional particles. Nanotechnology is an interdisciplinary branch of science, which emphasizes the study of materials in nano range 1-100nm. Cabbage Brassica oleracea var. capitata is one of major winter leafy vegetable which belong to cruciferae family. The aim of present study is the synthesis of Fe nanoparticles through green synthesis using Brassica oleracea var. capitata extract. In the present investigation synthesized Fe nanoparticles analyzed by using ultraviolet-visible spectroscopy (UV) was initially to be identified formation Fe nanoparticles. Furthermore, Fourier-transform infrared spectroscopy (FTIR) analysis to be confirmed functional groups of Fe nanoparticles. Scanning electron microscopy (SEM) and Energy dispersive X-ray spectroscopy (EDS) shows the shape of Fe nanoparticles and quantitative evaluation of Fe and O elements in the prepared samples.

Key words: Brassica oleracea var. capitata leaf extract, Ultraviolet spectroscopy (UV), Fourier transform infrared spectroscopy (FTIR), Scanning electron microscopy (SEM), Energy dispersive X-ray spectroscopy (EDS).

I. INTRODUCTION

“Nano” is derived from the Greek word for dwarf. Ananometer is one billionth of a meter (10⁻⁹) and might berepresented by the length of ten hydrogen atoms lined up in a row Nanotechnology implies the creation andutilization of materials, devices and systems through thecontrol of matter on the nanometer-length scale i.e. at thelevel of atoms, molecules and supramolecular structuresNanotechnology is mainly concerned with synthesisof nanoparticles of variable sizes, shapes, chemicalcompositions and controlled dispersity and their potentialuse for human benefits [1]. Various types of metal oxide nanoparticles (MONP), CuO, FeO and MgO NP have received global attention due to their inherited characteristics which have made these NPs a promising candidate in various applications; for example, CuO NPs are used as gas sensors, photoconductive applications and critical temperature superconductors [2-3]. On the other hand, NP FeOs receive solemn attention due to biocompatibility and many applications such as biosensors, separation processes,

environmental remediation, storage media, magnetic and electric fields have also been reported [4]. The synthesis of nanoparticles is usually performed by various chemical methods such as pyrolysis, sol-gel transition, supercritical fluid synthesis and chemical vapor deposition or with a variety of physical methods such as etching, mechanical milling, laser ablation, thermal decomposition and lithography. Many of these methods are costly and it requires the use of toxic solvents. On the other hand, great efforts have recently been made to use environmentally friendly methods for the synthesis of noble metal nanoparticles. This effort has produced so-called green methods, with the aim of delivering highly pure nanoparticles through simple, inexpensive and repetitive techniques [5]. Numerous studies have shown that plants, spices, and herbs have high levels of potent antioxidant compounds including reducing sugars, polyphenols, nitrogenous bases, and amino acids that are used as a reducing and protective agent for the synthesis of iron oxide nanoparticles. Plant extract synthesis methods can be scaled up appropriately for large-scale manufacturing [6].

II. EXPERIMENTAL METHODS

Ferric Nitrate [$\text{Fe}(\text{NO}_3)_3$] is standard research grade and experimental chemicals were procured from Hi-media Laboratory, Pune, India and used without any further purification step. All the experimental work was used by deionized water. Freshly *Brassica oleracea* var. capitata leaf purchased from local market of Aurangabad, Maharashtra region. The leaves along with stems were cut and dried in shade and then the dried leaves were taken in Morton pestle for making them in fine powder form. 10 g of plant leaf were taken into the 250 ml round bottom flask it contain 100 ml of deionized water and boiled above 100°C for 3 hours. The leaf extract was permeated through the whatman filter paper (No.1) then prepared leaf extract was stored in the cooled room for further studies.

GREEN SYNTHESIS OF IRON NANOPARTICLES

Synthesis of Iron nanoparticles by using 1M Ferric nitrate solution as a precursor, briefly the reaction mixture ferric nitrate was prepared in the deionized water was added into the 50 ml of *Brassica oleracea* var. capitata leaf extract solution under the continuously magnetic stirring at 80°C for 1 hour. During the stirring process the PH was adjusted by using of sodium hydroxide solution. After that reaction spontaneously color solution was changed from yellow to dark brown, which was indicated the development of iron nanoparticles. Then obtained precipitation was centrifuge and through washed with deionized water to remove excess impurities of organic and inorganic particles. After the precipitation was dried to obtained fine powder of iron nanoparticles was collected and used for further experiment purpose.

INSTRUMENTAL ANALYSIS

A Green Synthesis of Iron nanoparticle was confirmed using a UV-Visible spectroscopy, band gap energy determined at a wavelength between 277 and 375 nm. The identified functional groups of synthesized iron nanoparticles were performed by using a FT-IR spectroscopy peaks at 1070 cm^{-1} , 1636 cm^{-1} , 2800 cm^{-1} , and 3467 cm^{-1} were due to C-O, C=O, C-H, and OH bonds, respectively. The surface morphological characterization of the synthesized iron nanoparticles was imaged by using of FE-SEM analysis followed to identify the presence of elemental through the analysis of EDS [7-9].

III. CONCLUSION

From this present research work it is concluded that the greener method is cost effective and the electronic spectroscopic studies i.e., UV-visible, FT-IR and SEM-EDS shows the primary information of nanoparticles and functional groups present in it.

IV. REFERENCES

- [1]. Monalisa P., Nayak P.L., World Journal of Nano Science & Technology,2(1), 06-09, 2013.
- [2]. Azam A., Ahmed A.S., Oves M., Khan M.S., Memic A., International Journal of Nanomedicine, 7, 3527–3535, 2012.
- [3]. Selvam S., Seerangaraj V., Veerasamy V., Mythili S., Govindaraju R., Thamaraiselvi K., Fahad A.M., Journal of environmental Chemical Engineering, 9, 105033, 2021.
- [4]. Asifa N., Sumbal, Joham S.A., Muhammad L., Zarrin F.R., Sania N., Abdul M., Muhammad Z.,Materials Chemistry and Physics, 271, 124900, 2021.
- [5]. Amin J.A.A., Laouini S.E., Bouafia A., Alonso-Gonzalez M., Guerrero A., Romero A.,Sustainable Chemistry and Pharmacy, 17,100280, 2020.
- [6]. Mohammad Amin J. K., Nasrin B. , Saeed T., Ali Mohammad A.,Vahid A.,Adv. Nat. Sci.: Nanosci. Nanotechnol. 10, 015007, 2019.
- [7]. Mina J., Maryam K.B., Journal of Nanostructure in Chemistry, 10, 193–201, 2020.
- [8]. Gang W., Ke Z., Chunxia G., Jinyu W., Yucheng M., Xuesong Z., Peizhi Z.,Journal of Environmental Chemical Engineering, 9,10533,2021.
- [9]. YunqiangY., GuoquanT., Pokeung EricT., ShihuaX., Zhanqiang F., Materials Letters, 234, 388-39, 2019.

Synthesis and Characterization of Some 2- (Substituted Thiocarbamido) Aminophenothiazine

B. R. Deshmukh, R. D. Isankar

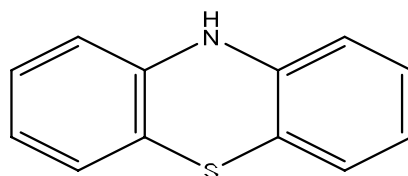
Department of Chemistry, Government Vidharbha Institute of Science and Humanities, Amravati,
Maharashtra, India

ABSTRACT

A series of 2-(Substitutedthiocarbamido) aminophenothiazine (IIIa-c) was successfully synthesized by the interactions of 2-chlorophenothiazine(I) with various thiourea (IIa-c) in isopropanol medium respectively. The structure determination and justification of the synthesized compounds were done on the basis of elemental analysis, chemical characteristics and spectral keywords: 2-Chlorophenothiazine, substitutedthioureas, isopropanol etc.

I. INTRODUCTION

Phenothiazine, abbreviated PTZ, is an organic compound that has the formula C₁₂H₉NS and is related to the thiazine-class of heterocyclic compounds. Although the parent compound has no uses, derivatives of phenothiazine are highly bioactive and have widespread use and rich history. The biological activities and industrial application of phenothiazines and their derivatives have created interest in the synthesis and study of the physiochemical properties of nuclear substituted phenothiazines¹. Phenothiazine (I) molecule is depicted below

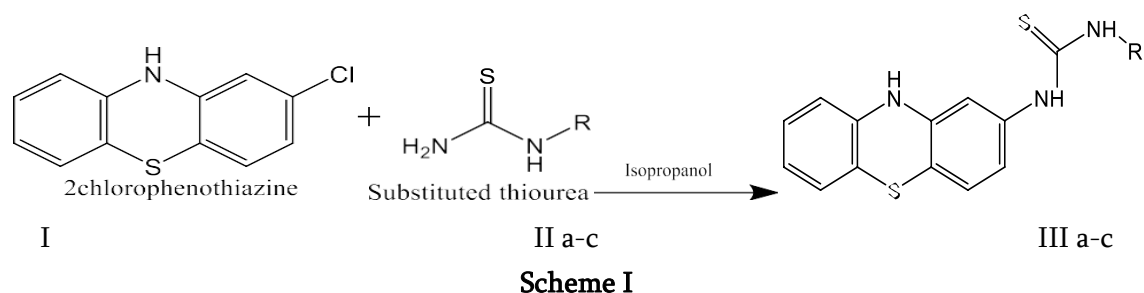


10H-dibenzo-[b,e]-1,4-thiazine

Phenothiazines are unanimously one of the most versatile compounds from the view of biological activity¹. Since their discovery, new exploitable pharmacological properties have emerged from time to time; thus, they have an important role in many areas of medicine and beyond²⁻⁴. This is why phenothiazines are basic compounds in pharmacology. A clear look at the proven physiologically active phenothiazine derivative reveal that compounds are mostly 2-10 disubstituted phenothiazines. At position 2 groups are -H, -OCH₃, -Cl, -CH₃, and -CF₃. A variety of substituents at position 10 have been promising medicinal properties⁵⁻⁹. As a wider programme of this laboratory in the synthesis of nitrogen, nitrogen and Sulphur containing hetrocycles, the interactions of 2- chlorophenothiazine with various thiourea had been investigated in sufficient details in various reaction conditions. As 2-chlorophenothiazine have thiazine nucleus and as a part

of research work presently been undertaken in this laboratory in the synthesis of nitrogen, nitrogen and Sulphur containing heteroacycles¹⁰⁻¹³. It was thought interesting to explore the interaction of 2-chlorophenothiazine with substituted thiourea in presence of isopropanol medium to obtained a novel series of 2-(substitutedthiocarbamido) aminophenothiazine This work describes somewhat suitable, cheaper and more practical utility.

II. MATERIALS AND METHODS



Preparation of 2-(ethylthiocarbamido) aminophenothiazine

A mixture of 2-chlorophenothiazine (0.1mol) and ethyl thiourea (0.1mol) were placed in a 30 ml of isopropanol contained round bottom flask equipped with a mechanical stirrer. The reaction mixture was stirred with a mechanical stirrer for 30 min and temperature of the mixture kept at about 25°C. The mixture was stirred and refluxed at 80° C for 4h on a water bath. It was cooled to room temperature and poured into 50ml of water. The precipitated solid was separated by a vacuum filter, washed with a small portion of cold water and recrystallized from ethanol.

Preparation of 2-(methylthiocarbamido) aminophenothiazine

A mixture of 2-chlorophenothiazine (0.1mol) and methyl thiourea (0.1mol) were placed in a 30 ml of isopropanol contained round bottom flask equipped with a mechanical stirrer. The mixture was stirred and refluxed at 80° C for 4h on a water bath. It was cooled to room temperature and poured into 50ml of water. The precipitated solid was separated by a vacuum filter, washed with a small portion of cold water and recrystallized from ethanol.

Preparation of 2-(phenylthiocarbamido) aminophenothiazine

A mixture of 2-chlorophenothiazine (0.1mol) and phenyl thiourea (0.1mol) were placed in a 30 ml of isopropanol contained round bottom flask equipped with a mechanical stirrer. The mixture was stirred and refluxed at 80° C for 4h on a water bath. It was cooled to room temperature and poured into 50ml of water. The precipitated solid was separated by a vacuum filter, washed with a small portion of cold water and recrystallized from ethanol.

III. RESULTS AND DISCUSSION

A total of 3 derivatives of Synthesized Phenothiazine compounds were recrystallized with appropriate solvents and all the compounds were identified and characterized by Physical and Spectral methods, the results were shown in Table 1 and Table.2.

Table 1: Physical Characterization Data of all the Synthesized Derivative Compounds

Compound Code	Mol. Formula	Mol. Weight (g/mole)	% Yield w/w	Melting Point(⁰ C)	Rf
III-a	C ₁₅ H ₁₅ N ₃ S ₂	301	83	203	0.72
III-b	C ₁₄ H ₁₃ N ₃ S ₂	287	87	215	0.87
III-c	C ₁₉ H ₁₅ N ₃ S ₂	349	82	210	0.82

*Ethyl Acetate: Pet ether 3:1

Table 2: Spectral analysis data of all synthesized compounds

Compound Code	Mol. Formula	Spectral data's
III-a	C ₁₅ H ₁₅ N ₃ S ₂	¹ H NMR (CDCl ₃ , 300MHz): -CH ₃ protons at δ 1.21 ppm, NH protons at δ 13.02 ppm, -NH proton side chain at δ 7.31ppm, -CH proton in fused ring at δ 6.82-7.41 ppm, CH ₂ protons at δ 4.43 ppm and -NH proton in ring at δ 8.30 ppm IR spectra: 3369 (-NH Str), 1590 (C=S Str), 1452 (C-S str), 2880 (C-H str in methyl), 1239.63(C-N str) Elemental Analysis: C, 59.77; H, 5.02; N, 13.94; S, 21.27
III-b	C ₁₄ H ₁₃ N ₃ S ₂	¹ H NMR (CDCl ₃ , 300MHz): -CH ₃ protons at δ 2.8 ppm, NH protons at δ 13.02 ppm, -NH proton side chain at δ 7.31ppm, -CH proton in fused ring at δ 6.82-7.41 ppm and -NH proton in ring at δ 8.30 ppm IR spectra: 3369 (-NH Str), 1600 (C=S Str), 1449 (C-S str), 2870 (C-H str in methyl), 1239.63(C-N Str) Elemental Analysis: C, 58.51; H, 4.56; N, 14.62; S, 22.31
III-c	C ₁₉ H ₁₅ N ₃ S ₂	¹ H NMR (CDCl ₃ , 300MHz): Ar-H protons at δ 7.09-7.70 ppm, NH protons at δ 13.02 ppm, -NH proton side chain at δ 11.32ppm, -CH proton in fused ring at δ 6.82-7.41 ppm and -NH proton in ring at δ 8.32 ppm IR spectra: 3369 (-NH Str), 1590 (C=S Str), 1439 (C-S str), 3089 (Ar-H), 1239.63(C-N Str) Elemental Analysis: C, 65.30; H, 4.33; N, 12.02; S, 18.35

IV. CONCLUSION

The synthesis of 3 derivative compounds were prepared, those are 3 derivatives of substituted phenothiazine were prepared in scheme 1 from 2-chlorophenothiazine and substituted thiourea. All the compounds were structurally elucidated with physical and analytical methods. The future studies of synthesized Phenothiazine derivatives need to develop QSAR methods and to bring potential effects.

V. REFERENCES

- [1]. Gabriela P. S., Martini M. F., Roxana G. V., Lucas E. F., Arabian Journal of Chemistry, Vol. 12, 21-32, 2019.
- [2]. Krystian P., Beata M. M., and Malgorzata J., European journal of Medicinal Chemistry, 46(8), 3179-3189, 2011.
- [3]. Shivkumar K., Ragi T. R., Journal of Bimolecular Structure and Dynamics, 1565-1574, 2019.
- [4]. Nodiff E. A., .Sharma H. L., Taunk P. C., .Shukla A. P., J. Heter. Chem., 18, 529, 1981. 5. Taunk P. C., J. Heter. Chem., 22, 1219, 1985.
- [5]. Srivastava S. K., Srivastava S. L., and .Srivastava S. D., Indian J. Chem., 3913, 464, 2000.
- [6]. Venkatesan, K., Satyanarayana, V. S. V., Sivakumar A., Ramamurthy, C., Thirunavukkarasu C., J. Heterocycl. Chem, 57, 2722-2728, 2020.
- [7]. Tayade D.T., Raut P. V and Waghmare S. A., JETIR, Vol. 7, 437-439, 2020/2.



Thermal Decomposition Kinetics of VO (IV) and Zr (IV) Complexes of Hydrazone Schiff Bases

Prashant R. Mandlik*, Pallavi R. Deshmukh, Pratik K. Deshmukh

P. G. Department of Chemistry, Shri Shivaji Science College, Amravati, Maharashtra, India

ABSTRACT

The thermal behaviour of VO(IV) and Zr(IV) complexes derived from different hydrazone Schiff bases was investigated by thermogravimetric analysis(TG). The thermodynamic analysis shows that the complexes lose hydrated and/or coordinated water molecules in the first step; followed by decomposition of ligand moiety in the further steps leading to formation of stable metal oxide. The decomposition steps were analyzed and the parameters like order of reaction(n), energy of activation (E_a), entropy change (ΔS), free energy change (ΔF) and apparent entropy (S^*) were calculated by using Broido and Horowitz-Metzger methods. The activation energies values obtained in the two sets are in good agreement. Thermodynamic parameters: entropy (ΔS) and Gibbs free energy (ΔF) of activation were calculated using standard relations and discussed. On the basis of half decomposition temperature, the thermal stability of the complexes was determined.

Keywords: Salicyloyl hydrazone, Metal complexes, Thermal decomposition, Thermodynamic parameters.

I. INTRODUCTION

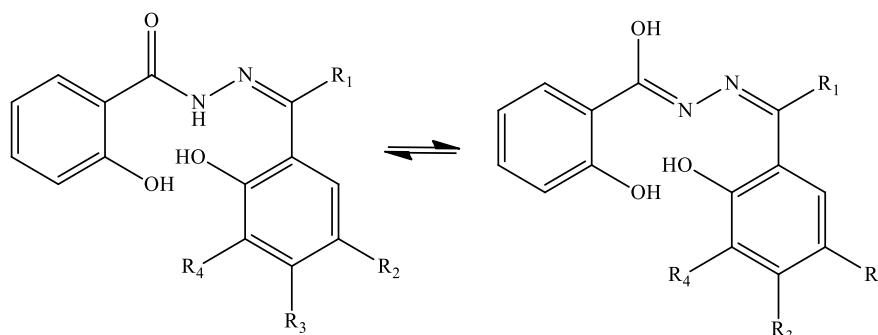
Schiff base complexes derived from hydrazone ligands containing strong donor sites such as oxygen and azomethine nitrogen atom have been the subject of particular investigation, not only due to variety of ways in which they can bonded to metal ions, their spectroscopic properties and biological applications [1-7], but also due to their remarkable thermal stability as compared to the Schiff base ligands [8-10]. In spite of the relatively large number of reports on Schiff base metal complexes, less work has been published on thermal stability of the complexes and calculation of their kinetic and thermodynamic parameters of decomposition. In this paper we report kinetics of the thermal decomposition pattern of VO(IV) and Zr(IV) complexes prepared by using five different Schiff base ligands. The thermal parameters were calculated using Broido [11] and Horowitz-Metzger [12] methods. The complexes are thermally stable and their thermal decompositions are multistage processes. The complexes are subjected to a TG analysis from 40-800°C.

II. MATERIAL AND METHODS

All the chemicals used as a starting material for the synthesis of the ligand and their metal complexes were of AR grade or chemically pure, solvents were purified and dried before use. The ligands used in the work were not commercially available, hence were synthesized in our laboratory. The metal complexes were prepared by mixing the ethanolic solution of metal salt with the ethanolic solution of ligands by setting the suitable reaction conditions. The VO(IV) and Zr(IV) metal salts used for the preparation of complexes were vanadylsulphate pentahydrate [VOSO₄.5H₂O] and zirconyloxchlorideoctahydrate [ZrOCl₂.8H₂O] respectively. The ¹H NMR spectra of the ligands were taken using TMS as the internal standard on a 90 MHz on a Perkin Elmer R-32 spectrometer. IR spectra (KBr) were recorded on a Perkin Elmer-842 spectrophotometer in the region 400-4000cm⁻¹ at RSIC, Punjab University, Chandigarh. Thermal analysis results of the complexes were obtained at a rate of 10°C per minute on a Rijaku-Thermo plus EVO2 thermodilatometer.

Synthesis of the Schiff base ligands:

All the ligands: SSH (Salicylaldehyde salicyloyl hydrazone), DHASH (2,4-dihydroxyacetophenone salicyloyl hydrazone), HMASH (2-hydroxy-5-methyl-acetophenonesalicyloylhydrazone), DHASH (2,4-dihydroxyacetophenone salicyloyl hydrazone), DHBSH (2,4-dihydroxybenzophenone salicyloyl hydrazone) and VSH (*o*-vaniline salicyloyl hydrazone) were prepared by the addition of hot ethanolic solution of salicyloyl hydrazide (0.05 mol) into hot ethanolic solution of respective aldehyde/acetophenone (0.05 mol). The reaction mixture was refluxed in a water bath for 4-6 hrs. The colored products so obtained were filtered off and recrystallized from dimethyl formamide.



Ligand	R ₁	R ₂	R ₃	R ₄
SSH	H	H	H	H
HMASH	CH ₃	CH ₃	H	H
DHASH	CH ₃	H	H	OH
DHBSH	C ₆ H ₅	H	OH	H
VSH	H	H	H	OCH ₃

Synthesis of VO(IV) and Zr(IV) Complexes:

Equimolar quantities of respective metal salt (0.02 mol VOSO₄.5H₂O or ZrOCl₂.8H₂O) and the ligands were dissolved separately in absolute ethanol (25 ml). Both the solutions were filtered and mixed in hot

condition. The reaction mixture was refluxed for 4-6 hrs in a water bath. The colored products obtained were filtered, washed several times with hot water followed by ethanol and diethyl ether and finally dried over fused calcium chloride.

III. RESULTS AND DISCUSSION

Infrared Spectra of the ligand:

The IR Spectra of the ligands were recorded for the identification of their donor sites and to compare the shifts in frequencies after their complexation with VO(IV) and Zr(IV) metal ions. A broad and strong band in the spectra of complexes in the region $3367-3269\text{ cm}^{-1}$ is assigned to intramolecular hydrogen bonded phenolic OH, a sharp band between $3221-3013\text{ cm}^{-1}$ is due to N-H Stretching. The other bands in the region $1651-1643$, $1620-1615$, $1303-1273$ and $1033-964\text{ cm}^{-1}$ are assigned to $\nu(\text{C}=\text{O})$, $\nu(\text{C}=\text{N})$, $\nu(\text{C}-\text{O})$ and $\nu(\text{N}-\text{N})$ respectively [13-17].

^1H NMR Spectral data of ligands:

L1-SSH - δ 12.39 (2 H,S, phenolic OH); 11.44 (1H,S, Imino NH); 6.95 - 7.95 (8H,M, Aromatic proton); 8.94 (1H,s, Azomethine HC=N) [18-21].

L2-HMASH - δ 12.86 (11.53 H,S, phenolic OH); 11.44 (1H,S, Imino NH); 6.99 - 7.99 (7H,M, Aromatic proton); 2.3 (3H,s, Methyl, Ar-CH₃); 2.55 (3H,S, Methyl, N=CCH₃).

L3-DHASH - δ 13.33 (2 H,S, Phenolic C₂-OH); 11.44 (1H,S, Imino NH); 6.98 - 7.99 (7H,M, Aromatic proton); 2.3 (3H,s, Methyl, N=CCH₃); 9.82 (1H,S, Phenolic C₄-OH).

L4-DHBSH - δ 12.4 (2 H,S, Phenolic C₂-OH); 11.22 (1H,S, Imino NH); 6.95 - 7.99 (12H,M, Aromatic proton); 12.01 (1H,s, Phenolic C₄-OH).

L5-VSH- δ 10.07 (2 H,S, phenolic OH); 11.43 (1H,S, Imino NH); 6.95 - 7.95 (7H,M, Aromatic proton); 3.79 (3H,s, Methyl, Ar-OCH₃); 8.96 (1H,s, Azomethine HC=N).

Table 1. The analytical and physical data of the complexes.

Sr. No.	Complex	Formula Weight g mol ⁻¹	Colour	Time of Reflux	M% Found (Calcd.)	C% Found (Calcd.)	H% Found (Calcd.)	N% Found (Calcd.)
1.	VO-L1	642.36	Black	6 h	15.86 (15.87)	52.35 (52.41)	3.14 (3.11)	8.72 (8.80)
2.	VO-L2	698.47	Black	6 h	14.59 (14.67)	55.03 (55.14)	4.04 (4.13)	8.02 (8.21)
3.	VO-L3	702.42	Black	6 h	14.50 (14.42)	51.30 (51.40)	3.44 (3.37)	7.98 (7.90)
4.	VO-L4	826.55	Black	6 h	12.33 (12.58)	58.12 (58.72)	3.41 (3.35)	6.78 (6.80)
5.	VO-L5	702.42	Black	6 h	14.50	51.30	3.44 (3.56)	7.98 (7.68)

					(14.98)	(51.44)		
6.	Zr-L1	599.71	Yellow	6 h	15.21 (15.27)	56.08 (56.17)	3.36 (3.45)	9.34 (9.47)
7.	Zr-L2	655.81	Yellow	6 h	13.91 (13.98)	58.61 (58.52)	4.30 (4.55)	8.54 (8.66)
8.	Zr-L3	659.76	Yellow	6 h	13.83 (13.84)	54.61 (54.44)	3.67 (3.61)	8.49 (8.41)
9.	Zr-L4	783.9	Yellow	6 h	11.64 (11.72)	61.29 (61.35)	3.60 (3.75)	7.15 (7.20)
10.	Zr-L5	659.76	Yellow	6 h	13.83 (13.99)	54.61 (54.78)	3.67 (3.49)	8.49 (8.56)

Thermogravimetric analysis of the complexes:

All the complexes are stable up to 70°C and are decomposed into two stages. The VO(IV) and Zr(IV) complexes remain stable up to ~240°C indicating absence of coordinated and lattice water molecules. Elimination of ligand moiety takes place in the first step and a part of coordinate ligand decomposed in second step followed by horizontal level beyond 650°C in all the complexes due to formation of stable metal oxides. The above pattern confirms the formation of metal complexes. The half decomposition temperature, entropy change (ΔS), free energy change (ΔF) and frequency factor (Z) of compounds were calculated by employing Broido and Horowitz-Metzger methods [22-24]. The kinetic parameter data for the complexes are given in the Table 3. On the basis of half decomposition temperature, the thermal stability of the VO(IV) and Zr(IV) metal complexes is found to be: VO-L₁ > VO-L₂ > VO-L₅ > VO-L₄ > VO-L₃ and Zr-L₅ > Zr-L₂ > Zr-L₄ > Zr-L₁ > Zr-L₃ respectively.

Table 2 Thermal decomposition data of VO(IV) and Zr(IV) complexes.

Sr. No.	Complex	Half decomposition temperature (°C)	Activation Energy Ea (kJ mole ⁻¹)		(n)	Entropy Change - ΔS (J/mol/K)	Free Energy Change ΔF (kJ/mol)	Apparent Entropy Change S* (kJ)	DTA Peak Temp. (°C)
			BR*	H-M**					
1.	VO-L1	420	18.68	7.61	1.00	-294.82	110.95	-35.79	270, 395
2.	VO-L2	421	5.17	21.16	0.90	-332.78	109.33	-33.34	315
3.	VO-L3	350	10.42	15.97	0.92	-253.83	89.88	-31.73	295
4.	VO-L4	390	22.59	17.32	0.90	-273.51	108.20	-30.25	301, 375
5.	VO-L5	420	20.00	31.1	0.90	-220.06	88.88	-30.25	335
6.	Zr-L1	348	10.73	22.89	0.90	-298.04	104.01	-31.54	275, 390
7.	Zr-L2	568	11.77	15.14	0.91	-329.87	115.01	-24.21	300, 385
8.	Zr-L3	330	9.56	19.23	0.90	-267.06	93.75	-32.88	260, 350

9.	Zr-L4	353	19.14	18.99	0.90	-217.44	87.19	-29.97	305, 325
10.	Zr-L5	590	46.61	36.16	0.90	-269.42	130.93	-25.03	300, 375

IV. CONCLUSION

The activation energy calculated by the Broido and Horowitz- Metzger methods are in good agreement with each other. Thermodynamic parameters have been calculated on the basis of thermal activation energy and values are given in Table 2. The thermal stability of the compounds can be correlated with the substituent group attached to the ligands. It is found that more substituted ligands may have more thermal stability than more substituted ligands.

V. ACKNOWLEDGMENT

P. R. Mandlik thanks the University Grants Commission, New Delhi, India for financial support in the form of Major research project [MRP. F. No. 41- 315/2012(SR)]. Thanks are also due to authorities of Shri Shivaji Science College, Amravati, India for providing necessary research facilities.

VI. REFERENCES

- [1]. Kajal, A., Bala, S., Sharma, N., Kamboj, S., & Saini, V. (2014). Therapeutic potential of hydrazones as anti-inflammatory agents. *International journal of medicinal chemistry*, 761030, 1-11. <https://doi.org/10.1155/2014/761030>
- [2]. Mohammed, A. A., Al-Daher, A. M., Mohamad, H. A., & Harrison, R. G., (2015). Synthesis and characterization of polydentate macrocyclic Schiff bases (14-membered atoms) and their complexes with Co(II), Ni (II), Cu (II) and Zn(II) ions. *Research Journal of Chemical Sciences*, 5(7), 12-19.
- [3]. Khorshidifard, M., Amiri Rudbari, H., Kazemi-Delikani, Z., Mirkhani, V. & Azadbakht, R. (2015). Synthesis, characterization and X-ray crystal structures of vanadium(IV), cobalt(III), copper(II) and zinc(II) complexes derived from an asymmetric bidentate schiff-base ligand at ambient temperature," *Journal of Molecular Structure*, vol. 1081, 494-505, 2015.
- [4]. Malik, S., Ghosh, S., & Mitu, L. (2011). Complexes of some 3d-metals with a Schiff base derived from 5-acetamido-1,3,4-thiadiazole-2-sulphonamide and their biological activity. *Journal of the Serbian Chemical Society*, 76(10), 1387-1394. <https://doi.org/10.2298/JSC110111118M>
- [5]. Abu-Khadra, A. S., Afify A. S., Mohamed A., Farag R. S., & Aboul-Enein, H. Y. (2018). Preparation, characterization and antimicrobial activity of Schiff base of (E) - N - (4-(Thiophen-2-ylmethyleneamino) Phenylsulfonyl) Acetamide metal complexes. *The Open Bioactive Compounds Journal*, 6, 1-10. <https://doi.org/10.2174/1874847301806010001>

- [6]. Ravoof, T. B., Crouse, K. A., Tahir, M. I., How, F. N., Rosli, R., & Watkins, D. J. (2010). Synthesis, characterization and biological activities of 3-methylbenzyl 2-(6-methyl pyridin-2-ylmethylene)hydrazine carbodithioate and its transition metal complexes. *Transition Metal Chemistry*, 35(7), 871-876.
- [7]. Gull, P., & Hashmi, A. A. (2015). Biological activity studies on metal complexes of macrocyclic schiff base ligand: synthesis and spectroscopic characterization. *Journal of the Brazilian Chemical Society*, 26 (7), 1331-1337. <https://doi.org/10.5935/0103-5053.20150099>
- [8]. Elemo, F., Gebretsadik, T., Gebrezgiabher, M., Bayeh, Y. & Thomas, M. (2019) Kinetics on thermal decomposition of Iron(III) complexes of 1,2-bis(imino-4'-antipyrinyl)ethane with varying counter anions. *Advances in Chemical Engineering and Science*, 9, 1-10. <https://doi.org/10.4236/aces.2019.91001>.
- [9]. Patel, K. R., Patel, D., & Patel, V. D. (2014). Characterization, activation energy & thermodynamic parameter of crystals synthesized from solvent evaporation method. *International Journal of Researches In Biosciences, Agriculture & Technology, J. Chem.* , 2(2), 746-753.
- [10]. Alshamsi, H. A., AL-Adilee, K. J., & Jaber, S. (2015). Thermal Decomposition Study on Solid Complexes of 7-[2-(Benzimidazolyl)azo]-8-hydroxy quinoline with Co(III), Ni(II) and Cu(II). *Oriental journal of chemistry*, 31(2), 809-818.
- [11]. Shamkuwar, R., & Juneja, H. (2013). Non isothermal kinetic study of some novel coordination polymers. *Research Journal of Pharmaceutical, Biological and Chemical Sciences*, 4(3), 1365-1377.
- [12]. Modi, C., & Thaker, B. (2008). Some novel tetradentate Schiff base complexes VO(IV) and Cu(II) involving fluorinated heterocyclic β -diketones and polymethylene diamines of varying chain length, *Journal of Thermal Analysis and Calorimetry*, 94(2), 567-577.
- [13]. Omar, M. M., Mohamed, G. G., & Ibrahim, A. A. (2009). Spectroscopic characterization of metal complexes of novel Schiff base. Synthesis, thermal and biological activity studies. *Spectrochim. Acta*, 73, 358-369. doi.org/10.1016/j.saa.2009.02.043
- [14]. Refat, M. S., El-Sayed, M. Y., Adam, A. (2013). Cu (II), Co (II) and Ni (II) complexes of new Schiff base ligand: synthesis, thermal and spectroscopic characterizations. *J. Mol. Struct.*, 1038, 62-72.
- [15]. Li, J., Xu, B., Jiang, W., Zhou, B., Zeng, W. & Qin, S. (2008). Syntheses, spectroscopic characterization and metal ion binding properties of benzo-15-crown-5 derivatives and their sodium and nickel(II) complexes. *Transition Metal Chemistry*, 33(8), 975-979. doi.org/10.1007/s10847-011-9973-y
- [16]. Maurya, M. R., Behl, S., Schulzke, C., & Rehder, D., (2001). Dioxo- and Oxovanadium(V) Complexes of Biomimetic Hydrazone ONO Donor Ligands: Synthesis, Characterisation, and Reactivity. *Eur. J. Inorg. Chem*, 3, 779-788.
- [17]. Makhijani, R. M., & Barhate, V. D. (2014). Synthesis, characterization and study of microbiological activity of complexes of Fe(II) and Cu(II) with (N-(o-methoxy benzaldehyde)-2-aminophenol}(NOMBAP). *International Journal of ChemTech Research*, 6(2), 1003-1012

- [18]. Rao, B., Ramesh, S., Bardalai, D., Rehman, H., & Shaik, H. A. (2013). Synthesis, characterization and evaluation of anti-epileptic activity of four new 2-pyrazoline derivatives compounds. *Scholar J. of Applied Medical Science*, 1(1), 20-27.
- [19]. Gupta, R., Gupta, N., & Jain, A. (2010). Improved synthesis of chalcones and pyrazolines under ultrasonic irradiation. *Ind. J. of Chemistry*, 49B, 351-355.
- [20]. Vidya, K., & Syed, S. (2014). Synthesis, characterization and antimicrobial studies of novel 2- pyrazoline derivatives. *Der Pharma Chemica*, 6(2), 283-287.
- [21]. Manoj, E., Kurup, M., Fun, H., & Punnoose, A. (2007). Self-assembled macrocyclic molecular squares of Ni(II) derived from carbohydrazones and thiocarbohydrazones: Structural and magnetic studies. *Polyhedron*, 26(15), 4451-4462.
- [22]. Akilandeswari J., Joseph S. & Saravanan D. (2019). Synthesis and characterisation of metal complexes of 2-[(1-methyl-1H-Tetrazole-5-yl)thio]-N'-[(1E)-4-methyl-1,3-thiazole-5-yl) methylene] acetohydrazide, *International Journal on Emerging Technologies*, 10(3), 311-317.
- [23]. Broido A.J. (1969). *Polym. Sci., A-2*, 7, 761.
- [24]. Horowitz H. H. & Metzger G. (1963). A new analysis of thermogravimetric traces. *Anal. Chem.*, 35 (10), 1464-1468. <https://doi.org/10.1021/ac60203a013>

Study the pH of Different Water Samples in Amravati City

Vaishnavi Pramod Gulhane, Kaiwalya Jwala Nagale

Students, Department of Chemistry, Bharatiya Mahavidyalaya, Amravati, Maharashtra, India

ABSTRACT

The study of pH of different water samples in Amravati were conducted by taking 10 water samples of municipal corporation, bore-well and well water respectively from different regions in Amravati. The pH is determined by using pH meter. According the parameters of WHO's, the finding of the study indicates that the water that are coming from Municipal corporation is suitable for drinking purpose along with this the water of bore-well and well water is also good for drinking purpose.

Keywords: assessment, pH meter, parameters, concentration of hydrogen ion and hydroxyl ion.

I. INTRODUCTION

pH is measure of how acidic, basic or neutral water is ? The range of pH is from 0-14. If pH of water is less than 7 then it is considered as acidic if the pH is greater than 7 then it is considered as basic. Eventually, it is a measurement of concentration of hydrogen ion or hydroxyl ion present in water. If there is a presence of hydrogen ion in water then it is considered as acidic and if there is a presence of hydroxyl ion in water then it is considered as basic. Hence, the pH of water is determined by the amount of chemicals present in water. Pure water contain equal level of hydrogen and hydroxyl ion.

There are two methods for the measuring the pH of water, one of the method is Colorimetric Method using indicator or pH paper and the more accurate Electrochemical Method using electrode i.e. pH meter. The pH is measured using pH meter consisting of glass electrode, probe, multifunctional electrode holder, display screen, host and keys which gives accurate pH of different water samples.

Objectives:

Following objectives have been set in this study.

1. To study the water is suitable for drinking purpose or not.
2. To study the variation in pH of water from one region to another.

Research methodology and tools:

There are many regions in Amravati from these, 10 regions were collected for the determination of pH of water.

II. EXPERIMENTAL

For the determination of pH, water samples were collected from different regions in Amravati, which is located in Maharashtra state. Samples of municipal corporation, bore-well and well water were collected in clean high density of plastic bottles which is use to store mineral water. Almost 10 samples of each water were collected from different regions. All the water samples were analysed in the laboratory of BharatiyaMahavidyalayaAmravati.

Table showing the pH of municipal corporation, bore-well and well water

- Table 1 showing the pH of municipal corporation water.
- Table 2 showing the pH of bore-well water.
- Table 3 showing the pH of well water.

Sr.no.	Area	pH
1.	Shegaon Naka	6.98
2.	Yashoda Nagar	7.72
3.	Badnera	7.63
4.	Rajapeth	6.31
5.	Gopal Nagar	7.2
6.	Sai Nagar	7.38
7.	Biyani square	7.5
8.	Panchavati	6.96
9.	Navsari	7.45
10.	Dastur Nagar	7.23

Table 1: Table showing thepH of municipal corporation water.

Sr.no.	Area	pH
1.	Shegaon Naka	6.99
2.	Yashoda Nagar	7.24
3.	Badnera	7.49
4.	Rajapeth	6.10
5.	Gopal Nagar	8.88
6.	Sai Nagar	7.43
7.	Biyani square	8.02
8.	Panchavati	7.15
9.	Navsari	4.98
10.	Dastur Nagar	6.87

Table 2: Table showing the pH of bore-well water.

Sr.no.	Area	pH
1.	Shegaon Naka	6.89
2.	Yashoda Nagar	7.33
3.	Badnera	7.88
4.	Rajapeth	7.34
5.	Gopal Nagar	7.41
6.	Sai Nagar	7.23
7.	Biyani square	7.54
8.	Panchavati	7.67
9.	Navsari	6.67
10.	Dastur Nagar	7.26

Table 3: Table showing the pH of well water.

III. RESULTS AND CONCLUSION

Eventually the pH values indicate the presence of hydrogen or hydroxyl ions in water. Higher the hydrogen ion lower the value of pH and the stronger acid. Lower the concentration of hydrogen ion higher the value of pH and the weaker acid. After the whole assessment it concluded that the pH level of different water samples in Amravati is suitable for drinking purposes as per WHO's parameters which is between 6.5-8.5.

IV. REFERENCES

- [1]. Dhawale, V.R. and Harle, S.M., ASSESSMENT OF GROUND WATER QUALITY OF AMRAVATI CITY OF MAHARASHTRA: INDIA.
- [2]. <https://www.tsijournals.com/articles/study-on-quality-of-underground-water-in-and-around-amravati-maharashtra-india.pdf>
- [3]. Vilaginès, P., Sarrette, B., Husson, G. and Vilagines, R., 1993. Glass wool for virus concentration at ambient water pH level. *Water Science and Technology*, 27(3-4), pp.299-306.

IOT Based Blood Glucose Measurement Using Optical Spectroscopy

Nilima Jajoo*¹, Dr. Gopaldas Agrahari*², Dr. Deepak Dhote*³

*¹Research Student, Department of Electronics, Brijlal Biyani Science College, Amravati, Maharashtra, India

*²Professor and HOD, Department of Electronics, Brijlal Biyani Science College, Amravati, Maharashtra, India

*³Principal, Brijlal Biyani Science College, Amravati, Maharashtra, India

ABSTRACT

This paper propose a device for measurement of glucose concentration in the human blood non-invasively using optical spectroscopy and IoT technology. The objective is to enhance the current technology with which the medical practitioner can monitor and get the update of the patient's glucose level without physically present at the patient place. This monitoring method also raises the patient's awareness of their blood sugar level. When the glucose level of diabetic is beyond the acceptance range, the system notifies the user or doctor [1]. This device uses Near Infra-Red (NIR) spectroscopy, Arduino Uno and IoT technology to reduce the agony of diabetic patients by providing easy and continuous monitoring of blood glucose non-invasively. Measurement system is basically able to monitor diabetic patients and save some data about name, age and blood glucose level of patient for future use.

Keywords: blood sugar, Arduinio, optical spectroscopy, IoT

I. INTRODUCTION

Diabetes Mellitus is one of the most life threatening diseases in the world that occurs not only in adults but also in infants and children. For diabetic blood glucose measurements is very essential to determine how much insulin dose intake should be taken [2]. Being a diabetic, it is necessary to check your blood glucose level regularly to maintain the glucose level within the normal range. The most widely used methods to measure blood glucose are invasive which are high in accuracy but regular use of an invasive method are usually a bit painful and has higher risk of infections [3]. The race for the next generation of painless and reliable glucose monitoring for diabetes mellitus is on. As technology advances, both diagnostic techniques and equipment improvement is important. Non-invasive glucose monitoring refers to the measurement of blood glucose levels required by the people with diabetes to prevent both chronic and acute complications from the disease without drawing blood, puncturing the finger, or causing pain or trauma [4].

There are three main types of Diabetes,

- 1) Type- I Diabetes
- 2) Type- II Diabetes
- 3) Gestational Diabetes.

In Type I body does not produce insulin. People usually had type I diabetes before their 40th year, often in early adulthood or teenage years. Type II occurs in childhood or occurs later in life perhaps after 40 years of age. The pancreas does not produce sufficient insulin or cells do not respond to insulin properly. Hence, requires insulin doses to maintain life. In addition healthy eating & exercise needed. Gestational Diabetes affects females during pregnancy. The majority of gestational diabetes patients can control their diabetes with exercise and diet. The acceptable range of glucose concentration is from 70 mg/dL to 110 mg/dL. But soon after eating, glucose concentration of a person may rise to a level up to 140 mg/dL [5,6,7].

II. NON-INVASIVE BLOOD GLUCOSE MONITORING TECHNIQUE

Non-invasive blood glucose monitoring, refers to the detection of human blood glucose without causing damage to human tissues. The advent of a pain free non-invasive technology would improve the patient's compliance for regular blood glucose monitoring. Subsequently the diabetic patient's life will improve considerably [7]. It prevents both chronic and acute complications, as this blood glucose measurement method is without drawing blood, puncturing the skin, causing pain or trauma. This technique is applied to overcome the pain, scare procedure, infections [8, 9]. In non-invasive blood glucose monitoring the most commonly approaches are by using optical detection or optical scanning methods. i.e. Polarimetry, Raman Spectroscopy, Photo Acoustic Spectroscopy, Mid-Infrared (MIR), Spectroscopy using an Attenuated Total Reflection (ATR) Prism, and Near- Infrared (NIR) spectroscopy. The NIR spectroscopy is one of the most promising optical methods and very useful in Non- Invasive blood glucose monitoring technique [10, 12].

2.1 NIR Spectroscopy

Spectroscopy is the branch of science concerned with the investigation and measurement of spectra produced when matter interacts with or emits electromagnetic radiation. Spectroscopic techniques are used to determine the presence or concentration of a substance by measuring how it interacts with light. This spectrum contains information about the optical properties and structure of the medium being measured. Near Infrared spectroscopy is a well established and constantly developing analytical technique which allows for the rapid, high-throughput, non-destructive analysis of a wide range of sample types [11]. It allows blood glucose measurement in tissues by variations of light intensity, based on transmittance and reflectance. The light focused on the body is partially absorbed and scattered, due to its interaction with the chemical components within the tissue [12]. In NIR spectroscopy, the absorption spectrum range of glucose is from 700nm to 2500nm. Molecular formula for glucose molecule is $C_6H_{12}O_6$. There is bonds C-H, O-H and C=O which causes absorption of NIR light in blood or other human bodily fluid. Glucose concentration could be estimated by variations of light intensity both transmitted through a glucose containing tissue and reflected by the tissue itself [13].

2.2 Arduino Uno

The Arduino Uno is a microcontroller board based on the ATmega328 ([datasheet](#)). It has 14 digital input/output pins of which 6 can be used as PWM outputs, 6 analog inputs, a 16 MHz crystal oscillator, a USB connection, a power jack, an ICSP header, and a reset button. It contains everything needed to support the

microcontroller; simply connect it to a computer with a USB cable or power it with a AC-to-DC adapter or battery to get started. The Uno features the Atmega8U2 programmed as a USB-to-serial converter. It is very cost efficient and also simple to use.

2.3 IoT – Internet of Things

The IoT (Internet of Things) is a new evolution of the Internet. IoT was used in 1999 for the first time which described the world where anything, including people, animals, plants and inanimate objects, being able to have their digital identity. Internet revolution in the recent decades showed that the new kinds of technologies can affect all aspects of the businesses [14, 15]. The IoT plays vital role in empowering the objects for connection at anytime, anywhere, with anything and any person that gets the ideal use of any route, service or network [16]. Advantages of IoT in healthcare include:

- **Continuous patient monitoring:** IoT enables patient monitoring in real time, continuous patient monitoring helps in diagnosing diseases at an early stage and can avoid serious impact of any disease.
- **Pocket Friendly:** IoT enables patient monitoring in real time, which causes cutting down unnecessary visits to doctors, hospital –admissions and stay.
- **Improved Treatment:** It enables physicians to make evidence-based informed decisions and brings absolute transparency. Continuous health monitoring opens the doors for providing proactive medical treatment.
- **Management of Drugs and Equipment:** In a healthcare industry management of drugs and medical equipment is a major challenge. Through IoT based connected devices, these are managed and utilized efficiently with reduced costs.
- **Fast decision making:** Data generated through IoT devices not only help in effective decision making but also ensure smooth healthcare operations with reduced errors, waste and system costs.

III. METHODOLOGY

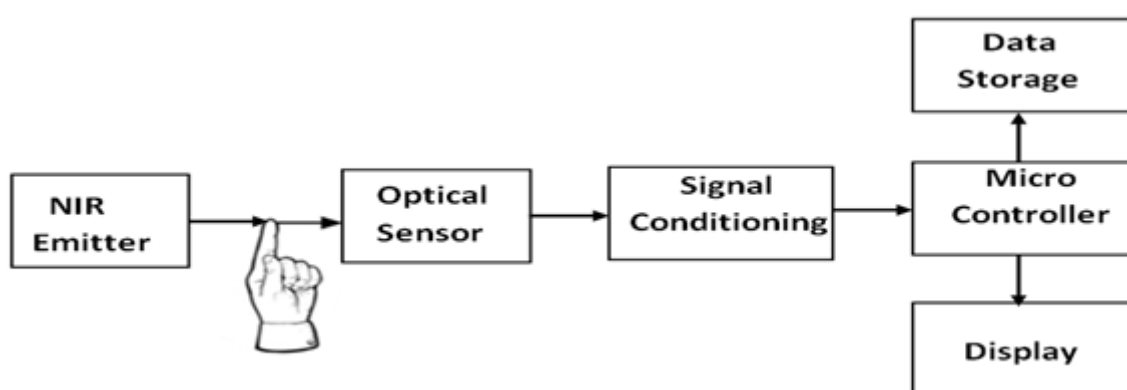


Figure -1

Our proposed module of blood glucose measuring system based on IOT has the following three units: (i) Sensing unit, (ii) Processing unit, (iii) Display unit.

The designed system consists of NIR emitter of range 900nm -1500nm which was placed over the fingertip to measure blood glucose optically and these optical signals are sent through the finger and reflected signals are detected by optical sensor. The main function of an optical sensor is to convert light rays into electronic signals. The glucose concentration of the blood was calculated depending on the intensity of the received light. The signals was then filtered and amplified before being fed into microcontroller. Here we used Arduino Uno a microcontroller board supported the ATmega328, The glucose readings were displayed on an LCD display. The glucose levels obtained are also displayed on smart phones through the Internet of Things (IoT) for remote monitoring.

Here we used Thingier.io is an Open-Source Platform for the Internet of Things. Thingier.io is a cloud IoT Platform which provides every needed tool to prototype, scale and manage connected products in a very simple way. Any device can be easily integrated with Thingier.io's infrastructure. Thingier.io WiFi Button is a ready-to-go Internet of Things based dash-button that integrates ESP8266 processor with WiFi connectivity among a simple integration with Thingier.io platform events. Thingier.io provides three essential tools to work with devices data that are Store, Show & Share Data

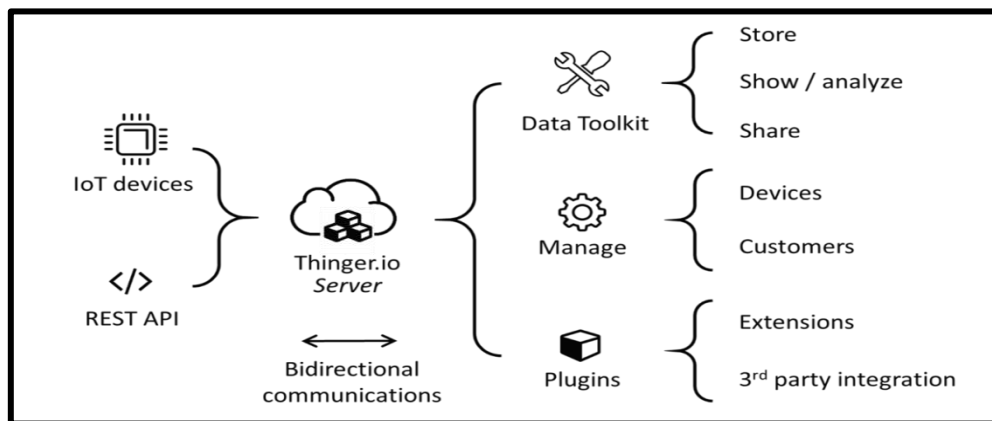


Figure 2

IV. RESULT AND DISCUSSION

Glucose concentration is measured non-invasively with the help of developed device. We have conducted the test with the some volunteers, male and female of different age and acquired the glucose concentration in mg/dl. The following tabulation is the results obtained from our non invasive glucose monitor. Good correlation is found with the blood glucose concentration value measured by the invasive method. The result obtained shows the feasibility of using IOT based non-invasive blood glucose measurement system.

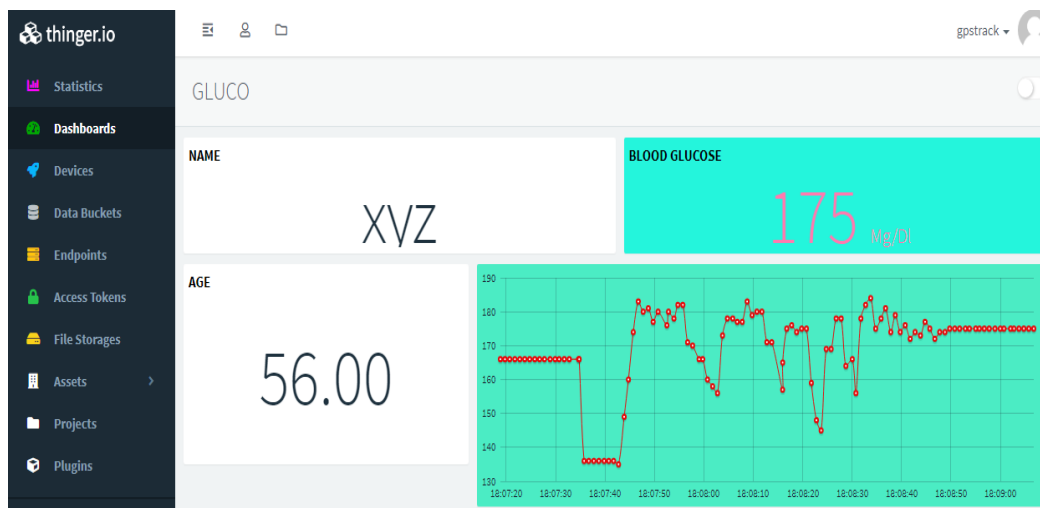


Figure – 3

SUBJECT	GENDER	AGE	GLUCOSE LEVEL IN (mg/dl)
1	Male	43	83
2	Female	27	85.3
3	Male	38	92
4	Male	49	123.7
5	Female	56	175

Table-1

V. CONCLUSION

In this project, we have designed and implemented a IoT based blood glucose measurement system that is working non-invasively using NIR spectroscopy. It makes convenient for the users to get their blood glucose reading without having to puncture their skin, encounter any pain and also reduce the risk of getting infection. As per latest technology, some IoT features are added to the prototype such as the accessibility for the family and doctors to monitor the glucose reading of the patient. Data from the glucose meter is sent via WiFi to their smart phone and also can store for future reference and medications. It helps the doctor to monitor the patients remotely without the need for the patient to come to the hospital, saving time and cost

VI. REFERENCES

[1]. Aznida Abu Bakar Sajak, “IOT-BASED GLUCOSE MONITORING SYSTEM” <https://www.researchgate.net/publication/343826910> August2020

[2]. Misgan Baig “Non-Invasive Blood Glucometer using NIR Spectroscopy” IRJET Volume: 04 Issue: 03 | Mar -2017

- [3]. Liu Tang “Non-Invasive Blood Glucose Monitoring Technology: A Review” International Conference on Electrical Engineering and Information & Communication Technology (ICEEICT) 2014.
- [4]. Gautam Talukdar, “ Non-Invasive Measurement of Glucose Content in Human Body: A Comparative Study” 2nd International Conference on Biomedical Engineering for Assitive Technologies ,2012.
- [5]. Jinit R. Patel “A Comprehensive Research on a Non-Invasive Glucometer using Near-Infrared Spectroscopy” JETIR April 2019, Volume 6, Issue 4, 2019.
- [6]. Bruen D.,”Glucose Sensing for Diabetes Monitoring: Recent Developments.” Sensors. 2017 ;17:1866. doi: 10.3390/s17081866.
- [7]. Gamble J.M., “ Incretin-based medications for type 2 diabetes: An overview of reviews.” Diabetes Obes. Metab. 2015;17:649–658. doi: 10.1111/dom.12465.
- [8]. Siddiqui S.A., “ Pain-Free Blood Glucose Monitoring Using Wearable Sensors: Recent Advancements and Future Prospects.” IEEE Rev. Biomed. Eng. 2018;11:21–35. doi: 10.1109/RBME.2018.2822301.
- [9]. Villena Gonzales W., “ The Progress of Glucose Monitoring-A Review of Invasive to Minimally and Non-Invasive Techniques, Devices and Sensors.” Sensors. 2019;19:800. doi: 10.3390/s19040800.
- [10]. Shyqyri Haxha, Jaspreet Jhoja, “Optical Based Non-invasive Glucose Monitoring Sensor Prototype” IEEE Photonics Journal,December 2016.
- [11]. Chi-Fuk So, Kup-Sze Choi, Thomas KS Wong, Joanne WY Chung, — Recent advances in noninvasive glucose monitoring| Medical devices : Evidence and research 27 Jun 2012.
- [12]. T.R.Jaya Chandra Lekha, C.Saravana kumar, “ NIR Spectroscopic Algorithm Development for Glucose Detection” IEEE Sponsored 2nd International Conference on Innovations in Information Embedded and Communication Systems(ICIECS),2015.
- [13]. Bazaev N.A., Masloboev I.P., Selishchev S.V. Optical methods for noninvasive blood glucose monitoring. Med. Tekh. 2011:29–33. doi: 10.1007/s10527-012-9249-x.
- [14]. Haxha S., “Optical Based Noninvasive Glucose Monitoring Sensor Prototype.” IEEE Photonics J. 2016.
- [15]. Premkumar, G., Roberts, M.: Adoption of new information technologies in rural small businesses. Omega 27(4), 467–484 (1999).
- [16]. Zainab Alansari, “The Rise of Internet of Things (IoT) in Big Healthcare Data: Review and Open Research Issues” Springer Nature Singapore Pte Ltd. 2018.
- [17]. Dr. Rajashekhar Karjagi , <https://www.wipro.com/business-process/what-can-iot-do-for-healthcare>

Synthesis and Physico-Chemical Parameters of Thiazine

Almas Farheen khan¹, Dr.Kolhe S.V¹

¹Department of Chemistry, Shri Shivaji Art's, Commerce & Science College, Akot-444101, Maharashtra, India

ABSTRACT

Thiazine area group of heterocyclic organic compounds Thiazine was synthesized from chalcone and purity check by TLC the characterization of Thiazine was done by IR H1 H1-NMR and mass spectrometer and UV Visible spectrophotometer .The physicochemical parameters of heterocyclic Thiazine such as density, viscosity,absorbance has been studied at different concentration, temperature and solvent.

Keywords:-Heterocyclic,density,absorbance,temperature,solvent etc.

I. INTRODUCTION

Thiazine is a six membered heterocyclic compound. Which contains two hetero atoms (N and S) are present in the heterocyclic ring at 1,4 position¹.the thiazine exists in three isomeric forms 1,2 thiazine,1,3 thiazine and 1,4 thiazine. Thiazine is a fairly basic diuretics supplement it reduces water and increase vascularity, so that it is also use as anabolic agent in medicine.². The ability of thiazine to exhibit antibacterial^{3,4},anti-inflammatory⁵ and used as cannabinoid receptor agonist⁶.Heterocyclic compounds are abundant in nature and are of great significance to life because their structural subunits exist in many natural products such as vitamins, hormones, antibiotics etc⁷.They have attracted considerable attention in the design of biologically active molecules⁸.A practical method for the synthesis of such compounds are of great interest in the synthetic organic chemistry.Theheterocycles, 1,3-thiazines are a class of heterocyclic compounds with a lot of biological activity, such as antimicrobial⁹, antitumor¹⁰, antioxidant¹¹ calcium channel modulators¹² and antipyretic¹³.Many people have synthesized different 1, 3-thiazines . Thiazines are very useful units in the fields of medicinal and pharmaceutical field and have been reported to shows a variety of biological activities such as blood platelet aggregation inhibitors¹⁴, antipsychotic¹⁵,antiviral, antimicrobial¹⁶.Thiazine nucleus is a pharmacophore of cephalosporin that occupy a very important place in the field of antibiotics and antifungal activity of thiazine nucleus is due to the presence of thiourea linkage in its structure. Chalcones and their analogues having α , β - unsaturated carbonyl system are very versatile substrates for the evolution of a various reactions and physiologically active compounds. The reaction of thiourea with α , β - unsaturated ketones results in 1, 3- thiazine.There has been well focused that the presence of 4-phenyl moieties as well as 2-substituted amino group present in the thiazine ring is an important structural feature, and resulting molecule would shows promising biological activities¹⁷.Physicochemical Parameter of Thiazine in physicochemical properties are important indicators used in hazards exposure and risk assessments hence in this experiment

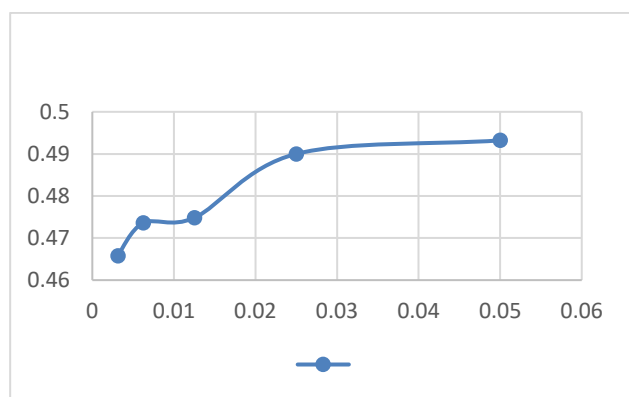
the physicochemical parameters were studied in solvent 1,4 dioxane also absorbance is taken from visible spectrophotometer. Density and Viscosity are affected by temperature and concentration, which exhibit. When the temperature is raised the particles in it start to move apart bringing down liquid density. The value of viscosity also decreases or liquid becomes less viscous the density and viscosity were taken in solvent 1,4 dioxane at different concentrations. The density was measured by using pycnometer and viscosity by Ostwald viscometer.

II. PHYSICAL ASPECT OF THIAZINE

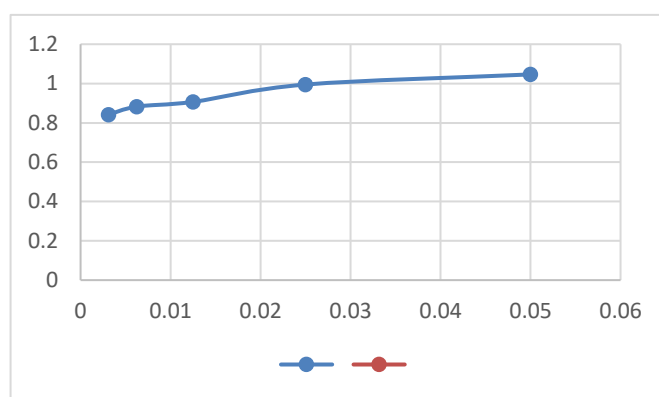
Solubility of Thiazine was studied in 1,4 Dioxane and DMF solvents.

A) Density and Viscosity of Thiazine in DMF solvent was taken at different concentrations at Temperature:- 312.15K

Conc.(M)	Density (ρ)(g.cm ⁻³)	Viscosity (η ·10 ⁻³)poise
0.05M	0.4932	1.04642
0.025M	0.49	0.99483
0.0125M	0.4748	0.90676
0.0625M	0.4736	0.88270
0.003125M	0.4658	0.84716



Graph A :-Conc. Vs density.

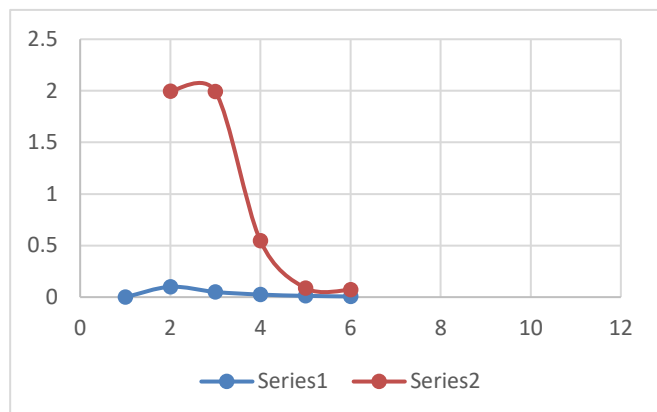


Graph B:-Conc.Vs Viscosity

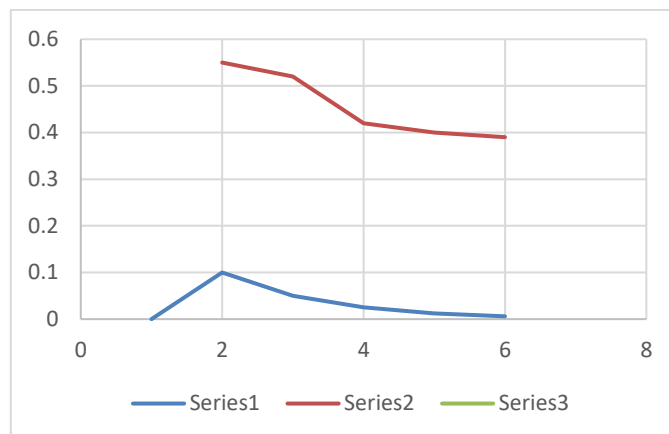
B) Conductance and Absorbance of Thiazine was taken at different concentrations in 1,4 Dioxane solvent at temperature:- 313.15K

Conc.(M)DMF Solvent	CONDUCTANCE(20 μ S)	ABSORBANCE (λ_{max480})
0.1M	0.55	1.995
0.05	0.52	1.993
0.025M	0.42	0.547

0.0125M	0.40	0.088
0.0625M	0.39	0.037



GraphC:- Conc.Vs Conductanc.



GraphD:-Conc Vs Absorbanc

III. RESULT AND DISSCUSION

In viscosity measurements different concentrations of solutions depend on the size of the molecule and molecular weight..If the concentration of solution increases then interaction between solute and solvent increases that leads to enhance intermolecular attraction that contribute to a resistance to flow and hence viscosity increases. The density slightly change by changing the concentration Astheir temperature increases,viscosity decreases at different concentrations, the viscosity is depend on solvent density and interaction between solute and solvent molecule,Here the solvent 1,4 Dioxane is having higher density .

CONDUCTANCE OF THIAZINE AT DIFFERENT CONCENCTRATION IN 1,4 DIOXANE SOLVENT-The conductance is measured by conductivity meter .Conductance study exhibit that as the concentration decreases conductance also decreases. Because on dilution as volume of solution increases .Thus, the number of ions per ml decreases. This results into decrease in conductance.

Visible spectroscopy studies shows that absorbance decreases with decrease in concentration. Because solution that are more concentrated have a larger number of molecules that interact with the light that enters, thus increasing its absorbance.

SYNTHETIC METHODS OF THIAZINE:-

The 1,3 thiazine is synthesized from the coumaran -3-one derivative were prepared from equimolar mixture of 2-hydroxyacetophenone and benzaldehyde.thechalcone undergoes cyclisation process in presence of mercuric acetate with solvent give coumaran-3-one derivative.Coumaran-3-one,thourea refluxed for 4 Hrs in alkaline medium followed by acidification product get separate out .Crystallized the product with ethanol.

IV. CONCLUSION

In this work the physico-chemical properties of thiazine was studied .it was concluded that physico-chemical properties of a compound depends upon nature of solvent concentration and temperature. If concentration decreases density, Viscosity, Conductance, and absorbance also decreases. Due to solute solvent interaction. Visible spectroscopy study exhibit that absorbance decreases with decrease in concentration.

V. REFERENCES

- [1]. Farooque H and Zulfeqar H, 2012. Synthesis and antimicrobial screening of some 1,3- thiazines, J. Chem. Pharm. Res. 4(4): 2263-2267.
- [2]. Doifode SK, Wadekar MP and Rewatkar S, 2011, Orient. J. Chem., 27(3), 1265-1267.
- [3]. Mohamed J.E. and HUSSNIYIA A.A, 2012. Synthesis of some heterocyclic compounds derived from chalcones, Sci. Revs. Chem. Commun. 2(2): 103-107.
- [4]. Kalirajan R. Sivakumar S.U. Jubie S. Gowramma B. and Suresh B, 2009. Synthesis and Biological evaluation of some heterocyclic derivatives of Chalcones, Int.J. ChemTech Res. 1(1): 27-34.
- [5]. Nagaraj A. and Sanjeeva R.C. 2008. Synthesis and Biological Study of Novel Bis-chalcones, Bis-thiazines and Bispyrimidines, J. Iran. Chem. Soc. 5(2): 262-267.
- [6]. Dabholkar V.V. and Parab S.D., 2011, Heterolett.org., 1, 176-188.
- [7]. J.U. Yuhong, R.S.Varma, J., 2006 Org. Chem. 71 135.
- [8]. Kawamoto M , T. Ikeda, A. Mori, A. Sekiguchi, K. Masui, T. Shimoda, M. Horie, M. Osakada, 2003 J. Am. Chem. Soc. 125 1700.
- [9]. Koketsu .M, Tanaka. K. Takenaka. Y, Kwong C.D, Ishihara H, Eur. 2002 J. Pharm. Sci. 307.
- [10]. Ei-Subbagh H.I, Abadi A, Al-Khawad I.E, Al-Pashood K.A, 1999 Arch. Pharm. 19 .332.
- [11]. Malinka .W, Kaczmarz M, Filipek .B, Sepa, J , Gold. .B , 2002 Farmaco I. L57 737.
- [12]. Lavilla R.J, 2002 Chem. Soc., Perkin Trans 1. 1141.
- [13]. Bonzsing .D, Sohar .P, Giggler.G, Kovacs .G, Eur. 1999 J. Med. Chem. 31 .663.
- [14]. Brown C. and Davidson R.N., 1,4-Benzothiazines, Dihydro-1,4-benzothiazines, and Related Compounds. 1985, Heterocycl. Chem., 38, 135.
- [15]. Wolff M.E., "Burger Medicinal Chemistry" 1995. 116 (Wolff Vol. IV part III), 889.
- [16]. Pnade V.K., Saxena S.K. and Bajpai S.K., Synthesis and antiviral activity of some novel substituted phenothiazines, 2004, Indian J. Chem., 43B, 1015
- [17]. Mahale J. D; Manoj, S. C; Belsare N G; Rajput, P. R. Synthesis and study of chlorosubstituted 4-aryloxy and 4-alkoxy-pyrazolines, pyrazoles and their effect on some flowering plants, 2010, Indian J. Chem., 49B(4), 505-511



Photo Degradation Study of LDPE/PEG Thin Film

Dr. V. S. Sangawar¹, S. A. Umale^{2*}, S. O. Sharma²

¹Department of Physics, Government Vidarbha Institute of Science & Humanities, Amravati, Maharashtra, India

²Shri. Deorao Dada Junior Science College, Tiosa, Maharashtra, India

ABSTRACT

Photodegradable plasticizer polyethylene glycol (PEG) is used as an additive for enhancement of properties of LDPE in 7 weight percent. The thin film samples of LDPE and LDPE + PEG were prepared by solvent casting method and its thickness is in the range of (20-30 μ m thickness). Degradation study of the samples were carried out by exposing to UV light for 30 days. The structural properties were studied by XRD, FTIR and degradation was estimated by weight loss measurement before and after weathering the sample.

Keywords: Photo-degradation, LDPE, PEG, XRD, FTIR

I. INTRODUCTION

The widespread use of polyethylene PE as packaging films is due to its mechanical properties, enabling the production of mechanically strong films [1]. Plastic is most useful synthetic manmade substance made up of different element extracted from the fossil fuel resources. Plastic have wide range of application in day to day life. Widely used plastic is generating huge amount of post use plastic wastes [2]. Excessive use of plastics in domestics, industrial and agriculture sectors exert pressure on capacities available for plastic waste disposal which cause an additional burden on the environment [3]. Polyethylene has a simple and semi crystalline molecular structure, high molecular weight but does not easily degrade in the natural environment because it does not absorb UV radiation [4,5]. Degradation of polymers is mainly due to photo-oxidation and thermo-oxidation reactions [6,7,8,9], causing the chain scission and cross-linking of polymer backbone, the formation of carbonyls (C=O) and vinyl (CH₂=CH) groups, and, finally, changes in the conformation and crystallinity of the polymer [10–12].

The present research is one of the way to solve such a problem is to find out ways for degradation of plastics. A photodegradable plastic is an innovation for solving the problems of plastic disposals. Since sunlight is natural energy source and best for UV radiation which is responsible for photo-oxidative degradation of plastic. Sunlight degrades the plastic waste at a very slow rate. Mimicking the role of sunlight, the photo catalytic degradation process could significantly accelerate by the addition of PEG in LDPE.

II. MATERIAL AND METHODS

Low density polyethylene (LDPE) is a soft, flexible, lightweight plastic material. LDPE noted for its low temperature flexibility, toughness and corrosion resistance. Commercial grade LDPE with density 0.924gm/cm^3 at 23°C , melt flow index $4\text{gm}/10\text{mins}$ melting range $105\text{-}109^\circ\text{C}$ were supplied from Nutan Gujarat Industrial Estate, Vadodara (India). Xylene solvent of AR grade and PEG with average molecular weights $3500\text{-}4000$ freezing point $53\text{-}50^\circ\text{C}$ and having PH in between 4.5 to 7.5.

Sample Preparation Technique:

LDPE+PEG based plastic thin film samples have been synthesized by solution evaporation technique. Tiny flakes PEG was added in LDPE granules by weight percentage. 7% PEG is added to LDPE. Thickness of film was measured with high accuracy and resolution using compound microscope in joining with an ocular micrometer. The thickness of the film ranges from $20\text{-}30\mu\text{m}$. For Degradation study U-V lamp (LABLINE, 8W) is used and the sample was irradiated for 30 days of duration. .

In this present work solvent evaporation technique is used for the preparation of thin film of LDPE and composites, as it is best for laboratory conditions.

The samples were characterized by XRD and FTIR. The degradation of samples was observed by weight loss percent method.

X-ray Diffraction (XRD):

X-ray diffraction is very important characterization technique employed for determination of crystalline and amorphous states of materials. Fig.1 shows XRD pattern of thin film of pure LDPE (LP_0),

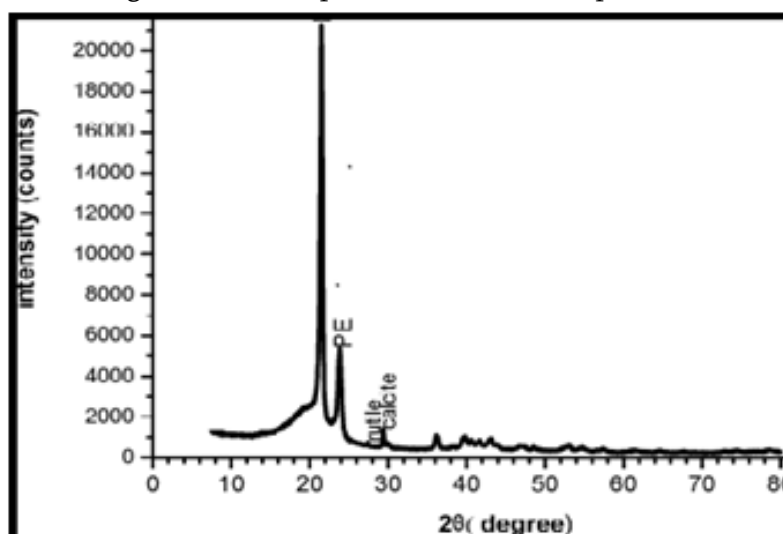


Fig.1.1(a) XRD of LP_0

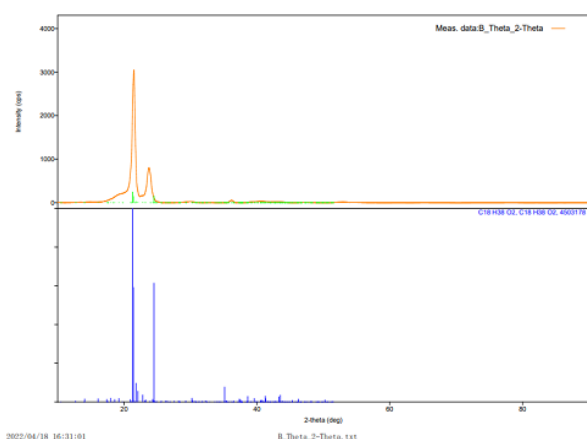
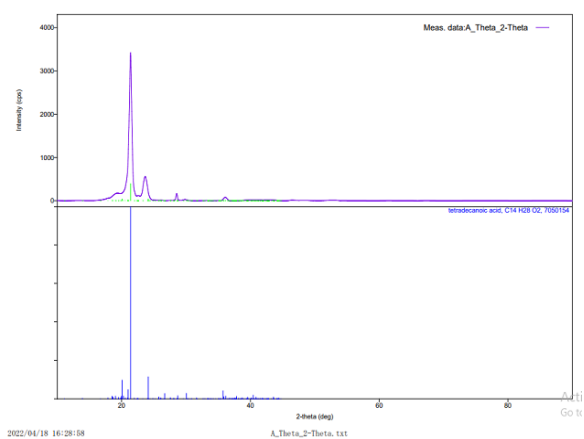
Fig1.1(b) XRD of LP7P₀Fig1.1(c) XRD of LP7P₃₀

Fig.1.1(b) shows XRD pattern of thin film of LDPE with 7% PEG (LP7P₀) without exposure to UV light and Fig.1.1(c) shows XRD pattern of thin film of LDPE with 7% PEG (LP7P₃₀) for 30 days exposure to UV light.

Diffraction from (110) and (200) planes in pure LDPE were centered at $2\Theta=21.9^\circ$ and $2\Theta=24.2^\circ$ corresponding to d-spacing of 4.04\AA and 3.75\AA respectively and XRD pattern of LP7P₀ fig.2 shows very sharp, small and prominent peaks at $2\Theta=21.44^\circ$ and $2\Theta=24.67^\circ$ corresponding to d-spacing values of 4.142\AA & 3.606\AA . The XRD pattern of LP7P₃₀ shows very sharp & prominent peaks at $2\Theta=21.64^\circ$, $2\Theta=24.42^\circ$ and $2\Theta=30.41^\circ$ for corresponding d-spacing of 4.103, 3.642 & 2.937. The XRD pattern of pure LDPE thin film shows small crystalline phase along with amorphous phase but with the addition of PEG in LDPE changes crystallinity. The crystallinity was higher for pure LDPE sample but with the composition of PEG with LDPE decreases the crystalline size. When this PEG added LDPE film was exposed to UV irradiation for 30 days the peak was slightly shifted towards higher angle and the intensity of the peak decreases after exposed to UV light.

This is calculated by using debye Scherrer's formula.

$$D = \frac{0.9\lambda}{\beta \cos\theta}$$

Where, D = Crystal size

λ = Wavelength of X-ray

Θ = Bragg's angle in radian

B = Full width at half maximum

The crystal size of LP7P₀ and LP7P₃₀ was found to be 37.6\AA and 30.9\AA . Thus it is found that physically hinder crystal growth resulting in lower polymer crystallinity [13,14].

Table 1.1 XRD 2Θ and d-spacing values of LP₀, LP7P₀ and LP7P₃₀ samples.

SAMPLE CODE	2Θ	d-spacing	2Θ	d-spacing
LP ₀	21.9	4.05	24.2	3.75
LP7P ₀	21.44	4.142	24.67	3.606
LP7P ₃₀	21.64	4.103	24.42	3.642

Fourier Transform Infrared Spectrometer (FTIR):

Fig.1.2(a) shows FTIR spectra of thin film of unfilled LDPE(LP₀)[15].

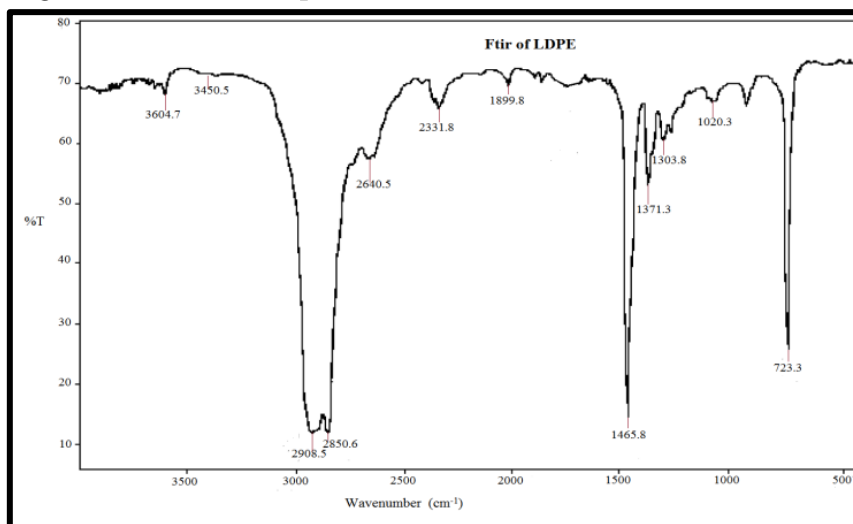


Fig 1.2(a) FTIR spectra of pure LDPE (LP₀).

FTIR spectra of LDPE show characteristics peaks at 2908.5cm⁻¹ and 2850.6cm⁻¹ due to asymmetrical and symmetrical CH₂ stretching vibrations of LDPE respectively. The peaks at 1465.8cm⁻¹ and 723.3cm⁻¹ corresponds to angular deformation (C-H bending) and asymmetrical angular deformation (C-H rocking) of CH₂ group respectively. The peak at 1371cm⁻¹ assigned for C-H bending of alcohol [16]. There are two very weak peaks at 1899.8cm⁻¹ and 1020.3cm⁻¹ which are assigned for C=O stretching and C-O stretching respectively formed during processing [17]. The peak at about 3450 cm⁻¹ belongs to O-H stretching vibration, which indicates the generation of alcohols during processing [18].

FTIR spectra of LDPE/PEG (LP7P₀) samples before degradation are represented in fig 1.2(b) and FTIR spectra of LDPE/PEG (LP7P₃₀) after degradation of 30days is shown in fig1.2(c).

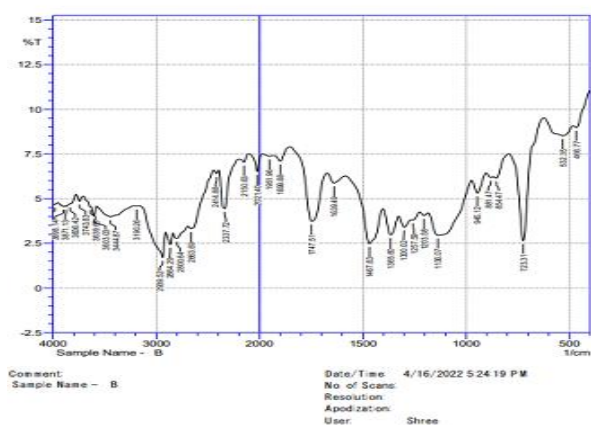


Fig 1.2(b) FTIR spectra of (LP7P₀)

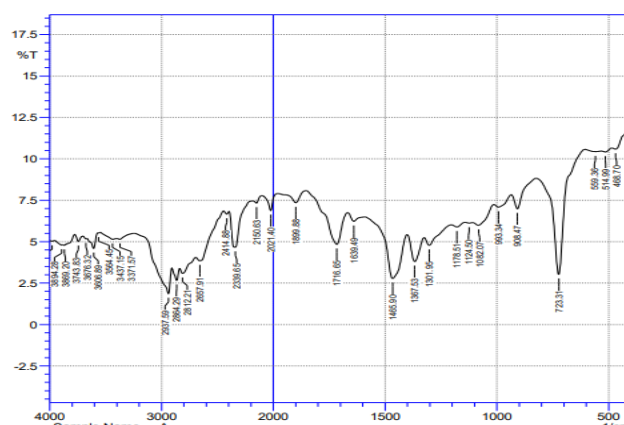


Fig 1.2(c) FTIR spectra of (LP7P₃₀)

FTIR spectra of PEG/LDPE (LP7P₀) shows peak at 3639.68cm⁻¹ due to O-H stretching vibration. The peak at 2939.52cm⁻¹ and 2864.29cm⁻¹are due to asymmetric and symmetric CH₂ stretching vibration of LDPE. The

peak at 1951.96cm^{-1} is due to C=C=C stretching which is absent in LP₀ and LP7P₃₀. The peak of 1467.83cm^{-1} and 1365.60cm^{-1} is occurs due to CH bending vibration and CH bending of CH₃. The peak at 945.12cm^{-1} is occur due to presence of C-O stretching of alcohol and 723.21cm^{-1} is due to C-H rocking (Asymmetric C-H bending).

FTIR spectra of PEG/LDPE (LP7P₃₀) shows peak at 3743.83cm^{-1} and 3676.32cm^{-1} due to O-H stretching. The sharp peak at 2937.59cm and 2864.29cm^{-1} are observed due to asymmetric and symmetric stretching of CH₂. The peak at 1716.65cm^{-1} and 1639.49cm^{-1} are present due to C=O stretching of carbonyl group and C=C stretching of vinyl group. Prominent peak at 1465.90cm^{-1} and 1301.95cm^{-1} are observed due to C-H bending vibration of CH₂. There is measurable change in peak value at 908.47cm^{-1} due to C-O stretching of alcohol. The peak at 723.31cm^{-1} is observed due to C-H rocking (Asymmetric C-H bending). Frequency correlation of FTIR of thin unfilled LDPE(LP₀) film and 7% added PEG/LDPE (LP7P₀) and (LP7P₃₀) samples shown in table 1.2 .

Table 1.2 represents peak frequencies and their correlation for unfilled LDPE and 7%PEG added LDPE samples with and without UV exposure.

Table 1.2 Frequency correlation table of LP₀, LP7P₀ and LP7P₃₀

Sr. No.	Frequency (cm ⁻¹)			Correlation
	LP ₀	LP7P ₀	LP7P ₃₀	
1	3604.7	3743.83	3743.83	O-H stretching free OH
	3450.4	3639.68	3676.32	O-H stretching vibration
2	2908.5	2939.52	2937.59	CH ₂ stretching (Asymmetric)
	2850.6	2864.29	2864.29	CH ₂ stretching (Symmetric)
3		1951.96		C=C=C stretching (Allene)
4		1747.51	1716.65	C=O stretching of carbonyl group
		1639.49	1639.49	C=C stretching of vinyl group
5	1465.8	1467.83	1465.90	C-H bending vibration
6		1136.07	1178.51	C-O stretching
	1371.3	1365.60	1367.53	C-H bending CH ₃
7	1303.8	1300.02	1301.95	C-N stretching Amine
8	1020.3	945.12	908.47	C-O stretching of alcohol
9	723.3	723.31	723.31	C-H rocking (Asymmetric C-H bending)
10	723.3	532.35	559.36	Alkyl halide

From the above tabular data, it is observed that FTIR spectra gives straight forward information of specific functional group. It also gives information about the changes in particular functional groups of polymeric material in different environments. The change in functional group gives the information about the various photo-degradation takes place during degradation.

Degradation of thin film by weight loss:

The weight loss of samples LP7P₀ and LP7P₃₀ before and after expose to UV light for 30 days is measured by using weighing balance with high accuracy is represented in table 1.3.

Table 1.3 Weight of LDPE/PEG sample before and after expose to UV light

Weight of sample before expose to UV light (LP7P ₀)	Weight of sample after expose to UV light (LP7P ₃₀)	Weight loss percentage of LDPE/PEG thin film
0.505gm	0.480gm	4.95%

The weight loss percentage of LDPE with 7% addition of PEG has been found to be 4.95%. From the present result it is observed that PEG supports the photo-degradation of LDPE.

III. CONCLUSION

From this present study, it can be concluded that the photo-degradation of LDPE can be accelerated using PEG. The XRD result shows that after addition of PEG in LDPE reduces the crystal size. This affects the crystallinity of LDPE and when this composite thin film is exposed to UV irradiation, it enhances the rate of photo-degradation of LDPE. FTIR +PEG studies show that the presence of some kind of oxidative product on the surface of the weathered sample was an indication of oxidative photo-degradation of the thin film of LDPE and PEG. The increase in carbonyl and vinyl group formation for LDPE after exposure to UV-irradiation is an indication of chain scission. A measurable 4.95% weight loss is observed after exposure to UV-irradiation. Among various methods of degradation, photo-degradation is a very effective method because it degrades plastic waste in sunlight, which is the best solution for the current plastic pollution problem. In the future, we will find out the best photodegradable plastic materials which are eco-friendly.

IV. REFERENCES

- [1]. P. K. Roy, P. Surekha, R. Raman, and C. Rajagopal, "Investigating the role of metal oxidation state on the degradation behavior of LDPE," *Polymer Degradation and Stability*, vol. 94, no. 7, pp. 1033–1039, 2009.
- [2]. P. Premkumar, C.G. Saravanan, M. Gopalakrishnan (IJETT) – Volume 16 Number 5 – Oct 2014.
- [3]. Shah et al., 2008, Zan et al., 2006.
- [4]. A. Valadez-Gonzalez, J. M. Cervantes-Uc, and L. Veleza, "Mineral filler influence on the photo-oxidation of high density polyethylene. I. Accelerated UV chamber exposure test," *Polymer Degradation and Stability*, vol. 63, no. 2, pp. 253–260, 1999.
- [5]. M. Koutny, J. Lemaire, and A.-M. Delort, "Biodegradation of polyethylene films with prooxidant additives," *Chemosphere*, vol. 64, no. 8, pp. 1243–1252, 2006.

- [6]. F. Khabbaz, A.-C. Albertsson, and S. Karlsson, "Chemical and morphological changes of environmentally degradable polyethylene films exposed to thermo-oxidation," *Polymer Degradation and Stability*, vol. 63, no. 1, pp. 127–138, 1999.
- [7]. M. Liu, A. R. Horrocks, and M. E. Hall, "Correlation of physicochemical changes in UV-exposed low density polyethylene films containing various UV stabilisers," *Polymer Degradation and Stability*, vol. 49, no. 1, pp. 151–161, 1995.
- [8]. A. Tidjani, "Comparison of formation of oxidation products during photo-oxidation of linear low density polyethylene under different natural and accelerated weathering conditions," *Polymer Degradation and Stability*, vol. 68, no. 3, pp. 465–469, 2000.
- [9]. J. D. Peterson, S. Vyazovkin, and C. A. Wight, "Kinetics of the thermal and thermo-oxidative degradation of polystyrene, polyethylene and poly(propylene)," *Macromolecular Chemistry and Physics*, vol. 202, no. 6, pp. 775–784, 2001.
- [10]. H. D. Hoekstra, J. L. Spoomaker, and J. Breen, "Mechanical and morphological properties of stabilized and non-stabilized HDPE films versus exposure time," *Angewandte Makromolekulare Chemie*, vol. 247, no. 1, pp. 91–110, 1997.
- [11]. F. Khoylou and S. Hassanpour, "The effect of environmental conditions on electron beam cross linked agricultural polyethylene films," *Iranian Polymer Journal*, vol. 14, no. 10, pp. 875–879, 2005.
- [12]. G. Scott, "Green' polymers," *Polymer Degradation and Stability*, vol. 68, no. 1, pp. 1–7, 2000.
- [13]. Sangawar VS, Dhokane RJ, Ubale AU, Chikhalikar PS and Meshram SD, *Bull. Mater. Sci.* 30(2)(2007)163-166.
- [14]. Xie X L, Li KY, Tjong S C, *Polym. Comp.* 23(2002)319.
- [15]. Meshram S D (2009).
- [16]. Mendoca R H et al (2003); Gupta B S (2006); Mishra A K and Luyt A S (2008)].
- [17]. Gugumus F (2007).
- [18]. Li Jet al (2008).



Ultrasonic Velocity and Other Acoustical Parameters of Leaf Extract Solution of Psidium guajava in Two Different Solvents: A Comparative Study

S. S. Kamble¹, S. R. Aswale², S. S. Aswale²

¹Department of Chemistry, Arts, commerce and Science College, Maregaon, Maharashtra, India

²Department of Chemistry, Lokmanya Tilak Mahavidyalaya, Wani, Maharashtra, India

ABSTRACT

Ultrasonic Velocity, density, viscosity have been measured experimentally for the solution of leaf extract of psidium guajava in 50% ethanol and also in distilled water solvent with various concentrations at 298.15 K, 303.15 K, 308.15 K keeping constant frequency of 4 MHz. As the acoustical parameters like adiabatic compressibility, intermolecular free length, relative association, relaxation time, specific acoustic impedance would prove to be more useful to predict and confirm the molecular interactions, these have been determined by measuring the Ultrasonic Velocity, density, viscosity of the prepared solution. A variation in these parameters will provide strong information regarding the molecular interactions taking place in the solution.

Keywords:- Ultrasonic Velocity, Adiabatic Compressibility, Relative Association

I. INTRODUCTION

Nowaday, ultrasonic technology is employed in diverse fields in investigating various organic liquids, polymers and their mixtures, drugs, aqueous and non- aqueous electrolyte solutions etc. It plays an important role in understanding the physico-chemical behavior of liquids^[1-5]. Ultrasonic velocity measurements and other acoustical parameters of liquid mixtures are the powerful technique in the understanding of chemical nature and the molecular interactions^[6-9]. Many researchers used ultrasonic velocity measurement for studying solutesolvent interaction in a number of system including organic liquid, dilute solutions^[10-12]. Different ultrasonic parameters have been calculated with a view to investigate the exact nature of the molecular interactions^[13-14]. The ultrasonic studies of liquid mixtures have of greater significance in understanding intermolecular interactions between the component molecules as they can locate numerous applications in industrial and technological processes^[15]. Ultrasonic velocity measurements and other acoustic parameters of liquid mixtures are the powerful technique in understanding of chemical nature and the molecular interactions.

Our country is very well known for Ayurveda, in the Ayurveda medicines are largely made up from plants, herbs. One of such herbs is psidium guajava which is also known as peru. It is known for its antifungal nature. The solution of leaf extract of psidium guajava in distilled water and 50% ethanol solvent is studied at 4 mhz for

the concentration of 1%, 0.5%, 0.25%, 0.125% at 298.15K, 303.15K, 308.15K. Here the effect of concentration at different temperature on molecular interaction will be predicted which may be helpful for predicting the reactivity of the extract.

II. METHODOLOGY

The leaf extract used in this study was of analytical range. For the preparation of solution 50% ethyl alcohol and distilled water solvent was used. A special thermostatic water bath arrangement was made to maintain constant temperature. 1%, 0.5%, 0.25%, 0.125% solutions of leaf extracts of *psidium guajava* was Prepared by taking accurate weights on electronic digital balance (Model CB/CA/CT-Series, Contech having accuracy ± 0.0001 g.) The ultrasonic velocity of the 1%, 0.5%, 0.25%, 0.125% solutions of leaf extracts of *ocimum tenuiflorum* was measured with the Multifrequency ultrasonic interferometer (Model M-83, Mittal Enterprises) at 4mhz with an accuracy of ± 2 m/s. All the readings were taken at 298.15 K, 303.15K, 308.15K. The viscosity was measured by using Ostwald's viscometer and the density of the solution was measured by using Digital densitometer (DMA-35, Anton Paar).

COMPUTATION :-

By using ultrasonic velocity following ultrasonic parameters are calculated. Adiabatic compressibility -

$$\beta = 1/v^2 d$$

Where, v - velocity of solution,

d - density of liquid

Intermolecular free length -

$$L_f = K\sqrt{\beta_s}$$

Where, K - temperature dependent known as Jacobson's constant

Specific acoustic impedance -

$$Z = v \times d_s$$

Relative association -

$$R_A = d_s / d_0 [v_0 / v_s]^{1/3}$$

Where, v₀ - ultrasonic velocity of solvent

v_s - ultrasonic velocity of solution

Relaxation time -

$$\tau = 4/3 \beta_s \times \eta$$

III. RESULT AND DISCUSSION

The experimentally determined values are listed in the following table.

Table 1: Density, Viscosity and Velocity (at frequency 4mhz) of *psidium guajava* leaf extract solution in 50% ethanol solvent.

Sr. No.	Conc. (%)	Temp. (K)	Density (d_s) (Kg m^{-3})	Velocity (v_s) (m/s)	Viscosity (η) ($\text{Kg m}^{-1}\text{s}^{-2}$)
1	1%	298.15	931.6	1822.7	23.50 E ⁻⁴
		303.15	922.5	1787.1	21.80 E ⁻⁴
		308.15	920.4	1770.1	17.42 E ⁻⁴
2	0.5%	298.15	936.7	1801.2	18.30 E ⁻⁴
		303.15	930.4	1767.0	20.50 E ⁻⁴
		308.15	928.9	1751.2	12.44 E ⁻⁴
3	0.25%	298.15	924.5	1787.8	21.27 E ⁻⁴
		303.15	927.4	1744.1	21.51 E ⁻⁴
		308.15	927.0	1717.1	16.85 E ⁻⁴
4	0.125%	298.15	925.0	1755.2	18.12 E ⁻⁴
		303.15	921.8	1701.1	16.05 E ⁻⁴
		308.15	918.4	1687.1	12.85 E ⁻⁴

Table 2 :- Acoustic parameters of psidiumgujava leaf extract solution in 50% Ethyl Alcohol at 4MHz.

Sr.No.	Conc. (%)	Temp. (K)	Adiabatic Compressibility	Specific Acoustic Impedence $\text{Kg M}^{-2}\text{S}^{-1}$	Intermolecular free length	Relative Association	Relaxation time
1.	1%	298.15	3.231 E ⁻¹⁰	1698027	3.697 E ⁻¹¹	2.997 E ⁻¹	10.098 E ⁻¹³
		303.15	3.394 E ⁻¹⁰	1648599	3.823 E ⁻¹¹	2.983 E ⁻¹	9.840 E ⁻¹³
		308.15	3.467 E ⁻¹⁰	1629200	3.899 E ⁻¹¹	2.979 E ⁻¹	8.023 E ⁻¹³
2.	0.5%	298.15	3.291 E ⁻¹⁰	1686996	3.731 E ⁻¹¹	3.055 E ⁻¹	8.00 E ⁻¹³
		303.15	3.442 E ⁻¹⁰	1644016	3.850 E ⁻¹¹	3.045 E ⁻¹	9.384 E ⁻¹³
		308.15	3.51 E ⁻¹⁰	1626689	3.923 E ⁻¹¹	3.037 E ⁻¹	5.807 E ⁻¹³
3.	0.25%	298.15	3.384 E ⁻¹⁰	1652821	3.783 E ⁻¹¹	2.986 E ⁻¹	9.573 E ⁻¹³
		303.15	3.544 E ⁻¹⁰	1617478	3.907 E ⁻¹¹	3.071 E ⁻¹	10.138 E ⁻¹³
		308.15	3.658 E ⁻¹⁰	1591751	4.005 E ⁻¹¹	3.092 E ⁻¹	8.197 E ⁻¹³
4.	0.125%	298.15	3.509 E ⁻¹⁰	1623560	3.852 E ⁻¹¹	3.092 E ⁻¹	8.456 E ⁻¹³
		303.15	3.748 E ⁻¹⁰	1568166	4.018 E ⁻¹¹	3.013 E ⁻¹	8.00 E ⁻¹³
		308.15	3.823 E ⁻¹⁰	1550015	4.094 E ⁻¹¹	3.119 E ⁻¹	6.533 E ⁻¹³

Table 3: Density, Viscosity and Velocity (at frequency 4 mhz) of Psidiumgujava leaf extract solution

Sr. No.	Conc. (%)	Temp. (K)	Density (d_s) (Kg m^{-3})	Velocity (v_s) (m/s)	Viscosity (η) ($\text{Kg m}^{-1}\text{s}^{-2}$)
1	1%	298.15	1002.8	1488.3	18.3 E ⁻⁴
		303.15	1002	1587.2	19.80 E ⁻⁴
		308.15	998.8	1582	21.2 E ⁻⁴
2	0.5%	298.15	998.9	1499.6	18.30 E ⁻⁴
		303.15	998.6	1596.2	20.50 E ⁻⁴
		308.15	997	1607.8	22.44 E ⁻⁴
3	0.25%	298.15	996.8	1508.7	21.27 E ⁻⁴
		303.15	996.3	1608.2	21.51 E ⁻⁴
		308.15	996.1	1625.7	23.85 E ⁻⁴
4	0.125%	298.15	996.3	1525	12.12 E ⁻⁴
		303.15	995.8	1627.2	16.05 E ⁻⁴
		308.15	995.2	1648.3	18.85 E ⁻⁴

Table 4. Acoustical parameters of psidiumgujava leaf extract in distilled water solvent at 4 mhz

Sr. No.	Conc. (%)	Temp. (K)	Adiabatic Compressibility	Specific Acoustic Impedance $\text{Kg M}^{-2} \text{S}^{-1}$	Intermolecular free length	Relative Association	Relaxation time
1.	1%	298.15	4.501 E ⁻¹⁰	1492467	4.363 E ⁻¹¹	3.059E ⁻¹	10.954 E ⁻¹³
		303.15	3.961	1590374	4.13 E ⁻¹¹	3.573 E ⁻¹	10.430 E ⁻¹³
		308.15	4.00	1580101	4.188 E ⁻¹¹	3.296 E ⁻¹	11.278 E ⁻¹³
2.	0.5%	298.15	4.451	1497950	4.339 E ⁻¹¹	3.024 E ⁻¹	10.833 E ⁻¹³
		303.15	3.930	1593965	4.114 E ⁻¹¹	3.539 E ⁻¹	10.715 E ⁻¹³
		308.15	3.88	1602976	4.125 E ⁻¹¹	3.238 E ⁻¹	11.579 E ⁻¹³
3.	0.25%	298.15	4.407	1503872	4.317 E ⁻¹¹	3.00 E ⁻¹	12.467 E ⁻¹³
		303.15	3.88	1602249	4.088 E ⁻¹¹	3.502 E ⁻¹	11.100 E ⁻¹³
		308.15	3.798	1619359	4.081 E ⁻¹¹	3.194 E ⁻¹	12.047 E ⁻¹³
4.	0.125%	298.15	4.315	1519357	4.272 E ⁻¹¹	2.965 E ⁻¹	6.955 E ⁻¹³
		303.15	3.792	1620365	4.041 E ⁻¹¹	3.461 E ⁻¹	8.094 E ⁻¹³
		308.15	3.698	1640388	4.027 E ⁻¹¹	3.15 E ⁻¹	9.271 E ⁻¹³

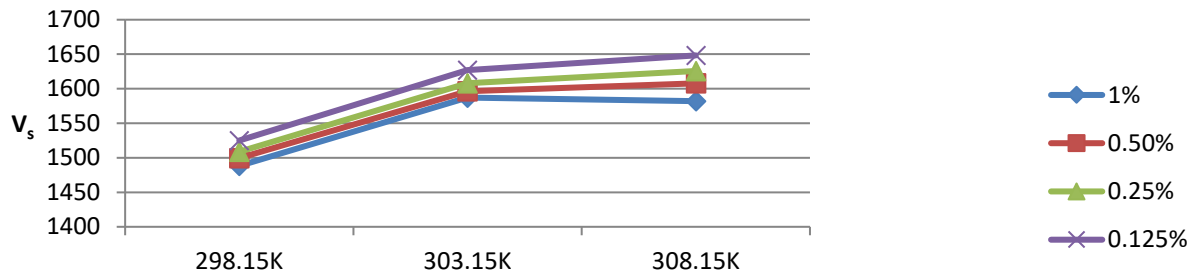


Fig.1b. Variation of ultrasonic velocity with temp. at diff. conc. in dist.water

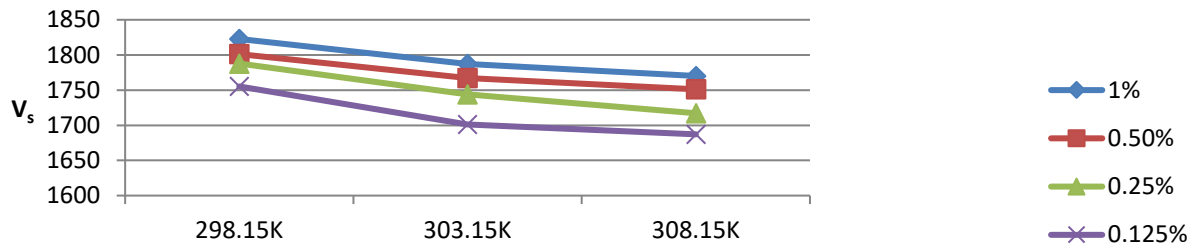


Fig.1a-Variation of ultrasonic velocity with temp. at diff. conc.in 50%alc. solvent.

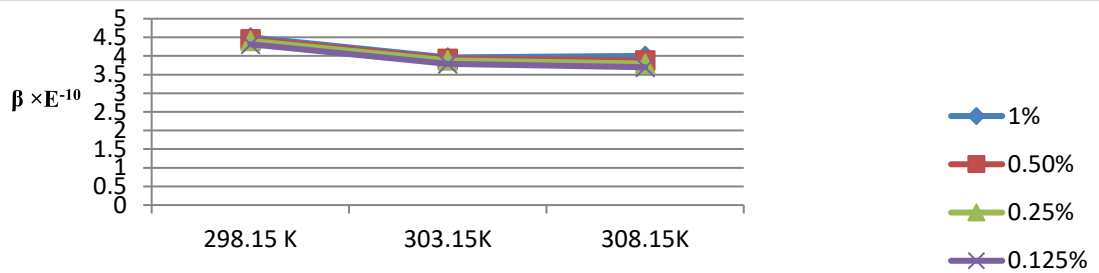


Fig.2b.-Variation of Adiabatic compressibility with temp. at different conc.in dist.water solvent

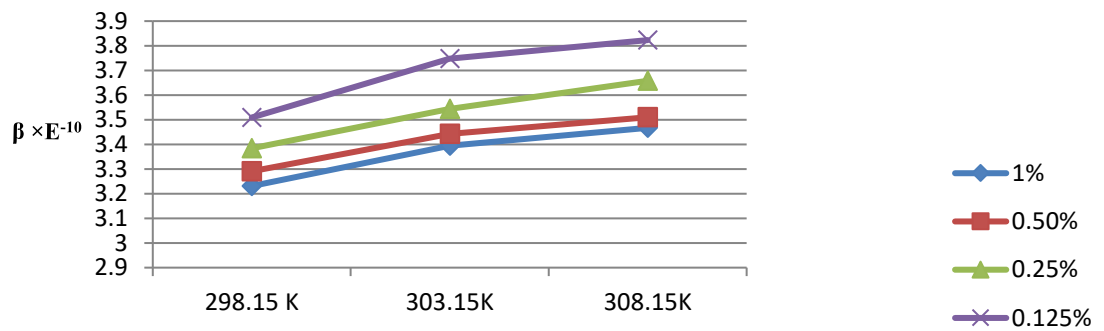


Fig.2a.-Variation of Adiabatic compressibility with temp. at diff. conc.in 50%alc. solvent.

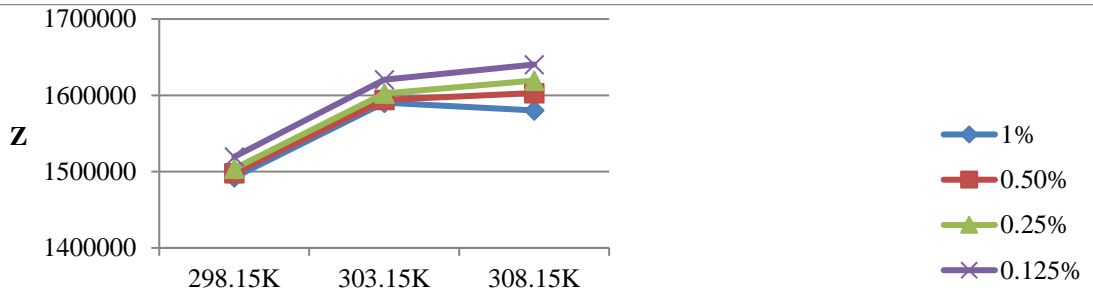


Fig.3b. Variation of Specific acoustic impedance with temperature at diff. conc.in dist.water solvent

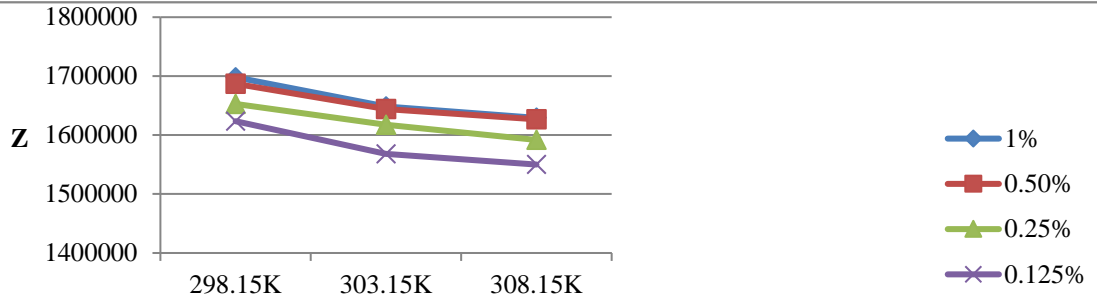


Fig.3a. Variation of Specific acoustic impedance with temperature at diff. conc. conc.in 50%alc. solvent.

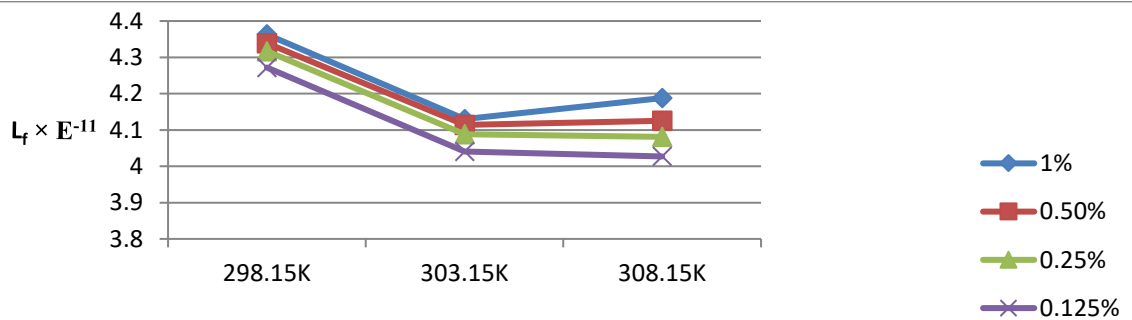


Fig. 4b. Variation of Intermolecular free length with temperature at various conc. in dist.water solvent

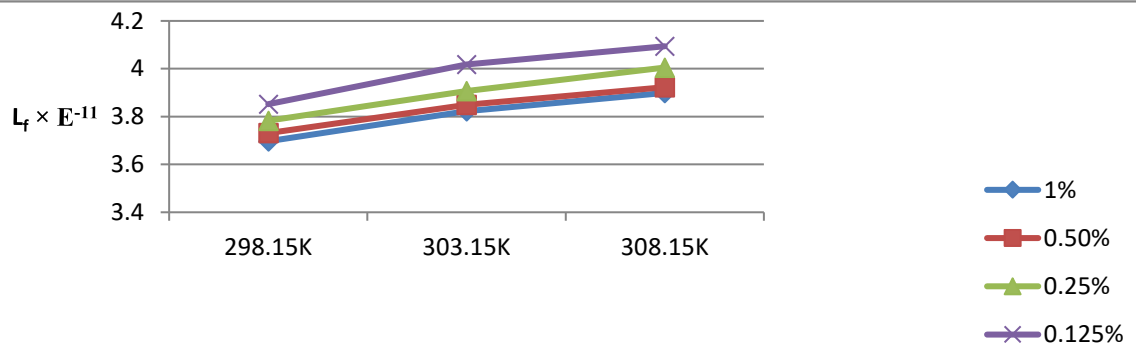


Fig. 4 a. Variation of Intermolecular free length with temperature at various conc. conc.in 50%alc. solvent.

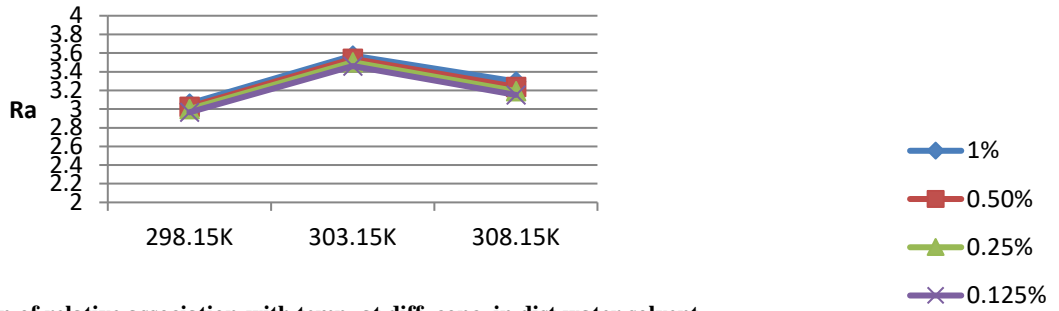


fig.5b.Variation of relative association with temp. at diff. conc. in dist. water solvent

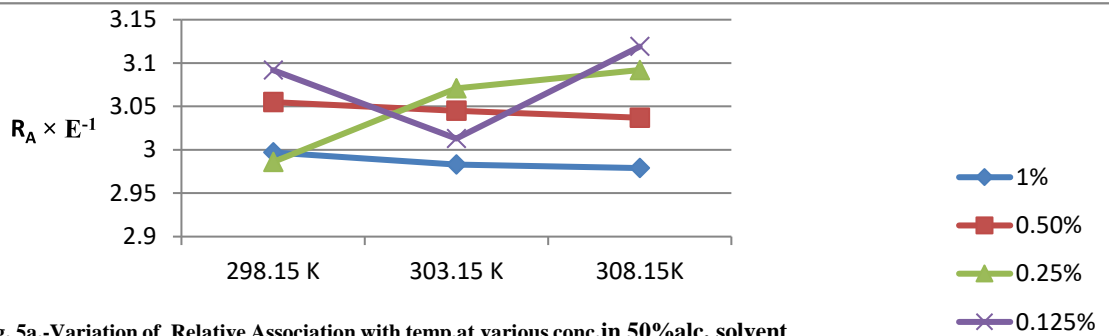


Fig. 5a.-Variation of Relative Association with temp. at various conc. in 50% alc. solvent.

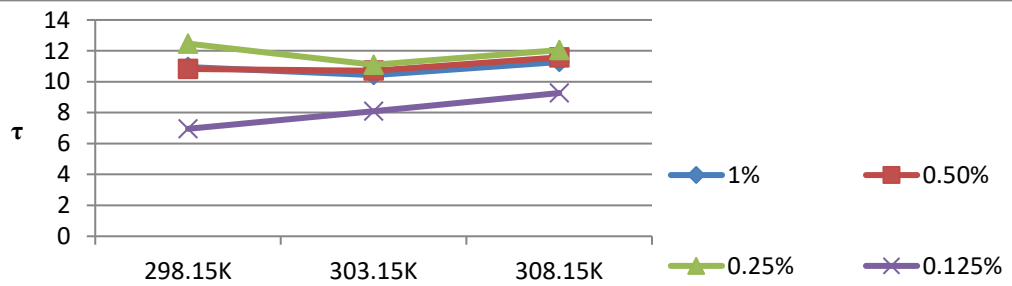


Fig.6b. Variation of Relaxation time with temperature at diff. conc in dist. water solvent

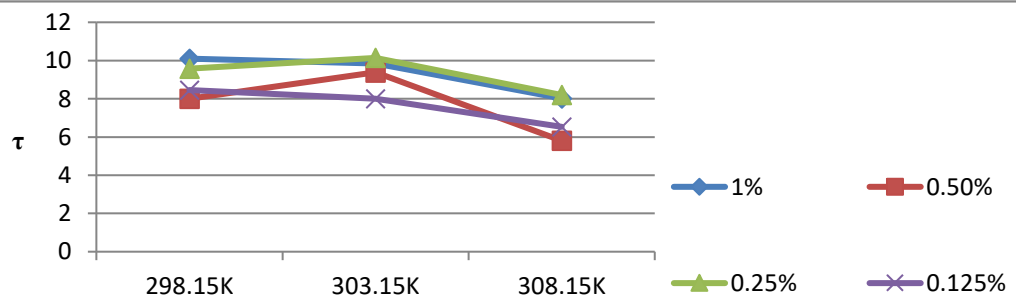


Fig.6. Variation of Relaxation time with temperature at diff. conc. in 50% alc. solvent.

The ultrasonic velocity of 1%, 0.5%, 0.25%, 0.125% psidiumgujavaleaf extract solution in 50% ethanol was measured at 298.15 K, 303.15K, 308.15K at 4mhz frequency. From table no.1and fig.no1a.it is observed that at different concentrations the ultrasonic velocity increases with increase in concentration, when the solvent is 50% ethanol. The ultrasonic velocity increases here with increase in concentration this is due to the salvation process of solute by two different solvent molecules like water and ethanol.But on the contrary when the solvent is distilled water a non linear variation of ultrasonic velocity with concentration is observed. From table no.3 and fig.1.(b) it is observed that ultrasonic velocity decreases with increase in concentration. This can be explained because of the formation of closed packed structure between solute and solvent molecules as the solvent molecules strongly associate through hydrogen bonding with leaf extract molecules.

From table no.2 and fig.2a.it is observed that Adiabatic compressibility decreases with increase in concentration. This can be explained as the solvent molecules strongly associate through hydrogen bonding with leaf extract molecules. Therefore bonds between solute- solvent strengthen the intermolecular forces resulting in decrease in adiabatic compressibility with increase in concentration. From table no.4 and fig.2b.it is observed that Adiabatic compressibility increase with increase in concentration. The increase in adiabatic compressibility shows significant molecular interactions.

From table 2 andfigure 3a.it is observed that there is increase in acoustic impedance with concentration shows the increase in molecular packing in the medium which gives the possibility of molecular interaction due to hydrogen bonding between solute- solvent. The reverse is found in the liquid system formed by water as a solvent, (table-4, fig-3b) here the acoustic impedance decreases with increase in concentration shows that there is decrease in molecular packing in the medium.

“ The intermolecular free length is the distance between the surfaces of the neighbouring molecules”. Here the intermolecular free length decreases with increase in concentration it indicates that asthe concentration of the system increases(table 2, fig.4a.) at particular temperature , one solute molecule and two solvent molecules arrange themselves resulting into a closed packed structure. Due to these closed packed structure , distance between these molecules decreases and intermolecular free length decreases. But in case of distilled water as solvent (table 4, fig.4b),on addition of solvent the gap between solute and solvent molecules which results in increase in intermolecular free length.

Relative association is a measure of extent of association of components in the medium. It is a property of understanding the molecular interaction in liquid mixtures and solutions. As discussed relative association depends on either of breaking of solvent molecules on addition of solute to it or the salvation of ions that are present.From table 4 and fig.5a.it is observed that relative association decreases with increase in concentration this is due to breaking up of associated solvent molecules on addition of solute. From table 4 and fig.5b.it is observed that there is increase in relative association with increase in concentration shows that the process of salvation of solute by solvent is predominant over the breaking of solvent molecules and results in the dipole-dipole interactions because both the solvents are polar in nature.

From table 2 and fig.6.a.it is seen that acoustical relaxation time increases with increase in concentration nonlinearly this may be due to presence of two solvent molecules around the solute molecules.Table 4 and

fig.6.b.shows that relaxation time increases with increase in concentration this is due to structural relaxation process showing presence of molecular interactions.

IV. CONCLUSION

From the above discussion it is observed that ultrasonic velocity increases with concentration in 50% ethanol solvent because of the salvation process on the other hand it decreases in distilled water due to formation of closed packed structure. Similar trend is also shown by intermolecular free length which clearly suggesting the contrary behavior of psidumgujava leaf extract solution in two different solvents. This also supports the molecular association occurring in the solution.

V. REFERENCES

- [1]. Parveen S., Shukla D., Singh S., Singh K.P , Gupta M. and Shukla J.P., Ultrasonic velocity, density, viscosity and their excess parameters of the binary mixtures of tetrahydrofuran with methanol and o-cresol at varying temperatures, *App. Acous.*,70(3),507-510, 2009.
- [2]. Umadevi M., Kesavasamy R.,Rathina K. and Mahalakshmi R., „Studies on liquid-liquid interactions of some ternary mixtures by density, viscosity and ultrasonic speed measurements“, *J. Mol. Liq.*, 219,820-822, 2016.
- [3]. Nayak N., Aralaguppi M.I. , and Aminabhavi T.M., Density, viscosity, refractive index, and speed of sound in the binary mixtures of 1,4- dioxane + ethyl acetoacetate, + diethyl oxalate, + diethyl phthalate, or + dioctyl phthalate at 298.15, 303.15, and 308.15 K, *Journal of Chemical and Engineering Data*, 48, (6), 1489–1494, 2003.
- [4]. Steele W. V., Chirico R. D. , Cowell A. B., Knipmeyer S. E., and Nguyen A, Thermodynamic properties and ideal-gas enthalpies of formation for methyl benzoate, ethyl benzoate, (R)-(+)- limonene, tert-amyl methyl ether, transcrotonaldehyde, and diethylene glycol, *Journal of Chemical and Engineering Data*, 47, (4), 667–688, 2002.
- [5]. Reis, J.C.R., Santos, A.F.S., Disas, F.A., Lampreia, I.M.S.: Correlated volume fluctuations in binary liquid mixtures from isothermal compressions at 298.15 K. *Chem. Phys. Chem.* (9), 1178–1188, 2008.
- [6]. Khasanshin, T.S., Shchemelev, A.P.: The thermodynamic properties of n-tetradecane in liquid state. *High Temp.* 40(2), 207–211 (2002)7 T. N. Srivastava, R. P. Singh and B. Swaroop, *Ind. J. Pure Phys.*, (21) 67-72, 1983.
- [7]. Kumar, A., Srivastava, U., Singh, A.K., Srivastava, K., Shukla, R.K.: Sound velocity and isentropic compressibility of binary liquid systems from various theoretical models at temperature range 293.15 to 313.15 K. *Can. Chem. Trans.* 4(2), 157– 167, 2016.
- [8]. Bhatt S.C., Hari Krishnan Semwak, Lingwal Vijendra, Singh Kuldeep, and Semwak B.S., Acoustical parameters of some molecular liquids, *J. Acous. Soc. India*, (28) 275-278, 2000.

- [9]. Murlijii D., Sekar. S., Dhanlaksmi A. And Ramkumar A.R., Study of ultrasonic velocity and Thermodynamic parameters of vaniline., J. Pure and Appl. Ultrasonics., (24) 63-67,2002.
- [10]. Vigneswari M., Saravanakumar S.S., Sureshbabu V.N., Sankarrajan S., Molecular interaction studies in solutions of polyvinyl alcohol: an ultrasonic study. International Journal of Advanced Chemistry, 4(2): 15-21,2016.
- [11]. Amruta R., Parsania P., ultrasonic velocity and acoustical parameters of poly (4,4-cyclohexylidenediphenyloxy-4,4-diphenylene-sulphone)solutions at different temperatures. Journal of scientific and industrial research, (65), 905-911,2006
- [12]. Bhuva B., Mehta N., Karia F., and Parsania P., Effect of temperature and solvents on ultrasonic velocity and allied acoustical parameters of epoxy oleate of 9,9-bis(4-hydroxy phenyl)anthrone -10 solutions. Journal of solution chemistry, (40), 719-726,2011.
- [13]. Bell W., and Pethrick R., Ultrasonic investigation of linear and star shaped polybutadiene polymers in solution of cyclohexane ,ethyl benzene and polymers (23), 369-373, 1982.
- [14]. Syal V., Chauhan A., Chauhan S., Ultrasonic velocity, viscosity and density studies of poly (ethylene glycols) (PEG-8000, PEG-20000) in acetonitrile and water mixtures at 250 C. Journal of pure and applied ultrasonics, (27), 61-69, 2005.
- [15]. Iqbal M., Siddiquah M., Partial molar volume of mefenamic acid in alcohol at temperature between $T = 293.15\text{K}$ and $T=313.13\text{K}$. Brazilian Chemical Society Journal, (17), 851-858, 2006.



Synthesis of Substituted-4, 6-Diaryl-2-Imino-6h-2, 3-Dihydro-1, 3-Thiazine

A. S. Dighade

Department of Chemistry, J.D. Patil Sangludkar Mahavidyalay, Daryapur, Maharashtra, India

ABSTRACT

Six different VII (a) –VII (f) thiazine were synthesized from flavanone VI (a) –VI (f) in ethanol containing little KOH and piperidine by the interaction of thiourea. The structures of some compounds were confirmed on the basis of IR, NMR, and Mass analysis.

Keywords: Iodo Acetophenone, Iodo- Diketone, Substituted iodo- Flavanone, Substituted iodo- 1, 3-Thiazine.

I. INTRODUCTION

The heterocyclic compounds which contain nitrogen, sulphur and oxygen possess an enormous significance in the field of medicinal chemistry. Heterocyclic compounds are abundant in nature and have acquired more importance because they form the structural subunits of many natural products such as vitamins, hormones, antibiotics and drug molecules. 1,3- thiazines which contains nitrogen and sulphur as a part of six membered heterocyclic ring (N-C-S). This ring also present in some of the medicinally important compounds like Xylazine(agonist at the α_2 - adrenergic receptor is used for sedation, anesthesia, muscle relaxation, and analgesia in animals¹)

Chhaya D. Badnakhe and P. R. Rajput² have synthesized and study of substituted 1,3-thiazine and their nanoparticles on phytotic growth of some vegetable crops. Koketsu et al.³, have synthesized 4- hydroxy-4-methyl-2, 6-diphenyl-5, 6-dihydro-4-H-1, 3-thiazine. Leflemme et al.⁴ have synthesized dihydro and tetrahydro-1, 3-thiazinederivatives from β aryl- β -amino acid.

Thiazine derivatives were reported to possess diverse biological activities including anticonvulsant⁵ antimicrobial^{6,7,8,9,10,11}, analgesic¹², anti-inflammatory and ulcerogenic^{13,14}, anticancer^{15,16,17,18,19}, antidiabetic²⁰, immunotropic²¹, antianxiety²², insecticidal and pesticidal²³, antitubercular²⁴, anthelmintic²⁵, anesthetic²⁶, and antiviral²⁷.

II. EXPERIMENTAL

Melting points of all synthesized compounds were determined in open capillary tube and are uncorrected. The purity of compounds were checked by TLC using silica G. I. R. spectra were recorded on Perkin-Climer-841 spectrometer (cm^{-1}) in KBr disc and NMR (Brucker Avance II 400 NMR) using CDCl_3 as solvent.

Synthesis of 2-hydroxy-3-iodo-5-methyl-acetophenone (Compound-1)

By known method from p-cresol to p-cresyl-acetate prepared and then by Fries migration-2-hydroxy-5-methyl acetophenone which on iodination gives 2-hydroxy-3-iodo-5-methyl acetophenone (Comp.-1).

Synthesis of 2-benzoyl-3-iodo-5-methyl acetophenone (IV)

2-benzoyl-oxy-3-iodo-5-methyl acetophenone was prepared from compound no. (I) by using benzoic acid, POCl₃ in pyridine and structure was confirmed on the basis of IR and NMR spectral analysis.

Synthesis of Diketone (1-(2-hydroxy-3-iodo-5-methyl phenyl)-3-phenyl-1, 3-propanedione) (V)

1-(2-hydroxy-3-iodo-5-methyl phenyl)-3-phenyl-1, 3-propanedione was prepared from by Baker – Venkatraman Transformation reaction. The structure was confirmed on the basis of IR, NMR and Mass spectral analysis.

Synthesis different substituted flavanone and chromanone VI (a) – VI (f)

Compound no. V propanedione was reacted with six different aromatic aldehydes in ethanol containing few drops of piperidine gave six different substituted flavanones and chromanones i.e. VI(a) – VI(f). The structures of some flavanone were confirmed on the basis of IR, NMR and Mass spectral analysis. The compounds prepared were listed in table 1.

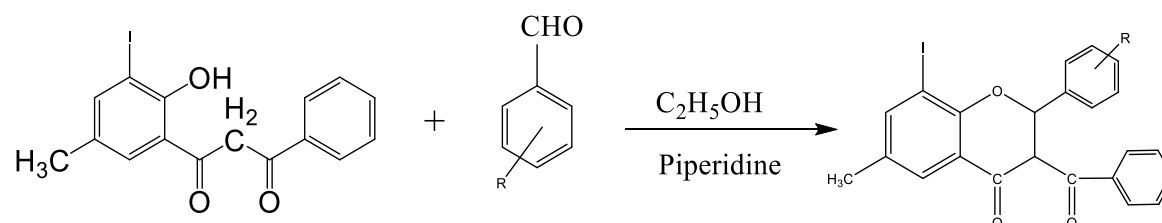


Table 1 3-aryl flavanones and 3-aryl chromanones VIa – VI f

Exp. No	Comp. No.	Name of compounds	M.P in °c	yield
82	VIa	3-benzoyl-2'-phenyl -6-methyl- 8 -iodo flavanone.	117 °c	76%
83	VIb	3-benzoyl-4'-methoxy -6-methyl- 8-iodo flavanone.	76 °c	68%
84	VIc	3-benzoyl-4'-ethenyl-6-methyl-8-iodo chromanone.	98 °c	63%
85	VI d	3-benzoyl-2'-furyl-6-methyl-8-iodo chromanone.	86 °c	65%
86	VIe	3-benzoyl-2'-hydroxy-6-methyl-8-iodo flavanone.	110 °c	66%
87	VI f	3-benzoyl-4'- chloro-6-methyl-8-iodo flavanone.	122 °c	70%

Characterization data of compounds

2-Hydroxy-3-iodo-5-methyl acetophenone

IR (KBr) ν_{\max} cm⁻¹: 3200 cm⁻¹ (s) – phenolic OH , 2919 cm⁻¹ (s) – Ar- C-H stretching, 1635 cm⁻¹ C = O stretching, 1082-1007 cm⁻¹ (S) CH₃ - stretching , 1020 cm⁻¹ (S) CH₃ stretching, 550 cm⁻¹ C-I stretching.

¹H NMR: [δ CDCl₃]: 2.3 δ (S, 3H, Ar- CH₃), 2.6 δ (S, 3H, COCH₃), 7.5 δ (S, 1H, Ar-H), 7.7 δ (S, 1H, Ar-H), 12.9 δ (S, 1H, Ar-OH).

TOF MS ES+: 345 Molecular ion at 275.1 m/z assign the molecular formula $C_9H_9IO_2$ and 1362 Base peak at 119.1 m/z assign the molecular formula C_8H_7O .

2-benzoyl-3-iodo-5-methyl acetophenone

IR (KBr) ν_{max} cm^{-1} : 3046 cm^{-1} (s) –C-H stretching in Ar-H, 1686 cm^{-1} C = O stretching, 2919 cm^{-1} (S) C-H stretching in CH_3 , 1562.09 cm^{-1} (S) **C=C ring** stretching, 1212.5 cm^{-1} (S) Ar-O stretching, 549 cm^{-1} C-I stretching.

1H NMR: [δ $CDCl_3$]: 2.25 δ (S, 3H, Ar- CH_3), 2.6 δ (S, 3H, Ar-CO- CH_3), 7.5 δ (S, 1H, Ar-H), 7.2-8.25 δ (m, 7H, Ar-H), 13 δ (S, 1H, Ar-OH).

(1-(2-hydroxy-3-iodo-5-methyl phenyl)-3-phenyl-1, 3-propanedione) Diketone

IR (KBr) ν_{max} cm^{-1} : 3045 cm^{-1} (s) Ar-H stretching, 1635 cm^{-1} C = O stretching, 3020 cm^{-1} (br) Ar-OH stretching, 1598-1447 cm^{-1} (S) **C=C ring** stretching vibration in aryl gp, 2919 cm^{-1} (S) Ar- CH_3 stretching, 536 cm^{-1} C-I stretching.

1H NMR: [δ $CDCl_3$]: 2.1-2.3 δ (S, 3H, Ar- CH_3), 8.3-8.45 δ (d, 2H, for CH_2), 7.1-7.85 δ (m, 7H, Ar-H), 12.8 δ (S, 1H, Ar-OH).

TOF MS ES+: 760 Molecular ion at 380.0 m/z assign the molecular formula $C_{16}H_{13}IO_3$ and 7173 Base peak at 335.9 m/z assign the molecular formula $C_{15}H_{11}IO$.

3-benzoyl-4'-methoxy-6-methyl- 8-iodo flavanone

IR (KBr) ν_{max} cm^{-1} : 3056 cm^{-1} (s) Ar-CH stretching, 1692.35 cm^{-1} C = O stretching of aroyl gp, 1253.64 cm^{-1} (S) Ar-O stretching, 1461.72-1439 cm^{-1} (S) **C=C ring** stretching vibration in aryl gp, 2914.56 cm^{-1} (S) Ar- CH_3 stretching, 1349.47 cm^{-1} (S) Pyrone, 573 cm^{-1} C-I stretching.

1H NMR: [δ $CDCl_3$]: 2.2-2.40 δ (S, 3H, Ar- CH_3), 3.8 δ (S, 3H, Ar-O- CH_3), 6.8-7.9 δ (m, 11H, Ar-H), 3.0 δ (S, 1H, CH_A), 5.5 δ (S, 1H, CH_B).

TOF MS ES+: 579 Molecular ion at 498.2 m/z assign the molecular formula $C_{24}H_{19}IO_4$ and 16634 Base peak at 229.1 m/z assign the molecular formula $C_{16}H_{13}IO_2$.

3-benzoyl-2'-hydroxy-6-methyl-8-iodo flavanone

IR (KBr) ν_{max} cm^{-1} : 3336 cm^{-1} (br) Ar-OH stretching, 3133-3005 cm^{-1} (s) Ar-CH stretching, 1596-1667 cm^{-1} (s) C = O stretching of aroyl gp, 1197-1257 cm^{-1} (s) Ar-O stretching, 1535-1444 cm^{-1} (s) **C=C ring** stretching vibration in aryl gp, 2948 cm^{-1} (s) Ar- CH_3 stretching, 1347 cm^{-1} (s) Pyrone, 514 cm^{-1} (s) C-I stretching.

1H NMR: [δ $CDCl_3$]: 2.1-2.6 δ (S, 3H, Ar- CH_3), 12.7-13.0 δ (br, 1H, Ar-OH), 7.2-7.85 δ (m, 13H, (1H) CH_A , (1H) CH_B & (11H) Ar-H),

TOF MS ES+: 520 Molecular ion at 484.0 m/z assign the molecular formula $C_{23}H_{17}IO_4$ and 6417 Base peak at 229.1 m/z assign the molecular formula $C_{15}H_{15}IO_2$.

Synthesis of substituted 4, 6-diaryl-2-imino-6H-2, 3-dihydro-1, 3-thiazine

Compound (VII_a-VII_f) 0.01 M, thiourea 0.01 M and 0.02 M KOH solution with a few drops of piperidine were refluxed in 25 mL ethanol for 2 to 2.5 hours. Dilute it with water and acidified with conc. HCl. The products were crystallized from ethanol. Physical data are shown in Table

Reaction

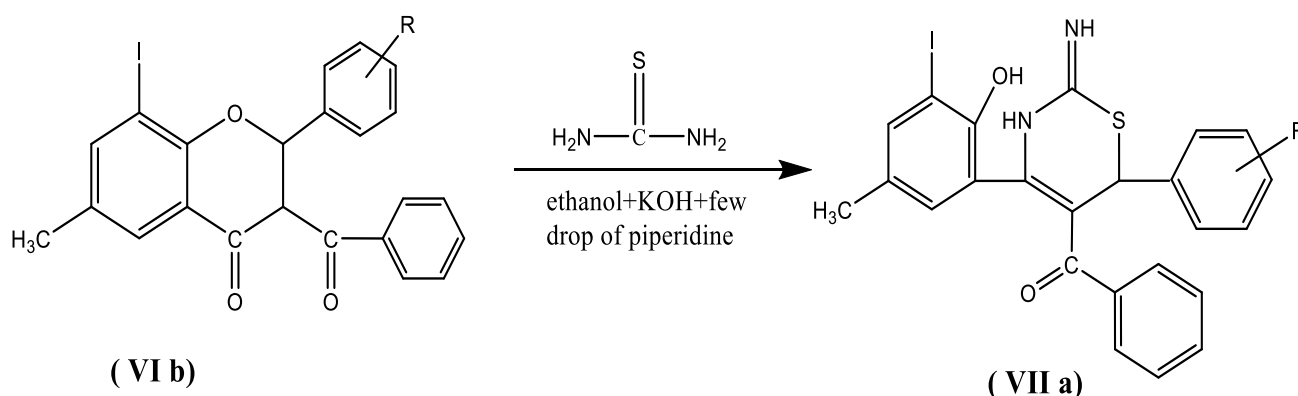


Table 2 4, 6-diaryl-5-aryl-2-imino-6H-2, 3-dihydro-1, 3-thiazines VIIa – VII f

Exp. No	Comp. No.	Name of compounds	M.P in $^{\circ}\text{C}$	Yield
88	VIIa	4- (2'- hydroxy -3-iodo-5-methylphenyl) -5-benzoyl -6- (phenyl) -2- imino- 6H- 2, 3- dihydro-1, 3-thiazine.	208 $^{\circ}\text{C}$	70%
89	VIIb	4- (2'- hydroxy -3-iodo-5-methylphenyl) -5-benzoyl -6- (4-methoxyphenyl) -2- imino- 6H- 2,3- dihydro-1,3-thiazine.	118 $^{\circ}\text{C}$	68%
90	VIIc	4- (2'- hydroxy -3-iodo-5-methylphenyl) -5-benzoyl -6- (-2-phenylethenyl) -2- imino- 6H- 2,3- dihydro-1,3-thiazine.	150 $^{\circ}\text{C}$	60%
91	VIIId	4- (2'- hydroxy -3-iodo-5-methylphenyl) -5-benzoyl -6- (2-furyl) -2- imino- 6H- 2,3- dihydro-1,3-thiazine.	89 $^{\circ}\text{C}$	62%
92	VIIe	4- (2'- hydroxy -3-iodo-5-methylphenyl) -5-benzoyl -6- (-2-hydroxyphenyl) -2- imino- 6H- 2,3- dihydro-1,3-thiazine.	98 $^{\circ}\text{C}$	64%
93	VIIIf	4- (2'- hydroxy -3-iodo-5-methylphenyl) -5-benzoyl -6- (-4-chlorophenyl) -2- imino- 6H- 2,3- dihydro-1,3-thiazine.	108 $^{\circ}\text{C}$	65%

Characterization data of compound

Synthesis of 4- (2'- hydroxy -3-iodo-5-methylphenyl) -5-benzoyl -6- (4-methoxyphenyl) -2-imino- 6H- 2, 3-dihydro-1, 3-thiazine

IR (KBr) ν_{max} cm^{-1} : 3368.81 cm^{-1} (s) O-H stretching in phenol, 3056.26 cm^{-1} (s) Ar-H stretching, 2836.03 cm^{-1} (s) C=N-H stretching, 2945.49 cm^{-1} (s) C-N-H stretching, 1691 cm^{-1} (s) C=N stretching, 1256 cm^{-1} (s) C-N stretching, 1637.47 cm^{-1} (s) C = O stretching of aroyl gp, 1555.67-1604.39 cm^{-1} (s) C=C ring stretching vibration in aryl gp, 536 cm^{-1} (s) C-I stretching.

^1H NMR: [δ CDCl_3]: 2.3 δ (s, 3H, Ar- CH_3), 3.95-4.2 δ (s, 3H, O- CH_3),

3.6-3.9 δ (s, 2H, N-H & =N-H), 2.7 δ (s, 1H CH_A), 6.5-8.2 δ (m, 11H, Ar-H).

TOF MS ES⁺: 425 Molecular ion at 554.2 m/z assign the molecular formula $\text{C}_{25}\text{H}_{21}\text{IN}_2\text{O}_3\text{S}$ and 12751 Base peak at 229.1 m/z assign the molecular formula $\text{C}_7\text{H}_6\text{IO}$.

III. RESULTS AND DISCUSSION

Compound **VI_a – VI_f** and **VII_a – VII_f** were synthesized through the route as shown in general reactions with R and R' as shown in Table 1 and 2. Physical data are given in Table 1 and 2. The synthesized compounds **I_e** and **II_e** were confirmed on the basis of IR, NMR spectral analysis.

IV. ACKNOWLEDGEMENT

Authors are thankful to Principal, J. D. Patil Sangludkar Mahavidyalaya Daryapur, H. O.D. Chemistry, J. D. Patil Sangludkar Mahavidyalaya Daryapur and thankful to RC SAIF Punjab University, Chandigarh for spectral analysis IR., NMR.

V. REFERENCES

- [1]. Greene SA, Thurmon JC, Xylazine--a review of its pharmacology and use in veterinary medicine. *J Vet Pharm and Ther* 1988; 11(4):295-313.
- [2]. Chhaya D. Badnakhe and P. R. Rajput, *European J. of biomedical and pharmaceutical Sciences* 5(9), 313-318(2018).
- [3]. M. Koketsu, M. Ebihara and H. Ishihara, *J. Acta Crystallographica Section E*, 62, Part 4, (2006) pp. 1218-1220.
- [4]. Nicolas Leftemme, Patrick Dallemagne and Sylvain Rault, *J. Tetrahydron Letters*, 45(7), 1503-1505 (2004).
- [5]. Ravindar B, Srinivasa Murthy M, Afzal Basha Shaik. Design, facile synthesis and biological evaluation of novel 1,3-thiazine derivatives as potential anticonvulsant agents. *Asian J Pharma Clin Res* 2016; 9(2):272-276.
- [6]. Ravindar Bairam and Srinivasa Murthy M. Synthesis characterization and biological screening of some novel substituted 1,3-thiazine derivatives. *Der Pharma Chemica* 2015; 7(10):150-154.
- [7]. Shaik K Yazdan, Gali V Sagar Afzal B Shaik. Biological and synthetic potentiality of chalcones. *J Chem Phar Res* 2015; 7(11):829-842.
- [8]. Rathore MM. Synthesis and antimicrobial activities of some bromo-substituted-1, 3-thiazines. *Int J Res Pham Biomed Sci* 2013;4(1):59-62.
- [9]. Silverstein R. Spectroscopic identification of organic compounds, 6th Edn, (John Wiley & Sons Inc., New York 1991; 60-70,119-176:191-200.
- [10]. Ibadur R Siddiqui, Pravin K Singh. Novel one pot synthesis of 1,3-dithiins and 1,3-thiazines under microwave irradiation. *Int J Chem* 2007; 46B: 499-504.
- [11]. Tarik El-Sayed Ali, Azza Mohammed El- Synthesis and antimicrobial activity of some new 1,3-thiazoles, 1,3,4- thiadiazoles, 1,2,4-triazoles and 1,3-thiazines incorporating acridine and 1,2,3,4-tetrahydroacridine moieties. *Eur J Chem* 2010; 1(1): 23.

- [12]. Srikanth Jupudi, Sandeep Talari, Divya Karunakaram, Govindarajan R. Screening of in vitro anti-inflammatory activity of some newly synthesized 1,3-thiazine derivatives. *Int J Rese Pharm Chem* 2013; 3(2):213-220.
- [13]. Vijay V Dabholkar, Sagar D Parab. 1, 3-Thiazines and 1, 3-pyrimidines derivatives and their biological evaluation for anti-inflammatory, analgesic and ulcerogenic activity. *Hetero Letters* 2011; 1(2):176-88.
- [14]. Udupi RH, Bhat AR, Jacob J. Synthesis and biological evaluation of some biphenyl ether and thiazine derivatives. *Ind J Hetro Chem* 2005; 15:89.
- [15]. Temple C, Wheeler GP, Comber RN, Elliot RD, Montgomery JA, Synthesis of potential anticancer agents, Pyrido[4,3-b][1,4]oxazines and pyrido[4,3-b][1,4] thiazines. *J Med Chem* 1983; 26:1641.
- [16]. Sayaji S Didwagh, Pravina B Piste Aravind S Burungale, Avinash M Nalawade. Synthesis and antimicrobial evaluation of novel 3-(4,6- diphenyl-6H-1,3-thiazin-2-yl)-2-(4-methoxyphenyl) thiazolidin-4-one derivatives. *J Appl Pharm Sci* 2013; 3(11):122-127.
- [17]. Roman Lesyk, Olena Vladzimirska, Serhiy Holota, Lucjusz Zprutko, Andrzej Gzella. New 5-substituted thiazolo[3,2-b][1,2,4]triazol-6-ones: Synthesis and anticancer evaluations. *Eur J Med Chem* 2007; 42: 641-648.
- [18]. Wei Wang, Bing Zhao, Chao Xu, Wenpeng Wu. Synthesis and antitumor activity of the thiazoline and thiazine multithioether. *Int J Org Chem* 2012; 2: 117-120.
- [19]. Beauchamp, Benardeau, Hilpert, Wang. 2-Aminodihydro [1,3] thiazines as bace 2-inhibitors, for the treatment of diabetes, patent scope. *Wor Inte Pro Org* 2011; 165.
- [20]. Syntheses and pharmacological analysis of new derivatives of tetra hydro-[1,3]-thiazine and 2-thiobarbituric acid. *Nat Cen Biot Inf* 1981; 29(2):235-248.
- [21]. Hong Min Wu, Kuo Zhou, Tao Wu, Yin Guang Cao. Synthesis of pyrazine-1,3-thiazine hybrid analogues as antiviral agent against HIV-1, influenza A (H1N1), enter virus 71(EV71), and coxsackievirus B3(CVB3). *Chem Biol Drug Des* 2016; 88:411-21.
- [22]. Syntheses and pharmacological analysis of new derivatives of tetrahydro-[1,3]-thiazine and 2-thiobarbituric acid. *Nat Cen Biot Inf* 1981; 29(2): 235-48.
- [23]. Srikanth Jupudi. Screening of in vitro anti-inflammatory activity of some newly synthesized 1,3-thiazine derivatives. *Int J Res Phar and Chem* 2013; 3: 213-20.
- [24]. Foks H. Synthesis, structure and biological activity of 1, 2, 4-triazolo-1,3-thiazine derivatives. *Pharm* 1992; 47(10): 770-73.
- [25]. Bhusari PK, Khedekar PB, Umathe SN, Bahekar RH, Rama R. *Ind J Hete Chem* 2000; 69:
- [26]. Al-Khamees HA, Bayomi, SM, Kandil, HA, El-Thahir K. Microwave assisted green chemical synthesis of novel spiro[indole-pyrido thiazines], a system reluctant to be formed under thermal conditions. *Eur J Med Chem* 1990; 25: 103.
- [27]. Turaska Rao, Bhongade S L, More SM, Dongarwar A S, Shende V S and Pande V B. Effects of lippia nodiflora extracts on motor coordination, exploratory behavior pattern, locomotor activity, anxiety and convulsions on albino mice. *Asian J Pharm Clin Res* 2011; 4(3):133--138.



Insight Details Of X-Ray Diffraction Analysis and Infrared Spectra of Polypyrrole Composites Decorated With TiO₂ and SnO₂ Metal Oxides

Aditya V.Tiwari, A.P.Deshmukh, P.S.Awandkar, S. P. Tiwari, S. P. Yawale

Department of Physics, Government Vidarbha Institute of Science and Humanities, Amravati, Maharashtra, India

ABSTRACT

Pure Polypyrrole and its composite with metal oxides namely Ppy-TiO₂ and Ppy-SnO₂ were synthesized by in-situ chemical oxidative polymerization of pyrrole using FeCl₃ as an oxidant. Composite samples were prepared by (10 $\frac{w}{v}$ %) of the pyrrole monomer. The crystallinity of composites were studied by X-ray diffraction (XRD) technique. The composites were analyzed by Fourier transform infrared (FTIR) spectroscopy. The infrared spectra of pure Polypyrrole, Ppy-TiO₂ and Ppy-SnO₂ composites were measured over wavelength range 400-4000 cm⁻¹ in an attempt to study their structures systematically. The shifting of X-ray peaks provided useful information regarding rutile and anatase phase change ratio of the TiO₂ (TiO₂ in Ppyanatase to rutile phase becomes 57:43) in Ppy matrix. Some of the characteristic FTIR peaks of Ppy shifts to higher wavenumber and wavelength sides in Ppy-TiO₂ and Ppy-SnO₂ hybrid composites, which are attributed to the interaction of metal oxide with the Ppy molecular chains.

Keywords: Titanium dioxide, Tin oxide, Polypyrrole-TiO₂, Polypyrrole-SnO₂, XRD, FTIR

I. INTRODUCTION

Conducting Polymers have gained the interest of many researchers due to their diverse structures, special doping mechanism, excellent environmental stability and high conductivity based applications[1]. One of the conducting polymer polypyrrole (Ppy) has properties like high electrical conductivity and appreciable air stability which have been exploited for application purposes in its pure form and as different Ppy nano composites[2]. Polypyrrole has also emerged as material having efficient electron donor properties, high mobility of charge carriers, high absorption Coefficient rates showing optical and redox properties [3-4]. Although PANI is widely used conducting polymer, Ppy shows higher conductivity than PANI [1]. Embedding metal oxides like TiO₂ and SnO₂ the electrical properties of the nano composites can be improved showing rather good thermal stability than pure Ppy[5-7]. Hence to study these properties efficiently it is important to analyze the structural pattern of composite and their infrared spectroscopy behavior.

TiO₂ is an n-type semiconductor material with an energy band gap of about 3.33 eV, which cannot be found in other nanomaterials, thus rendering it suitable for providing useful sensing ranges [8]. SnO₂ is an n-type

semiconductor material with an energy band gap of about 3.6 eV at room temperature shows an excellent adsorption behavior in presence of ambient gas environment [9]. Thus in view of the importance of both the metal oxides TiO_2 and SnO_2 in material science, it is noteworthy as well as interesting to study the properties of Ppy- TiO_2 , Ppy- SnO_2 composite, which may have unique properties along with their individual properties overlapping with pure Ppy. Hence an Endeavour is made to study the detailed structure of samples through infrared spectroscopy and X-ray technique.

Conducting polymers are easy to be synthesized through chemical or electrochemical processes, and their molecular chain structure can be modified conveniently by copolymerization or structural derivations [10]. Furthermore, polypyrrole has good mechanical properties, which allow a facile fabrication of sensors such as gas sensors and bio-sensors [11]. It also finds applications in batteries [12], electro-chemical supercapacitors [13], electrical-magnetic shields, microwave absorbing materials [14]. Hence, Polypyrrole (PPy) was chosen as a conductive polymer for this study since it can be in situ generated [15].

II. EXPERIMENTAL

2.1 Chemicals

Pyrrole monomer procured from Himedia, Methanol and Stannic dioxide (SnO_2 99.9% pure) received from Lobha Chemical, Titanium dioxide (TiO_2 99.9% pure) obtained from Ultrananotech, Ferric Chloride (FeCl_3) anhydrous A.R. from Himedia used as oxidizing agent to start the polymerization reaction, Whatmann grade one filter paper were used for filtering the product, Distilled water and methanol were used for washing the product.

2.2 Synthesis of pure Polypyrrole (Ppy)

For the preparation of polypyrrole methanol is taken as a solvent. The ratio of pyrrole monomer to the oxidizing reagent FeCl_3 (1:2.33) is taken in such a way to obtain maximum yield of the polypyrrole out of polymerization. Firstly 9.01 g of FeCl_3 is added into the 40 ml of methanol under constant stirring in a beaker for 10 min. As soon as the FeCl_3 is added into the methanol produces heated fumes and solution becomes warm, showing exothermic reaction. This freshly prepared solution is further ultrasonicated for 30 min in a sonication bath for homogeneous solution of FeCl_3 . Then 4 ml Pyrrole monomer is added drop wise into the prepared oxidizing solution slowly for 30 min under constant stirring. Reaction is kept under stirring for 2 hrs. As the methanol evaporates the oxidizing potential of the reaction increases forming thick greenish black polypyrrole paste in a beaker.

The reaction is again kept unagitated to have complete polymerization for 2 hrs and obtained product was filtered and washed several times with distilled water and methanol till the filtrate obtained was colorless. Washing removes excess of ferric chloride and ferrous chloride present due to polymerization. Product was finally dried in an oven (Gallenkamph British made) at 60-70 °C for 12 hrs. Then, the resulting polymer was milled to convert the powder and fine Greenish-black polypyrrole powder was obtained.

2.3 Synthesis of Ppy-TiO₂ and Ppy-SnO₂ composites

Composites were prepared by following the same procedure as mentioned above. While following the above synthesis process the powder of TiO₂ and SnO₂ is added into the FeCl₃ followed by 1 hr of sonication for two samples. Sonication allows the dispersion of these metal oxides into the oxidizing reagent solution and homogeneity of the polymer can be achieved after the polymerization with the Pyrrole monomer as per above procedure. Hence two composite samples Ppy-TiO₂ and Ppy-SnO₂ are obtained.

III. CHARACTERIZATION

3.1 X-ray diffraction

The X-ray powder diffraction data for all the scrutinized samples were obtained from Physics Instrumentation laboratory Government Vidarbha Institute of Science Humanities, Amravati. The Rigaku Miniflex X-ray Diffraction unit having benchtop X-ray diffractometer with advanced detector is employed for the recording of results. The operating conditions of the X-ray generator were as mentioned: Tube voltage 40 kV, tube current 15 mA; radiation: CuK α (angle range: 0 to 80°, step size: 13 mm, water flow 4.3 L/min).

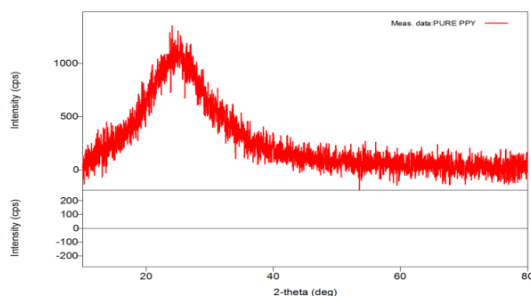
3.2 Infrared Spectra

The FT-IR spectrum has been taken on Shimadzu IR Affinity-1S model having a maximum resolution of 0.5 cm⁻¹. The smooth moving mirror system monitored by the Dynamic Alignment system allows the IR Affinity-1S to provide optimum and stable quality spectra after only a short warm-up time. Sampling at over 5000 times /second the Dynamic Alignment keeps the IR Affinity-1S in optimum operating condition for powder samples. The vibration spectra of samples were obtained in the range 400-4000 cm⁻¹.

IV. RESULTS AND DISCUSSION

4.1 X-ray Analysis

X-ray diffraction was used to check the nature of the samples. For pure PPy, the XRD pattern showed a broad, amorphous diffraction peak at approximately $2\theta = 26^\circ - 30^\circ$ hence found to have complete long chain amorphous nature throughout the polymer matrix [16].



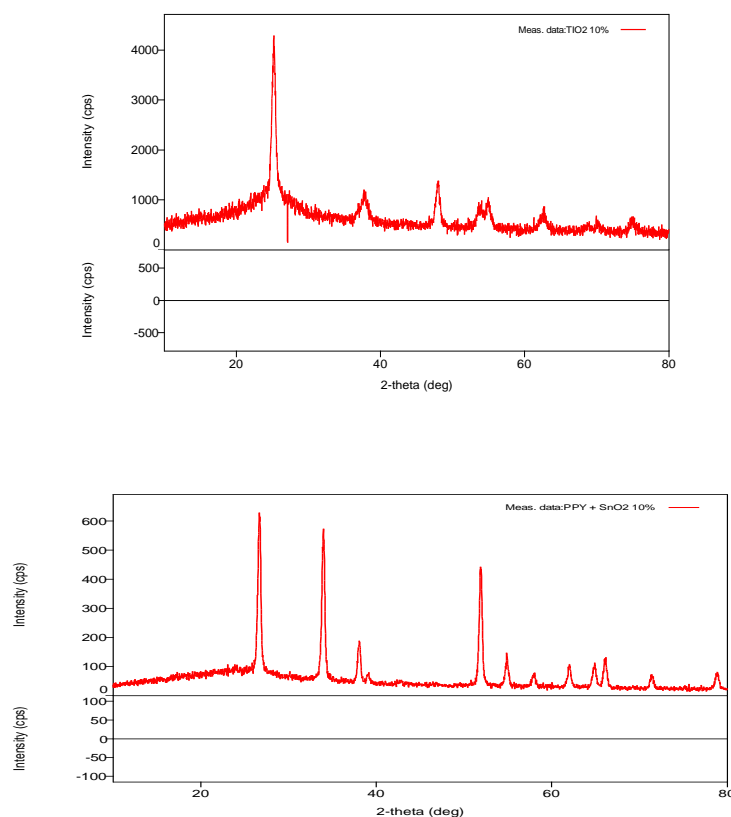


Fig 1. XRD spectra of: (a)Ppy (b) Ppy- TiO₂(10%) (c)Ppy- SnO₂ (10%)

In case of Ppy-TiO₂, XRD pattern shows crystalline peaks of TiO₂ in a polymer composite. The patterns shows strong diffraction peaks at 27.35°, 37.92° and 54.05° with specific assignment to the (110), (101), and (105) planes of rutile TiO₂, respectively. Similarly, the diffraction peaks at 25.27° and 47.93° which correspond to the Bragg's reflections from the (101) and (200) planes respectively indicate the presence of TiO₂ in anatase phase. Obtained peaks are in a good agreement with the standard spectra (JCPDS numbers 88-1175 and 84-1286). Peaks attributed to the higher Bragg's angles like 62.57° and 74.70° correspond to the (204) and (215) planes assigned to the crystal anatase phase of TiO₂ [17]. It has been found from XRD that in TiO₂ the ratio of anatase and rutile phases is almost 75:25 and upon an addition of TiO₂ in Ppy the ratio of anatase to rutile phase becomes 57:43, this indicates that the anatase phase is predominant compared to rutile one in the composite sample. This observation concludes that the synthesized composites have a dominant crystalline nature with TiO₂ particles which is not much absorbed by Ppy.

The XRD spectra of SnO₂ shows obvious prominent peaks at $2\theta = 26.55^\circ, 33.84^\circ, 37.92^\circ, 38.92^\circ, 42.62^\circ, 51.74^\circ, 54.74^\circ, 57.82^\circ, 61.86^\circ, 64.69^\circ, 66^\circ, 71.26^\circ$ and 78.70° which are assigned to scattering from (110), (101), (200), (111), (210), (211), (220), (002), (310), (112), (301), (202) and (321) reflection planes of tetragonal SnO₂ (JCPDS Card No. 41-1445) [18].

The XRD spectra of PPy–SnO₂ composite confirm the shift of prominent peaks (of SnO₂) 26.72°, 33.99°, 38.09°, 39.10, 42.70, 51.95°, 54.93°, 57.95°, 62.07°, 64.87°, 66.11°, 71.36° and 78.86° in their respective planes. After addition of SnO₂ into PPy matrix, the 2 θ values of prominent peaks of SnO₂ are shifted towards higher values, indicating the loss of conjugation of PPy. Hence, show that the obtained composite have a dominant crystalline nature with SnO₂. From the XRD data it is observed that for the pure SnO₂ the ratio of anatase to rutile phases is almost constant. Also on an addition of SnO₂ in PPy matrix will not affect the structure.

4.2 FT-IR Analysis

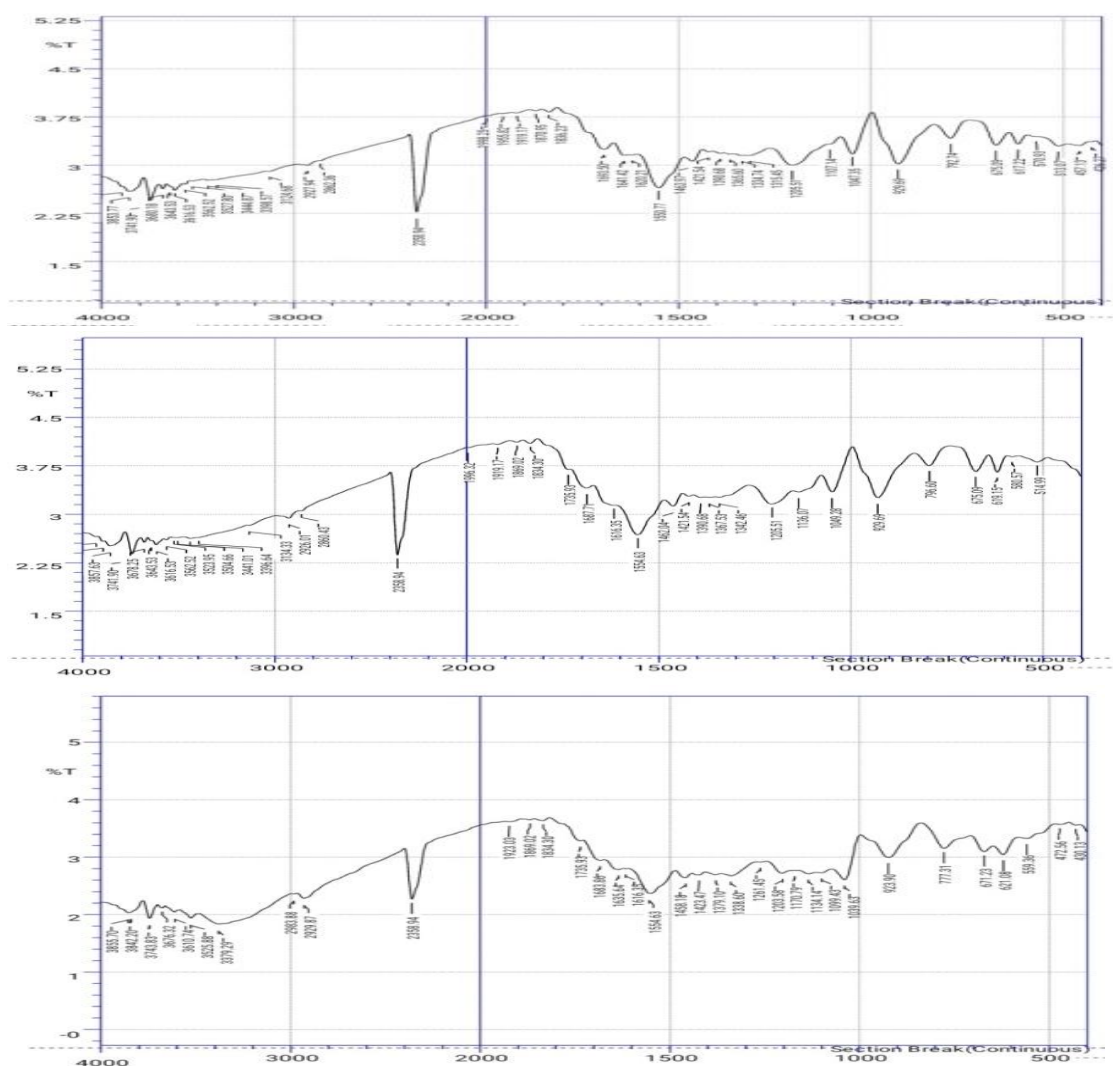


Fig 2(a).IR spectra of pure Polypyrrole Fig 2(b).IR spectra of PPy- TiO₂ (10%) Fig 2 (c).IR spectra of PPy- SnO₂ (10%)

FT-IR spectroscopy reveals the presence of interaction between conducting Ppy with TiO₂ and SnO₂. Fig. 2 (a-c) shows the FTIR spectra of pure Ppy, Ppy-TiO₂ and Ppy-SnO₂ composite materials where the absorption peak of PPy at 930 cm⁻¹, shows C-H bonding in Ppy ring and shifted absorption peaks of composites at lower wave numbers 928 cm⁻¹ and 924 cm⁻¹ shows C-H wagging in respective composites [19]. The band at 1554 cm⁻¹

in Ppy, Ppy- SnO₂ and 1550 cm⁻¹ in Ppy- TiO₂ are assigned to stretching vibrations of C=C shows stretching mode of pyrrole ring. Similarly weak band at 1462 cm⁻¹ in pure and 1458 cm⁻¹ and 1463 cm⁻¹ in respective composites are due to the stretching vibration of C-C in Pyrrolering. The peaks observed in above samples from 1317 to 1334 cm⁻¹ can be attributed to C-N bonding in plane deformation. The C-C stretching vibrations are observed at 1207 cm⁻¹ and 1203 cm⁻¹ in Ppy and PPy- TiO₂ composite. The peak obtained at 1049 cm⁻¹ is assigned to the C-H deformation of Ppy. The peak obtained at 794 cm⁻¹ in Ppy and Ppy-TiO₂ while 777 cm⁻¹ for Ppy-SnO₂ confirms that the pyrrole is being polymerized.

In PPy-TiO₂ The broad band at about 3997 cm⁻¹ is assigned to stretching vibrations of hydroxyl group (-OH) and the band at about 1614 cm⁻¹ corresponds to deformative vibration of Ti-OH which is adsorbed water on the TiO₂ surface. The absorption bands that appear in the low-frequency region of spectra located in the range 450-750 cm⁻¹ characteristic of a Ti-O-Ti symmetric stretching vibration mode and of Ti-O vibrations [20]. Also, the appearance of peaks in the wavelength range from 2000 to 2500 cm⁻¹ corresponds to the N-C=O bonds referred peak at 2360 cm⁻¹, this is due to Ti-O-C=N and Ti-O=C-N structures as results of PPy and TiO₂ interactions [21]. Similarly in Ppy-SnO₂, the peak at 2358 cm⁻¹ corresponds to the N-C=O bonds. The interaction between PPy and TiO₂ vibration bands can be explained by shifting of peaks to higher wave number like peaks at 3446, 3531, 3618, 3747 and 1695, 1739 cm⁻¹, indicating the strong interaction on the interface [22].

Figure 2(a) and 2(c) shows the FTIR spectra of the PPy and PPy-SnO₂ (10%) hybrid composite. The peaks at 621, 777, 924 cm⁻¹ are attributed to C-H wagging. The peaks obtained at 1040 and 1100 cm⁻¹ are attributed to the C-H in plane deformation vibration, 1203 and 1339 cm⁻¹ attributed to N-C stretching band, the peak at 1458 cm⁻¹ is due to a C-C asymmetric stretching vibration and peak at 1555 cm⁻¹ is on account of the stretching mode of pyrrole ring [23]. The bending motion of N-H and C-H stretching is observed at 1684 cm⁻¹ to 1736 cm⁻¹. The peak at 2984 cm⁻¹ is due to N-H stretching in PPy [24].

The following table shows comparison of shifting of PPy peaks in the PPy- TiO₂(10%), PPy-SnO₂ (10%) composites.

PPy peak (cm ⁻¹)	PPy- TiO ₂ peaks (cm ⁻¹)	PPy- SnO ₂ peaks (cm ⁻¹)	Assignments
619	615	621	C-H wagging
794	794	777	C-H wagging
929	928	924	C-H wagging
1049	1049	1040	C-H in plane deformation vibration
1109	1097	1100	C-H in plane deformation vibration
1207	1203	1203	N-C stretching
1334	1334	1339	N-C stretching
1462	1464	1458	C-C asymmetric stretching
1554	1550	1555	Stretching of pyrrole ring
1687	1695	1684	Bending motion of N-H
1734	1740	1736	C-H stretching
2931	2978	2983	N-H stretching in PPy

Fig 3. IR peaks comparison

Some peaks of PPy are shifted in FTIR spectra of PPy–SnO₂ composite towards higher wave number side. These shifts in peak positions regards to the loss in conjugation and molecular order after modification of PPy with SnO₂ and hence attributed to a strong chemical interaction between active sites in PPy and SnO₂ in forming changes to the polymer composition.

V. CONCLUSION

Polypyrrole and its PPy–TiO₂, PPy–SnO₂ composites were synthesized by one step insitu oxidation polymerization using FeCl₃ as oxidizing reagent. The process of synthesis of composites yield bulk product out of polymerization and hence can be utilized for further studies in generous amounts. These composites were analyzed by XRD and FTIR techniques. For pure PPy, the XRD pattern showed a broad peak hence found to have complete long chain amorphous nature throughout the polymer matrix. From the 2θ values the major peaks of TiO₂ and SnO₂ shifts towards higher side in their composites indicating their loss of conjugation within Ppy matrix. In TiO₂ the ratio of anatase and rutile phases is almost 75:25 and upon an addition of TiO₂ in Ppy the phase ratio becomes 57:43 shows the anatase phase is predominant compare to rutile one in the PPy–TiO₂ composite sample. For SnO₂ the phase ratio of anatase to rutile almost remained constant on addition of SnO₂ in Ppy matrix. From the FTIR spectra, it is revealed that the characteristic absorption peaks of Ppy are shifted significantly for both metal oxide composites, indicating an existence of different interfacial interactions between TiO₂, SnO₂ particles with Ppy. Thus it is evident to conclude that by overlapping the properties of TiO₂, SnO₂ metal oxides with Ppy can lead to various structurally functionalized composites by making modifications in synthesis process towards better applications.

VI. REFERENCES

- [1]. N.K. Guimard, N. Gomez, C.E. Schmidt, Prog. Polym.Sci. 32, 876 (2007).
- [2]. A. Bhattacharya, D.C. Mukherjee, J.M. Gohil, Y. Kumar, S. Kundu, Desalination 225, 366 (2008).
- [3]. G. Chakraborty, K. Gupta, A.K. Meikap, R. Babu, W.J. Blau, Solid State Commun. 152, 13 (2012).
- [4]. F. Han, D. Li, W.-C. Li, C. Lei, Q. Sun, A.-H. Lu, Adv. Funct. Mater. 23, 1692 (2013)
- [5]. Akhil D Prabhu ,Bharathesh B M , Aaditya V B, Chaluvaraju B V, Raghavendra U P, Murugendrappa M, Materials Today Proceedings, Elsevier 5, (10) Part 1, 21217-21224, (2018).
- [6]. S. Roy, S. Mishra, P. Yogi, S. K. Saxena, P. R. Sagdeo, R. Kumar, J. Organo. Polym. And mate., Springer, 27, 257–263, (2017).
- [7]. M. S. Bhende, S.P. Yawale, S.S. Yawale, Int. J. Inno. And Emer. Research in Eng. 3, (1), ICSTSD, 569-573, (2016).
- [8]. Y. Wu, S. Xing, J. Fu, J. Applied Polymer Science 118, 3351– 3356, (2010).
- [9]. A Doyan, Susilawati, Imawanti, Y.D. Gunawan, E. R., Taufik M., J. Physics, 1097, 1-9, (2017).
- [10]. K. Zakrzewska, Thin Solid Films, 391, 229-238, (2001).
- [11]. R. Jain, N. Jadon, A. Pawaiya, TrAC Trends in Ana. Chemistry, Elsevier, 97, 363-373, (2017).

- [12]. X. Liu, M. Yang, X. Zhu, H. Yang, K. Zhou, D. Pan, J. Mate. science: Mate. inEle., 29, 6098–6104, (2018).
- [13]. M. Zhang, A. Nautiyal, H. Du, J. Li, Z. Liu, X. Zhang, R. Wang, Electro.Acta,357, (10)136877, (2020).
- [14]. N. Velhal, N.D.Patil, G. Kulkarni, S.K. Shinde, N.J. Valekar, H.C. Barshilia, V. Puri, J. Alloys and Compounds, 777, 627-637, (2019).
- [15]. A. Imani, G. Farzi, A. Ltaief, Springer, Int. Nano Lett. 3, Article number: 52, (2013).
- [16]. S. A. Waghule, S. M. Yenorkar, S. S. Yawale and S. P. Yawale, Sens. and Actu. B, 128, 366-373, (2008).
- [17]. Wei Kong, Bo Liu, Bo Ye, Zhongping Yu, HuaWang, GuodongQian, and ZhiyuWang, J. Nanomaterials, Article ID 467083, (2011).
- [18]. X. Zhou, L. Yu, X.W. Lou, Adv. Energy. Mater., 6, 1600451, (2016).
- [19]. H.J. Kharat, K.P. Kakde, P.A. Savale, K. Datta, P. Ghosh, M.D. Shirsat, Polym. Adv.Technol.,18, 397 (2007).
- [20]. L.K. Krehula, J. Stjepanovic, M. Perlog, S. Krehula, V. Gilja, J. T. Sejdic, Z. H. Murgic, Polym. Bull. 76, 1697–1715, (2019).
- [21]. S. H. Pine, J. B. Hendrickson, D. J. Cram, G. S. Hammond Organic chemistry, 4th edn. McGrawHillKogakusha LTD, (1980).
- [22]. R. P. Turcu, D. Bica, L. Vekas, N. Aldea, D. Macovei, A. Nan, O. Pana, O. Marinica, R Grecu, Pop CVL, Romanian Rep Phys 58, 359–367, (2006).
- [23]. E. Pretsch, P. Buhlmann, M. Badertscher,4th Revised and Enlarged Edition,Springer, 283, (2000).
- [24]. R. D. Sakhare, Y. H. Navale, S. T. Navale, V. B. Patil,J. Mate. Science: Mate.Electron.,Springer,28, 11132–11141, (2017).



Photoluminescence Properties of $\text{Cs}_2\text{Ba}(\text{MoO}_4)_2:\text{Eu}^{3+}$ Red Emitting Phosphor

A.S.Khobragade^{1*}, B.V.Tupte², D.H. Gahane¹, S. V. Moharil³

^{1*}Department of Physics, N.H. College, Bramhapuri– 441206, Maharashtra, India

²Department of Physics, SGM College, Kurkheda– 441209, Maharashtra, India

³Department of Physics, PGTD RTMNU, Nagpur-440001, Maharashtra, India

ABSTRACT

$\text{Cs}_2\text{Ba}(\text{MoO}_4)_2:\text{Eu}^{3+}$ phosphor ($x=0.01, 0.03, 0.07$ and 0.09 mole %) molybdate red phosphors had been synthesized using a combustion Method at a temperature 760°C and their photoluminescence characterization was performed. The excitation and emission spectra indicated that this phosphor could be excited successfully by the visible light, and then emitted red light with the peaks positioned at 615 nm . Upon 270 nm UV excitation, this phosphor shows characteristic fluorescence $^5\text{D}_0 \rightarrow ^7\text{F}_j$ ($J = 0, 1, 2, 3, 4$) of the Eu^{3+} ions. The electronic transition located at 615 nm corresponding to $^5\text{D}_0 \rightarrow ^7\text{F}_2$ of Eu^{3+} ions, which is superior than the magnetic dipole transition located at 593 nm corresponding to $^5\text{D}_0 \rightarrow ^7\text{F}_1$ of Eu^{3+} ions. Concentration quenching has been observed for Eu^{3+} concentration $5\text{ mole}\%$. Eu^{3+} doped $\text{Cs}_2\text{Ba}(\text{MoO}_4)_2$ is a promising phosphor for applications in displays and optical devices.

Keywords: *Combustion Method, Crystal Structure, Molybdates, Photoluminescence, Phosphor,*

I. INTRODUCTION

Molybdates are good hosts for phosphors and promising candidates in optical fibers, scintillators, and laser host material applications [1]. The host of molybdate material exhibits strong absorption under n-UV radiation and transfers the absorbed energy from the matrix to the activators, resulting in strong color emission [2]. In particular, the scheelite molybdate type is an excellent matrix of inorganic materials with stable tetrahedral symmetry MOO_4^{2-} group, which is expected to be applied in luminescent materials [3,4]. In 2019, Lim et al. reported the scheelite-type ternary molybdate $\text{NaPbLa}(\text{MoO}_4)_3:\text{Er}^{3+}/\text{Yb}^{3+}$ phosphor, which is found to be an efficient up-conversion material [5]. In 2012, Zhang et al. discovered high efficient red emission $\text{Na}_5\text{La}(\text{MoO}_4)_4:\text{Sm}^{3+}$ compounds and confirmed their applications in n-UV LED [6]. $\text{Cs}_2\text{Ba}(\text{MoO}_4)_2$ is made of layers in the ab plane of corner-sharing BaO_6 octahedra and MoO_4 tetrahedra alternating with CsO_{10} decahedra sharing faces with the BaO_6 octahedra and edges plus corners with the MoO_4 tetrahedra [7]. Eu^{3+} is known to be an efficient activator. Its characteristic energy transfer generates a strong emission with a high color purity [8,9]. Eu^{3+} has excellent PL properties with various host materials. Among these host materials, double molybdate have shown efficient emitting properties. [10,11] These hosts show efficient charge transfers

(CT), because they are transition-metal compounds in their highest oxidation states,^[12] and the intense excitation properties in the near UV–blue region were able to be used in GaInN-based LED phosphors.^[13] In the present work, red-emitting phosphors $\text{Cs}_2\text{Ba}(\text{MoO}_4)_2:\text{xEu}^{3+}$ ($x=1,3,5$ & 7 mole%) were prepared by Combustion Method and Photoluminescence of prepared phosphors is studied,

II. EXPERIMENTAL

The Eu^{3+} activated $\text{Cs}_2\text{Ba}(\text{MoO}_4)_2:\text{xEu}^{3+}$ (where $x = 0.01, 0.03, 0.05$ & 0.07 mole) phosphors were prepared by the combustion synthesis. The starting AR grade materials (99.99% purity) were taken as Cesium Nitrate (CsNO_3), Eu oxide (Eu_2O_3), Barium Nitrate ($\text{Ba}(\text{NO}_3)_2$), Ammonium molybdate ($(\text{NH}_4)_6\text{Mo}_7\text{O}_{24}\cdot 6\text{H}_2\text{O}$) and $(\text{NH}_2\text{CONH}_2)$ were used as the starting materials without further purification and were weighted by stoichiometric ratio. In the present investigation, materials were prepared according to the chemical formula $\text{Cs}_2\text{Ba}(\text{MoO}_4)_2:\text{xEu}^{3+}$ (where $x = 0.01, 0.03, 0.05$ & 0.07 mole). The mixture of reagents was grind together to obtain a homogeneous powder. Eu^{3+} ion was introduced as a $\text{Eu}(\text{NO}_3)_3$ solution by dissolving Eu_2O_3 into a dil. HNO_3 solution. The molar ratio of the rare earth was varied in $\text{Cs}_2\text{Ba}(\text{MoO}_4)_2:\text{xEu}^{3+}$ (where $x = 0.01, 0.03, 0.05$ & 0.07 mole) phosphors relative to the Ba/Cs/Mo ions. For various compositions of the metal nitrates (oxidizers), the amount of urea (fuel) was calculated maintaining total oxidizing and reducing valences of the components equal to unity, so that the heat liberated during combustion is a maximum. After stirring for about 30 min, the precursor solution was transferred to a furnace which was preheated to 760°C . Porous products were obtained. Rare-earth ion doped $\text{Cs}_2\text{Ba}(\text{MoO}_4)_2:\text{xEu}^{3+}$ (where $x = 0.01, 0.03, 0.05$ & 0.07 mole) phosphors were prepared by introducing Eu ion as $\text{Eu}(\text{NO}_3)_3$ solutions with different concentrations, respectively, and the processes were repeated as explained above.

III. RESULT AND DISCUSSION

3.1 X-ray diffraction of $\text{Cs}_2\text{Ba}(\text{MoO}_4)_2$

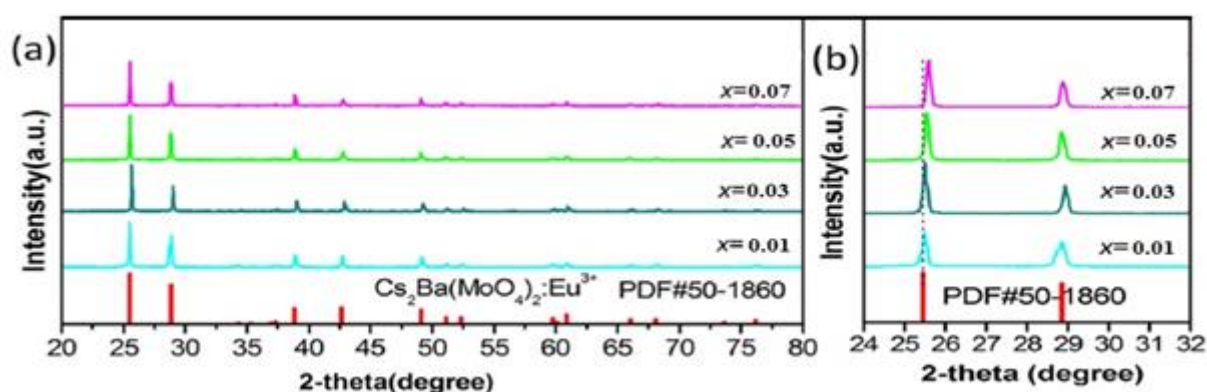


Fig. 1. [a] XRD patterns of $\text{Cs}_2\text{Ba}(\text{MoO}_4)_2:\text{xEu}^{3+}$ (1,3,5 & 7 mole %) phosphors. [b] The magnified view of the peak position between 24 – 32° .

XRD samples of $\text{Cs}_2\text{Ba}(\text{MoO}_4)_2:x\text{Eu}^{3+}$ ($x=1,3,5$ & 7 mole%) phosphor are shown in Figure 1 (a). The diffraction peaks of the formed phosphor are consistent with the standard card of $\text{Cs}_2\text{Ba}(\text{MoO}_4)_2$ (PDF # 50–1860) without any impurity peaks, indicating that doping of Eu^{3+} ions has no obvious effect on the structure of the host. Thus, single-phase phosphors are successfully generated. From the XRD data, we can determine that $\text{Cs}_2\text{Ba}(\text{MoO}_4)_2$ has a rhombohedral structure with lattice parameters $Z = 3$, $a = b = 6.1836 \text{ \AA}$, $c = 23.0636 \text{ \AA}$, and V (unit cell volume) = 763.73 \AA^3 , which is related Space group $R3m$ (166) [14]. When the coordinate number (CN) is 6, the ionic radius of Ba^{2+} is 1.35, which is close to Eu^{3+} ($r = 0.947 \text{ \AA}$, CN = 6). Therefore, the Eu^{3+} ions replace the Ba^{2+} ions in the $\text{Cs}_2\text{Ba}(\text{MoO}_4)_2$ host. The substitution of Ba^{2+} by Eu^{3+} significantly reduces the lattice constants of $\text{Cs}_2\text{Ba}(\text{MoO}_4)_2: \text{Eu}^{3+}$ due to the small radius of Eu^{3+} ions. The result is verified using the Bragg diffraction formula $2d\sin\theta = n\lambda$ ($n\lambda$ is constant). When the interplanar distance d decreases, should be greater. Fig. As shown in 1 (b), XRD samples show a slight shift to the right with increasing concentration of Eu^{3+} ions compared to $\text{Cs}_2\text{Ba}(\text{MoO}_4)_2$'s standard data.

3.2 PL Characteristics of $\text{Cs}_2\text{Ba}(\text{MoO}_4)_2: x\text{Eu}^{3+}$ ($x=1,3,5$ & 7 mole %) Phosphor

The excitation spectrum of $\text{Cs}_2\text{Ba}(\text{MoO}_4)_2:5\text{mol}\%\text{Eu}^{3+}$ phosphor ($\lambda_{\text{em}} = 615 \text{ nm}$) is shown in Fig. 2. The photoluminescence excitation spectrum contains two parts. The first part contains a broad band at a range of 200–325 nm with a center at 270 nm, which belongs to the charge transfer band (CTB) from the fully filled $2p$ orbitals of O^{2-} to the partially filled $4f$ orbitals of Eu^{3+} and $4d$ state of Mo^{6+} ions [15].

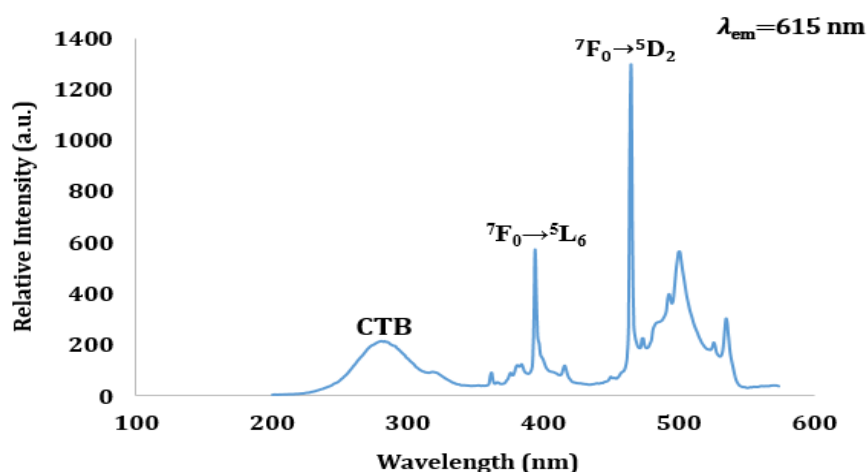


Fig.[2]The excitation spectrum of the $\text{Cs}_2\text{Ba}(\text{MoO}_4)_2:5\text{mol}\%\text{Eu}^{3+}$ phosphor ($\lambda_{\text{em}} = 615 \text{ nm}$).

The second part contains several sharp peaks in the range of 360 nm–600 nm, which belongs to the typical f–f forbidden transitions of Eu^{3+} . These sharp peaks are centering at 396 (${}^7\text{F}_0 \rightarrow {}^5\text{L}_6$) and 465 nm (${}^7\text{F}_0 \rightarrow {}^5\text{D}_2$) [16].

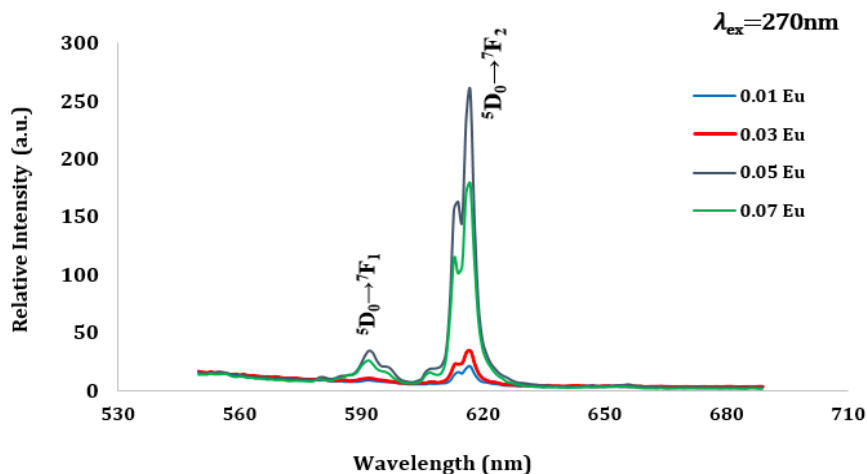


Fig. [3] Emissions spectra of $\text{Cs}_2\text{Ba}(\text{MoO}_4)_2:\text{xEu}^{3+}$ ($\text{x}=1,3,5$ & 7 mole%) phosphor

The emission spectrum of $\text{Cs}_2\text{Ba}(\text{MoO}_4)_2:\text{xEu}^{3+}$ ($\text{x}=1,3,5$ & 7 mole %) is shown in Fig (3). Emission spectrum of $\text{Cs}_2\text{Ba}(\text{MoO}_4)_2:\text{xEu}^{3+}$ phosphor under the excitation of 270 nm consists of narrow and strong emission band at 615 nm and a number of small emission bands. The main emission band should be recognized as the transition from splitting level ${}^5\text{D}_0 \rightarrow {}^7\text{F}_2$ of Eu^{3+} . The emission spectra must be recognized as the transitions ${}^5\text{D}_0 \rightarrow {}^7\text{F}_j$. The spectra which are attributable to the transitions ${}^5\text{D}_0 \rightarrow {}^7\text{F}_j$ consist of some bands according to the number of stark components of ${}^7\text{F}_j$, the number of stark components of Eu^{3+} in $\text{Cs}_2\text{Ba}(\text{MoO}_4)_2$ crystal follows $2J+1$ rule. The bands due to the transition ${}^5\text{D}_0 \rightarrow {}^7\text{F}_1$ is 593nm and transition ${}^5\text{D}_0 \rightarrow {}^7\text{F}_2$ is 615 nm [17]. The hypersensitive band at 615 nm can be attributed to the electric dipole transition ${}^5\text{D}_0 \rightarrow {}^7\text{F}_2$ of Eu^{3+} ions. The emission wavelengths of these $4f-4f$ transitions are only moderately influenced by way of the environment of the lanthanide ions since the partially filled $4f$ shell is properly shielded by the filled $5s$ and $5p$ orbitals [18, 19]. In PL emission, we have observed that the luminescence intensity increased with the increasing Eu^{3+} concentration.

Effect of Eu^{3+} concentration on the red emission of $\text{Cs}_2\text{Ba}(\text{MoO}_4)_2:\text{xEu}^{3+}$ ($\text{x}=1,3,5$ & 7 mole%) phosphors

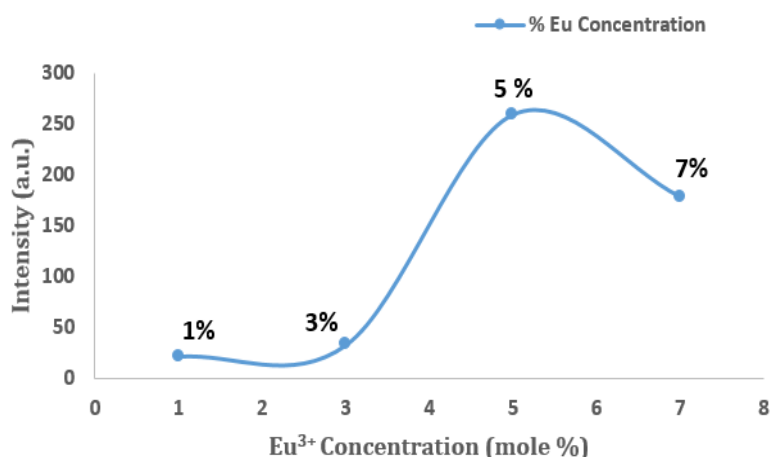


Fig.[4]. Luminescence intensity of $\text{Cs}_2\text{Ba}(\text{MoO}_4)_2:\text{xEu}^{3+}$ ($\text{x}=1,3,5$ & 7 mole %) as function of Eu^{3+} concentration.

Generally speaking, the doping concentration of luminescent centers has a significant effect on the phosphor performance. Therefore, it is necessary to confirm the optimum doping concentration. For the $\text{Cs}_2\text{Ba}(\text{MoO}_4)_2:\text{xEu}^{3+}$ ($\text{x} = 0.01, 0.03, 0.05$ & 0.07 mole) phosphors, the effect of Eu^{3+} doping concentration on the relative intensity of the electric dipole transition (${}^5\text{D}_0 \rightarrow {}^7\text{F}_2$) is shown in the inset of Fig. 4 As can be seen, the emission intensity initially increases, then reaches a maximum at 5 mole % Eu^{3+} , and finally decreases with further increasing Eu^{3+} doping concentration. Thus, the optimal doping concentration of Eu^{3+} in $\text{Cs}_2\text{Ba}(\text{MoO}_4)_2:\text{xEu}^{3+}$

IV. CONCLUSION

In summary, Double Molybdate $\text{Cs}_2\text{Ba}(\text{MoO}_4)_2:\text{xEu}^{3+}$ ($\text{x} = 0.01, 0.03, 0.05$ and 0.07 mole) phosphors were synthesized successfully by Combustion method. XRD patterns show the prepared samples are single-phase. An intense broad band from 250 to 450 nm, which matches well with the emission wavelength of near-UV LEDs chips, is observed in the excitation spectrum. $\text{Cs}_2\text{Ba}(\text{MoO}_4)_2:\text{xEu}^{3+}$ shows an intense red emission at 617 nm under the excitation of 270 nm. The optimal doping concentration of Eu^{3+} in $\text{Cs}_2\text{Ba}(\text{MoO}_4)_2:\text{xEu}^{3+}$ is about 5 mole % and the energy transfer type among Eu^{3+} ions in $\text{Cs}_2\text{Ba}(\text{MoO}_4)_2:\text{xEu}^{3+}$ phosphors is exchange interaction. Therefore, the $\text{Cs}_2\text{Ba}(\text{MoO}_4)_2:\text{xEu}^{3+}$ red phosphors may have a potential application for lamp industry and display devices.

V. REFERENCES

- [1]. A.A. Marques, R. Künzel, N.K. Umisedo, R.M. Latini, E.M. Yoshimura, E. Okuno, J. Alloys Compd. 735 (2017) 707.
- [2]. G.S. Yi, B.Q. Sun, F.Z. Yang, D.P. Chen, Y.X. Zhou, J. Cheng, Chem. Mater. 7 (2002) 2910.
- [3]. D. Peng, Y. Jae Su, RSC Adv. 74 (2015) 60121.
- [4]. Y.B. Hua, J.S. Yu, J. Alloys Compd. 783 (2018) 969.
- [5]. C.S. Lim, A.S. Aleksandrovsky, V.V. Atuchin, M.S. Molokeyev, A.S. Oreshonkov, J. Alloys Compd. 9 (2019) 111.
- [6]. Y. Zhang, L. Xiong, X. Li, J. Guo, Z. Wang, Mater. Sci. Eng., B 177 (2012) 341.
- [7]. A.L. Smith, N. de Zoete, M. Rutten, L. van Eijck, J.-C. Griveau, E. Colineau, Inorg. Chem. 59 (2020) 13162.
- [8]. He, X.; Zhou, J.; Lian, N.; Sun, J.; Guan, M. , J. Lumin. 2010, 130, 743–747.
- [9]. Stambouli, W.; Elhouichet, H.; Gelloz, B.; Férid, M. J. Lumin. 2013, 138, 201–208.
- [10]. Macalik, L.; Tomaszewski, P. E.; Lisięcki, R.; Hanuza, J. J. Solid State Chem. 2008, 181, 2591–2600.
- [11]. Loiko, P. A.; Yumashev, K. V.; Kuleshov, N. V.; Pavlyuk, A. A. Appl. Phys. B: Lasers Opt. 2012, 106, 663–668.

- [12]. Daub, M.; Lehner, A. J.; Hoppe, H. A. Dalton Trans. 2012, 41, 12121–8.
- [13]. Wang, Z.; Liang, H.; Wang, Q.; Chen, M.; Gong, M.; Su, Q. Phys. Status Solidi A 2009, 206, 1589–1593.
- [14]. A.L. Smith, N. de Zoete, M. Rutten, L. van Eijck, J.-C. Griveau, E. Colineau, Inorg. Chem. 59 (2020) 13162
- [15]. Y.B. Hua, J.S. Yu, J. Alloys Compd. 783 (2018) 969.
- [16]. J. Wang, M. Song, H.J. Seo, J. Lumin. 87 (2020) 117185.
- [17]. Rainho JP, Carlos LD, Rocha J. Journal of Luminescence, Elsevier, Science Direct. 2000 May; 87–89:1083-6.
- [18]. G. Blasse, A. Bril, and W. C. Nieuwpoort, J. Phys. Chem. Solids 27(10), 1587–1592 (1966).
- [19]. K. Binnemans, Chem. Rev. 109(9), 4283–4374 (2009).



Ultrasonic Velocity, Adiabatic Compressibility, Intermolecular Free Length and Other Acoustical Parameters of Leaf Extract Solution of *Cymbopogon Citratus*

S. S. Kamble¹, S. R. Aswale², S. S. Aswale²

¹Department of Chemistry, Arts, commerce and Science College, Maregaon-445303, Maharashtra, India

²Department of Chemistry, Lokmanya Tilak Mahavidyalaya, Wani-445304, Maharashtra, India

ABSTRACT

Ultrasonic Velocity, density, viscosity have been measured experimentally for the solution of leaf extract of *Cymbopogon Citratus* in 50% ethyl alcohol with various concentrations at 298.15 K, 303.15 K, 308.15 K keeping constant frequency of 4 MHz. As the acoustical parameters like adiabatic compressibility, intermolecular free length, relative association, relaxation time, specific acoustic impedance would prove to be more useful to predict and confirm the molecular interactions, these have been determined by measuring the Ultrasonic Velocity, density, viscosity of the prepared solution. A variation in these parameters will provide a strong information regarding the molecular interactions taking place in the solution. Ultrasonic velocity together with density and viscosity data will furnish a wealth of information about the interactions between ions, dipoles and hydrogen bonding. In the present study it is observed that ultrasonic velocity increases with concentration due to solvation process.

Keywords: Ultrasonic velocity, Adiabatic compressibility, Intermolecular free length.

I. INTRODUCTION

Ultrasonic velocity measurements and other acoustical parameters of liquid mixtures are the powerful technique in understanding the chemical nature and the molecular interactions [1-4]. Many researchers used ultrasonic velocity measurement for studying solute-solvent interaction in number of systems including organic liquid, dilute solutions in organic acid and complexes [5-7]. Ultrasonic velocity in liquids and liquid mixtures provide valuable information about their physico-chemical properties and the nature of molecular interactions in them. The structure, nature and prevailing conditions of solvent and solute plays an important role on resulting properties and interactions occurring in the solution [8-10]. Our country is very well known for Ayurveda, in the Ayurveda medicines are largely made up from plants, herbs. One of such herbs is *Cymbopogon Citratus* which is also known as lemongrass. It is known for its antifungal nature. The solution of leaf extract of *Cymbopogon Citratus* in distilled water and 50% ethanol solvent is studied at 4 mhz for the concentration of 1%, 0.5%, 0.25%, 0.125% at 298.15K, 303.15K, 308.15K. Here the effect of concentration at

different temperature on molecular interaction will be predicted which may be helpful for predicting the reactivity of the extract.

II. METHODOLOGY

The leaf extract used in this study was of analytical range. For the preparation of solution 50% ethyl alcohol solvent was used. A special thermostatic water bath arrangement was made to maintain constant temperature. 1%, 0.5%, 0.25%, 0.125% solutions of leaf extract of cymbopogon citratus was Prepared by taking accurate weights on electronic digital balance (Model CB/CA/CT-Series, Contech having accuracy ± 0.0001 g.) The ultrasonic velocity of the 1%, 0.5%, 0.25%, 0.125% solutions of leaf extracts of cymbopogon citratus was measured with the Multifrequency ultrasonic interferometer (Model M-83, Mittal Enterprises) at 4mhz with an accuracy of ± 2 m/s. All the readings were taken at 298.15 K, 303.15K, 308.15K. The viscosity was measured by using Ostwald's viscometer and the density of the solution was measured by using Digital densitometer (DMA-35, Anton paar).

III. COMPUTATION

By using ultrasonic velocity following ultrasonic parameters are calculated.

Adiabatic compressibility -

$$\beta = 1/v^2 d$$

Where, v - velocity of solution,

d - density of liquid

Intermolecular free length -

$$L_f = K\sqrt{\beta_s}$$

Where, K - temperature dependent known as Jacobson's constant

Specific acoustic impedance -

$$Z = v \times d_s$$

Relative association

Sr. No.	Conc. (%)	Temp. (K)	Density (d_s) (Kg m^{-3})	Velocity (v_s) (m/s)	Viscosity (η) ($\text{Kg m}^{-1}\text{s}^{-2}$)
1	1%	298.15	930.6	1807.7	23.50 E ⁻⁴
		303.15	919.5	1755.1	21.80 E ⁻⁴
		308.15	919.2	1750.7	17.42 E ⁻⁴
2	0.5%	298.15	936.7	1801.2	18.30 E ⁻⁴
		303.15	929.4	1767.0	20.50 E ⁻⁴
		308.15	928.9	1751.2	12.44 E ⁻⁴
3	0.25%	298.15	924.5	1755.8	21.27 E ⁻⁴

		303.15	927.4	1744.1	21.51 E ⁻⁴
		308.15	927.0	1717.1	16.85 E ⁻⁴
4	0.125%	298.15	925.0	1750.2	18.12 E ⁻⁴
		303.15	921.8	1701.1	16.05 E ⁻⁴
		308.15	918.4	1687.1	12.85 E ⁻⁴

$$R_A = d_s / d_0 [v_0 / v_s]^{1/3}$$

Where, v_0 - ultrasonic velocity of solvent

v_s - ultrasonic velocity of solution

Relaxation time $-\tau = 4/3 \beta_s \times \eta$

IV. RESULT AND DISCUSSION

Table 1: Density, Viscosity and Velocity (at frequency 4 MHz) of cymbopogon citratus leaf extract solution in 50% ethanol solvent.

Table 2. Acoustic parameters of Cymbopogon leaf extract solution in 50% Ethyl Alcohol at 4 MHz.

Sr.N o.	Conc . (%)	Temp. (K)	Adiabatic Compressibiliy	Specific Acoustic Impedenc e Kg M ⁻² S ⁻¹	Intermolecular free length	Relative Association	Relaxation time
1.	1%	298.15	3.281 E ⁻¹⁰	1697127	3.755E ⁻¹¹	2.997 E ⁻¹	7.55 E ⁻¹³
		303.15	3.394 E ⁻¹⁰	1648599	3.823 E ⁻¹¹	2.983 E ⁻¹	6.330 E ⁻¹³
		308.15	3.467 E ⁻¹⁰	1629200	3.899 E ⁻¹¹	2.979 E ⁻¹	5.023 E ⁻¹³
2.	0.5%	298.15	3.391 E ⁻¹⁰	1686696	3.761 E ⁻¹¹	3.055 E ⁻¹	8.00 E ⁻¹³
		303.15	3.442 E ⁻¹⁰	1644016	3.850 E ⁻¹¹	3.045 E ⁻¹	7.220 E ⁻¹³
		308.15	3.51 E ⁻¹⁰	1626689	3.923 E ⁻¹¹	3.037 E ⁻¹	5.807 E ⁻¹³
3.	0.25 %	298.15	3.524 E ⁻¹⁰	1652521	3.783 E ⁻¹¹	2.986 E ⁻¹	9.573 E ⁻¹³
		303.15	3.544 E ⁻¹⁰	1617478	3.907 E ⁻¹¹	3.071 E ⁻¹	8.138 E ⁻¹³
		308.15	3.658 E ⁻¹⁰	1591751	4.005 E ⁻¹¹	3.092 E ⁻¹	8.197 E ⁻¹³
4.	0.125 %	298.15	3.533 E ⁻¹⁰	1623260	3.852 E ⁻¹¹	3.092 E ⁻¹	8.456 E ⁻¹³
		303.15	3.748 E ⁻¹⁰	1568166	3.960 E ⁻¹¹	3.013 E ⁻¹	8.00 E ⁻¹³
		308.15	3.823 E ⁻¹⁰	1550015	4.001 E ⁻¹¹	3.119 E ⁻¹	6.533 E ⁻¹³

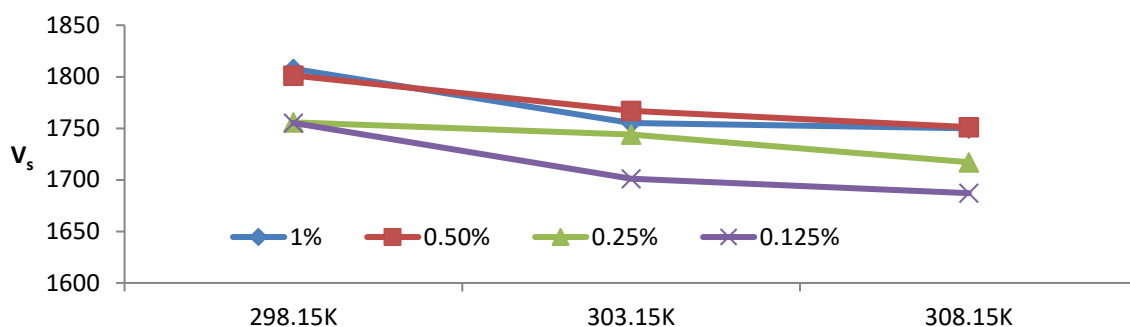


Fig.1. Variation of ultrasonic velocity with temp. at diff. conc.in 50%alc. solvent

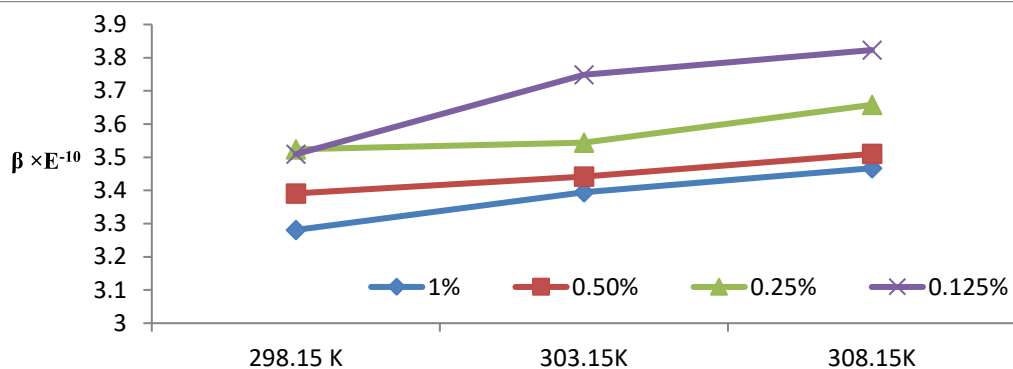


Fig.2.-Variation of Adiabatic compressibility with temp. at diff. conc.in 50%alc. solvent.

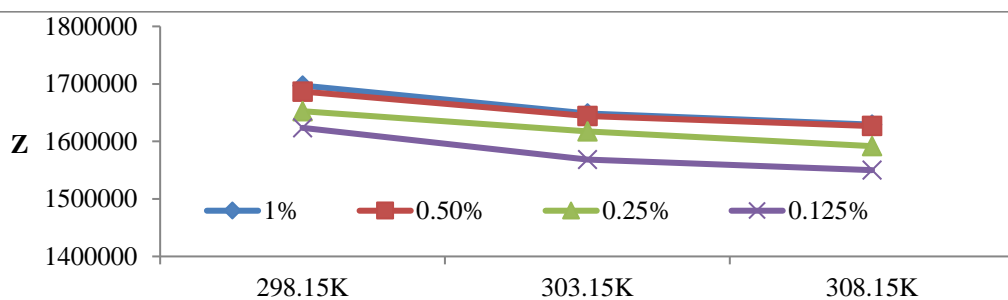


Fig.3 Variation of Specific acoustic impedance with temperature at diff. conc. conc.in 50%alc. solvent.

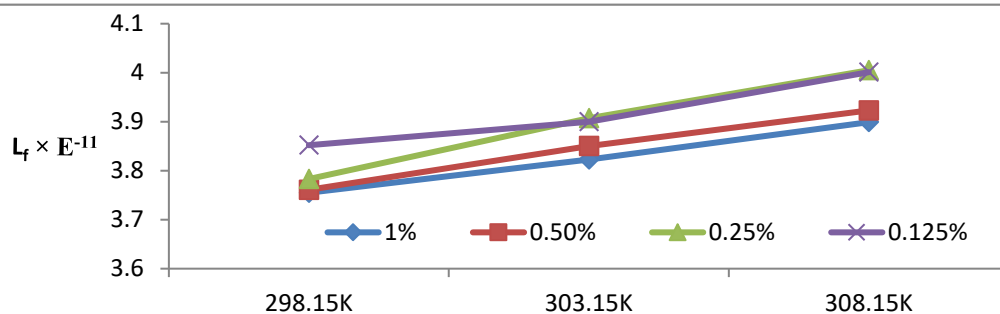


Fig.4 . Variation of Intermolecular free length with temperature at various conc. conc.in 50%alc. solvent.

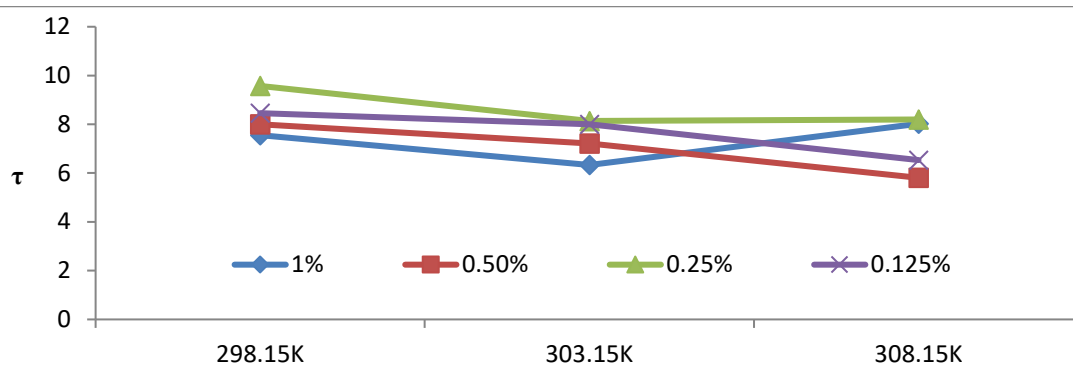


Fig.6. Variation of Relaxation time with temperature at diff. conc.in 50%alc. solvent.

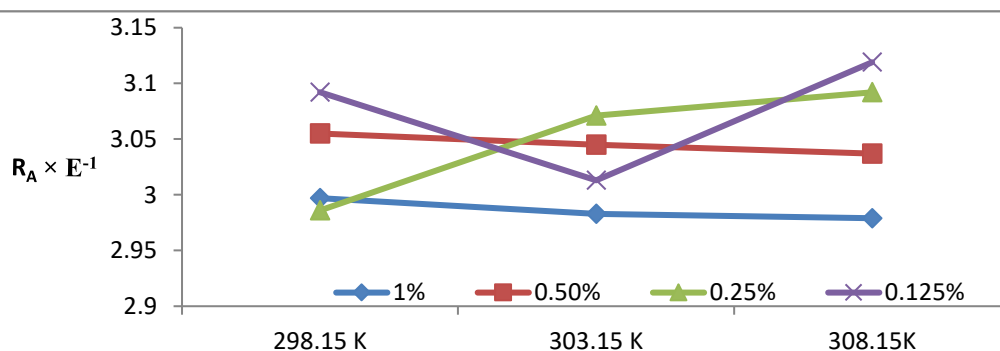


Fig. 5a.-Variation of Relative Association with temp.at various conc.in 50%alc. solvent.

The ultrasonic velocity of 1%, 0.5%, 0.25%, 0.125% cymbopogon citratus leaf extract solution in 50% ethanol was measured at 298.15 K, 303.15K, 308.15K at 4 MHz frequency. From table no.1 and fig.no1. it is observed that at different concentrations the ultrasonic velocity increases with increase in concentration. The ultrasonic velocity increases here with increase in concentration this is due to the salvation process of solute by two different solvent molecules like water and ethanol.

From table no.2 and fig.2 it is observed that Adiabatic compressibility decreases with increase in concentration. This can be explained as the solvent molecules strongly associate through hydrogen bonding with leaf extract molecules. Therefore, bonds between solute- solvent strengthen the intermolecular forces resulting in decrease in adiabatic compressibility with increase in concentration.

From table 2 and figure 3 it is observed that there is increase in acoustic impedance with concentration shows the increase in molecular packing in the medium which gives the possibility of molecular interaction due to hydrogen bonding between solute- solvent.

“The intermolecular free length is the distance between the surfaces of the neighboring molecules”. Here the intermolecular free length decreases with increase in concentration it indicates that as the concentration of the system increases (table 2, fig.4.) at particular temperature, one solute molecule and two solvent molecules arrange themselves resulting into a closed packed structure. Due to this closed packed structure, distance between these molecules decreases and intermolecular free length decreases.

Relative association is a measure of extent of association of components in the medium. It is a property of understanding the molecular interaction in liquid mixtures and solutions. As discussed, relative association depends on either of breaking of solvent molecules on addition of solute to it or the salvation of ions that are present. From table 2 and fig.5 it is observed that relative association decreases with increase in concentration this is due to breaking up of associated solvent molecules on addition of solute.

From table 2 and fig.6 it is seen that acoustical relaxation time increases with increase in concentration nonlinearly this may be due to presence of two solvent molecules around the solute molecules.

V. CONCLUSION

From the above discussion it is observed that molecular association between *Cymbopogon citratus* leaf extract and solvent may arise from intermolecular hydrogen bonding which supports the molecular association occurring in the solution.

VI. REFERENCES

- [1]. Praveen S, Shukla D, Singh S, Singh K.P, Shukla J.P., ultrasonic velocity, density, viscosity and their excess parameters of the binary mixtures of tetrahydrofuran with methanol and o- cresol at varying temperatures. *App Acous.*, 70 (3) (2009) 507.
- [2]. Umadevi M., Keshavswamy R., Rathina K., Mahalaxmi R., Studies on liquid-liquid interactions of some ternary mixtures by density ,viscosity and ultrasonic speed measurements *J. Mol. Liq.*, 219 (2016) 820-823.
- [3]. Nayak N., Aralaguppi M.I., Aminabhavi T.M., Density, viscosity, refractive index and speed of sound in the binary mixture of 1,4- dioxane + ethyl acetoacetate, + diethyl oxalate, + diethyl phthalate, or + dioctyl phthalate at 298.15, 303.15, 308.15K. *J.Chem. Engr.DT.*, 48(2003)1489-1494.
- [4]. Steele W. V., Chirico R.D., Cowell A.B., Knipmeyer S.E., Nguyen A., Thermodynamic properties and ideal- gas enthalpies of formation for methyl benzoate, ethyl benzoate, (R) – (+)- limonene, tert-amyl methyl ether, trans- crotonaldehyde, and diethylene glycol. *J.Chem.Engr.DT.*,47 (4) (2002) 667- 688.
- [5]. Reis J.C.R., Santos A.F.S., Disas F.A., Lampreia I.M.S., Correlated volume fluctuations in binary liquid mixtures from isothermal compressions at 298.15K.*Chem.Phys.Chem.*, 9 (2008)1178-1188.
- [6]. Khansanshin T.S., Shchemelev A.P., Srivastava T.N., Singh R.P., Swaroop B., The thermodynamic properties of n-tetradecane in liquid state *Ind.J.Pure Phys.*,21 (1983) 67-72.
- [7]. Kumar A., Srivastava U., Singh A.K., Srivastava U., Singh A.K., Shukla R.K., Sound velocity and isentropic compressibility of binary liquid systems from various theoretical models at temperature range 293.15 to 313.15 K. *Can. Chem. Trans.*4 (2) (2016) 157-167.
- [8]. Jayakumar S., Karunanidhi N., Kannapan V., Ultrasonic study of molecular interactions in binary liquid mixtures. *Indian J. Pure & Appl. Phy.*34 (1996) 761-764.

- [9]. Kulkarni S.S. and Khadke U.V., Effects of solvents on Ultrasonic velocity and Acoustic parameters of PolyvinilideneFlouride Solutions. Indian j.mater.sci.2 (2016) 1-6.
- [10]. Hazare R.S., Aswale S.S, Aswale S.R., Relative association, specific acoustic impedence, and free volume of antibiotic cefotaxime sodium. Int.j.curr.eng.sci.res. 6 (1) (2019) 332-337.



Synthesis and Optical Properties of Lanthanum Doped Nanocrystalline Tin Dioxide Thick Films

L.P.Chikhale^{*1}, F.I.Shaikh², A.V.Rajgure³, S.S.Suryavanshi⁴

^{*1}Department of Physics, Venkatesh Mahajan Senior College, Osmanabad, Maharashtra, India

²Department of Physics, Government Institute of Forensic Science, Aurangabad, Maharashtra, India

³G.S.Tompe Arts, Commerce & Science College, Chadur Bazar, Dist-Amravati 444704, Maharashtra, India

⁴Department of Physics, Solapur University, Solapur, Maharashtra, India

ABSTRACT

To study the effect of pure and La doped tin dioxide thick films on their optical properties and the oxide powders were prepared by the chemical co-precipitation method. The thick films of La doped SnO₂ were prepared by the screen-printing technique and further sintered at 750° C. The samples were characterized by X-ray diffraction (XRD), thermo gravimetric-differential thermal analyzer (TG-DTA) and Fourier transformation infrared spectroscopy (FTIR) and UV-VIS techniques. XRD studies reveal formation of fine nanocrystalline material. The particle size of sintered powder of pure and La (2 and 4 mol %) doped SnO₂ powders were 15, 10 and 9 nm respectively. These results were further confirmed by FTIR studies. Crystallite size was observed to vary from 16 to 9 nm as the La content increased from 0 to 4 mol%, suggesting the prevention of crystal growth with La doping. It was evident from the absorption spectra that the absorbance increases with the dopant concentration. Optical band gap was estimated by using Tauc relation which decreases with the increase in La content confirming the size reduction as a result of La doping. Raman spectroscopic measurements showed that the broadening of intense peak observed at 647 cm⁻¹ with La doping, indicating that the La ions are substituted at the Sn sites in SnO₂ lattice.

Keywords: Tin oxide; Thick film; Screen printing; Lanthanum

I. INTRODUCTION

In catalyst, it is desirable to produce materials with nanometric-scale structures to obtain improvement in some specific properties [1]. To prepare active nanocrystalline powders, several chemical techniques have been investigated and reported in the literature. Among the various methods of preparation of nanostructured SnO₂, polymeric precursor method [2], sol-gel method [3], hydrothermal method [4], electrospinning technique [5], co-precipitation [6], chemical vapor deposition (CVD)[7], sol-gel method[8], combustion method[9], spray pyrolysis technique [10] etc. are popular. Many workers proposed the use of nanocrystallite of SnO₂ in thin film form and reported that SnO₂ thin films can have maximum gas sensitivity only if the crystallite size of the film is comparable with its space-charge thickness which is below 10 nm [14].

The purpose of the present work is to investigate the effect of La doping SnO₂ on its structural, morphological and optical properties. We have chosen La as dopant material as it is catalytically active material and has been investigated by several researchers [15].

II. EXPERIMENTAL PROCEDURE

The details of the preparation of undoped and doped SnO₂ powder as well as thick film technique are described elsewhere [16].

2.1. Characterization:

The thermal analysis of the prepared powder was obtained by thermo gravimetric differential thermal analysis (TG-DTA) performed on SDT Q600 V20.9 Build20 instruments in ambient air with increasing the temperature at a rate of 10° C /min. The structural properties of pure and La doped SnO₂ thick films are studied by computer controlled X-ray diffractometer (BRUKER AXS D8-Advanced) using Cu-K α ($\lambda=1.54056$ Å) radiation. The scanning angle 2θ was in the range of 20° to 90°. The average crystallite size (D) of sintered pure and La doped SnO₂ was estimated using the Scherrer equations as follows:

$$D = \frac{0.9\lambda}{\beta \cos\theta} \dots\dots\dots (2)$$

Where, λ , β and θ are the X-ray wavelength, the full width at half maximum (FWHM) of the diffraction peak, and the Bragg's diffraction angle respectively.

The UV-absorption spectra of pure SnO₂ and La doped SnO₂ were performed using JASCO (Model V-670) UV-VIS-NIR spectrophotometer. The spectra were taken in the wavelength range of 200-1000 nm for studying the optical band-gap of the samples. FTIR spectroscopic measurements of sample powder sintered at 750°C in air has been studied in the wave number range of 400-4000 cm⁻¹, using JASCO Model FTIR -6100 type spectrophotometer for studying the chemical groups on the surface of samples.

III. RESULTS AND DISCUSSION

3.1. TGA and DTA analysis:

Fig. 1 shows the TG-DTA curves of as prepared powder for L2. Significant weight loss was observed from room temperature to 300°C. The weight change up to temperature of 300°C was due to release of adsorbed water, crystal water and other gases which was also observed as weak endothermic peak in DTA curve. Above 600°C there is no weight loss indicating phase formation of L2. From the TGA-DTA studies we have opted 750°C as a optimum sintering temperature for pure and La doped SnO₂ samples.

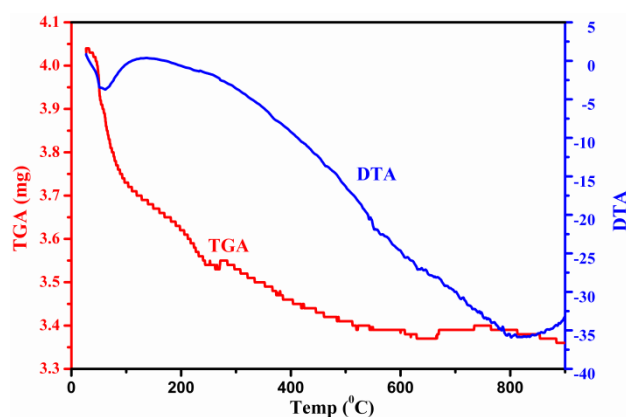


Fig.1 TGA-DTA profile of the precipitate precursor of pristine SnO₂.

3.2. XRD analysis:

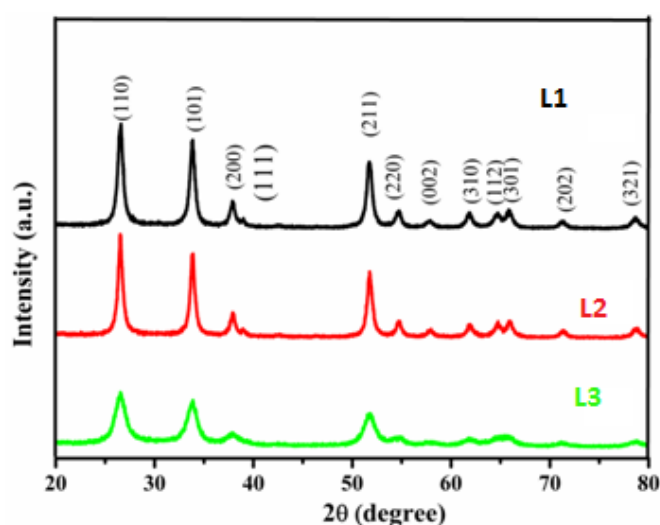


Fig. 2 XRD patterns of undoped (L1) , 2 mol % La-doped (L2) , and 4 mol % La-doped SnO₂ (L3).

Fig. 2 show the XRD patterns of SnO₂ thick films with different La concentrations. All patterns exhibit peaks corresponding to the rutile structure of polycrystalline SnO₂ with the maximum intensity peak corresponding to (110) planes and are indexed on the basis of joint committee on powder diffraction standards (JCPDS) data [17]. However, the relative intensity of the peaks decreases with an increase in the La content. It is also observed that the full width at half maxima (FWHM) of the diffraction peaks increases with increasing La content which is in good agreement with the earlier studies [18]. The increase in FWHM along with a decrease in peak intensity suggests that La incorporation into the SnO₂ lattice results in a decrease in crystallite size of the films. The decrease in the crystallite size is further supported by the decrease in the sharpness of the peaks with the incorporation of La. Pure SnO₂ has an average crystallite size of 15nm, while 2 mol % La doped SnO₂ shows reduced crystallite size of 10 nm and 8 nm in case of 4mol % La-doped SnO₂.

3.3. Optical analysis:

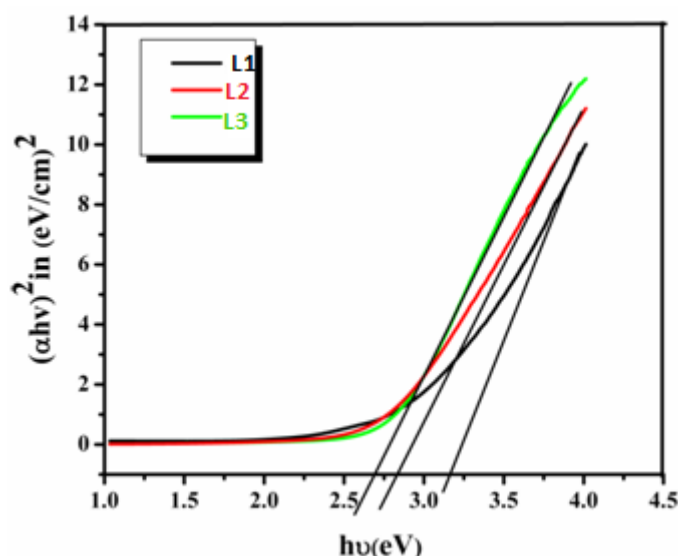


Fig. 3 UV spectra of undoped (L1) , 2 mol % La-doped (L2) , and 4 mol % La-doped SnO₂ (L3)

UV absorption spectra were carried out on the JASCO Model V-670 Spectrophotometer in the wavelength range 200-1000nm. Fig.3 shows the optical absorbance spectra for of pure and La doped SnO₂ powder samples sintered at 750°C in the wavelength range 200–1000 nm. The nature of the transition is determined by using the relation:

$$\alpha = \text{const} \times \frac{(hv - E_g)^{1/2}}{hv} \dots\dots\dots (2)$$

Where, E_g is the optical band gap energy which was calculated from $(\alpha hv)^2$ versus energy (hv) plot, A is a constant, α is the absorption coefficient, hv is the photon energy taken from the UV-spectra. The plot of $(\alpha hv)^2$ as a function of the energy (hv) of the incident radiation has been shown in Fig. 3. It is found that the nature of the plot is nonlinear indicating absence of indirect transition. The band edge can be evaluated from the intercept of the extrapolated linear part of the curve with the energy axis. The corresponding value of the optical band gap (E_g) for pristine SnO₂ is found to be 3.17 eV. La doping also has influence on optical band gap of the La-doped SnO₂ films. Data from this study showed the direct optical band gap of La-doped SnO₂ thick films for La-doping levels in the range 0 to 4 mol% were found to be 3.17 to 2.69 eV respectively (Fig. 3). It should be noted that reduction in optical band gap was observed after La doping which is consistent with the direct optical band gap of various La doped SnO₂ thick films reported by [19]. The reason for optical band gap reduction might be due to the appearance of the La-Sn metallic compounds, as seen in XRD analysis results.

3.4. FTIR analysis

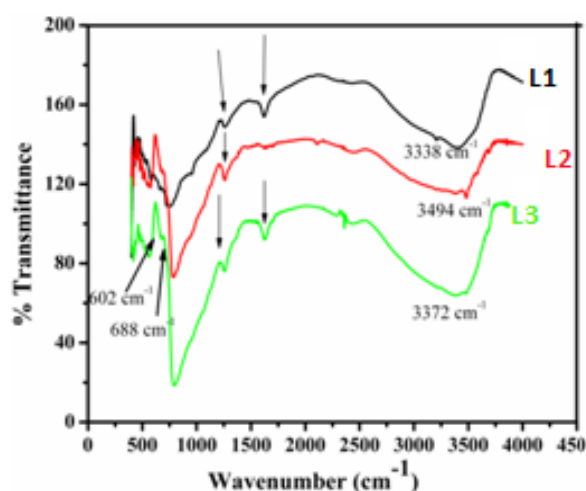


Fig. 4 Shows the FTIR spectrum for studying the chemical composition on the surface of the samples L1, L2, and L3 sintered at 750°C in air after mixing in KBr powder. All FTIR spectra contain absorption bands in the range of 2500–3500 cm^{-1} associated with water and absorption of Sn-OH groups. The peak which appeared at 602 cm^{-1} relates to the terminal oxygen vibration of Sn-OH, while the peak appearing at 688 cm^{-1} is due to the O-Sn-O bridge functional group of SnO₂ (L1). The broad band centered on 3250 cm^{-1} region is due to the stretching vibration of O-H (Sn-OH) bond [20]. Addition of dopants changed the positions of two characteristic vibration peaks of the Sn-O bond in SnO₂ [21]. The sample doped with La (L2) changed the positions of these two peaks to 776 cm^{-1} and 1200 cm^{-1} , respectively. The positions of these two peaks changed to 741 cm^{-1} and 957 cm^{-1} , respectively in the La doped SnO₂ (L3). The additional absorption peaks were observed with La addition, indicating its homogeneous dispersion in the support material.

IV. CONCLUSIONS

The films of co precipitation synthesized undoped and La doped SnO₂ were successfully deposited using screen printing technique. The XRD, UV-Vis, FTIR spectroscopic analysis confirmed that the La doping in SnO₂ can significantly affects particle size and band gap of La doped SnO₂. These results indicate that the La doped SnO₂ material can be used as a potential candidate for fabricating the optoelectronic devices.

V. REFERENCES

- [1]. D. Wang, J. Jin, D. Xia, Q. Ye, J. Long, The effect of oxygen vacancies concentration to the gas-sensing properties of tin dioxide-doped Sm. *Sensors and Actuators B* 66 (2000) 260–262
- [2]. A.P. Maciel, P.N. Lisboa-Filho, E.R. Leite, C.O. Paiva-Santos, W.H. Schreiner, Y. Maniette, E. Longo, Microstructural and morphological analysis of pure and Ce-doped tin dioxide nanoparticles, *Journal of the European Ceramic Society* 23 (2003) 707–713.

- [3]. G. T. Ang, G. Hoon Toh, M. Z. Abu Bakar, A. Z. Abdullah, M. R. Othman. High sensitivity and fast response SnO₂ and La-SnO₂ catalytic pellet sensors in detecting volatile organic compounds, *Process Safety and Environmental Protection* 89 (2011) 186–192.
- [4]. P. Sun, Y. Cao, J. Liu, Y. Sun, J. Ma, G. Lu. Dispersive SnO₂ nanosheets: Hydrothermal synthesis and gas-sensing properties, *Sensors and Actuators B* 156 (2011) 779–783.
- [5]. H. Zhang, Z. Li, L. Liu, X. Xu, Z. Wang, W. Wang, W. Zheng, B. Dong. Enhancement of hydrogen monitoring properties based on Pd-SnO₂ composite nanofibers, *Sensors and Actuators B* 147 (2010) 111–115.
- [6]. J. Zhang, S. Wang, Y. Wang, M. Xu, H. Xia, S. Zhang, W. Huang, X. Guo, S. Wu. Facile synthesis of highly ethanol sensitive SnO₂ nanoparticles, *Sensors and Actuators B* 139 (2009) 369–374.
- [7]. H. T. Feng, R. F. Zhuo, J. T. Chen, D. Yana, J. J. Feng, H. J. Li, S. Cheng, P. X. Yan. Axial periodical nanostructures of Sb-doped SnO₂ grown by chemical vapor deposition, *Physica E* 41 (2009) 1640–1644.
- [8]. M. Hubner, S. Hafner, N. Barsan, U. Weimar. The influence of Pt doping on the sensing and conduction mechanism of SnO₂ based thick film, *Sensors Procedia Engineering* 25 (2011) 104 – 107.
- [9]. A. Ayeshamariam, C. Sanjeeviraja, M. Jayachandra. Synthesis, characterization and gas sensing properties of SnO₂ nanoparticles, *International Journal of Chemical and Analytical Science* 2(6) (2011) 54-61.
- [10]. V. Brinzari, G. Korotcenkov, V. Golovanov, J. Schwank, V. Lantto, S. Saukko, Morphological rank of nano-scale tin dioxide films deposited by spray pyrolysis from SnCl₄.5H₂O water solution, *Thin Solid Films* 408 (2002) 51–58.
- [11]. Z. Wang, L. Liu. Synthesis and ethanol sensing properties of Fe doped SnO₂ nanofibers, *Materials Letters* 63 (2009) 917–919.
- [12]. K. Galatsis, L. Cukrov, W. Wlodarski, P. McCormick, E. Comini, G. Sberveglieri. p- and n-type Fe-doped SnO₂ gas sensors fabricated by the mechanochemical processing technique, *Sensors and Actuators B* 93 (2003) 562–565.
- [13]. S. Chakraborty, A. Sen, H.S. Maiti, Selective detection of methane and butane by temperature modulation in iron doped tin oxide sensors, *Sensors and Actuators B* 115 (2006) 610–613.
- [14]. S. Bose, S. Chakrabortya, B.K. Ghoshb, D. Dasc, A. Sena, H.S. Maitia, Methane sensitivity of Fe-doped SnO₂ thick films, *Sensors and Actuators B* 105 (2005) 346–350.
- [15]. L.A. Patil, D.R. Patil, Heterocontact type CuO-modified SnO₂ sensor for the detection of a ppm level H₂S gas at room temperature, *Sensors and Actuators B* 120 (2006) 316–323.
- [16]. L.K. Bagal, J.Y. Patil, I.S. Mulla, S.S. Suryavanshi, Influence of Pd-loading on gas sensing characteristics of SnO₂ thick films, *Ceramics International* 38 (2012) 4835–4844.
- [17]. JCPDS Data Card No.14-4145.
- [18]. S. Rani, S. C. Roy, M.C. Bhatnagar. Effect of Fe doping on the gas sensing properties of nano-crystalline SnO₂ thin films, *Sensors and Actuators B* 122 (2007) 204–210.
- [19]. N. Timonah, C. Yang, L. Sun, Structural, optical and electrical properties of Fe doped SnO₂ fabricated by sol-gel dip coating technique, *Materials Science in Semiconductor Processing* 13 (2010) 125–131.

- [20]. M.V. Vaishampayan, R.G. Deshmukh, P.Walke, I.S. Mulla, Fe-doped SnO₂ nonmaterial: A low temperature hydrogen sulfide gas sensor, *Materials Chemistry and Physics* 109 (2008) 230–23416.
- [21]. M. M. Bagheri-Mohagheghi, N. Shahtahmasebi, M.R. Alinejad, A. Youssefi, M. Shokooh-Saremi, Fe-doped SnO₂ transparent semi-conducting thin films deposited by spray pyrolysis technique: Thermoelectric and p-type conductivity properties, *Solid State Sciences* 11 (2009) 233-239.
- [22]. R.Adnan, N.A. Razana, I. A.Rahman, M. A.Farrukh, Synthesis and characterization of high surface area tin oxide nanoparticles via the sol-gel method as a catalyst for the hydrogenation of styrene, *Journal of the Chinese Chemical Society*, (2010) 222-229.
- [23]. L. S. Chuah, M. Y. Yaacob, M. S. Fan, S. S. Tneh, Z. Hassa, Synthesis, characterization and optical properties of Ni-doped nanocrystalline SnO₂, *Optoelectronics and Advanced Materials*, Vol. 4, No. 10, October 2010, p. 1542 – 1545.



Synthesis and Structural Properties of Lanthanum Doped Tin Dioxide Nanocrystalline

L.P.Chikhale^{*1}, F.I.Shaikh², A.V.Rajgure³, S.S.Suryavanshi⁴

^{*1}Department of Physics, Venkatesh Mahajan Senior College, Osmanabad, Maharashtra, India

²Department of Physics, Government Institute of Forensic Science, Aurangabad, Maharashtra, India

³G.S.Tompe Arts, Commerce & Science College, Chadur Bazar, Dist-Amravati 444704, Maharashtra, India

⁴Department of Physics, Solapur University, Solapur, Maharashtra, India

ABSTRACT

The present work to study effect of pure and La doped tin dioxide thick films on their optical properties and the oxide powders were prepared by the chemical co-precipitation method. The thick films of La doped SnO₂ were prepared by the screen-printing technique. Thick films of functional material were prepared by using a screen printing technique and then sintered at 750 °C for 2 h. The samples were characterized by X-ray diffraction (XRD), transmission electron microscopy (TEM), scanning electron microscopy (SEM), energy dispersive X-ray analysis (EDAX) techniques. XRD studies reveal formation of fine nanocrystalline material. The particle size of sintered powder of pure and La (2 and 4 mol %) doped SnO₂ powders were 15, 10 and 9 nm respectively.

Keywords: TEM; SEM; Screen printing; Thick Film

I. INTRODUCTION

Nanostructured semiconductor oxides are attracting a great deal of attention due to their exclusive properties and novel applications. In the recent years, atmospheric pollution has become a major global concern. Gases released from automobile exhausts and industries are severely polluting the environment. Thus, it has not only imperative to develop sensors for the detection but also the quantitative measurement of the toxic and inflammable gases to determine the exact concentration which could be ascertained before some natural disaster may occur. The gas sensor would also facilitate on line monitoring of the hazardous gases and providing safety of working environment [1]. In this paper we are reporting the effect of La doping on the structural and optical of SnO₂ thick films prepared by chemical co-precipitation technique. We have chosen this technique because of the easy of selectivity of resistivity and transmittance by controlling preparative parameters[2-4]

II. EXPERIMENTAL PROCEDURE

2.1 Preparation of undoped and doped SnO₂ powder:

We have opted the simple and economical co-precipitation method for synthesis of undoped and La doped SnO₂. The analytical grade stannic chloride (SnCl₄.5H₂O) and ammonia (NH₃.H₂O) was used as raw materials. The stannic chloride was dissolved in distilled water to form a transparent solution. Ammonia was added drop wise into the solution under continuous stirring until pH attains around 8 where the precipitation was occurred. The precipitate was washed with de-ionized water for several times to remove chlorine ions [5]. The precipitate was dried under IR lamp for about 2 h and then calcined at 600°C for 2 h in air to obtain fine nanocrystalline powder. The sample was labeled as S1. The as synthesized powder was subjected to TGA to know the phase formation temperature and to decide calcination or sintering temperature. The 98 mol% stannic chloride and 2 mol% lanthanum nitrate were added together in distilled water to form precursor solution. Dilute ammonia was added to the solution to precipitate the constituents together. The precipitates were filtered and washed using de-ionized water and further procedure was same as adopted in case of L1. In a similar way 2 mole and % 4 mol% La doped SnO₂ was prepared and the sample was labeled as L2 and L3 respectively.

2.2. Preparation of thick films:

The thixotropic paste was formulated by mixing the fine powder of SnO₂ with a mixture of organic solvents (a temporary binder) namely ethyl cellulose, butyl carbitol acetate and terpineol. In formulating the thixotropic paste, the ratio of the inorganic to organic part was kept at 75:25 [6]. This thixotropic paste was further used to deposit thick films on ultrasonically cleaned alumina substrate (10mm X 20mm) by using screen printing technique with the nylon cloth of 140 mesh counts. The details of the technique are described elsewhere [7]. The thick films were sintered at 750°C for 2 h in air.

III. RESULTS AND DISCUSSION

3.1. XRD analysis

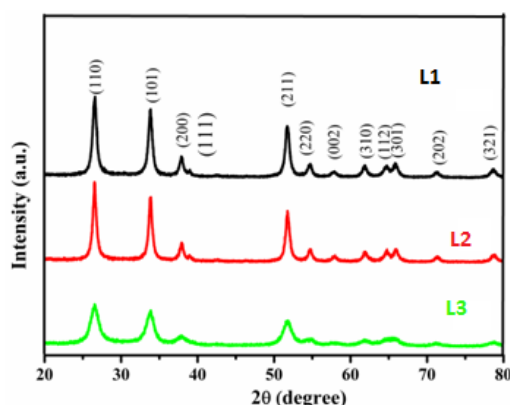


Fig. 1 XRD patterns of undoped (L1) , 2 mol % La-doped (L2) , and 4 mol % La-doped SnO₂ (L3).

Fig.1 show the XRD patterns of SnO₂ thick films with different La concentrations. All patterns exhibit peaks corresponding to the rutile structure of polycrystalline SnO₂ with the maximum intensity peak corresponding to (110) planes and are indexed on the basis of joint committee on powder diffraction standards (JCPDS) data [8]. However, the relative intensity of the peaks decreases with an increase in the La content. It is also observed that the full width at half maxima (FWHM) of the diffraction peaks increases with increasing La content which is in good agreement with the earlier studies [9]. The increase in FWHM along with a decrease in peak intensity suggests that La incorporation into the SnO₂ lattice results in a decrease in crystallite size of the films. The decrease in the crystallite size is further supported by the decrease in the sharpness of the peaks with the incorporation of La. Pure SnO₂ has an average crystallite size of 15nm, while 2 mol % La doped SnO₂ shows reduced crystallite size of 10 nm and 8 nm in case of 4mol % La-doped SnO₂. A small crystallite size provides a larger surface area for adsorption of oxygen species and exposure to the test gas, which increases the probability of gas solid interaction, thereby increasing the response. The presence of La in the crystallographic structure increases the formation of oxygen vacancies as required by the charge balance. This effect is in conjunction with the smaller ionic radius of La³⁺ (250 pm) as compared to Sn⁴⁺ (71 pm) [10]. These end result suggest that, the increment of the doping concentration leads to decrease of the lattice parameter and crystalline size, and prevent the growth of SnO₂ Crystallites. The role of La as grain growth inhibitor is also supported by earlier studies [11].

3.2. SEM and EDAX analysis:

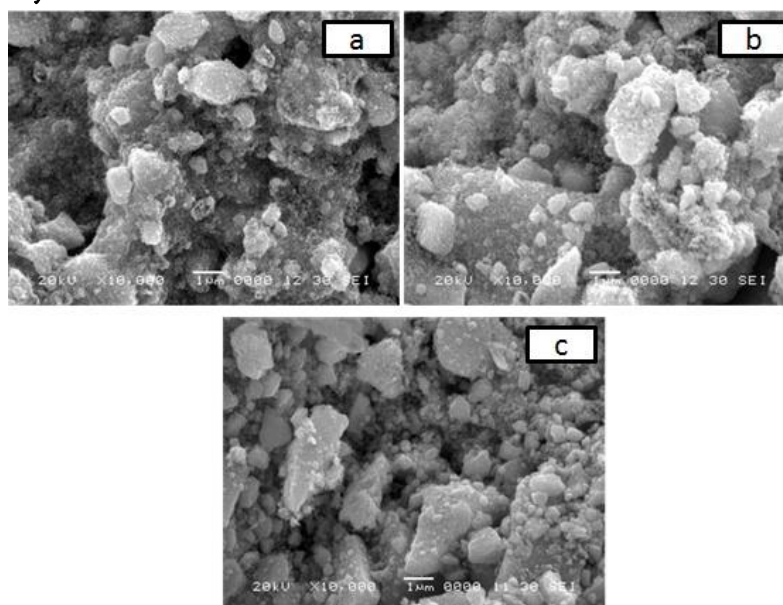


Fig. 2 SEM images of the surface of SnO₂ thick films: (a) undoped SnO₂ (b) 2mol % La doped SnO₂ (c) 4 mol % La-doped SnO₂.

Fig.2 illustrates SEM images of sintered thick film samples. It shows evidence of splintered surface morphology, covering the micro pores on the surface. Pure SnO₂ shows large pore with non-uniform grains (Fig. 2(a)), however; agglomerates can be seen for L2 sample (Fig. 2(b)). In case of 4 mol % doped SnO₂, dispersed nanoparticles with significant porosity were observed. (Fig.2(c)). It is clearly seen that with

incorporation of La the particle size of SnO₂ decreases changes distinctly suggesting La playing imperative role in the growth embarrassment for the SnO₂ material. The decrease of crystallite size caused by doping of La results in high surface energy, thereby agglomerates are favored to form. A chemical composition of thick film was investigated by energy dispersive X-ray analysis (EDAX) and is shown in Fig.3.

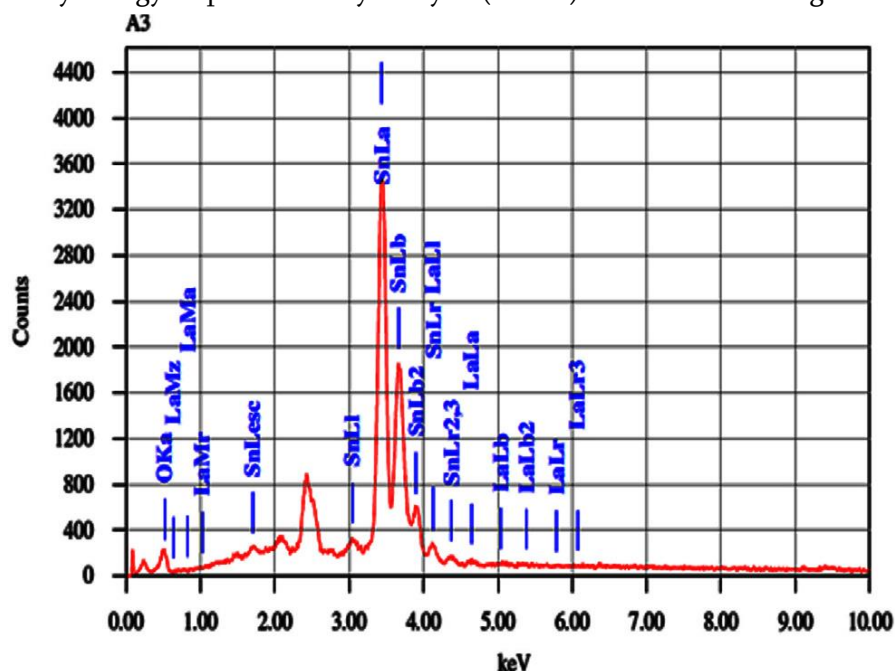


Fig. 3 EDAX spectrum of 2 mol % La-doped SnO₂ thick film.

The EDAX data is in good agreement with the initial precursor concentration. It was found that the La doped SnO₂ thick film was tin deficient and oxygen rich, indicating that the La doped SnO₂ thick film was non-stoichiometric.

3.3. TEM analysis:

The morphology of powders was examined with TEM and the images of pure, 2 mol% and 4 mol% La doped SnO₂ sintered powders are shown in Fig 4(a-c) respectively. There is a noticeable reduction in average particle size of SnO₂ when La is doped into the SnO₂. For pure SnO₂, the size of the crystallites was about 15 nm while the crystallite size decreases to 10 and 8 nm for SnO₂ doped with 2mol% La and 4mol% La respectively. The average crystallite size estimated from XRD is comparable with the size observed from TEM images. In addition, a significant amount of agglomeration was observed in the micrographs especially for L2 and L3 sample.

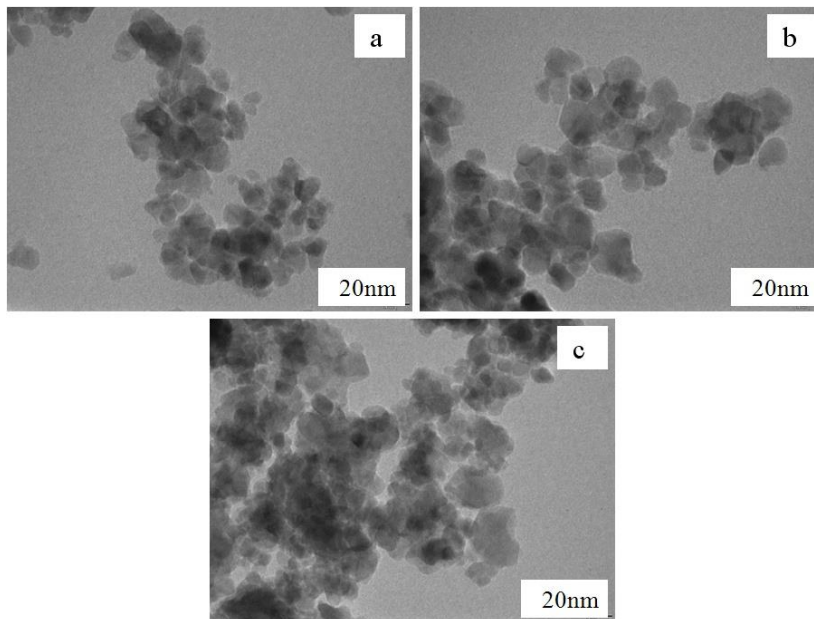


Fig. 4 TEM images of SnO₂ thick films: (a) undoped SnO₂ (b) 2mol % La –doped SnO₂ (c) 4 mol% La –doped SnO₂.

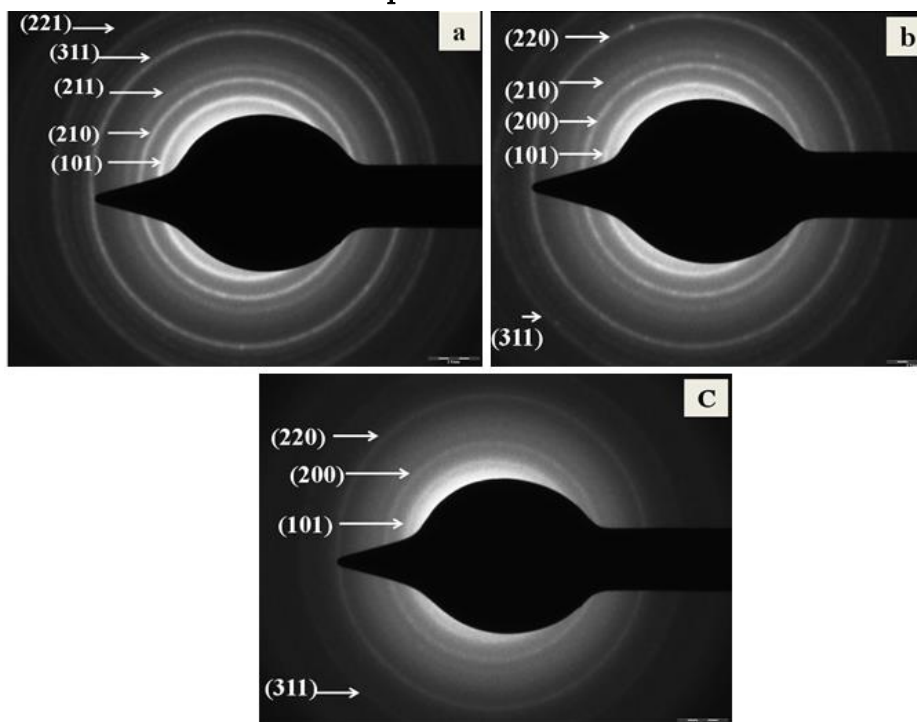


Fig. 5 SAED pattern of SnO₂ thick films: (a) undoped SnO₂ (b) 2mol % La –doped SnO₂ (c) 4 mol% La –doped SnO₂.

The selected area electron diffraction (SAED) pattern of an isolated particle for various SnO₂ thick film samples is shown in Fig.5. The SAED shows bright rings corresponding to the (101), (210), (211), (311), (221) lattice planes of SnO₂ which are in good agreement with the X-ray diffraction pattern.

IV. CONCLUSIONS

The films of co precipitation synthesized undoped and La doped SnO₂ were successfully deposited using screen printing technique. XRD and TEM studies confirmed the nanocrystallinity of undoped and La doped SnO₂ material. The structural and morphological studies were proved the role of La as grain growth inhibitor. The XRD, SEM-EDAX, TEM, SAED analysis confirmed that the La doping in SnO₂ can significantly affects morphology and particle size of La doped SnO₂.

V. REFERENCES

- [1]. D. N. Suryavanshi, D.R. Patel, L.A. Patil, Fe₂O₃-activated Cr₂O₃ thick films as temperature dependent gas sensors, *Sensors and Actuators B* 134 (2008) 579–584.
- [2]. L.A. Patil, D.R. Patil, Heterocontact type CuO-modified SnO₂ sensor for the detection of a ppm level H₂S gas at room temperature, *Sensors and Actuators B* 120 (2006) 316–323.
- [3]. Y. Niti, V. Patama, V.Voranipit, S.Pachara. Sinterability and microstructure of Bi-Added SnO₂ nanomaterials by precipitation method, *Journal of Metals, Materials and Minerals* 20 (3) (2010) 67-72.
- [4]. T.D. Senguttuvan, R. Rai, S.T. Lakshmikummar, Gas sensing properties of lead doped tin oxide thick films, *Materials Letters* 61 (2007) 582–584.
- [5]. S. Bose, S. Chakrabortya, B.K. Ghoshb, D. Dasc, A. Sena, H.S. Maitia, Methane sensitivity of Fe-doped SnO₂ thick films, *Sensors and Actuators B* 105 (2005) 346–350.
- [6]. L.A. Patil, D.R. Patil, Heterocontact type CuO-modified SnO₂ sensor for the detection of a ppm level H₂S gas at room temperature, *Sensors and Actuators B* 120 (2006) 316–323.
- [7]. L.K. Bagal, J.Y. Patil , I.S. Mulla, S.S. Suryavanshi, Influence of Pd-loading on gas sensing characteristics of SnO₂ thick films, *Ceramics International* 38 (2012) 4835–4844.
- [8]. JCPDS Data Card No.14-4145.
- [9]. S. Rani, S. C. Roy, M.C. Bhatnagar. Effect of Fe doping on the gas sensing properties of nano-crystalline SnO₂ thin films, *Sensors and Actuators B* 122 (2007) 204–210.
- [10]. N. Timonah, C.Yang, L.Sun, Structural, optical and electrical properties of Fe doped SnO₂ fabricated by sol–gel dip coating technique, *Materials Science in Semiconductor Processing* 13 (2010) 125–131.
- [11]. M.V. Vaishampayan, R.G. Deshmukh, P.Walke, I.S. Mulla, Fe-doped SnO₂ nonmaterial: A low temperature hydrogen sulf.ide gas sensor, *Materials Chemistry and Physics* 109 (2008) 230–23416.



Effect of Synthesis Temperature on Structural, Electrical and Optical Properties of Mn₃O₄ Thin Films

K.S. Iqbal¹, M.S Dixit¹, A.U Ubale²

¹Department of Physics, Jagadamba Mahavidyalaya, Achalpur City-444806, Maharashtra, India

²Nanostructured Thin Film Materials Laboratory, Department of Physics, Govt. Vidarbha Institute of Science and Humanities, VMV Road, Amravati-444604, Maharashtra, India

ABSTRACT

In the present work to study the effect of synthesis temperature on structural, electrical and optical properties of Mn₃O₄, thin films were prepared using a simple and low-cost chemical spray pyrolysis technique by varying substrate temperature. The XRD patterns have revealed that Mn₃O₄ films exhibit nanocrystalline structure, with crystallite size ~ 28nm and after annealing it increases. The optical absorption studies showed that Mn₃O₄ exhibit direct optical band gap energy that changes from 2.19 to 2.27 eV depending on substrate temperature. The electrical resistivity and thermo-emf studies confirmed that Mn₃O₄ films are semiconducting in nature with p-type conductivity.

Keywords: Thin films, Chemical synthesis, X-ray diffraction, Electrical properties, Optical properties.

I. INTRODUCTION

Recently, synthesis of nanometal oxides by chemical method is one of the most promising research area in the field of nanotechnology. Metal oxides such as manganese oxide, zinc oxide, cobalt oxide, nickel oxide, iron oxide and their composites are increasing day by day [1- 10]. Among these manganese oxide may become a functional oxide material in future due to its low cost and ecofriendly nature [11]. As manganese oxide has different oxidation states Mn²⁺, Mn³⁺, and Mn⁴⁺, it shows different phases such as MnO, MnO₂, Mn₂O₃ and Mn₃O₄[12]. Among them, Hausmannite Mn₃O₄ is one of the most stable oxide of manganese. Now a days, considerable interest has been generated towards manganese oxide due to its variety of applications such as supercapacitor [13,14], electrochemical material [15,16], humidity sensor [17], catalyst [18,19], rechargeable lithium batteries [20,21], water oxidation [22], antibacterial and antioxidant material in medicinal science [23]. Various methods have been used to prepared manganese oxide thin films such as chemical bath deposition [24,25], dip coating [26], electrochemical deposition [27], atomic layer deposition, electrostatic spray deposition, pulsed laser deposition, chemical vapor deposition and SILAR method [11]. Spray pyrolysis technique is a simple, low cost and ecofriendly chemical method to grow large area, high quality adherent films of uniform thickness.

II. EXPERIMENTAL PROCEDURE

2.1 Preparation of Mn₃O₄ thin films:

To synthesize Mn₃O₄ thin films, 0.05 M, C₄H₆ MnO₄.4H₂O was prepared in deionised water. The solution was then filled in a spray gun and 10 ml solution was allowed to spray onto heated glass substrate at constant temperature of 473 K. As deposited thin film sample is labeled as A1. By keeping all deposition parameters fix films are prepared by varying substrate temperature viz. 473, 523, 573, 623, 673 and 723 K. As deposited thin film samples are then labeled as A2, A3, A3, A4, A5, A6 respectively. As deposited films were further annealed at 673 K for 4 hours, and are labeled as A1*, A2*, A3*, A4*, A5*, A6* respectively.

III. RESULTS AND DISCUSSION

The film thickness of Mn₃O₄ deposited at 723K temperature is of the order of 121nm and it increases to 289nm as the deposition temperature decreases to 473K. However, if the deposition temperature increases above 473K, film thickness decreases. It may due to evaporation of material at higher temperature

3.1 Structural studies

The diffraction patterns obtained for as deposited Mn₃O₄ films A1, A2, A3, A4, A5, A6 are shown in Fig.3.1 It is clearly seen that the as deposited Mn₃O₄ film A4 shows nanocrystalline structure and exhibit peak corresponding to (200) plane and crystallite size is found to be 28 nm. As deposited Mn₃O₄ films are further annealed at 673K for 4 hours, after annealing Mn₃O₄ films shows crystalline nature(fig.3.2). The observed XRD patterns were compared with the JCPDS data (card no. 24 - 0734) . Fig.3.3 shows that after annealing, the crystallite size increases as temperature of the substrate increases. The crystalline nature of film increases upto 573K temperature and decreases as annealing temperature increases. In spray process, above 573K i.e towards higher side of temperature, the Mn₃O₄vapour molecules exhibits excess kinetic energy that creates unfavorable situation on the substrate surface for nucleation and growth, giving amorphous phase.

3.2 Optical studies

The optical absorption studies of Mn₃O₄ thin films were carried out in the wavelength range 200–800 nm at room temperature. Fig.3.4 shows the variation of % transmittance of Mn₃O₄ film with wavelength. It is observed that % transmittance of Mn₃O₄ increases with substrate temperature. However, as expected the absorption coefficient shows opposite trend fig(3.5). This happens because crystalline nature of film is improved with substrate temperature. Fig(3.6) and fig(3.7) shows variation of % transmittance and absorption coefficient with wavelength for annealed films. The increase in transmittance is due to decrease in thickness of the film as substrate temperature increases.

3.3 Electrical studies

The dc two point probe method was employed to understand the variation of electrical resistivity of Mn₃O₄ thin films with temperature. Fig. 3.8 and 3.9 shows the variation of log(ρ) with reciprocal of temperature. It is clearly seen that the resistivity of Mn₃O₄ decreases as temperature increases indicating semiconducting nature.

3.4 Thermo-emf measurement

Thermo-electric Power is the ratio of thermally generated emf to the temperature difference across the semiconductor. The emf was measured for all samples as a function of temperature in the temperature range 273 - 325

K. linear variations for as deposited and annealed Mn_3O_4 thin films are as shown in fig.3.10 and fig.3.11. The polarity of thermally generated voltage was found to be negative towards the hot end, which confirms that Mn_3O_4 films are p-type semiconducting material.

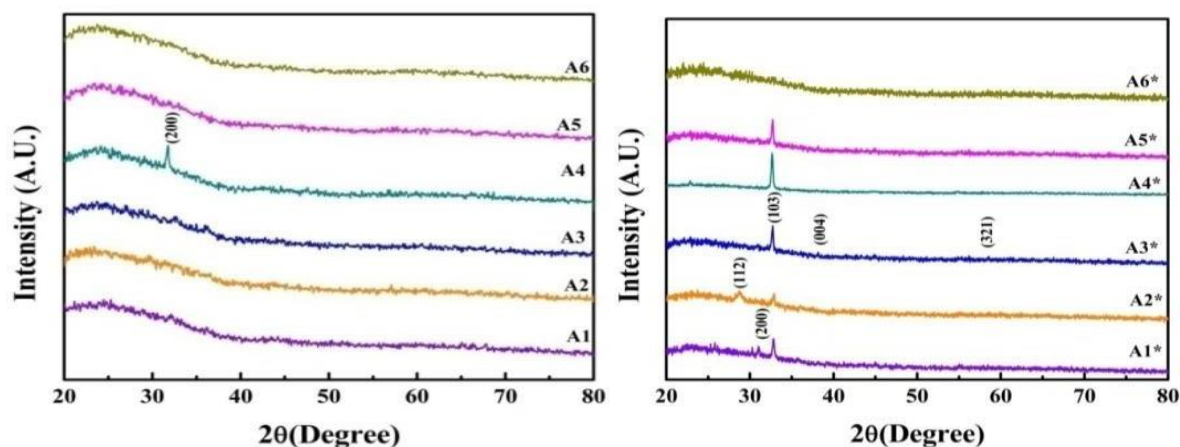


Figure 3.1 XRD pattern of as deposited Mn_3O_4 films. Figure 3.2 XRD patterns of Mn_3O_4 films after annealing.

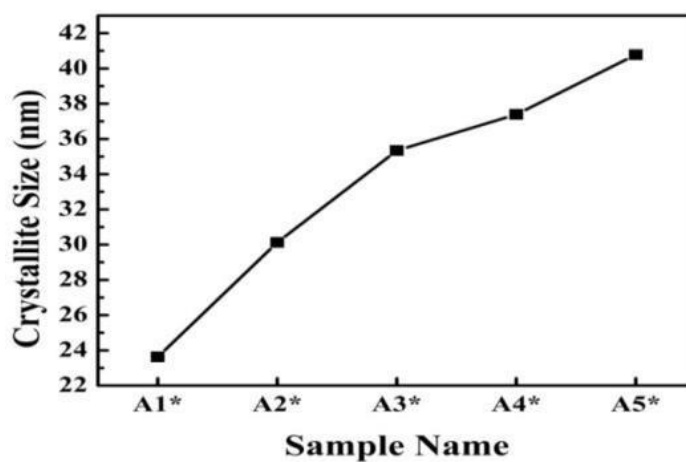


Figure 3.3 Variation of Crystallite size of Mn_3O_4 with deposition temperature (after annealing).

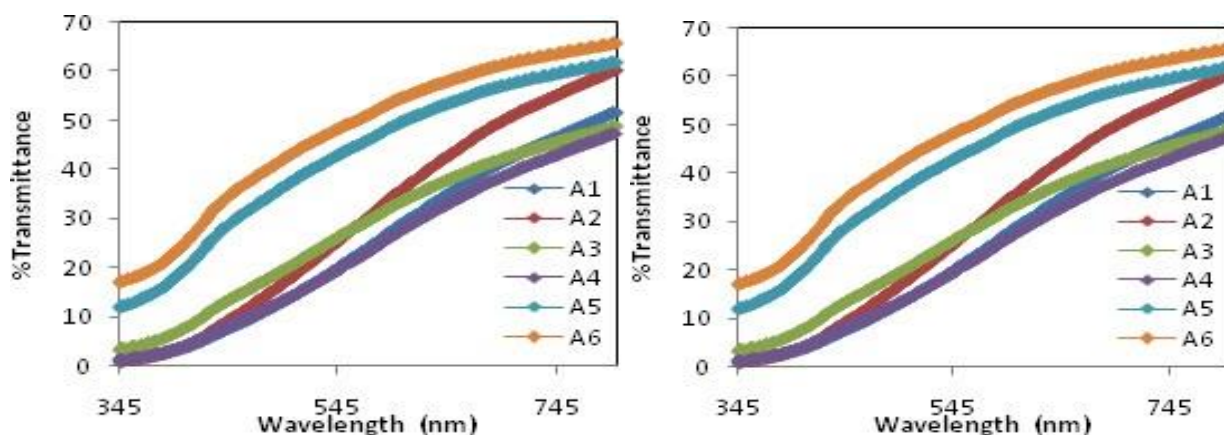


Figure 3.4 Plots of % transmittance versus wavelength of as deposited Mn₃O₄ films.

Figure 3.5 Plots of optical absorption coefficient versus wavelength as deposited Mn₃O₄film

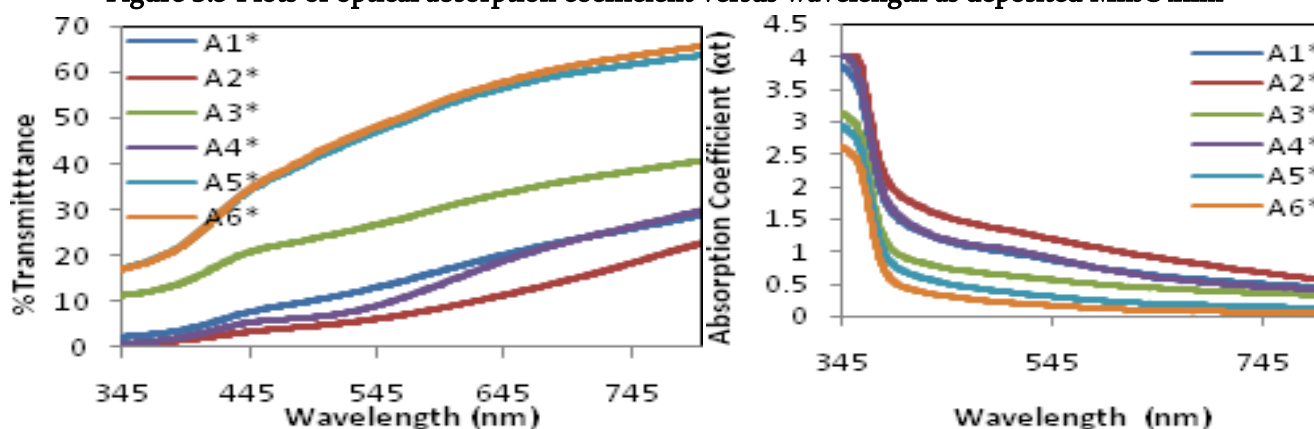


Figure 3.6 Plots of % transmittance versus wavelength of annealed Mn₃O₄films.

Figure 3.7 Plots of optical absorption coefficient versus wavelength of annealed Mn₃O₄ thin films

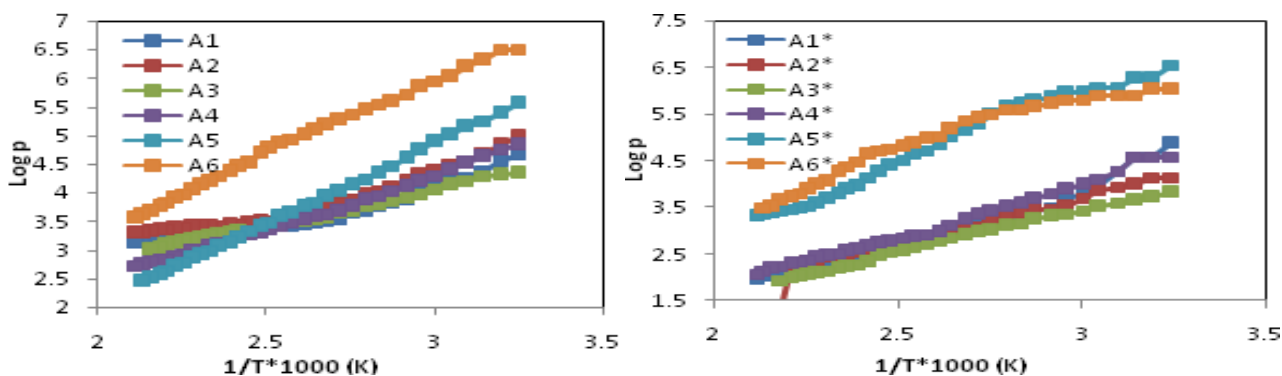


Figure 3.8 Plots of log ρ versus 1/T*1000 of as deposited Mn₃O₄ thin films.

Figure 3.9 Plots of log ρ versus 1/T*1000 of annealed Mn₃O₄ thinfilms.

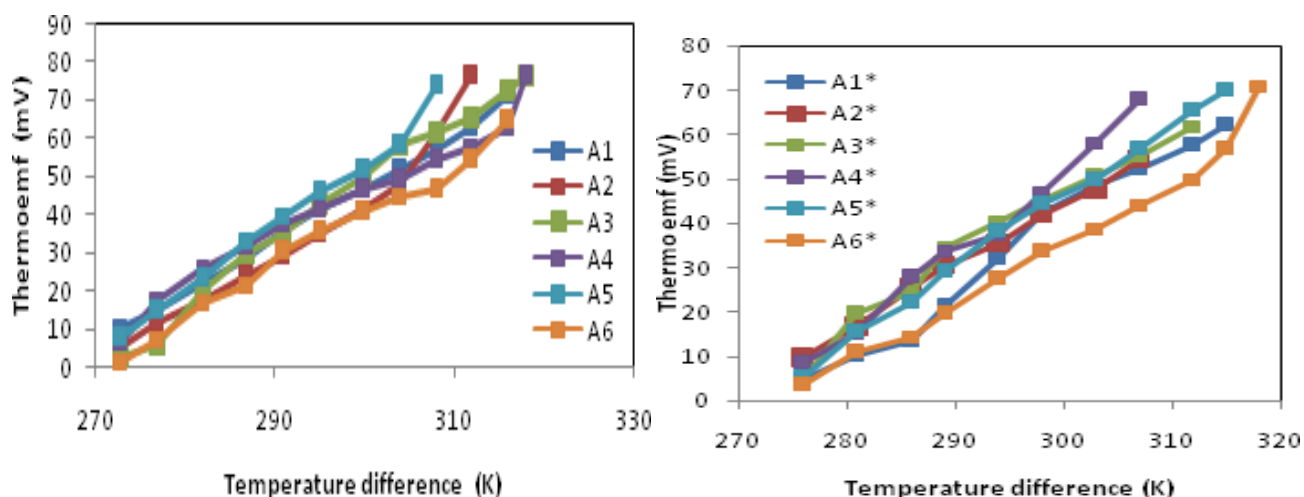


Figure 3.10 Plots of induced thermo-emf versus applied temperature difference across the films.

Figure 3.11 Plots of induced thermo-emf versus applied temperature difference across annealed Mn₃O₄ thin films.

IV. CONCLUSIONS

In the present work, nanocrystalline Mn₃O₄ thin films were successfully synthesized by Spray pyrolysis technique by varying substrate temperature. The XRD confirms the nanocrystallinity of the deposited Mn₃O₄. The optical studies reveals that the band gap energy of Mn₃O₄ deposited film was found to vary between 3.19 to 3.27 eV depending on substrate temperature. However after annealing all samples shows almost equal values of band gap energy (~3.24) for the different substrate temperature. The electrical studies showed that the resistivity of Mn₃O₄ decreases as temperature increases. The thermo-emf measurements confirmed p-type nature of Mn₃O₄ films.

V. REFERENCES

- [1]. M. Wang, J. Iocozia, L. Sun, C. Lin, Z. Lin, *Energ. Environ. Sci.* 7 (2014)2182.
- [2]. J.S. Jang, K.Y. Yoon, X. Xiao, F.R.F. Fan, A.J. Bard, *Chem. Mater.* 21 (2009) 4803.
- [3]. A. Gulino, G. Compagnini, A.A. Scalisi, *Chem. Mater.* 15 (2003)3332.
- [4]. D.M. Robinson, Y.B. Go, M. Mui, G. Gardner, Z. Zhang, D. Mastrogiovanni, E.Garfunkel, J.Li, M. Greenblatt, G.C. Dismukes, *J. Am. Chem. Soc.* 135 (2013) 3494.
- [5]. M. Sultan, A.A. Tahir, M. Mazhar, M. Zeller, K.G.U. Wijayantha, *New J. Chem.* 36 (2012)911.
- [6]. T.H. Shin, S. Ida, T. Ishihara, *J. Am. Chem. Soc.* 133 (2011)19399.
- [7]. M.A. Mansoor, A. Ismail, R. Yahya, Z. Arifin, E.R.T. Tiekink, N.S. Weng, M.Mazhar, A.R.Esmaeili, *Inorg. Chem.* 52 (2013)5624.
- [8]. Y.J. Kim, B. Gao, S.Y. Han, M.H.Jung, A.K. Chakraborty, T. Ko, C. Lee, W.I. Lee, *J. Phys. Chem.* 113 (2009) 19179.

- [9]. Y. Qu, W. Zhou, H. Fu, Chem. Cat.Chem. 6 (2014)65.
- [10]. M.A. Mansoor, N.M. Huang, V.M Kee, T.A.N. Peiris, K.G.U. Wijayantha, Z. Arifin, M. Misran, M. Mazhar, Sol. Energ. Mater. Sol. Cells 137 (2015) 258.
- [11]. M.R. Belkhedkar, A.U. Ubale, J. Mol.Struct. 1068 (2014)94.
- [12]. J.D. Lee, Concise Inorganic Chemistry, fourth ed., Chapman-Hall, London (1991)734.
- [13]. M. Baldi, E. Finocchio, F. Milella, G. Busca, Appl. Catal. B: Environ. 16 (1998)43.
- [14]. Q. Huang, X. Wang, J. Li,Electrochim. Acta 52 (2006)1758.
- [15]. D.P. Dubal, R. Holze, Energy 51(2013) 407.
- [16]. W. Gao, S. Ye, M.W. Shao, J. Phys. Chem. Solid. 72 (2011)1027.
- [17]. S. Xing, Z. Zhou, Z. Ma, Y. Wu,Mater. Lett. 65 (2011)517.
- [18]. M.L. Singla, S. Awasthi, A. Srivastava, Sens. Actut. B 127 (2007)580.
- [19]. J. Zhang, J. Du, H. Wang, J. Wang, Z. Qu, L. Jia, Mater. Lett. 65 (2011)2565.
- [20]. N. Li, Z. Geng, M. Cao, L. Ren, X. Zhao, B. Liu, Y. Tian, C. Hu, Carbon 54 (2013)124.
- [21]. E. Macheaux, A. Verbaere, D. Guyomard, J. Power Sources 157 (2006)443.
- [22]. M.M. Thackeray, W.I.F. David, P.G. Bruce, Mater. Res. Bull. 18 (1983) 461.
- [23]. A. Ramirez, D. Friedrich, M. Kunst, S. Fiechter, Chem. Phys. Lett. 569(2013) 157.
- [24]. A.N. Chowdhury, M.S. Azam, M. Aktaruzzaman, A. Rahim, J. Hazard. Mater. 172(2009)1229.
- [25]. D.P. Dubal, D.S. Dhawale, R.R. Salunkhe, V.J. Fulari, C.D. Lokhande, J. Alloy Compd. 497 (2010)166.
- [26]. H.Y. Xu, S.L. Xu, X.D. Li, H.Wang, H. Yan, Appl. Surf. Sci. 252 (2006) 4091.
- [27]. S.C. Pang, M.A. Anderson, T.W. Chapman, J. Electrochem. Soc. 147 (2000)444.



Synthesis of Some Substituted 4H-Chromene Derivatives by Using Nanostructured Doped Polyaniline as a Catalyst

Sharad N. Pawar¹, Deepak M. Nagrik²

¹Department of Chemistry, SSES Amravati's Science College, Pauni Dist. Bhandara-441910, Maharashtra, India

²Department of Chemistry, G.S. Science, Arts and Commerce College, Khamgaon, Dist. Buldhana-444303, Maharashtra, India

ABSTRACT

4H-benzopyran (Chromene) are synthesized through one-pot Knoevenagel-Michael cyclo-condensation reaction. Multicomponent reaction (MCR) are considered as one of the most important synthetic strategies which consists two or more reactants added together in a one-pot reaction to form targeted products. The 4-H chromene compounds are of biological interest synthesized from the variety of aldehydes and its derivatives, malononitrile and various nucleophiles including 1,3-dicarbonyl, indole, secondary amines, cyanides compounds using various catalysts. These reactions were extensively well studied and reported in the literature. This study aimed at investigating the synthesis of Substituted 4H-Chromene (benzopyran) from (a) salicylaldehyde and (b) malononitrile or different active methylene moieties by using nanostructure Ammonia Doped Polyaniline Graphitic Carbon Nitride composite (NPGCN) as Catalyst was carried out. The effective method for the synthesis of 4-H chromene derivatives of biologically important compounds has been coined. We synthesized the different 4-H chromene (benzopyran) derivatives which give up to 86 % yield. The Ammonia Doped Polyaniline Graphitic Carbon Nitride composite (NPGCN) as Catalyst has been used as an efficient and eco-friendly, metal free catalyst in the synthesis of 4H- chromene derivatives.

Keywords: chromene, catalyst, Multicomponent reactions (MCR), polyaniline.

I. INTRODUCTION

Six-membered oxygen-containing heterocycles are wide-ranging through both the areas of naturally and completely synthetic molecules. Numerous naturally occurring compounds containing pyrans and benzopyrans display interesting biological activity which has in part motivated substantial attention from the chemical community at the degrees of structure and reactivity, and synthesis and properties [1].

4H- chromene derivatives have been considered as a main unit in maximum oxygen-containing heterocyclic compounds. 4H-benzopyrans are synthesized through one-pot Knoevenagel-Michael cyclo-condensation reaction. In addition, they have been attracted a substantial interest related to their biological and pharmaceutical properties similar as antibacterial, antitumor, antitubercular and antiviral activities [2]. Thus,

numerous researchers have been developed many protocols for 4H-Pyrans synthesis by reacting aldehydes, malononitrile and 1,3-dicarbonyl compounds using various catalysts such as SnCl₂/ SiO₂, MgO, potassium phthalimide, silica nanoparticles and silica bonded N-propylpiperazine sodium n-propionate [3]. Multicomponent reactions (MCR) are considered as one of the most important synthetic methodology which consists three or more reactants attached together in a one- pot reaction to form targeted products. The characteristic advantage of MCR's is that the targeted products contain nearly all portions of substrates, generating generally no by- products. That makes MCRs really novel, green and eco-friendly reaction system. Targeted products can be gained in one- pot with truly less steps. Thus, MCRs have been attracted significant attention in numerous research fields, similar as discovery of vital compounds in medicinal chemistry, combinatorial chemistry and medicinal discovery [4,5].The heterogeneous catalytic reactions have played important role in developing organic synthesis. Because of their, functional simplicity, environmental compatibility, reusability, non-toxicity, profitable and easy removal from reaction mixture [6,7], so we have employed the following catalytic system Ammonia Doped Polyaniline Graphitic Carbon Nitride (PANI-GCN) in the synthesis of some important 4H- chromene derivatives.

The generalschematic representation ofsynthesis ofSubstituted 4H-benzopyran (Chromene) from (a) substituted salicylaldehyde and (b) malononitrile or reactive methylene compounds by using nanostructure Ammonia Doped Polyaniline Graphitic Carbon Nitride (NPGCN) as Catalysts given in **Fig.1**

This extended synthesis protocol [8] was found to be the convenientmethod for the synthesis of the number of 4H- chromene derivatives which was characterized and found tohavetheextensiveuseinthemedicinalchemistry.

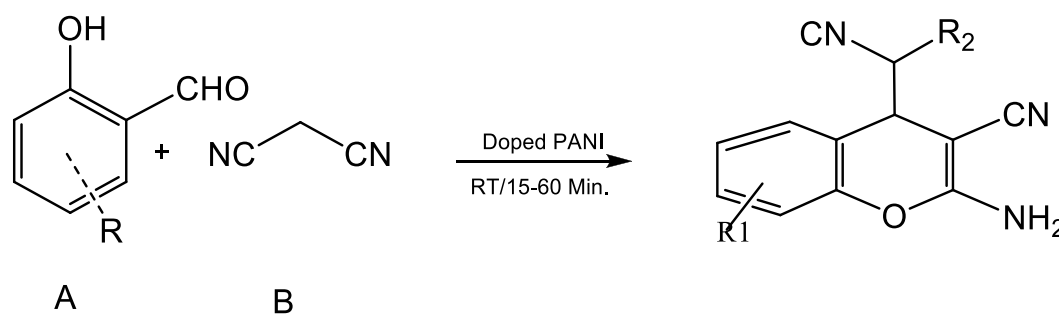


Fig.1 The generalschematic representation ofsynthesis of substituted 4H- chromene derivatives from (a) substituted salicylaldehyde and (b) malononitrile by using nanostructure doped PANI as Catalyst.

II. EXPERIMENTAL DETAILS

2.1 Material and Methods:

All chemicals supplied by the Merck (Extra pure) Chemical Companies and used were without further purification. IR spectra were recorded on a Perkin-Elmer 1640 FT-IR instrument. The ¹H- and ¹³C-NMRspectrawererecordedonaBrukerDPX-300NMRmachine.Unlessotherwisespecified, CDCl₃ was used as solvent.

2.2 Preparation Of Polyaniline (PANI):

The polyaniline was synthesized by the chemical oxidization technique at low temperature (0 to 50° C). Ammonium Persulphate and Hydrochloric acid used as a oxidizing agent as took without additional purification. 15 ml Aniline was first dissolve in 2 M 100 ml Hydrochloric Acid (HCl) (Merk). Also this solution is kept in the ice bath below 50° C temperature. Ammonium Persulphate solution (Generally 10) was added to the aforementioned solution with constant stirring. This polymerization process were completed within the three to four hours and the finally the green colour polyaniline was formed. It's washed with the hot dilute HCl and dried it in the oven for 24 Hours.

2.3 Doping of PANI :

In a RBF vessel containing 50 mL of deionized water, 1.5

g of GCN, 550 mg of ammonium persulfate ((NH₄)₂S₂O₈), and 18 mL of 1 M HCl were added. The above mixture after stirring for 1 h at 0 °C, 1.5 mL of aniline was added dropwise to the cooled mixture and the reaction mixture was stirred at 0 °C for 10 h. After completion of reaction, the green precipitate of PANI-GCN (PGCN nanocomposite) was filtered off and washed repeatedly with ethanol and water until the filtering solution becomes colourless. Lastly, the obtained PANI-GCN (1:1) composite was dried at 70 °C for 12 h. Similarly, other nanocomposites of PANI-GCN with (1:1), (1:2) and (1:4) were synthesized by varying the amount of aniline in the above mentioned procedure.

2.4 Synthesis of N-PANI-GCN Nanocomposite :

For this purpose, 500 mg of the PANI – GCN (PGCN) nanocomposite was taken in a round- bottom flask and 50 mL of 1 M NH₃ solution was added to it. after, the reaction mixture was stirred for 3 h at RT. After 3 h, a dark blue solid of N – PANI – GCN (NPGCN nanocomposite) was filtered off. The solid material acquired was washed with 50 mL of NH₃ solution and was dried in an oven at 70 °C for 12h.

2.5 General procedure of synthesis of substituted 4H-benzopyran (Chromenes).

In a RBF of 10 ml capacity, salicylaldehyde (1 mmol), malononitrile (2 mmol), NPGCN catalyst (5 wt), and ethanol (2 mL) were taken, and the admixture was stirred at temperature of 55 °C. The progress of the reaction and the conformation of the product were constantly judged by silicagel- coated aluminum thin-layer chromatography (TLC). After completion of the reaction, water was decanted from the reaction mixture and ethanol was added to it for extraction of the product. The admixture was also centrifuged for the separation of the catalyst used. The ethanol layer was dried over anhydrous sodium sulphate, and the solvent was evaporated to get the crude mixture using a rotary evaporator. The obtained crude admixture was purified by silica gel column chromatography using eluting admixture of hexane and ethyl acetate.

III. RESULTS AND DISCUSSION

The structure and functionality of synthesized bare PANI catalysts material were confirmed by FTIR spectroscopy shown in Fig.2. The bands at 1560 and 1480 cm⁻¹ can be assigned to C=N and C=C of aromatic systems. The bands at 1300 and 1245 cm⁻¹ can be assigned to C-N stretching vibrations of the benzenoid unit, and the band at 1115 cm⁻¹ corresponds to the quinoid unit of the PANI polymer.[9,10]

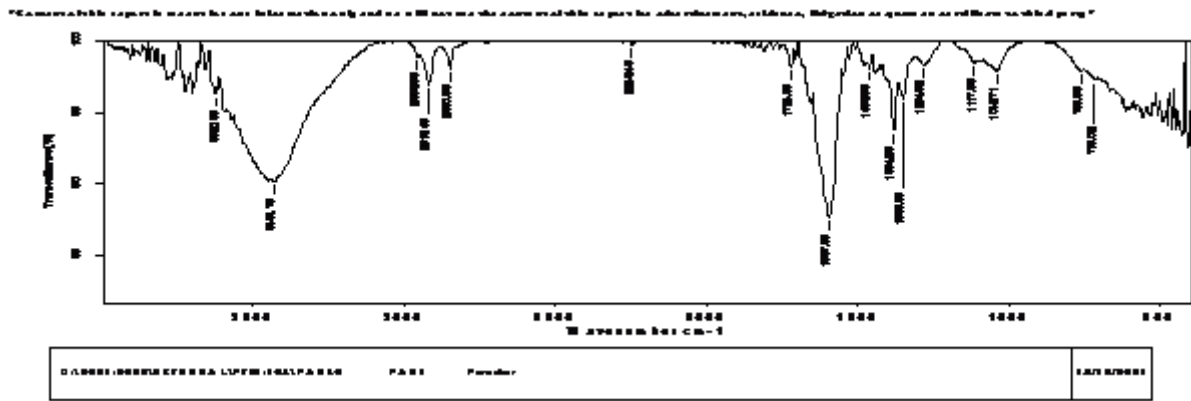


Fig.2 FTIR images PANI (Emeraldine Salt)

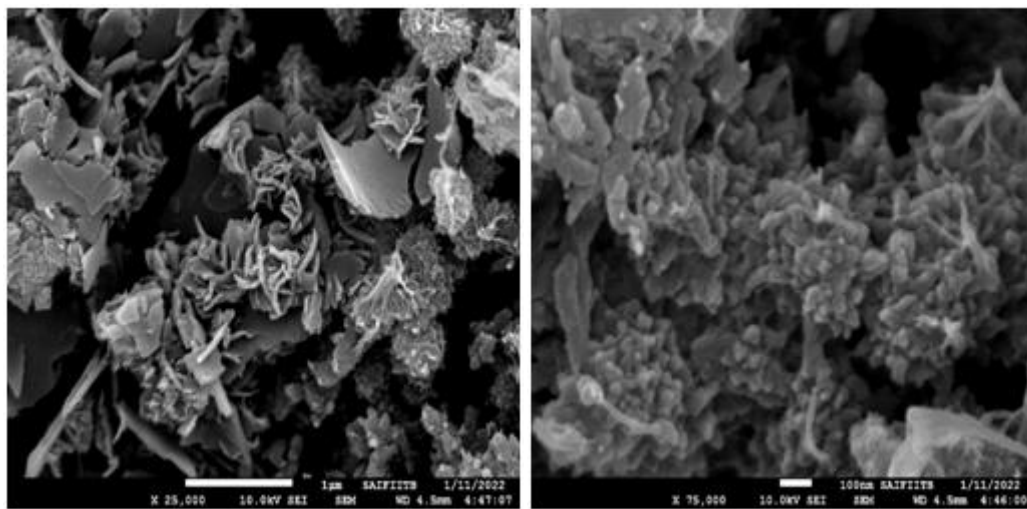


Fig.3 FEG-SEM images of PANI

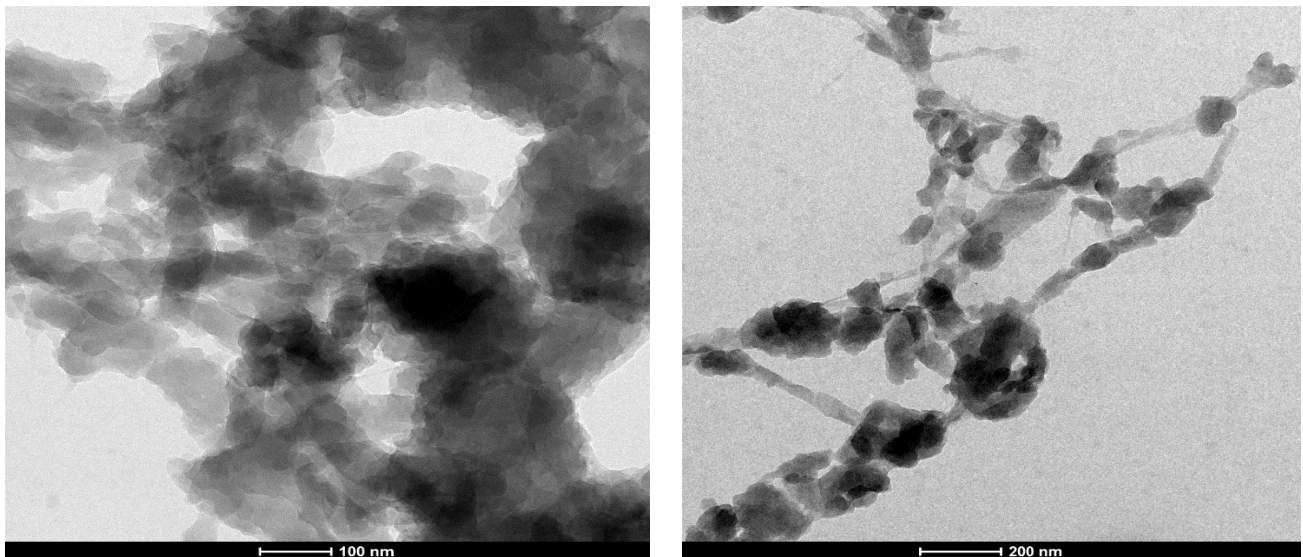
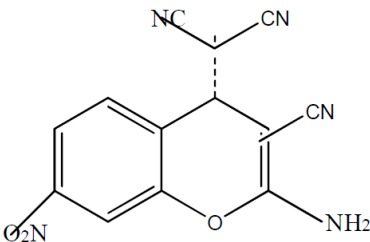
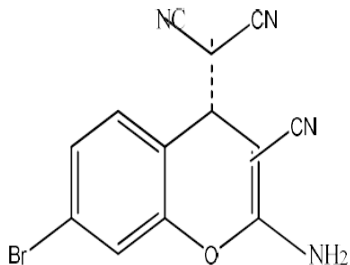
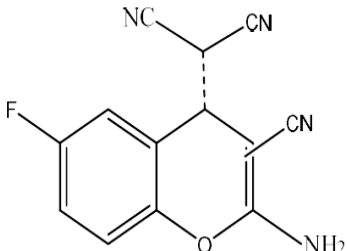


Fig.4 TEM images of PANI

The synthesis of some substituted 4-H chromene from salicylaldehyde and malonitrile as a reactive methylene compound by using nanostructure NPGCN composite as Catalyst was carried out according to the reaction as shown in the Fig.1 and found to be the most effective method for the synthesis of 4-H benzopyran derivatives of medicinally important compounds. The synthesized compounds have not yet been evaluated for their antimicrobial activities.

There are four substituted 4-H derivatives that have been synthesized from the (a) various substituted Salicylaldehyde and (b) Malonitrile by using Ammonia Doped Polyaniline Graphitic Carbon Nitride composite (NPGCN) as Catalyst and they were found to have good results and yield of the product.

Sr. No.	Product	R ₁ in a	R ₂ in b	Time in Min.	Isolated Yield (%)	
					Observed	Reported
1		-NO ₂	-CN	56	81	---
2		-Br	-CN	60	90	
3		-F	-CN	57	84	85 [15]

Reaction conditions: In a round-bottom 10 mL reaction flask, salicylaldehyde (1 mmol), malonitrile (2 mmol), NPGCN catalyst (5 wt %), and ethanol (2 mL) were placed, and the reaction mixture was stirred at 55 °C temperature.

3.1 The Representative analytical data of few Compounds:

2-(2-Amino-3-cyano-7-nitro-4H-chromen-4-yl)-malononitrile (Table Entry01)

Molecular Formula- $C_{13}H_7N_5O_3$ Mol. Weight-281.23 Light yellow solid, 81%; ¹H NMR (500 MHz, DMSO-d₆) δ (ppm) 8.51 (d, 1H, J = 2.75 Hz), 8.24 (dd, 1H, J = 2.75 Hz, J = 8.9 Hz), 7.80 (s, 2H), 7.39 (d, 1H, J = 7.45 Hz), 5.22 (d, 1H, J = 4.1 Hz), 4.80 (d, 1H, J = 4.1 Hz). ¹³C NMR (125 MHz, DMSO-d₆) δ (ppm) 162.7, 154.1, 143.8, 125.9, 125.3, 119.3, 118.8, 117.9, 112.8, 112.6, 48.5, 36.7, 32.5

2-(2-Amino-7-bromo-3-cyano-4H-chromen-4-yl)- malononitrile (Table Entry02)

Molecular Formula- $C_{13}H_7N_4OBr$ Mol. Weight-315.12 white solid, 84%; ¹H NMR (500 MHz, DMSO-d₆) δ (ppm) 7.70 (d, 1H, J = 2.1 Hz), 7.62–7.56 (m, 3H), 7.11 (d, 1H, J = 8.9 Hz), 5.15 (d, 1H, J = 3.45 Hz), 4.62 (d, 1H, J = 3.41 Hz). ¹³C NMR (125 MHz, DMSO-d₆) δ (ppm) 163.2, 149.0, 132.8, 131.4, 120.4, 119.2, 117.8, 116.4, 112.9, 112.8, 47.4, 36.7, 32.4

2-(2-Amino-3-cyano-6-fluoro-4H-chromen-4-yl)- malononitrile (Table Entry03)

Molecular Formula- $C_{13}H_7N_4OF$ Mol. Weight-254.22 Creamy white solid, 85%; ¹H NMR (500 MHz, DMSO-d₆) δ (ppm) 7.57 (s, 2H), 7.34–7.32 (m, 1H), 7.31–7.27 (m, 1H), 7.19–7.18 (m, 1H), 5.13 (d, 1H, J = 4.1 Hz), 4.60 (d, 1H, J = 3.4 Hz). ¹³C NMR (125 MHz, DMSO-d₆) δ (ppm) 163.5, 159.3, 157.3, 146.1, 119.7, 119.6, 119.3, 118.3, 118.2, 117.3, 117.1, 115.2, 114.9, 115.1, 114.7, 112.9, 112.8, 48.1, 37.1, 32.3.

IV. CONCLUSION

In the above reported work we extended the methodology for the synthesis of substituted 4-H chromene by using nanostructure NPGC composite as Catalyst. We synthesize the four different substituted 4-H chromene by using nanostructure NPGCN composite as metal free Catalyst.

V. ACKNOWLEDGMENT

The authors wish to gratefully acknowledge support from the Research Centre Department of Chemistry, G.S. College, Khamgaon Dist. Buldhana, SAIF, IIT, Powai, Mumbai. The author is also thankful to Principal, Science College Pauni Dist. Bhandara for providing laboratory facilities.

VI. REFERENCES

- [1]. A. J. Phillips, J. A. Henderson, and K. L. Jackson University of Colorado, Boulder, CO, USA 2008, p338
- [2]. Kumar KA, Renuka N, Kumar GV, et al. Pyrans: Heterocycles of chemical and biological interest. J Chem Pharm Res. 2015;7: pp 693-700
- [3]. (a) Mansoor SS, Logaiya K, Aswin K, Sudan PN. An appropriate one-pot synthesis of 3,4-dihydropyrano[c]chromenes and 6-amino-5-cyano-4-aryl-2-methyl-4H-pyrans with thiourea dioxide as an efficient, reusable organic catalyst in aqueous medium. J Taibah Univ Sci. 2015;9:213-26. (b) Smits R, Belyakov S, Plotniece A, et al. Synthesis of 4H-Pyran Derivatives Under Solvent-Free and Grinding

- Conditions. *Syn Commun.* 2013;43:465-75. (c) Romdhane A, Janne HB. Synthesis of new pyran and pyranoquinoline derivatives. *Arabian J Chem.* 2017;10:S3128- S34.
- [4]. Khaligh NG, Abd-Hamid SB. 4-(Succinimido)-1-butane sulfonic acid as a Brönsted acid catalyst for the synthesis of pyrano[4,3-b]pyran derivatives using thermal and ultrasonic irradiation. *Chin J Catal.* 2015;36: pp 728-33.
- [5]. Anatoly NV, Michail NE, Fedor VR, et al. Multicomponent assembling of salicylaldehydes, malononitrile, and 4- hydroxy-6-methyl-2H-pyran-2-one: A fast and efficient approach to medicinally relevant 2-amino-4H-chromene scaffold. *C R Chimie.* 2015;18:1344-9.
- [6]. Niknam KM, Mohammad R, Mohamed S. Silica-bonded S-sulfonic Acid as a Recyclable Catalyst for Synthesis of 2,3- Dihydroquinazolin-4(1H)-ones. *Chin J Chem.* 2011;29:1417- 22.
- [7]. Viviana M, Elsa MF, Torres N, et al. Sol-gel synthesis of V2O5-SiO2 catalyst in the oxidative dehydrogenation of nbutane. *Appl Catal A: General.* 2006;312:134-4
- [8]. Ashish Bahuguna, Priyanka Choudhary, Tripti Chhabra, and Venkata Krishnan *ACS Omega* 2018, 3, 12163–12178
- [9]. Ge, L.; Han, C.; Liu, J. J. *Mater. Chem.* 2012, 22, 11843–11850.
- [10]. Pillalamarri, S. K.; Blum, F. D.; Tokuhiko, A. T.; Bertino, M. F. *Chem. Mater.* 2005, 17, 5941–5944.
- [11]. Khalafi-Nezhad, A.; Nourisefat, M.; Panahi, F. *Org. Biomol. Chem.* 2015, 13, 7772–7779.
- [12]. Gao, Y.; Du, D.-M. *Tetrahedron: Asymmetry* 2013, pp 2, 1312– 1317.
- [13]. Harichandran, G.; Parameswari, P.; Kanagaraj, M.; Shanmugam, P. *Tetrahedron Lett.* 2015, 56, 150–154
- [14]. Wang, Y.; Wang, X.; Antonietti, M. *Angew. Chem., Int. Ed.* 2012, 51, 68–89.
- [15]. Datta, K.; Reddy, B. S.; Ariga, K.; Vinu, A. *Angew. Chem.* 2010, 122, 6097–6101.
- [16]. Yang, F.; Wang, Z.; Wang, H.; Wang, C.; Wang, L. *RSC Adv.* 2015, 5, 57122–57126
- [17]. Bhat, S. I.; Choudhury, A. R.; Trivedi, D. R. *RSC Adv.* 2012, 2, 10556–10563.
- [18]. Yadav, J.; Reddy, B. S.; Gupta, M. K.; Prathap, I.; Pandey, S. *Catal. Commun.* 2007, 8, 2208–2211



Synthesis of Substituted Triazine and Its Derivatives, with Their Study of Antimicrobial Activity

Pratibha S. Deulkar, Ramkrushna P. Pawar

Department of Chemistry, Govt. Vidarbha Institute of Science and Humanities, Amravati 444604,
Maharashtra, India

ABSTRACT

The present study focuses on the synthesis of triazine derivatives, prepared by using the conventional and microwave irradiation methods, its characterization and antimicrobial activity were studied. These types of derivatives might have special interest in coordination and medicinal chemistry. Triazine and their derivatives has found many applications in industry particularly for drug development and pharmaceutically applicable molecule. Microwave irradiation were carried out in less solvent which was affordable for the target product, obtained good yield. Spectroscopic techniques such as Ultra, ¹H NMR, Fourier Transform Infrared spectroscopy (FTIR) was carried out. Similarly newly synthesised compound has been tested for their microbial activity.

Keywords- Synthesis, microwave, triazine, Characterization, antimicrobial activity.

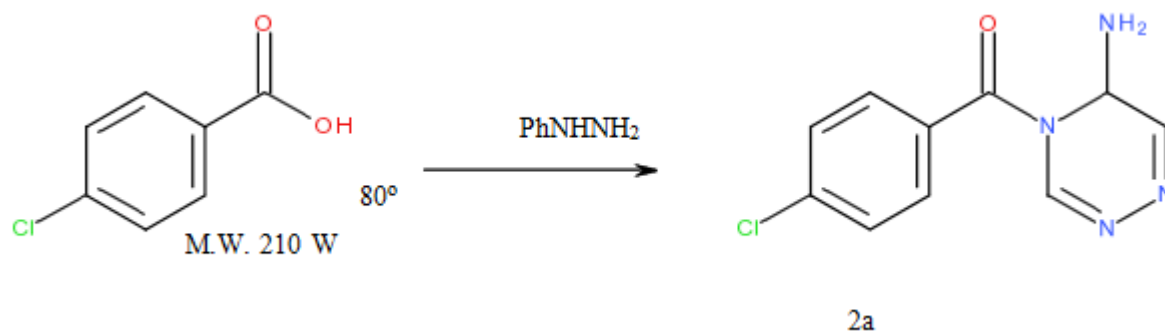
I. INTRODUCTION

Microwave assisted organic synthesis continuous to affect synthetic chemistry significantly by enabling rapid reproducible scalable chemistry development 1-5 the use of microwave irradiation is an established tool in organic synthesis for achieving better selectivity enhancement and reduction of thermal degradation of by product. Triazine derivative and metal complex interesting biological activities. The pharmaceutical importance of these compounds lies in the fact that they can be effectively utilized as a antimicrobial agent. Currently used antimicrobial agent are not effective due to the resistance developed by microbes so that it is on going efforts to synthesize new antimicrobial agent. 6-7 The importance of studying triazine chemistry remains unabated because of their uses as intermediates for synthesis of new heterocyclic compounds. 1,2,4-Triazine derivatives exhibit antifungal, anti-inflammatory, analgesic, antihypertensive. 8-9 The derivatives of 1,3,5-triazine are well-known compounds of considerable interest because of their applications in many different fields. 10 1,2,4-Triazines and their analogues have gained considerable attention because they are found in numerous natural and synthetic biologically and pharmacologically active targets. Present work deals with synthesis and biological study of some new triazine derivatives and their metal complexes characterization by elemental analysis, IR and ¹H NMR analysis

II. EXPERIMENTAL METHOD

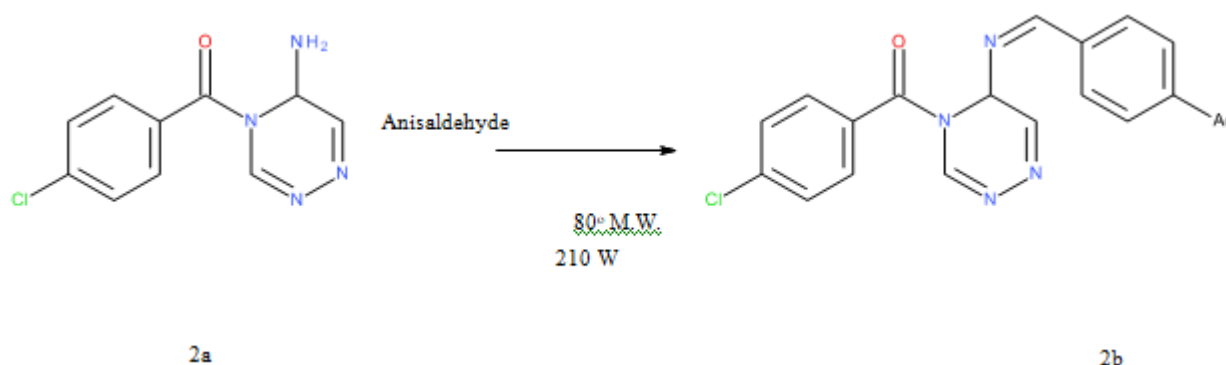
Synthesis of 2a

4-chloro benzoic acid and phenyl hydrazine in presence of micro wave irradiation of 240W at 80⁰ C for 20 minutes then add acetic acid and sodium benzoate in it. Repeat the procedure. Cool it at room temperature. Poured into ice cold water. Filter the precipitated and recrystallized the product with alcohol.



Synthesis of substituted triazine

2a compound react with anisaldehyde in presence of micro wave (240W) at 80⁰ C for 30 minutes . Cool it at room temperature. Poured into ice cold water. Filter the residue and recrystallized the product with alcohol.



IR Characterization of 2a

IR(vmax) cm⁻¹: 3430 (OH str), 3199 (N-N triazine), 1660 (C-O), 1597(C=N str.), 3205 (NH₂ str)

NMR study of 2a

(ppm) 3.10 -3.18(dd, 1H, H), 3.79-3.82(dd, 1H, H), 3.85(s, 3H, OCH₃) 5.19-5.21 (dd, 1H, H), 5.95 (s, 2H, NH₂), 6.91 – 7.92 (m, 9 Ar-H), 9.95 (s, 1H, OH).

Table 1: Physical data of synthesized compound

Sr. no.	Compound no.	Molecular formula	Melting point	Colour of compound	% yield	% of N
1	2a	C ₁₀ H ₉ ClN ₄ O	276	yellowish	68%	23.5
2	2b	C ₁₉ H ₁₅ ClN ₄ O ₂	257	Brown	67.7%	15.2

Biological Study:

Above synthesized triazine derivatives and their metal complex have been studied for their antimicrobial activity against *Escherichia coli*, *proteus mirabilis*, *staphylococcus aureus*,

A. Nigar. The culture of each species was incubated at 37 °C and the zone of inhibition was measured after 24 hr. Most of these compounds were found active

Sr. No.	Compound	Antimicrobial activity			
		<i>E.coli</i>	<i>P.mirabilis</i>	<i>S. aureus</i>	<i>P.aeruginosa</i>
1	2a	12	10	09	08
2	2b	15	11	13	16

Strongly active range : 15-18 mm , weakly active range : 7-10 mm Moderately active range : 11-14 mm

Thus from above result it was observed that the heterocyclic compound were found effective against *Escherichia coli*, *proteus mirabilis*, *staphylococcus aureus*, and *A. Nigar* so all synthesized compound can easily be used for the treatment of disease caused by these above pathogens only when they do not have poisons and other side effects.

III. ACKNOWLEDGEMENT

The authors are thankful to head of department of chemistry Government Vidarbha institute of science and Humanities , Amravati their valuable guidance and cooperation .

IV. REFERENCES

- [1]. Chow, W.S.; Chan, T.H. Microwave-assisted solvent-free N-arylation of imidazole and pyrazole. *Tetrahedron Lett.* 2009, 50, 1286-1289.

- [2]. Abdul Rauf, S.S.; Gangal, S. Microwave assisted efficient one-pot synthesis of 3,5,6-trisubstituted-1,2,4-triazines from fatty acid hydrazides under solvent-free conditions and their antimicrobial activity. *ARKIVOC* 2007, xvi, 137-147
- [3]. Kappe, C.O.; Dallinger, D. The impact of microwave synthesis on drug discovery. *Nat. Rev. Drug Discov.* 2006, 5, 51-64.
- [4]. Shipe, W.D.; Wolkenberg, S.E.; Lindsley, C.W. Accelerating lead development by microwave-enhanced medicinal chemistry. *Drug Discov. Today Tech.* 2005, 2, 155-161.
- [5]. Leadbeater, N.E. Fast, easy, clean chemistry by using water as a solvent and microwave heating: The Suzuki coupling as an illustration. *Chem. Commun.* 2005, 2881-2902.
- [6]. M. Kidwai, Y. Goel, and R. Kumar, "Synthesis of novel antibacterial cephalosporin derivatives using microwaves," *Indian Journal of Chemistry*, vol. 37B, p. 174, 1998.
- [7]. B. S. Holla, R. Gonsalves, B. S. Rao, S. Shenoy, and H. N. Gopalakrishna, "Synthesis of some new biologically active bis-(thiadiazolotriazines) and bis-(thiadiazolotriazinyl) alkanes," *Farmaco*, vol. 56, no. 12, pp. 899-903, 2001.
- [8]. Koç ZE (2011) Complexes of iron (III) and chromium (III) salen and salophen Schiff bases with bridging 1, 3, 5-triazine derived multidirectional ligands. *J Heterocycl Chem* 48(4):769-775
- [9]. Carofiglio T, Varotto A, Tonellato U (2004) One-pot synthesis of cyanuric acid-bridged porphyrin-porphyrin dyads. *J Org Chem* 69(23):8121-8124
- [10]. Mooibroek TJ, Gamez P (2007) The s-triazine ring, a remarkable unit to generate supramolecular interactions. *Inorg Chim Acta* 360(1):381-404

Study of Molecular Interaction in Various Liquid Mixtures by Acoustical Technique : A Review

Krishna Kumar Pandey*, Shilpa Kundrakpam

Acoustics Research Laboratory, Department of Physics, School of Basic Sciences and Research, Sharda University, Greater Noida-201310, Uttar Pradesh, India

ABSTRACT

The knowledge of molecular interactions between the atoms of any liquid or mixtures of two liquids is very much required for their several types of applications. There are several methods and tools available for explaining that how the atoms in a liquid mixture interacts with each other. In this review paper we have reviewed several research papers related to the study of molecular interactions. Here the authors of various research papers have used a very important technique known as the acoustical technique for which they have used the ultrasonic waves for study of molecular interactions. They have used the ultrasonic interferometer for the measurement of ultrasonic wave velocity. Density of liquid has been found by using the specific gravity bottle. For viscosity measurement, the Oswald viscometer has been used. By measuring the three parameters such as ultrasonic wave velocity, density of a particular liquid mixture and its viscosity, the several acoustic and thermodynamic parameters can be evaluated. This study helps a lot for understanding the molecular interactions in a particular sample. The various observed parameters have been explained in detail.

Keywords: Molecular Interaction; Ultrasonic Waves; Specific Gravity Bottle; Oswald viscometer; Liquid Mixtures

I. INTRODUCTION

The contents in this review paper includes the ultrasonic study which has been trending in the present-day scenario for its ability to dig up information about molecular structure and interaction between binary liquid mixtures, ternary liquid mixtures and as well as organic liquid mixtures. Not only in this field of area, ultrasonic study is widely used for its non-destructive nature to fulfil other applications in the area of medical and science, agriculture, industries and many more. But the focus in this review paper mainly focuses on finding deep information about the interaction between different binary, ternary and organic solution in accordance to different criteria used for evaluation. The thermo properties, excess functions and acoustic parameters are the main component of this study which is calculated in every research paper studied so far. Many researchers also begin their research on nano fluids which were recently announced as new type of thermal fluids (Singh Kuljeet et al 2020). The study of nano-materials mixed with some aqueous solutions has

been growing due to their wide application in various fields of study. The study of physical properties and thermodynamic properties in finding out the behaviour between liquids and liquid mixtures has been considered as the fundamental knowledge and importance in going further study.

Polyacrylonitrile (PAN), polyvinylpyrrolidone (PVP), polyvinyl chloride (PVC) and polymethyl methacrylate (PMMA) and using dimethylformamide (DMF) as solvent (A. Upmanyu et al 2020) were the most trendy and popular polymers in the field of industries for their outstanding performance in contributing wide range of applications in present day scenario such as PVP polymer is used as plasma volume expander in treating trauma victims and not only this it is also used in medical products, hair products etc. and many more.

The binary mixtures of 1-butanol mixed with three different molecular weights of polyethylene glycols (PEG 200 and PEG 400) or tetraethylene glycol dimethyl ether (TEGDME) at varied temperature are the study which uses the viscosity data correlated by the one-parameter Grunberg–Nissan model, two-parameter Eyring–UNIQUAC and three-body McAlister model and the Eyring–NRTL model (N. Živkovi'c et al 2013). Continuous research regarding volumetric, acoustic and viscometric of liquid mixture provide huge contribution in discovery of new information between component of liquid mixture. Therefore, these kinds of studies help in numerous technological and biological procedures.

II. RESEARCHED METHODOLOGY

Researchers used different methods and techniques to measure the ultrasonic velocity, viscosity and density of the various liquid which is to be analysed. The ultrasonic interferometer is one of the most popular and frequently used devices to measure ultrasonic velocity where the ultrasonic wave with known frequency is made to pass through the liquids by keeping the temperature constant using water bath. Specific gravity bottle is mostly used to measure density but some researcher used other method like hydrostatic sinker (Bhandakkar V.D. et al 2012) and bicapillary pycnometer (S. Bahadur Alisha et al 2017). Ostwald's viscometer is used to measure the viscosity of the liquids.

Theory:

Given below are list of some of the acoustical parameters used by the researchers to study physico-chemical properties of various liquid mixtures as well as to further derive other acoustical parameters:

1. Acoustic impedance, $Z = \rho \times U$ (Here ρ is the density of the sample and U being the velocity of Ultrasonic waves)
2. Adiabatic compressibility, $\beta = 1 / (U^2 \times \rho)$
3. Intermolecular free length, $L_f = K_B \times \beta^{1/2}$ Where, $K_B = \text{Jacobson constant}$
4. Ultrasonic Attenuation $\alpha/f^2 = 8\pi^2 \eta / 3\rho U^3$ (Here η is the Viscosity)
5. Relaxation Time $\tau = 4\beta\eta/3$

III. RESULTS AND DISCUSSION

The table as given below shows the different liquids studied by various researchers and their evaluation for the various acoustical parameters. In Most of the cases, the liquids were studied by either varying the temperature or keeping at a constant and increasing the molar concentration of the liquid mixtures used. Like in the case of binary mixtures of propranol hydrochloride with water at different temperature ranging from 303 to 313 K in different concentration have been studied. The ultrasonic velocity and acoustic impedance show nonlinear behaviour at increasing molar concentrations. This result gives the information about intermolecular weak association which is caused by hydrogen bonding in the solution.

On contrary, the adiabatic compressibility shows opposite behaviour to the ultrasonic velocity and acoustic impedance at increasing molar concentration. This predicts that there is powerful association in between the liquids at solute concentration. The free length path also shows nonlinearity in increasing molar concentration.

In ternary mixtures of 1-alkanols in di-isopropyl ether and 2,2,2-trifluoroethanol the strength of the association between the liquids faded as temperature rises. This is due to the existence of weak intermolecular forces and thermal dispersion forces.

Therefore, as shown in the above table the study of different liquid mixtures has been carried out by different researchers to understand the physico-chemical properties of various types of liquids using ultrasonic method. Variety of acoustical parameter as well as thermal properties has been calculated for better understanding and findings of the studied liquids.

Table : Information of the various reviewed samples

S.No.	Name of liquid studied in the research papers	Conc. %	Fixed Frequency.	T (K)	Density Kg/m ³	Viscosity NSm ⁻²	Ultrasonic Velocity m/s	A. Comp. ($\beta \times 10^{-10}$ (N ⁻¹ m ²))	Impedance Kg ⁻² /s	Free path length X 10 ⁻¹¹	References
1	Acrylonitrile with methanol, cyclohexane and 1,4-dioxane	1.0	10 MHz	303K	0.8066	0.3060	1425.0	10.925	0.8428	0.6594	1
2	Triethylamine with different types of carbitols	0.1006	2M Hz	308.15K	0.7144	0.9792	1079.9	----- ---	1.3268	4.9393	2
3	Aqueous paracetamol solutions	0.001	2M Hz	303K	932.5	0.8279	1501.21	4.7584	----- -----	----- ---	3
4	Dilute solutions of	0.0	----	328K	856.5		1163.	8.6287	0.996	0.637	4

	poly (ethylene glycol)	118	---			----- ---	2		3	1	
5	Propranolol hydrochloride	0.0 2	1M Hz	303 K	1002. 2	1.27	1531	4.26	1.54	4.10	5
6	Aqueous l- glutamic acid	0.0 2	2M Hz	323K	----- -	----- ----	1540	4.200 E-10	----- ----	4.200 E-11	6
7	Ternary mixtures of 1-alkanols in di-isopropyl ether and 2,2,2-trifluoroethanol	0.0 210	3M Hz	303K	821.4	0.466 2	924.3	----- --	----- ----	----- -	7
8	2,3-dichloroaniline and PEG	0.2	2M Hz	300K	1.389	5.717	1460. 7	3.5	1.83	0.371	8
9	CuO nanoparticles with aqueous solution of ethylene, propylene and hexylene- glycol	0.0 2	2M Hz	303K	----- -	----- ---	----- ---	----- ---	----- ---	----- --	9
10	PAN, PVP, PVC, PMMA	0.1	2M Hz	303.1 5K	----- -	----- ---	----- ---	----- --	----- --	----- -	10
11	Polymer solutions of polyisobutylene (PIB)	0.0 2	2M Hz	333K	-----	41	1228	----- -	103	68	11
12	Tetrahydrofuran with Benzenes	0.2	2M Hz	302K	1.389	5.717	1460. 7	3.374	2.202 9	0.364	12
13	1-Butanol with PEG200, PEG400, TEGDME	0.0 999	2M Hz	288.1 5K	0.805 8	2.59	----- ----	----- --	----- ---	----- ---	13
14	Aqueous sodium methyl p-hydroxybenzoate with polyethylene glycols	0.0 982	2M Hz	298K	-----	0.898 7	----- --	4.482	1.491	90.61 45	14
15	1,1'-Binaphthalene-2,2'-diyl Diacetate Solutions	0.9 25	2M Hz	308.1 5K	1464	0.547	957.6	----- --	0.882	0.979	15
16	p-chlorotoluene in benzene	0.1 311	2M Hz	303.1 5K	915.6	----- -	1284. 12	6.6234	11.75 74	----- --	16

IV. CONCLUSION

The Non-Destructive Technique such as the Ultrasonic method has been becoming a highly demandable technique to study the physico-chemical properties of different binary, ternary and organic liquid mixtures. This reviewed paper highlighted the different types of liquids used by various researchers. The values of the different acoustical parameters for these liquids are also highlighted in the table by reviewing the research paper of the similar area.

V. REFERENCES

- [1]. Bhandakkar, V.D. and Rode, S. (2012), Acoustical studies on molecular interactions in binary liquid mixtures at 303K, *Advances in Applied Science Research*, 1-7.
- [2]. Bahadur Alisha, S., Nafeesa Banu, S., Krishna Rao, K.S., Subha, M.C.S. (2017), Ultrasonic Studies on Binary Liquid Mixtures of Triethylamine with Carbitols at 308.15K, *Indian Journal of Advances in chemical Science*, 2-8.
- [3]. Aswale, S.R. Aswale, S.S. Dhote, A.B. and Tayade, D.T. (2011), Ultrasonic Investigation of Molecular Interaction in Paracetamol Solution at Different Concentrations, *Journal of chemical and pharmaceutical Research*, 1-5.
- [4]. Sannaningannavar, F.M., Navati, B.S. and Ayachit, N.H. (2012), Studies on thermo-acoustic parameters in the dilute solutions of poly (ethylene glycol), *Polym. Bull.*, 1- 16.
- [5]. Naik Ritesh, R., Bawanka, S.V. and Kukade, S.D. (2015), Acoustical Studies of Molecular Interaction in the Solution of Propranolol Hydrochloride Drug at Different Temperatures and Concentrations, *Russian Journal of Physical Chemistry*, 1-6.
- [6]. Shamkumar Priyanka and Chimankar, O.P. (2015), Ultrasonic Characterisation of Aqueous L-Glutamic Acid at different temperatures, *international journal of Advanced Information Science and Technology*, 1-4.
- [7]. Palani, R. and Balakrishnan, S. (2010), Acoustical properties of ternary mixtures of 1- alkanols in di-isopropyl ether and 2,2,2-trifluoroethanol mixed solvent, *Indian Journal of Pure & Applied Physics*, 1-7.
- [8]. Kumar Mahendra, Khan Aftab Mohd, Yadav Prasad Chandreshvar, Pandey Kumar Dharmendra and Singh Dhananjay, (2021), Ultrasonic characterisation of binary mixture of 2,3-dichloroaniline and polyethylene glycols, *J. Chem. Thermodynamics*, 1- 8.
- [9]. Singh Kuljeet, Dhiman Monika, Kumar Pankaj, Gupta, D. P., Singh, D. P. and Arun Upmanyu, (2020), Thermo-acoustic investigations of molecular interactions in CuO nano particles contained aqueous solutions of some glycols, *AIP Conference Proceedings*, 3-8.
- [10]. A. Upmanyu, D. P. Gupta, M. Dhiman, P. Kumar, K. Singh and D. P. Singh, (2020), Theoretical Investigations of Effective Debye Temperature, Pseudo-Gruneisen Parameter, and Bayer's Nonlinear Parameter of Some Polymers and Their Blends in Dimethylformamide at 303.15 K, *Journal of Biochemistry & Molecular Medicine*, 2-6.

- [11]. Upmanyu Arun, and Singh D.P., (2014), Ultrasonic Studies of Molecular Interactions in Polymer Solution of the Polyisobutylene (PIB) and Benzene, *Acta Acustica United with Acustica*, 1-6.
- [12]. K. Vijaya Lakshmi, D. Suhasini, M. Jayachandra Reddy, C. Ravi, K. Chowdoji Rao, M.C.S. Subha, (2014), Ultrasonic Studies on Binary Liquid Mixtures of Tetrahydrofuran with Benzenes At 308.15 K, *Indian Journal of Advances in Chemical Science*, 1-11.
- [13]. N. Živkovi'c, S. Šerbanovi'c, M. Kijev'canin, and E. Živkovi'c, (2013), Volumetric Properties, Viscosities, and Refractive Indices of the Binary Systems 1-Butanol + PEG 200, + PEG 400, and + TEGDME, *Int J Thermophys*, 1-19.
- [14]. Thakur Ashima, K.C. Juglan, and Kumar Harsh, (2020), Acoustic and viscometric studies of ternary liquid mixtures of aqueous sodium methyl p-hydroxybenzoate with polyethylene glycols at 25°C, *Journal of Physics: Conference Series*, 2-12.
- [15]. P. Pooja Adroja, S. P. Gami, J. P. Patel and P. H. Parsania, (2010), Ultrasonic Speed and Related Acoustical Parameters of 1,1'-Binaphthalene-2,2'-diyl Diacetate Solutions at 308.15 K, *E-Journal of Chemistry*, 1-5
- [16]. G. Pavan Kumar, Praveen Babu, K. Samatha, A. N. Jyosthna and K. Showrilu, (2014), 'Acoustical studies of binary liquid mixtures of p-chlorotoluene in benzene at different temperatures', *International Letters of Chemistry, Physics and Astronomy*, 2-14



A Synthesis and Fluorescence Properties of Trivalent Europium Doped Yttrium Vanadate and YVO₄ : Eu₃₊ @SiO₂ for Biological Application

R. G. Korpe¹, K. A. Koparkar^{2*}, G. V. Korpe³, S. K. Omanwar⁴

¹Department of Physics, Shri Shivaji Science College Amravati-444003, Maharashtra, India

^{2*}Department of Physics, M. S. P. Arts, Science and K. P. T. Commerce College, Manora, Dist: Washim-444404, Maharashtra, India

³Department of Chemistry, Shri Shivaji Science College, Amravati-444603, Maharashtra, India

⁴Department of Physics, S.G.B.A. University, Amravati-444602, Maharashtra, India

ABSTRACT

The red emitting Eu³⁺ doped YVO₄ phosphor were synthesized via co-precipitation method. The Core shell structured of Europium doped Yttrium Vanadate capped with SiO₂ was obtained by using TEOS (Tetraethyl Orthosilicate) to modified the biological properties. The structure confirmation and morphological properties of as-synthesized material were investigated by using powder X-ray diffraction (XRD) and Scanning electron microscopy (FE-SEM). The photoluminescence (PL) study of as-synthesized material were studied using spectrophotometer which reveals that intense red emission corresponds to ⁵D₀ -⁷F₂ transition of Eu³⁺ ions in the host lattice under the UV excitation. The biocompatibility of as-synthesized material shows the good potential for biological applications.

Keywords: Co-precipitation method; YVO₄:Eu³⁺@SiO₂; biological application; optical material.

I. INTRODUCTION

The red emitting Eu³⁺ doped YVO₄ is one of the best and very demanding phosphor in the in the field of luminescence [1]. Because of its high chemical and thermal stability as well as low phonon energy. The quantum efficiency of YVO₄:Eu³⁺ phosphor is almost 70%. YVO₄:Eu³⁺ phosphor is an important commercial red emitting luminescence material used in display applications. Various dopants can act as luminescent centre (activator) and/or as a sensitizer in YVO₄ host, which absorbs the light energy and transfer to the luminescent centre [2, 3]. In the resent years, luminescence materials capped with core shell of SiO₂ are widely used for various applications [4]. Moreover, the SiO₂ silica shell can enhance the photochemical and stability of the core particles. Such kinds of materials are generally used in biomedical targeting and drug-delivery systems [5, 6]. There are several reports on luminescence materials capped with tetraethyl orthosilicate (TEOS) with improving the luminescence intensity such as Lin et al. synthesized Gd₂O₃:Eu³⁺@SiO₂ nanophosphor by using sol-gel method with size of silica spheres in the range 60 -250 nm

[7], Yu et al. synthesized $\text{YVO}_4:\text{Eu}^{3+}@\text{SiO}_2$ by using Pechini sol-gel process [8], Bao et al. synthesized $\text{YVO}_4:\text{Eu}/\text{SiO}_2$ core-shell composite by using simple citrate sol-gel method with particles size in the range of 300–500 nm [9], Cheng et al. synthesize $\text{YVO}_4:\text{Eu}^{3+}@\text{SiO}_2$ composite microspheres. The microspheres were fabricated by using facile surface protected etching method for biological application [10] and Lai et al. synthesized functional $\text{YVO}_4:\text{Eu}^{3+}$, $\text{Bi}^{3+}@\text{SiO}_2$ submicron-sized core-shell particles by using hydrothermal and sol-gel methods for solar cell application [11] etc. Most of the researcher preferred sol-gel method and pechini method but these methods required very costly organic additives at the time of synthesis.

Inspiring from the above discussions, the present work planned to study the luminescent properties of Europium doped Yttrium Vanadate and $\text{YVO}_4:\text{Eu}^{3+}@\text{SiO}_2$ phosphor synthesized by using simple co-precipitation methods for biological application, which is main accomplishment of the present work.

II. EXPERIMENTAL

Synthesis

The phosphor $\text{YVO}_4:\text{Eu}^{3+}$ was prepared by co-precipitation method. The starting chemicals Y_2O_3 (99.99%, AR) and Eu_2O_3 (99.90%, AR) were mixed together in a china clay basin. A small quantity of deionized water added then HNO_3 was added drop by drop and heated slowly at 50°C . After that the solution was further heated to get excess of acid boiled off. The resulting solution was considered as $\text{Y}(\text{NO}_3)_3:\text{Eu}$, to this soluble solution, NH_4VO_3 (AR) dissolved in deionized water and then added drop by drop [12]. The precipitate so obtained was filtered out, washed with deionized water and acetone, and dried at 50°C . The final product was calcined at 900°C .

Preparation of $\text{YVO}_4:\text{Eu}^{3+}@\text{SiO}_2$ core-shell particles

The particles of $\text{YVO}_4:\text{Eu}^{3+}$ with 20 ml of deionized water, sonicated for 30 min and then the silica shells capped over $\text{YVO}_4:\text{Eu}^{3+}$ were prepared by hydrolysis of TEOS in an alcohol solvent in the presence of water with ammonia was added drop by drop in the solution of $\text{YVO}_4:\text{Eu}^{3+}$. The mixture was stirred 30 min and to agitated by using ultrasonification for 1 h to disperse the core particles. The reaction was continue in the ultrasonicator to obtain more dispersed core and uniform SiO_2 coating on the core [13, 14]. Then $\text{YVO}_4:\text{Eu}^{3+}@\text{SiO}_2$ core-shell particles were formed.

Characterization of samples

The phase purities of $\text{YVO}_4:\text{Eu}^{3+}$ samples were studied using Rigaku miniflex II X-ray Diffractometer and $\text{Cu K}\alpha$ ($\lambda = 1.5406 \text{ \AA}$) radiation in the range 10° to 90° . PL and PL excitation (PLE) spectra were measured on fluorescence spectrophotometer (Hitachi F-7000) at room temperature. The parameters such as spectral resolution, width of the monochromatic slits (1.0 nm), photomultiplier tube (PMT) detector voltage and scan speed were kept constant throughout the analysis of samples.

III. RESULTS AND DISCUSSION

X-ray diffraction

The formation of the YVO₄ in the crystalline phase synthesized by co-precipitation synthesis method was confirmed by XRD pattern as shown in Fig. 1. The XRD pattern for YVO₄:Eu³⁺ agreed well with the standard data from ICDD file (01-082-1968). Also the XRD pattern show that the formed material was completely crystalline and in single phase, where $a = b = 7.11$ and $c = 6.28$ Å. The space group for YVO₄ is I41/amd(141) [3].

Scanning electron microscopy

Fig. 2 (A) shows the SEM images of the YVO₄:Eu³⁺ and YVO₄:Eu³⁺@SiO₂ core-shell particles. In Fig. 2 (A) that the YVO₄:Eu³⁺ particles have an average particle size in the range of 100-120 nm and the surfaces of the YVO₄:Eu³⁺ particles were smooth. After coating SiO₂ on the YVO₄:Eu³⁺ particles, the particle size of YVO₄:Eu³⁺@SiO₂ core-shell became increases with spherical nature as shown in Fig. 2 (B) [15].

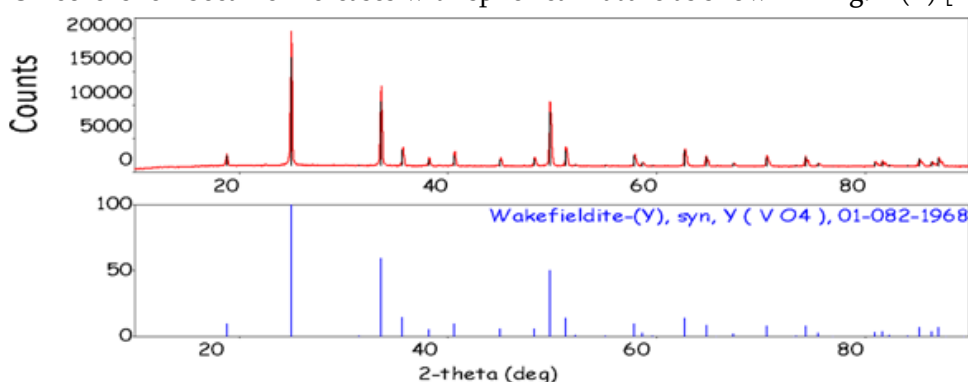


Figure 1: XRD pattern of YVO₄:Eu³⁺.

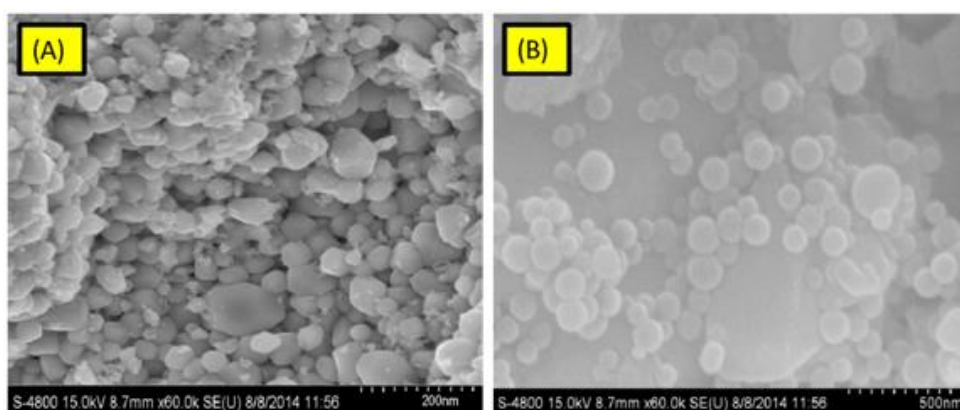


Figure 2: SEM image of YVO₄:Eu³⁺ (A) and YVO₄:Eu³⁺@SiO₂ (B).

Photoluminescence study

In Fig. 3 shows YVO₄:Eu³⁺@SiO₂ core-shell particles gives strong red emission under UV excitation than YVO₄:Eu³⁺ with similar peak position. The most intense excitation band centered at 318 nm monitoring at

621 nm is due to the overlapping of the O²⁻-Eu³⁺ charge transfer band (CTB) and the VO³⁻ absorption [16]. One small peak was observed at 395 nm due to the 4f-4f transitions of Eu³⁺. The emission spectra consist of number of peaks in the visible range. From the Fig. 3 It is clearly seen that the two emission spectra of YVO₄:Eu³⁺ and YVO₄:Eu³⁺@SiO₂ consist of five peak in the range 500 to 700 nm corresponds to 5D₀ to 7F_J (J= 1, 2 and 3) transitions of Eu³⁺ ions. The emission peak at 539 nm and 596 nm is corresponding to magnetic dipole of 5D₀-7F₁ transition, whereas the two peak at 617 and 621 nm corresponding to 5D₀-7F₂ transition of Eu³⁺ ions which are due to the electric dipole transitions. The electric dipole transition exhibits more intense peak than magnetic dipole transition only when the impurity ion is situated at the non-inversion center of the crystal. Moreover, the emission peak at 648 nm is corresponding to 5D₀-7F₃ transition [12].

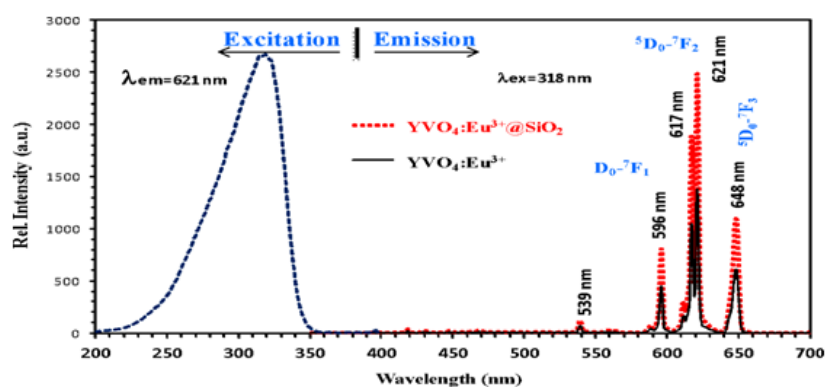


Figure 3: PL excitation and two emission spectra of YVO₄:Eu³⁺ (Black solid line) and YVO₄:Eu³⁺@SiO₂ (Red dotted line).

HeLa cell cytotoxicity and drug release properties of YVO₄:Eu³⁺@SiO₂ material

The potential use of the luminescence phosphors in biological fields, the cytotoxic measurements by MTT assays (It is a colorimetric assay for assessing cell viability) on HeLa cells was studied. The effects of YVO₄ with different concentrations on HeLa cell viabilities are depicted in Fig. 4. It is clearly a show that the assay results demonstrate the YVO₄:Eu³⁺@SiO₂ was almost no toxicity upon incubation with HeLa cells. The viability of HeLa cells varied with increasing concentration. Thus it was found that the prepared sample shows no cytotoxicity using the MTT assays [17].

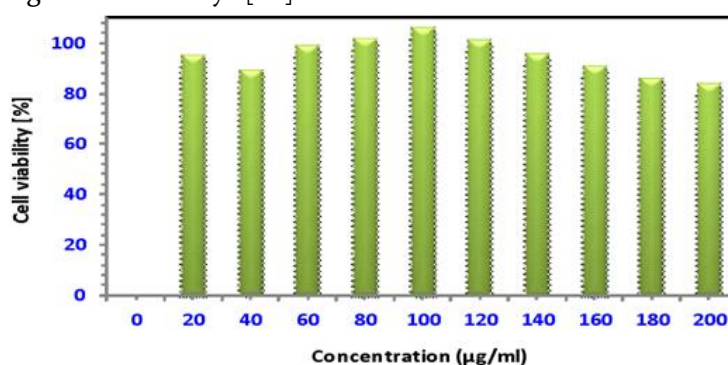


Figure 4: Viability experiments of Hela cells with various concentrations of YVO₄@SiO₂ after 24 h of incubation.

IV. CONCLUSIONS

The YVO₄ synthesized by co-precipitation method which is low cost, low temperature and not required any other additive for initiation of process of synthesis. The YVO₄:Eu³⁺@SiO₂ shows optimum PL emission than YVO₄:Eu³⁺ phosphor. The obtained YVO₄:Eu³⁺@SiO₂ core-shell phosphor has spherical morphology, submicron size and narrow size distribution. The cytotoxicity tests of as prepared sample indicate that the YVO₄:Eu³⁺ particles capped with SiO₂ show the no cytotoxicity. Moreover, our strategy developed other core-shell yttrium based phosphor in the future.

Acknowledgements

One of the authors K. A. Koparkar is thankful to the Chairman FIST-DST Project, for providing XRD facility for this work.

V. REFERENCES

- [1]. Tang L, Gui W, Ding K, Chen N. and Du G. 2014 J. Alloys Compd. 590 277.
- [2]. Zhang S, Liang Y, Gao X Y and Liu H T 2014 PHYSICA POLONICA A 125 105.
- [3]. Koparkar K. A and Omanwar S. K. 2014 J. Lumin. 175 175.
- [4]. Darbandi M, Hoheisel W and Nann T. 2006 Nanotechnol 17 4168.
- [5]. Xiaoxing Sun. "Mesoporous silica nanoparticles for applications in drug delivery and catalysis, Iowa State University, 2012.
- [6]. O'Farrell N, Houlton A and Horrocks B. R. 2006 Int J Nanomedicine. 1 451.
- [7]. Lin K M, Lin C C and Li Y Y 2006 Nanotech 1 745.
- [8]. Yu M, Lin J and Fang J 2005 Chem. Mater. 17 1783
- [9]. Bao A, Lai H, Yang Y, Liu Z, Tao C. and Yang H 2010 J Nanopart. Res. 12 635.
- [10]. Cheng Z, Ma P, Hou Z, Wang W. Dai Y. Zhai X. and Lin J. 2012 Dalton Trans. 41 1481.
- [11]. Lai H, Wang Y, Du G, Li W. and Han W 2014 Ceram. Int. 40 6103.
- [12]. Koparkar K.A., Bajaj N.S., Omanwar S.K. 2015 Opt. mater. 39 74.
- [13]. Stöber, Werner; Fink, Arthur and Bohn 1968 J. Colloid and Interface Science. 26 62.
- [14]. Han J.K., Hirata G.A., Talbot J.B. and McKittrick J., 2011 Materials Sci. and Eng: B 176436.
- [15]. Lai H., Wang Y., Du G., Li W., Han W. 2014 Cer. Int. 40 6103.
- [16]. Xia Z, Chen D, Yang M. and Ying T 2010 J. Phys. Chem. Solids 71 175.
- [17]. Zhang J, Wang Y, Xu Z, Zhang H, Dong P, Guo L, Li F, Xin S and Zeng W 2013 Mater. Chem. B 1 330.

MgSe Thin Films Deposited By Successive Ionic Layer Adsorption and Reaction Method

Kailas C. Shinde¹, Raghavendra J. Topare², Yogesh S. Sakhare^{*3}

¹Department of Physics, Madhavrao Patil Mahavidyalaya, Murum, Dist: Osmanabad, Maharashtra, India

²Department of Physics, Yogeshwari Mahavidyalaya, Ambajogai, Dist: Beed, Maharashtra, India

^{*3}Department of Physics, Late Pundalikrao Gawali Arts and Science College, Shirpur (Jain), Dist: Washim, Maharashtra, India

ABSTRACT

Manganese selenide have generated considerable scientific and technological interest due to their remarkable physical and chemical properties and associated applications. Magnesium Selenide thin films were fabricated using Successive Ionic Layer Adsorption and Reaction (SILAR) deposition technique at different SILAR cycles. These deposition techniques are a very simple and produce thin films at room temperature. The structural and morphological characterizations of the as deposited MgSe films have been carried out by means of X-ray diffraction (XRD), Field Emission Scanning Electron Micrograph (FESEM).

Keywords: Thin Films, XRD, SILAR method, Morphological properties

I. INTRODUCTION

Transition metal chalcogenide systems have recently attracted unlimited consideration due to the fact that they possessed exceptional physical and chemical properties which open windows for various applications. From last two decades, nanocrystalline thin films of metal chalcogenide grown by chemical route have been extensively studied due to their commercial outstanding applications in optoelectronic devices. The SILAR method is inexpensive, simple and convenient for large area deposition[1,2]. A variety of substrates such as insulators, semiconductors, metals and temperature sensitive substrates can be used since the deposition is carried out at or near to room temperature. Metal chalcogenide thin films prepared by SILAR method are of particular interest as in recent years, thin film technology has developed enormously due to the fact that one dimension of film is negligible and that is relatively easy to produce by SILAR method. The technology of thin films deals with the films of thickness between tenths of nanometers and several micrometers can be easily prepared by SILAR. The SILAR plays a pivotal role in the deposition of materials. This method is suitable for industrial application to develop synthetic materials of tailored properties for communication, information and solar energy conversion with decreased size of active electronic components, a higher packing density, higher seed performance and lower cost[3,4]. In this work, Magnesium selenide thin films

were deposited by SILAR method. Number of SILAR cycles was optimized to determine its effect on the structural properties of the deposited thin film materials.

II. EXPERIMENTAL

2.1 Deposition of thin films

SILAR method, to develop thin film the substrate is immersed repeatedly into separately placed cationic and anionic precursor alternately. To eliminate freely bound variety, after each precursor immersion, the substrate is rinsed in de-ionized water. For the current work the glass slides of size 75×25×1 mm were used as substrates. Before actual deposition cleaning of the substrate is very important as it affects the development system. Initially, the slides were washed with liquid detergent, then boiled in concentrated acid for 2 hour, and then kept in it for next 48 hours. The substrates were then washed with double distilled water and cleaned in ultrasonic cleaner for 10 min. Finally, the substrates were dried using AR grade acetone. The SeO₂ solution was prepared by dissolving 1g of selenium powder (99% purity, Merck) with 10 ml nitric acid (HNO₃). It was then boiled for few minutes to get white residual powder. To it 100 ml of distilled water was added to prepare 0.13 M SeO₂ solution. The deposition of MgSe films was done at room temperature in a reactive solution prepared in a beaker. Glass substrates were immersed in the 80 ml of MgCl₂ solution for 10 s. It was then to immersed in 80 ml of freshly prepared SeO₂ solution for 10 s. This forms one SILAR deposition cycle. Deposition cycles were varied from 100 to 350 cycles in the steps of 35 cycles. All the prepared samples were annealed for 48 h for the complete transformation. The X-ray diffraction was used to study the structure of the film. X-ray diffraction patterns of the films were taken with a PANalytical X'Pert PRO MRD X-ray diffractometer with CuK α radiation in the 2 θ range from 20 to 90. The morphological study of the film was carried out using scanning electron microscopy (SEM) with a Park Scientific Instruments and SEM/EDAX with JOEL's JSM -7600F. The scanning electron microscope gives topographical and elemental information at various magnifications.

2.2 X-ray diffraction

MgSe thin films were prepared onto glass substrates using simple and economic SILAR technique. The inter-planar spacing's d was calculated using the relation,

$$d_{hkl} = \frac{a}{\sqrt{h^2 + k^2 + l^2}}$$

Figure 1 shows the x-ray diffraction pattern of MgSe thin film deposited on glass substrate at room temperature. The diffraction peaks of MgSe is found at 2 θ values of 28.28, 32.31 and 47.00 corresponding to the lattice plane (111) (200) and (220). The d value calculated using equation confirm well with available JCPDS standered (NBS monograph 25-section 5) for MgSe. The average crystallite size of the deposited material is determined by using Debye- Schererformula

$$d = 0.9 \lambda$$

$$\beta \cos \theta$$

Where β is Full Width at Half Maximum of the peak in radians, λ is the wavelength of CuK α radiation ($\lambda=1.5418 \text{ \AA}$), θ is the Bragg's diffraction angle at peak position in degrees. The X- ray diffraction study revealed that the films are nanocrystalline in nature with cubic structure[5,6,7].

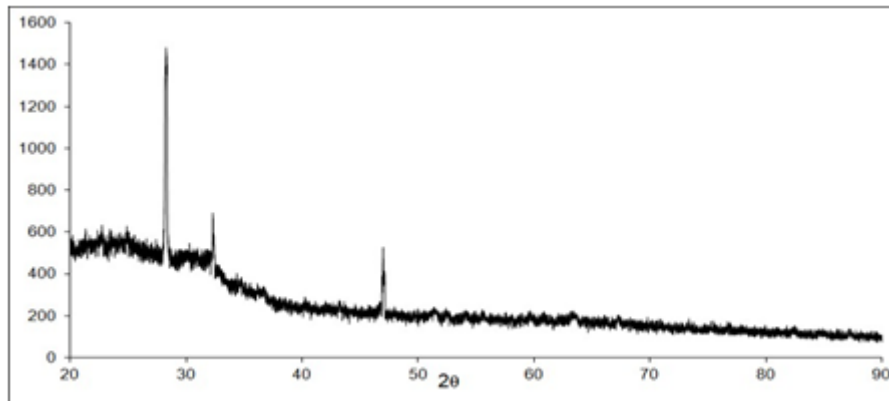


Fig. 1 Shows the x-ray diffraction pattern of MgSe thin film deposited on glass substrate at room temperature.

2.3 Morphology

Fig.2. shows, the SEM image of as deposited MgSe thin film on to glass substrate. From SEM, we can examined that as-deposited MgSe film is homogeneous and covering the substrate without cracks. The surface investigation from two dimensional micrograph showed that the film surface is even.

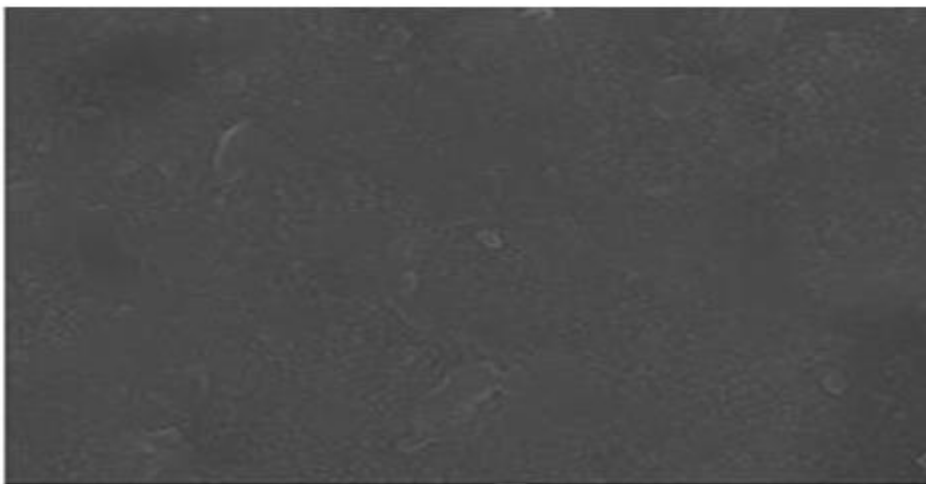


Fig.2 shows, the SEM image of as deposited MgSe thin film on to glass substrate

III. CONCLUSIONS

The structural properties of MgSe thin films deposited by successive ionic layer adsorption and reaction deposition technique have been studied. These XRD and SEM results are in good union with the available research paper.

IV. REFERENCES

- [1]. A.U.Ubale Y.S.Sakhare S.G.Ibrahim M.R.Belkhedkar, Solid State Sciences,23(2013), 96.
- [2]. D.M. Jeroh, A.J. Ekpunobi, D.N. Okoli, East Eur.J. Phys. 4 (2018)13
- [3]. Y.S.Sakhare, N.R.Thakare, A.U.Ubale, Archives of Physics Reserch,6 (2015)12.
- [4]. S. Joshua Gnanamuthu , S. Johnson Jeyakuma, A. R. Balu , K. Usharani & V. S. Nagarethinam Int. J. Thin. Fil. Sci. Tec. 4, (2015) 121
- [5]. P.Prete, N.Lovergine, L.Tapfer, C.Z.Fregonara, A.M.Mancini,J Cryst. Growth,214 (2000)119.
- [6]. P.X. Feng, J.D.Riley, R.C.G.Leckey, L.Ley, J.Phys. D: Appl.Phys., 34 (2001) 1293.
- [7]. M. Sohel, M. Munoz, M. C. Tamargo, Appl. Phys. Lett., 85 (2004) 2794.



To Study the Adsorption Efficiency of Pb (II) from Aqueous Solution Using Low-Cost Adsorbent

Anil R. Somwanshi

Department of Chemistry, J.D. Patil Sangludkar Mahavidyalaya, Daryapur, Maharashtra, India

ABSTRACT

Lead is toxic to living systems and therefore it is essential to remove it from wastewater. The removal of Lead (II) ions from aqueous solution by using *Phyllanthus emblica* tree bark was investigated. Adsorption studies were performed by batch experiments. The effect of contact time, pH, adsorbent dose and temperature were explored. From the experimental data, the isotherm parameters of Freundlich and Langmuir were calculated. The equilibrium was best represented by the Langmuir. Langmuir adsorption capacity (Q_0) was found to be 3.28 mg/g.

Keywords: Adsorption, Lead (II), Langmuir, Freundlich

I. INTRODUCTION

Many heavy metal ions are present in the form of pollutants in industrial effluent. Ground water and surface water gets contaminated by heavy metal ions released from the industries such as metal plating, metal finishing, rubber processing, fertilizers, mining etc¹⁻². Rapid industrialization has led to increased disposal of heavy metals into the environment. The Groundwater that contains an appreciable amount of iron or manganese or both is always devoid of dissolved oxygen and high in carbon dioxide content³. As far as is known, humans suffer no harmful effects from drinking water containing lead. However, lead interferes with laundering operation, imparts objectionable stains to plumbing fixture, and causes trouble in distribution systems by supporting growths of iron bacteria⁴. With better awareness of the problems associated with lead came an increase in research studies related to methods of removing lead from wastewater, for which a number of technologies have been developed over the years⁵. These technologies include chemical precipitation, electro flotation, ion exchange, reverse osmosis and adsorption onto activated carbon. These methods are not cost-effective in the Indian context. Low-cost and nonconventional adsorbents include agricultural wastes, such as natural compost, Irish peat, planer shell, walnut shell, and biomass⁶⁻⁷.

II. MATERIALS AND METHODS

Preparation of Adsorbent

Phyllanthus emblica bark were collected from the Mahendri Forest region. It was wash with triple distilled water to remove impurities from it and then sundried for 4 days. Later on, the bark was cut in to small pieces with the mesh size 100. To activate the adsorption power of adsorbent the bark was wash with 0.1 N H₂SO₄ and 0.1 N NaOH solution.

Preparation of Solutions

Standard solution of Lead was prepared in deionised water. The concentration of Pb (II) was analysed by UV-Visible spectrophotometer (model-117) at the wavelength of 460 nm.

III. RESULTS

Effect of pH

The effect of pH can be done experimentally by taking 0.5 gm of adsorbent with working volume of Pb (II) 200 ml having constant initial metal ions concentration and the contact time of 3 hours with shaking speed 1000 rpm in the pH range 1 to 7 shown in fig.1.

Effect of Contact time

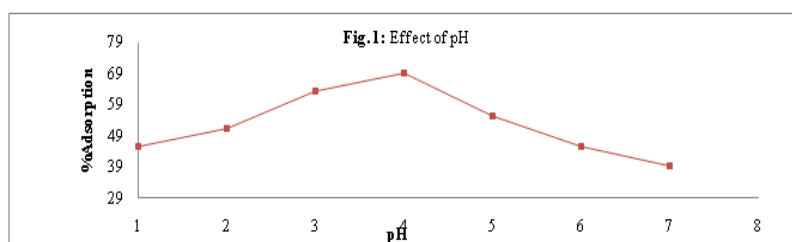
Study was carried out by taking 0.5 gm of adsorbent with working volume of Pb (II) 200 ml with known concentration of metal ions. It was observed that initially rate of adsorption is rapid up to 180 min with shaking speed 1000 rpm and then there was no further change in equilibrium concentration. Equilibrium time was found to be 300 minutes for this adsorption shown in fig.2.

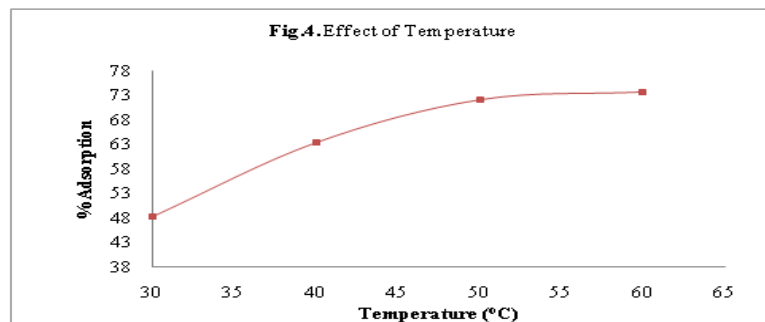
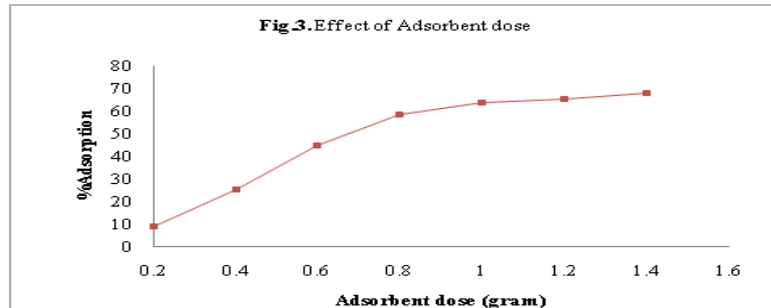
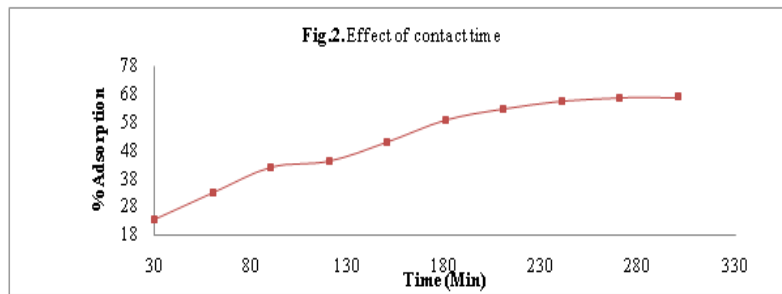
Effect of Adsorbent dose

The effect of varying the adsorbent dosage (AC-PETB, AC- PETB-SLS and AC- PETB-AMPSA) from 0.2–1 gram for adsorption of Mn (II) from their aqueous solutions having known volume of initial concentration was studied at pH 4 It has been found that the percent removal of Mn (II) increases with increase in adsorbent dose up to some extent, thereafter further increase adsorbent dose shown in fig.3.

Effect of Temperature

Effect of temperature was studied by varying the temperature from 30°C to 60°C with working volume 200 ml having known concentration. Study was carried out at pH 4 and at 1000 rpm with contact time 3 hours shown in fig.4. As the temperature increases porosity increases and percent of adsorption increases up to certain extent and then remains constant this is due to chemisorptions process.





Isotherm Modelling

Langmuir Adsorption Isotherm The Langmuir isotherm model can be given as:

$$\frac{1}{q_e} = \frac{1}{Q^0 b} \times \frac{1}{C_e} + \frac{1}{Q^0}$$

The Langmuir constant Q^0 is a measure of adsorption capacity and b is the measure of energy of adsorption. In order to observe whether the adsorption is favourable or not, a dimensionless parameter ' R_L ' obtained from Langmuir Isotherm. The values of Q^0 and b were evaluated from the intercept and slope of linear plots of $1/q_e$ vs. $1/C_e$ respectively.

Freundlich Adsorption isotherm It is most commonly used adsorption isotherm model which describes adsorption on heterogeneous surfaces with interactions among adsorbed molecules. It helps to investigate the nature of adsorption and the adsorption capacity of an adsorbent. The linear form of Freundlich isotherm model is

$$\log q_e = B \cdot \log C_e + \log K_f$$

Where, B and K_f are Freundlich constant. These constants represent the adsorption capacity and the adsorption intensity respectively. q_e is the amount adsorbed at equilibrium (mg/g), C_e is the equilibrium concentration of adsorbate.

Table 1: Adsorption Isotherm Constants

Metal ion	Langmuir Isotherm				Freundlich Isotherm		
	Q_0	b	R_L	R^2	K_f	$1/n$	R^2
Pb(II)	3.2820	0.2584	0.1492	0.999	1.544	0.025	0.999

IV. CONCLUSION

Tree bark prepared from *Phyllanthus emblica* shows good adsorption efficiency for the removal of lead (II). The removal efficiency was found to be rapid at initial stage and then slow down. The adsorption isotherm data was best revealed by the Langmuir adsorption isotherm where maximum adsorption capacity for the removal of Pb (II) was found to be 3.28 mg/g. The maximum removal efficiency was found to be at pH 4. Batch study indicates that as the temperature, adsorption dose, contact time increases adsorption capacity increases.

V. REFERENCES

- [1]. A.K. Wanjari, Adsorption of manganese (II) by nitric acid treated granular activated charcoal prepared from Cordia Macleodii tree bark. Der Pharma Chemica. 2016, 8(18): 87-94.
- [2]. Atul Wanjari et al, Removal of Cr(VI), Pb(II), Mn(II) and Bi(III) From Aqueous Solutions Using Granular Activated Charcoal Prepared From Cordia Macleodii Tree Bark. Rasayan Journal of Chemistry. 2017, 10(1): 82-85 <http://dx.doi.org/10.7324/RJC.2017.1011556>
- [3]. Atul Wanjari, Evaluation of Adsorption Efficiency of Ferronia Elefantum Fruit Shell for Rhodamine-B Retrieval from Aqueous Solution. International Journal Of Pharmaceutical And Chemical Sciences. 2013 2(1): 457-460.
- [4]. U.E. Chaudhari et al, Adsorption, Kinetics and Equilibrium Studies on Removal of Mn (II) From Aqueous Solutions Using Surface Modified Granular Activated Charcoal as a Low-Cost Adsorbent. International Research Journal of Environment Sciences. 2016.5(12): 47-55.
- [5]. A.K. Wanjari et al, Surface Modified Granular Activated Charcoal With Anionic Surfactant For Scavenging of Co(II) Metal Ions From Aqueous Solution : Thermodynamics and Kinetics. International journal of research in biosciences, agriculture & technology, 2015 special issue 3:93-99.
- [6]. U.E. Chaudhari et al, Sodium Dodecyl Sulfate Impregnated Granulated Activated Charcoal for the Scavenging of Cr (VI) Metal Ions from Aqueous Solution, International Journal of Chemical and Physical Sciences, Vol. 4 Special Issue – NCSC Jan-2015, 261-266.
- [7]. Atul K. Wanjari, Maheshkumar Prakash Patil, Umesh E. Chaudhari, Vaibhav N. Gulhane, Gun-Do Kim & Anley T. Kiddane (2022) Bactericidal and photocatalytic degradation of methyl orange of silver-silver chloride nanoparticles synthesized using aqueous phyto-extract, Particulate Science and Technology, DOI: 10.1080/02726351.2022.2056552



Photoluminescence Investigation Of $\text{Li}_2\text{Al}_2\text{Si}_2(\text{Po}_4)_4 \text{Eu}^{3+}$ for WLEDs Lighting Applications

R.G. Deshmukh, P.A Fartode

Shri Shivaji Science College, Amravati, Maharashtra, India

ABSTRACT

Inorganic phosphate phosphors have wide range of applications in the field of lighting devices The white light emitting diode (WLED) has the advantages like high energy-efficiency, good life-durability, and environmental friendliness in comparison to the conventional light sources, so it is a promising green solid-state lighting source [1,2]. In the proposed work Eu^{3+} activated $\text{Li}_2\text{Al}_2\text{Si}_2(\text{Po}_4)_4\text{Eu}^{3+}$ phosphors have been synthesized via low temperature simple combustion method using urea as a fuel. Phase confirmation and crystal structure determination of proposed sample were confirmed by Reitveld refinement analysis. Vibrational features of these phosphors have been investigated by FT-IR analysis. Photoluminescence study of the proposed sample confirms the spectra in blue and yellow region. These are results confirms the Eu^{3+} activated $\text{Li}_2\text{Al}_2\text{Si}_2(\text{Po}_4)_4\text{Eu}^{3+}$ phosphors are the potential candidate for WLEDs lighting applications.

Keywords: Luminescent, Rietveld, Refinement, Lighting,

Specifications Table

Subject area	<i>Spectroscopy</i>
Compounds	$\text{Li}_2\text{Al}_2\text{Si}_2(\text{Po}_4)_4\text{Eu}^{3+}$
Data category	<i>Spectral, synthesized</i>
Data acquisition format	<i>XRD, Photoluminescence study, CIE chromaticity</i>
Data type	<i>analyzed</i>
Procedure	<i>Synthesis procedure</i>
Data accessibility	<i>There is no data with this article</i>

I. INTRODUCTION

Inorganic phosphate phosphors have wide range of applications in the field of lighting devices[1,2], electronic display[3], solid state lighting lasers[4], biological applications[5] so attracted tremendous attention of all. LEDs(Light emitting diodes) are the fourth and latest generation of lighting system due to their advanced abilities like less power consumption[7], environmental friendliness[8], long lifetime[9], chemical and thermal stability[10] etc. Different kind of rare earths has been used for obtaining red blue and green component for the WLEDs. Among then Ce^{3+} , Eu^{3+} Tb^{3+} is the main rare earths .

Among the various lighting systems, WLEDs are the most remarkable lighting system due to their high reliability and energy efficiency levels. Some of the phosphors used commercially as good quality phosphors for WLEDs. The commercial white LEDs are commonly composed of blue GaInN chips and yellow light-emitting phosphors (YAG:Ce³⁺), which display the serious problems of poor colour-rendering index[11–13].

In recent times, Dy³⁺ activated luminescence phosphor shows their worth in the field of solid state lighting and display applications due to their blue yellow combine colour emitting capacity. This combination of emission is enough to give white light emission. Recently, Kadam et al[14] reported Dy³⁺ activated SrYAl₃O₇ phosphor shows white light emission. Chen et al[15] in 2017 reported the Tm³⁺/Dy³⁺ activated phosphate glasses shows color tunability in the glass sample under UV excitation reported by Han et al[16]. Kadam et al[17] reported Na₂Sr₂Al₂PO₄Cl₉:Eu³⁺ phosphor shows bright red emission with singly, doubly and triply ionized ions. Sebastian et al[18] explains the luminescence characteristics of Dy³⁺ doped borofluorophosphate glasses for white emission applications.

In the present study, Li₂Al₂Si₂(Po₄)₄ phosphors activated via Eu³⁺ ions are synthesized by Solid diffusion method. XRD of the proposed phosphor gives the analysis of phase determination of the proposed phosphor. Photoluminescence study shows these samples worth in the field of solid state lighting and display devices applications.

II. EXPERIMENTAL PROCEDURE

A series of phosphors Li₂Al₂Si₂(Po₄)₄ (x = 0.02, 0.04, 0.08, 0.12 and 0.16) with different concentrations are prepared by the high-temperature solid-state diffusion method. Li₂CO₃(AR), Al₂O₃, SiO₂, NH₄H₂PO₄(AR) and Eu₂O₃(AR) are selected as the raw materials and mixed in a grinding bowl. All the precursors are weighed in the stoichiometric ratio. The every sample crushed for 1/2 h. After homogeneous mixing, they are loaded into a corundum crucible and heated in a furnace at 800°C for 24 hrs. After this annealed phosphor is cooled at room temperature and final product is used for further characterizations.

III. RESULTS AND DISCUSSION

The XRD pattern of the phosphor

Fig. 1 displays the XRD pattern of the synthesized phosphors Li₂Al₂Si₂(Po₄)₄ activated via Eu³⁺ ions. This proposed phosphor compared with the standard ICSD database card No1000059. There are certain some extra peaks are observed in the XRD pattern which are might be due to improper allocation of temperature and incorporation of rare earth ions in the host matrix.

Fig 1: XRD pattern of Li₂Al₂Si₂(Po₄)₄ :Eu³⁺ ion compared with the standard ICSD database.

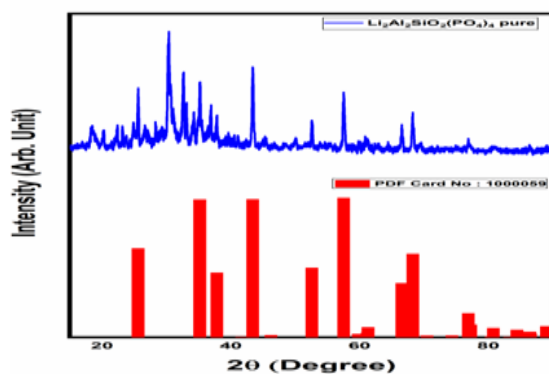


Fig 1 depicts the XRD patterns of a series of the as-synthesized $\text{Li}_2\text{Al}_2\text{Si}_2(\text{Po}_4)_4$ ($x = 0.005, 0.01, 0.03, 0.05,$ and 0.07), and the standard pattern (ICSD-1000059) of $\text{Li}_2\text{Al}_2\text{Si}_2(\text{Po}_4)_4$ is taken as a reference. The XRD patterns agree well with the reference .

Photoluminescence Study:

PL excitation spectra of $\text{Li}_2\text{Al}_2\text{Si}_2(\text{Po}_4)_4$: x mol % of Eu^{3+} phosphors with different doping concentrations of Eu^{3+} are fabricated and their emission spectra at 618 nm wavelength are tested to analyse the influence of different doping concentrations on the luminescent properties. The emission spectra of different doping concentrations at the 618 nm near- ultraviolet excitation wavelength are shown in Fig. 4. Under the excitation of 395 nm light, the emission intensity of the samples with different doping concentrations varies with the different concentrations. At $x = 0.12$, the emission intensity of the samples reaches the maximum, and then decreases with the increase of the concentration because of the concentration quenching of the Eu^{3+} doping ions. PL excitation spectra of proposed material consist of three peaks positioned at 394nm, 411, 466 due to transitions of Eu^{3+} ions. On pumping this phosphor with 394 nm excitation, two characteristic emission peaks are observed at 395nm and 466 nm. Eu^{3+} -doped phosphorous are most sought red emitting phosphorous due to their red emission from 590nm to 650 nm. and red component pure color purity is obtained by ${}^5\text{D}_0$ - ${}^7\text{F}_2$ TRANSITION OF Eu^{3+} . Eu^{3+} ions are known for characteristics excitation and emission peaks corresponding to f-f transition.

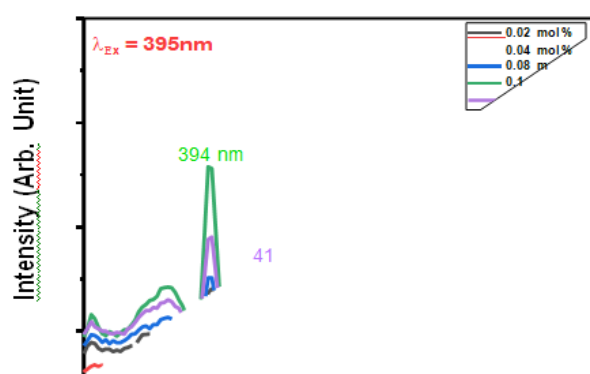


Fig 2. : PL emission spectra of $\text{Li}_2\text{Al}_2\text{Si}_2(\text{Po}_4)_4$: x mol % of Eu^{3+} ($x = 0.02, 0.04, 0.08, 0.12$ And 0.16 mol%) under excitation wavelength 395 nm.

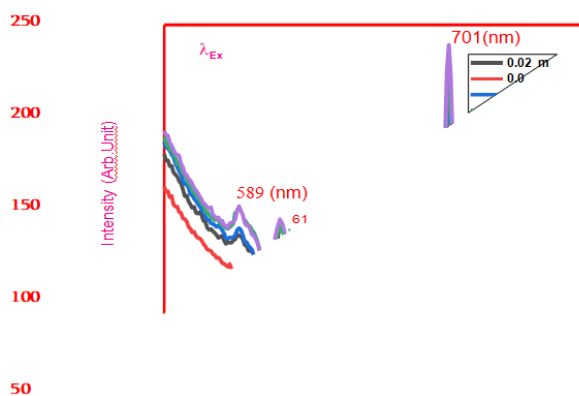


Fig 3: PL excitation spectra of $\text{Li}_2\text{Al}_2\text{Si}_2(\text{Po}_4)_4$:x mol % of Eu^{3+} (x = 0.02, 0.04, 0.08 , 0.12and 0.16 mol %) under emission wavelength 466 nm.

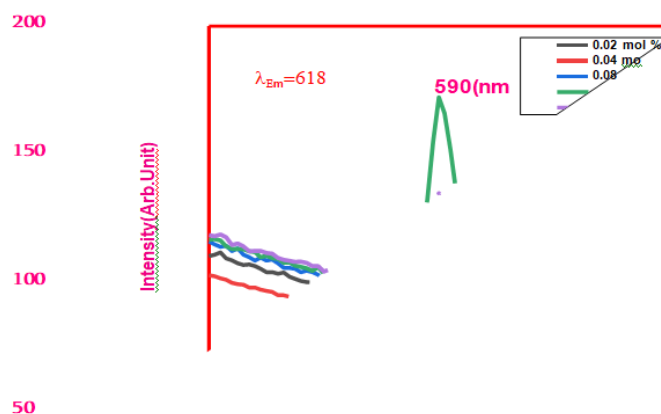
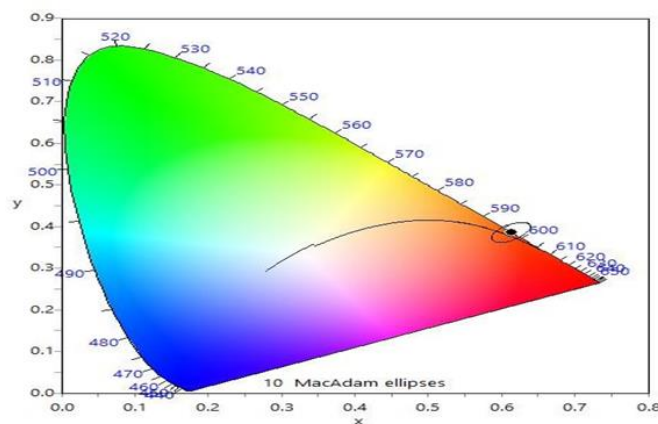
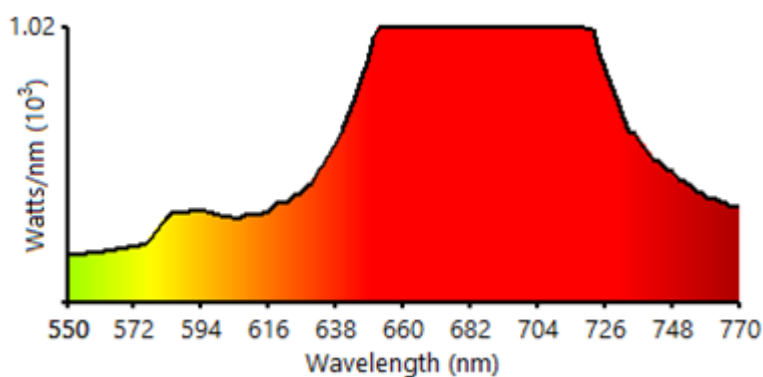


Fig 4: PL excitation spectra of $\text{Li}_2\text{Al}_2\text{Si}_2(\text{Po}_4)_4$:x mol % of Eu^{3+} (x = 0.02, 0.04, 0.08 , 0.12 and 0.16 mol %) under emission wavelength 618 nm.

CIE Chromaticity:

The International commission on Illumination (CIE)[22] chromaticity coordinates is calculated as a function of PL emission spectra of Eu^{3+} activated $\text{Li}_2\text{Al}_2\text{Si}_2(\text{Po}_4)_4$ phosphor demonstrated in Fig. 5. The value of CIE coordinates are falls in bluish white region in the CIE1331 chromaticity diagram. The values of CIE coordinates are (0.6132, 0.3862).





IV. CONCLUSION

In this work, Eu^{3+} activate $\text{Li}_2\text{Al}_2\text{Si}_2(\text{PO}_4)_4$ phosphor has been synthesized via Solid Diffusion method. Proposed phosphor has been characterized by XRD to confirm its crystalline nature. This XRD pattern is in good agreement with the standard database confirming this phosphor has been synthesized successfully. Photoluminescence study of this phosphor shows two characteristic emission peaks 466nm and 618nm. On combining these two characteristic peaks sample shows color coordinates in bluish white region which are almost near to white light region. All these results conclude that the proposed phosphor shows its potential for solidstate lighting and WLEDs applications.

V. REFERENCES

- [1]. S.U. Khan, W.U. Khan, W.U. Khan, D. Khan, S. Saeed, S. Badshah, M. Ikram, T.A. Saleh, Eu^{3+} , Sm^{3+} Deep-Red Phosphors as Novel Materials for White Light-Emitting Diodes and Simultaneous Performance Enhancement of Organic–Inorganic Perovskite Solar Cells, *Small*. 16 (2020) 1–10. <https://doi.org/10.1002/sml.202001551>.
- [2]. A.R. Kadam, R.L. Kohale, G.C. Mishra, S.J. Dhoble, Eu^{3+} -Doped tri-calcium $\text{Ca}_3(1-X-Z)\text{MZ}(\text{PO}_4)_2\text{AX}:\text{X}$ host array: optical investigations of down-conversion red phosphor for boosting display intensity and high color purity, *New J. Chem.* 45 (2021) 7285–7307. <https://doi.org/10.1039/d0nj05930g>.
- [3]. X. Wang, E. Song, L. Qin, D. Gui, Z. Xu, J. Xie, M. Lei, H. Zhang, Y. Wang, Y. Wang, Z. Xia, W. Liu, W. Du, S. Wang, Fabrication of a Wide Color Gamut pc-WLED Surpassing 107% NTSC Based on a Robust Luminescent Uranyl Phosphate, *Chem. Mater.* 33 (2021) 6329–6337. <https://doi.org/10.1021/acs.chemmater.1c00862>.
- [4]. M. Shoaib, R. Rajaramakrishna, G. Rooh, N. Chanthima, H.J. Kim, C. Saiyasombat, R. Botta, N. Nuntawong, S. Kothan, J. Kaewkhao, Structural and luminescence study of Dy^{3+} doped phosphate glasses for solid state lighting applications, *Opt. Mater. (Amst)*. 109 (2020) 110322. <https://doi.org/10.1016/j.optmat.2020.110322>.

- [5]. Y. Zhang, S. Sheng, S. Mao, X. Wu, Z. Li, W. Tao, I.R. Jenkinson, Highly sensitive and selective fluorescent detection of phosphate in water environment by a functionalized coordination polymer, *Water Res.* 163 (2019) 114883. <https://doi.org/10.1016/j.watres.2019.114883>.
- [6]. A.R. Kadam, G.B. Nair, S.J. Dhoble, Insights into the extraction of mercury from fluorescent lamps: A review, *J. Environ. Chem. Eng.* 7 (2019) 103279. <https://doi.org/10.1016/j.jece.2019.103279>.
- [7]. X. Liu, G. Chen, Y. Chen, T. Yang, Luminescent characteristics of Tm³⁺/Tb³⁺/Eu³⁺ tri- doped phosphate transparent glass ceramics for white LEDs, *J. Non. Cryst. Solids.* 476 (2017) 100–107. <https://doi.org/10.1016/j.jnoncrysol.2017.09.032>.
- [8]. H.N. Van, P.D. Tam, V.H. Pham, Red and Yellow Luminescence of Eu³⁺/Dy³⁺ Co-Doped Hydroxyapatite/ β -Tricalcium Phosphate Single Phosphors Synthesized Using Coprecipitation Method, *J. Appl. Spectrosc.* 85 (2018) 738–742. <https://doi.org/10.1007/s10812-018-0713-6>.
- [9]. M. Runowski, A. Shyichuk, A. Tyimiński, T. Grzyb, V. Lavín, S. Lis, Multifunctional Optical Sensors for Nanomanometry and Nanothermometry: High-Pressure and High- Temperature Upconversion Luminescence of Lanthanide-Doped Phosphates - LaPO₄/YPO₄:Yb³⁺-Tm³⁺, *ACS Appl. Mater. Interfaces.* 10 (2018) 17269–17279. <https://doi.org/10.1021/acsami.8b02853>.
- [10]. M. Xia, X. Wu, Y. Zhong, H.T. Bert Hintzen, Z. Zhou, J. Wang, Photoluminescence properties and energy transfer in a novel Sr₈ZnY(PO₄)₇:Tb³⁺,Eu³⁺ phosphor with high thermal stability and its great potential for application in warm white light emitting diodes, *J. Mater. Chem. C.* 7 (2019) 2927–2935. <https://doi.org/10.1039/c8tc06235h>.
- [11]. D.A. Hakeem, J.W. Pi, G.W. Jung, S.W. Kim, K. Park, Structural and photoluminescence properties of La_{1-x}NaCaGa₃PZrO₁₂ doped with Ce³⁺, Eu³⁺, and Tb³⁺, *Dye. Pigment.* 160 (2019) 234–242. <https://doi.org/10.1016/j.dyepig.2018.06.047>.
- [12]. J. Zhong, W. Zhao, W. Zhuang, W. Xiao, Y. Zheng, F. Du, L. Wang, Origin of Spectral Blue Shift of Lu³⁺-Codoped YAG:Ce³⁺ Phosphor: First-Principles Study, *ACS Omega.* 2 (2017) 5935–5941. <https://doi.org/10.1021/acsomega.7b00304>.
- [13]. B. Yildirim, O. Yasin Keskin, S. Oguzlar, I. Birlik, F. Ak Azem, K. Ertekin, Manipulation of brightness and decay kinetics of LuAG: Ce³⁺ and YAG: Ce³⁺ by simple metal oxides in polymeric matrices, *Opt. Laser Technol.* 142 (2021) 107226. <https://doi.org/10.1016/j.optlastec.2021.107226>.
- [14]. A.R. Kadam, S.B. Dhoble, G.C. Mishra, A.D. Deshmukh, S.J. Dhoble, Combustion assisted spectroscopic investigation of Dy³⁺ activated SrYAl₃O₇ phosphor for LED and TLD applications, *J.Mol.Struct.* 1233(2021) 130150. <https://doi.org/10.1016/j.molstruc.2021.130150>.
- [15]. Y. Chen, G. Chen, X. Liu, C. Yuan, C. Zhou, Tunable luminescence mediated by energy transfer in Tm³⁺/Dy³⁺ co-doped phosphate glasses under UV excitation, *Opt. Mater. (Amst).* 73 (2017) 535–540. <https://doi.org/10.1016/j.optmat.2017.09.011>.
- [16]. and G.S. Xiaowen Yu, Miao Zhang, Wenjing Yuan, High-performance three- dimensional Ni-Fe layered double hydroxide/graphene electrode for water oxidation, *J. Mater. Chem. A.* (2014) 1–9. <https://doi.org/10.1039/x0xx00000x>.

- [17]. A.R. Kadam, R.S. Yadav, G.C. Mishra, S.J. Dhoble, Effect of singly, doubly and triply ionized ions on downconversion photoluminescence in Eu^{3+} doped $\text{Na}_2\text{Sr}_2\text{Al}_2\text{PO}_4\text{Cl}_9$ phosphor: A comparative study, *Ceram. Int.* 46 (2020). <https://doi.org/10.1016/j.ceramint.2019.10.032>.
- [18]. J. Sebastian, S. Gopi, E. Sreeja, A. Jose, T. Krishnapriya, P.R. Biju, Luminescence characteristics of Dy^{3+} doped borofluorophosphate glasses for white emission applications, *AIP Conf. Proc.* 2269 (2020). <https://doi.org/10.1063/5.0019646>.
- [19]. A.R. Kadam, S.J. Dhoble, Synthesis and luminescence study of Eu^{3+} -doped SrYAl_3O_7 phosphor, *Luminescence.* 34 (2019) 846–853. <https://doi.org/10.1002/bio.3681>.
- [20]. N. Baig, A.R. Kadam, K. Dubey, N.S. Dhoble, S.J. Dhoble, Wet chemically synthesized $\text{Na}_3\text{Ca}_2(\text{SO}_4)_3\text{Cl}:\text{RE}^{3+}$ (RE= Ce, Dy, Eu) phosphors for solid-state lighting, *Radiat. Eff. DefectsSolids.*176(2021)493–507. <https://doi.org/10.1080/10420150.2021.1871735>.
- [21]. A.R. Kadam, S.J. Dhoble, Energy transfer mechanism of $\text{KAlF}_4:\text{Dy}^{3+}$, Eu^{3+} co-activated down-conversion phosphor as spectral converters_ An approach towards improving photovoltaic efficiency by downshifting layer, *J. Alloys Compd.* 884 (2021) 161138. <https://doi.org/10.1016/j.jallcom.2021.161138>.
- [22]. A.R. Kadam, G.C. Mishra, A.D. Deshmukh, S.J. Dhoble, Enhancement of blue emission in Ce^{3+} , Eu^{2+} activated BaSiF_6 downconversion phosphor by energy transfer mechanism: A photochromic phosphor, *J. Lumin.* 229 (2021) 1–9. <https://doi.org/10.1016/j.jlumin.2020.117676>.



Degradation Studies of UV Irradiated Polystyrene/ Polyisoprene Thin Films

Dr. V. S. Sangawar¹, S. O. Sharma^{*2}, S. A. Umale²

¹Department of Physics, Government Vidarbha Institute of Science & Humanities, Amravati, Maharashtra, India

²Moolji Jetha College, Jalgaon, Maharashtra, India

ABSTRACT

Thin films of polystyrene/ polyisoprene composites of thickness 20 to 30 micron were prepared by solution evaporation technique. PS/PI thin films were exposed to UV irradiation of wavelength 280nm for varied time intervals. As synthesized thin films were characterized using weight loss method, X- ray diffraction (XRD), Fourier Transform Infrared (FTIR) spectroscopy and UV- Visible spectroscopy. The crystalline nature of films were found to be decreased and % of weight loss increases with varying time of irradiation.

Keyword: Polystyrene, PI, XRD, FTIR, and UV-Visible

I. INTRODUCTION

The photo induced degradation and photodegradation of polymer has been investigated extensively to clarify their reaction mechanism. Polystyrene (PS) is one of the commercial polymers widely used in various industrial fields and its stabilization against light is also an important problem[s]. Polymers can be degraded by illumination either directly or using a photosensitizer. Although direct irradiation of the polymer may be simplest method, the introduction of photosensitive structure to polymer presents some advantages. The photosensitization method is preferred when there is a need of controlling the photodegradation as well as when using light of wavelengths that are not absorbed by the polymers[1,2].

The excitation of photosensitizers by light usually results in the production of free radicals that initiate the polymer degradation processes[3,4]. In general, these radicals abstract a hydrogen atom from macromolecules forming a polymeric alkyl radical react with oxygen, initiating an oxidative chain reactions.

Cis-1,4- polyisoprene is a natural rubber used as a additive to enhanced the photodegradation reaction of polystyrene. Continuing our research on the sensitized photodegradation of polymer films[5]. We present here the results on the evaluation of efficiency of polyisoprene in the degradation of polyisoprene films.[6]

II. EXPERIMENTAL SECTION

Materials:

Commercial polystyrene (Aldrich, $M_w = 500000$) was used as received. The photosensitizer were Cis - 1,4-polyisoprene (Aldrich, $M_w =$). The solvent Toluene were used as further purification.

Sample Preparation:

Solution of polystyrene containing 7% w/w of polyisoprene were prepared in toluene. Thin films of PS (about 20 - 30 μ m) containing photosensitizers were obtained by evaporation of solutions from horizontal glass plate. After solvent evaporation, films were dried. The films were exposed to 8W BLB Philips UV light of 280nm in wavelength in irradiation chamber.

III. RESULT AND DISCUSSION

Optical absorption:

The energy band gap for semiconductor materials can be investigated through the UV- Visible spectrum []. The UV-Visible data obtained from the absorbance characteristic of PS/PI were used to calculate the energy band gap by equation (1).

$$\alpha = A/T \dots\dots\dots(1)$$

Where, α = Absorption coefficient, T= thickness of the sample

Using Tauc's equation (2), the direct and indirect bands can estimate the energy band gap.

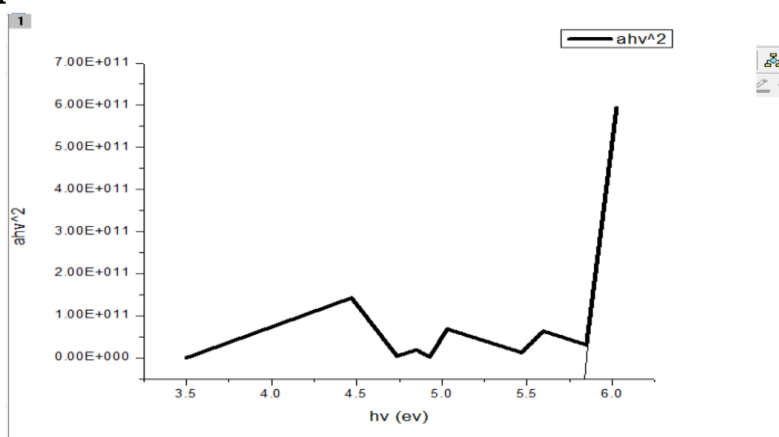
$$\alpha hv = \beta(hv - E_g)^n \dots\dots\dots(2)$$

Where β is band tailing parameter which relies on the electron hole mobility, h is the energy of photon and n is the constant that ascertain the type of transition, such as for the direct allowed and forbidden transition is $n = \frac{1}{2}$ and $n = \frac{3}{2}$ respectively. For the indirect allowed and forbidden transition is $n = 2$ and $n = 3$ respectively[7].

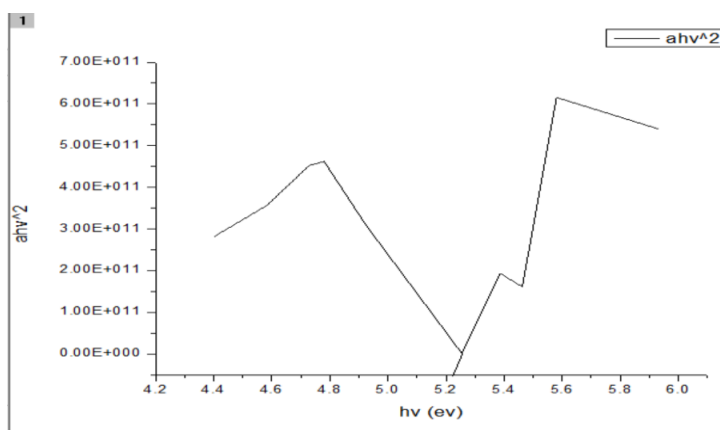
Energy band gap:

The values of the energy band gap at different ratio concentrations and time exposure were determined by $(\alpha hv)^2 = 0$ from the graph of $(\alpha hv)^2$ versus hv as shown in fig. the Tauc's equation (2) show the relation of incident photon energy hv with absorption coefficient .the extrapolation of straight lines gives the direct band gap where value of n used in this is $\frac{1}{2}$ for direct transition[7].

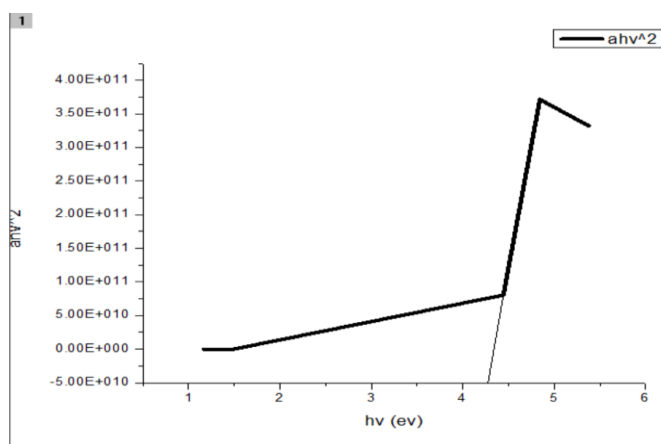
The optical Band gap of PS/PI with irradiation time 0hr, 24hr and 48hr is as shown in fig1, fig 2 and fig3.



Fig(1). PS/PI 0 Hour



Fig(2). PS/PI 24 Hour



Fig(3). PS/PI 48 Hour

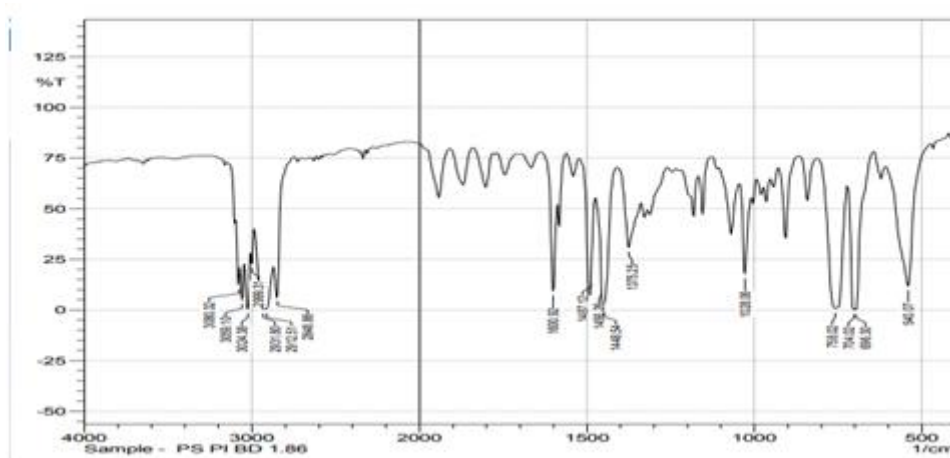
In present work the optical band gap of PS doped with 7% of PI were reduced as increased in irradiation time from 0 hr to 48 hr. The values of energy bandgap as shown in paper table.1.

Table :1

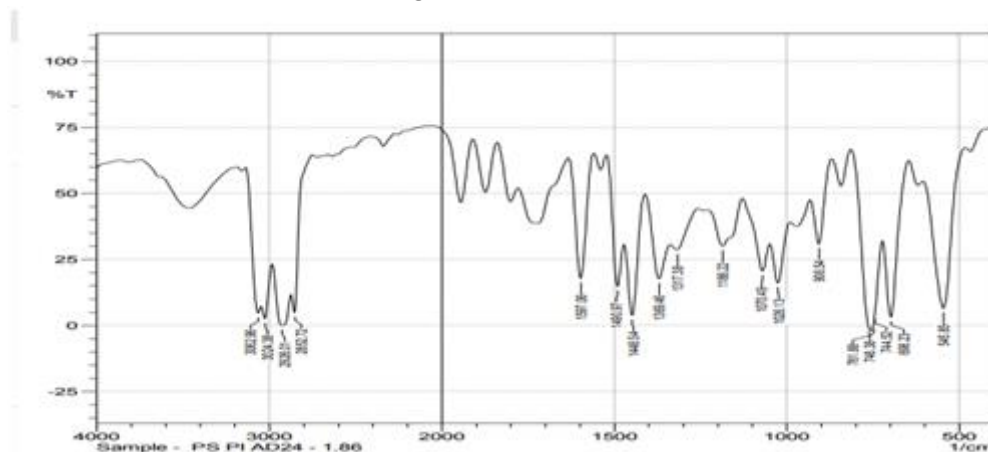
Sr. No.	Samples	Irradiation time	Direct Band gap
1	PS+7%PI	0 hr	5.83
2	PS+7%PI	24hr	5.22
3	PS+7%PI	48hr	4.26

FTIR Absorption:

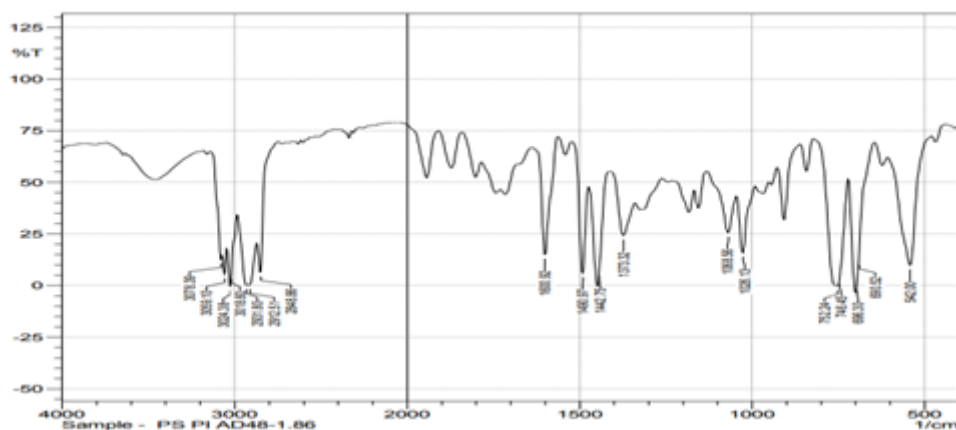
The FTIR absorption spectra of non-irradiated and irradiated blended PS films with 7% PI for 0.0 hr, 24hr and 48hr as shown in figure.



Fig(4): PS/PI 0 Hour



Fig(5): PS/PI 24 Hour



Fig(6): PS/PI 48 Hour

FTIR absorption band positions of PS films blended with 7% of PI before and after irradiation is as shown in table 2.

Table:2

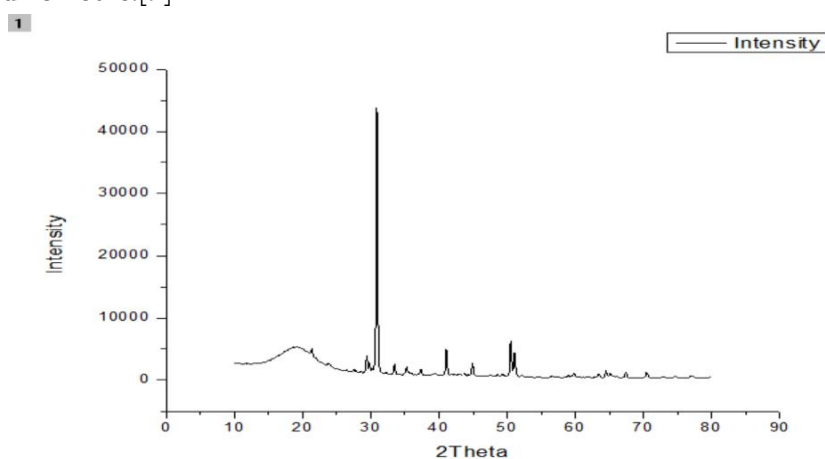
Polymer	Band (cm ⁻¹)	Time of irradiation			Types of vibration
		0hr	24hr	48hr	
PS +7%PI	3200-2700	3080.32	3062.96	3078.62	O-H stretching
		3059.10	3059.10	
		3024.38	3024.38	3024.38	
		2999.31	3018.60	
		2912.51	2912.51	
		2848.86	2852.72	2848.86	
	1600	1600.92	1597.06	1600.92	C=C stretching in conjugated alkene
	1500	1487.12	1490.97	1490.97	N-O stretching
	1450	1456.26	1448.54	1442.75	C-H bending in alkane
		1448.54			
	1375	1375.20	1371.38	1373.32	None
	1250-1020	1028.06	1026.06	1026.13	C-N stretching in amine
	1085-1050	1070.49	1068.13	C-O stretching
	750±20	758.02	761.81	752.24	C-H stretching in alkane
542	540.07	545.85	542.00	Monosubstituted benzene ring	

As can be noticed from the figure, modifications occur in the intensity of different absorption bands in the FTIR spectra of irradiated pure and blended PS films. These changes correspond to photo oxidation and photo degradation of polymeric change. Transformation is clearly demonstrated by the decrease in absorption in the band at 3200-2700cm⁻¹, and by the formation of new absorption band corresponding to new compounds resulting from the polymer change photo degradation in different regions reported that the presence of absorption 3200-2700cm⁻¹ shows the OH starching as can be noticed from figure and table. The increase in

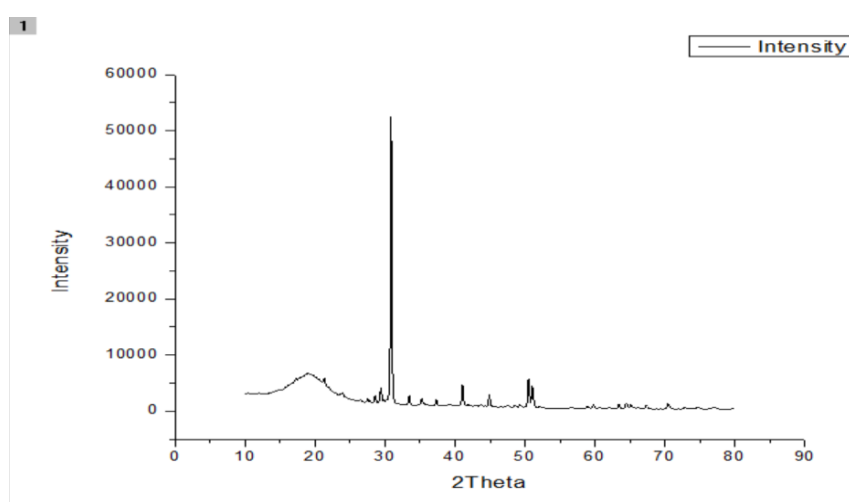
the irradiation time resulted in the absorption intensity band at 1600 cm^{-1} (C=C stretching) and formation of new band at 1450 cm^{-1} (C-H stretching) and absorption band at 1500 cm^{-1} (N-O stretching) may also influence carbonyl compound and diene type structure during photo oxidation and photo degradation of chromosphere. Absorption peak at $1250\text{--}1020\text{ cm}^{-1}$ shows (C-N stretching) and also assigned to (C-O-C anti symmetric stretching) vibration increase with plasticization and irradiation of polymer films. The shift in absorption band as well as the formation in new absorption bands upon irradiation of the PS films is good indication of the confirmation operation in the polymeric chromophores and the increases in the efficiency of photo degradation of polymeric chains.[8]

X- Ray Diffraction:

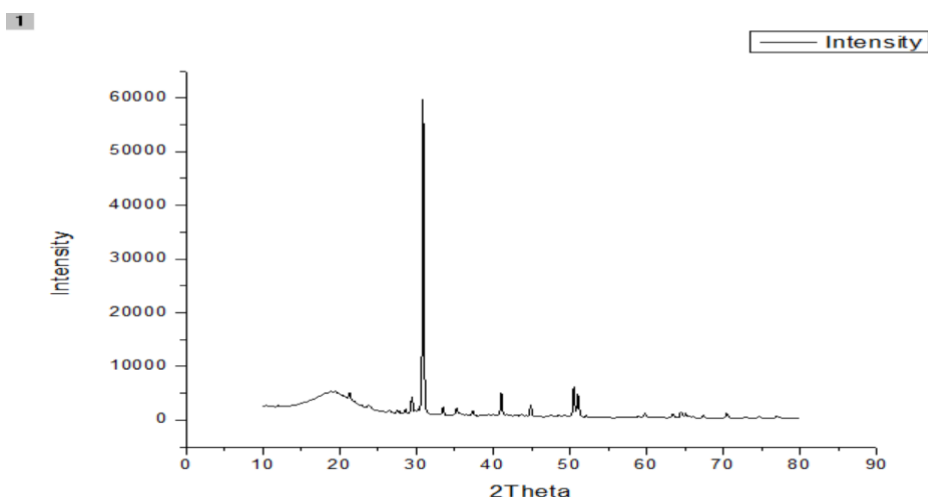
The X- Ray diffraction is used for structural analysis of thin films figure and table shows the X- Ray Diffraction of PS blended with 7% of PI thin films irradiated for 0 hour, 24hour, 48 hour. From XRD we can calculate the crystal size of the material in present study debye-scherrer formula use to calculate the crystalline size of the PS/PI thin films. Crystalline size of PS/PI thin films decreased with irradiation time of 0 hours, 24 hours and 48 hours.[9]



Fig(7). PS/PI 0 Hour



Fig(8). PS/PI 24 Hour



Fig(9). PS/PI 24 Hour

IV. CONCLUSION

We have demonstrated the synthesis of PS/PI thin films through mixing process. The polyisoprene worked as a photosensitizer to enhanced the photodegradation process. From UV we can conclude that energy band gap of PS/PI thin films decreased as irradiation time increased. Also from weight loss method, 6% of the samples get degraded in 48hr. The absorption bands are due to the different stretching and vibration modes of different functional groups of PS and PI and a new C=O group is found after degradation and crystalline size of the material decreased as irradiation time increased.

V. REFERENCES

- [1]. Torikai A, Takeuchi T, Fueki K. Photodegradation of polystyrene and polystyrene containing benzophenone. *PolymPhotochem* 1983; 3: 307- 20.
- [2]. Ammala A, Bateman S, Dean K, Pentinakis E, Sangwan P, Wong S, et al. An overview of degradable and biodegradable polyolefins. *ProgPolymSci* 2011 ; 36: 1015- 49
- [3]. Kaczmarek H, Kaminska A, Swiatek M, Sanyal S. Photoinitiated degradation of polystyrene in the presence of low molecular organic compounds. *EurPolym J* 2000; 36: 1167- 73
- [4]. Yousif A, Salimon J, Salih N. New stabilizers of polystyrene based on 2-N-Salicylidine-5-(substituted) - 1,3,4-thiadizole compounds. *J Saudi ChemSoc* 2012; 16: 299-306.
- [5]. Manangan T, Shawaphun S, Sirirat W. Acetophenone and benzophenone derivatives as Catalyst in Photodegradation of PE and PP films. *Adv Mater Res* 2010; 93- 94: 284-87.
- [6]. Leticia F.A. Pinto, Beatriz E. Goi, Carla C. Schmitt and Miguel G. Neumann. Photodegradation of polystyrene films containing UV- visible sensitizers, *J research updates in polymsci*, 2013, 2, 39-47.

- [7]. Mohd. A. Agam, NurulN.Awal, Siti A. Hassan, Jibrin A. Yabagi, Maytham Q. Hamzah, Azman T. Energy band gap investigation of polystyrene copper oxide nanocomposites bombarded with laser, J AdvRes FldMech and ThermSci 66, Issue 2(2010) 125-135.
- [8]. Khalid A. Al Ani, Afrah E. Ramdhan, Kinetic study of the effect of plasticization on photodegradation of Polystyrene Solid Films, Mate Sci and Appl, 2015, 6 , 617-633.
- [9]. K. Maragatham, S. Muruganand, N. Manikanandan, XRD, FTIR and the Optical study of pure polystyrenefilms, Int J Recent and Innovation trends in Comp and Comm. , ISSN: 2321-8169, 1148-1151.

Refractometric Studies of 2,4,6-Triazinobutylthio-Carbamides In Dioxane-Water Systems

P.V.Raut¹, K.P.Jumde², M.S.Lunge³, D.T.Tayade⁴

¹Department of Chemistry, Smt. Radhabai Sarda Arts, Commerce and Science College, Anjangaon Surji, Amravati- 444, Maharashtra, India

²Department of Chemistry, Nilakanthrao Shinde Science and Arts College, Bhadrawati, Chandrapur- 442 902, Maharashtra, India

³Department of Chemistry, Jagadamba Mahavidyalaya, Achalpur (City), Amravati- 444 905, Maharashtra, India

⁴Department of Chemistry, G.V.I.S.H., Amravati, Maharashtra, India

ABSTRACT

Recently in this laboratory, the refractometric study of 1-(4-hydroxy-6-methyl)- 2,4,6-triazino-3-p-tolylthiocarbamide (M1), 1-(4-hydroxy-6-methyl)- 2,4,6- triazino-3-m-tolylthiocarbamide (M2), 1-(4-hydroxy-6-methyl)- 2,4,6-triazino-3-o-tolylthiocarbamide (M3) were carried out at various percentage compositions of solvent to investigate effects of various groups on 2,4,6- triazinothiocarbamides. The results obtained during this investigation gave detail information regarding drug pharmacokinetics and pharmacodynamic activities of these.

Keywords: 1-(4-hydroxy-6-methyl) – 2,4,6-triazino-3-p-tolylthiocarbamide (M1), 1-(4-hydroxy-6-methyl)- 2,4,6-triazino-3-m-tolylthiocarbamide (M2), 1-(4-hydroxy-6-methyl)- 2,4,6-triazino-3-o-tolylthiocarbamide (M3), dioxane-water various percentage composition, refractometer.

I. INTRODUCTION

When we go to literature survey it was observed that symmetrical triazine and thiocarbamide nucleus containing drugs have importance in drug chemistry. Many of them are used as muscle relaxant¹, hypoglycemic agent², blood pressure depressant³, anti-diabetic drug⁴. They also showed anti-tumour⁵⁻⁶, anti-bacterial⁷⁻⁹, anti-inflammation¹⁰, anti-cancer¹¹ hormone antagonists¹² and antipsychotic properties¹³. Some are used in industries such as finishing and brightening agents¹⁴. They are also been used as herbicides¹⁵⁻²⁰, sea water algicides²¹, fungicidal²², insecticidal²³ and pesticidal²⁴. In our chemistry, concentration of unknown binary dilute solution was determined by the refractometric method²⁵. Refractometric study of s-triazinothiocarbamides in 80% dioxane-water mixture at different temperature was carried out by Kshirsagar²⁶. From this it can be concluded that the symmetrical triazino compounds initiated the new branches of development in the medicinal, pharmaceutical, agricultural and biochemical fields. The drug absorption,

distribution (transmission), activity and effects will directly predicted by refractometric study of the solute (drug) and solvent in the human physiology. This information is essential for deciding dose of drug to the patient, drug activity and effects of drug in pharmaceutical and medicinal sciences. Results of refractometric study directly gave information regarding solute-solvent, solvent-solvent interactions. This study is an important tool for pharmaceutical and medicinal sciences. Considering all these facts and as a wider programmed of this laboratory in the synthesis of nitrogen and sulphur containing heterocyclic and heteroacyclic compounds, it was thought interestingly to carry out the refractometric study of newly synthesized compounds in this laboratory. This study throw the light on the potency of newly synthesized drugs, stability of drug and will also renovate and modify the traditional drugs preparative methods which are used by medicinal practitioners. One of a unique and important property of liquid is refractive index, when a ray of light passes from less dense to denser medium then there is a change in the direction of refraction and angle of refraction changes and ultimately the refractive index gets changed. The result obtained during this investigation directly through light on the dipole association of ligand, intermolecular attraction between solute and solvent, dielectric constant of medium, polarizability, and mutual compensation of dipoles. These results are much more useful for distribution, stability, activity and effect of drug hence this study was carried out. M1, M2 and M3 in dioxane were studied at various percentage compositions. This study may become milestone in the drug, medicinal, pharmaceutical of triazinothiocarbamido molecules.

II. EXPERIMENTAL

The 0.1M solution of ligands in different percentage of dioxane-water and the solutions of different concentration of ligands (0.1M, 0.075M, 0.050M, 0.025M) in 65%, 75% and 85% dioxane-water mixture were prepared. All weighing were made on Mechaniki Zaktady Precyzying Gdansk Balance [Poland make, ($\pm 0.001\text{gm}$)] The densities of solutions were determined by a bicapillary Pyknometer ($\pm 0.2\%$) having a bulb volume of about 10cm^3 and capillary having an internal diameter of 1mm. The refractive indices of solvent mixture and solutions were studied by Abbe's refractometer (± 0.001). The refractometer was calibrated with glass piece ($n=1.5220$) provided with the instrument.

III. OBSERVATIONS AND CALCULATIONS

The present work deals with the study of molar refraction and polarizability constant of ligand (M1), ligand (M2) and ligand (M3) in 65% dioxane-water, 75% dioxane-water and 85% dioxane-water mixtures at different composition at 303.15°K (30°C). The data obtained during work was used to study intermolecular interactions. The refractometric readings were taken as described in literature. Here, (M1) is 1-(4-hydroxy-6-methyl)-symmetrical triazino-3-p-tolylthiocarbamide, (M2) is 1-(4-hydroxy-6-methyl)-symmetrical - triazino-3-m-tolylthio-carbamide and (M3) is 1-(4-hydroxy-6-methyl)-symmetrical triazino-3-o-tolylthiocarbamide.

IV. RESULT & DISCUSSION

The molar refraction of solutions of ligand in dioxane-water mixtures were determined by a following equation, $R_{mixture} = [(\eta^2 - 1)/(\eta^2 + 2)] \{ [X_1 m_1 + X_2 m_2 + X_3 m_3] / d \}$ Where, η is the refractive index of solution, X_1 is mole function of dioxane, X_2 is mole function of water, X_3 is mole function of solute, m_1 , m_2 , m_3 are molecular weights of dioxane, water and solute respectively, D is density of solution The molar refraction of ligand is calculated as,

$$R_{lig} = R_{mixture} - R_{Dioxane-Water}$$

Where, $R_{Dioxane-Water}$ - The molar refraction of solvent, dioxane-water mixture

The polarizability constant (α) of ligand is calculated from the following relation,

$$R_{lig} = (4/3) \pi N_0 \alpha \quad \text{Where, } N_0 \text{ is Avogadro's number.}$$

Table 1: Molar Refraction of Different Percentage of Dioxane-Water Mixture

% of Dioxane- Water	Molar Refraction (RM) (cm ³ mole ⁻¹)
100	20.5977
90	14.4584
80	10.9390
70	10.6564
60	9.0551

A] Molar Refraction and Polarizability constant at different concentration for M1

Table No. 2:		System: 65% Dioxane –Water		Temp:30±0.1°c	
Concentration C(M)	Density $\rho \times 10^3$ (Kg-m ⁻³)	Refractive Index(η)	R_{mix} (m ³ mole ⁻¹)	R_{Lig} (m ³ mole ⁻¹)	$(\alpha) \times 10^{-23}$ (cm ³)
0.1	1.0109	1.3074	8.3864	0.3321	0.01614
0.075	1.0108	1.3032	8.3461	0.2831	0.01408
0.050	1.0107	1.3920	8.2928	0.2314	0.01236
0.040	1.0106	1.3016	8.2911	0.2407	0.01221

Table No. 3:		System: 75% Dioxane –Water		Temp:30±0.1°c	
Concentration C(M)	Density $\rho \times 10^3$ (Kg-m ⁻³)	Refractive Index(η)	R_{mix} (m ³ mole ⁻¹)	R_{Lig} (m ³ mole ⁻¹)	$(\alpha) \times 10^{-23}$ (cm ³)
0.1	1.0153	1.3074	8.8846	0.2269	0.01262
0.075	1.0143	1.3022	8.8133	0.1558	0.00951
0.050	1.0131	1.3020	8.7622	0.1054	0.00750
0.040	1.0110	1.3314	8.7218	0.0715	0.00523

Table No. 4: System: 85% Dioxane –Water

Temp: 30±0.1°c

Concentration	DensityPx10 ³ (Kg-m ⁻³)	Refractive Index(η)	Rmix (m ³ mole ⁻¹)	RLig (m ³ mole ⁻¹)	(α)x10 ⁻²³ (cm ³)
C(M)					
0.1	1.0165	1.3060	8.1613	0.2223	0.01160
0.075	1.0153	1.3052	8.1055	0.1665	0.00910
0.050	1.0137	1.3044	8.0555	0.1120	0.00720
0.040	1.0124	1.3032	8.0032	0.0643	0.00535

B] Molar Refraction And Polarizability constant at different concentration for M2

Table No. 5

System: 65% Dioxane –Water

Temp: 30±0.1°c

Concentration	DensityPx10 ³ (Kg-m ⁻³)	Refractive Index(η)	Rmix (m ³ mole ⁻¹)	RLig (m ³ mole ⁻¹)	(α)x10 ⁻²³ (cm ³)
C(M)					
0.1	1.0212	1.3032	9.3664	0.3320	0.01623
0.075	1.0140	1.3030	9.3452	0.3107	0.01511
0.050	1.0139	1.3016	9.3216	0.2835	0.01414
0.040	1.0036	1.3012	9.3105	0.2706	0.01340

Table No. 6

System: 75% Dioxane –Water

Temp: 30±0.1°c

Concentration	DensityPx10 ³ (Kg-m ⁻³)	Refractive Index(η)	Rmix (m ³ mole ⁻¹)	RLig (m ³ mole ⁻¹)	(α)x10 ⁻²³ (cm ³)
C(M)					
0.1	1.0244	1.3072	9.9119	0.2627	0.01322
0.075	1.0242	1.3056	9.8841	0.2332	0.01227
0.050	1.0133	1.3042	9.8716	0.2142	0.01130
0.040	1.0130	1.3028	9.8706	0.2122	0.01121

Table No. 7

System: 85% Dioxane –Water

Temp: 30±0.1°c

Concentration	DensityPx10 ³ (Kg-m ⁻³)	Refractive Index(η)	Rmix (m ³ mole ⁻¹)	RLig (m ³ mole ⁻¹)	(α)x10 ⁻²³ (cm ³)
C(M)					
0.1	1.0230	1.3123	10.1508	0.2112	0.01117
0.075	1.0125	1.3112	10.1320	0.1910	0.01034
0.050	1.0123	1.3071	10.1064	0.1674	0.01006
0.040	1.0112	1.3054	10.0811	0.1409	0.00881

C] Molar Refraction and Polarizability constant at different concentration for M3

Table No. 8

System: 65% Dioxane –Water

Temp: 30±0.1°c

Concentration	DensityPx10 ³	Refractive	Rmix	RLig	(α)x10 ⁻²³ (cm ³)
---------------	--------------------------	------------	------	------	---

C(M)	(Kg-m ⁻³)	Index(η)	(m ³ mole ⁻¹)	(m ³ mole ⁻¹)	
0.1	1.0234	1.3124	8.4007	0.3451	0.01648
0.075	1.0207	1.3072	8.3706	0.3132	0.01522
0.050	1.0164	1.3048	8.3331	0.2830	0.01422
0.040	1.0114	1.3032	8.3229	0.2732	0.01342

Table No. 9

System: 75% Dioxane –Water

Temp:30±0.1°c

Concentration	DensityPx10 ³	Refractive	Rmix	RLig	(α)x10 ⁻²³ (cm ³)
C(M)	(Kg-m ⁻³)	Index(η)	(m ³ mole ⁻¹)	(m ³ mole ⁻¹)	
0.1	1.0259	1.3966	9.0116	0.2632	0.01340
0.075	1.0206	1.3126	9.0074	0.2616	0.01322
0.050	1.0162	1.3116	9.0050	0.2538	0.01315
0.040	1.0129	1.3060	9.0032	0.2310	0.01215

Table No. 10

System: 85% Dioxane –Water

Temp:

30±0.1°c

Concentration	DensityPx10 ³	Refractive	Rmix	RLig	(α)x10 ⁻²³ (cm ³)
C(M)	(Kg-m ⁻³)	Index(η)	(m ³ mole ⁻¹)	(m ³ mole ⁻¹)	
0.1	1.0269	1.3124	10.1620	0.2208	0.01162
0.075	1.0230	1.3112	10.1310	0.1919	0.01040
0.050	1.0223	1.3110	10.1233	0.1822	0.01023
0.040	1.0148-	1.3106	10.1024	0.1634	0.01022

The values of molar refraction of dioxane- water mixtures were presented in Table No 1. The values of molar refraction and polarizability constant of ligand M1, M2, M3 in 65%, 75% and 85% of dioxane-water mixtures were presented in Table No. 2 to 10. The values of molar refraction and polarizability constant at different concentrations of ligands M1, M2, M3 at 65%, 75% and 85% dioxane- water mixtures were given in Table No. 2 to 10. It was observed from these Tables that, the molar refractions and polarizability constants of the ligands decreases in the concentration of ligand. From the data, it can be predicted that, when the percentage of dioxane increases, the molar refractivity (true molar volume) continuously increases. At the same time the polarizability constant of ligand (α) decreases. This may be attributed to the fact that with the increase in percentage of dioxane it causes decrease in dielectric constant of medium and also considerable dipole association (intermolecular attraction) take place, which would be accompanied by decrease in polarizability. It was observed from Table No.2-10 when concentration of dioxane increases the refractive index also increases for M1, M2 and M3. It was also observed that the refractive index was increase from M1 to M3. The resonance stabilization in the ring or in the molecule directly affects the solute –solvent interactions which affect on the result refractive index. From this investigation it was clear that M3 is more suitable drug than M1 and M2 at preliminary stage. Much more anatomical, biochemical and medicinal study is required for these synthesized drugs. Then these drugs will renovate the old drug therapies in malaria, typhoid, ulcer and cancer like diseases. It means that

when the percentage of dioxane increases the solute-solvent interactions i.e. Interactions of ligands (drugs) and dioxane increases, which may stabilize the drug activity at higher percentage of dioxane .From this it can be concluded that the drug absorption, drug transmission and drug effect of M1, M2 and M3 is more effective at higher concentration of dioxane.

V. REFERENCES

- [1]. Dandia A, Arya K, Sati M, 2004, *Synthetic Communication*, 34(6),1141.
- [2]. Nitha B, Strayo De, Adikari S.K., Devasagayam T.P.H. and Janardhanan K., 2010, *Pharmaceutical Biology*, 48(4), 453.
- [3]. Yang J.J., Tian Y.T., Yang Z. and Zhang T., 2010, *Tuxicology in Vitro*, 24(2), 397.
- [4]. Gorinstein, Najaman K., Park Y.S., Heo B.G., Cho J.Y., and Bae J.H., 2009, *Food Control*, 20(4), 407.
- [5]. Saczewski F. and Bulakowska A., 2006, *European J. Medicinal Chem.*, 41(5), 611.
- [6]. Krauth F., Dalise H.M., Ruttinger H.H., and Erobbeg P., 2010, *Bioorganic and Medicinal Chem.*, 18(5), 1816.
- [7]. Gang Cheng, Nir Shapir, Michael J., Sadowsky, and Lawrence P., Wackett, *Applied and Environmental Microbiology*, 2005, 71(8), 4434.
- [8]. Vicente Garcia-Gonzalez, Fernando Govantes, Odil Porrua, and Eduardo Santero, *J. Bacteriology*, 2005, 187(1), 155.
- [9]. Srinivas K., Srinivas W., Bhanuprakash K., Harkishore K., Murthy U.S.N., and Jayathirtha Rao V., 2006, *European J. Medicinal Chem.*, 41(11), 1240.
- [10]. Adebisi A.O., Koekemoer T., Adebisi A.P. and Smith N., 2009, *Pharmaceutical Biology*, 47(4), 320.
- [11]. Paquin Isabelle, Lu Aihua, Claude Marie and Delcome Daniel, 2008, *Bioorganic and Medicinal Chem. Lett.*, 18(3), 1067.
- [12]. Pontillo Joseph, Guo Zhiqiang, Wu Dongpei, Scott R. Struthers and Chen, 2005, *Bioorganic and Medicinal Chem. Lett.*, 15(19), 4363.
- [13]. Frankenburg Frances R. and Baldessanini Ross J., 2008, *Harvard Review of Psychiatry*, 16(15), 299.
- [14]. Mansoon Iqbal, 2008, *Scribd Textile Dyes*, 76,231.
- [15]. Sanchez M., Garbi C., Martinez-Alvarez R., Ortiz I.T., Allende J.L. and Martin M., 2005, *Applied Microbiology and Biotechnology*, 66(5), 589.
- [16]. Marcacci Sylvie, Raveton Muriel, Ravanel Patrick and Schwitzguebel Jean-Paul, 2006, *Environmental and Botony*, 56(2), 205.
- [17]. Trimble A.J., and Lydy M.J., 2006, *Archives of Environmental and Experimental Contamination and Toxicology*, 51(1), 29.
- [18]. Sergeyeva T.A., Brovko O.O., Piletska E.V., Piletsky S.A., Goncharova L.A. and El'skaya A.V., 2007, *Analytic Chimica Acta*, 582(2),311.
- [19]. Salmain M., Fischer-Durand N. and Pradier C.M., 2008, *Analytical Biochemistry*, 373(1), 61.

- [20]. Herranz S., Azcon J.R., Pena E.B., Maruzuela M.D., Marco M.P., and Mereno-Bundi M.C., 2008, *Analytical and Bioanalytical Chem.*, 391(5), 1801.
- [21]. Hase Y., Tatsuno M., Nishi T., Kotaoka K., Kabe Y. and Watanabe H., 2008, *Biochemical and Biophysical Research Communication*, 366(1), 66.
- [22]. Franek M. and Hruska K., 2005, *Vet Medi-Czech*, 50(1), 1.
- [23]. Dolaptsogloy C., Karpouzas D.G., Spiroudi D.M., Eleftherohorinos I. and Voudrias E.A., 2005, *J. Environ. Qual*, 38,782.
- [24]. Petrov M., 2021, *Academia Journal of Scientific Research*, 9(1), 009-018.
- [25]. Kshirsagar A.M., 2012, *Sci. Revs. Chem. Commun.*, 2(3), 503-509.



Preparation & PL Analytical Study of Red and Blue Emitting KCaPO_4 Phosphor for Lighting Industry

G.R.Rahate^{*1}, V.R.Panse², K.V.Sharma³, N.S.Bajaj⁴, Odi Martin Ntwaeaborwa⁵

^{*1}Department of Basic Science & Humanities G. H. Rasoni University, Amravati, Maharashtra, India

²Department of Physics, Late B.S. Arts, Prof. N.G. Science & A.G. Commerce College, Sakharkherda, Maharashtra, India

³Department of Physics, Shri Ramdeobaba College of Engineering & Management, Nagpur, Maharashtra, India

⁴Department of Physics, Toshniwal Arts Commerce & Science College, Sengaon, Maharashtra, India

⁵Department of Physics, University of the Witwatersrand, Johannesburg, South Africa

ABSTRACT

Under this investigation, the compounds $\text{KCaPO}_4:\text{Ce}^{3+}$ & Eu^{3+} was orchestrated by an altered wet chemical synthesis strategy and actuated by alkaline earth Ce^{3+} & Eu^{3+} ion, concerning the relating host material. The characterization of the prepared compound is done under XRD, SEM, PL and CIE coordinates. A wide absorption band in the scope of 280 to 380 nm due to the 4f-5d change of Ce^{3+} ions topping at 332 nm is noticed that shows a blue emission band focused at 442 nm. $\text{KCaPO}_4:\text{Eu}^{3+}$ phosphor presented several emission peaks, which corresponded to the $^5\text{D}_0 \rightarrow ^7\text{F}_j$ ($J=0, 1, 2, 3, 4$) transition of Eu^{3+} , respectively. The highest emission is observed at 620 nm. The excitation spectrum contained 200~350 nm and 350~450 nm two excitation bands, which corresponds to a weak charge transition broad band absorption CTS and a strong f-f transition absorption of Eu^{3+} , respectively. The highest peak of excitation is positioned at 396 nm.

Keywords: Photoluminescence , XRD, SEM,CIE

I. INTRODUCTION

Inorganic phosphors are investigated for their luminescent properties and are widely used in optical arena [1]. This prepared material is a blend of a better return, emanation frequency with a good reaction, quicker decay investigations of iridescence, and stable temperature which makes them advantageous for utilizes in clinical imaging applications [2] and high energy physical science research region [3].

While light comprises of many tones of blue shades which in turn is derived by UV-blue LED (appropriately covered mounted with inorganic phosphors sensitive by LED lights. This set-up results into white light age. This process is successful way to utilize the luminicent properties into reasonable phosphor material [4]. Accessible W-LEDs have lower color re-generation as they regularly rely upon the blending of a blue LED with yellow transmitting inorganic phosphor.[5] The red and green wavelengths of the spectrum of white

tone forms the major portion of white LED.[6] Prepared phosphors are the creation of an optically energized actuated rare earth ion and an inactive host material, generally 3d in any case 4f Metallic electron which are Ce^{3+} , Tb^{3+} or Eu^{3+} , Cr^{3+} Oxide inorganic phosphors material have been widely used in a fitting for vacuum fluorescent display (VFD), electroluminescent (EL) gadgets, field emission display (FED) and (PDP) plasma display panel gadgets [7-8-9-10].

Few researchers have been reported the Eu^{2+} doped soluble earth aluminates based phosphors work in recent past such as D. Ravichandran etl. A very least investigations has been observed based on blue producing trivalent cerium doped phosphor. However, because of their exceptional properties for certain applications like higher effectiveness of luminous, energy saving abilities, longer life length, and short of harmful mercury, light-emitting diodes become considered as cutting-edge lighting sources.[8] To create white light by [1-8] various methodologies are accessible to deliver the white light with the assistance of blue/NUVLEDs. Nichia Co. presents beginning W-LED (blue LED is covered with a yellow shading phosphor of YAG: Ce^{3+}) which has been promoted in market. However, in the discharge spectra, an absence of a red segment is noticed so that,[7] this sort of white LED experiences the detriment of yellow/blue shading allotment and helpless color-rendering index (CRI) noticed. One more methodology is to get white light by joining various lights of colors produced by different chips.[9] Creation of white LEDs revealed in 1997, by Nakamura with the assistance of blending three essential regular colors LEDs (for example green just as blue InGaNSQ W-LEDs with a red AlGaAs LED). In spite of the fact that for such kind of component which adjusts distinctive tone debases among the red, green, and blue chips an unpredictable IC control framework is required. To generate white light and to excite two or tricolor phosphors the third loom with the help of NUV or blue LED sources is needed.

II. EXPERIMENTAL

A synthesis process of wet chemical was used to take over with the advancement of Merck analytical grade inorganic materials which are as follows.

1) KNO_3 (99.99% purity Merck), 2) $Ca(NO_3)_2$ (99.99% purity Merck), 3) KPO_4 (99.99% purity Merck), with double distillation water and 4) Cerium Nitrate ($Ce(NO_3)_3$, 5) REI 99.9 %), 6) Eu_2O_3 and the concentration of Ce^{3+} varies from 1-10 mol % with concentration of Eu^{3+} varies from 0.1 to 1 mol % approximately at the temp of $100^\circ C$ using an oven.

Primarily, According to the stoichiometric ratio in an agate glass beaker with double distillation water, all the ingredient are choosen. Secondly, it is proceeded for stirring process with the help of a magnetic stirrer and keep that homogeneous mixture in an oven whose temp maintain at $100^\circ C$ for 24 hours durations and at long last a pasty solution was framed. At this stage, the entire arrangement is switched to a silica crucible and placed inside a muffle furnace which was kept up at a constant temperature of around $100^\circ C$. A foamy powder with the flame is formed. A collected was further dissected for emission and excitation spectra for photoluminescence estimation. This process results a foamy powder after a crush, the collected fine powder was further analyzed by XRD and PL measurement.

III. RESULTS AND DISCUSSION

X-ray diffraction pattern of KCaPO_4 phosphor

To investigate the crystalline nature of the phosphor products, the prepared sample was carried out XRD measurements at room temperature. Fig. 1 shows the XRD patterns of prepared $\text{KCaPO}_4:\text{Ce}^{3+}$ phosphors. The prepared powder compound was characterized and its phase purity and crystallinity is investigated with the help of X-beam powder diffraction (XRD) by utilizing a PAN Analytical X'pert Pro diffractometer. The XRD diffractometer was used to study the XRD pattern of prepared powder compound using $\text{Cu-K}\alpha$ of radiation (1.54060 nm) with a scanning scan step time 10.3377s with continuous scan type.

We arranged this KCaPO_4 material with Ce^{3+} & Eu^{3+} ion on the reference of standard JCPDS information source document phosphor and discovered it is in acceptable concurrence with JCPDS information source record no. 033-1002. The XRD example of the KCaPO_4 compound is as per the following. The XRD-pattern shows phosphor has great glass like nature. The X-beam diffraction example of the KCaPO_4 compound is appeared in the fig 1. The example was heated reach up to 100°C with a steady rate of 20°C , in a climate of argon. Good crystalline nature powders have synthesized by wet chemical, as indicated by the XRD-pattern

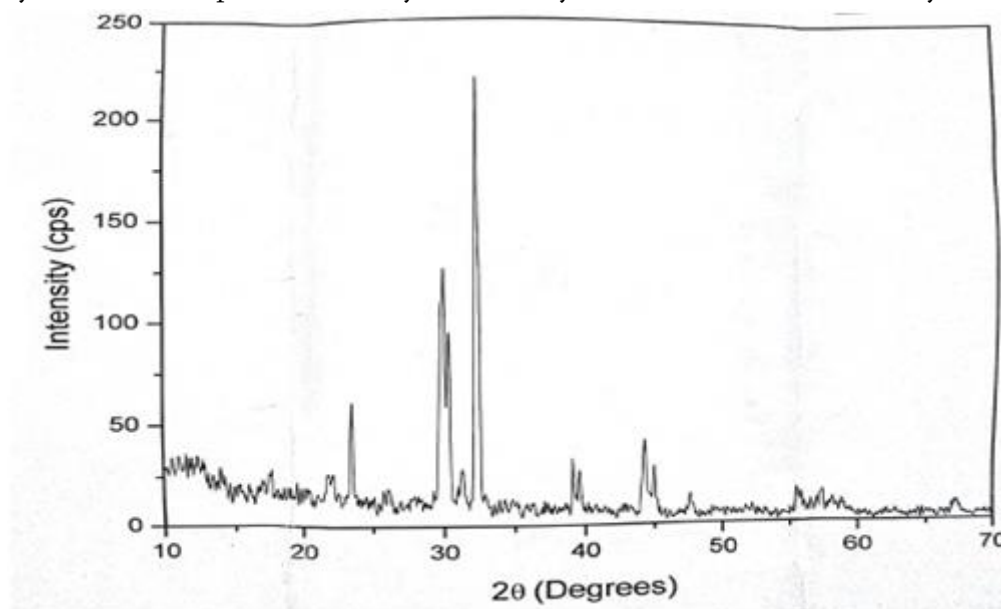


Fig. 1 XRD-pattern of KCaPO_4 lamp phosphors.

Ce^{3+} luminescence in KCaPO_4 phosphors

The Photoluminescence excitation and emission spectra of $\text{KCaPO}_4:\text{Ce}^{3+}$ phosphors are shown in Fig. (3- 4). A wide absorption band in the wavelength of 280 to 380 nm is noticed due to the $4f-5d$ change of Ce^{3+} ions topping at 332 nm wavelength. In Fig.4, the Photoluminescence emission spectra of $\text{KCaPO}_4:\text{Ce}^{3+}$ phosphor shows a blue emission band focused at 442 nm. For the most part, the ground state arrangement of the Ce^{3+} particle is partition into two levels viz., $^2F_{5/2}$ and $^2F_{7/2}$ while the excited configuration of $5d_1$ is partition by the crystal playing field going from 2 to 5 segments. In the present work, a wide blue emission band in the scope of 400-650 nm cresting at 442 nm has observed in the emission spectra of the prepared samples.[8] According

to the available literature [11], it is tracked down that the progress of an electron from the energized province of 2D_1 to the Ce^{3+} ions ground states viz., $^2F_{5/2}$ and $^2F_{7/2}$ of in the prepared sample of $KCaPO_4:Ce^{3+}$ host materials. A deficiency of the doublet characteristic for trivalent cerium ion is seen in the emission spectra [9]. In the T section, the photoluminescence emission spectra are appearing due to the spectral overlapping of different emissions peaks associated with trivalent cerium particles fill in for five Sr locales [12]. The excitation occurs among the most extreme ground level parting to the 5d levels while the emission occurs from the energized level of most minimal level toward the two parting ground levels state. As a result of trivalent cerium ion, there is an extra 4f-5d absorption in the photoluminescence emission spectra while the 5d-4f emission is observed in the photoluminescence emission range is a characteristic twofold band profile. The trivalent 5d-4f emission spectra of cerium ion which firmly dependent on the crystallographic field. Typically, the trivalent cerium ions characteristic emission results the casual most minimal 5d condition of excitation a particular lattice site that occurs as doublet bands with the changes in the 2F_1 ($J=5/2,7/2$) spin-orbit splitting 4f ground state. The partition of energy of the two groups relating to the normal spin-orbit splitting of (2000 cm^{-1}). According to clarifying in the current case as in fig 3 and 4, the peak of excitation was communicated by the energy difference between the most minimal 5d level of excitation of Ce^{3+} ion (332 nm) and the current Sr^{2+} host material equate with the free Ce^{3+} ion (6.118 eV). The emission spectra are probably from a similar discernible site. Non attendance of another emission band in the emission spectra demonstrating that Ce^{3+} possesses one class of destinations in the host material. The nine-fold synchronization Sr^{2+} is seen with Cs evenness in an indistinct tri-covered three-sided trigonal prismatic geometry. Accordingly, $KCaPO_4:Ce^{3+}$ among blue emission can discover possible applications as a blue radiating light phosphor.

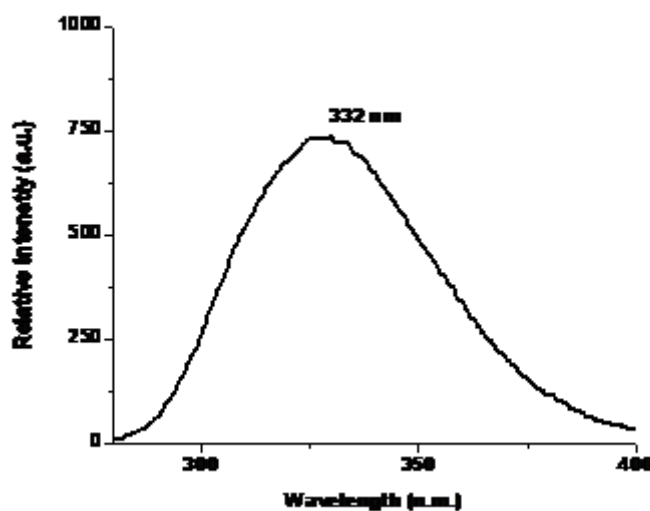


Fig.3 Excitation Spectra for $KCaPO_4:Ce^{3+}$ phosphors, $\lambda_{em}= 442$ nm

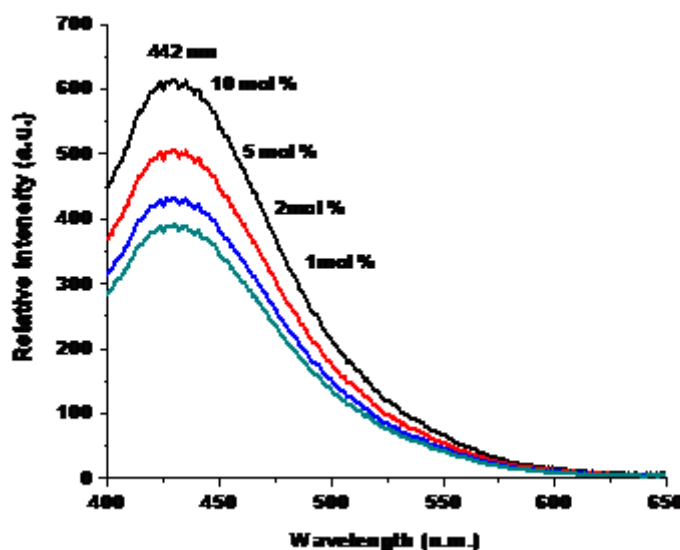


Fig. 4 Emission spectra for $\text{KCaPO}_4:\text{Ce}^{3+}$ phosphor $\lambda_{\text{ex}}=332$ nm

Eu^{3+} luminescence in KCaPO_4 phosphors

The compounds $\text{KCaPO}_4:\text{Eu}^{3+}$ were synthesized by an altered wet chemical synthesis strategy and actuated by alkaline earth Eu^{3+} ion, changes from 0.2 to 1 m% concerning the relating host material. The peaks of emission frequencies of the prepared fluoride aluminates based are contrasted and compound arranged by the high-temperature reaction are aggregated through the graphical representation of emission spectrum. The emission spectra of our prepared red radiating phosphor gives at 620 nm displaying a orange rediesh shift moderately with economically accessible phosphor in the investigations and has forthcoming applications for red light lighting businesses. The excitation as well as emission spectra of $\text{KCaPO}_4:\text{Eu}^{3+}$ phosphor is shown in Fig. (5-6). The highest intensity of emission is observed at the Eu^{3+} concentration of 1 mole% Eu. The decrease in the average distance among Eu^{3+} ions, owes to the increasing concentration of Eu^{3+} , and favors the energy transfer as well as the significant concentration correspond to an adequate decrease in the standard distance. The emission stroke at 594 nm (equivalent to the magnetic dipole $^5\text{D}_0 \rightarrow ^7\text{F}_1$ change of Eu^{3+}), is much weaker than the emission line at 620 nm assign to the required electric dipole $^5\text{D}_0 \rightarrow ^7\text{F}_2$ evolution of Eu^{3+} . We can conclude that Eu^{3+} engaged the lattice sites by means of irregularity. It is well recognized that the $^5\text{D}_0 \rightarrow ^7\text{F}_2$ red color emission of Eu^{3+} ions fit in to basic transitions with $J = 2$ (strongly influenced by the outside surroundings). When Eu^{3+} ions are positioned at local sites of high symmetry (with inversion regularity center), the $^5\text{D}_0 \rightarrow ^7\text{F}_2$ emission is frequently weaker than the $^5\text{D}_0 \rightarrow ^7\text{F}_1$ emanation in the spectrum. The 396 nm wavelength of excitation - an emission wavelength of near-UV as well as blue LED chips, is stronger than the other transition of Eu^{3+} . This implies that the illustration can be efficiently athirst by radiations of wavelength in the nearby UV regions along with red. The luminescent intensity of $\text{KCaPO}_4:\text{Eu}^{3+}$ increases with Eu^{3+} ions concentration and reaches the maximum at value of 1 m% molar fraction of Eu^{3+} ions.

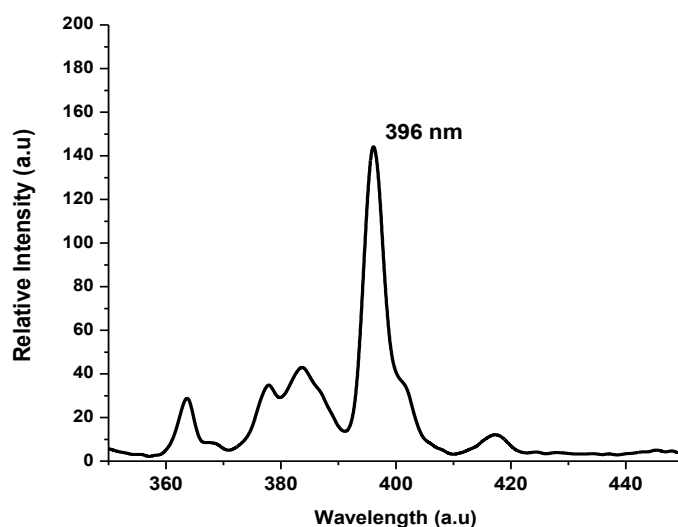


Fig.5 Excitation Spectra for KCaPO₄:Eu³⁺ phosphors, $\lambda_{em}= 620$ nm

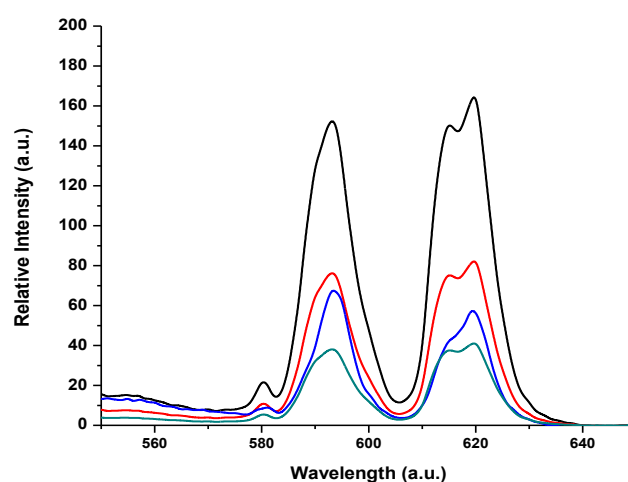


Fig. 6 Emission spectra for KCaPO₄:Eu³⁺ phosphor $\lambda_{ex}=396$ nm

Relationship between Emission Intensity and Concentration of Ce³⁺ ion in KCaPO₄:Ce³⁺ phosphor

The emission intensity of KCaPO₄: Ce³⁺ and Eu³⁺ ion in prepared phosphor was researched in a progression of KCaPO₄:Ce³⁺ blue emitting phosphor with different Ce³⁺ concentrations viz., (1-10) mol % was prepared and the impact of dopant Ce³⁺ concentration. While in the case of KCaPO₄:Eu³⁺ doing with the concentration ranges from 0.1-1 mol %. Fig 7 and 8 shows the greatest emission intensity with review solid emission of Ce³⁺ and Eu³⁺ ion. As we observed from the examples, the emission intensity of Ce³⁺ for 10 m% concentrations are to be 594.3889 nm, which is the maximum intensity shown for the as-prepared KCaPO₄:Ce³⁺ phosphor by using a modified combustion synthesis method, and for 1 m% concentration of Ce³⁺, the smallest amount intensity for emission spectra is found to be 368.858 nm. All the ions of these excitation and emission spectra

are observed at room temperature. For Eu^{3+} cases, the maximum intensity is observed to be 167 nm and minimum intensity to be 41 nm.

The emission intensities of the readied phosphors differ with the substance Ce^{3+} & Eu^{3+} illustrated in following figures..

S.N.	Conc. of Ce^{3+} in KCaPO_4 phosphor	Emission intensity (a.u.)
1	1 mol%	368.858
2	2 mol%	411.176
3	5 mol%	491.226
4	10 mol%	594.3889

Fig /Table 7 : Emission intensities w.r.to conc. of Ce^{3+}

S.N.	Conc. of Eu^{3+} in KCaPO_4 phosphor	Emission intensity (a.u.)
1	1 mol%	167
2	0.5 mol%	83
3	0.25 mol%	57
4	0.1 mol%	41

Fig /Table 7 : Emission intensities w.r.to conc. of Eu^{3+}

The total characteristics of Ce^{3+} & Eu^{3+} doped KCaPO_4 reveal that it is a promising blue & red emitting single-host phosphor for businesses related to light. Moreover, it very well may be valuable as a blue light phosphor and blended in with other shading outflow phosphors to acquire white light.

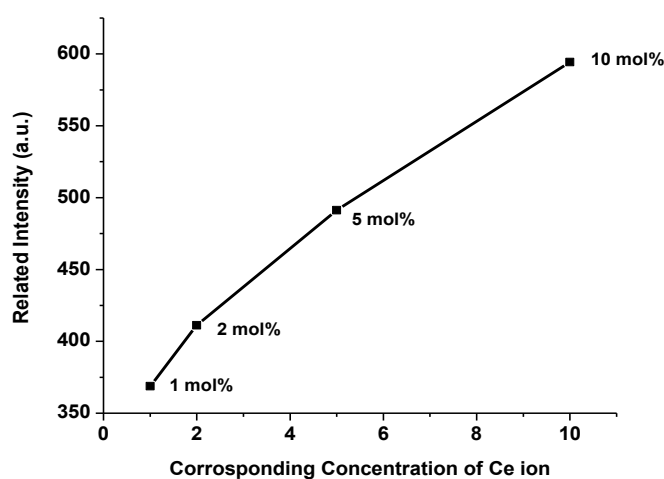


Fig 8(a) Effect of conc. of dopant Ce^{3+} on the emission intensity

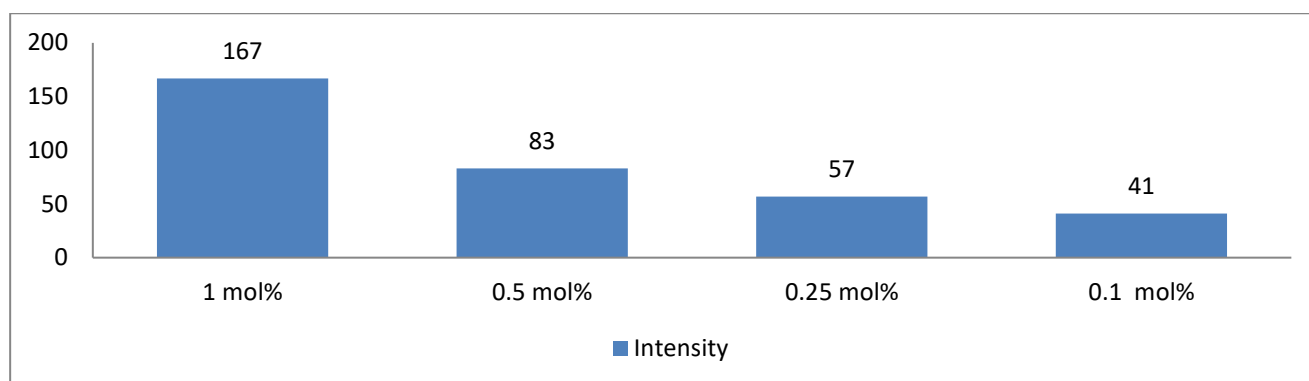


Fig 8(b) Effect of conc. of dopant Eu^{3+} on the emission intensity

Chromatic properties of $\text{KCaPO}_4:\text{Ce}^{3+}$ & Eu^{3+} phosphor

We have observed that the trivalent cerium particle is available with host lattice then the measure of energy can be switched to the activator ion, coming about because of the particular extraordinary emission peak of these activator ions. [14-15] The observations include that the properties of arranged inorganic phosphors in powder structure resulting from the luminescence, rely on the concentration of activator ion, and subsequently, the acknowledgment of the dopant concentration is fundamental [16]. The emission spectrum of Ce^{3+} (located in the blue locale) is considered for additional logical examination and characterization. The luminescent properties of $\text{KCaPO}_4:\text{Ce}^{3+}$ blue-emitting phosphors, accomplish the total discharge of color. Here, we decide the coordinate of chromaticity ordered with the help of the emanation spectra of Ce^{3+} . In 1931, chromaticity facilitate outline was imagined by a famous Commission of International de l'Eclairage (CIE). It is a two-dimensional graphical pictorial delineations of any visible color through the eye arrangement of a person on the x and y-hub. [17]

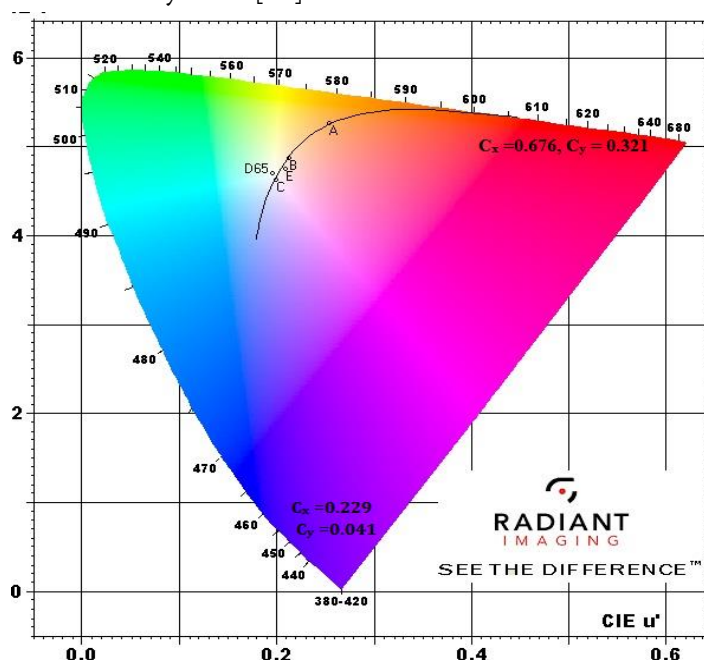


Fig 9 CIE chromatic diagram for $\text{KCaPO}_4:\text{Ce}^{3+}$ phosphor.

Generally, lighting enlightenment implies colors alluding to lighting in states of the chromatic color coordinate which perceives by the individual perception conspire it utilizes 03 significant colors: for example, blue, red, and green [17-18]. The CIE chromaticity diagram of $\text{KCaPO}_4:\text{Ce}^{3+}$ & Eu^{3+} phosphor has appeared in Fig 9, that the shading directions of the $\text{KCaPO}_4:\text{Ce}^{3+}$ phosphor and in the blue area ($C_x = 0.229$, $C_y = 0.041$) phosphor is additionally in the blue region and in case of Eu^{3+} it could be ($C_x = 0.676$, $C_y = 0.321$)

Concerning the CIE diagram, it is effectively clarified that the $\text{KCaPO}_4:\text{Ce}^{3+}$ & Eu^{3+} phosphors are close to the CIE chart casing and shows the most extreme color clarity of the readied phosphor material. Accordingly, the emission and excitation system saw that by connecting these focuses in the arrangement of a tri-point [jointly with white light (0.31 and 0.32)] just as the go-between arrangement can create a white light between an exacting percentage of arranged inorganic blue-emitting phosphor.[19-20] The chromaticity coordinates system (x, y) is determined with the assistance of the color calculator program brilliant imaging. The main wavelength of the spectrum is only the particular wavelength of monochromatic light which seems to have a comparable color of the light source. Such type of wavelength is determined by outlining a singular line elite of a delay from one finish of the chromaticity white illuminants (0.31, 0.32) through the coordinates of x and y-axis to be determined and fully expecting the line to meet the external region locus point hence to the limit of the spectral region of 1931 C.I.E. chromatic graphical representation [21]. The outcome is plotted by the Commission of International de l'Eclairage (CIE) 1931 chromaticity graphical representation in fig. 9.

IV. CONCLUSION

The investigation of the photoluminescence characteristics of trivalent cerium actuated blue-emitting $\text{KCaPO}_4:\text{Ce}^{3+}$ & Eu^{3+} phosphors which is very close to UV-vis range, shows the excitation groups at 332 nm. Due to the corresponding energy level, the emission characteristics of $\text{KCaPO}_4:\text{Ce}^{3+}$ shows an emission band at 442 nm.

$\text{KCaPO}_4:\text{Eu}^{3+}$ phosphor presents several emission peaks, which corresponds to the $^5\text{D}_0 \rightarrow ^7\text{F}_j$ ($J=0, 1, 2, 3, 4$) transition of Eu^{3+} , respectively. In the highest emission at 620 nm, the excitation spectrum contained 200~350 nm and 350~450 nm two excitation bands, which corresponds to a weak charge transition broad band absorption CTS and a strong f-f transition absorption of Eu^{3+} , respectively. The highest excitation peak is located at 396 nm. XRD-pattern of arranged phosphor demonstrates a decent crystalline nature. the morphology of the phosphor as per images obtained from the Scanning Electron Microscope shows at microns to sub few microns. The prepared phosphors have planned in blue applications for the lamp phosphor.

V. REFERENCES

- [1]. A. M. Lejus, N. Pelletier-Allard, R. Pelletier and D. Vivien, Opt. Mater., 1996, 6, 129.
- [2]. V. Bachmann, C. Ronda and A. Meijerink, Chem. Mater., 2009, 21, 2077..
- [3]. V.R.Panse, Alok shukla, S.J.Dhoble, J. of Optik 2017, 130, , 539-542

- [4]. Bajaj N S, Omanwar SK, J. Optical Materials 2013;35:1222.
- [5]. V.R. Panse, N.S. Kokode, K.N. Shinde, S.J. Dhoble, J. of Results in Physics 8 (2018) 99–103
- [6]. V. R. Panse, A. N. Yerpude, S. J. Dhoble, N. S. Kokode, Renu Choithrani, J Mater Sci: Mater Electron, 2017, Vol 28, Issue 22, pp 16880–16887
- [7]. A. N. Yerpude, V. R. Panse, S. J. Dhoble, N. S. Kokode, M. Srinivas, The J. of Bio. and Chem. Lumin. DOI: 10.1002/bio.3340
- [8]. R.L. Kohale, S.J. Dhoble, J. of Lumin 138 (2013) 153–156
- [9]. V.R. Panse, Alok Shukla, S.V. Panse, N. S. Dhoble, S. J. Dhoble, J. of Mat. Sci. : Material In Electronics, 2017, Vol, 28, Issue 2, pp 2193–2199
- [10]. Seed Ahmed HAA, Ntwaeaborwa OM, Kroon RE. J Lumin 2013;135:15–9.
- [11]. Gedam SC, Dhoble SJ, Moharil SV. J Lumin 2007;126:121–9.
- [12]. V.R. Panse, N.S. Kokode, A.N. Yerpude, S.J. Dhoble, Optik 127 (2016) 1603–1606
- [13]. Natarajan V, Dhoble AR. J Lumin 2009;129:290–3.
- [14]. N. Yerpude, V.V. Shinde, V.R. Panse, S. J. Dhoble, N.S. Kokode, IJCESR, Vol-5, Issue-1.
- [15]. J. K. Sheu et al., IEEE Photonics Technol. Lett., vol. 15, no. 1, pp. 18–20, 2003.
- [16]. R. R. Patil, and S. V. Moharil, Phys. Status Solidi A, vol. 187, no. 2, pp. 557–562, 2001.
- [17]. N.S. Kokode, V.R. Panse, S.J. Dhoble, J. of advanced material letter 2015, 6(7), 616–619.
- [18]. V. R. Panse, N. S. Kokode, and S. J. Dhoble, J. of Optik, vol. 126, no. 23, pp. 4782–4787, 2015.
- [19]. Weng M, Yang R, Peng Y, Chen J. Ceram Int 2012;38:1319–23.
- [20]. Zhu L, Lu A, Zuo C, Shen W. J Alloys Compd 2011;509:7789–93.
- [21]. Zhou Li-Ya, Weia Jian-She, Shib Jian-Xin, Gongb Meng-Lian, Liang Hong-Bin. J Lumin 2008;128:1262–6.



Synthesis and Photoluminescence Properties of $\text{ZnB}_4\text{O}_7 : \text{Eu}^{3+}$ Phosphor

V. R. Kharabe

Department of Physics, Kamla Nehru Mahavidyalaya, Nagpur 440024, Maharashtra, India

ABSTRACT

The solid state diffusion technique was used to successfully prepare the $\text{ZnB}_4\text{O}_7 : \text{Eu}^{3+}$ phosphor. The PL's excitation spectra exhibited a broad band between 240 and 330 nm with a peak around 257 nm and many lesser excitation peaks between 240nm and 340nm. In the broad band at 250-300 nm, the $\text{O}^{2-} \rightarrow \text{Eu}^{3+}$ charge transfer transition in the Eu^{3+} doped ZnB_4O_7 phosphor was seen. The phosphor may be efficiently activated with mercury as well as UV rays, based on excitation peaks at 257nm and 393nm. In the wavelength range of 580nm to 680nm, a number of emission peaks are detected, which correspond to the transitions of $5\text{D}_0 \rightarrow 7\text{F}_1$ (orange emission), 7F_2 (orange emission), and 7F_3 (orange emission) (red emission). The $\text{ZnB}_4\text{O}_7 : \text{Eu}^{3+}$ phosphor is a new red-orange color emitting phosphor, according to the comprehensive investigation of the emission and excitation spectra. In the future, XRD and SEM could be employed to examine the material's structural properties and surface morphology.

Keywords: ZnB_4O_7 , PL, XRD, SEM.

I. INTRODUCTION

Luminescent materials have grown in popularity in recent years as their features have been related to a wide range of scientific applications. It involves the design and development of novel optical devices like white light emitting diodes (WLEDs), plasma display panels (PDPs), solid-state lasers, [1-4]. Researchers were interested in getting glasses for various optical devices like activated phosphors, up converters, optical amplifiers and laser because of the glasses's unique visible emission. [5]. The type of bonding, chemical composition, and structure of RE ions in glasses affect both luminescence and absorption properties [6]. Because of their size, composition flexibility borate glasses are excellent hosts for RE ions [7]. The Eu^{3+} ion, a popular spectroscopic tool, is extensively employed to analyze structure in glasses, near RE ions because of its relative simplicity of energy level structure with non-degenerate ground (7F_0) and excited (5D_0) states [8-15]. In Eu^{3+} doped phosphors a $5\text{D}_0 \rightarrow 7\text{F}_2$ transition produces narrow, monochromatic radiation at 613nm (red) which is commonly used in technologies for field emission. Zinc borates are multifunctional compounds containing ZnO , B_2O_3 , and H_2O in various ratios. They are vital chemical raw materials required in a wide range of applications. They're prominent in flame-resistant polymer materials [16]. Zinc borate has garnered a lot of attention as a luminescence host material in recent decades. LaBO_3 and YBO_3 are rare earth orthoborates that

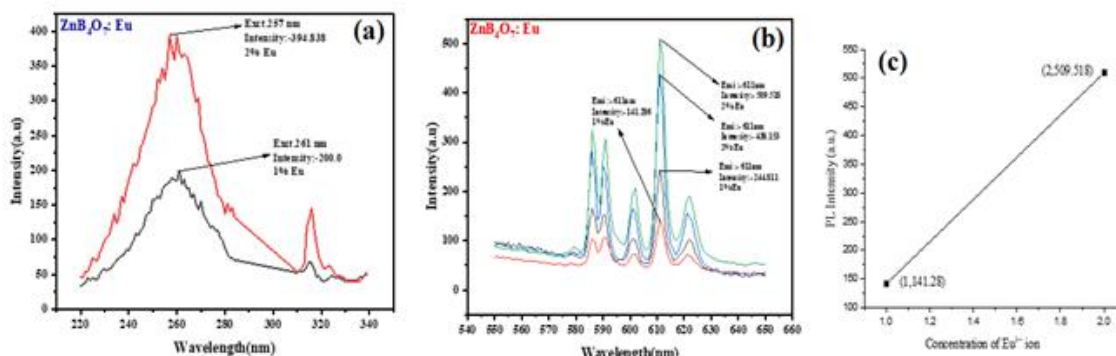
have been shown to be the best for Eu^{3+} and Tb^{3+} luminescence in all lattices. Hg-free fluorescent lighting, plasma display panels, and field emission displays are some of the latest innovations. [17,18] The red and green elements, for example of PDP television are now $\text{YBO}_3:\text{Eu}^{3+}$ and $\text{YBO}_3:\text{Tb}^{3+}$ [19, 20]. Due to poor absorption (parity prohibited transitions) within the 4f shell when excitation occurs in the soft UV or blue energy range, the emission efficiency of Eu^{3+} ions in most hosts is quite low. Indirect excitation via the energy transfer process via host absorption or connected host absorption (charge transfer band) the Eu^{3+} ions show some good efficiency under UV light. By manipulating/selecting suitable host materials with minimal band gaps or generating a crystal lattice with low symmetry, the photoluminescence efficiency in the soft UV to blue excitation region can be improved. As a result, low-cost phosphors with better thermal, optical efficiency and stability when activated between UV and visible light are needed. The hydrates of zinc borate and zinc borate have been researched as afterglow suppressants, flame retardants, smoke suppressants, synergistic agents, and corrosion inhibitors in the past [21–24]. Borate of zinc is an optically and thermally stable chemical that is significantly less expensive than borates doped with rare earth such as lanthanum-borate and yttrium-borate. The $[\text{B}_4\text{O}_7]^{2-}$ unit is made up of two BO_3 triangles and two BO_4 tetrahedra with a shared vertex in the crystal structure of ZnB_4O_7 . These flats are scattered around the structure. In an unequal and twisted tetrahedron, each zinc atom (ZnO_4) is surrounded by four oxygen atoms. The six O-Zn-O angles range from 89.1 to 125.5 degrees [25], allowing the Eu^{3+} ion's prohibited f-f transitions to be improved by the poor symmetry crystal. There are, however, only a few publications on zinc's luminescence qualities. However, there are fewer articles on the luminescence properties of zinc borates. [26–28]. As a result, this paper discusses the PL characterization of $\text{ZnB}_4\text{O}_7:\text{Eu}^{3+}$ phosphor.

II. EXPERIMENTAL

At a high temperature, the sample $\text{ZnB}_4\text{O}_7:\text{Eu}^{3+}$ was produced using a traditional solid-state diffusion approach. In a mortar pestle, the initial components were a stoichiometric mixture of reagent ZnCO_3 , H_3BO_3 , and Eu_2O_3 (99.99 percent). Weighing was done using an extremely precise balance with an accuracy of up to four digits, or 0.0001 gm. Then, depending on the molar concentration (0.5, 0.1, 1, 2) mole percent, Europium oxide (Eu_2O_3) was added. The entire ingredient was crushed for around 30-35 minutes till it was converted to a very fine powder. Moisture absorption is not a negative thing; on the contrary, it aids in the formation of a homogeneous mixture. This mixture was transferred to china crucible and placed it in a furnace maintained at temperature 500°C and kept at this temperature for 5 hours. The powder was thoroughly mixed into the mortar pestle, and the entire ingredient was crushed for another 30-35 minutes till powder was formed. This combination was transferred to a china crucible, which was then placed in a furnace and heated to 900°C in air for 5 hours. After the reaction was completed, the china crucible was removed from the furnace and the sample was crushed in a mortar pestle for 30 minutes to obtain a fine powder that can now be used to determine the PL characteristic of ZnB_4O_7 . At room temperature, the samples' photoluminescence (PL) emission spectra were recorded using a SHIMADZU Spectrofluorophotometer (RF-5301 PC) equipped with a 150W Xenon lamp as the excitation source. In each example, the same amount of sample was used.

III. RESULT AND DISCUSSION

3.1 Photoluminescence of $\text{ZnB}_4\text{O}_7:\text{Eu}^{3+}$ Phosphor



The excitation (Fig. a) and emission spectra (Fig.b) of as prepared $\text{ZnB}_4\text{O}_7:\text{Eu}^{3+}$ and Fig.(c) shows dependence of Emission Intensity On Concentration Of Eu^{3+} Ions

Monitoring one of the principal emission wavelengths, 611 nm, was used to record the excitation spectra (Fig. a). Excitation spectra revealed a broad band between 240 and 330 nm, with maximum peak around 257 nm and multiple weak excitation peaks between 240 and 340 nm. The transition from one charge to the next ($\text{O}^{2-} \rightarrow \text{Eu}^{3+}$) in the Eu^{3+} doped ZnB_4O_7 phosphor was significant in the 250-300 nm broad band [29,30]. The charge is transferred from O^{2-} 's 2p orbital to Eu^{3+} , the core metal ion's 4f orbital. It suggests that mercury has the ability to successfully activate the phosphor. Due to the transitions to the inner shell of Eu^{3+} ions, the substantial excitation peaks at 257 nm and 261 nm are the weaker peaks. [31]. The excitation edge located from 220-340 nm is large against other Eu^{3+} doped host materials [32,33,34], which could be related to the extremely advantageous as the electric dipole infra 4f transitions are boosted by the poor symmetry crystal structure of borate. The emission peaks of the Eu^{3+} sample were 370 nm, 380 nm, and 393 nm, respectively. $7\text{D}_0-5\text{D}_4$ transitions take place at 370 nm, $7\text{D}_0-5\text{G}_2$ transitions take place at 380 nm, and $7\text{D}_0-6\text{L}_2$ transitions take place around 400 nm. It indicates that blue and near ultraviolet light the phosphor can be effectively activated. The UV to blue edge of the transition spectrum exactly fits LED near UV/blue, implying that white LED is provoked by blue LED generation is achievable. Fig. (b) shows the emission spectra of $\text{ZnB}_4\text{O}_7:\text{Eu}^{3+}$ phosphor at room temperature. A series of emission peaks have been recorded in the wavelength range of 580 nm to 680 nm, which correspond to the transitions of $5\text{D}_0-7\text{F}_1$ (orange emission), 7F_2 (orange emission), and 7F_3 (orange emission) (red emission). The phosphor's luminous effect gradually enhanced after Eu^{3+} was introduced at a doping concentration of between 1% and 2% (Fig. c). When the concentration of Eu^{3+} is low, it is impossible to produce a major luminescent centre, hence the luminescence is low.

IV. CONCLUSION

The $\text{ZnB}_4\text{O}_7:\text{Eu}^{3+}$ phosphor was successfully synthesized using the solid state diffusion process. The prominent peak at 611 nm was caused by Eu^{3+} ions in the ZnB_4O_7 host transitioning from 5D_0 to 7F_2 , and the optimal concentration of Eu^{3+} ions for the best PL intensity was found to be 2 mole percent. When compared to the

other sites, the temperature-dependent photoluminescence results suggest that $\text{ZnB}_4\text{O}_7:\text{Eu}^{3+}$ is a phosphor with potential with good temperature stability, implying that it is a favorable environment when Eu^{3+} ions undergo a forced electric dipole transformation [35]. When stimulated at 611nm, all samples showed orange fluorescence, with the main component peaking at 257nm. According to a careful investigation of the emission and excitation spectra, the $\text{ZnB}_4\text{O}_7:\text{Eu}^{3+}$ phosphor is a new red-orange color emitting phosphor that may be proposed for near ultraviolet or blue-light excitation and has a favorable effect.

V. REFERENCES

- [1]. H.M. Yang, J.X. Shi, M.L. Gong, *J. Solid State Chem.* 178 (2005) 917.
- [2]. M.K. Chong, K. Pita, C.H. Kam, *J. Phys. Chem. Solids* 66 (2005) 213.
- [3]. E.J. Nassar, L.R. Avila, P.F.S. Pereira, C. Mello, O.J. de Lima, K.J. Ciuffi, C. Mello, L.D. Carlos, *J. Lumin.* 111 (2005) 159.
- [4]. V. Lavin, P. Babu, C.K. Jayasankar, I.R. Martin, V.D. Rodriguez, *J. Chem. Phys.* 115
- [5]. M. Nagami, Y. Abe, *J. Non-cryst. Solids* 197 (1996) 73.
- [6]. M.J. Weber, *J. Non-cryst. Solids* 123 (1990) 208.
- [7]. V. Venkatramu, P. Babu, C.K. Jayasankar, *Spectrochim. Acta A* 63 (2006) 276.
- [8]. J.A. Capobianco, P.P. Proulx, M. Bettinelli, F. Negrisolo, *Phys. Rev. B* 42 (1990) 5936.
- [9]. S. Todoroki, S. Tanab, K. Hirao, N. Soga, *J. Non-cryst. Solids* 136 (1991) 213.
- [10]. J.L. Adam, V. Poncon, J. Lucas, G. Boulon, *J. Non-cryst. Solids* 91 (1987) 191.
- [11]. V. Lavin, V.D. Rodriguez, I.R. Martin, U.R. Rodriguez-Mendoza, *J. Lumin.* 72 (1997) 437.
- [12]. R. Balda, J. Fernandez, J.L. Adam, M.A. Arriandiaga, *Phys. Rev. B* 54 (1996) 12076.
- [13]. R. Balakrishnaiah, R. Vijaya, P. Babu, C.K. Jayasankar, M.L.P. Reddy, *J. Non-cryst. Solids* 353 (2007) 1397.
- [14]. P. Babu, C.K. Jayasankar, *Physica B* 279 (2000) 262.
- [15]. W.T. Carnall, P.R. Fields, K. Rajnak, *J. Chem. Phys.* 49 (1968) 4450.
- [16]. Mu Z F, Hu Y H, Chen L, Wang X J. Enhanced red emission in $\text{ZnB}_2\text{O}_4:\text{Eu}^{3+}$ by charge compensation. *Opt. Mater.*, 2011, 34(1): 89.
- [17]. Z. H. Li, J. H. Zeng, C. Chen, and Y. D. Li, "Hydrothermal synthesis and luminescent properties of $\text{YBO}_3:\text{Tb}^{3+}$ uniform ultrafine phosphor," *Journal of Crystal Growth*, vol. 286, no. 2, pp. 487–493, 2006.
- [18]. S. Shionoy and W. M. Yen, *Phosphor Handbook*, CRC Press, New York, NY, USA, 2nd edition, 1998.
- [19]. C.-H. Kim, I.-E. Kwon, C.-H. Park et al., "Phosphors for plasma display panels," *Journal of Alloys and Compounds*, vol. 311, no. 1, pp. 33–39, 2000.
- [20]. X. Zhang, H. Lang, and H. J. Seo, "On the luminescence of Ce^{3+} , Eu^{3+} , and Tb^{3+} in novel borate $\text{LiSr}_4(\text{BO}_3)_3$," *Journal of Fluorescence*, vol. 21, no. 3, pp. 1111–1115, 2011.
- [21]. Z. Li, P. Wu, X. Jiang, Z. Zhang, and S. Xu, "The synthesis of rare earth borate glasses and their luminescence properties," *Journal of Luminescence*, vol. 40–41, pp. 135–136, 1988.

- [22]. C. Ting, D. Jian-Cheng, W. Long-Shuo, Y. Fan, and F. Gang, "Synthesis of a new netlike nano zinc borate," *Materials Letters*, vol. 62, no. 14, pp. 2057–2059, 2008.
- [23]. F. Samyn, S. Bourbigot, S. Duquesne, and R. Delobel, "Effect of zinc borate on the thermal degradation of ammonium polyphosphate," *Thermochimica Acta*, vol. 456, no. 2, pp. 134–144, 2007.
- [24]. A. Genovese and R. A. Shanks, "Structural and thermal interpretation of the synergy and interactions between the fire retardants magnesium hydroxide and zinc borate," *Polymer Degradation and Stability*, vol. 92, no. 1, pp. 2–13, 2007.
- [25]. M. Martinez-Ripoll, S. Martínez-Carrera, and S. García-Blanco, "The crystal structure of zinc diborate ZnB₄O₇," *Acta Crystallographica Section B Structural Crystallography and Crystal Chemistry*, vol. 27, no. 3, pp. 672–677.
- [26]. A. Ivankov, J. Seekamp, and W. Bauhofer, "Optical properties of Eu³⁺-doped zinc borate glasses," *Journal of Luminescence*, vol. 121, no. 1, pp. 123–131, 2006.
- [27]. Y. Zheng, Y. Qu, Y. Tian et al., "Effect of Eu³⁺-doped on the luminescence properties of zinc borate nanoparticles," *Colloids and Surfaces A: Physicochemical and Engineering Aspects*, vol. 349, no. 1–3, pp. 19–22, 2009.
- [28]. Z. Mu, Y. Hu, L. Chen, and X. Wang, "Enhanced red emission in ZnB₂O₄:Eu³⁺ by charge compensation," *Optical Materials*, vol. 34, no. 1, pp. 89–94, 2011.
- [29]. L. Lou, D. Boyer, G. Bertrand-Chadeyron, E. Bernstein, R. Mahiou, and J. Mugnier, "Sol-gel waveguide thin film of YBO₃: preparation and characterization," *Optical Materials*, vol. 15, no. 1, pp. 1–6, 2000.
- [30]. C.-H. Kim, I.-E. Kwon, C.-H. Park et al., "Phosphors for plasma display panels," *Journal of Alloys and Compounds*, vol. 311, no. 1, pp. 33–39, 2000.
- [31]. L. Guan, Y. Wang, W. Chen et al., "Fabrication and luminescent properties of red phosphor M₃BO₆:Eu³⁺ (M=La, Y)," *Journal of Rare Earths*, vol. 28, no. 1, pp. 295–298, 2010.
- [32]. G. Bertrand-Chadeyron, R. Mahiou, M. El-Ghozzi, A. Arbus, D. Zambon, and J. C. Cousseins, "Luminescence of the orthoborate YBO₃: Eu³⁺. Relationship with crystal structure," *Journal of Luminescence*, vol. 72–74, pp. 564–566, 1997.
- [33]. Z.-W. Zhang, X.-Y. Sun, D.-D. Jia, S.-T. Song, J.-P. Zhang, and S.-F. Wang, "Tunable full color emission from single phase LiSr_{3.99-x}Dy_{0.01}(BO₃)₃:xEu³⁺ phosphors," *Ceramics International*, vol. 39, no. 4, pp. 3965–3970, 2013.
- [34]. X. Zhang, H. Lang, and H. J. Seo, "On the luminescence of Ce³⁺, Eu³⁺, and Tb³⁺ in novel borate LiSr₄(BO₃)₃," *Journal of Fluorescence*, vol. 21, no. 3, pp. 1111–1115, 2011.
- [35]. V. Venkatramu, P. Babu, and C. K. Jayasankar, "Fluorescence properties of Eu³⁺ ions doped borate and fluoroborate glasses containing lithium, zinc and lead," *Spectrochimica Acta—Part A: Molecular and Biomolecular Spectroscopy*, vol. 63, no. 2, pp. 276–281, 2006.

Application of Graphene Oxide - Cadmium Oxide Nano Composite as Photo Catalyst in Degradation of Nitro Benzene

M. N. Zade, D. T. Tayade

Department of Chemistry, Govt. Vidarbha Institute of Science and Humanities, Amravati, Maharashtra, India

ABSTRACT

Graphene oxide based metal oxide nano composite act as a photo catalyst in various organic transformations and selective degradation of organic dye, act as a water purifying agent. In this work the synthesis of grapheme oxide cadmium oxide nanocomposite was done and degradation of nitro compound dye was studied in visible region of electromagnetic spectrum using different concentration of dye and catalyst.

Keywords:- Graphene oxide, cadmium oxide, nanocomposite, and nitrobenzene.

I. INTRODUCTION

The discovery of the 2D nanostructure of graphene was in fact the beginning of a new generation of materials. Graphene itself, its oxidized form graphene oxide (GO), the reduced form of GO (RGO) and their numerous composites are associates of this generation. . GO can be functionalized with metals (Ag and Mg) and metal oxides (CuO, MgO, Fe₂O₃, Ag₂O, etc.)¹⁻⁵ nanoparticles (NPs), organic ligands (chitosan and EDTA) and can also be dispersed in different polymeric matrices (PVA, PMMA, PPy, and PAN).⁶⁻⁸ All these combinations give rise to nanohybrid materials with improved functionality.

The functional properties of GO were synergistically modified by photoactive semiconductor NPs; as a result, the GO– MO hybrids acquired excellent photocatalytic ability and were able to degrade a large variety of organic dyes (MB, RhB, MO, MR, etc.)¹⁰⁻¹² and pathogens. GO as filler enhanced the strength, flexibility and functional properties of common polymers, such as PVA and PVC, to a large extent while, GO–CP composites with polyaniline and polypyrrole are considered suitable for the fabrication of biosensors, supercapacitors, and MEMS as well as efficient photo thermal therapy agents.

During the past few years, various GR-based composite photo catalysts used for “non- selective” degradation of pollutants, photo-inactivation of bacteria and water splitting to H₂ and O₂, for “selective” organic transformations, including reduction of CO₂ to renewable fuels, reduction of nitro-aromatic compounds to amino compounds, oxidation of alcohols to aldehydes and acids, epoxidation of alkenes, hydroxylation of phenol, and oxidation of tertiary amines.

Nitro compounds constitute a large family among organic compounds and are widely used for various purposes; Reduction of nitro compounds is one of the important methods for the preparation of aryl amines.

Nitro compounds have traditionally been reduced by high-pressure hydrogenation. The application of NaBH_4 $\text{NaBH}_4/\text{CoCl}_2$, $\text{NaBH}_4/\text{FeCl}_2$, $\text{NaBH}_4/\text{CuSO}_4$, NaBH_4/Co , $\text{NaBH}_4/\text{Cu}(\text{acac})_2$, borohydride exchange resin (BER); BER/ $\text{Ni}(\text{OAc})_2 \cdot 4\text{H}_2\text{O}$, CoCl_2 , PdCl_2 , $\text{Cu}(\text{OAc})_2$ are effective for the reduction of aliphatic or aromatic nitro compounds. Sn in HCl is also powerfull tools.¹⁹⁻²⁵

Although various methods for degradation of nitro compounds are reported but they have one or more limitation such as used of hazardous solvent toxic materials and costly catalyst. Present work provide green method by suing graphene oxide cadmium oxide based nanocomposite is catalyst in visible region of light using water as a reaction medium for degradation of nitro compounds.

II. EXPERIMENTAL SECTION

Synthesis of graphene oxide.

A mixture of grapheme powder sodium nitrate concentrated Sulfuric acid Potassium permanganate, 30 volume hydrogen peroxide was stirred a bright yellow color precipitate is obtained . Filter the reaction mixture; wash the ppt with 10% HCl solution. A brownish chocolate colored crystalline solid, insoluble in water was obtained. IR spectrum of compound shows following data. 3178.26cm^{-1} indicates sp^2 C-H stretching frequency, 2085.32cm^{-1} indicates C-H (bend) sretching frequency 1569.12cm^{-1} indicates carbonyl stretching frequency 1324.74cm^{-1} indicates C-O stretching frequency. TGA Analysis shows Loss of substituent is observed in first step from 110-2400C. Loss of remaining part is observed from 260-3200C. The compounds are degraded completely in the range 320-4000C indicates that the material is fully organic. Half decomposition temperature was found to be 180oC

Synthesis of G.O.-CdO-Nanocomposite

Mixture of graphene oxide , cadmium sulphate. Potassium permanganate. Was Reflux in water the for 24 hours at160oC brownish chocolate colored crystalline ppt obtained IR spectrum shows 3334cm^{-1} indicates sp^2 C-H stretching frequency 2093.32cm^{-1} indicates C-H (bend) stretching frequency 1576.12cm^{-1} indicates carbonyl stretching frequency 1334.77cm^{-1} indicates C-O stretching frequency further XRD report and SEM, TEM confirm the properties of nanocomposite material

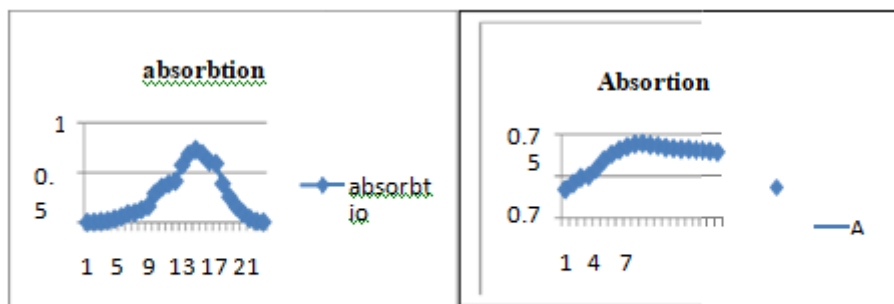
Application of GO Nanocomposite in Reduction of Nitro compound Optimization of Reduction of spectrophotometrically

Source of visible light

White LED of 5w,10w, 20w used as a source of photon for the reaction. The observed result indicate that 5w LED take 20hours to complete the reaction. 10 w last 12 hours, 20w take 3-4 hours for this conversion. So 20 w LED used as a photo source throughout the process. Optimization for various concentration of nitrobenzene with various concentration of catalyst discussed below

Determiation of λ max for 1M Solution of M-dinitrobenzene

The λ max was calculated by observing the absorption of sample in all range of spectrophotometer. The result of experiment summarized in graph.

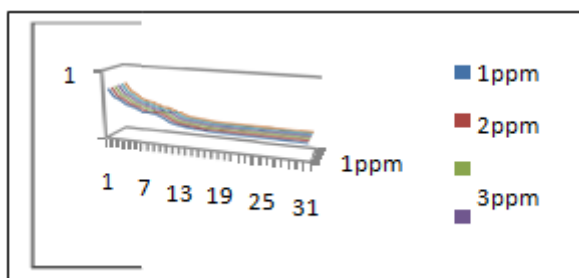


On x axis 1 unit= 20 nm, Y axis 1 unit = 0.2 absorbtion.

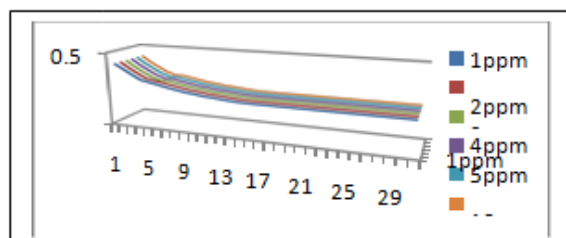
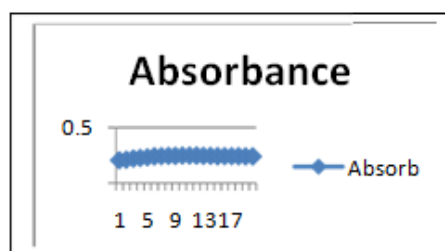
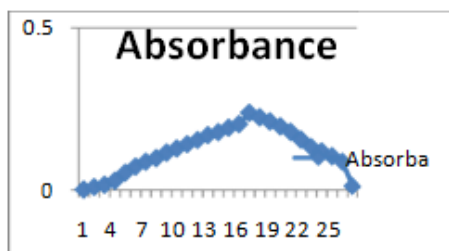
From above observation the maximum wavelength for m-dinitrobenzene is 510 nm.

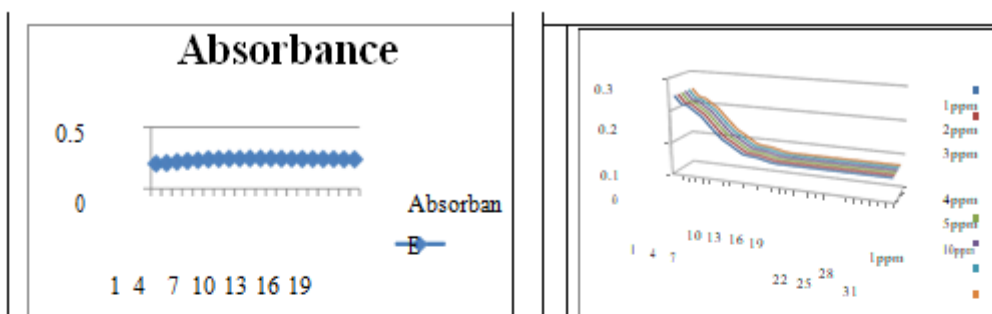
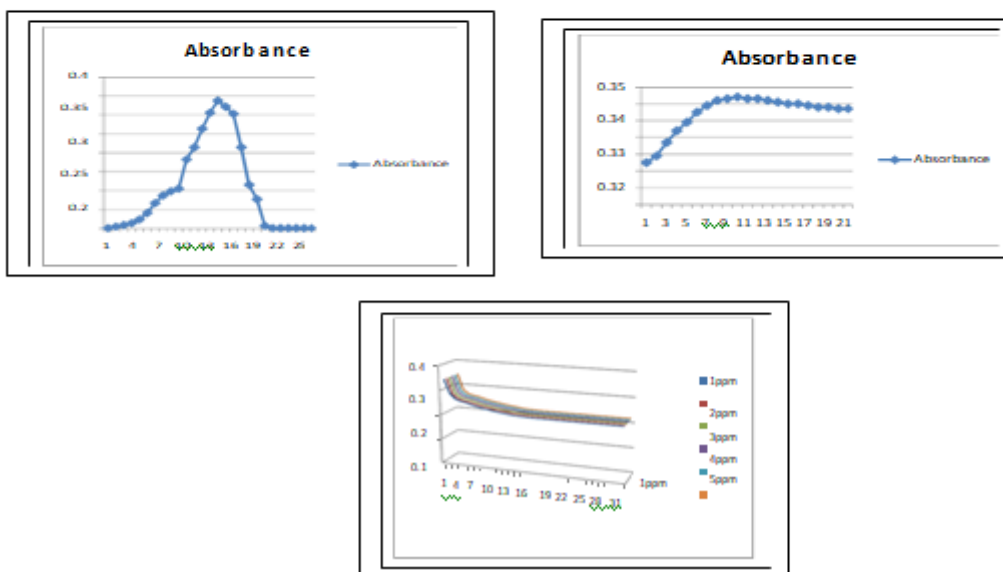
Optimization of time and conc. of catalyst

In λ max the conversion of nitro to amine observed by various concentration of catalyst. Initially reaction was examined with respect to 1ppm of catalyst. To complete reaction it take 190 minute, then the effect of different concentration of catalyst (2ppm, 3ppm, 4ppm, 5ppm, 10ppm) was studied. The increasing conc. of catalyst initially affects the rate of conversion but it also take almost same time to complete the reaction. Hence 1ppm catalyst is the transformation. best choice for this



Following similar method optimization was carried out for different concentration summarized in graphs. Optimization at different concentration for 0.1 M solution



For 0.001 M solution**For 0.02M solution****III. RESULT AND DISCUSSION**

Synthesis of graphene oxide was done by following Hummers method. Synthesis of graphene oxide based metal nanocomposite did by using potassium permagnate hydrogen peroxide oxidation method. Synthesized nano composite were use as a photo catalyst by optimizing reaction in various reaction conditions using different concentration of nitro dye and various proportion of catalyst in range of visible radiation of light. Characterization of synthesized material was done using IR, TGA, SEM, TEM and XRD.

IV. CONCLUSION

Present work provide green method by suing graphene oxide cadmium oxide based nanocomposite is catalyst in visible region of light using water as a reaction medium for degradation of nitro compounds. Even very low concentration of catalyst does degradation of nitro benzene in visible region. So that graphene oxide cadmium oxide nanocomposite found to be excellent photo catalyst. So present method is better alternative way for

degradation of nitro compound instead using hazardous solvent and costly catalyst. since reaction proceeded in water and using light the provided method is ecofriendly environmental benign and energy efficient.

V. REFERENCES

- [1]. Dordevic L., Arcudi f., Cacioppo M., Prato M. . *Nature Nanochem* . 2022 17, 112-130
- [2]. Liu Z., Ling Q., Cai Y., Xu L., Su J., Yu K., Wu X., Xu J., Hu B. , Wang X. . *Nanoscale Adv.* 2022 DOI: 10.1039/d1na00843a
- [3]. András G., Ábrányi-Balogh P. *Catalysts* . 2021, 11, 1081.
- [4]. Jiang Z., Zhu H., Guo W. , Ren Q., Ding Y., Chen S., Chend J. , Jiad X.. *RSC Adv.*,2022, 12, 7671
- [5]. Sandeep V., Bhaskar H. ,Maddilia S., kumar K., *Arabic journal of chemistry.* 2020,1142-1178 , 13
- [6]. Kondo T., Mistudo T., *Chem. Rev.* 2000, 100, 8, 3205–3220
- [7]. Kumar G., Hussain F., Gupta R.. *Dalton transaction*,2017,43.
- [8]. Luo J. , Wei W. <https://doi.org/10.1002/adsc.201800205>
- [9]. Shelvaraj V., Swarna T., Karthika C., Algar M.doi.org/10.1016/j.molstruc.2020.129195
- [10]. Alajilani H., Jamjoum A., Umar K., Adnan R., Razali M., Nasir M., Ibrahim M.,1 [doi: 10.3389/fchem.2021.752276](https://doi.org/10.3389/fchem.2021.752276)
- [11]. cková A., Jankovský O. , Sofer Z. , Sedmidubský D.. *Materials* 2022, 15, 920
- [12]. Palmisano G., Augugliaro V., Pagliaro M., Palmisano L., *Chem. Commun.*, 2007, 3425- 3437.
- [13]. Tahoon M.A., Siddeeg S.M., Salem Alsaieri N., Mnif W., Ben Rebah F., A review. *Processes* 2020, 8, 645.
- [14]. Siddeeg S.M., Tahoon M.A., Rebah F.B., *Mater. Res. Express* 2019, 7, 012001.
- [15]. Siddeeg S.M., Tahoon M.A., Alsaieri N.S., Shabbir M., Rebah F.B., *Curr. Anal. Chem.*2021, 17, 4–22.
- [16]. Jalees M.I. , *J. Water Sanit. Hyg. Dev.* 2020, 10, 56–65.
- [17]. Batool A., Valiyaveetil S. , *J. Environ. Chem. Eng.* 2021, 9, 104902.
- [18]. Aitbara A., Khelalfa A., Bendaia M., Abrane R., Amrane A., Hazourli S., *Euro Mediterr.J. Environ. Integr.* 2021, 6, 19.
- [19]. Cohen-Tanugi D. and Grossman, J. C. *Nano Lett.*, 2012, 12, 3602.
- [20]. Georgakilas V., Otyepka M., Bourlinos A. B., Chandra V., Kim N., Kemp K. C., Hobza P., Zboril R. , Kim K. S., *Chem. Rev.*, 2012, 112, 6156.
- [21]. Allen M. J., Tung V. C., Kaner R. B., *Chem. Rev.*, 2010, 110, 132.
- [22]. Park S., Ruoff R. S., *Nat. Nanotechnol.*,2009, 4, 217.
- [23]. Huang X., Zeng Z., Fan, Z. Liu J. Zhang H., *Adv. Mater.*, 2012, 24, 5979.
- [24]. Xiang Q., Yu J., Jaroniec M., *Chem. Soc. Rev.*, 2012, 41, 782.
- [25]. Liu Y., Dong X., Chen P., *Chem. Soc. Rev.*, 2012, 41, 2283.



Synthesis of 3- (4-Substituted Phenyl) 2- Chloractamide and Its Some Physical Aspects

Miss. Raibole Shital, Dr. Kolhe S.V*

*Department of Chemistry, Shri Shivaji Arts Commerce and Science College, Akot-444101, Maharashtra, India

ABSTRACT

The work emphasis on the synthesis the starting material amino acetophenone, dissolve in dichloromethane, in ice cold condition .Add potassium carbonate with stirring after complete addition chlorocetyl chloride was added drop-wise so that temp of reaction set maintained. After complete addition stir the reaction for hrs. at room temperature. Due to presence of pharmacophores hybrid molecule may act on different biological targets which may result in amplification of activity and evaluation of the physical properties like, conductance, viscosity, density, solubility. etc was studied for resulting compounds in different solvents at different concentration.

KEYWORDS:-Pharmacophores hybrid, Chlorocetyl chloride, Viscosity, Density, Solubility. etc

I. INTRODUCTION

Bacteria, viruses, fungi, protozoa, and worms are main pathogenic organisms cause diseases such as hepatitis B and C, malaria, dengue, and tuberculosis¹. The development of antimicrobial drugs based on their modes of mechanism to reduce or prevent resistant pathogens².The problems of medical community could be reduce the risk of diseases caused by pathogenic used effective and low toxic antimicrobials and challenging request a capability of researches to design new antimicrobial drugs ³. In addition, the increasing of fungal infections with limited therapeutic treatment, leads to discover novel antifungal drugs via set new approaches to target the chemical matter⁴.

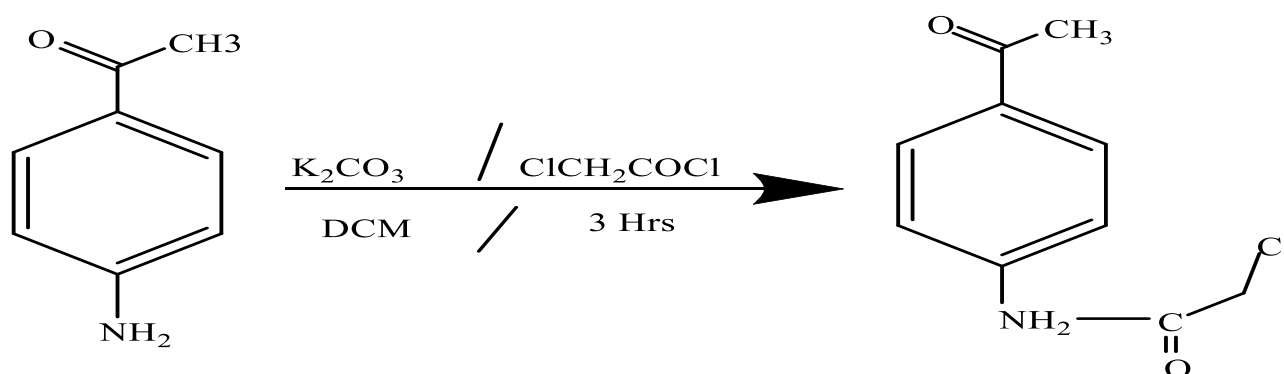
The chalcones and hydantoin are very important pharmacophores, which are present in many biologically active compounds^{5,6}. Synthetic analogues of hydantoin are of great interest in chemical industry due to their versatile applications such as anticonvulsants, in epilepsy treatment, as herbicides, fungicides, antimicrobial, virucidal agents, stabilizers in photographic film, and in the preparation of high temperature epoxy resins ⁷.Therefore, this pharmacophores is of considerable interest both for medicinal and agrochemical industry⁸. Further, hydantoin derivatives have also been used as new drugs for treatment of various diseases, for example, nilutamide, which was approved by the FDA in 1996 as a non-steroidal, orally active antiandrogen in the therapy of metastatic prostate cancer ⁹⁻¹⁰. Chalcone derivatives are also reported to exhibit diverse biological activities¹¹⁻¹⁹.

In order to overcome the problem of drug resistance several approaches such as targeting bacterial virulence, genome hunting, high throughput screening (HTS) structure based discovery and combinatorial chemistry have been explored ²⁰⁻²². A newer concept in the field of drug discovery is a concept of hybrid molecules, whereby two pharmacophores are incorporated in a single molecule to exert dual drug action. Due to presence of two pharmacophores hybrid molecule may act on different biological targets which may result in amplification of activity. The probability of these hybrid molecules to act on different target may help to overcome problem of drug resistance.

II. EXPERIMENTAL METHOD

The melting points will take in open capillary tube; IR spectra will be recorded in Nijol, ¹H NMR spectra were recorded in CDCl₃ with TMS as an internal standard. The purity of a synthesized compound will be check by TLC. The structural elucidation of compound will be done on the basis of chemical and spectral data. The starting Para amino acetophenone, dissolve in dichloromethane, in ice cold condition .Add 0.01m potassium carbonate with stirring after complete addition 0.01m chloroacetyl chloride was added drop-wise so that temp of reaction set maintained. After complete addition stir the reaction for 3hrs. at room temperature .Decomposed the product with acidic ice cold water.

Chemical reaction

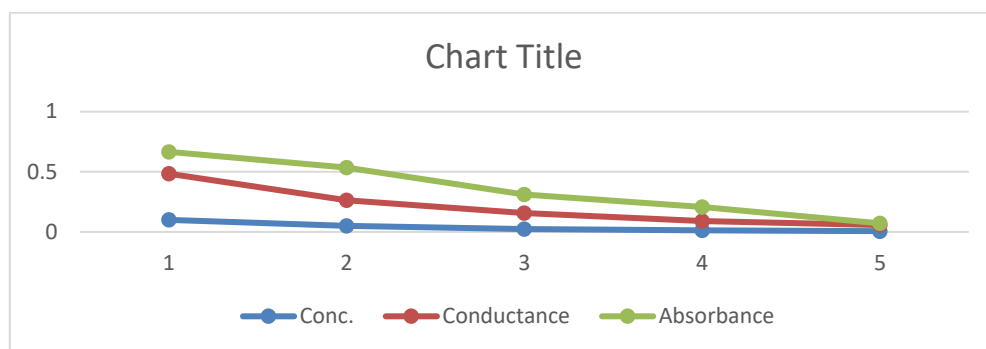


III. RESULTS AND DISCUSSIONS

Physical Aspect of 3-(4-substituted phenyl)-2-chloroacetamide.

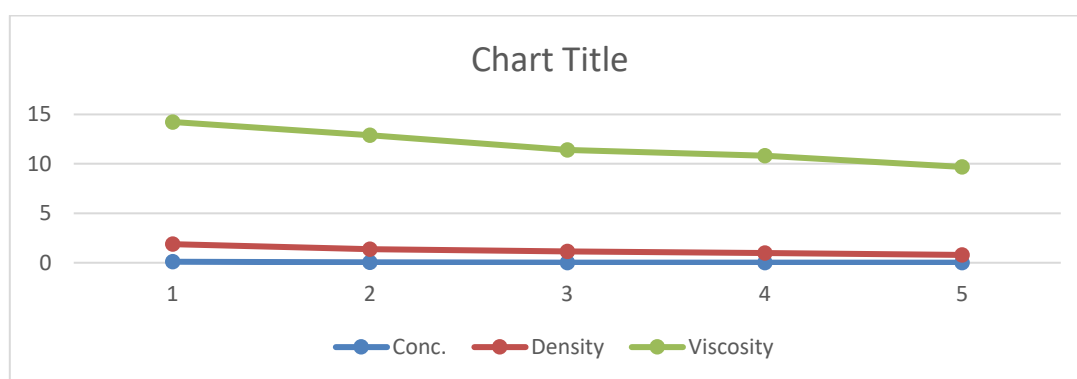
A. Conduction and Absorbance

Sr.	Conc.	Conductance(s/cm ³)	Absorbance
1	0.1	0.384	0.482
2	0.05	0.213	0.272
3	0.025	0.132	0.154
4	0.0125	0.079	0.116
5	0.00625	0.051	0.014



B. Density and viscosity

SR.NO	Conc.	Density (gm/cm ³)	Viscosity (poise)
1	0.1	1.778	12.362
2	0.05	1.334	11.526
3	0.025	1.123	10.263
4	0.0125	0.963	9.856
5	0.00625	0.782	8.902



The concentration of solution decreases with viscosity and conductance decreases due to solute solvent polar interaction.

IV. REFERENCES

- [1]. M.A.El-Sharief, S.Y.Abbas,K.A. El-Bayouki,E.W. El-Gammal, 2011. Synthesis of thiosemicarbazones derived from N-(4-hippuric acid) thiosemicarbazide and different carbonyl compounds as antimicrobial agents. *Eur. J. Med Chem.*, 67, 263-268.
- [2]. D.K.Aneja, P. Lohan, S. Arora, C. Sharma, K.R. Aneja, O. Prakash, 2011. Synthesis of new pyrazolyl-2, 4- thiazolidinediones as antibacterial and antifungal agents. *Bioorg. Med.Chem. Lett.* 1- 15.
- [3]. J.Rai, G.K Randhawa, M Kaur, 2011. Recent advances in antibacterial drugs. *Int J Appl Basic Med Res.* 3(1), 3-10.

- [4]. T.Roemer, D.J. Krysan, 2014. Antifungal drug development: challenges, unmet clinical needs, and new approaches. *Cold Spring HarbPerspect Med.* 4(5), a019703.
- [5]. K. Lavrador, D. Guillerm and G. Guillerm, *Bioorg. Med. Chem. Lett.*, 1998, 8, 1629.
- [6]. F. Tellier, F. Acher, I. Brabet, J.-P. Pin and R. Azerad, *Bioorg. Med. Chem.*, 1998, 6, 195.
- [7]. C. Syldatk, R. Muller, M. Pietzsch and F. Wagner, *Microbial and enzymaticproduction of L-amino acids from DL-5- monosubstitutedhydantoin*s, in J. D. Rozell and F. Wagner (eds.), *Biocatalytic Production of Amino Acids and Derivatives*, Hanser Publishers, New York, 1992, 131.
- [8]. W. B. Yeh, M. J. Lin, M. J. Lee and C. M. Sun, *Mol. Divers.*, 2003, 7, 185.
- [9]. Ware, Elinor (1950). *The Chemistry of the Hydantoin*s. *Chem. Rev.* 46 (3): 403–470.
- [10]. Urech, Friedrich (1873). *UeberLacturaminsäure und Lactylharnstoff*. *Liebigs Ann.* (M. Lamothe, M. Lannuzel and M. Perez, *J. Comb. ChemJ. Anderson, BJU Int.*, 2003, 91, 455.
- [11]. Y. B. Vibhute and M. A Basser, *Indian J. Chem., Sect. B*, 2003, 42, 202.
- [12]. B. A. Bhat, K. L. Dhar, A. K. Saxena and M. Shanmugavel, *Bioorg. Med. Chem.*, 2005, 15, 3177.
- [13]. L. E. Michael, M. S. David and S. S. Prasad, *J. Med. Chem.*, 1990, 33, 1948.
- [14]. R. Kalirajan, M. Palanivelu, V. Rajamanickam, G. Vinothapooshan and K. Andarajagopal, *Int. J. Chem. Sci.*, 2007, 5, 73.
- [15]. R. H. Udipi, R. Bhat and K. Krishna, *Heterocycl. Chem.*, 1998, 8, 143.
- [16]. P. Alka and V. K. Saxena, *Indian J. Chem., Sect. B*, 1987, 26, 390.
- [17]. G. Urmila, S. Vineeta, K. Vineeta and C. Sanjana, *Indian J. Heterocycl. Chem.*, 2005, 14, 265.
- [18]. V. K. Pandey, V. D. Gupta and D. N. Tiwari, *Indian J. Heterocycl. Chem.*, 2004, 13, 399.
- [19]. R. O. Clinton, A. J. Manson, F. W. Stonner, A. L. Beyler, G. O. Potts and A. Arnold, *J. Am. Chem. Soc.*, 1959, 81, 1513.
- [20]. Y. M. Lee, F. Almqvist and S. J. Hultgren, *Curr. Opin. Pharmacol.*, 2003, 3, 513.
- [21]. R. Bax, N. Mullan and J. Verhoef, *Int. J. Antimicrob. Agents*, 2000, 16, 51.
- [22]. I. Chopra, J. Hodgson, B. Metcalf and G. Poste, *J.A.M.A.*, 1996, 275, 401.



Synthesis and Characterization of Copper Oxide (CuO) Doped Conducting Polymer Polyaniline

M. N.Pawar¹, D.R. BIjwe¹, A.V. Rajgure¹, P.S. Deole², S. Kavitkar², M.S.Khandekar²

¹Department of Physics, G.S.Tompe Arts, Commerce & Science College, Chadur Bazar, Dist Amravati 444704, Maharashtra, India

²Department of Physics, Maharashtra Udayagiri Mahavidyalaya, Udgir, Tal-Udgir, Dist-Latur-413517, Maharashtra, India

ABSTRACT

In this present paper, Nano crystalline and bulk CuO are prepared by thermal decomposition of freshly prepared Cu(OH)₂. The PANi-CuO samples are prepared with 10 and 35 wt%. The structural changes of prepared composite materials were carried out by X-ray diffraction (XRD) tool.

Keyword:-PANI, CuO, XRD

I. INTRODUCTION

Rapid development of industrialization need to stable, low cost ecofriendly effective battery. Day to Day Advance in technology leads to the need of energy storage systems of eco-friendly nature with fast charging and discharging time[1-3]. Nanotechnology is wide progressing to produce growing media with public interest since from the past decade which has broad application in many research areas, development and industrial application. The electrical conductivity of the PANi can be modified by the process of doping with suitable metal oxide. The CuO nanoparticles are the primary dopants which vary the structural, magnetic, optical and/or electronic properties of the PANi and it is accompanied by large increase in conductivity[4-5]. Nanoparticles of copper oxide exhibit the nature of a semiconductor with a band gap of 1.5 to 1.8 eV with their application in photo detectors, solar cells, gas sensors, biosensors, super capacitors, removal of organic, magnetic storage media etc8.

In this research work, Copper oxide nanoparticles were prepared by ecofriendly low temperature solution Co-pracipated synthesis and the polyaniline- CuO Nano Composites of doping concentrations (10,35wt%) were synthesized . The samples were characterized by XRD, studies and specific surface area.

II. EXPERIMENTAL

2.1 Synthesis of Polyaniline (PAni):

The analytical grade 0.2M aniline hydrochloride and 0.25 M ammonium peroxydisulfate were used as precursors. Aniline hydrochloride was dissolved in distilled water to form a transparent solution; ammonium peroxydisulfate was added drop-wise to the solution under continuous stirring until pH becomes around 8. The precipitate obtained was washed with distilled water for several times to remove chlorine ions. It was further dried at 60°C for 2 h in air to obtain fine Nanocrystalline powder.

2.2 Synthesis of CuO Nano Composite

CuO nanoparticles are synthesized by Co-precipitation method using copper (II) acetate [$\text{Cu}(\text{CH}_3\text{COO})_2 \cdot \text{H}_2\text{O}$] and Ammonia (NH_3). In short, 0.2 M copper (II) acetate solutions (100 ml) and Ammonia were added drop wise to maintained pH in a round-bottom flask and under magnetic stirrer. The colour of the solution turned from blue to black instantaneously and a black suspension formed simultaneously. The reaction was carried out under stirring and boiling for 3 hr. The mixture was cooled to room temperature wet CuO precipitate was obtained. The precipitate was filtered and washed with distilled water for several times. The resulting product was dried at 60°C for 2 hr to obtain the dry powder of CuO Nano Composite. Similarly 10wt% & 35Wt% PAni doped CuO Nano Composite was obtained. The X-ray Diffraction Study was carried out using X-ray diffractometer in the 2θ range from 10° to 80°.

III. RESULTS AND DISCUSSION

3.1 XRD analysis

X-ray diffraction (XRD) method is used for materials characterization as it provides important information about the internal structure of matter such as crystallite size and crystal structure. All patterns exhibit peaks corresponding to the rutile structure of polycrystalline CuO with the maximum intensity peak corresponding to (110) plane [6]. It was observed that the relative intensities of all the peaks reduce with an increase in PAni Content. It was also observed that the peak broadening takes place with the increasing PAni content which is in good agreement with the earlier studies [7-9]. The increase in FWHM along with the reduction in peak intensity suggests that PAni incorporation into CuO lattice results in lowering of crystallite size of CuO. The Pure PAni shows larger voids Fig. 3(a) as compared to doped samples which have smaller uniformly distributed voids in Fig. 3(b and c).

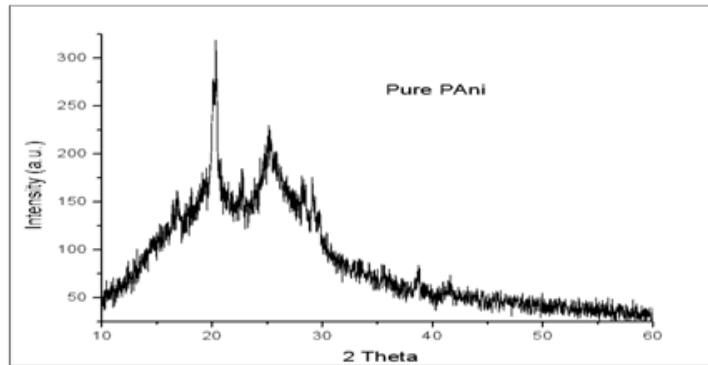


Fig. 1(a) XRD of Pure Polyaniline(PAni)

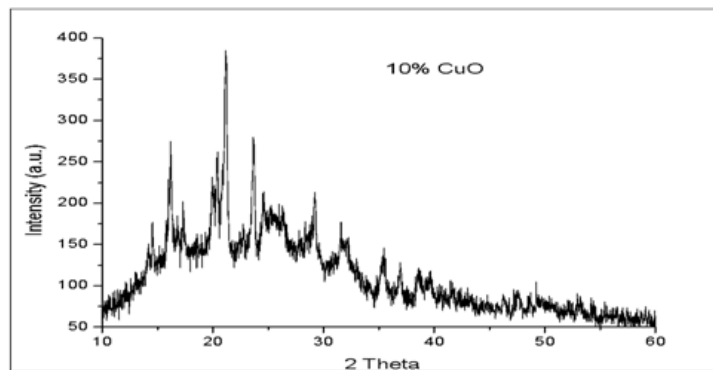


Fig.1(b)XRD of 10wt%CuO-PAni Nano Composite

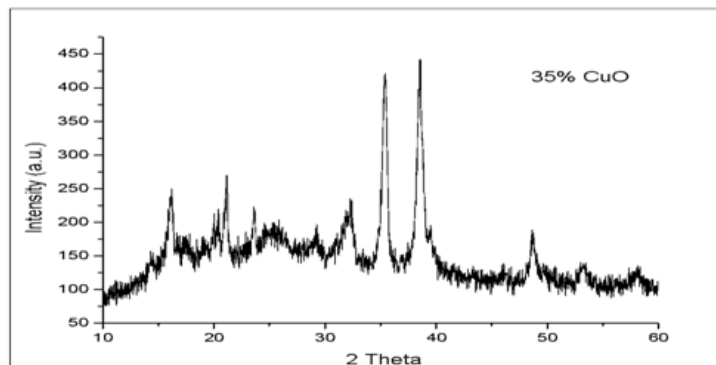


Fig.1(c)XRD of 35wt%CuO-PAni Nano Composite

IV. CONCLUSION

The study of the pure PANi and (10 & 35wt%) PANi doped CuO polyaniline increases due to addition of PANi wt %. The 35wt% PANi nano composite plays the important role in the contribution Surface modification.

V. REFERENCES

- [1]. Sexena, V, Malhotra, B D, Curr. Appl. Phys., 3, 293-305 (2003)

- [2]. M. Chang, H. Liu and C.Y. Tai (2011) Powder Technology 207, 378–386.
- [3]. Chaudhari, S, Mandate, AB, Patil, KR, Sainkar, SR, Patil, PP, J. Appl. Polym. Sci., 106,220-229 (2007)
- [4]. Gupta K, Jana P C, Meikap A K., Synthetic Metals 160 (2010) 1566-1573.
- [5]. Mathai C J, Saravanan S, Anantharaman M R, Venkitachalam S, Jayalekshmi S., J. Phys. D: Appl. Phys., 35 (2002) 240
- [6]. Amnerkar R H, Adgaonkar C S, Yawale S S, Yawale S P., Bull. Mater. Sci. 25 (2002) 431-434
- [7]. Lanje, A.S., Sharma, S.J., Pode, R.B., Ningthoujam, R.S., Advances in Applied Science Research, 1 (2) 36-40, (2010)
- [8]. A. B. Kaiser, C. K. Subramaniam, P. W. Gilberd and B. Wessling, Synth. Met., 69, 197 (1995).
- [9]. Mittal, H., Kaith B., Jindal R, Advances in Applied Science Research, 1 (3) 56-66, (2010)



To Study the Potency Of Newly Synthesized Substituted Thiocarbamidonaphthol by Conductometrically

Saleem Khan R.Khan, D.T.Tayade

Department of Chemistry, Government Vidarbha Institute of Science and Humanities, Amravati -444 604, Maharashtra, India

ABSTRACT

To foster more intensity drugs since microorganisms become more dynamic than past one. Numerous physicist and scientists has gotten an extraordinary consideration in the perspective on human powerlessness and insurance of conditions. According to the need of this age they combined many mixtures and particles and prime to evaluate their meanings and applications in different fields. Conductometric concentrate on got more qualities. Conductometric examination fostered an interconnecting join in the middle to substance science and life sciences. Consider above reality as a top priority present examination plot planned as to concentrate on the strength of 5-phenylthiocarbamido-1-naphthol at blended dissolvable media. In which decided the conductometric boundaries and thermodynamics boundaries of 5-phenylthiocarbamido-1-naphthol at various fixations and 310 K in 60% ethanol-water combination. Present work assists with understanding various associations like solute-dissolvable connection, solute cooperation, solute dissolvable collaboration and solute-dissolvable communication that are utilized in present work. This study assists with figuring out Pharmacodynamics of the recently integrated atoms.

KEYWORDS: 5-Phenylthiocarbamido-1-naphthol, conductometric parameters, thermodynamic parameters and conductometric study.

I. INTRODUCTION

Portability of particles in electrolytic arrangement is known as conductivity. As medications action perspective versatility of particles got more qualities since it worries to the conductivity particle in arrangement that additionally assists with figuring out the separation of solute in dissolvable. Separation of solute additionally called as ionization of solute that impact the portability and bioavailability of solute particles. Conductivity of medication assists with understanding the pharmacodynamics of medication. Versatility of particles is additionally treated as transmission of particles. Ionic transmissions of electrolyte in electrolytic arrangement firmly impact on solvency and penetrability of medications proficiently Shuiqin Li et al¹ reported green synthesis of gold nanoparticles using aqueous extract of Mentha Longifolia leaf and investigation of its anti-human breast carcinoma properties in the in vitro condition. Shengmei Chen et al² carried out Ziziphoraclinopodioides Lam leaf aqueous extract mediated novel green synthesis of iron

nanoparticles and its anti-hemolytic anemia potential: A chemobiological study. Elsayed M. AbouElleef et al³ studied Conductometric Association Parameters for Cd Br in the Presence and Absence of Ceftazidime in Water and 30% Ethanol–Water Mixtures. BingxiFenget al⁴ studied Self-template synthesis of spherical mesoporous tin dioxide from tin-polyphenol-formaldehyde polymers for conductometric ethanol gas sensing. ReemAlzahrani et al⁵ carried out Synthesis and characterization for new Mn(II) complexes conductometry, DFT, antioxidant activity via enhancing superoxide dismutase enzymes that confirmed by in-silico and in-vitro ways. GhenadiiKorotcenkov et al⁶ reported their Electrospun Metal Oxide Nanofibers and Their Conductometric Gas Sensor Application, in Nanofibers and Features of their Forming. ArwaAlharbiet al⁷ carried out Studies on new Schiff base complexes synthesized from d¹⁰metal ions: Spectral, conductometric measurements, DFT and docking simulation. Dafne Musino et al⁸ studied Hydroxyl groups on cellulose nanocrystal surfaces form nucleation points for silver nanoparticles of varying shapes and sizes. K.V. Stepurska et al⁹ carried out Feasibility of application of conductometric biosensor based on acetylcholinesterase for the inhibitory analysis of toxic compounds of different nature. Ahmad I. Ayesh et al¹⁰ studied Conductometric graphene sensors decorated with nanoclusters for selective detection of Hg traces in water. PheerayaJaikang et al¹¹ reported their Conductometric determination of ammonium ion with a mobile drop. AgnieszkaChylewska et al¹² studied Spectrophotometric, potentiometric, and conductometric studies of binary complex formation between copper(II) and three forms of vitamin B6 in aqueous solutions. Considering these above realities present exploration work intended to assurance of thermodynamic boundaries (viz. ΔH ; ΔS and ΔG) and conductometric boundaries of 5-phenylthiocarbamido-1-naphthol conductometrically at various focuses and 310 K in 60% ethanol-water blend. This review assists with understanding the different bury and intra-atomic communication like dissolvable, solute-dissolvable and solute-dissolvable associations. That data assists with understanding the pharmacodynamics of recently blend particle.

II. MATERIALS AND EXPERIMENTAL METHODS

Newly pre-arranged arrangements are utilized through current work. All AR grade synthetics are utilized through present examination. The solvents were decontaminated by standard strategy before utilized. To arranged 0.01M, 0.005M, 0.0025M and 0.0012M convergences of 5-phenyl thiocarbamido-1-naphthol 60% ethanol-water blend. Warm balance kept up with at temperatures 310 K) of medications arrangement by utilizing indoor regulator individually. Conductivity estimated for every focus arrangement in the wake of getting warm balance.

III. RESULT AND DISCUSSION

Arranged the arrangement of 0.01 M grouping of 5 phenylthiocarbamido-1-naphthol then by utilizing sequential weakening strategy arranged arrangements of 0.005M, 0.0025M and 0.0012M with 60% ethanol-water combination separately. To estimated conductance for every arrangement by utilizing Conductivity

Bridge at 310 K. The got result classified in given in Table-1 and Table-2. Noticed conductance (G), explicit conductance (k) and molar conductance (μ) were analyzed with helps of known writing technique from resultant information

TABLE – 1 - CONDUCTOMETRIC MEASUREMENTS AT DIFFERENT CONCENTRATIONS OF 5-PHENYLTHIOCARBAMIDO-1-NAPHTHOL				
DETERMINATION OF G, k and μ AT DIFFERENT CONCENTRATIONS AND DIFFERENT TEMPERATURES IN 60% E-W MIXTURE				
Temp	Concentration C (M)	Observed conductance (G) mS	Specific conductance (k) mSm ⁻¹	Molar conductance (μ) mSm ² mol ⁻¹
310 K	0.01	0.04608	0.0023084 X10 ⁻³	0.23084
	0.005	0.03502	0.031848 X10 ⁻³	0.63696
	0.0025	0.03064	0.021365 X10 ⁻³	0.8546
	0.0012	0.02912	0.021147X10 ⁻³	0.17622

Noticed conductance (G), explicit conductance (k) diminishes and molar conductance (μ) values are arranged in Table 1. Here G, k and μ increments alongside diminishing fixations and G, k and μ increments alongside expanding temperatures. The particular conductance increments with expanding temperature. Determined values the particular steady (Ksp), log (Ksp) and thermodynamic boundaries viz. (ΔG), (ΔS) and (ΔH) of 5-phenylthiocarbamido-1-naphthol by known writing techniques at various fixation with various temperatures. Gotten outcome figured in Table 2.

TABLE – 2 - CONDUCTOMETRIC MEASUREMENTS AT DIFFERENT CONCENTRATION AND DIFFERENTS TEMPERATURES OF 5-PHENYLTHIOCARBAMIDO-1-NAPHTHOL						
DETERMINATION OF Ksp, log Ksp, ΔG , ΔH and ΔS AT DIFFERENT CONCENTRATIONS AND DIFFERENT TEMPERATURES						
SYSTEM: L ₂ [PTCN]			MEDIUM - 60% Ethanol-Water Mixture			
Temp.(K)	Conc. M	Ksp	Log Ksp	ΔG kJmlo ⁻¹	ΔH kJmlo ⁻¹	ΔS kJK ⁻¹ mlo ⁻¹
310 K	0.01	0.05595	-4.58701	-2705092	-88357.6	377.639
	0.005	0.03930	-5.03159	-29672.75	-96920.5	413.007
	0.0025	0.03507	-5.29433	-31224.52	-101989	435.5
	0.0012	0.033584	-5.44574	-32115.3	-104898	447.837

IV. CONCLUSION

From above table - 1 and 2 it is reasoned that the variety in molar fixations firmly connected with conductometric and thermodynamic boundaries upsides of 5-phenylthiocarbamido-1-naphthol.As noticed,

the μ values increment with diminishing in focus that shows less solvation or higher portability of particles. This is because of the way that more prominent bond breaking because of weakening. Additionally regrettable upsides of ΔG showed the response is unconstrained. Negative upsides of enthalpy change (ΔH) recommended the response is exothermic. Good at lower temperature and positive worth of (ΔS) delights entropically great. The adjustment of thermodynamic boundaries esteems firmly impacted by molar fixations and rate pieces. Additionally solute (drug)- dissolvable collaborations, dissolvable connections, dissolvable solute associations and - solute-dissolvable communications significantly impact on these boundaries. Interior calculation as well as inward and intra hydrogen holding are likewise answerable for the variety of these boundaries.

V. REFERENCES

- [1]. Shuiqin Li, Fahad A. Al-Misned , Hamed A. El-Serehy , Linlin Yang, Arabian Journal of Chemistry, 2021, 14, 102931.
- [2]. ShengmeiChen, Ailing Fang , Yanfa Zhong , Jin Tang, Arabian Journal of Chemistry, 2022,15, 103561.
- [3]. Elsayed M. AbouElleef, Mahmoud N. Abd El-Hady, Esam A. Gomaa, Anwer G. Al-Harazie, Journal of Chemistry Engineering Data, 2021,2, 66, 878–889.
- [4]. BingxiFeng ,Youyou Feng , Jing Qin , Zheng Wang , Yalong Zhang , Fei Du , Yongxi Zhao, Jing Wei, Sensors & Actuators: B. Chemical,2021 , 341, 129965,.
- [5]. Reem Alzahrani ,IsmailAlthagafi ,AmerahAlsoliemy ,KhloodS.Abou-Melha ,Abdulmajeed F.Alrefaei ,GaberA.M.Mersal ,Nashwa El-Metwaly, Journal of Molecular Structure, 2021, 1243,130855.
- [6]. GhenadiiKorotcenkov, Nanomaterials, 2021,11, 1544.
- [7]. Arwa Alharbi ,SerajAlzahrani ,FatmahAlkhatib ,Khulood Abu Al-Ola ,Alia AbdulazizAlfi,RaniaZaky ,Nashwa M.El-Metwaly, Journal of Molecular Liquids, 2021,334, 116148.
- [8]. Dafne Musino ,CamilleRivard ,Gautier Landrot ,Bruno Novales ,Thierry Rabilloud Isabelle Capron, Journal of Colloid and Interface Science, 2021, Volume 584, 360-371.
- [9]. K.V. Stepurska, Soldatki, I.S. Kucherenko, V.M. Arkhypova ,S.V. Dzyadevych, A.P. Soldatkin, Analytica Chimica Acta, 2015,854, 161–168.
- [10]. Ahmad I. Ayesh ,Zainab Karam ,Falah Awwad ,Mohammed A. Meetani, Sensors and Actuators B: Chemical, 2015, Volume 221, 201-206.
- [11]. PheerayaJaikang ,KateGrudpan ,TinakornKanyanee, Talanta, 2015,Volume 132, 884-888.
- [12]. Agnieszka Chylewska, MałgorzataOgryzek, Lech Chmurzyński , Mariusz Makowski, Journal of Coordination Chemistry, 2015, Vol. 68, No. 21, 3761–3775.



pH Metric Studies of Some Substituted 2-Oxo-2H-Chromene-3-Carbohydrazide Derivatives at 0.1 M Ionic Strength at 52oC

P. P. Choudhari^{*1}, P. R. Yawale², S. S. Ubarhande², M. P. Wadekar²

^{*1}G. S. Tompe Arts, Commerce and Science College, Chandur Bazar, Amravati, Maharashtra, India

²Government Vidarbha Institute of Science and Humanities, Amravati, Maharashtra, India

ABSTRACT

Stability Constant are determined for complex formation of substituted 2-oxo-2H-chromene-3-carbohydrazide derivatives with metal ions Fe(III), Mn(II), and Cr(III). The present study involves pH metric study of substituted 2-oxo-2H-chromene-3-carbohydrazide derivatives with metal ions Fe(III), Mn(II), and Cr(III) at constant ionic strength (0.1M) in 70 % DMF-water mixture at temperature 52oC. Bjerrum and Calvin's method as adapted by Irving and Rossotti is used for calculations of $n\bar{A}$ and $n\bar{}$.

Keywords: Substituted 2-oxo-2H-chromene-3-carbohydrazide derivatives with metal ions Fe(III), Mn(II), and Cr(III), metal-ligand stability constant (logK) and proton-ligand stability constant (pK).

I. INTRODUCTION

Stability of complexes is express in terms of formation constant. Temperature plays crucial role in complex formation reaction. It affects on metal-ligand stability constant (logK) and proton-ligand stability constant (pK). The magnitude of formation constant is the direct reflection of the sign and magnitude of Gibbs energy of formation of complex . This factor can be understood by considering following well known relationship . Stability constant of complex of O-(N- α -oxindolimino) benzoic acid and O-(N- α -oxindolimino) propanoic acid with lanthanum(III) metal ions at different temperature is reported . The complexes of Ca(II), Mg(II) and Zn(II) with amino acid phenylalanine (phe) in ethylene glycol-water mixture have studied . The complex formation between Cu, Cd, Co, Ni, Pb and Zn metal ion with benzaldehydethiosemicarbazone and pyridine 2-carbaldehyde in 50% dioxane-water are studied . Measurement of step-wise stability constant of mixed ligands complexes of Th(IV), Pr(III) and Yb(III) metal ions with 3-(acetophenonehydrazone)-6-phenylpyridazine,3(p-hloroacetophenhydrazone)-6-henylpyridazine and amino acetophenone hydrazone-6-phenylpyridazinebypotentiometry in 75% dioxane-water mixture is reported . The metal ligand stability constant of transition metals and substituted pyrazoles have reported by many workers . The metal ligand stability constant of some β -diketones are reported . Stability constants have investigated for some substituted pyrazolines, isoxalline and diketone . The mixed ligand complex compounds of alkaline earth metals Mg(II), Ca(II), Sr(II) and Ba(II) with 5-nitrosalicyladehyde and β -diketones are reported . Metal ligand stability constant is determined for lanthanide metal ions with substituted schiff's bases at 0.1M ionic strength by pH

metric method . Various experimental methods are used to determine composition and stability constants of complexes. These are potentiometry , pH-metry , polarographic , UV-VIS spectrophotometry , paper electrophoretic technique , electroanalytical method , fluorescence quenching titration , gel chromatography , spectrophotometrically ,

The present study involves pH metric study of substituted 2-oxo-2H-chromene-3-carbohydrazide derivatives with metal ions Fe(III), Mn(II), and Cr(III) at constant ionic strength (0.1M) in 70 % DMF-water mixture at temperature 52oC. Bjerrum and Calvin's method as adapted by Irving and Rossotti is used for calculations of n and n^- .

II. METHODS AND MATERIAL

Metal Ions and Ligands

The following metal ions and ligands are used in present study.

a) **Metal Ions** Following metals in the form of their salts are used for complexing with chelating agents (Ligands): 1. Fe(III) 2. Mn(II) 3. Cr(III)

b) **Ligands** In the present work, following substituted coumarines have synthesized by standard method Following substituted-2-oxo-2H-chromene-3-carbohydrazide derivatives are used as chelating agents (Ligands).

Ligand (LA) = N-[(E)-1-(5-bromo-2-hydroxy-phenyl)ethylideneamino]-2-oxo- chromene-3-carboxamide

Ligand (LB) = N-[(E)-1-(5-chloro-2-hydroxy-phenyl)ethylideneamino]-2-oxo- chromene-3-carboxamide

Bjerrum's original titration method is modified by Calvin and Wilson for determining the stability constants of metal complexes in mixed aqueous solution. This Bjerrum-Calvin titration technique as modified by Irving and Rossotti has employed in the present study.

The following three sets of titrations are carried out in sequence.

- i) Acid titration: Nitric acid (1.00×10^{-2} M)
- ii) Ligand titration: Nitric acid (1.00×10^{-2} M) and ligand (20.00×10^{-4} M)
- iii) Metal titration: Nitric acid (1.00×10^{-2} M), the ligand (20.00×10^{-4} M) and the metal salt (4.00×10^{-4} M) against standard 0.1N sodium hydroxide solution.

All the titrations are carried out in 70% DMF-water mixture and the reading are recorded for each 0.2 ml addition of alkali. Titrations are carried out in inert atmosphere by bubbling nitrogen gas. Ionic strength of solution is maintained constant at 0.1M by adding an appropriate amount of 1M KNO₃ solution.

Calculation of \bar{n} , \bar{n}^- and pK

The experimental data obtained from titration curves is useful in calculation of \bar{n} , \bar{n}^- and pK by applying following relationships:

Proton ligand formation number (\bar{n}) for different pH values are obtained from expression:

$$\bar{n}^- = (\text{total concentration of proton bound to ligand}) / (\text{total concentration of ligand not bound to metal})$$

$$\bar{n}^- = y - (V_2 - V_1) (N + E^{\circ}) / ((V_o + V_1) T_L)$$

Where V_0 is the initial volume of the solution, E_0 and T_L are the total concentrations of the mineral acid and ligand respectively, V_1 and V_2 are the volumes of alkali of given normality required during the acid titration and acid + ligand titration respectively at given pH, y is the number of replaceable hydrogen ions and N is the normality of NaOH solution.

The metal ligand formation number (α_n) is calculated from the following expression

$$\alpha_n = (\text{total concentration of ligand bound to metal}) / (\text{total concentration of metal})$$

$$\alpha_n = (V_3 - V_2)(N + E^0) / ((V_0 + V_2) \alpha_A - T_M)$$

The values of α_n are calculated by Irving Rossotti's expression

$$\alpha_n = y - (V_2 - V_1)(N + E^0) / ((V_0 + V_1) T_L)$$

Where V_0 is the initial volume of solution, E_0 and T_L are initial concentrations of mineral acid and ligand respectively, V_1 and V_2 volumes of alkali required during acid and ligand titration at given pH, y is the no. of replaceable protons from the ligand.

The difference ($V_2 - V_1$) is estimated from the plot between volume of NaOH and pH of solution. The values of α_n calculated along with the values of ($V_2 - V_1$) at various pH are presented in tables 6 to 9.

a) Half Integral Method

The graphs are plotted between α_n vs pH and the values of $\log K_1$ and $\log K_2$ are determined. The values of $\log K_1$ and $\log K_2$ are determined from the formation curves by knowing the values of pH at which $\alpha_n = 0.5$ and $\alpha_n = 1.5$ respectively.

b) Pointwise Calculations Method

For value of $\alpha_n < 1.0$, metal ligand stability constants for 1:1 complex formations are calculated by using .

$$\log \frac{\alpha_n}{(1 - \alpha_n)} = \log K_1 - pH$$

For value in the region $1 < \alpha_n < 2$, metal ligand stability constants for 1:2 complex are calculated by using equation.

$$\log \left(\frac{\alpha_n - 1}{2 - \alpha_n} \right) = \log K_2 - pH$$

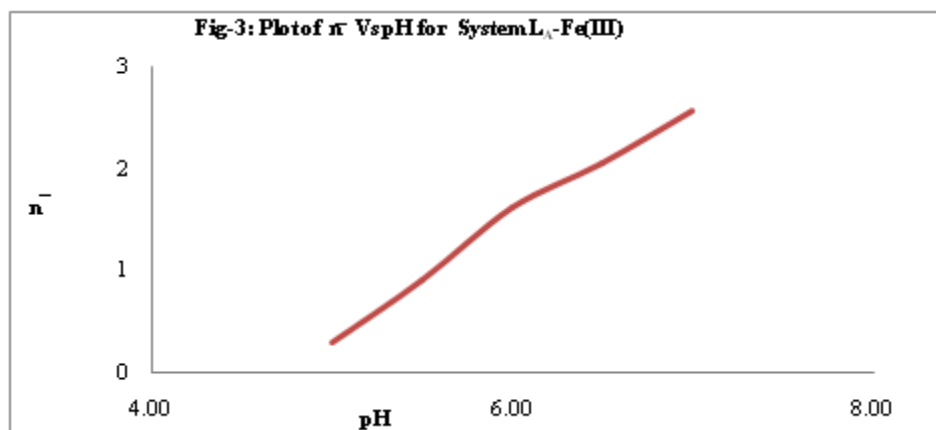
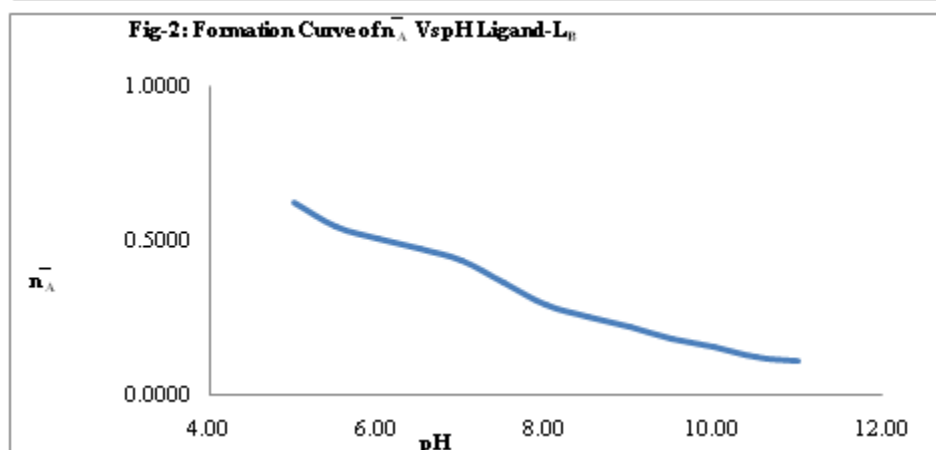
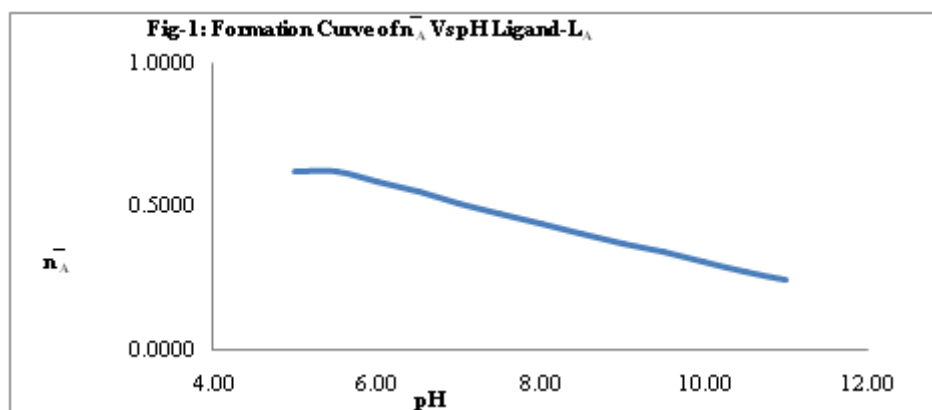
The values of $\log K_1$ and $\log K_2$ are shown in table no. 32. The values of $\log K$ calculated by point wise calculation methods are in good agreement with the values obtained by the half integral method.

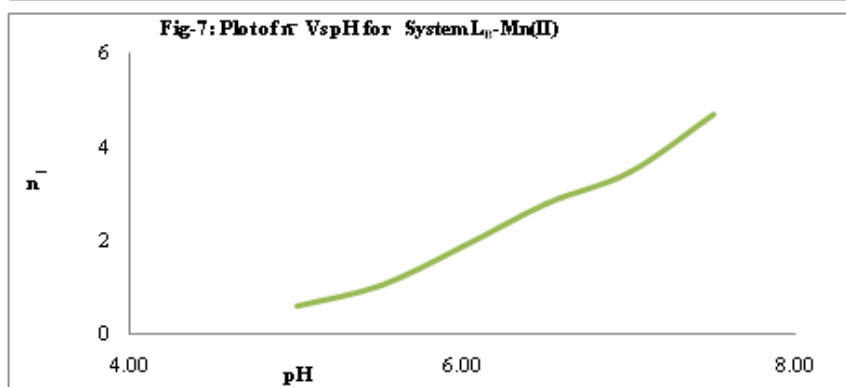
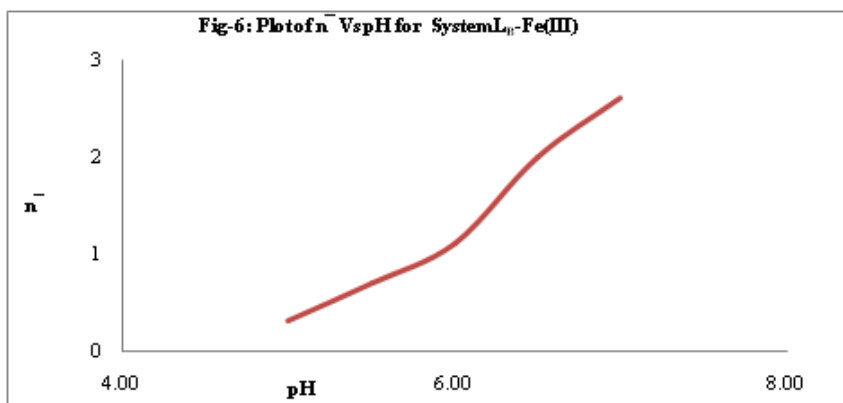
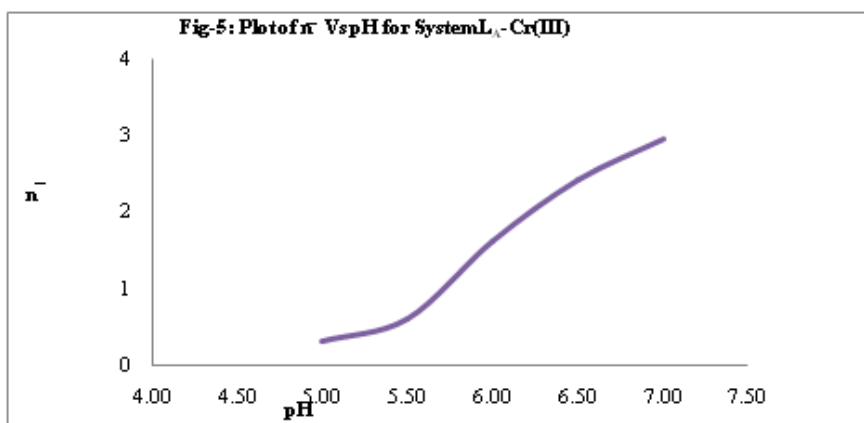
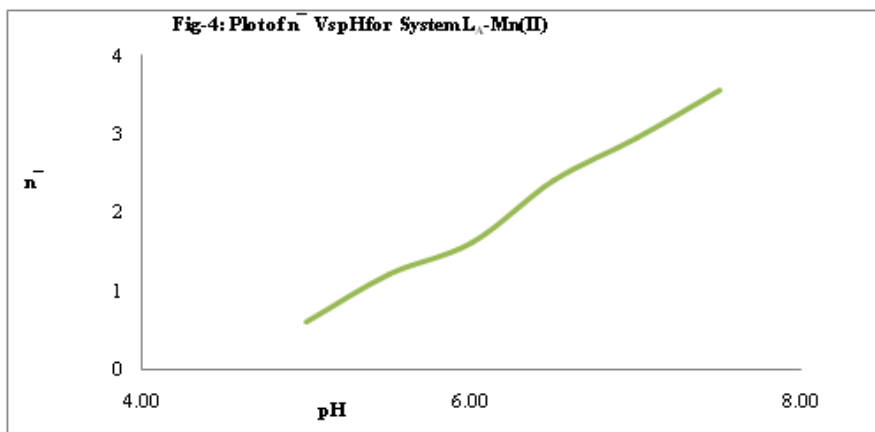
III. RESULT AND DISCUSSION

The ratio $\log K_1 / \log K_2$ give very crucial information about the complex. If the ratio is less than 1.5 then simultaneous complex formation takes place. If this ratio is greater than 1.5 then stepwise complex formation occurs. In present study it is smaller than 1.5 in all cases, indicating simultaneous complex formation. The difference between $\log K_1 - \log K_2$ is usually positive . If the difference between $\log K_1$ and $\log K_2$ is less than 2.5, simultaneous formation of 1:1 and 1:2 complex takes place and if it is more than 2.5 then stepwise complex formation occurs . In the present case, in all the systems it is less than 2.5. This indicates simultaneous formation of 1:1 and 1:2 complexes. Thus difference and ratio factors give same result.

IV. CONCLUSIONS

In the present work the interaction between Substituted 2-oxo-2H-chromene-3-carbohydrazide derivatives with metal ions Fe(III), Mn(II), Cr(III) and Ti(III) at temperature 52oC is determined by pH metric. From it is observed that there is formation of complex. In this two method, half integral and point wise calculation method gives same result. The values of metal–ligand stability constants for all the systems indicate that complex formed in these processes are stable.





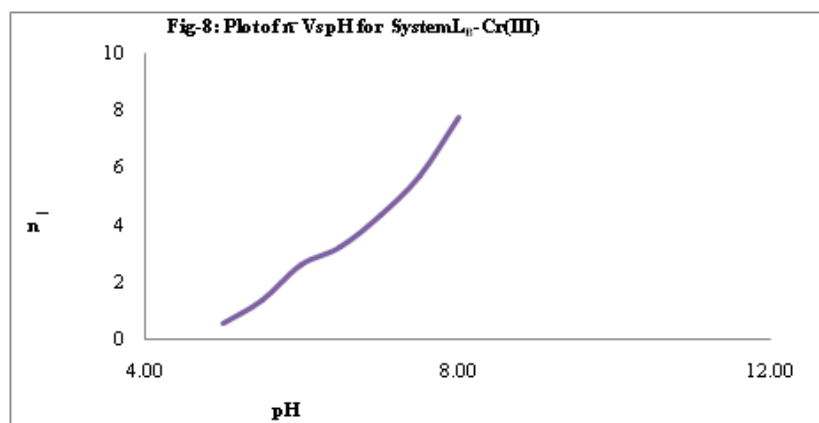


Table – 1pK Values of Various Ligands

Temp. = 52 ± 0.1°C

 $\mu = 0.1$ M

Ligands	pK (Half Integral Method)	pK (Pointwise Calculation Method)
L _A	7.10	7.23
L _B	6.25	7.03

Table –2 Data of logK₁ and logK₂, Difference and Ratio between them at 52°C

Ligand	Metal	logK ₁	logK ₂	logK ₁ /logK ₂	logK ₁ -logK ₂
L _A	Fe(III)	4.7347	3.9538	1.1975	0.7809
	Mn(II)	4.7447	4.1438	1.1450	0.6009
	Cr(III)	4.6247	4.0038	1.1550	0.6209
L _B	Fe(III)	3.7947	3.2038	1.1844	0.5909
	Mn(II)	3.8947	3.3538	1.1612	0.5409
	Cr(III)	3.9147	3.5838	1.0923	0.3309

Table-3

Ligand	Metal	Half integral method	Pointwise calculation method
		logK	logK
L _A	Fe(III)	4.7347	4.8447
	Mn(II)	4.7447	4.9147
	Cr(III)	4.6247	4.7847
L _B	Fe(III)	3.7947	3.8547
	Mn(II)	3.8947	4.0047
	Cr(III)	3.9147	4.0147

V. REFERENCES

- [1]. a) Shriver D F, Atkin P W, Inorganic Chemistry, 3rd Edition, Oxford University Press, Oxford, (2002), 242; b) Manku G S, Theoretical Principles of Inorganic Chemistry, Tata McGraw- Hill, Delhi, (2006), 505.
- [2]. Sarkar K, Garg B S, *Thermochim. Acta*, 113, (1987), 07.
- [3]. Jain L, Jangid S, Singh H, Mehta N R K, *J. Indian Inst. Sci.*, 72, (1992), 495.
- [4]. Sreevaram T, Kumar N V, Sailaja B V, *Int. J. Aca. Res.*, 3(1), (2016), 107.
- [5]. Mahajan R K, Vora K K, Arora P, Sharma E, Lobana T S, *J. Coord. Chem.*, 63 (7), (2010), 1220.
- [6]. Saleem H S, *Commun. Fac. Sci. Uni. Ank. Seris B.*, 48 (2), (2002), 13.
- [7]. a) Sawalakhe P D, Narwade M L, *J. Indian Chem. Soc.*, 71, (1994), 49; b) Agrawal P B, Burghate A S, Narwade M L, *Orient. J. Chem.* 17(1), (2001), 54.
- [8]. Bodkhe P S, Patil K N, Narwade M L, Doshi A G, *Asian J. Chem.*, 15(3), (2003), 1739.
- [9]. Tekade P V, Patil K N, Narwade M L, *Acta Ciencia Indica*, 31(4), (2005) 287.
- [10]. Prasad R N, Agrawal M, Ratnani R, Sarswal K, *J. Indian Chem. Soc.*, 82, (2005), 137.
- [11]. Thakur S D, Munot K P, Raghuvanshi P B, Tayade D T, *Acta Ciencia Indica*, 30(3), (2010), 425.
- [12]. Zelichowicz N, Gaudyn A, *Chem. Papers*, 45(6), (1991), 735.
- [13]. Wadekar M P, Shirrao A S, Tayade R R, *Adv. Appl. Sci. Res.*, 5(6), (2014), 132.
- [14]. Nezhadali A, Sharifi H, *Engineering*, 2, (2010), 1026.
- [15]. Reková M, Vanura P, Krizova V J, *Int. Chem. J.*, 3, (2009) 26.
- [16]. Tewari B B, *Rev. Soc. Quim. Peru.*, 76(3), (2010), 293.
- [17]. Ernst R, Allen H E, Mancy K H, *Water Res.*, 9, (1975), 969.
- [18]. Ryan D K, Weber J H, *Anal. Chem.*, 54, (1982), 986.
- [19]. Yoza N, *J. Chem. Educ.*, 54(5), (1977), 284.
- [20]. Eldossoki F I, Elseify F A, *J. Chem. Eng. Data*, 55, (2010), 3572.
- [21]. Ramganesha C K, Yadav D, Bodke S, Venkatesh K B, *Indian J. Chem. Sect. B*, 49, (2010), 1151.
- [22]. Bjerrum J, *Metal Ammine Formation in Aqueous Solution*, P. Haase and Son, Copenhagen, (1941).
- [23]. Calvin M, Wilson K W, *J. Am. Chem. Soc.*, 67, (1945), 2003.
- [24]. a) Irving H M, Rossotti H S, *Acta Chem. Scand.*, 10, (1956), 72; b) Seleem H S, Mostafa M, Hanafy F I, *Spectrochim. Acta Part A*, 78, (2011), 1560.
- [25]. Agrawal Y K, Tandon S G, *J. Inorg. Nucl. Chem.*, 36, (1974), 869.
- [26]. Deorankar D S, Deshpande Y H, *Indian J. Chem. Sect. A*, 26, (1987), 68.

Structural Characterisation of Ppy/Rhodamine-B Dye Composites Synthesized by Simple Chemical Oxidation Method

N.S. Dixit¹, M.S. Dixit², S.G. Khobragade³, A.S. Dixit³

¹Department of Chemistry, G.S.Tompe Arts, Commerce & Science college, Chandur Bazar, Amravati, Maharashtra, India

²Jagadamba Mahavidyalaya, Achalpur, Maharashtra, India

³Department of Chemistry, Brijlal Biyani Science College, Amravati-444605, Maharashtra, India

ABSTRACT

In the present research work PPy/ Rhodamine-B dye composites were synthesized by using simple oxidative polymerization method by using ammonium peroxydisulphate as an oxidizing agent with simultaneous doping during the synthesis at 0.00001 and 0.0001M concentration of dopant Rhodamine-B. Structural characterization of synthesized composites was carried out by Mass and NMR spectroscopic analysis. These studies suggest that they exhibit amorphous behavior and change in structure due to insertion of dopant.

Key words: PPy, PPy/Rhodamine-B, APS.

I. INTRODUCTION

Until about 30 years ago all carbon based polymers were rigidly regarded as insulators. The breakthrough happened in year 1977 when somewhat accidentally Alan J. Heeger, Alan G. MacDiarmid and Hideki Shirakawa discovered that plastics that are generally referred to as insulators can under certain circumstances be made to behave like metals. Organic conducting polymers and their composites have become increasingly important for technical applications and the use of organic or inorganic fillers (dopants or composites) can prepare a new polymeric material with interesting combinations of physical mechanical and electrical properties.¹⁻³

Among all organic conducting polymers polypyrrole is one of the most promising materials for multifunctionalised applications. For the commercial use of this conducting polymer, a complete understanding of its properties is necessary. The conducting properties of PPy are not only depend upon nature, concentration and oxidation state of dopant but also on doping level with type and concentration of different types of oxidant used. The properties of the polymers can be modified by adding various concentrations of different types of dopant to their structure.⁴⁻⁶

In this present research work conducting polymer PPy/Rhodamine-B dye composite was synthesized through chemical oxidative polymerization route by using ammonium peroxydisulphate as an oxidant at low temperature. The monomer to oxidant ratio was 1:1M. The concentration of fluorescein was varied from

0.00001-0.0001 M. All the composite samples were characterized through Mass and NMR spectroscopic analysis.

II. EXPERIMENTAL

All the chemicals required in the present work like monomer pyrrole, oxidizing agent, ammonium peroxydisulphate and dopant Rhodamine-B are of A. R. Grade. PPy/Rhodamine-B composites were synthesized by simple chemical oxidative polymerization method. The aqueous solution of 0.1 M Ammonium peroxydisulphate was prepared. To this solution 0.00001 M aqueous solution of dopant was added with constant stirring. After a vigorous stirring at 50°C drop by drop 0.1 M solution of monomer pyrrole was added. The reaction was stirred for few hours on magnetic stirrer which gives rise to formation of precipitate of polymer composite. This reaction mixture was allowed to stand for 24 hours in order to complete polymerization process. The resulting product was vacuum filtered. The precipitate was washed with copious amount of triply distilled water. Until the washing was clear. Similarly 0.0001 M PPy/ Rhodamine-B composite was also synthesized. The polymer composite was dried in desiccators and again dried in an oven at 40-500°C. The synthesized product was further characterized by Mass and NMR spectroscopic Analysis.

III. RESULT AND DISCUSSION

The structural characterization of PPy/Rhodamine-B composite was carried out through Mass and NMR spectroscopic analysis.

1. Mass spectrometric analysis

The mass spectra of PPy/Rhd-B dye (0.00001 and 0.0001M concentration) composite gives molecular ion peak at m/z 740 and 745 indicates incorporation of dopant in the polymeric structure of oligomer having 9-10 number of monomer unit. The molecular ion peak gives an idea regarding molecular weight of polymeric composite materials. The abundance of molecular ion peak is very less indicating decomposition of oligomer during spectral analysis. The detail of molecular ion peak is given in the table below.

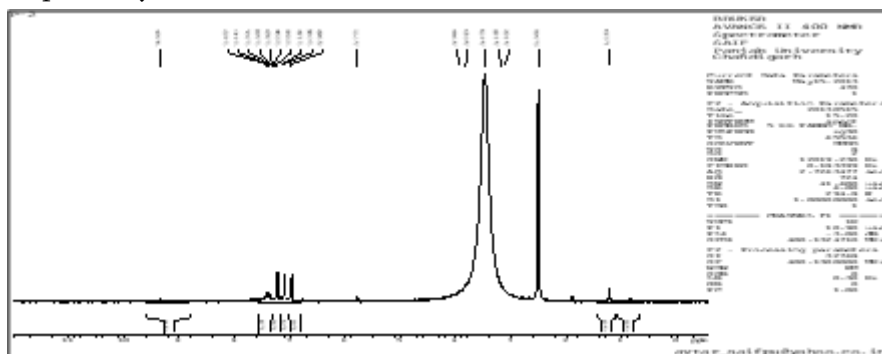
Molecular ion peaks of PPy/Rhd-B composites

S.N.	PPy composite	Molecular weight M^+ (m/z)
1.	PPy	580
2.	PPy/0.00001M Rhd-B	~740 (weak)
3.	PPy/0.0001 M Rhd-B	~745 (weak)

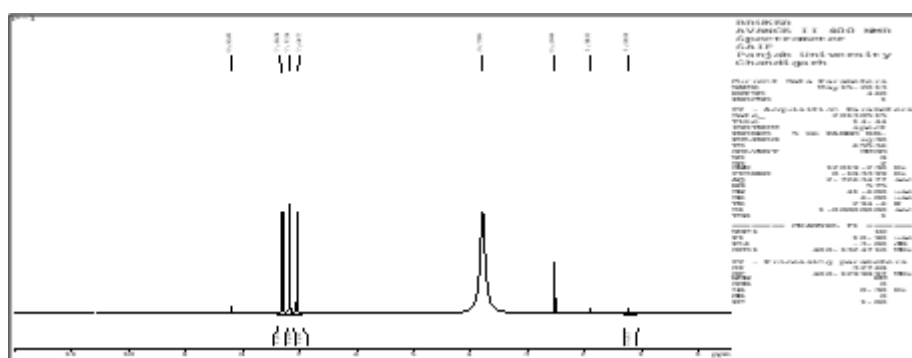
2. NMR spectral analysis of PPy/fluorescein composites

The NMR Spectra of PPy/Rhodamine-B dye composites are given in following figures which revealed that NMR spectrum of PPy, PPy/0.00001 M Rhd-B and 0.0001 M Rhd-B show three distinct peaks. The first peak is obtained for C=C-H proton at δ 2.5082, 2.5344 and 2.5083 ppm for PPy, PPy/0.00001 Rhd-B and PPy/0.0001M Rhd-B composites respectively. The second peak corresponding to N-H proton is obtained at δ

3.9097, 3.7950 and 3.4793 for PPy, PPy/0.00001 Rhd-B and 0.0001M Rhd-B respectively. This peak is deshielded because the proton is attached to more electronegative nitrogen atom. The peaks corresponding to aromatic protons are assigned at δ 7.1535, 7.1754 and 7.3239 for PPy, PPy/0.00001 Rhd-B and PPy/0.0001 M Rhd-B composites respectively.



NMR spectra of PPy/0.00001 M Rhd-B



NMR spectra of PPy/0.0001 M Rhd-B

The specific peak at 8.2030 and 9.3351 (w) is observed in the spectra which may be due acidic proton present in the dye. While higher value of acidic proton in 0.0001 M Rhd-B may be due to increase in hydrogen bonding in high concentration of dye. The presence of such bulkier dye may affect hindrance in conjugation which may become consequence to alter conductivity of the material.

IV. CONCLUSIONS

The PPy/ Rhodamine-B dye composites were synthesized by chemical polymerization method. It is a simple and low cost method for synthesis. The composite formation was confirmed by Mass and NMR spectroscopic analysis. The Mass study reveals that the interaction exists between PPy and Rhodamine-B dye and the dye particles were successfully incorporated in polymeric structure. The specific peaks obtained for NMR spectrum of each composite confirms aromatic and highly conjugated polymeric structure.

V. REFERENCES

- [1]. Fichou D, Handbook of Oligo- and Polythiophenes. Wiley-VCH: Weinheim, Germany, 1999.
- [2]. Steudel S, Myny K, Arkhipov V, Deibel C, De Vusser S, Genoe J, Heremans P, Nature Materials, 4 (8), 2005, 597-600.
- [3]. Kirchmeyer S, Reuter K, Journal of Materials Chemistry, 15 (21), 2005, 2077-2088.
- [4]. Hoppe H, Sariciftci N S, Journal of Materials Research, 19 (7), 2004, 1924-1945.
- [5]. Berridge R, Wright S P, Skabara P J, Dyer A, Steckler T, Argun A A, Reynolds J R, Ross W H, Clegg W, Journal of Materials Chemistry, 17 (3), 2007, 225-231.
- [6]. Roncali J, Chemical Reviews, 97 (1), 1997, 173-205.
- [7]. Tonzola C J, Alam M M, Bean B A, Jenekhe S A, Macromolecules, 37 (10), 2004, 3554-3563.
- [8]. Skotheim T A, Ed. Handbook of conducting Polymers, Vols. 1&2, Marceldekker, New York, 1986.
- [9]. Kaiser A B, et al, Curr. Appl. Phys., 4, 2004, 497-500.

Morphometric Analysis using Remote Sensing and GIS of Bhiram Ka Sand River (Pili River) Basin Amravati District, Maharashtra

Akshay D. Ghatol, Pravin S. Parimal

Department of Geology, G. S. Tompe Arts, Commerce & Science College, Chandur Bazar, District Amravati – 444702, Maharashtra, India

ABSTRACT

The aim of this paper is to perform morphometric analysis of Bhiram Ka Sand River (Pili river) with the help of remote sensing and GIS. Morphometric analysis of the river catchment was done by using geospatial techniques. The morphometric analysis of a drainage basin and its stream channel system can be better achieved through the measurement of linear aspect of drainage network and area aspect of drainage basin. The linear aspects of the channel system are; Stream order (Su), Stream length (Lu) and Bifurcation ratio (Rb) and Areal Aspect of drainage basin placed on the evaluation of morphometric parameters such as drainage density (Dd), stream frequency (Fs), circularity ratio (Rc), texture ratio (T), form factor ratio (Rf), Constant channel maintenance (C) and elongation ratio (Re). The study area is a 5 order drainage basin. The drainage pattern of the area ranged from dendritic to sub dendritic and at places the drainage was structurally controlled by lineament.

Keyword: Morphometric analysis, Remote sensing, GIS, Bhiram Ka Sand River (Pili river) basin

I. INTRODUCTION

Generally, morphometric analysis, quantitative description and analysis of landforms as practiced in geomorphology that may be applied to a particular kind of landform or to drainage basins and large regions. With regard to drainage basins, many quantitative measures have been developed to describe valley side and channel slopes, relief, area, drainage network type and extent, and other variables [1]. Attempts to correlate statistically parameters defining drainage basin characteristics and basin hydrology, as in studies of sediment yield, are generally designated as morphometric analysis [2].

In the study area stream number, order, frequency, density and bifurcation ratio are derived and tabulated on the basis of areal and linear properties of drainage channels using GIS based on drainage lines as represented over the topographical maps (scale 1:50,000). The various morphometric parameters for the study area were determined and summarized as given;

II. STUDY AREA

Bahiram Ka Sand River (Pili river) basin located in Amravati district, lying between latitude $20^{\circ}32'$ to $21^{\circ}46'$ North and longitudes $76^{\circ}37'$ to $78^{\circ}27'$ East (Fig 1). It occupies an area of 193 square kilometers is covered under survey of India Toposheet Nos. T 55G/11 and T 55G/12. The area experience sub-tropical climate and is characterized by a hot summer that normally starts from mid-March and continues up to mid-June. During summer, the maximum temperature may shoot up to 47°C whereas; the minimum is around 26°C . May is the hottest month. Winter season is moderately cold and normally extends from November to mid-March. During winter the maximum temperature is around 29°C which goes down to the minimum of 14°C . December is the coldest month[3].

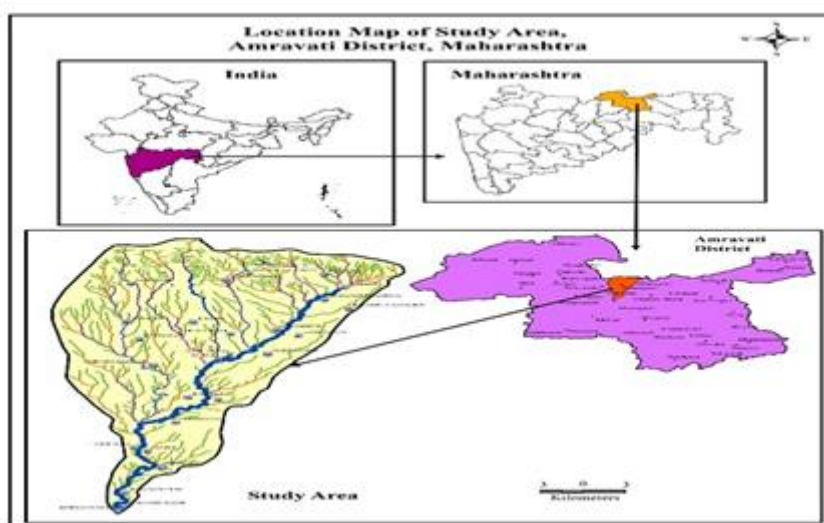


Figure 1: Location map of the study area.

III. DATA METHOD

In the study area, the satellite remote sensing data has been used for the updated drainages used for morphometric analysis. Topographical map T 55G/11 and T 55G/12 of scale factor 1:50,000 from Survey of India. The toposheet are geometrically rectified and mosaic. After mosaicking we extract study area by joining first order stream to the outlet of the river. The software used is ARCGIS (9.3) for the computation of various morphometric parameters and layout of map.

IV. RESULT AND DISCUSSION

The drainage map of the study area was prepared with the help of survey of India toposheet no. T 55 G/11 and T55G/12 was further utilized for morphometric analysis. The drainage pattern of the study area ranged from dendritic to sub dendritic and at places the drainage was structurally controlled by lineament Figure 2.

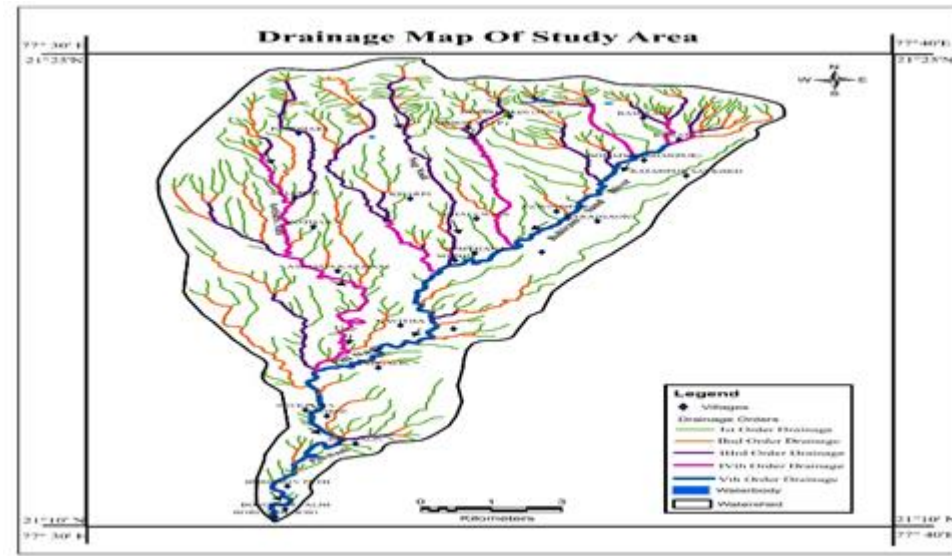


Figure 2: Drainage map of study area

Linear aspects of drainage network

1] Stream order (S_n)

In the drainage basin the first step is to determine the stream orders. The channel segment of the drainage basin has been ranked according to Strahler's stream ordering system [4]. According to Strahler (1964), the smallest fingertip tributaries are designated as order 1. Where two first order channels join, a channel segment of order 2 is formed, where two of order 2 joins, a segment of order 3 is formed; so forth. The study area is a 5 order drainage basin (Table 1). The total numbers of 179 streams were identified of which 119 are first order streams, 40 are second order, 14 are third order stream and 5 are fourth order stream and 1 is fifth order streams.

2] Stream length (L_n)

According to Horton's, (1945) the mean length of the stream is the ratio of the length of the stream of each order to the number of segments of same order. The total length of stream segments is maximum in first order and decreases length of stream as the stream order increases [5]. In the basin area total 460 streams are found. Out of which number of first order stream is 345 having stream length 243.65km. Similarly, second order stream are 86 with stream length 88.24km, 22 streams of third order with length of 55.54km, 6 fourth stream order having stream length 32.10km and there is a only stream of fifth order with stream length 30.97 km respectively (Table 1).

3] Bifurcation ratio (R_b)

Bifurcation ratio is relation between number of streams of one order and of next higher order which was obtained by dividing number of streams in one order by the number of stream in the next higher order for all the orders of the stream. These calculations were also based on Strahler (1964) method. The mean bifurcation ratio value is 4.3 for the study area in which 3.90 is the second order bifurcation ratio nearer to the value of mean value of bifurcation ratio, 3.66 is the third order bifurcation ratio, 6 is the fourth order bifurcation ratio and 0 is the fifth order bifurcation ratio (Table 1).

Table 1 - Linear aspects of drainage network

Stream order	No of segment	Bifurcation ratio	Stream length (in km)
1	345	4.01	243.65
2	86	3.90	88.24
3	22	3.66	55.54
4	6	6	32.10
5	1	0	30.97
Total	460	17.5	450.5
Mean	92	4.3	90.1

Areal Aspect of drainage basin

1] Drainage Density (Dd)

Drainage density (Dd) is an important indicator of the linear scale of landform element in stream eroded topography [6]. It is the ratio of total channel segments lengths cumulated for all orders within a basin to the basin area, which is expressed in terms of mi/ sq.mi or km/sq.km. It is expressed as the channel length in kilometers falling in unit 193 sq.km. The drainage density of the basin area is 2.33 km/sq. km indicating dendritic drainage pattern. (Table 2).

2] Stream Frequency (Fs)

Stream frequency is the number of streams of all the orders of the basin divided by the surface area of the same basin. Higher values of stream frequency in one area n the other depicts the growth of new channel of lengthening of the existing streams [6]. The stream frequency of the basin area is 2.38 km/sq. km. indicating low stream frequency (Table 2).

3] Drainage Intensity (Di)

Drainage intensity refers to the multiplication of drainage density with stream frequency. The drainage intensity of the study area is 5.55 km/sq. km. indicating low f drainage intensity implies that drainage density and stream frequency have little effect on the extent to which the surface has been lowered by agents of denudation (Table 2).

4] Circularity ratio (Rc)

Circularity ratio is the ratio of area to the area of circle having the same perimeter of the basin [7]. According to Miller (1953) the circularity ratio is helpful to interpret shape, discharge of runoff and permeability of subsoil condition. In the study area circularity ratio value is 17.95 indicating that the basin is elongated in shape (Table 2).

5] Texture Ratio (T)

Textural ratio is a ratio of total number of first order streams and perimeter of watershed. The ratio depends on the underlying lithology, in filtration capacity and relief aspect of the terrain. The texture ratio of the basin area is 5.11 indicating moderate texture ratios (Table 2).

6] Form Factor ratio (Rf)

Quantitative expression of drainage basin outline form was made by Horton (1932) through a form factor ratio (Rf), which is the dimensionless ratio of basin area to the square of basin length. The form factor ratio of the basin area is 0.31 (Table 2).

7] Constant channel maintenance (C)

Constant channel maintenance is the area of basin surface needed to sustain a unit length of stream channel and is expressed by the inverse of drainage density. The constant (C) is expressed as km. 0.42 depends upon not only the rock type and permeability, climatic regime, vegetation cover and relief (Table 2).

8] Elongation ratio (Re)

Elongation ratio (Re) is the ratio between the diameter of the circle having the same area (as that of the basin) and the maximum length of the basin [8]. It is a very significant criterion in basin shape determination the values near 1.0 are typical of regions of very low relief. Elongation ratio value of the basin area is 0.01 which indicate elongates in shape (Table 2).

Table 2: Areal aspect of drainage basin

Morphometric parameters	Formula	Values
Area (sq.km)	A	193
Perimeter (km)	P	67.5
Drainage density (km / km ²)	$D = Lu/A$	2.33
Stream frequency(Km/Sq.Km)	$F_s = N_u/A$	2.38
Texture ratio	$T = N_i/P$	1.775
Basin length (km)	L_b	450
Circulatory ratio	$R_c = 4\pi A/ P^2$	17.95
Bifurcation ratio (mean)	N_u/N_{u+1}	4.3
Elongation Ratio	$R_e = 2 \sqrt{A/\pi}/ L_u$	0.01
Form Factor ratio	$R_f = A/l_b^2$	69.48
Drainage Intensity(Km.)	$D_i = D_d * F_s$	5.55
Cost. Channel Maint.	$C = 1/D_d$	0.42

V. CONCLUSION

Detail morphometric analysis of Bahiram Ka Sand river (Pili river) basin has been carried out. Linear aspects of drainage network of the basin indicates that the basin is fifth order with total stream length is 450.5 km. Areal Aspect of drainage basin like drainage density (Dd), stream frequency (Fs), circularity ratio (Rc), texture ratio (T), form factor ratio (Rf), Constant channel maintenance (C) and elongation ratio (Re) indicating that the basin is elongated in shape. In the area indicating low f drainage intensity implies that drainage density and stream frequency have little effect on the extent to which the surface has been lowered by agents of denudation. The drainage pattern of the study area is from dendritic to sub-dendritic.

VI. REFERENCES

- [1]. S. K Nag and S. Chakraborty (2003) Influence of rock types and structures in the development of drainage network in hard rock area. *J Indian Soc Remote Sens*, V 31(1), pp. 25–35
- [2]. M. D. Nautiyal (1994) Morphometric analysis of a drainage basin, district Dehradun, Uttar Pradesh. *J Indian Soc Remote Sens*, V 22(4)., pp. 251–261
- [3]. A. K. Srivastava and P. S. Parimal (2014) Hydrochemical Facies and Ionic Ratios of Groundwater in Purna Alluvial Basin, Maharashtra. *Gond. Geol. Magz., Special Volume No.14*, pp. 117-126.
- [4]. A. N. Strahler (1964). “Quantitative geomorphology of drainage basins and channel networks,” in *Handbook of Applied Hydrology*, V. T.Chow,Ed.,section4–11,McGraw-Hill,NewYork,NY,USA.
- [5]. R. E. Horton (1945). “Erosional development of streams and their drainage basins: Hydrophysical approach to quantitative morphology”. India, using remote sensing and GIS techniques. *Environ Earth Sci.* 68:1967–1977.
- [6]. R. E. Horton (1932). Drainage basin characteristics. *Transactions of American Geophysics Union*, 13: 350–361.
- [7]. V. C. Miller (1953). “A quantitative geomorphic study of drainage basin characteristics in the Clinch mountain area, morphology”. *Geological Society of America Bulletin*, 56(3): 275–370.
- [8]. S. A. Schumn (1956). “Evolution of drainage system and slopes in badlands at perth Amboy, New Jersey”. *Geol. Soc. Am. Bull.* 67: 597-646.

Ionic Ratios of Groundwater in Northern part of Akola District, Maharashtra

P. S. Parimal

Department of Geology, G. S. Tompe Arts, Commerce & Science College, Chandur Bazar, District Amravati – 444702, Maharashtra, India

ABSTRACT

The present work is aimed at assessing various ionic relations of groundwater from northern part of Akola district, Maharashtra. The interpretations are based on a total of 55 samples each were collected in pre- and post-monsoon periods of the years 2006. Interrelationship plots of certain ions of groundwater are a significant tool to interpret sediment water chemistry, geochemical setup and weathering patterns. The scatter diagrams of Ca+Mg vs HCO₃+SO₄ and Na vs Cl indicate the prevalent of silicate weathering.

Keyword: Source rock weathering and major ion composition

I. INTRODUCTION

Hydrological condition, natural recharge rates and over limit of irrigations are increasing the salinity of groundwater [1]. Groundwater salinity increases due to change of hydrogeological conditions, rate of natural recharge and irrigation [2][3]. In the study area, the northern part of the Akola district represented mostly by the Deccan trap basaltic terrain exhibits dendritic pattern which is characterized by irregular branching of tributaries in many directions at almost any angle. The dendritic drainage pattern is developed upon the rocks of almost uniform resistance and implies a notable lack of structural control. Average rainfall of Akola district during 1st June to 30th September is 697.29 mm. The total actual rainfalls in the years 2006 high with an average of 911.27 mm (130.60%) as compared to the annual average rainfall *i.e.*, 697.29 mm. All these northward tributaries originate in the Satpura Hills. These are markedly influent in the gravel-conglomerate zone lying in the northern part of the basin. The aim of the present study is find out various ionic relations of groundwater from northern part of Akola district, Maharashtra.

II. STUDY AREA

The study region, located between longitudes 76°41' to 77°37' E and latitudes 20°08'31" to 21°40'30"N. Mostly covered by the basalt of Deccan Trap while the alluvial tract occupy mostly the central part. The region experiences a tropical humid type and experiences very hot summers and moderately cold winters.

The rainy season starts in mid-June and ends in mid September, with high peaks in July and August. The area experiences salinity problem, covering major northern part of Akola districts.

III. METHODOLOGY

Fifty five groundwater samples were collected from dug wells and bore wells during pre- and post-monsoon periods of the year 2006 to evaluate the quality of ground water. Water samples were collected in one liter pre-washed polyethylene bottles. The water from the wells was pumped for 5–10 minutes and the polyethylene bottles were rinsed for 2 – 3 times with the water to be sampled. Electrical Conductivity (EC) and Hydrogen ion concentration (pH) were noted on the site by using the portable EC and pH meters respectively. The analyses of major ions were carried out as per the standard procedure recommended by [4]. The representative samples collected from the study area were analyzed for alkalinity (Al), calcium (Ca), chloride (Cl) and total hardness (TH) were determined by respective volumetric titration methods. Magnesium (Mg) is measured by subtracting calcium value from the total hardness. Bicarbonate (HCO_3) was calculated by the numerical calculation of pH and phenolphthalein alkalinity values. Sodium (Na) and potassium (K) were determined by using flame photometer, whereas, SO_4 and NO_3 by UVVIS spectrophotometer. Total dissolved solids (TDS) concentration was calculated from EC adhering to the procedure [5].

IV. RESULT AND DISCUSSION

In the present attempt, interrelationships of $\text{Ca}+\text{Mg}$ vs SO_4+HCO_3 and Na vs Cl have been plotted Figure 1. In the study area, evidences for chemical weathering can be explained by the relationships between major ions in groundwater [6]. The scatter plots ($\text{Ca}+\text{Mg}$) vs. SO_4+HCO_3 (Figure.1) in general, show that the majority of the samples fall below the equiline. It indicates that the concentration of HCO_3 is more than $\text{SO}_4+\text{Ca}+\text{Mg}$, which is due to silicate weathering [7][8]. However, the samples falling above the equiline indicates high ratio of Calcium and magnesium. The high ratio of calcium and magnesium indicating excess of $\text{Ca}+\text{Mg}$ are attributed from carbonate weathering [8]. The high value of ($\text{Ca}+\text{Mg}$) indicating dissolution of alkaline earth minerals from rock/soil into groundwater [9]. A plot between Na vs. Cl (Fig. 2) indicates that most of the data points fall below equiline which indicates that excess of sodium values (Figure. 2). The dominance of sodium indicates silicate weathering due the presence halite mineral dissolution is responsible for the release of sodium. Some of the points falling above the equiline, indicating excess of chloride are attributed from carbonate weathering. However, the increasing value of sodium probably controlled by water-rock interaction, most likely by feldspar weathering [10]

V. CONCLUSION

Overall evaluation of groundwater during the period of study the scatter diagram of Ca+Mg vs HCO +SO and Na vs Cl plots suggest that the rock weathering is the dominant factor affecting the major ion composition. Scatter diagram of Ca+Mg vs HCO +SO and Na vs Cl shows that the most of samples of groundwater falling below the equiline. It indicates that the concentration of SO₄+HCO₃ and Na is more than Ca+Mg and Cl which is due to silicate weathering.

VI. REFERENCES

- [1]. Greggio Nicolas, Antonellini Marco, Mollema Pauline, RamAmy Murugan, Sadhasivam Satish, "Effects of natural recharge and irrigation on groundwater salinity in a costal unconfined aquifer, Lido Di, Ravenna, Italy" Conference paper 10.1474/Epitome.04.0100. 2011
- [2]. P.S. Eagleson, "Climate, soil, and vegetation,". Water Resources Research, vol. 14, pp. 705–776. 1978.
- [3]. P.S Eagleson, "The annual of water balance," J. Hydro. Division ASCE, 1979, vol. 105, pp. 923–941.
- [4]. APHA, Standard Method for the Examination of Water and Waste Water, 16th edn. American Public Health Association. Washington, D.C. 2. 1992.
- [5]. J. D. Hem, Study and interpretation of chemical characteristics of natural water, 1991, 3 rd edn. USGS Water Supply Paper 2254, 264 p.
- [6]. Manavalan Satyanarayanan & Vysetti Balaram & Mohammed Saad Al Hussin & Majed Abdul Rahman Al Jemali & Thota Gnaneshwar Rao & Ramavati Mathur & Bonathu Dasaram & Soday Laxman Ramesh "Assessment of Groundwater Quality in a Structurally Deformed Granitic Terrain in Hyderabad, India" Environmental Monitoring and Assessment, Vol.131(1-3), pp. 117-127, 2007.
- [7]. P. S. Datta, and S. K. Tyagi, "Major ion chemistry of groundwater in Delhi area: chemical weathering processes and groundwater flow regime," J. Geol. Soc. India. vol. 47, pp. 179–188, 1996
- [8]. E. Lakshmanan, R. Kannan and M. Senthilkumar, "Major ion chemistry and identification of hydrogeochemical processes of groundwater in a part of Kancheepuram district, Tamil Nadu, India," Env. Geosci., vol. 10 (4), pp. 157–116, 2003.
- [9]. S. Manavalan, B. Vysetti, M. S. A. Hussin, M. A. R. Al Jemali, G. R. Thota, R. Mathur, D. Bonathu and L. R. Soday, "Assessment of Groundwater Quality in a Structurally Deformed Granitic Terrain in Hyderabad, India." Env. Monit Assess, vol. 131(1-3), pp. 117-127, August 2007.
- [10]. G. F. Zhu, Y. H. Su, and Q. Feng, "The hydrochemical characteristics and evolution of groundwater and surface water in the Heihe River Basin, northwest China," Hydrogeol. J, vol. 16, pp. 167-182, 2008

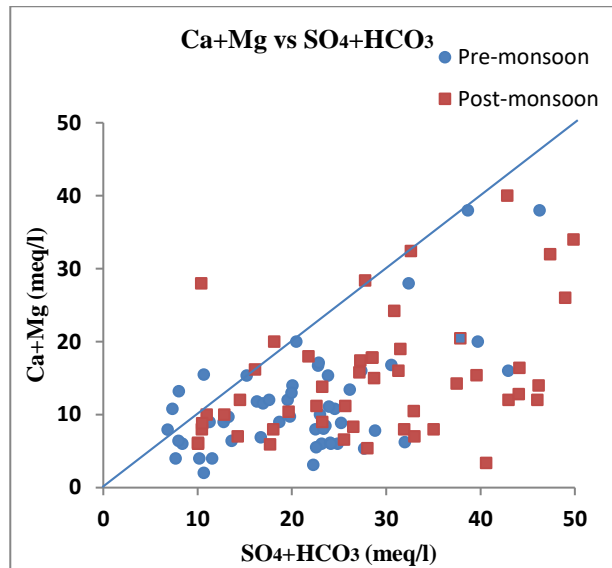


Fig. 1:Ca+Mg vs SO₄+HCO₃ scatter diagram showing high concentration of SO₄+HCO₃ as compared to Ca+Mg indicating silicate weathering.

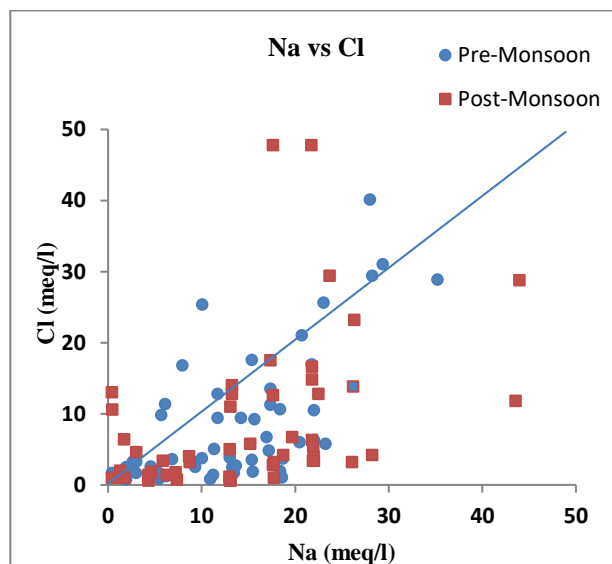


Fig. 2: Na vs Cl scatter diagram showing high concentration of Na as compared to Cl indicating silicate weathering.

Sr No.	Parameter	monsoon/ period	1) Dug well		2) Bore well		WHO Standard		Indian Standard	
			Concentration in Mg/l*	Mean	Concentration in Mg/l*	Mean	Highest Desirable	Highest Permissible	Highest Desirable	Highest Permissible

1.	pH	Pre- Post-	6.9-9.6 7-9.4	7.51 7.78	6.8-8.6 6.9-9.3	7.23 7.62	6.5-8.5	7.0- 8.5	6.5-8.5	-
2	EC	Pre- Post-	300-18300 210-15800	-	200-18200 300-18200	-	-	-	-	-
3.	TDS	Pre- Post-	186-11346 130-9796	2993 2726	124-11284 186-11656	2028 1853	500	1000	500	2000
4.	Ca	Pre- Post-	28.8-901.8 20-665.3	167. 6 129. 1	14.4-681.3 12-877.7	97.9 111.8	75	200	75	200
5.	Mg	Pre- Post-	36.9-1978 32.9-2050	253 402. 8	13.1-4681 26.3-2670	332.4 304.3	-	150	30	100
6.	Na	Pre- Post-	4.5-565 30.4-2545	296. 6 621	5-676 10-2008	288.7 363.7	-	200	-	-
7.	Cl	Pre- Post-	25.3-3990 35.5-1491	749. 7 463. 4	28.4-5424 20.5-1697	497.8 332.5	200	600	250	1000
8.	SO ₄	Pre- Post-	3.01-296 15-350	129. 5 113. 8	5-296 3-275	107.2 90.3	200	400	200	400**
9.	NO ₃	Pre- Post-	0.2-22 0.1-27	14.9 16.3	0.8-26 0.1-25.2	14.8 18.4	45	-	45	100
10	TH	Pre- Post-	140-5250 100-4770	792. 5 934. 4	140-8550 70-5370	765.3 733.5	100	500	300	600

Molar Concentration Dependent Capacitive Performance of Ultrasonic Spray Pyrolysed Ruthenium Oxide (RuO₂) Thin Films

B.Y. Fugare¹, A.V. Rajgure², G.T. Chavan³, P. K. Tawalare¹, B.J. Lokhande⁴

¹Jagadamba Mahavidyalaya, Achalpur City-444805, Maharashtra, India

²G.S. Tompe Arts, Commerce and Science College, Chandur Bazar, Amaravati-444704, Maharashtra, India

³College of Information and Communication Engineering, Sungkyunkwan University, Suwon, 440-746, Republic of Korea

⁴School of Physical Sciences, Solapur University, Solapur 413255, Maharashtra, India

ABSTRACT

Ultrasonic spray pyrolysis technique used for preparation of RuO₂ thin films on stainless steel substrate for different molar concentration (0.001-0.006 M) of RuCl₃.nH₂O as a precursor, dissolved in double distilled water. The decomposition temperature 723 K and volume 50 ml was kept constant for all depositions. All the deposited samples exhibit amorphous nature as indorses by XRD analysis. It was observed that the thickness of the materials strongly depends on the concentration of precursor solutions. Surface morphological evaluations like SEM elucidates the formation of continuous uniformity, structural homogeneity, interconnected granular morphology. The morphological outcomes reveals that the interconnected granular morphology offers large surface area for electrochemical activities as compared to dense, flat, bulky morphology. Wettability glimpses exhibit hydrophilic nature of all the deposits. Electrochemical studies of RuO₂ were carried out in 1 M KOH electrolyte for all electrodes. Optimized RAM5 electrode shows 218 F/g SC at 2 mV/s scan rate.

Keywords: Ultrasonic spray; Mesoporous (RuO₂), Supercapacitor; Energy and power.

I. INTRODUCTION

In the 21st century, there is a daily requirement of electric energies for storage and power supplies. Now a day, batteries, capacitors and supercapacitors are used for energy storage and supplies. Unlike batteries and capacitors, supercapacitor offers high energy densities than capacitors and high-power densities than batteries. As results, supercapacitor is a very powerful solution to crossover this problem cause supercapacitor is a bridge between capacitor and battery. Supercapacitor delivers high specific capacitance (SC) in micro sachets to completion of the daily necessitate of power supplies. It stores the charges by its unique charge storage mechanisms like faradic, non-faradic and combined reaction mechanisms. The performance of supercapacitor based on nature of deposited materials. Basically carbon, metal-oxides, conducting polymers and more

materials established for fabrication of supercapacitors [1-6]. Because of high conductivity and current research concern, ruthenium oxide is mainly admirable metal oxide for production of supercapacitor, due to its ample range of physical and electrochemical properties such as amorphous nature, mixed electro-protonic conductivity, multi oxidation states, wide potential window, very low electrochemical series resistance and high porosity [7,8]. Current research concern, ruthenium oxide (amorphous phase) exhibits very high SC [9]. Numerous literatures are found to get better SC value of RuO₂, but not found on the reproducibility of SC. As results, achievement of high energy and power density and excellent reproducibility is strongly depending on the choice of materials and method of preparation of deposit [10].

Now days, RuO₂ thin films were prepared by number of techniques such as electro deposition [11], sol-gel [12], e- beam evaporation [13], ultrasonic spray pyrolysis [14, 15], etc. Amongst them, Ultrasonic spray pyrolysis (USP) is most simplified promising method for preparation of single and multilayered dense, porous, thin films at low decomposition temperature, broad surface area coatings, thickness variations and highly adherence film formations in one step only. In the present work USP deposited RuO₂ thin films are carefully investigated to study the effect of different molar concentrations and electrochemical performance for supercapacitor application.

II. EXPERIMENTAL DETAILS

The deposition of RuO₂ thin films was done on smoothly polished stainless steel (SS-304) substrates by ultrasonic spray pyrolysis technique. All the precursors used in this study are of analytical grade reagents (AR) and (99.9%) pure purchased from SD Fine-Chem Limited. In actual synthesis process, Initial precursor was dissolved in double distilled water. To see the effect of solution concentration, samples were carried out by varying the molarity of precursor solution from 0.001, 0.002, 0.003, 0.004, 0.005 and 0.006 M and nominated as RAM₁, RAM₂, RAM₃, RAM₄, RAM₅ and RAM₆ respectively. The decomposition temperature 723 K and volume 50 ml was kept constant for deposition. The as-prepared precursor solution sprayed on pre-heated SS substrate at 08 ml/min spray rate, at a compressed air (flow rate of 10 L min⁻¹).

III. RESULTS AND DISCUSSION

3.1 Thickness variations

Fig.1 illustrates the variation of thickness of the RuO₂ thin films prepared using RAM₁ to RAM₆ solution concentrations of the ruthenium tri chloride precursor. It was observed that the thickness of the materials strongly depends on the concentration of precursor solutions. As the concentration of solution increases, thickness of the materials increases gradually due to loading of precursor mass on to the substrate. The RAM₁ sample shows minimum thickness and sample RTA₆ shows maximum thickness may due to effect of solution concentration, residue gas evaporation during thermal decomposition and reduced mass transport to the substrate.

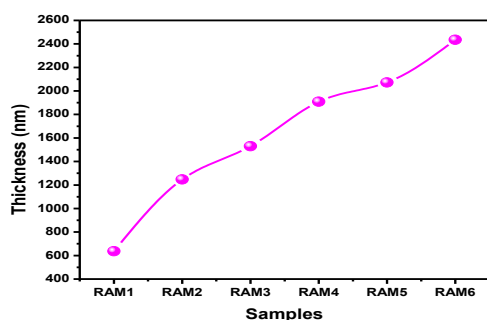


Fig.1

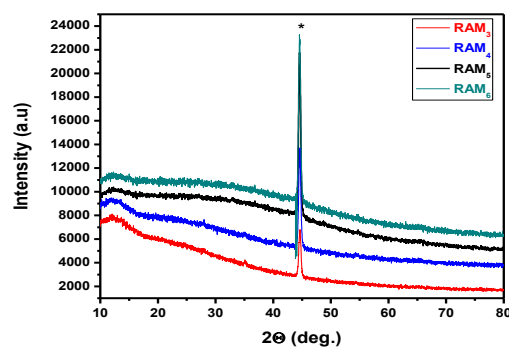


Fig.2

Fig.1. illustrates the variation of sample thickness and Fig.2 illustrate XRD pattern of typical RAM₃, RAM₄, RAM₅ and RAM₆ samples.

3.2 Structural properties

Structural study of as deposited RuO₂ thin films was carried out using XRD in range from 10 to 80°. Fig.2 illustrate XRD pattern of RAM₃, RAM₄, RAM₅ and RAM₆ thin films. All the diffracted peaks show the substrate peaks (SS). No any deposit peak observed for all samples, which illustrate that the deposited material shows amorphous nature. Similar results are observed in the literature survey [11-12]. The observed peaks are indicated by asterisk (*).

3.3 Surface Morphological studies

Fig.3 illustrate the SEM images of RAM₃, RAM₄, RAM₅ and RAM₆ thin films at 60,000 X magnification for all samples. Sample shows continuous uniformity, structural homogeneity, interconnected granular morphology. It is also shows that the surface morphology changes with change in precursor concentration. As the concentration increases, morphology changes granular to nano flower, may due to proper solution concentration and thermal decomposition of the material evidenced by RAM₅, afterward morphology changed nanoflowers to flat, dense, overgrowth was also observed, it may due to high mass loading on to the surface of substrate.

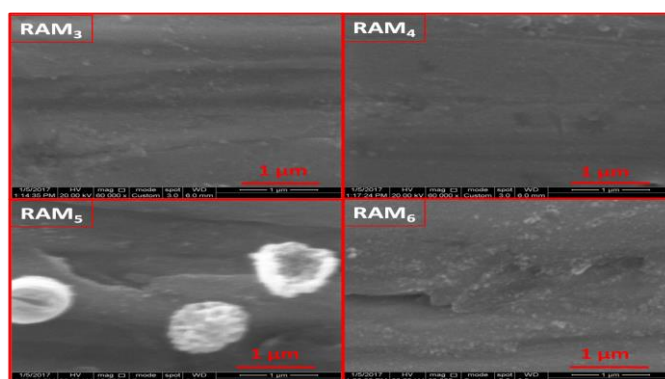


Fig.3 illustrate the SEM images of RAM₃, RAM₄, RAM₅ and RAM₆ samples

IV. ELECTROCHEMICAL MEASUREMENTS

4.1 Cyclic voltammetry studies

The supercapacitive performance of spray deposited RuO₂ thin films were scrutinized by CVs in the wide potential range -1.6 to -0.2 V/ Ag/AgCl in 1 M KOH. To evaluate the SC values using cyclic voltammetry, following relations are used [14].

$$C = \frac{dQ}{dv} = \frac{I}{dv/dt} \quad 1$$

$$SC = C/W \quad 2$$

Where C- capacitance, Q - accumulated charges on the surface of electrode, I-average current, V- applied potential, dv/dt- scan rate and W- active mass of deposit (0.20 mg). The RAM₅ electrode achieved maximum value of SC is 218 F/g with a scan rate (mVs⁻¹), which are tabulated in Table 1. Fig.5 (a) represents the CVs of different RAM₁ to RAM₆ electrodes at 100 mV/s scan rates. During the CV analysis, it was illustrated that, as solution concentration increases the area under curve (anodic-cathodic current) increases. This illustrates that the voltammetric current is directly proportional to the solution concentration and scan rate. The solution concentration increases, SC values increase up to achievement of optimum condition of the deposit then after it becomes decreases. As concentration increases beyond the optimum condition, which shows that the area under curve decreases and curve shows tails at the tip of curve, which is not suitable for supercapacitive properties and SC values of the deposit also decreases. It may be due to improper solution concentration and thermal decomposition of the deposit [14].

Fig.5 (b) represents the CVs of RAM₅ electrodes scanned for different scan rate variations. It shows that, the scan rate increases, area under curve is decreases. As the scan rate increases, SC values of the deposit decrease with increasing scan rate. This is implying that, higher scan rate leads either saturation or depletion of ions in KOH electrolyte during redox mechanism, due to slow transfer of ions diffusion effect of ions within the electrode [15].

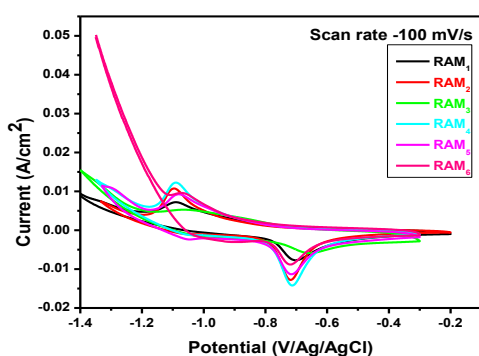


Fig. 5 (a)

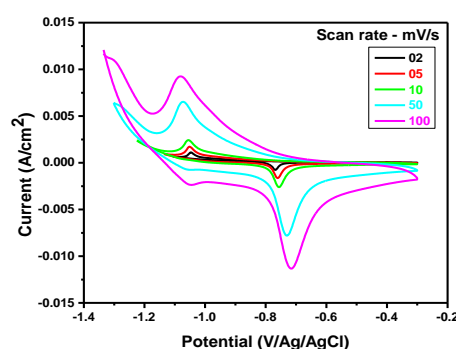


Fig. 5 (b)

Fig.5 (a) represents the CVs of different RAM₁ to RAM₆ electrodes at 100 mV/s scan rates and Fig.5 (b) represents the CVs of RAM₅ electrodes at different scan rates in 1 M KOH.

V. CONCLUSION

The ingredient (RuCl_3) was used to prepare the RuO_2 films by varying the different solution concentrations like 0.001 M to 0.006 M. The XRD of all samples shows amorphous nature. Film deposited with 0.005 (RAM_5) M, 50 ml solution concentration shows better performance. The SEM studies of the films shows continuous, porous, crack's free growth of the deposit. All deposited RuO_2 electrodes shape of CVs curve shows mixed capacitive behavior. Electrode deposited at 0.005 M (RAM_5) concentration solution CVs curve shows large area under the curve, mixed capacitive nature and observed maximum value of SC is 218.52 F/g at scan rate 2 mV/sec. which is more feasible for electrochemical performance.

VI. REFERENCES

- [1]. B.E. Conway, J. Electrochem. Soc. 138 (1991) 1539.
- [2]. C.C. Hu, Y.H. Huang, J. Electrochem. Soc. 146 (1999) 2465.
- [3]. J. Wen, Z. Zhou, Mater. Chem. Phys. 98 (2006) 442.
- [4]. J.K. Chang, W.T. Tsai, J. Electrochem. Soc. 152 (2005) A-2063.
- [5]. K.W. Nam, K.B. Kim, J. Electrochem. Soc. 149 (2002) A-346.
- [6]. C.C. Hu, C.H. Chu, Mater. Chem. Phys. 65 (2000) 329.
- [7]. J.P. Zheng, P.J. Cygan, T.R. Jow, J. Electrochem. Soc. 142 (1995) 2699.
- [8]. W.C. Chen, C.C. Hu, C.C. Wang, C.K. Min, J. Power Sources 125 (2004) 292.
- [9]. C.C. Hu, K.H. Chang, Electrochem. Acta 45 (2000) 2685.
- [10]. B.O. Park, C.D. Lokhande, H.S. Park, K.D. Jung, O.S. Joo, J. Power Sources 134 (2004) 148.
- [11]. I. Oja Acik, A. Junolainen, V. Mikli, M. Danielson, M. Krunk, Appl. Surf. Sci. 256 (2009) 1391.
- [12]. R. Mechiakh, N. Ben Sedrine, R. Chitourou, R. Bensaha, Appl. Surf. Sci. 257 (2010) 670.
- [13]. C. Sima, C. Grigoriu, Thin Solid Films 518 (2009) 1314.
- [14]. B.Y. Fugare, B.J. Lokhande, Mater. Sci: Mater. Electron., 27 (2016) 5788.

Synthesis and Electronic Study of Iron Nanoparticles of *Trigonella Foenum-Graceum*

Saifuddin Quazi¹, Dipak Tayade²

¹Department of Chemistry, Maulana Azad College, Dr Rafiq Zakaria Campus, Aurangabad, Maharashtra, India

²Department of Chemistry, G V.I.S.H. Amravati, Maharashtra, India

ABSTRACT

The use of natural materials and less hazardous or toxic materials for the synthesis of nanoparticles is known as green method. The present work deals with the synthesis of iron nanoparticles by greener approach. The electronic spectroscopic studies i.e. ultraviolet-visible spectroscopy and Fourier transform infra-red spectroscopic studies of iron nanoparticles of *trigonella foenum-graceum* were studied in this present research work. The absorption band in UV around 310 nm is obtained and FTIR values around 3300 cm⁻¹ and 1720 cm⁻¹ provides the information of formation of iron nanoparticles from *trigonella foenum-graceum*.

Keywords: - Ultraviolet-visible, Fourier Transform infra-red, *Trigonella Foenum-Graceum*, iron nanoparticles.

I. INTRODUCTION

Nowadays nanoparticles are emerging a great interest due to its tremendous applications in science and technology¹. Due to its unique dimensions and properties nanoparticles are almost studied in every field of science, medicines²⁻⁴. Nanoparticles have small particle size and large surface to volume ratio which make them unique for wide applications⁵⁻⁷. Nanoparticles can be synthesized by various methods such as sol-gel method, chemical methods, ion sputtering, etc. The most efficient and ecofriendly methods were used for synthesis of nanoparticles are green method from plant extract⁸. The nanoparticles shows biological properties such as antibacterial, antifungal, antioxidant, etc⁹.

The plant mediated synthesis of metal nanoparticles shows numerous applications such as antibacterial, antifungal, etc¹⁰⁻¹². Iron has been known from ancient period and iron nanoparticles shows good biological properties. *Trigonella foenum-graceum* is medicinally important plant and have wide applications in diabetes, anemia. Many studies shows that Fenugreek has applications in antiulcer, antibacterial, etc.

II. MATERIALS AND EXPERIMENTAL METHODS

Freshly prepared solutions are used through current work. All AR grade chemicals are used through present analysis. The solvents were purified by standard method before used. The fenugreek plant leaves were

purchased from local market in Aurangabad. The leaves along with stems were cut and dried in shade and then the dried leaves were taken in morton pestle for making them in fine powder form.

10gm of powder extract was taken in 250ml round bottom flask and 100ml deionized water was poured in it . The distillation is done for 3 hours and after that the filtration is done with simple filter paper and plant extract was collected. 1M Fe(NO)₃ solution is prepared in standard flask as metal solution. The plant extract is made little basic in nature by few NaOH pallets and the ferric nitrate solution is kept on magnetic stirrer and the plant extract is added slowly .i.e. dropwise addition is done the color change from light green to brown ppt shows the formation of nanoparticles and the stirring was done for 4 hrs .After stirring the beaker is kept in dark covering with foil paper for 48hrs. Lastly the ppt is centrifuge at 1500rpm centrifuge machine for 15 minutes and the collected precipitate is calcined for 2 hours at 600° c in silica crucible . The collected sample is characterized by UV and FTIR Spectroscopy

III. RESULT AND DISCUSSION

The iron oxide nanoparticles are prepared by green method and the characterization and confirmations of formation of iron oxide nanoparticles of trigonella foenum graecum is as follows

ULTRAVIOLET-VISIBLE SPECTROSCOPY

The ultra violet- visible spectroscopy is great technique and tool for studing or identifying the nanomaterials. In this technique the light is absorb by the material and which allow the electrons to shift of electron to higher energy level and again come back to ground level . These transition of electron from different energy levels provides the informations of electronic transitions and these study of electron shifting is based on formula $E=hv$. The UV is recorded between range of 200nm to 600 nm absorbtion band is obsereved on uv visible spectroscopy around 310 nm which confirms the formation of iron oxide nanoparticles from trigonella foenum graecum . This peak of iron oxide nanoparticles gives primary information of formation of iron nanoparticles from trigonella foenum graecum.

FOURIER TRANSFORM INFRA RED SPECTROSCOPY

The Fourier transform infra red spectroscopy (FTIR) characterization technique provides the information of functional groups present in the sample. The nanoparticles of iron oxide from trigonella foenum graceum contains alkaloids, amino acids , saponins in its extract and the newly synthesized nanoparticles of iron oxide has the same. The stretching frequencies such as around 1720 cm⁻ confirms the presence of carbonyl group and stretching frequency around 3300 cm⁻ confirms the presence of phenolic -OH group. These functional group i.e. acid and phenol is present in amino acid and isovitexin respectively. Such information of functional groups present in iron oxide nanoparticles of trigonella foenum graceum is confirmed by the fourier transform infra red spectroscopy. The bands around 2900 cm⁻ gives the information about presence of CH₂ C-O-C asymmetric stretching and a band around 580 cm⁻ confirm formation of Fe-O surface vibration at iron oxide core.

IV. CONCLUSION

From this present research work it is concluded that the greener method is cost effective and the electronic spectroscopic studies i.e. UV-visible and FTIR study shows the primary information of nanoparticles and functional groups present in it .

V. REFERENCES

- [1]. Laxmanan S, Joster S, International Journal of Nanoscience and Nano Technology,2021,17(2),109-121
- [2]. Toumey C, Reading Feyman into Nanotechnology,2003,12(3)133-138.
- [3]. Roja G, Melanie L, David R, Journal of Hazardous Materials, 2016, 302,362-374.
- [4]. Majid N, Majid M, Hossen B, Journal of Photochemistry and Photobiology,2018,179,98-104.
- [5]. Megarajan S, Dhinesh V, Materials Research Bulletin, 2018, 100,386-393.
- [6]. Samreen F, Abdul A, Mazahar F, Pathan A, Chemistry Journal, 2019, 2,134-140.
- [7]. Sheng P, Chao W, Jin E, Journal of American Chemical Society,2006,128,10676-10677.
- [8]. Smuler V, Varma R, Sikdar R, Journal of Membrane science,2011, 379(1), 131-137.
- [9]. Shrivastav G, Das C, Das A, Singh S, Journal of Royal Society of chemistry Advances, 2014, 4(104),58495-58500.
- [10].Aila E, Ayed H , Yassen A, International Journal of Environment, 2019,4,181-185.
- [11].Samreen F, Shirsat M, Mazahar F, Pathan A, International Journal of Nano Dimension,2019, 10(2),163-168.
- [12].Hulla J, Sahu S, Hayes A, Human and Experimental Toxicology,2015,34(12),1318-1321

Evaluating The Performance of Artificial Recharge Structures Towards Ground Water Recharge in Amravati District, Maharashtra

Sumit D. Ingle¹, Ketki A. Jadhav²

ABSTRACT

The images can be processed in order to get desired results for many other applications by Digital image

Keywords: Raspberry pi, USB camera, motor driver, motor, LCD display, road side speed sign controlling.

I. INTRODUCTION

The main objective of artificial recharge structures is to conserve excess surface water in underground for future use. To achieve these objectives, it is essential that the site selected for recharge satisfies the basic requirements of storage and retrieval and requires proper scientific investigations. Sites of artificial recharge structures should be geologically and hydrogeologically sound, otherwise the very purpose of construction of these structures may be defeated and the expenditure incurred thereon will be infructuous. For evaluating the performance of artificial recharge structure towards ground water recharge nine structures from Amravati district Maharashtra has been selected (Fig.1).

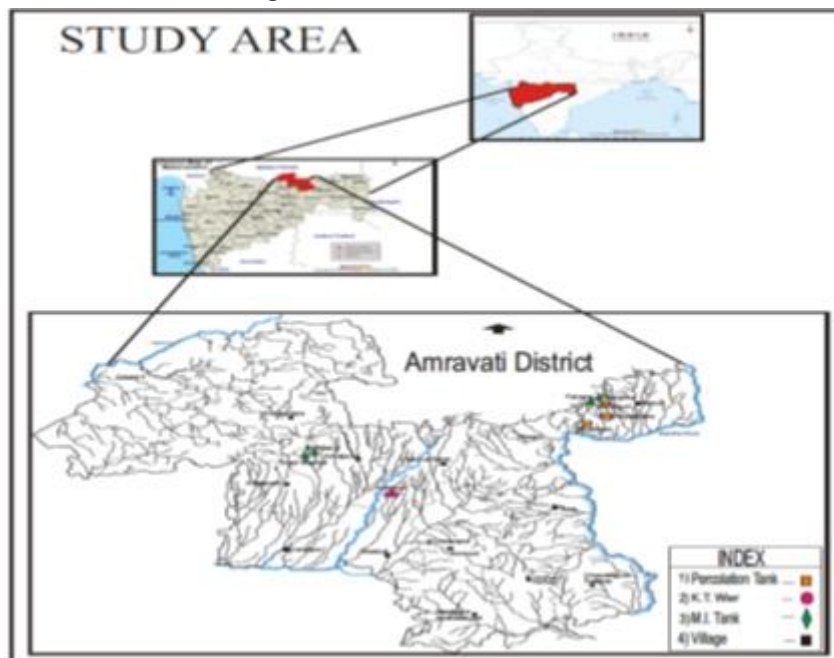


Fig 1. Location map of the study area

II. AIMS AND OBJECTIVES

1. To study the geomorphic control of site for artificial recharge structures.
2. To study the geologic control on feasibility of an artificial recharge structures.
3. To study the hydrogeologic control of an artificial recharge structures on feasibility.
4. Evaluate the performance of artificial recharge structures in terms of geological and hydrological set up
5. Evaluate cost benefit analysis of artificial recharge structures.

III. METHODOLOGY

1. Preparation of drainage map for all the nine artificial recharge structures from Survey of India toposheets on 1:25,000 scale.
2. Determine linear, aerial and relief parameters for each structure following standard techniques.
3. Field mapping and preparation of geological map of the study area.
4. Conducting two to three Vertical Electrical Sounding at each structure to determine range of resistivity of subsurface material, with ANVIC-500 Aquameter.
5. Establishing observation wells around each structure and monitoring of tank water levels and groundwater levels (monthly) in observation wells.
6. Construction of hydrographs of tank water levels and groundwater levels and determining their correlation coefficients.
7. Determining the dugwells being benefited (based on cut-off value of 50% correlation coefficient) and area benefited from the artificial recharge structure.
8. Ultimately determining the efficiencies of artificial recharge structures by adopting the water balance technique.
9. Attempting a correlation between the geomorphic, geologic, hydrogeologic and electrical resistivity for evaluating efficiencies of artificial recharge structures and cost benefit analysis.

IV. OBSERVATIONS AND DISCUSSION

Morphometric investigations have been carried over nine structures and the linear areal and relief characteristics presented in Table No.1 while representative drainage maps of four structures given in Fig.2.

The geological set up was studied by taking field traverses and the geological map was prepared. Representative maps of four structures are presented in Fig.3. Two main geological set up were noted for artificial recharge structure, the Deccan trap and alluvium.

Geologically, the Deccan trap set up can be further divided into three model- zeolitic and amygdaloidal top followed by zone of sheeted joint followed by massive basalt. Second situation is of sheeted joint followed by massive basalt and third is of massive basalt. On alluvium geological set up, the percentage of sand, silt and clay in alluvium controls the type of model (TableNo.2).

Two or three vertical electrical soundings was carried at each structure using Schlumberger method and data interpreted using IPI2Win software to determine the resistivity range for first layer and represented in Table 2.

Ten to twelve observation wells have been fixed over each structure on upstream as well as downstream side. These wells have been monitored on monthly basis along with the water levels in artificial recharge structures (Table No.3a, 3b.) along with the correlation coefficient.

The wells being benefited have been determined by assuming 50% as direct correlation existing between water level in structures and ground water level. The range of rise in water level along with area benefited is represented in Table No.4 (Fig 4).

Ultimately geomorphological (morphometric), geological, hydrogeological and resistivity investigation results were integrated to compared for evaluating efficiencies of artificial recharge structures.

Table No.1. Morphometric aspects of artificial recharge structures in Amravati district, Maharashtra.

S. No	Artificial Recharge structure	Linear Aspects			Aerial Aspects				Relief Aspects
		Stream Order	Bifurcation Ratio (RB)	Length of overlaid flow	Drainage Density (DD)	Drainage Frequency (DF)	Form Factor (F)	Circulatory Index (C)	Hypsometric Integral
1	Pimpalkhuta PT	2	5	0.27	1.85	1.35	0.14	0.46	46.13%
2	Mangona PT	4	3.83	0.14	3.52	6.39	0.13	0.32	35.71%
3	Manikpur PT	2	5	0.19	2.55	3.23	0.24	0.85	41.66%
4	Palsona M.I	2	1.2	0.22	2.2	1.99	0.16	0.56	43.15%
5	Asegaon K.T	3	3.38	0.18	2.66	4.16	0.34	0.77	43.15%
6	Changapur P.T	2	5	0.46	1.08	0.72	0.51	1.04	53.57%
7	Mamdapur C.P	3	3.83	0.17	2.98	3.23	0.22	0.63	23.80%
8	Gond wagholi M.I	3	3.17	0.18	2.78	3.61	0.51	0.21	43.15%
9	Khatijapur M.I	4	3.38	0.2	2.45	5.11	0.38	0.17	47.61%

Table No.2 Geological set up of the artificial recharge structures in Amravati district, Maharashtra

S. No.	Artificial Recharge structure	Geological Set up			Earth resistivity of first layer in
		Aquifer	Depth to weathering (in m)	Earth Model	

					ohm-m
1	Pimpalkhuta PT	Deccan Trap	4.58	Weathered sheeted- columnar	36-45
2	Mangona PT	Deccan Trap	5.42	Weathered amygdaloidal-sheeted	32-38
3	Manikpur PT	Deccan Trap	4.24	sheeted- massive	42-56
4	Palsona M.I	Deccan Trap	3.86	Part. weathered amygdaloidal-massive	38-45
5	Benoda P.T	Deccan Trap	--	Highly weathered amygdaloidal-sheeted	26-28
6	Changapur P.T	Laterite	4.12	Laterite	28-32
7	Mamdapur C.P	Alluvium	2.46	Highly weathered massive	58-66
8	Gond wagholi M. I	Alluvium	--	Sandy alluvium-clayey alluvium	22-26
9	Khatijapur M.I	Alluvium	--	Sandy alluvium-clayey alluvium	24-27
10	Benoda	Deccan Trap	3.82	Weathered amygdaloidal-sheeted-columnar	35-38
11	Loni-I	Deccan Trap	3.18	Weathered sheeted- massive	48-56
12	Loni-II	Deccan Trap	2.96	Weathered sheeted- massive	52-64

Table No.3a Tank water levels and groundwater levels near Pimpalkhuta percolation tank

Month.	Tank R.L (In m).	OBW -1 (In m)	OBW -2 (In m).	OBW -3 (In m).	OBW -4 (In m).	OBW -5 (In m).	OBW -6 (In m).	OBW -7 (In m).	OBW -8 (In m).	OBW -9 (In m).	OBW-10 (In m).
Jn-09	391.89	384.9	383.8	382	382.2	377.2	384.5	380.7	379.1	381.0	380.38
Jl-09	393.24	389.5	388.9	387.6	386.2	384.7	390.8	386.6	386.5	383.0	383.38
Ag-09	393.73	389.5	389.0	387.8	386.5	384.9	391.6	386.8	386.9	384.0	384.58
Sp-09	394.79	389.2	388.6	387.2	386.4	384.2	391.9	386.2	386.6	383.6	383.13
Ot-09	394.61	389.0	388.2	385.4	385.4	382.0	391.9	384.3	385.2	382.1	383.78

Nv-09	393.99	388.8 3	387.8 3	384.8 2	378.6 8	377.9 8	391.7 4	382.6	382.6 9	382.7 3	383.68
Dc-09	393.55	388.9 3	387.7 5	382.3 2	381.0 8	378.8	391.9 9	381.9	380.8 4	382.2 3	359.88
Jn-10	393.22	389.0 3	387.6 9	384.4 4	383.8 4	376.5	391.7 9	381.1	383.5 9	382.2 3	382.46
Fb-10	392.67	385.5 3	386.6 3	383.2 2	382.2 8	375.3 8	388.5 9	379.4	383.6 9	381.4 3	378.98
Mr-10	392.28	388.7 3	387.6 3	383.9 2	380.8 8	379.3 8	389.2 4	378.6	382.9 9	381.6 3	383.08
Ar-10	391.44	388.0 3	385.8 3	383.7 2	383.1 1	375.9 3	389.6 9	378	380.5 9	381.0 8	380.68
My-10	390.26	387.7 3	385.7 5	383.7 2	382.1 3	374.9 3	388.6 9	378	379.2 9	379.8 8	379.68
Corr. Coeff.		58.4	74.1	58.7	35.8	62.4	73.6	76.6	67.5	75	6.3

Table No.3b Tank water levels and groundwater levels near Mangona percolation tank

Mont h.	Tank R.L (In m).	OBW -1 (In m)	OBW -2 (In m).	OBW -3 (In m).	OBW -4 (In m).	OBW -5 (In m).	OBW -6 (In m).	OBW -7 (In m).	OBW -8 (In m).	OBW -9 (In m).	OBW 10 (In m).	OBW11 (In m).
Jn-09	442.56	446.1 8	444.5 7	445.5 2	445.5 7	446.3 1	438.3 3	439.7 8	439.3 4	434.7 5	445.5 5	427.93
Jl-09	441.66	446.4 3	445.0 5	446.1 6	446.7 2	447.3 7	438.5 1	440.7 3	439.8 8	435.8 4	445.8 5	429.28
Ag- 09	440.77	448.1 3	446.1 2	446.2 2	447.7 2	448.7 2	447.7 1	440.9 3	440.2 9	440.9 9	446.7 5	430.08
Sp- 09	440.76	449.0 3	448.9 5	445.9 2	443.9 2	447.6 4	439.9 1	441.6 3	440.5 3	442.4 4	443.9 5	434.76
Ot- 09	440.92	448.5 3	448.6 5	447.9 6	447.8 3	448.0 3	440.6 2	441.7 4	439.9 4	441.7 4	445.3 5	434.43
Nv- 09	441.76	447.8 3	447.5 7	445.4 4	442.7 3	444.6 8	437.9 2	439.0 2	435.7 9	439.1 2	446.7 5	433.88
Dc- 09	442.46	445.5 3	446.9 5	445.7 8	446.2 3	446.9 8	437.1 2	439.7 4	438.7 4	436.9 4	446.3 5	433.13
Jn-10	443.12	446.8 3	447.0 5	446.6 5	447.2 5	447.1 8	439.9 2	440.1 4	438.3 4	440.5 4	446.4 7	443.11

Fb-10	444.08	446.0	443.9	444.6	443.3	445.8	437.2	438.8	438.3	439.2	445.3	432.71
Mr-10	444.72	445.5	444.7	444.8	445.2	445.8	438.2	437.1	439.9	439.4	445.4	433.04
Ar-10	445.68	443.3	444.5	445.5	441.6	442.2	438.1	437.5	439.7	436.6	444.2	432.23
My-10	446.64	443.2	443.0	443.5	443.9	445.9	439.1	437.0	439.1	437.5	443.5	432.13
Corr. Coeff		91.8	77.3	73.7	53.5	80.7	43.96	92.05	7.22	40.36	52.28	6.8

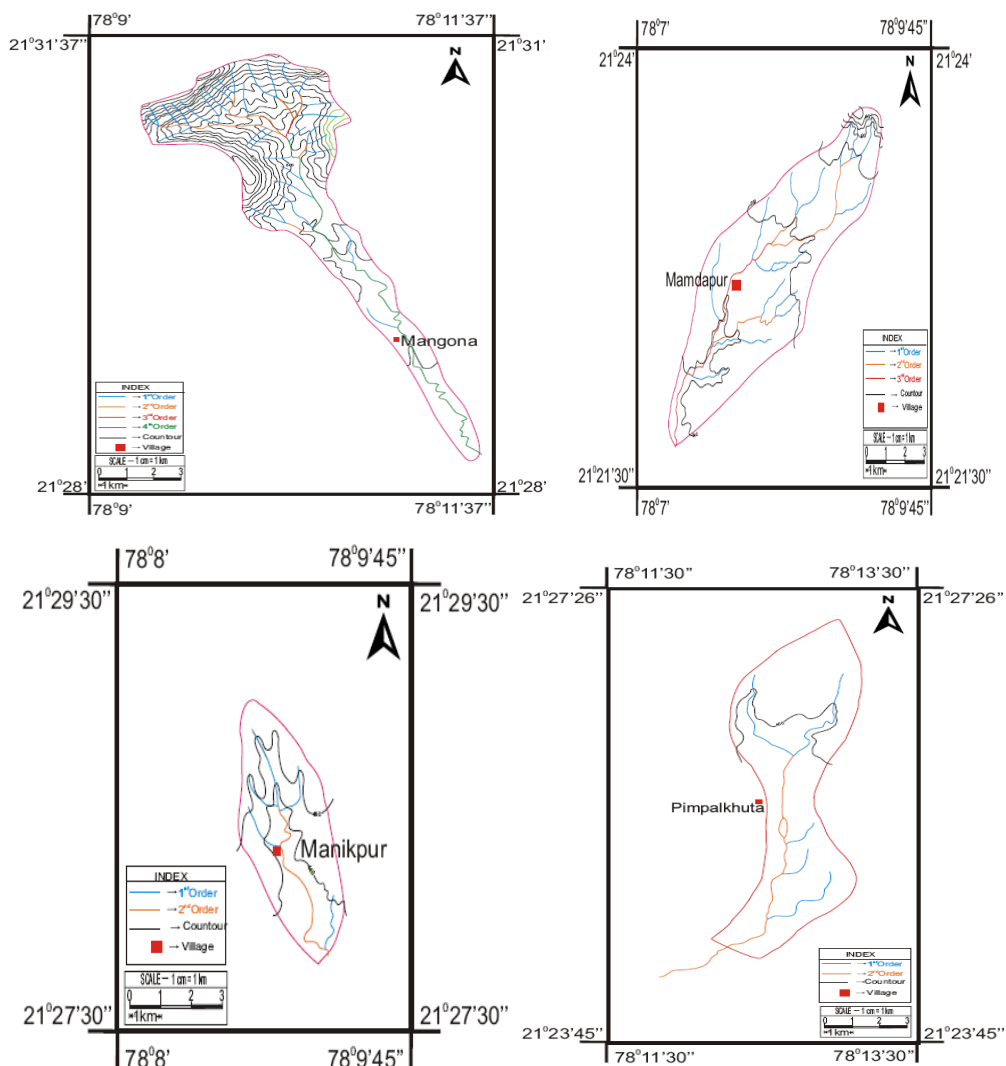
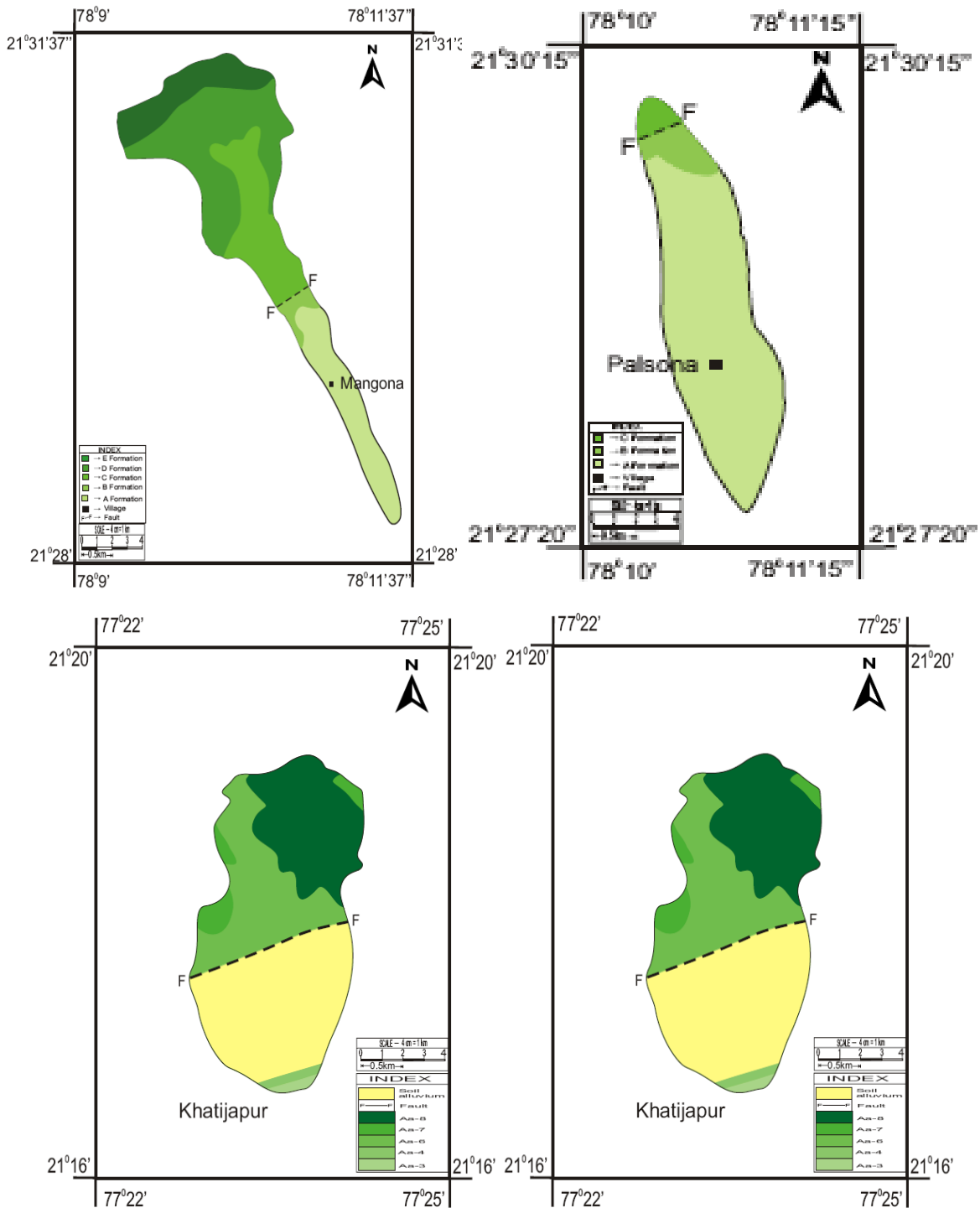
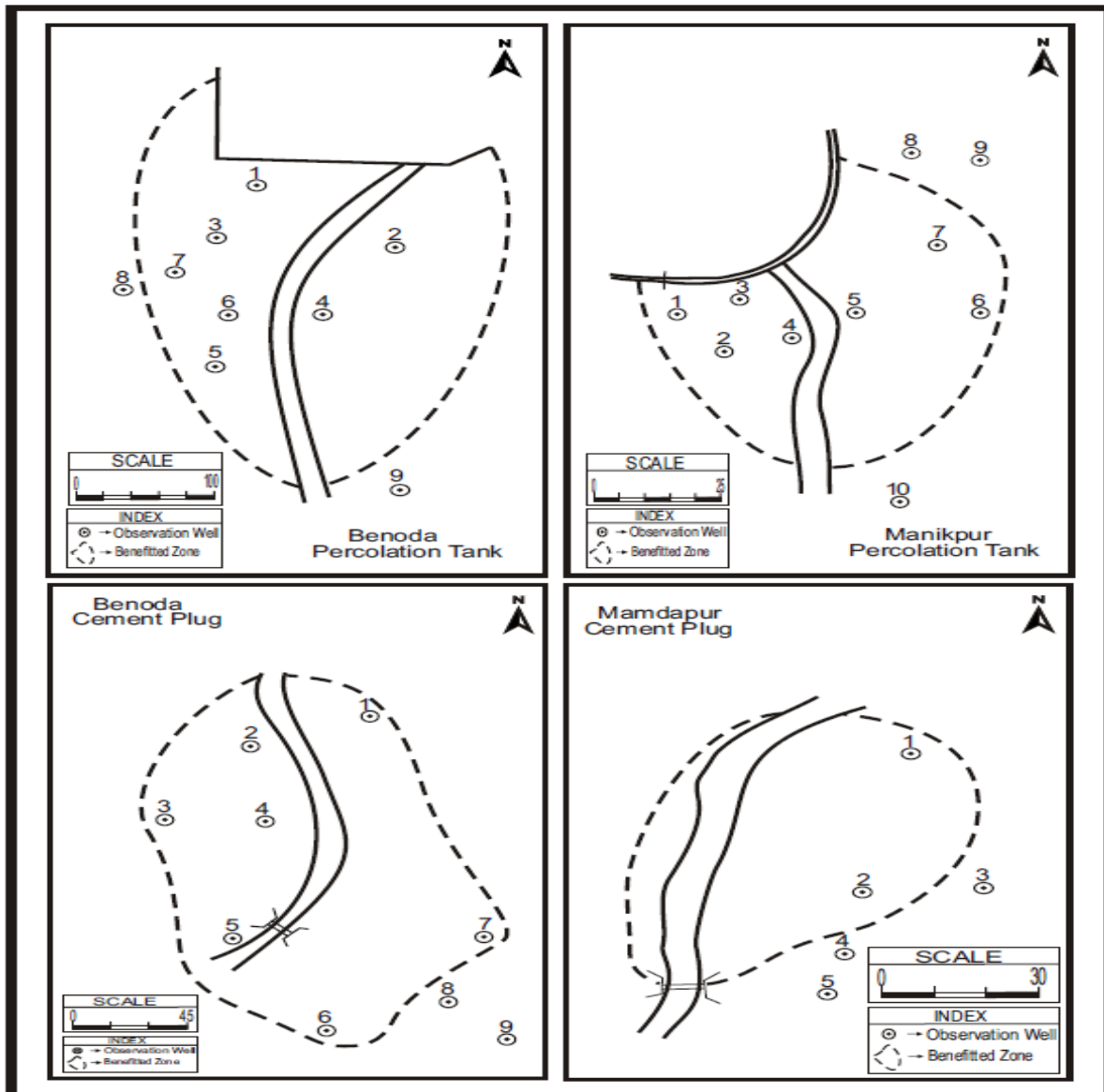


Fig.2 Drainage map of four Artificial recharge structures, a.Mangona, b. Mamdapur, c. Manikpur and d. Pimpalkhuta.



Geological set up at four artificial recharge structures,
a. Mangona, b. Palsona, c. Khatijapur and d. Gond wagholi.



Area benefited in four by artificial recharge structures of Amravati district, Maharashtra.

V. CONCLUSIONS

Geologically, artificial recharge structures have good efficiencies if there exists a weathered bed rock more than 3 m. In alluvial area the site is beneficial if sandy zone is present. In Deccan trap thick weathered zeolitic / amygdaloidal followed by sheeted jointed zone with massive / columnar jointed rocks are good sites. In case of alluvium, presence of thick clayey zone hinders the site. Sandy zone at shallow depth, trapped between two clayey zones are most favorable sites.

Morphometric characteristics do not control significantly on the sites of artificial recharge, though higher order streams are more favorable.

Resistivity value range of 25-35 with layer thickness more than 3.0 m are very good sites for artificial recharge.

Efficiencies of artificial recharge structure indicate that the efficiencies of percolation tanks vary from 63 to 82% while that of cement plug vary from 78 to 90.5%. Seepage loss range in percolation tank varies from 5.2 to 14% while for cement plug it ranges from 8.2 to 20.5%.

Evaporation losses accounts up to 10.6% in percolation tanks. Higher evaporation losses were observed in cement plugs.

Rise in water level ranges from 2 to 8 m in percolation tanks and 1-2.5m in case of cement plugs. The area benefited varies from 60-110 hectars in percolation tanks and 2-10 hectars in cement plug.

Findings of this can easily be replicated with modification based on site conditions in major parts of Maharashtra where the geological set up along with other parameters are similar.

VI. REFERENCES

- [1]. Bagade,S.J., (1990) Construction of jacket well by radial bore blast technique. Proc.All India Sem. Modern tech. Of Rainwater Harvesting, Water conservation and Art. Rec. for drinking, Afforestation, horticulture and agriculture, Pune. pp.773- 782.
- [2]. C.G.W.B., (1998) Artificial Recharge project in Orange Growing Area Amravati District and Banana Growing Area, Jalgoan District, Maharashtra.CGWB (CR).
- [3]. Edmunds, M.W., Darling, W.G., and Kinniburgh, D.G., (1990) Solute profile techniques or recharge estimation in semi-arid and arid terrain. Groundwater Recharge, IAH. V. 8, pp. 257-270.
- [4]. Eriksson, E., and Khunakasem, V., (1969) Chloride concentration in groundwater, recharge rate of deposition of chloride in Israel coastal plain. J. of Hydrology.V. 7, pp. 178-197.
- [5]. GEC, (1997) Groundwater resource estimation methodology.Report of the Ground Water Estimation Committee, Ministry of Ground Water Resources, Government of India. 105 p.
- [6]. Gee, G.W., and Hillel, D., (1988) Groundwater Recharge in Arid Regions. Review and Critique of Estimation methods Hydrological Processes. Vol.2 pp. 255- 266.
- [7]. Jadhav,F.J., (1990) Augmentation of groundwater by Artificial recharge at village Dindnerli, district Kolhapur and experiment by bore blasting technique. Proc. All India Sem. Modern Techniques of Rainwater harvesting, water conservation and Art.Rec. for drinking water, Afforestation, horticulture and agriculture, Pune. Pp 858-863.
- [8]. Raju,K.C.B.,(1985) Recharge through percolation tanks and subsurface dykes, India.Proc. Semi. On Art. Rec. of Groundwater held at Ahmadabad, India. Pp. 12c-1.
- [9]. Sharma, S.C., (1985) Recharge in Gujrat State by injection, spreading through percolation tanks, check dams, bandharas and other methods. Proc. Semi. On Artificial Recharge of Groundwater, held at Ahmadabad, India. Pp. 160.
- [10].Siddiqui, M.A.,et al, (1990) "Application of Hydrofractured Stimulation Techniques to Rejuvenate the poor yielding Borewells in the Basaltic Terrain of Deccan Provience" All India Seminar on Modern

Techniques of Rainwater Harvesting water Conservation, and Artificial Recharge for Drinking Water, Afforestation, Horticulture and Agriculture Rural Devel. Dept. Govt.of Maharashtra, Directorate of GSDA p.127.

- [11].Sukhija, B.S., Reddy, D.V., et al, (1997) A method for evaluation of artificial recharge through percolation tanks using environmental Chloride. Groundwater. V.35, No. 1., pp 161-165.

A Discriminatively Trained Fully Connected Conditional Random Field Model for Blood Vessel Segmentation in Fundus Images

Durgeshwari Vairale*¹, Dr. Ram K. Nawasalkar²

*¹Department of Computer Science, G.S. Tompe Arts, Comm. and Science College, Chandur Bazar, Dist. Amravati, Maharashtra, India

²Department of Comp. Science, G.S. Tompe Arts, Comm. and Science College, Chandur Bazar, Dist. Amravati, Maharashtra, India

ABSTRACT

Automated retinal blood vessel segmentation is critical for early computer-aided diagnosis of certain ophthalmological and cardiovascular illnesses. Traditional supervised vessel segmentation algorithms are often based on pixel classification, which classifies all pixels as vessel or non-vessel. In this research, we present a novel retinal vascular segmentation approach that uses cross-modality dictionary learning to extract vessels based on vessel block segmentation. First, we use multi-scale filtering to improve the structural information of vessels. Then, for the aim of vessel segmentation, cross-modality description and segmentation dictionaries are learnt in order to create the intrinsic link between the augmented vessels and the labelled ground truth vessels. Effective pre-processing and post-processing are also used to improve performance. Experiment findings on three benchmark data sets show that the suggested technique is capable of producing satisfactory segmentation results.

Keywords: Vessel Segmentation, Pixel, Vessel block.

I. INTRODUCTION

The retina is a light-sensitive tissue that makes up the inner layer of the eye. It comprises brain cells and blood vessels and is the only tissue in the human body that can be used to visualize blood vessels non-invasively, which is important in the diagnosis and treatment of many disorders including as diabetes, hypertension, cardiovascular disease, and cancer. Because of the diversity of lighting settings, low contrast tiny vessel identification, and the trade-off between accuracy and computing efficiency, segmenting retinal blood vessels is a difficult challenge. The fundus camera may be used to see retina as an image. These pictures are often noisy, poorly contrasted, and non-uniformly lighted; also, brightness differences exist within the same image as well as across separate photos.. In medical practice, retinal scans are often utilized to diagnose vascular and non-vascular disease. Retinal pictures give information about retinal changes. vascular structure, which is shown in disorders such Diabetes, occlusion, glaucoma, hypertension, and cardiovascular disease are

all possibilities. Ailment and stroke These disorders often evolve. Reflectivity, tortuosity, and blood vessel patterns If left alone These medical problems, if left untreated, may lead to blindness. Deterioration, if not blindness Early exposure to these change is necessary for adopting preventative measures and as a consequence, severe vision loss might be averted. The fundus pictures with diabetic retinopathy show a portion of the eye tissues that are already damaged. This is more appropriately known as a red lesion. These red lesions may induce swelling in the retina, blood arteries termed micro aneurysms, and bleeding. In the event of brilliant lesions, a mass cell aggregation and fluffy areas in the retina may ensue. The primary goal is to distinguish micro aneurysms from stretched out formations. Although micro aneurysms are early indicators of diabetic retinopathy, haemorrhages are more important and beneficial in determining the severity of the illness. Personal use of allows clinicians to study the retina and its anatomical components, including the vascular tree, the optic disc, and the fovea, in a non-invasive manner [2]. The development of automatic tools for the early detection of retinal diseases is beneficial because they can be easily integrated into screening programs where large numbers of images are collected from patient populations and careful evaluation by physicians is not feasible in a reasonable time [3]. These methods are often supplemented by an investigation of the morphological characteristics of retinal blood vessels, which provides useful information for the diagnosis, screening, treatment, and assessment of the aforementioned illnesses [3]. In other circumstances, vessels must be discovered beforehand in order to automate the diagnosis of lesions of comparable intensity [4]. However, any automated examination of the retinal vasculature must first be precisely segmented. This work is now conducted manually by qualified professionals, despite the fact that it is exceptionally tedious and time-consuming. Furthermore, imaging process difficulties, such as insufficient contrast between vessels and background and uneven background illumination, as well as variability in vessel width, brightness, and shape, reduce the coincidence between segmentations performed by different human observers significantly [5]. These findings inspire the development of autonomous blood vessel segmentation systems that do not need human involvement [3]. Despite multiple efforts, the topic of automated retinal vascular segmentation remains an important area of study owing to the potential significance of having more precise findings [2]. Existing techniques may be divided into two categories: supervised and unsupervised. To develop a model or a classifier, supervised approaches need a collection of training samples—typically constituted of pixels features and their known annotations.

II. BACKGROUND

Ming Li et al 2018 Fundus images are one of the main methods for diagnosing eye diseases in modern medicine. The vascular segmentation of fundus images is an essential step in quantitative disease analysis. Based on the previous studies, we found that the category imbalance is one of the main reasons that restrict the improvement of segmentation accuracy. This paper presents a new method for supervised retinal vessel segmentation that can effectively solve the above problems. In recent years, it is a popular method that using deep learning to solve retinal vessel segmentation. We have improved the loss function for deep learning in order to better handle category imbalances. By using a multi-scale convolutional neural network structure

and label processing approach, This results have reached the most advanced level. This approach is a meaningful attempt to improve blood vessel segmentation and further improve the diagnostic level of eye diseases.

Zafer Yavuzet al 2014 Usage of Computer Aided Diagnostic (CAD) systems is increasing rapidly. Blood vessel segmentation on retinal fundus images could be used as a CAD system for diagnosis of various retinal diseases. In This paper, blood vessels are segmented on retinal fundus images. Firstly, Gabor filter and morphological top-hat transform are applied after pre-processing step in order to enhance blood vessels. Afterward, performed p-tile thresholding method to obtain binary vessel image. At the last step a post processing method is applied to increase accuracy. In order to test the developed system, the images obtained from STARE and DRIVE databases are used. Finally, 94.02% of accuracy for STARE database and 94.59% of accuracy for DRIVE database are obtained as a result, which is promising.

M. Usman Akram et al 2009 The appearance and structure of blood vessels in retinal images play an important role in diagnosis of eye diseases. This paper proposes a method for segmentation of blood vessels in color retinal images. We present a method that uses 2-D Gabor wavelet to enhance the vascular pattern. Segmentation of the blood vessels using adaptive thresholding. The technique is tested on publicly available DRIVE database of manually labeled images which has been established to facilitate comparative studies on segmentation of blood vessels in retinal images. The proposed method achieves an area under the receiver operating characteristic curve of 0.963 on DRIVE database.

The improper circulation of blood flow inside the retinal vessel is the primary these of most of the optical disorders including partial vision loss and blindness. Accurate blood vessel segmentation of the retinal image is utilized for biometric identification, computer-assisted laser surgical procedure, automatic screening, and diagnosis of ophthalmologic diseases like Diabetic retinopathy, Age-related macular degeneration, Hypertensive retinopathy, and so on. Proper identification of retinal blood vessels at its early stage assists medical experts to take expedient treatment procedures which could mitigate potential vision loss. This paper presents an efficient retinal blood vessel segmentation approach where a 4-D feature vector is constructed by the outcome of Bendlet transform, which can capture directional information much more efficiently than the traditional wavelets. Afterward, a bunch of ensemble classifiers is applied to find out the best possible result of whether a pixel falls inside a vessel or non-vessel segment. The detailed and comprehensive experiments operated on two benchmark and publicly available retinal c image databases (DRIVE and STARE) prove the effectiveness of the proposed approach where the average accuracy for vessel segmentation accomplished approximately 95%. Furthermore, in comparison with other promising works on the a foremen This paper presents a novel three-stage blood vessel segmentation algorithm using fundus photographs. In the first stage, the green plane of a fundus image is pre-processed to extract a binary image after high-pass filtering, and another binary image from the morphologically reconstructed enhanced image for the vessel regions. Next, the regions common to both the binary images are extracted as the major vessels. In the second stage, all remaining pixels in the two binary images are classified using a Gaussian mixture model (GMM) classifier using a set of eight features that are extracted based on pixel neighborhood and first and second-order gradient

images. In the third post processing stage, the major portions of the blood vessels are combined with the classified vessel pixels.

III. SIGNS OF DIABETIC RETINOPATHY

Ophthalmologists visually assess and analyze retinal pictures to identify retinal disorders such as diabetic retinopathy (DR). The DR is the Diabetic eye complications are the most prevalent. Retinopathy. Diabetic patients must be tested for Diabetic eye should be detected early and treated promptly. Illnesses that may dramatically lower the chance of visual loss. Large boats are generally simple to detect because to their stark contrast with the backdrop in the photographs however, detecting tiny vessels is significantly more challenging owing to due to the photos' poor contrast The suggested To remove the thin vessels, a new filter is used. So discovery of a blockage in the retinal blood vessels owing to the ability to identify both big and thin vessels Early Patients may benefit from early diagnosis and therapy. Individuals suffer from comparable eye illnesses

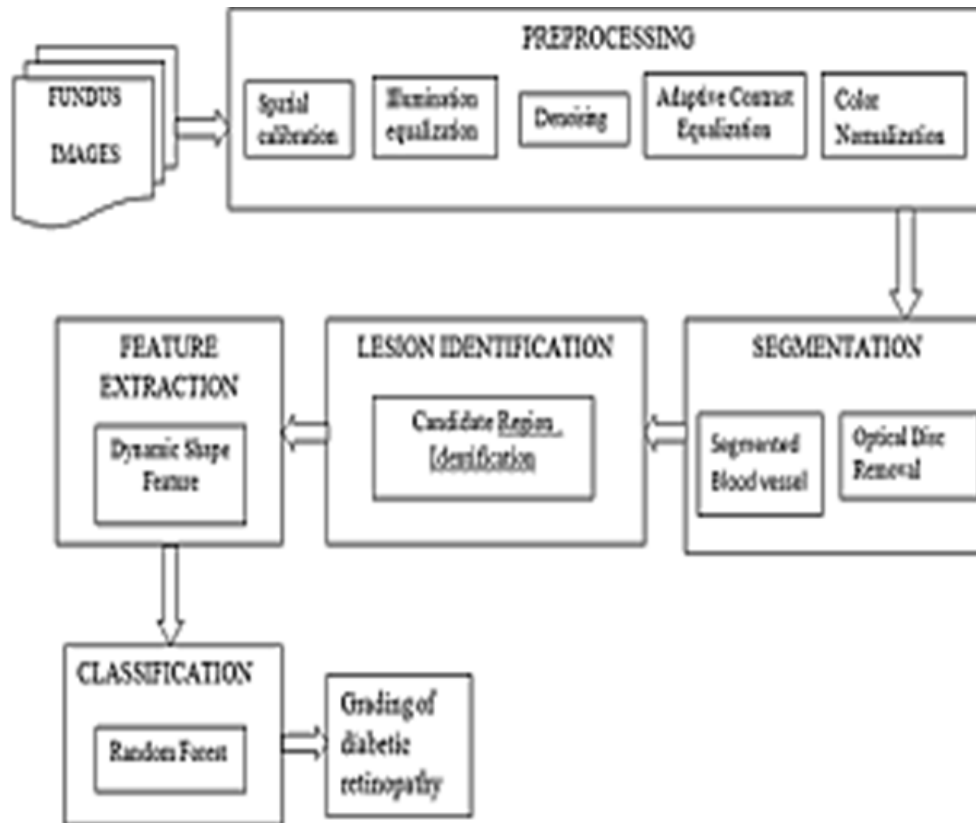
1. Micro-aneurysms: These are balloon-like formations on the sidewalls of capillaries that form when the capillary walls deteriorate. Micro-aneurysms appear as solitary red spots that are not connected to any blood artery. They are often the first indicators of DR that may be identified.
2. Hemorrhages: Capillary wall breakdown leads in blood leakage, which may vary in size and shape depending on the retinal layer in which the veins are situated. Dot, blot, and flame hemorrhages are the three types of hemorrhages.
3. Exudates: Oedema leaking is often caused by capillary collapse. Oedema accumulation causes retinal thickening. Exudates are oedema-related lipid residues. They manifest as waxy yellow lesions with a variety of patterns such as isolated patches, tracking lines, rings (circinates), and macular stars.

IV. METHODOLOGY

Exact recognition of the optic disc in color retinal pictures is a critical challenge in an automated retinal image processing system. The detection of the same is required for the segmentation of other normal and diseased retinal characteristics. In these photos, the position of the optic disc is employed as a reference length for measuring distances, particularly when identifying the macula. The optic disc appears as a brilliant spot with a circular or oval shape that is broken up by outgoing vessels. Optic nerves and blood vessels may be seen emerging from the optic disc into the retina. As a result, it is also known as the blind area. Ophthalmologists visually assess and analyze retinal pictures to identify different retinal disorders such as diabetic retinopathy (DR). To make their task simpler, a retinal image analysis system may be built to make diagnosis more efficient. Diabetic Retinopathy (DR) is the most prevalent eye consequence in diabetes. Diabetic patients must be examined in order to discover and treat diabetic eye disorders early, which may dramatically minimize the risk of vision loss. To make their task simpler, a retinal image analysis system may be built to make diagnosis more efficient. To remove the thin vessels, the suggested approach employs a novel

filter. The initial stage in any automated retina analysis system is to segment retinal anatomical structures. Large boats are reasonably simple to spot because to their significant contrast against the backdrop in the photographs, while tiny vessels are considerably more difficult to detect due to their low contrast in the images. To remove the thin vessels, the suggested approach employs a novel filter.

V. BLOCK DIAGRAM



VI. INTERPRETATION

1. Vessel Segmentation: The segmentation task can be posed as an energy minimization problem in a conditional random field (CRF). In the original definition of CRFs, the respective images are mapped to graphical representation, where each pixel represents a node, and every node is connected with an edge to their neighbors according to a certain connectivity rule.
2. Lesion Detection: Among the candidates, several regions correspond to no lesions, such as vessel segments and remaining noise in the retinal background. To discriminate between these false positives and true lesions, an original set of features, the DSFs

The expected outcome of the project is:

- Detection both MAs and HEs in eye

- Analysis of diameter and tortuosity of the vessels, classification of veins and arteries, calculation of the arteriovenous ratio.
- Automated or semi-automated segmentation methods would have improvements in efficiency and accuracy.
- Fast, readily available, highest spatial resolution.

VII. CONCLUSION

This research focuses on the segmentation of blood vessels in retinal fundus pictures for the possible use of automated diabetic retinopathy diagnosis. Five algorithms were built in this research based on methodologies from relevant literature. These five algorithms were then integrated using two separate ways to maximize their respective benefits. To assess the performance of each of the created approaches, many performance metrics were generated. These metrics include precision, sensitivity, and specificity. Each of the algorithms created offers trade-offs between these performance indicators. However, when all performance indicators are averaged, the improved hybrid algorithm results tend to outperform.

VIII. REFERENCES

- [1]. L. Dai, L. Wu, H. Li et al., "A deep learning system for detecting diabetic retinopathy across the disease spectrum", *Nat Commun*, vol. 12, no. 3242, 2021.
- [2]. Kangrok Oh, Hae Min Kang, Dawoon Leem, Hyungyu Lee, Kyoung Yul Seo and Sangchul Yoon, "Early detection of diabetic retinopathy based on deep learning and ultra-wide-field fundus images", *Scientific Reports*, vol. 11, pp. 1897, 2021.
- [3]. Sam E Mansour, David J Browning, Keye Wong, Harry W Flynn and Abdhish R Bhavsar, "The Evolving Treatment of Diabetic Retinopathy", *Clinical Ophthalmology*, vol. 14, pp. 653-678, 2020.
- [4]. M. Xu et al., "High-performance coherent optical modulators ", *Nature Commun.*, vol. 11, pp. 1-7, 2020.
- [5]. Mona Leeza and Humera Farooq, "Detection of severity level of diabetic retinopathy using Bag of features model", *IET Computer Vision*, vol. 13, no. 5, pp. 523-530, 2019
- [6]. M. Tsukikawa and A. W. Stacey, "A review of hypertensive retinopathy and chorioretinopathy", *Clin. Optometry*, vol. 12, pp. 67-73, May 2020.
- [7]. B. Bateman, A. R. Jha, B. Johnston and I. Mathur, *A New Interactive Approach to Understanding Supervised Learning Algorithms*, Birmingham, U.K.:Packt Publishing, pp. 342-346, 2020.
- [8]. K. D. Kirange, "Diabetic retinopathy detection and grading using machine learning", *Int. J. Adv. Trends Comput. Sci. Eng.*, vol. 8, no. 6, pp. 3570-3576, 2019.
- [9]. R. Buló, G. Neuhold and P. Kotschieder, "Loss maxpooling for semantic image segmentation", *CVPR*, vol. 7, July 2017..

- [10]. N. Strisciuglio, G. Azzopardi, M. Vento and N. Petkov, "Supervised vessel delineation in retinal fundus images with the automatic selection of b-cosfire filters", *Machine Vision and Applications*, vol. 27, no. 8, pp. 1137-1149, 2016.
- [11]. S. Aslani and H. Sarnel, "A new supervised retinal vessel segmentation method based on robust hybrid features", *Biomedical Signal Processing and Control*, vol. 30, pp. 1-12, 2016.
- [12]. D. Maji, A. Santara, P. Mitra and D. Sheet, *Ensemble of deep convolutional neural networks for learning to detect retinal vessels in fundus images*, 2016.
- [13]. A. Lahiri, A. G. Roy, D. Sheet and P. K. Biswas, "Deep neural ensemble for retinal vessel segmentation in fundus images towards achieving label-free angiography", *Engineering in Medicine and Biology Society (EMBC) 2016 IEEE 38th Annual International Conference of the. IEEE*, pp. 1340-1343, 2016.
- [14]. M. Melinscak, P. Prentasic and S. Loncaric, "Retinal vessel segmentation using deep neural networks", *VISAPP 2015 (10th International Conference on Computer Vision Theory and Applications)*, 2015.

EEG Signal Processing for Fetus and Mother Using MATLAB

Ankita Gurjar^{*1}, Dr. Ram K. Nawasalkar¹

^{*1}Department of Computer Science, G.S. Tompe Arts, Commerce and Science College, Chandur Bazar, Dist. Amravati, Maharashtra, India

ABSTRACT

During pregnancy, it is critical to diagnose the mother's and child's heartbeats, and fetal electrocardiogram (FECG) extraction is the method utilised to do so. During pregnancy and labour, the signal carries accurate information that might assist doctors. Independent component analysis has been used to build an easy-to-use technique. An efficient approach has been proposed using the ICA. For FECG extraction, the technique employs PCA and ICA. An algorithm written in MATLAB was used to implement the FECG extraction approach. The FECG signal that was recovered is noise-free. Post processing was utilised to detect the QRS complex, which used an adaptive noise filtering method to count the R-R peaks. The detection method can count the heart rate of the FECG signal, as shown in the end result. This project creates a complete FECG extraction model utilising effective algorithms and adaptive filters, and then produces the FECG data.

Keywords: ECG(Electrocardiography), FECG (Fetal Electrocardiogram), ICA (Independent Component Analysis),PCA(Principal component analysis)

I. INTRODUCTION

Every year, one in every one hundred kids is born with a heart defect. This can be caused by a genetic syndrome, an inherited condition, or environmental causes such as drug abuse. In any event, regular monitoring of the baby's heart is required prior to birth. As a result, Fetal ECG (FECG) signals are required to monitor the baby's heart status, so that any anomalies discovered can be treated clinically by the concerned specialists. Fetal ECG monitoring is a common method for detecting and diagnosing fetal abnormalities. By diagnosing the fetal ECG signal during the prenatal stage, the clinician can readily prepare himself or herself for any fetal anomalies. It's the simplest and least invasive way to diagnose a variety of cardiac conditions. The Fetal ECG (FECG) represents the heart's varied electrical activities and so provides useful information about its physiological state. The FECG signal can be easily collected from a pregnant woman's abdomen, whereas the maternal electrocardiogram (MECG) signal can be taken from her chest. The addition of the MECG signal to the FECG signal is usually a source of irritation. The FECG signal generated by putting electrodes on the maternal belly provides minute details about the fetal status that are particularly important during diagnosis. The maternal ECG (MECG) signal and electromyogram (EMG) signal are contaminated by various noise and skin impedance, whereas the FECG signal is contaminated by various noise and skin

impedance. The electrocardiogram (ECG) is a method of describing the electrical activity of the heart. Three basic types of waves make up ECG signals. The heart rate of the abdominal ECG (AECG) signal is determined by the peaks value of the QRS complex. As a result, it is critical for doctors to diagnose heart problems before they cause harm to the fetus or the mother. When the ECG signals from the abdomen leads are combined, a composite signal is created. Adaptive filtering, wavelet Transform, Independent component Analysis, Principle Component Analysis, Fetal ECG Extraction from Maternal Abdominal ECG Using Neural Network, Fetal ECG Extraction for Fetal Monitoring Using SWRLS Adaptive Filter and Extraction of Fetal ECG from Maternal ECG using Least Mean Square Algorithm are some of the methods for extracting FECG from AECG. Every year, one in every one hundred kids is born with a heart defect. This can be caused by a genetic syndrome, an inherited condition, or environmental causes such as drug abuse. In any event, regular monitoring of the baby's heart is required prior to birth. As a result, Fetal ECG (FECG) signals are required to monitor the baby's heart status, so that any anomalies discovered can be treated clinically by the concerned specialists. Fetal ECG monitoring is a common method for detecting and diagnosing fetal abnormalities. By diagnosing the fetal ECG signal during the prenatal stage, the clinician can readily prepare himself or herself for any fetal anomalies. It's the simplest and least invasive way to diagnose a variety of cardiac conditions. The Fetal ECG (FECG) represents the heart's varied electrical activities and so provides useful information about its physiological state. The FECG signal can be easily collected from a pregnant woman's abdomen, whereas the maternal electrocardiogram (MECG) signal can be taken from her chest. The addition of the MECG signal to the FECG signal is usually a source of irritation. The FECG signal generated by putting electrodes on the maternal belly provides minute details about the fetal status that are particularly important during diagnosis. The maternal ECGb(MECG) signal and electromyogram (EMG) signal are contaminated by various noise and skin impedance, whereas the FECG signal is contaminated by various noise and skin impedance. The electrocardiogram (ECG) is a method of describing the electrical activity of the heart. Three basic types of waves make up ECG signals. The heart rate of the abdominal ECG (AECG) signal is determined by the peaks value of the QRS complex. As a result, it is critical for doctors to diagnose heart problems before they cause harm to the fetus or the mother. When the ECG signals from the abdomen leads are combined, a composite signal is created.

II. BACKGROUND

Manisha Dodatale et al 2021 says that During pregnancy, it is critical to diagnose the mother's and child's heartbeats, and fetal electrocardiogram (FECG) extraction is the method utilised to do so. During pregnancy and labour, the signal carries accurate information that might assist doctors. Independent component analysis has been used to build an easy-to-use technique. An efficient approach has been proposed using the ICA. For FECG extraction, the technique employs PCA and ICA. An algorithm written in MATLAB was used to implement the FECG extraction approach. The FECG signal that was recovered is noise-free. Post processing was utilised to detect the QRS complex, which used an adaptive noise filtering method to count the R-R peaks. The detection method can count the heart rate of the FECG signal, as shown in the end result. This

project creates a complete FECG extraction model utilising effective algorithms and adaptive filters, and then produces the FECG data.

Esha Ahuja et al 2016 The extraction of Fetal Electrocardiogram (FECG) is vital to know the well being of the fetus and useful for doctors to decide the mode of delivery and period. The FECG contains activity of electrical depolarization and repolarization of fetal heart. In this paper, a simple algorithm, Independent Component Analysis (ICA), is used to extract FECG from Abdominal Electrocardiogram (AECG) of mother. The database used is non-invasive fetal electrocardiogram and direct fetal electrocardiogram, taken from physionet.org. ICA comes under the classification of Blind Source Separation (BSS) method. ICA is basically a filtering solution which gives the signal from an unknown source. In this problem, the signal from an unknown source is Fetal ECG. It is to be derived from the pure maternal ECG that is thorax signal and abdominal ECG.

Md. Kafiul Islam et al 2020 EEG recordings are usually affected by various artifact types come from non-neural sources and make it difficult for accurate signal classification in the later stage. Thus reliably detecting and removing artifacts from EEG by an automated signal processing algorithm is an active research area. In this paper we have developed a wavelet based artifact removal algorithm from EEG data that selects the best (optimal) threshold parameters, and hence consequently provides the best performance of artifact removal. In the proposed algorithm we choose to sweep both the wavelet filter parameter and threshold parameters until the best accuracy and/or least distortion is achieved by making a decision based on a reference dataset. The criteria for optimized selection are based on the metrics that quantify both amount of artifact removal and amount of distortion in the signal in both time and frequency domain. The algorithm is tested on synthesized EEG data that include different artifact templates and thus quantifies the performance based on several time and frequency domain measures. The achieved results prove that by selecting the optimum mother wavelet and parameter values adaptively would give the best performance both with regard to amount of artifact removal and least signal distortion compared with selecting any predefined mother wavelet and/or constant threshold parameter. This research would help the EEG signal analysis community a platform to work further in future on such problem to be able to properly select the wavelet parameters.

III. ADAPTIVE FILTERING BASED FECG EXTRACTION

An adaptive filter is one that self-adjusts its transfer function in response to an error signal that drives an optimization process. For the separation of fetal and maternal signals, various adaptive filters have been applied. These approaches extract the deadly QRS waves by training an adaptive or matching filter with one or more reference maternal signals[1][2], For MEEG cancellation and FECG extraction, the kalman filter, a broad form of adaptive filter, requires simply an arbitrary MEEG as a reference. The temporal dynamics of AECG signals were synthesized using a collection of state-space equations and a Bayesian filter, which was employed for ECG de noising. However, when the maternal and deadly components are completely overlapped in time, the filter is unable to distinguish between them. When the waves of mixed signals fully overlap in time, it is said to be wholly overlapped. This filter makes it difficult to filter out the required ECG.

A superior strategy was proposed in Buses multistage adaptive filtering for FECG extraction, where MECG cancellation was conducted using thoracic ECG as a reference signal, and de noising methods were used to improve the quality of the resultant signal. Normally, an adaptive filter requires two input signals (AECG signal and Thoracic ECG), but in this case, the thoracic ECG has been scaled and squared. Adaptive filters were well calibrated to conduct the extraction once scaling factors were chosen. The advantage of this technique is that the input thoracic signal does not have to be original, as it was collected from a pregnant lady whose AECG was also provided as primary input; alternatively, a signal that is very similar can be used. This self-adjusting filter uses three alternative methods to boost the SNR ratio by altering filter coefficients: LMS, RLS, and NLMS. The FECG was extracted using a linear adaptive filter[3].The FECG was extracted using abdominal ECG as primary inputs and thoracic ECG collected from the mother's chest as reference inputs. Despite the fact that the offered method gives a solution, it fails to extract when maternal and fetal signals coincide. As a result, it is not appropriate for clinical use.

IV. METHODOLOGY

The subjective signal and the wavelet function are convoluted in the Wavelet Transform. The Wavelet Transform divides a signal into two parts, the detail signal and the approximation signal. The detail signal is found in the upper half of the frequency component, while the approximation signal is found in the lower half. In the discrete wavelet domain, multi-resolution analysis is thus possible. A significant number of well-known wavelet families and functions are available for a wide range of applications. Bi-orthogonal, Coiflet, Harr, Symmlet, and db (Daubechies) wavelet are some of the wavelet families. The wavelet function is utilized depending on the application. These wavelet families have been used in a variety of research projects. It is not possible to select a certain wavelet. To obtain the wavelet analysis, we use the MATLAB application. The wavelet toolkit in MATLAB is quite extensive. We employ the db (Daubechies) wavelet in the algorithm because it resembles the waveform of a human heart beat outcome of the daubechies is excellent. In this research, we employ the daubechies wavelet transform to construct an algorithm in MATLAB that decomposes the signal into approximation and detailed coefficients. The Wavelet Transform is based on the convolution of the subjective signal and the wavelet function. An automated approach is used to extract the Fetal Electrocardiogram (FECG) from the Abdominal Electrocardiogram. In [23], a (AECG) recording was described. The information was gathered in a non-invasive manner. Data is collected using external electrodes inserted on the abdomen. An AgAgCl transducer is used to boost SNR, and electrode positions are altered. To capture signals, electrodes were placed on the mother's abdominal wall. The.edf format of the abdominal electrocardiogram (AECG) data employed in this technique was converted to a Matlabreadable format. There are three main procedures that are considered. Pre-processing, FECG extraction and post-processing are all steps in the process. First read the recorded mothers Abdominal ECG signal in MATLAB and then use PCA to eliminate undesirable noise from the AECG signal. After preprocessing, the FECG signal was extracted using the ICA approach. Then R-Peak is discovered, and Fetal Heart Rate Calculation is performed.

V. BLOCK DIGRAM

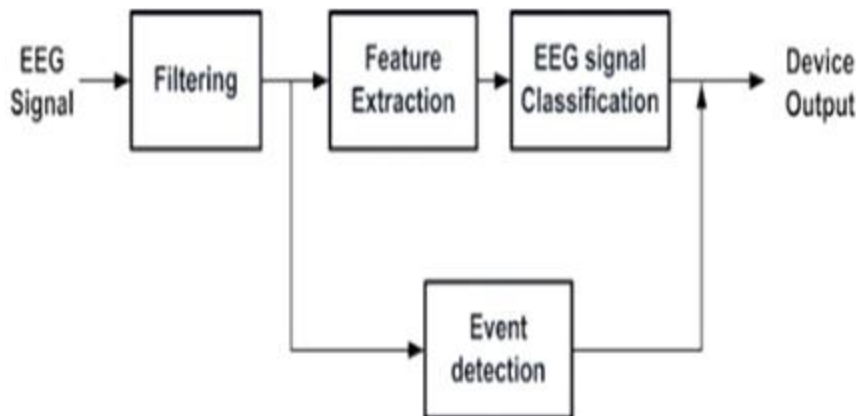


Fig 1: Block Diagram of the overall system

VI. INTERPRETATION

- EEG Signals are functionally fast, relatively cheap and safe way of checking the functioning of different areas of brain.
- High precision time measurements
- Today's EEG technology can accurately detect brain activity at a resolution of a single millisecond.
- EEG electrodes are simply stuck onto the scalp. It is therefore a non-invasive procedure.
- .EEG equipment is relatively inexpensive compared with other devices and is simple to operate.

An automated approach is used to extract the Fetal Electrocardiogram (FECG) from the Abdominal Electrocardiogram. In [23], a (AECG) recording was described. The information was gathered in a non-invasive manner. Data is collected using external electrodes inserted on the abdomen. An AgAgCl transducer is used to boost SNR, and electrode positions are altered. To capture signals, electrodes were placed on the mother's abdominal wall. The.edf format of the abdominal electrocardiogram (AECG) data employed in this technique was converted to a Matlabreadable format. There are three main procedures that are considered. Pre-processing, FECG extraction and post-processing are all steps in the process. First read the recorded mothers Abdominal ECG signal in MATLAB and then use PCA to eliminate undesirable noise from the AECG signal. After preprocessing, the FECG signal was extracted using the ICA approach. Then R-Peak is discovered, and Fetal Heart Rate Calculation is performed.

VII. CONCLUSION

The fatal electrocardiogram (FECG) has a humble beginning dating back to 1901, when the first expansion of research in the associated arena was severely limited. The identification of the waveform was greatly eased with the introduction of improved amplifiers and filters, yet waveform morphology surveillance was a difficult issue due to the presence of background noise after the contaminated signal was filtered. The signal-

to-noise ratio of the original FECG was dramatically improved thanks to sophisticated processing and computer technologies, notwithstanding the signals.

VIII. REFERENCES

- [1]. X. Shen, J. Wu, Y. Zhang, Y. Li, and Y. Ma, "Towards an evaluation model of online learning behavior and learning effectiveness for moocap learners," *Distance Education in China*, vol. 7, 2022.
- [2]. A. H. Ansari, P. J. Cherian, A. Caicedo, G. Naulaers, M. De Vos and S. Van Huffel, "Neonatal seizure detection using deep convolutional neural networks", *Int. J. Neural Syst.*, pp. 1850011, 2022.
- [3]. H. Abbasi, A. Gunn, L. Bennet and C. Unsworth, "Deep convolutional neural network and reverse biorthogonal wavelet scalograms for automatic identification of high frequency micro-scale spike transients in the post-hypoxic-ischemic EEG", *EMBC*, vol. 20, 2020.
- [4]. O'Shea, G. Lightbody, G. Boylan and A. Temko, "Neonatal seizure detection from raw multi-channel EEG using a fully convolutional architecture", *Neural Networks*, vol. 123, pp. 12-25, 2021.
- [5]. H. Abbasi, A. Gunn, C. Unsworth and L. Bennet, "Wavelet spectral time-frequency training of deep convolutional neural networks for accurate identification of micro-scale sharp wave biomarkers in the post-hypoxic-ischemic EEG of preterm sheep", *EMBC*, vol. 20, 2020..
- [6]. H. Abbasi and C. P. Unsworth, *Applications of advanced signal processing and machine learning in the neonatal hypoxic-ischemic electroencephalogram*, vol. 15, no. 2, pp. 222-231, 2020.
- [7]. B. Bateman, A. R. Jha, B. Johnston and I. Mathur, *A New Interactive Approach to Understanding Supervised Learning Algorithms*, Birmingham, U.K.:Packt Publishing, pp. 342-346, 2020.
- [8]. A. H. Ansari, P. J. Cherian, A. Caicedo, G. Naulaers, M. De Vos and S. Van Huffel, "Neonatal seizure detection using deep convolutional neural networks", *Int. J. Neural Syst.*, pp. 1850011, 2018.
- [9]. X. Shen, J. Wu, Y. Zhang, Y. Li, and Y. Ma, "Towards an evaluation model of online learning behavior and learning effectiveness for moocap learners," *Distance Education in China*, vol. 7, 2019..
- [10]. H. Abbasi and C. P. Unsworth, *Electroencephalogram studies of hypoxic-ischemic encephalopathy in fetal and neonatal animal models*, vol. 15, no. 5, pp. 828-837, 2020.

Line width-Tolerant Joint Digital Signal Processing for 16QAM Nyquist Wdm Super Channel

Avantika Upase*, Dr. Ram K. Nawasalkar

*Department of Computer Science, G.S. Tompe Arts, Commerce and Science College, Chandur Bazar, Dist. Amravati, Maharashtra, India

ABSTRACT

The performance of Nyquist wavelength division multiplexing (WDM) super channel, using 16-ary quadrature amplitude modulation (16QAM), is severely degraded due to the existence of inter-channel interference and full-response equalization-enhanced in-band noise. Here, we propose a joint digital signal processing (DSP) technique incorporating digital spectral shaping and maximum likelihood sequence detection for 16QAM Nyquist WDM super channel with a symbol rate of 28 GBd. Compared with traditional joint DSP, we can obtain 1.8-dB required-OSNR improvement at a bit error rate of 10^{-3} for back-to-back measurement. In addition, 0.9-dB peak Q-factor improvement is also secured after 960-km standard single mode fiber transmission. Furthermore, using the proposed joint DSP technique, linewidth tolerance is relaxed from 80 to 230 kHz given 1-dB required-OSNR penalty. Meanwhile, reduction of block-size for carrier phase recovery is also secured, taking 100-kHz linewidth into account.

Keywords: WDM, Superchanned, linewidth

I. INTRODUCTION

In order to meet the capacity requirements of future optical networks, the design of transport systems capable of supporting 1Tb/s and greater channel rates based on "superchannel" architectures necessitates a careful selection of modulation formats, channel spacing, and signal processing in order to achieve the maximum channel capacity without limiting reach or incurring unacceptable complexities, as well as the use of advanced signal processing techniques. In superchannel coherent systems, Nyquist-WDM and Coherent Optical-OFDM (CO-OFDM) are two complementing techniques that may be utilised to achieve ultra-high spectral efficiency via the use of coherent optical-of-diode modulation (CO-OFDM). In an ideal world, they are completely orthogonal systems.

At such tight channel spacing, however, the production and preservation of these ideal orthogonal superchannel signals is very challenging, and even the smallest imperfection results in significant inter-channel interference (ICI).

Linear ICI is most likely to be formed largely at the transmitter during multiplexing or at the receiver during demuxing since the subchannels of Nyquist superchannels are most likely to be transmitted and routed as a

bonded group. ICI mitigation techniques used on the transmitter side include aggressive optical filtering, Nyquist-like optical filtering, and electrical spectrum shaping enabled by high-speed DACs. ICI may occur on the receiver side during the process of subchannel separation. This is true for both optical demux and electrical demux, which is the case in the case of colourless receivers.

The receivers' capacity to handle inter-symbol interference (ICI) and inter-symbol interference (ISI) impairments is what determines the complexity of the generation and mux/demux processes in the end, though. Up to this point, coherent detection in Nyquist-WDM systems has been performed only by operations on a single channel, with no consideration given to neighbor-channel information.

Future DSP implementations, on the other hand, are anticipated to have sufficient processing capability to enable neighbor-channel information to be employed in the demodulation of any given channel, assuming that this is possible.

So we propose and show an architecture for Nyquist-WDM systems that we refer to as a "super receiver," which detects and demodulates several channels at the same time while being coherent. Using information from side channels and joint DSP to cancel ICI, we are able to achieve much better performance than typical receivers that analyse each channel in isolation from the others.

The suggested architecture has a receiver complexity that is comparable to that of MIMO methods that have been presented for crosstalk cancellation in single-mode fibres. At the same time, in contrast to the MIMO method, which investigates mode-division multiplexing, the suggested "super receiver" design is based on standard WDM systems and eliminates inter-channel interference (ICI) caused by frequency overlap between surrounding subchannels. Additional to this, we offer a carrier phase estimation approach that takes use of the carrier information of numerous subchannels in Nyquist-WDM systems that are carrier phase-locked by the carrier phase.

II. BACKGROUND

Zhongqi Pan et al 2015 says that single-carrier wavelength-division-multiplexing (WDM) systems, the spectral efficiency can be increased by reducing the channel spacing through digital signal processing (DSP). Two major issues of using tight filtering are crosstalk between channels and inter-symbol interference (ISI) within a channel. By fulfilling the Nyquist criterion, Nyquist spectral shaped WDM systems can achieve a narrow channel spacing close to the symbol rate (R_s) with negligible crosstalk and ISI. In principle, DSP can generate any signals with arbitrary waveforms and spectrum shape.

Junyi Wang et al 2013, investigate transmitter-side digital signal processing to generate 16-ary quadrature-amplitude-modulation (16QAM) Nyquist wavelength-division-multiplexing (WDM) signals by simulations. We first study required digital finite-impulse response (FIR) filter tap numbers and optimum roll-off factors to generate Nyquist 16QAM WDM signals. We show that a root-raised cosine spectrum with a roll-off factor of 0.1 is optimal for Nyquist 16QAM signals considering the trade-off between the system performance and complexities, and a digital FIR filter with 37 taps is sufficient to generate such signals.

Shin Takano et al 2020 numerically demonstrate DBP applying field intensity averaging for 28-Gbaud-10-channel-Nyquist-WDM with SP-16QAM signals. The method shows 0.63 dB improvement in Q 2 compared to conventional-DBP at a distance of 1000 km and power of 1 dBm. The ever increasing bandwidth demand has driven fiber-optic communication system to target higher spectral efficiency (SE) transmission. In order to achieve higher SE, three major competitive technologies for forming spectrally-efficient wavelength division multiplexing (WDM) superchannels have been proposed so far instead of increasing serial interface rate [1]. One is the orthogonal frequency-division multiplexing (OFDM) technique [1–3], where frequency domain sink-like subcarriers are spaced exactly at the symbol rate to obtain high SE. Another one is referred to Nyquist-WDM, which requires an ideal rectangular shaped spectrum with bandwidth equal to the symbol rate [4–6]. The last one is offset quadrature amplitude modulation (OQAM) based WDM superchannel with channel spacing equal to the symbol rate, where the tolerance of inter-channel interference (ICI) is improved by offsetting the in-phase and quadrature components of QAM-based carrier with half symbol period and controlling the phase difference ($\Delta\Phi$) between individual wavelength channels equal to either 90 or 270 degree [7–10]. For the OQAM based WDM superchannel, the deviation of optimal phase difference leads to severe performance degradation, and error-free transmission is impossible for offset-16QAM based WDM (16-OQAM-WDM) superchannel in case the deviation of phase difference from its optimal value is more than 60 degree [10]. Consequently, sensitivity of phase difference for the OQAM based WDM superchannel hinders its practical implementation due to the random environment perturbations, although such technique can relax the stringent requirements on devices and shows performance improvement with respect to that of OFDM and Nyquist-WDM. Recently, a practical receiver-side digital spectral shaping wavelength division multiplexing technique (RS-DSS WDM) has been proposed to build up multi-carrier superchannels as a supplementary to Nyquist-WDM [11–15]. In such superchannel, the RS-DSS technique can relax the stringent requirements on the transmitter-side filter, and permits the use of the conventional optical components. After receiver-side spectral shaping, the maximum likelihood sequence detection (MLSD) is applied to detect the shaped signal with optimum performance. It is well known that 16QAM exhibits low tolerance to the linear crosstalk. Consequently, RS-DSS WDM superchannel suffers from large performance degradation using 16QAM with narrow channel spacing, due to the co-existence of both inter-symbol interference (ISI) and ICI, especially when the channel spacing is reduced to the symbol rate. Therefore, the symbol rate is commonly set below the channel spacing for 16QAM based RS-DSS WDM superchannel to avoid significant ISI and ICI, which is defined as quasi-Nyquist WDM [13, 15].

In this research work, Nyquist WDM superchannel using offset-16QAM and RS-DSS. The generation and transmission of 3-carrier 672 Gbit/s superchannel is numerically demonstrated with 28 GHz channel spacing over 12×80 km standard single-mode fiber (SSMF) with Erbium-doped fiber amplifiers (EDFAs) only, indicating a SE up to 7.44 bit/s/Hz assuming 7% hard-decision forward error correction (HD-FEC) overhead. Performance comparison between 16QAM based RS-DSS Nyquist WDM superchannel and the proposed Nyquist WDM superchannel is comprehensively investigated and significant performance improvement is secured. Furthermore, good tolerance of phase difference deviation is also achieved for our proposed Nyquist WDM superchannel, indicating of the potential towards practical implementation

III. SYSTEM CONFIGURATION AND OFFLINE DSP FLOW

System configuration of 16QAM based RS-DSS WDM superchannel together with digital signal processing (DSP) flow is schematically shown in following figure. The multi-carrier is obtained from an optical comb generator (OCG). The linewidth of each carrier from OCG is 10 kHz. The signal data trains consist of 28Gbit/s 217-1 pseudo-random binary sequences (PRBS) and differential coding is used to solve the phase ambiguity problem. These logic data trains are used to generate 4-level electrical signals. Then 3 carriers are, respectively, introduced to three parallel IQ modulators driven by these 4-level electrical signals. Polarization multiplexing is achieved through adding a delay of 180 symbols between two polarization tributaries. Then, each carrier is filtered by a 4th-order Gaussian optical filter, whose response is available in commercial products, in order to shape the optical spectrum for the purpose of achieving a trade-off between ICI and ISI. After spectrum shaping, all the carriers are launched into the 12×80 km EDFA-only SSMF link with launched optical power controlled by a variable optical attenuator (VOA). At the receiver-side, amplified spontaneous emission (ASE) noise loading is used to adjust the optical signal-to-noise-ratio (OSNR) for the back-to-back (B2B) measurement. Then, the signals are electrically amplified after the polarization-diverse and phase-diverse coherent detection. After amplification, four 5th electrical Bessel filters with 3dB bandwidth of 21GHz are applied to suppress the out-of-band noise. Finally, the received analog signals are sampled by ADCs with two samples per symbol and feed into the offline DSP module.

The offline DSP flow is firstly started with I/Q imbalance compensation [16]. The electronic dispersion compensation (EDC) is next performed to compensate the accumulated dispersion in the SSMF link [16]. The adaptive equalization and polarization demultiplexing are performed by four butterfly L-tap T/2-spaced finite impulse-response (FIR) filters. These FIR filters are first adapted by the standard constant modulus algorithm (CMA) for pre-convergence. Final equalization is done by switching CMA to decision-directed least-mean-square (DD-LMS) algorithm. In the DD-LMS loop, the carrier recovery includes frequency offset compensation (FOC) using the fast Fourier transform (FFT) method [17] and the carrier phase recovery (CPR) using the blind phase search (BPS) method [18]. Instead of using hard decision after CPR, a simple two-tap FIR filter with a transfer function $H(z)=1+\alpha \times z^{-1}$ is applied to each of the four quadrature components for post-filtering, where α with a range of 0 to 1 is chosen as an optimized parameter [15]. Symbol decision is finally done by a 4-state MLSD algorithm with 16 branches. Note that no channel estimation after post-filtering is required for the implementation of MLSD [12–14]. As we can see, the post-filtering and MLSD can be easily switched to hard decision by setting α equal to zero since no spectral shaping is done and the MLSD does not have any memory to use.

IV. METHODOLOGY

In this project, we have designed a low-overhead low-complexity carrier phase tracking scheme for OFDM-based superchannel transmission system enabled by optical frequency combs. In this scheme, taking advantage of the broadband phase coherence provided by optical frequency combs among the OFDM-bands,

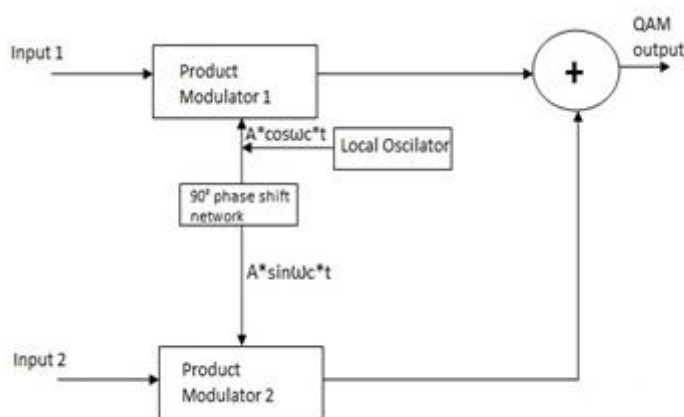
the carrier phase retrieved from pilot-subcarriers of the OFDM-band on the central wavelength channel is reused for the OFDM-bands on the other wavelength channels. In this case, the overall pilot-subcarrier overhead and DSP complexity is significantly reduced since the pilot-subcarriers occupy a small fraction of the overall OFDM bandwidth.

The feasibility of this joint-carrier phase tracking scheme has been verified successfully via comprehensive simulation, where results show that the BER threshold for soft-decision FEC could be achieved for 50GHz-spaced 5-band 4-QAM, 8-QAM, 16-QAM and 32-QAM OFDM-based superchannel signals with zero guard-band and both laser and nonlinear phase noise effects after 7000km, 4000km, 3000km and 2000km SSMF transmission respectively. The simulation results show that there exist chromatic dispersion-induced differential phase offset among the OFDM-bands whose impact on joint-carrier phase tracking depends on the modulation format, channel count and fiber length. Finally, we demonstrate experimentally the feasibility performance of the designed master-slave carrier phase tracking technique for comb-based OFDM-based superchannels.

For Nyquist-WDM superchannel systems, the ideal spectral shape for each subchannel is rectangular with the channel spacing (Δf) equal to the baud rate B , Fig. 1. Therefore, no inter-channel interference (ICI) exists. On the other hand, due to the rectangular spectrum, the pulse within each subchannel is sinc shape in the time domain with zero-crossing points at integer multiples of the symbol period T , thus a Nyquist pulse (inter-symbol interference (ISI) free) is achieved.

In contrast, for CO-OFDM system, each carrier is sinc shape in the frequency domain, and rectangular in the time domain. Therefore, theoretically both schemes can be ICI and ISI free simultaneously

V. BLOCK DIAGRAM



VI. INTERPRETATION

In practical implementation of the proposed Nyquist WDM super channel, the precise phase difference ($\Delta\Phi$) between channels is hard to realize due to random environment perturbations. Thus, it is essential to

investigate the effect of phase difference deviation between channels for the proposed Nyquist WDM superchannel. As a comparison, we also take traditional 16-OQAM-WDM superchannel into account by switching post-filtering and MLSD into hard decision

VII. CONCLUSION

The performance of Nyquist WDM superchannel using advanced modulation formats with coherent detection is degraded due to the existence of both inter-symbol interference (ISI) and inter-channel interference (ICI). Here, we propose and numerically investigate a Nyquist WDM superchannel using offset-16QAM and receiver-side digital spectral shaping (RS-DSS), achieving a spectral efficiency up to 7.44 bit/s/Hz with 7% hard-decision forward error correction (HD-FEC) overhead. Compared with Nyquist WDM superchannel using 16QAM and RS-DSS, the proposed system has 1.4 dB improvement of required OSNR at BER = 10⁻³ in the case of back-to-back (B2B) transmission. Furthermore, the range of launched optical power allowed beyond HD-FEC threshold is drastically increased from -6 dBm to 1.2 dBm, after 960 km SSMF transmission with EDFA-only. In particular, no more than 1.8 dB required OSNR penalty at BER = 10⁻³ is achieved for the proposed system even with the phase difference between channels varying from 0 to 360 degree.

VIII. REFERENCES

- [1]. P. Ying et al., "Low-loss edge-coupling thin-film lithium niobate modulator...", *Optics Lett.*, vol. 46, pp. 1478-1481, 2021
- [2]. Xi Chen; Prashanta Kharel; Greg Raybon; Di Che; Christian R et al., "Demonstration of 120-GBaud 16-QAM Driver-less Coherent Transmitter with 80-km SSMF Transmission", *IEEE Xplore: 13 April 2022 Optical Fiber Communications Conference and Exhibition (OFC)*.
- [3]. P. Ying et al., "Low-loss edge-coupling thin-film lithium niobate modulator...", *Optics Lett.*, vol. 46, pp. 1478-1481, 2021.
- [4]. M. Xu et al., "High-performance coherent optical modulators ", *Nature Commun.*, vol. 11, pp. 1-7, 2020..
- [5]. B. Tang et al., "Low complexity two-stage FOE using modified Zoom-FFT for coherent optical M-QAM systems", *IEEE Photon. Technol. Lett.*, vol. 32, no. 5, pp. 263-266, Mar. 2020.
- [6]. G. Campobello, A. Segreto and N. Donato, "A novel low-complexity frequency estimation algorithm for industrial Internet-of-Things applications", *IEEE Trans. Instrum. Meas.*, vol. 70, pp. 1-1, 2021.
- [7]. K. Li, X. Chen, J. E. Hurley, J. Stone and M.-J. Li, "Modal delay and modal bandwidth measurements of bi-modal optical fibers through a frequency domain method", *Opt. Fiber Technol.*, vol. 55, Mar. 2020.
- [8]. C. Li et al., "Fiber Nonlinearity Mitigation in Single Carrier 400 G and 800 G Nyquist-WDM Systems", *IEEE J. Lightwave Technol.*, vol. 36, no. 17, pp. 3707-3715, Sep. 2018.
- [9]. C. Fougstedt et al., "ASIC Implementation of Time-Domain Digital Back Propagation for Coherent Receivers", *IEEE Phot. Technol. Letters*, vol. 30, no. 13, pp. 1179-1182, July 2018.

- [10].H. Yao et al., "A Modified Adaptive DBP for DP 16-QAM Coherent Optical System", IEEE Phot. Technol. Letters, vol. 28, no. 22, pp. 2511-2514, Nov. 2016.
- [11].S. B. Amado et al., "Low Complexity Advanced DBP Algorithms for Ultra-Long-Haul 400 G Transmission Systems", IEEE J. Lightwave Technol., vol. 34, no. 8, pp. 1793-1799, April 2016.
- [12].S. Takano and H. Uenohara, "Low Computational Complexity of Optical Nonlinear Compensation with Phase Linear Approximation Method for Single Polarization-64QAM Signals", OECC/PSC 2019, pp. TuP4-B3, July 2019.
- [13].S. Takano and H. Uenohara, "Low complexity DBP with phase linear approximation for DP-16QAM coherent optical communication systems", IEICE Communications Express, vol. 8, no. 8, pp. 329-334, Aug. 2019.
- [14].S. Takano and H. Uenohara, "Low-Complexity DBP Using Optical-field-intensity Averaging for Digital Coherent System", IEICE Communications Express, 2020.
- [15].R. Schmogrow et al., "Error Vector Magnitude as a Performance Measure for Advanced Modulation Formats", IEEE Phot. Journal, vol. 24, no. 1, pp. 61-63, Jan. 2012..

Green Synthesis of Magnesium Oxide Nanoparticles using Aloe Vera and its Application

D. R. Bijwe¹, A.V. Rajgure¹, A.M. Shirbhate¹, S. S. Kavar²

¹P. G, Department of Physics, G. S. Tompe Art, Commerce and Science College, Chandur bazar, Dist. Amravati, Maharashtra, India

²Dr. R. G. Rathod Arts & Science College, Murtijapur, Dist. Akola, Maharashtra, India

ABSTRACT

Green synthesis of nanoparticles is of significant interest in recent years and has become the one of the most desired methods for the production of metal oxide nanoparticles. Synthesis of MgO Nanoparticles by green synthesis using aloe vera leaves which can be easily used for various bio-medical applications. In this study MgO nanoparticles have been synthesized with aloe vera leaves extract. The synthesized MgO nanoparticles were characterized using UV-vis spectroscopy, X-ray diffraction (XRD) study was used to confirm the crystalline nature of the synthesized nanoparticles and confirm the crystalline size of the nanoparticles as 0.43nm.

Keywords: MgO nanoparticles, aloe vera extract, UV-vis, XRD

I. INTRODUCTION

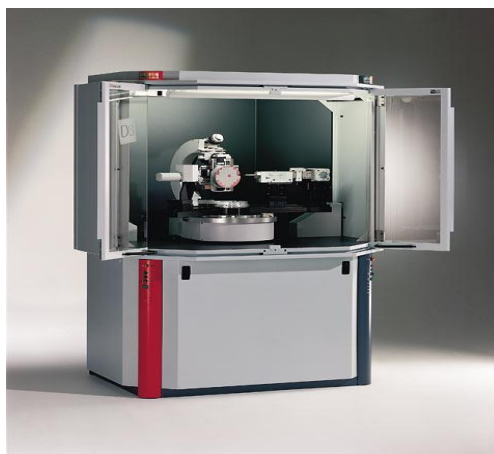
There are various methods for the synthesis of nanoparticles. Among all these green synthesis is the most efficient, cheap, Eco-friendly, and harmless method of green synthesis [1]. MgO nanoparticles are synthesized by using eco friendly method & All over the world people using this safest method. The MgO nanoparticles have been effectively produced by green synthesis which is environmental friendly, non toxic with greater stability & has broad range of opportunity for the production of these material in the nanoscale[2]. Aloe Vera plant extract acts as an agent and an on hazardous gelling agent for stabilizing the nano structures [3] MgO nanoparticles has been used in wide range of application such as catalysis, catalyst support, toxic waste remediation, refractory materials and absorbents, additive in heavy fuel oils, refracting and anti-refracting coatings, superconducting and ferroelectric thin films as the substrate, super-conductor, lithium ion batteries and so on[4-5]. It is used in medicinal field for the relief of heartburn, sore stomach, bone regeneration and tumor treatment [6].

II. MATERIALS AND METHOD

- Material: Magnesium nitrate {Mg (NO₃)₂}, Sodium hydroxide solution(NaOH), distilled Water, Aloe Vera leaves.

- Aloe Vera were collected from the botanical garden of G.S. Tompe Art's Commerce & Science College, Chandur Bazar.

Apparatus: Magnetic stirrer, breaker, funnel, filter paper, test tube, dropper, UV-visible spectrometer, X-ray diffraction (XRD)



X-ray Diffraction (XRD) Instrument

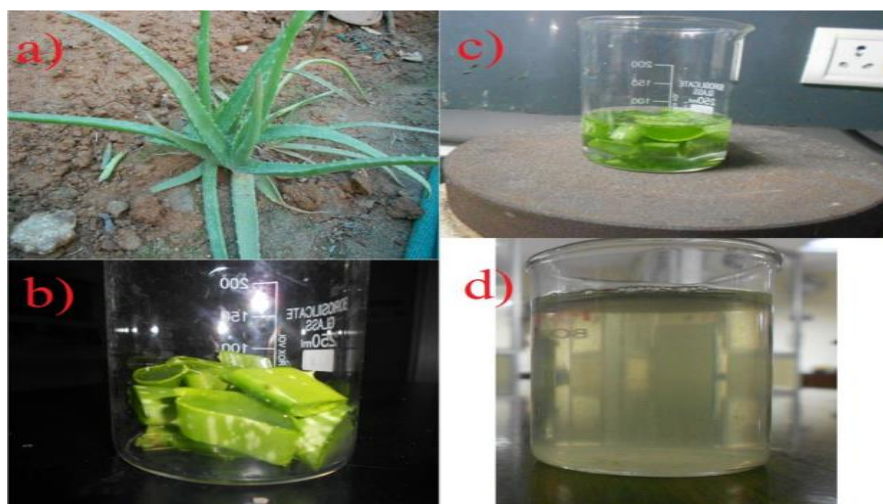


UV-Vis Spectroscopy Instrument

III. SYNTHESIS

2.1. Preparation of aloe Vera leaf extract:

50 g of Aloe Vera leaves were thoroughly washed, dried and then boiled in 50 ml of deionised water for half an hour. The resulting extract was cooled and used as a gelling agent for the synthesis of magnesium oxide nano particles.



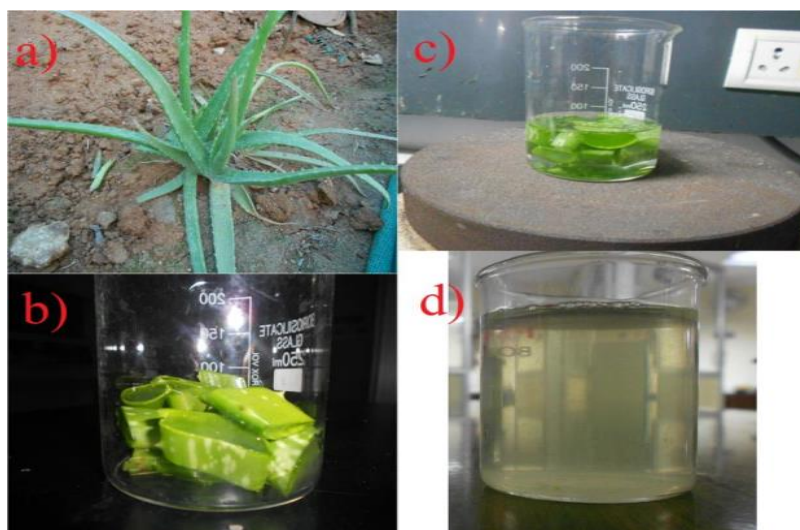


Fig.1. Preparation of Aloe Vera Leaf Extract

2.2. Preparation of MgO nano particles by using aloe Vera leaf extract:

Ten mL of magnesium nitrate solution was added to 10 mL of aloe Vera extract. Then, the mixture was stirred in a magnetic stirrer for about half an hour. NaOH was added drop wise while stirring till a white precipitate of magnesium hydroxide was obtained. The precipitate was filtered and dried in an air oven for an hour. The content was washed repeatedly with distilled water to remove the basicity of the solution. Further, the calcinations was done in the muffle furnace at 500°C for three hours



Fig. 2. Preparation of MgO nano particles by using aloe Vera leaf extract

IV. RESULT AND DISCUSSION

4.1 Characterization of catalysts: -

Powder X-ray diffraction studies The XRD spectra of as synthesized nanoparticles was carried out using XRD For 2θ values ranging from 10 to 80° using $\text{CuK}\alpha$ radiation at $\lambda = 1.5406\text{\AA}$. The 2θ values at 57.01 for

MgO were observed. The crystallite size was calculated using Debye-Scherer formula. The crystallite size of MgO nanoparticles was found to be 0.43nm

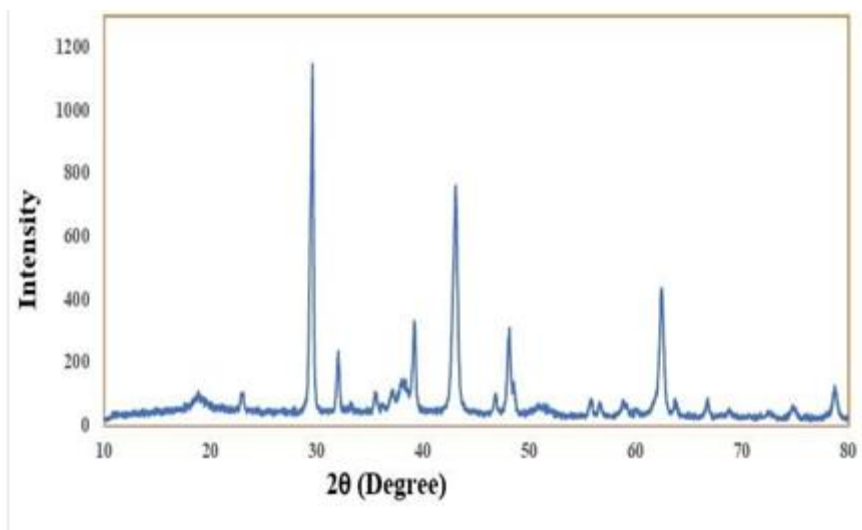


Fig.3. X-ray Diffraction MgO Nanoparticles

4.2 UV characterizations:-

UV-Visible Diffuse Reflectance Spectroscopic studies extract. The UV absorption measurements were carried out using JASCO UV Vis spectrophotometer and was scanned in the range of 150-1200nm. The UV-Reflectance spectrum of the synthesized MgO nano particles is shown below figure. The band gap energy of the magnesium oxide nano particles was calculated using the Planck's equation. The band gap energy is found to be 2.86 eV for magnesium oxide nano particles from Aloe Vera extract.

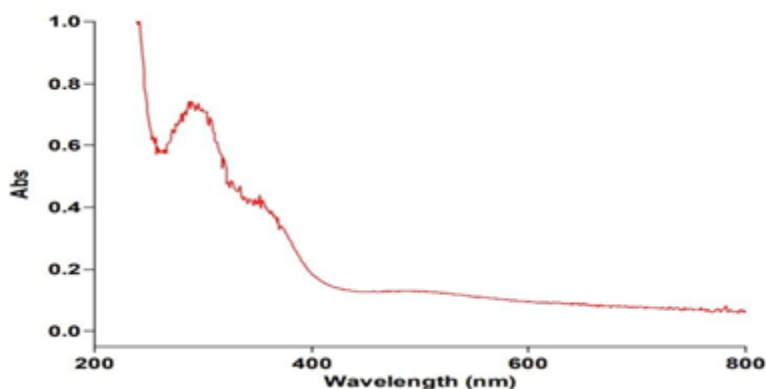


Fig.4.UV-Vis spectrum of MgO nano particles

V. REFERENCES

- [1]. P.Ouraipryvan, T. Sreethawong and S.Chavadej, "Synthesis crystalline MgO nanoparticle with mesoporous-assembled structure via a surfactant-Modified sol-gel process. Materials Letters, 2009 63, 1862-1865.

- [2]. Department of Chemistry, Faculty of Engineering and Technology, SRM Institute of Science and Technology, Ramapuram Campus, BharathiSalai, Ramapuram, Chennai, 600089, TN, India
- [3]. H. Mirzaei and A. Davoodnia, Microwave assisted sol-gel synthesis of MgO nanoparticles and their catalytic activity in the synthesis of hantzsch 1,4-dihydropyridines Chinese journal of catalysis,2012,33,1502-1507
- [4]. L. Bertinetti, C. Drouet, C. Combes, C. Rey,A. Tampieri, S. Coluccia, and G. Martra, Surface characteristics of nanocrystallineapatites: Effect of MgO surface enrichment on morphology, surface hydration species, and cationic environments, Langmuir, 2009, 25, 5647-5654.
- [5]. C. M. Boubeta, L. Bacells, R. Cristofol, C. Sanfeliu,E. Rodriguez, R. Weissleder, S. Piedrafita, K. Simeonidis, M. Angelakeris, F. Sandiumenge, A. Calleja, L. Casas, C. Monty and B. Martinez, "Selfassembled multifunctional Fe/MgO nano-spheres for magnetic resonance imaging and hyperthermia", Nanomedicine, 2010, 6, 362-370.
- [6]. D. R Di,z. Z He, Z. Q. sun, and J. Liu, "A new nanocryosurgical modality for tumor treatment using biodegradable MgO nanoparticles",Nanomedicine, 2012 8 1233-1241.

Green Synthesis and Characterisation of Copper Oxide Nanoparticles using *Azadirachta indica* (Neem Leaves)

D. R. Bijwe¹, A. R. Rajgure¹, P. S. Deole¹, M. N. Pawar¹, G. P. Gorle¹, S. P. Deshmukh¹, D. A. Pund²

¹Post Graduate, Department of Physics, G. S. Tompe Arts, Commerce & Science College, Chandur Bazar, Dist. Amravati, Maharashtra, India

²Department of Chemistry, R. R. Lahoti Science College, Morshi, Dist. Amravati, Maharashtra, India

ABSTRACT

The green Nanotechnology is generating interest in Researchers for the Synthesis of Nano Particle in simple, cost effective, less toxic and eco friendly manner. In this study CuO-NPS have been bio-synthesized with *Azadirachta indica* leaf extract. The formation of Nano particles was confirmed by UV-Spectra studies. In UV spectrum the peak was obtained at 213 nm. The average particle size of synthesized Nano particles confirmed by the XRD studies. The particles size of CuO NPs are found in different sizes of nm.

Keywords: - Copper nanoparticles, X-ray diffraction, UV-vis spectroscopy

I. INTRODUCTION

Nanoparticles are ultra-small particles of size 10^{-9} m. Because they are very small in size, they are highly chemically active because of their high surface to volume ratio. Many physical and chemical methods which have been developed for preparing metallic nanoparticles, currently we need clean and environment friendly options to develop them, so researcher are focusing on green options.

In metal oxide nanoparticles in which Cupric oxide (CuO) nanostructures are of particular interest because of their interesting properties and promising applications such as in solar cell technology, field emission, magnetic storage media, lithium-ion batteries, gas sensing, drug delivery, magnetic resonance imaging, and field emission devices, super capacitors and in medicines because of their anti-bacterial properties. Copper oxide is one of the important metal-oxide which has attracted recent research because of its low cost, abundant availability as well as its unusual properties. [1-3]

CuO shows superconductivity at high temperature so it is used as superconducting material. [3]

Figure.1 shows the image of neem leaf. It shows anthelmintic, antifungal, antidiabetic, antibacterial, antioxidant, Anti-inflammatory and antiviral properties.



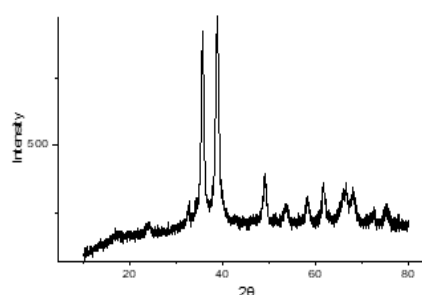
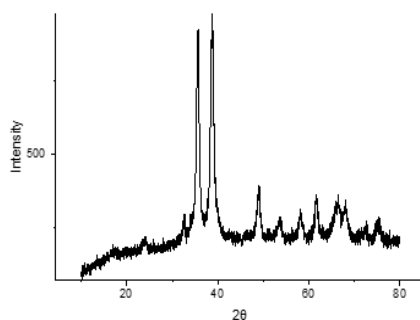
Plant Description

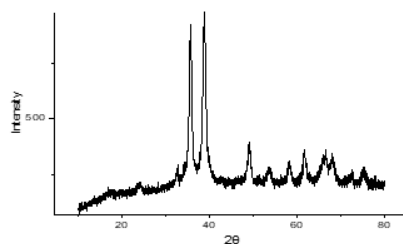
- *Family Name* :-Meliaceae
- *Binomial Name* :-Azadirachta indica
- *Common Name*:- Neem Plant
- Plant Taken:- Leaves

II. EXPERIMENTAL METHODS

2.1. Neem Extract:

For the synthesis neem leaves are used. Neem leaves were collected during the month of December 2021 from G. S. College campus, ChandurBazar. The healthy leaves were washed by running tap water two times and again two times washed with distilled water and dried it for room temperature. About 60 g of leaves weighted and taken in beaker and 600 ml of distilled water was added to it. This was heated for 1 hour at 70 to 80 °c. In the process the water turn into yellow brownish colour. After cooling down the extract was filtered byWhatmann No.1 filter paper. This filtrate extract was made upto 550 mL of in a standard measuring flask.





2.2. Copper Acetate Solution:

About 5 gm of copper acetate was weighed and made up-to 250 mL of solution.

2.3. Synthesis of CuO Nanoparticles

150 mL of copper acetate which is blue in colour and 500 mL of Neem extract which is brownish in colour is taken and mixed in a beaker. After mixing it is observed that the colour of mixed solution is turn into dark green and after 2 to 3 minutes the particles are settling down at the bottom of beaker as shown in Figure. 2. This precipitate is filtered by Whatmann no.1 filter paper, washed with distilled water and left to dry it for almost 24 hours at room temperature. After drying, crushed and made fine powder and collected



(Neem Extract)



(Mixture)



(Solution of cupric acetate)



(CuO NPs)

III. RESULTS AND DISCUSSION

3.1 UV-Vis spectra of CuO nanoparticles

UV spectral analysis of sample was done in wavelength range of 200-800 nm. The peak was obtained at 214 nm. The UV spectrum of CuO NPs are shown in Fig.no.1.[1-3]

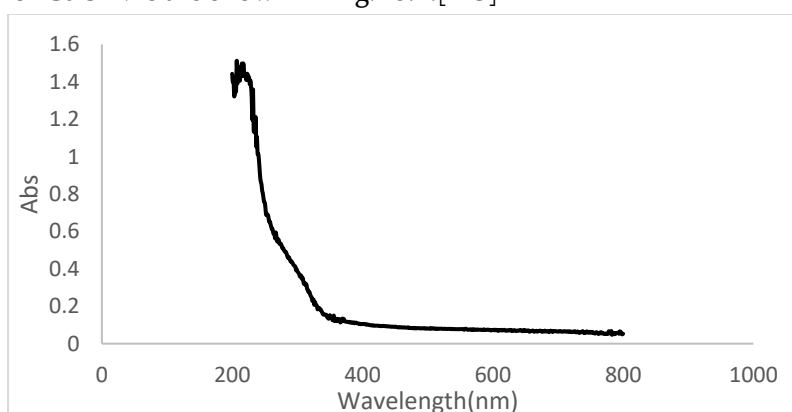


Fig.1. UV- spectrum of CuO NPs

3.2 X-Ray Diffraction Studies (XRD):-

XRD for synthesized CuO NPs synthesized using extract of neem leaves (*Azadirachta indica*) shows crystallinity of sample with diffraction angle 2θ of 37.26° , 45.82° and 66.76° which corresponding h,k,l values of reflection from (111), (200) and (220). The XRD pattern of CuO NPs is identical to simple cubic crystalline structure. The XRD pattern are shown in Fig. no. 2 & 3. [1-3]

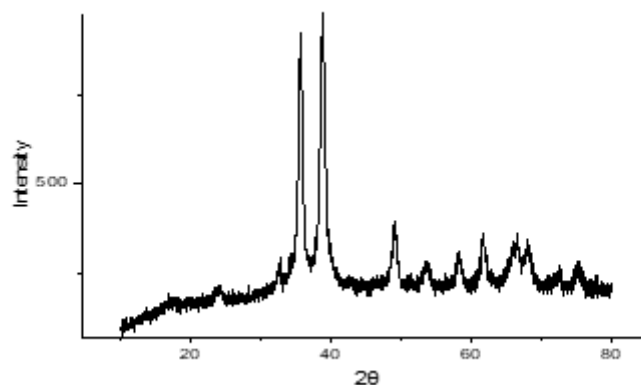


Fig. 2. XRD pattern of CuO NPs

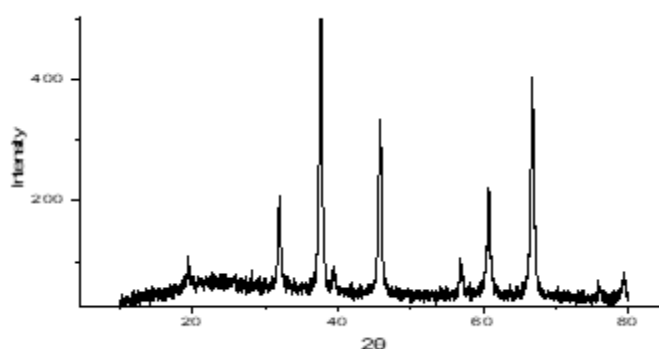


Fig. 3. XRD pattern of CuO NPs using Neem extract

IV. CONCLUSION

In conclusion, we can say that the methods are easily available, low cost materials are needed and procedure is easy to carry out in any laboratory, the process is pollution free, here we report an eco-friendly synthesis of CuO NPs using neem leaves extract (*Azadirachta indica*). The XRD analysis confirms the obtained NP is simple cubic crystalline having inter molecular spacing 2.3975 nm for first order peak of h,k,l values are (111). The UV spectrum analysis shows the absorption values at 214 nm.

V. REFERENCES

- [1]. S. Ansilin, J. Kavya Nair, C. Aswathy, V. Rama, J. Peter, J. Jeyachynthaya Persis. Green Synthesis and Characterisation of Copper Oxide Nanoparticles using *Azadirachta indica* (Neem) Leaf Aqueous Extract.2(5) (2016) 221–223.
- [2]. Yilleng, Samuel, Stephen, Akande, Agende, Madaki. Biosynthesis of Copper and Iron Nanoparticles using Neem (*Azadirachta indica*) Leaf Extract and their Anti-bacterial Activity.24 (11) (2020) 1987-1991
- [3]. R. Chopra, N. Kashyap, Amit Kumar, D. Banerjee. Chemical Synthesis of Copper Oxide Nanoparticles Study of its Optical and Electrical Properties.9(1)(2020) 2278-0181
- [4]. Ayona Jayadev and Neethu Krishnan. Green Synthesis of Copper Nanoparticles and its Characterization.64(1)2021
- [5]. N.V. Surmawar, S.R. Thakare, N.T. Khaty, One-Pot, single step green synthesis of copper nanoparticles: spr nanoparticles, Inter. J. Green Nanotechnology.3(4) (2011) 302-308.

Green Synthesis of Zinc Oxide (ZnO) Nanoparticles Using *Ocimum Tenuiflorum* Leaves

P. S. Deole, D. R. Bijwe, A. V. Rajgure, M. N. Pawar, K. H. Chavhan, A. R. Bodkhe

P. G., Department of Chemistry, G. S. Tompe Arts, Commerce & Science College, Chandur Bazar, Dist. Amravati, Maharashtra, India

ABSTRACT

This contribution reports on the synthesis and characterization of ZnO nanoparticles synthesized by a completely green process using leaves of *Ocimum Tenuiflorum* plant as reducing agent in the synthesis of ZnO nanoparticles.

Green synthesis of nanoparticles represents an advance over other methods because it is simple, cost-effective, and relatively reproducible, and often results in more stable material. Prepared ZnO nanoparticles were characterized by X-ray diffraction (XRD) and (UV) Rays. The average particle size was calculated as 28.08 nm by using Scherrer's formula.

Keywords: *Ocimum Tenuiflorum*, ZnO nanoparticles, Green synthesis, XRD, UV

I. INTRODUCTION

In nanotechnology world, nanoparticles play a major role in many applications because nanotechnology is hailed as having the potential to increase the efficiency of energy consumption, help clean the environment, and solve major health problems. It is said to be able to massively increase manufacturing production at significantly reduced costs.

Nanoparticles are materials with overall dimensions in the nanoscale, i.e. under 100 nm. In recent years, these materials have emerged as important players in modern medicine, with clinical applications ranging from contrast agents in imaging to carriers for drug and gene delivery into tumors.

Nanostructure ZnO materials have received broad attention due to their distinguished performance in electronics, optics and photonics. From the 1960s, synthesis of ZnO thin films has been an active field because of their applications as sensors, transducers and catalysts. In the last few decades, especially since the nanotechnology initiative led by the US, study of one-dimensional (1D) materials has become a leading edge in nanoscience and nanotechnology. With reduction in size, novel electrical, mechanical, chemical and optical properties are introduced, which are largely believed to be the result of surface and quantum confinement effects. Zinc Oxide has amazing applications in diagnostics, biomolecular detection, microelectronics.

A variety of synthetic techniques are used for the synthesis of ZnO. These techniques broadly can be divided into three type, that is chemical, biological and physical methods. Chemical synthesis can further be divided into liquid phase synthesis and gas phase synthesis liquid phase synthesis includes precipitation, caprecipitation method, colloidal method , sol-gel processing, water – oil microemulsions method, hydrothermal synthesis, solvothermal and sonochemical, and polyol method. And vapor phase fabrication includes paralysis and inert gas condensation methods.

In recent green synthesis of ZnO nanoparticles was achieved by using leves extract of *Ocimum Tenuiflorum* plant . *Ocimum Tenuiflorum* also called holy basil, tulsi, *Ocimum Sanctum*. It is belong to Lamiacece family *ocimum Tenuiflorum* mostaly present in tropical region. The chemical constituents of *Ocimum Tenuiflorum* are linalool, alkaloids, ursolic acid, glycosides, carvacrd, tannins rosmarinic acid, aromatic compound etc.

Recently leaves extract of *Ocimum Tenuiflorum* plant have been utilized in the synthesis of copper nanoparticles, gold nanoparticles, and silver nanoparticles. To the best of our knowledge, the use of leaf extract *Ocimum Tenuiflorum* plant for green synthesis of ZnO nanoparticles has not been revealed. Hence the present task was carried out to synthesis and characterization of ZnO nanoparticles using leaves extract of *Ocimum Tenuiflorum* plant. Figure 1 show the plant of *Ocimum Tenuiflorum* which is use in leaf extract preparation.



Figure 1: *Ocimum Tenuiflorum* Plant.

II. EXPERIMENTAL

2.1 Material

All the chemicals such as zinc nitrate, distilled water, the leaves of *Ocimum Tenuiflorum* plant collected from college ground area in Chandur bazar Dist. Amravati, Maharashtra , India.

2.2 METHODS: -

2.2.1 Preparation of Leaves Extract of *Ocimum Tenuiflorum*:-

For the preparation of leaves extract of *Ocimum Tenuiflorum* first washed leaves many times with water and dried in sunlight. Then taking 10 gm of dried leaves in 250 ml borosil beaker along with 100 ml distilled

water. The solution mixture of leaves and distilled water boiled for 10 min. until solution colour turns in redish colour. The mixture solution cooled at room temperature. The leaves extract filtered utilizing filter paper and stored in refrigerator for synthesis of ZnO nanoparticles. Figure 2 shows the sample of leaves extract of *Ocimum Tenuiflorum* plant.



Figure 2: Sample of Leaves Extract of *Ocimum Tenuiflorum* Plant.

2.2.2 Green synthesis of ZnO nanoparticles using leaf Extract of *Ocimum Tenuiflorum* Plant:-

For the ZnO nanoparticles synthesis, 50 ml of *Ocimum Tenuiflorum* leaf extract was taken boiled to 60-80°C. using magnetic stirrer heater. Then 5 gm of Zinc nitrate was added to the leaf extract of *Ocimum Tenuiflorum* plant when temperature reach 70°C. and boiled it reduced deep reddish paste. This paste dried in dryer at temperature 100-130°C. For 40-50 min. Zinc Oxide nanoparticles obtained in form of light yellow coloured powder. This powder mashed in ceramic mortar pestle to get finer nature for characterization purpose. Figure 3 show the sample picture of ZnO nanoparticle.



Figure 3: ZnO Nanoparticles

III. RESULTS AND DISCUSSION

3.1 X-ray Diffraction (XRD)

XRD pattern of the prepared Zinc oxide nanopowder is shown in Figure 4. The observed diffraction peak of ZnO at $2\theta = 36.33^\circ$ with correspond to lattice plane. The crystallite average size D_p of the prepared nanopowder can be calculated by using Scherrer's formula

$$D_p = 0.9 \lambda / \beta \cos \theta$$

Where λ is the wavelength of X rays used (0.15406 \AA), β is the full width at half maximum (FWHM) = 0.29781 and θ is the angle of diffraction. The crystallite average size of prepared nano powder is found to be around 28.08 nm which is in the order of nano size. In comparison with the standard card of bulk ZnO with hexagonal structure see Figure 5. No diffraction peaks of other impurities are detected, which testify that the prepared sample is ZnO.

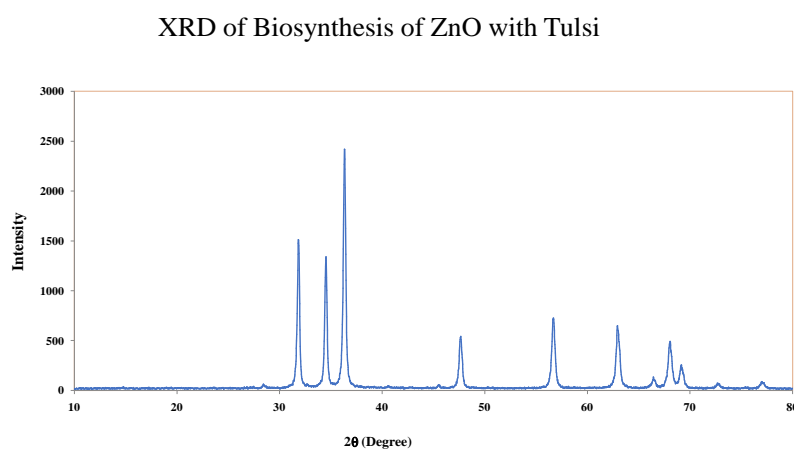


Figure 4: XRD pattern of Zinc Oxide nanoparticles

UV of Leaves extract of *Ocimum Tenuiflorum*:-

The extracts were analyzed using Shimadzu UV-Visible spectrophotometer (model: UV-1800). The samples are scanned at wavelength ranging from 400 to 800 nm using Shimadzu UV-Visible spectrophotometer and the characteristic peaks are detected. The UV spectra are shown in figures 5[11]

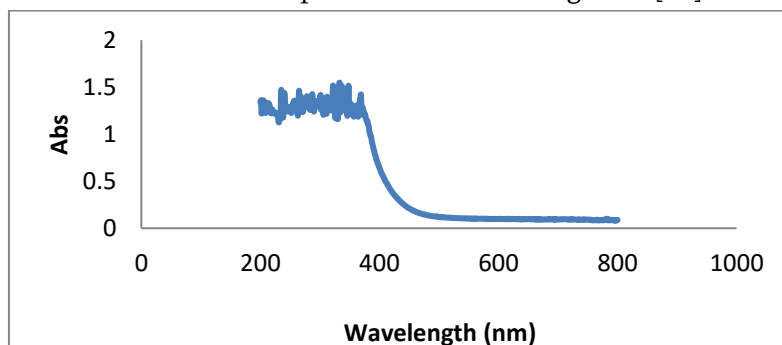


Figure 5: UV of Leaves extract of *Ocimum Tenuiflorum*

IV. CONCLUSION

In summary, ZnO nanoparticles are prepared with help of green synthesis method by using leaves extract of *Ocimum Tenuiflorum*. Green synthesis method are simple, non toxic, rapid method. The size and structure of nanoparticles is confirmed with the XRD technique. The synthesized ZnO average particle size is calculated as 28.08 nm by using scherrer Formula. The SEM image showed hexagonal shape nanoparticle formed with diameter 28.08 nm. These ZnO nanoparticles can be used in various industrial applications like active medium for lasers, luminescent material for fluorescent tubes, paints, and so forth.

V. REFERENCES

- [1]. Sagar Raut¹, Dr. P. V. Thorat², Rohini Thakre³ International Journal of Science and Research (IJSR) ISSN (Online): 2319-7064 Index Copernicus Value (2013): 6.14 | Impact Factor (2013): 4.438
- [2]. H. S. Nalwa, Encyclopedia Of Nanoscience and Nanotechnology, American Scientific Publishers, Vol. 10, pp. 1-46, 2007.
- [3]. E. Fortunato et. al., "Recent Advances in ZnO Transparent Thin Film Transistors", Journal Of Thin Solid Films Vol. 487, pp.205-211,2005.
- [4]. X. L. Cheng et. al., "ZnO Nanoparticulate Thin Film: Preparation, Characterization and Gas Sensing Property", Journal Of Sens. Actuators, Vol. 102, pp. 248-252,2004.
- [5]. M. Fonrodona et. al., "PEN as Substrate For New Solar Cell Technologies", Journal Of Sol. Energy Mater. Sol. Cells, Vol. 89, pp. 37-47, 2005.
- [6]. R. P. Wanga et. al., "Ultraviolet Lasing With Low Excitation Intensity In Deep Level Emission Free ZnO Films", Journal Of Cryst. Growth, Vol. 282, pp.359-364, 2005
- [7]. M. Vaseem, A. Umar, ZnO Nanoparticles: Growth, Properties, and Applications, American Scientific Publishers, Vol. 5, pp.2-3, 2010.
- [8]. M. Vafee, M. S. Ghamsari, "Preparation and characterization of ZnO nanoparticles by a novel sol-gel route", Journal of Material Letters, Vol. 61, pp. 3265- 3268, 2007.
- [9]. D. Tiwari et. al., "Application Of Nanoparticles In Waste Water Treatment", Journal Of World Applied Science, Vol. 3(3), pp. 417-433, 2008.
- [10]. Ganasangeetha D. et.al., "One Pot Synthesis Of Zinc Oxide Nanoparticles via Chemical and Green Method", Research Journal Of Material Science, Vol. 1(7), pp. 1- 8, 2013.
- [11]. Delia-Gabriela Dumbrava, Camelia Moldovan, Diana-Nicoleta Raba, Mirela-Viorica Popa, "Vitamin C, chlorophylls, carotenoids and xanthophylls content in some basil (*Ocimum basilicum* L.) and rosemary (*Rosmarinus officinalis* L.) leaves extracts", Journal of Agroalimentary Processes and Technologies, 18 (3), (2012), p 253-258.

Green Synthesis and Characterization of Copper Oxide Nanoparticle Using Ficus Panda Leaf (Mehendi) Aqueous Extract

A.V. Rajgure, D. R. Bijwe, P. A. Mandale, N. C. Ingle, N. G. Pokle

P. G., Department of Physics, G. S. Tompe Arts, Commerce & Science College, Chandur Bazar, Dist. Amravati, Maharashtra, India

ABSTRACT

The method of generating nanoparticle here which is copper oxide is very unique and most importantly ecofriendly method. As it says, it is ecofriendly it means it is less hazardous than others technical and chemical methods. We don't have to deal with chemical substances. And because of that it is also a cheaper method to perform. The copper oxide nanoparticle is generated using 150 ml of ficus panda extract mixing it with 50 ml of copper acetate solution. After adding them together, leave it to set the precipitate to settle down. Then filter all the solution using filter paper. Then leave it to dry.

Keywords:- UV, Ficus Panda, CuO

I. INTRODUCTION

Scientists are frequently researching for various methods which will be useful for mankind. To make their life journey more smooth. Discovery of nanoparticle and its application is one of their achievements toward human's development. Besides of all that extracting nanoparticle and its practical application in day to day life was not that much easy task. It's not should be useful but also should be harmless unlike other chemical methods. That's why scientist discovers the most convenient method for extraction of nanoparticle, which is GREEN SYNTHESIS. It is very convenient and nature friendly method which is also very safe and chemical free, universally accepted method for generating metal oxide nanoparticle. The most important phytochemicals in plants are phenols and flavonoids, found in different parts of the plants, such as shoots, leaves, stems, flowers, roots, and fruits. These phenolic compounds possess hydroxyl and ketone groups, contributing to the iron chelation and subsequently demonstrating a strong antioxidant property [1]. NPs synthesized through this green method increased in stability, prevented the agglomeration and deformation of the NPs and allowed adsorption of phytochemicals on the surface of the NPs, which enhance the reaction rate of NPs [2]. One of the common techniques in synthesizing Cu and CuO NPs is mixing a known concentration of plant extract to a known concentration of precursor and heating the mixture to a fixed temperature, with continuous stirring at a given time.

There are various types of metal oxide nanoparticles available, but besides all this copper oxide is easily available, safe, cheap, harmless and very productive chemical for using in this process of nanoparticle extraction.

Other uses of Cu Nanoparticles:

- 1) As heat transfer system, antimicrobial materials, super strong materials, sensors and catalyst
- 2) Among various metal oxides copper nanoparticles, due to their excellent physical and chemical properties and low cost of preparation have been of great interest.
- 3) Copper is a good alternative materials for noble metals such as Au and Ag and it is highly conductive and much more economical than them.
- 4) Also copper plays an important role in electronic circuit because of their excellent electrical conductivity
- 5) Act as an antifungal , antibiotic agent added to plastics, coatings and textiles, thermal conductive material, capacitor materials , nonmetals lubricant additives, microelectronic devices
- 6) Various plants can be used for green synthesis, here it is Ficus Panda

About F. Panda

Kingdom = Plantae, Clade = Tracheophytes, Clade = Angiosperms,
Clade = Eudicots, Clade = Rosids, Order= Rosales, Family = Moraceae
Genus = Ficus, Species = F. Retusa, Binomial name = Ficus Retusa
Synonyms = Ficus truncata (Miq) Miq. Nom. Illeg.

Uses of Ficus Panda:

There are many uses of ficus panda in cosmetic and medical field.

It's rich in fragrance and very useful for hair growth. That why it uses in different kind of hair products.

II. EXPERIMENTAL METHODS

Collection of sample

Ficus panda leaves were collected from the Campus of G. S. Tompe College Chandur Bazar during the month of December 2021. The fresh and green leaves were collected

Preparation of Extract

The leaves were cleaned properly by washing it, firstly with normal water and then with distilled water. After washing the leaves were wiped with clean cloth. Then cut it into small pieces.

It took 250 ml of water and 25 gm. of ficus panda leaves in a beaker and boiled it on 70-80 degree Celsius temperature. While this copper acetate solution is making, the heterogeneous mixture of ficus panda leaves and water turned its color into dark green solution after a certain time of interval. Then kept it for cooling. After cooling down the solution filtered it with filter paper and collected the green extract.

Instruments and Chemicals

Copper acetate ($\text{Cu}(\text{CH}_3\text{COO})_2 \cdot \text{H}_2\text{O}$), distilled water, UV Spectrometer, etc

Preparation of Copper acetate solution

5gm of copper acetate with 250ml of water was taken in a beaker.

Synthesis of CuO Nanoparticles:-

For the synthesis of copper oxide Nanoparticles, 150ml of green extract and 50ml of copper acetate solution mixed together by dropping method with the help of burette. The precipitate was formed at the bottom of the solution which was then filtered by filter paper and kept it to dry for nearly 24 hours.

After complete filtration the sample was collected from filter paper in china dish and crushed it into fine powder.

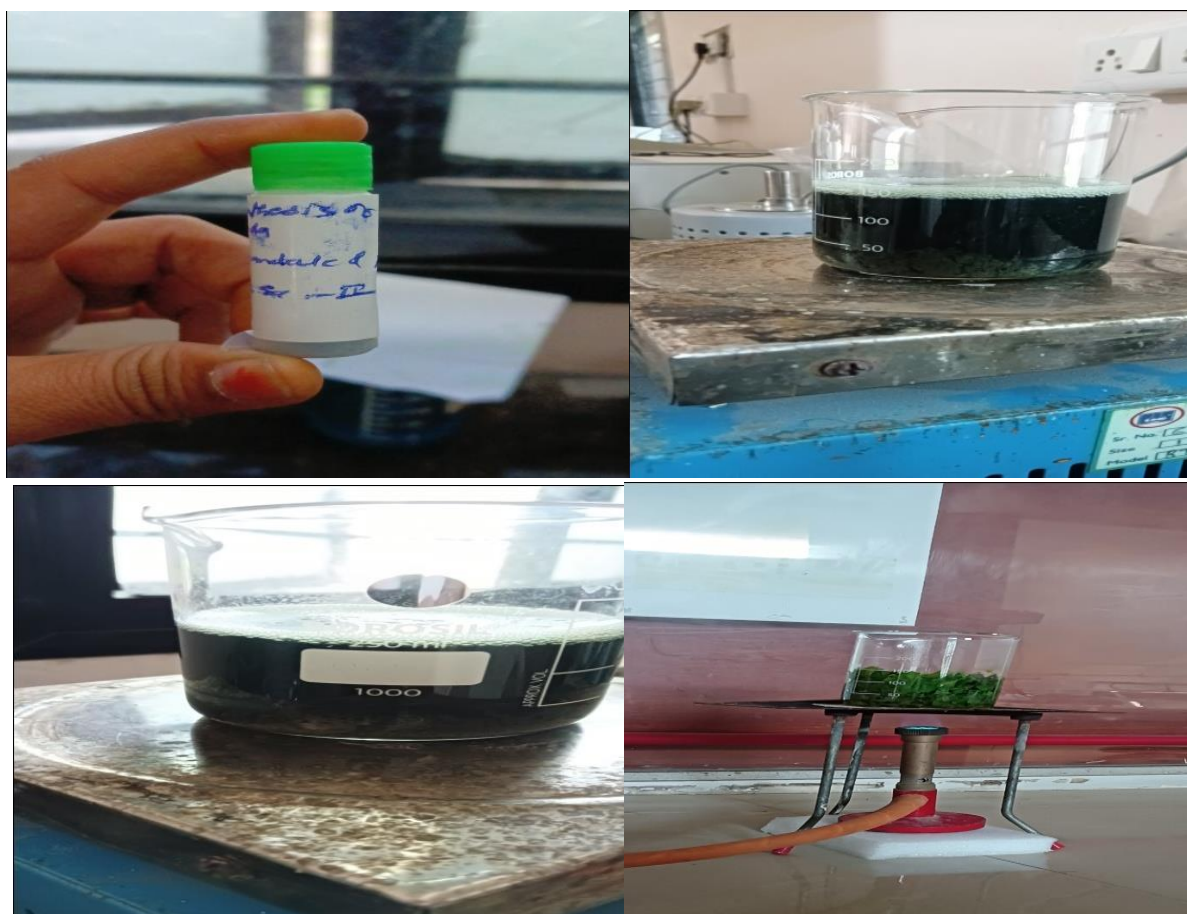


Fig. 1 Synthesis of CuO Nanoparticles using extract of Ficus Panda

III. RESULT AND DISCUSSION

UV-Vis spectral analysis of CuO NPs was done in the wavelength range of 200-800 nm. A peak was obtained at 250 nm due to inter band transition of core electrons of CuO NP and the spectrum was represented in Fig. 2.

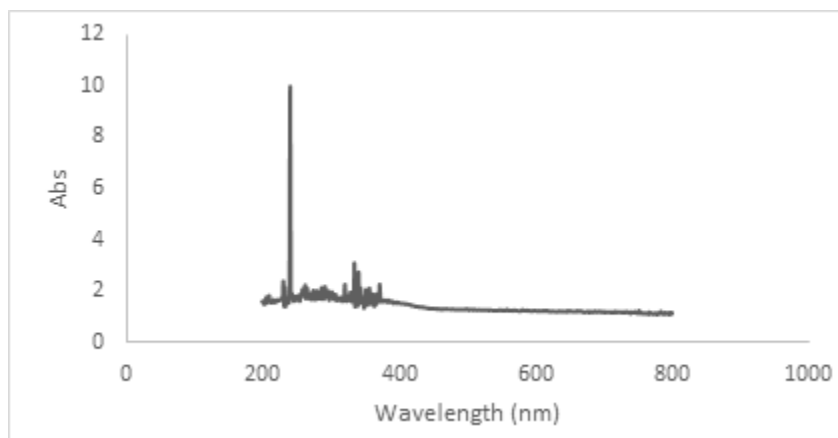


Fig.2 UV-Vis Spectra of CuO Nanoparticles

IV. CONCLUSION

By performing the method of green synthesis, it is concluded that, this is ecofriendly and economically useful method and can be done in any normal laboratory. It doesn't need much expense and toxins free.

V. REFERENCES

- [1]. Singh, S.; Kumar, N.; Kumar, M.; Agarwal, A.; Mizaikoff, B. Electrochemical sensing and remediation of 4-nitrophenol using bio-synthesized copper oxide nanoparticles. *Chem. Eng. J.* 2017, 313, 283–292
- [2]. Nasrollahzadeh, M.; Sajadi, S.M.; Rostami-Vartooni, A.; Hussin, S.M. Green synthesis of CuO nanoparticles using aqueous extract of *Thymus vulgaris* L. leaves and their catalytic performance for N-arylation of indoles and amines. *J. Coll. Interface Sci.* 2016, 466, 113–119.
- [3]. V. Bansal, A. Bharde, R. Ramanathan, S.K. Bhargava *Adv. Colloid Interf. Sci.*, 179 (2012), pp. 150-168
- [4]. J. An, D. Wang, Q. Luo, X. Yuan *Mater. Sci. Eng. C Mater. Biol. Appl.*, 29 (2009), pp. 1984-1989
- [5]. R. Sankar, R. Dhivya, K.S. Shivashangari, V. Ravikumar *J. Mater. Sci. Mater. Med.*, 25 (2014), pp. 1701-1708
- [6]. J. Wang, G. Zhang, Q. Li, H. Jiang, C. Liu, C. Amatore, X. Wang *Sci. Rep.*, 3 (2013), p. 1157
- [7]. R. Sankar, A. Karthik, A. Prabu, S. Karthik, K.S. Shivashangari, V. Ravikumar *Colloids Surf. B*, 108 (2013), pp. 80-84
- [8]. G.M. Sulaiman, W.H. Mohammed, T.R. Marzoog, A.A.A. Al-Amiery, A.A.H. Kadhum, A.B. Mohamad *Asia Pac. J. Trop. Biomed.*, 3 (2013), pp. 58-63
- [9]. J.M. Tranquada, B.J. Sternlieb, J.D. Axe, Y. Nakamura, S. Uchida *Nature*, 375 (1995), pp. 561-563
- [10]. Ya-Nan Chang, M. Zhang, L. Xia, J. Zhang, G. Xing *Materials*, 5 (2012), pp. 2850-2871
- [11]. F. Perreault, S.P. Melegari, C.H. da Costa, A.L. de Oliveira Franco Rossetto, R. Popovic, W.G. Matias *Sci. Total Environ.*, 441 (2012), pp. 117-124

Green Synthesis and Characterization of MgO Nanoparticles by Using Neem Leaves

D. R. Bijwe¹, S. P. Deshmukh¹, G. P. Gorle¹, A. R. Bhojane¹, R. V. Barde²

¹Post Graduate, Department of Physics, G. S. Tompe Arts, Commerce and Science College, Chandur Bazar,
Dist.- Amravati, Maharashtra, India

²Department of Physics, G. V. I. S. H., Amravati, Maharashtra, India

ABSTRACT

Nano Particle fabrication using plant extracts is an important alternative method because it is non-toxic, biocompatible and environmentally friendly. Synthesis of MgO Nanoparticles by green synthesis using Neem leaves which can be easily used for various biomedical applications. In this study MgO Nanoparticles have been bio-synthesized with Neem leaf extract. The synthesized MgO nanoparticles was characterized using UV-vis spectroscopy, X-ray Diffraction (XRD) study was used to confirm the crystalline nature of the biosynthesized nanoparticles and confirm the crystal size of the nanoparticles as 29.6 nm.

Keywords: MgO nanoparticles, Neem extract, UV-Vis, XRD

I. INTRODUCTION

Green synthesis is an eco-friendly, low cost, non-toxic chemical free method presenting a different way thinking in chemistry intended to eliminate toxic waste reduce energy consumption and to use ecological solvent. Nanoparticles due to their smaller size and large surface to volume ratio exhibit remarkable novel properties and methodical application in the field of biotechnology, sensor, medical, optical devices, DNA labelling, drug delivery and they are rewardingly treated as bridge between bulk material and atomic and molecular structures. Metal oxide nanoparticles have a high specific surface area and a high friction of surface atom. Because of the unique physiochemical characteristics of nanoparticle including their catalytic activity, optical properties electronic properties, antibacterial properties and magnetic properties, synthesis of oxide nanoparticle is a important topic in research in modern science.

Plant provide a better platform for nanoparticle synthesis as they free from toxic chemicals as well as provide natural capping agents moreover use of plant extract also reduce is the most adopted method green, eco-friendly production of nano particles and it can also a special advantage that the plants are widely distributed, easily available, much safer to handle and act as a source of several metabolites. Magnesium is an important mineral that act as a co factor of several enzymes and constituent for bon and teeth. It has been used in many application such as catalysis, catalyst supports, toxic west etc.



Neem leaves

Plant Description

Family Name :-Meliaceae, Binomial Name :-Azadirachtaindica, Common Name :-NeemPlant, Part Taken :- Leaves

shows the image of neem leaf. It shows anthelmintic, antifungal, antidiabetic, antibacterial, antioxidant, Anti-inflammatory and antiviral properties.

II. EXPERIMENTAL METHODS

• Material and Methodology

Present investigation is focused on the synthesis of the magnesium oxide the green synthesis method is used to synthesis the MgONPs using the precursor materials such as a magnesium nitrate and neem (*Azadirachta indica*) leaf extract has been used as reducing agent to synthesis the corresponding NPs.

• Preparation of neem leaf extract

To prepare the neem leaves extract 15 gram Neem leaves is washed properly in two to three times and and cut small pices and dry for 20-30 minutes at room temperature. The extract solution was prepared by boiling dried leaves in 500ml beaker consist 350 ml double distilled water for one hour at 100°C. Freshly prepared neem leaf extract was used for the synthesis of MgONPs. After cooling down the extract was filtered by Whatmann No.1 filter paper. Freshly prepared extracts alone have been used throughout the study.

• synthesis of Mgo Nanoparticles

In the experiment 20 ml fresh neem extract and 80 ml double distilled water was added to 500ml beaker and heated at 60°C and after some time this solution was added 20 gm Magnesium nitrate and heated at 80°C with continuous stirring for 260 min by using magnetic stirrer with hot plate. The magnesium nitrate ions was reduced to magnesia or Magnesium oxide Nanoparticles by using Neem leaves extract. The formation of magnesium oxide Nanoparticles (MgONPs) have been observed by change of the solution from yellow to yellowish-brown colour.



Neem Extract Magnesium Nitrate $Mg(NO_3)_2$ Solution heated & continuous stirring Magnesium oxide nanoparticles

Solution= Neem extract + magnesium nitrate + double distilled water

Influence of Neem (*Azadirachta indica*) leaf extract

The green synthesis of Nanoparticles of magnesium oxide was mediated by using different concentration of Neem leaf extracts. Different concentration ex 5ml, 10ml, 20ml, 25ml, 50ml concentrations used 5ml of extract was found too good for the synthesis of MgONPs.

Effect of stirrer temperature

The influence of stirring temperature for the green synthesis of MgONPs were studied by exposing the precursors in range of temperature from 35°C to 150°C. Among 35°C, 50°C, 80°C, 100°C, and 150°C stirring temperature used 80°C of stirring temperature was found to good for the synthesis of nanoparticles of magnesium oxide.

Influence of Calcination Temperature

The calcination Temperature is used for the crystallisation purpose. The study exposed the synthesised magnesium oxide nanoparticles in various calcinations Temperature such as 300°C, 500°C, and 700°C for one hour and average size of the magnesium oxide nanoparticles have been measured using Debye Scherer's formula ($0.9 / (B \cdot \cos)$). Among 300°C, 500°C and 700°C calcination Temperature was found good for the synthesis of magnesium oxide nanoparticles.

III. RESULT AND DISCUSSION

Magnesium oxide was synthesized by green method from Magnesium nitrate $Mg(NO_3)_2$ using Neem leaf extract. The influence of various parameters

UV-Vis spectra of Magnesium oxide Nanoparticles

UV spectral analysis of sample was done in wavelength range of 100-800 nm. The peak was obtained at 207 nm. The UV spectrum

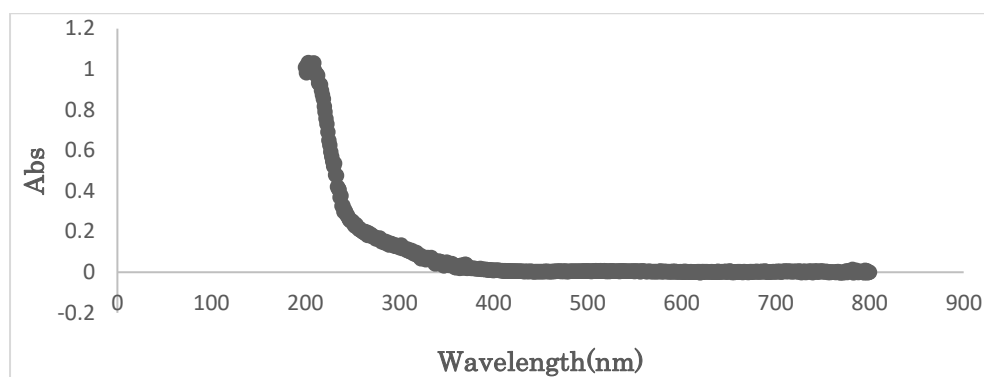


Fig. 1 UV-Vis spectra of Magnesium oxide Nanoparticles

XRD of Magnesium oxide Nanoparticles:-

A white coloured MgO nanoparticles were obtained as powder and the result of the XRD showed the structure was found to be cubic in nature. Debye Scherer's formula is used to find the particle size of synthesised MgO nanoparticles $D = K\lambda / (\beta * \cos\theta)$ (where, D is the crystal size, $K = 0.94$) and the size was found to be 29.6nm.

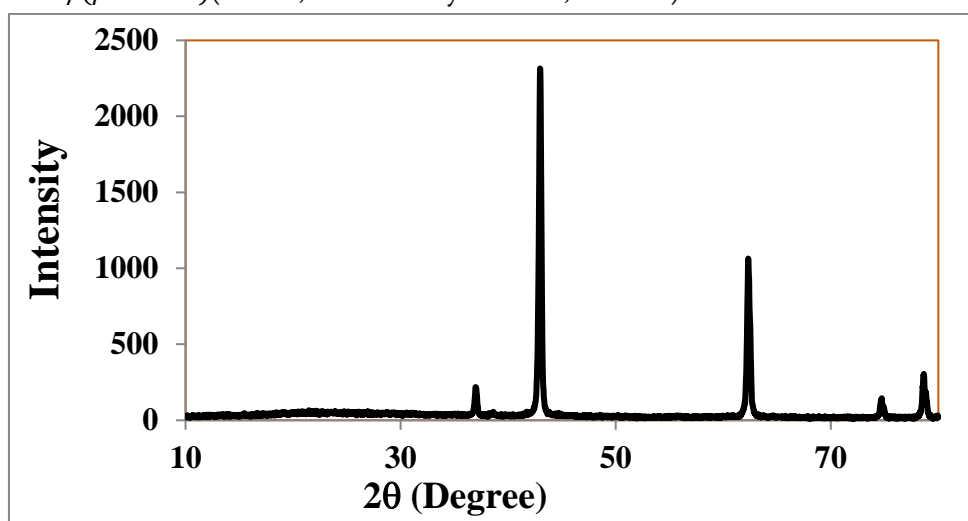


Fig. 2 XRD of MgO Nanoparticles

IV. CONCLUSION

Magnesium oxide was synthesized by Green synthesis method from Magnesium Nitrate $Mg(NO_3)_2$ using Neem (*Azadirachta indica*) Leaf extract. The influence of various parameters. Stirring temperature, concentration of Neem Leaf extract and calcination temperature were also checked and condition were optimized for the synthesis of Magnesium oxide Nanoparticles. The synthesis of magnesium oxide Nanoparticles are investigated by using the characterization techniques such as XRD and UV to confirm the presence of Magnesium oxide Nanoparticles. The green synthesised MgONPs were used in the study of seed germination. The study result revealed that the germination process was influenced by magnesium oxide Nanoparticles

V. REFERENCES

- [1]. S Krishna Moorthy, CH Ashok, K Venkateswara Rao, C Viswanathan(2015) 4360-4368.
- [2]. WaniAH and Shah MA (2012) A unique and profound effect of Mgo and ZnO nanoparticles on same plant pathogenic fungi 02(03), 40-44
- [3]. Akl M. Awwad and Ninda (2012) A green and Facile Approach for synthesis of magnetite Nanoparticles, Nanoscience and nanotechnology 2(6), 208-213
- [4]. Joy Sarkar, Manosij Ghosh, AnitaMukherjee, Dipankar Chattopadhyay and Krishnendu Acharya Biosynthesis and safety evaluation of ZnOnanoparticles (2013)
- [5]. Siti Fatimah, RistiRagadhita, DwiFitria Al Husaeni, AsepBayu Dani Nandiyanto how to calculate the crystallite size from XRD using Scherrer method.2(1) 2022 65-76.
- [6]. S. Prathap Chandran, Minakshi Chaudhary, Renu Pasricha, Absar Ahmad, Murali Sastry (2006) 22,577-583.
- [7]. Kannan Badri Narayanan, Natarajan Sakthivel (2010) Biological synthesis of metal nanoparticles 156(1-2),-13.
- [8]. Lei Zheng, Fashuihong, Shipenglu and Chao liu(2009) 5(10),1128-1132.
- [9]. HeneistC,Mathieu JP, Vogels C, Rulmont A, Clootsr (2003) Morphological study of magnesium hydroxide nanoparticles precipitated in dilute aqueous solotion249,321-330.
- [10].Avinash C Pandey, Sharda S. Sanjay and Raghvendra S. Yadav,(2010) Application of ZnO nanoparticles in influencing the growth rate of cicer arietinum5(6), 488-97
- [11].Sohail Yasin, Lin Liu and JumingYao(2013)A green And Facile Approach for synthesis of magnetite nanoparticles 2(6), 208-213.
- [12].Dalip Kumar, Buchi Reddy V, Braj G. Mishra, Rana RK, Allikarjuna N. NadagoudaandRajender S. Varma(2007). Nanosized magnesium oxide as catalyst for the rapid and the green synthesis of substituted 2-amino-2-chromenes. 63, 3093-3097.
- [13].Rahman TR, S Hossain MI, Islam MT, Rahman TS, Kharun H synthesis and characterization of MgO Nanoparticles using Neem leaves with their photocatalytic and Antioxidant properties 2021
- [14].Kavitha, K. S,Baker, S, Rakshith D. Kavitha, H. U, Yashwantha Rao, H. C. Harini, B. P. & Satish S. (2013). Plants as green source towards synthesis of nanoparticles 2(6),66-76.

Molecular Interaction Between the Monosaccharide and Salt Solution by Acoustical Approach

Akshay M. Jirkuntwar*, Urvashi P. Manik, Paritosh L. Mishra

PGT Department of Physics, Sardar Patel Mahavidyalaya, Chandrapur, Maharashtra, India

ABSTRACT

The different Thermo-acoustical properties have been investigated from the ultrasonic velocity & density measurement through ultrasonic velocity interferometer and 10 ml specific gravity density bottle. The sound velocity and density of monosaccharide (D- Glucose) in aqueous electrolytic solution (Magnesium chloride) provide valuable information regarding the ilk, strength of interaction and the formation of hydrogen bonds. The result is analyzed and explains on the basics of possible molecular interaction in term of structure – making and structure- breaking effects of monosaccharide in the aqueous solution of magnesium chloride at different temperature.

Keywords: Monosaccharide, electrolyte, thermo-acoustic property, intermolecular interaction.

I. INTRODUCTION

Ultrasonic sound refers to instantaneous sound pressure with a high frequency than human audible sound frequency (20Hz to 20 kHz). Ultrasonic is most useful in the investigation of various specialization like excess pressure grain size microstructure, elastic constant etc. ultrasonic is the non-destructive flexible method. Acoustical parameter calculating from the values determined by the ultrasonic viscosity, velocity and density. [1]

Ultrasonic measurements are astronomically used to study the intermolecular interaction in pure and mixtures of liquids. residual acoustical properties of mixture are used in the study of arrangement and Molecular interaction. [2] Theoretical treatment and analysis of the experimental thermodynamic properties of liquids and mixtures depends upon reliable equations of the parameters for the pure liquids. Properties of liquid-liquid mixtures are thermodynamically very important as a part of studies of thermodynamic, acoustic and transport aspects [3]. The present Work mainly deals with aqueous solution of monosaccharide the (D-glucose), they are of the same family and having many common properties with a sharp feature differences, which are the most expressive bimolecular of life on the earth. The carbohydrates, constantly termed as sugars are “Staff of life” for most living organism. They are widely distributed in plant and animal.[4] All the carbohydrates (D-glucose, sucrose,-B-D lactose) were made anhydrous. The low conductivity of water as used for preparing the Solution, which is made up of passing distilled water through a cation and anion Resin’s. [5]

D-Glucose is the most common naturally occurring simple sugar and is a building block for disaccharides sucrose and lactose and higher oligo- and polysaccharides. It is the only sugar unit in cellulose and starch. Animals and plants produce D-glucose by glycogenolysis and photosynthesis, respectively, and use it as a primary energy source empirical formula for monosaccharide is $(C_{12}H_{22}O_{12})_n$, predict the great variety of structures and interesting conformational flexibility. The physical properties of monosaccharide in aqueous solution are monosaccharides are colorless and crystalline compound. They are readily soluble in water, they have sweet taste. D- glucose and L-glucose are mirror images of each other, the presence of asymmetric carbon atoms in a compound give rise to the formation of isomers of that compound, etc. [6]

II. EXPERIMENTAL DETAILS

A. MATERIALS

In the present work, we have used analytical reagent (AR) grade with 99% purity of D-Glucose {[CAS No-50-99-7] [molecular wt. – 180.156 g/mol]} used as solute , magnesium chloride with 99% purity of {[CAS No-7786-30-3][molecular wt-203.30 g/mol]} and fresh distilled water having [molecular wt. 18.01528 g/mol with density – 1000 kg/m³] was used as a pure universal solvent and this work was done at different temperatures (i.e.283.15,288.15, 293.15 & 298.15K) and concentrations.

B. METHOD

A digital ultrasonic velocity interferometer was used for measuring the ultrasonic velocity operating at frequency 2 MHz supplied from Vi Microsystems Pvt. Ltd., Chennai (Model VCT:71) with an overall accuracy 0.0001m/s.

The densities of the solutions were determined using 10ml specific gravity bottle having accuracy $\pm 2 \cdot 10^{-2}$ kg/m³ and digital electronic balance (Contech CA-34) having accuracy ± 0.0001 gm. an average of triple measurements was taken into account for better accuracy. The experimental temperature was maintained constant by circulating water with the help of an automatic thermostatic water bath supplied by Lab-Hosp. Company Mumbai having an accuracy ± 1 K temperature.

III. DEFINING RELATIONS

For the derivation of several acoustical and thermo-dynamical parameters the following defining relations reported in the literature are used:

- Adiabatic Compressibility (β) = $1/(U^2\rho)$
- Acoustic Impedance (Z) = $U\rho$
- Non linearity parameter by Hartmann: $B/A= 2+0.98 \cdot 10^4/ u$
- Relative association (R_A): $(R_A) = (\rho/\rho_0) (u_0/u)^{1/3}$

IV. RESULT AND DISCUSSION

A. ULTRASONIC VELOCITY & DENSITY:

In the present work ultrasonic velocity of pure water has been measured at temperature and the observed data tabulated in the *table (1)* The ultrasonic velocity of the system grow with the grow of temperature as well as concentration In *table (2)* this indicates that increscent in the molecule of solute and solvent due to dipole-Dipole, ion dipole interaction. [8]

In the present Investigation of D-glucose in aqueous solution of magnesium chloride increases with the increase in concentration and decrease with an increasing temperature in *table (1)* thus particle become loosely packed to cause a decrease in density as the temperature increases.[9]

Table 1: Experimentally determined values of Ultrasonic velocity at different concentration and temperature.

Velocity				
Conc.	283.15K	288.15K	293.15K	298.15K
0	1447.101	1466.032	1481.496	1498.101
0.001	1447.437	1466.822	1482.906	1484.514
0.005	1447.653	1467.661	1482.692	1512.688
0.01	1449.001	1467.870	1483.105	1498.284
0.05	1448.53	1468.403	1484.722	1499.554
0.1	1449.441	1470.802	1484.735	1500.560

Table 2: Experimentally determined values of Density at different concentration and temperature.

Density				
Conc.	283.15K	288.15K	293.15K	298.15K
0	999.76	999.1	998.202	997.031
0.001	1020.982	1019.197	1015.667	1013.9009
0.005	1024.2287	1019.1567	1017.1951	1014.4769
0.01	1024.916	1021.2209	1018.4	1017.033
0.05	1029.9534	1025.2821	1022.254	1021.0031
0.1	1032.9516	1029.34	1026.9552	1023.767

B. ADIABATIC COMPRESSIBILITY:

Physico-chemical properties of liquid can be understood by adiabatic compressibility (β) as the hydrogen bonding between the unlike components in the solutions decreases with the compressibility. In the present case it is found that the adiabatic compressibility decreases with increase in concentration. Because, as water is polar solvent and when salts and monosaccharide mixed, the well intermolecular interaction occurred, resulting in close packing of molecules. The decrease values of adiabatic compressibility listed in *table (3)* indicate the strong association of monosaccharide and salts molecules. The compressibility of the solvent is higher than that of solution and decreases with increase in concentration of the solution.[10]

Table 3: Calculated values of Adiabatic Compressibility at different concentration and temperature.

Adiabatic Compressibility(β)*10 ⁻¹⁰				
Conc.	283.15K	288.15K	293.15K	298.15K
0	4.77646	4.65698	4.56437	4.46899
0.001	4.67501	4.56023	4.47735	4.47544
0.005	4.6588	4.5552	4.47192	4.30784
0.01	4.64702	4.5447	4.46414	4.38003
0.05	4.6273	4.52341	4.43763	4.35561
0.1	4.60807	4.49089	4.41724	4.33803

C. ACOUSTIC IMPEDANCE:

In *table (4)* the acoustic impedance is a acoustical parameter which depends on the temperature and concentration of solution. Acoustic impedance is increases with increasing concentration. The increase of acoustic impedance is an indication of strong interaction between D-glucose and aqueous magnesium chloride. [11]

Table 4: Experimentally determined values of Acoustic Impedance at different concentration and temperature.

Acoustic Impedance (Z)				
Conc.	283.15K	288.15K	293.15K	298.15K
0	1446753.6	1464712.5	1478832.2	1493653.1
0.001	1477807.1	1494980.5	1506138.6	1505150.0
0.005	1482727.7	1495776.5	1508187.0	1534587.0
0.01	1485104.3	1499019.5	1510394.1	1523804.2
0.05	1491918.3	1505527.3	1517763.0	1531049.2
0.1	1497202.4	1513955.3	1524756.3	1536223.8

D. NON LINEARITY PARAMETER BY HARTMANN:

This interaction can be described in terms of Non linear parameters which measure how much each compound contributes to the mixtures overall polarity and internal pressure in *table (5)*. [12]

Table 5: Calculated values of Non Linearity parameter at different concentration and temperature.

Non Linearity Parameter				
Conc.	283.15K	288.15K	293.15K	298.15K
0	8.77216	8.684710	8.614935	8.54161
0.001	8.770588	8.681110	8.608645	8.601486
0.005	8.769578	8.677291	8.609599	8.478577
0.01	8.763280	8.676340	8.607758	8.546027

0.05	8.765479	8.673917	8.60056	8.576489
0.1	8.761227	8.663031	8.600504	8.531214

E. Relative association (RA):

It is studied to understand the ion-ion or ion-solvent interaction. In present study the relative association increases as increase in concentration due to decrease in intermolecular free length. It suggests that the salvation of D-glucose predominates over breaking up to the solvent structure, as observed in table 8 it is varying irregularly with increase in temperature due to addition of D-glucose in *table (6)*. [13]

Table 6: Calculated values of Relative Association at different concentration and temperature.

Relative Association (RA)				
Conc.	283.15K	288.15K	293.15K	298.15K
0	1	1	1	1
0.001	1.021148	1.019931	1.017173	1.020013
0.005	1.024344	1.019697	1.018753	1.014216
0.01	1.024713	1.021714	1.019865	1.020020
0.05	1.029861	1.025653	1.023353	1.023712
0.1	1.032643	1.029152	1.028056	1.026004

V. CONCLUSION

It is concluded that the system explained on the basis of molecular interaction in terms of structure-making and structure-breaking effects of monosaccharide in the aqueous solution of magnesium chloride at different temperatures was determined.

VI. REFERENCES

- [1]. Thrahim P., Vinatagum V, Murgan V, Edward V, Jr. Information and Computational Sci. 9(2019) PP 391-399
- [2]. Palanir, Kalavathy S., J. Pure Appl. Ultrasonic 33 (2011) PP 33-383
- [3]. Babavali S, Narendra K., Shakira P., Srinivasu Ch., International J Phys. Math. Sci., 6, (2016) pp 3
- [4]. Nithiyantham S., Palaniappan L., Arabian J. Chemistry 5 (2012) PP 25-30.
- [5]. Ahmada S Nasir K, Saleem R J. Sci Ind. Res. 47(2004) PP 349-355. J Stenger, M. Cowman, F. Eggers, E. Eyring, U. Kautze, S. Petrucci, J. Phys. Chem. B 104(2000) PP 4782-7990.
- [6]. Greenspan M., Tschiegg C.E. (1957) J. of Research of the National Bureau of Standards, 59(4), 249-254.
- [7]. Eyring H. and Kincaid F., Chem J. Phys, Vol.6, pp.620-629, (1938).
- [8]. Mirikar S., Pawar P. & Bichile G. Ame J. Pharm. Pharma., Vol. 2(1), pp; 19-25, (2015)
- [9]. Endo H., (1973) Bull. Chem. Soc. Jpn, 46(4), 1106-1111.

- [10].Khan R., Khan I, Thermo. J. Acta., Vol. 45 (2009),pp: 483.
- [11].Mishra P., Lad A., Manik U., Int. Res. J. Sci. Eng., 2020 pp 260-265.
- [12].Jahagirdar B., Arbad B., Walvekar A., Shankarwer A. and Lande M., J. Mol. Liq., Vol.85 (2000) pp-361-37.

Molecular Interaction and Thermodynamic Properties of Potassium Nitrate at Various Concentrations and Temperatures by Ultrasonic Method

Neha Pathan, Dr. Urvashi Manik, Paritosh Mishra

PGT, Department of Physics, Sardar Patel Mahavidyalaya Chandrapur-442401, Maharashtra, India

ABSTRACT

In the present manuscript, we intend to examine the type of solute-solvent interactions present in such a system which is valuable to various sector. Systematic knowledge of the thermodynamic properties in conjunction with other volumetric properties provides useful information about water-solute interactions. We examine, therefore velocity, density, and viscosity of various concentrations of KNO_3 that have been measured in various aqueous solutions at 2MHz and 283.15K to 298.15K, to study the ion-solvent interactions. With the use of these experimental values desired thermodynamical and acoustical parameters such as available volume, ultrasonic attenuation, entropy, enthalpy, and L.J.P have been calculated.

Keywords- KNO_3 , Acoustical parameters, ultrasonic velocity

I. INTRODUCTION

Ultrasonic studies help in characterizing the acoustical and thermodynamic behavior of various liquid mixtures.[1-2]Ultrasonic and thermodynamic properties of a liquid mixture are of great significance in obtaining an in-depth knowledge of inter and intra-molecular interactions.[3]The thermophysical parameters are a very easy tool for understanding and correlating the result. This result predicts a direct correlation of physical parameters of the liquid system. The study of ultrasonic is found to be useful in measuring several physicochemical parameters [4-6]

Potassium nitrate is used as a diuretic in medicines. It is also used as an ingredient in toothpaste. It makes the teeth less sensitive to pain, by interfering with the transmission of pain signals to the nerves of the teeth. It is also added to the drugs for back pain and joint pain. Potassium nitrate affects nucleic acid synthesis in the greening cucumber cotyledons [7] and the stability of tropomyosin [8]

Hence present work mainly provides useful information on the measurement of velocity, density, and viscosity values of KNO_3 solution at different temperatures and concentrations. This information is useful to understand various biochemical reactions occurring in living organisms.

II. MATERIAL AND METHOD

AR grade of Potassium Nitrate having a molecular weight of 101.1032g/mol was obtained from HIMEDIA private ltd. The purity of the compound is 99.99%. The various concentrations ranging from 0.01-0.10 mole/Kg were prepared from the standard formula and used on the day were prepared.

In the proposed work we have planned to measure Ultrasonic velocity at different solutions using a digital Ultrasonic interferometer or pulse-echo overlap technique with the function of concentration and temperature. The density measurement of solutions would be carried out using specific gravity density bottles respectively. The temperature variation of different samples will be maintained constant using a thermostatically controlled digital water bath with a flowing water technique. The viscosity has been calculated with the help of Oswald's Viscometer.

III. DEFINING RELATION

Using measured data, the following acoustical parameters have been computed using the standard relations,

Ultrasonic Attenuation (α) :

Ultrasonic attenuation has been calculated using the relation

$$\alpha = \frac{0.1151}{v} U_t \dots \dots \dots 1$$

Available volume (V_a) :

Available volume can be calculated as

$$V_a = V_m \left(\frac{1-c}{c_\infty} \right) \dots \dots \dots 2$$

Where C is the Velocity of the compound and C_∞ infinite velocity

Enthalpy (ΔH_i): Enthalpy can be calculated using the equation

$$\Delta H_i = \frac{P_i \times V_m}{M_{eff}} \dots \dots \dots 3$$

M_{eff} is an effective molar mass and P_i is internal pressure and V_m is the molar mass

Entropy (ΔS): Entropy is given by the formula

$$\Delta S = \frac{(\Delta H_i - \Delta G)}{T} \dots \dots \dots 4$$

Where ΔH_i is Enthalpy of the system ΔG is Free energy of activation of the system, and Absolute temperature in Kelvin

Lenard Jones Potential (L.p.j): It can be calculated using the relation

$$(LJ) 6 - \left(\frac{v_m}{v_a} \right) - 13 \dots \dots \dots 5$$

IV. RESULT AND DISCUSION

- 1) **Graph:** Graphical representation of Potassium Nitrate at temperatures 288.15k, 288.15K, 293.15K 298.5K respectively the ultrasonic attenuation, available volume, enthalpy, are calculated by using the following standard relation [1-5]

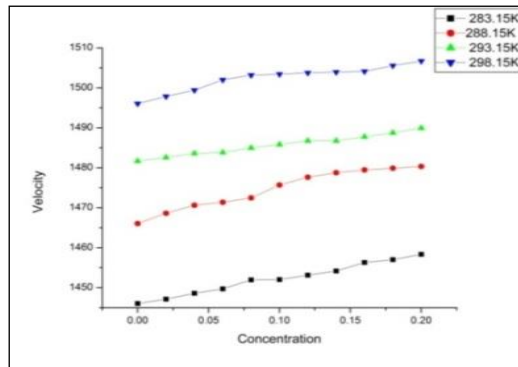


Fig IV.a Variation of velocity with concentration

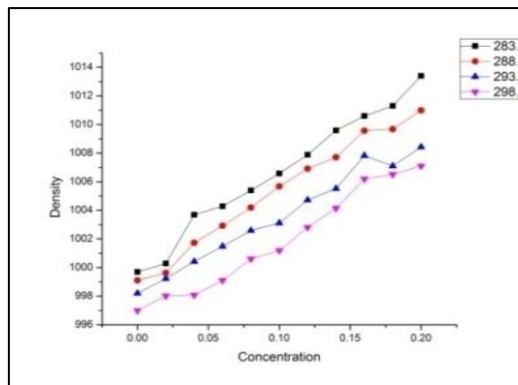
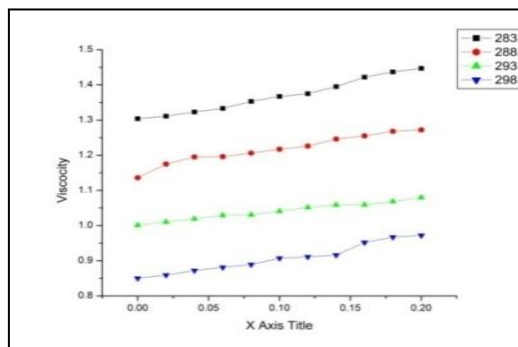
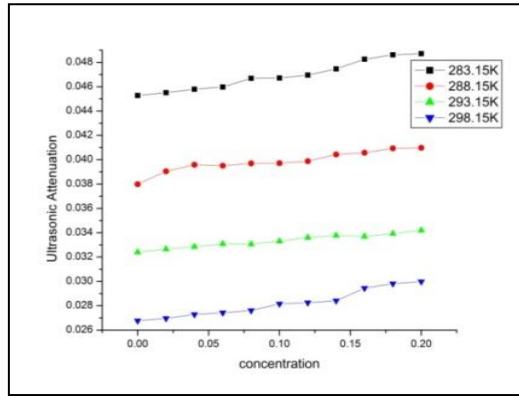


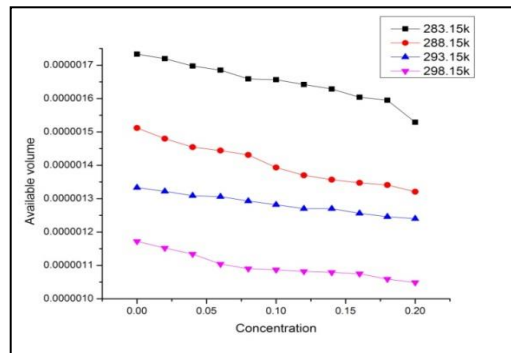
Fig IV.b Variation of density with concentration



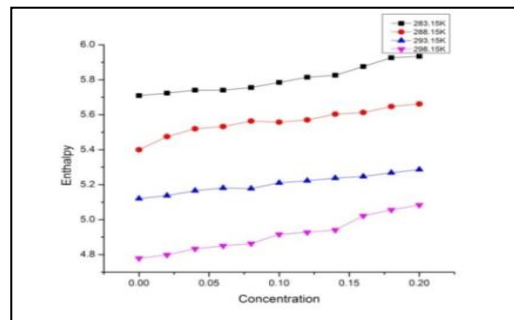
FigIV.c Variation of viscosity with concentration



FigIV.d Variation of ultrasonic attenuation with concentration



FigIV.e Variation of available volume with concentration



FigIV.f Variation of enthalpy with concentration

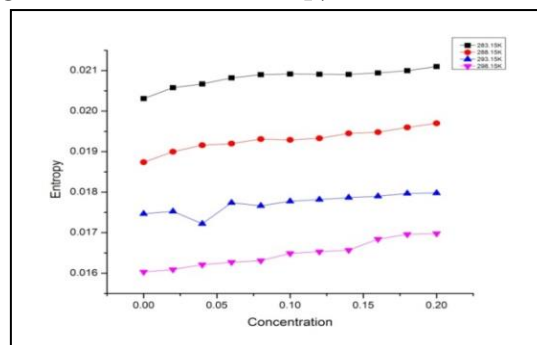


Fig IV.g Variation of entropy with concentration

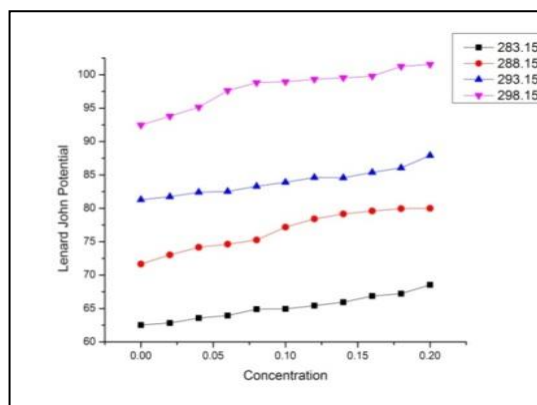


Fig IV.h Variation of L.J.P with concentration

From the graph IV.a to IV.b we observe the trends of all acoustical parameters with variation in concentration and temperature. The ultrasonic velocity increases with the molar concentration of solute as well rise in temperature. This increase in ultrasonic velocity, in the aqueous solution of potassium nitrate may be attributed to the cohesion brought by the ionic hydration. The increase in density with molar concentration may be due to enhancing solute-solvent, and solvent-solvent interaction exists between water and potassium nitrate. [9-10]

Fig IV.(c) suggests that the viscosity of potassium nitrate increases with an increase in molar concentration. An increase in viscosity of solution indicates a greater association among the molecules of solution. A decrease in viscosity with temperature is because of cohesion and frictional forces diminished due to frictional forces of the molecule.[11]

Ultrasonic attenuation values increase with an increase in the concentration of solute fig IV.(d). Decrease in viscosity and density whereas, an increase in sound speed with the temperature affects the absorption of ultrasonic waves causing a decrease in the attenuation with temperature.[12]

The variation of available volume is shown in Fig IV.(e) it is observed that the fig that the available volume of potassium nitrate solution decreases with the rise in concentration and also with temperature. This indicates that there exists a significant solute-solvent interaction that leads to structure-promoting behavior. [13] Fig IV.(f) shows that the Entropy increases with an increase in the concentration of potassium nitrate. This indicates the availability of more solute molecules in a given region, giving rise to solute-solvent interaction. [14]

From the fig IV.(g) shows the variation of Entropy with temperature. From the observed graph, it is concluded that the entropy decreases with the increasing value of temperature. [15] This variation leads to the conclusion that the medium is closely packed and favors the solute-solvent interactions, constant is given in fig All these constant shows a minor increase in their respective values due to an increase in concentration. These variations conclude that the medium is closely packed and favors the increase in solute-solvent interactions.[16] As monitored from fig IV.(h) values of Lenard john's potential increase with an increase in concentration and decrease with an increase in temperature the Lenard John Potential values indicate that dipole-dipole attraction is stronger than induced dipole-dipole attraction.[17]

V. CONCLUSION

The ultrasonic study of the aqueous solution of potassium nitrate confirms the presence of strong ion-dipole interactions. The experimental parameters give valuable information regarding ion-solvent interaction in an aqueous solution. KNO_3 is added as a solute result breaking hydrogen bonds in the solvent system and thus producing free solvent molecules. This result increases the value of ultrasonic velocity and decreases with available volume with concentration which shows the solute-solute interaction is smaller than solute-solvent interactions.

VI. REFERENCES

- [1]. SB Alisha; MCS Subha; KC Rao, J. Pure Appl. Ultrason., 2001,23, 26.
- [2]. MCS Subha; P Srinivasa Rao; G Narayanaswamy, Acoustica acta acustica,1996,82,155.
- [3]. Indu Saxena; RN Pathak; Vijay Kumar; Rikkam Devi, Int.J. Of Appl. Research.2015,1(9), 562-569
- [4]. Varada Rajulu; Mabu Sab, Bull. Mater.Sci.,189(3),247-253
- [5]. R Paladhi; R.P.Sing, Acoustica, 1990,72,90-95
- [6]. RP Singh; GV Reddy; S Majumdar and YP Singh, J.Pure Appl.Ultrason.1983,5,52-54
- [7]. J Knypl; S Chylinksa and M Krystyna, M.Int.Phy.Cytol.,1974,166,345-350
- [8]. S Leher; A Yua., J.Struct.Biol.,1998,122,176-179
- [9]. VA Tabhane; OP Chimankar; S Manja;TK Naminarayan. Pure Appl. Ultrason.1999,(21),67
- [10].S Thirumaran; AN Kannapan, Global J. of Mole.Sci.,2009.49(2) 160
- [11].KC Patil; CM Dudhe, Der Pharm. Chemical.,2015,7(12),219-226
- [12].VV Surnychev; VI Kovalenko;AS Lagunov and VV Belyaev, Tech Phys.,2005,50(10),1379-1382
- [13].S Takeda; I Morioka; K Miyashita; A Okumura; Y Yoshida; K Matsumoto, European J. of Appl. Physiology. (1992), 65(5), 403– 408.
- [14].Ezil Pvai; P Vasantrani; A Kanappan.J.of pure and applied physics, 2004, 42,934-936.
- [15].R Rani;A Kumar, R sharma ;B saini; RK Bamezai RK. Acta chimica slovenica (2016)
- [16].G Jones; M Dole. J.of the American chemical society. 1929;51
- [17].A Dhanalakshmi; Vasanta Rani, J. of pure and applied ultrasonics. 1999,21(3),79-82

Measurement of Thermo-Acoustic and Volumetric Properties of Zinc Sulphate in Aqueous Solution of Monosaccharide

Pooja V. Lande*, Urvashi P. Manik, Paritosh L. Mishra

*PG, Department of Physics, Sardar Patel Mahavidyalaya, Chandrapur-442401, Maharashtra, India

ABSTRACT

Ultrasonic velocity and density measurement of Zinc Sulphate have been performed by ultrasonic interferometer technique in aqueous solution of monosaccharides (glucose) as a function of concentration (i.e. 0.2 and 0.5 Mole/kg) and temperature (i.e. 298.15k, 293.15K 288.15k and 283.15k). The different acoustical properties have been explore data from the density and ultrasonic velocity such as adiabatic compressibility, acoustic impedance, specific heat ratio, non-linearity parameter, relative association and isothermal compressibility. The result have been explain on the basis of association or dissociation exist between zinc sulphate and aqueous glucose solution or effect of structure making and breaking of solute in solvent.

Keywords: acoustical parameters, density, ultrasonic velocity and Zinc Sulphate.

I. INTRODUCTION

Ultrasonic measurement are astronomically used to study the intermolecular interaction in pure and mixtures of liquids. Residual acoustical properties of mixture are used in the study of arrangement and molecular interaction.[1] Ultrasonic sound refers to instantaneous sound pressure with a high frequency than human audible Sound frequency (20Hz to 20kHz). Ultrasonic is most useful in the investigation of various specialization like excess pressure grain size microstructure, elastic constant etc. ultrasonic is the non-destructive flexible method. Acoustical parameter calculating from the values determined by the ultrasonic velocity and density.[2] ultrasonic is the resourceful or all around and non-destructive techniques and gives an extensive large application in distinguish thermodynamic and physiochemical behavior of liquid mixture. [3]

The current work mainly deals with aqueous solution of monosaccharide (glucose) which is the most expressive biomolecule of life on the earth. The carbohydrates, constantly termed as sugars are "Staff of life" for most living organism. They are widely distributed in plant and animal. [4] $C_n (H_2O)_n$ is the general formula for all carbohydrates. This formula is only valid for simple sugars, which are made up of the same amount of carbon and water. All the carbohydrates (D-Glucose, sucrose, -B-D lactose) were made anhydrous. The low conductivity of water as used for preparing the Solution, which is made up of passing distilled water through a cation and anion resins. [5]

Empirical formula For monosaccharide is $(CH_2O)_n$, predict the Great variety of structures and interesting conformational flexibility. The physical properties of monosaccharide in aqueous solution are monosaccharide are colorless and crystalline compound. They are readily soluble in water; they have sweet taste. D-glucose and L-glucose are mirror images of each other, the presence of asymmetric carbon atoms in a compound give rise to the formation of isomers of that compound, etc. [6]

II. MATERIAL AND METHOD

In the present work, we have used analytical reagent (AR) grade with 99% purity of Glucose {[CAS No- 50-99-7] [molecular wt. – 180.156 g/mol]} used as solute, Zinc Sulphate with 99% purity of {[CAS No-7733-02-0][molecular wt-161.47 g/mol]} and fresh distilled water having [molecular wt. 18.01528 g/mol with density – 1000 kg/m³] was used as a pure universal solvent and this work was done at different temperatures (i.e.283.15,288.15, 293.15 & 298.15K) and concentrations

1. This experiment was carried out at different temperatures (i.e.283.15, 288.15, 293.15 & 298.15K) which were maintained by a digital water bath.
2. The measurement of weight was done by using a digital weighing machine having an accuracy of ± 0.1 mg.
3. Some basic parameters like, Ultrasonic velocity were measured on a digital ultrasonic interferometer with a 2MHz frequency having an accuracy of 0.1%.
4. The ultrasonic density of this solution was accurately determined by using a 10ml density gravity bottle.
5. Using the measured data, some other acoustical parameters have been calculated using standard relation.

Defining Relation:

- 1 **Adiabatic Compressibility** The adiabatic compressibility is defined as ‘the fractional decrease volumeter unit Increase of pressure. $\beta_a = 1/u^2\rho$,
Where, u=ultrasonic velocity and ρ =densityof solution
- 2 **Acoustic Impedance** The specific acoustic impedance is given by $Z = u\rho$
Where, u=ultrasonic velocity ρ =densityof solution
- 3 **Specific Heat Ratio:** $\gamma = (17.1/ T^{4/9} \rho^{1/3})$
Where, T= temperature and ρ = Density
- 4 Nonlinear it y parameter by Hartmann.[10]
 $B/A = 2 + 0.98 \cdot 10^4 / u$
Where, u is ultrasonic velocity, u is in m/s
- 5 **Relative association (RA):** The relative association parameter is the relative association between the component’s molecules in a liquid mixture and is given by $(R_A) = (\rho/\rho_0) (u_0/u)^{1/3}$ where, ρ is density, u ultrasonic velocity, ρ_0 is the density of water, u_0 is the ultrasonic velocity of water.
- 6 **Isothermal compressibility (β_i):** Isothermal Compressibility is a useful concept in determining the compressible properties of the reservoir. $\beta_i = \gamma B_a$, Where γ =specific heat ratio

III. RESULT & DISCUSSION

The experiment value of ultrasonic velocity (U) density (ρ), and other allied parameter of zinc sulphate in aqueous solution of monosaccharides for the experimental system at different temperature (283.15k, 288.15k, 293.15k & 298.15k) and Concentration are demonstrated in figures.

The Ultrasonic velocity, density have been used by many workers to calculate different acoustical parameters such as adiabatic compressibility, acoustic impedance and so on these parameters were successfully employed to understand the structural change and the nature of molecular interactions between the interacting component in the mixtures. These parameters were used to explain different types of molecular interaction, such as strong, weak charge transfer, complex formation and hydrogen bonding interaction and the structure making and breaking properties of the interacting components

Ultrasonic velocity is the most important parameter that gives information concerning the nature of molecular interaction & is affected by temperature and concentration. The ultrasonic velocity of the system increases with the increase in concentration as well as temperature (as show in fig.1). This suggests, association in the molecular of solute and solvent, due to ion-dipole, dipole-dipole interaction.[7]

The density of zinc sulphate in aqueous glucose in the present investigation increases with the increase in concentration and decreases with an increase in temperature (as shown in fig. 2) as the temperature increases, particle become loosely packed to cause a decrease in density. [8]

The dependence of adiabatic compressibility of zinc sulphate in aqueous solution of glucose on concentration at different temperature is as shown in fig (3) It is obvious that if ultrasonic velocity increases, then adiabatic compressibility of solution decreases as there exists inversely proportional relationship between them. In the present investigation, the decrease in adiabatic compressibility value with rise in concentration at constant temperature is observed. The decrease in adiabatic compressibility with rise in temperature at a given concentration is observed. [7]

The acoustic impedance is the parameter which depends on concentration and temperature of solution. Acoustic impedance increases with increase in concentration. The increase of acoustic impedance is an indication of strong interaction between zinc sulphate and aqueous solutions of glucose. [9]

Fig. 5 displays the variation of specific heat ratio at different concentration of zinc sulphate biomolecules in 0.2 mol/kg solution of glucose at different temperature. The heat capacity ratio constantly decreasing which throw light on the fact that specific heat at constant volume is decreasing constantly with increasing concentration. [10]

Nonlinear parameter (B/A) obtain by to the Hartmann Balizer is related to the internal pressure hardness intermolecular potential, molecular structure & molecular interaction of liquid. fig. 6 shows the non-linearity parameter for zinc sulphate biomolecules as a function of concentration in glucose at various temperature. [10]

Relative association (R_A) is depended upon the factor. The breaking of solvent structure on addition of solute to shown in fig 7 increase of relative association (R_A) with concentration suggest that close association of component of molecule and there exist intermolecular interaction. [10].

The overall trends in the isothermal compressibility (β_i) are as shown fig 8. It has been found to be decrease in concentration. The decrease in isothermal compressibility (β_i) value with increase in concentration of biomolecules seems to be the result of corresponding decreases in free volume and average kinetic energy of the constituent solute - solvent molecules in the aqueous solution of glucose.[10]

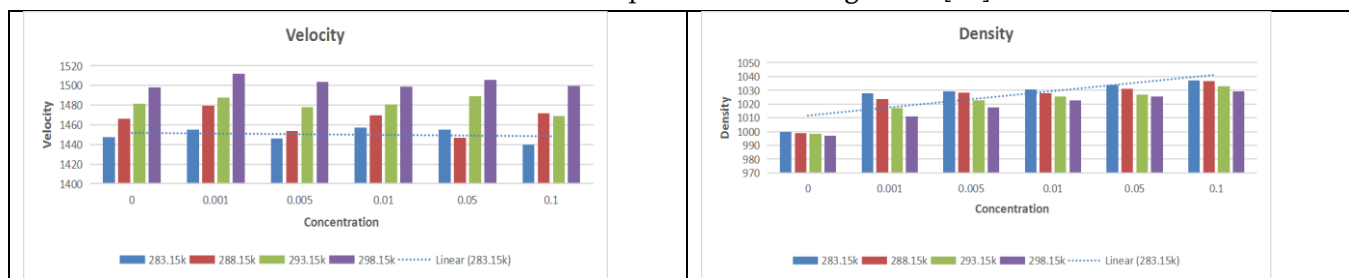


Fig.1 Variation of Ultrasonic Velocity with Concentration and temperature

Fig.2 Variation of Density with Concentration and temperature

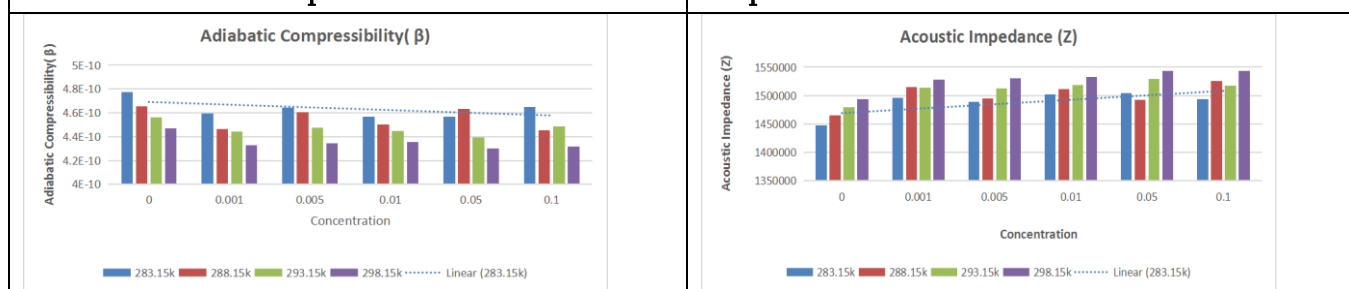


Fig.3 Variation of Adiabatic compressibility Concentration and

Fig.4 Variation of Acoustic Impedance with Concentration and temperature.

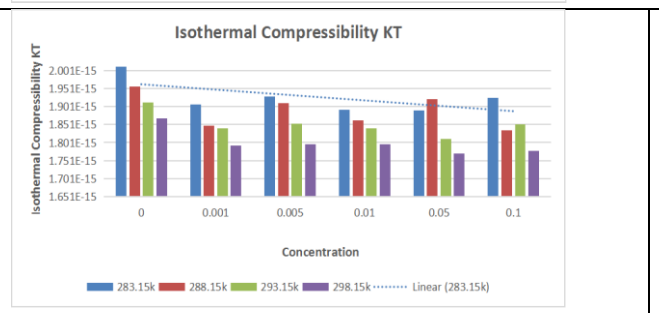
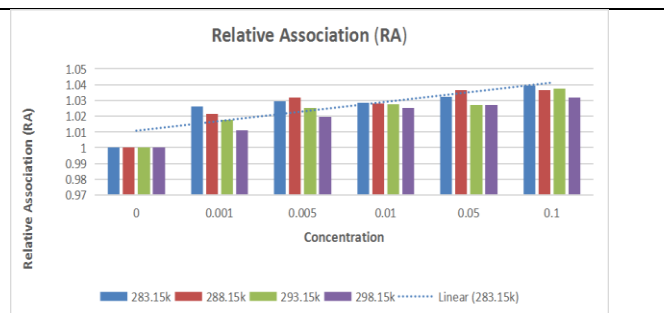
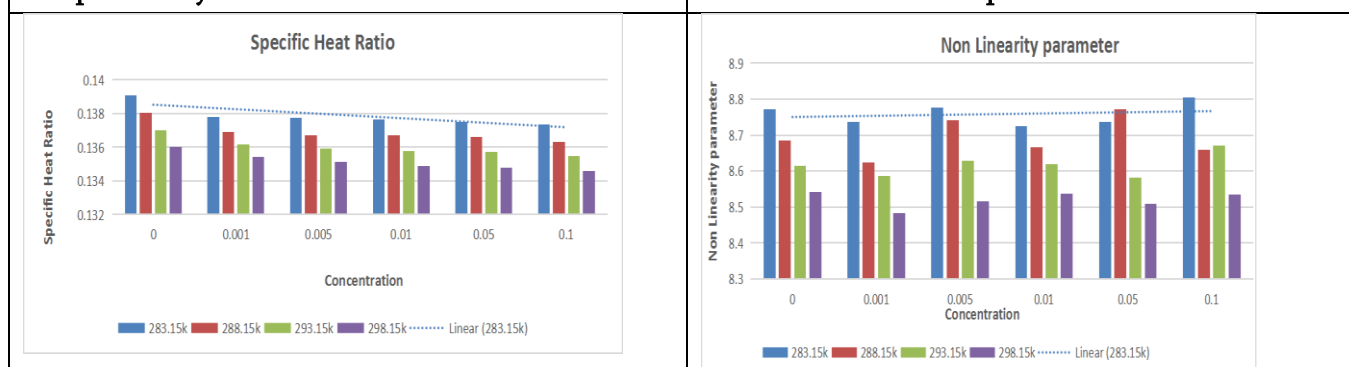


Fig.7. Variation of Relative association with concentration and temperature.

Fig.7. Variation of Isothermal compressibility with concentration and temperature.

IV. CONCLUSION

Basic physical parameters such as ultrasonic velocity and density of zinc sulphate in aqueous solution of glucose of different concentration and temperatures were measured initially. Using these basic parameters various acoustical parameters were calculated. The effect of temperature and concentration of this parameter was discussed appropriately. The addition of solute in solvent has been structure making tendency through molecular hydrogen bonding. It concluded that the system explains on the basis of association or dissociation exist between zinc sulphate and aqueous glucose solution or effect of structure making and breaking of solute in solvent and This information suggest the molecular interaction of liquid mixture.

V. REFERENCES

- [1]. R. Palani, S. Kalavathy, J. Pure Appl. Ultrason., Vol.33,(2011) pp 33-38.
- [2]. P. Thrahim, S. Vinatagum, J. Murgan, J. Edward, Jr. Inform. and Comput. Sci, vol.9, (2019) pp 391-399.
- [3]. V. Giratkar, R. Lanjewar, Int. J. Sci. Res., vol. 4.438, (2003), pp 2319-7064.
- [4]. S. Nithiyantham, L. Palaniappan, Arab. J. of Chem., vol 5, (2012), pp 25-30.
- [5]. S. Ahmada, K. Nasir, R. Saleem, J. Sci Ind. Res. 47(2004) PP 349-355.
- [6]. J Stenger, M. Cowman, F. Eggers, E. Eyring, U. Kautze, S. Petrucci, J. Phys. Chem. Vol.104, (2000), pp 4782-799
- [7]. V. Girakar, R. Lanjewar, S. Gadegone, K. Patil, Der. Pharma. Chem. Vol.13, (2017), pp 46.549
- [8]. S. Mirikar, P. Pawar, G. Bichile, Am. J. Pharma. Vol. 2, (2015), pp 19-25.
- [9]. S. Chauhan, K. kumar, B. Patil, Ind. J. Pure Appl. Phys., Vol.51, (2013), pp 531-541
- [10]. P. Mishra, A. Lad, U. Manik, J. Pure Appl. Ultrason., vol. 43 (2021), pp 27-34.

A Physico-Chemical and Thermo-Acoustical Study of Aqueous Potassium Sulphate at Different Temperature and Concentrations

Pooja R. Sonune*, Urvashi P. Manik, Paritosh L. Mishra, Mohini G. Wankhade

PGT, Department of Physics, Sardar Patel Mahavidyalaya, Chandrapur-442401, Maharashtra, India

ABSTRACT

The experimentally determined quantity such as ultrasonic velocity, density and viscosity for aqueous potassium sulphate solution of various concentrations have been determined at different temperatures (288.15, 293.15 & 298.15K). These data have been used to calculate various thermos-acoustical parameters{viz. Free volume (V_f), Wada's constant (W), Hydration number(n_H), Specific heat ratio(γ), Relaxation strength(r), Solubility parameter(δ),and Ballou's constant(B/A)²}. These all parameters proved the intermolecular interaction between solute (potassium sulphate) and solvent (water) and also observed the Physico-chemicalbehaviour of the solution. Thermo-acoustical studies could also be used successfully and well supported in this regard.

Keywords: Density, potassium sulphate, thermos-acoustical parameters, ultrasonic velocity, viscosity.

I. INTRODUCTION

Today, ultrasonic is one of the best-suited techniques for Physico-chemical as well as thermo-acoustical studies to determine the solute-solute, solute-solvent, ion-solvent interaction of the liquid system. In recent years ultrasonic waves have acquired the status of an important study of the structure and properties of matter. In an infield of technology, the waves are being used for detection of flaws, testing of material, mechanical cleaning of surfaces etc. And also, these waves are used in medical science, agricultural industry, chemical industry, computer technology, underwater acoustic and many other industrial areas. In the agriculture industry, fertilizer is the most important factor. Fertilizers replace the nutrient that crops remove from the soil, without the addition of fertilizer agriculture productivity would be reduced. That's why mineral fertilizer is used in the soil as a supplement that can be quickly absorbed and supply more nutrients for the better growth of plants.

Thus, in this paper, we are studying the different thermo-acoustical parameters of aqueous potassium sulphate solution which is mainly used as fertilizer at different temperatures and concentrations. Potassium is needed to complete many essential functions in plants, (such as activating enzyme reactions, synthesizing protein, forming starch & sugar and regulating water flows in cells & leaves. And the salt index of potassium

sulphate solution is very low near about 0.88. By using this fertilizer, we can reduce the risk of soil-salt build up in agriculture.

II. MATERIAL AND METHOD

In the present paper, we have used potassium sulphate [molecular wt. – 174.259 g/mol] as a solute of AR grade with 99% purity and fresh distilled water having [molecular wt. 18.01528 g/mol] was used as a pure universal solvent and this work was done at different temperatures (i.e., 288.15, 293.15 & 298.15K) and concentrations (0.2.....2M).

This experiment was carried out at different temperatures (i.e., 288.15, 293.15 & 298.15K) which were maintained by a digital water bath. The measurement of weight was done by using a digital weighing machine having an accuracy of ± 0.1 mg. Some basic parameters like Ultrasonic velocity, density and viscosity, (ultrasonic velocity were measured on a digital ultrasonic interferometer with a 2MHz frequency having an accuracy of 0.1%, Ultrasonic viscosity was determined by using Ostwald's viscometer with ± 0.001 pa-sec accuracy and the ultrasonic density of this solution was accurately determined by using a 10ml density gravity bottle). Using the measured data, some other thermos-acoustical parameters have been calculated using standard relation.[1]

Defining Relation:

The thermo-acoustical parameters can be calculated using the following relation:

- Free volume (V_f): $V_f = (M_{eff} \cdot U) / K\eta$

M_{eff} – effective molar mass, $K = 4.28 \cdot 10^9$, U – ultrasonic velocity and η – viscosity

- Wada's constant (W): $W = \beta_a^{1/7} \cdot V_m$

β_a – adiabatic compressibility & V_m – molar volume

- Hydration number (n_H): $n_H = \{(n_1/n_2) \cdot (1 - \beta/\beta_0)\}$

n_1 – number of moles of solute, n_2 – number of moles of solvent, β – adiabatic compressibility of solute and β_0 – adiabatic compressibility of the pure solvent.

- Specific heat ratio (γ): $\gamma = \{17.1 / (T^{4/9} \cdot \rho^{1/3})\}$

T – temperature & ρ – density of the solution

- Relaxation strength (r): $r = \{1 - (U/U_\infty)^2\}$

U – ultrasonic velocity of solution & $U_\infty = 1600$ m/s

- Solubility parameter (δ): $\delta = (\pi_i)^{1/2}$

π_i – internal pressure

- Ballou's constant (B/A): $(B/A)_2 = \{-0.5 + [(1.2 \cdot 10^4) / U]\}$

U – Ultrasonic velocity of solution

III. RESULTS AND DISCUSSION

The thermos-acoustic parameter of aqueous potassium sulphate solution at different concentrations (0.2 to 2 M) and temperatures (288.15, 293.15 & 298.15K) is given in below fig. 1-10. The increase in ultrasonic velocity with concentration shown in fig.1 in solution indicates the presence of solute-solvent interaction.[2] An increase in velocity with a concentration in the present system confirms the greater molecular association. And also, as temperature increases breaking of hydrogen bonding increases and thus ultrasonic velocity increase with the increase in temperature.[3]The measured density of all systems increases with rising in concentration (shown in fig. 2),this indicates a good association between solute and solvent molecules.[4] It is also found that the density decreases as the temperature increases. This is because the thermal motion of a particle of the medium also increases. Thus, particles become loosely packed to cause a decrease in density.[5] From graph 3 it is observed that the viscosity of the solution is found to increase with the increase in concentration which suggests that a strong association in potassium sulphate solution may be due to the intermolecular hydrogen bonding, dipole-dipole and ion-dipole interaction between solute and solvent molecules.[6] It is also found that viscosity decreases as the temperature of the system increases. This is because as the temperature increases, the kinetic energy of the molecules increases which diminishes the viscosity of the medium.[5]From fig. 4 it concludes that free volume is decreasing with an increase in concentration and increase with the increase in temperature which suggests the structure making and breaking tendency of the solute molecule[7] in a solvent can be properly understood with the help of an important physical parameter free volume. Wada constant is also known as molar isothermal compressibility. from fig. 5 it is found that as concentration increases, The value of the Wada constant decreases, and it confirms existing intramolecular interaction between solute and solvent molecule.[8] The hydration number is also known as the solvation number. It is one of the important parameters in terms of explaining the degree of interaction structure making or breaking behaviors of solute molecules. From fig. 6, it is observed that the n_H value of fertilizer decrease with an increase in concentration. This decreasing trend is due to a lack of solvent for all ions.[9] And when rise in a temperature drops in hydration number. Specific heat ratio is an important property which depends upon the density and temperature of liquid mixture fig. 7 displays the variation of specific heat ratio, it constantly decreases with a variation of concentration of solute fact that closer packing of the molecule in a solution through hydrogen bonding.[10] And also fig.7 shows that increases with the temperature rise.

It is an important property to elucidate the molecular interaction present in the system. Relaxation strength directly correlates with adiabatic compressibility. It can be calculated by using the formula.[11] The decrease in values of relaxation strength with an increase in concentration and temperature indicates solute-solvent interaction in the system (shown in fig.8). This suggests a greater association between fertilizer and salts as compared to fertilizer and water.[12]Solubility parameter data are useful in the description and interpretation of different phenomena occurring between solute and solvent such as their miscibility, compatibility or adsorption.[4] Variation of the solubility parameter of potassium sulphate solution at different temperatures and concentrations (shown in fig. 9) shows the value of this parameter increases with increasing

concentration due to an increase of internal pressure in the solution. The increasing trend of the solubility parameter exhibits that the solution has more tendency to be soluble. Ballou's constant is also known as the non-linearity parameter, the value of this parameter has been interpreted as the quantity representing the magnitude of the hardness of liquid. Fig. 10 show the non-linearity parameter for potassium sulphate fertilizer at different concentration and all temperature, from observation it is clear that the value of B/A is decreasing with an increase in concentration and temperature. Thus, it leads to the tight packing of the medium and enhancement in molecular interaction.[13] This tightening of the medium creates a better way for the propagation of sound waves or ultrasonic waves.

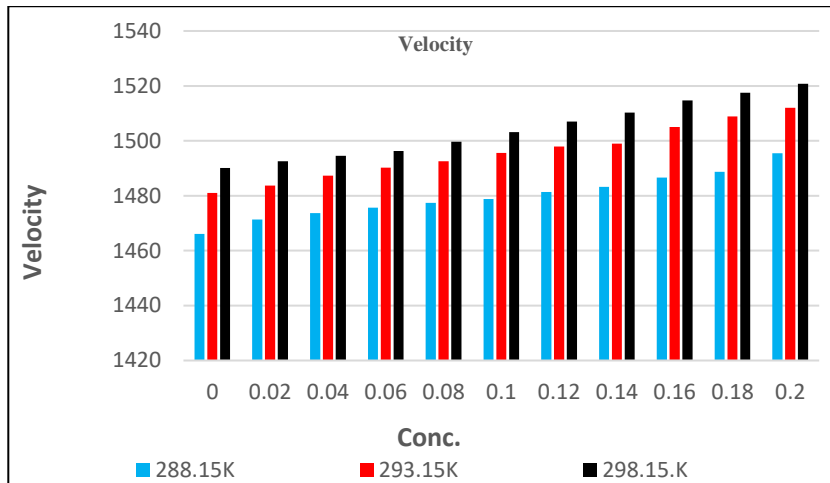


Fig.1 Variation of Velocity with Conc.

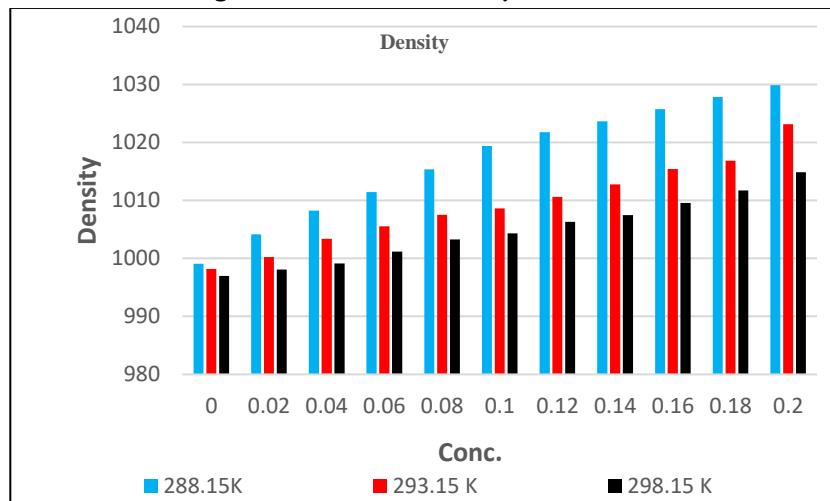


Fig.2 Variation of Density with Conc.

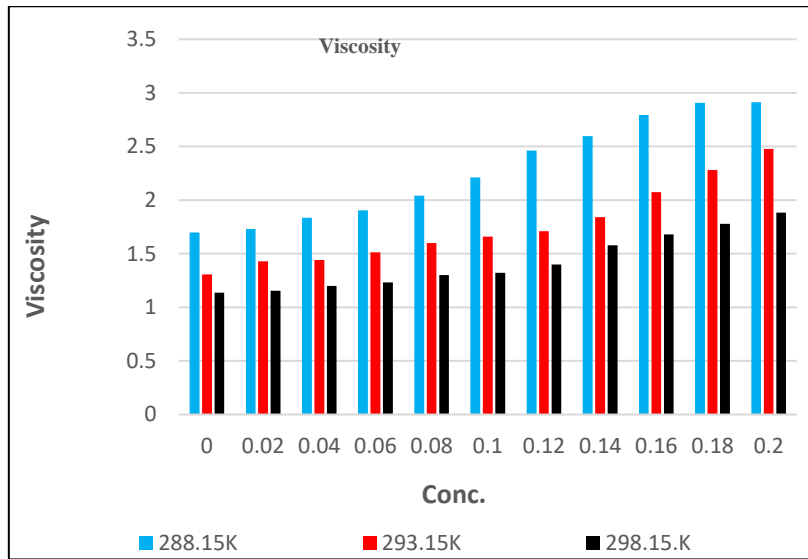


Fig.3 Variation of Viscosity with Conc.

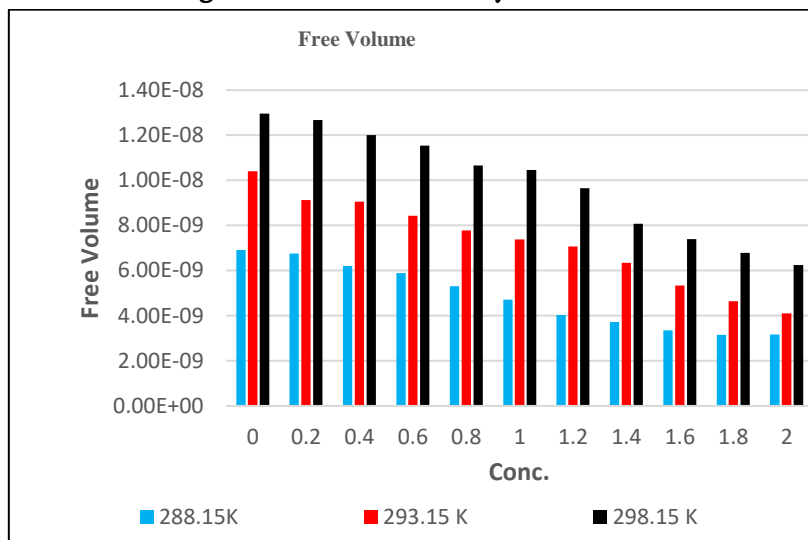


Fig.4 Variation of Free vol with Conc.

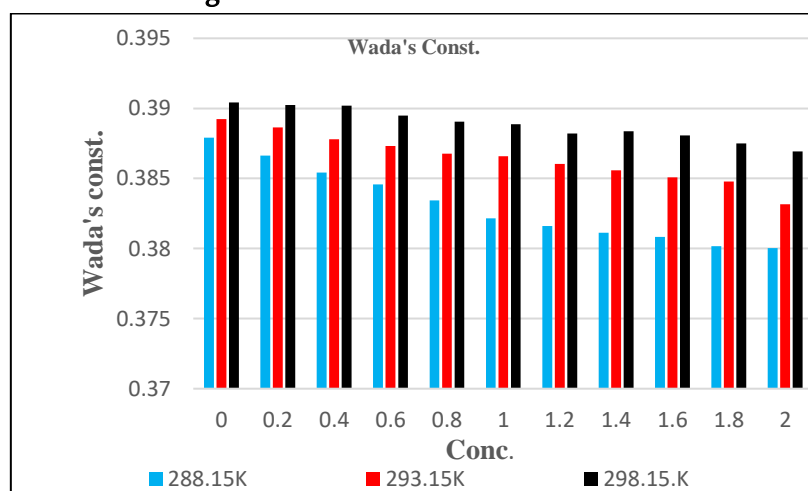


Fig.5 Variation of W. C. with Conc.

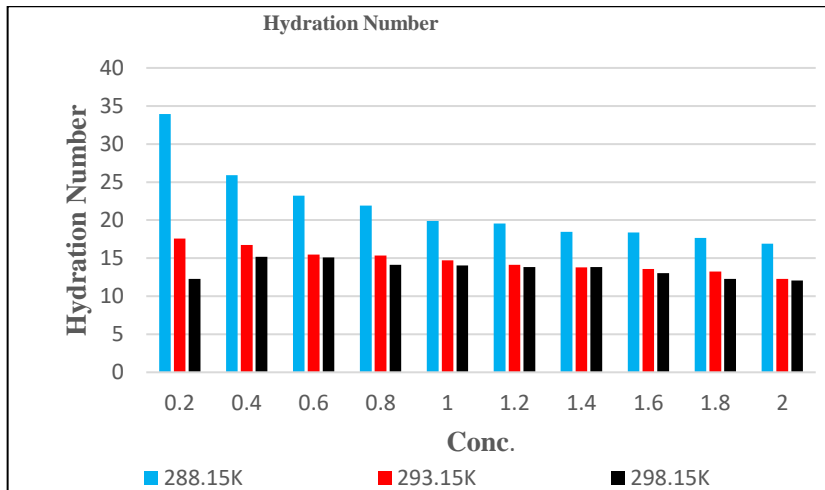


Fig.6 Variation of H. N. with Conc.

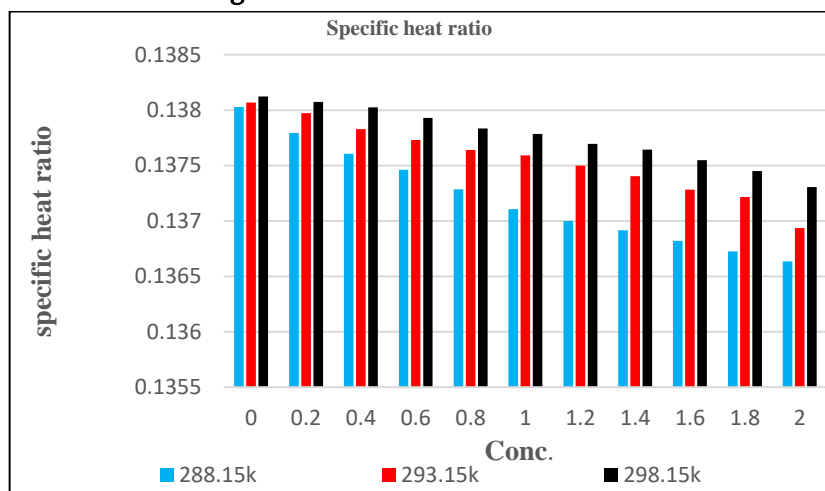


Fig.7 Variation of S.H.R. with Conc.

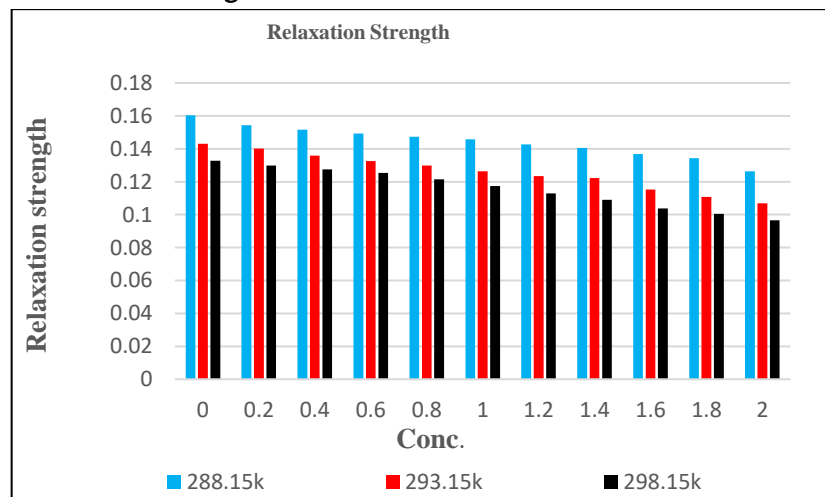


Fig.8 Variation of R.S. with Conc.

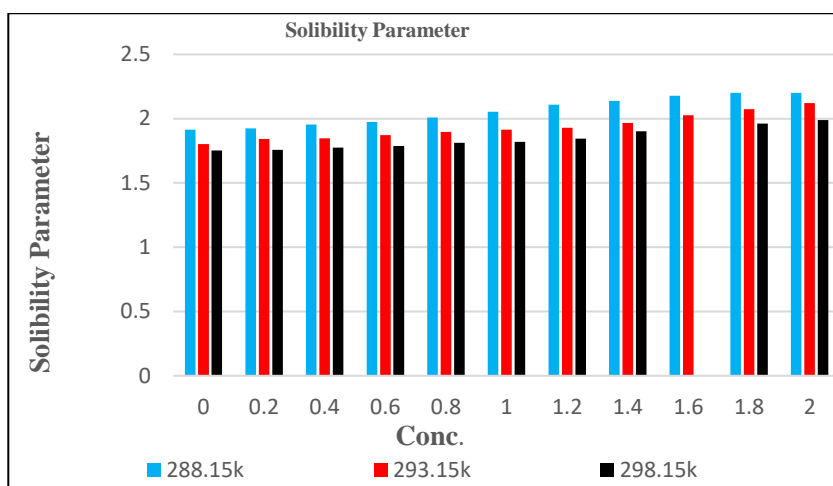


Fig.9 Variation of S.P. with Conc.

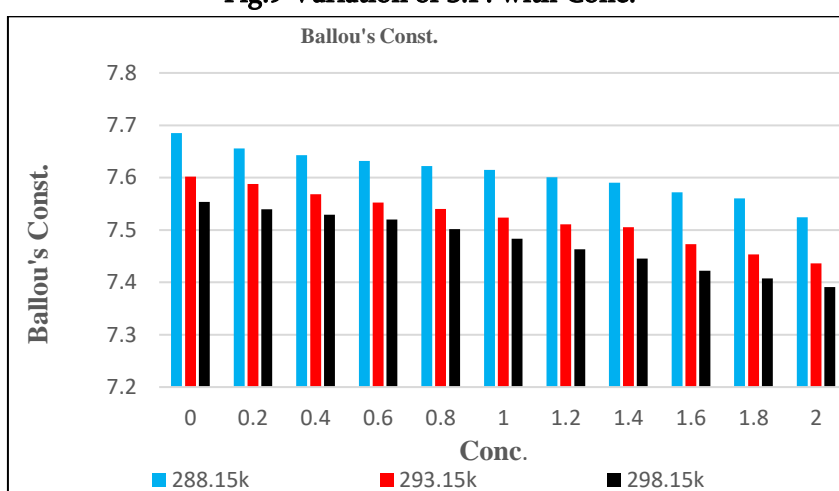


Fig.10 Variation of B. C. with Conc.

IV. CONCLUSION

The various Physico-chemical and thermo-acoustical parameters were determined by using the experimentally measured values of density, velocity and viscosity at different concentrations (0.2.....2) and temperatures (288.15, 293.15 & 298.15K). All computed thermo-acoustical parameter shows the intermolecular interaction between solute and solvent and observed Physico-chemical behaviour of potassium sulphate solution. Thermo-acoustical studies could also be used successfully and well supported in this regard.

V. REFERENCES

- [1]. Giratkar V. A., Gadegone S. M. and Lanjewar R. B., NCMAM, pp; 41-45, 2017.
- [2]. Godhani D. R., Dobariya P. B. and Saghani A. M., J. Mol. Liq., Vol. 168, pp; 28-35, 2012.
- [3]. V. A. Giratkar, R. B. Lanjewar and S. M. Gadegone, IJRBAT, Vol. 3, pp; 37-40, 2017.

- [4]. Greenspan M., J. Res. Nat. Bure. Stand., Vol. 59, pp; 249-254, 1957.
- [5]. V. A. Giratkar, R. B. Lanjewar and S. M. Gadegone, JCBPS J. Sci., Vol. 6, pp; 1319-1325, 2016.
- [6]. V. Pagare, S. Mirgane, A. Mahajan and S. Deshmukh, Mate. Sci. Res. Ind., Vol. 4 (2), pp; 475-480, 2007.
- [7]. Arul G., Palanippan, Ind. J. of App. & Pure Phy., Vol. 43, pp; 755-758, 2005.
- [8]. S. Govindarajan. V. Kannappan, K. Senthilkumar, V. Ponnyswamy, J. Mol. Liq., Vol. 202, pp; 115-124, 2015.
- [9]. E. Jasmine, Vasantha Rani, K. K. Annagi, R. Padmavathy and N. Radha, Ind. J. Pure Appl. Ultrason., Vol. 28, pp; 20-28, 2006.
- [10]. P. Kietczynski, M. Szalewski, Balcerzak and K. Wieja, IEEE, Int. Ultrason. Symposium, Chicago USA, 2014.
- [11]. A. Moses Ezhil Raj, L. B. Resma, V. Bena Jothy, M. Jaychandran and C. Sanjeeviraja, Fluid phase Equilibria, Vol. 281, pp; 78-86, 2009.
- [12]. S. Baluja and F. Karia, J. Pure Appl. Ultrason., Vol. 22 (3), pp; 82-85, 2000.
- [13]. R. Joshi, K. Tamta, B. Chandra and N. D. Kandpal, Int. J. Appl. Chem., Vol. 13, pp; 611-630, 2017.

An Acoustical Study to Explore the Interaction Between Dextrose and Electrolyte Solution Using Ultrasonic Technique

Prajakta S. Mohare, Paritosh L. Mishra, Urvashi Manik

PGT, Department of Physics, Sardar Patel Mahavidyalaya, Chandrapur-442401, Maharashtra, India

ABSTRACT

The impact of solute in solvent has a great importance in to drug delivery in body as well as in nutrient uptake by plants from the soil. This will be studied by observing the tendency of structure making and breaking effect and their interactions by the introduction on of solute in solvent. In this work an attempt is made to evaluate the ultrasonic velocity and density for dextrose in 0.5mol/kg solution of aq. Potassium chloride. The different acoustical and transport properties of the given system using the sound speed and density of solute as well as solvent at different temperatures (viz. 283.15k, 288.15k, 293.15k, 298.15k).

Keywords: Acoustical Parameter, Density, Dextrose, Potassium chloride, Ultrasonic velocity, water.

I. INTRODUCTION

Ultrasonic investigation have been extensively used for characterizing the thermodynamics properties and to predict the solute and solvent and ion solvent interaction in aqueous solution. [1] This technology has been used for quite some time to determine bonding and formation of complexes at different temperatures. polysaccharides has been the subject of wide research and ultrasonic velocity measurements allow to accurately measure some [2] important and applicable thermodynamics and acoustic parameter. These excess ultrasound, intrinsically molecular free length, adiabatic compressibility and acoustic impedance in liquid mixtures plays an important role to understand the interaction between the solute and the solvent. Ultrasonic velocity measurements can reveal the molecular interaction that are present in binary and ternary liquid mixtures.[3]

Jackfruit seed starch was obtained by hydrolysis with alpha amylase enzyme and then dried to form malto dextrin . The characteristic of jack fruit seed. Maltodextrin had a brownish yellow color, 64% yield a water content of 3.07%, PH 6, dextrose equivalent 15.44, and water solubility 95.5 %.[4]. The density measurements are made with a density balance which provides a resolution of 0.0001g/ cm³ . The ultrasonic velocity is measured by pulse-echo techniques with an accuracy of 1 m/s . In the work, glycerine a non-electrolyte dextrose a monohydric alcohol were chosen as probe molecules. In these system Na₂CO₃ and NaHCO₃ were used as buffer because they exhibit different types of behaviour in their solutions. [5]

II. MATERIAL AND METHOD

The compound dextrose (molecular wt. 180.16g/mol. Used in present work is of analytical reagent which use as solute and potassium chloride (molecular wt. 74.56g/mol) used as solvent and fresh distilled water (Molecular wt. 18.01528g/mol with density 1000 kg/m³ is used as universal solvent. This process is done at different temperatures (viz. 283.15k, 288.15k, 293.15k, 298.15k) which were maintained by using a digital water bath.

The measurement of weight has done by using a digital weighing machine having having an accuracy of +- 0.1%. Some basic parameter like, [(a) ultrasonic velocity were measured on a digital ultrasonic interferometer with 2MHZ frequency having an accuracy of 0.1% [(b) ultrasonic viscosity was calibrated by using Ostwald's viscometer with an accuracy of +- 0.001pa-sec and (c) The Ultrasonic density of this solution was accurately determine by using a 10ml density gravity bottle. By using this three basic parameters of KCl solution measured at different temperatures and concentration we can calibrate other various acoustic parameter.

Defining relation :

For the derivation of several acoustical and thermo-dynamical parameters the following defining relation reported in the literature are used.

1. Acoustic Impedance : Acoustic impedance (also known as shock impedance) is defined as ratio of sound pressure (p) to particle velocity (U) at a single frequency and is expressed as 'rayals'.

$$Z = Ue$$

2. Adiabatic compressibility: it can be calculated from the speed of sound (U) and the density (ρ) of the medium using the equation of Newton's laplace as, Adiabatic compressibility : $\beta = 1/ U^2e$
3. Specific Heat Ratio: Specific heat ratio is the ratio of isothermal compressibility and adiabatic compressibility and can be calculated using the following relation.

$$\text{Specific Heat Ratio: } \{17.1/ T^{4/9} *()\}^{1/3}.$$

4. Non-Linearity parameter: $(B/A) = \{2+ [0.98 \cdot 10^4/U.]\}$
5. Isothermal Compressibility: $(K_t) = 1.33 \cdot 10^{-8} / (6.4 \cdot 10^{-4} U^{3/2} e^{3/2})$
6. Relative association: The value of relative association (RA) for liquid system have been (dextrose +water+ KCl) estimate using relation.

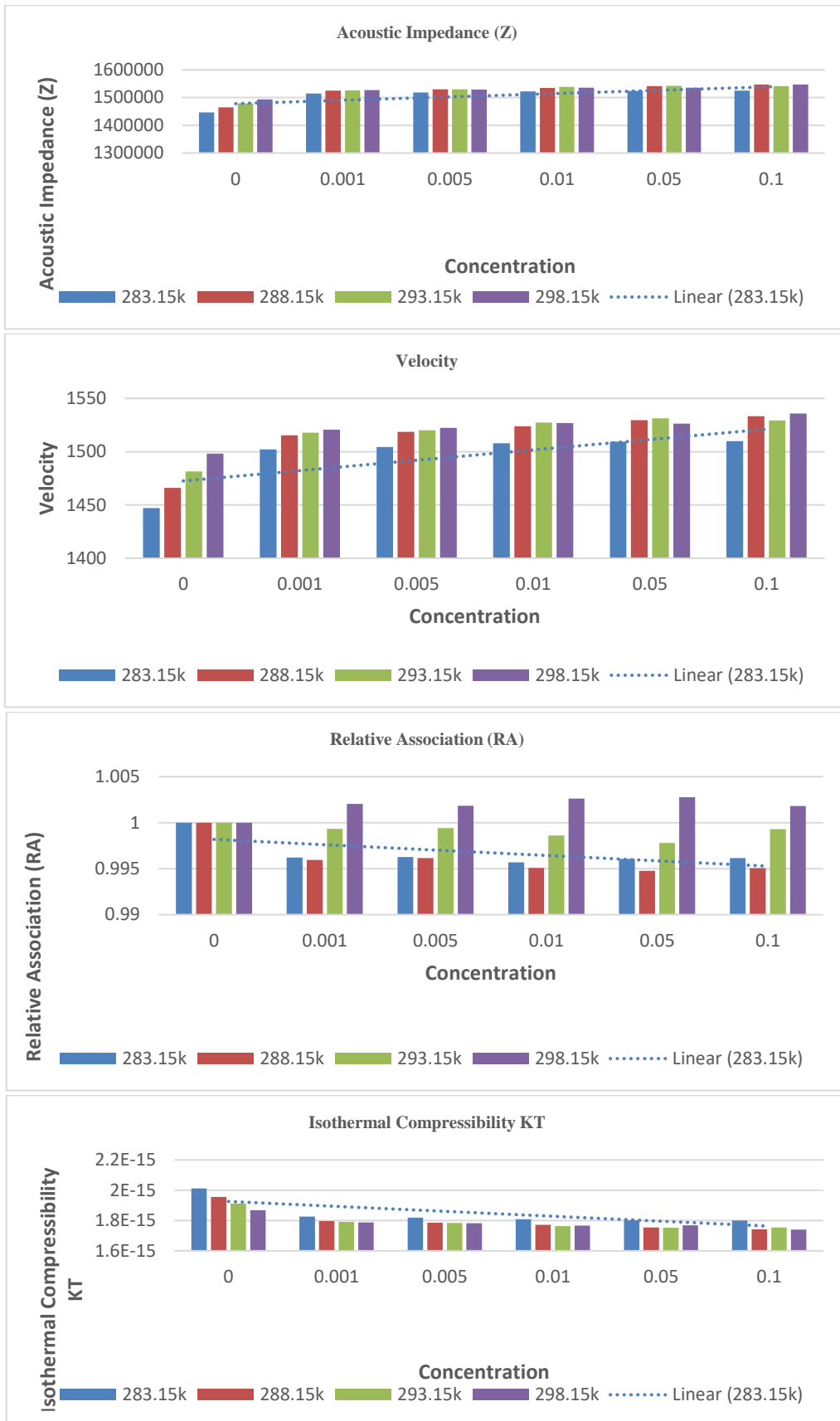
$$(RA) = \{(\rho/\rho_0 (U/U_0)^{1/3}.$$

III. RESULT AND DISCUSSION

Ultrasonic density and velocity of dextrose compound have been found to have various values to understand the effect of structuring on molecular interaction. Several acoustic and thermodynamic parameter were derived from experimental measurements of ultrasonic velocities and density. In dextrose compound the variation of density of dextrose compound increases as gradually with increasing concentration of the solution. The Ultrasonic velocity is measured with the frequency of ultrasound i.e. at 3and 10 MHz of

concentration of solution. At both frequencies ultrasonic velocities increases gradually with an increases of concentration . However there is an increase in velocity at low frequency at high frequency.





In addition these compounds increases acoustically impedance as concentration increases. Our scientist aren't 100% sure why this happens, but they think it might have something to do with the fact that most of the molecules in the compound are interacting with each other via. Hydrogen bonds but more research is needed to confirm this hypothesis.[6].The adiabatic compressibility decreases in concentration of dextrose in shown in fig it indicates that there is strong solute solvent interaction. The solution become more and more compressible as adding the concentration of drug.[7].

The heat capacity ratio is constantly decreasing which thrown light on the fact that specific heat at constant volume is decreasing constantly with increasing both concentration as well as temperatures. When chemical compounds are mixed together, they interact with each other through the bonds between their molecules. This interaction can be described in terms of Non linear parameters which measure how much each compound contributes to the mixtures overall polarity and internal pressure.[8] Decrease in kinetic energy – The decrease in isothermal compressibility (KT) value with increase in concentration of biomolecules seems to be the result of corresponding decreases K.E of the constituent solute-solvent molecules in an aq. Solution of dextrose . This relative association of a given solute is a function of its concentration, it has been observed that the breaking of solvent on addition of solute to it increases this is shown in fig. Increases of relative association R_a with concentration on suggest that close association of component of molecule and their exist intermolecular interaction.

IV. CONCLUSION

The result shown in this section indicate that there is a positive association between potassium chloride and dextrose, which means that there is more structure formation between the two solutes at higher concentration.

V. REFERENCES

- [1]. S. Rathika, K Renuka Devi, S. Geetha , A. Gamathiyalini, IOSR J. Pure Appl. Vol.6, Sep-Oct 2014 pp 19-24.
- [2]. N. Chakravarti Kc Juglan H. Kumar Plants archives Vol. 20, 2020 pp 3089 – 3102.
- [3]. B. A Gop, S. K, Chavan Acad. J. Env . Sci. Jan 2020 pp 015-021.
- [4]. Z . Rayhani, E. Kurniasih , R. Fadhilah IOP Conference Series : Material sci. And Eng. 2018 pp 420.
- [5]. Y. Akhtar, Chem. Sci. Int. J. ISSN 2016 pp 2249-0205.
- [6]. S. K Swain , Pragnya P. Priyadarshani, Ind. J. Pure Appl. Phy . VOL. 48, Aug 2010 pp 539-542.
- [7]. P. Nalle, B. Shinde, S. Shinde , R. Dorik, K. Jadhav , J. Pure Appl. Ultrason 2017 pp 1-7.
- [8]. P. Mishra, A. Lad, U. Manik, Int. Res. J. Of sci. Engineering, 2020 pp 260-265.

Intermolecular Interaction Between Ascorbic Acid & Salt Solution: A Thermo-Acoustical Study

Rahul J. Raut*, Urvashi P. Manik, Paritosh L. Mishra

PG, Department of Physics, Sardar Patel Mahavidyalaya, Chandrapur – 442401, Maharashtra, India

ABSTRACT

The ultrasonic velocity, density of different concentration of ascorbic acid (Vitamin C) have been studied at various temperature. The measurement of ultrasonic velocity & density were carried out by using the ultrasonic digital velocity interferometer & 10ml specific gravity density bottle. By using this experimental data other thermo-acoustical relation like adiabatic compressibility, internal pressure, acoustic impedance, etc. have been calculated & studied. The aim of these study is to determine the geometry, nature, kind & strength of interaction of the liquid mixture. Such experimental data is helpful in pharamaceutical& food industries due to its wide application.

Keywords: Ultrasonic velocity, density, viscosity, ascorbic acid, sodium chloride, molecular interaction

I. INTRODUCTION

Ultrasonic is a branch of physics in which frequency sound wave is concerned. Usually, people can capable to perceive sounds with a frequency range varies between 16 Hz to 20 KHz (20,000 cycles per second). Ultrasonic was very useful & powerful tool for research areas in the field of physics. [1] Ultrasonic is used to measure the distance & also used to detect the obstacles. It is also used in medical field. Ultrasonic velocity in chemical physics, biochemical science, industrial technology and food industries. The measurement of the ultrasonic enables the accurate determination of some useful acoustical and thermodynamic parameters.

Vitamin C, also known as ascorbic acid or ascorbate, is a six-carbon compound naturally found in many fruits and vegetables. It is required in many “ reaction involved in body process, including collagen synthesis , carnitine synthesis, tyrosine synthesis and catabolism, and neurotransmitter synthesis ”, etc. Nevertheless, vitamin C is not just an essential nutrient for maintaining human health. In fact, due to its multiple biological and chemical properties, vitamin C plays a useful role in different areas, such as food and cosmetic industries. In food industry, vitamin C has double role; it act as a nutrient as well as food antioxidant and product improver. Due to its physical structure, vitamin C is highly unstable. It is extremely heat-sensitive & can be easily destroyed under various conditions, such as enzymatic reaction, exposure to oxygen or light, use of inappropriate containers, & the presence of antioxidants or preservatives. Vitamin C i.e. Ascorbic acid can be significantly reduced during food manufacturing and storage process. The use of vitamin C is not only limited to food related areas; actually its application extend to areas other than just food and beverages

industry. Like the role of vitamin C plays in food industry, its excellent reducing capacity makes it an effective ingredient in cosmetic products. It protects & strengthens skin tissues and cells against external attacking factors such as oxidation damage resulting from attack of free radical and oxygen derived species, ultra violet radiation, pollutants and other exogenous agents which lead of elasticity of skin, etc. [2]

In the present study, we report the value of density, ultrasonic velocity for different molar concentration of ascorbic acid with NaCl solution at different temperature. The various physical parameters were calculated by using density , ultrasonic velocity.

II. MATERIALS AND METHODS

In the present work, analytical reagent (AR) grade with 99% purity of L-Ascorbic acid ($C_6H_8O_6$) {[CAS No-50-81-7] [Mol.Wt.-176.12 g/mol]} used as solute, Sodium Chloride (NaCl) with 99% purity of {[CAS No-7647-14-5] [Mol.Wt.-58.44 g/mol]} & fresh distilled water [havingMol.Wt.-18.01528 g/mol with density – 1000g/m³] was used as universal solvent and this work was done at different temperatures& different concentrations.

1. This experiment was carried out at different temperatures (i.e. 283.15K, 288.15K, 293.15K & 298.15K) which werw maintained by using a digital water bath.
2. The ultrasonic velocity have been measured by using ultrasonic digital velocity interferometer with an accuracy of 0.1%.
3. The measurement of weights was done by using a digital weighing machine accurately.
4. The ultrasonic density of the solution were measured accurately by using 10ml specific gravity density bottle.

The various acoustical parameters were calculated from the measured data by using some standard relations. [3]

Defining Relation :

1. **Ultrasonic Velocity** : The formula used to determine the ultrasonic velocity is, $u = 2d / t$

Where, d = separation between transducer and reflector

t = travelling time period of ultrasonic wave

2. **Density** : The formula by which density calculated is, $\rho = (W / W_w)\rho_w$

Where, ρ = density of liquid mixture at experimental temperature

W = weight of liquid mixture at experimental temperature

W_w = weight of water at experimental temperature

ρ_w = density of water at experimental temperature

3. **Adiabatic Compressibility** : The adiabatic compressibility is defined as ‘ the fractional decrease to volume per unit increase of pressure ’.

$$\beta_a = 1 / u^2\rho$$

where, u = ultrasonic velocity

ρ = density of solution

4. **Acoustic Impedance** : The specific acoustic impedance is given by ,

$$Z = \rho u$$

Where, u = ultrasonic velocity

ρ = density of solution

5. **B/A for Hartmann** : Non linearity parameter B/A is,

$$B/A = 2 + 0.98 \times 10^4 / U$$

Where, U is in m/s.

6. **Relative Association** : The relative association parameter is the relative association between the components molecule in a liquid mixtures and is given by

$$R_A = (\rho/\rho_0)(u_0/u)^{1/3}$$

7. **Isothermal Compressibility (β_i)** : Isothermal compressibility is a useful concept in determining the compressible properties of the reservoir.

$$\beta_i = \gamma \cdot B_a$$

III. RESULTS & DISCUSSION

By the experimental data, the variations in ultrasonic velocity, density, adiabatic compressibility & acoustic impedance and variation in different parameters are shown in the graphs (fig.1-8) for different temperature & different concentrations.

The variation of ultrasonic velocity and adiabatic compressibility with molar concentration are shown in fig.1 & fig.3. It is observed that ultrasonic velocity and adiabatic compressibility are increases and decreases in molar concentration of ascorbic acid. This shows that the strong intermolecular force exists between solute and solvent. This enhance the degree of association among molecules of solute-solvent components. [4]

The variation of the density with molar concentration is shown in the fig.2 . The density of solution increases as the molar concentration of ascorbic acid also increases. [5]

Fig.4 shows the variation of acoustic impedance (Z) with different molar concentrations. As the concentration of ascorbic acid increases, the acoustic impedance also increases. It shows that molecular interaction is associative.[6] Fig.(5,6,7)& fig.(8) shows the variation in the specific heat ratio, non-linearity parameter, relative association (RA) & isothermal compressibility with different molar concentration of ascorbic acid. Fig.(5,6) indicates that as the concentration increases the specific heat ratio and non-linearity parameter decreases. These are inversely proportional to the concentration of solute.[7] The variation in relative association (RA) increases as the concentration of solute increases. This variation is shown in the fig.(7). And fig.(8) gives the variation in the isothermal compressibility with concentration. As the concentration of the solute increases, the isothermal compressibility decreases. It is inversely proportional to the concentration of solute.

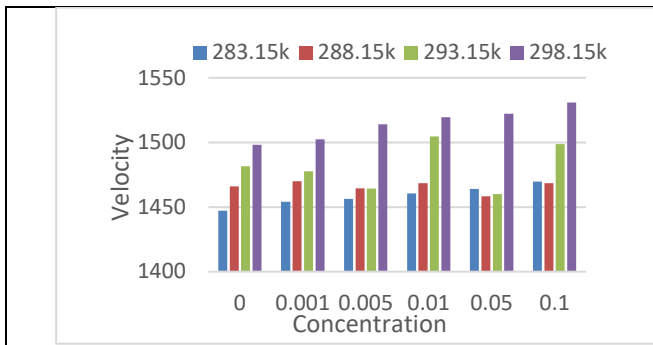


Fig1.Variation of ultrasonic velocity with concentration & temperature

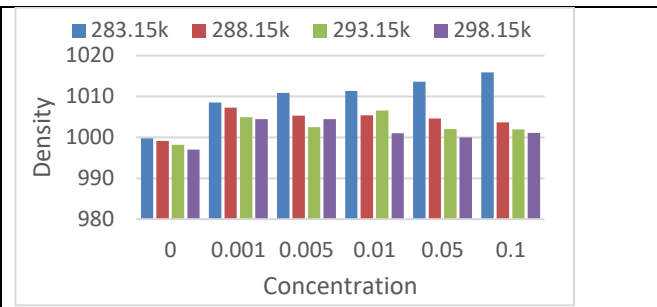


Fig2.Variation of density with concentration & temperature

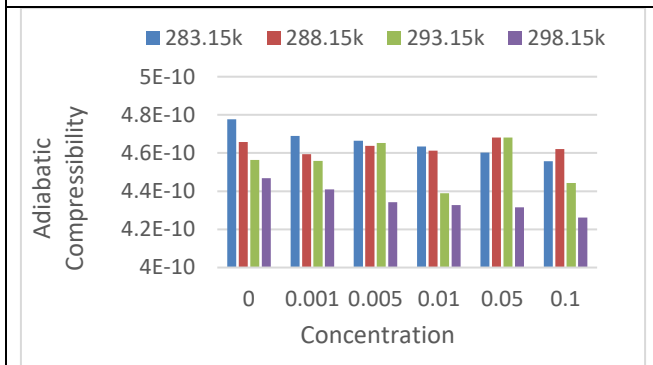


Fig3.Variation of adiabatic compressibility with concentration & temperature

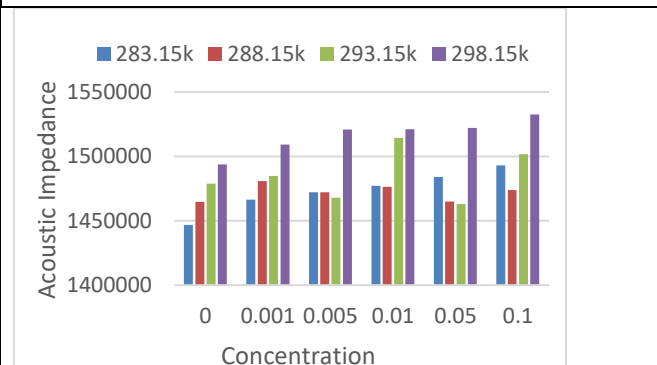


Fig4.Variation of acoustic impedance with concentration & temperature

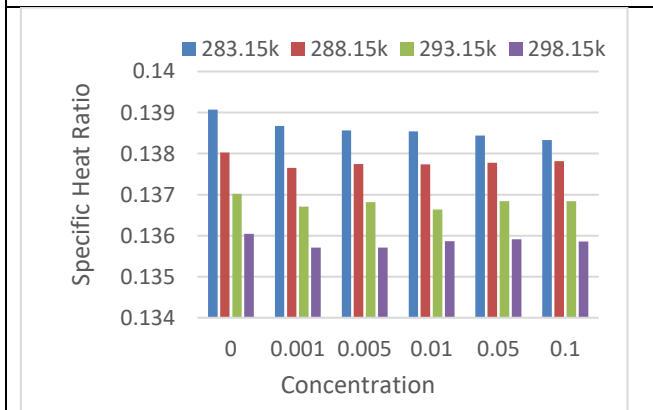


Fig5.Variation of specific heat ratio with concentration & temperature

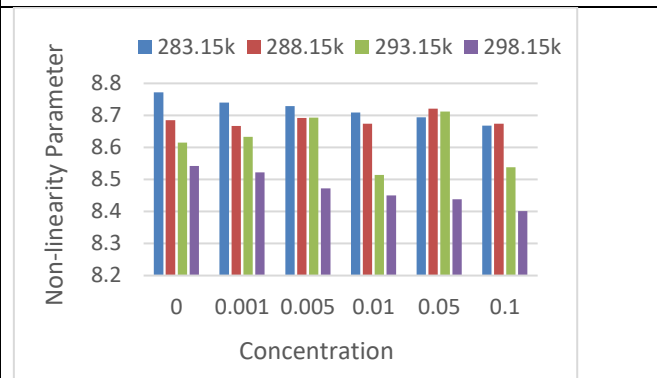
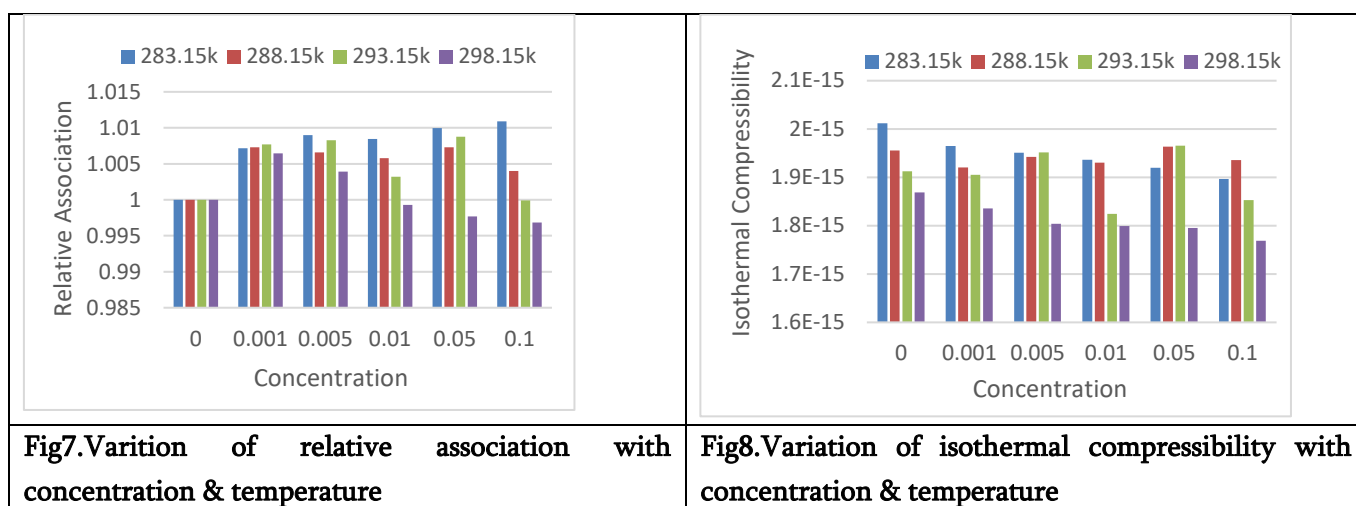


Fig6.Variation of non-linearity parameter with concentration & temperature



IV. CONCLUSIONS

The ultrasonic velocity, density of ascorbic acid of different concentration measured at different temperature & the thermos-acoustical parameters are calculated. The ultrasonic velocity, density & acoustic impedance (Z) are increases with the concentration. This indicates that solute-solvent interaction are present in the solution. The adiabatic compressibility decreases with rise in the concentration shows that there is strong solute-solvent interaction in a system. Hence, association takes place.

V. REFERENCES

- [1]. Tripathi P.; Shrivastava S. K.; Bhambhani P.; Verma S.K.; Khare V., IJEDR 2019, Vol.7, Issue 3, ISSN:2321-9939
- [2]. Dange S. P.; Chimankar O. P.; Hiwarkar S. T.; Borkar P. D., IJSR 2015, pp.286-288 (ISSN:2319-7064)
- [3]. Sarkar A.; Pandit B. K.; Sinha B., J.Chem.Thermodyn. 2016, 103 pp.36-43
- [4]. Dudhe V.G.; Tabhane V.A.; Chimankar O.P., IJSR 2016, Vol.5, Issue-4, pp.2398-2401
- [5]. Sagar S.; Kumari L. & Gupta M., J. Pure Appl. Ultrason. 2017, 39, pp.71-78
- [6]. Dhudhe V.G.; JETIR 2019, Vol.6, pp.30-37, (ISSN:2349-5162)
- [7]. Asargar J. & Ahamed S.B., IJRAR 2018, Vol.5, I.3, pp.18-20

Ultrasonic Characterization on Solution of Niacinamide in Aqueous Sodium Sulphate

Sanchit M. Bhatarkar*, Urvashi P. Manik, Paritosh L. Mishra

*PG, Department of Physics, Sardar Patel Mahavidyalaya, Chandrapur-442401, Maharashtra, India

ABSTRACT

The Purpose of this paper is to Expose the Observable and Extraordinary Nature of Intermolecular Interaction in Niacinamide of Concentration (0.001N, 0.005N, 0.01N, 0.05N, 0.1N mol/kg) in the Aqueous Solution of Sodium Sulphate of (0.2 N & 0.5N mol/kg). The main Velocity and Density data for the said system were used to calculate the various Acoustical and Thermodynamic parameter in view to specify the Nature of Solute in the Solvent. These studies will help in View to investigate the tendency of structure Making and Breaking Effect, as well as Existence of a Significant Solute – Solvent Interaction.

Keywords: Niacinamide, Sodium Sulphate, Acoustical Parameter, Thermodynamic parameters, Ultrasonic Velocity.

I. INTRODUCTION

The viscosity of the medium has a significant impact on the speed with which an ultrasonic wave propagates. This property can be a useful tool in investigating the viscosity of materials. Because different viscosities distinguish different regions of a living cell, acoustical microscopy can exploit this property of cells to "see" inside living cells, as detailed below under Medical Application. The Thermodynamic features of compressed liquids, which are crucial substances in numerous industries such as pharmaceutical, chemical, leather, cosmetics, and so on, are obtained by acoustic studies of liquid mixes. Because of the intimate links between the structure of the liquid and its macroscopic properties, measuring density and sound speed for any liquid mixture has become a valuable approach for analysing its condition. Because it is a non-destructive approach, ultrasonic research has grown in importance as a vital instrument for determining the molecular structure of matter and its properties. [1]

The intramolecular and intermolecular interactions of Niacinamide with Sodium sulphate and water were studied using ultrasonic velocity and density measurements. Ultrasonic has a wide range of practical applications, including underwater explanation, bottle and can sanitation for leak detection, ultrasonic cleaning, and medical applications (diagnosis, therapy and surgery). Niacinamide, commonly known as Nicotinamide, is a vitamin B3 derivative. Meat, fish, milk, eggs, green vegetables, and cereals are just a few of the foods that contain Niacinamide.

Niacinamide is needed for the body's fats and sugars to work properly, as well as to keep cells healthy. When niacin is consumed in quantities more than what the body requires, it is transformed to niacinamide. Niacinamide, unlike niacin, does not aid in the treatment of elevated cholesterol.

Vitamin B3 deficiency and disorders like pellagra are treated with niacinamide. It's also used to treat acne, diabetes, cancer, osteoarthritis, ageing skin, skin discoloration, and a host of other conditions, though most of these claims are unsubstantiated.

II. MATERIAL AND METHOD

In the present work, we have used analytical reagent (AR) grade with 99% purity of Niacinamide {[CAS No-98-92-0] [molecular wt. – 122.13 g/mol]} used as solute, Sodium sulphate with 99% purity of {[CAS No-7757-82-6][molecular wt-142.04 g/mol]} and fresh distilled water having [molecular wt. 18.01528 g/mol with density – 1000 kg/m³] was used as a pure universal solvent and this work was done at different temperatures (i.e.283.15,288.15, 293.15 & 298.15K) and concentrations.

1. This experiment was carried out at different temperatures (i.e.283.15, 288.15, 293.15 & 298.15K) which were maintained by a digital water bath.
2. The measurement of weight was done by using a digital weighing machine having an accuracy of ± 0.1 mg.
3. Some basic parameters like, Ultrasonic velocity were measured on a digital ultrasonic interferometer with a 2MHz frequency having an accuracy of 0.1%.
4. The ultrasonic density of this solution was accurately determined by using a 10ml density gravity bottle.
5. Using the measured data, some other acoustical parameters have been calculated using standard relation.

Defining Relation :

1. Adiabatic Compressibility

The adiabatic compressibility is defined as the fractional decrease in volume per unit increase of pressure. $\beta_a = 1/u^2\rho$. Where, u =ultrasonic velocity and ρ =density of solution.

2. Acoustical Impedance

The specific acoustic impedance is given by, $Z=up$

3. Non linearity parameter

Nonlinearity parameter B/A is,

$$B/A = 2 + 0.98 \cdot 10^4 / U$$

Where U is in m/s

4. Relation association (RA):

The relative association parameter is the relative association

Between the component's molecules in a liquid mixture and is given by $(R_A) = (\rho/\rho_0) (u_0/u)^{1/3}$

5. **Isothermal compressibility (β_i):** Isothermal Compressibility is a useful concept in determining the compressible properties of the reservoir.

$$\beta_i = \gamma \cdot \beta_a$$

III. RESULT AND DISCUSSION

For the systematic study the variation in ultrasonic velocity and density of the niacinamide with aqueous sodium sulphate solution under the study at different concentrations and temperatures (283.15, 288.15, 293.15 & 298.15K) are plotted. These are shown in fig. (1-8).[2]

In the present study one can observe that in given fig. 1 the niacinamide system, the value of ultrasonic velocity is increased with an increase in concentration and Temperature. This increasing trend of ultrasonic velocity in the mixtures suggests a moderate strong electrolytic in which the solute (Niacinamide) tends to attract solvent (Aqueous Sodium Sulphate) molecules [3]. i.e., it shows a greater association between solute and solvent molecules.[4] From fig. (2) it is found that slightly density increases for some concentration of Niacinamide solution. Thus, the increase in density with concentration may be due to the closed packing of solute-solvent interaction among the constituent particles of the mixture. [5] It is found that the density slightly decreases as the temperature increases. This is because as the temperature increases, the thermal motion of a particle of the medium also increases. Thus, particles become loosely packed to cause a decrease in density. [6]

The dependence of adiabatic compressibility of Niacinamide in aqueous solution of sodium sulphate on concentration at different temperature is shown in fig (3) It is obvious that if ultrasonic velocity increases the adiabatic compressibility of solution decreases as there exists an inversely proportional relationship between them. In the present investigation, the decrease in adiabatic compressibility value with rise in concentration at constant temperature is observed. The decrease in adiabatic compressibility with rise in temperature at given concentration is observed [6]. From fig (4), It is seen that expansion in Acoustical impedance (Z) increases with convergence of niacinamide at all temperature might be ascribed to the powerful solute-dissolvable cooperation. The acoustic impedance also increases with increase in temperature due to structural properties of niacinamide in the solution and there occurs a structural rearrangement as a result of hydration (solvation) leading to a comparatively more ordered state.[7]

Non-linear parameter (B/A) obtained by Hartmann-Balizer and Ballou is related to the internal pressure, hardness, intermolecular potential, molecular structure and molecular interaction of liquid Fig (6) shows the non-linearity parameter for niacinamide with aqueous sodium sulphate as a function of concentration and temperature. It is observed that the values of B/A show a decreasing trend with increasing temperature. This trend indicates that less array of molecules at low temperature hence high value of B/A and confirms the less interaction at low temperature. [8] It is studied to understand the ion-ion or ion-solvent interaction. In present study the relative association increases as increase in concentration due to decrease in intermolecular free length. It suggests that the solvation of niacinamide predominates over breaking up to the solvent structure, as observed in fig (7), it is varying irregularly with increase in temperature due to addition of niacinamide [9]

From fig (8), It is observed that the isothermal compressibility decreases with the increase in concentration of the solute at all temperature. That's what the explanation is, when solute breaks down in fluid sodium sulphate (dissolvable) a portion of the encompassing dissolvable atoms are firmly connected to the particles

because of the impact of electrostatic field of the particles. Since the dissolvable particles are arranged in the ionic field, the dissolvable atoms are minimalistic ally pressed in the essential solvation shell as thought about without a trace of the particles.[10]

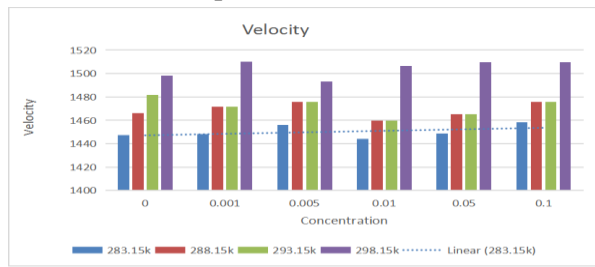


Fig.1 Variation of Ultrasonic Velocity with concentration and temperature.

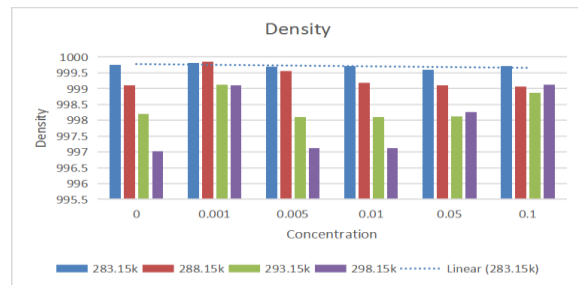


Fig.2 Variation of Ultrasonic Density with concentration and temperature.

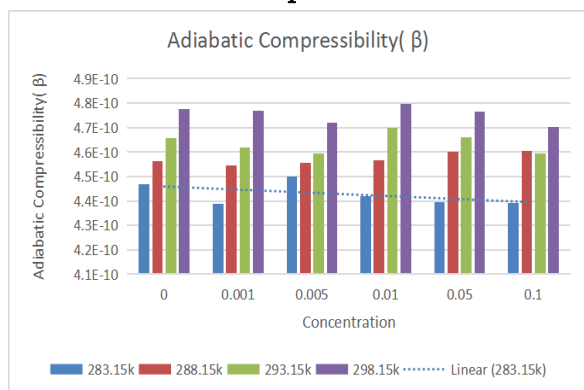


Fig.3 Variation of Adiabatic Compressibility with concentration in and temperature.

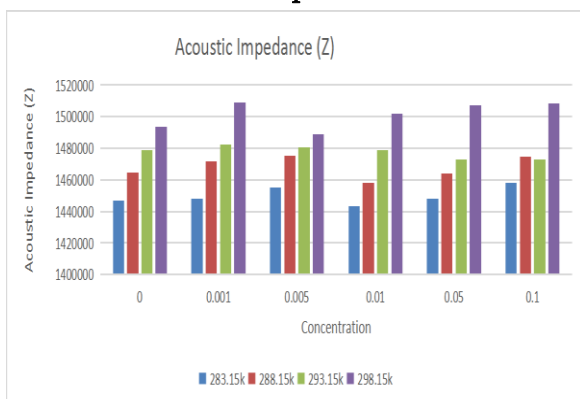


Fig.4 Variation of Acoustic Impedance with concentration in and temperature

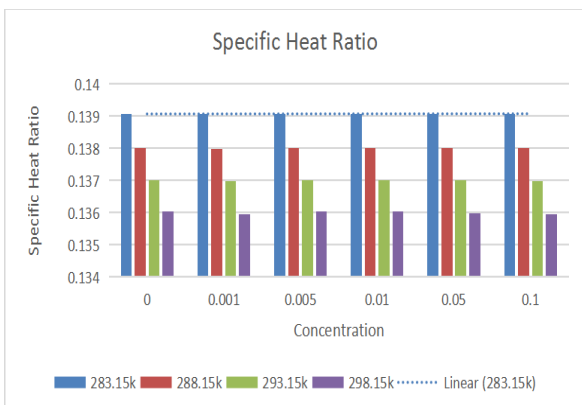


Fig.5 Variation of Specific heat ratio with concentration in and temperature.

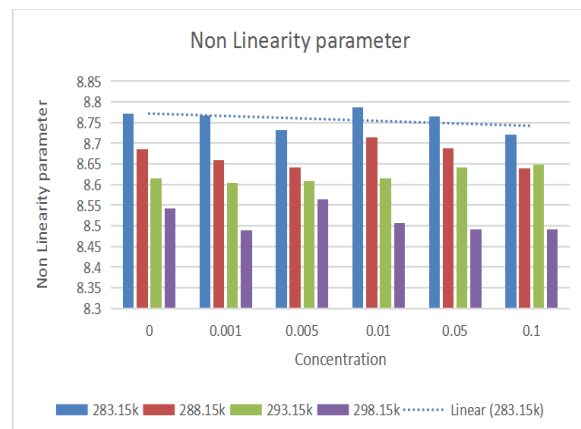


Fig.6 Variation of Non linearity parameter with concentration in and temperature

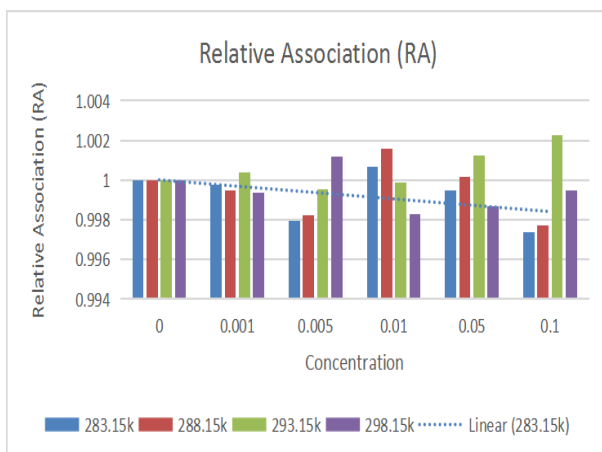


Fig.7 Variation of Relative association with concentration in and temperature.

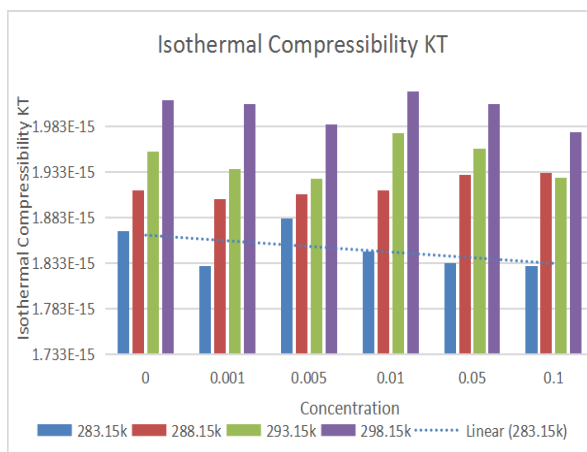


Fig.8 Variation of Isothermal Compressibility with concentration in and temperature

IV. CONCLUSION

From the present experiment it is concluded that the solute-solvent interaction exists in the systems of Niacinamide and aqueous sodium sulphate and structural changes may occur. The ultrasonic investigation of niacinamide in aqueous sodium sulphate determine the presence of strong ion-dipole interaction, there is complex interaction found for the system (Niacinamide + Sodium sulphate + water), there is solvent, solute and substituent are playing vital role in finding the interaction happening in the solutions.

V. REFERENCES

- [1]. Sarkar A., Pandit, B. K., Sinha B., (J. Chem. Thermodyn.), Vol.103, pp-36-43, (2016)
- [2]. Giratkar V., Lanjewar R., Gadegone S., Patil K., (J. Sci.), Vol. 7, pp- 615-630, (2017)
- [3]. Thirumaran S., Sabu k., (J. App. Sci.), Vol. 18, pp; 3256-3266, (2011)
- [4]. Giratkar V., Lanjewar R., Gadegone S., (Int. J. Res. Biosci. Agric. Techn.), Vol. 3, pp;41-45, (2017)
- [5]. Mirikar S., Pawar P., Bichile G., (American J. Pharm. & Pharma.), Vol. 2(1), pp; 19-25, (2015)
- [6]. Giratkar V., Lanjewar R., Gadegone S., (J. Sci.), Vol. 6, pp; 1319-1325, (2016)
- [7]. Kanhekar S., Pravina P., Govind K., (Indian J. Pure Appl. Phys.), Vol-48, pp-51-53, (2010)
- [8]. Pandey J., Dey R., Sanguri V., Soni N., Yadav M., Journal of Indian Chemistry Soc, Vol-83 pp-649-651, (2006)
- [9]. Jahagirdar B., Arbad B., Walvekar A., Shankarwer A., Lande M, J. Mol. Liq., Vol-85, pp-361-373, (2000)
- [10]. Fort J., Moore W., (Faraday Soc.), Vol-61, pp-2120-2143, (1965)

Enhancement of Electrical Conductivity in PVA Film by Doping with Li⁺ ion

A. S. Wadatar^{1*}, A. V. Turkhade²

¹Department of Physics, Vinayak Vidnyan Mahavidyalaya, Nandgaon Khandeshwar, Amravati-444708, Maharashtra, India

²Smt. Shevantabai Kalmegh Arts and Science Junior College, Chausala, Anjangaon Surji, Amravati-444806, Maharashtra

*Corresponding author's e-mail address: anantwadatar@gmail.com

ABSTRACT

The electrical characteristics of polyvinyl alcohol (PVA) films doped with different concentration of (0, 5, 10, 20 wt%) of LiClO₄ Salt were studied. The electrical conductivity for (PVA -LiCO₄) polymer electrolyte films as a function of the concentration inorganic lithium perchlorate (LiCO₄) salt at room temperature and the relationship of electrical conductivity for (PVA-LiCO₄) films of different concentration of LiClO₄ Salt with the temperature are calculated. It is found that electrical conductivity of polyvinyl alcohol (PVA) is increase with increasing LiClO₄ Salt content and also temperature. In temperature range 313–343 K, the conduction mechanism is due to carries excited into the localized states at the edge of the band. Pure PVA and (PVA + 5wt% LICO₄), (PVA + 10wt% LICO₄), (PVA + 20wt % LICO₄), polymer electrolyte films have been prepared by solution casting method. These films were characterized by X-ray diffraction technique for structural studies. In XRD pattern PVA shows broad peak at 2θ= 19.84°. This diffraction peak reveals the semi-crystalline nature of PVA. The addition of LiClO₄ causes the decrease in the degree of the crystallinity and consequently the increase in the amorphicity of the material and its conductivity.

I. INTRODUCTION

Ion conduction in polymer was first reported in 1973. Ion doped polymer finds many applications in solid polymer electrolyte[1]. An electrolyte is a material in which when dissolved solvent it could form a medium that is capable to conduct electricity the dissolved electrolyte will split into cation & anion which could help in the electric Conduction of the medium[2]. Generally, in order to produce a highly efficient electrolyte, the medium needed to be able to allow fast ionic transport, inert to all the cell component such as electrode, thermally stable and chemically stable[3-6]. Polymer electrolyte are thus different and consist of a host polymer dissolved in suitable solvent and additionally an inorganic salt is added to the polymer solution and excess solvent is evaporated. The concept of dissolving inorganic salts in functional (polar) polymer, thus creating an ion conducting solid electrolyte is known as a solid electrolyte is known as a solid polymer

electrolyte (SPE)[7-13]. The interaction of metal ions with polar group of polymer are mainly resulting from electrostatic force and according the formation of coordinating bonds. There are some important factors that may have effect on the polymer metal ion interaction, such as nature of the functional groups attached to the polymer backbone, composition and distance between functional groups, molecular weight degree of branching, nature and charge of metal cation, and counter ions. The cations can transfer from one coordinated site to another when subjected to an electric field[10, 13-18]. This is due to the weak coordinate of the cations to sites along the polymer chain for a better understanding of these technologically important material, further study has to be conducted in this field, with a particular emphasis on their complex chemistry and ionic transport properties.

In recent years, studies on the electrical properties of polymer electrolyte have attracted much attention in view of their applications in electronic devices[19-21]. The electrical properties are aimed to understand the nature of the charge transport prevalent in these materials and these properties of polymer can be suitably modified by the addition of dopant depending on their reactivity with the host matrix. Moreover, the advantage of polymer materials such as high strength good mold ability, and flexibility could be combined with the great properties of inorganic materials such as high strength, heat stability and chemical resistance through producing composite material.

The ion transport in solid polymer electrolyte may occur by a combination of several events namely ion motion, local motion in the polymer segments and intra polymer transitions between ion coordinating sites. Thus, ion conductivity in solid polymer electrolyte depends not only upon ion solvation but also on the morphology of physical structure nature of phase State of polymer transport properties of ionic species and their mobility several macroscopic models are proposed to explain and understand the ionic conductivity mechanisms in polymer electrolyte[22, 23]. These models are based on liquid like and solid like mechanism for the ionic conductivity. Electrical properties of solid polymer electrolyte can be tailored to a specific requirement by the addition of suitable dopant material. Depending on the chemical nature of the doping substance and the way in which they interact with the host matrix, the dopant alters the properties to different degrees.

1. Experimental

2. *Materials and Chemicals*

The raw materials used in this work were as a powder of commercial polyvinyl alcohol (PVA) doped by lithium perchlorate LiClO_4 inorganic salt with weight percentage (0, 5, 10 and 20 %). Raw materials were procured by Merck of analytical reagent (AR) grade and used as supplied without any further purification.

3. *Synthesis of oleic acid-coated ferrite and preparation of magnetic nanofluids.*

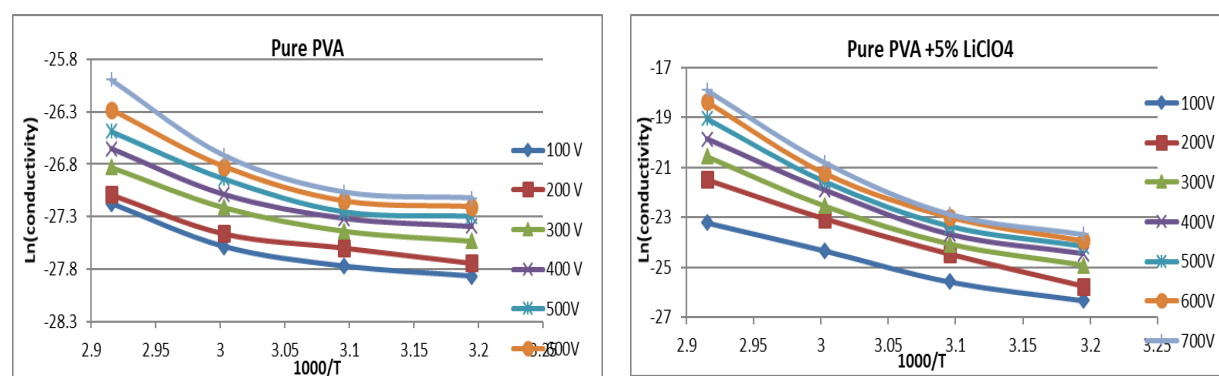
Polyvinyl alcohol (PVA) is a polymer with carbon chain backbone with hydroxyl groups attached to methane carbon these OH group can be a source of hydrogen bonding and hence assist in the formation of polymer electrolyte. Also it has several interesting physical properties, which are very useful in material science and technical application polyvinyl alcohol (PVA) is semi-crystalline, water soluble with low

electrical conductivity polymer, PVA has certain physical properties resulting from crystal amorphous interfacial effect. For a solid type of polymer electrolyte, doping the lithium salt into the polymeric complex tends to increase the charge carriers in the polymer electrolyte system. The lithium perchlorate has smaller ionic radius and smaller dissociation energy which is highly soluble in most of the organic solvent. Therefore, the lithium perchlorate (LiClO_4) is selected as a doping salt for this research. The films of pure (PVA + 5% LiClO_4), (PVA + 10% LiClO_4) and (PVA + 20% LiClO_4) were prepared using the conventional solution casting method by dissolving the powders with the appropriate percentage in distilled water. The powders were completely dissolved by using magnetic stirrer then placed in Petri dish. The thickness of the dried sample measured by digital micrometer.

4. Results and Discussion:

5. Temperature dependence ionic conductivity

PVA was found to exhibit the highest ionic conductivity of 2.3×10^{-8} S/m with addition of 20wt% of LiClO_4 at temperature 343K figure given above indicates that the ionic conductivity of polymer electrolyte increases with increasing temperature. Migration of the charge carriers (Li^+) in polymer electrolyte films probably occurs quite similar to that in ionic crystals, where ions jump into neighboring is known as ion hopping mechanism. At low temperature, the bonding between oxygen atom of polyvinyl alcohol and Li^+ ions of LiClO_4 becomes weaker. the DC ionic conductivity with temperature in PVA with different concentration of LiClO_4 polymer electrolyte film to segmental motion, which results in increase in the free volume of the system. This results in the ion to hop from one site and provide a pathway for ions to move in polymer films i.e. the segmental movement of the polymer facilitated the translational ionic motion.



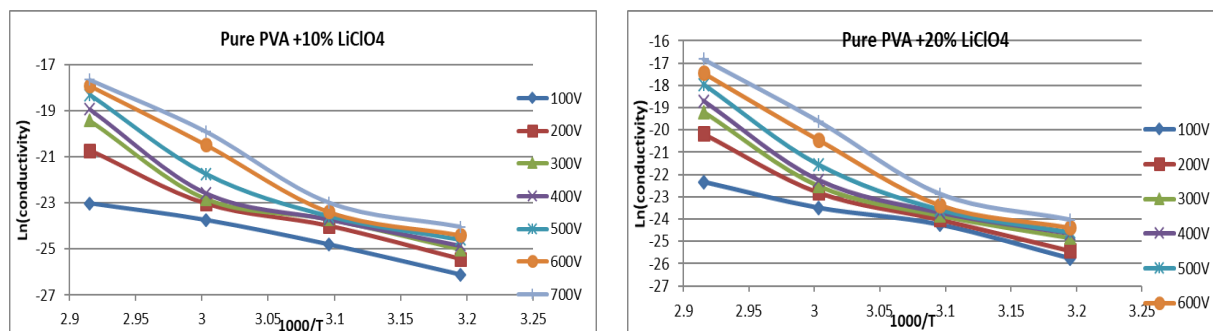


Fig. 1 : Conductivity of films of pure (PVA + 5% LiClO₄), (PVA + 10% LiClO₄) and (PVA + 20% LiClO₄)

6. Concentration dependent ionic conductivity:

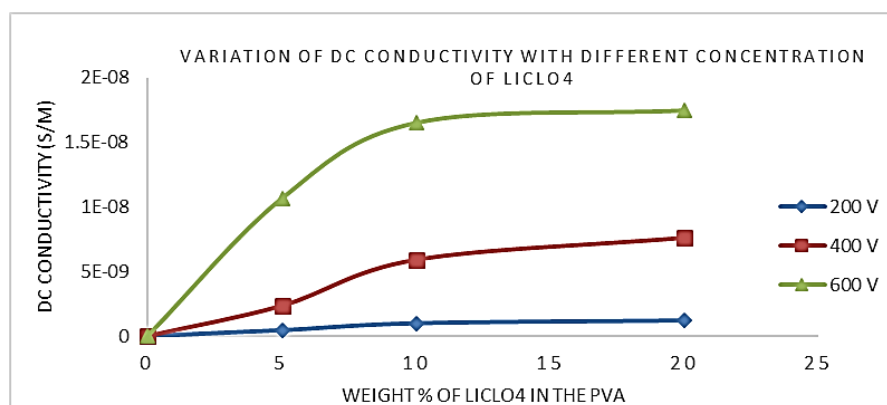


Fig. 2 : Concentration dependent DC Conductivity of polymer electrolyte.

Fig.2. depicts the concentration dependent DC ionic conductivity of pure PVA and PVA with different wt% of LiClO₄ for voltage 200v,400v, 600v and at temperature of 343K. As concentration of LiClO₄ increase (0, 5, 10, 20wt%), amorphous nature of the polymer electrolyte increases which fever inter and intra chain ion hopping and thus attained high degree of conductivity.

7. Conclusions

A series of PVA with different wt. % of LiClO₄ (0, 5, 10, 20) polymer electrolyte was successfully prepared by solution casting technique. XRD of PVA shows broad peak at $2\theta = 20^\circ$ reveals the semi-crystalline nature of polyvinyl alcohol. The polymer electrolytes films obeys the Arrhenius rule which infer the ionic hopping mechanism as shown in temperature dependence ionic conductivity studies. The ionic conductivity also increases with increase in LiClO₄ salt concentration as more Li⁺ ions available to flow increases the amorphous nature of polymer electrolyte attained high degree of conductivity.

References

[1] S. Ramesh, O.P.J.P.C. Ling, Effect of ethylene carbonate on the ionic conduction in poly (vinylidene fluoride-hexafluoropropylene) based solid polymer electrolytes, 1 (2010) 702-707.

- [2] A.R. Mainar, E. Iruin, L.C. Colmenares, A. Kvasa, I. De Meaza, M. Bengoechea, O. Leonet, I. Boyano, Z. Zhang, J.A.J.J.o.E.S. Blazquez, An overview of progress in electrolytes for secondary zinc-air batteries and other storage systems based on zinc, 15 (2018) 304-328.
- [3] W. Zhang, Z. Tu, J. Qian, S. Choudhury, L.A. Archer, Y.J.S. Lu, Design principles of functional polymer separators for high-energy, metal-based batteries, 14 (2018) 1703001.
- [4] S. Liang, W. Yan, X. Wu, Y. Zhang, Y. Zhu, H. Wang, Y.J.S.S.I. Wu, Gel polymer electrolytes for lithium ion batteries: Fabrication, characterization and performance, 318 (2018) 2-18.
- [5] A. S. Wadtkar, P.B. Kharat, A.V. Ambhore, S. Onkar, Low-cost Fabrication of Cu doped ZnO (Zn_{0.95}Cu_{0.05}O) Film for Enhanced Gas Sensing Applications, Journal of Physics: Conference Series, IOP Publishing, 2020, pp. 012059.
- [6] S. Onkar, S. Nagdeote, A. Wadtkar, P.B. Kharat, Gas sensing behavior of ZnO thick film sensor towards H₂S, NH₃, LPG and CO₂, Journal of Physics: Conference Series, IOP Publishing, 2020, pp. 012060.
- [7] A. Wadtkar, P.B. Kharat, A. Turkhade, S. Onkar, P. Bodkhe, The DC electrical properties of Lithium ion conducting solid polymer electrolyte based on polyvinyl alcohol, Journal of Physics: Conference Series, IOP Publishing, 2020, pp. 012037.

RAMAN
2022

12th - 14th May 2022